

europhysics
conference
abstracts

1992 International Conference on Plasma Physics

Joint Conference of the

9th Kiev International Conference on PLasma Theory
and the
9th International Conference on Waves and Instabilities in Plasmas
combined with the
19th EPS Conference on Controlled Fusion and Plasma Physics

Innsbruck, 29 June - 3 July 1992
Editors: W. Freysinger, K. Lackner, R. Schrittwieser, W. Lindinger

Contributed Papers, Part I

shed by: The European Physical Society
s Editor: Prof. K. Bethge, Frankfurt/M
aging Editor: G. Thomas, Geneva

VOLUME 16C Part I

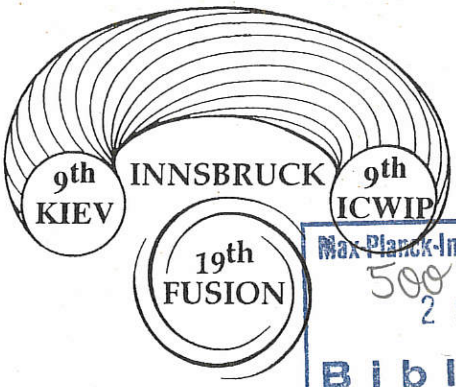

Max-Planck-Institut für Plasmaphysik
5006068
2 9. OKT. 1992
Bibliothek

Topics 1-3

1992 International Conference on Plasma Physics

Joint Conference of the

9th Kiev Interational Conference on Plasma Theory

and the

9th International Conference on Waves and Instabilities in Plasmas

combined with the

19th EPS Conference on Controlled Fusion and Plasma Physics

Innsbruck, 29 June - 3 July 1992
Editors: W. Freysinger, K. Lackner, R. Schrittwieser, W. Lindinger

Contributed Papers, Part I

0783-92

EUROPHYSICS CONFERENCE ABSTRACTS is published by the European Physical Society, © 1992

Reproduction rights reserved.

This volume is published under copyright of the European Physical Society. We wish to inform the authors that the transfer of the copyright to the EPS should not prevent an author from publishing an article in a journal quoting the original first publication or to use the same abstract for another conference. This copyright is just to protect EPS against using the same material in similar publications.

The Proceedings may be purchased from the Institute for Ion Physics, University of Innsbruck, Technikerstr. 25, A-6020 Innsbruck, Austria

PREFACE

The 1992 International Conference on Plasma Physics is held as a joint conference of the 9th Kiev International Conference on Plasma Theory and the 9th International Congress on Waves and Instabilities in Plasmas with the 19th EPS Conference on Controlled Fusion and Plasma Physics in Innsbruck, Austria, from 29 June to 3 July 1992. The conference is organized by the Institute of Ion Physics of the University of Innsbruck.

The programme, format and schedule of the Conference were determined by the International Programme Committee, which also selected the plenary and topical invited lectures based on suggestions from the International Advisory Committee of the ICPP and from other members of the scientific community. Some topical invited lectures were selected from among the contributed papers. The programme included 12 plenary, 35 topical invited lectures presented orally, and 532 poster contributions.

Innsbruck, May 1992

The Editors

Acknowledgement:

The conference organizers acknowledge the financial support of the following agencies and institutions:

The Austrian Federal Ministry of Science and Research
The State Government ofyrol
The City of Innsbruck
The International Union of Pure and Applied Physics (IUPAP)
The Kongresshaus Innsbruck

INTERNATIONAL ADVISORY COMMITTEE

K. Appert . . . . . Switzerland
D.E. Baldwin . . . . . USA
H.A.B. Bodin . . . . . UK
T.J.M. Boyd . . . . . UK
F.F. Cap . . . . . Austria
F.F. Chen . . . . . USA
B. Chirikov . . . . . Russia
A. Dalgarno . . . . . USA
J.M. Dawson . . . . . USA
F. De Marco . . . . . Italy
S. Denus . . . . . Poland
F. Engelmann . . . . . Germany
E. Fabre . . . . . France
B.D. Fried . . . . . USA
A. Gibson . . . . . UK
D. Grésillon . . . . . France
M. Haines . . . . . UK
S. Hamberger . . . . . Australia
A. Hasegawa . . . . . USA
M.A. Hellberg . . . . . South Africa
Y.H. Ichikawa . . . . . Japan
R. Janev . . . . . Yugoslavia
A.N. Kaufman . . . . . USA
P.K. Kaw . . . . . India
T. Kawabe . . . . . Japan
L.M. Kovrizhnykh . . . . . Russia
H.J. Kunze . . . . . Germany
S. Lee . . . . . Malaysia
Zhengwu Li . . . . . China
W. Lindinger (Chairman) . . . . . Austria
J. Lingertat . . . . . Germany
P. Michelsen . . . . . Denmark
G. Murtaza . . . . . Pakistan
K. Nishikawa . . . . . Japan
T.M. O'Neil . . . . . USA
A.P. Rodrigo . . . . . Argentinia
P.H. Rutherford . . . . . USA
D.D. Ryutov . . . . . Russia
P.H. Sakanaka . . . . . Brasil
K. Sauer . . . . . Germany
F.C. Schüller . . . . . Netherlands
A.G. Sitenko . . . . . Ukrainia
H.M. Skarsgard . . . . . Canada
F.W. Sluijter . . . . . Netherlands
M.P. Srivastava . . . . . India
P. Šunka . . . . . CSFR
S. Tanaka . . . . . Japan
J.B. Taylor . . . . . UK
F. Troyon . . . . . Switzerland
P. Vandenplas . . . . . Belgium
R.R. Weynants . . . . . Belgium
H.P. Winter . . . . . Austria

PROGRAMME COMMITTEE

K. Lackner (Chairman) . . . . . Germany
W. Lindinger (Vice-chairman) . . . . Austria
F. Engelmann . . . . . Germany
V.E. Golant . . . . . Russia
G. Haerendel . . . . . Germany
M.G. Haines . . . . . UK
R. Janev . . . . . Yugoslavia
G. Laval . . . . . France
T.D. Märk . . . . . Austria
D. Robinson . . . . . UK
D.D. Ryutov . . . . . Russia
K. Sauer . . . . . Germany
F.W. Sluijter . . . . . Netherlands
R.R. Weynants . . . . . Belgium

LOCAL ORGANIZING COMMITTEE

F.F. Cap (Honorary Chairman), Institute for Theoretical Physics, University of Innsbruck;
W. Lindinger (Chairman), W. Freysinger (Scientific Secretary), M. Heigl, T.D. Märk, and R. Schrittwieser, Institute for Ion Physics, University of Innsbruck;
S. Kuhn (Minutes Secretary), Institute for Theoretical Physics, University of Innsbruck.

CONTENTS

PART I	Topic 1:	Tokamaks	I-1
	Topic 2:	Stellarators	I-487
	Topic 3:	Alternative Magnetic Confinement Schemes	I-593
PART II	Topic 4:	Plasma Edge Physics	II-721
	Topic 5:	Heating and Current Drive	II-879
	Topic 6:	Diagnostics	II-1029
	Topic 7:	Inertial Confinement Fusion	II-1223
	Topic 8:	General Plasma Theory	II-1269
PART III	Topic 9:	Space and Astrophysical Plasmas	III-1565
	Topic 10:	Basic Collisionless Plasmas	III-1675
	Topic 11:	Partially Ionized Plasmas	III-1955
	Topic 12:	Elementary Processes in Plasmas	III-2053
	Topic 13:	Plasma Applications	III-2107

LIST OF TITLES

P A R T I

Topic 1: Tokamaks

Poster-No. Volume/Page
Title,
Author(s)

1-1 I-3
High current, high power H-modes in JET,
Jones T.T.C., Balet B., Brusati M., Bures M., Hugon M., Lawson K.D., Lomas P.J., Morgan P.D., Morsi H., Nielsen P., Sadler G., Sartori R., Start D.F.H., Summers D.D.R., Tanga A., Taroni A., Thomsen K., Ward D.J.

1-2 I-7
Influence of divertor geometry and boronization on the ELM-free H-mode confinement in ASDEX,
Ryter F., Kardaun O.J.W.F., Kus A., Vollmer O., Stroth U., Wagner F., ASDEX-, NI-Teams

1-3 I-11
VH-mode discharges in the DIII-D tokamak,
Greenfield C.M., Jackson G.L., Burrell K.H., DeBoo J.C., Lao L.L., Osborne T.H., Rettig C., Schissel D.P., Taylor T.S., Winter J.

1-4 I-15
Current scaling of plasma confinement,
Christiansen J.P., Challis C., Cordey J.G., Gormezzano C., Gowers C., Kramer G.J., O'Rourke J., Taroni A., Tibone F., Tubbing B., Stubberfield P.M.

1-5 I-19
Dependence of confinement on plasma ion species in JET,
Tibone F., Balet B., Bures M., Cordey J.G., Jones T.C.C., Lomas P.J., Lawson K., Morsi H.W., Nielsen P., Start D.F., Tanga A., Taroni A., Thomsen K., Ward D.J.

1-6 I-23
Energy confinement of FTU ohmic plasma,
Alladio F., Berton F., Bracco G., Buratti P., Tudisco O., FTU Team, Bruschi A., De Luca F., Jacchia A., Mantica P.

1-7 I-27
Global energy confinement in TORE SUPRA,
Hoang G.T., Bizarro J.P., De Gentile B., Hutter Th., Laurent L., Litaudon X., Moreau D., Peysson Y., Tonon G., Van Houtte D.

1-8 I-31
Energy confinement in the tight aspect ratio tokamak, START,
Appel L.C., Duck R., Fielding S.J., Gibson K.J., Hugill J., Li J., Manhood S.J., Morris A.W., Robinson D.C., Sykes A., Turner M.F., Valovic M., Walsh M.J.

1-9 I-35
Confinement scaling for the ASDEX L-mode in different divertor configurations,
Stroth U., Kardaun O.J.W.F., Kus A., the ASDEX-, the NI-Teams

1-11 I-39
Recycling perturbations of supershot plasmas,
Scott S.D., McCune D.C., Bell M.G., Bell R., Budny R.V., Fredrickson E., Grek B., Hill K.W., Jassby D., Jobes F., Johnson D.W., Johnson L.C., Mansfield D.K., Park H.K., Ramsey A.T., Snipes J.A., Stratton B.E., Synakowski E.J., Taylor G., Towner H.H., Zarnstorff M.C.

1-12 I-43
Simulations of beam-fueled supershot-like plasmas near ignition,
Budny R.V., Grisham L., Jassby D.L., Manickam J., McCune D., McGuire K.M., Sabbagh S.A., Scott S.D., Stotler D., Wieland R., Zarnstorff M.C., Zweben S.J.

Poster-No. Volume/Page
Title,
Author(s)

1-13 I-47
The investigation of properties of ohmic, ion-cyclotron plasma heating in the condition of boronized tokamak first wall,
Azizov E.A., Buzhinskij O.I., Chernobaj A.P., Dmitriev V.I., Jakovenko V.P., Kanaev A.I., Kovan I.A., Krasilnikov A.V., Mirnov S.V., Monakhov I.A., Petrov A.A., Petrov V.G., Portnov D.V., Romannikov A.N., Semenov I.B., Sharapov V.M., Sotnikov S.M., Tugarinov S.N., Sharapov V.M., Zakharov A.P.

1-15 I-51
Confinement scaling for kinetic energy in tokamak L-mode plasmas,
Takizuka T.

1-16 I-55
The effect of current profile changes on confinement in the DIII-D tokamak,
Ferron J.R., Lao L.L., Taylor T.S.

1-17 I-59
Heat transport with strong on/off axis heating,
Balet B., Boucher D., Cordey J.G., Muir D., Neudatchin S.V., Schmidt G.

1-18 I-63
Energy confinement in high performance JET D-T plasmas,
Stubberfield P.M., Balet B., Cordey J.G., O'Brien D.P., Thomsen K., Von Hellermann M.

1-19 I-67
Determination of the ion thermal diffusivity from neutron emission profiles in decay,
Sasao M., Adams J.M., Conroy S., Jarvis O.N., Marcus F.B., Sadler G., Van Belle P.

1-21 I-71
Local power balance analysis in ohmic, ECR heated plasmas in RTP,
Konings J.A., Hogeweij G.M.D., Lopes Cardozo N.J., Oomens A.A.M., Schüller F.C., RTP Team

1-22 I-75
Perturbative transport analysis in RTP,
Hogeweij G.M.D., Lopes Cardozo N.J., Peters M., RTP Team, De Luca F., Gorini G., Jacchia A., Mantica P.

1-23 I-79
Experiments on heat pulse propagation generated by localized electron cyclotron heating on the WT-3 tokamak,
Tanaka S., Hanada K., Minami T., Maehara T., Makino K., Kisigami Y., Kishino T., Nakamura M., Maekawa T., Terumichi Y.

1-24 I-83
Characteristics of heat pulse propagation at JT-60U,
De Haas J.C.M., Nagashima K., Shirai H.

1-25 I-87
Gas puff modulation experiment on JT-60U,
Nagashima K., Sakasai A., De Haas J.C.M., Fukuda T.

1-27 I-91
Modeling simultaneous sawtooth measurements of the thermal and energetic electron diffusivities from the TEXT tokamak,
Catto Peter J., Myra J.R., Bengtson Roger D., Wootton A.J.

1-28 I-95
Asymmetry of radial heat pulse propagation at TEXTOR,
Krämer-Flecken A., Tokar M.Z., Waidmann G., Wolf G.H.

1-29 I-99
Transport studies in TJ-1 tokamak from steady and perturbative methods,
Pardo C., Rodriguez-Yunta A., Vega J., Branas B., Estrada T., Ochando M.A., Tabares F.L., Zurro B.

1-30 I-103
Magnetic turbulence measurement from pellet striations: first comparison with energy transport,
Dubois M.A., Pégourié B., Sabot R., Hoang G.T.

Poster-No. Volume/Page
Title,
Author(s)

1-31 I-107
Transport and turbulence in TORE SUPRA ohmic discharges,
Garbet X., Payan J., Laviron C., Devynck P., Saha S.K., Capes H., Chen X.P., Coulon J.P., Gil C., Harris G., Hutter T., Pecquet A.L., Truc A., Hennequin P., Gervais F., Quéméneur A.

1-32 I-111
Study of the plasma turbulence by means of reflectometry methods in the TUMAN-3, FT-2 tokamaks,
Aleksandrov V.O., Bulanin V.V., Korneev D.O.,Sergeyev A.A.

1-33 I-115
Particle flux in a tokamak: fundamental experimental constraints on the form and relation to fluctuations,
Gentle K.W., Richards B., Austin M.E., Bravanec R.V., Brower D.L., Gandy R., Li W.L., Phillips P.E., Ross D.W., Rowan W.L., Schoch P.M., Sing D.C., Valanju P.M., Wootton A.J.

1-34 I-119
Diffusion of fast electrons after a monster sawtooth crash,
Hugon M., Bartlett D., Brusati M., Froissard P., Gormezano C., Morgan P., Porte L., Rimini F., Stamp M.

1-35 I-123
Electron temperature and density gradients across magnetic m=2 structures in RTP,
Van Milligen B.Ph., Van Lammeren A.C.A.P., Lopes-Cardozo N.J., Schüller F.C., Verreck M.

1-37 I-127
Profile consistency on FTU,
Buratti P., Zerbini M., Bracco G., Segre S.E., Zanza V.

1-38 I-131
Theory-based transport simulation of tokamaks: density scaling,
Ghanem E.-S., Kinsey J., Singer C.

1-40 I-135
Role of Alfvén-Wave filaments in tokamak transport,
Morales G.J., Ramachandran H.

1-41 I-139
Energy and current transport: symmetry breaking and degradation,
Coppi B., Pegoraro F.

1-42 I-143
On relaxation of tokamak discharges with toroidal plasma rotation,
Throumoulopoulos G.N., Pantis G.

1-45 I-147
Perturbative measurement of suprathermal electron diffusion in JET,
Gonhhalekar A., Bartlett D., Lomas P., Martin-Solis R., O'Brien M.

1-46 I-151
Measurements of MeV energy ICRF driven minority ions in JET,
Khudoleev A.V., Afanasyev V.I., Corti S., Gondhalekar A., Maas A.C., Petrov M.P.

1-47 I-155
Observation of relativistic runaway electrons by synchrotron radiation in TEXTOR,
Jaspers R., Finken K.H., Mank G., Rusbüldt D., Lopes-Cardozo N.J., Schüller F.C., Boedo J., Hoenen F.

1-48 I-159
Combined repetitive pellet injection and lower hybrid current drive experiments in TORE SUPRA,
Géraud A., Foster C.A., Pégourié B., Peysson Y., Bibet P., Chatelier M., Drawin H.W., Moreau D.

1-49 I-163
Observations of suprathermal electrons in the edge region on JET H-mode plasmas,
Bartlett D.V., Porte L., Costley A.E., Jones S.E., Smith R., Zolfaghari A.

Poster-No.
Title,
Author(s)

Volume/Page

1-50
Effects of enhanced toroidal field ripple on JET plasmas, I-167
Sadler G., Barabaschi P., Bertolini E., Conroy S., Deksnis E., Dietz J., De Esch B., Green B., Huguet M., Huart M., Jacquinot J., Jarvis O.N., Khudoleev A., Loughlin M.J., König R., Last J., Maas A., Petrov M., Putvinskii S., Sborchia C., Stork D., Tubbing B., Van Belle P.

1-51
Two-dimensional measurement of heat load on the first wall due to fast ion ripple loss in JT-60U with near-perpendicular NBI, I-171
Tobita K., Tani K., Neyatani Y., Takeuchi H., Miura S., Nishitani T., Matsuoka M.

1-52
Profile measurements of localized fast electrons and ions in TORE SUPRA, I-175
Basiuk V., Roubin J.-P., Becoulet A., Carrasco J., Martin G., Moreau D., Saoutic B.

1-53
Investigation of microturbulence drive and damping mechanism in DIII-D, I-179
Rettig C.L., Peebles W.A., Burrell K.H., Doyle E.J., Groebner R.J., La Haye R.J., Luhmann Jr. N.C., Philipona R., Rhodes T.L.

1-54
Edge ion dynamics in H-mode discharges in DIII-D, I-183
Groebner R.J., Burrell K.H., Gohil P., Kim J., Seraydarian R.P.

1-55
Investigation of the effect of large core changes in toroidal plasma rotation and radial electric field on confinement in H-mode discharges in the DIII-D tokamak, I-187
La Haye R.J., Groebner R.J., Hyatt A.W., Scoville J.T.

1-56
Characteristic features of density fluctuations associated with the L-H-transition in the ASDEX tokamak, I-191
Dodel G., Holzhauer E.and the ASDEX-Team

1-57
H-mode power threshold in ASDEX, I-195
Ryter F., Stroth U., Wagner F., ASDEX-Group, NI-Group

1-58
Measurement of the toroidal motion of fine-scale density structures in JET plasmas, I-199
Costley A.E., Cripwell P., Fukuda T.

1-60
Plasma flows and fluctuations during H-modes in TFTR, I-203
Bush C.E., Stratton B.C., Synakowski E., Bretz N., Budny R., Darrow D.S., Durst R., Fonck R., Fredrickson E.D., Mazzucato E., McGuire K.M., Medley S.S., Nazikian R., Paul S., Ramsey A.T., Schivell J., Scott S.D., Taylor G., Wieland R.M., Zweben S.

1-61
Autooscillating L-H transitions under ECCD in T-10, I-207
Voitsekhovich I.A., Kislov D.A., Parail V.V., Razumova K.A.

1-62
Rotation in ohmically heated tokamaks: a detailed comparison of experiment with theory, I-211
Rowan W., Calvin M., Hazeltine R., Meigs A., Solano E., Valanju P.

1-63
Divertor plate biasing and current injection on TdeV, I-215
Lachambre J.-L., Couture P., Boileau A., Boucher C., Decoste R., Gregory B., Janicki C., Lafrance D., Le Clair G., Liu-Hinz C., MacLatchy C., Martin F., Michaud D., Ross G.G., Stansfield B., St.-Onge M., Terreault B., Wang Z.

1-64
Edge fluctuations at regimes with improved confinement on CASTOR tokamak, I-219
Stöckel J., Kryska L., Zacek F., Badalec J., Jakubka K., Mlynar J., Magula P., Kletecka P.

Poster-No. Volume/Page
Title,
Author(s)

1-66 I-223
H mode induced by the biased electrode and transition of low density to high density with optimized gas puffing in HL-1,
Ran L.B., Yang H.R., Yang S.K., Zhang S.X., Zheng Y.Z., Wang E.Y., Wang Z.H., Yao L.H., Sun S.Q., Qin Y.W., Dong J.F., Deng Z.C., Deng H.C., Guo G.C., Jiang Y.X., Li H.Z., Li K.H., Zuo H.N., Yang J.W., Yang Q.W., Huang K.Q., Yuan C.J., HL-1 Team

1-67 I-227
ELM precursors in JET,
Ali-Arshad S., Campbell D., Colton A., Cripwell P., De Kock L., Kramer G.J., Nave M.F.F., Neill G.F.

1-68 I-231
Reflectometry measurements of the m=1 satellite mode in L-, H-mode plasmas in ASDEX,
Serra F., Manso M.E., Silva A., Matias J., Wagner F., Zohm H., Kallenbach A., Varela P.

1-69 I-235
A quantitative analysis of the effect of ELMS on H-mode thermal energy confinement in DIII-D,
Schissel D.P., Osborne T.H., Carlstrom T.N., Zohm H.

1-70 I-239
Steady state H-modes in JET,
Thomas P.R., Campbell D.J., Gondhalekar A., Lowry C.J.

1-71 I-243
ELM studies on DIII-D and a comparision to ASDEX results,
Zohm H., Osborne T.O., Burrell K.H., Chu M.S., Doyle E.J., Gohil P., Hill D.N., Lao L.L., Taylor T.S., Turnbull A.D.

1-72 I-247
MHD stability models of edge localized modes in JET discharges,
Huysmans G.T.A., De Blank H.J., Kerner W., Goedbloed J.P., Nave M.F.F.

1-73 I-251
Neutron profile measurements during the tritium experiments in JET,
Marcus F.B., Adams J.M., Bond D.S., Conroy S. Howarth P.J.A., Jarvis O.N., Loughlin M.J., Sadler G., Smeulders P., Van Belle P., Watkins N.

1-74 I-255
Fuelling of JET limiter, x-point plasma by deuterium pellet injection,
Schmidt G.L., Bartlett D., Baylor L., Bures M., Edwards A., Gadeberg M., Gottardi N., Jones T., Kupschus P., Lomas P., Morgan P., Morsi H., Nielsen P., O'Rourke J., Sadler G., Start D.F.H., Stubberfield P., Tanga A., Ward D.

1-75 I-259
Measurements of the electron source distribution and implications for particle transport,
O'Rourke J., Kramer G.J., Simonini R., Sips A.C.C.

1-76 I-263
Particle transport during the tritium experiments in JET,
Balet B., Cordey J.G., Jones T.T.C., König R., Marcus F., Sadler G., Stubberfield P.M., Von Hellermann M.

1-79 I-267
First results of pellet injection in ECR and ohmic heated discharges in RTP,
Oomens A.A.M., da Cruz Jr. D.F., Van Dijk G., Van Gelder J.F.M., Lok J., Rommers J.H., Tielemans A.J.H., RTP-Team

1-80 I-271
On the bootstrap current calculations based on values of the radial electron transport,
Petrzilka V.

1-81 I-275
Helium transport studies on DIII-D,
Finkenthal D., Hillis D.L., Wade M.R., West W.P., Hogan J.T., Burrell K.H., Seraydarian R., Groebner R.J., Gohil P., Klepper C.C., Mioduszewski P.K.

Poster-No. Title, *Author(s)*	Volume/Page
1-83 Poloidal asymmetry of impurity in co-, counter-injection experiment at JET, *Giannella R., Christensen M., De Angelis R., Gottardi N., Lauro-Taroni L., Mattioli M., Pasini D.*	I-279
1-84 Scaling of impurity transport in JET, *Pasini D., Giannella R., Lauro-Taroni L., Magyar G., Mattioli M.*	I-283
1-85 Particle and impurity transport in JET versus neoclassical theory, *Lauro-Taroni L., Giannella R.*	I-287
1-86 Components of P_{rad} and Z_{eff} derived from X-ray spectroscopy of the main inpurities in JET, *Barnsley R., Brzozowski J., Coffey I.H., Lawson K.D., Melnick I.M., Patel A., Patel T.K., Peacock N.J.*	I-291
1-87 Effective ion charge and impurity behavior in the Frascati tokamak upgrade, *McNeill D.H., Zanza V., Mazzitelli G., Bracco G., Condrea I., De Angelis R., Orsitto F., Panaccione L., Segre S.*	I-295
1-88 Studies of impurity confinement injected by laser blow-off in the TJ-1 tokamak, *Zurro B., Vega J., Aragon F., Burgos C., Pacios L., Pardo C.*	I-299
1-89 Toroidal diffusion of injected impurities in the MT-1M tokamak, *Zoletnik S., Veres G., Bakos J.S., Bürger G., Ignacz P.N., Kardon B., Kalvin S., Kocsis G., Szigeti J.*	I-303
1-94 Long pulse operation in JET, *Brusati M., Bures M., Clements S., Ehrenberg J., Horton L., Jones T.T.C., Lawson K., Lomas P., Morgan P., Nielsen P., Sartori R., Schmidt G., Stamp M., Summers D.*	I-307
1-95 Evolution of the current profile in JET high bootstrap current plasmas, *O'Rourke J., Challis C.D., Jacquinot J., O'Brien D., Stamp M.F., Stork D., Stubberfield P., Tibone F., Tubbing B.J., Zwingmann W.*	I-311
1-96 Bootstrap current driven by alpha particles in a fusion reacting tokamak, *Chang C.S.*	I-315
1-97 Fast wave spectral properties in ITER tokamak, *Elfimov A.G., Medvedev S.Yu., Pestryakova G.A.*	I-319
1-99 Expansion of the ablated pellet substance along the magnetic field lines, *Spathis P.N. , Lengyel L.L.*	I-323
1-100 Identification of ion cyclotron emission from fusion alpha particles during JET deuterium-tritium experiments, *Cottrell G.A., Bhatnagar V.P., da Costa O., Dendy R.O., Edwards A., Jacquinot J., Nave M.F.F., Schmid M., Sibley A., Smeulders P., Start D.F.H.*	I-327
1-102 MHD limiting phenomena in high performance JET plasmas, *Alper B., Edwards A.W., Gill R.D., Pasini D., Smeulders P.*	I-331
1-103 High-β_p MHD activity in JET, *Hender T.C., Alper B., Ali-Arshad S., DeBlank H.J., Challis D.C., Gimblett C., Han J., Jacquinot J., Kramer G.J., Kerner W., Nave M.F., O'Brien D.P., O'Rourke J., Smeulders P., Stamp M., Summers D., Tibone F., Tubbing B., Zolfaghari A., Zwingmann P.W.*	I-335

Poster-No. Title, *Author(s)*	Volume/Page
1-104 High β studies in the H-mode and hot ion H-mode in JET, *Stork D., Alper B., Ali-Arshad S., De Blank H.J., De Esch H.P.L., Edwards A., Hender T.C., König R., Kramer G., Marcus F.B., Nave M.F., O'Brien D.P., O'Rourke J., Smeulders P., Stamp M., Tibone F., Tubbing B.J.D., Zolfaghari A., Zwingmann P.W.*	I-339
1-105 Ideal-MHD operational limits for highly elongated tokamaks, *Eriksson G., Bondeson A., Ward D.J., Hofmann F., Villard L.*	I-343
1-107 Fine structure in tokamak operating region, *Li L.H., Deng C.B., Li G.X., Guo D.Q., Xie J.K., Huang R.*	I-347
1-108 The high density and high β_{pol} disruption mechanism on TFTR, *Fredrickson E., Manickam J., McGuire K.M., Monticello D., Nagayama Y., Park W., Taylor G., Drake J.F., Kleva R.G.*	I-351
1-109 Generation and loss mechanisms of runaway electrons following disruptions in JET, *Gill R.D., Edwards A.W.*	I-355
1-110 Density turbulence and disruptive phenomena in TEXTOR, *Waidmann G., Jadoul M., Kuang G.*	I-359
1-111 Electron density profile and microturbulence modification by MHD instabilities, *Brower D.L., Yu C.X., Jiang Y., Chen J.Y., Lin H., Luhmann Jr. N.C., Peebles W.A., Yang X.Z., Zhao S.J.*	I-363
1-112 Investigation of tearing modes with toroidal coupling in a tokamak with arbitrary cross-section and aspect ratio, *Atanasiu C.V., Zakharov L.E., Subbotin A.A., Chudin N.V.*	I-367
1-115 Internal MHD perturbations in T-10 tokamak, *Savrukhin P., Kislov D., Lyadina E., Razumova K., Bagdasarov A., Volkov V.*	I-371
1-117 The sawtooth collapse in rotating JET plasmas, *Büchse R., Campbell D.J., Edwards A.W., Gill R.D.*	I-375
1-118 A comparison of JET sawtooth behaviour in plasmas with co- and counter-neutral beam injection, *Edwards A.W., Bickley A., Büchse R., Challis C.D., König R., Marcus F.B., O'Rourke J., Stork D.*	I-379
1-119 Investigation of the sawtooth precursor oscillations of electron density and electron temperature in ohmic tokamak discharges on TEXTOR, *Koslowski H.R., Krämer-Flecken A.*	I-383
1-120 The influence of mode locking by resonant helical fields on fluctuations induced particle transport in Tokoloshe Tokamak, *Van Vurren G.W., Roberts D.E., Fletcher J.D., Hellberg M.A., De Villiers J.A.M.*	I-387
1-122 Sawtooth oscillations with q_o, the safety factor on axis, below unity, *Anderson D., Kolesnichenko Ya.I., Lisak M., Wising F., Yakovenko Y.V.*	I-391
1-123 Sawtooth activity and photoneutron production, *Guo G.C., Zhong Y.Z., Dong J.F., Fu B.Z., Yang J.W., Zhang G.Y., Liang W.X., Gong D.F., Shi M.L.*	I-395

Poster-No. Volume/Page
Title,
Author(s)

1-124 I-399
MHD properties of low-aspect-ratio tokamak plasmas,
Gryaznevich M., Bondeson A., Duck R., Hender T., Robinson D.C., Sykes A.

1-125 I-403
Excitation of fast density oscillations by pellet injection and its relation with sawtooth activity in TEXTOR plasmas,
Sato K.N., Akiyama H., Kogoshi S., Noda N., Sakamoto M., Dippel K.H., Finken K.H., Fuchs G., Koslovski H.R., Soltwisch H., KFA TEXTOR Team

1-126 I-407
First measurements of fast MHD fluctuations in JET by ECE correlation radiometry,
Zolfaghari A., Bartlett D.V., Costley A.E., Cripwell P., Jones S.E., Kesner J., Luckhardt S.C., Porte L., Ramos J.J., Smith R.J., Woskov P.P.

1-128 I-411
Fluid rotation and resonant magnetic perturbations in COMPASS-C,
Carolan P.G., Fitzpatrick R., Hender T.C., Morris A.W.

1-129 I-415
A study of the difference in confinement properties between large rotating and large locked modes on Tokoloshe tokamak,
Fletcher J.D., Roberts D.E., Nothnagel G., Van Vuuren G.W., De Villiers J.A.M.

1-130 I-419
Activation/inibition of plasma instabilities caused by resonant magnetic fields,
Araujo M.S.T., Vannucci A., Caldas I.L.

1-131 I-423
Feedback stabilisation of resistive tearing modes in tokamaks,
Morris A.W., Fitzpatrick R., Hender T.C., O'Brien M.R.

1-132 I-427
Nonlinear mechanism for the suppression of error field magnetic islands by plasma flow,
Parker R.D.

1-133 I-431
Observations of beam ion losses in TFTR during TAE modes and other MHD activity,
Darrow D.S., Fredrickson E.D., Mynick H.E., Nazikian R., White R.B., Wong K.-L., Zweben S.J., Tuszewski M.

1-135 I-435
Global Alfvén Eigenmodes in DIII-D,
Turnbull A.D., Chu M.S., Strait E.J., Heidbrink W.W., Duong H., Lao L.L., Greene J.M., Chance M.S., Taylor T.S.

1-136 I-439
Energetic particle driven instabilities at JET,
Nave M.F.F., Borba D., Cripwell P., Von Hellermann M., Kerner W., Porcelli F., Sadler G., Smeulders P.

1-137 I-443
Plasma characteristics during soft disruptions,
Lazzaro E., Simonetto A., Tanga A.

1-138 I-447
Disruption behavior of plasma and vacuum vessel in JT-60U,
Neyatani Y., Ushigusa K., Matsukawa M., Ninomiya H.

1-140 I-451
Discharge scenarios for the first operational phase of ASDEX-Upgrade,
Seidel U., Gruber O., McCarthy P., Cha S.S., Köppendörfer W., Krause A., Mertens V., Woyke W. and ASDEX-Upgrade Team

1-141 I-455
Performance of the equilibrium control system for ASDEX upgrade,
Woyke W., Gernhardt J., Gruber O., Jülich A., Lackner K., McCarthy P.J., Seidel U., ASDEX-Upgrade Team

Poster-No. Volume/Page
Title,
Author(s)

1-142 I-459
MHD equilibrium identification on ASDEX-upgrade,
Mc Carthy P.J., Schneider W., Lackner K., Zehrfeld H.P., Büchl K., Gernhardt J., Gruber O., Kallenbach A., Lieder G., Wunderlich R., ASDEX-Upgrade Team

1-143 I-463
Volt-second consumption and current ramp experiments on FTU,
Apruzzese G., Crisanti F., Frigione D., Kroegler H., Lovisetto L., Mazzitelli G., Podda S., Buratti P., Zerbini M., Romanelli F., Tudisco O.

1-144 I-467
Stabilization of axisymmetric modes and the effects of plasma deformability in elongated tokamak plasmas using active feedback coils inside and outside the vacuum vessel,
Ward D.J., Hofmann F.

1-145 I-471
Plasma performance, equilibrium and stability in spherical tokamak GLOBUS,
Belyakov V.A., Bender S.E., KavinA.A., Kostsov Yu.A., Minyaev O.A., Vasiliev V.I., Golant V.E., Levitsky A.N., Sakharov N.V., Fedorov O.V., Shakhovets K.G.

1-146 I-475
Rapid controlled shutdown of a burning plasma,
Pacher G.W., Pacher H.D.

1-147 I-479
Neutral beam heating in Alvand IIC tokamak,
Ghoranneviss M., Moradshahi M., Avakian M.

1-149 I-483
Operational start-up and vessel conditioning of the Novillo tokamak,
Melendez-Lugo L., Lopez-Callejas R., Valencia-Alvarado R., Chavez-Alarcon E., Colunga-Sanchez S., Jimenez-Dominguez H., Gaytan-Gallardo E.

Topic 2: Stellarators

Poster-No. Volume/Page
Title,
Author(s)

2-1 I-489
Confinement studies in recent NBI experiments of Heliotron E,
Sano F., Kondo K., Zushi ., Sudo S., Sato M., Mizuuchi T., Matsuura H., Hanatani K., Nakasuga M., OKada H., Besshou S., Nakamura Y., Nagasaki K., Ijiri Y., Iima M., Senju T., Yaguchi K., Baba T., Kobayashi S., Toshi K., Sakamoto K., Wakatani M., Obiki T.

2-2 I-493
Electron heat transport in the LMFP-regime for the stellarators W7-A, W7-AS and L2,
Dyabilin K.S., Gasparino U., Maaßberg H., Renner H., Ringler H., W7-AS Team, ECRH Group

2-3 I-497
Diffusive and convective transport modelling from analysis of ECRH-stimulated electron heat wave propagation,
Erckmann V., Gasparino U., Giannone L., Hartfuß H.J., Maaßberg H., Tutter M., W7-AS Team, IPF-ECRH Group, KFK-Gyrotron Group

2-4 I-501
Towards higher β in the stellarator Wendelstein W7-AS,
Renner H., Ringler H., Kißlinger J., Kühner G.and the W 7AS-Team, NBI-Group

2-5 I-505
The optimum ion confinement mode in W7-A stellarator induced by fast orbit losses of the nearly perpendicular NBI,
Gasparino U., Kick M., Maaßberg H., Renner H., Ringler H., Sardei F., W7-AS Team

Poster-No. Volume/Page
Title,
Author(s)

2-6 I-509
Local neutral particle density in the W7-AS stellarator,
Junker J., Kick M., Maaßberg H., Sardei F., Stroth U., Zöpfel S., WVII AS-Team, NBI-Team

2-7 I-513
ECH power deposition control in CHS,
Kubo S., Idei H., Hosokawa M., Takita Y., Iguchi H., Yamada I., Arimoto H., Ueda M., Ida K., Matsuoka K., Morita S., Nishimura K., Okamura S., Takahashi C., Yamada H., Fujiwara M., Noda N., Sagara A., Sanuki H., Todoroki J., Toi K.

2-8 I-517
Density profile and particle transport of NBI-heated plasmas in the low-aspect-ratio Heliotron/torsatron CHS,
Iguchi H., Ida K., Morita S., Yamada H., Okamura S., Matsuoka *K., Akiyama R., Arimoto H., Hosokawa M., Idei H., Kaneko O., Kohmoto T., Kubo S., Nishimura K., Noda N., Ozaki T., Sagara A., Sakakibara S., Sanuki H., Takeiri Y., Takita Y., Takahashi C., Ueda M., Yamada I., Uchino K., Takenaga H., Muraoka K., Maeda M.*

2-9 I-521
Transport studies using modulation of dimensionless parameters in the advanced toroidal facility,
Murakami M., Bigelow T.S., Carreras B.A., Dory R.A., Wilgen J.B., Baylor L.R., Dyer G.R., England A.C., Hutchinson D.P., Isler R.C., Jernigan T.C., Ji H., Ma C.H., Morimoto S., Motojima O., Rasmussen D.A., Sato M., Wing W.R., Yamada H., the ATF Group

2-10 I-525
Fluctuation studies of ECH plasmas in the ATF torsatron,
Harris J.H., Hanson G.R., Wilgen J.B., Bell J.D., Murakami M., Carreras B.A., Baylor L.R., Aceto S., Bigelow T.S., Colchin R.J., Dunlap J.L., Dominguez N., Dyer G.R., England A.C., Isler R.C., Jernigan T.C., Leboeuf J.N., Lee D.K., Lyon J.F., Ma C.H., Quallis A.L., Rasmussen D.A., Thomas C.E., Uckan T., Zielinski J., Shats M.G., Likin K.M., Sarksyan K.A., Kovrizhnykh L.M.

2-11 I-529
Results of the heavy ion beam probe measurements on the advanced toroidal facility,
Aceto S.C., Schwelberger J.G., Connor K.A., Zielinski J.J., Glowienka J.C., Isler R.C., Murakami M., Bell J.D., Uckan T.

2-13 I-533
A general solution of the ripple-averaged kinetic equation (GSRAKE),
Beidler C.D., W.D. D'haeseleer

2-14 I-537
Influence of electric fields on the heating efficiency in the W7-AS stellarator,
Teubel A., Penningsfeld F.-P.

2-15 I-541
Change of adiabatic invariant in trap-detraping processes in stellarator,
Bulanov S.V., Shasharina S.G.

2-16 I-545
-particle behaviour outside the last closed magnetic surface in divertor stellarators,
Alladio F., Batistoni P., Mancuso A.

2-17 I-549
Mode activity at high plasma pressure in the stellarator Wendelstein W7-AS,
Weller A., Jaenicke R., Kißlinger J., Lazaros A., Maaßberg H., Sardei F., Schwab C., W7-AS Team, ECRH Group, NI Group

2-18 I-553
Finite ion gyro radius stabilization of ideal MHD ballooning modes in optimized stellarators,
Nührenberg J., Zheng L.-J.

2-19 I-557
Linear MHD stability computations in 3D plasmas,
Cooper W.A., Nakamura Y., Wakatani M., Gruber R., Merazzi S., Anderson D.V., Schwenn U.

2-20 I-561
Interchange modes in torsatrons, heliacs,
Jimenez J.A., Varias A., Dominguez N.

Poster-No. Title, *Author(s)*	Volume/Page
2-21 Ideal MHD studies of the TJ-IU Torsatron, *Alejaldre C., Ascasibar E., Garcia L., Lopez-Fraguas A., Varias A., Carreras B., Dominguez N.*	I-565
2-22 Progress in the studies of URAGAN-2M stability and transport properties, *Besedin N.T., Grekov D.L., Pavlichenko O.S., Shishkin A.A., Zolotukhin A.V., Beidler C.D., Kißlinger J., Maaßberg H., Rau F., Wobig H., Carreras B.A., Dominguez N., Lynch V.E.*	I-569
2-23 Destruction of Alfvén modes on a torus due to large nonaxisymmetry, *Salat A.*	I-573
2-24 Study of magnetic surfaces with islands using the PIES code, *Lopez-Fraguas A., Salas A., Reiman A.H., Monticello D.A., Johnson J.L.*	I-577
2-25 Modifies vacuum fields and compensation of islands in the stellarator W7-AS, *Beidler C., Harmeyer E., Gasparino U., Kißlinger J., Kühner G., Maaßberg H., Rau F., Ringler H., Wobig H., W 7-AS Team, ECRH-Group, W7-X Team*	I-581
2-26 Optimization of coils and a sweep coil system for W7-X, *Merkel P., Kißlinger J.*	I-585
2-27 Anisotropic pressure numerical 3D MHD equilibria, *Hirshman S.P., Cooper W.A., Merazzi S., Gruber R.*	I-589

Topic 3: Alternative Magnetic Confinement Schemes

Poster-No. Title, *Author(s)*	Volume/Page
3-1 Confinement studies of a high current density RFP in the extrap T1 upgrade device, *Drake J.R., Brzozowski, Brunsell P., Hellblom G., Karlsson P., Mazur S., Nordlund P., Welander A., Zastrow K.-D.*	I-595
3-2 Reversed field pinch equilibria and profile dynamics in a high aspect ratio geometry, *Nordlund P., Mazur S., Drake J.R.*	I-599
3-3 Stability of kink modes in a noncircular z pinch surrounded by a resistive and a conducting wall, *Jiang Z.X., Wahlberg C.*	I-603
3-4 Studies of edge plasma and impurities in extrap T1 using surface probes, *Bergsåker H., Gudowska I., Emmoth B., Tennfors E.*	I-607
3-5 Plasma spectroscopy at the extrap T1 RFP experiment, *Zastrow K.-D., Hörling P., Brzozowski J., Källne E.*	I-611
3-6 RFP set-up and confinement in SWIP-RFP device, *Zhang P., Fang S., Li J., Luo C., Li Q., Zhang S., Yi P., Xu Y.*	I-615

Poster-No. Title, *Author(s)*	Volume/Page
3-7 Ion temperature measurements in the reversed field pinch plasmas, *Schiavi A., Buffa A., Costa S.*	I-619
3-8 Generation of fast electrons by magnetic reconnection processes in RFP plasmas, *Erba M., Martin P., Ortolani S., Rossi A.*	I-623
3-9 Relaxed states for a driven reverse field pinch, *Paccagnella R.*	I-627
3-10 Electron diffusion and energy loss in a reversed field pinch plasma, *Antoni V., Bagatin M., Martines E.*	I-631
3-11 Self-similar solutions for trapping and diffusion of magnetic flux during formation of field-reversed configuration, *Bud'ko A., Karlson E.T., Liberman M.A.*	I-635
3-12 Study of current drive and particle flux in the SPEX spheromak, *Browning P.K., Cunningham G., Gee S.J., Al-Karkhy A., Martin R., Roe G., Rusbridge M.G.*	I-639
3-13 Toroidal current enhancement with strong poloidal plasma current drive in FBX-II spherical torus, *Irie M.*	I-643
3-14 Parametric investigation of the rotamak discharge in a 10-litre spherical vessel, *Donaldson N., Hahnheuser R., Jones I.R., Staines G.W., Xu S.*	I-647
3-17 An alternative configuration of axially pinched spherical torus, *Sinman S., Sinman A.*	I-651
3-18 Centrally peaked temperature profiles due to the Ettinghausen effect, *Haines M.G., Chittenden J.P.*	I-655
3-19 Viscous effects on equilibrium states of isolated z-pinches, *Miyamoto T.*	I-659
3-21 FIGARO: A large larmor radius stability code, *Coppins M., Scheffel J.*	I-663
3-22 The interrupted z-pinch dynamics modeling, *Kubes P., Kravarik J., Hakr J., Kulhanek P., Pichal J.*	I-667
3-23 Stabilization of the long wavelength sausage and kink modes of a Z-pinch by nonlinear radial oscillations, *Bud'ko A., Karlson E., Liberman M.A.*	I-671
3-25 Ideal and resistive MHD analysis of rotational instabilities in FRC, *Sakanaka P.H., Machida M., Honda R.Y., Aramaki E.A., Berni L.A., Santiago M.A.A., Tsui K.-H., Tavares-Azevedo M.*	I-675
3-26 Discrete Alfvén waves in reversed field pinches, *Sakanaka P.H., Shigueoka H., Azevedo C.A., Assis A.S.*	I-679

Poster-No. Title, *Author(s)*	Volume/Page
3-27 Hot spot X-ray and microwave emission of the DPF-78 plasma focus, *Antsiferov P., Franz D., Pfau R., Rupasov A., Schmidt H., Schulz D.*	I-683
3-28 The relative role of the macroscopic and microscopic phenomena in the plasma focus performance, *Zambreanu V., Zoita V.*	I-687
3-29 Investigation of charged-particle and X-ray pulses emitted from PF-type discharges, *Sadowski M., Szydlowski A., Zebrowski J., Al-Mashhadany E.M.*	I-691
3-30 Fusion reaction yield in focused discharges with variable energy and plasma fine structure, *Bortolotti A., Brzosko J.S., DeChiara P., Kilic H., Mezzetti F., Nardi V., Powell C., Wang J.*	I-695
3-35 Parametric study of mirror plasma based neutron source FEF-II, *Mizuno N., Yamaguchi H., Kawabe T., Hirayama S.*	I-699
3-37 Direct conversion of a fusion energy into an electric one in the DRACON-trap, *Glagolev V.M., Kuvshinov B.N., Proshin M.A., Timofeev A.V.*	I-703
3-39 Electrodynamics of plasma-molecular systems with drift motion of charged and neutral particles, *Moiseev S.S., Suyazov N.V., Yakimenko I.P.*	I-707
3-41 D-^{3}He fusion reactor based on a dipole magnetic field, *Hasegawa A., Fowler T.K., Mauel M.E.*	I-711
3-42 Proposed experiment with injection of a small angular spread beam in the oscillated REB regime, *Piffl V., Sunka P., Clupek M., Raus J.*	I-713
3-43 Confinement of laser-produced plasma by a strong external magnetic field, *Miklaszewski R., Farynski A., Fiedorowicz H., Mroczkowski M., Parys P., Pisarczyk T., Szczurek M.*	I-717

PART II

Topic 4: Plasma Edge Physics

Poster-No. Title, *Author(s)*	Volume/Page
4-1 Edge measurements in the divertor region in high density discharges at JET, *Clement S., Erents S.K., Gottardi N., Harbour P.J., Jaeckel H., Janeschitz G. De Kock L., Loarte A., Lowry C., Saibene G., Summers D., Tagle J.A., Vlases G.*	II-723
4-2 High power operation with a radiative divertor in JET, *Janeschitz G., Clement S., Gottardi N., Lesourd M., Lingertat J., Lowry C., Radford G., Saibene G., Stamp M., Summers D., Taroni A., Thomas P.R., Vlases G.*	II-727
4-3 Energy exhaust through neutrals in a tokamak divertor, *Watkins M.L., Rebut P.-H.*	II-731

Poster-No. Title, *Author(s)*	Volume/Page
4-4 Modelling of the density limit in JET beryllated limiter discharges, *Borrass K., Campbell D., Clement S., Vlases G.*	II-735
4-5 Modelling of neutral and charged helium transport in scoop of a pump limiter, *Tokar M.Z., Reiter D.*	II-739
4-6 Marfe detection by radiation monitoring and control of density limit disruptions, *Steuer K.-H., Junker W., Röhr H., Büchl K., Engelhardt W., Gruber O., Kaufmann M., Mertens V., Neuhauser J., Stäbler A., Zohm H., ASDEX-, ASDEX-Upgrade Teams*	II-743
4-7 Modelling of the ASDEX-Upgrade scrape-off layer plasma, *Bosch H.-S., Neuhauser J., Bachmann P., Schneider R., Kaufmann M., Reiter D., Baelmans T., Braams B.*	II-747
4-8 Modeling the DIII-D plasma boundary with the LEDGE code, Porter G.D., Rensink M.E., Rognlien T.D., Jong R.A., Hill D.N.	II-751
4-9 2-D edge modelling: convergence and results for next step devices in the high recycling regime, *Pacher H.D., D'haeseleer W.D., Pacher G.W.*	II-755
4-10 Modelling of TEXTOR edge plasma in discharges with auxiliary heating, neon puffing, *Tokar M.Z., Samm U.*	II-759
4-12 A study of the SOL density profile behaviour in ASDEX, *McCormick K., Schweinzer J., Pietrzyk Z.A.*	II-763
4-13 Power flux widths in the ASDEX divertor, *Kyriakakis G., Kakoulidis E., Tsois N., McCormick K., Neuhauser J.*	II-767
4-14 Spatial distribution of carbon ions and ion temperature measurements in the plasma edge of TEXTOR using emission spectroscopy, *Telesca G., Claaßen H.A., Graffmann E., Van Oost G.*	II-771
4-15 Poloidal rotation in the limb of the TEXTOR plasma measured by the Doppler shift of a BII-line, *Conrads H., Euringer H., Rusbüldt D.*	II-775
4-16 The effect of radial electric field on fast ion losses in divertor tokamaks, *Chankin A.V., Summers D.D.R., McCracken G.M.*	II-779
4-17 Density, potential and temperature fluctuations in Wendelstein 7-AS, ASDEX, *Balbin R., Carlson A., Endler M., Giannone L., Hidalgo C., Niedermeyer H., Rudyj A., Theimer G., W7-AS Team, ASDEX Team*	II-783
4-18 Attempt to model the edge turbulence of a tokamak as a random superposition of eddies, *Endler M., Theimer G., Weinlich M., Carlson A., Giannone L., Niedermeyer H., Rudyj A., the ASDEX-Team*	II-787
4-19 Mechanisms inducing changes on the edge turbulence in the TJ-I tokamak, *Pedrosa M.A., Garcia-Cortes I., Balbin R., Hidalgo C., Ochando M.A., Liniers M.*	II-791
4-20 m=1 activity prior to the onset of sawtoothing on Tokoloshe tokamak, *Nothnagel G., Sherwell D., Roberts D.E., Fletcher J.D., De Villiers J.A.M., Walters P.E.*	II-795

Poster-No. Title, *Author(s)*	Volume/Page
4-21 Role of edge plasma in a high ß very low q tokamak regime, *Kiyama H., Kiyama S.*	II-799
4-22 Fluctuations and transport in a tokamak with high MHD activity, *Heller M.V.A.P., Castro R.M., Caldas I.L., da Silva R.P., Brasilio Z.A., TBR-1 Team*	II-803
4-23 Kinetic instabilities in a plasma in E x B fields, *Shoucri M., Bertrand P., Ghizzo A., Knorr G.*	II-807
4-24 Coherent vortical structures in two-dimensional plasma turbulence, *Lynov J.P., Nielsen A.H., Pécseli H.L., Rasmussen J.J.*	II-811
4-25 Guided Alfvén beams in the Tortus tokamak, *Cross R.C., Miljak D.G.*	II-815
4-26 Measurement of sputtering yields at the JET beryllium and carbon x-point tiles, *Stamp M.F., Thomas P.R.*	II-819
4-27 Radial carbon flux profiles in the upper divertor in JET at high target load, *Jäckel H.J., Clement S., Lesourd M., Lingertat J., Maggi C.F., Matthews G.F., Summers D.D.R., Summers H.P.*	II-823
4-28 Chemical impurity production under boronized wall conditions in TEXTOR, *Philipps V., Vietzke E., Erdweg M.*	II-827
4-29 Divertor retention for recycling impurities, *Krieger K., Roth J., Fussmann G.*	II-831
4-30 Particle influx and impurity behaviour in the ASDEX-Upgrade tokamak, *Kallenbach A., Fuchs C., Fussmann G., Jenichen F., Mast K.F., H.-M.Mayer, Schumacher U., the ASDEX-Upgrade Team*	II-835
4-31 Reduction in SOL Φ_p increases and impurity generation caused by RF near ω_{ci} by the use of insulating Faraday shield limiters in the Phaedrus-T tokamak, by elimination of Faraday shields, *Hershkowitz N., Majeski R., Diebold D., Tanaka T., Sørensen J., Breun R., Brouchous D., Fonck R., Intrator T., McKee G., Probert P.*	II-839
4-32 Plasma induced material transport on limiter probes in the boundary plasma of fusion experiments, *Naujoks D., Behrisch R.*	II-843
4-33 Production and control of an edge radiating layer with the ergodic divertor on TORE SUPRA, *Poutchy L., Vallet J.C., DeMichelis C., Grosman A., Hess W., Mattioli M., Monier-Garbet P.*	II-847
4-34 Edge transport induced by the interaction of a stochastic layer with the wall, *Nguyen F., Ghendrih Ph., Samain A., Grosman A.*	II-851
4-35 Control of the MHD activity with the ergodic divertor on TORE SUPRA, *Vallet J.C., Edery D., Van Houtte D., Mohamed-Benkadda M.S., Joffrin E., Lecoustey P., Pecquet A.L., Samain A., Talvard M.*	II-855

Poster-No. Volume/Page
Title,
Author(s)

4-36 II-859
Plasma edge structure of a tokamak with ergodic magnetic limiter,
Takamura S., Oda Y., Sakurai S.

4-37 II-863
Stochastic broadening in the scrape-off layer of a single-null divertor tokamak,
Punjabi A., Verma A., Boozer A.

4-38 II-867
On stationary flow in the boundary region of toroidal systems,
Wobig H.

4-39 II-871
Sheath potential at a target with almost parallel magnetic field,
Chodura R.

4-41 II-875
Boundary conditions for the momentum and energy flux of ions at the plasma-sheath interface,
Günther K.

Topic 5: Heating and Current Drive

Poster-No. Volume/Page
Title,
Author(s)

5-1 II-881
Enhanced performance of neutral beam heated hot-ion H-modes on JET by central ICRF heating,
Bures M., Balet B., Campbell D., Cottrell G.A., Elevant T., Eriksson L-G., Jacquinot J., Jarvis N., Jones T., König R., Lomas P., Marcus F., Righi E., Sadler G., Start D.F.H., Tanga A., Van Belle P., Von Hellerman

5-2 II-885
RF heating and current drive experiments in TORE SUPRA,
Hoang G.T., Agarici G., Beaumont B., Becoulet A., Berger G.By, Bibet P., Bizarro J.P., Capitain J.J., Carrasco J., Goniche M., Joffrin E., Kupfer K., Kuus H., Litaudon X., Moreau D., Parlange F., Peysson Y., Rey G., Saoutic B., Tonon G., Van Houtte D.

5-3 II-889
ICRF power limitation relation to density limit in ASDEX,
Ryter F., ICRH-Group, ASDEX-Group

5-4 II-893
Fast wave current drive experiments on the DIII-D tokamak,
Petty C.C., Pinsker R.I., Porkolab M., Baity F.W., Chiu S.C., Goulding R.H., DeGrassie J.S., Harvey R.W., Hoffman D.J., James R.A., Kawashima H., Lohr John, Luce T.C., Mayberry M.J., Prater R.

5-5 II-897
Observation of fast wave ion current drive effects on sawteeth in JET,
Start D., Bhatnagar V., Bosia G., Brusati M., Bures M., Campbell D., Cottrell G., Cox M., DeEsch H., Edwards A., Eriksson L-G., Gormezano C., Jacquinot J., Lomas P., Marcus F., O'Brien M.R., Porcelli F., Rimini F., Stork D., Tanga A., Tubbing B., Warrick C.D., Wesson J.

5-6 II-901
Resistive internal kinks and ICRF phasing current drive,
Porcelli F., Bhatnagar V.P., Bosia P., Cherubini A., Jacquinot J., Start D., Taroni A.

5-7 II-905
Kinetic effects in fast wave current drive,
Becoulet A., Giruzzi G., Kupfer K., Moreau D., Saoutic B.

5-8 II-909
Theoretical studies of fast wave plasma heating and current drive in tokamaks,
Moroz P.E., Hershkowitz N., Tataronis J.A.

Poster-No. Volume/Page
Title,
Author(s)

5-9 II-913
Influence of various physics phenomena on fast-wave current drive in advanced tokamaks,
Batchelor D.B., Jaeger E.F., Carter M.D., Goldfinger R.C., Stallings D.C.

5-11 II-917
Current density profile control in reversed field pinch plasma by RF current drive,
Shiina S., Saito K., Kondoh Y., Ishii H., Shimada T., Hirano Y.

5-15 II-921
A method of increasing the ion Bernstein wave excitation efficiency in plasmas,
Longinov A.V., Lukinov V.A., Pavlov S.S.

5-16 II-925
The local power dissipation of ion Bernstein waves in a weakly inhomogeneous plasma,
Werthmann H., Brambilla M.

5-17 II-929
The slot-in-recess antenna system for ion Bernstein wave excitation in plasmas,
Gribok V.A., Longinov A.V., Lukinov V.A.

5-18 II-933
RF system for plasma production, heating in TJ-IU torsatron,
Ascasibar E., Castejon F., Rodriguez L., Navarro A.P., Dyakov V.E., Longinov A.V., Pavlichenko O.S., Pavlov S.S., Stepanov K.N.

5-20 II-937
The separation of ion Bernstein waves and incoherent ion gyroresonant ballistic waves in a dispersive, spatially varying medium,
Flå T., Cook D., Tracy E., Kaufmann A.N.

5-21 II-941
Plasma heating and generation current drive study in the torsatron U-2M using ion Bernstein wave,
Dyakov V.E., Longinov A.V.

5-22 II-945
Resistive flux saving, current profile control during lower hybrid waves assisted current rise in TORE SUPRA,
Van Houtte D., Hoang G.T., Joffrin E., Lecoustey P., Moreau D., Parlange F., Tonon G., Vallet J.C.

5-23 II-949
Initial lower hybrid current drive results and first two-dimensional images of hard X-ray emission in PBX-M,
Von Goeler S., Asakura N., Bell R., Bernabei S., Chance M., Chu T.K., Dunlap J., England A., Fishman H., Gettelfinger G., Greenough N., Harris J., Hatcher R., Herrmann H., Ignat D., IslerR., Jardin S., Jones S., Kaita R., Kaye S., Kesner J., Kugel H., LeBlanc B., Luckhardt S., Levinton F., Manickam J., Okabayashi M., Ono M., Paul S., Preische S., Roney P., Sauthoff N., Seki S., Sesnic S., Stevens J., Takahashi H., Valeo E., Voss K.

5-24 II-953
Performance of the LHCD in high current regime in JT-60U,
Imai T., Ushigusa K., Ikeda Y., Ide S., Naito O., Seki M., Kondoh T., Nemoto M., Wolfe S., Sato M., Takeuchi H.

5-25 II-957
Change of internal inductance and anisotropy during lower hybrid current drive in ASDEX,
Leuterer F., Söldner F.X., Bartiromo R., Bernabei S.

5-26 II-961
Electron and ion heat transport with LH, NBI heating in ASDEX,
Söldner F.X., Pereverzev G.V., Bartiromo R., Fahrbach H.U., Leuterer F., Murmann H.D., Steuer K.-H., LH-Team, NBI-Team, ASDEX-Team

5-27 II-965
Experimental studies of high energy X-ray emission and bootstrap current generation in high β_p lower hybrid driven plasmas,
Squire J.P., Porkolab M., Bonoli P.T., Colborn J.A., Villasenor J.

Poster-No. Volume/Page
Title,
Author(s)

5-28 II-969
Investigation of high energy electrons produced by lower hybrid waves with measurement of the hard X-ray in JT-60U,
Kondoh T., Ide S., Imai T., Ushigusa K., Ikeda Y., Seki M., Takeuchi H.

5-29 II-973
Characterization of LH induced current carrying fast electrons in JET,
Ramponi G., Airoldi A., Bartlett D., Brusati M., Froissard P., Gormezano C., Rimini F., da Silva R.P., Tanzi C.

5-30 II-977
A phenomenological description of fast electrons induced by LH waves in tokamaks,
Conceicao P., Brusati M., Froissard P., Varandas C.A.F.

5-31 II-981
Impurity transport during RF current drive in WT-3 tokamak,
Nakamura M., Sawada K., Kawachi T., Suemitu H., Maekawa T., Terumichi Y., Tanaka S.

5-32 II-985
The distant coupling of LHCD launcher in the JT-60U,
Seki M., Ikeda Y., Imai T., Ushigusa K., Naitou O., Ide S., Kondoh T., Nemoto M., Takeuchi H., Suganuma K., Sawahata M., Takasa A., Takahashi S., Yamamoto T.

5-33 II-989
Coupling analysis and experiment of the multijunctional grill near the lower hybrid frequency,
Ohkubo K., Matsumoto K.

5-36 II-993
Modulational instability development and current drive,
Popel S.I., Vladimirov S.V., Tsytovich V.N.

5-39 II-997
Fast ion generation during RF discharge on the FT-2 tokamak and parametric decay instabilities,
Budnikov V.N., Dyachenko V.V., Esipov L.A., Its E.R., Lashkul S.I., Novik K.M., Stepanov A.Yu., Shcherbinin O.N., Alexandrov V.O., Sakharov I.E., Shatalin S.V.

5-43 II-1001
Measurements of electron cyclotron emission during high power ECRH in the W7-AS stellarator,
Gasparino U., Hartfuß H.J., Tribaldos V., Tutter M., W7-AS Team, ECRH Group

5-44 II-1005
Simulations of fast electron generation by stimulated Raman forward scattering in a magnetized plasma,
Bertrand P., Ghizzo A., Karttunen S.J., Pättikangas T.J.H., Salomaa R.R.E., Shoucri M.

5-45 II-1009
Effects of fluctuations on magnetohydrodynamic wave heating and current drive,
Tataronis J.A., Antani S.N.

5-46 II-1013
Radial diffusion of toroidally trapped particles induced by lower hybrid and fast waves,
Krlin L.

5-47 II-1017
ICRF Minority plasma heating in realistic geometries,
Friedland L., Cohen D.

5-48 II-1021
Simulation of runaway electrons in a toroidal geometry,
Sipilö S.K., Heikkinen J.A., Pättikangas T.J.H.

5-49 II-1025
Modelling of the FMS wave propagation and transformation in the ion-cyclotron frequency domain for the TUMAN-3 tokamak plasma,
Irzak M.A., Pavlov I.P., Shcherbinin O.N.

Topic 6: Diagnostics

Poster-No. Volume/Page
Title,
Author(s)

6-2 II-1031
Neutral particle analysis in the MeV range in JET,
Petrov M.P., Afanasyev V.I., Corti S., Gondhalekar A., Khudoleev A.V., Korotkov A.A., Maas A.C.

6-3 II-1035
Investigation of alpha particle slowing-down features in helium neutral beam fuelling experiments at JET,
Von Hellermann M., Core W.G.F., Frieling J., Horton L.D., König R., Mandl W., Summers H.P., Wolle B.

6-5 II-1039
Prospects for investigation of alpha particles velocity distribution by charge exchange spectroscopy in ITER,
Korotkov A.A., Belik V.P., Shmaenok L.A., Platonov Yu.Ya., Salashchenko N.N.

6-6 II-1043
Helium stopping cross-section in fusion plasma taking into account the multistep collision processes,
Korotkov A.A.

6-7 II-1047
Neutron spectrometry concepts for diagnosing DT plasmas of Q ≈ 1,
Källne J., Gorini G., Condé H., Renberg P.U.

6-8 II-1051
Effects of neutron on the JET soft X-ray detectors,
Gill R.D., Alper B., Edwards A.

6-9 II-1055
The application of x-mode reflectometry to the study of large scale density fluctuations in TFTR,
Mazzucato E., Nazikian R., the TFTR-Group

6-11 II-1059
A multi-channel reflectometer for the RTP tokamak,
Heijnen S.H., Hugenholtz C.A.J., Van de Pol M.J.

6-12 II-1063
A microwave reflectometric system for tokamak ASDEX upgrade,
Silva A., Manso M.E., Serra F., Söldner F.X., Cupido L., Pereira J., Neves J., Nunes F., Varela P., Moreira A., Fernandes C., Loureiro C., Correia C., Santos J., Zilker F.

6-13 II-1067
Simulation of correlation reflectometry,
Michelsen P., Pécseli H.L.

6-14 II-1071
Microwave reflectometry as a density fluctuation diagnostic: a comparison between a controlled laboratory experiment and a one dimensional numerical model,
Rhodes T.L., Baang S., Chou A.E., Domier C.W., Luhmann Jr. N.C., Peebles W.A.

6-15 II-1075
Amplitude modelation reflectometry for large fusion devices,
Sanchez J., Zhuravlev V., De la Luna E., Estrada T., Branas B.

6-17 II-1079
Fluctuations spectra in TORE SUPRA from scattering experiment,
Gervais F., Grésillon D., Hennequin P., Quéméneur A., Truc A., Devynck P., Garbet X., Payan J., Laviron C., Saha S.K.

6-18 II-1083
From incoherent to collective scattering,
Maafa N., Grésillon D., Cabrit B.

Poster-No. Title, *Author(s)*	Volume/Page
6-19 Effects of the ohmic plasma current on collective scattering spectra, *Tartari U., Castiglioni S., Lontano M.*	II-1087
6-20 Ion temperature measurements by Rutherford scattering at TEXTOR, *Tammen H.F., Van Blokland A.A.E., Oyevaar Th., Schüller F.C., Donné A.J.H.*	II-1091
6-21 CO_2-scattering and RF probe measurements of lower-hybrid wave spectra in the presence of low-frequency fluctuations, *Fischer B., Krämer M.*	II-1095
6-22 Measurement of coherent temperature fluctuations on the stellarator Wendelstein 7-AS, *Hartfuß H.J., Sattler S., W7-AS Team, NBI-Team, ECRH-Group*	II-1099
6-23 Electron cyclotron non thermal spectra during ohmic and RF assisted discharges on TORE SUPRA, *Talvard M., Giruzzi G., Liu W.D.*	II-1103
6-24 First electron cyclotron emission and electron temperature profile measurements on ASDEX-upgrade, *Salmon N.A.,Eberhagen A.*	II-1107
6-26 The heavy ion beam diagnostic for the tokamak ISTTOK, *Cabral J.A.C., Malaquias A., Praxedes A., Van Toledo W., Varandas C.A.F., Dias J.M.*	II-1111
6-27 Development of Boxcar imaging system for visualizing magnetic field structure in tokamak plasma, *Sakurai S., Ohno N., Takamura S.*	II-1115
6-29 Statistical analysis of luminescence signals observed during pellet injection, *Baldzuhn J., W7-AS Team*	II-1119
6-31 Dispersion interferometer for controlled fusion devices, *Drachev V.P., Krasnikov Yu.I., Bagryansky P.A.*	II-1123
6-32 Visible spectroscopic measurements on FTU, *Condrea I., Bartiromo R., Mazzitelli G., McNeill D.H.*	II-1127
6-33 Determination of O^{8+} to electron density ratio by the intensity ratio of the charge exchange recombination and the Doppler-shifted H_α emissions of the injected neutral beam, *Kondo K., Sano F., Sudo S., Zushi H., Mizuuchi T., Okada H., Besshou S., Nagasaki K., Higashijma S., Hanatani K., Nakasuga M., Wakatani M., Obiki T.*	II-1131
6-34 Spatial structure of nonthermal fluctuating electric fields in the TJ-I tokamak, *Zurro B., Castejon F., Burgos C.*	II-1135
6-37 Fast analysis of spectral data using neural networks, *Roach C.M.*	II-1139
6-38 Tomography algorithms for visible light tomography on RTP, *Pickalov V.V., Ingesson L.C., Donne A.J.H., Schram D.C.*	II-1143
6-39 Investigation of the sensitivity of visible continuum $Z_{eff}(0)$ to edge radiation, *Telesca G., Van Oost G., Ongena J., Leys C., Schoon N.*	II-1147

Poster-No. Title, *Author(s)*	Volume/Page
6-40 Spatially resolved diagnostics of inhomogeneous low temperature plasmas: new techniques, *Neger T., Jäger H.*	II-1151
6-41 Localized impurity flux measurements on Wendelstein 7-AS, *Hofmann J.V., W7-AS Team, ECRH Group, NI Group*	II-1155
6-42 Diagnostic for hydrogen behaviour at edge regions of high temperature plasmas, *Muraoka K., Maeda M., Honda C., Okada T., Uchino K., Kajiwara T., Takenaga H.*	II-1159
6-43 Determination of plasma edge parameters with fast lithium beams, *Schweinzer J., McCormick K., Fiedler S., Aumayr F., Pöckl M., Winter H.*	II-1163
6-44 Sniffer probe measurements in W7-AS, *Wolff H., Grigull P., Poschenrieder W., Roth J., Pech P., the W7-AS Team*	II-1167
6-47 Electric current collection by Langmuir probe in strong magnetic fields, *Stanojevic M., Cercek M., Jelic N., Gyergyek T.*	II-1171
6-48 A double probe for electron flux measurements in inhomogeneous and time-varying plasmas, *Axnäs I., Torvén S.*	II-1175
6-49 A processing method of the probe characteristic in a two electron temperature plasma, *Ruscanu D., Popa G., Stamate E.*	II-1179
6-50 Comparison of the wavenumber sensitivity and spatial resolution between Langmuir probes and reflectometry in a longitudinally magnetized RF plasma waveguide, *Anabitarte E., Senties J.M., Bustamante E.G., Calderon M.A.G., San Jose M.A.G., Monterde P., Vila J.*	II-1183
6-51 RF pulse interaction with low density plasma diagnosed by gated Langmuir probe, *Cicconi G., Paris P.J., Rosatelli C., Tarditi A.*	II-1187
6-57 Development of a diagnostic system for high power microwave (FEL) electric fields in the microwave tokamak experiment, *Oda T., Odajima K., Takiyama K., Foote J.H., Mizuno K., Ogawa T., Sato K., Ohasa K., Hoshino K., Maeda H., Nilson D.G.*	II-1191
6-59 Laser shadowgraphic study of plasma sheath in dense plasma focus in the presence of external axial magnetic field, *Rawat R.S., Srivastava M.P., Mohanty S.R.*	II-1195
6-61 Measurement of plasma drifts in space and laboratory plasmas by the resonance cone technique, *Rohde V., Piel A.*	II-1199
6-62 The time-delay of a microwave signal, backscattered at the hybrid resonance and new possibilities for the diagnostics of small-scale plasma fluctuations, *Arhipenko V.I., Simonchik L.V., Budnikov V.N., Gusakov E.Z., Piliya A.D., Selenin V.L.*	II-1203
6-65 Excimer laser driven soft X-ray plasma source: preliminary results, *Palladino L., Reale A., Taglieri G., Batani D., Bollanti S., Di Lazzaro P., Flora F., Letardi T., Schina G., Belli M., Scafati A.*	II-1207

Poster-No. Title, *Author(s)*	Volume/Page
6-67 Measurements of intense plasma streams with Faraday-type collectors, *Baranowski J., Sadowski M., Skladnik-Sadowska E.*	II-1211
6-68 New Cerenkov detectors for studies of fast electron beams from plasma discharges, *Jakubowski L., Sadowski M., Zebrowski J.*	II-1215
6-70 Application of laser induced ionisation to atomic hydrogen density measurements in high temperature plasma, Gladuschak V.I., Gusev V.K., Kantor M.Yu., Petrov Yu.V., Razdobarin G.T., Semenov V.V., Tolstyakov S.Yu.	II-1219

Topic 7: Inertial Confinement Fusion

Poster-No. Title, *Author(s)*	Volume/Page
7-1 Absorption of KrF laser pulses in laser produced plasmas, *Matsushima I., Koyama K., Tomie T., Matsumoto Y., Owadano Y.*	II-1225
7-3 Nonstationary stimulated Brillouin scattering in laser plasma, *Rubenchik A.M., Ochirov B.D., Kozochkin S.M., Maluyta D.D., Strel'tsov A.P., Shirokikh A.V.*	II-1229
7-4 Absorption process by ion acoustic turbulence, *Torres-Silva H., Sakanaka P.H.*	II-1233
7-5 Absorbed power into the plasma by laser radiation and determination of reflection coefficient in the implosion of deuterium-tritium pellets corresponding to the inertial confinement fusion, *Blazquez J.F.M.*	II-1237
7-7 Effect of electron velocity distribution on the heating of core by corona in spherical pellet, *Singh D.P., Giammanco F., Salvetti A., Vaselli M.*	II-1241
7-8 Influence of partial charge exchange on effective charge of swift heavy ions flowing through dense hydrogen plasmas, *Maynard G., Katsonis K., Deutsch C.*	II-1245
7-9 Numerical simulations of X-ray diagnostics in ICF, *Humbert P.*	II-1249
7-11 Plasma driven liners, *Kilic H., Linhart J.G., Bortolotti A., Bilbao L., Nardi V.*	II-1253
7-13 Axial magnetic field generation in a nonuniform laser produced plasma, *Srivastava M.K., Lawande S.V., Khan M., Das C., Chakraborty B.*	II-1257
7-14 Stabilization of the Rayleigh-Taylor instability by convection and thermal conduction in smooth density gradient: WKB analysis, *Bud'ko A., Liberman M.A., Bondarenko E.A.*	II-1261

Poster-No. Title, *Author(s)*	Volume/Page
7-17 Fusion-fission triggers for advanced fuels, *Linhart J.G.*	II-1265

Topic 8: General Plasma Theory

Poster-No. Title, *Author(s)*	Volume/Page
8-1 Wave collapse of strong lower-hybrid turbulence, *Bingham R., Su J.J., Dawson J.M., Shapiro V.D., Shevchenko V., Tsytovich V.N.*	II-1271
8-2 Empirical spectral codes for tokamak turbulence, *Smith G.R., Cohen R.H., Boerner E.D., Dimits A.M.*	II-1275
8-5 Frequency and heater power dependency of RF generated Langmuir turbulence, *Hanssen A., Mjølhus E.*	II-1279
8-7 Nonlinear modulational instability of whistler waves, *Karpman V.I., Lynov J.-P., Michelsen P., Rasmussen J.J.*	II-1283
8-8 Low-frequency kinetic structures in plasma quasiparticle concept, *Sitenko A.G., Sosenko P.P.*	II-1287
8-15 A novel approach to the interaction between the plasma wake field and the driving relativistic electron beam, *Fedele R., Shukla P.K.*	II-1293
8-18 Simultaneous emissions at harmonics and half harmonics of the electron gyrofrequency, *Krafft C., Matthieussent G., Belmont G.*	II-1297
8-20 Intense laser pulse propagation in a plasma, *Kaw P.K., Sen A., Katsouleas T.*	II-1301
8-21 Nonlinear depletion of short, relativistically strong laser pulses in an underdense plasma, *Bulanov S.V., Inovenkov N., Kirsanov V.I., Naumova N.M., Sakharov A.S.*	II-1305
8-25 Nonlinear modulated waves near marginal state of instability, *Flå T., Wyller J.*	II-1309
8-27 Plasma oscillations wave breaking in inhomogeneous collisional plasmas, *De Nicola S., Nappi C.*	II-1313
8-30 Nonlinear absorption on the front of relativistically strong electromagnetic pulse in an underdense plasma, *Bulanov S.V., Inovenkov I.N., Kirsanov V.I., Naumova N.M., Sakharov A.S., Shah H.A.*	II-1317
8-31 "Plasma maser" effect in turbulent plasma with regular and random magnetic fields, *Pryadko J.M., Tsytovich V.N.*	II-1321

Poster-No. Title, *Author(s)*	Volume/Page
8-32 Nonlinear evolution of the modulational instability and chaos by using ID-Zakharov equations, *Sharma R.P., Verga A.D.*	II-1325
8-33 Energy of linear quasi-neutral electrostatic drift waves, *Pfirsch D., Correa-Restrepo D.*	II-1329
8-34 General theory of modulational interactions of two modes, *Vladimirov S.V., Tsytovich V.N.*	II-1333
8-35 Nonlinear evolution of solitons with oscillations under the influence of resonant ions, *Honzawa T., Arakawa M., Singh S.*	II-1337
8-36 3D non-linear kinetic equation for the calculation of neoclassical effects in tokamak plasmas, *Zaitsev F.S., O'Brien M.R., Cox M.*	II-1341
8-37 Nonlinear Langmuir pulses in the active plasma, *Bachin I.V., Prudsky V.V.*	II-1345
8-39 Soliton formation in quasiparallel MHD waves, *Hamilton R.L., Kennel C.F., Mjølhus E.*	II-1349
8-41 Nonlinear wave behaviour determined by high-frequency plasma response, *Georgieva M., Khristova D., Shivarova A.*	II-1353
8-42 Evolution of electron two-stream instability and generation of nonlinear structure, *Tanaka M.*	II-1357
8-44 Gyroinvariant second order drifts in electric fields of the same order of the magnetic field, *Martin P.*	II-1361
8-45 Charge shielding by trapped ion orbits in a dusty plasmas, *Goree J.*	II-1365
8-48 Vlasov solution describing nonabdiabatic plasma heating by magnetic compression, *Persson H., Ågren O.*	II-1369
8-50 The Pade approximate method for solving problems in plasma kinetic theory, *Jasperse J.R., Basu B.*	II-1373
8-51 Correlation theory of particle distribution near the plasma boundary in the presence of strong electric field, *Korchinsky G.M., Yakimenko I.P., Zagorodny A.G.*	II-1377
8-54 Possible changes of temperature and density power law exponents in expressions for plasma transport quantities under many particle interaction conditions, *Larenz R.W.*	II-1381
8-56 Dynamical screening in the Coulomb relaxation of anisotropic plasmas, *Wolf U., Schamel H.*	II-1385

Poster-No. Title, *Author(s)*	Volume/Page
8-57 Wiedemann-Franz-Law for magnetized plasmas, *Hensler E.*	II-1389
8-58 The influence of toroidicity, pressure and local profile changes on tearing mode stability, *Connor J.W., Cowley S.C., Hastie R.J., Martin T.J.*	II-1393
8-60 Linear and non-linear modelling of island control in tokamaks, *Hansen B.M.S., Hellberg M.A., Sherwell D., Roberts D.E., McLoud W.S.*	II-1397
8-61 Resistive wall instabilities for axisymmetric systems, *Berge G., Freidberg J.P.*	II-1401
8-62 Stability of force-free axisymmetric spherical plasma with flow, *Sugimoto H., Ashida H., Kurasawa T.*	II-1405
8-64 Internal disruption = catastrophic ergodisation, *Dubois M.A., Hennequin P., Nakach R., Sabot R.*	II-1409
8-65 Stability of ideal ballooning modes near a magnetic island, *Hegna C.C., Callen J.D.*	II-1413
8-66 Sheared flow effects on resistive pressure-gradient-driven turbulence, *Garcia L., Carreras B.A., Lynch V.E., Diamond P.H.*	II-1417
8-67 Mechanism of MHD modes stabilization by the ergodic divertor, *Edery D., Samain A., Vallet J.C., Morera J.P., Joffrin E., Lecoustey P., Pecquet A.L., Talvard M.*	II-1421
8-68 Nonlinear island dynamics, *Schep T.J., Pegoraro F., Rem J.*	II-1425
8-69 Magnetic reconnection in electron-magnetohydrodynamics, *Bulanov S.V., Pegoraro F., Sakharov A.S.*	II-1429
8-70 Radial propagation of microturbulence in tokamaks, *Garbet X., Laurent L., Roubin J.P., Samain A.*	II-1433
8-71 On the threshold of the ion temperature gradient driven mode, *Guo S.C., Romanelli F., Rewoldt G., Tang W.M.*	II-1437
8-72 Stability and transport due to ITG modes in a toroidal plasma with impurities, trapped electrons and vortex formation effects, *Jarmen A., Fröjdh M., Pavlenko V., Weiland J.*	II-1441
8-74 Dissipative-drift wave instability in the presence of impurity radiation, *Bharuthram R., Shukla P.K.*	II-1445
8-75 Nonadiabaticity and toroidal mode coupling in collisional drift waves, *Schlüter M., Scott B.D.*	II-1449

Poster-No. Title, *Author(s)*	Volume/Page
8-76 On the "captured" energy in freely decaying two-dimensional hydrodynamic and drift-wave plasma turbulence, *Bazdenkov S.V., Kukharkin N.N.*	II-1453
8-77 Effect of parallel heat flows on electron heat conduction losses due to electrostatic turbulence, *Becker G.*	II-1457
8-79 An energy balance approach to L-H transition at the edge, *Martinell J.J., Ramos G.*	II-1461
8-80 Pedestal sustenance, heat transport at the edge in the H-transition, *Minardi E.*	II-1465
8-81 Non-standard high energy ion orbits, *Eriksson L.-G., Berk H., Porcelli F., Stankiewicz R.*	II-1469
8-83 Plasma transport as a dissipative structure, *Uehara K.*	II-1473
8-84 Ambipolar transport in a magnetically perturbed tokamak edge-region, *Wittenberg R.W., Hellberg M.A., Feneberg W.*	II-1477
8-85 Neoclassical transport with surface variation of the macroscopic quantities, *Feneberg W.*	II-1481
8-87 Time-dependent neutron rate interpretation for deuterium injection into deuterium plasmas, *Wolle B., Eriksson L.-G., Hübner K., Morgan P.D., Sadler G., Tsintsadze L.N., Von Hellermann M.G.*	II-1485
8-88 Multidimensional WKB solution of a wave equation, *Pereverzev G.V.*	II-1489
8-89 Electron cyclotron emission and absorption in two dimensional momentum distribution, *Bornatici M.*	II-1493
8-90 Oblique propagation of electron-cyclotron-waves in non-maxwellian, weakly relativistic Vlasov-plasmas, *Moser F.*	II-1497
8-92 Partially transient plasma response near an attainable harmonic state, *Lim C.S., Suchy K.*	II-1501
8-94 Mode coupling of the ordinary and extraordinary waves in a cylindrical plasma, *Ramsay D., Laing E.W.*	II-1505
8-97 High frequency electrostatic plasma instabilities and turbulence in the lower ionosphere, *Basu B., Jasperse J.R., Retterer J.M., Decker D.T., Chang T.*	II-1509
8-99 Numerical calculation based on multipole expansions was used to study the linear instability in a DP-Machine, *Cereceda C., Ruiz J., Puerta J.*	II-1513

Poster-No. Title, *Author(s)*	Volume/Page
8-100 Dispersion characteristics of electromagnetic waves in dipolar (m=+/-1) modes travelling along a magnetized plasma column, *Benova E., Ghanashev I., Zhelyazkov I.*	II-1517
8-102 Cyclotron autoresonance current drive in tokamaks, *Kuyanov A.Yu., Skovoroda A.A., Timofeev A.V., Zvonkov A.V.*	II-1521
8-103 Application of a reconstructive MHD code based on the formalism of the toroidal multipoles to the ITER tokamak, *Alladio F., Lalousis P., Micozzi P.*	II-1525
8-105 MHD theory with induced surface current effects, *Lehnert B.*	II-1529
8-107 Exact surface waves on spheres, cylinders, *Yu M.Y., Stenflo L.*	II-1533
8-109 1st and 2nd elliptic solutions to the extended Grad-Shafranov-Schlüter equation for asymmetric tokamak plasma with stationary flows, *Zelazny R., Stankiewicz R., Galkowski A., Potempski S.*	II-1537
8-110 A new fast 2-d MHD-equilibrium solver, *Hübner G.*	II-1541
8-111 A civil engineering approach to ideal MHD, *Jensen V.O.*	II-1545
8-112 A general formulation of the nonlinear plasma theories, *Kuhn S., Assis A.S.*	II-1549
8-113 Uniqueness of solution to a stationary boundary kinetic problem, *Zhykharsky A.*	II-1553
8-114 Solution to the boundary kinetic problem presenting the interaction of plasma flows with a solid, *Zhykharsky A., Shmykov V.*	II-1557
8-115 A theoretical model for transient cataphoretic segregation, *Dumitrascu N., Berbece D., Popa Gh.*	II-1561

PART III

Topic 9: Space and Astrophysical Plasmas

Poster-No. Title, *Author(s)*	Volume/Page
9-1 Modulational instability of lower hybrid wave in a cylindrical plasma, *Sharma S.K., Sudarshan A.*	III-1567

Poster-No. Title, *Author(s)*	Volume/Page
9-5 Interaction of a magnetized plasma stream with an immobile ion cloud, *Baumgärtel K., Sauer K.*	III-1571
9-7 Rayleigh-Taylor instability favoured drift turbulence in a spread F simulation experiment, *Prasad G., Bora D., Saxena Y.C.*	III-1575
9-9 Simulation of electron beam-driven instabilities by a 3-D electromagnetic particle code, *Nishikawa K.-I., Buneman O., Neubert T.*	III-1579
9-13 Night time equatorial spread F simulation in a laboratory plasma, *Prasad G., Bora D., Saxena Y.C.*	III-1583
9-14 Stimulated attachment instability of electromagnetic waves in the ionosphere, *Shukla P.K., Stenflo L., Borisov N.D.*	III-1587
9-17 Radar collective backscattering and the high latitude plasma turbulence, *Grésillon D., Cabrit B., Hanuise C., Villain J.P., Greenwald R.A., Baker K.B.*	III-1591
9-19 Stimulated scattering of EM wave by ICW in a two electron temperature plasma, *Sudarshan A., Sharma S.K.*	III-1595
9-20 Binding energy and triplet-splitting of the hydrogen molecule in ultrahigh magnetic fields, *Korolev A., Liberman M.A.*	III-1599
9-21 Behaviour of two-dimensional ion-acoustic soliton in relativistic plasmas of radiation belts, *Singh S., Honzawa T.*	III-1603
9-23 The Rayleigh-Taylor instability in a super-dense igniting plasma, *Garcia D., Serichol N., Bravo E., Diaz-Pinto A.*	III-1607
9-26 New electrostatic instabilities in nonuniform partially ionized magnetoplasmas, *Shukla P.K., Dwivedi C.B., Das A.C.*	III-1611
9-27 Spontaneous formation of intermediate shocks, *Chao J.K., Chiu C.Y., Chiueh T.H.*	III-1615
9-33 Spectrum of MHD waves in cometary tails, *Matsuura O.T., Azevedo C.A., Assis A.S., Shigueoka H., Sakanaka P.H.*	III-1619
9-34 Low-frequency resonant ion-beam turbulence in cometary plasmas, *Verheest F., Lakhina G.S.*	III-1623
9-35 Lower hybrid resonance acceleration of electrons and ions in the aurora and solar flares, *Bingham R., Bryant D.A., Hall D.S., Su J.J., Dawson J.M.*	III-1627
9-38 Solar flare mechanism based on MHD relaxation model, *Kusano K., Kubo H., Tamano T., Sato T.*	III-1631

Poster-No. Title, *Author(s)*	Volume/Page
9-39 Nonlinear MHD surface waves on plasma interfaces and their evolution equation in solar and magnetospheric conditions, *Nenovski P., Zhelyazkov I., Murawski K.*	III-1635
9-42 Generation of large amplitude plasma waves in space phenomena, *Dudnikova G.I., Vshivkov V.A.*	III-1639
9-43 Parametric instabilities of Langmuir waves in dusty plasmas, *Shukla P.K., Feix G., Rao N.N.*	III-1643
9-44 Magnetic reconnection in the plasma within clusters of galaxies, *Jafelice L.C., Friaca A.C.S.*	III-1647
9-46 Quantitative analysis of cosmic noise coming from plasma jets of quasar, *Tanizuka N., Kawaguchi N., Mikoshiba H., Inoue M.*	III-1651
9-47 A theory on the evolution process of the fine structure in space, *Nejoh Y.*	III-1655
9-48 The effects of slightly oblique propagation on nonlinear Alfvén waves, *Spangler S.R., Plapp B.B.*	III-1659
9-50 Mathematicl theories of resonant absorption of Alfvén waves in space plasmas: time dependent solution, *Uberoi C.*	III-1663
9-51 Runaway electrons in the presence of kinetic Alfvén waves, *Assis A.S., Leubner C.*	III-1667
9-52 Polarization changes through stimulated Raman scattering, Krishan V., Gangadhara R.T.	III-1671

Topic 10: Basic Collisionless Plasma Physics

Poster-No. Title, *Author(s)*	Volume/Page
10-1 Transition to chaos in periodically driven thermionic diodes at low pressure, *Klinger T., Timm R., Piel A.*	III-1677
10-3 Equilibrium double layers in extended Pierce diodes, *Ciubotariu-Jassy C.I.*	III-1681
10-4 New results on weakly nonlinear driven oscillations in the Pierce diode, *Hörhager M., Kuhn S.*	III-1685
10-7 Laboratory study of collisionless interaction processes between supernova-like ejectas and magnetized background under conditions of a laser-produced-plasma experiments, *Zakharov Yu.P., Orishich A.M., Ponomarenko A.G., Snytnikov V.N.*	III-1689

Poster-No. Title, *Author(s)*	Volume/Page
10-8 Total energy conservation, Manley-Rowe relations for plasma-maser interaction, *Nambu M.*	III-1693
10-9 Phase-space topology in the dynamics of cyclotron-masers, *Pakter R., Schneider R.S., Rizzato F.B.*	III-1697
10-10 RF production of long, dense plasma columns, *Chen F.F., Chevlaier G.*	III-1701
10-11 Plasma potential formation in the presence of localized radio-frequency electric fields, *Sato N.Y., Hatakeyama R., Sato N.*	III-1705
10-12 Inward and outward plasma motion induced by axisymmetric electromagnetic fields around the ion cyclotron frequency, *Hatakeyama R., Miyakuni S., Sato N.Y., Sato N.*	III-1709
10-13 The exact and drift Hamiltonian, *Yao Q., Boozer A.H.*	III-1713
10-14 Collisionsless driftwaves in anisotropic cylindrical plasmas, *Korn J., Schamel H.*	III-1717
10-15 Instabilities of gyro-kinetic plasmas with a guiding center density gradient, finite Larmor radius and polarization drift, *Knorr G., Shoucri M.*	III-1721
10-16 The launching and propagation of drift waves in a steady-state plasma, *Sandeman J., Elliott J.A., Sutcliffe M., Rusbridge M.G.*	III-1725
10-17 Studies of non-linear interactions of drift waves in the UMIST quadrupole "GOLUX", *Duncan P.J., Chekroud D., Rusbridge M.G.*	III-1729
10-18 Excitation of electron cyclotron waves and related physics experiments, *Tanaka M., Tamaoki M., Shoyama H., Nagao K., Komori A., Kawai Y.*	III-1733
10-19 An Eulerian Vlasov plasma simulation code for ion phase space phenonema, *Cherkhani R., Bonhomme G., Ghizzo A., Bertrand P.*	III-1737
10-20 An Eulerian code for the study of the gyro-averaged kinetic Vlasov equation, *Ghizzo A., Bertrand P., Shoucri M., Fijalkow E., Feix M.*	III-1741
10-21 Relativistic Vlasov-Maxwell equilibria of anisotropic charge-separation-free plasmas, *Kamp L.P.J., Van Bruggen-Kerkhof M.J., Sluijter F.W.*	III-1745
10-22 A new action principle for the Vlasov-Maxwell system, *Larsson J.*	III-1749
10-23 Negative-energy waves in an inhomogeneous force-free Vlasov plasma with sheared magnetic field, *Correa-Restrepo D., Pfirsch D.*	III-1753

Poster-No. Title, *Author(s)*	Volume/Page
10-24 Electrons passing through a negatively biased grid due to collective trapping, *Popa G., Schrittwieser R.*	III-1757
10-26 Experimental analysis of a low frequency instability in a magnetized discharge plasma, *Gyergyek T., Cercek M., Jelic N., Stanojevic M.*	III-1761
10-27 Ion cyclotron oscillations induced by an emissive electrode floating in a magnetized collisionless plasma column, *Sato N., Hatakeyama R., Aoyama K., Ding W.X.*	III-1765
10-28 On the double layer phenomenology, *Sandulovicіu M., Lozneanu E.*	III-1769
10-29 A probe sheath instability in a double plasma device, *Dempers C.A., Krumm P., Schrittwieser R.*	III-1773
10-30 Progress in the kinetic modeling of collisionless two-dimensional bounded plasma systems, *Pedit H., Kuhn S.*	III-1777
10-31 Anisotropic conductivity of the collisionsless magnetized plasma, its application to the cylindrical plasma column, *Kiyama S.*	III-1781
10-32 Analytic solution to longitudinal eigenmodes in a collisionless bounded plasma, *Kuhn S., Schupfer N., Assis A.S., Santiago M.A.M.*	III-1785
10-36 A collisionless **ExB** instability with large ion orbits, *Chen F.F.*	III-1789
10-37 Influence of the thermoionic emission on the current-driven ion-acoustic instability, *Donoso G., Martin P.*	III-1795
10-38 Modulational instability of relativistic ion acoustic waves in a plasma with trapped electrons, *Nejoh Y.*	III-1799
10-39 Cross-field ion acoustic instability and turbulence in a weakly magnetized plasma, *Barrett P.J., Popov G.H.*	III-1803
10-40 Numerical study of potential formation and negative resistance in a current-carrying ion sheath, *Ohno N., Komori A., Takamura S., Kawai Y.*	III-1807
10-41 Asymmetric **ExB** equilibria and diocotron adiabatic invariants, *Chu R., Wurtele J.S., Notte J., Fajans J.*	III-1811
10-43 Compression of multiple ion acoustic solitons at the plasma sheath edge, *Nagasawa T., Nishida Y.*	III-1815
10-44 The effects of finite electron mass on ion-acoustic solitons, *Rice W.K.M., Hellberg M.A., Mace R.L., Baboolal S.*	III-1819

Poster-No. Title, *Author(s)*	Volume/Page
10-45 Effect of second ion species on ion-acoustic rarefactive soliton in two-el/ *Sayal V.K., Yadav L.L., Sharma S.R.*	
10-46 Transport of time-varying currents by whistler waves, *Urrutia J.M., Stenzel R.L., Rousculp C.*	III-1951
10-47 Excitation of low-frequency whistlers by magnetic loops, *Stenzel R.L., Urrutia J.M., Rousculp C., Golubyatnikov G.Yu.*	
10-49 Non-stationary propagation of nonlinear ion acoustic waves in a plasma with negati, *Uehara M., Maciel H.S.*	
10-52 Relaxation and self-organization of a nonneutral plasma, *Ramachandran H., Morales G.J., Decyk V.K.*	
10-53 Low-dimensional attractors arising from the interaction of drift waves with low frequency instabilities, *Klinger T., Piel A.*	III-1
10-54 Ion-holes associated with rarefactive ion acoustic pulse, *Singh A.K., Saxena Y.C.*	III-1847
10-55 Cascading bifurcations to chaos in a current carrying ion sheath, *Kono M., Komori A.*	III-1851
10-56 Experimental measurements of cascading bifurcations to chaos in an ion sheath, *Komori A., Kono M., Norimine T., Tanaka M., Kawai Y.*	III-1855
10-57 Nonlinear evolution and localized structure of unstable waves in an electron-beam plasma, *Yamagiwa K., Mieno T., Tanaka M.*	III-1859
10-58 Observation of two wave induced chaos in a magnetized plasma, *Fasoli A., Paris P.J., Tran M.Q., Skiff F.*	III-1863
10-59 Observations of intermittent structures in association with low frequency turbulence in toroidal magnetized plasma, *Singh A.K., Saxena Y.C.*	III-1867
10-60 Lower hybrid turbulence excited by electron diamagnetic drifts, *Stenzel R.L.*	III-1871
10-61 Experimental studies of anomalous potential drops due to ion density inhomogeneities, *Axnäs I., Bohm M., Torvén S.*	III-1875
10-62 Ion resonance cones and intrinsic diffraction, *Pierre T., Bonhomme G.*	III-1879
10-63 Reflection of a divergent resonance cone near the plasma layer in a magnetized inhomogeneous plasma, *Boucher I., Pierre T., Leclert G.*	III-1883

Poster-No. Title, *Author(s)*	Volume/Page
10-64 Production of a high density plasma by helicon waves, *Komori A., Sugimoto M., Kono M., Tanaka M., Kawai Y.*	III-1887
10-65 Development of spiral structures on a rotating plasma column with large ion-gyroradius, *Ikehata T., Mase H.*	III-1891
10-66 Waves driven by strong transverse potential structures, *Koepke M.E., Alport M.J., Sheridan T.E., Amatucci W.E., Carroll III J.J.*	III-1895
10-67 Experimental dynamics of 2-D vorticity rings, *Peurrung A.J., Fajans J.*	III-1899
10-68 Dynamics of non-stationary dipole vortices in the Hasegawa-Mima equation, *Hesthaven J.S., Lynov J.-P., Nycander J.*	III-1903
10-69 Localized vortices in η_i-modes, *Nycander J., Lynov J.-P., Rasmussen J.J.*	III-1907
10-72 Breaking of waves into wave packets observed in a beam-plasma system, *Honzawa T., Singh S.*	III-1911
10-74 Experimental measurement of the deflection of an electron beam due to the ponderomotive force of a HF wave in a waveguide, Hadjoudj Y., Heuraux S., Pierre T., Leclert G.	III-1915
10-76 Generation of ion cyclotron wave in an ion beam by a periodic magnetic field, *Mieno T., Hatakeyama R., Sato N.*	III-1919
10-77 Non-linear ion acceleration in electrostatic wave fields, *Alava M.J., Heikkinen J.A.*	III-1923
10-78 Electron acceleration by $\mathbf{v}_p \mathrm{x} \mathbf{B}$ mechanism in vacuum, *Yugami N., Nishida Y.*	III-1927
10-79 Plasma wave wake field excited by short pulse microwave, *Nishida Y., Kusaka S., Yugami N.*	III-1931
10-82 Direct measurements of velocity space transport in a fully ionized plasma, *Rynn N., Bowles J., McWilliams R.*	III-1935
10-83 Phase conjugation via Brillouin enhanced four-wave mixing in a plasma, *Domier D.W., Luhmann Jr. N.C., Peebles W.A.*	III-1939
10-84 High frequency modes of a plasma column loaded in a sheath helix, *Ganguli A., Appala N.P., Umesh G.*	III-1943
10-85 Estimation of electron temperature and density by deconvolving the absorption part of the plasma dispersion function, *Jimenez-Dominguez H., Cabral-Prieto A., Melendez-Lugo L., Lopez-Callejas R., Colunga-Sanchez S., Valencia-Alvarado R., Cruz-Jimenez S., Gaytan-Gallardo E., Chavez-Alarcon E.*	III-1947

Poster-No. Title, *Author(s)*	Volume/Page
10-86 Kinetic description of modulated electromagnetic wave in relativistic plasma, *Ekiel-Jezewska M., Flå T., Kaufman A.N.*	III-1951

Topic 11: Partially Ionized Plasmas

Poster-No. Title, *Author(s)*	Volume/Page
11-2 Experimental evidence of self-organization and chaos in some plasma devices, *Sanduloviciu M., Alexandroaei D., Talasman S.J. and Ianopol B.*	III-1957
11-5 Tomographic time-resolved reconstruction of the three dimensional electron velocity distribution in a partially ionized RF plasma, *Matsumoto K., Iwama N., Ishii S.*	III-1961
11-6 Large amplitude striations in an RF discharge, *Sato T., Shoji T., Sakawa Y., Hori M.*	III-1965
11-9 Ionization front structure in the lateral spreading of a DC discharge along cylindrical coaxial electrodes, *Gavrilescu C., Popa G.*	III-1969
11-10 Plasma heating in low pressure RF discharges, *Skorik M.A., Braithwaite N.St.J., Allen J.E.*	III-1973
11-11 Ion energy distribution in an RF Argon plasma, *Annaratone B.M., Skorik M.A., Goruppa A.A., Allen J.E.*	III-1977
11-12 Observation of coherent drift structures in the turbulence of a DC discharge, *Kauschke U., Schlüter H.*	III-1981
11-13 Effects of magnetic field on a magnetron discharge, *Mase H., Tanabe T., Ikehata T., Sato N.Y.*	III-1985
11-17 The Langmuir probe study of the electron energy distribution function in the flowing afterglow plasma, *Glosik J., Cermak I., Sicha M., Tichy M., Zakouril P.*	III-1989
11-18 Computer simulation of RF discharges and comparison with laboratory results, *Vahedi V., Surendra M., DiPeso G., Mirrashidi P., Birdsall C.K.*	III-1993
11-19 On modelling of steady states in toroidal machines for basic plasma physics, *Øien A.H.*	III-1997
11-23 A one-dimensional q-machine model taking into account charge-exchange collisions, *Maier H., Kuhn S.*	III-2001
11-24 Determination of composition and physical properties of partially ionized plasmas in the function of temperature, *Zaporowski B.*	III-2005

Poster-No. Title, *Author(s)*	Volume/Page
11-25 Thermodynamic functions for partially ionized plasmas in the mean spherical approximation, *Kahlbaum T., Schneidenbach H.*	III-2009
11-26 Dielectric constant of weakly-ionized magnetized plasmas, *Kiss'ovski Zh., Pironkova A., Shivarova A.*	III-2013
11-28 Ion Bernstein waves in a toroidal steady-state device, *Batani D., Fontanesi M., Galassi A., Riccardi C., Sindoni E.*	III-2017
11-33 Study of low frequency flute type oscillations, their nonlinear interaction in toroidal plasma, *Prasad G., Bora D., Saxena Y.C., Sethia G.C.*	III-2021
11-39 Behaviour of charged particle motion along an inhomogeneous magnetic field and a retarding electric field - evidence for the existence of discrete energy states, *Varma R.K., Punithavelu A.M.*	III-2025
11-40 Unstable behaviour of globular anode structures, *Biborosch L., Toma M., Sanduloviciu M.*	III-2029
11-41 On the electrodynamic explanation of the retrograde motion of the electric arc, *Hong J.S., Allen J.E.*	III-2033
11-42 Nonequilibrium transport phenomena of a plasma in a nonuniform electric field, *Cicconi G., Molinari V., Sumini M.*	III-2037
11-43 Experimental study of the axial structure of an argon plasma column sustained by an electromagnetic wave in the presence of an external magnetic field, *Staikov P., Grozev D., Zhelyazkov I., Benova E.*	III-2041
11-46 Electromagnetic surface waves for large-area RF plasma productions between large-area planar electrodes, *Nonaka S.*	III-2045
11-49 CO_2-TE laser-produced cadmium plasma in vacuum experiment, kinetics, *Apostol I., Bahrim B., Bahrim C., Vasilescu C.*	III-2049

Topic 12: Elementary Processes in Plasmas

Poster-No. Title, *Author(s)*	Volume/Page
12-1 Measured and calculated charge density in Ce, Cu vapor produced by an electron gun, *Blumenfeld L., Gonella C., Morin M.*	III-2055
12-5 Stokes parameters for Compton scattering in a strong magnetic field, *Chou C.K., Chen H.H.*	III-2059

Poster-No. Title, *Author(s)*	Volume/Page
12-6 CTMC study of collisions of Carbon ions with H and He, relevant to magnetically confined fusion plasmas, *Katsonis K., Maynard G.*	III-2063
12-8 Investigation on the metastable fragmentation of mixed argon-oxygen, argon-krypton cluster ions: the observation of two new fragmentation decay channels - evidence for the existence of metastable excited dimer ions ArO^{+*}, $ArKr^{+*}$, *Foltin M., Lukac P., Märk T.D.*	III-2067
12-12 Ion attachment to van der Waals clusters: reactions of NO^+ with Ar_m, *Lezius M., Scheier P., Märk T.D.*	III-2071
12-13 On the interation of low energy electrons with vdW-Clusters: electron attachment reactions, auto-scavenging, *Rauth T., Lezius M., Foltin M., Grill V., Märk T.D.*	III-2075
12-16 Particle exchange reactions at low kinetic energies, *Praxmarer C., Freysinger W., Hansel A., Lindinger W.*	III-2079
12-17 Collisional induced dissociation of Kr_2^+, $(CO)_2^+$, N_4^+, N_2Ar^+, *Praxmarer C., Glosik J., Smith D., Freysinger W., Lindinger W.*	III-2083
12-18 Theoretical studies of the vibrational relaxation of $N_2^+(v=1)$ in collisions with He using the semiclassical method, *Zenevich V.A., Freysinger W., Lindinger W.*	III-2087
12-20 Ionization, recombination processes in dense nonideal plasmas, *Bornath Th., Schlanges M., Kremp D., Bonitz M.*	III-2091
12-23 Experimental, theoretical determination of electron impact ionization cross sections of atoms and molecules, *Grill V., Margreiter D., Walder G., Scheier P., Winkler C., Kurdel M., Poll H.U., Deutsch H., Stephan K., Märk T.D.*	III-2095
12-26 Microwave determination of the coefficient of dissociative recombination of molecular ions of argon, *Okada T., Sugawara M.*	III-2099
12-27 On the laser cooling of ions in oscillating traps, *Reyna L.G., Sobehart J.*	III-2103

Topic 13: Plasma Applications

Poster-No. Title, *Author(s)*	Volume/Page
13-2 One-dimensional modeling for magneto-microwave plasma using the Monte Carlo method, *Ikegawa M., Kakehi Y., Kobayashi J.*	III-2109
13-3 ECR plasma source in ICR separation device, *Meis C., Compant La Fontaine A., Louvet P., Meyer R.L.*	III-2113

Poster-No. Title, *Author(s)*	Volume/Page
13-6 Current and geometry dependence of mass and energy fluxes in capillary, ablative critical flows, *Cuperman S., Zoler D., Ashkenazy J., Caner M., Kaplan Z.*	III-2117
13-7 New method of ion extraction from plasma by using radio-frequency electric field, *Matsui T., Tuchida K., Nishio R., Suzuki K., Shoji T.*	III-2121
13-8 Density and temperature measurements by laser absorption diagnostic on a magnetized plasma, *Compant La Fontaine A., Le Gourrierec P., Louvet P.*	III-2125
13-9 The plasmachemical reactions in negative corona discharges, *Skalny J.D., Lukac P., Gabris R.*	III-2129
13-12 Plasma parameter profiles and fluctuation properties of an ECR process plasma source for Si etching at LN_2 temperatures, *Kim S.K., Park C.W., Cho S., Choi E.H., Kwak J.K., Park J.K., Rhee C.*	III-2133
13-14 Magnet plasma dynamic accelerator with ultra high frequency resonator, *Kubarev Y.V., Tashaev Y.N., Safronov V.P., Kholin N.N.*	III-2137
13-16 Ion irradition studies from dense plasma focus for change of phase for thin film of CdS, *Sagar R., Srivastava M.P., Rawat R.S.*	III-2141
13-17 Influence of metastable atoms on the characteristics of surface wave produced plasmas, *Kortshagen U., Schlüter H.*	III-2145
13-19 Use of cold plasmas in film deposition and structuring, *Edlinger J., Pulker H.K., Rille E., Vogl G.*	III-2149
13-22 Experimental study of plasma effect on oxidation of solid surface, *Kitajima M., Kuroki H., Shinno H., Kawabe T.*	III-2155

Topic 8: General Plasma Theory
(Contribution added in print)

8-116 Langevin-equation for charged particles in microturbulent plasma, *Meister C.-V.*	III-2159

Topic 1:

Tokamaks

HIGH CURRENT, HIGH POWER H-MODES IN JET

T T C Jones, B Balet, M Brusati, M Bures, M Hugon, K D Lawson[1],
P J Lomas, P D Morgan, H W Morsi, P Nielsen, G Sadler, R Sartori,
D F H Start, D D R Summers, A Tanga, A Taroni, K Thomsen and D J Ward
JET Joint Undertaking, Abingdon, Oxfordshire OX14 3EA, UK
[1] *Culham Laboratory, UKAEA / Euratom Fusion Association, Abingdon, Oxfordshire OX14 3DB, UK*

The range of plasma currents accessible in the JET double null X-point (DNX) configuration has been increased. The maximum plasma shaping capability has been employed at plasma currents up to 5MA. For plasma currents of 4MA and above, the field null was formed outside the vacuum vessel. The resulting plasmas were, strictly speaking, limiting directly on the X-point dump plates. Nevertheless, H-modes were readily obtained in these configurations, including the 5MA case in which the null was located approximately 8cm beyond the surface of the dump plates. Up to 10MW ICRH and 17MW D^0 NBI were applied in the H-mode; global confinement and fusion performance are examined in the range of plasma currents 3-5MA including data for discharges with and without sawteeth, and with varied proportions of ICRH and NBI heating. The discharges interacted predominantly with the top CFC graphite X-point dump plates, which formed a continuous toroidal surface whose geometry had been optimised with respect to the incident power distribution. By operation at sufficiently high density or with a D_2 gas puff localised in the X-point region , in excess of 20MJ conducted energy into the scrape-off layer could be tolerated without large C influxes (blooms) even at maximum power. In this way, H-modes could be maintained for up to 2.5 s with nearly stationary stored energy content, with D-D neutron production dominated by thermonuclear reactions, and with equivalent $Q_{DT} \gtrsim 0.2$.

Magnetic configuration The poloidal field system was symmetrically configured; the maximum shaping amplifier current of 50kA was utilised and the primary circuit was operated with 35kA less current in the end subcoils, the maximum permissible difference current, to give the plasma equilibrium shown in Fig.1 at 5MA. A slight upward shift, necessary to avoid the possibility of damage to the bottom Be X-point dump plates before completion of critical tile characterisation experiments, was applied using the vertical position control system. In order to optimise the match of the plasma boundary to the shape of the ICRH antennae, a reduced subset of the vertical field coil was energised which resulted in increased plasma triangularity. The combination of high plasma current and large elongation posed a serious potential problem of very large mechanical vessel forces in the event of loss of vertical position control, e.g. during disruptions. A major factor in the development of these discharges was the successful commissioning of automatic protection in which the shaping and plasma currents were ramped down upon detection of a disruption precursor, namely the onset of a quasi stationary mode /1/. This measure substantially reduced the mechanical forces experienced by vessel components due to disruptions, and no in-vessel damage at all was sustained.

Global confinement Fig.2 gives the plot of diamagnetic stored energy versus plasma loss power $P_{tot} - dW_{DIA}/dt$. The data are for 3-5MA H-modes in the DNX configuration taken in the 1991-2 operating period. Despite the marginal nature of the X-point configuration at 4MA and above many of the discharges featured ELM-free phases and the data in Fig.2 is restricted to such cases. Time traces for the highest power H-mode discharges at 4MA and 5MA are shown in Figs.3 and 4 respectively; the former attained the highest ever stored energy of

12.7MJ, for 23MW total input power. The 4MA data set in Fig.2 includes discharges with early X-point formation where the main heating pulse was applied before the onset of sawteeth, and, as a result the solid points are mainly representative of sawtooth-free periods. In some cases, a monster sawtooth developed during the main heating pulse after the start of normal sawteeth; Fig.4 shows such an example, in which 10MW D^0 NBI was supplemented by 1.5MW H-minority ICRH. Fig.2 also indicates the stored energy expected on the basis of the 1990 ITER H-mode empirical scaling /2/ which is almost linear with plasma current. The main result is that W_{DIA} scales with current more weakly than linearly, especially between 4 and 5MA. However, there is substantial scatter in the data and the 5MA data set is not extensive. Previously observed saturation of L-mode confinement current scaling at high I_p (e.g./3/) suggested effects due to sawteeth at low q_{cyl} and unfavourable NBI power deposition profiles at high n_e. The present sawtooth-free data and in addition, lack of any systematic difference between confinement of NBI and ICRH dominated discharges rules out either of the aforementioned deleterious effects. The most likely explanation for the H-mode data remains the progressive reduction in edge shear in the plasma as the X-point moves further away at high current. There is some evidence for this effect at 3MA where there is scope for significant variation of the X-point position, although unfortunately the range of this parameter in the 3MA DNX data set does not overlap the values at 4-5MA.

Impurity influxes The evolution of D_α and CIII emission (measured on vertical viewing chords), Z_{eff} and radiated power P_{rad} shown in Fig.3 are typical of the behaviour at high power. No sudden large C influx is observed to occur (C bloom), although there is a jump in P_{rad} on termination of the H-mode following removal of the heating power. Such bloom resilience was generally observed when pre-programmed D_2 gas injection into the X-point region was employed as in Fig.3. Comparable resilience was also observed at sufficiently high density of the X-point target plasma ($<n_e> \gtrsim 3\times10^{19}m^{-3}$) e.g. Fig.5. The bloom limits under these conditions were not fully explored, but are at least a factor two better than low density hot-ion H-modes in terms of energy lost by conduction from the bulk plasma. Nevertheless, Z_{eff} can still rise to a large value, particularly during ELM-free periods (Figs.3 and 4). For the data within a given range of $P_{tot}/<n_e>$, the average value of n_D/n_e decreases strongly with plasma current. This trend implies either enhanced impurity confinement in the bulk plasma or a reduction of screening; certainly the latter would be expected at high current in the absence of any divertor plasma when the X-points are external.

Fusion performance The present DNX H-mode data is plotted in the T_i versus $n_D(0)\tau_E T_i(0)$ plane in Fig.6, labelled according to plasma current. The $T_i(0)$ values are mainly from charge exchange spectroscopy and deuteron dilution is derived from the bremsstrahlung Z_{eff}. Much of the data falls in the region in which $T_i \sim T_e$ irrespective of heating method, a natural constraint due to ion-electron coupling when $\tau_{ei}^{eq} \lesssim \tau_E$ /4/. A few points taken at low density with NBI heating enter the hot ion regime where $T_i >> T_e$; these shots have the highest equivalent Q_{DT} and measured Q_{DD} within the present DNX dataset, but were not optimised for hot-ion performance and the single-null configuration (SNX) was favoured for maximum fusion yield studies including the preliminary tritium experiment /5/. According to Fig.6 the best discharges with $T_i \sim T_e$ achieve Q_{DT} equivalent of 0.2-0.3. The best conditions are obtained without sawteeth due to more peaked temperature profiles; $n_e(r)$ was generally flat or slightly hollow for the moderate to high density shots similar to Figs.3-5. Pulse 25945, whose time traces are given in Fig.5, is identified in Fig.6 and represents steady conditions of n_D, T_i and τ_E held for over two seconds. The experimental Q_{DD} values may be taken as a third

coordinate in the T_i versus $n_D(0)\tau_E T_i(0)$ plane and a smoothed surface of average Q_{DD} obtained. Assuming $Q_{DT}/Q_{DD}\sim 200$, the average experimental Q_{DD} values scale to within a factor$\sim$2 of the equivalent Q_{DT} inferred from $T_i(0)$and $n_D(0)\tau_E T_i(0)$, as expected if the DD reactions are mainly thermal in origin. A significant feature of the data in Fig.6 is the lack of improvement of Q_{DT} equivalent in going to high current; this can be explained in terms of degraded n_D/n_e which offsets the gain in τ_E. The present data has lower performance than the best SNX hot-ion H-modes, which attain Q_{DT} equivalent of $\sim$1 /5/. This is due in part to the improvement in global confinement of the latter over standard H-mode confinement at 3MA by as much as 50%, equalling or exceeding the confinement gain obtained by going from 3 to 5MA in the DNX configuration.

Conclusions Purity of the background (pre-bloom) plasma, and scaling of confinement weaker than linear with current are identified as factors limiting the H-mode fusion yields in the existing JET high current double-null configuration. The H-mode regimes presented here therefore have potential for further development in the JET pumped divertor phase, resulting in at least improved n_D/n_e and possibly better confinement in optimised X-point magnetic configurations designed for currents up to 6MA.

References

/1/ A Tanga *et al*, Proceedings, Symposium on Fusion Engineering, San Diego, CA, USA (1991), p201

/2/ J P Christiansen *et al*, Nucl.Fusion Vol.32 (1992) p291

/3/ T T C Jones *et al*, 16th European Conference on Controlled Fusion and Plasma Physics, Europhys. Conf. Abstracts, Vol.13B Part I (1989), p11

/4/ R J Bickerton, Plasma Physics and Controlled Fusion, Vol.29 No.10A (1987), p1219

/5/ The JET Team, Nuclear Fusion, Vol.32 (1992), p187

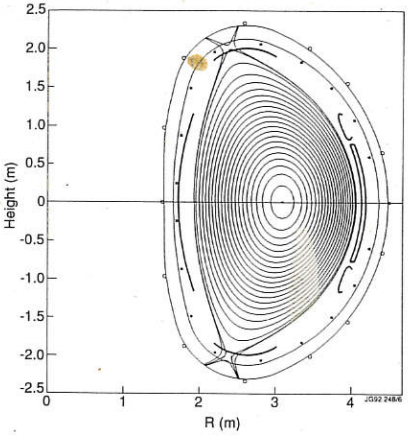

Fig.1 Equilibrium for 5MA DNX discharge using maximum shaping capability in symmetric configuration.

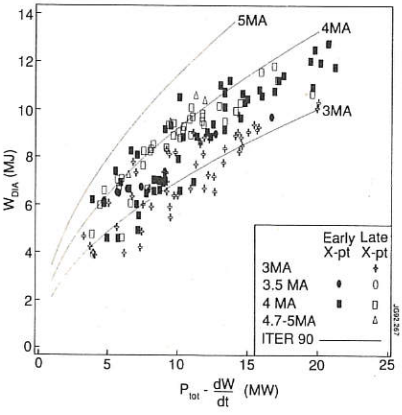

Fig.2 Diamagnetic stored energy versus plasma loss power for 1991-2 DNX H-modes measured during ELM-free periods; solid lines give ITER90-HP scaling.

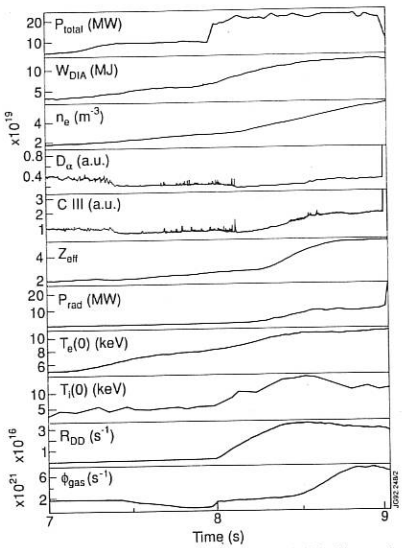

Fig.3 Record stored energy DNX H-mode (#25803, 4MA/2.8T, 14MW D⁰ NBI, 8MW H-min. ICRH, early X-pt. formation). ELM-free, sawtooth-free H-mode terminates on removal of power.

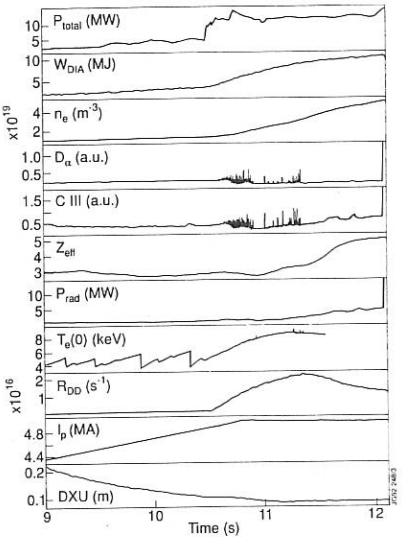

Fig.4 5MA/2.8T DNX H-mode (#27278, 10MW D⁰ NBI, 1.5MW H-min. ICRH) with ELM-free and sawtooth-free phase; H-mode terminates spontaneously. DXU = upper null distance beyond tile surface.

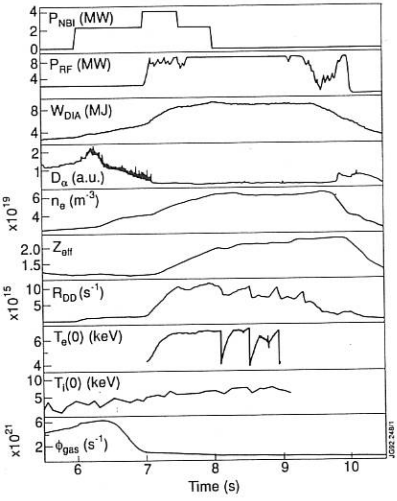

Fig.5 Long duration ELM-free DNX H-mode (#25945, 4MA/2.8T), achieving near stationary conditions.

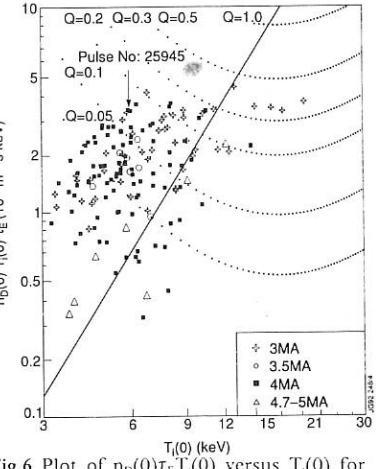

Fig.6 Plot of $n_D(0)\tau_E T_i(0)$ versus $T_i(0)$ for the 1991-2 DNX H-modes. Solid line defines boundary of hot-ion domain ($\tau_{ei}^{eq} \gtrsim \tau_E$). Thermal Q contours assume D:T ratio = 1:1 and stationary conditions, as observed for most points with $T_i \sim T_e$.

Influence of divertor geometry and boronization on ELM-free H-mode confinement in ASDEX

F. Ryter, O.J.W.F. Kardaun, A. Kus, O. Vollmer, U. Stroth, F. Wagner, ASDEX-, NI-Teams

Max-Planck-Institut für Plasmaphysik, EURATOM-IPP Association
D-8046 Garching, FRG

1. Introduction

The confinement desirable to reach ignition in ITER must be improved by a factor of two above the usual L-mode [1]. The H-mode is one of the most promising regimes to reach this goal. It is therefore of importance to identify the conditions that possibly influence the H-mode confinement. In particular, the question was risen whether the divertor configuration might play a role [2]. This question can be addressed in the ASDEX tokamak which went through 3 main divertor configurations [3]. First: the original divertor ("DV-I",1980-1986) a so-called closed divertor for which the by-pass conductance between divertor chamber and main chamber was comparable to the divertor neck conductance. Secondly: an open divertor ("DV-II open",1987-1989) for which the by-pass conductance was clearly larger than the neck conductance. Thirdly and finally: this divertor DV-II was made tight ("DV-II closed",1989-1990) and the conductance was again of the order of that of the divertor neck. During this last experimental period the vessel was boronized whereas the wall conditions were stainless steel for the two other cases. In the open divertor the neutral gas density in the main chamber was higher than in the closed cases. The influence of the configuration was shown in [3] for ELMy discharges: for the open divertor the confinement of such discharges was on the average 30% lower than in the closed case. This was attributed to an increase of the ELM activity possibly linked with the higher neutral density. In ref [3], was also shown that the power threshold for the open divertor was higher than for the closed ones.
A study of the influence of the divertor configuration on the intrinsic H-mode confinement must be performed with ELM-free (H*) discharges analysed under similar conditions to avoid the non-quantified influence of the ELM activity. This is the aim of the present paper.

2. Experimental conditions and analysis

ELM-free discharges in ASDEX required an adequate positioning of the plasma column with respect to the vessel and a heating power above the threshold of ELMy discharges [4]. Under these conditions, ELM-free discharges in ASDEX were fairly reproducible. An example of the type of ELM-free discharges used in the present work is given in Fig.1.

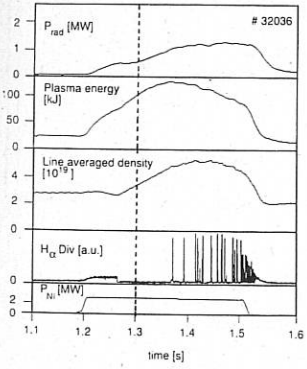

Fig. 1 Time evolution of some signals for an ELM-free discharge: NBI power, H_α in divertor, line density, plasma energy from the diamagnetic loop, volume integrated radiation. The time of the analysis, as described in the text, is indicated by the vertical line.

The ELM-free phase is clearly shown by the H_α signal drop in divertor as well as by the increase of the electron density and of the plasma energy.

Fig. 2 gives the Ip/Bt operational window of the H* discharges analyzed for this paper. Due to the higher power threshold for DV-II open [3], the H* operation was.limited during this period. The available datasets for the three divertor configurations only allow the comparison of hydrogen NBI-heated deuterium plasmas. This introduces a small uncertainty on confinement due to the isotope effect. This error remains small because, although the species concentrations in the plasma core are not precisely known, they are probably reproducible for similar discharges under comparable conditions. This should allow a rather fair comparison of the confinement time for the three divertor configurations.

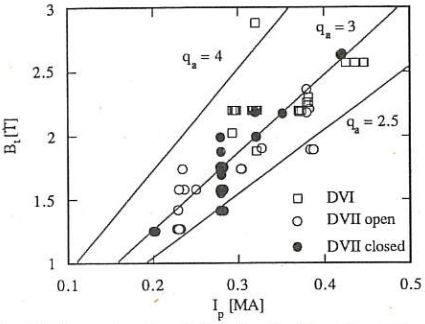

Fig. 2. Operational window for the 3 configurations

The confinement time analysis was performed at the time point where $dW/dt = 0.3\ P_{tot}$. W is the plasma energy, P_{tot} is the total heating power $P_{tot} = P_{OH} + P_{abs}$, with P_{OH} residual Ohmic power and P_{abs} NBI power absorbed by the plasma. The reasons for this choice of the analysis time point are that, at this stage of the discharge, the H-mode is well developed but that the radiation in the plasma core is still small compared to the central heating power. Therefore, the confinement time is practically not affected by radiation losses. Moreover, due to this condition, the confinement time is measured well before the discharges reach the beta limit. These two important conditions would not be fulfilled if the analysis were made at the maximum of the plasma energy.

The confinement time is derived from the diamagnetic loop measurement by the expression: $\tau_E = W_{dia} / P_L$ with $P_L = P_{tot} - dW/dt$. The error on the confinement time is estimated to be ±15%. Under the conditions of the discharges considered here (rather high density), this measurement includes a 10% - 15% contribution due to the of fast beam ions.

3. Results

To get an impression of the experimental reproducibility for comparisons with the following results, we analyzed one series of 28 boronized H* discharges performed consecutively with identical operational machine parameters. The results are given in Fig. 3 which shows the confinement time normalized to the corresponding L-mode scaling presented in [6]. This distribution has a mean value of 1.76 and a standard deviation of 0.04. This means a relative error of 2.3% which is 6 times narrower than the assumed experimental error on τ_E. This estimate from Fig. 3 is an absolutely lowest value of the experimental error. It does not include any systematical error or changes with plasma and machine conditions from day to day over a long period of time, as it is based on a small number of homogeneous discharges.

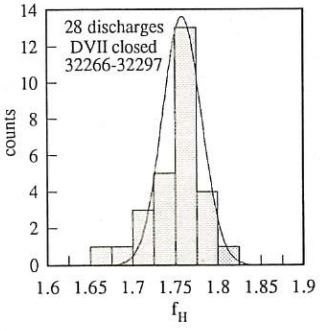

Fig. 3. Statistical distribution of the normalized confinement time.

A good visualisation of the influence of the divertor configuration is provided by the confinement quality factor, τ_E/I_p, plotted versus P_L in Fig. 4.

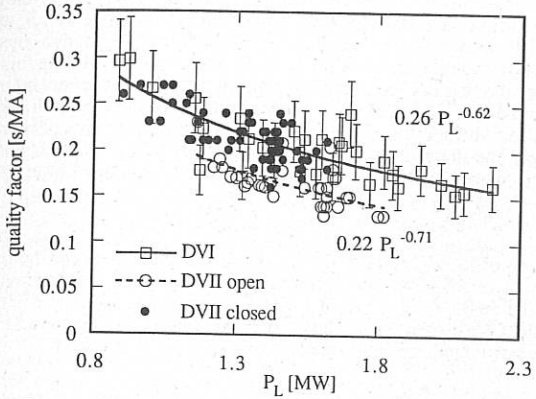

Fig. 4. Quality factor, τ_E/I_p, for the 3 divertor configurations. The lines indicate the fits versus power. The individual fits for the closed versions are so similar that only that of DV-I is given.

The two closed versions have the same quality factor and the same power dependence: $\tau_E/Ip = 0.26\ P_L^{-0.62}$. The lack of points with $P_L > 1.7$ for DV-II closed is due to the limited available NBI power during this period. The quality factor for DV-II open is systematically 15-20% lower than the closed versions and has a somewhat stronger power dependence: $\tau_E/Ip = 0.22\ P_L^{-0.71}$. The difference between closed and open configurations is only slightly larger than the measurement errors (±15%). The change due to the open configuration for these ELM-free discharges is however about half of that for the ELMy discharges [3], in agreement with the hypothesis [3] of an increased ELM degradation of confinement with the open divertor. It must be noticed, as shown by Fig. 4, that the boronization (DV-II closed) did not improve the confinement time as it did for DIII-D with the VH-mode [7]. The change of the confinement time with divertor configuration is not a particular feature of the H-mode. In fact the L-mode study described in [6] shows similar effects. Normalizing the H-mode confinement during the

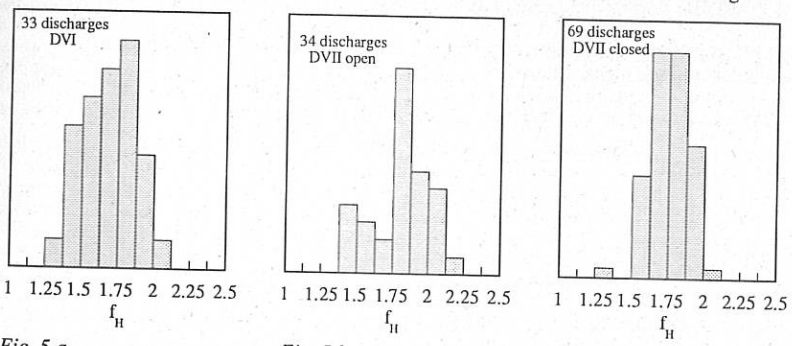

Fig. 5 a. *Fig. 5 b.* *Fig. 5 c.*

Statistical distribution of the normalized confinement time for the 3 configurations.

three periods with the corresponding expressions for the L-mode taken from [6] gives the H-mode enhancement factor relative to the ASDEX L-mode. The results are given in Fig. 5 a-c. For each of the 3 periods, the mean enhancement factor is between 1.7 and 1.8. The degradation for DV-II open is comparable for the L and H mode as shown by Fig. 5 b. As indicated in [6], the power degradation for the L-mode is also stronger during this period. This common behaviour of the H and L mode confinement suggests a global effect on transport. The broader spectrum found for DV-I is due to a larger scattering of the data both for the L and H mode. It is not yet clear whether this scattering is due to the measurements or is actually due to confinement changes. The shape of the distribution for the DV-II open case is possibly related to the restricted H-mode accessibility during this period due to the higher power threshold.

4. Conclusion

The confinement time of ELM-free H-mode phases have been studied for the three different divertor configurations of ASDEX. The results are believed to represent the behaviour of the intrinsic H-mode confinement. They indicate that the open version had a 15% to 20% lower confinement time than the closed ones. This affects both the H and L mode as shown in [6] such that the enhancement factor remains roughly constant.

Acknowledgement

The efforts of the technical and experimental teams are greatly acknowledged.

References

[1] D. E. Post, et al., ITER Physics, ITER Documentation Series No. 21, International Atomic Energy Agency, Vienna, 1991.

[2] J. P. Christiansen, et al, Nucl. Fus. **32** 291 (1992)

[3] F. Wagner, et al., proceedings of the 13th IAEA Int. Conf. on Plasma Physics and Controlled Nuclear Fusion, Washington DC, 1-6 October 1990, Vol.1, 277, (Vienna 1991)

[4] F. Ryter, et al., H-mode power threshold in ASDEX, this conference

[5] ASDEX Team, Nucl. Fus. **29** 1959 (1989)

[6] U. Stroth, et al., Confinement scaling for the ASDEX L-mode in different divertor configurations, this conference

[7] G. L. Jackson, et al. Phys. rev. Lett. **67** 3098 (1991)

VH–MODE DISCHARGES IN THE DIII–D TOKAMAK*

C.M. GREENFIELD, G.L. JACKSON, K.H. BURRELL, J.C. DEBOO, L.L. LAO, T.H. OSBORNE, C. RETTIG,† D.P. SCHISSEL, T.S. TAYLOR, J. WINTER‡

General Atomics, San Diego, California, USA

Introduction. A regime of very high confinement (VH–mode) has been observed in divertor discharges in DIII–D.[1] The VH–mode, first seen following the initial boronization of the DIII–D vessel[2] in 1991, exhibits total energy confinement a factor of 2.5 to 3.5 greater than that predicted by the ITER89-P L–mode scaling relation.[3] Also, confinement of thermal energy alone is greater than 1.6 times that of the JET/DIII–D H–mode scaling[4] and in many cases has exceeded twice that amount.

VH–mode is observed during a long ($\leq$0.8 sec) ELM-free phase of the discharges. At the beginning of the ELM-free period, the plasma appears to be in H–mode, with confinement near that predicted by the JET/DIII–D scaling. In the usual H–mode, confinement is observed to decrease or remain constant over time. In the present discharges, confinement has been observed to remain nearly constant for up to hundreds of milliseconds, after which the behavior sharply deviates from H–mode as the confinement begins to increase over time (Fig. 1). This increase in confinement continues until the occurrence of a beta-related ($\beta > 2.8\,\mathrm{I/aB}$) global MHD event, which rapidly decreases the plasma stored energy with a temperature reduction across the entire profile. Magnetic measurements indicate that at least in some cases, this event includes both an internal $n = 1$ mode and a more localized $high - n$ mode near the edge. After this event, the plasma relaxes into an ELMing H–mode phase.

As a consequence of the boronization, the plasmas in these discharges are unusually clean, with very low radiated power ($P_{\mathrm{rad}}/P_{\mathrm{aux}} \leq 0.25$). In previous H–mode discharges, the radiated power increased during the ELM-free phase, sometimes reaching levels comparable with the input power if the ELM-free period was long enough. Also, Z_{eff} is constant or decreasing over the length of the discharge, with a central value of $\approx$1. It is noted that most of the energy in these discharges is thermal energy, with $\leq$10% contained in fast ions.

We have obtained VH–mode over a wide range of conditions on several different occasions. In all cases, boronization of the vessel was required. Most of the VH–mode discharges to date have been double-null divertor configurations, although we have also been able to achieve VH–mode in a single-null configuration with high triangularity (shape similar to double-null, but biased toward the lower null). VH–mode has been obtained at plasma currents of 1 to 2 MA, with toroidal fields of 1.6 to 2.1 T and moderate to high (4–16 MW) neutral beam power. Low ohmic target density ($\approx 3\times10^{19}\,\mathrm{m}^{-3}$ with $I_P = 1.6$ MA) is found to be essential. Discharges with higher target densities result in the early onset of ELMs, which limit the time available for the development of VH–mode. Although the data set is insufficient to determine how confinement scales with plasma current, it is consistent with a linear scaling.

Internal Features of VH–mode. The high confinement of the VH–mode is seen to coincide with the broadening of the steep temperature-gradient region of both the ions and electrons in the outer portion of the plasma. The radial electric field shear region seen in H–mode broadens, corresponding to a decrease in turbulence. The current profile also shows a unique feature: modeling indicates that a region of high current density develops near the plasma edge, which is caused by a large bootstrap current. This is believed to be associated with the access of the outer portion of the plasma volume to the second regime of ballooning stability.

* This is a report of work sponsored by the U.S. Department of Energy under Contract No. DE-AC03-89ER51114.

† University of California, Los Angeles, California, USA

‡ Kernforschungsanlage GmbH, Jülich, Germany

The transition from the L–mode to H–mode in these discharges looks quite similar to that seen previously.[5–8] Within 100 μs of the transition, density fluctuations decrease inside the separatrix ($\rho > 0.9$); as shown by reflectometer and FIR scattering measurements; within 1 msec of the transition, a shear in the electric field develops in this region (both time scales above represent the temporal resolution of the measurement). Over the next few tens of milliseconds, the FIR scattering shows a decrease of about a factor of 2 in the amplitude of the density fluctuations in the bulk of the plasma around $\rho = 0.8$, similar to that seen previously.[7]

When the VH–mode develops out of the H–mode in the present discharges, the electric field shear region is seen to broaden and move deeper into the plasma (Fig. 2). Although the data are incomplete, indications are that the density fluctuations in the region $0.7 < \rho < 0.9$ decrease further by a factor of about 2.

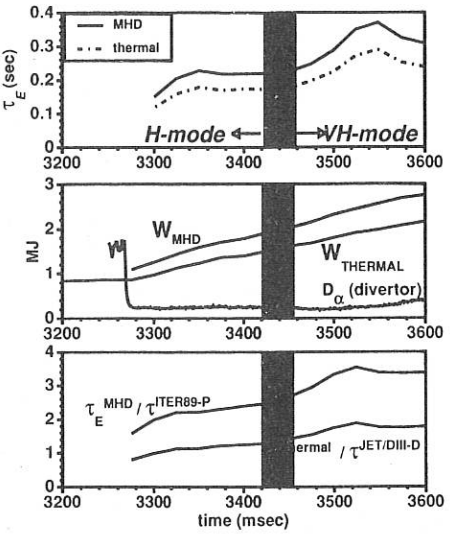

FIG. 1. Time traces of a double-null divertor discharge which evolves from H– to VH–mode. Shaded region denotes transition from H– to VH–mode. Shot 72220, $I_p = 1.6$ MA, $B_T = 2.1$ T, $P_{NBI} = 12.5$ MW.

Examination of ion (from CER) and electron (from Thomson scattering) temperature profiles during the ELM-free phase (Fig. 3) shows that the steep gradient regions seen near the edge in H–mode continue to extend deeper into the plasma during the transition to VH–mode. Whether this effect is strongest for the ions or electrons varies somewhat from shot-to-shot. The density profiles (Fig. 3) develop in a way that is roughly consistent with "normal" H–mode, with the usual increase of density over time.

Time-dependent transport analysis using the ONETWO[9] code shows that the single-fluid diffusivity χ_{eff} during the early (H–mode) phase of the ELM-free period is approximately the values previously obtained for H–mode discharges with similar parameters. At the time of the sudden increase in confinement, however, χ_{eff} decreases sharply, by as much as a factor of 2 to 4 (Fig. 3), most notably in the region $0.5 \leq \rho < 0.9$ with little change in convection or other power balance terms. Note that the region of largest decrease in χ_{eff} corresponds to the region of increased electric field shear. Accordingly, one possible explanation for the VH–mode confinement improvement is electric field shear stabilization of turbulence. The VH–mode bulk confinement improvement would then be a further extension of the bulk confinement improvement seen in H–mode.[8,10]

Bootstrap Current and Implications. As previously mentioned, after boronization, we find that DIII–D discharges have low radiated power, low neutral density and low recycling. These conditions lead to rather low $n_e(a)$ and high $T_e(a)$, and therefore low collisionality ($\nu^* \approx 0.6$ at $\rho = 0.9$). This combined with the high pressure gradient seen in H–mode make the conditions ideal for production of a large bootstrap current near the edge.

Modeling with the ONETWO code reproduces this high edge bootstrap current (Fig. 4). The resulting current profile shape is consistent with the results of modeling the equilibrium with the EFITD[11] code. Although it is possible to generate an equilibrium from the magnetics data which does not contain the bump in the current profile, the best fit (lowest χ^2) is obtained when this feature is included.

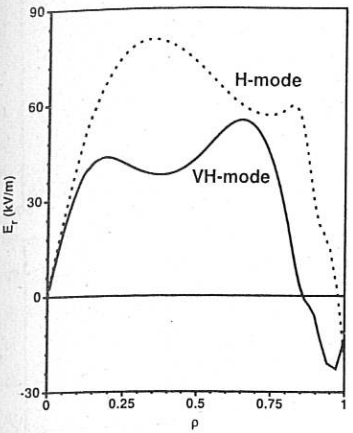

FIG. 2. The radial electric field shear region is both broadened and pushed deeper into the plasma during VH–mode. Shot 73290, I_p = 1.6 MA, B_T = 2.1 T, $P_{\rm NBI}$ = 10.6 MW.

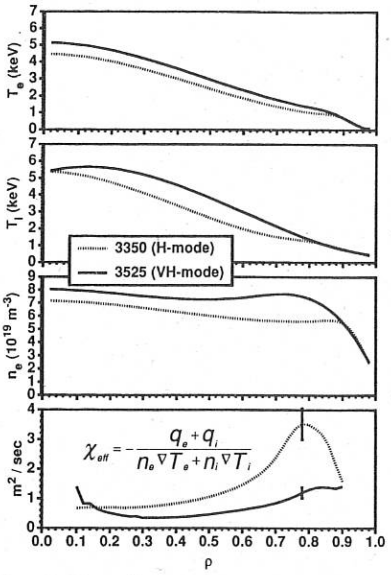

FIG. 3. The profiles of the VH–mode contain steep gradient regions which are extended further inward than those in H–mode. Transport analysis shows that this corresponds to a decrease in the single-fluid diffusivity, most notably in the outer half of the plasma. Shot 72220, I_p = 1.6 MA, B_T = 2.1 T, $P_{\rm NBI}$ = 12.5 MW.

This large edge current produces low shear, which in this high triangularity plasma configuration, is associated with possible access to the second regime of stability to ballooning modes.[12] In the VH–mode discharges studied, it appears that access to second stability may be correlated with the improvement in confinement.

In Fig. 4, we see that the confinement begins to improve after the bootstrap current has begun to increase. The MBC code[13] predicts that when the bootstrap current at $\rho = 0.85$ reaches 50 A/cm^2, 30% of the plasma volume will have entered the second stable regime to ideal ballooning modes. Note that this calculation requires the edge current density to be known with greater accuracy than is available, so this result is qualitative. However, for any reasonable value of edge current density, the MBC code prediction is similar. With the assumption of zero current density at the plasma edge, the (first) marginal stability pressure gradient is below the measured pressure gradient.

Conclusions. We have observed a regime of very high confinement (VH–mode) in the boronized DIII–D tokamak, during which the confinement has been observed to exceed 3.5 times that of the ITER89-P L–mode scaling relation. In this ELM-free phase, confinement is seen to increase with time, and is terminated by a global MHD event which is associated with high β. Low radiated power, $Z_{\rm eff}$, and a low fast-ion fraction are also characteristics of the VH–mode.

In the VH–mode, we observe that the steep gradient regions of the temperature profiles are extended inwards more deeply than previously seen in H–mode. This high-gradient region is also seen to correspond to an extended radial electric field shear layer, and a decrease in density fluctuations of perhaps a factor of two below H–mode. Transport calculations in this region show a sharp decrease in the single-fluid heat diffusivity.

Another remarkable feature of these plasmas is the existence of a region near the plasma boundary with high bootstrap current, which modeling predicts to correspond with a significant fraction of the plasma volume accessing the second regime of ballooning stability.

Although a causal relationship has not been established between these characteristics, it is believed that both the electric field shear stabilization of turbulence and the second stability access play important parts in the observed confinement improvement. Further experimentation and analysis is expected to shed some light on these issues.

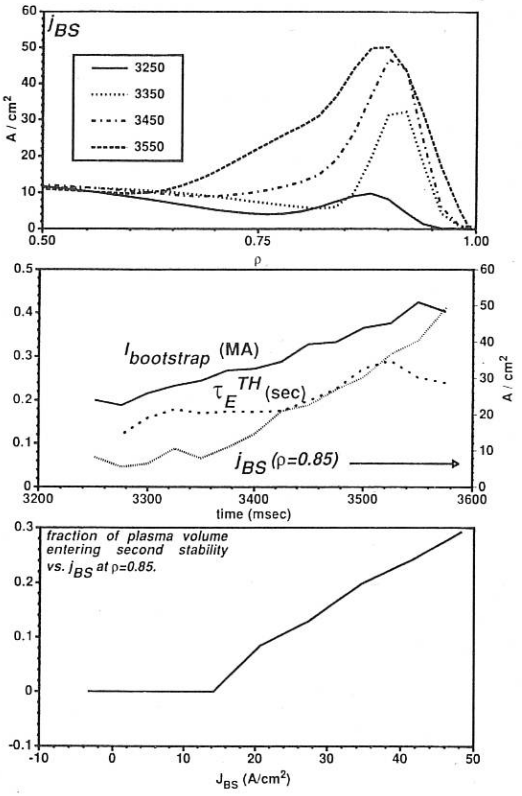

FIG. 4. As the plasma evolves from H- to VH-mode, the calculated bootstrap current increases near the edge. Modeling using the MBC code predicts that a large portion of the plasma volume is entering the second stability regime. Shot 72220, $I_p = 1.6$ MA, $B_T = 2.1$ T, $P_{NBI} = 12.5$ MW.

REFERENCES

1. Jackson, G.L., *et al.*, Phys. Rev. Lett. **67**, (1991) 3098.
2. Phillips, J.P., *et al.*, to be published in J. Vac. Sci. Tech. (1992).
3. Yushmanov, P.N., *et al.* Nucl. Fusion **30**, (1990) 1999.
4. Schissel, D.P., *et al.* Nucl. Fusion **31**, (1991) 73.
5. Burrell, K.H., *et al.* Phys. Fluids B **2**, (1990) 1405.
6. Groebner, R.J., *et al.* Plasma Physics and Controlled Nucl. Fusion Research 1990 (IAEA, Vienna, 1991), Vol. 1, p. 453.
7. Doyle, E.J., *et al.* Phys. Fluids B **3**, (1991) 2300.
8. Kurki-Suonio, T., *et al.* Nucl. Fusion **32**, (1992) 133.
9. Pfeiffer, W., *et al.* Nucl. Fusion **25**, (1985) 655.
10. Burrell, K.H., *et al.* Plasma Physics and Controlled Nucl. Fusion Research 1990 (IAEA, Vienna, 1991), Vol. 1, p. 123.
11. Lao, L.L., *et al.* Nucl. Fusion **30**, (1990) 1035.
12. Bishop, C.M., Nucl. Fusion **26**, (1986) 1063.
13. Moore, R.W., General Atomics Report GA-A16243 (1981).

CURRENT SCALING OF PLASMA CONFINEMENT

J.P. Christiansen, C. Challis, J.G. Cordey, C. Gormezzano, C. Gowers, G. Kramer, J. O'Rourke, A. Taroni, F. Tibone, B. Tubbing, P.M. Stubberfield,
JET Joint Undertaking, Abingdon, Oxon, OX14 3EA, U.K.

1. Introduction

The dependence of global confinement properties in a Tokamak upon global plasma parameters has been well established empirically and is often represented by for example the ITER89P scaling law for L-mode plasmas /1/

$$\tau_E = 0.048\ a^{0.3}\ R^{1.2}\ n^{0.1}\ I_\phi^{0.85}\ B_\phi^{0.2}\ P^{-0.5}\ \kappa^{0.5}\ A^{0.5} \qquad (1)$$

τ_E is the confinement time which scales with respectively minor-major radius, density, current, field, power, plasma elongation and ion mass. The dependence of local confinement, the local thermal diffusivity χ, upon local values of representation plasma parameters, i.e.

$$\chi = \chi\left(x, n, B_p, s, B_\phi, T, \kappa, A, L_j,\right) \qquad (2)$$

is however not very well known; in (2) x is a flux surface label, $0 \le x \le 1$, B_p the poloidal field, T the temperature, s the shear and L_j denotes scale lengths like $(\nabla n/n)^{-1}$. The scalings of (1) that are best determined are those with I_ϕ, n and P; the origin of such scalings must arise from the B_p, s, n, T and L_j scalings of χ. This can be seen from the relation derived by Callen et al /2/

$$\tau_E = \frac{W_1}{P} + \frac{1}{P}\int_o^1 \frac{3}{2} N(x)\ \frac{P(x)\,dx}{n(x)V' < |\nabla x|^2 > \chi} \qquad (3)$$

where $W_1 = \frac{3}{2}$ e N(x = 1) T(x = 1) and N(x) is the total particle inventory up to radius x with $n(x) = n_e(x) + n_i(x)$; the effective diffusivity χ is calculated from

$$\chi = \frac{P(x)}{eV' < |\nabla x|^2 > \left(n_e T_e' + n_i T_i'\right)} \qquad (4)$$

V and P(x) are the total volume and power inside a flux surface x and the prime denotes a derivative w.r.t. x while the angular bracket represent a flux surface average.

Several authors claim to be able to explain the B_p, n, T, L_j dependence of χ required to yield the scaling (1). In this paper we examine the link between the scaling with I_ϕ of (1) and those with B_p, L_j of (2). The study is based on data from a series of experiments on JET in which all global parameters of (1) are held constant except for I_ϕ which is ramped up or down by a factor 2. The ramping of total current during the time τ_{RAMP} decorrelates I_ϕ from the steady state profile shape of the current density J_ϕ over a period of many confinement times since

$$\tau_E < \tau_{RAMP} < \tau_\eta \qquad (5)$$

Typical values for JET are $\tau_\eta \approx 5$ sec, $\tau_{RAMP} \approx 2$ sec, $\tau_E \approx 0.2$ - 0.5 sec. The ramp is needed to investigate if the origin of the I_ϕ scaling of τ_E is purely due to a B_p dependence of χ or if shear is important.

The JET diagnostic measurements are used in TRANSP calculations and a set of consistency checks are made. Such checks include cross-correlations of data on loop volts, diamagnetic energy, polarimetry, interferometry and soft x-rays /3/. An example of a consistency check is given by Fig. 1 showing the evolution of q_ψ at three radlii as calculated by TRANSP and as inferred from polarimetry data. The diffusivity χ is calculated from (4); T_i (x) is calculated by assuming $\chi_i = \alpha\,\chi$ (Neoclassical) α being determined by T_i (x = 0) from the x-ray crystal spectrometer. The TRANSP calculations show that the resistive field diffusion during the current ramp with a neoclassical resistivity provides a good description of the data.

2. Global confinement

Data from 8 ramp up or down pulses and 2 reference pulses with no ramps is analysed. Fig. 2 shows the time evolution of stored energy W for 4 pulses: I = 1.5. MA, 3 MA 1.5 ramped up to 3 MA and 3 MA ramped down to 1.5 MA. W evolves on the resistive diffusion timescale τ_n and not on the ramp timescale τ_{RAMP}. AT t = 10s W ≈ 3 MJ for I_ϕ = 1.5 and 3 MA: W does therefore not depend on I_ϕ alone but also on some measure of the J_ϕ shape, e.g. internal inductance ℓ_i. Data fitting to: log W = log C + z_n log n + z_I log I_ϕ + z_p log P + z_ℓ log ℓ_i yields

$$W = C\left(\ell_i\, I_\phi^2\right)^{2/3} \qquad (6)$$

3. Local transport

Ramping I_ϕ causes changes to B_p to propagate inwards from the edge where the applied voltage changes during the ramp as shown in Fig. 3 with $\Delta B_p/\Delta B_{pmax}$ vs time traces at three

radii. The changes propagate (by resistive diffusion) faster for the ramp up than for the ramp down pulse, the latter starting from a higher T_e in the outside region. To demonstrate that no "action at a distance" model needs to be invoked we show in Fig. 4 $\Delta\chi/(\Delta\chi_{max})$ vs time for $x = 0.55, 0.65, 0.75$. The changes $\Delta\chi$ start at $x = 0.75$ some 2 sec. before they reach $x = 0.55$. Therefore χ is linked to the resistive field diffusion, i.e B_p, q or shear s. Since this particular JET data does not determine the n or T dependence of χ, the well known "bowl-shape" of the χ (x) profile cannot be described either; this is because density and power are kept constant. We therefore represent at each radius x the diffusivity by $\chi_{model} = \chi_o C_\chi s^\mu q_\psi^\lambda$. A fit of the data on χ to χ_{model} serves to determine the dimensionless parameters C_χ, μ and λ at each radius. While C_χ describes the "bowl shape" itself we choose the diffusivity χ_o as either the Bohm ($\chi \sim T/B_p$) or gyro-Bohm ($\chi \sim T^{3/2}/B_p^2$) forms. For both forms we find some shear dependence in the outer region. A regression analysis on the data gives the following result if we take into account that both χ_o, s and q_ψ depend on B_p

$$\chi \sim B_p^y s^\mu \quad , \quad -2 < y < -1 \quad , \quad -1 < \mu < 0 \quad . \qquad (7)$$

4. Summary

The JET current ramp experiments decorrelates, at constant plasma parameters n, B_ϕ etc, the current I_ϕ from its shape J_ϕ. The global and local scalings Eqs. (6) and (7) are fully consistent. This can be seen by inserting (7) in (3) assuming $P'(x) = P\delta(x)$, $n = n_o$. For $y = 1$ or - 2 Eq. (3) gives $\tau_E \sim h_i I_\phi$ or $l_i I_\phi^2$ respectively. Since $\chi = \chi(B_p)$, Eq. (3) shows that τ_E depends on some integral involving B_p, e.g. the internal inductance ℓ_i or the flux inductance h_i.

References

/1/ P.N. Yushmanov, et al., Nucl. Fusion 30, 1999 (1990)

/2/ J.D. Callen, et al, Nucl. Fusion 27, 1857 (1987)

/3/ C.D. Challis, et al., Current ramp experiments on the scaling of Energy confinement, JET-Preprint, subm. to Nucl. Fusion.

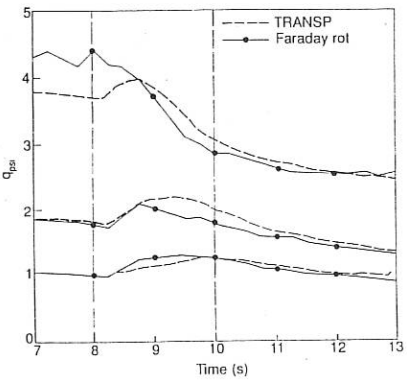

Fig. 1 Safety factor at 3 radii by TRANSP agrees with values from polarimetry data

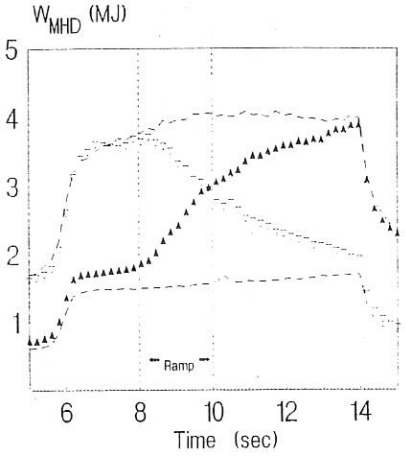

Fig. 2 Evolution of stored energy at constant 1.5 and 3 MA and ramp up-down from 1.5 to 3 MA

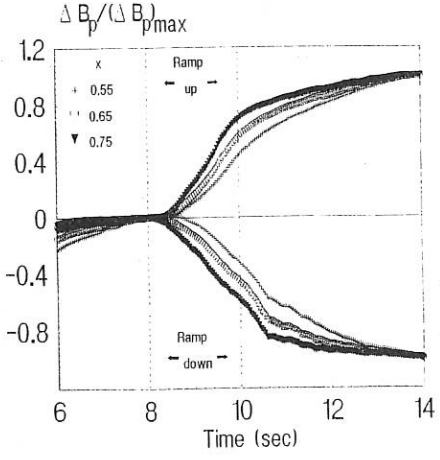

Fig. 3 Changes to B_p during ramp up-down at 3 radii

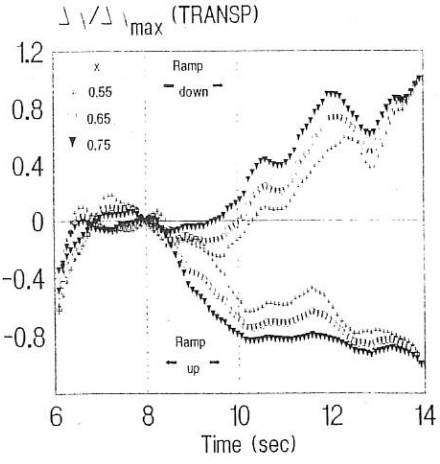

Fig. 4 Changes to χ at 3 radii follow resistive field diffusion

DEPENDENCE OF CONFINEMENT ON PLASMA ION SPECIES IN JET

F. Tibone, B. Balet, M. Bures, J. G. Cordey, T. C. C. Jones, P. J. Lomas, K. Lawson, H. W. Morsi, P. Nielsen, D. F. Start, A. Tanga, A. Taroni, K. Thomsen, D. J. Ward
JET Joint Undertaking, Abingdon Oxon OX14 3EA, UK.

In a recent experiment in JET the composition of both the target plasma and the injected neutral beams (NB) has been varied to investigate the dependence of confinement on ion species. Hydrogen, deuterium and helium-3 were used in limiter discharges (with plasma current of 3 MA, toroidal field of 3 T and elongation 1.4 - 1.5) with several seconds of NB heating, leading to stationary sawtoothing L-mode plasmas. In hydrogen and helium plasmas, the residual concentration of deuterium was measured to be $\leq 10\%$.

The auxiliary power for hydrogen NB injection, was limited to ≤ 7 MW. We compare here hydrogen and deuterium data for a density scan with $P_{NB} \simeq 6.0 \pm 0.5$ MW. In these discharges the electron density profile remains approximately constant during the heating, in the absence of external gas puff. Its shape is - regardless of the ion species - parabolic at low density and becomes less peaked at high density. The effective ionic charge varies over the density range from 3.0 to 1.5, with marginally better plasma purity in deuterium. Both Ohmic power and power lost by radiation are ~ 20 - 30% of the total input; the fraction does not change systematically with the isotope used.

The NB power deposition profiles on electrons and ions, as modelled using either the PENCIL or the TRANSP code, are the same to within 10% for hydrogen and deuterium at any given density. The particle source also has a similar radial distribution, but is stronger in hydrogen than in deuterium, as a result of the lower injection energy and of the higher proportion of input power in the fractional energy components.

The time evolution of a pulse in deuterium (140 keV $D^\circ \rightarrow D^+$) is compared with that of a similar pulse in hydrogen (100 keV $H^\circ \rightarrow H^+$) in Figure 1. The total diamagnetic energy content is 15 - 20% larger in deuterium. A similar difference is observed in the measured electron temperature profile, at all radii. The central T_e signal in Figure 1 shows that the sawtooth period is very sensitive to the change in ion species , with major internal disruptions occurring twice as frequently for the lighter isotope.

In order to highlight systematic differences in global and local energy confinement, hydrogen and deuterium plasmas have been analysed using the same diagnostic signals and modelling assumptions. Data from microwave interferometry and electron cyclotron emission are used for electron density and temperature profiles. Ion temperature profile measurements in the deuterium discharges show that $T_i \simeq T_e$ within 10% at all radii, which is

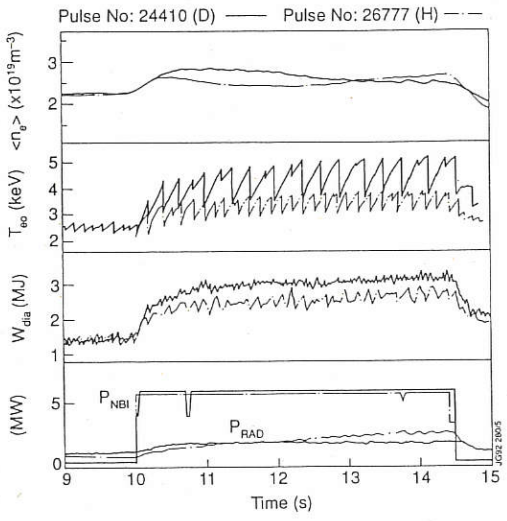

Figure 1

consistent with the independent measurements of D-D neutron yield and energy content. For the hydrogen plasmas, where the T_i profile measurement is not available, we have also assumed $T_i \simeq T_e$. This is equivalent to assuming that heat losses through the ion channel are at least as important as through the electron channel. Z_{eff} is assumed to be radially uniform, and equal to the average value inferred from a vertical visible Bremsstrahlung measurement; together with the measured T_e, this is found to be consistent with the measured loop voltage and neoclassical resistivity. The radiative power loss is assumed to take place predominantly in the vicinity of the plasma edge.

Figure 2

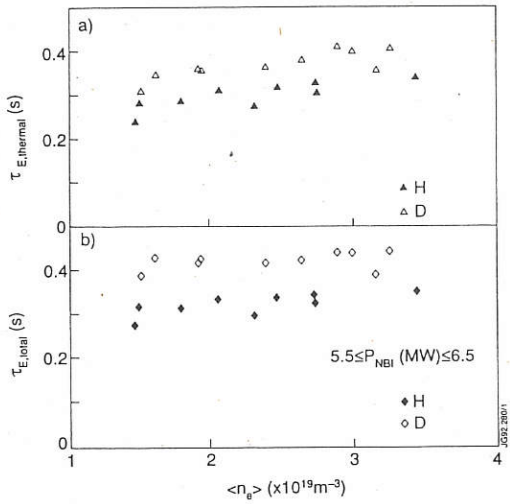

The behaviour of the inferred kinetic energy replacement time is shown in Figure 2a for the L-mode density scan, indicating an average improvement ~ 15 - 20% when going from hydrogen to deuterium. A similar result is found with Ohmic heating only, but this result is less firm owing to larger uncertainties in the determination of W_{kin} and P_{OH}. With NB heating, the improvement in deuterium is larger if one considers the

total energy replacement time, including the non-thermal part of the energy as estimated by the PENCIL code (Figure 2b). Note that the increase in fast ion energy with isotope mass might also be responsible for the change in sawtooth behaviour.

Particle confinement is significantly worse in hydrogen than in deuterium, since similar density profiles are sustained in spite of stronger beam fuelling, Figure 3 shows the electron confinement time $\tau_p \equiv \int n_e dV / \Gamma_e$ where Γ_e is the local electron flux, for a radial position well outside the region affected by sawteeth. An "effective" diffusion coefficient for the electrons, defined as ratio of local particle flux to density gradient, is found to be 50% larger in hydrogen than in deuterium. Correspondingly, the convective contribution to the local heat loss is systematically larger in H^+, accounting throughout the plasma for ~ 20% of the total heat flux (as opposed to ~ 10% in D^+). In Figure 4 a one-fluid thermal conductivity defined as $\chi_{eff} \equiv -(q_{tot} - 3/2\Gamma_{tot}T_e)/[(n_e + n_i)\nabla T_e]$ is plotted as a function of the average input power per particle, at two different radial positions. This transport coefficient is only marginally - if at all -

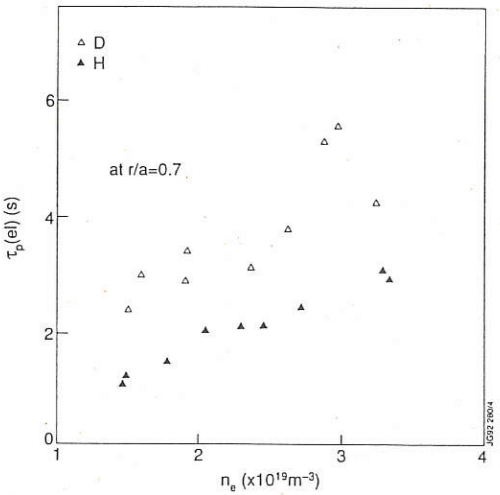

Figure 3

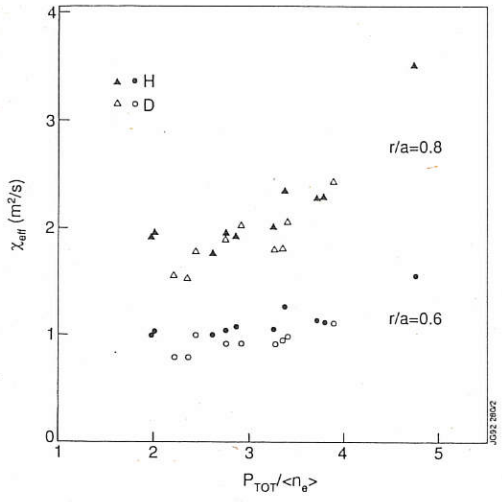

Figure 4

larger in hydrogen than in deuterium. The difference in global confinement in Figure 2a appears therefore to be due at least as much to the change in particle confinement as to a change in conductive energy transport.

The comparison between confinement in deuterium and helium-3 is based on a series of discharges at higher density, with additional NB power up to 12 MW and an injection energy ~ 140 keV for both ion species. The helium plasmas have 10% larger volume, lower impurity content and a larger fraction of the auxiliary power heating the electrons. As shown in Figure 5, no significant difference is observed in the estimated thermal energy replacement time; inclusion of the fast ion energy would again make the total confinement in deuterium marginally better. There is no clear evidence for a difference in particle confinement. The one-fluid effective thermal conductivity is inferred to be ~ 20% larger in the outer region of the He^3 plasmas, where more power has to be conducted away because of significantly lower radiative losses.

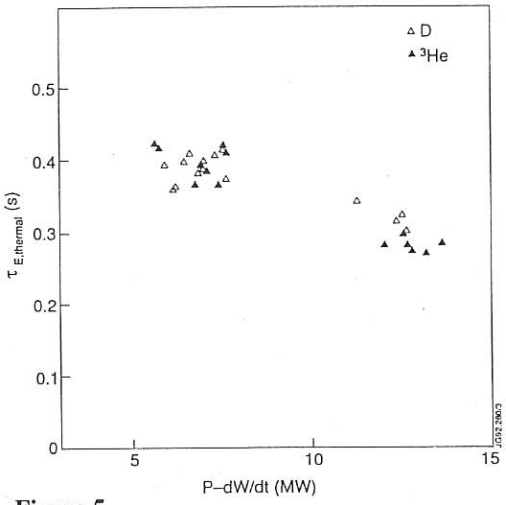

Figure 5

In summary, observations in JET point to a weak dependence of thermal energy confinement on the ion species used, and do not support the hypothesis of a scaling of τ_E with the square root of the ion mass. In hydrogenic plasmas, particle confinement and sawtooth activity display the strongest isotopic dependence. Their effect on the energy balance, together with the increased fast ion population and possibly a modest decrease in conductive heat transport, seem to account for the observed improvement ~20% in energy confinement from hydrogen to deuterium.

ENERGY CONFINEMENT OF FTU OHMIC PLASMA

F. Alladio, F. Berton*, G. Bracco, P. Buratti, O. Tudisco and FTU team, A. Bruschi**, F. De Luca+, A. Jacchia**, P. Mantica**
Associazione EURATOM-ENEA sulla Fusione, Centro Ricerche Energia Frascati, C.P. 65 - 00044, Frascati, Rome (Italy)

Introduction

FTU (a=0.3 m, R=0.93 m) has been operated in a wide range of the plasma parameters /1/: line averaged density n_e ($2x10^{19}$: $2.5x10^{20}$ m^{-3}) magnetic field B_t (4:8 T), plasma current I_p (0.2:1 MA) and hydrogen, deuterium and helium as working gases. Most of the performed plasma discharges are included in a subset of the operation space defined as ne ($2x10^{19}$:$1.5x10^{20}$ m^{-3}), B_t=6 T magnetic field, I_p (0.35:0.75.MA), hydrogen and deuterium. FTU operates with a stainless steel wall and an inconel limiter.

Plasma energy content has been evaluated making use both of the kinetic and magnetic measurements. Plasma geometry is obtained as the reconstruction of the plasma equilibrium from the data the magnetic diagnostics. The electron temperature T_e has been measured by ECE analysis and the n_e profile is reconstructed using the equilibrium geometry and data from a 5 points DCN interferometer. Diamagnetic energy and equilibrium beta are also available. Z_{eff} is measured by an array of bremsstrahlung radiation detectors. Passive NPA and neutrons provide informations on the peak ion temperature T_i while the T_i profile is computed by solving the ion energy balance equation as in /2/. A database containing the confinement results for 500 plasma pulses has been prepared, choosing the most stationary conditions of each discharge.

The most striking feature of FTU plasma is the variety of the ne profiles which can be divided in two classes: flat profiles ($n_{eo}/\langle n_e\rangle$ between 1.2 and 2, becoming flatter at high n_e) and peaked profiles ($n_{eo}/\langle n_e\rangle$ between 2 and 3 irrespectively of the n_e value). T_e profiles /3/ are in close agreement with the peaking factor expected using Spitzer resistivity and the assumption that the safety factor q on axis is 1 ($q_a=T_{eo}^{1.5}/\langle T_e^{1.5}\rangle$). The volume averaged T_e scales as $\langle T_e\rangle \approx I_p^{1.2}\, n_e^{-0.6}$ (hydrogen values are 30% lower than deuterium or helium). Z_{eff} from plasma resistivity without neoclassical corrections is in agreement with Z_{eff} from bremsstrahlung measurement /4/. Z_{eff} depends on n_e and ohmic power P_{oh} as $Z_{eff}\approx P_{oh}/\langle n_e\rangle$ and at low currents it attains the values Z_{eff} =1÷2 while at high current $Z_{eff}>3$. T_i from NPA is in agreement with the neoclassical prediction (error bars ±15%). For deuterium plasma the experimental neutron flux is typically a factor 2 lower than the neoclassical prediction. This difference can be explained by the deuterium dilution both due to low Z impurity and hydrogen contamination. P_{oh} ranges from 0.5 MW at low current to 2 MW at high currents with a small n_e dependence. Plasma energy content W scales as $W\approx I_p\, n_e^{0.6}$ (H and He data are 20% lower than deuterium).

Confinement Results

In Fig. 1a,b the confinement time τ_E as a function of n_e is shown respectively for deuterium, helium and hydrogen plasma. The scaling of τ_E with the ion species in FTU is similar to FT /2/ while the τ_E dependence on n_e shows that the saturation of the τ_E increase with n_e takes place at n_e= 5×10^{19} m^{-3}, while FT value was n_e=10^{20} m^{-3}. In the analysis of FT data /2/ it was pointed out that τ_E saturation took place at the same n_e at which T_i=T_e, Z_{eff}=1 and at which the sawtooth period τ_{ST} saturated. FTU

* ENEA Fellow
** Istituto di Fisica del Plasma, Associazione EURATOM-ENEA-CNR, Milano, Italy
+ Dipartimento di Fisica, Universita' degli Studi di Milano, Milano, Italy

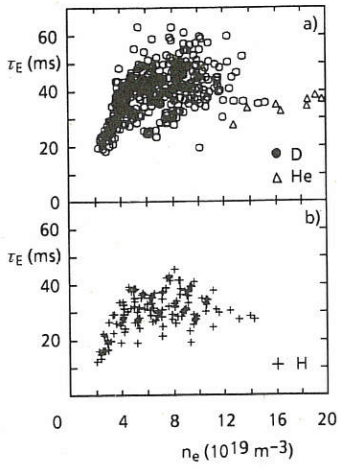

Fig 1: Energy confinement time vs line averaged density a) D,He b) H

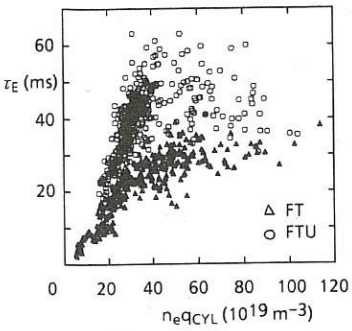

Fig 2: Energy confinement time vs $n_e q$ for FT and FTU (deuterium)

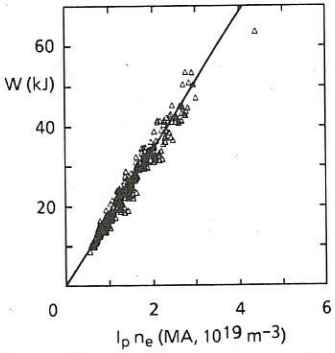

Fig 3: Plasma energy versus I_p $n_e^{0.6}$ (deuterium)

data show that $T_i=T_e$ at the same n_e as FT and also τ_{ST} does not show any saturation at n_e lower than in FT. Z_{eff} on the contrary is greater in FTU than in FT and its importance in τ_E saturation can not be ruled out. In Fig. 2 τ_E is shown versus $n_e q$ both for FT and FTU deuterium plasma. The increase of τ_E from FT(a=0.2 m, R=0.83 m) to FTU is a factor 1.7 which is somehow smaller than the NeoAlcator scaling aR^2 (factor 1.9). Lackner-Gottardi scaling which was able to provide the best fitting to FT data /2/, is again in good agreement with FTU data. The dependence of saturated τ_E ($n_e>6\times10^{19}$ m^{-3}) from other plasma parameters has been examined. No strong dependence of τ_E on n_e peaking factor has been found in stationary conditions. If the resistive voltage V_r is included between the considered parameters the scaling $\tau_E \approx n_e^{0.6}/V_r$ is found which corresponds to the total energy content scaling $W \approx I_p\, n_e^{0.6}$ as previously quoted. The scaling is shown in Fig. 3 for all the deuterium data in the full n_e range. This scaling is also found in FT data and in ASDEX /5/. It is not clear if this scaling originates from the combined effects of the ohmic constraint, which connects the average of the $T_e^{3/2}$ with I_p, Z_{eff} and V_r, and of the observed Z_{eff} dependence on P_{oh} and n_e, or indicates an intrinsic plasma behaviour. A dependence of W on I_p and on plasma radial velocity u_r is suggested by the poloidal Ohm's law constraint /6/. u_r has been evaluated by assuming a constant value for neutral density at plasma edge $n_o(a)=1\times10^{15}$ m^{-3}. The poloidal Ohm's law expression which neglects the plasma viscosity has been used in computation of W foreseen by the constraint. The comparison between computed and experimental W shows that a good agreement can be found that by changing $n_o(a)$ of less than an order of magnitude around the chosen value.

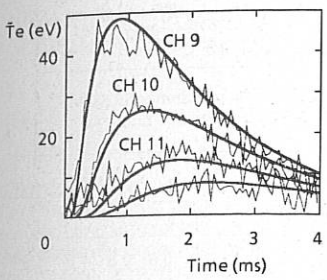

Fig 4: Measurement and simulation of the time evolution of T_e perturbation

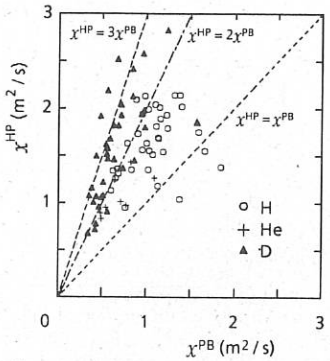

Fig 5: Heat pulse conductivity vs averaged power balance conductivity

Heat Pulse Propagation

The temperature perturbation induced by sawteeth are measured with a 12 channels grating polychromator with a spatial resolution better than 3 cm. The channel spatial separation is about 4 cm. Coherent addition of many sawteeth is performed in order to improve the S/N ratio. Typically from 20 to 100 sawtooth cycles are added during the flat-top of the discharge obtaining, at the last significant channel, a S/N ratio ranging from 2 to 6. The Fourier analysis of the temperature perturbation shows that the heat pulse behaviour is diffusive for frequencies ranging from 100 to 500 Hz. The χ^{fou} value and the damping time τ are obtained following Ref. /7/ as: $\chi^{fou}=3\ \omega/4\phi'^2R$, $1/\tau=3\ \omega(R^2-1)/4R$ where $R= (A'/A+1/2r+1/2r_n)/\phi'$, A and ϕ are the amplitude and the phase of the harmonic component of of temperature perturbation, the prime indicates the derivatives respect to the radius r. χ^{fou} and $\chi^{HP}=\Delta(r^2)/9\Delta t_p$ are in good agreement in the whole range of density analyzed so far independently of damping constant. The measured damping time is also in good agreement with e-i equilibration time /8/. Figure 4 shows typical temperature signals and their simulation with a damped diffusive model and a reduced transport inside the inversion radius. A database containing the time-to-peak χ^{HP} for 85 discharges at 5.7 t with three different gases (H,D and He), has been made with plasma current ranging from 350 to 700 kA, line density from 0.3 to 2×10^{20} m^{-3}, Z_{eff} from 1 to 7 and q_{cyl} from 3.2 to 7. The comparison of χ^{HP} with a volume averaged power balance conductivity χ^{PB} is shown in Fig. 5 where different marks are for different gases. Data of different gases clearly separate in two groups (D, H-He).The result of least square fit for deuterium yields $\chi^{HP}=2.2\ \chi^{PB}$ whilst with a greater dispersion $\chi^{HP}=1.5\ \chi^{PB}$ for the H-He group, this is a consequence of the fact that χ^{PB} (as τ_E) is different for different gases whilst χ^{HP} is almost insensitive to the gas species.

Peaked Density Profiles

Peaked density profiles ($n_{e0}/<n_e> \geq 2$) can be obtained in FTU by means of a programmed outward displacement and/or by a decrease in the gas puffing rate. These actions lead to the development of a very strong density gradient at the edge which is subsequently lost and the density profile starts to peak. A detachment of the internal side (R >0.8 m) of the Te profile becomes pronounced when the density profile peaking begins. Such evolutions of n_e and T_e profiles can occur both in Hydrogen as well as in Deuterium plasmas and the peaked density regime can be sustained up to 1 s. A number of plasma parameters bear signs of n_e peaking (Fig. 6a). At B_t=6 T in the plasma current flat top, the maximum value of $\beta_p+l_i/2$, as deduced from the magnetic

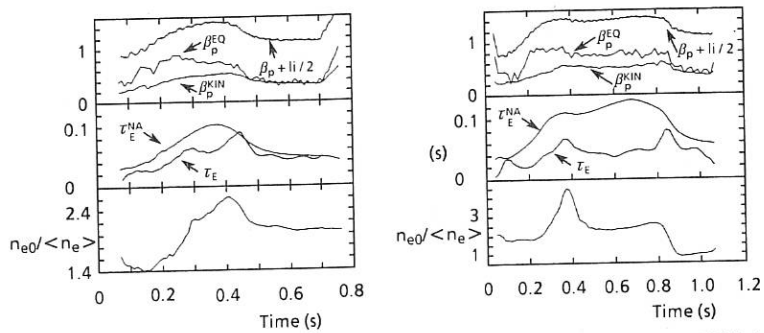

Fig 6: Waveforms of a) $\beta_p + l_i/2$, β_{pEQ} and β_{pKIN}; b) τ_E^{NA} and τ_E; c) $n_{e0}/<n_e>$ for FTU shots 2120 and 2226 (B_t = 6 T, I_p = 350 kA)

measurements, increases from 1.1 to 1.65 at I_p=350 kA and from 1.05 to 1.20 at 500 kA. The increase of the maximum value of β_{pKIN} ,as desumed from the kinetic measurements, is is from 0.27 to 0.8 at 350 kA and from 0.25 to 0.40 at 500 kA. Only a slight increase (0.9 to 0.95) in $\beta_p+l_i/2$ is detected at I_p=700 kA. The plasma internal inductance seems not to be much affected by n_e evolution: maximum variations of $l_i/2$ of 0.15 have been observed. The neutron emission is remarkably enhanced and, although n_e goes up by a factor of two, the peak T_e does not decrease. A hysteresis loop in the behaviour of the dynamic total energy confinement time τ_E=W/(VI$_p$-dW/dt) is observed (Fig. 6b): at the end of the n_e rise and then during n_e decay, until the density profile remains peaked, the dynamic τ_E is very near to the Neo-Alcator value τ_E^{NA}=0.066 n_{e20} q_{cyl} R^2 a (s) for values of n_e q such that τ_E^{NA} <80 ms. On the other hand for values of n_eq such that τ_E^{NA} >80 ms the dynamic τ_E decreases with n_eq. The data of the dynamic τ_E are not in contradiction with the steady state analysis as values of τ_E >80 ms are observed for time intervals not longer than 80 ms. Whereas the agreement of β_{pDIA} from the diamagnetic measurement with β_{pKIN} is quite good, a remarkable discrepancy is observed with the equilibrium reconstructed β_{pEQ} during the density profile evolution. An intriguing possibility is that the extra energy detected by the equilibrium measurements is plasma toroidal rotation: as a matter of fact during the peaked density regime an (m=2÷3,n=1) MHD mode structure appears and rotates toroidally in the direction opposite to I_p at a speed of 1×10^5 m/s. It has to be recalled that an explanation for the long standing question of the shapes and modifications of ne profiles in tokamaks connected to plasma toroidal rotation was put forward by Itoh and Itoh /9/.

References

/1/ This conference -Paper 1-1/184c187
/2/ F.Alladio et al., 13th Int.Conf. on Plasma Physics and Controlled Nuclear Fusion Research, Washington 1990, IAEA-CN-53/A2-5
/3/ This conference -Paper 1-1/180c189
/4/ This conference -Paper 1-1/185c186c190
/5/ P.J.McCarthy et al., Nucl. Fusion, 31,1595, (1991)
/6/ S.E.Segre,V.Zanza,Nucl. Fusion,31, 819, (1991)
/7/ A.Jacchia et al., Phys of Fluids B, 3 11, (1991)
/8/ W.Goedheer, Nucl. Fusion, 26 1043, (1986)
/9/ S.I. Itoh and K. Itoh, 13th Int.Conf. on Plasma Physics and Controlled Nuclear Fusion Research, Washington 1990, IAEA-CN-53/D-412.

Global Energy Confinement in TORE SUPRA

G.T. Hoang, J.P. Bizarro, B. de Gentile, Th. Hutter, L. Laurent, X. Litaudon, D. Moreau, Y. Peysson, G. Tonon, D. van Houtte.

Département de Recherches sur la Fusion Contrôlée, Association Euratom-CEA
Centre d'Etudes de Cadarache - 13108 Saint-Paul-Lez-Durance- FRANCE.

Abstract. The global energy confinement behaviour of mixed Ohmic/Lower Hybrid driven Tore Supra plasmas has been analysed at various densities. In contradiction with L-mode ITER scaling law, this analysis indicates that the global energy confinement time depends strongly on the plasma density and the isotopic dependence seems not to be observed. The thermal electron energy content of steady-state discharges is in good agreement with the offset linear Rebut-Lallia scaling law.

During current ramp experiments, the global energy confinement time was found to depend on the internal self-inductance (li). Improved confinement has been obtained for a steady-state 0.8MA plasma where the plasma current profile is peaked by LH waves (li ≈1.8). In this case, the global confinement time is found to be about 40% higher than the value predicted by the Rebut-Lallia scaling law.

High power LH experiments have been carried out at B_T = 3.9 Teslas on axis, a plasma current 0.5MA $\leq I_p \leq$ 1.6 MA and at various densities (2×10^{19} m$^{-3} \leq n_e(0) \leq 9\times10^{19}$ m^{-3}). A maximum total power (OH + LH + ICRF) of up to 7.5 MW was injected into the plasma. The bulk electrons are heated by slowing down of suprathermal electrons. At high densities, $n_e(0) \approx 5 \times 10^{19}$ m^{-3}, the temperature on axis increases linearly with power and the profile peaking, defined as Te(0)/<Te>, was almost unchanged indicating that all of the plasma volume was heated. At lower densities the electron heating occured preferentially in the center of the plasma (within the small surface, $\rho \approx 0.3$), thus the volume averaged temperature was practically unchanged: for example, at $n_e(0) = 2.2 \times 10^{19}$ m^{-3}, the central electron temperature reached 8 keV with 3.6 MW LH power injected [1].

In figure 1, the diamagnetic energy, W_{dia}, for both He and D_2/1.6MA plasmas at a central density of 4.5 x 10^{19} m^{-3}, is plotted versus total input power. This shows that the total energy content increases linearly with the additional power and reaches 0.75 MJ at a maximum input power of 4.2MW LH + 2.5MW ICRH + 0.8MW OH. Nevertheless, the power degradation of the global energy confinement time, defined as $\tau_E = W_{dia} / (P_{tot} - dW_{dia}/dt)$, is found to be more pessimistic than L-mode scaling law ($\tau_E \propto P^{-0.5}$): τ_E drops from 0.25s to 0.1s when the total injected power varies from the ohmic level of 1.5MW to 7.5MW. We plotted in this figure the ITER predictions calculated for the effective mass M=1 and M=2.

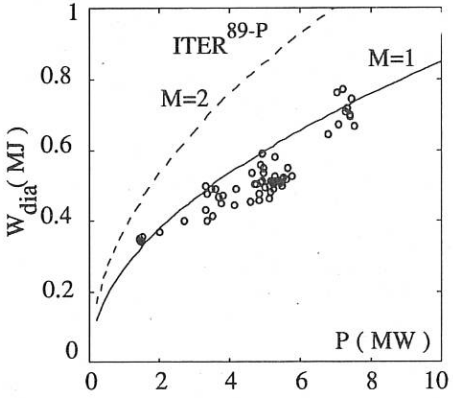

Figure 1: Energy content deduced from diamagnetic measurements versus total power

With M=2, ITER values are always two times higher than the experimental values, especially at low densities ($n_e(0) = 2.4 \times 10^{19}$ m^{-3}) where the most important discrepancy was found. However the fit seems to be better with M=1, although the hydrogen content was negligible in all of these discharges. Therefore, the isotopic dependence of the energy confinement time is not clearly observed. It should be noted that we can neglect the fast particle contribution in the energy balance. Indeed, during high frequency modulations of the LH power, the energy content of the fast electron tail could be deduced from the time evolution of the magnetic and diamagnetic signals and was found to be lower than 1% of the total plasma energy content. With additional ICRF power, the fast ion contribution was larger due to their longer slowing down time, but never exceeded 10% of the total energy. Moreover, for some discharges where both ion and electron energy contents were available (from charge exchange, interferometry and Thomson scattering diagnostics), we found $W_{dia} \approx W_e + W_i$ by assuming that the ion and electron density profiles were the same and n_i was between 0.7 - 0.8 n_e. Generally, the ratio W_{dia}/W_e was found to be between 1.6 and 1.8.

The global confinement time versus the total power is plotted in figure 2 together with the ITER scaling corresponding to M=1. These data contain both helium and deuterium 1.6 MA discharges and three different density regimes ($n_e(0)$=2.4x10^{19} m^{-3}, 4.5x10^{19}m^{-3} and 6x10^{19} m^{-3}).

A significant dependence of the global confinement time upon the plasma density is observed, in a regime where the ohmic power is still an important component of the total input power: the global confinement time increases by a factor of two when the central density rises from 2.4 x 10^{19} m^{-3} to 6 x 10^{19} m^{-3}. This density effect can be attributed to the reminiscence of the neo-Alcator ohmic heating scaling, but is not described correctly by the ITER scaling in which the density dependence is negligible. Instead, we have compared the thermal electron energy alone, obtained from interferometry and Thomson scattering diagnostics, with the offset linear Rebut-Lallia scaling law [2]:

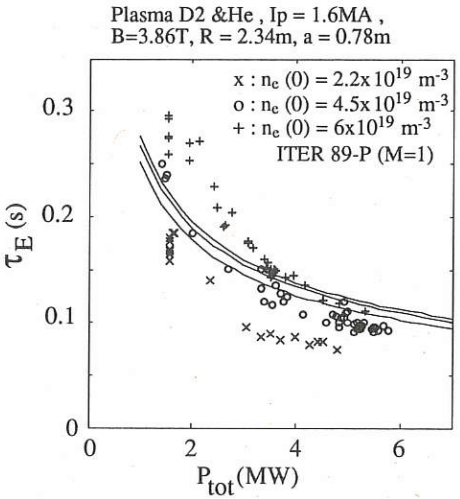

Figure 2: Global confinement time versus total power at different densities

$$W_e^{R-L} = 2.6 \times 10^{-2}\, \bar{n}_e^{3/4}\, Z_{eff}^{1/4}\, B_0^{1/2}\, I_p^{1/2}\, (\kappa a^2 R)^{11/12} + 1.2 \times 10^{-2}\, I_p\, P_{tot} Z_{eff}^{-1/2}\, (\kappa a^2 R)^{1/2}$$

in units of 10^{19} m^{-3}, Teslas, MA, MW, MJ, meters and seconds. This comparison is shown in Fig. 3, and we find the experimental results in fair agreement with the prediction over the whole density range, for I_p = 1.6 MA and I_p = 1 MA, and for total input powers ranging from 0.8 MW to 7.5 MW.

However, it must be noted that the global confinement follows fairly well the Rebut-Lallia law only for the Tore Supra standard steady-state regime.

Indeed, when we include the current ramp data, the experimental values were found to be no more given by the Rebut-Lallia scaling: first, the global confinement is poorer than the prediction during plasma current ramp-up and, second, it is better than the predicted one during ramp-down. This behaviour of the confinement time could be explained by the current profile dependence of the global confinement. The ratio between the experimental confinement time and the fitted values is plotted versus internal self-inductance in figure 4, where the Rebut-Lallia values were calculated by taking $W_i = W_{dia} - W_e$ when the ion energy content measurements were not available. As shown in this figure, for li varying between 0.9 to 2.8, this ratio rises from 0.8 to about 1.5 approximately as $(l_i/l_{i0})^{0.7}$ [3], where l_{i0} is a standard value of the internal inductance in the stationnary discharges (l_{i0}≈1.25 for q_a=3 - 4).

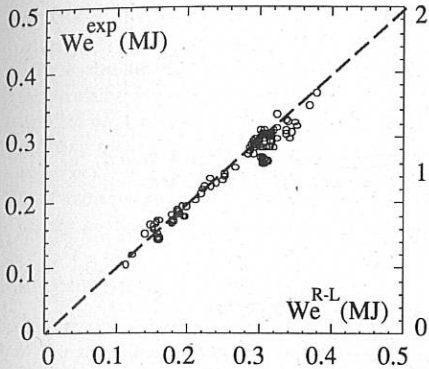

Figure 3 : Electron energy content versus Rebut-Lallia prediction
Plasma He&D2, Ip = 1/1.6MA,
B = 3.9 T
P_{tot} = 0.8 -7.5 MW,
n_e (0) = 2 - 6 x10^{19} m^{-3}

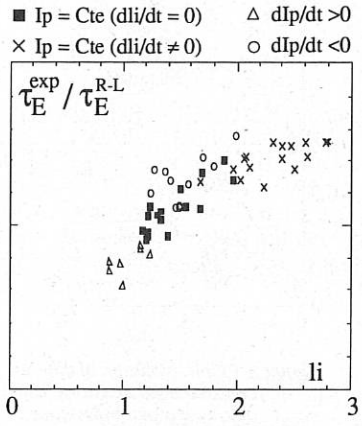

Figure 4 : Electron energy content normalized to Rebut-Lallia prediction versus plasma self inductance
Ip = 0.5 - 1.6 MA, B = 3.9 T,
P_{LH}= 1.5 - 4 MW
n_e (0) = 2 - 4.5 x $10^{19}$$m^{-3}$

In order to obtain steady-state plasmas with a high value of the li parameter, a series of experiments were performed in which the plasma current was ramped down from 1.7MA to a 0.8MA plateau (with dIp/dt = - 1MA/s) at a central density of 2.4 x 10^{19} m^{-3}, during the LH power application. With such a scenario, li is higher than the one which is obtained without LH power. As shown in figure 5, during the 2.9MW LH pulse the quasi- stationnary value of li reaches about 1.8 instead of 1.4 (q_a value is about 7 in this case), thanks to the modified current profile. As a consequence, an improved confinement was obtained while li and central density current obtained from Faraday rotation measurements were constant during about one second: the confinement time was about 40% higher than the Rebut-Lallia prediction (we note that the diamagnetic energy was not correctly calculated during the 1.7/0.8MA ramp-down because the eddy current effect due to the rapid drop of the plasma current was not estimated). During these experiments, the bulk electrons were heated the whole plasma volume. The central temperature reached 5 keV and the peaking factor, Te(0)/<Te>, rose from 2 to 4, and the volume averaged

temperature increased from 0.7 to 1.4 keV (figure 6). A weak increase of the ion temperature was also observed.

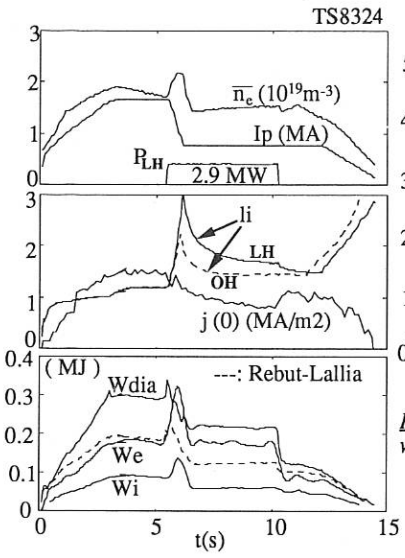

Figure 5 : Time evolution of different parameters (shot TS8324) line-averaged density, plasma current, LH power, plasma internal inductance, central curent density (from Faraday rotation measurements), diamagnetic energy, electron and ion energy contents, and electron energy given by Rebut-Lallia law

Figure 6 : Te profile with and without LH at Ip=0.8MA

Summary

Global confinement studies during RF additional heating up to 7.5MW injected power have shown a more significant density dependence than the ITER 89-P law would predict. Moreover, the effective mass dependence was not observed. The electron energy content, however, follows fairly well the offset linear Rebut-Lallia scaling.

Current ramp experiments have shown that confinement depends on the plasma internal inductance, li. The ratio between the experimental confinement time and the predicted one reaches 1.5 above li ≈ 2 following a $(l_i/l_{i0})^{0.7}$ scaling.

Using LH waves, a series of promising experiments have been investigated in order to obtain a high and stationnary value of li parameter, in which an improved confinement has been obtained for steady-state plasmas where the confinement time was about 40% higher than the L-mode prediction while li was constant (li=1.8) during 1s.

References:

[1]: D. Moreau and Tore Supra Team, invited paper at the 33rd Annual Meeting of the APS, Tampa (1991), to be published in Phys. Fluids (1992)

[2]: P. H. Rebut, P. P. Lallia, M. L. Watkins, in *Plasma Physics and Controlled Nuclear Fusion Research*, Proceedings of the 12th International Conference, Nice, 1988 (IAEA, Vienna, 1989), Vol. 2, p. 191.

[3]: M.C.Zarnstorff, in *Plasma Physics and Controlled Nuclear Fusion Research*, Proceedings of the 13th International Conference,Washington, 1990 (IAEA,Vienna, 1991), Vol. 1, p. 109.

Energy confinement in the tight aspect ratio tokamak, START

L C Appel, R Duck†, S J Fielding, K J Gibson, J Hugill, J Li, S J Manhood, A W Morris, D C Robinson, A Sykes, M F Turner, M Valovič and M J Walsh
(Culham Laboratory, Abingdon, Oxon, OX14 3DB, UK. Euratom/AEA Fusion Association
†UMIST, P.O. Box 88, Manchester, M60 1QD, UK.)

Introduction

START is the world's first tokamak operating at aspect ratios $A \lesssim 1.5$ [1]. It provides a unique opportunity to extend heating and confinement studies to a regime where toroidal effects are greatly enhanced. Various scaling laws have been derived to empirically describe confinement in tokamaks but to date these laws have only been applied to a regime where the aspect ratio is greater than 2.3. At low aspect ratio existing scaling laws diverge, with predicted energy confinement times varying by up to an order of magnitude. One of the primary aims of the START experiment is to test confinement predictions at low aspect ratio. In this paper we compare the measured energy confinement with various scaling law predictions.

Experimental Results

The energy content of the plasma has been separately determined from measurements of the electron density and ion and electron temperatures, and from the plasma diamagnetism.

In recent flat-top discharges, the electron temperature profile was determined from pulse height analysis of SXR measurements made with a scanning Si(Li) detector. The measured temperatures of ~300eV, with a flat profile out to 0.13m(Fig.1), are consistent with spectroscopic observations from low-Z impurity charge states.

The line-integrated electron density is measured along a horizontal tangential chord using an HCN(337μm) interferometer. The plasma dimensions and hence the HCN path length are determined from CCD observations of the H_α emission. Line of sight densities of up to $8\times10^{19}\mathrm{m}^{-3}$ have been measured.

Central ion temperatures of up to 150 eV have been measured using a neutral particle analyser (NPA), with high resolution Doppler spectroscopy of CV yielding similar values. Approximate ion temperature profiles are constructed from Doppler measurements of other impurity ion emission lines, Fig.1.

Because of the flatness of the temperature profile and lack of information on the density profile we use the following approximation for the plasma stored energy:

$$W_p = \frac{3}{2}\rho\bar{n}_e(T_e + \gamma T_i)V$$

where ρ is the ratio of the volume average to line-of-sight-average density ($\bar{n}_e$) and γ is the ion depletion factor. With density profiles of the form $(1 - r^2/a^2)^\alpha$ and

$0 < \alpha < 4$, then $1 < \rho < 0.5$. We choose $\rho = 0.75$ (corresponding to $\alpha = 1$) with a probable error of $< \pm 0.25$ and $\gamma = 0.7$ corresponding to Z_{eff}=2 with carbon as the dominant impurity. Fig.2 shows the time history of the relevant plasma parameters for these kinetic measurements. At current flat-top (t=23.5ms) $R_0 \simeq 0.20$m, $a \simeq 0.15$m, $\kappa \simeq 1.3, I_p \simeq 110$kA, $\bar{n}_e \simeq 5 \times 10^{19}\mathrm{m}^{-3}$, $B_\phi(R_0) \simeq 0.48$T and W_p is estimated to be 390±155J. The ohmic power is calculated from $P_{oh} = V_l I_p - \frac{d}{dt}\left(0.25\mu_0 R_0 l_i I_p^2\right)$. At t=23.5ms $\dot{I}_p \sim 0$, $V_L \sim 2.1$, $P_{oh} \sim 230$kW giving τ_E=1.7±0.7ms, where it is assumed that $\dot{l}_i \sim 0$, $\dot{R}_0 \sim 0$, and corrections due to finite $\dot{W}$ (not included) are estimated at less than 15%.

START has no conventional diamagnetic loop. The plasma diamagnetism has been estimated from the difference of toroidal flux, $\Delta\Phi$, measured across the poloidal gap on the vacuum tank. The main toroidal field flux is compensated for using the signal from a Rogowski coil, mounted on one of the toroidal field coils. Errors resulting from the flux diffusing into the tank wall, and stray signals induced by ohmic heating and vertical field currents, are subtracted numerically using vacuum shot data. Any residual signal before and after the plasma current is treated as a linear drift and subtracted out. The absolute error from the correction procedure is estimated at ±0.5mWb. Fig.3 shows data from two similar discharges with opposite toroidal field. The spike in $\Delta\Phi$ in the first part of the current rise is believed to be generated by poloidal currents flowing along the field lines before the tokamak magnetic field configuration is formed. After major radius compression there is a quasi-stationary phase (23.5-24.5ms) during which the plasma dimensions show little change ($|\dot{R}_0| < 8m/s$) and diamagnetic measurements are possible. In order to determine the plasma energy, W_{dia}, from $\Delta\Phi$, toroidal corrections must be considered. Free boundary equilibrium calculations have been performed to quantify this relationship. For small poloidal beta where $\beta_p \equiv 2\langle p\rangle (\oint dl)^2/(\mu_0 I_p^2)$

$$\mu_I \equiv \frac{8\pi B_\phi \Delta\Phi}{(\mu_0 I_p)^2} = C - D\beta_p.$$

Parameters C and D depend on plasma geometry and current profile. For t=24ms in Fig 3., $R_0 \approx 0.18$m, $a \approx 0.13$m, $\kappa \approx 1.3$, $I_p \approx 82$kA, $B_\phi(R_0) \approx 0.52$T and calculations give $C = 0.62 + 0.17 l_i$, $D = 0.59$. l_i is estimated by simulating the measured vertical field B_θ at the inboard side of the plasma and agreement is obtained with $\beta_p + l_i/2 \approx 0.78$. From this, with $\Delta\Phi = 0.47 \pm 0.05 mWb$ we find: $\beta_p = 0.32 \pm 0.2$, $l_i \approx 0.92$ and $W_{dia} = 170 \pm 100J$. Similarly, from the measured rates of $\dot{B}_\theta$, $\dot{I}_P$, and $\Delta\dot{\Phi}$ we obtain $\dot{l}_i \approx 65s^{-1}$ and $\dot{W}_{dia} \approx -20kW$. For these values $P_{oh} - \dot{W}_{dia} \approx 290kW$ and $\tau_E = 0.6 \pm 0.4ms$.

An attempt was made to derive the density dependence of μ_I from the diamagnetic data, however no change was observed within experimental error over the density range $\bar{n}_e = (2-7) \times 10^{19}\mathrm{m}^{-3}$. Note that extrapolation from conventional tokamak data predicts saturation of energy confinement in START at $\bar{n}_e \approx 3.6 \times 10^{19} m^{-3}$.

The measured values of τ_E are compared with scaling law predictions in the Table. It can be seen that in all cases the measured values exceed conventional aspect ratio predictions.

Scaling Law [2]	τ_E(ms) R_0=0.20m,a = 0.15m I_p=110kA,$\bar{n}_e = 5 \times 10^{19}$m^{-3}	τ_E(ms) R_0=0.18m,a = 0.13m I_p=82kA,$\bar{n}_e = 5 \times 10^{19}$m^{-3}
Experiment Method	Kinetic 1.7±0.7	Diamagnetic 0.6±0.4
Neo-Alcator	0.52	0.44
Rebut-Lallia	1.15	0.61
T-10	0.59	0.53

Conclusions

Two independent experimental estimates have been made of the energy confinement time for ohmic discharges on START. When compared with scaling law predictions the results show that confinement at low aspect ratio is at least as good as for a conventional tokamak of similar dimensions.

References

[1] A. Sykes *et al*, (To appear Nuclear Fusion, 1992)

[2] ITER Concept Definition, IAEA Vienna Vol.2 (1989) 8

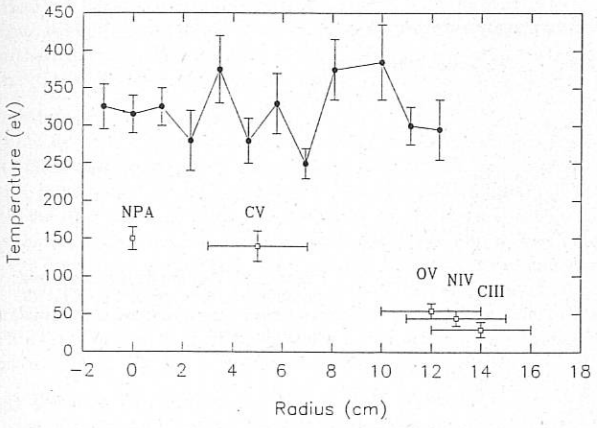

Figure 1: *Electron (solid points) and ion temperature (open points) profiles at current flat-top (110kA) in* START, T_e *from Si(Li),* T_i *from NPA and Doppler spectroscopy.*

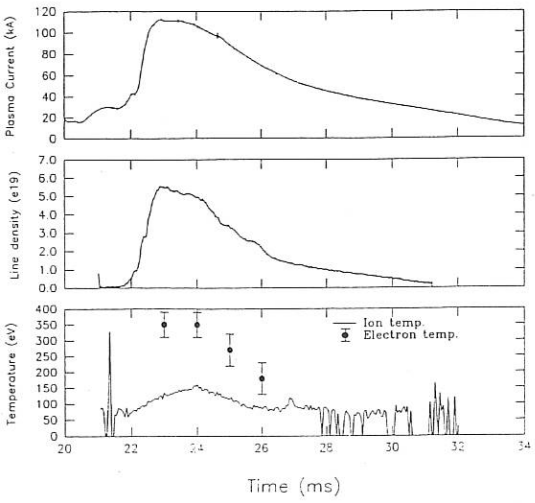

Figure 2: *Principal plasma parameters for a typical* START *discharge.*

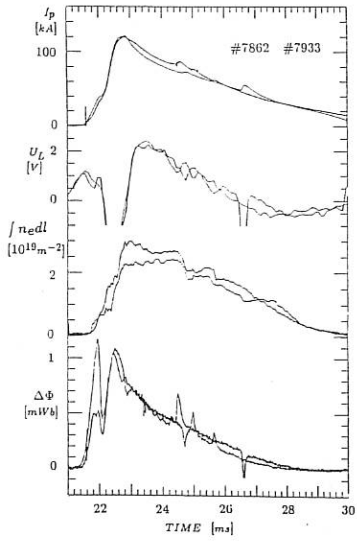

Figure 3: *Plasma parameters and diamagnetic data from two START discharges with opposite toroidal magnetic field*

Confinement Scaling for the ASDEX L-Mode in Different Divertor Configurations

U. Stroth, O.J.W.F. Kardaun, A. Kus,
the ASDEX and the NI Teams

Max-Planck-Institut für Plasmaphysik,
EURATOM-IPP Association, D-8046 Garching, FRG

1. Introduction

We present some results of confinement studies on a L-Mode database which covers 10 years of operation of ASDEX. During this period, ASDEX has been modified several times. The most important modifications were made on the 2 divertors. Operation of ASDEX started with closed divertors (DV-I), went through a period with open divertors (DV-II *open*), which allowed for high neutral gas recycling through by-passes, back to situations with first the by-passes in the upper and later in the lower divertor closed. In addition, different techniques of wall conditioning were employed on ASDEX so that discharge conditions under stainless steel, carbonized and boronized walls can be studied.

In global energy scaling expressions subtleties like divertor type and wall coating are not always taken into consideration. The systematic differences due to such effects which can occur from one tokamak to the other are then hidden in the dependencies on geometrical parameters. For example, improved energy confinement due to a specific divertor of a small tokamak compared to a larger tokamak with a different divertor would lead to a softened dependence on major radius. This will lead to inaccuracies when extrapolating to future devices. Beside documentation of the ASDEX L-Mode, one of the goals of this paper is therefore to investigate the influence of the divertor type on the global diamagnetic and MHD confinement times. Furthermore, we give first results of the scaling of the thermal energy confinement time, which is more relevant when comparing to transport theories.

2. Description of the Database

In total, 2131 different observations have been stored in the database, each consisting of data for about 100 plasma parameters. The same type of variables were defined and stored as in the ASDEX contribution to the ITER H-mode database. In addition full profile information is available for 1096 validated cases. Kinetic values for the thermal energy content are stored as well as the estimated contribution of fast ions. Only time points from phases with stationary values of the plasma parameters were included. The values are understood to represent sawtooth averages. Sawtooth-free discharges and others, which transition later into the H-mode were labeled as subsets and not yet included in the analyses. The ranges covered by the database are listed in Tab. 1. For comparison to ohmic confinement scaling, for each discharge the preceding ohmic phase has been stored in the database.

3. Energy Content from Magnetic and Kinetic Data

A comparison of diamagnetic and MHD plasma energy contents, E^{dia} and E^{MHD}, at sufficiently high density, to avoid dominant contributions from fast particles, was made as a check for systematic measurement errors.

Another important check and a prerequisite for the investigation of thermal confinement times is to compare both energy measurements to the corresponding estimates from kinetic

quantities:

$$E_{kin}^{dia} = c_i E_e^{th} + 1.5\alpha E_{fast} \quad (1)$$

$$E_{kin}^{MHD} = c_i E_e^{th} + (1.5 - 0.75\alpha) E_{fast} + 1.5 E_{rot}. \quad (2)$$

We compared all discharges for which the electron energy content, E_e^{th}, could be calculated from Thomson scattering measurements for electron temperature and density profiles. It was not possible to include ion temperature and Z_{eff} profiles. Therefore, the ion contribution had to be taken into account by a factor c_i.

The rotation energy E_{rot} contributes by not more than 10% (see Fig. 1). We estimated it using scaling laws for the toroidal torque and the central rotation velocity [1].

For the fast particle energy content, E_{fast}, and the fraction of it into the perpendicular direction, α, Kardaun and Stäbler derived formulas based on Freya code simulations for a number of different temperature and density profile combinations:

$$E_{fast}^{u} = e^{5.36} \bar{n}_e^{-1.25} E^{0.75} P_{inj}^{0.95} (E^{th})^{0.5}. \quad (3)$$

The units are $[10^{19} m^{-3}, 5 \times 10^4 eV, MW, J]$. P_{inj} is the total injected power and E the energy of the main beam component. Eq. 3 is valid for $D \rightarrow D^+$ injection; for $H \rightarrow D^+$ the same formula with a different constant was postulated. and the thermal energy is calculated iteratively with help of eq. 1.

In Fig. 1 we depict the comparison of results from Eq. 1, 2 and 3 to the magnetic data. From the comparison at high densities we estimated the ion contribute to be 85% of the electron contribution: $c_i = 1.85$. This factor is taken the same for all discharges. At lower density no agreement between kinetic and magnetic measurements is found. One possibility is that Monte-Carlo codes like Freya underestimate the fast ion population and that slowing down of fast particles might be slower than expected. At lower densities roughly a factor of 2 higher fast ion content is needed to restore agreement in Fig. 1. The discrepancy can not be explained by a change in the ion contribution which is with 85% of the electrons more likely overestimated.

We also employed the database to find an alternative relation for the fast ion energy content. We resolved eq. 1 for E_{fast} and fitted a power law to data calculated from this formula. The result, E_{fast}^{h}, showed a stronger density dependence. Using this formula for the fast particle content gives very satisfactory results also for the comparison with E^{MHD} as shown in the upper part of Fig. 1. The few discharges for which E_{kin} overestimates the corresponding magnetic measurements by more than 20% are discharges at low density and high heating power. An improved fit for these discharges we could get when we took saturation effect account in adding $(\log \bar{n}_e^2)^2$ into as additional regression variable.

Divertor type	I_p kA	Δ	min,max	B_t T	Δ	min,max	P_{tot} MW	Δ	min,max	$\bar{n}_e$ $10^{19} m^{-3}$	Δ	min,max
DV-I+II	359	59	98,463	2.23	0.25	1.26,2.82	1.59	0.58	0.52,3.99	3.57	1.47	0.77,12.7
DV-I	353	56	242,452	2.28	0.22	1.86,2.82	1.58	0.57	0.72,3.60	3.32	1.18	1.59,8.86
DV-II *c.*	350	58	218,449	2.26	0.18	1.89,2.80	1.57	0.50	0.74,2.83	3.37	1.37	1.51,12.7
DV-II *o.*	364	27	287,420	2.21	0.08	1.87,2.45	1.74	0.59	0.93,2.97	3.79	1.21	1.92,10.5

Table 1: Ranges of the database in the various divertor configurations: Mean values, standard deviation, minimum and maximum. The first row represent the entire database, the other rows various subsets which were used for the regression analyses.

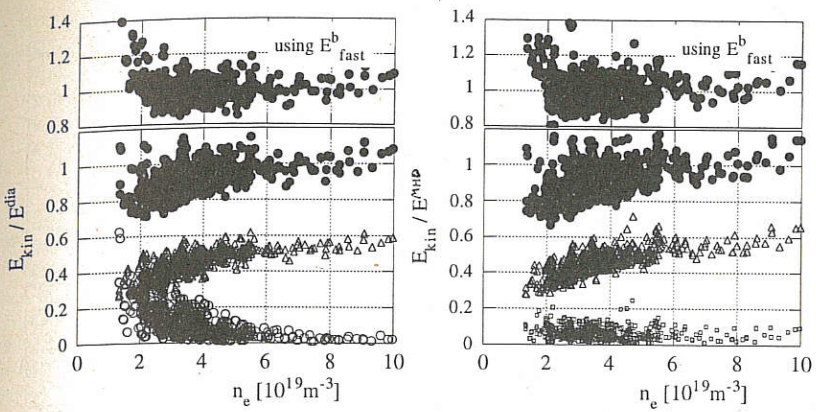

Figure 1: The different contributions to E_{kin}^{dia} and E_{kin}^{MHD} normalized to E^{dia} and E^{MHD}, respectively. Left hand side: $1.5E_{fast}^{a}$ (○), E_e^{th} (△) and the sum E_{kin}^{dia} (•) according to Eq. 1. Right hand side: $1.5E_{rot}$ (□) and the sum E_{kin}^{MHD} (•) according to Eq. 2. In the upper part the alternative expression E_{fast}^{b} is used.

4. Power law expressions for the confinement time

In table 2 results from regression analyses of the energy confinement time are listed. The data set was restricted as follows: $q_{95} \geq 2.5$, $I_P \geq 200kA$ and $B_t \geq 2T$; in order to single out discharges in which fast particles tend to dominate thermal ions and those which might not yet clearly transition from ohmic to L-mode conditions, $\bar{n}_e \geq 2.5 \times 10^{19} m^{-3}$ and $P_{abs} \geq 0.5MW$ were used as additional restrictions. Relaxing any of the constraints does not alter the results.

The energy confinement time we calculate from both, diamagnetic (τ_E^{dia}) and MHD equilibrium (τ_E^{MHD}) measurements. As input power we use the sum of ohmic and neutral beam heating, corrected for shine through losses: $P_{tot} = P_{OH} + P_{abs}$

The agreement of the scaling laws for τ_E^{dia} and $\tau_E^{MHD}$is satisfactory. The most remarkable result is a substantial change of the current dependence when going from a closed to an open divertor. Discharges in the open divertor configuration show a much stronger dependence on current than discharges done in closed divertor configurations. The difference in B_t scaling, although statistically significant, should be taken with some caution, since it relies only on about 10% of the discharges. Omitting B_t as a regression variable in DV-II *open* does not notably change the dependence on the other variables. The rmse increases only by 0.2%.

The current dependence in DV-II *open* could not be estimated with the same accuracy as in the other cases, because there are only very few discharges hat higher I_P in this subset. Nevertheless, the difference to the scaling of closed divertor discharges is significant and could be a key to the different scaling on finds for other tokamaks with open divertors Ref. [2].

The power degradation is weaker for τ^{MHD} than for τ^{dia} because E^{MHD} is more sensitive to the fast ions which are better confined and of increasing importance with increasing power. In addition one finds a worse degradation for discharges done in the open divertor configuration.

The isotope effect is present in all scaling expressions. It is weaker in the open divertor configuration. From ASDEX it is known that the improvement in energy confinement of D

L-Mode scaling for τ_E^{dia}										
Selection	e	I_P	P_{tot}	m_P	$\bar{n}_e$	B_t	τ_E^a	τ_E^b	Obs.	τmse
DV-I+II	-7.9±.1	.75±.02	-.52±.01	.35±.01	.10±.01	.08±.03	.032	.038	1473	10.5
DV-I	-7.4±.2	.65±.03	-.44±.02	.31±.03	.12±.02	.24±.07	.035	.041	406	10.2
DV-II	-8.1±.1	.78±.02	-.56±.01	.33±.01	.14±.01	.07±.03	.032	.039	1067	9.2
closed	-7.6±.1	.68±.02	-.43±.01	.29±.02	.17±.01	.09±.04	.032	.037	319	7.4
open	-11.1±.5	1.24±.08	-.74±.02	.20±.02	.17±.02	.58±.15	.028	.039	236	9.0
L-Mode scaling for τ_E^{MHD}										
DV-I	-7.1±.3	.64±.04	-.33±.02	.39±.03	.03±.02	.18±.09	.043	.051	406	12.5
DV-II *c.*	-7.5±.1	.70±.02	-.35±.01	.28±.02	.05±.01	.08±.04	.036	.043	319	6.2
DV-II *o.*	-10.7±.6	1.22±.1	-.66±.02	.18±.03	.09±.03	.41±.19	.031	.042	238	11.3
L-Mode scaling for τ_E^{th}										
DV-I	-7.1±.2	.55±.04	-.66±.02	.25±.03	.47±.02	.07±.07	.026	.030	406	10.5
DV-II *c.*	-7.5±.3	.55±.04	-.73±.02	.21±.04	.65±.02	.00±.07	.020	.023	319	13.1
DV-II *o.*	-10.8±.4	1.08±.1	-.82±.02	.17±.02	.48±.03	.63±.12	.020	.026	236	7.3
Combined OH and L-Mode scaling for τ_E^{dia}										
DV-I+II	-7.7±.1	.71±.02	-.60±.01	.37±.01	.15±.01	.06±.03	.031	.038	1942	12.1

Table 2: Power law scaling coefficients for τ_E^{dia}, τ_E^{MHD} and τ_E^{th} for different divertor configurations: DV-I: both divertors closed; DV-II periods with *closed* and *open* divertors. Number of included observations, root mean square error and τ_E values in s for two typical discharges ($I_P = 350[kA]$ (^{a}) and $I_P = 450[kA]$ (^{b}), $P_{tot} = 2[MW]$, $m_p = 2$, $\bar{n}_e = 3[10^{19}m^{-3}]$, $B_t = 2[T]$) are given.

versus H discharges is connected to more peaked density profiles in D discharges. One could speculate, that enhanced recycling in DV-II *open* lowers the capabilities of the density profile to peak and that a similar reason might be responsible, that open divertor tokamaks have less clear sings of the isotope dependence of confinement.

If the data from the ohmic phases are included in the regression (s. Tab. 2) the scaling does not alter substantially. The power dependence is somewhat stronger but the current scaling remains the same within one standard error.

For the thermal confinement time we used the diamagnetic measurement for the total energy content and substracted the fast ion contribution according to our alternative formula for E_{fast}^b. The scaling laws for the thermal confinement time show the same trends as discussed above. But they show different aspects like a stronger dependence on density and a worse degradation with power. Further work is in progress to investigate wether the density dependence can be related to the density dependence in the linear ohmic confinement regime.

Acknowledgement: We would like to thank M. Porbadnik, E. Speth and O. Vollmer for the support in extracting the database.

References

[1] KALLENBACH, A., MAYER, H. M., FUSSMANN, G., MERTENS, V., STROTH, U., et al., Plasma Phys. Controlled Fusion **33** (1991) 595.

[2] RIEDEL, K. S. and KAYE, S. M., Nucl. Fusion **30** (1990) 731.

Recycling Perturbations of Supershot Plasmas[1]

S.D. Scott, D.C. McCune, M.G. Bell, R. Bell, R.V. Budny, E. Fredrickson, B. Grek, K.W. Hill, D. Jassby, F. Jobes, D.W. Johnson, L.C. Johnson, D.K. Mansfield, H.K. Park, A.T. Ramsey, J.A. Snipes[2], B.E. Stratton, E.J. Synakowski, G. Taylor, H.H. Towner and M.C. Zarnstorff

Plasma Physics Laboratory, Princeton University
Princeton, New Jersey USA 08543

Introduction

Thermal heat transport in the core ($r/a \leq 0.5$) of beam-heated TFTR plasmas varies by more than a factor of five between L-mode and supershot plasmas for the same I_p, B_T, and P_b. Operationally, this variation is strongly correlated with the density of the ohmic target plasma, which in turn is determined by the particle recycling coefficient of the carbon-carbon composite inner bumper limiter, but the mechanisms underlying this correlation are not understood. Initial theoretical explanations for reduced transport rates in supershots focussed on stabilization of the ion-temperature-gradient-driven turbulence (ITGDT), which might be expected in peaked-density plasmas. However, local heat transport was not observed to increase when the threshold for ITGDT was greatly exceeded by transiently flattening the density profile with a pellet or with a gas puff[1]. This result does not exclude suppression of ITGDT as the cause of improved τ_E in supershots, but it does indicate that supershot temperature profiles are not marginally stable with respect to a strong transport mechanism. More recently, Mynick[2] has suggested that orbit-averaging effects should reduce heat transport in supershot plasmas due to the high ratio of T_i/T_e, which is ≥ 3 in supershots versus ~ 1 in L-mode plasmas. This paper describes studies of the edge ion temperature, which is an important parameter if τ_E is controlled by ITGDT, and perturbative studies of the effect of edge recycling and density on the evolution of supershot plasmas.

Scaling of Edge Temperatures

The scaling of edge ion temperature is of considerable interest for transport mechanisms involving ITGDT, since the threshold is related to $\eta_i \equiv d(\log T_i)/d(\log n_i)$, which, qualitatively, causes the central T_i to be a *multiple* of the edge T_i. Higher edge ion temperatures might be expected in supershot plasmas due to reduced ion-electron coupling (due to lower edge density), or to reduced convective or atomic physics losses (ionization, charge-exchange) arising from the lower neutral density. Fig. 1a,b plots the measured T_i and T_e 10 cm inside the plasma edge as a function of total beam power divided by local electron density for a variety of L-mode and supershot scans. The edge T_e scales rather simply with power-per-particle, showing little dependence on the recycling status of the limiter. But recycling strongly affects the edge T_i: temperatures of only a few hundred eV are obtained by saturating the limiter with deuterium, while temperature of 1-3 keV are obtained under low-recycling conditions. Puffing near-unity recycling helium gas into an otherwise low-recycling plasma systematically reduces the edge T_i.

To ascertain the causes of higher edge T_i in low-recycling plasmas, edge transport in these scans has been analyzed using the SNAP equilibrium transport code. For this study, the ion temperature was measured by charge-exchange recombination spectroscopy, electron temperature by Thompson scattering or by ECE radiometry, and electron density by a 10-channel microwave interferometer. Plasma composition was inferred from a single-chord visible bremsbtrahlung measurement (Z_{eff} assumed flat) and from soft x-ray measurements of the metallic impurity

[1]Work supported by U.S. DOE contract DE-AC02-76-CHO-3073.
[2]Massachusetts Insitute of Technology

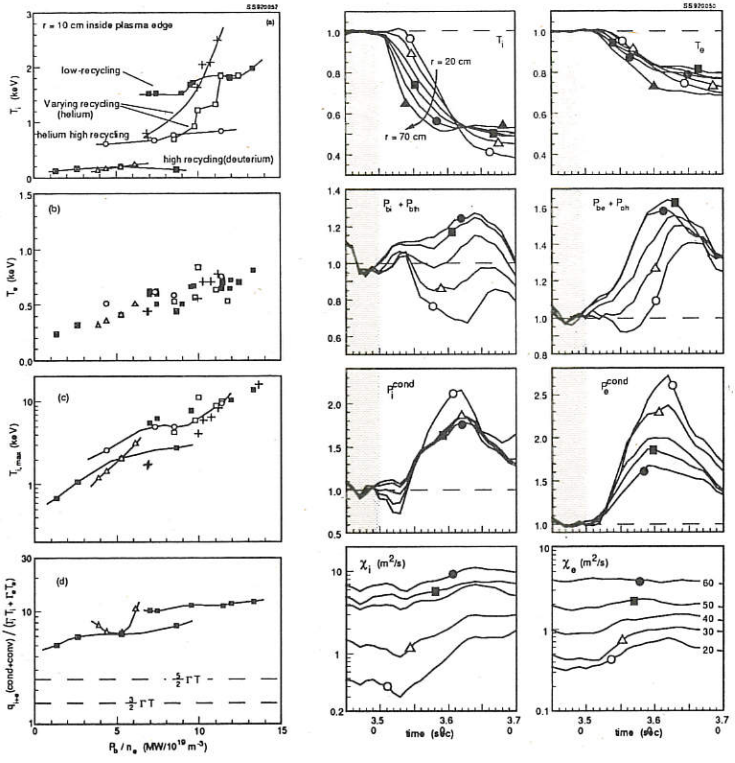

Figure 1: (a,b) Measured T_i and T_e 10 cm inside the plasma edge in various scans. Low recycling: P_b scan (7-21 MW) at $I_p = 1.3$ MA. Variable recycling: variable helium in target plasma at (P_b=22 MW, $I_p = 1.4$ MA) or (P_b=16 MW, $I_p = 1.3$MA). Helium high recycling: P_b scan (7-21 MW) at $I_p = 1.3$ MA. Deuterium high recycling: P_b scan (2-17 MW) at I_p=1.2 MA, $\overline{n}_e \approx 3.5 \times 10^{19}$m^{-3} and density scan at $I_p = 1.2$ MA, $P_b = 8$ MW. (c) Maximum edge T_i allowed by ion-electron coupling. (d) Ratio of total heat flux to convection. (e-l) TRANSP analysis of transport following helium puff into a supershot plasma. Curves are normalized to their value in the shaded region.

content. Neutral transport modelling by the DEGAS code [3] was used to estimate the total neutral source rate from wall neutrals (with factor 2-3 uncertainty) from measurements of the $D\alpha$ emission intensity along a poloidal array of 5 sightlines viewing the inner bumper limiter. Beam ion thermalization and power delivery to the thermal plasma was calculated by a numerical solution to the Fokker-Planck equation.

Surprisingly, atomic physics processes (ionization and charge exchange) remain a small term in the edge power balance even in high-recycling plasmas. The volume-integrated power loss calculated from known atomic cross sections and a neutral density profile consistent with the $D\alpha$ measurements typically represents only ~5% of the power being conducted and convected into the edge region by the ions.

Next, we consider a crude calculation to assess the conjecture that the L-mode edge T_i is determined primarily by ion-electron power coupling. Neglecting all other loss processes, the edge T_i will rise until the total power transferred from ions to electrons in the edge volume equals the power conducted and convected *into* the edge by the ions. For the calculations shown in Fig. 1c, the "edge" plasma volume is defined as the outer 20% of the minor radius, with a constant n_e and T_e equal to the measured values at $r/a = 0.875$. At high beam power, ion-electron coupling alone would limit the edge T_i to values of order 1-2 keV in high-recycling plasmas, considerably larger than the edge T_i actually obtained. This result suggests mechanisms other than ion-electron coupling are dominant in the edge, but we caution that measurements of n_e, T_e, and especially Z_{eff} are difficult in the 10 cm region just inside the plasma edge.

Finally, we consider whether convective power flows (i.e. the energy carried by the radial particle flux) represents a substantial loss term, which could impose low edge T_i in high-recycling plasmas. Fig. 1d plots the ratio of total heat flow (conduction + convection, ions + electrons) to a convective term $\Gamma_i T_i + \Gamma_e T_e$ for the high-recycling deuterium scans, at 10 cm inside the plasma edge. The relatively large values of this ratio (5-10) suggest that convection could be the dominant edge transport mechanism only by assuming a large convective multiplier (i.e. $q_{conv} = 2.5\Gamma T$) and that the neutral density is near or above the upper bound of the estimated factor 2-3 uncertainty.

To summarize, low-recycling plasmas do obtain considerably higher edge ion temperature compared to high recycling plasmas. Assuming that some form of ITGDT controls transport in L-mode and supershot plasmas, this behavior could, in principle, establish a favorable edge condition in supershots that would improve confinement everywhere. We are unable to clearly identify a mechanism associated with recycling or high edge density responsible for the low edge T_i in L-mode plasmas.

Time-Dependent Perturbations

To explore the effects of recycling on transport in more detail, a reproducible series of supershot plasmas was perturbed by strong helium gas puffs and by lithium pellet injection, both just prior to beam injection and during beam injection. The lithium pellet transiently perturbs the plasma density but does not increase recycling, while helium puffing increases both density and recycling. As shown in Fig. 2, the plasma fully recovers the favorable supershot τ_E following pellet injection with a few hundred milliseconds. This is also true for pre-beam pellets which increase the target density a factor of ~7. By contrast, τ_E drops rapidly (time scale $\leq \tau_E$) and permanently to near L-mode values following a helium gas puff. The plasma's ability to attain supershot confinement following the pre-beam lithium pellet injection implies that supershots do not result from high T_i/T_e being driven in the initial period (first ~100 ms) of beam injection in supershot target plasmas – whose low density, in principle, allows the ions to be heated on a time scale considerably shorter than τ_E.

This section discusses the time response of the local transport coefficients (χ_i, χ_e) to the helium puff, as analyzed by the TRANSP time-dependent transport code using measured profiles of $n_e(R,t)$, $T_e(R,t)$, $T_i(R,t)$ and other diagnostic data (including $Z_{eff}(t)$ from single-chord visible bremsstrahlung emission, and neutral density from $D\alpha$ emission). For this analysis, the evolution

of the helium density following the puff was calculated from a particle transport simulation using a particle diffusivity $D(r)$ taken from measurements in similar supershot and L-mode plasmas. There is good agreement between measured diamagnetic beta, total neutron emission, and collimated neutron emission with TRANSP's simulations, providing some confidence that the assumed helium evolution is reasonable.

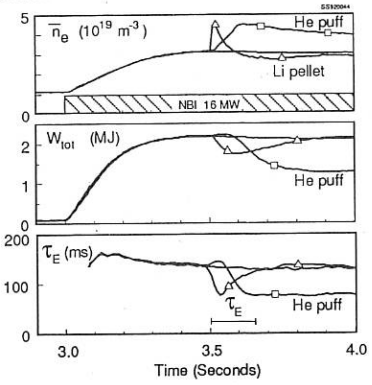

Figure 2: Evolution of supershot plasma perturbed by a lithium pellet or a helium puff.

Plasma conditions prior to the helium puff were typical of moderate-power supershots (T_{io} = 21 keV , T_{eo} = 7.5 keV, n_{eo} = 5 x 10^{19}m^{-3}, $\tau_E = 2.3\tau_E^{L-mode}$), with a core power balance dominated by convection. The density introduced by the helium puff, which propagates to the center in ~100 ms, causes a local adiabatic temperature response, a transient dump of beam-ion energy into the thermal plasma (W_{beam} decreases 0.6 MJ in 200 ms), and changes in beam power deposition and power split between ions and electrons. The global thermal energy confinement time decreases about 35% during the 200 ms following the puff, due to rather large (factor ~4) increases in core χ_i and smaller increases at the edge. Fig. 1(e-l) illustrates the plasma response. All quantities except χ_i and χ_e are expressed as a ratio to their value prior to the puff. An interesting feature of the data is that power flows and confinement in the core ($r \leq 30$ cm) deteriorate *before* they do further out in radius, despite the fact that the perturbations of local density and temperature propagate inward. This behavior is more suggestive of phenomena that involve a threshold (or, more generally, a sensitive dependence on gradients) than with forms of turbulence which yield transport that varies smoothly with local plasma conditions. The data does appear to exclude a major role for $j(r)$ as a cause of improved confinement in supershots, because the core transport increases on a time scale much shorter than the current penetration time (which is ~seconds).

[1] ZARNSTORFF, M., BARNES, C., EFTHIMION, P., HAMMETT, G., HORTON, W., et al., Advances in transport understanding using perturbative techniques in TFTR, in *Plasma Physics and Controlled Nuclear Fusion Research 1990*, volume 1, IAEA,Vienna, 1991.

[2] MYNICK, H. and ZWEBEN, S., Nucl. Fusion **32** (1992).

[3] HEIFETZ, D., ERHRARDT, A., RAMSEY, A., DYLLA, H., BUDNY, R., MCNEILL, D., MEDLEY, S., and ULRICKSON, M., J. Vac. Sci. Technol. A **6** (1988) 2564.

SIMULATIONS OF BEAM-FUELED SUPERSHOT-LIKE PLASMAS NEAR IGNITION[a]

R.V. Budny, L. Grisham, D.L. Jassby, J. Manickam, D. McCune, K. M. McGuire,
S. A. Sabbagh[b], S. D. Scott, D. Stotler, R. Wieland, M. C. Zarnstorff, and S. J. Zweben
Princeton Plasma Physics Laboratory, Princeton University,
Princeton NJ 08543, USA

In certain conditions, neutral beam injection (NBI) and low recycling result in supershot plasmas/1/. These are characterized by peaked density profiles and high central ion temperatures. We discuss the potential advantages of NBI fueled supershot-like plasmas in tokamaks operating near ignition. The goal is to investigate the feasibility of these plasmas to aid in the design of future advanced tokamaks.

NBI has been very successful in advancing tokamak plasmas close to ignition conditions. The primary benefits of NBI are heating and particle fueling, but the plasma currents generated by the beam ions are also of considerable interest. The optimal injection energy E_{inj} for the beam ions depends on the desired role of the NBI. For central particle fueling, E_{inj} should be low to maximize the particle current at fixed P_B, but high enough to penetrate to the center. For heating and current drive, higher E_{inj} is preferable for deepest penetration. With the standard positive ion beam technology, the neutralization efficiency becomes too low for useful power densities if E_{inj} is significantly greater than about 120 keV. Negative ion beam sources would be useful for heating and current drive at very high E_{inj} (500 keV or more), but the fueling rate of NBI is too low be practical. It seems generally accepted that future tokamaks which operate closer to ignition will have to be fueled and heated by means other than NBI since it is argued that the beams with low E_{inj} can not penetrate deeply into the dense plasmas of interest.

We show that contrary to the standard belief, for certain plasmas which are close to, or at ignition conditions, D and T neutral beams with $E_{inj} < 120$ keV can penetrate into the core. This offers potential solutions to some of the challenges for ignited plasmas. For instance, the NBI sources of D and T in the plasma core might keep the Z_{eff} low by displacing impurities and the He ash. If the core fueling rate is 10 times the DT fusion rate, and if the He concentration is 10 % of the fuel concentration, then the He should be displaced by the NBI ions along with thermal D and T, maintaining a steady state. Also it may prove difficult to replenish the fusing D and T if the inward pinch velocity is small. Pellet injection may be too disruptive for steady state ignition. Also pellets will not penetrate deeply when the plasma temperatures become too high. Unlike pellets, the NBI penetration becomes deeper as the temperature increases. Other potential uses of NBI are heating

---

[a] Work supported by the US DoE Contract No. DE-AC02-76-CHo-3073.
[b] *Department of Applied Physics, Columbia University, NY, NY 10027, USA*
/1/ J.D. Strachan, M. Bitter, A.T. Ramsey, M. Zarnstorff, et al., Phys. Rev. Lett. **58** (1987) 1004.

for reactor startup, or heating ions to complement the electron heating of the α particles in tokamaks operating close to ignition.

Yet another possible advantage of NBI is that supershot-like profiles with peaked density profiles may be produced, and these profiles appear advantageous for several reasons. The region of high density is concentrated in the region of highest temperature, so the pressure and stored energy are used efficiently to maximize the DT fusion rate. The fusion power depends roughly on $\langle n^2T^2 \rangle$ whereas the stored energy depends on $\langle nT \rangle$. MHD stability calculations/2/ have shown that the TFTR plasmas with more peaked pressure profiles have increased stability at high β. Also long pulse tokamaks will need large non-inductive currents, such as the bootstrap current. The bootstrap current is maximum where the gradient of the plasma pressure is maximum, which should be centrally located, as is the case for supershot profiles. A study of the ignition probability in BPX has shown that peaked profiles can significantly reduce the operating parameters required to achieve a desired fusion performance level relative to those needed with flat profiles/3/. Lastly, supershots might be used for reactor startup, with central ignition/4/ in a supershot that later might develop into an L-mode or H-mode plasma.

There are disadvantages which may preclude NBI from being of use in commercial reactors. One is the problem of shielding the neutrons since the neutral beams need straight lines of flight into the plasma. Also if an electrical power reactor were fueled continuously and entirely by NBI, economics imposes a lower bound on Q_{DT} and an upper bound on E_{inj}. The Carnot cycle would convert the fusion yield Y to electricity with an efficiency η which is typically about 1/3. Some fraction of this electricity, f, would be diverted to the NBI system, and converted to injected power P_B with an efficiency ν which is typically also about 1/3 using positive ion beams. Then

$$Q_{DT} \equiv \frac{Y}{P_B} = \frac{1}{f\nu\eta} \qquad (1)$$

must be greater than 50 to keep f small enough to be attractive, say less than 20% , if $\nu\eta = 10\%$. Also, the rate of D and T deposition must be at least as large as the DT fusion rate if NBI is the only fueling source. Each fusion reaction generates 17 MeV of fusion yield, so

$$\frac{Y}{17\ \text{MeV}} = \frac{P_B}{f\nu\eta\ 17\ \text{MeV}} < \frac{P_B}{2E_{inj}} \qquad (2)$$

requires $E_{inj} < f$ MeV if $\nu\eta$ is about 0.1. Thus with f = 0.1, E_{inj} = 100 keV could balance the DT fusion rate. In order for the NBI fueling rate to be much larger than the burnup rate, E_{inj} would have

---

/2/ J. Manickman, V. Arunasalam, C. W. Barnes, M.G. Bell, et al., "Stability of TFTR Plasmas", in *Plasma Physics and Controlled Nuclear Fusion Research*, (IAEA, Vienna) **1** (1989) 395.
/3/ D. Stotler and R. Goldston, Fusion Technol. **20** (1991) 7.
/4/ M. Redi, S.J. Zweben, and G. Bateman, Fusion Technol. **13** (1988) 57.

to be too small for penetration. Due to these bounds and potential disadvantages, NBI may be useful only for prototype reactors, or for partial fueling of power reactors.

We give specific examples of NBI fueled supershot-like profiles in which the fueling rate is greater than the DT fusion rate. The NBI penetration depends on the plasma profiles and NBI parameters. We studied NBI for the tokamaks in the following Table.

Generic tokamaks and plasmas with NBI fueling greater than the fusion rate

tokamak class	R (m)	a (m)	B (T)	I (MA)	$n_e(0)$	$T_e(0)$	P_B	Q_{DT}	I_{boot}(MA)
Small R	1.3	0.47	12	13	6	16.5	16	3.6	1.0
Medium R	3.0	0.69	5	3.5	4.4	15	30	5.7	3.1
Large R	7.0	1.1	12	6.5	3.6	47	50	29	5.8

The units of n_e, T_e, and P_B, are $10^{20}/m^3$, keV, and MW respectively, and I_{boot} is the calculated bootstrap current. The small R case is similar to the proposed IGNITOR tokamak/5/. The medium R case is similar to the proposed SSAT/6/, although DT is not planned to play a significant role in this tokamak. The large R case is similar to the ARIES-1 reactor/7/. The plasmas for all three were chosen to have an elongation and triangularity of approximately 1.8 and 0.3 respectively, and a relatively small minor radius which facilitates NBI penetration along the midplane. The plasma boundaries are compared in Figure 1.

Figure 1 Cross sections of plasma boundaries

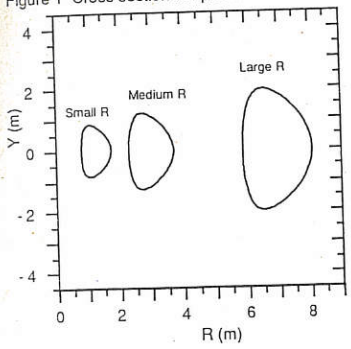

Figure 2 n_e profiles for the large R simulations

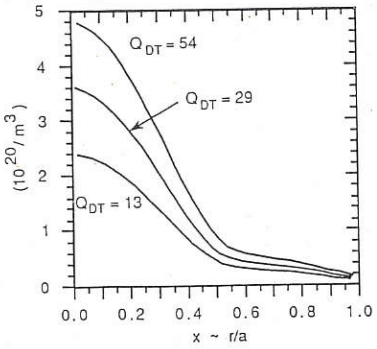

/5/ B. Coppi, M. Nassi, and L.E. Sugiyama, Physica Scripta, **45** (1992) 112.
/6/ K. Thomassen, R. Goldston, et al., "Steady State Advanced Tokamak (SSAT)," UCRL-ID-109807 (1992).
/7/ F. Nejmabadi, R.W. Conn, et al., "The ARIES-1 Tokamak Reactor Study," UCLA-PPG-1323 (1992).

The plasma transport for these unexplored plasmas is unknown, so we assumed density and temperature profiles representative of supershots, scaled to give the desired fusion yields. The n_e profile is assumed to have a peaked central region proportional to $\{1-(2x/3)^2\}^2$ and a broad pedestal proportional to $(1-x^2)$, where x = the square-root of the normalized toroidal flux. Examples are shown in Figure 2. The electron and ion temperatures are assumed to be equal and proportional to $(1-x^2)$.

The TRANSP plasma analysis code was used to calculate steady state conditions in these plasmas. The simulations calculate the heating profiles of the neutral beams and of the fast α particles/8/. They also predict the neutron emission profiles and the current profiles from the bootstrap and beam driven currents. The predicted α parameters include profiles of the α density, average energy, slowing down time, and β_α.

TRANSP calculates the transport coefficients required by the assumed profiles. These can be compared with those measured in presently operating tokamaks, or with theoretical predictions. The penetration depends on n_e, T_e, and E_{inj}. We choose $E_{inj} \approx 110$ keV, with the full and half energy fractions of the TFTR beam lines, and we explored bounds on n_e and T_e. As n_e increases, the beam penetration to the center decreases. This is shown in Figure 3 for the large R tokamak with 25 MW of D and 25 MW of T NBI into the densities shown in Figure 2. The thermal D fueling rates from NBI and wall recycling for the intermediate density case are compared with the DT fusion rate in Figure 4. The thermal T fueling rates are comparable to the thermal D fueling rates.

Figure 3 Varation of NBI fueling rate with n_e

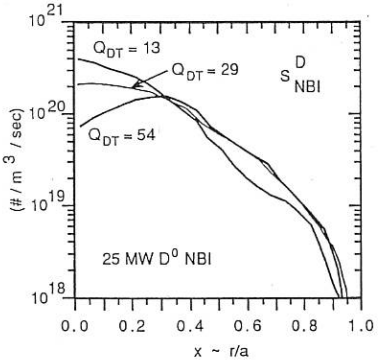

Figure 4 Fueling and burnup for the Q_{DT} = 29 case

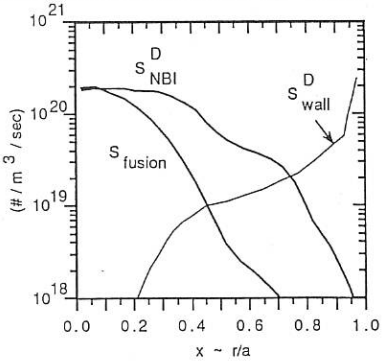

The other examples given in the Table also have predicted core beam fueling rates greater or equal to the DT fusion rates. The calculated bootstrap currents, as shown in the Table, can be large. We conclude that NBI fueled supershot-like plasmas could play an important role in future advanced tokamaks.

/8/ R.V. Budny, M.G. Bell, H. Biglari, M. Bitter, et al., Nucl. Fusion **32** (1992) 429.

THE INVESTIGATION OF PROPERTIES OF OHMIC AND ION-CYCLOTRON PLASMA HEATING IN THE CONDITIONS OF BORONIZED TOKAMAK FIRST WALL.

Azizov E.A., Buzhinskij O.I., Chernobaj A.P., Dmitriev V.I., Jakovenko V.P., Kanaev A.I.*, Kovan I.A., Krasilnikov A.V., Mirnov S.V., Monakhov I.A., Petrov A.A., Petrov V.G., Portnov D.V., Romannikov A.N, Semenov I.B., Sharapov V.M.*, Sotnikov S.M., Tugarinov S.N., Zakharov A.P.*

TRINITI , Troitsk, Moscow region, 142092, Russia
* Institute of Physical Chemistry, Academy of Science, Moscow, Russia

Different methods of the first wall coating with the low-Z materials are now actively investigated in view of the problem of impurity content reduction and plasma thermal isolation in tokamak discharge. Recent experiments have shown that the use of graphite limiters and protection screens favours reduction of the plasma effective charge, but at the same time it leads to significant gas flux from the walls during both ohmic and auxiliary heating. The boronization appeared to be very effective way of the impurity control and the gas release.

An original method of the first wall boronization was tested recently on the T-11M tokamak [1]. The method is based on carborans ($C_2B_{10}H_{12}$) decomposition in helium discharge. The elaborated technique of the wall conditioning allowed to improve characteristics of the ohmic stage of the tokamak discharge and to rise the ion-cyclotron heating efficiency.

The distinctive feature of the T-11M tokamak construction (R = 70 cm, B_T = 1.2 T, $I_p \leq$ 150 KA) [2] is complex structure of its first wall. In order to maximize the stabilizing role of the copper shell it is placed inside the SS vacuum chamber (a_{ch} = 25 cm) in the nearest vicinity of the plasma and is protected from erosion by thin

molibdenum screen. The extended surface of the vacuum chamber interior makes the problem of the wall conditioning on T-11M especially important.

As a result of the wall boronization application the ohmically heated discharges (I_p = 80 KA, a_p = 20 cm) appeared to be much more stable with higher achievable parameters ($\bar{n}_e \simeq 3.5 \cdot 10^{13}$ cm^{-3}, $T_e \simeq$ 350 - 400 eV) and better plasma thermal isolation. Particularly after the boronization the total radiative losses power was registered twice as low as before the boronization in spite of the total stored energy increase. The 1.5 decrease of the discharge circumference voltage after the boronization should be noted also.

The main components of the ICRF heating system on T-11M are: the high power triode autogenerator with the selective feedback circuit (2 MW, 17.3 MHz, 100 ms), matching 3/4λ coaxial feeders (50 Ω) , the poloidal 1/3 turn loop antenna which is placed at the low magnetic field side of the tokamak. The compact modular resonant antenna of T-11M is the TSP high power ICRH antenna prototype. It is basically tank circuit with very low characteristic impedance ($\rho \simeq$ 18 OHm) which is achieved by the special design of the parallel plate vacuum capacitor and its location inside the tokamak standard port in the vicinity of the current loop. All elements of the antenna are mounted on the port flange and are enclosed by the metal casing with radial slots on its plasma facing side. The modular principle of the construction allows independent antenna assembling and tuning. The antenna is capable to deliver up to 1 MW RF power to the plasma, the surface density of radiated power is being 5 KW/cm^2.

The experiments on ion-cyclotron heating were performed in conditions of the fast magnetosonic wave dumping on hydrogen minority in D-plasma ($n_H/n_D \simeq 5 \div 20$ %). The fast wave eigenmode resonances with low quality factor were observed. The RF generator switching on during the plasma density fall caused recurrence of the eigenmode tracking

regime which has been discovered earlier on TO-2 tokamak [3]. RF power input without boronization ($n_H/n_D \simeq 20$ %) was accompanied by significant increase of the radiative losses power P_R (Fig.1). The value of delivered RF power $P_{RF} \leq 100$ KW was limited by the major discharge disruptions. The ICRF heating efficiency in this conditions was not higher then $\eta \simeq 1.0$ eV/(KW cm^3 10^{13}).

The wall boronization notably changed the picture of ICRF heating (Fig.2). During the RF pulse the radiative losses remained nearly the same as in the ohmic stage. (The P_R increase just after the RF pulse is explained by the lack of plasma equilibrium control.) RF power input in conditions of $n_H/n_D \simeq 7 \div 10$ % led to effective deutron heating (Fig.3). The ion heating efficiency increased thrice comparing with the discharges without boronization (Fig.4). It should be noted that observed heating efficiency decrease with the delivered RF power rising can be explained by poor confinement of RF-accelerated high energy protons in low density plasma. In discharges with more dense plasma $n_e \simeq 3.5 \cdot 10^{13}$ cm^{-3} the heating efficiency has typical value of $\eta \simeq 3.5$ eV/(KW cm^3 10^{13}). The reduction of additional gas flux from the chamber walls during RF heating was also registered after the boronization.

The results of investigation of the tokamak first wall boronization encourage further efforts on delivering up to 1 MW RF power during ICRF plasma heating on T-11M, certain measures on plasma equilibrium control improvement and plasma current rise being also necessary.

[1] Azizov E.A., Buzhinskij O.I., Belov A.M., et.al., to be published in Journ.of Nucl. Mat., 1992.

[2] Mukhovatov V.S. Heating in Toroidal Plasmas, Proc. Joint Grenoble-Varenna Int. Symp., Como, 1980, Vol.II, p.761.

[3] Kovan I.A.,Kovrov P.E.,Monakhov I.A., Proc. 17th Eur. Conf. on Cont. Fus. and Pl. Heat., Amsterdam, 1990, Pt.III, p.991.

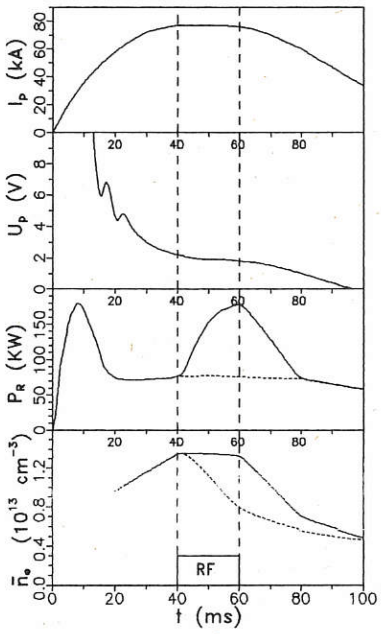

Fig.1 ------ OH ——— OH+ICRH without boronization

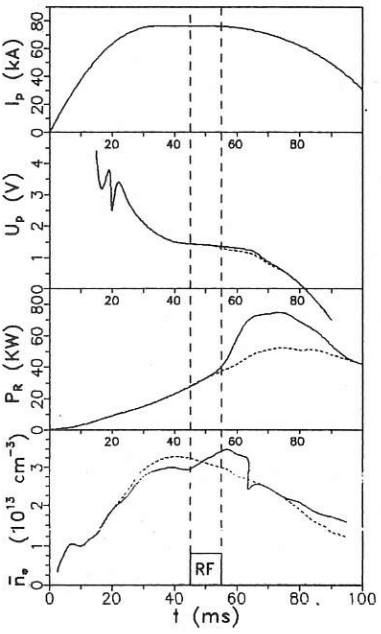

Fig.2 ------ OH ——— OH+ICRH with boronization

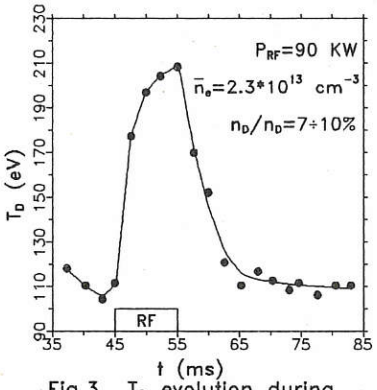

Fig.3 T_D evolution during OH+ICRH after boronization

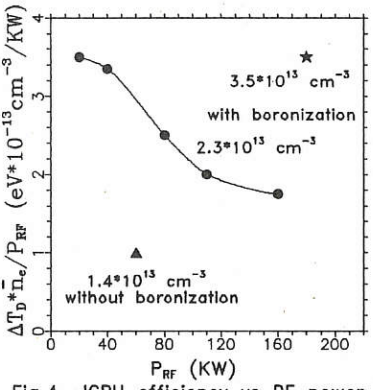

Fig.4 ICRH efficiency vs RF power for different plasma concentration

CONFINEMENT SCALING FOR KINETIC ENERGY IN TOKAMAK L-MODE PLASMAS

T. Takizuka
Japan Atomic Energy Research Institute, Naka Fusion Research Establishment
Naka-machi, Naka-gun, Ibaraki-ken, 311-01 Japan

1. Introduction

Scaling for the global energy confinement in tokamak L-mode plasmas has been studied by many authors with the use of the ITER confinement database [1]. Dimensionally correct analysis by Lackner and Gottardi [2] showed the L-mode confinement determined a gyro-Bohm type transport ; $\tau_E \sim B^{0.8} (n/P)^{0.6}$, while the analysis by Christiansen et al. [3] indicated that a high-β collisional model can describe the L-mode confinement ; $\tau_E \sim B^{1.14} n^{0.16}/P^{0.6}$ (τ_E is the global energy confinement time, B the magnetic field, n the plasma density, and P the heating power). The dependence of τ_E on n_e is weak [1,3], which has been explained to be a decreased beam penetration at higher density and an increased beam ion contribution at lower density [1]. The parameter dependence of τ_E is found to be not unique among different tokamak devices. Even in the JT-60 tokamak, dependence of τ_E on such plasma current I_p is different between for limiter discharges and for divertor discharges [1]. The causes of these facts have not been clarified yet, and should be explained physically in order to use scaling expressions accurately for designing future tokamak reactors.

In the present paper, we analyze in detail the kinetic database of the JT-60 tokamak [5] in order to identify a satisfactory transport model for L-mode confinement and to clarify the cause of the above mentioned difference in JT-60 limiter and divertor discharges.

2. Results

The database used here is of neutral beam heating experiments in the JT-60 tokamak with the circular plasma cross section. Data points for limiter discharges and divertor discharges are 55 and 67, respectively. Major radius R is 3.0-3.1m, minor radius a is 0.8-0.9m, plasma current Ip is 1-3MA, toroidal magnetic field B_t is 3-4.5T. Data for two types of wall materials, TiC/Mo (44 pts) and Graphite (78 pts), are included. As is shown in Fig.1, the density

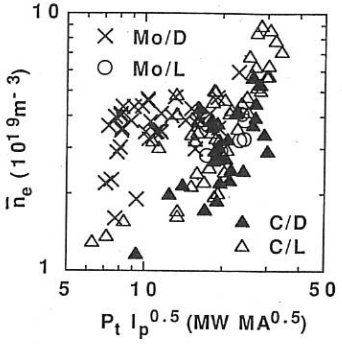

Fig.1 Correlation between $\bar{n}_e$ and $P_t I_p^{0.5}$

control in graphite-wall-divertor discharges is difficult, and the line averaged electron density $\bar{n}_e$ depends strongly on the plasma current I_p and total heating power P_t. The note, Mo/D, in the figure means a TiC/Mo-wall-divertor discharge, Mo/L a TiC/Mo-wall-limiter, C/D a graphite-wall-divertor and C/L a graphite-wall-limiter discharges. Data for TiC/Mo wall, on the other hand, spread widely in the P_t-$\bar{n}_e$ plane, and they enable us to separate the P_t dependence and $\bar{n}_e$ dependence of the energy confinement.

Since there are many data points for I_p =1.5MA and B_t =3.9-4.5T (73 pts), we analyze at first these data set. Figure 2 shows P_t~0.5 dependence of the total stored energy W_{tot}, which agrees well with the prediction by ITER 89P scaling law. The $\bar{n}_e$ dependence of $W_{tot} \propto \bar{n}_e^{0.25}$ is a little stronger than the prediction. The standard deviation σ from a fitting expression, $W_{tot}^{fit} = C\, P_t^{0.5}\, \bar{n}_e^{0.25}$, is 9.7%, where C is a constant for $\Sigma\,(W/W^{fit} - 1) = 0$ and $\sigma^2 = N^{-1}\Sigma\,(W/W^{fit} - 1)^2$ with N data points. The fraction of beam ion energy in W_{tot} is usually 8-20% and sometimes becomes up to 50%.

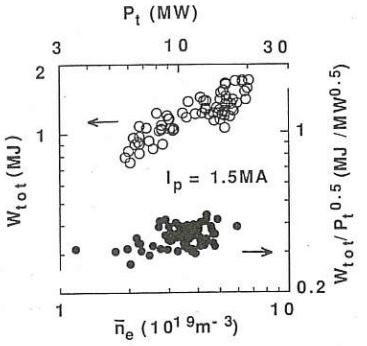

Fig.2 Dependence of W_{tot} on P_t and $\bar{n}_e$

The dependence of the kinetic energy W_k on P_t and n_e for I_p=1.5MA is studied now; $W_k^{fit} = C\, P_t^{\alpha_P}\, \bar{n}_e^{\alpha_n}$. To determine a suitable set of (α_P, α_n), we search for the minimum of σ. Figure 3 shows the standard deviation as functions of α_P and α_n. We also refer the 61-pts subset excluding very-low-density data points, and take account of the dependences of W_e, the electron energy, and W_i, the thermal ion energy, as $W_e^{fit} \propto P_t^{\alpha_P}\, \bar{n}_e^{\alpha_n}$ and $W_i^{fit} \propto P_t^{\alpha_P}\, \bar{n}_i^{\alpha_n}$. Subscripts k0 and k1 denote the total kinetic values for 73 pts and for 61-pts subset, i the ion component and e the electron component. Values of thermal ion density $\bar{n}_i$ are measured from figures of profile database in Ref.[4], and the ratio n_i/n_e is affected by impurity as

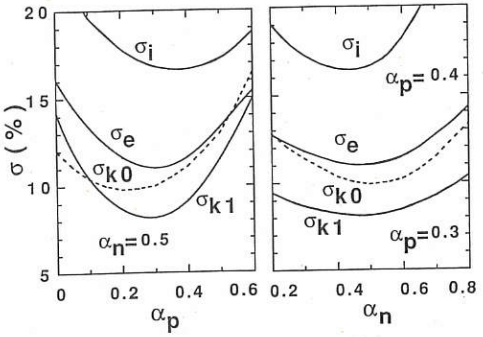

Fig.3 Standard deviation σ vs α_P and α_n

well as by $\bar{n}_e$ and P_t. Although the minimum of σ_{k0} is at (α_P=0.25, α_n=0.5), other minimums of σ_{k1}, σ_e and σ_i are at $\alpha_P > 0.3$. This is due to the correlation among n_i, n_e and P_t. We set therefore the following fitting forms;

$$W_k^{fit} = C_k P_t^{1/3} \bar{n}_e^{1/2}, \quad W_e^{fit} = C_e P_t^{1/3} \bar{n}_e^{1/2}, \text{ and } W_i^{fit} = C_i P_t^{2/5} \bar{n}_i^{1/2}.$$

The cause of larger σ_i value is supposed to be the error in the measurement of W_i or the existence of unknown parameters such as η_i value or effect of sawtooth oscillations. The scatter in W_k/W_k^{fit} is found mainly due to the scatter in W_i/W_i^{fit} and the value of σ for a fitting form $W_k/W_k^{fit} \propto (W_i/W_i^{fit})^{0.5}$ is drastically reduced to σ = 5.3% from σ_{k0} = 9.8%. On the other hand, the correlation between W_k and W_e is weak; $W_k/W_k^{fit} \propto (W_e/W_e^{fit})^{0.4}$ with σ = 8.7%, which is only 1% reduction from σ_{k0}. If we identify the cause of larger σ_i value, we can make a scaling expression with small σ_k, which consists of only physical quantities without using $(W_i/W_i^{fit})^{0.5}$. From the viewpoint of physics, at present, we use only uncorrected scaling expressions hereafter.

Next we study the dependence of W_k on I_p and B_t. There are 17 points for I_p = 1MA and 12 points for I_p = 2MA, and the scaling of $W_k^{fit} \propto P_t^{1/3} \bar{n}_e^{1/2}$ fits well these data. The I_p dependence is found to be $W_k \propto I_p^{1/2}$ in the range of I_p = 1-3MA. The B_t dependence, on the other hand, is difficult to be determined accurately because of small number of data for lower B_t. ; $W_k \propto B_t^{\alpha_B}$ with $0 < \alpha_B < 1$. Finally we have a fitting expression for the kinetic energy confinement time τ_{Ek} ;

$$\tau_{Ek}^{fit} = C_k (\bar{n}_e I_p B_t)^{1/2} P_t^{-2/3},$$

where we choose α_B equal to 0.5 for simplicity. Justification of this scaling is demonstrated by Fig.4, where all 122 points are plotted and σ_k is 11.5%.

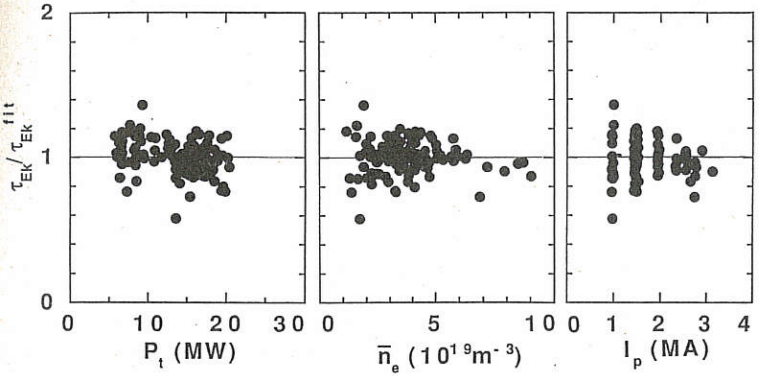

Fig.4 Dependence of $\tau_{Ek}/\tau_{Ek}^{fit}$ on P_t, $\bar{n}_e$, and I_p

The present result differs much from former results by using the database of total stored energy. Power degradation of τ_{Ek} is stronger than that predicted by the gyro-Bohm transport model. The n_e dependence of τ_{Ek} is rather strong compared with that of τ_E. These differences originate in the effect of beam ion component. There is no discrepancy in the parameter dependence of τ_{Ek} between divertor and limiter discharges, and the difference in τ_E between them is due to lower density in divertor operations. Lastly we note that this expression is also applicable to the ohmic confinement at higher density (so called saturated ohmic confinement) without change of any coefficients.

3. Summary and discussion

By detailed analysis of the kinetic database of JT-60 experiments, we obtain a scaling expression, $\tau_{Ek} \propto (\bar{n}_e I_p B_t)^{1/2} P_t^{-2/3}$, for L-mode discharges as well as for ohmic discharges at higher density. The beam ion component plays important roles in the global confinement property. There are significant differences between parametric dependences of τ_{Ek} and τ_E.

The effective heat diffusivity χ near $r/a \approx 2/3$ is almost proportional to $a^2/4\tau_{Ek}$, and the effect of edge transport on τ_{Ek} is found to be small. The present result suggests that the energy confinement in tokamak L-mode plasmas is described by a collisionless or weakly-collisional high-β transport model . We presume the heat diffusivity of a form $\chi \propto q^{3/2} \beta^{1/2} (\rho/a) (T/eB)$, where q is the safety factor, β the ratio of plasma- to magnetic- pressures, ρ the Larmor radius, and T the temperature. The size scaling of τ_{Ek} predicted by this model becomes $\tau_{Ek} \propto I_p a^2 (\bar{n}_e q)^{1/2} P_t^{-2/3}$, where the aspect ratio dependence cannot be determined. The effect of the heating profile, i.e., a decreased beam penetration at higher density, has not been considered here. The applicability of the present result and model will be checked by using new database of JT-60 and JT-60U experiments.

Acknowledgment I wish to thank authors of Ref.[4] for their efforts to complete the database, which is just a base of the present analysis. I am also indebted to the members of the JT-60 team for their contributions to the database.

References

[1] for example, P. Yushmanov, T. Takizuka, K. Riedel, O. Kardaun, J. Cordey, S. Kaye, D. Post, Nucl. Fusion **30**, 1999 (1990).

[2] K. Lackner, N. Gottardi, Nucl. Fusion **30**, 767 (1990).

[3] J. Christiansen, J. Cordey, O. Kardaun, K. Thomsen, Nucl. Fusion **31**, 2117 (1991).

[4] M. Kikuchi, K. Kikuchi, T. Aoyagi, K. Tani, " Kinetic Database of the JT-60 Tokamak during 1985 - 1987 Experiments," JAERI-M 91-057 (1991).

THE EFFECT OF CURRENT PROFILE CHANGES ON CONFINEMENT IN THE DIII-D TOKAMAK*

J.R. Ferron, L.L. Lao, T.S. Taylor

General Atomics, San Diego, California, USA

Experiments in the DIII-D tokamak have demonstrated that the effect of changes in the current profile on plasma confinement varies with the discharge shape. The results are similar in many respects to those from other tokamaks.[1-3] In all cases, a rapid change in the plasma current in an L-mode, circular or moderately elongated, discharge has been used to produce a transient change in the current density profile. Although the detailed results vary among tokamaks, it is generally observed that during and immediately following a negative plasma current ramp, the stored energy does not follow the L-mode scaling that predicts that confinement should be proportional to the total plasma current. The stored energy changes on the time scale of the relaxation of the current density profile rather than the shorter time scales of the energy confinement time or the change in the total current. Because of the discharge shaping capability of the DIII-D tokamak it has been possible to extend these current ramp experiments beyond the L-mode, moderate elongation case ($\kappa \leq 1.5$) to highly elongated ($\kappa \leq 2$) double-null divertor discharges in H-mode. In separate experiments, a rapid change in the discharge elongation has also been used to vary the current density profile. This paper shows that the dependence of the plasma confinement on the current profile changes when the discharge shape is changed. This variation with discharge shape provides evidence for a model that predicts that changes in the local magnetic shear resulting from the changes in the current profile can result in decreased local transport.

In L-mode, nearly circular, inside-wall-limiter discharges in DIII-D the plasma confinement varies approximately linearly with the internal inductance, ℓ_i. To demonstrate this, a rapid decrease in the plasma current has been used to induce transient changes in the current density profile. Higher values of ℓ_i result from a more peaked current density distribution and from a region of zero or negative current density in the outer portion of the discharge produced by the negative surface voltage that drives the current ramp. With a factor of 2 decrease in the current and a current ramp rate of $dI/dt \approx -4$ MA/sec, ℓ_i increases from 1 to as high as 2.75. The time evolution of this type of discharge is illustrated in Fig. 1 along with the evolution of a comparison discharge for which the plasma current was constant. Here, $\kappa = 1.2$, the neutral beam power is constant at 10 MW and $n_e \approx 6 \times 10^{19}\,\mathrm{m}^{-3}$. The thermal stored energy shown in the figure is obtained by subtracting the calculated value of the energy of the unthermalized fast ions from the total stored energy calculated from the MHD equilibrium reconstruction. The thermal stored energy changes by less than 10% during the current ramp. If the confinement time depended only on the total plasma current the stored energy would be expected to decrease by a factor of 2 on the time scale of the current ramp, a period of approximately $3\tau_E$. Instead, about one second is required before the factor of 2 decrease is complete, the same time scale as the relaxation of the current profile, or the decay of ℓ_i.

The observed changes in the thermal stored energy occur because of changes in the electron temperature and density. On the time scale of the current ramp, there is no measurable change in the electron density or ion and electron temperature profiles. After the current profile relaxation, both n_e and T_e have decreased by 20% to 30% while there is still no change in the ion temperature. The data in Fig. 2, obtained from several discharges during the current profile relaxation, show that there is an approximately linear relation between ℓ_i and the confinement time. The figure shows the confinement time normalized to the JET/DIII-D scaling law for

* This is a report of work sponsored by the U.S. Department of Energy under Contract No. DE-AC03-89ER51114.

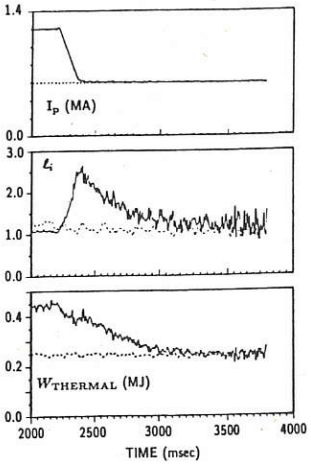

FIG. 1. The time evolution of an L–mode, $\kappa = 1.2$ discharge during and after a rapid current ramp (solid lines). The dashed lines show a comparison discharge for which the plasma current was constant.

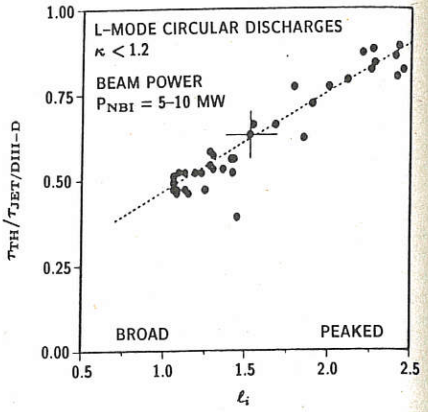

FIG. 2. The observed scaling of thermal energy confinement normalized to the JET/DIII–D H–mode energy confinement scaling as a function of ℓ_i.

H–mode[4] which has no ℓ_i dependence. There is nearly a factor of 2 improvement in confinement obtained through modification of the current density profile and the discharges with the highest values of ℓ_i have confinement close to that observed in H–mode.

In similar experiments with high elongation ($\kappa = 1.95$), high triangularity ($\delta = 0.85$), double-null divertor, H–mode discharges there is a large change in stored energy during the current ramp. The time evolution of this type of discharge is illustrated in Fig. 3. Here the neutral beam power is constant at 6.3 MW, $n_e = 1.1 \times 10^{20}\,\mathrm{m}^{-3}$, and the discharge is in a steady-state H–mode with ELMs by 2100 ms, well before the beginning of the current ramp. During the factor of 2 current ramp, the stored energy decreases to 65% of the value present before the ramp even though ℓ_i increases from 1 to 2.8. The current ramp is followed by a period of nearly constant stored energy, even as ℓ_i decays, which lasts until 3500 ms. The change in stored energy during the current ramp is accompanied by a drop in electron density of as much as 60%, primarily in the outer half of the discharge, and a 30% drop in electron temperature.

There is some variation with time of the ELM character in these H–mode discharges, but this variation has no effect on conclusions drawn about the connection between the current profile and confinement. During the ramp the elongation decreases from 1.95 to 1.75 because of the effect of the increase in ℓ_i on the control of the discharge shape. This results in a decrease in the ELM frequency which lasts until 3500 ms. The rapid drop in stored energy during the current ramp cannot, however, result from the change in ELM frequency since a decrease in ELM frequency would be expected to result in an increase in the confinement time. The period of constant stored energy before 3500 ms during which the ELM frequency is approximately constant and ℓ_i decays indicates a weak dependence of the confinement on ℓ_i. The slow drop in stored energy after 3500 ms coincides with a slow increase in the ELM frequency. A comparison of confinement in the period after 4000 ms with the confinement in the period before the current ramp agrees only approximately with the linear scaling of τ with total current that is commonly observed in H-mode because of the difference in ELM character in these two periods.

The observed changes in the global confinement are consistent with a model of the diffusivity which depends on both the plasma current and the local current profile. In both the low

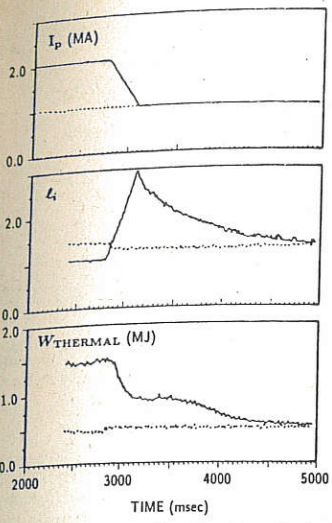

FIG. 3. The time evolution of an H–mode, double-null divertor discharge during and after a rapid current ramp (solid lines). The dashed lines show a comparison discharge for which the plasma current was constant.

elongation discharge and the high elongation discharge, on the short time scale of the current ramp, the current density change is localized to the outer portion of the discharge. Scaling of energy confinement with the total plasma current has been well established for both L–mode and H–mode, so in the case of the negative current ramp in the circular discharge, the local change in the current density profile must offset the change in plasma current because there is no net change in local transport and no net change in confinement. In the double-null case, the effect of the local change in the current profile must be weak because the confinement scales with current during the ramp. These observations are consistent with theories that link pressure gradient driven turbulence and energy confinement.[5] These theories suggest that the level of transport is proportional to the ratio of the local pressure gradient to a function of the local magnetic shear which is approximately the critical pressure gradient for the onset of instability (P'_{crit}). An increase in the local magnetic shear which results from the change in the current profile can result in an increase in P'_{crit}, offsetting the decrease which would result from a decrease in the total current.

A simple test of this idea has been made using a global parameter, β, rather than the local parameter, P'. The time evolution of the energy confinement is compared to the ratio of the critical beta to the measured value of beta: $\tau \propto f(\beta^{\alpha}_{crit}/\beta)$. Since $\beta \propto \tau P_{aux}$, we expect that the time evolution of energy confinement will be similar to the time evolution of the critical value of beta: $\tau \propto h(\beta^{\gamma}_{crit}/P_{aux})$. Here α and γ represent unknown power laws, P_{aux} is the auxiliary heating power which is constant in these experiments, and β_{crit} is obtained from the integral of P'_{crit}. The pressure gradient driven mode which might be responsible for the turbulence is not known at this point, so we use the well established stability theory[6] for the infinite-n, ideal ballooning mode to provide a value for β_{crit}. The modes actually responsible for the turbulence would be expected to be unstable at values of β below β_{crit} for the ideal mode, but the assumption is made here that the value of the critical pressure gradient which drives the turbulence scales in the same manner as P'_{crit} for the ideal mode.

In both the near-circular discharge and the strongly shaped discharge the time evolution of $\tau_{thermal}$ is similar to that of the critical beta for the ideal ballooning mode. Figure 4(a) shows the result of calculations for the $\kappa = 1.2$, L–mode discharge shown in Fig. 2. With no change in the form of the current profile, the factor of 2 change in the total current during the ramp would be expected to be responsible for a factor of 2 change in β_{crit}. However, ideal ballooning stability calculations show that in a circular discharge the value of β_{crit} increases nearly linearly with ℓ_i,[6] so that the change in total current is offset by the change in ℓ_i and the values of β_{crit} before and after the ramp are nearly equal. β_{crit} decays slowly as the current profile relaxes, as does $\tau_{thermal}$. Numerical calculations for a strongly shaped discharge such as the double-null divertor show that the scaling of β_{crit} with ℓ_i is much weaker than it is in the case of the circular discharge.[6] Thus an increase in ℓ_i would be expected to have a smaller effect on confinement. Figure 4(b) illustrates the calculated time evolution of β_{crit} for the discharge in Fig. 3. There is a comparable, large, difference in both $\tau_{thermal}$ and β_{crit} after the current ramp compared to the value before the current ramp. In the period after the current ramp, as ℓ_i decays there is only a small change in both β_{crit} and $\tau_{thermal}$.

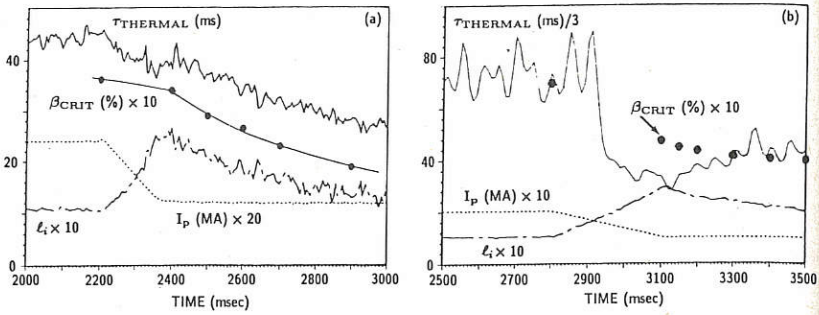

FIG. 4. The time evolution of τ_{thermal} and β_{crit} for the infinite-n, ideal ballooning mode during and after a current ramp. Also shown are total current and ℓ_i. (a) L–mode, nearly-circular discharge, (b) H–mode, double-null divertor discharge.

This difference between the circular and the strongly shaped discharges in the comparison of the time evolution of β_{crit} and τ_{thermal} provides the evidence for a connection between the local magnetic shear and the effect of the current ramp on confinement. In the near circular discharge the confinement remains constant during the negative current ramp because the increase in local shear can offset the decrease in the total current. In contrast, in the strongly shaped discharge the change in magnetic shear has a weaker effect and as a result the effect of the total current dominates the changes in confinement during the current ramp.

A rapid increase in the discharge elongation, at constant total current, has also been used to make the current profile more peaked. Changing κ from 1.2 to 1.8 in 200 ms in an L–mode, inside wall limiter discharge increased ℓ_i from 1.1 to 1.7. When the peak value of κ is below 1.8, the discharge remains in L–mode. In this case, a comparison with a discharge with κ constant at 1.8 shows that there is a small increase in confinement that results from the increase in ℓ_i but that most of the increase in confinement probably results from the increase in κ. This is consistent with the idea that in more strongly shaped discharges, changes in ℓ_i have a weaker effect on confinement, as in the double-null experiments.

In summary, for low elongation discharges there is a linear dependence of energy confinement on the internal inductance and for strongly shaped discharges, such as a double-null divertor or an elongated limiter, the dependence of energy confinement on ℓ_i is much weaker. This behavior is consistent with a model that proposes that a local change in the magnetic shear can reduce the level of transport which results from pressure gradient driven turbulence. This model has been tested using global parameters and been shown to be consistent with the time evolution of the data.

REFERENCES

1. Zarnstorff, M.C., *et al. Proc. of the 13th Int. Conf. on Plasma Phys. and Controlled Nuclear Fusion Research*, (IAEA, 1991) Vol. 1, p. 109.
2. O'Rourke, J., *et al. Proc. of 18th European Conf. on Controlled Fusion and Plasma Physics*, (EPS, Berlin, Petit-Lancy, Switzerland, 1991), Vol. 1, p. 37.
3. Murmann, H., *et al. Proc. of 18th European Conf. on Controlled Fusion and Plasma Physics*, (EPS, Berlin, Petit-Lancy, Switzerland, 1991), Vol. 1, p. 109.
4. Schissel, D.P., *et al.* Nucl. Fusion **31**, 73 (1991).
5. Connor, J.W., and Taylor, J.B., *Proc. of the 10th Int. Conf. on Plasma Phys. and Controlled Nuclear Fusion Research*, (IAEA, 1988) Vol. 2, p. 13.
6. Lao, L.L., *et al.* Phys. Fluids B, 4, 232 (1992).

HEAT TRANSPORT WITH STRONG ON/OFF-AXIS HEATING

by B. Balet, D. Boucher, J.G. Cordey, D.G. Muir, S.V. Neudatchin* and G. Schmidt+
JET Joint Undertaking, Abingdon, Oxfordshire, OX14 3EA

* I.V. Kurchatov Institute of Atomic Energy, Moscow, Russia
+Princeton Plasma Physics Laboratory, Princeton, U.S.A.

1) Introduction In this paper we describe recent experiments on JET in which comparisons have been made between on and off-axis ICRH following pellet injection. The reason for the injection of the pellet is twofold, first to suppress the sawteeth by flattening the current profile and second to provide a large heat sink in the plasma centre, such that with off-axis heating, regions in which the heat flux Q is - ve can be examined. Previous experiments with off-axis ICRH on JET [1] were done without pellet injection and although both the temperature profile and the energy content were sensitive to the location of the resonance, the heat flux was always outward. These experiments along with the more recent JET experiments are in sharp contrast to many other experiments [2] [3] [4] in which the temperature profile is somewhat insensitive to the location of the heating profile. One key difference between the JET ICRH experiments and other experiments is the lack of sawtoothing in the JET data, as well as flattening the temperature and density profiles sawteeth may also disturb the fast ion/electron heating profile.

2. Description of the data The main plasma parameters are shown in Fig. 1, for the off and equivalent on axis heated pulses. In both pulses, a 4 mm pellet is injected 3.8 secs after the commencement of the discharge, just after the current reaches its flat top, this causes the central temperature to drop by approximately 2 KeV. The time development of the electron temperature profiles after the injection of the pellet are shown in Fig. 2. Immediately after the start of the heating it can be seen that an off-axis peak in the temperature is formed at the resonance position for the off-axis heated peaks. Some 0.2 secs later the profile has become profoundly hollow and remains hollow for a further 1 sec. The reason for the peaking being the ohmic heating which is peaked on axis 2 secs after the start of heating. In contrast the on axis heating pulse has a strongly peaked electron temperature profile throughout.

3. Transport Analysis Both interpretative (TRANSP) and predictive codes have been used to analyse the data. The power balance consists of five significant terms, the ICRH (P_{ICRH}) and ohmic (P_{OH}) input terms, the thermal inertia (W) and radiation (P_{rad}) loss terms and the conductive heat flux, the convected heat flux is very small. The radiation loss term is

also very small in the plasma centre being $\sim\frac{1}{4}$ of the ohmic heating term. The equation for the total (ion + electron) conducted heat flux Q has the form

$$QS = \int_o^\rho P_{ICRH} + \int_o^\rho P_{OH} - \int_o^\rho \dot{W} - \int_o^\rho Prad \quad , \qquad (1)$$

where S is the surface area of the flux surface ρ. (ρ ≡ horizontal width of the magnetic surface normalised to the width of the outer magnetic surface). For the off-axis heating case, initially in the plasma centre the thermal inertia term is larger than the power input terms which are mainly ohmic hence the heat flux Q is initially - ve.

The development Q versus -nΔTe is shown in Fig. 3 at several different radial positions for the two radial positions close to the plasma centre both Q and - nΔTe start negative at the beginning of the heating phase, then eventually become positive after passing close to the origin. Moving out further in radius on the outboard side of the resonance the starting point moves further away from the origin but the curves are still approximately straight lines and extrapolate to pass close to the origin. At the outermost radii $0.6 < \rho < 0.8$ there is not a sufficient range in - nΔTe to make a meaningful extrapolation.

To investigate further the region in which q and -nΔTe are negative, an inward heat pulse propagation technique [5] has been developed, using the grating polychrometer data in the region R = 3.58 → 3.12m. Essentially the time dependent heat transport equation is solved with the boundary condition imposed at R = 3.58 and χ_e varied to obtain the best fit to the polychrometer data at locations nearer the centre, a typical example is shown in Fig. 4. It is found that the χ_e varies from 0.7 m^2/s if one ignores the ohmic heating altogether down to 0.3 m^2/s when one includes the ohmic heating, and that the maximum value for the inward heat velocity is 0.4 m/s. This is in agreement with the interpretative analysis presented in Fig. 3.

In Fig. 5 we compare the χ's of the on and off-axis heating pulses at the same time t = 4.8 s just before the first sawtooth in the on axis heating case. The χ's are very similar in the region $\rho > 0.5$, but in the inner region the off-axis heating χ is lower. The lower value of χ in the off-axis heating case no doubt being due to the lower value of T or ΔT.

4. Discussion From the results presented in Figs (2) - (5) the following conclusions can be drawn. In the absence of sawteeth the electron temperature profile responds strongly to the location of the heating profile (Fig. 2), and there is no evidence of any significant heat pinch in the total Q (Fig. 3). Hence a model of the form

$$Q = -\chi n \Delta T \qquad (2)$$

can adequately describe the data. In principle it should be possible to determine separately the T, ∇T and r/R dependence of χ from these pulses and our future studies will be concentrated in this direction.

We have also compared the data with an existing transport model namely the RLW (6) one, which is of the same form as Eq. (2) with a strongly nonlinear form for χ as a function of ∇T. The fit to the off-axis heating case, which is shown in Fig. 5, is good, indicating that this model has the right behaviour of Q with ∇T at low values of ∇T of either sign.

References

1) J.D. Callen, J.P. Christiansen, J.G. Cordey, etal, Nucl Fusion 27 (1987) 1857.

2) F. Wagner, et al., Phys. Rev. Lett 56 (1986) 2187.

3) T.C. Luce, C.C. Petty, and J.C.M. Hass, Phys. Rev. Lett. 68 (1992) 52.

4) D.P. Schissel, T.H. Osborne, J.C. DeBoo, etal, GA - A20696 (1991) submitted to Nuclear Fusion.

5) S.V. Neudatchin, Contr. Fus. and Plasma Heating, (Proc. 15th Euro. Conf. Dubrovnik, 1988), V12B Part 111, EPS, 1988, 1147.

6) P.H. Rebut, M.L. Watkins, D.J. Gambier and D. Boucher, Phys. Fluids B3 (8) 2209 (1991).

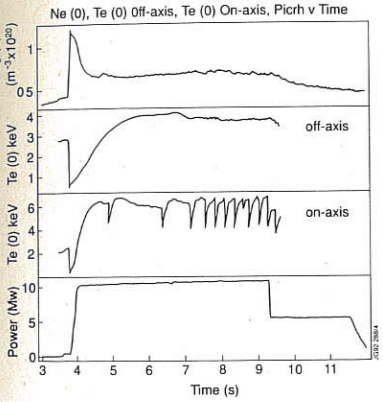

Fig. 1 The central density (off/on axis very similar), the central electron temperature (off axis case) the central temperature (on axis case), ICRH power (off/on very similar)

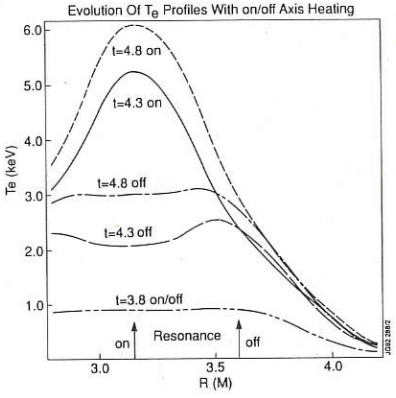

Fig. 2 The radial electron temperature profile at several different times for on/off axis heating

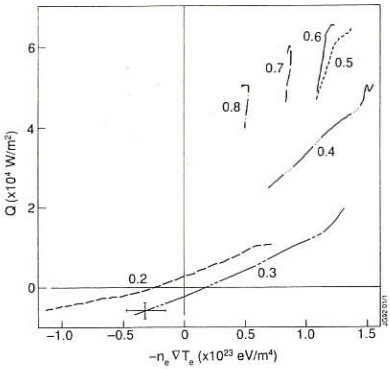

Fig. 3 The total heat flux Q versus -n∇Te at different values of the normalised radius ρ

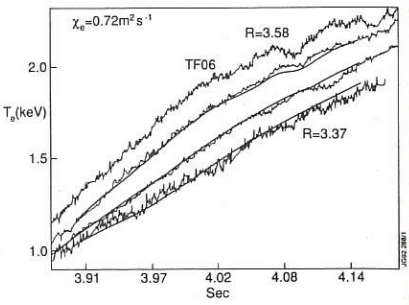

Fig. 4 The time development of the electron temperature at the radial positions R = 3.58, 3.52, 3.45, 3.37, and the fit from the inward heat pulse propagation analysis without heat sources inside R = 3.58.

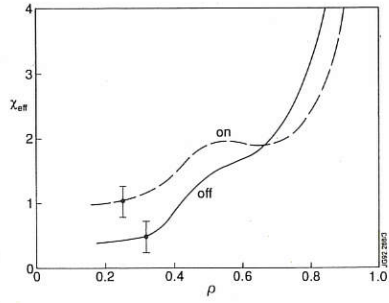

Fig. 5 The χ_{eff} versus normalised radius at $\tau = 4.8$ for the on and off heated cases

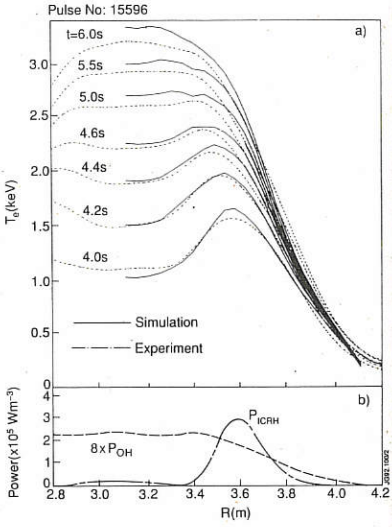

Fig. 6 a) Evolution of the measured temperature profile (dotted curves) and the prediction from the RLW model versus time, b) Input power profiles

ENERGY CONFINEMENT IN HIGH PERFORMANCE JET D-T PLASMAS

P.M. Stubberfield, B. Balet, J.G. Cordey, D.P. O'Brien, K. Thomsen, M. von Hellermann
JET Joint Undertaking, Abingdon, Oxon, OX14 3EA, U.K.

Introduction It has been shown previously that high fusion performance JET plasmas are obtained in the hot ion H-mode regime (1). This regime was therefore chosen for the tritium experiments in JET (2), and in the course of these experiments a number of pulses having good central confinement were obtained. However the good confinement is only maintained for a short time before the ion temperature falls causing a dramatic drop in the thermal-thermal component of the neutron yield. The degradation of the performance does not clearly follow the same pattern in each discharge and careful analysis is needed in order to understand the sequence of events. The $1\frac{1}{2}$D transport analysis code TRANSP (3) is being used to analyse the performance of these pulses. Details of the results obtained for one discharge are described in this paper. It is important to get an understanding of the good confinement regime since, if it can be extended in future JET experiments, values of Q_{DT} substantially above unity could be obtained.

High Performance JET Pulses Figure 1 shows the time evolution of the thermal confinement time for four discharges compared to the value predicted by the DIII-D/JET H-mode confinement scaling law (4). The first pulse #18246 is a conventional medium density H-mode discharge with similar neutral beam heating power to that in the series of hot ion H-mode pulses and the confinement does indeed follow the DIII-D/JET scaling law. Pulse #26087 is the best pure deuterium discharge, its thermal confinement being about double that predicted by the confinement scaling law. The third pulse #26095 is a deuterium-tritium discharge, with a 1% mixture of tritium in deuterium introduced into one PINI. It shows the largest enhanced confinement phase of any discharge in this series and it is a factor 2 above the DIII-D/JET scaling law and a factor 3 above the Goldston L-mode scaling law (5). The last pulse #26148 is a tritium-deuterium discharge with a 100% mixture of tritium introduced into two PINIS. All these three pulses show a period of enhanced confinement prior to a decrease of the thermal confinement some time before the neutron yield falls and the plasma returns to the normal H-mode confinement regime. The degradation in confinement leads to a large heat flow to the X-point target which causes the "carbon bloom".

Experimental Data Diagnostic data is used wherever possible to define plasma parameters and the consistency of the data is checked by comparing measurement and simulation of neutron rates (2), and other quantities. The pulse with the longest period of enhanced confinement #26095 was chosen for the initial extensive analysis with TRANSP. The large influx of impurities, the so called "carbon bloom", which always occurs at the end of

these pulses is not obviously triggered by an MHD event in this particular discharge. Figure 2 shows the time evolution of data from charge exchange recombination spectroscopy for the ion temperature T_i and Z_{eff} at 3.15 and 3.9 m, the data points marked by the symbols are available at 50 ms time intervals. Figure 2 also shows the time behaviour of the CIII light emission from the plasma edge which does not start to increase until 13.75 s. The total neutron yield also given in Figure 2 falls at the same time. The ion temperature profile is fairly constant from 13.25 s until 13.7 s when it falls. The value of Zeff at the edge is steadily increasing at a slow rate until 13.7 s when it increases sharply.

Results of transport analysis The power balance is dominated by the ion channel, the principle losses being equipartition and conduction. The pulse has good central confinement ($\chi_i \approx 0.2$ m^2/s) during the high confinement phase as shown in Figure 3a and the conductivity is only a factor 2 to 3 above neoclassical. Near the edge the conductivity is an order higher than neoclassical. During the normal H-mode phase the conductivity is higher across the whole radius. Figure 3b shows that χ_i at the edge is increasing slowly until 13.7 s when it increases abruptly. The central value remains roughly constant until that time.

As the density rises throughout the discharge there will be some reduction in the fast particle deposition rate at the plasma centre. Figure 4 shows firstly the injected power, there is a loss of about 1 MW between 13.56 and 13.7 s. The central density rises steadily as shown in the second trace except during the sawtooth at 12.8 s. The drop in the central particle deposition rate is shown in the third curve but the heating of the thermal plasma within the inner third continues to increase slightly until 13.9 s due to increased beam heating with increased density. The loss in good confinement does not therefore appear to be connected to any degradation in the beam heating.

Discussion The reasons for the formation of the enhanced confinement phase and its loss are not clear. Attempts have been made to correlate the change in χ_i with $\frac{1}{n_D}\frac{dn_D}{dr}$ near the centre of the plasma and it is possible that as the density profile flattens the good confinement disappears. However, it is difficult to come to a firm conclusion due to the poor time resolution of the data.

These pulses exhibit some of the same characteristics found in the DIII-D V-H mode [6]; particularly steep edge gradients and a large edge bootstrap current as shown in Figure 5. The fact that the predicted value of the bootstrap current density is larger than the total current density at the edge is confirmed by the measurement of a negative loop voltage. Previous analysis of a similar JET pulse [7] shows that this sort of current profile permits entry to the second region of stability and therefore may improve the stability against ballooning modes. A possible explanation of the improved confinement in the VH-mode is that a significant portion of the plasma near the boundary has entered the second stable region to ballooning modes [8].

An extensive analysis of more pulses is needed to understand the enhanced confinement phase and its collapse.

References

(1) B. Balet, et al., Nuclear Fusion Vol. 30 No. 10 (1990) 1229

(2) The JET team Nucl. Fusion 32 (1992) 187

(3) R.J. Goldston, et al., J. Comput. Phys. 43 (1981) 61.

(4) D.P. Schissel, et al., Nuclear Fusion 31 (1991) 73.

(5) R.J. Goldston, et al., Plasma Phys. Contr. Fusion 26 (1984) 87.

(6) G.L. Jackson, et al., Phys. Rev. Lett 67 (1991) 3098.

(7) D.P. O'Brien, et al, EPS Venice 1989.

(8) L.L. Lao, et al, Fifth Transport Task Force Workshop (1992).

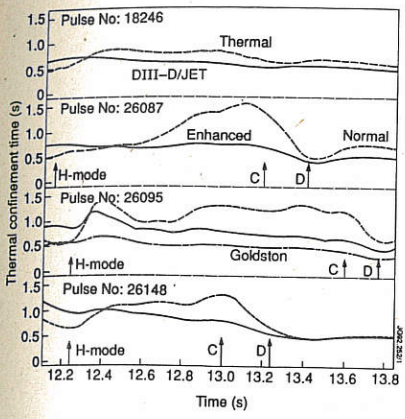

Fig. 1: The thermal confinement times for pulses #18246, #26087, #26095 and #26148 compared to the values from the JET-DIII-D H-mode scaling law. C: confinement collapse, D: decay of neutron yield.

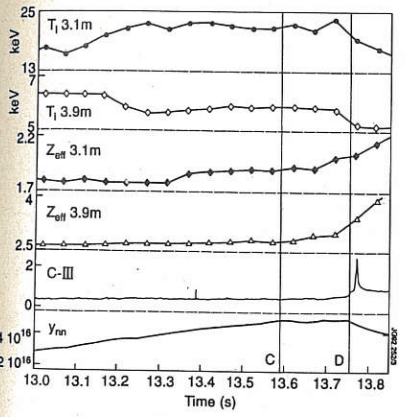

Fig. 2: The time development of data for shot #26095: Central and edge T_i values: Central and edge values of Zeff; CIII light emission: total neutron yield Ynn. C: confinement collapse, D: decay of neutron yield.

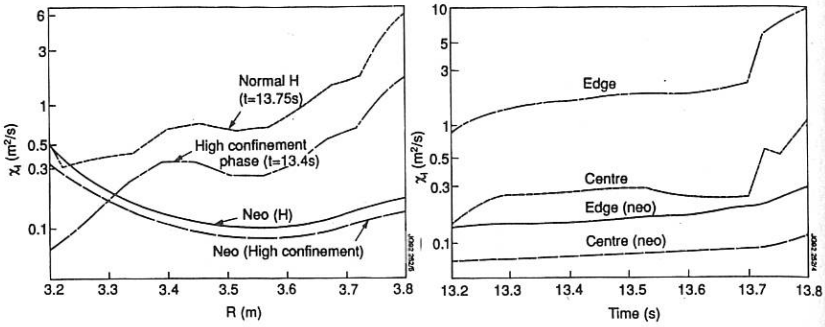

Fig. 3. a) Radial profiles of χ_i and χ_{ineo} in the high confinement phase 13.4 secs and in the normal H-mode phase 13.75 secs. b) Change with time of the ion thermal conductivities χ_i at the centre and edge of the plasma compared to neoclassical values.

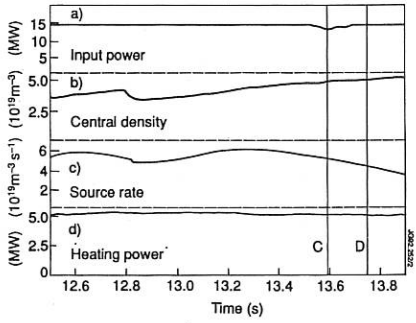

Fig. 4: Neutral beam power deposition to the centre of the plasma a) total injected power b) central electron density c) central beam source rate d) heating power to the centre third of the plasma. C: confinement collapse, D: decay of neutron yield.

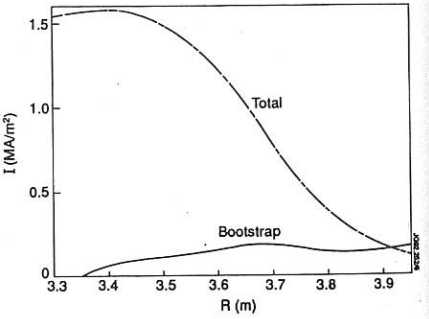

Fig. 5. Radial profiles of total and bootstrap currents at 13.7 secs.

DETERMINATION OF THE ION THERMAL DIFFUSIVITY FROM NEUTRON EMISSION PROFILES IN DECAY

M.Sasao[1], J.M.Adams[2], S.Conroy, O.N.Jarvis, F.B.Marcus, G.Sadler and P.van Belle
JET Joint Undertaking, Abingdon, Oxfordshire. OX14 3EA, U.K.
[1]National Institute for Fusion Science, Nagoya-464, Japan
[2]AEA Industrial Technology, Harwell Laboratory, Oxon, OX11 ORA,U.K.

Abstract

Spatial profiles of neutron emission are routinely obtained at the Joint European Torus (JET) from line-integrated emissivities measured with a multi-channel instrument [1]. It is shown that the manner in which the emission profiles relax following termination of strong heating with Neutral Beam Injection (NBI) permits the local thermal diffusivity (χ_i) to be obtained with an accuracy of about 20%. The radial profiles of χ_i for small minor radius ($r/a < 0.6$) were found to be flat and to take values between 0.3 and 1.1 m^2/s for H-mode plasmas with plasma current I_p = 3.1 MA and toroidal field B_T = 2.3T. The experimental value of χ_i is smallest for Z_{eff} = 2.2 and increases weakly with increasing Z_{eff}. The experimental results disagree by two orders of magnitude with predictions from an ion temperature gradient driven turbulence model.

Concept

Fig. 1, opposite, shows an example of the time evolution of the line-integrated neutron emissivities (raw data) of the central chord and that of the upper-most chord of the JET neutron profile monitor [1] during and after periods of neutral beam injection for discharge 22871. The dotted line indicates the time at which the subsequent analysis was performed. The similarity of the decay rates for the two time-traces is a result of χ_i possessing a flat radial dependence for $r/a < 0.6$. The time trace of the input power of the 80 keV neutral beam is also shown.

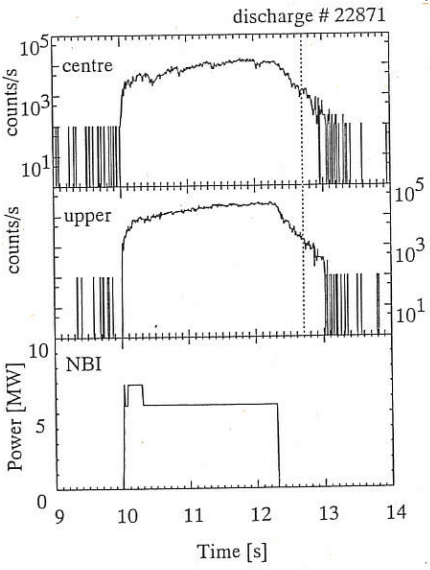

When the NBI is terminated, the neutron emission starts to decay. If there is no significant MHD activity, the neutron decay rate immediately after the NBI termination is due to an approximately equal admixture of beam-plasma and thermal interactions, with the beam particles slowing down classically. After a full slowing down-time of the beam particles, the decay in neutron emission is due primarily to the cooling of the thermal plasma ions. This is the time interval of interest. The local ion power balance of this region can be expressed as:

$$\frac{dW_i}{dt} = Q_{ei} - Q_{cond}$$

$$= \frac{3}{2}\frac{n_e(T_e - T_i)}{\tau_{ei}} + \frac{1}{r}\frac{\partial}{\partial r}\left[r n_i(r)\, \chi_i(r) \frac{\partial T_i}{\partial r} \right] \qquad (1)$$

The convection and charge exchange losses are considered to be negligible [2,3] and have been omitted from eq.1. In the present work, the ion temperature profile, $T_i(r)$, and the change in the ion stored energy, dW_i/dt, were provided by the neutron profile monitor. The line-integrated neutron emission recorded by the 19 chords were analyzed by means of the ORION code [4], which assumes that the magnetic flux surfaces are contours of the neutron emissivity, $Y_n(r)$. Here, a parabolic function, $Y_n(r) = Y_n(0)(1-r^2)^{\alpha}$, where r = r/a, was used. The parameter α was determined by the fitting procedure to an accuracy of 5-20 %.

If the relationship between the neutron emission rate and the ion temperature can be expressed as $Y_n = \frac{1}{2}\, n_d^2\, T_i^{\beta}$, then the change of the local neutron emissivity can be related to the change in the ion stored energy by

$$\frac{1}{W}\frac{dW_i}{dt} = \frac{1}{\beta}\frac{1}{Y_n}\frac{\partial Y_n}{\partial t} + \left(1 - \frac{2}{\beta}\right)\frac{1}{n_d}\frac{\partial n_d}{\partial t} \qquad (2a)$$

$$= \frac{n_e(T_e - T_i)}{n_d T_i \tau_{ei}} + \frac{2}{3 n_d T_i}\frac{1}{r}\frac{\partial}{\partial r}\left[r n_d\, \chi_i(r) \frac{\partial T_i(r)}{\partial r} \right] \qquad (2b)$$

This is the equation used to obtain χ_i in the present paper. During the time interval of the analysis, the change of plasma parameters was moderate so that the contributions from the second term of the right side in Eq.(2a) and from the first term of Eq. (2b) were small. For the remaining terms of Eq.(2a) and (2b), only relative changes in the values of n_d, T_e, T_i, Y_n

are needed and the χ_i values are determined primarily by the neutron emission decay constant and the radial profile peaking factor of T_i. Further details of the analysis are provided in Ref.3.

Results and Discussions

Nine discharges were selected from the range 22866-22890 of single-null (upper) discharges run as part of the H-mode study programme. The plasma current I_p was fixed at 3.1 MA and toroidal field B_T was 2.3-3.5 T. The zone defined by $\chi_i \pm \Delta\chi_i$ for 22871 and 22874 is shown in fig 2. In the most reliable region for the present analysis, i.e. $0.25 < r/a < 0.55$, the $\chi_i(r)$ profiles were found to be flat. The neoclassical predictions [5] are also presented.

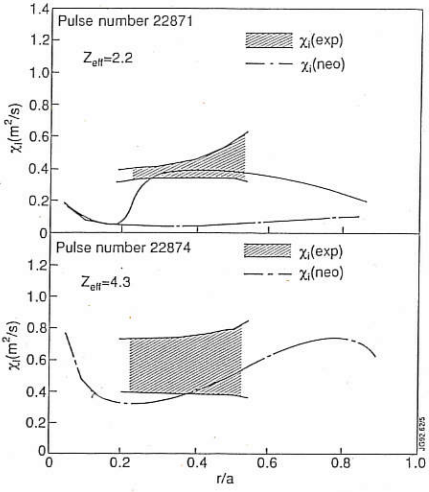

Fig.2. The χ_i profiles for discharges 22871 and 22874 are shown opposite. The hatched areas indicate the regions of $\chi_i \pm \Delta\chi_i$. The neoclassical χ_i profiles are indicated. For discharge 22871, the sum of the neoclassical χ_i and that of the ion temperature gradient model (although scaled down by over an order of magnitude), is shown by the solid line to illustrate its radial dependence.

The theoretical models of the ion temperature gradient driven turbulence were tested in the parameter range of $0.5 < \eta_i < 4.5$. The experimental χ_i values are typically two orders of magnitude less than the theoretical predictions [6]. The flat χ_i profiles of the present analysis also disagree with the theoretical predictions in that they do not show any major changes near η_{crit}. In fig 2(upper), the theoretical values from the ion temperature gradient model [6] have normalized to the experimental data and then added to the neoclassical χ_i for comparison

with the experimental results for discharge 22871 in order to illustrate the region of r/a for which abrupt changes in χ_i are to be expected.

In Fig.3, the experimental χ_i(r/a=0.3) are plotted against Z_{eff}. They are much larger than the simple neoclassical predictions except for high Z_{eff}.

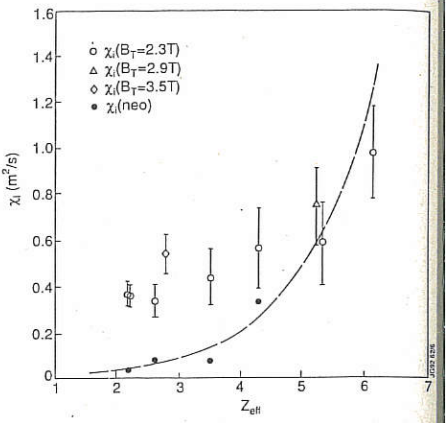

Fig.3. The Z_{eff} dependence of χ_i^{exp} (r/a=0.3) values for discharges 22866-22890, which were single null discharges with Ip=3.1A. The dashed line connects the calculated χ_i^{neo} values.

Conclusions

It has been shown that, under appropriate circumstances, neutron emission profile measurements can be analyzed directly to obtain reasonably accurate estimates of local ion thermal diffusivities. For clean plasmas, $Z_{eff} < 3$, the experimental χ_i values are much larger than the predictions of neoclassical theory but much smaller than those of the ion temperature gradient driven turbulence model.

References

[1] ADAMS,J.M., CHEETHAM.A., CONROY,S., et al., in Controlled Fusion and Plasma Physics (Proc. 16th Eur. Conf. Venice, 1989) Vol.**13B**, Part I, European Physical Society (1989) 63

[2] BALET,B., BOYD,D.A., CAMPBELL,D.J., et al., Nucl. Fusion **30** (1990) 2029.

[3] M.SASAO et al., to be published as a JET report.

[4] CONROY,S., Diagnosis of Fusion Products for Reactor Relevant Plasmas, PhD Thesis, Imperial College, London (1990)

[5] CHANG,C.S., HINTON,F.L., Phys. Fluids **29** (10) (1986) 3314.

[6] R.R.DOMINGUEZ and R.E.WALTZ, Nucl. Fusion **27** (1987) 65.

LOCAL POWER BALANCE ANALYSIS IN OHMIC AND ECR HEATED PLASMAS IN RTP

J.A. Konings, G.M.D. Hogeweij, N.J. Lopes Cardozo,

A.A.M. Oomens, F.C. Schüller, and the RTP team

FOM-Instituut voor Plasmafysica 'Rijnhuizen', Association Euratom-FOM,

P.O. Box 1207 3430 BE Nieuwegein, the Netherlands

INTRODUCTION

The Rijnhuizen Tokamak Project (RTP) is dedicated to the study of steady-state and perturbative transport processes in tokamak plasmas. In this paper we report on the steady-state analysis in ohmic and electron cyclotron resonance heated (ECRH) plasmas, for varied I_p, n_e, $Z_{\rm eff}$ and $P_{\rm ECRH}$. The global energy confinement time is compared to scaling laws. The electron thermal diffusivity $\chi_e(r)$ is obtained by solving the local power balance equation. A comparison is made to the Rebut-Lallia model, which attributes anomalous transport to turbulence in the magnetic field topology.

EXPERIMENTAL CONDITIONS

In the RTP experiment ($R_0 = 0.72$ m, $a = 0.164$ m, $B_T \leq 2.4$ T, pulse duration ~ 250 ms) ohmic plasmas are obtained with $n_e(0) = 1$ to $9 \cdot 10^{19}$ m^{-3}, $T_e(0) = (0.6 - 0.9)$ keV and $Z_{\rm eff} = 2 - 4$ ($Z_{\rm eff} = 1 - 2$ after boronization of the vacuum vessel). Additional ECR power is launched from a single gyrotron (200 kW, 60 GHz, 100 ms, O-mode, TE_{11}) from the low field side. With the localized ECR power deposition, a power density of ~ 50 MW/m^3 is obtained and temperature gradients up to 50 keV/m are reached.

T_e-profiles are obtained from a scannable single-point Thomson scattering system and a 20-channel ECE radiometer. A 19-chord FIR interferometer yields $n_e(r)$ after Abel inversion. Further diagnostics include magnetics, soft X-ray pulse height analysis, an 80-channel 5-camera SXR tomographic system, XUV spectroscopy, hard X-ray and visible light monitors, a bolometer and a neutral particle analyser.

LOCAL POWER BALANCE ANALYSIS

A local power balance analysis is performed using an adapted version of the SNAP transport code from TFTR, Princeton. In a 1-dimensional analysis, the electron heat flux $q_e(r)$ in steady state is obtained from the power balance equation for electrons:

$$p_{\rm ohmic} + p_{\rm ECRH} - p_{\rm ei} - p_{\rm rad} \quad - \langle \nabla_r q_e \rangle \quad = \quad \frac{\partial}{\partial t}(\frac{3}{2} n_e T_e) \quad \approx 0.$$

The ohmic power density ($p_{\rm ohmic}$) is calculated from the loop voltage assuming neoclassical resistivity and the current distribution. The ECR power deposition ($p_{\rm ECRH}$) is deduced from measurements of the single pass transmitted power and by ray-tracing studies. Electron-ion coupling ($p_{\rm ei}$) is included using the classical equipartition term, where T_i is measured by the neutral particle analyser. Radiation losses ($p_{\rm rad}$) are estimated from XUV-spectroscopy and bolometry, and are modelled by the predictive transport code ICARUS [1]. The electron heat diffusivity is given by $\chi_e^{PB}(r) = -q_e(r)[n_e(r)\nabla T_e(r)]^{-1}$.

REBUT - LALLIA MODEL

The Rebut-Lallia transport model [2] describes enhanced thermal transport in terms of chaotic magnetic field zones. The electron heat flux is given by:

$$q_e = n_e \chi_{e,\mathrm{neo}} \nabla T_e + n_e \chi^{\mathrm{RL}}_{e,\mathrm{anom}} (1 - \frac{(\nabla T_e)_c}{\nabla T_e}) \cdot \nabla T_e \cdot H[\nabla T_e - (\nabla T_e)_c] \; H[\nabla q] \; ,$$

where

$$\chi^{\mathrm{RL}}_{e,\mathrm{anom}} = \alpha \, [\frac{\nabla T_e}{T_e} + \frac{2 \nabla n_e}{n_e}] \sqrt{\frac{T_e}{T_i + T_e}} (1 - \sqrt{\frac{r}{R}}) \sqrt{1 + Z_{\mathrm{eff}}} (\frac{q^2}{\nabla q B_T R^{1/2}}) \; .$$

Here $\chi_{e,\mathrm{neo}}$ is the neoclassical thermal diffusivity, q the safety factor, r and R are the major and minor radius, respectively, and H is the Heaviside step function. The critical gradient is given by:

$$k(\nabla T_e)_c = \frac{\beta}{q} \, (\frac{\eta j \; B_T^3}{n_e (k T_e)^{1/2}}) \; ^{1/2}$$

where η is the plasma resistivity, j the current density and B_T the toroidal magnetic field. The dimensionless parameters α and β are tuned by confinement studies in JET. The same values have been used in this study. The effective electron thermal diffusivity is given by:

$$\chi^{\mathrm{RL}}_e = \chi_{e,\mathrm{neo}} + \chi^{\mathrm{RL}}_{e,\mathrm{anom}} (1 - \frac{(\nabla T_e)_c}{\nabla T_e}) \; .$$

The model leads to the global energy confinement scaling law [3]:

$$\tau_E = 2.6 \cdot 10^{-2} \; n_e^{3/4} \; Z_{\mathrm{eff}}^{1/4} \; B_T^{1/2} \; I_P^{1/2} \; (Rab)^{11/12} \; P_\Omega^{-1} \; + \; 1.2 \cdot 10^{-2} \; I_P \; (Rab)^{1/2} \; Z_{\mathrm{eff}}^{-1/2}$$

in units [s], [$\cdot 10^{19}$ m^{-3}], [T], [MA], [m] and [MW]. The second term must be included for additionally heated plasmas.

RESULTS

Ohmically heated plasmas with $n_e(0) = 1.5$ to $9 \cdot 10^{19}$ m^{-3} ($q_a \sim 3.5$ - 7) and ECR heated discharges with $n_e(0) = 1.5$ to $4 \cdot 10^{19}$ m^{-3} have been analysed. The energy confinement time is compared to the Goldston scaling law [4] and the Rebut-Lallia scaling (see Fig. 1). For low density and low power ECRH, an improved confinement is observed [5].

The results of the local power balance analysis for varied I_P and P_{ECRH} with constant density are summarized in Table 1. The radiation losses are obtained from the bolometer data. During ECRH, the total radiated power does not change significantly. For $T_e(r)$, a smooth curve has been fitted through the measured data points, within the experimental error bars. The electron thermal diffusivity from the experiment and from the Rebut-Lallia model are given at $\rho = 0.5$. There is a good agreement between the model and the experimental observations within a factor 2. Figure 2 shows a typical result for low density, ECR heated plasmas for $P_{\mathrm{ECRH}} = 60$ and 180 kW.

P_{OH} (kW)	P_{ECR} (kW)	P_{RAD} (kW)	I_P (kA)	$T_e(0)$ (keV)	∇T_e (keV/m) $\rho = 0.5$	Z_{eff}	W (kJ)	τ_E (ms)	χ_e^{PB} (m^2/s) $\rho = 0.5$	χ_e^{RL} (m^2/s) $\rho = 0.5$
150	60	30	125	1.2	5.1	1.3	0.9	4.5	3.8	2.9
235	180		125	1.3	10.3	3.7	1.1	2.7	4.2	2.1
142	0		90	0.8	5.5	1.5	0.6	3.8	2.5	
90	60	30	90	1.2	7.0	1.0	0.8	5.5	2.2	1.2
98	180		90	1.6	8.3	2.1	0.9	3.2	4.7	2.1
130	0		60	0.6	4.3	2.6	0.4	2.9	4.0	
60	60	30	60	1.3	5.7	1.8	0.7	5.8	2.6	2.7
47	120		60	1.3	10.7	1.6	0.6	3.5	3.2	4.3
83	180		60	1.4	8.6	3.0	0.6	2.2	4.8	4.4

Table 1: Local power balance analysis for plasmas with density $n_e(0) = 2.5 \cdot 10^{19}$ m^{-3}, for various plasma currents and additional ECR power. T_e- and n_e-profiles are obtained by Thomson scattering. From NPA measurements $T_i = 0.7\ T_e$ in ohmic phase. The thermal diffusivity χ_e from local power balance analysis and the Rebut-Lallia model are calculated at $r/a = 0.5$. For some profiles no bolometer data is available.

For ohmically heated plasmas, the difference between the electron temperature gradient and the critical gradient is very small, as shown in Fig. 3. In this case, the temperature profile calculated by the Rebut-Lallia model should be compared to the measured profiles.

CONCLUSIONS

For varied I_P, n_e, Z_{eff} and P_{ECRH}, a global and local transport analysis has been performed. The global confinement is consistent with both the Goldston and the Rebut-Lallia scaling law. The local power balance analysis shows for ohmic plasmas an electron temperature gradient which approximates the critical gradient. For ECR heated plasmas, the thermal diffusivity from the Rebut-Lallia model corresponds to the local power balance χ_e^{PB} within a factor 2.

ACKNOWLEDGEMENTS

The authors are indebted to Dr. M.C. Zarnstorff (Princeton) for making the SNAP code available, and to Dr. D. Boucher (JET) for the discussions about the Rebut-Lallia model. This work was performed under the Euratom-FOM association agreement with financial support from NWO and Euratom.

REFERENCES

[1]: M.L. Watkins *et al.*, Methods Comput. Phys., **16** (1976) 165.
[2]: P-H. Rebut *et al.*, Contr. Fusion and Plasma Physics (Proc. 14th Eur. Conf. on Contr. Fusion and Plasma Phys., Madrid (1987) Part I, 172)
[3]: P-H. Rebut *et al.*, Plasma Physics and Controlled Nuclear Fusion Research (1988) (Proc. 12th Int. Conf. Nice, 1988) **2** IAEA Vienna (1989) 191
[4]: R. Goldston, Plasma Physics and Controlled Fusion **25** (1984) 65
[5]: F.C. Schüller *et al.*, Proc. 18th Eur. Conf. on Contr. Fusion and Plasma Phys., Berlin (1990)

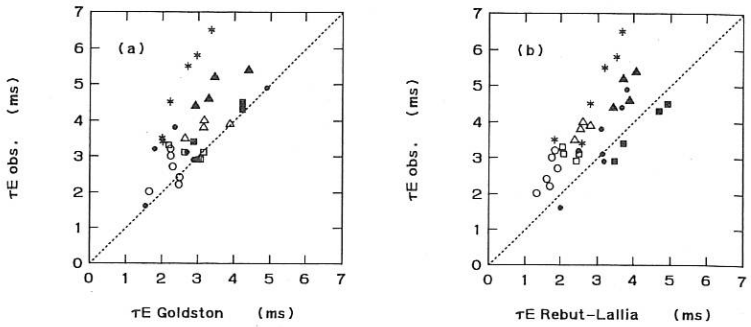

Figure 1: *The observed τ_E versus Goldston scaling (a) and Rebut-Lallia scaling (b). Profiles are measured by Thomson scattering and heterodyne ECE. Different symbols mean:* (•): *ohmic, Thomson scattering;* (o): P_{ECRH} *= 180 kW, Thomson scattering;* (⋆): P_{ECRH} *= 60 kW, Thomson scattering;* (▲): *ohmic, ECE;* (△): P_{ECRH} *= 180 kW, ECE;* (■): *ohmic, helium plasmas.* (□): P_{ECRH} *= 180 kW, ECE, helium plasmas.*

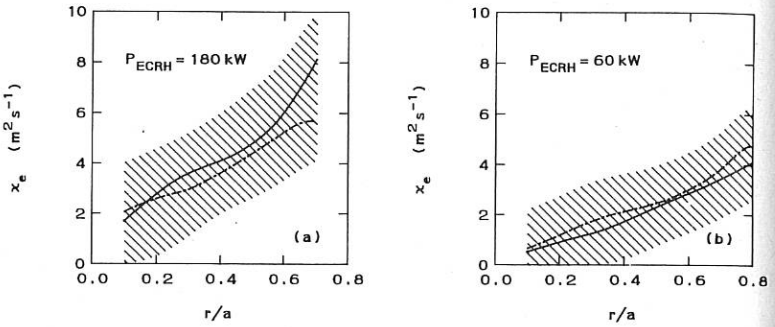

Figure 2: $\chi_e(r)$ *from steady-state local power balance (full line) and from the Rebut-Lallia model (dashed line). Plasma conditions are:* $n_e(0) = 2.5 \cdot 10^{19}$ m^{-3}, $I_p = 60$ *kA,* $Z_{\text{eff}} = 2$ *- 3. Additional ECRH power is 180 kW (a) and 60 kW (b).*

Figure 3: *Typical electron temperature gradient in ohmic discharge (dashed curve), compared to the critical gradient from the Rebut-Lallia model (full curve).*

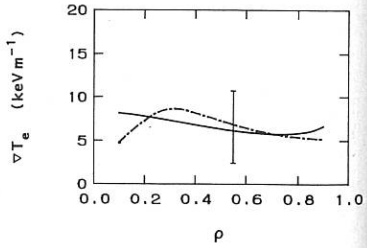

PERTURBATIVE TRANSPORT ANALYSIS IN RTP

G.M.D. Hogeweij, N.J. Lopes Cardozo, M. Peters and the RTP team
FOM Instituut voor Plasmafysica Rijnhuizen, Associatie EURATOM-FOM, P.O.BOX 1207, 3430 BE Nieuwegein, The Netherlands

F. De Luca*, G. Gorini*, A. Jacchia, P. Mantica
Istituto di Fisica del Plasma, Associazione EURATOM-ENEA-CNR, Milano, Italy
** Dipartimento di Fisica, Università degli Studi di Milano, Milano, Italy*

Introduction

The Rijnhuizen tokamak project (RTP) is dedicated to the study of transport processes in tokamaks. In addition to the examination of steady state conditions of plasmas with ohmic and intense additional heating, temperature and density perturbations are used for transport analysis.

In this paper we report both on the analysis of sawtooth induced heat and density pulses and on transport studies by means of ECR input power modulation.

Diagnostics used are a 20-channel heterodyne ECE radiometer for the T_e-profiles and a 19-chord interferometer for the n_e-profile. The perturbations are also followed with a 5-camera, 80-channel SXR tomography system.

Experimental conditions

The RTP tokamak has a stainless steel vessel with R_0=0.72 m, r_0=0.23 m and a poloidal carbon limiter, usually at 0.164 m. The toroidal field used was 2.14 T; I_p=60-145 kA. For additional heating and power modulation, two 60 GHz, 200 kW gyrotrons are available, one from the low field side in O-mode, one from the high field side in X-mode. The results reported here have been obtained with LFS heating only. In the experiments Z_{eff} has been varied by using hydrogen, helium and nitrogen as puffing gas.

Techniques used in the analysis

Two different techniques have been used in the analysis. One method uses the ACCEPT code, fitting a numerical solution of the linearized transport equations to the signals, taking into account possible coupling between the heat and density perturbation and the effect of damping and inward propagating particle and heat pinch terms. The other method uses Fourier decomposition of the signals, thus deriving a frequency dependent diffusion coefficient from the phase velocity and the radial amplitude decay of each harmonic component of the signals; see /1/ for a detailed description of the method.

Both methods have been compared using sawtooth induced heat pulses in JET, and checked against the extended time-to-peak method. The three methods have proven to give consistent results; see /2/.

Sawtooth induced heat and density pulses in ohmic and ECR heated plasmas

Sawtooth induced heat and density pulses have been studied in ohmic plasmas with central densities of 3 to $10*10^{19}$ m^{-3}. A wide Z_{eff} range has been covered by using H, He and N as puffing gas. Values of χ^{inc} between 3 and 8 m^2/s are found. In most cases, the density pulse propagates with the heat pulse, indicating that the time evolution of temperature and density is dominated by a single, fast eigenmode of the system /3/. Sometimes indications are found that the density pulse also contains a slow part. Results are summarized in Table 1; a typical case is plotted in Fig.1. In high density hydrogen plasmas the density pulse often shows an asymmetry between low and high field side, as reported earlier /4/.

discharge nr.	*puffing gas*	$n_e(0)$ $10^{19}m^{-3}$	Z_{eff}	*sawtooth period (ms)*	$\chi^{inc,st}$ (m^2/s)
R19910423.012	H_2	10.0	1.3	2.1	3.0
R19910423.053	He	9.2	1.9	1.7	5.5
R19910423.057	He	7.0	2.4	1.7	5.7
R19910424.019	N_2	4.2	2.8	0.6	8.3
R19910424.020	N_2	5.5	4.4	0.9	6.3

Table 1. χ^{inc} determined with ACCEPT from sawteeth in ohmic discharges at 115-145 kA. The Z_{eff} values have been estimated from the loop voltage and $T_e(0)$, assuming a standard T_e profile.

For comparison, some discharges with 60 and 180 kW ECR heating with the LFS gyrotron have been studied. Because of the cutoff limit, this is only possible in low to medium density plasmas, $n_e(0) \approx 2\text{-}3*10^{19}$ m^{-3}. T_e profiles tend to be very peaked during ECR heating, thus causing large sawtooth crashes of ≈30% of the unperturbed value in the centre. In this regime, values of χ^{inc} are found from 6 m^2/s for clean plasmas with $Z_{eff} \approx 1.5$, to 8-9 for dirty plasmas with $Z_{eff} \approx 4$.

Results of ECR power modulation and comparison with sawteeth

Power modulation experiments have been performed with central resonance ECR heating, using a 60 GHz, 200 kW gyrotron, either from the low field side in O-mode, or from the high field side in X-mode. Modulation frequencies between 0.1 and 1.0 kHz have been used, with duty cycles from 0.1 to 0.8. Experiments have been performed at 60, 90 and 125 kA.

At RTP, best results are obtained with a modulation frequency of 300-500 Hz, a central density of $2.5\text{-}3.5*10^{19}$ m^{-3}, and with plasma current 90 or 125 kA. At higher density, refraction of the EC beam is a problem; at lower density, the power deposition profile is too broad and suprathermals contaminate the ECE signals.The 60 kA experiments suffer from a large modulated plasma displacement. In Fig.2 a typical example is given.

At 125 kA, big sawteeth continue during the power modulation with well separated frequency; see Fig.3. This gives the opportunity to derive χ^{inc} from both the modulation and the sawteeth in the same time window. For the sawtooth case, the ACCEPT and Fourier methods of analysis have been used and show good agreement. Results at 90 and 125 kA are summarized in Table 2. For these discharges, $\chi^{inc,st}$ was also determined for the ohmic part of the discharge, with about the same values as $\chi^{inc,st}$ during the modulation.

discharge nr.	*puffing gas*	I_p *kA*	$n_e(0)$ $10^{19}m^{-3}$	Z_{eff}	$\chi^{inc,st}$ *ACCEPT*	$\chi^{inc,st}$ *Fourier*	$\chi^{inc,pm}$ *Fourier*
R19920224.023	H_2	90	3.2	1.1	4.2	3.9	7.5
R19920226.017	H_2	125	2.8	1.7	5.4	6.3	12.1
R19920226.045	N_2	90	2.8	3.1	-	-	7.8
R19920226.041	N_2	125	3.6	2.9	9.6	11.2	15.3

Table 2. χ^{inc} determined from power modulation and sawteeth. For one of the 90 kA cases the sawteeth were too weak to determine a χ^{inc}.

Discussion

As is seen from table 2, $\chi^{inc,pm}$ is always larger than $\chi^{inc,st}$. Work is still in progress to find the cause for this difference. One explanation could be an effect of the ECRH power deposition profile extending from the plasma centre out into the radial interval $2 < r < 8$ cm where $\chi^{inc,pm}$ is determined (only 65% of the power is deposited within 2 cm from the plasma centre, according to ray tracing calculations). A similar effect is reported in /5/. A second effect which could contribute to increase the observed $\chi^{inc,pm}$ values at high current (125 kA), is the presence of the sawtooth activity. Since the inversion radius is at $r \approx 5$ cm, an m=1 island could be present in the measurement region of $\chi^{inc,pm}$, causing a flattening of the phase profile.

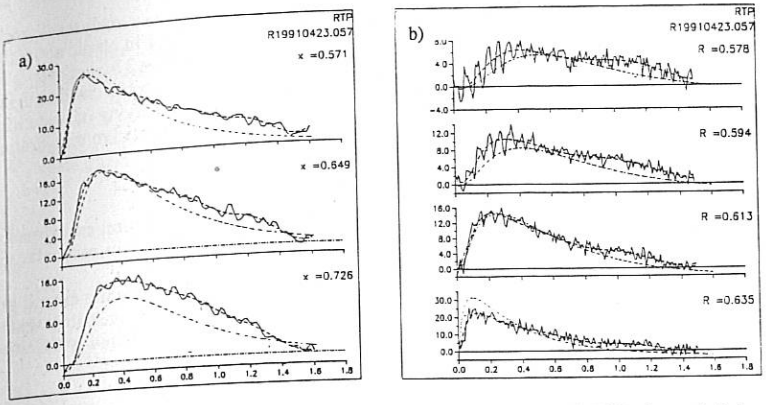

Fig. 1. Heat and density pulse of discharge R19910423.057, seen at 3 ECE channels (a) and 4 interferometer channels (b). The data are given by solid lines, spline fits through the data by dashed lines, and the ACCEPT fits by dotted lines. Radial positions are given in x=r/a for the temperature data, and in major radius for the line integrated density data. Time is in ms; the vertical scale is in arbitrary units. Uncertainties in the calibration may be the cause of the discrepancy in the amplitude between the simulation and the measurements.

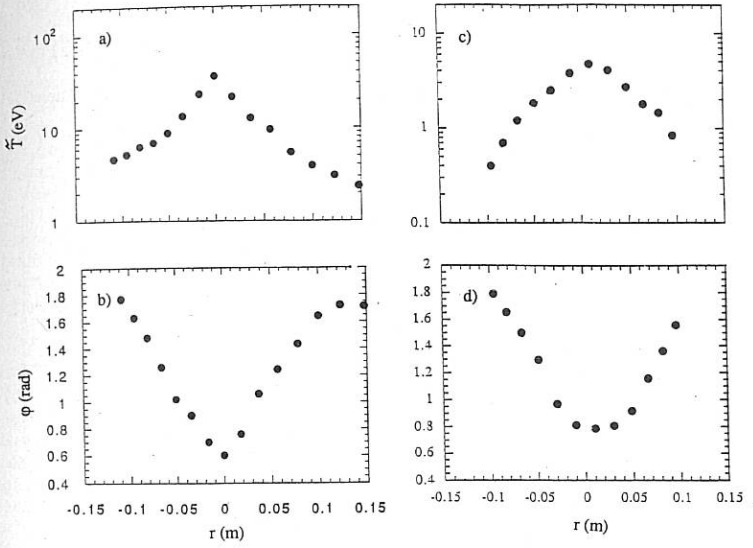

Fig. 2. Amplitude and phase plots of pulse R19920226.017 (power modulation). On left hand side the amplitude (a) and phase (b) of the ECE data; on the right hand side (c,d) the same for the data of the horizontal SXR camera. Note the flatter behaviour of the SXR data in the centre because of line integration.

The results presented here have been compared with local power balance analysis. Typical values for χ^{pb} at r/a=0.5, i.e. in the measurement region of χ^{inc}, are 2.5 to 4 in ohmic and ECR heated plasmas with central density $2.5*10^{19}m^{-3}$, /6/. So χ^{inc} is only a factor 2 higher than χ^{pb}.

The heat pulse propagation shows no dependence on the size of the sawtooth crash, ranging from 5% in 90 kA ohmic plasmas to 30% in ECR heated plasmas, thus justifying (a posteriori) the linearization of the problem. For power modulation experiments the relative temperature perturbation is 5%.

Conclusions

RTP has proven to be able to perform very successful power modulation experiments. There are however still some uncertainties in the determination of $\chi^{inc,pm}$, in particular the power deposition profile.

The Fourier and simulation method give consistent results for $\chi^{inc,st}$; the values exceed χ^{pb} by only a factor of 2. Although the diffusion coefficient shows a significant scatter, it is weakly increasing with Z_{eff}. The variation in the data has not yet been large enough to draw a definitive conclusion. The density pulse is generally dominated by a single, fast eigen mode.

Acknowledgements

This work was performed under the Euratom-FOM and the Euratom-ENEA-CNR association agreements, with financial support from ZWO, CNR and Euratom.

References

/1/ A.Jacchia et al, Phys. Fluids (B) **3**, 3033 (1991).
/2/ P.Mantica et al, submitted to Nuclear Fusion.
/3/ J.C.M. de Haas, J.O'Rourke, A.C.C. Sips and N.J. Lopes Cardozo, Nuclear Fusion **31**, 1261 (1991).
/4/ A.C.A.P. van Lammeren et al, in 18th European Conf. on Controlled Fusion and Plasma Physics (Berlin, 1991), Vol **15 C** part II, p.73.
/5/ L.Giannone et al, 'Electron thermal conductivity from heat wave propagation in Wendelstein 7-AS', Submitted for publication.
/6/ J.A.Konings et al, this conference.

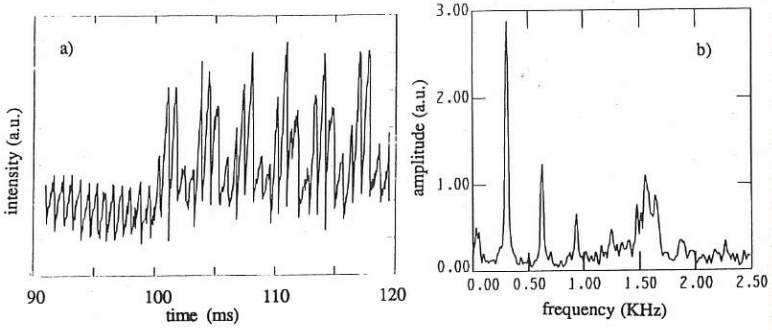

Fig. 3a. Central ECE channel of pulse R19920226.041, showing sawteeth superimposed on the fluctuation caused by the power modulation. Fig. 3b shows the corresponding spectrum, with narrow peaks at 0.3, 0.6 and 0.9 KHz (first and higher harmonics of the power modulation), and a broader peak at 1.5 KHz caused by the sawteeth.

Experiments on Heat Pulse Propagation Generated by Localized Electron Cyclotron Heating on the WT-3 Tokamak

S.Tanaka, K.Hanada, T.Minami, T.Maehara, K.Makino, Y.Kisigami, T.Kishino, M.Nakamura, T.Maekawa and Y.Terumichi

Department of Physics, Faculty of Science, Kyoto University, Kyoto 606, Japan

Electron heat diffusivity χ_e was measured by the heat pulse propagation of the electron cyclotron heat and the sawtooth collapse signals and both values are agreed with each others. Further χ_e decreases when the sawtooth is stabilized by the lower hybrid current drive in the ohmic heating plasma.

Recently the intense studies to understand the tokamak transport have been carried out. The determination of the electron heat diffusivity (χ_e) from the propagation of the heat pulse after a collapse induced by sawtooth oscillations (STO) has been made on several tokamaks/1-6/. We have measured χe by propagation of the heat perturbation induced by a short ECH pulse. Experiments were carried out in the WT-3 tokamak with major and minor radii of R=65cm and a=20cm, respectively. The toroidal field was $B_T \leq 1.75$ T, and the plasma current was $I_p \leq 150$ kA. Microwaves from a gyrotron ($\omega/2\pi$=56GHz, $P_{EC} \leq 200$kW) were transferred through circular wave guides to a Vlasov antenna with an elliptic reflector placed along the major radius and injected into the plasma from the low-field-side. The sharply focused wave, propagating as X mode with an angle of θ=84° to the toroidal field, is absorbed at the second-harmonic ECH resonance layer, R_{2e} and produces local heat pulse around R_{2e}. The perturbations caused by the ECH pulse and by sawtooth are measured with a soft X-ray (SXR) detector array installed on the radial port in WT-3.

Fig. 1 shows the time evolution of SXR signals at various spatial positions on the sawtoothing plasma. The difference between the STO and ECH pulse can clearly be seen. The STO pulse (open arrows) is propagating faster and the amplitude decreases faster than the ECH pulse (closed arrows).

A short ECH pulse is capable of making a monopole perturbation to the electron temperature profile, that is, a localized perturbation which has the same sign everywhere. While, the initial perturbation of sawteeth has a dipole character, that is, the perturbation is negative inside the inversion radius but positive between the inversion and

mixing radius. Analysis gives the following expressions for the delay time of the heat perturbation induced by both ECH and STO;

$$\tau^{ECH} \simeq \frac{3}{8\chi_e} r^2 \qquad (1)$$

and

$$\tau^{STO} \simeq \frac{1}{9\chi_e} r^2. \qquad (2)$$

So χ_e can be determined by plotting τ^{ECH} and τ^{STO} versus r^2 which give the straight lines with a slope inversely proportional to χ_e in both ECH and STO cases. The difference is, however, that τ^{STO} is a factor 9/(8/3)=3.375 times smaller than τ^{ECH}.

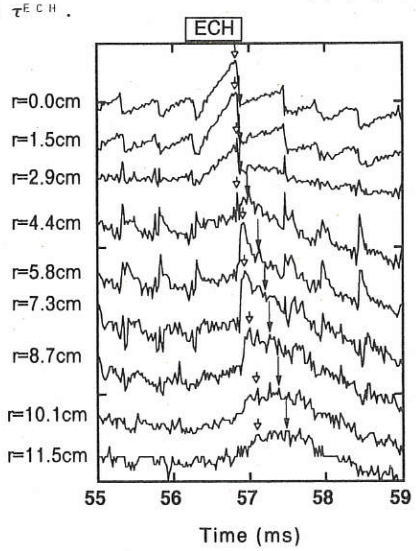

Fig. 1 Illustration of the ECH and the STO pulse propagation for a sawtoothing plasma at B_T=1.015 T, I_P=79 kA, q_L=3.7, and n_e=0.5x10^{13} cm^{-3}. The waveforms are measured by a SXR detector array installed on a radial port and have been normalized to the same excursion height. The times are after the initiation of the discharge. The ECH power is applied from 56.2 ms to 56.9 ms and its resonance layer is located r=0.0 cm (magnetic axis). Black and white arrows show the peak position of the ECH and the STO pulse for each detector.

To examine the difference, the delay times for ECH and STO pulses are plotted against r^2 as shown in Fig. 2. Fits by straight lines to the remaining data points weighted according to their standard deviations are also shown there.

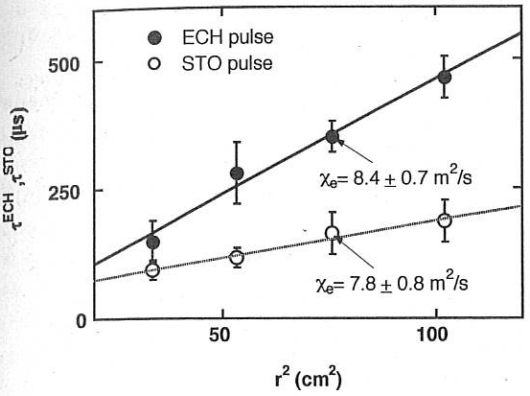

Fig. 2 Illustrative plot of τ^{STO} and τ^{ECH} versus r^2 to determine χ_e for the data shown in Fig. 2. Close and open circles show the delay time of ECH and STO pulse respectively. χ_e is determined by the slope of fitting lines.

The slope of the lines for minor radii between 6 and 10 cm are $\Delta t/\Delta r^2$ = 0.0145 + 0.0013 s/m² for STO and 0.0448+ 0.0035 s/m² for ECH, respectively. From these slopes the values $\chi_e{}^{STO}$ and $\chi_e{}^{ECH}$ can be determined by using Eqs. (1) and (2) as follows,

$$\chi_e{}^{STO} = \frac{1}{9}\frac{\Delta r^2}{\Delta t} = 7.8 \pm 0.8 \text{ m}^2/\text{s} \qquad (3)$$

and

$$\chi_e{}^{ECH} = \frac{3}{8}\frac{\Delta r^2}{\Delta t} = 8.4 \pm 0.7 \text{ m}^2/\text{s}. \qquad (4)$$

The conclusions from the values in Eqs. (3) and (4) are: 1) the values determined by both methods are coincident within error bars and 2) χ_e is not enhanced during a sawtooth period including a sawtooth crash. If there is enhanced transport due to the sawtooth crash, the STO pulse propagates under an enhanced condition, while the ECH one does not. Consequently, $\chi_e{}^{STO}$ should be larger than $\chi_e{}^{ECH}$. However the experimental results show that $\chi_e{}^{STO}$ and $\chi_e{}^{ECH}$ are equal, so there is no enhanced transport due to the sawtooth crash.

Next, we measure χ_e by using the short ECH pulse for the OH discharges superposed by LHCD. In Fig. 3, χe is plotted as the function of P_{LH} and χe is decreased abruptly with P_{LH}, where STO is stabilized. The effect ascribed to LHCD are as follows: 1) when injection power of LH wave, P_{LH}, is small the periods of STO increases, but STO persists and 2) when P_{LH} increased STO is stabilized and m=1 oscillations appear and 3) the more increased P_{LH} attains the complete stabilization of both the STO and the m=1 oscillations, as shown in Fig. 3. We are now investigating why this change of the transport appears with the stabilization of STO.

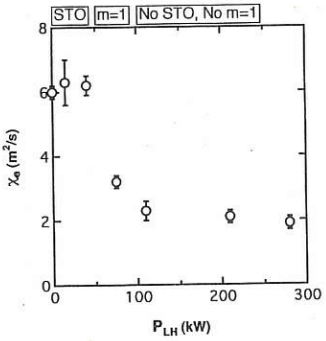

Fig. 3 χe determined by the ECH plotted against the injection power of LH wave. LHCD superposes in the OH plasma at B_T=1.015 T, I_P=79 kA, q_L=3.7, and n_e=0.8x10^{13} cm^{-3} and the ECH (P_{EC}=200 kW) is applied on the magnetic axis. The boundary of STO or m=1 oscillations are shown on the top of the figure.

The authors express their thanks to Dr. J.C.M. de Haas for useful discussions.

/1/ J.D. Callen, G.L. Jahns, Phys. Rev. Lett. 38, 491 (1977)
/2/ J.D. Bill, J.L. Dunlap et al., Nucl. Fusion 24, 997 (1984)
/3/ E.D. Fredrickson, J.D. Callen, K. McGuire, et al., Nucl. Fusion 26, 849 (1986)
/4/ J.C.M. de Haas, J. O'Rourke, A.C.C. Sips, N.J. Lopes Cardozo., Nucl. Fusion 31, 1261 (1991)
/5/ A.C.C. Sips, G.M.D. Hogeweji, A.E. Costley, J. O'Rourke, N.J. Lopes Cardozo, J.C.M. de Haas, Nucl. Fusion 31, 1545 (1991)
/6/ E.D. Fredrickson, K. McGuire, A. Cavallo, R. Budny, A. Janos, D. Monticello, Y. Nagayama, W. Park, G. Taylor, M.C. Zarnstorff, Phys. Rev. Lett. 65, 2869 (1990)

CHARACTERISTICS OF HEAT PULSE PROPAGATION AT JT-60U

J.C.M. de Haas*, K. Nagashima, and H. Shirai
Japan Atomic Energy Research Institute, Naka Fusion Research Establishment,
Naka-machi, Naka-gun, Ibaraki-ken, 311-01 Japan
*Present address: Association EURATOM-CEA sur la fusion controlée
CEN Cadarache, F-13108 Saint-Paul-Lez-Durance Cédex, France

I. Introduction

In the next few years, transport analysis at JT-60U will be performed using different perturbations, diagnostics and analysis techniques. Some experimental data concerning transient processes and perturbations at JT-60U have been analyzed to obtain information about heat (and density) transport in the plasma. Using the present diagnostics capabilities, data has been analyzed to test different techniques (see also /1/). In this paper the first results of the analysis of heat pulses caused by sawtooth crashes are given and the resulting heat diffusivities are compared with those obtained from power balance analysis.

II. Experimental conditions and analysis

Sawteeth induced perturbations have been looked at for a number of ohmic and beam heated shots. The sawteeth induce both temperature (HP=heat pulse) and density (density pulse = DP) perturbations which are moving out from the so-called mixing radius which is determined by the q = 1 surface. For the shots for which power balance analysis has been performed so far /2,3/, the set of two Soft X-Ray (SXR) arrays with a total of 64 channels is the only diagnostic with enough spatial and temporal resolution to analyze these perturbations. The disadvantages of the SXR are that the signals depend on both the temperature and the density, and that the signals are line integrated emissivities, not local values. The signals still could be used for e.g. a heat pulse analysis in case the perturbation seen on the SXR signals is mainly caused by the perturbation in the electron temperature. Because the HP is generated near the center of the discharge and its amplitude is largest there, the perturbation of the line integrated data tends to be dominated by the perturbation at the flux surface tangent to the line of sight of the channel. The characteristic shape of a heat pulse signal is an initial rise and then a relatively slow decrease back to the original value. The perturbation at a specific spatial location can be characterized by the time between the sawtooth crash and the peak of the perturbation (ttp = time-to-peak). A plot of the ttp versus spatial location gives information about the transport in the plasma. Assuming cylindrical geometry and fully diffusive transport (in the perturbation), the electron heat diffusivity can be derived from the

change of the ttp with radial position according to /4/: $\chi_e^{HP} = \frac{1}{9}\frac{\Delta r^2}{\Delta ttp}$ (Eq. 1). For the spatial location the r/a value of the tangent flux surface is used and the geometry is taken into account by the horizontal minor radius a and the ellipticity ε: $\chi_e^{HP} = \frac{a^2\varepsilon}{9}\frac{\Delta(r/a)^2}{\Delta ttp}$ (Eq. 2). Because the analysis is done just outside the mixing radius, the spatial location of the analysis depends on the plasma current and the magnetic field. This dependence of the perturbation on the mixing radius also gives a restriction on the currents for which the analysis can be done. Only shots with $I \geq 3$ MA have large mixing radii and therefore large enough amplitudes to be seen on the SXR data. In the ohmic shots the amplitudes are still small and therefore the signal to noise level is small. The S/N was improved by averaging over a number of sawteeth, for which the AVERSA code obtained from JET was used. The neutral beam heated signals have larger amplitudes and the time between sawteeth is very large. Therefore the analysis has to be done on a perturbation caused by one single crash. Because the data acquisition of the SXR cameras is set-up to look at very fast phenomena, there is a lot of high frequency noise which is filtered out by the application of a smoothing procedure. Sawtooth crashes near the end of the neutral beam heating were chosen to avoid a strongly increasing background of the SXR signal due to the rising density.

III. Experimental Results and Comparison with Power Balance

The time-to-peak versus the square of the normalized minor radius has been plotted in Fig. 1 for a two different Ohmic discharges in deuterium at 4 T. The difference between these shots is that one of them has a highly elongated configuration while the other one has the standard configuration filling the JT-60U vacuum vessel. The two lines are best fits of straight lines to the data. The intersections with the abscissa give the mixing radii of r/a = 0.34±0.03 (high elongation, 3 MA) and 0.45±0.04 (standard configuration, 3.3 MA). The slopes can be used to calculate χ_e^{HP} according to Eq. 2, using a = 0.87 m, ε = 1.64 and a = 0.97 m, ε =1.46 respectively. The resulting values for χ_e^{HP} are (2.3±0.3) m^2/s and (2.8±0.4) m^2/s, so the value for the standard configuration is slightly larger than that for the high elongation case. A power balance analysis, yielding χ_e^{PB}, was done for both shots. Because there is no ion temperature data available, an ion heat diffusivity χ_i which is constant over the minor radius was used to calculate the ion temperature profile. The resulting (calculated) neutron rate is very sensitive to the assumed value of χ_i and agrees in both cases with the experimental neutron rate for $\chi_i = 1$ m^2/s. At r/a =0.5, this procedure yields $\chi_e^{PB} = 1.0$ m^2/s and $\chi_e^{PB} = 0.8$ m^2/s respectively. So while χ_e^{PB} is similar for both cases, χ_e^{HP} is a factor of 2 to 4 higher. A similar plot of ttp versus the square of the normalized minor radius is given in

Fig. 2 for a beam heated, high elongation plasma. Note that the ttp is given by the open circles and is larger than in the Fig. 1 for the Ohmic case. The increase is linear for $(r/a)^2 < 0.3$ and the resulting value for $\chi_e^{HP} = (0.44 \pm 0.04)$ m^2/s, being much smaller than the value for χ_e^{HP} in the ohmic case. This is contrary to what was expected because for discharges with additional heating the heat conductivity is normally larger. In this analysis however, only part of the experimental information is used, namely the time-to-peak value of the experimental signals. The SXR signals can have widely different shapes while still having the same time-to-peak values. To characterize the shape of the SXR signals, the time in which the signals reach half the peak value (time-to-half peak = tth) can be compared to the ttp. The tth is also plotted in Fig. 2 (closed circles) and is at most 25% of the ttp, indicating that the SXR signals have a relatively steep rise and a long flat top.

IV. Discussion

The results described above are quite unexpected: 1) the values of χ_e^{HP} for both ohmic shots are quite different though the confinement times and the χ_e^{PB} values are similar; 2) χ_e^{HP} is smaller for the beam heated case than for the ohmic plasmas as opposed to what can be expected from the degradation of confinement with power. Though the experimental SXR data shows clear differences in the time-to-peak, one still has to consider that this diagnostic is not ideal for this kind of analysis. First the perturbation seen on the SXR data might not be caused by a pure temperature perturbation but also by a density perturbation. Second the analysis method used to obtain the values for χ_e^{HP} assumes that there is no coupling between the temperature perturbation and the density perturbation which is certainly caused by the sawtooth crash /5/. Third the data is line-integrated instead of local. As for the comparison between χ_e^{HP} and χ_e^{PB} one also has to consider the error bars on the latter: thought the results are very sensitive to the electron density, the values of χ_e^{PB} of the ohmic discharges are reasonable when compared with the confinement times of about 700 ms. There is however an indication that the ttp of the SXR is slower than that of the temperature: as found at JET the D_α signals go up when the temperature pulse reach the edge of the plasma. For both Ohmic shots the D_α signal peaks at around 10 msec which is earlier than could be expected from an extrapolation of the SXR ttp to the edge. So the ratio between χ_e^{HP} and χ_e^{PB} is probably bigger than stated above. One or more of the effects described above could also explain why the value of χ_e^{HP} found for a beam heated plasma is smaller than that in the Ohmic case: a strong indication is the small ration between tth and ttp which should be between 0.4 and 0.5 according to simulations with a single diffusive equation.

V. Conclusions

First results of the analysis of heat pulses induced by sawteeth in JT60-U are given and a comparison with power balance results is made. The values of χ_e^{HP} are at least a factor of 2 to 4 higher than χ_e^{PB} for ohmic shots. The heat diffusivity from the ttp is unexpectedly low in beam heated plasmas, but the shape of the SXR signals indicate that this can be caused by a density perturbation. Also effects of line integration effects should be considered. More experiments with improved diagnostic capabilities are necessary to resolve such effects.

Acknowledgements

The authors wish to thank the members of the JT-60U team for their cooperation and Drs. A.C.C. Sips and P.E. Stott of JET for making the AVERSA code available.

References

[1] K. Nagashima, A. Sakasai, J.C. M. de Haas and T. Fukuda, "Gas Puff Modulation Experiment on JT60-U", this conference.
[2] H. Shirai, T. Hirayama, and M. Azumi, "Transport Analysis of Ohmically Heated Plasmas in JT-60U", Sect. 5.1, JT-60U Review Report, JAERI-M92-073 (1992).
[3] H. Shirai, T. Hirayama, and M. Azumi, "Transport Analysis of L mode Plasmas in JT-60U", Sect. 5.2, JT60-U Review Report, JAERI-M92-073 (1992).
[4] E.D. Fredrickson, J.D. Callen, K. McGuire et al., Nucl. Fusion 26 (1986) 849.
[5] J.C.M. de Haas, J. O'Rourke, A.C.C. Sips, and N.J. Lopes Cardozo, Nucl. Fusion, 31 (1991) 1261.

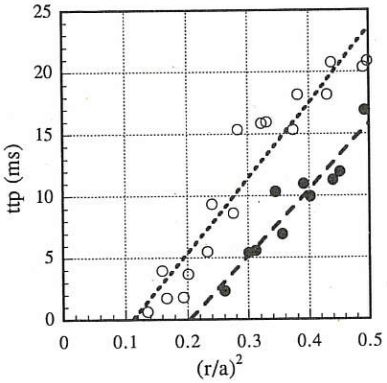

Fig. 1. Time-to-peak of heat pulses as measured with the SXR cameras versus $(r/a)^2$ and best fits of a straight line for two Ohmic shots in deuterium at 4 T; open circles: # 13733, high elongation, 3 MA; closed circles: # 13627, standard configuration, 3.3 MA.

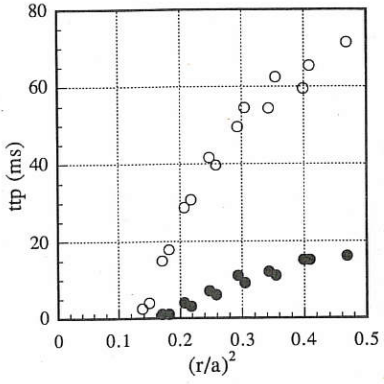

Fig. 2. Time-to-peak (open circles) and time-to-half (closed circles) of a heat pulse measured with the SXR cameras versus $(r/a)^2$ in a beam heated, high elongation shot in deuterium at 3 MA, 4 T and 16 MW.

GAS PUFF MODULATION EXPERIMENT ON JT-60U

K. Nagashima, A. Sakasai, J. C. M. de Haas and T. Fukuda

Department of Fusion Plasma Research, Naka Fusion Research Establishment,
Japan Atomic Energy Research Institute
Naka-machi, Naka-gun, Ibaraki-ken, Japan

I. Introduction

In fusion plasma experiments, the physics of heat and particle transport is one of the most important problems and is not fully understood until now. Especially, in tokamak plasmas, many experiments have been performed to determine local transport coefficients as the particle and heat diffusion coefficients, D and χ. In these experiments, source modulation methods are popular and effective, and many kinds of sources have been used to analyze the response of the corresponding plasma parameters. For example, the response of the electron temperature was analyzed using modulation of additional heating power[1], and the electron and impurity densities were analyzed using modulations of working gas[2] and of impurity injection[3]. Here, we show the experimental results of gas puff modulation experiments performed on JT-60U plasma.

II. Experimental Conditions

In these experiments, the injection of hydrogen working gas was modulated sinusoidally during the steady state phase of ohmically heated plasma. As a result, the electron density and temperature were modulated in the same form with some phase delay. The injected gas is ionized in the peripheral region of plasma and becomes a particle source for the electron density. As the source profile is highly peaked in the peripheral region, the particles penetrate into the inner region with a characteristic time delay which is dominated by the transport. In these experiments, we used the H-alpha intensity as the particle source signal.

The discharge conditions were plasma current of 2.5 MA, toroidal magnetic field of 4.0 T, major and minor radii of 3.29 and 0.90 m, plasma ellipticity of 1.58, effective safety factor of 4.5, and the line averaged electron density of $1.8\text{-}4.0\times10^{19}$ m^{-3}. The modulation frequency of gas puff was scanned from 1 to 7 Hz, and the same quantity of gas puff was injected. The configuration of the outermost magnetic surface of these discharges is shown in Fig.1.

The perturbations of electron density, electron temperature and H-alpha intensity were measured using the FIR interferometer, the ECE Fourier spectrometer and the spectroscopic method using the optical interference filters, respectively. In these discharges, the measurement chords of the interferometer were located at radii of r/a=0.67 and 0.30 (a is plasma minor radius), which are shown as U-1 and U-2 chords in Fig.1. We used the

experimental data from the H-alpha/ch.1 and 2 to prevent the effect of the high recycling region near the divertor plate.

III. Experimental Results

In Fig.2, the modulated quantities of the H-alpha intensity, the chord integrated electron density (U-1 chord) and the electron temperature at r/a=0.5 in a case of f=1 Hz are shown. A slight phase difference can be recognized between the H-alpha intensity and the electron density. The modulation of the electron temperature is out of phase with respect to the density, i.e. the phase difference is about π.

The measured amplitudes of the density modulation were plotted in Fig.3 as a function of the modulation frequency. In the figure, open and solid circles represent the data measured from the U-1 and U-2 chords. The amplitude decreases with the increase of the modulation frequency in the both measurement chords. In Fig.4, the phase differences between the H-alpha intensity and the electron density are plotted. The phase measured at U-1 chord decreases with the frequency, but the one at U-2 chord is almost constant or slightly decreasing. These data points intersect in the region of f=3-5 Hz. This peculiar feature is caused by the line integral of the measurement.

The modulation of electron temperature was measured only in a case of f=1 Hz. In this case, both values of modulation amplitude and phase delay decrease with a increase of radius. The analysis of this temperature perturbations is now under consideration.

IV. Analysis of Density Modulation

In order to determine the particle diffusion coefficient, we simulated the experimental results by numerically solving the particle diffusion equation. In a cylindrical geometry, the dynamics of the plasma density is described using a particle diffusion coefficient D and a flow velocity V as

$$\frac{\partial n}{\partial t} = -\frac{1}{r}\frac{\partial}{\partial r} r\Gamma + S \qquad (1)$$

$$\Gamma = -D\frac{\partial n}{\partial r} - V n \qquad (2)$$

where n, Γ and S represent the particle density, flux and source, respectively. We analyzed Eqs.(1)-(2) using a simple numerical method[4]. Dividing the density and source terms into equilibrium and perturbed parts as $n(r,t)=n_0(r)+n(r)\exp(i\omega t)$ and $S(r,t)=S_0(r)+S(r)\exp(i\omega t)$, Eqs.(1)-(2) are rewritten as follows

$$\frac{\partial^2 n}{\partial r^2} + \left(\frac{1}{r} + \frac{1}{D}\frac{\partial D}{\partial r} + \frac{V}{D}\right)\frac{\partial n}{\partial r} + \left(\frac{V}{D}\frac{1}{r} + \frac{1}{D}\frac{\partial V}{\partial r}\right) n - i\frac{\omega}{D} n + \frac{S}{D} = 0 \qquad (3)$$

where n(r) and S(r) are complex functions.

To obtain a solution of Eq.(3), a set of appropriate boundary conditions and profiles of D(r), V(r) and S(r) are necessary. In this analysis, we used the boundary conditions $\partial n/\partial r=0$ at r=0 and n=0 at r=a. In these discharges, the equilibrium density profile $n_0(r)$ was found to be almost flat. Therefore, it could be inferred that the inward pinch term is negligible, i.e. V=0. The source profile S(r) is peaking in a peripheral region, and it is considered that the half width of the edge source region is estimated to be about 0.05 m[5]. To represent the source profile with this half width, we used a functional form of $S(r)=S(a)(r/a)^{15}$.

To determine the particle diffusion coefficient D(r), we have calculated the chord integrated density perturbation using Eq.(3), and compared with the experimental results. In this calculation, it was assumed that a profile form of the diffusion coefficient is $D(r)=(D(0)-D(a))(1-(r/a)^2)+D(a)$, where D(0) and D(a) are the center and edge values. The best fitted case was D(0)=0.15 and D(a)=0.8 m^2/sec, and it was confirmed the profile of D(r) increases with an increase of radius.

V. Conclusion

Gas puff modulation experiments were performed on JT-60U plasma using a sinusoidal modulation of hydrogen working gas. The experimental results were analyzed using a numerical solution of the particle diffusion equation. The obtained particle diffusion coefficients were 0.15 m^2/sec in the central region and 0.8 m^2/sec in the peripheral region. From the experiments, a high particle confinement in the core region was confirmed. In the next experiment, a dependence on isotope will be examined.

Acknowledgements

The authors are grateful for many useful discussions with members of the JT-60U team. In particular, we would like to thank Dr. A. Funahashi and Dr. R. Yoshino for their useful comments.

References

1) G. L. Jahns, S. K. Wong, R. Prater, S. H. Lin, S. Ejima, Nucl. Fusion 26 (1986) 226
2) K. W. Gentle, B. Richards, F. Waelbroeck, Plasma Physics and Controlled Fusion 29 (1987) 1077
3) K. Krieger, G. Fussmann and the ASDEX Team, Nucl. Fusion 30 (1990) 2392
4) K. Nagashima and A. Sakasai, JAERI-M 92-057 (1992)
5) P. C. Stangeby, G. M. McCracken, Nucl. Fusion 30 (1990) 1225

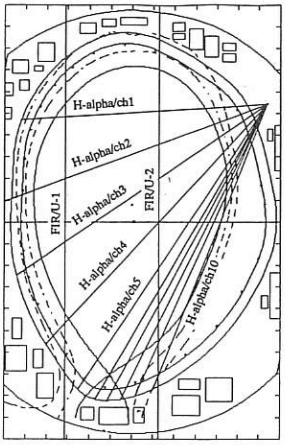

Fig.1 The plasma configuration and the measurement chords of FIR interferometer and H-alpha monitor.

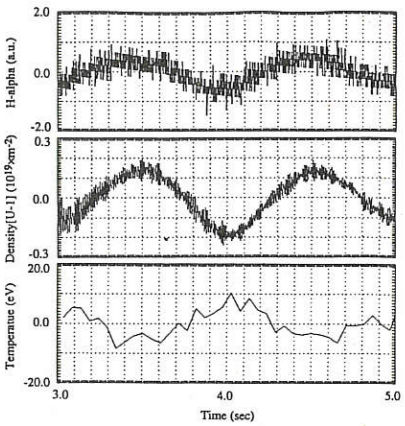

Fig.2 Time evolutions of the modulated quantities of the H-alpha intensity, the chord integrated electron density (U-1 chord) and the electron temperature at r/a=0.5 in a case of f=1 Hz.

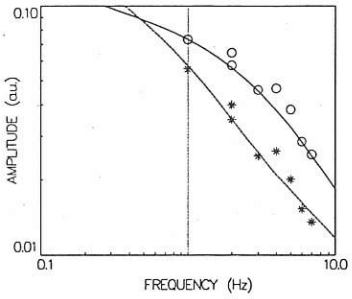

Fig.3 The measured and calculated perturbation amplitudes of the chord integrated electron density. Open circle and asterisk represent the values obtained from the two measurement chords of U-1 and U-2. Solid and dashed lines represent the calculated solutions of the two chords.

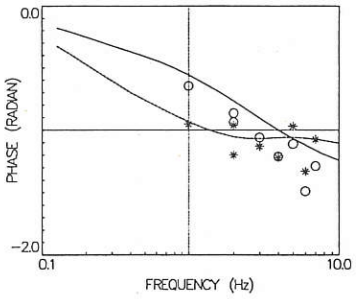

Fig.4 The measured and calculated phase differences of the chord integrated electron density. Open circle and asterisk represent the values obtained from the two measurement chords of U-1 and U-2. Solid and dashed lines represent the calculated solutions of the two chords.

MODELING SIMULTANEOUS SAWTOOTH MEASUREMENTS OF THE THERMAL AND ENERGETIC ELECTRON DIFFUSIVITIES FROM THE TEXT TOKAMAK

Peter J. Catto and J. R. Myra
Lodestar Research Corporation, 2400 Central Ave., Boulder, Colorado 80301 U.S.A.

Roger D. Bengtson and A. J. Wootton
Fusion Research Center, The University of Texas at Austin, Austin, Texas 78712 U.S.A.

The pioneering work of Callen and Jahns[1] demonstrated that the electron temperature perturbations produced by internal disruptions provided an important diagnostic of the electron heat conduction coefficient or thermal diffusivity in tokamaks. Subsequent work improved the mathematical modeling[2-4] and investigated additional effects such as spatially and temporally varying diffusivities,[4,5] the coupling of the density and heat fluxes,[6-8] perturbations to the diffusivities,[7,8] and perturbations in sources and sinks in the heat transport equation.[4,9] Retention of these effects generally lowers the measured value of the thermal diffusivity χ_e and thereby removes much of the discrepancy between the heat pulse and power balance measurements.

Nearly all investigations of sawtooth phenomena focus on thermal particles; however, energetic electrons are also sensitive to internal disruptions. Barnes and Strachan[10] observed sawtooth oscillations on hard x-ray detectors due to the increase in thick target bremsstrahlung emission caused by runaway electrons striking the limiter. They suggested the hard x-ray sawtooth events as a useful transport measure, investigated the parametric dependence of the time delay to the sawtooth peak, and noted that external heating helped to increase the amplitude of the signal beyond the background noise.

The question quite naturally arises as to whether the underlying loss mechanisms of the energetic and thermal electrons are related.[11] To help answer this question it is useful to have heat pulse propagation models capable of determining both the thermal and runaway or energetic diffusivities, during the discharge if possible. Previous Green's function solutions[2,3] are inadequate because they are obtained on the semi-infinite domain ($0 \leq r < \infty$) and, therefore, fail near the limiter[4] ($r = a$) as well as inside and in the vicinity

of the mixing radius (r = b). Moreover, a radially increasing diffusivity is needed[5] to obtain good fits of the data over a range of r. Finally, at the large r ≈ a where the runaway diffusivity is measured in TEXT, single crash models may no longer be valid. Because the energetic diffusivity may be substantially less than its thermal value[11-13] the delay time to the sawtooth peak may become comparable to or greater than a sawtooth period.[3,4]

Convenient mathematical models appropriate for simultaneously measuring the thermal and energetic electron diffusivities by their responses to internal disruptions are used to analyze simultaneous soft and hard x-ray data from the TEXT tokamak. An eigenfunction expansion technique is employed and first applied to a constant diffusivity, single sawtooth crash model. This model is unable to give a satisfactory fit to the TEXT soft x-ray data from disparate radii even with an initial condition of a flattened temperature profile out to the mixing radius.

A more sophisticated single crash eigenfunction expansion model having a parabolic radial dependence for the thermal diffusivity and a flattened profile initial condition substantially improves the fit to the TEXT soft x-ray data. The parabolic diffusivity model is a potentially important extension of previous analytic models. It provides a parabolic fit to the thermal diffusivity over a wide range of radii without the extensive numerics normally needed to solve the diffusion equation with a spatially varying diffusion coefficient. Fitting TEXT soft x-ray data, for which there is simultaneous hard x-ray data, gives $\chi_e(r=0) = 2.4\ m^2/sec$ and p = 15 in the parabolic thermal diffusivity model

$$\chi_e = \chi_e(r=0)\left(1 + \frac{pr^2}{2a^2}\right) \quad . \tag{1}$$

The extra freedom provided by the parabolic model allows a much improved fit to the soft x-ray sawtooth peaks.

Single sawtooth crash models assume that the perturbation becomes vanishingly small before the end of a sawtooth period. However, for a given sawtooth period, a single crash model will fail if the energetic diffusivity is significantly smaller than its thermal

value because the maximum of the response (which scales as the diffusion time) shifts to a substantially later time, which eventually exceeds the sawtooth period. Consequently, multiple crashes are of particular concern for the runaway electron response in TEXT since the observations of the thick target bremsstrahlung from the limiter are made at r = a by a hard x-ray detector and the runaway diffusivity D is expected to be much smaller than its thermal value[11-13] χ_e.

A periodic crash model makes it possible to measure energetic diffusivities for smaller D than can be measured with a single crash model. In the long sawtooth period limit the single crash results are recovered. But for shorter sawtooth periods, periodic crash modifications[4] alter the temporal behavior of the lower eigenfunctions, thereby changing the response and allowing TEXT hard x-ray data to be fit by more than one value of the energetic diffusivity. Using the periodic crash model to fit the simultaneous hard x-ray data one finds that more than one value of the energetic diffusivity is possible because of the uncertainty in the delay to the sawtooth peak by multiples of a sawtooth period. The highest value of D ~ 5.6 m^2/sec cannot be ruled out at this time. However, only the next lower value of D ~ 0.6 m^2sec seems consistent with previous measurements[11,12] and it could not have been obtained by a single crash model. Still lower values of D seem unlikely because the amplitude of the response to a crash decreases dramatically as the delay to the sawtooth peak increases.

The runaway electron losses in TEXT are due to the stochasticity of the intrinsic magnetic fields.[11,12] If the energy loss mechanism for the thermals were the same then[14] $D/\chi_e(0) \sim (E_r/T_e)^{1/2} \gg 1$, where $E_r \sim 1$ MeV for the runaway electrons at the limiter and $T_e \sim 1$ keV for the core electron temperature. The simultaneous soft and hard x-ray data give $D/\chi_e(0) \lesssim 1$. As a result, the thermal losses in TEXT are not due to the intrinsic stochasticity of the fluctuating magnetic fields.

References

1. J. D. Callen and G. L. Jahns, Phys. Rev. Lett. 38, 491 (1977).
2. G. L. Jahns, et al., Nucl. Fusion 18, 609 (1978); and M. Soler and J. D. Callen, Nucl. Fusion 19, 703 (1979).
3. E. D. Fredrickson, et al., Nucl. Fusion 26, 849 (1986).
4. W. J. Goedheer, Nucl. Fusion 26, 1043 (1986).
5. E. D. Fredrickson, et al., Phys. Rev. Lett. 65, 2869 (1990); and N. J. Lopes Cardozo and A. C. C. Sips, Plasma Phys. and Cont. Fusion 33, 1337 (1991).
6. M. Hossain, et al., Phys. Rev. Lett. 58, 487 (1987); D. L. Brower, et al., Phys. Rev. Lett. 65, 337 (1990); S. K. Kim, et al., Phys. Rev. Lett. 60, 577 (1988); C. M. Bishop and J. W. Connor, Plasma Phys. and Controlled Fusion 32, 203 (1990); and T. L. Rhodes, et al., Phys. Rev. Lett. 65, 583 (1990).
7. K. W. Gentle, Phys. Fluids 31, 1105 (1988).
8. J. C. M. de Haas, et al., Nucl. Fusion 31, 1261 (1991); and A. C. C. Sips, et al., Nucl. Fusion 31, 1545 (1991).
9. N. J. Lopes Cardozo, et al., Nucl. Fusion 28, 1173 (1988); and J. D. Bell, et al., Nucl. Fusion 24, 997 (1984).
10. C. W. Barns and J. D. Strachan, Nucl. Fusion 22, 1090 (1982).
11. J. R. Myra, P. J. Catto, A. J. Wootton, R. D. Bengtson, and P. W. Wang, "Runaway Electrons as a Diagnostic of Magnetic Fluctuations in the TEXT Edge Plasma," to be published in Phys. Fluids B.
12. P. J. Catto, et al., Phys. Fluids B3, 2038 (1991); P. W. Wang, Ph.D. thesis, University of Texas at Austin, 1991; and P. W. Wang, et al., submitted to Phys. Fluids B.
13. S. C. McCool, et al., Nucl. Fusion 29, 547 (1989).
14. J. R. Myra and P. J. Catto, Phys. Fluids B4, 176 (1992) and references therein.

Asymmetry of Radial Heat Pulse Propagation at TEXTOR

A. Krämer-Flecken, M.Z. Tokar, G. Waidmann, G.H. Wolf
Institut für Plasmaphysik, Forschungszentrum Jülich
Association EURATOM-KFA, D-5170 Jülich

Introduction

It is usually assumed that electron heat transport is governed by a diffusive process across the entire magnetic surface, and consequently that $\chi_e(r)$ is a useful characteristic quantity. Experimentally $\chi_e(r)$ is derived from the (quasi-)stationary energy balance.

Complementing this standard procedure, pertubation methods have been applied to calculate the χ_e-values from the radial propagation of transients on the T_e- and n_e-profiles[1,2,3]. An intrinsic pertubation source of such transients is the sawtooth collapse phase occuring under many discharge conditions in tokamaks.

Previous analyses were based on observations along one radial direction only addressing the question whether and to which extent the χ_e-values derived from heat pulse propagation differ from those obtained from the stationary power balance.

The present paper reports on the simultaneous observation of heat pulse propagation along two opposite radial directions, i.e. along both the high field side (HFS) and the low field side (LFS).

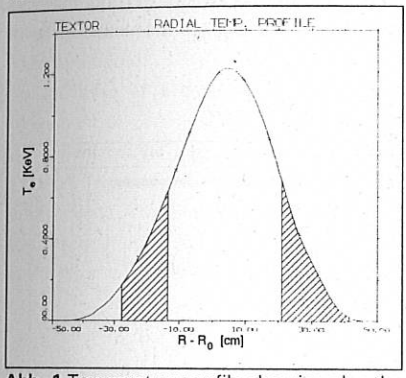

Abb. 1 Temperature profile showing also the regions covered by the tuneable radiometers.

At TEXTOR ($R = 1.75m$, $a = 0.46m$) the radial heat pulse propagation after a sawtooth crash was studied in ohmically heated discharges ($I_p = 350KA$, $B_T = 2.25T$ and $\bar{n}_e = 2.1 * 10^{13} cm^{-3}$). The propagation time was measured using a ten channel heterodyne ECE-radiometer system. Two radiometers, one on the LFS (102-112GHz) and one on the HFS (137-150GHz), are tuneable in frequency. The ECE-diagnostic with a spatial resolution of $\Delta r = \pm 0.5cm$ was operated with a time resolution of $\Delta t = 100\mu s$. The frequencies of the tuneable radiometers were varied (after each discharge) in steps of 1GHZ corresponding to a radial stepwidth of $\Delta r = 1cm$ on the high field side and $\Delta r = 2cm$ on the low field side (Fig. 1).

T_e-profile development during the sawtooth crash

The T_e-profiles were deduced from local ECE-measurements after a coherent averaging procedure. Initially, the sawtooth crash starts at the LFS and moves then towards the HFS as is shown in curve 1 in Fig. 2, where the temperature differences ΔT_e between the T_e-profile immidiately before and 100μs after the onset of the sawtooth crash are plotted. However, already 200μs later, i.e. 300μs after the onset (curve 2), the pattern has become rather more symmetric in shape. Furthermore comparing curve 1 and curve 2 we found that the radial position, where the temperature changes in the plasma center are largest, has moved more inward.

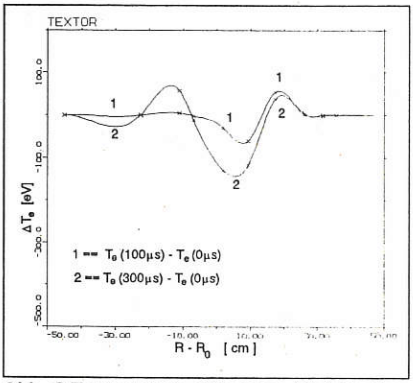

Abb. 2 Temperature difference $\Delta T_e(r)$ before and after the onset of the crash (curve 1: 100μs; curve 2: 300μs).

Comparing this development with the corresponding dynamics of the n_e-profile, measured by a multi-chord interferometer located 180° toroidally away from the ECE-diagnostic, suggests the existence of an $m = 1, n = 1$ helical structure before the start of the sawtooth crash[14]. Therefore we assume that the heat pulse is launched from a helical line winding around the $q = 1$ surface.

Heat pulse propagation analysis

In order to obtain a reference frame for the analysis of the heat pulse propagation in the radial direction of the HFS and the LFS, the unperturbed electron pressure profiles (p_e-profiles) where constructed for two cases: (i) immidiately before the onset of the sawtooth crash and (ii) one millisecond after the sawtooth crash. For this purpose the n_e-profile was taken from the interferometric measurements. The isobar radii in the interesting radial range ($16 \leq r \leq 35$cm) were deduced from the p_e-profiles and conicide within a margin of $0.1 \leq \Delta r \leq 0.3$cm. With respect to these radii, a distinct and systematic difference

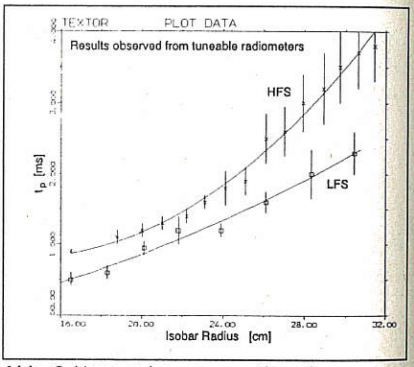

Abb. 3 Heat pulse propagation time versus isobar radius (observed by the tuneable radiometers)

between the HFS and LFS heat pulse propagation time has been found, lying outside any uncertainty of the relative isobaric positions before and after the crash. In fact, to obtain fictiously equal propagation speeds along both directions an inward shift of the whole plasms column of more than 2cm would be required. The heat pulse propagation time table is shown in Fig. 3. The time difference between HFS and LFS increases with increasing radius of the isobar and yields a time difference of $\Delta t \approx 1$ms for an isobar radius of 30cm. These results remain essentially the same if, instead of the p_e-profiles, the T_e-profiles or the n_e-profiles were taken as reference frames.

In a further experiment where the horizontal plasma position was changed from $R\text{-}R_0 = -0.7$cm $R\text{-}R_0 = -8.0$cm with fixed radiometer frequency settings we obtained again a faster radial heat transport on the LFS than on the HFS.

Attempt of an interpretation

We cannot interpret these heat pulse propagation data with the concept of a predominantly diffusive process across the entire magnetic surfaces and with $\chi_e(r)$ being a useful characteristic quantity. Instead, the primary electron heat transport appears to be mainly driven by some kind of poloidally localized (i.e. here the LFS) "break down" of the magnetic barriers, followed by heat equilibration parallel to the magnetic field lines towards the HFS. This is in analogy to the pulsating flow of water in an axisymmetric circular cascade which consists of bassins that are not properly aligned in horizontal direction but slightly tilted to one side. In order to examine this hypothesis, the electron heat transport time τ_T between the LFS and the HFS along the magnetic field lines has been estimated.

In the case of a collisionless plasma the transport of heat is associated with the movement of particles. Assuming a local heating of the electrons, caused by the radial movement of the heat pulse on the LFS, a temperature gradient along the isobar is created. This temperature gradient is balanced by the electric field between the electrons and the ions. The electric field drives the ions to the HFS. The characteristic time τ_T for the propagation of the heat from the LFS to the HFS is given by equation 1, where ΔT_e is the largest temperature difference between the HFS and the LFS on the same isobar,

$$\tau_T = \frac{\pi \cdot q \cdot R}{\sqrt{\Delta T_e / m_i}} \qquad \text{equ. (1)}$$

when the heat pulse crosses this isobar. For an isobar radius of $r = 30.5$cm we observe $\Delta T_e = 5$eV. Assuming the standard current profile we obtain $q = 2.34$ at an isobar radius of $r = 30.5$cm. The time difference between LFS and HFS results then to $\tau_T = 800\mu$s. This estimated value is in reasonable agreement with our experimental observations.

Derivation of χ_e-values

Although, according to our interpretation, the use of a $\chi_e(r)$ is misleading in this case, χ_e-values are derived in order to permit the quantitative comparision with previous experiments of this kind. Since outside of an isobar radius of $r \geq 24$cm no significant density pulse pertubation was observed by the interferometer, χ_e can formally be deduced from the assumption of a diffusive process using equation 2 according to ref[3,5].

$$\chi_e = \frac{r^2 - r_{mix}^2}{8 \cdot t_p} \qquad \text{equ. (2)}$$

The mixing radius r_{mix} was deduced from the linear dependence between heat pulse propagation time and the radial ECE-position for an isobar radius for $r \geq 24$cm. This yields $\chi_e = 1.7 m^2/s$ on the HFS and $\chi_e = 2.9 m^2/s$ on the LFS.

According to our interpretation, however, the real heat pulse driven χ_e at the HFS would be smaller and would be substitute that part of the heat flow which is not supplied by parallel transport from the LFS. By contrast, "χ_e" at the LFS has not only to compensate for this, but can even become still larger considering the amount of localization of the radial transport there.

Conclusion

At the toroidal position of the ECE-diagnostic, used to measure the time-resolved T_e-profiles, we observed a much faster heat pulse propagation towards the LFS than towards the HFS. The time delay between HFS and LFS increases with increasing isobar radius reaching values of the order of one millisecond. This suggests that the primary and predominant heat transport during the sawtooth crash occurs localized at the LFS and that the HFS is subsequently fed from the LFS by parallel heat equilibration along the connecting magnetic field lines. This questions the concept of a simple diffusive transport across the entire magnetic surface and the use of a $\chi_e(r)$ to characterize this process.

References

[1] Soler, M., Callen, J.D., Nucl. Fusion **19** (1979) 703

[2] Jahns, G.L., Soler,M., Wadell, B.V., Callen, J.D., Hicks, H.R., Nucl. Fusion **18** (1978) 609

[3] Fredrickson, E.D., Callen, J.D., McGuire, K., et al., Nucl. Fusion **26** (1986) 849

[4] Koslowski, H. R., this conference

[5] Tubbing,B.J., Lopez Cardozo,N.J., Van der Wiel,M.J.,Nucl. Fusion **27** (1987) 1843

TRANSPORT STUDIES IN TJ-I TOKAMAK FROM STEADY AND PERTURBATIVE METHODS.

C.Pardo, A.Rodríguez-Yunta, J.Vega, B.Brañas, T.Estrada, M.A.Ochando, F.L.Tabarés and B. Zurro.

Asociación EURATOM-CIEMAT para Fusión. 28040 Madrid. SPAIN

Introduction

Transport understanding is an essential task for the development of a future tokamak fusion reactor. In a general formulation, the dependence of particle and electron energy fluxes on density and temperature gradients, may be written as:

$$\Gamma = -D\nabla n - D_T n\frac{\nabla T}{T} - nV$$

$$q = Q - \frac{5}{2}\Gamma T = -\chi_n T\nabla n - \chi n\nabla T - nTU$$

where both fluxes are related to both gradients, and the particle and energy pinches V and U may depend on any other force as could be the parallel electric field. The transport coefficients must be expected to be functions of local plasma parameters such as B, q, n, T, ∇n, ∇T,.. etc. This means that the fluxes may be non-linear functions of the gradients.

Transport analysis in the steady state gives values, from experimental data, for fluxes and gradients. This is not enough to determine the values of the six transport coefficients. A perturbative experiment, such as the simultaneous measurement of density and temperature pulses induced by a sawtooth collapse, give us the incremental transport coefficients or the derivatives of the fluxes with respect to the gradients. By making a coupled analysis of both pulses as is described in ref [1], we can obtain values for the four derivatives: $\partial\Gamma/\partial\nabla n$, $\partial\Gamma/\partial\nabla T$, $\partial q/\partial\nabla n$ and $\partial q/\partial\nabla T$. The combination of both steady and perturbative studies in discharges with different plasma parameters could give us a better picture of transport processes in a tokamak.

Experimental results.

TJ-I is an ohmically heated tokamak (R=30cm, a=10cm, I≤60kA, B≤1.5T) In order to make the steady state transport analysis the density and electron temperature profiles were obtained from Thomson scattering measurements [2]. Particle flux was estimated from a neutral influx simulation code compared with H_α measurements [3]. The electron energy flux was calculated assuming for the ohmic power a current profile given by Spitzer conductivity and the classical electron-ion energy transfer rate. The radiation profile was measured by a bolometer array. To make the perturbative analysis, the temperature pulses

induced by sawtooth were measured with soft-X-ray tomography [4], and density pulses with microvawe interferometer and a two-channel reflectometer [5].

We start with the results of the perturbative experiments. Following the method of coupled analysis of ref [1], the density and temperature pulses are combinations of a fast and a slow eigenmodes. By least square fitting to the experimental pulses we obtain these fast and slow eigenvalues and their relative contribution to each pulse. A typical fit is shown in figures 1 and 2. As can be seen in the TJ-I tokamak temperature pulse goes mainly with the fast component and density pulse with the slow one plus the effect of pulse overlapping.

Fig. 1. Temperature pulse in TJ-I

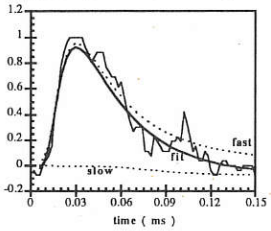

Fig. 2. Density pulse in TJ-I

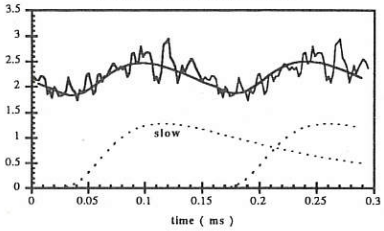

From this data the matrix A that rules the pulse propagation is obtained:

$$\frac{\partial}{\partial t}\begin{pmatrix}\tilde{n}/n\\ \tilde{T}/T\end{pmatrix}=-\begin{pmatrix}A_{11} & A_{12}\\ A_{21} & A_{22}\end{pmatrix}\nabla^2\begin{pmatrix}\tilde{n}/n\\ \tilde{T}/T\end{pmatrix}$$

$$A_{11}=-\frac{\partial\Gamma}{\partial\nabla n} \qquad A_{12}=-\frac{T}{n}\frac{\partial\Gamma}{\partial\nabla T}$$

$$A_{21}=\frac{2}{3}\left(A_{11}-\frac{1}{T}\frac{\partial q}{\partial\nabla n}\right) \qquad A_{22}=\frac{2}{3}\left(A_{12}-\frac{1}{n}\frac{\partial q}{\partial\nabla T}\right)$$

For a plasma radius r/a = 0.4 not far from the inversion one, local density = $2.x10^{19}m^{-3}$ and B = 1T the experimental results are typically the following:

$$A_{11}=1.2\pm0.1\ m^2/s \qquad A_{12}=0.0\pm0.3\ m^2/s$$

$$A_{21}=0.8\pm0.3\ m^2/s \qquad A_{22}=5.9\pm0.1\ m^2/s$$

By changing plasma parameters, matrix coefficients scale with the inverse of local density and the square of magnetic field $A_{ij}=A_{ijo}/nB^2$

We are interested in the matrix D, D_T, χ_n and χ. If the nonlinearities of the fluxes in the gradients are negligible, they can be obtained readily from the A matrix. The matrix obtained in this way, normalized to the value of D, and compared to the results of TEXT and JET [6], is:

$$D\begin{pmatrix} 1 & D_T/D \\ \chi_n/D & \chi/D \end{pmatrix} \qquad \begin{matrix} \text{TJ-I} \\ 1.2\begin{pmatrix} 1.0 & 0.0 \\ 0.0 & 7.4 \end{pmatrix} \end{matrix} \qquad \begin{matrix} \text{TEXT} \\ 0.8\begin{pmatrix} 1.0 & 0.4 \\ 0.0 & 3.4 \end{pmatrix} \end{matrix} \qquad \begin{matrix} \text{JET} \\ 0.3\begin{pmatrix} 1.0 & -1.6 \\ 0.0 & 11.7 \end{pmatrix} \end{matrix}$$

The results of the three machines are compatible with a null contribution of the density gradient to the conductive heat flux, but they show very different results in the contribution of temperature gradient to the particle flux. None of the matrixes shows Onsager´s symmetry. It must be remembered that nondiagonal terms are affected by large errors, and that TEXT results came from a non pure sawtooth analysis [4]. The ratio χ/D is around one order of magnitude in TJ-I and JET, and the absolute values of D in the three machines are compatible with a scaling in 1/B.

To check the reliability in TJ-I of the negligibility of nonlinearities, we represent in figure 3 the total energy flux versus the predicted flux using the coefficients obtained from the sawtooth analysis $Q= -1.2 \times (2.x10^{19}/n) \times (2.5\, T\nabla n + 7.4\, n\nabla T)$ in r/a=0.4 and B=1.T, for different discharges with different values of density, current and temperature. As can be seen the agreement is very good, what implies than nonlinearities are not important and the heat pinch is not needed for r/a=0.4. The agreement also means that χ obtained from sawtooth coupled analysis and χ from steady state transport analysis have roughly the same value.

Fig.3 Heat flux (kW/m^2) in TJ-I

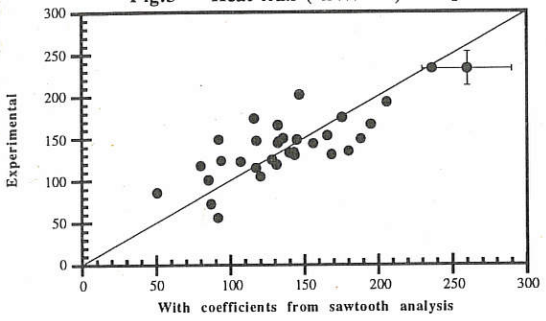

From the previous results we can expect to have a good description of transport in the plasma core, writing the fluxes in TJ-I as: $\Gamma = -D\nabla n - nV$ $\qquad q = -\chi n\nabla T$

If we also assume that the value for the ratio $\chi/D=7.4$ is valid for different plasma radius, we can determine from steady state analysis the radial profiles of χ and D, together with the particle pinch V.

Figure 4 shows the ratio between the obtained pinch V and the neoclassical value versus the plasma radius, for two discharges with roughly the same parameters but one with

and the other without sawteeth due to a different Z_{eff} profile. As can be seen the factor in the plasma core is of order one. Going to the plasma edge, for $q > 2$, the factor becomes negative what means that there are outwards convection. Figure 5 shows the radial profile of D for the discharge without sawtooth, compared with the neoclassical value and with the scaling 1/n. The experimental value is one order of magnitude greater than the neoclassical one in the plasma core.

Fig.4 $V / V_{neoc.}$ in TJ-I

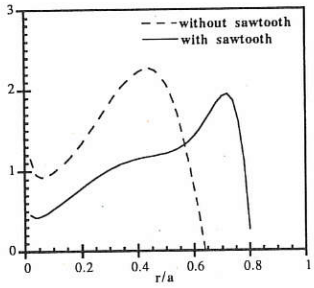

Fig.5 $D\ (m^2 s^{-1})$ in TJ-I

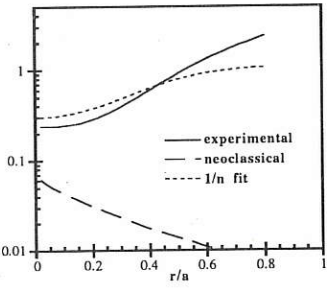

Discussion and conclusions.

The results obtained in this work allow us to describe the transport in the plasma core ($r/a < 0.6$) in a way valid to explain at the same time the steady state and the sawtooth pulse propagation. In this description the particle flux is independent of the temperature gradient and have a pinch very close to the neoclassical Ware pinch. Nevertheless, the diffusion coefficient is an order of magnitude higher than the neoclassical one. The conductive electron heat flux depends only on the temperature gradient with a heat conductivity seven times greater than the diffusion coefficient.

The fluxes are linear in the gradients of temperature and density. Transport matrix has not Onsager´s symmetry, although the nondiagonal terms could be affected by large errors. This means that the plasma distribution function is not too close to the Maxwellian one, for the velocities which gives the main contribution to the transport. This and the high value of χ/D can suggest a transport mechanism dominated by the faster electrons. For example transport due to some kind of magnetic activity.

References

1 J.C.M.de Haas et al. Nucl. Fus. **31**, 1261 (1991)
2 C.Pardo and B.Zurro. Report CIEMAT-610. Madrid. (1987)
3 B.Zurro, F.L.Tabarés et al. Proc. 18th EPS Berlin, I-69 (1991)
4 J.Vega and A.P.Navarro. Proc. 18th EPS Berlin, II-29 (1991)
5 J.Sanchez et al. to be published in Rev. Sci. Instrum. (1992)
6 A.C.C.Sips. et al Nucl. Fus. **31**, 1545 (1991)

MAGNETIC TURBULENCE MEASUREMENT FROM PELLET STRIATIONS: FIRST COMPARISON WITH ENERGY TRANSPORT

M.A.Dubois, B.Pégourié, R.Sabot , G.T.Hoang

Association Euratom-CEA sur la Fusion Contrôlée, CE Cadarache, 13108 Saint-Paul-lez-Durance, France

INTRODUCTION

Ablation of matter during pellet injection in Tore Supra is monitored by fast Hα signal acquisition. It is well known that the stronger dips in this signal are explained by the encounter of rational surfaces (e.g. in the vicinity of q =1). Assuming this explanation to be valid for the whole set of striations, we have been able to deduce q -profiles from the Hα signals, by identification of the more important dips. These q -profiles always exhibit shear plateaus on rational surfaces which do not appear systematically, but with a seemingly unpredictable frequency. Interpreting these shear plateaus as due to preexistent magnetic islands, we compute the local field line diffusion coefficient and derive a profile of the electron thermal conductivity.

q -PROFILE DETERMINATION

Method

Striations during pellet ablation have been related to resonant surfaces. The mechanism can be understood as follows. Let us define: Φ_p and V_p the pellet diameter and velocity; R the major radius of the torus; r the minor radius of the resonant surface and $v_{//}$ the electrons parallel velocity. For rational values of q=m/n, the energy reservoir available to ablate the pellet is smaller than elsewhere in a ratio $m\Phi_p/\pi r$ ($\approx$ m/150 in Tore Supra). If $\tau_p=\Phi_p/V_p$ (the time during which the pellet intersects a given magnetic surface) is longer than $\tau_{//}=2\pi Rm/v_{//}$ (the time of transit of the electrons on a closed field line, i.e. the time required to empty the tube of flux of its energy), a striation can appear whose depth is close to $\tau_{//}/\tau_p$. For typical parameters of ohmic discharges on Tore Supra, striations can exist for every m smaller than 15 to 20.

In a previous paper [1], it is shown that the rational q -values should be associated with a shear plateau to yield a striation. The analysis of the strong dip observed on the Hα signal when a pellet crosses the q=1surface supports this interpretation since shear plateaus as wide as 15cm are measured on JET [2]. Moreover, the fact that striations do not appear systematically on every strongly rational surface suggests that the shear plateaus are due to

preexistent structures which the pellet may or may not intersect depending on the poloidal phase (X or O point) and turbulence activity (width of the island). Supporting this idea, we show in a recent paper [3] that, even though the striation associated with the q=3/2 surface can not always be identified on every Hα signal of a series of about 10 pellets, it is clearly visible on their average. It is therefore highly tempting to associate each striation to shear plateaus due to small scale magnetic islands and to use the Hα modulation to determine the q -profile with a high accuracy.

The identification of the q -profile is performed in two steps:

-1- From each Hα signal, a set of radii r_i and depths $\alpha(r_i)$ are extracted for the most visible striations (the attenuation factor $\alpha(r)$ is equal to the ratio of the Hα signal divided by the value of its envelope at the same radius). To determine the q -profile is then equivalent to identify the corresponding $q_i=m_i/n_i$ yielding the best possible agreement between the α_i and the theoretical values $(\tau_{//}/\tau_p)_i$.

-2- The optimal set of (m_i, n_i) is determined by simulated annealing (a minimization method which allows to avoid local minima). The functional to be minimized is built requiring the solution to follow three constraints: q must increase with r, the experimental α_i must be in agreement with the theoretical bounds of the striation depths $(\alpha_i \geq (\tau_{//}/\tau_p)_i)$ and, with a much lesser weight, q (r) must approach the rough q -profile given by the equilibrium code IDENTC. The width of the shear plateaus is calculated according to [1].

Experimental results

We present results for two ohmic discharges: i) shot #4159, with a safety factor at the edge q (a)=3.8 and ii) shot #6435 for which q (a)=2.8. During shot #4159, the inductance $\beta+l_i/2$ varies and therefore the position of rational surfaces is expected to vary: we present on Figure 1a the q -profile for only one pellet (with the Hα signal and the envelope used to compute the α_i). The same q -profile (on which each plateau is labelled with its corresponding m and n values) is compared in Figure 1b with the one given by IDENTC. Shot #6435 is more interesting since the inductance stays constant: Figure 2 displays the q -profiles deduced from the three last pellets injected during this shot (a horizontal adjustement of the Hα signal of 4mm - that is below the experimental error - has been effected for the last pellet). The q -profile given by the code IDENTC is identical and the profiles determined from the striations analysis are within a ±5% range. A careful analysis of the signal shows that for the last pellet, all the striations corresponding to rational surfaces with $m \leq 9$ are present.

COMPARISON WITH ENERGY TRANSPORT

We assume that the measured shear plateaus δ_r correspond to small scale magnetic islands and more precisely to the island-like KAM torii remnants of interacting islands in a stochastic sea (see e.g. [4]). In these conditions, one can deduce for each striation the equivalent separatrix width δ_s (as would exhibit each island if isolated) from the relation $\delta_r=1.7\delta_s\exp(-\delta_s/l)$, where l is the separation between two adjacent resonant surfaces (this relation was derived numerically and is valid for $\delta_s/l>0.6$). A stochastic field line diffusion coefficient between two successive surfaces, χ_{STO}, can then be deduced following [5]. A rough estimate of the electron energy diffusion coefficient is then given by:

$$\chi_e = \chi_{STO} \frac{(r_i - r_{i+1})^2 / (2\pi)^2}{2\pi Rm / v_{//}}$$

We use $v_{//}=v_{the}$ as a first approximation. Figures 3a and 3b show, for the two shots mentionned above, three χ_e profiles obtained from this method for three different pellets and a fit of the averaged value. In fact, only averaged values can be compared to energy balance results since magnetic turbulence creates intermittent percolation paths rather than a smooth, constant value of χ_e (see [6] for an illustration).

The average value of the order of $1 m^2 s^{-1}$ and the tendency of χ_e to slowly increase with r are in good agreement with the value of χ_e obtained by transport analysis. A detailed comparison will be presented in a forthcoming study.

References

[1] Pégourié B. and Dubois M.A., Nucl. Fus. **29**, 745 (1989)

[2] Pégourié B. and Dubois M.A., Nucl. Fus. **30**, 1575 (1990)

[3] Dubois M.A., Sabot R., Pégourié B.et al., Report EUR-CEA-FC-1446 (1992), submitted to Nuclear Fusion.

[4] Hugon M., Rebut P.H., Plasma Physics and controlled Fusion Research (Proc. 10th Int. Conf. London, 1984) **2**, 197 (1985)

[5] Beaufumé P., Dubois M.A. and Mohamed Benkadda M.S., Physics Letters A **147**, 87 (1990)

[6] Dubois M.A., Beaufumé P. and Fromont B., Report EUR-CEA-FC-1444 (1991), submitted to Nature.

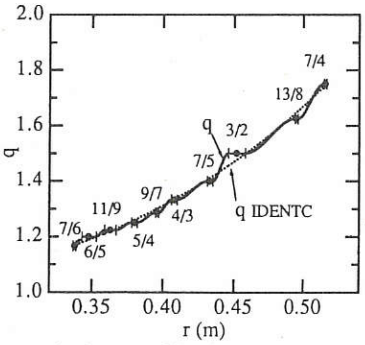

fig 1a : q-profile with shear plateaus for shot #4159

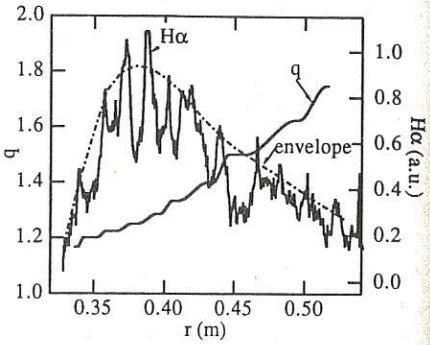

fig 1b : q-profile superimposed on the Hα signal

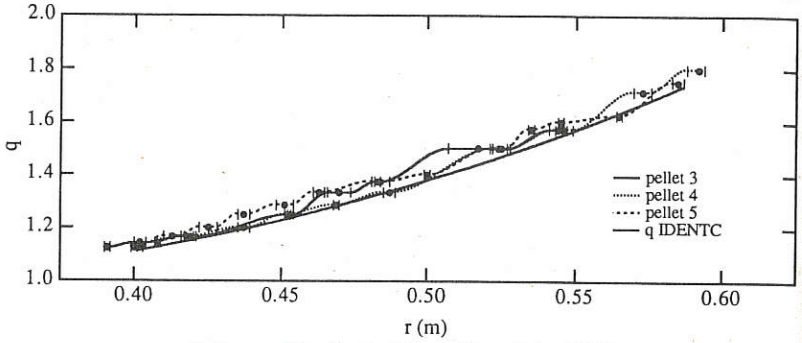

fig 2 : q profiles for the 3 last pellets of shot #6435

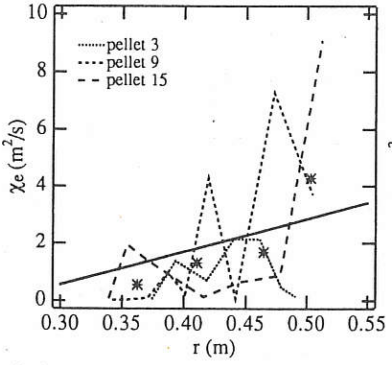

fig 3a : χ_e profils for 3 pellets of shot #4159,
* are averaged values,
the solid line is the linear fit

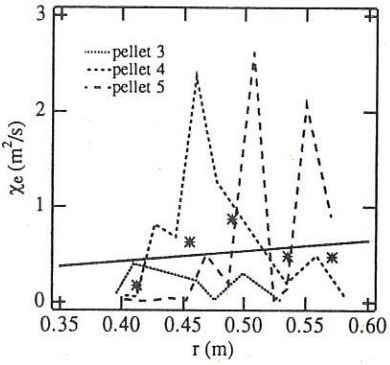

fig 3b : same as 3a for shot #6435

TRANSPORT AND TURBULENCE IN TORE SUPRA OHMIC DISCHARGES

X.Garbet, J. Payan, C. Laviron, P. Devynck, S.K. Saha, H. Capes, X.P. Chen, J.P. Coulon, C. Gil, G. Harris, T. Hutter, A.L. Pecquet.
Association Euratom-CEA
CE Cadarache, 13108 St Paul lez Durance Cedex, France
A. Truc, P. Hennequin, F. Gervais, A. Quéméneur,
PMI-Ecole Polytechnique, 91128 Palaiseau, France

1 - INTRODUCTION

The mechanisms underlying the energy confinement behaviour in ohmic tokamak discharges are not yet understood. It is well known that the confinement time increases with the average density and saturates above a critical value of the density, but several explanations exist for this saturation: the onset of ionic turbulence, an impurity content effect on Drift Trapped Electron Modes, or η_e modes stabilization by the increase of β (see ref.1 for a review). The present study is an analysis of a set of ohmic discharges in TORE SUPRA with I_p=1.6 MA , B=4 T , R=2.35 m and a=0.78 m, where the average density was increased from 0.9 to 4.2 10^{19} m^{-3}. For these plasma parameters, the energy confinement time given by magnetic measurements saturates for $\langle n_e \rangle \geq 2.5\ 10^{19}\ m^{-3}$ (fig.1). It is emphasized here that the onset of ionic turbulence is unlikely in TORE SUPRA. This conclusion relies on a transport analysis and turbulence measurements by CO_2 laser scattering, whose results are presented in this paper.

2 -LOCAL TRANSPORT ANALYSIS

A local transport analysis has been performed using the LOCO code [2]. Electron density and temperature measured by interferometry and Thomson scattering are input data to this code. The ion heat diffusivity is adjusted so that the calculated ion temperature agrees well with the one measured by charge exchange. Figure 2 shows the electron and ion heat diffusivities in the gradient zone (r=2/3a) as a function of average density. The electron heat diffusivity χ_{Te} decreases with $\langle n_e \rangle$ for $\langle n_e \rangle \leq 2.\ 10^{19}\ m^{-3}$, while the ion heat diffusivity χ_{Ti} also decreases, from 0.9 to $0.5 m^2 s^{-1}$. The latter values are well above the neoclassical estimate (the ratio is close to 15 at low densities). For $\langle n_e \rangle \geq 2.\ 10^{19}\ m^{-3}$, χ_{Te} saturates at a value close to $1 m^2 s^{-1}$, while χ_{Ti} saturates at a value close to $\chi_{Te}/2$. This behavior can only be guaranteed up to $\langle n_e \rangle = 3.\ 10^{19}\ m^{-3}$, where error bars on χ_{Ti} become too large to

allow a clear conclusion. The saturation of χ_{Te} is also confirmed by heat pulse analysis [3] which shows a similar behavior, except that values obtained for χ_{Te} are larger than the ones given by LOCO: a classical result in tokamaks. The change of slope seems also to occur for a larger density. The saturation of the confinement time therefore seems to be well explained by a saturation of the electron heat diffusivity. The variations of ion and electron diffusivities with density are apparently similar, although a degradation of χ_{Ti} (or χ_{Te}) at very large densities cannot be excluded. Note that the saturation of the energy confinement time with density occurs after the saturation of χ_{Te} at $\langle n_e \rangle = 2.\ 10^{19}\ m^{-3}$: this is because equipartition is not yet attained and Z_{eff} is not at its minimum value at this density. The cause of the electron heat diffusivity saturation cannot be clarified in these experiments. The effective charge number varies in fact as $1/\langle n_e \rangle$, and the average electron temperature as $\langle n_e \rangle^{-2/3}$: it is therefore not possible to know if the key parameter is the impurity content, the collisionality or the plasma beta.

3 - TURBULENCE MEASUREMENTS

Density fluctuations are measured in TORE SUPRA by using a CO_2 laser scattering experiment, ALTAIR [4]. This diagnostic allows localized measurements and its heterodyne detection permits the direction of wave propagation to be measured. The level of turbulence integrated over frequency, for a wave number $k_\perp = 600 m^{-1}$ and a scattering volume localized at the edge, is indicated in fig.2: it shows a good correlation with the electron heat diffusivity. Fluctuation spectra at low and high densities are shown in fig.3: it turns out that waves propagating in the ion diamagnetic direction exist at all densities. There is therefore no onset of an ionic turbulence at $\langle n_e \rangle = 2.\ 10^{19}\ m^{-3}$. Whether there always exists an ionic turbulence in TORE SUPRA remains an open question. It is nevertheless possible that this ion feature is due to a doppler shift linked to the inversion point of the radial electric field near the edge. This hypothesis is under investigation : preliminary calculations based on pure electron drift turbulence and a shear layer localized at $r/a = 0.90 \pm 0.03$ give a reasonable agreement between calculated and measured spectra [5]. Finally, it must be stressed that the theoretical threshold for ionic turbulence is never reached in TORE SUPRA ohmic discharges, a result which supports the above conclusion [6].

IV.-CONCLUSION

The saturation of the energy confinement time in TORE SUPRA is governed by the behavior of the electron confinement. This appears through a saturation of the electron heat

diffusivity, correlated to similar variations of the density fluctuation level. Ion heat transport is not neoclassical at low densities and is correlated to the electron heat transport. No dramatic changes of ion heat transport appear at the saturation point and so an ion turbulence is not necessary to explain the saturation. Moreover, no ion turbulence onset is observed in coherent scattering spectra at the saturation. Although an ion feature is always present in these spectra, it is likely to be due to the presence of a shear layer near the plasma edge. Consequently, the saturation of the confinement time seems to be correlated with the behavior of the electron drift turbulence.

REFERENCES

[1] Romanelli, F., Plasma Phys. Cont. Fusion, **31** (1989) 1543.

[2] Harris, G., et al., Rep. EUR-CEA-FC1452, submitted to Nucl. Fus.

[3] Pecquet, A.L., et al.,Workshop on perturbative transport studies and relation to global confinement, Utrecht,1992,unpublished.

[4] Laviron, C., et al., in Proc. 18th European Conf. on Cont. Fus. and Plasma. Phys., Berlin 1991, vol.IV,p 337.

[5] Gervais, F., et al., this conference.

[6] Garbet, X., et al., Phys. Fluids **B4** (1992) 136.

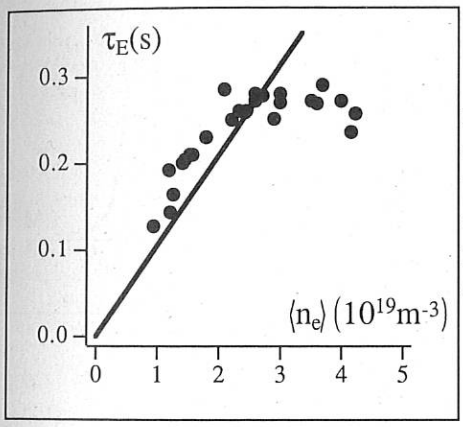

Fig.1: Energy confinement time versus average density for TORE SUPRA deuterium discharges with I_p=1.6MA, B=4T, R_0=2.35m, a=0.78m. The solid line indicates the Alcator law.

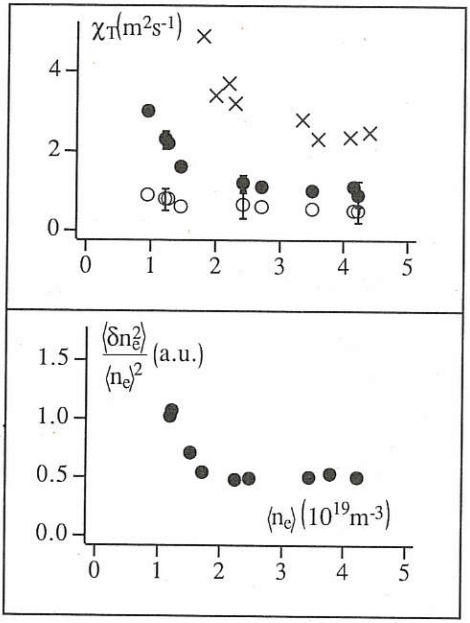

fig.2:Electron (black points) and ion (circles) heat diffusivities at r=2/3a and turbulence level versus average density. Crosses indicate values obtained from a sawteeth heat pulse analysis

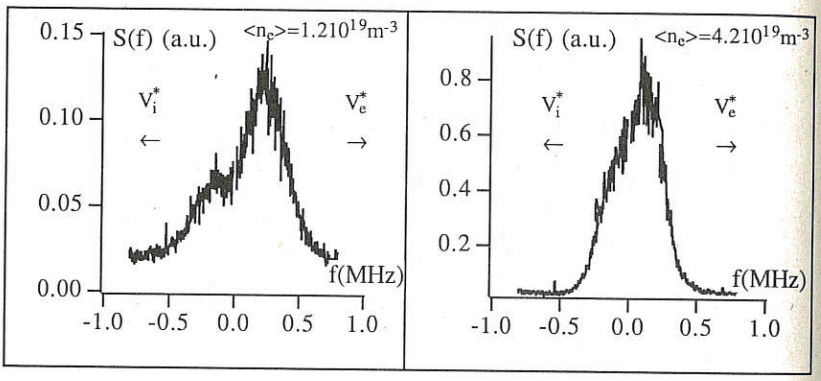

fig.3 : Density fluctuation spectra from CO_2 laser scattering for $k_\perp=600m^{-1}$, at low and high densities. Positive frequencies correspond to waves propagating in the electron diamagnetic direction.

1-32

STUDY OF THE PLASMA TURBULENCE BY MEANS REFLECTOMETRY IN TUMAN-3 AND FT-2 TOKAMAKS

V.O.ALEKSANDROV, V.V.BULANIN, D.O.KORNEYEV, A.A.SERGEYEV

St.Petersburg Technical University
195251 St.Petersburg (Russia)

In recent years microwave reflectometry has been more and more used as a convenient method for the plasma turbulence study in the tokamak. However some problems have been encountered in experimental data interpretation connected with the coupling of the phase and amplitude oscillations in the output reflectometer signals. The decoupling of the oscillations may be achieved with the cross-detection reflectometers. The initial investigations of the plasma edge turbulence in the Tuman-3 tokamak were carried out with the simple homodyne reflectometer [1]. Some features of the received signal have been similar to those of the DIII-D tokamak [2]. Namely the high frequency spectral components were drastically decreased just after the L-H transition. The homodyne reflectometer output signal is well known to be influenced by phase oscillations (fringes) and amplitude one. For the fringe component has not been evidently observed in the output signal the strong amplitude modulation is assumed to be existing near the Tuman-3 tokamak periphery.

The cross-detection (or sine-cosine) reflectometer has been used for the decoupling of the phase and amplitude oscillations. The simple single antenna scheme has been designed for this purpose (Fig. 1). There are two similar homodyne channels in which the reference signal phases have been tuned to obtain the additional phase shift $\pi/2$ between two output signals of detector sections. This shift is achieved using the adjustable short circuits in the directional couplers. The shift $\pi/2$ could be measured and tuned while observing the 2D phase diagram on the oscilloscope. The sine and cosine output signals are amplified and memorized in the digital form with the sampling step of 1 or 0.5 μs. The corresponding algorithm has been used for the step by step phase calculation provided the phase jump is no more than π to exclude the phase ambiguities.

The cross-detection reflectometer was installed on the Tuman-3 tokamak. The main tokamak and reflectometer parameters as follows: R = 55 cm, a = 24 cm, B_t = 0.4 - 0.6 T, I_p = 90 - 130 KA, F = 16 - 26 GHz (O or X mode), $n_c = (0.3 - 0.8) \times 10^{13}$ cm^{-3} (O - mode), $n_c = (0.1 - 0.5) \times 10^{13}$cm^{-3} (X - mode). Here : F-microwave probing frequency, n_c -cut-off layer electron density. The experiments were performed in the various tokamak discharge condition : with the ohmic H-mode initiated by means of gas puffing or radial electric field switching on and in the fast current ramp down. The circular antenna of 6 cm in diameter placed at the low magnetic field side was taken to probe the plasma. A few experiments were made with low gain antenna with the 2 cm horn diameter. The antenna was taken for plasma probing along the central vertical chord.

While using the cross-detection reflectometer the amplitude and phase oscillations could be treated separately. The Fig. 2 shows the typical calculated phase and amplitude spectra. The amplitude spectra are commonly broader than the phase ones. The step by step reconstruction procedure allows to obtain the phase evolution over the all period of the discharge. The calculated phase is observed to correspond to the actual cut-off layer

displacement only in a few ms just after the plasma current start and during the period of plasma decay after current disappearance. The data obtained in these periods prove the correct action of the total cross-detection scheme. During the main tokamak discharge the rate of the phase changing is observed to be anomalously large (Fig. 3). The 100π per division is here. So this phase variation is equvalent to cut-off displacement which happened to be large than tokamak minor diameter. It is clear that the long time periods of phase rump up or down are not due to the cut-off movement and are of another origin. It is important to note that the runaway effect are strongly connected with the discharge condition changing. Fig. 3 illustrates different cases of plasma condition changing due to the application of various potentials to the biased electrode. At zero potential the phase run away sing change was observed just after the spontaneous improvement of the confinement and the D_α emission fall down. Fig. 3(b) shows the event of the positive potential application to the biased electrode which leads to the D_α emission uprising and to the fast phase run away. The negative potential application initiates the well defined L-H transition (Fig. 3(c)) and prevents the phase falling down observed without potential. The phase run away change occurs after the two fold fast current rumpdown (Fig. 4). One can see the phase run away is slowing off in a few ms after the rumpdown.

The phase runaway phenomena may be induced by different reasons. According to simulation experiments the fault of the $\pi/2$ phase shift can not be responsible for the anomalous phase changing. The low level secondary reflection between antenna horn and plasma was stated to be unimportant as well. The phase distortion could be happened if the high frequency range of spectrum is virtually lost. However the experiments with two different sampling steps (1 and 0.5 μs) have shown the same phase behavior.

As we assume the phase run away effect is induced by the grating-like cut-off layer which rotates in the poloidal (or toroidal) direction. For the case of assimetrical grating groove the rotation liads to continuous shift of the cut-off layer in the antenna direction with the speed of $V_c = V_\theta \delta / \lambda_\theta$ (Here: δ is the depth of grating groove modulation, λ_θ- the poloidal wave length of the fluctuation). The microwaves are reflected from this rippling layer and interfere into the antenna directivity diagram. As a result the Doppler frequency shift have to be appeared Ω. The frequency shift leads to the linear phase uprise Ωt. Such effect is known to be commonly used in the laser interferometry for the frequency shift due to the rotation of the reflection grating. With this view the experiments with the low gain antenna are worth to be mentioned. Because of the wide directivity diagram the wide range of the reflection angles is accessible and so the profile of the plasma grating and its displacement could be determined. While using the low gain antenna the phase run away disappeared just after the L-H transition and the cut-off layer displasement was observed by well defined fringes. The phase run away effect would occur also due to the strong back (or forward) scattering process. The scattering has to induce the frequency shift signal and therefore the linear phase changing provided the existence of the radial component of the plasma wave veloscity. The assumption on the grating-like plasma fluctuations is in accordance with the theoretical outlook on the tokamak turbulence [3]. According to this theory the high poloidal wave number islands which are turned over their magnetic axes form the grating-like space structure. These plasma perturbations perhaps could be observed using the cross-detection reflectometry technique.

FT-2 experement.

An X-mode, U-band homodyne reflectometer with probing from high field side was used for density profile control and turbulence investigation. A slow change of toroidal magnetic field during a discharge leads to scan of cut-off layer along the major radius. Time evolution of the one of the obtained signals is presented on Fig. 5 together with electron density averaged over central chord and toroidal magnetic field. Note that three modes of operation of the diagnostic took place. While B_t was relatively low the interferometer mode with reflection from vacuum chamber wall at the low field side was observed (I). With the B_t increase the upper cut-off layer occurred in plasma and diagnostic transmuted into reflectometer mode (II). Further B_t increase led to the entrance of ECR layer into the plasma from the high field side. In this case the probing beam dissipated in the vicinity of UHR layer and only scattered radiation was received (III).

Two ADC was used for data acquisition: 1 MHz sampling rate during the whole discharge and 20 MHz one during 50 μs. The spectra of signal in interferometer and reflectometer modes were different. First spectrum was falling down up to 200 KHz with well defined peak connected with low frequency fringes. MHD oscillations were also observed. Contrary, in reflectometer mode spectrum was broader: 500 KHz near the plasma edge and up to 1.5–2 MHz in inner part of plasma column. The discharges were investigated with the following parameters: $B_t = 0.2$ T, $I_p = 50$ KA, $N_e = 1 - 2 \times 10^{13}cm^{-3}$. In the discharge with low plasma density (about $10^{13}cm^{-3}$) these oscillations were so strong that no any fringes connected with slow cut-off layer motion due to B_t change were not observed. In discharges with $N_e = 2 \times 10^{13}cm^{-3}$ the fringes were detected and density profiles were reconstructed. Fig. 6(a) presents the profile obtained from data shown on Fig. 5. The comparison of averaged density obtained from the profiles and 2-mm interferometer data (only one central chord was available) shows a good agreement. It is possible to estimate the radial distribution of turbulence intensity because the cut-off layer moved through the large part of minor radius during the discharge. On Fig. 6(b) we present the averaged power of reflectometer signal with frequencies upper 200 KHz normalized on fringe amplitude Us/Uf. This distribution consist of well defined peaks. On one hand they would be connected with distribution of resonance magnetic surfaces, but on other hand they would reflect the change of turbulence intensity in whole plasma column due to B_t change.

In conclusion the authors express the gratitude to Tuman-3 and FT-2 groups for their assistance in performing the experiments.

References.

[1] Bulanin V V, et al 1991 *Proc. 18th EPS Conf., Berlin* **IV** 321
[2] Doyle E L, et al 1990 *Proc. 17th EPS Conf., Amsterdam* **14B**,1 203
[3] Kadomtsev B B 1991 *Nuclear Fusion* **31**, N **7** p1301

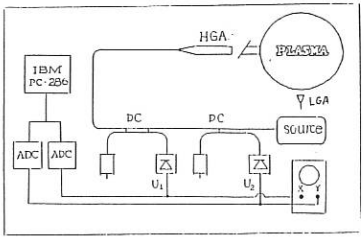

Fig. 1 Cross-detection reflectometer layout on Tuman-3. HGA,LGA - high and low gain antenna.

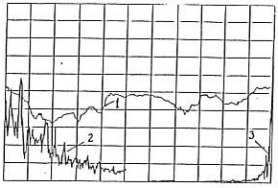

Fig. 2 Reconstructed phase-(1). Spectra of amplitude (2) and phase (3).

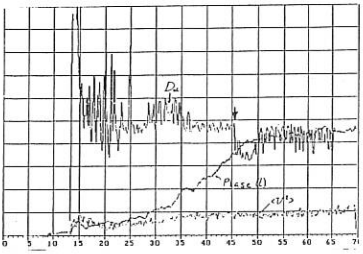

t, ms

Fig. 4 Discharge with current rumpdown.

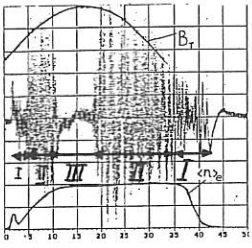

t, ms

Fig. 5 Temporal behavior of reflectometer signal (U), toroidal magnetic field (Bt) and average density (nxe. I-III -the modes of aperation of microwave diagnostic.

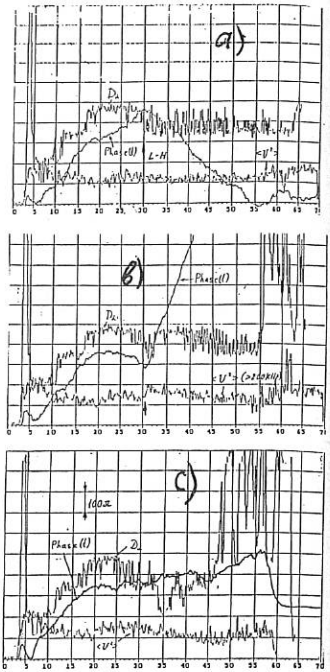

t, ms

Fig. 3 Discharges with potential application. a - zero potential, b-positive, c - negative. $\langle U^2 \rangle$ - RMS value of sine output signal in the frequency band above 200 KHz(arb. units)

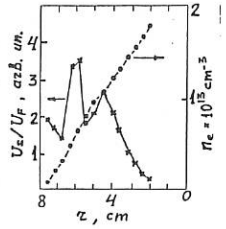

Fig. 6 The reconstructed density profile (1) and relative amplitude of oscillations (2).

1-33

PARTICLE FLUX IN A TOKAMAK: FUNDAMENTAL EXPERIMENTAL CONSTRAINTS ON THE FORM AND RELATION TO FLUCTUATIONS

K.W. Gentle, B. Richards, M.E. Austin, R.V. Bravenec, D.L. Brower, R. Gandy, W.L. Li, P.E. Phillips, D.W. Ross, W.L. Rowan, P.M. Schoch, D.C. Sing, P.M. Valanju, A.J. Wootton

Fusion Research Center,University of Texas, Austin, Texas, USA

The local density may be significantly (~10%) modulated in a tokamak by control of the gas feed; the electron temperature and the level of density fluctuations are also modulated. From a transport analysis of such experiments in the TEXT tokamak, the perturbed particle and energy fluxes can be determined and compared with the equilibrium values as a function of minor radius. The analysis implies that the particle flux does not obey Fick's law $\Gamma=-D\nabla n$ -- additional terms are required -- and that the amplitude of electrostatic turbulence is not an index of Γ. The energy flux is equally complex.

The continuity equations for the equilibrium, $\Gamma_0(r)$, and perturbed, $\Gamma_1(r)$, particle flux with $e^{i\omega t}$ time dependence are

$$\frac{1}{r}\frac{\partial}{\partial r}(r\Gamma_0) = S_0(r) \qquad (1)$$

$$i\omega n_1 = -\frac{1}{r}\frac{\partial}{\partial r}(r\Gamma_1) + S_1(r) \qquad (2)$$

in terms of the density n(r) and the source S. The radial shape of $S_0(r)$ is determined from a neutral particle penetration code, and the scale factor is fixed by the measured particle confinement time (absolute H_α measurements.) Then Γ_0 follows from direct integration of Eq.(1). The density is measured with a multichannel interferometer, from which seven independent chord integrals are determined. The amplitude and phase of the Fourier component at the imposed modulation frequency ω are determined for each chord and subjected to a extensive transport analysis as discussed in /1/, from which Γ_1 is easily inferred. The magnitude of the flux ratio, $|\Gamma_1|/\Gamma_0$, is plotted in Fig. 1 for a typical discharge of average density 3.2 x $10^{19}/m^3$, 200 kA plasma current, and 2 T toroidal field. This dimensionless ratio makes it easy to compare equilibrium and perturbed transport. Results for three different perturbation strengths are shown, indicated by the amplitude of the central density perturbation amplitude, $|n_1(0)|/n_0(0)$. To demonstrate the linearity of the process, $\Gamma_1 \propto n_1$, the data for the weaker perturbations is also scaled to the strongest. If linearity were perfect, the three uppermost curves would superimpose.

From Fig. 1, which has been confirmed for various conditions and at values of $|n_1(0)|/n_0(0)\leq 0.15$, the linearity of the process is quite clear, but the values of $|\Gamma_1|/\Gamma_0$ are remarkably large. Since these perturbations are not steep, $|\nabla n_1|/\nabla n_0 \sim |n_1|/n_0$, such large

values are inconsistent with a simple Fick's law Γ=-D∇n, for which $|\Gamma_1|/\Gamma_0 \sim |n_1|/n_0$. Not even a nonlinear D can explain the observations. No homogeneous function of the local variables, e.g.

$$\Gamma = C_\alpha n^{\alpha 1}(\nabla n)^{\alpha 2} T^{\alpha 3}(\nabla T)^{\alpha 4} \qquad (3)$$

can be satisfactory. Since all perturbations ($|n_1|/n_0$, $|T_1|/T_0$, etc.) are small, linearization of Eq.(3) could produce a large $|\Gamma_1|/\Gamma_0$ only if some of the α_i were quite large, of order 15 for this case. Besides being physically unsatisfactory, such large values of an exponent would imply a nonlinearity in the response for the perturbation amplitudes here, contrary to the observed linearity. The resolution of this inconsistency is the use of an inhomogeneous form for Γ, in this context usually termed a diffusive-convective (D and V) model, and in other contexts an offset model. Such models naturally accommodate a small equilibrium Γ_0 as the balance of two larger terms while permitting large, but linear, Γ_1. These experiments require such models.

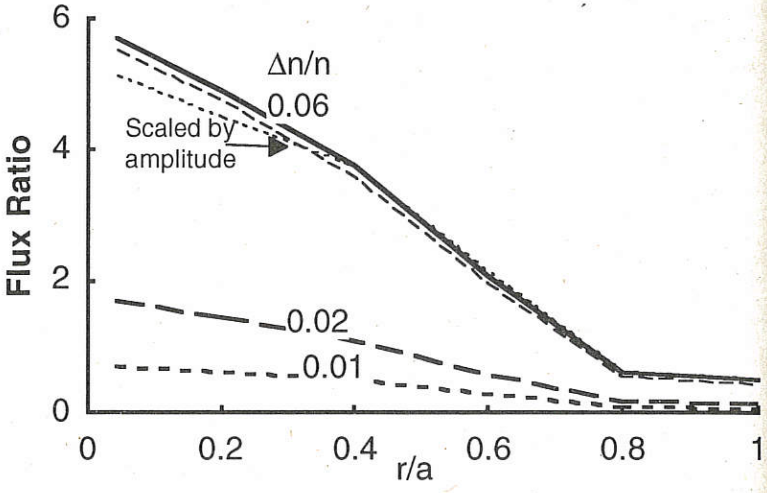

Fig. 1 Ratio of perturbed to equilibrium particle flux as a function of minor radius.

Another common working hypothesis of the same sort as Eq.(3) is the statement that $\Gamma \propto (\tilde{n}/n)^\beta$, with $\beta \sim 2$ and $\tilde{n}$ being the amplitude of the turbulence responsible for the transport. The electrostatic turbulence is measured in these experiments by a Heavy Ion Beam Probe and represented by the rms value of density fluctuations $\tilde{n}$ integrated over all frequencies (above 5 kHz to include only turbulence) and wave numbers within the range of the instrument

($0<k<2$ cm^{-1}; $k\rho_s < 0.25$), which seems to include the spectral peak. As with other parameters, both the equilibrium turbulence level $\tilde{n}_0$ and the Fourier component associated with the modulation at ω, $\tilde{n}_1$, are measured, a clear distinction because the 30 Hz modulation is much less than the frequencies of the turbulence. The absence of a simple relation between turbulence level and particle flux is shown in Fig. 2, which repeats the particle flux data for the case of Fig. 1, largest perturbation, and includes the associated modulation in the turbulence level. The 6% density modulation is associated with a 10%-20% modulation in the turbulence level, a reasonable physical effect, but much too small to account for the large perturbed flux. The simple relation between turbulence level and flux is quite wrong; the relation must be much more subtle. The turbulence level should not be used as an indicator of transport rates.

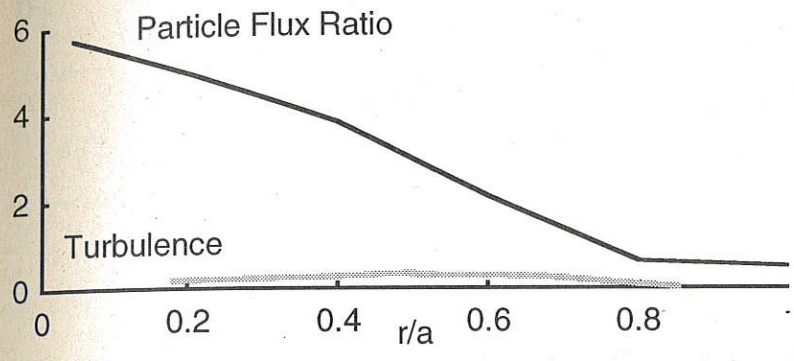

Fig. 2 Ratio of perturbed to equilibrium particle flux and perturbed to equilibrium turbulence level, $|\tilde{n}_1|/\tilde{n}_0$.

Using a calibrated Electron Cyclotron Emission system to measure $T_{e0}(r)$ and $T_{e1}(r)$, a similar analysis (/2/) can be performed on these ohmic discharges to obtain the energy fluxes $q_0(r)$ and $q_1(r)$. The modulation frequency is sufficiently high that the current distribution is frozen; the ohmic dissipation is modulated only through the temperature modulation of the conductivity. The simplest models, for which energy and particle are transported together with $q=\alpha kT\Gamma$ (α~5) are clearly inadequate, as shown in Fig. 3. In fact, examination of the perturbations suggests that the energy transport may be as complex as the particle transport. In Fig. 4, estimates for the conducted energy $Q = q - (5/2)kT_e\Gamma$ in the electron channel are shown for the equilibrium and perturbation as Q_1/Q_0 and compared with the electron temperature gradient T'_1/T'_0. Both the amplitude and phase for each quantity are shown. Neither is consistent with a simple sort of $q = \kappa T'$ relation. However, these results do not

Eq.(3) could be possible, the linearization of which would give $Q_1 = AT'_1 + BT_1 + Cn_1 + ...$, which could provide an adequate resolution of the paradox of Fig. 4.

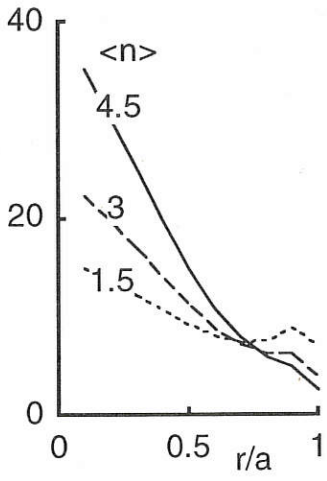

Fig. 3 Ratio of energy to particle flux times temperature for the equilibrium at several densities.

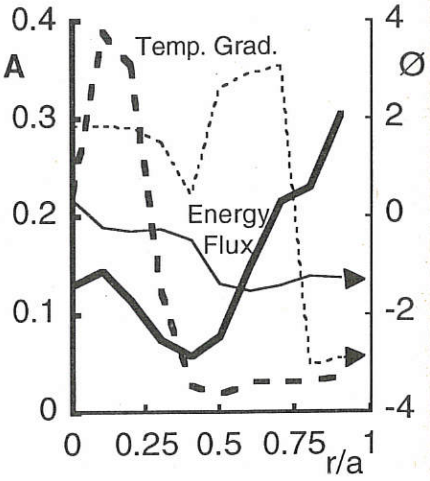

Fig 4. Amplitude (left) and phase (radians, right) for the ratio of perturbed to equilibrium temperature gradient (dashed) and convected energy flux (solid).

The complexity of the relations among particle flux, energy flux, and turbulence has also been demonstrated in experiments using ECRH to induce temperature modulation. Local turbulence levels have been modulated in the absence of apparent local changes in any driving term and without changes in local transport.

This work was supported by the U.S. Department of Energy under Grants DE-FG05-88ER53267 and DE-FG05-88ER53266.

/1/ K.W. Gentle, O. Gehre, and K. Krieger, Nuclear Fusion **32**, 217 (1992).
/2/ K.W. Gentle, B. Richards, M.E. Austin, R.V. Bravenec, D.L. Brower, R.F. Gandy, W.L. Li, P.E. Phillips, D.W. Ross, W.L. Rowan, P.M. Schoch, P.M. Valanju, and A.J. Wootton, Phys. Rev. Lett. **68**, 2444-2447 (1992).

DIFFUSION OF FAST ELECTRONS AFTER A MONSTER SAWTOOTH CRASH

M. Hugon, D. Bartlett, M. Brusati, P. Froissard,
C. Gormezano, P. Morgan, L. Porte, F. Rimini, M. Stamp

JET Joint Undertaking, Abingdon, Oxon, OX14 3EA, United Kingdom

Introduction

Monster sawteeth have been produced during Lower Hybrid Current Drive and Ion Cyclotron Resonance Heating campaigns. In these experiments, the Lower Hybrid wave generates fast electrons in the plasma bulk with energies in excess of 100 keV /1/. The fast electrons are observed to reach the limiters after the sawtooth crash well in advance of the heat pulse due to thermal electrons. Analysis of this process could give an insight into the nature of the turbulence responsible for anomalous transport in tokamaks.

Experimental conditions

The observations described in this paper have been carried out in 3 MA, 3.1 T limiter Deuterium plasmas with central electron density $n_{eo} \simeq 2.5\ 10^{19}\ m^{-3}$ and temperature $T_{eo} \simeq 8 - 10$ keV. Effective electron heating was achieved through H minority (10 % H concentration), central resonance ICRH at ~ 6 MW power level. Lower Hybrid Current Drive (LHCD) was applied in these discharges at 1.5 MW coupled power level with a narrow power spectrum peaking at $N_{\parallel} = 1.8 \pm 0.2$, corresponding to an Electron Landau Damping resonant energy of 100 keV. The application of LHCD produces a loop voltage drop ≤ 30 % in these conditions and the combined effect of the residual electric field and synergism with the IC Fast Wave /1/ leads to an LH induced fast electron density $n_{fe} \simeq 10^{-3} n_e$ in the energy range 100 to 300 keV, corresponding to ~ 2 % of the total electron energy (fig. 1). The fast electron profile is assessed by means of the FEB diagnostic /2/ and is found in these plasmas to be peaked on axis with a half width at half maximum $\simeq r_{q=1} \simeq 0.5$ m.

Two series of experiments have

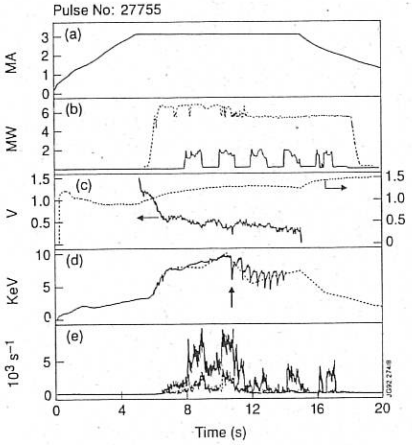

Fig. 1 - Time evolution of the main plasma parameters for the JET pulses in these experiments. (a) Plasma current. (b) ICRH (—) and LH (—) power. (c) Loop voltage (—) and internal inductance (—). (d) Central electron temperature from ECE (—) and LIDAR (—) measurements. The arrow indicates the sawtooth crash where the fast data acquisition window was set. (e) FEB emission in the 100 - 150 (—) and 200 - 250 (—) keV energy windows.

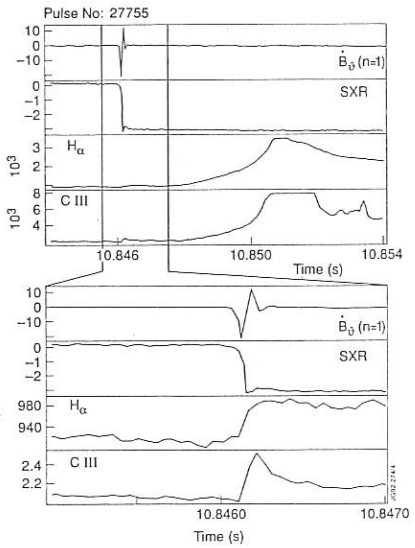

Fig. 2 - Blow-up of the time interval around the sawtooth crash selected in fig. 1, showing the growth of the m=1 mode, the sawtooth crash as detected by the central soft x-ray channel and the behaviour of Hα and C III associated with the arrival of fast and thermal electrons at the limiter. All units are arbitrary.

been carried out for plasmas leaning either on the beryllium or on the carbon limiter. Both sets of data lead to the same conclusions as far as the dynamics of fast electrons is concerned.

Scaling studies have shown that the inversion radius increases with the sawtooth period /3/ and that the heat pulse propagation time decreases with increasing mixing radius. These observations indicate that the heat wave propagation time is much shorter for a monster sawtooth crash than the 20 - 30 ms of a normal sawtooth collapse. In addition, the time behaviour of the Hα emission at the plasma edge (limiter or X-point tiles) after a sawtooth crash mainly reflects the arrival of the heat pulse.

In the experiments reported here the Hα and CIII emission signals from the carbon limiter show a small increase starting immediately after the crash and lasting about 1 ms. This behaviour is ascribed to the arrival of fast electrons on the limiter, and the observed amplitude is consistent with the fast electron energy content. Subsequently, these signals exhibit a 5 to 40 fold increase 2 to 5 ms after the crash, when thermal electrons reach the limiter (fig. 2).

The time evolution of the electron cyclotron emission measured by a heterodyne radiometer at frequencies where there is contribution to the overall signal by fast electrons outside $r_{q=1}$ show a structure about 0.5 ms long. It occurs at the time of the sawtooth crash and is superimposed on the thermal signal (fig. 3). Similar observations can be made in absence of LH, suggesting that fast electrons could be also created during the flux reconnection process.

The arrival of fast electrons at the limiter while the sawtooth is actually collapsing may be explained by the fast growth of the instability, which starts about 0.25 ms before the crash. In JET, this instability is measured as an m=1 displacement in the plasma centre and as a fast poloidal magnetic perturbation $\tilde{b}_\theta$ lasting about 0.5 ms at the edge. The n=1 component of $\tilde{b}_\theta$, $\tilde{b}_{\theta n=1}$, is identical to the m=1 radial plasma shift. For monster sawteeth, $\tilde{b}_{\theta n=1}$ is the dominant harmonic with a poloidal mode number m=int(q_ψ) and can reach a maximum of a few 10^{-3} T at the crash. The

maximum amplitude of $\tilde{b}_{\theta n=1}$ increases with the relative central temperature drop $\Delta T_e(0)/T_e(0)$ and with the sawtooth period /4/. Note that the sawtooth instability is only observed at the wall on large machines of tight aspect ratio, such as JET, TFTR and DIII-D, probably because of strong mode coupling.

Consequences for the nature of the turbulence

These observations are consistent with the existence of magnetic turbulence in the tokamak plasma. This turbulence would result from a mixture of islands of the size of the ion Larmor radius and a chaotic region, where the magnetic field lines link the inside to the outside of the plasma /5/. The 100-300 keV electrons generated by the LH waves have a 0.3-0.5 mm Larmor radius at most and are collisionless, when comparing their transit time (≤ 1 ms) to their relativistic collision time (≃ 20 - 40 ms). Consequently they follow the magnetic field lines closely and are expected to reach the limiter before thermal electrons do.

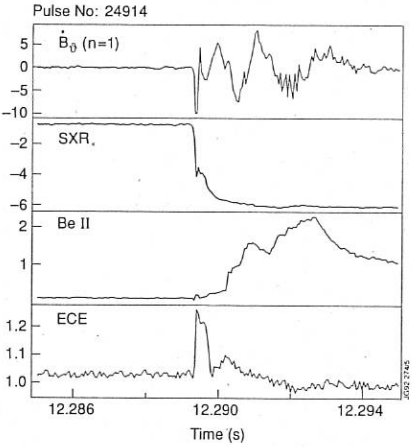

Fig. 3 - Similar to fig. 2, where the fast electron behaviour is monitored by the Be II detector and the non thermal EC emission radiometer.

Quasi-neutrality in the chaotic region arising from island overlap is ensured by a radial ambipolar electric field directed outwards in the reference frame of the islands /5/. When the fast electrons are ejected at the plasma edge after the monster sawtooth crash, quasi-neutrality is maintained by the increase of the radial electric field.

It has been shown that the chaotic field lines satisfy a diffusion process across the island chains /6/. Under these conditions, the transit time t of the fast electrons assumed to be collisionless is given by: $t = 1.6\pi RN^2/(\gamma-0.75)^{2.1}v$, where R is the major radius, N the number of crossed island chains between the q=1 surface and the limiter, γ the overlapping parameter and v the velocity of the electrons along the field lines

When comparing the predictions of this formula with experiment, two phases have to be considered:

a)- During the sawtooth instability, the large amplitude of $\tilde{b}_{\theta n=1}$ measured at the edge indicates that $N = int(q_\psi)$ modes are coupled and that γ is probably larger than 1, the value corresponding to the steady state. q_ψ is between 3.6 and 5.6 for the pulses investigated. This phase leads to very small values for t (≤ 0.1ms).

b)- After the sawtooth crash and after $\tilde{b}_{\theta n=1}$ has decreased substantially, N is of the order of 15 - 30 and $\gamma \simeq 1$ as in steady state conditions. The corresponding transit time is larger ($0.1 \leq t \leq 1$ms).

The measured values for t of 0-1 ms are consistent with the above equation, when considering the velocity and spatial distributions of the fast electrons, with the fast electron population being mostly emitted during phase a).

Conclusions

LH induced fast electrons in the energy range 100 - 300 keV, located near the q = 1 surface are observed to be ejected by the plasma following a monster sawtooth collapse in less than 1 ms, well before thermal electrons (~ 5 ms in these experiments). The diffusion speed is of the order of $5\ 10^3$ m/s.

These values are consistent with a diffusion mechanism based on magnetic stochasticity, in the initial phase of large $\tilde{b}_\theta$ fluctuations during a sawtooth crash.

References

/1/ C Gormezano et al., Proc. IAEA Technical Committee on Fast Wave Current Drive in Reactors, Arles (France), 1991.
/2/ P Froissard et al., Proc. 18th EPS Conference, Berlin (Germany), 1991.
/3/ Pearson D., Campbell D., Edwards A. and O'Rourke J., in Controlled Fusion and Plasma Physics (Proc. 18th Eur. Conf. Berlin, 1991), Vol.15C, Part II, European Physical Society (1991) 25.
/4/ Duperrex P.A., Pochelon A., Edwards A. and Snipes J., JET-P(91)43, submitted to Nuclear Fusion.
/5/ Rebut P.H., Brusati M., Hugon M. and Lallia P. (1987) Proc. 11th Int. Conf. on Plasma Physics and Controlled Nuclear Fusion Research, Kyoto, 1986, Vol.II, p.187, IAEA, Vienna.
/6/ Hugon M., Mendonça J.T. and Rebut P.H. (1989) C.R. Acad. Sci. Paris 308, Série II, 1319.

Electron Temperature and Density gradients across magnetic m=2 structures in RTP

B.Ph. van Milligen, A.C.A.P. van Lammeren, N.J. Lopes Cardozo, F.C. Schüller, M.Verreck

FOM Instituut voor Plasmafysica 'Rijnhuizen' P.O.Box 1207, 3430 BE Nieuwegein, The Netherlands

Introduction

This paper investigates the existence of temperature and pressure gradients across m=2 magnetic islands. Measurements of both T_e and n_e in a very large m/n=2/1 island preceding a disruption are analysed. The T_e and n_e perturbations are compared to the position and width of the island as deduced from magnetic measurements, and we investigate whether there are closed isothermal and isobaric surfaces within the island. Further, the incremental current in the island O-point is computed, and the coupling between the m=1 and m=2 modes is considered. The results are discussed in the context of the theory of tearing modes and transport in the collisional outer region of the plasma.

RTP Tokamak and diagnostics

The experiments are performed in the RTP tokamak (R_0=0.72m, a=0.165m, circular cross-section, boronized vessel). The discharge under study had B_T=2.14T, I_p=145 kA , q(a)=2.80, with $n_e(0)\approx 6\times10^{19}m^{-3}$. Diagnostics include: 20 channel ECE heterodyne radiometer and 6-channel grating polychromator, 19-channel FIR interferometer and single channel 2 mm interferometer, magnetics, neutral particle analyser, soft X-ray pulse height analysis. The magnetic diagnostic consists of a set of 12 B_θ pick-up coils and 12 saddle loops. The B_θ pick-up coils are located at r_{coil}=0.213 m. The 20-channel radiometer measures 2nd harmonic ECE X-mode, from which T_e is deduced. The radial resolution varies from ≈1.5 cm at R = 0.62 m to ≈2.5 cm at R = 0.82 m. The noise equivalent temperature is typically 2-3 eV at 10 kHz video-bandwidth. The computation of T_e includes optical depth effects, using the n_e-profile from the interferometer. The channels of the FIR-interferometer have variable spacing. For this study, the spacing of the 14 available channels was 2.4 cm on average. λ(FIR)=432μm; the intermediate frequency between the plasma and reference beams is 1 MHz, allowing high time resolution. The accuracy in the line-integrated density is better than $2\cdot10^{16}$ m^{-2}.

Experimental results.

Fig.1 gives an overview of the discharge under study: the current plateau of 145 kA is reached at t=100ms; note the sawtooth activity on both the central interferometer channel and the central temperature, and the occurrence of strong MHD activity starting at t≈135ms, leading to a minor disruption at t=143ms and a major disruption at t=147ms. The mode activity is shown in Fig.2, where the contributions of the different m-numbers have been separated.

Magnetic measurements

We concentrate on the strong m=2 mode around t=142ms, i.e. prior to the minor disruption. The radial island width (w) can be expressed in terms of the radial field perturbation at the rational surface: $w=4\{(s\hat{B}_r)/(mB_\theta)\}^{0.5}$ [1] where $\hat{B}_r$ is the amplitude of the radial field perturbation due to the island, $s=\partial\ln q/\partial\ln r$ is the shear, and all quantities are to be evaluated at the radius r_2 of the q=2 surface. $\hat{B}_r(r_2)$ can be deduced from measurements of $\hat{B}_\theta$ outside the plasma: $\hat{B}_r(r_2)\approx\hat{B}_\theta(r_{coil})(r_{coil}/r_2)^2$. From the amplitude of the m=2 mode S_2=47 Ts^{-1} (Fig. 2) and the frequency f =4.7kHz at t=142 ms it follows that $\hat{B}_\theta(r_{coil})=1.5\times10^{-3}$T. To determine r_2,

the q-profile is approximated by a parabola, which is fixed by q(a) and the sawtooth inversion radius (r_{inv}=6cm, as deduced from T_e-sawteeth): $q = 0.73 + 2.06\,(r/a)^2$. This procedure leads to r_2=13 cm and w=6.1 cm. The corresponding incremental current in the O-point is $\delta I \approx 1.1$kA, running anti-parallel to I_p.

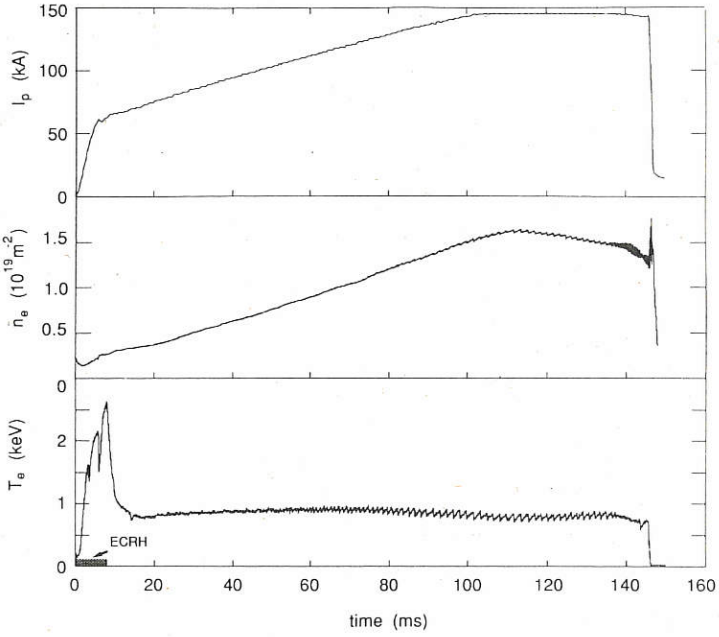

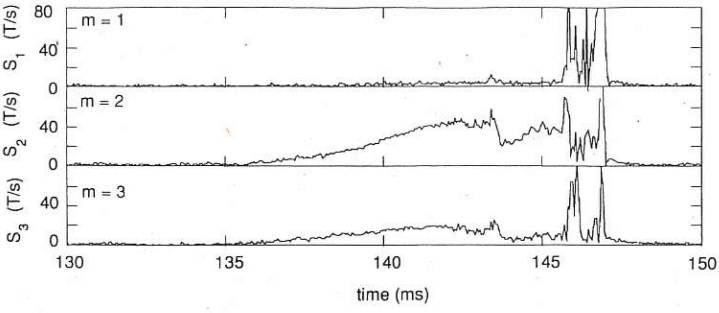

Figure 1. Evolution of plasma current, line integrated density and central electron temperature.
Figure 2. Evolution of the mode activity (magnetic measurements) in the disruptive phase.

Temperature measurements

Fig.3a shows $T_e(R)$ at the minimum and maximum of an oscillation, fig.3b shows T(R,t) in a contour plot. The oscillations in the region $0.60<R<0.64$ m are in phase with the oscillations at $0.80<R<0.88$ m and are attributed to the m/n=2/1 mode. The oscillations in the regions $0.64<R<0.70$ m and $0.74<R<0.80$ have opposite phase and are associated with the m=n=1 mode. All modes have the same frequency, indicating that they are coupled and have the same toroidal mode number (n=1), assuming toroidal rotation. The modes are coupled in such a way that the O-point of the m=1 mode locks to the X-point at the high field side of the m=2 mode.

Density measurements

To interpret the oscillations of the interferometer signals, line integrated signals were simulated with an m=2 mode structure, Gaussian in the radial and poloidal directions. The amplitude, the radial position, and the radial and poloidal width are determined from a fit to the measured data, yielding: r=13.5 cm, radial full width at 1/e: 6 cm. This agrees well with the position and size of the island as deduced from the magnetic measurements. The amplitude $(n_{max}-n_{min})/2 = 0.67$ 10^{19} m^{-3}, which is 30% of the local time-averaged density.

Phase relation of the B, n, and T oscillations

After correction for the different toroidal locations of the diagnostics, it is found that the B_θ , T_e and n_e oscillations are all nearly in phase. Since s>0, the island O-point corresponds to a minimum in $B_\theta(r_{coil})$. Hence, the observations show that the m=2 O-point is a relatively cold region with low density. There is a phase difference ($\approx 50°$) between the T_e and n_e oscillations. This could be due to a non-zero poloidal rotation: $\omega_\theta/\omega_\phi = 0.2$ would be sufficient to explain it.

Profiles

Assuming the classical magnetic island structure, with magnetic surfaces forming closed, nested tubes within the island, an in-out symmetry is expected for p_e, and for T_e because of the good thermal conduction along the field lines. In our experiment, neither T_e nor n_e show such a feature: see contour plot. With w=6cm, the island covers 3 channels of the T_e diagnostic, so that a local flattening of the profile should be observable. The typical shape of flux surfaces of an island is sketched in the T_e-contour plot (Fig 3b). This shows that only for $T_e \geq 250$eV the T_e-contours may follow the flux-surfaces. At lower T_e the T_e-contours cross the flux contours at increasingly large angle. For n_e the situation is similar.

Discussion and Conclusions

From the above observations we conclude that flux surfaces may be isothermals and isobars down to $T_e \approx 250$ eV, below which temperature increasing gradients of T_e and p_e are maintained on a flux surface. The absence of a flattening of the T_e-profile across large m=2 islands was also reported in JET [2]. In m=1 islands in JET, however, a local minimum in T_e could be demonstrated [3]. A possible explanation could be the reduction of the transport over the island flux surfaces because of a very large local q^* value (which then needs to be $O(10^2)$, with vanishingly small shear), in combination with the high collision frequency in the low T_e plasma. To make this explanation work, an anomalous collision frequency is required which exceeds the classical value by two to three orders of magnitude. This also produces a cross-field diffusivity close to the experimental value, but predicts a far too large resistivity. An alternative possibility is that the observed m=2 magnetic perturbation is not a magnetic island, but a m=2 helical deformation (kink) of the plasma.

Acknowledgements

This work was performed with financial support from NWO and Euratom.

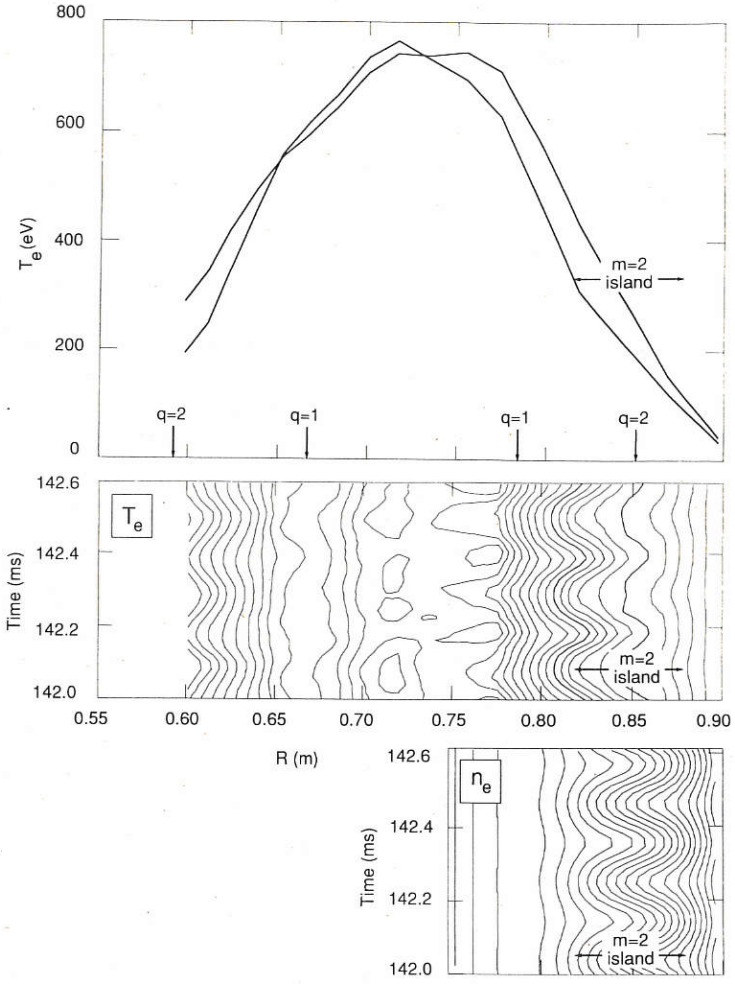

Figure 3a. The electron temperature at the minimum and maximum of the m=2 oscillation (ECE-data)
Figure 3b. Contour plots of the electron temperature and density during the strong m=2 mode activity. The position of the m=2 magnetic island, as deduced from the magnetic measurements, is indicated.

References

[1] J.A. Wesson, Tokamaks, Clarendon Press, Oxford (1987)
[2] J.A. Wesson et al., Disruptions in JET, Nucl. Fusion **29** (1989) 641
[3] E.Westerhof, P.Smeulders and N.J. Lopes Cardozo, Nucl. Fusion **29** (1989) 1056

PROFILE CONSISTENCY ON FTU

P. Buratti, M. Zerbini, G. Bracco, S.E. Segre*, V. Zanza.
Associazione EURATOM-ENEA sulla Fusione Centro Ricerche Energia Frascati,
C.P.65 - 00044 Frascati (Rome), Italy

1 - Introduction

The analysis of several tokamak experiments /1,2/ has revealed that the electron temperature profile shape is not influenced by plasma parameters such as current, density and magnetic field, excepting a dependence on the edge safety factor q_a for $r/a<0.6$. Both this dependence and the law governing the peaking factor, i.e. $T(0)/\langle T\rangle \approx q_a$, can be explained as effects of the sawtooth instability that keeps the central q close to one.

In this paper we present the first observations on the shape of the electron temperature profile on FTU tokamak (major radius 0.935 m; limiter radius 0.3 m; magnetic field $B \leq 8$ t).

2 - Database Description

Electron temperature profiles have been obtained from second harmonic electron cyclotron emission as measured by Fourier transform spectroscopy. The plasma is viewed along a major radius on the equatorial plane; spatial resolution is better than 3 cm both in this direction and in the transverse one. Averaging on many profiles makes detector noise and signal fluctuations negligible excepting the edge region. Systematic errors could arise from inaccuracies in the spectral calibration but selection of data at fixed magnetic field makes them ininfluent. Profile distortions due to finite optical thickness (τ) at low temperature and density are avoided by restricting the analysis to regions with $\tau > 1.5$.

Stationary periods have been selected in FTU discharges, requiring for plasma current and density variation times much larger than the resistive diffusion time; plasma horizontal position has been required to be constant within 1 cm and the maximum allowed vertical displacement was 3 cm. Only stationary intervals longer than 0.1 s have been considered. Temperature profiles have been precompressed by averaging within each stationary interval; data with suprathermal signatures (bursts in raw signal or profiles with a bump at the outer edge) have been discarded and only intervals with more than 10 valid profiles have been considered. Selecting data with $B=5.8\pm0.1$ t we obtained 415 compressed profiles, originated from 28855 raw profiles. The explored plasma current range was 301÷771 kA; the range for line average density n_e was $1.6\div21.6\times10^{19}$ m^{-3}. The database only includes ohmic discharges with poloidal limiter; a few ones with low current, low n_e are sawtooth free.

3 - Profile Shape Analysis

Measured temperature profiles (Fig. 1) are monothonic from the center to the edge and symmetric about the center. Three regions can be clearly distinguished: 1) a central region, in which the profile is flat or convex; 2) an intermediate region, with mostly concave profile and large gradient; 3) a cold external region. In some cases, only the second region is present, i.e. the profiles are almost triangular; this is typical of non-sawtoothing discharges. The size of the third region is practically negligible for almost all the data, but the exceptions (detached plasmas) are important.

The central flattening can be attributed to sawtooth; if we define the flat region as the one in which $T(r)/T(0) \geq 0.95$, we find for the radius r_f of this region that $r_f/a \approx 1/q_a$, where a is the radius of the last closed magnetic surface within the limiter and qa is the safety factor.

For a quantitative study of profile shape, we consider the quantity $S_T = aT'/T$, i.e. the inverse fall-off length normalized to plasma radius, rather than the normalized temperature itself, so that the results do not depend on the choice of an arbitrary normalization point.

At r/a=0.2, S_T increases with q_a (fig. 2a); this is simply a consequence of the variation of r_f with q_a. At low q_a, S_T does not depend on n_e, while at high q_a it decreases for increasing n_e.

At r/a=0.45, S_T is independent from n_e at low q_a, while at high q_a it strongly increases with n_e (fig. 2b). Larger values of r/a are not considered since some profiles could be distorted by finite τ effects.

A closer inspection to data with large S_T revealed that these originate from detached profiles; we then repeated the analysis replacing the nominal plasma radius, a, with the hot plasma radius a_h. The definition of such radius is rather arbitrary, but we verified that different reasonable choices do not change much the results. The definition $T(a_h)=0.2T(0)$ has been adopted to avoid finite τ effects.

Assuming that all the current flows within a_h, we can define an effective safety factor q_h; for low current detached discharges, q_h takes the same values as for high

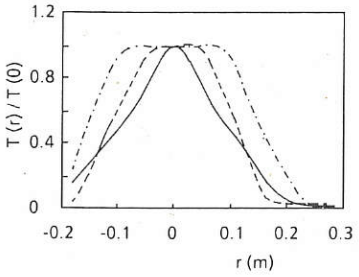

Fig: 1: Electron temperature profiles at low current, without sawteeth (solid line); low current, detached (dashed); high current (dotted-dashed).

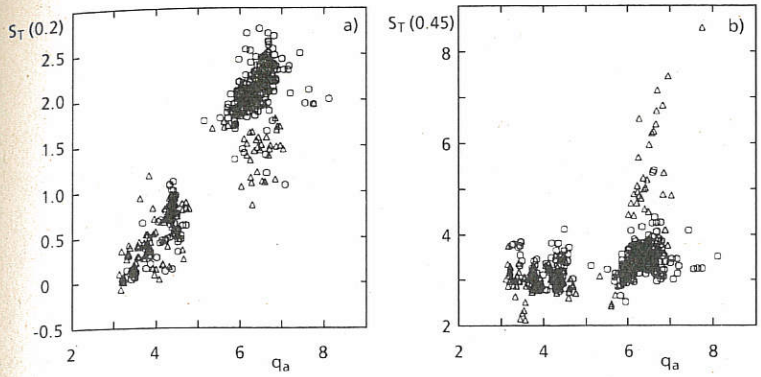

Fig 2: a) variation of $S_T(0.2)$ with q_a for $n_e < 7\times10^{19}$ m^{-3} (circles) and for $n_e > 7\times10^{19}$ m^{-3} (triangles). b) The same for $S_T(0.45)$.

current discharges; inspection of $T(r/a_h)/T(0)$ shows that profiles with currents differing by a factor two, but with the same q_h, can be superimposed very well.

Profiles are free from finite τ effects up to $r/a_h=1$. At $r/a_h \leq 0.5$, we find that $S_h=a_hT'/T$ increases with q_h; this is nicely consistent with the fact that r_f ranges up to 0.5 a_h.

For $r/a_h \geq 0.6$ (to be compared with $r/a=0.45$), the spread in S_h is much smaller than the one found for S_T at $r/a=0.45$, and detached discharges can no longer be distinguished. The residual spread can be ascribed to mild dependence on plasma parameters; regression analysis at $r/a_h=0.7$ gives $S_h \propto q_h^{-0.99} n_e^{-0.13}$.

4 - Explanation of Detachment

The reduction of the equivalent minor radius of the plasma, occurring in many low current FTU discharges, may be explained in terms of the constraint imposed by the poloidal Ohm's law to the plasma profiles /3/. Using the notation of /3/ we can write

$$dp/dr = -[EB_p(1+q^2\varepsilon^{-3/2}K) + v_r B_t^2(1+\varepsilon^{1/2}K)]/[2\eta(1+q^2+q^2\varepsilon^{-3/2}K/2)] \quad (1)$$

$$(1/\mu_o r)[d(rB_p)/dr] = (E/\eta) + [B_p v_r(1+2q^2+q^2\varepsilon^{-3/2}K)]/[2\eta(1+q^2+q^2\varepsilon^{-3/2}K/2)] \quad (2)$$

v_r is the radial plasma velocity which is given by:

$$v_r(r) = (1/n_e r)\int_0^r r' S(r')\,dr' \quad (3)$$

where $S(r)$, given by $S(r)=S_{ion}(r)+S_{rec}(r)$ is the particle source strength. S_{ion} is the source strength due to ionization of neutral atoms. This term is proportional to the neutral atom density, n_a, and is dominant when $S(r)$ is significant. S_{rec} represents the

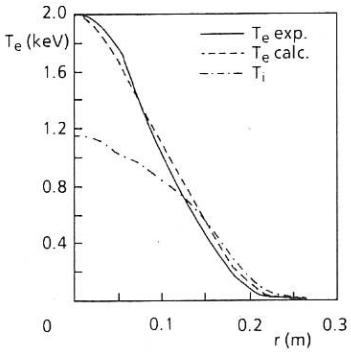

Fig 3: Comparison of the electron temperature profile obtained from the integration of eqs. (1) and (2) with the experimental one.

contribution due to ion-electron recombination which is proportional to the product $n_e n_i$.

If n_a is determined by the analysis of neutral particle emission measurements as described in /3/, v_r can be calculated by eq. (3). Using the experimental density profile eqs. (1) and (2) can be integrated, starting from the experimental value of $T_e(0)$. The ion temperature profile, required to integrate eqs (1) and (2), can be, self consistently, calculated by the ion energy balance using the neoclassical thermal conductivity.

The electron temperature profile obtained from the integration, for a 350 kA FTU discharge, is shown in Fig. 3 compared with the experimental one. In this case the effective radius is as low as 15 cm, that is about half the nominal radius.

5 - Conclusions

The shape of electron temperature profiles on FTU shows, besides the usual q_a dependence in the plasma core, a strong dependence on density.

The hot plasma radius a_h can be significantly smaller than the nominal one (detachment); normalizing the radial coordinate to a_h, the dependence on density disappears.

Plasma detachment may be explained in terms of the profile constraint imposed by the poloidal Ohm's law.

Footnote and References

* Dip. di Fisica, Università degli Studi di Roma II, Tor Vergata (Rome) Italy

/1/ E. D.Fredrickson, et al. Nucl. Fusion **27**, 1897 (1987)
/2/ P. J. Mc Carthy, et al. Nucl Fusion **31**, 1595 (1991)
/3/ S.E. Segre and V. Zanza, Nucl. Fusion **31**, 819 (1991)

Theory-Based Transport Simulation of Tokamaks: Density Scaling

E-S. Ghanem, Jon Kinsey, and Clifford Singer
Department of Nuclear Engineering
University of Illinois at Urbana-Champaign, U.S.A.

Glenn Bateman, Princeton Plasma Physics Laboratory

There has been a sizeable amount of work in the past few years using theoretically based flux-surface-average transport models to simulate various types of experimental tokamak data. Here we report two such studies, concentrating on the response of the plasma to variation of the line averaged electron density. The first study reported here uses a transport model described by Ghanem et al. [1] to examine the response of global energy confinement time in ohmically heated discharges. The second study reported here uses a closely related and more recent transport model described by Bateman [2] to examine the response of temperature profiles to changes in line-average density in neutral-beam-heated discharges. Work on developing a common theoretical model for these and other scaling experiments is in progress [3].

1 Density Scaling in Ohmic Plasmas

In applying the model of Ghanem et al. [1, 4] to scaling of global energy confinement in ohmic discharges, our primary interest was the relative importance of resistive ballooning and ion temperature gradient effects. The total anomalous flux-surface-averaged radial energy flux in this work was a sum of drift/η_i effects of the form

$$Q^{DR} = -0.75 n f_\beta \left[f_{te} \frac{\partial (T_e + T_i)}{\partial r} + \left(f_i \frac{\partial T_i}{\partial r} - \frac{3}{5} f_{te} \frac{\partial T_e}{\partial r} \right) f_{ith} \right] \hat{D}^{DR} \quad (1)$$

and resistive ballooning effects of the form $Q^{RB} = -\Lambda_S^2 \chi_e^{res.ball} n \partial T_e / \partial r$. Here the ion temperature gradient threshold function, $f_{ith} = \{1+\exp[-4(\eta_i - \eta_i^{th})]\}^{-1}$, changes rapidly from zero towards unity as the logarithmic derivative of the ion temperature, $\eta_i = L_n / L_{T_i} = \partial \ln T_i / \partial \ln n$, exceeds a prescribed value of η_i^{th}. The remaining parameters in these formulas not described below are given by

Ghanem et al. [1, 4]. The methodology of the present study is to vary the value of η_i^{th} from zero (beyond the theoretically expected η_i effect) through unity (approximately the theoretically expected η_i effect) to infinity (no η_i effect). We then see whether or not the saturation of global energy confinement time with increasing line average density disappears as f_{ith} is made to disappear. The results we show will be for discharge parameters typical of the ASDEX experiment, where we expect neoclassical effects to play relatively little role.

The demonstrable contribution of large η_i effects in this model to saturation of energy confinement with increasing density may be connected to the different multipliers of the basic diffusivity, $D^{DR} = \omega_e^*/(0.3\rho_s)^2$, where $\omega_e^* = 0.3c_s/L_n$, $\rho_s = c_s/\omega_{ci}$, $c_s = [k_b T_e/(m_i)]^{1/2}$, $L_n = -n/(\partial n/\partial r)$, k_b is Boltzman's constant, T_e is the electron temperature, m_i is the ion mass, and r is the midplane halfwidth of a flux surface. These multipliers are $f_{te} = \epsilon^{1/2} min(1, 0.1/\nu_e^*)$ for drift waves, and

$$f_i = \left(\frac{2T_i}{T_e} \frac{L_n}{L_{T_i}} \frac{L_n}{R_0} \right)^{1/2} \tag{2}$$

for η_i effects (where ν_e^* is the electron collisionality and $R_0 = r/\epsilon$ is the major radius [4]). Within much of the plasma, the density scale length factor, L_n, in f_i increases with increasing line-average density for two reasons. First, we impose an experimentally calibrated increase in density near the plasma boundary density with increasing line-average density [5]. Second, we include a Monte-Carlo model of neutral gas fuelling, with feedback as in the experimental operations to match a line average density evolution scaled up or down proportionally from detailed information for a reference discharge. Together with neoclassical particle fluxes and an anomalous particle flux of the form $\Gamma^{DR} = -0.3 f_\beta [1 - f_{ith}/(1 + \nu_e^*)] f_{te} D^{DR} (\partial n/\partial r)$, this gives flatter density profiles as the line-average density increases. (Here the curvature stabilization coefficient f_β is near unity, and a leading coefficient in the drift model has been independently adjusted empirically to match a sizeable set of profile and confinement data [4].)

The increasing contribution of resistive ballooning energy fluxes with increasing plasma density in the present study results from the well-known "unfavorable" scaling of energy transport with increasing pressure, as documented in detail elsewhere [1, 4, 3]. The question of interest here is whether saturation of energy confinement with increasing line-average density in ohmic plasma is due solely to finite η_i effects in the model used, or whether resistive ballooning effects also play role. The answer to this question is shown in Fig. 1. This figure shows the results of varying the η_i threshold and the line average density using full time-dependent simulations based on a well-documented ASDEX tokamak reference discharge. It can be seen that saturation of global energy confinement with increasing line-average density occurs even in the absence of η_i effects (i.e. with $\eta_i^{th} = \infty$), up to the maximum densities obtained experimentally ($\overline{n} = 6 \times 10^{19} \mathrm{m}^{-3}$). However, a good match to data from similar

experiments is best obtained with η_i^{th} between 1 and 2. We conclude that η_i effects only partly determine saturation of global energy confinement with line average density for the ohmically heated plasma simulated, in the context of the present model when $\eta_i^{th} \sim 1$.

2 TFTR L-mode Density Scaling

This section will describe simulations of an L-mode density scan carried out on TFTR in which both the density and the power were increased together in order to hold the temperatures nearly constant. In this experiment, the line-averaged electron density and heating power were increased from 3.6×10^{19} m^{-3} and 7.44 MW in TFTR shot 62270 to 5.5×10^{19} m^{-3} and 14.8 MW in TFTR shot 62248. All other conditions were held fixed ($R = 2.45$ m, $a = 0.80$ m, $I = 1.78$ MA, $B = 4.77$ T, and $Z_{\rm eff} \sim 1.9$ to 2.0).

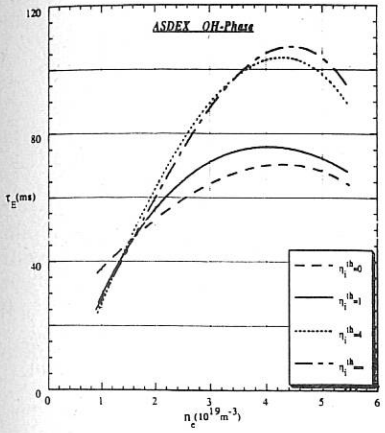

Fig. 1. Energy confinement time versus n_e for different values of η_i^{th} in ASDEX Ohmic Heating phase as predicted by the model.

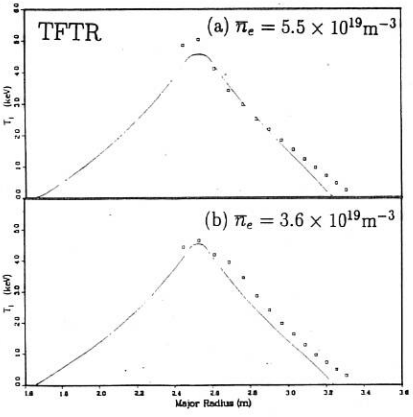

Fig. 2. Simulated (curve) and experimental (points) T_i for TFTR shots (a) 62248 and (b) 62270.

Max-Planck-Institut für Plasmaphysik
8046 Garching bei München

The simulation model used in this section is nearly the same as that described in Ref. 2 by Bateman. The latest version of this model used here computes the impurity radiation using a nonequilibrium coronal model (following each ionization state of the carbon impurity as it moves around) and computes the density profiles using theory-based diffusivity models.

Figure 2 shows the ion temperature profiles as a function of major radius from the simulations (solid curves) and the experimental data points. The temperature profiles do not change appreciably even though the density and density gradient scale length increased by factors of 1.5 and 1.76 respectively. The thermal diffusivity remains nearly unchanged in these simulations because the thermal diffusivity over most of the plasma is dominated by the η_i mode which scales like $(\eta_i - \eta_i^{th})/L_n \simeq 1/L_T - 5/R$. Note $\eta_i^{th} = \max(1, 5L_n/R) = 5L_N/R$ in this model (see Ref. 2). The resistive ballooning mode is confined to a narrow region near the edge of the plasma and the trapped electron modes are smaller than the η_i mode in these simulations.

The full variety of plasma conditions available in tokamaks covers the range between the extremes just described. Thus, in the context of the present type of theory-based transport simulations, dependence of plasma transport on density should vary between dominance by drift/η_i effects to significant contribution from other mechanisms, depending on the plasma parameters available in various tokamaks.

Acknowledgments:

The TFTR experimental data was provided by Drs. P. C. Efthimion, S. D. Scott, E. J. Synakowski, B. C. Stratton, G. Taylor, D. K. Mansfield, and H. K. Park.

References

[1] E-S. Ghanem, C. E. Singer, G. Bateman, and D. Stotler, Nuclear Fusion **30** (1990) 1595.

[2] G. Bateman, Phys. Fluids **B4** (1992) 634.

[3] C. E. Singer and G. Bateman, "Predictive Tokamak Transport Simulations," University of Illinois Fusion Studies Laboratory Report FSL-333 (1991).

[4] E-S. Ghanem, "Theoretical Transport Model for Tokamaks," University of Illinois at Urbana-Champaign Department of Nuclear Engineering PhD Thesis (1991).

[5] C. E. Singer, G. Bateman, and D. D. Stotler, "Boundary Conditions for OH, L, and H-mode Simulations," Princeton University Plasma Physics Laboratory Rep. PPPL-2527 (1988).

ROLE OF ALFVEN-WAVE FILAMENTS IN TOKAMAK TRANSPORT

G.J. Morales and H. Ramachandran

Physics Department
University of California, Los Angeles
Los Angeles, CA 90024-1547 USA

I. Overview

A series of experiments (started in 1991) by R.J. Taylor strongly suggest that filamentary structures having radial dimensions on the order of the ion Larmor radius (comparable to the electron skin depth) play an important role in the CCT device, and possibly in major tokamaks. The present analytical study examines those properties of kinetic Alfven waves that result in filamentary behavior. The space-time evolution of filaments launched by a fixed exciter is investigated and the role of electron Landau damping is assessed. The picture that emerges is that energy transport may result from the damping of radially evanescent filaments without causing particle transport (a feature well documented in H-mode experiments). In a sense each magnetic field-line behaves as an in-situ Alfven-wave antenna and the problem of energy transport reduces to self-consistent RF heating. Ultimately, the heating source has its origin in the non-thermal equilibrium nature of the electron distribution function.

II. Properties of Filaments

A useful background to this topic is the analytical study by Shoucri, et al.[1], concerning the generation of Alfven waves by thermal modulation of the electrical conductivity and also the toroidal experiments by Borg, et al.[2], using small antennas. Essentially, it is found that collimated radiation of shear waves results from cross-field excitation in the range of frequencies $\omega \sim 0.1\ \Omega_i$; the energy carried-out by the fast mode being less than 10%. Accordingly, the phenomenon can be well described by neglecting the off-diagonal components in the dielectric tensor.

The simplest space-time evolution of the filaments is obtained in slab geometry in the cold plasma limit, described by

$$\left[\partial_z^2 - \frac{1}{v^2(k_\perp)}\,\partial_t^2\right] \tilde{E}_x\,(k_\perp,\, z,\, t) = 0 \qquad ,$$

where z is the direction along the confining magnetic field (and x perpendicular). $v = v_A\,(1 + (k_\perp/k_s)^2]^{-1/2}$ is the speed at wavenumber $k_\perp$ with v_A the cold Alfven speed and k_s^{-1} the skin depth. The kinetic ion response is introduced by setting

$$v_A^2 = (\Omega_i c/\omega_{pi})^2 \; be^b/2I_1(b)$$

with $b = (k_\perp \rho_i)^2$.

Figure 1 illustrates the characteristic space-time evolution of a filament. It consists of a collimated core of extent ρ_i surrounded by cones of spreading radiation. When hot ion effects are included the sources having $\omega/k_\parallel < v_A$ contribute to the collimated part, while those having $\omega/k_\parallel > v_A$ result in the spreading radiation. Figure 2 illustrates how an initial perturbation evolves in a periodic system. After several transits along the confining magnetic field, one observes a core filament embedded in continuum shear waves. Sources whose radial correlation length is less than ρ_i retain their shape, while larger radial correlations lead to radiation.

The excitation of a cylindrical filament in a collisionless plasma by a current source $\tilde{j}_\parallel (k_\parallel, \omega)$ is described by

$$[1 - (k_\parallel/k_A)^2]^{-1} \left[\partial_r^2 + \frac{1}{r}\partial_r\right] \tilde{E}_\parallel - k_s^2 \xi^2 Z'(\xi)\, \tilde{E}_\parallel = -\frac{4\pi}{c^2} i\omega \tilde{j}_\parallel \quad ,$$

with $k_A = \omega/v_A$, $\xi = v_\parallel/\sqrt{2}\,\bar{v}_e$, and Z the plasma dispersion function. Using this equation, the effective radiation resistance experienced by a field-aligned current fluctuation (having velocity $v_\parallel$) due to collisionless excitation of a filament is found to be

$$R_{eff} = \frac{\pi}{2}\left[1 - (v_A/v_\parallel)^2\right] \tan^{-1}\,(\mathrm{Im}Z'/\mathrm{Re}Z') \quad .$$

For a collisional plasma the effective resistance of a radially correlated layer of skin-depth size is on the order of the Spitzer resistance. Hence, the magnitude of the current fluctuations required to maintain a thermal steady-state must be on the order of the Ohmic current. In this steady-state the energy is transported radially by overlapping evanescent filaments.

II. Filament Maintenance

Presently a self-consistent description of the maintenance of Alfven-wave filaments in a tokamak is not available. We conjecture that in reality the electron distribution function is not a local Maxwellian, but rather it exhibits finite amplitude fluctuations in velocity space about a mean value which coarse diagnostics tend to sample as a "thermal equilibrium". We envision that the fluctuations δf are relatively short-lived and exhibit spatial structure; they are elongated along the magnetic field and are short across, typically on the order of the skin-depth or ρ_i. A picture of filament maintenance may be as follows.

Field-aligned currents $\tilde{j}_{\parallel}$ having perpendicular scale length ρ_e transfer energy to an existing filament. In this manner a larger correlation length develops, i.e., on the filament scale ρ_i. This momentary correlation acts as a transverse in-situ antenna that radiates a collimated wave along $\underline{B}$. The Landau damping of this collimated wave distorts the electron distribution in the form of a streaming perturbation. The evolution of this perturbation in turn becomes δf and results in $\tilde{j}_{\parallel}$, and the process repeats. Ultimately, the magnitude of δf is related to the external non-equilibrium constraints that define the macroscopic behavior of a tokamak, namely the major and minor radii, R and a, the external power input P_{ext} and particle fueling. Basic experiments that relate the dependence of filamentary structures to these parameters may shed significant insight on the process of energy transport in tokamak devices.

Acknowledgment:

This work is sponsored by the U.S. Department of Energy. The underlying principles are the outgrowth of discussions with R.J. Taylor.

References:

1. M.M. Shoucri, G.J. Morales, and J.E. Maggs, Phys. Fluids 28, 2458 (1985).

2. G.G. Borg, M.H. Brennan, R.C. Cross, L. Giannone, and I.J. Donnelly, Plasma Physics and Controlled Fusion, 27, 1125 (1985).

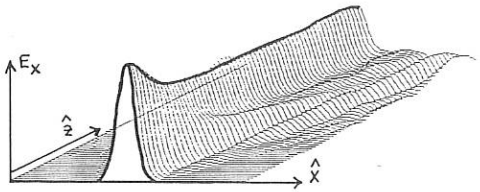

Figure 1. Time evolution of a launched pulse viewed in a frame moving at the Alfven speed ($z \rightarrow z + v_A t$). Initial width is ρ_i, $\rho_i = 2c/\omega_{pe}$.

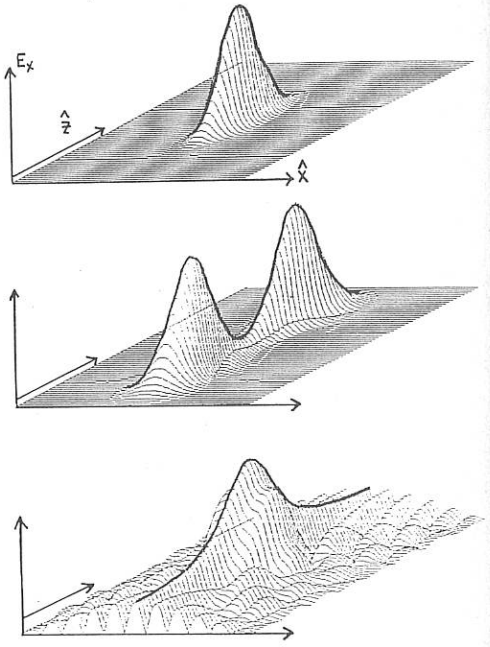

Figure 2. Space-time evolution of an initial perturbation shown on top panel. System is periodic along z and length displayed is 64 k_A^{-1}. Transverse dimension displayed is $18\rho_i$. Center panel shows pulse splitting after $\Omega_i t = 16$. Bottom panel ($\Omega_i t = 128$) has a core filament surrounded by shear waves.

ENERGY AND CURRENT TRANSPORT: SYMMETRY BREAKING AND DEGRADATION

B. Coppi [a] and **F. Pegoraro** [b]

[a] Massachusetts Institute of Technology, USA. [b] Università di Torino, Italy.

The anomalous transport of the electron thermal energy and that of the longitudinal current density are assumed to be interdependent and to be described by a common diffusion matrix equation. This transport matrix is taken to be symmetrical in the case where the applied electric field is responsible both for driving the current and heating the plasma. The transport coefficients that appear in the diffusion matrix are an electron thermal conductivity and a "thermo-viscous" coefficient that are of non-collisional origin. The latter coefficient describes the energy and current transport arising from the combined gradients of the electron temperature and current density. The energy transport related to this coefficient can take the form of a thermal energy inflow and provides an interpretation of the so called "heat pinch".

We interpret the degradation in the energy transport that occurs when externally injected heating is dominant over Ohmic heating in terms of the breaking of the symmetry of the transport matrix. This breaking leads to a change in the relationship between the electron temperature and the current density profiles, to a non-linear dependence of the electron heat flow on the temperature gradient, and to an enhancement of the effective thermal conductivity.

We assume that the electron temperature and the current density transport is described by a matrix equation [1-3] which, under steady state conditions, we write in the form

$$-\nabla\cdot\left[(\underline{D}^{T}+\underline{D}^{TJ})\cdot\nabla\begin{vmatrix}T\\J\end{vmatrix}\right]=\begin{vmatrix}S_1\\S_2\end{vmatrix}. \qquad (1)$$

The transport matrix $\underline{D}$ has been written as the sum of two positive definite symmetrical matrices, $\underline{D}^{T}$ and $\underline{D}^{TJ}$, $J\equiv J_{\parallel}(r)$ is the parallel current density, S_1 represents an effective entropy density production rate ($S_1>0$), S_2 is the difference between the electric field and the "resistive field", $S_2 = E - \eta J$, $E\equiv E_{\parallel}$ is the applied electric field and η is the appropriate collisional resistivity. In the limit where Ohmic heating is dominant, we write $\underline{D}^{T}$ and $\underline{D}^{TJ}$ in the form

$$\underline{D}^{T}=\frac{\kappa_e}{T}\begin{vmatrix}1&0\\0&0\end{vmatrix}, \qquad \underline{D}^{TJ}=L\begin{vmatrix}\alpha^2&-\alpha\\-\alpha&1\end{vmatrix}, \qquad (2)$$

where κ_e is the thermal conductivity, L is the thermo-viscous coefficient, $\alpha = c_0 J/T$, and c_0 is a numerical coefficient. Each of the two diffusion matrices is of rank one and describes a transport process that is one-dimensional in $(\nabla T,\nabla J)$ space; $\underline{D}^{T}$ describes the electron energy transport produced by the gradient of the electron temperature, while $\underline{D}^{TJ}$ describes the mixed

energy and current density transport produced by the gradients of the electron temperature and of the parallel current in the combination $-\alpha\nabla T+\nabla J$. The entropy source S_I can be written as

$$S_I = \frac{\eta J^2}{T} + \kappa_e \frac{(\nabla T)^2}{T^2} + \frac{L}{T}\left[\alpha^2(\nabla T)^2 - 2\alpha(\nabla T)(\nabla J) + (\nabla J)^2\right], \quad (3)$$

where the second and the third terms represent the irreversible entropy density production rate. If we take $c_o=3/2$, the thermo-viscous term in the entropy production rate vanishes when $J \propto T^{3/2}$. This is the case when the current density obeys Ohm's law in the standard form $E = \eta J$, with η the classical resistivity that does not include electron trapping effects, and the applied electric field E is uniform over the plasma cross section. The electron thermal energy balance equation is obtained by multiplying Eq.(1) times the vector |T,J|. Combining the resulting equation with the second component of Eq.(1) we obtain the following transport equations

$$EJ = -\nabla\cdot\left\{\kappa_e\nabla T - (c_o-1)LJ\left[\nabla J - c_o\frac{J}{T}\nabla T\right]\right\}, \quad (4)$$

$$E-\eta J = -\nabla\cdot\left\{L\left[\nabla J - c_o\frac{J}{T}\nabla T\right]\right\}. \quad (5)$$

If $\nabla J - c_o(J/T)\nabla T$ is negative, that is, if the temperature profile is sufficiently flatter than the current density profile, the thermo-viscous flux in the energy balance equation produces a thermal energy inflow [4]. The value of the electric field E is commonly found to be consistent with that predicted by the collisional (neoclassical) resistivity. Thus, we take E to be equal, on average, to the resistive field ηJ, i.e. we take $E = \langle\eta J\rangle$,where $\langle..\rangle$ denotes spatial average over the plasma cross section. This condition implies that the thermo-viscous flux vanishes at the plasma boundary. Then the thermo-viscous contribution to Ohm's law amounts simply to a current redistribution within the plasma column, while the thermal energy inflow vanishes at the plasma boundary and does not contribute directly to the the global electron energy confinement. We take the point of view that the thermo-viscous flux is caused by a class of microscopic processes that are different from those responsible for the electron energy flux described by κ_e. The processes that lead to the thermo-viscous flux can be stronger than those responsible for the energy diffusion coefficient without causing, in Ohmic discharges, a significant increase in the electron energy transport. In the energy balance the effect of the thermo-viscous coefficient is absorbed by the combination $\nabla J - (c_oJ/T)\nabla T$ which, as follows from the current equation, decreases if L is increased. Thus, in the presence of Ohmic heating only, the main effect on the thermo-viscous transport is to link the profiles of the electron energy and of the parallel current density.

The conditions that we have considered so far are those where the applied electric field E determines both the plasma heating and the plasma current density. When a form of externally injected heating is added, there is strong experimental evidence that the electron

energy confinement is degraded. This degradation does not originate necessarily from the excitation of new instabilities that are not present in the Ohmic regime, but can result from the loss of the symmetry of the mixed electron energy and current transport matrix $\underline{D}^{TJ}$. This loss of symmetry has the effect that the combination $\nabla J - c_0(J/T)\,\nabla T$ is no longer capable of "buffering" the influence of the thermo-viscous coefficient, leading to the appearance of an effective electron thermal conductivity that first adds to, and then effectively replaces κ_e, while acquiring a non-linear dependence on the electron temperature gradient. In order to identify the changes introduced by the externally injected heating, we refer again to Eq.(1). First we include the additional source term P_{inj}/T in the entropy density source term S_1, where P_{inj} is the injected power density; second, we assume that the expression (3) for the irreversible entropy density production rate, given by the quadratic forms in the temperature and current density gradients, is not modified. This implies that only an anti-symmetric matrix can be added to the transport matrix $\underline{D}$. Furthermore we assume that the symmetry breaking involves the link between the current density and the electron temperature only and rewrite $\underline{D}^{TJ}$ in the form

$$\underline{D}^{TJ} = L \begin{vmatrix} \alpha^2 & -\alpha(1+\delta) \\ -\alpha(1-\delta) & 1 \end{vmatrix}, \qquad (6)$$

where δ is a parameter that vanishes if the injected power is negligible. The modified matrix $\underline{D}^{TJ}$ has rank two, ($\det \underline{D}^{TJ} = (c_0 L J \delta/T)^2 > 0$), and thus no longer describes a transport process that is one-dimensional in $(\nabla T, \nabla J)$ space. This means that its effect is not limited to making the modified profile combination $\nabla J - c_0(1-\delta)(J/T)\,\nabla T$ small. Then we have

$$EJ + P_{inj} = -\nabla\cdot\left\{\left[\kappa_e + \frac{c_0^2 L J^2 \delta^2}{T}\right]\nabla T - [c_0(1+\delta)-1]LJ\left[\nabla J - c_0(1-\delta)\frac{J}{T}\nabla T\right]\right\}, \qquad (7)$$

$$E - \eta J = -\nabla\cdot\left\{L\left[\nabla J - c_0(1-\delta)\frac{J}{T}\nabla T\right]\right\}, \qquad (8)$$

where the electron energy transport equation has been written in such a way that, despite the asymmetry of the matrix $\underline{D}^{TJ}$, the thermo-viscous flux has the same form as in the current density equation and a new effective thermal conductivity $c_0^2 L J^2 \delta^2/T$ has appeared besides κ_e. This new thermal conductivity represents the degradation of the energy confinement caused by the loss of the symmetry of the transport equation, while the term in Eq.(7) that is proportional to the combination $\nabla J - c_0(1-\delta)(J/T)\nabla T$ describes a modified thermal energy inflow.

We write the electron thermal conductivity κ_e in the form that follows[5] from applying the "profile consistency" condition to Ohmically heated discharges

$$\kappa_e \approx \frac{E^*}{T}\frac{a^2}{4x}\int_0^x J(x')dx' \ , \qquad (9)$$

where dx' denotes integration over the plasma cross section, with x the normalised surface area variable [$x = (r/a)^2$ for a circular cross section of minor radius a]. In Eq.(9) E_* is a parameter with the dimensions of an electric field that, through the condition $E \approx E_*$ which is valid in Ohmically heated discharges, can be used to express the near invariance of the loop voltage observed in widely different toroidal devices. The value of E_* is determined [1,5] in terms of the characteristic parameters considered to be involved in the anomalous electron energy transport by inferring the value of the remaining free numerical coefficient from a fit of a set of Ohmically heated experiments where the electron thermal conductivity can be taken to be the prevalent form of energy loss. In the presence of injected heating, $E \neq E_*$ and κ_e, as given by Eq.(9), is determined up to a multiplicative function of E_*/E which reduces to unity in the case where Ohmic heating dominates. If we choose this function to be $(E_*/E)^\gamma$, the Ohmic thermal conductivity becomes nearly independent of the value of the central electron temperature when we take $\gamma = 2/3$. A possible form of the thermo-viscous coefficient L is obtained by identifying the effective thermal conductivity $c_0^2 L J^2 \delta^2/T$ brought about by the symmetry breaking with the anomalous thermal conductivity that applies to injected heating regimes given in Refs.[1,6,7]. This conductivity is considered to result from the combined excitation of the collisionless trapped electron mode, the so called "ubiquitous mode", in the main part of the plasma column and of collisional, impurity-driven modes at the periphery. If we take $c_0 = 3/2$, $\delta = [(E^* - E)/E^*]f$, and consider the limit where Ohmic heating is negligible, we have $E \ll E^*$ and $\delta \approx f$, where f, $f > 1/3$, is a function of the gradients that drive the modes producing L. We observe that Eq.(8) leads to J-profiles that are broader than the T-profiles, as numerical simulations[8] appear to require. The form of $LJ^2\delta^2/T$ must be chosen in such a way that it leads to the same class of temperature profiles regardless of the magnitude and the form of the energy deposition profile P_{inj}. We choose L to be independent of the temperature gradient and the function f to depend linearly on $d\ln T/d\ln x$, thus suggesting that the asymmetry of $\underline{D}^{TJ}$ is associated with the combined effects of the injected heating and of the electron temperature gradient.

References

[1] B.Coppi and F.Pegoraro, Phys Fluids **B3**, 2582, (1991). [2] B.Coppi, R.C.Englade, M.Nassi. L.E.Sugiyama and F.Pegoraro in "Plasma Physics and Controlled Nuclear Fusion Research 1990", (Publ. IAEA **2**, 337, 1991). [3] B.Coppi and F.Pegoraro, "International Topical Conference on New Ideas in Tokamak Confinement", La Jolla, California, (January 1992). [4] B.Coppi, Bull. Am. Phys. Soc. **30**, 1631 (1985). [5] B.Coppi and E.Mazzucato, Phys. Lett **71**, 337 (1979). [6] B.Coppi, Phys. Letters **128**, 193 (1988). [7] B.Coppi, Comm. Plasma Phys. Cont. Fusion, **12**, 319 (1989). [8] R.C.Englade, B.Coppi and F.Pegoraro, Bull. Am. Phys. Soc. **36**, 2414 (1991).

On Relaxation of Tokamak discharges with toroidal plasma rotation

G.N. Throumoulopoulos and G. Pantis
Dept. of Physics, University of Ioannina Ioannina 45110 Greece

Abstract

From the equilibrium solution of a toroidal plasma with toroidal velocity it is possible to define a relaxed energy state. This state corresponds to the minimum total energy at a given current and under certain assumptions retains the current and pressure profiles of the static case. For large toroidal radius it produces unique current and pressure profiles which however are completely different to those of the static case.

Equilibrium and stability of plasmas with toroidal flow have been studied extensively in the last years, both for cylindrical symmetric and axisymmetric configurations in ideal magnetohydrodynamics. Axisymmetric equilibria are described by the vectorial Mashke-Perrin [1] equation for the poloidal flux function

$$(\Delta^* \Psi + FF') \nabla\Psi + R^2 \nabla p - \varrho R^3 \omega^2 \nabla R = 0 \qquad (1)$$

where $\omega(\Psi)$ is the angular rotation frequency of each magnetic surface. We shall note here that eq. (1) is still valid for a resistive plasma if the toroidal field is much larger than the poloidal one. In this case the Ohm's law reads: $\vec{E} + \vec{V} \times \vec{B} = \eta \vec{J}_{\varphi}$, and one can show that while the toroidal velocity V_{φ} is redefined through the electric potential, the angular rotation frequency $\omega = V_{\varphi}/R$ still remains a surface quantity, just as it is for a plasma with infinite conductivity.

For plasmas with purely toroidal flow the heat conduction along the magnetic field is fast compared to the transport time scale and therefore the assumption that the temperature T is a surface function, $T=T((\psi)$, is a good approximation[2]. In this case eq. (1) can be reduced to the scalar equation[3]

$$\Delta^* \Psi + \left\{ FF' + R^2 \left[X' + X \frac{R^2}{2} \left(\frac{\omega^2}{\tilde{R}T} \right)' \right] \right\} \exp\left(\frac{R^2\omega^2}{2\tilde{R}T} \right) \qquad (2)$$

which contains the four arbitrary surfance quantities $F(\psi)$, $\omega(\psi)$, $T(\psi)$ and $x(\psi)$. The function $x(\psi)$ is releted to the plasma pressure P, $\left(X = P \exp\left[- \left(\frac{R^2\omega^2}{2\tilde{R}T} \right) \right] \right)$, and $\tilde{R}$ is the

proportionality constant in the ideal gass low $P = \tilde{R}T\varrho$. Several authors have considered solutions of eq. 2 both analytically and numerically, see for example ref. 3 and references cited there, and they have found that inertial flow forces disturb the static equilibrium formation so that the surfaces of constant pressure do not any more coincide with the magnetic surfaces.

In the theory of relaxation of magnetised plasmas[4] it has been shown that one can arrive at a relaxed state by minimising the magnetic energy subject to a constant magnetic helicity. This concept was developed further[5-7] to determine relaxed equilibria through nonideal MHD perturbations using the total current as a constant of motion. The idea is that one can determine the functional form of the current in a way such that if current and pressure are functions of Ψ only and retain their functional dependence on Ψ during evolution, arbitrary variations $\delta\Psi$ of the magnetic flux, which keep the total current constant, will also not change the energy, thus defining an extremal energy state.

In this work we shall apply this approach to a toroidal plasma with purely toroidal rotation and we shall show that despite the introduction of mass flow we can arrive, at a completely relaxed equilibrium through successive resistive equilibrium states. We shall start from the total energy of the system

$$W = \int_V \left(\frac{|B|^2}{2} + \frac{p}{\gamma - 1} + \frac{1}{2} \varrho V_\varphi^2 \right) d^3r$$

which now contains a term due to the toroidal velocity. The equilibrium defined in eq. (2) can relax fully if we minimise the energy by holding the total current constant

$$J = \frac{1}{2\pi} \int_V \left(\frac{FF'}{R^2} + f(p_T, \omega, T, R) \right) d^3r ,$$

with

$$f = \left[p'_T + p_T \frac{R^2}{2} g' \right] \exp w, \quad g(\psi) = \frac{\omega^2}{\tilde{R}T}, \quad w = \frac{R^2}{2} g$$

Using the method of Langrancian multipliers the variational principle gives:

$$2FF' + \frac{5}{2} R^2 \, P'_T \exp w + \frac{R^4}{2} (7/2 \, p_T g' + p'_T g) + \frac{R^6}{4} \, p_T g g' =$$

$$2\mu \left\{ \frac{\partial (FF')}{\partial \Psi} + R^2 p''_T \exp w + \frac{R^4}{2} (2 p'_T g' + p_T g'') + \frac{R^6}{4} p_T (g')^2 \right\} \qquad (3)$$

From eq. (3) the resulting four indentities:

$FF' = \mu FF'$, $\frac{5}{4} P'_T = \mu P''_T$, $\frac{7}{2} p_T g' + p'_T g = 2\mu (2p_T'g' + p_T g'')$ and $gg' = 2\mu(g')^2$

determine the functional form of the current, of the pressure and of the angular frequency i.e., $FF' = C_F \exp e^{\Psi/\mu}$, $p'_T = C_p \exp(\frac{5\Psi}{4\mu})$

and $g = C_\omega \exp(\psi/2\mu)$, giving for the minimum energy state the expression

$$\Delta^*\Psi = - C_F \exp(\Psi/\mu) - C_p R^2 e^{5\Psi/4\mu} (1 + \frac{C_\omega}{5} R^2 \exp(\Psi/2\mu))$$

$$\exp (C_\omega \frac{R^2}{2} \exp(\Psi/2\mu)) \qquad (4)$$

Equation (4) is a highly non-linear differential equation which can only be solved numerically. It reveals the influence of the mass-flow on the pressure profile while retaining the equilibrium conditions, the current profiles and the energy content reported in ref. (6) for the force-free state i.e., for $C_p = 0$. On the other hand it reduces to the minimum energy state of refs. (5-7) in the case of no mass flow (C_ω=0).

It is possible to get a rough idea of how the solution of eq.(4) could look like. From the expression of the angular frequency $\omega^2 = \tilde{R}TC_\omega \exp(\Psi/2\mu)$ one can see that for low angular velocities or very high temperatures we can reduce eq. (4) to

$$\Delta^*\Psi = - C_F e^{\Psi/\mu} - C_p R^2 e^{5\Psi/4\mu} - \frac{C_p C_\omega}{5} R^4 \exp(7\Psi/4\mu) \qquad (5)$$

which for values of β_p near unity, in example in the case of $C_F = 0$, it can be approximately investigated by considering two characteristic domains.i) Systems with small toroidal radius (R_o) i.e., R small and ii) systems with large toroidal values i.e., R large. In the first case the last term can be omited and approximate solutions of the resulting equation $\Delta^*\Psi = -C_p R^2 \exp(5\Psi/4\mu)$ can be found in the cylindrical approximation in the form $\Psi = \Psi_o - \frac{4}{5}\mu \ln(1+\alpha x^2)^2$, $\alpha = \frac{5}{4\mu}\frac{C_p}{8} a^2 \exp(\frac{5\Psi_o}{4\mu})$, $x = r/a$, $\Psi_o = \Psi(r=r_o=0)$. This solution is the same with the solution of ref. (7) in the large aspect ratio, thus retaining the pressure profiles and the energy content in this case. On the other hand if R is large then, one can assume that the last term dominates and the resulting equation

$\Delta^*\Psi = - \frac{C_p C_\omega}{5} R^4 \exp(7\Psi/4\mu)$ has, in the cylindrical approximation, the solution $\Psi = \Psi_o - \frac{4\mu}{7} \ln(1+\alpha x^4)^2$, $\alpha = \frac{C_\omega C_p}{5}\frac{7}{4\mu}\frac{a^4}{32} \exp(7\Psi_o/4\mu)$, $x = r/a$ which produces completely different pressure profiles even in this approximation.

This can be seen by the following arguments: for the current profile in the confinement region $r_o<r<a$ the above solution gives: $j = j_m \frac{(1+\alpha x_m^4)^2}{x_m^2} \frac{x^2}{(1+\alpha x^4)^2}$, where j_m is the peak current located at $x = x_m$. This shows that, in contrast to no-flow case, the current is zero at the center (r=0) and it has its peak at $x_m = (1/3\alpha)^{1/4}$ with the values of α restricted to $1/3 \leq \alpha < \infty$. In addition, for the peak to everage ($\bar{J} = \sqrt{j_m j_a}$, $j_a = j(r=a)$) current ratio we have $j_m/\bar{j} = \frac{x_m}{4}(1+\alpha)$ as against $(1+\alpha)$ in the no-flow case.

Similary for the pressure profile, if we define, with $p_o = p(r = 0)$ and $p_a = p(r =a)$, the pressures at the center and at the edge, we have:
$\frac{p-p_o}{p_a-p_o} = (1+\alpha)^2 x^2/(1+\alpha x^4)^2$. Also a complete different pressure profile still holding a kind of proportionality between p and j profiles which however is different from the one shown to exist in the static case. In fact if $p_o = 0$ then, the current and pressure profiles become identical i.e. $p/p_m = j/j_m$ and $p_m/\bar{p} = j_m/\bar{j} = (1 + \alpha)\frac{3x_m}{4}$

It is clear that we also have a complete different q - profile: $q/q_a = (1 + ax^4)/ (x^2 (1 + a))$ which is infinite at the center and it has its minimum at $x_1 = (1/a)^{1/4}$ showing, $J_m/\bar{J} = \frac{3}{2}(\alpha/3)^{1/4} q_a/q_1$, another kind of proportionality between the current (pressure) ratio of peak to average and the safety factor ratio of edge to the center.

In summary, a relaxed energy state can be derived for resistive equilibria with mass-flow and the functional dependences of pressure current and angular frequency have been determined. Within the limits of our approximation and under the assumption of very high temperatures unique pressure and current profiles have been determined. In systems with small toroidal radius these profiles are similar to those of the static case while in systems with large toroidal radius the profiles are completely different. Neither of these peaks at the center and they do hold a different proportionality than that of the static case.

REFERENCES

/1/ E.K. Maschke and M. Perrin Plasma Physics and Contr. Fusion 22, 578 (1980), Phys. Letts. A102, 106 (1989)
/2/ J. W. Connor, S. C. Cowley, R. J. Hastie and L.R. Pan, Plasma Phys. Contr. Fusion 29, 919 (1987)
/3/ G.N. Throumoulopoulos and G. Pantis Phys. fluids B1, 1827(1989)
/4/ J.B. Taylor, Rev Mod. Phys. 58, 741 (1986)
/5/ B.B. Kadomtsev, sov. J. Plasma Phys. 13(7), 443 (1987)
/6/ D. Biskamp, Comments plasma Phys. Controlled fusion 10, 165(1986)
/7/ J.Y. Hsu and M.S. Chu, Phys. fluids 30, 1221(1987)

PERTURBATIVE MEASUREMENT OF SUPRATHERMAL ELECTRON DIFFUSION IN JET

A.Gondhalekar, D.Bartlett, P.Lomas, R.Martin-Solis, and M.O'Brien[+]
JET Joint Undertaking, Abingdon, OX14 3EA, UK
[+]Culham Laboratory, AEA-EURATOM Association, Culham, UK.

Above a certain energy electrons in a tokamak plasma become collisionless and closely follow magnetic field lines, probing the field structure. Due to orbit averaging at very large energy, only electrons in the intermediate energy range, hundreds of keV, are useful for probing small scale magnetic stochasticity. Such electrons are produced in JET during Lower Hybrid Current Drive(LHCD) experiments, during which a broad steady state profile of suprathermal(st-) electron density $n_e^{ST}(r)$ with energy E_e^{ST}=50-300 keV is evidenced by hard X-ray bremsstrahlung measurements[1]. Experiments have been performed to determine the spatial diffusivity D_e^{ST} of these electrons using a perturbative method employed previously to measure electron and ion thermal, and electron density diffusivities in JET, using evolution of perturbations caused by injection of a small superficially penetrating D_2 pellet into the plasma[2,3]. During LHCD the pellet is very rapidly ablated by st-electrons and instantaneously depletes n_e^{ST} in the region $r \geq r_p$, where r_p is the pellet penetration radius. Cooling of the thermal plasma is not evident. D_e^{ST} is inferred from evolution of n_e^{ST} in region $r \leq r_p$.

OBSERVATIONS: Fig.1 shows the key data. A target plasma with I_ϕ=3MA and B_ϕ=2.8T was produced in limiter configuration. The steady state Ohmically heated deuterium plasma had $T_e(0)$=4keV and $\bar{n}_e = 1.45 \times 10^{19} m^{-3}$. Shown too are signals from channels of a fast sampling 12-channel grating polychromator, tuned to receive E-mode thermal second harmonic electron cyclotron emission (ECE) from different points in the plasma, showing thermal emission during OH, from which T_e is usually deduced. When LHCD is applied the ECE greatly increases at all frequencies due to growth of the st-electron population, notably at frequencies above and below second harmonic where the plasma is optically thin[4]. We attribute the increase at second harmonic frequencies during LHCD to down-shifted non-thermal third harmonic, with only a small increase in thermal emission. The ECE occurs at frequencies given by the resonance condition $\omega_m = m\Omega_c \cdot (1-\beta^2)^{1/2} \cdot (1-\beta_\parallel \cos\theta)^{-1}$, where m=1,2,3,...etc. m is the harmonic number, Ω_c is the non-relativistic electron cyclotron frequency, $\beta = v/c$, $\beta_\parallel = v_\parallel/c$, and $\theta = \pi/2$ in our experiments. The intensity

of ECE from st-electrons, besides being proportional to n_e^{ST}, is weighted by the higher energy electrons, the m=3 ECE varies as $\sim E_\perp^2$. Examination of the variation of EC harmonic frequencies and cutoffs in a tokamak magnetic field shows that the frequency of a higher harmonic (eg. m=3) ECE from st-electrons can be downshifted to that of thermal emission from a lower one (eg. m=2). As seen in fig.2 downshifted m=3 emission originating from radii smaller than that of the optically thick thermal m=2 emission is reabsorbed and only downshifted emission coming from electrons in front of the thermal m=2 layer, those with E≤255keV in our case, can be seen. Fig.2 shows where contributions to ECE seen in the twelve polychromator channels, comprising thermal m=2 and downshifted non-thermal m=3 ECE, originate. The computation uses the resonance condition for ECE and the magnetic field profile.

INTERPRETATION: In fig.1, at 7.6s a small pellet was injected into the plasma, penetrating to R_p= 3.8m, where R_p was determined as before[2,3]. The effect of pellet injection was to interrupt the LHCD and extinguish all st-electrons at $r \geq r_p$. When LHCD restarted 100ms later no st-electrons were produced at $r \leq r_p$, as evidenced by absence of recovery in the ECE signals in the polychromator channels. Thus evolution of $n_e^{ST}(r,t)$ subsequent to pellet injection was source free. Fig.1 shows evolution of the ECE after pellet injection in three channels with the following second harmonic resonance locations, one at $r > r_p$, one at r slightly less than r_p, and one at $r \ll r_p$. At $r \geq r_p$ transition to a new equilibrium was instantaneous while for channels at $r < r_p$ evolution was seen to be characteristically diffusive. Analysis of ECE evolution at $r < r_p$ was used to determine diffusion of n_e^{ST}.

When LHCD is terminated in the normal way, the non-thermal ECE decays, its evolution determined by spatial diffusion and slowing-down of st-electrons. The effect of injecting a pellet is to increase $\nabla n_e^{ST}(r=r_p)$, amplifying the diffusive flux and speeding the decay of n_e^{ST} while the slowing-down time in the region $r < r_p$ is unchanged. The observed increase in the rate of decay of non-thermal ECE from $r < r_p$ is a manifestation of spatial diffusion of n_e^{ST}. The low energy st-electrons make only a small contribution, since emission is strongly energy dependent. This is seen by examination of the signal in channels #11(fig.1); absence of a fast reduction in ECE signal following pellet injection indicates that in channel #11 electrons of E≤200 keV from $r > r_p$ contribute very little to the signal. Similarly for the other channels

not crossed by the pellet (efforts to simulate this behavior of the ECE by tailoring $n_e^{ST}(r)$ and its energy distribution have not yet been successful). We thus define an energy band $220 \leq E_e^{ST}(keV) \leq 255$ for electrons contributing most to the observed non-thermal ECE. This energy can be assumed to be constant, since the electron slowing down time at this energy is longer than the decay of the ECE signals. Then the position of the radiating electrons is fixed to a small range of radii, and the ECE is proportional to st-electron density n_e^{ST}, and evolution of downshifted m=3 ECE after pellet injection represents evolution of n_e^{ST}.

SIMULATION: St-electron density evolution is described by the continuity equation $dn_e^{ST}(r,t)/dt = -div\Gamma_e^{ST}(r,t) + S_e^{ST}(r,t)$. The flux is assumed diffusive and given by $\Gamma_e^{ST}(r,t) = -D_e^{ST}\nabla n_e^{ST}(r,t)$; $S_e^{ST}(r,t)$ is the source. Cylindrical geometry is used, with conditions $S_e^{ST}(r,t)=0$, $n_e^{ST}(r<r_p,0)=n_0$, $n_e^{ST}(r\geq r_p,0)=0$ and $n_e^{ST}(r=a,t)=0$. Slowing-down of st-electrons is neglected because it is much slower than the decay of the ECE signals. Fig.3 shows a comparison between the measured evolution of $n_e^{ST}(r,t)$ and simulation of it using the above model. The diffusivity D_e^{ST} is iterated until a best fit between simulation and measurement is obtained, taking E_e^{ST}=250keV. In the example shown the best value obtained was $D_e^{ST}=15 m^2/s$. Varying E_e^{ST} within the band mentioned above, gave $9 \leq D_e^{ST}(m^2/s) \leq 15$.

The continuity equation given above has an analytic solution of the form

$$n_e^{ST}(r,t)/n_0 = 2r_p/a^2 \sum [J_1(\alpha_i r_p) J_0(\alpha_i r)/\{\alpha_i J_1^2(\alpha_i a)\}] \exp(-D_e^{ST}\alpha_i^2 t)$$

where $J_0(\alpha_i a)=0$. When $t \gg 1/(D_e^{ST}\alpha_2^2)$, or when $r/a \ll r_p/a$, then the i=1 term is dominant and $n_e^{ST}(r,t)/n_0$ can be represented by a single exponential. Then the measured decay time τ_m is related to the diffusion time τ_D and slowing down time τ_{SD} thus $1/\tau_m = 1/\tau_D + 1/\tau_{SD}$. Here $\tau_D = 1/(D_e^{ST}\alpha_1^2)$ and $\tau_{SD} \cong 70ms$. Using this correction the diffusivity of st-electron density is $6 \leq D_e^{ST}(m^2/s) \leq 10$.

CONCLUSIONS: (i) For suprathermal electrons with $220 \leq E_e^{ST}(keV) \leq 255$ a radial density diffusivity, $6 \leq D_e^{ST}(m^2/s) \leq 10$ at $r/a \cong 0.5$ is inferred. Such a value for D_e^{ST} has been deduced for LHCD modulation experiments in TORE SUPRA [5]. (ii) The magnitude of D_e^{ST} above appears to be larger than D_e^{ST} deduced from steady state LH power balance. (iii) Analogous measurements of electron thermal and density diffusivity gave[2,3] $\chi_e \cong 3 m^2/s$ and $D_e \cong 0.4 m^2/s$ at $r/a \cong 0.5$. That $\chi_e \gg D_e$, and that suprathermal electrons diffuse more rapidly than

thermal ones, $D_e^{ST} \gg \chi_e$, both indicate that micromagnetic stochasticity may play an important role in anomalous electron thermal transport in JET.

References:

[1] P. Froissard, et al., Europhys. Conf. Abstracts, 15C(1991)III-389.

[2] A. Gondhalekar, et al., Plasma Phys. and Contr. Fusion, 31(1989)805.

[3] A. Cheetham, et al., Proceedings of IAEA Conference on Plasma Physics and Controlled Nuclear Fusion, Nice, France. 1(1989)483.

[4] G. Ramponi, et al., 1992, this conference.

[5] D. Moreau, 18th European Conference on Controlled Fusion and Plasma Physics, Berlin, Germany. June 3-7, 1991.

Figure 1

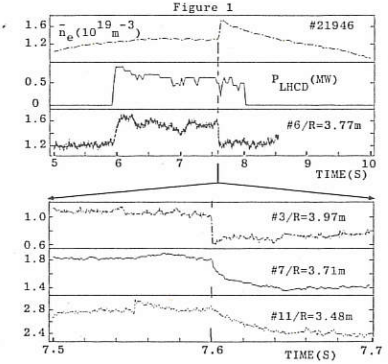

Figure 2

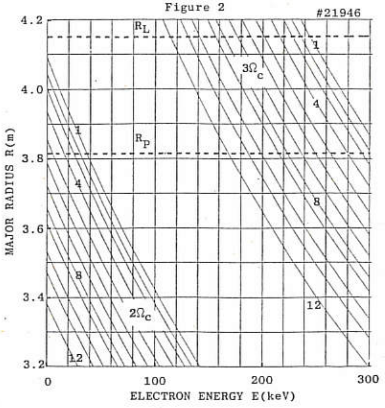

Figure 3

Pellet Penetration Radius $r_p/a = 0.78$

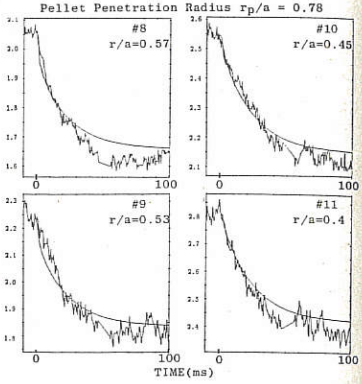

Fig. 1 Evolution of plasma density, LHCD, and ECE during measurement of st-electron density diffusivity.

Fig. 2 Plot of energy and location of electrons contributing thermal second harmonic and nonthermal third harmonic ECE in twelve measurement channels of the polychromator.

Fig. 3 Simulation of diffusivity of st-electrons of 250keV energy, with best match to measurement given by $D_e^{ST} = 15\ m^2/s$.

MEASUREMENTS OF MEV ENERGY ICRF DRIVEN MINORITY IONS IN JET

A.V.Khudoleev[+], V.I.Afanasyev[+], S.Corti, A.Gondhalekar,
A.C.Maas, and M.P.Petrov[+].

JET Joint Undertaking, Abingdon, OX14 3EA, United Kingdom
[+]A.F.Ioffe Physical-Technical Institute, St.Petersburg, Russia

Measurements have been made of flux and energy spectra of 0.5-2MeV hydrogen atoms, produced during H-minority ICRF heating in JET, using a high energy neutral particle analyzer(NPA)[1]. The ions, neutralized by charge-exchange and recombination processes, exit the plasma and reach the NPA installed at the top of the torus with its line of sight intercepting the plasma center at R=3.07m. The NPA has eight energy channels spanning $0.5 \leq E(MeV) \leq 3.5$, with common mass selection, enabling time resolved measurements of the flux and energy spectra of hydrogenic and helium atoms emitted by the plasma.

The beam line geometry determines that only atoms with $v_\phi/v_z \leq 7 \times 10^{-3}$ reach the NPA detectors. Moreover the birth point of the atoms has to be at the intersection of the NPA line of sight, the ICRF deposition region, and the banana tips of the parent H^+ ions. We infer from orbits computed using the above boundary conditions that the observed flux arises mainly from H^+ ions near the center of the plasma. A typical deuterium target plasma with parameters I_ϕ=3.6MA, B_ϕ=2.8T, $n_e(0)=2 \times 10^{19} m^{-3}$ and $T_e(0)$= 2keV was heated using fundamental frequency H-minority ICRF. The applied ICRF power, P_{ICRF}, was ramped to 10 MW in 1s, whereby electron density and temperature increase to $n_e(0)=4 \times 10^{19} m^{-3}$ and $T_e(0)$=6keV. Fig.1 shows evolution of the 'passive'[1] hydrogen flux $\Gamma_H(E)$ and its spectrum for different P_{ICRF}. The 'temperature' of the flux, defined as $T_{EXP}=-[\delta(ln\Gamma_H(E))/\delta E]^{-1}$, increases for data shown, from $T_{EXP} \cong 0.17$ MeV to a steady state value of $T_{EXP} \cong 0.44$ MeV. The saturation behavior of T_{EXP} may be an artifact of effective 'temperature' associated with the velocity dependence of the reaction rates for neutralization of the H^+ ions[1]. The two orders of magnitude increase at all energies in $\Gamma_H(E)$ can not be understood either as due to increase in the H-minority temperature at constant density, or due to influx of hydrogen into the plasma during the ICRF heating. The increase in Γ_H may again be an artifact related to the neutralization process! Details of the ion neutralization processes and influence of other plasma parameters on them is a subject of ongoing investigations.

Experiments were performed to measure the width of the ICRF resonance by sweeping it across the NPA line of sight. A target deuterium plasma with $I_\phi \cong 3$MA was heated with ICRF in the fundamental frequency H-minority mode at 42.6MHz. B_ϕ was increased from 2.3T to 3.4T in 12s, causing the position of peak of resonance, R_{RES}, to move through $2.6 \leq R_{RES}(m) \leq 3.69$. Evolution of heating and plasma parameters is shown in fig.2. Also shown is the count rate R_H for hydrogen flux measured by the NPA in the 0.97MeV channel. In fig.3 the normalized flux from two NPA channels, at 0.5MeV and 1.8MeV, is shown as a function of R_{RES}. We see that the full width at half maximum (FWHM) of the resonance is $\approx$0.17m, and nearly the same for the two extreme energy ions measured. Assuming that $T_\parallel \approx T_\perp/10$, which is usual for ICRF heating of deuterium plasma with low density H-minority[2], $T_\perp$=0.3MeV, and $k_\parallel = 7.5 m^{-1}$, which is appropriate for the dipole phasing employed in the experiments, the Doppler broadening of the resonance, $\Delta R = R_{RES} \mathbf{k}_\parallel \cdot \mathbf{v}_\parallel / \omega$, will give a FWHM of $2 \times \Delta R \cong 0.3$m. ΔR is the width of the resonance, R_{RES} the resonance position for $v_\parallel = 0$, $\mathbf{k}_\parallel$ the parallel component of the wave vector, $v_\parallel$ the parallel thermal velocity of the ions, and ω the ICRF frequency.

Experiments were performed to measure the effects of toroidal field ripple on confinement of high energy ions in JET. The ripple magnitude was changed by operating JET with 16 TF coils instead of the normal 32 TF coils, giving $\Delta B_\phi / B_\phi \cong 12.5\%$ for 16 coils and $\Delta B_\phi / B_\phi \leq 1\%$ for 32 coils, on the torus midplane at the outer limiter. High energy H^+ ions were produced by second harmonic H-minority ICRF heating of a target deuterium plasma with I_ϕ=2.5MA, $n_e(0) \cong 1.8 \times 10^{19} m^{-3}$, and $T_e(0) \cong 4$keV, with B_ϕ=1.4T. 3-5MW of ICRF power was applied and the frequency changed shot-by-shot from 42.6MHZ to 52MHz, thereby moving R_{RES} from 3.33m to 2.73m. Fig.4 shows the spectrum of 'passive' H^0 flux in the NPA, for $0.5 \leq E(MeV) \leq 1.8$, with 16 TF and 32 TF coil operation with R_{RES}= 3.33m. Under nearly similar heating and plasma conditions, the flux at the highest energy measured by the NPA, is reduced by a factor $\cong$35 in the 16 TF coil operation compared to that with 32 TF coils, for R_{RES}= 3.33m. Fig.5 shows Γ_H(32 coil)/Γ_H(16 coil), the ratio of fluxes for 32 and 16 coil operation, for different NPA energy channels, as the ICRF resonance position was scanned $2.73 \leq R_{RES}(m) \leq 3.33$. We see that when $R_{RES} \geq 3.1$m, the ratio of fluxes dramatically increases, indicating large ion losses which increase with ion energy, in the 16 coil operation. The point where these losses become large in 16 TF coil operation, $R_{RES} \geq 3.1$m, coincides with the

boundary of the ripple trapping region calculated for the topology of the toroidal field ripple prevailing in the experiment[3], shown in fig.6. Thus it seems that direct ripple related loss of high energy H^+ ions on the low field side of the tokamak takes place during 16 TF coil operation of JET.

In conclusion, the newly developed high energy NPA has been used to study different aspects of H-minority ICRF heating, and dynamics of high energy ions in JET. The measured FWHM of ICRF resonance is compared with expected Doppler broadening. In the toroidal field ripple experiments large direct high energy ion losses are observed in the 16 coil configuration.

The authors thank P.van Belle for help with the ion orbit computations, and D.Muir for ray tracing calculations of ICRF power deposition.

1. M.P.Petrov, et al., 1992, paper at this conference.
2. V.P.Bhatnager, et al., 1992, to be published.
3. S.Putvinskii, private communication.

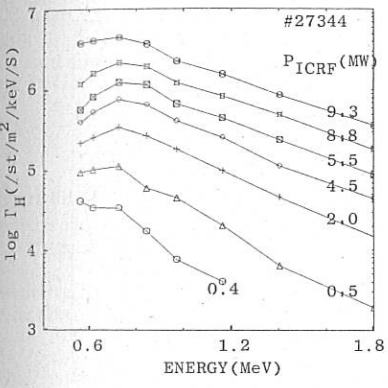

Fig.1 Evolution of 'passive' H^0 flux and its energy spectrum with level of applied ICRF power.

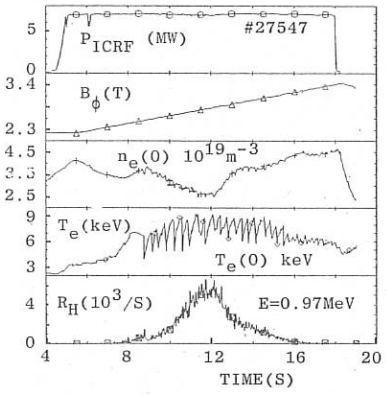

Fig.2 Evolution of heating and plasma parameters during toroidal field ramp experiments.

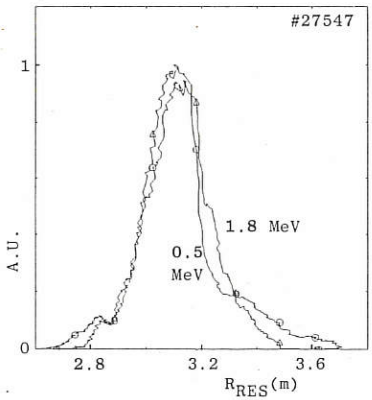

Fig.3 Normalized flux in two NPA channels, for 0.5MeV and 1.8MeV, plotted against R_{RES}.

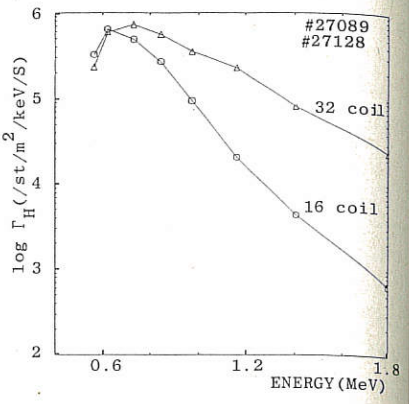

Fig.4 Comparison of spectra of H^0 flux for 32 TF coil and 16 TF coil operation of JET showing effect of increased ripple on energetic ions

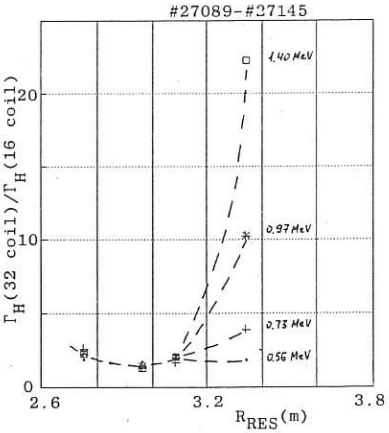

Fig.5 Ratio Γ_H(32coil)/Γ_H(16coil) for different energies as function of position of ICRF resonance.

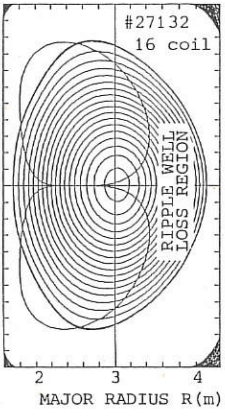

Fig.6 Contours of ripple well trapping and regions of enhanced fast ion loss due to TF ripple in the 16 TF coil configuration.

Observation of Relativistic Runaway Electrons by Synchrotron Radiation in TEXTOR

R. Jaspers[1], K.H. Finken[2], G. Mank[2], D. Rusbüldt[2], N.J. Lopes Cardozo[1], F.C. Schüller[1], J. Boedo[3], F. Hoenen[2]

[1]FOM Instituut voor Plasmafysica Rijnhuizen, Ass. Euratom-FOM, P.O. Box 1207, Nieuwegein, The Netherlands
[2]Institut für Plasmaphysik, Ass. Euratom-KFA, Forschungszentrum, 517 Jülich, Germany
[3]Institute for Plasma and Fusion Research, University of California at Los Angeles, USA

Introduction

Runaway electrons are a promising tool to study magnetic turbulence in a tokamak plasma. Recently, several studies have been devoted to this issue [1, 2]. In these studies hard X-rays, created when runaways hit the limiter, have been analysed. This paper also addresses the question of confinement of runaways. Here, however, not the runaways leaving the plasma are studied, but the runaways in the interior. They were diagnosed by means of the infrared synchrotron radiation which relativistic runaways (> 10 MeV) emit, as was shown by Finken et al. [3]. With this tool information can be obtained about runaway- confinement times, energy, birth-rate, dimensions of the runaway beam and perhaps about their energy distribution. In this paper at first a presentation of the measurements is given and the energy and pitch angle is deduced from the data. Then a comparison of the runaway confinement in low density plasmas ($n_e(0) < 0.8\ 10^{19}$ m^3) is made for three different conditions: normal ohmic discharge, discharge with a gas puff and one with neutral beam injection (NBI).

Experimental Set Up

Synchrotron radiation is emitted because electrons moving along the drift orbits experience an acceleration perpendicular to their path. In the relativistic limit the spectrum becomes continuous with a sharp fall off at the short wavelength limit. This radiation is predominantly emitted in forward direction with an opening angle of $\approx 1/\gamma$ (γ being the relativistic energy factor). The spectral intensity of synchrotron emission is given by the Schwinger equation [4]:

$$P^e_\lambda = \frac{4\pi}{\sqrt{3}} \frac{m_0 c^3 r_e}{\gamma^2 \lambda^3} \int_{\frac{4\pi R_{curv}}{3\lambda\gamma^3}}^{\infty} K_{(5/3)}(x)\, dx \qquad 1$$

where the average radius of curvature $R_{curv} = [(1 - \theta^2) / R + e B \theta / \gamma m c]^{-1}$
and the pitch angle $\theta = \arctan(V_\perp / V_{//}) \approx V_\perp / c$,
r_e = classical electron radius, $K_{(5/3)}$ = modified Bessel function.

With two I.R.scanners (Inframetrics, model 600) the plasma was observed tangentially in the direction of electron approach. Window and lens-material was CaF_2, having a long wavelength cutoff of approximately 9 µm. One scanner looked in the horizontal plane and was sensitive in the spectral range 3-14 µm. Because of a limited field of view only the high field side could be observed (r=[-15 cm,0 cm]). The other scanner detected the radiation under an oblique angle of approximately 12° with respect to the equator and had a spectral range from 3-6 µm.
Measurements were performed at TEXTOR (R_0=1.75 m, I_{pl}=350 kA, B_t=2.25 T, a=0.46 m). Time traces for several plasma parameters are given in fig.1 for the three conditions we investigated: 1.low-density deuterium discharges, to see the synchrotron radiation developing under normal conditions 2.same discharges but with a gas puff (deuterium) at t=3.0 s, to see the influence of higher densities on runaways 3.low-density deuterium discharges with 400 kW deuterium NBI from t=3.0 to t=3.4 s, to look for different loss mechanisms for runaways under additional heating.

Spectrum and Energy

To deduce the energy of the runaways from the synchrotron radiation some measurements were performed with 3 different filters in front of the I.R. scanner 1. These quartz filters transmit the I.R. up to a certain wavelength. They had different thicknesses and therefore different long wavelength cut-offs (≈3.5, 4, 4.5 μm resp.). The spectral information, obtained through comparison of the intensities for the different filter measurements, gives the maximum runaway energy to an accuracy of better then 4 MeV. The thermal contribution from the liner, transmission functions of optics and detector response were taken into account. The information was not sufficient to deduce the energy distribution *f(E)*. Therefore two extreme cases were analysed, the first being that of a mono-energetic distribution, the second being a constant energy distribution up to a maximum energy E_{max}. Whereas these distributions are substantially different only a difference of less then 20 % in E_{max} is found. In fig.2 is plotted the energy of the runaways as a function of time, together with the expectation from free-fall acceleration. Here a pitch angle of $\theta = 0.1$ (see next section) has been used.
During the first second of the discharge the energy obeys the free fall expectation quite well. After this it departs from this line and reaches a maximum energy of 35 MeV at about 2.5 s. Here-after there seems to be a tendency of decrease in energy. It should be remarked that this is in the current ramp down phase, where the loop voltage is decreased to approximately 0.4 V.
The feature that for high energies runaways do not obey the free fall acceleration has also been seen on other tokamaks, e.g TORE SUPRA, where the discrepancy was attributed to the interaction of the runaways with the magnetic field ripple [5]. At a certain energy (for TEXTOR the second harmonic ≈ 35 MeV) a resonance will occur, resulting in a pitch angle scattering. Then an effective energy-blocking can occur, because the radiated power equals the power gained from the electric field. Another explanation could be that the observed energy limit is simply the result of orbit shift. The runaways will disappear from the diagnosed area as they gain energy. In fig. 3 is plotted the maximum energy for which the runaways are still confined, calculated from this orbit shift for a peaked current profile according to Schüller [6]. This plot also includes the radiation limit for several values of the pitch angle θ, together with some measured values at t=3.0 s. The radiated power is given by [4]:

$$Pe = \frac{2}{3} \frac{r_e \, m_0 \, c^3}{R^2_{curv}} \gamma^4 \qquad 2$$

Pitch angle

One of the I.R.scanners made an angle of approximately 12° with the equatorial plane, observing the thermal radiation from the limiter blades. On this camera also synchrotron radiation was observed, that could clearly be distinguished from the thermal radiation. Knowing the apparent position of this radiation, the divergence of the synchrotron radiation could be calculated, resulting in a value of 6° in the vertical plane, corresponding to a pitch angle $\theta = 0.10$. It should be noticed that with this value and the value we find for E_{max}, the runaways are indeed close to the radiation limit. Measurements will be made at the low field side in the future, to see if the runaway energy is really limited by the radiation limit.

Confinement

The effect of high electron densities on the runaways and effects of additional heating has been studied by comparing normal low density deuterium discharges, with discharges where deuterium was puffed into the plasma at t=3.0 s, and with discharges where from t=3.0 s to t=3.4 s a neutral beam was injected. All other plasma conditions were kept the same, resulting in a very reproducible synchrotron signal, that varied in amplitude only by a factor of 1.5 on shot to shot basis, but had the same shape. In fig.4 three time traces are given for this signal for the various conditions. In fig.1 the corresponding plasma parameters are shown (line averaged n_e, V_{loop}, I_{pl} and Hard X-rays). The most remarkable features are:

1. Normal case: The synchrotron signal increases until it reaches a constant level after ≈ 3.0 s. As is seen in fig.2 the energy does not increase after 2.5 s, so the population of runaways must be growing. This leads to the conclusion that the runaways are not only created at the beginning but also during the discharge. One possibility for this creation can be the close collisions between runaway and tail electrons, in which the latter also becomes runaway. That this process can be substantially has been pointed out by Besedin and Pankratov [7]. The leveling off at t=3.0 s can be either the result of the decrease in energy or a change in source rate. Enhanced losses are not observed on the hard X-ray signal. It has to be remarked that at t=2.7 s the loop voltage is decreased by a factor of two. The electrical field in the centre, however, behaves different. The current density in the centre can only change on a magnetic diffusion time. The resistivity η then determines the electrical field, which therefore does not decrease.

2. Gas puff: In contrast to the previous situation the signal keeps increasing after the gas puff, reaching its maximum value at ≈ 3.4 s. This is observed in every gas puff experiment. Only then the signal decays, much more rapidly than in the case without gas puff. The further increase could be understood in the sense of birth-rate changes or in electrical field changes. The higher density increases the frequency for the close collisions between runaways and thermal electrons, resulting in more runaways. Another effect of the gas puff is the temperature drop and therefore the increased resistivity η and electrical field in the centre. If the runaways were in radiation equilibrium, then the total emission can now be increased. As can be seen at the hard X-ray signal (fig.1) also runaways are lost, explaining the decrease of the signal after t=3.4 s. What kind of mechanism this is, is not yet investigated. The decrease in signal cannot be explained by a decrease in energy because slowing down effects can be neglected for the observed electrons (collision time > 1000 s).

3. With NBI (co-injected with respect to the current): The signal starts decreasing immediately after the beam is turned on. Two possibilities are suggested to explain the immediate decrease. The first is the drop in the electrical field in the centre if the beam is turned on, which results in an effective deceleration of the runaways if it is assumed that they were already in a phase where the radiated power equated the power gained from the electrical field, as shown in the previous section. The second explanation for the decrease could be a new loss mechanism, like enhanced levels of fluctuating electrical and / or magnetic fields. This is in agreement with the observed hard X-ray signal (fig. 1. bottom) which shows a strong increase in the NBI - phase. Another remarkable fact is the further decrease if the beam is turned off, whereas the hard X-ray signal falls back to a low level.

Conclusions

Runaway electrons with energies up to 35 MeV have been observed by synchrotron radiation in TEXTOR. During the first second they obey the free fall acceleration very well. Then the observed energy saturates after approximately 2.5 s. Explanations for this energy limit can be given by orbit shift effects, the second harmonic runaway ripple interaction, or by reaching the radiation limit. The latter is consistent with the value observed for the pitch angle. For a conclusive answer, measurements will be made at the low field side. Measurements show also that runaways are not just created in the start up phase, but also during the discharge. Loss mechanisms of runaways were found in the cases of gas puff experiments and NBI. To determine these mechanisms will be one of the aims of further investigation.

References

1.O.J. Kwon et al., Nucl.Fusion 28, 1931, (1988).
2.P.J. Catto et al. , Phys.Fluids B 3, 2038, (1991).
3.K.H.Finken et al. , Nucl. Fusion 30, 859, (1990).
4.J.Schwinger,Phys.Rev. 75, 1912, (1949).
5.L. Laurent and J.M. Rax, Europhysics Lett. 11, 219, (1990).
6.F.C.Schüller et al., Proc. 18th Eur. Conf. on Controlled Fus. and Plasma Phys., 15C, IV 185,Berlin 1991.
7.N.T. Besedin and I.M.Pankratov, Nucl.Fusion 26, 807, (1986).

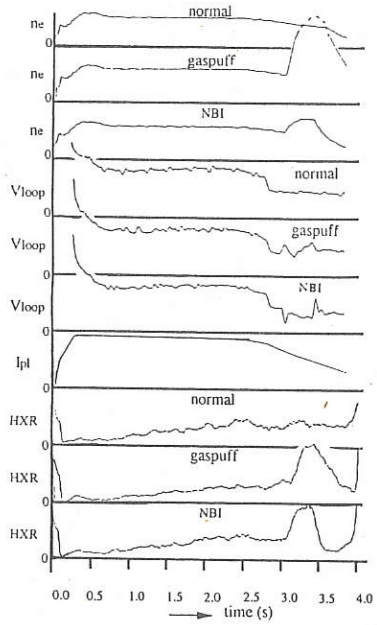

Figure 1: *Experimental conditions. From top to bottom: electron density (scale:0-1.2 10^{19} m^{-3}), Loop voltage (scale : 0 -1 V),Plasma current (scale 0-375kA) and Hard X-ray signal (scale 0-2.5 kHz).*

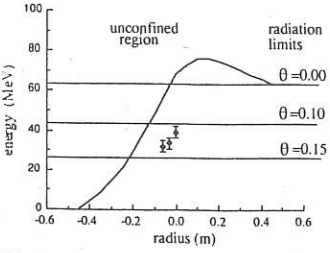

Figure 3: *Maximum energy for which the runaways are still confined. Values measured at t=3.0 s are also included, together with the radiation limit for different pitch angles.*

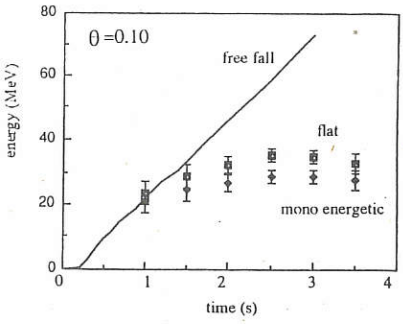

Figure 2: *Development of the maximum observed energy as a function of time for two cases: flat energy distribution function (squares), and mono-energetic distribution function (diamonds).The values expected from free fall acceleration are also included.*

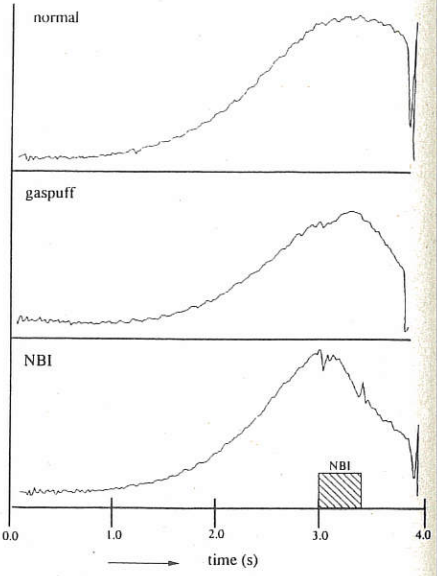

Figure 4: *Time traces (same scale) for the synchrotron radiation for normal conditions (top), gaspuff (middle) and NBI (bottom).*

COMBINED REPETITIVE PELLET INJECTION AND LOWER HYBRID CURRENT DRIVE EXPERIMENTS IN TORE SUPRA

A.Géraud, C.A.Foster*, B.Pégourié, Y.Peysson, P.Bibet, M.Chatelier, H.W. Drawin, D.Moreau

Association Euratom-CEA sur la Fusion Contrôlée, CE Cadarache, 13108 Saint-Paul-lez-Durance, France
* Oak Ridge National Laboratory, 37830 Oak Ridge, Tennessee, USA

INTRODUCTION

In order to control the plasma density during long shots (>10-20s), attemps to combine repetitive pellet fuelling and lower hybrid current drive have been carried out in Tore Supra. As expected from previous studies [1,2], the penetration of pellets injected during LH pulses is small and corresponds to a poor fuelling efficiency. Nevertheless, a partial recovery of the penetration depth is obtained by switching off the LH power just before each injection, which yields a significant increase of the fuelling efficiency. This difference in the pellet penetrations is interpreted in the frame of an ablation model [2] taking into account the heating in volume of the pellet by the fast electron tail.

EXPERIMENTAL SET-UP

The ORNL centrifugal pellet injector used on Tore Supra [3] can inject up to 100 pellets during a single discharge at a velocity ≤800m/s and a frequency ≤10Hz. The particle content of the pellets can be ajusted between 2 10^{20} and 10^{21} deuterium atoms. For the combined pellets/LHCD experiments, the injector was operated at 600m/s, 4Hz, the pellet size was 5±2 10^{20} atoms and the number of pellets per shot limited to 28, according to the duration of the current plateau. One launcher of the 3.7 GHz LH system was used and the injected power was ≤ 3MW ($n_{//}$=1.8; 0° phasing). During the modulation experiments, pellets were triggered by the LH control generator. Tore Supra (R=2.34m, a=0.78m) was operating with Bt=3.9T and Ip=1.6MA. The volume averaged plasma density varied from 1 to 4 $10^{19}m^{-3}$ and the particle pumping capacity available was that of the inner carbon wall (estimated to about 50-60 pellets [4]).

Pellet ablation and penetration are monitored by H_α, H_β photodiodes viewing along the injection path and by a CCD camera mounted in the vertical port at the injection toroidal location. The fuelling efficiency η is defined as the ratio of the instantaneous increase of the total number of electrons in the plasma to the pellet content measured with a microwave cavity.

GLOBAL PLASMA PARAMETERS AND FUELLING EFFICIENCY

CONTINUOUS LH

The time evolution of the main plasma parameters is given on fig.1 for two consecutive shots: the LHCD case (2MW during 4.6s) corresponds to solid lines and markers ●, while the dotted curves and markers **0** are for the similar ohmic shot. Pellets have no significant effect on the wave coupling, since the reflected power remains ≈ 5%, as in the gas injection case. When LH is applied, the volume averaged density increase following each injection becomes small although the pellet size remains constant. The corresponding poor fuelling efficiency $\eta \approx 15$-30% (instead of 80-90% for ohmic plasmas) is closely linked with the reduced penetration of the pellets $L_p \approx 10$cm (instead of ≈ 35cm for ohmic plasmas). Edge pressure spikes (see fig.1) well correlated with pellets are measured on a gauge close to the injector port, indicating that probably a large fraction of the injected matter is lost by charge exchange reactions ($\lambda_{cx} \approx 5$ to 10cm). Owing to the outer matter deposition profile, the density peaking factor $ne(0)/\langle ne \rangle$ is slightly reduced (15%) and remains nearly constant, except during the central filling up transient phase. Central heating [5] by LH waves avoids the electron temperature drop following the very first pellets, as seen on the central channel of the Thomson scattering signal. The density increase compensates for the presence of LH power, yielding a quasi-constant Z_{eff}.

NOTCHED LH

Switching off the LH power before every pellet results in a significant increase of the penetration depth. The delay $\Delta\tau$ between the end of the LH pulse and the injection is taken in the 100-300keV electron slowing-down time and is varied from shot to shot. The evolution of L_p is displayed versus $\Delta\tau$ on fig.2 for different volume averaged densities and for 2MW of LH power. The comparison with the penetrations obtained without notching ($\Delta\tau = 0$) shows that L_p increases very rapidly for small $\Delta\tau$ and reaches an asymptotic value for $\Delta\tau > \Delta\tau_c \approx 30$ms. An example is given on fig.3 for shot TS6035. Twenty-height pellets ($\Delta\tau = 90$ms) are injected during the 9s of the current plateau. Spikes are observed on the loop voltage ($\Delta V \approx 1$V) when the LH generator is switched off. The progressive density increase from 1 10^{19} to 3 10^{19}m^{-3} compensates the Z_{eff} reduction from 4.5 to ≈ 2.5 yielding only a small increase of the mean loop voltage throughout the discharge (2.6Vs saved).

FUELLING EFFICIENCY

The high fuelling efficiency of pellets is due to the deep matter deposition. In the preceding paragraph, an experimental procedure is described wich allows deep penetrations. Nevertheless, the viability of the simultaneous use of LHCD and pellet fuelling will only be demonstrated if the corresponding fuelling efficiency is shown to be high enough. The behaviour of η with the penetration depth is displayed on fig.4 for ohmic (**0**) and LHCD discharges, with (+) and without (●) switch off. For the experiments reported in this paper, a penetration larger than ≈ 20cm is required for the fuelling efficiency to recover a quasi-ohmic

value (i.e. $\eta \approx 60\text{-}80\%$). This condition is only fulfilled for a time delay $\Delta\tau$ of few tens of milliseconds between the LH power switch off and the pellet injection. For steady LH pulses, the penetration depth is limited to $\approx$ 10cm. In that case, the fuelling efficiency does not exceed 20-30%, which does not correspond to a significant improvement with respect to gas puff.

DISCUSSION

It is shown in [2] that, in presence of a fast electron tail, the pellet ablation rate depends crucially on the density of fast electrons whose penetration in the ice is of order of the pellet size. In these conditions, the increase in the pellet penetration suggests that during the time interval $\Delta\tau$, the number of these fast electrons strongly decreases. Qualitatively, the evolution of the suprathermal population can be understood as follows: at a time δt after the power switch off, the electrons whose initial slowing down time τ_{SD} is shorter than δt have lost their energy by collisions while those for which τ_{SD} is larger than δt have been accelerated by the electric field. The condition for the pellets to recover a deep penetration is therefore that the density of the electrons for which $\tau_{SD} \leq \Delta\tau_c$ dramatically decreased. The condition $\tau_{SD} \approx 30$ms corresponds to an energy $E_c \approx 100$keV, for which the stopping length in solid hydrogen is about 1mm, which compares well with the pellet radius.

Acknowledgements

Part of this research is performed under a US-DoE / Association EUR-CEA Collaboration Agreement sponsored by the office of Fusion Energy, US-DoE, under contract DE-AC05-84OR2400 with Martin Marietta Energy Systems, Inc.

References

[1] Söldner F.X. et *al.*, Plasma Physics and Controlled Fusion, Vol.33, No 5, p 405, 1991

[2] Pégourié B. and Peysson Y., Proc.17th EPS, Amsterdam 1990, Vol.III, p 1227

[3] Foster C.A. et al., Proc.IAEA Technical Meeting Gut Ising 1988, IAEA-TECDOC-534

[4] Grosman A., Proc.18th EPS, Berlin 1991, Vol.I, p 317

[5] Moreau D. and the Tore Supra Team, Physics of Fluids B.Plasma Physics, to be published

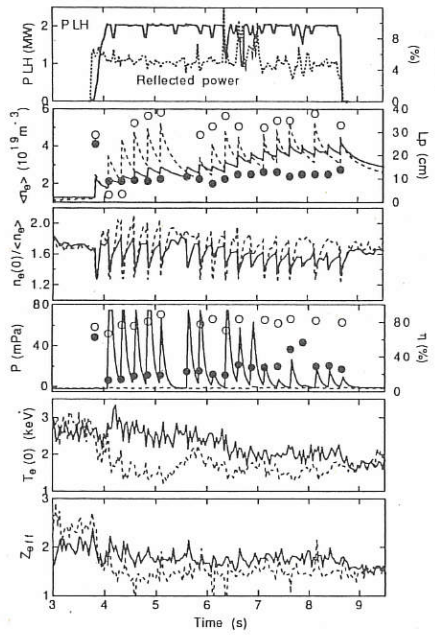

Fig.1: Time evolution of the main plasma parameters for ohmic (-- and o #7033) and LH (- and • #7034) shots

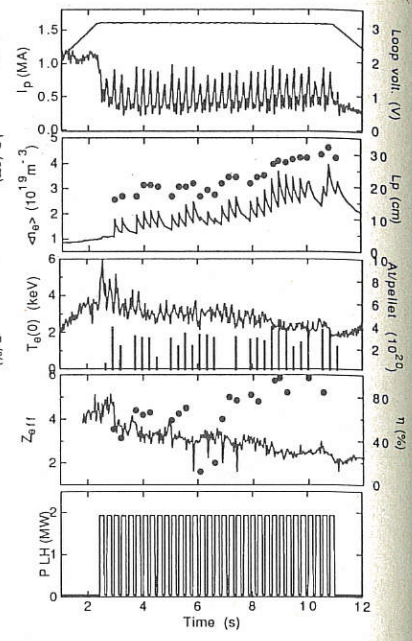

Fig.3: Time evolution of the main plasma parameters and pellet characteristics for a notched LH shot (#6035)

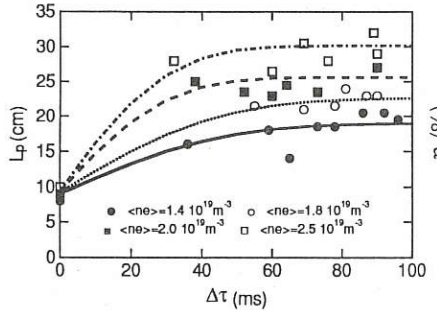

Fig.2: Penetration depth versus Δτ

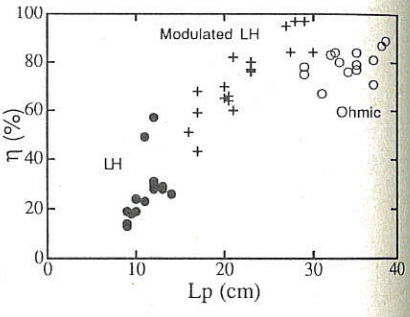

Fig.4: Fuelling efficiency versus penetration depth

OBSERVATIONS OF SUPRATHERMAL ELECTRONS IN THE EDGE REGION OF JET H-MODE PLASMAS

D V Bartlett, L Porte*, A E Costley, S E Jones+, R Smith, A Zolfaghari+

JET Joint Undertaking, Abingdon Oxon OX14 3EA, UK

* *University of Strathclyde, Glasgow G4, UK.*

\+ *MIT Plasma Fusion Centre, Boston MA, USA*

INTRODUCTION. Measurements of the edge plasma parameters are an important part of understanding the behaviour of H-mode plasmas. In previously reported work [1], the JET electron cyclotron emission (ECE) heterodyne radiometer has been used to study the evolution of the edge electron temperature profile. However, this has been limited during H-modes by the presence of two non-thermal features: enhanced emission (not present during the L-mode) at radiation frequencies normally associated with the extreme edge of the profile, and brief intense bursts of emission coincident with ELMs and in the same range of frequency. These phenomena are investigated in this paper. The enhanced emission is explained in terms of a small population of moderately suprathermal electrons. Experimental evidence showing that this suprathermal population is located in the edge region, and estimates of its energy range and density are presented. Rapid changes to this population, caused by the ELMs, are believed to be responsible for the observed bursts of ECE.

MEASUREMENT SYSTEM. The JET ECE heterodyne radiometer [1,2] is a powerful tool for studying the temporal evolution of ECE from the edge plasma since it combines high sensitivity with good spatial and temporal resolutions. It has a total of 44 channels spread over the frequency bands 73-103GHz and 115-127GHz, each channel having a frequency resolution of 500MHz. Either ordinary mode emission (for first harmonic measurements) or extraordinary mode emission (for second harmonic measurements) can be selected, allowing edge measurements over a wide range of toroidal field values. A recent upgrade of the data acquisition [3] allows a large quantity of data to be taken at sample rates up to 1MHz. The data on the ELMs presented in this paper was recorded in eight channels at 200 kHz, while all channels were simultaneously acquired at a rate of a few kHz.

MEASUREMENTS. In H-mode discharges the electron temperature profile can be determined from radiometer measurements to within about 5 cm of the separatrix. At frequencies corresponding to locations closer to the separatrix, the emission over a narrow range of frequency is enhanced to well above the local thermal level. This "hump" on the emission profile always appears at the L to H transition and remains through the entire H-mode phase. Figure 1 shows E-mode spectra of the edge ECE measured by the radiometer at times before, during and after the L-H transition. The intensities are given as radiation temperature (ie equivalent to electron temperature for a thermal optically thick plasma). The steeply rising intensity on the high frequency side is optically thick second harmonic

emission from the steep edge temperature profile. The slowly rising level at low frequencies is due to harmonic overlap: at these frequencies the second harmonic resonance is outside the plasma, but the first harmonic is resonant on the inboard side. The nature of the hump can be investigated by examining the behaviour of the emission in two particular circumstances.

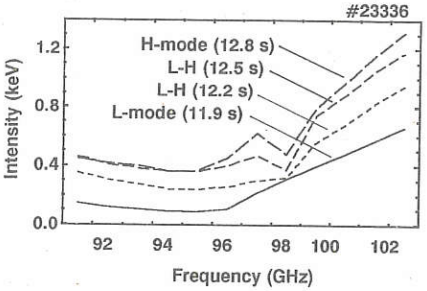

Figure 1: E-mode ECE spectra measured using the heterodyne radiometer at frequencies in the second harmonic edge region. The build up of the non-thermal hump as the plasma enters the H-mode is clearly seen.

First, the optical depth at the edge frequencies can be estimated by making use of a brief spike of emission which is usually observed at the sawtooth collapse. In the edge channels, this spike is (to within the response time of the acquisition) simultaneous with the collapse at the plasma centre, and clearly separated from the heat pulse which propagates to the edge. The electrons generating the spike must therefore be near the plasma centre and have sufficient energy to give a relativistic downshift to a range of edge frequencies. The mechanism by which this radiation spike is generated is not well understood, but its rapidly changing intensity across the radiometer channels, which is due to changing absorption by the thermal edge plasma, can be used to estimate the optical depth profile in the edge region. In these plasmas, with steep edge gradients, the transition from optically thin to optically thick occurs over only one or two radiometer channels (ie a few cm). Applied to data like that in figure 1, this analysis shows that the non-thermal H-mode hump is located at frequencies where the thermal second harmonic is optically thin. The lowest frequency channel for which the thermal plasma is optically thick corresponds to the minimum just above the hump.

Secondly, it can be shown that the electrons which produce the hump are in the edge region by examining discharges in which the density rises sufficiently to produce cut-off of the edge ECE frequencies. The density profile in the edge of these discharges is very steep, reaching its plateau value about 40 cm from the separatrix. When the central density rises to about 10^{20} m^{-3} (for the conditions of figure 1), the cut-off layer is about 40 cm from the separatrix for the frequencies corresponding to the hump. As the density rises further, the cut-off layer moves rapidly to the plasma edge. Since radiation emitted inboard of the cut-off layer cannot propagate to the receiving antenna on the outboard side, the falling intensity of the hump during this time shows where the emitting electrons are located. In these discharges, the intensity of the hump starts to be affected when the cut-off is within 30-40 cm of the separatrix, and it almost disappears when the cut-off is 5-10 cm from the separatrix.

During ELMs the ECE exhibits brief, very intense bursts, as illustrated in figure 2 which shows the time history of an ELM on two edge channels. These spikes occur at the same radiation frequencies as the non-thermal hump, and sometimes extend to slightly higher frequencies. The intensity of the spikes saturates the detection system at a radiation temperature of ~10 keV. Negative saturation of the signal after the ELM is caused by high-pass filtering. The D-alpha signal shows that an ELM occurs at the same time as the burst of ECE, but it is recorded with insufficient time resolution to detect any fine structure of the kind visible on the ECE. Although the magnetics and density reflectometer diagnostics frequently show precursor oscillations leading up to the ELMs, they are not seen on the ECE.

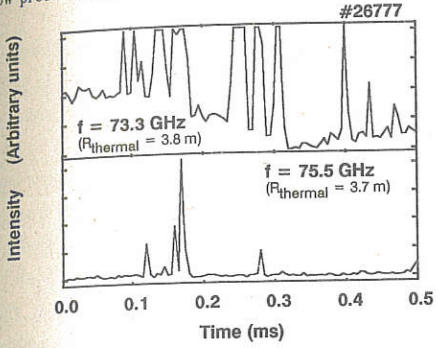

Figure 2: Time evolution of ECE from two edge channels during an ELM. The time origin of this plot is at 13.2 s from the start of the discharge.

The onset of the ECE ELM bursts can be difficult to identify precisely, but it is generally not exactly simultaneous in all the edge radiometer channels. Although there is considerable variation from ELM to ELM, the large number of ELMs (65) recorded over a 0.6 s period in the discharge of figure 2 show a trend of increasing start time delay (with respect to the start time in the lowest frequency channel) as the radiation frequency increases. This is illustrated by figure 3, which plots the start and end times (averaged over all 65 ELMs) as a function of emission frequency. The end time shows very large variability, but there is a marked tendency for the ELM duration to fall with increasing radiation frequency.

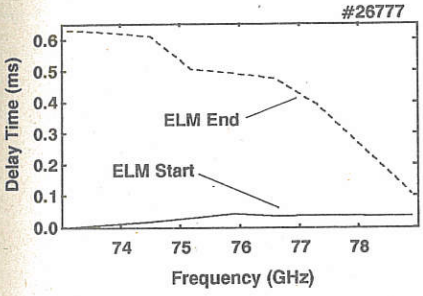

Figure 3: Start and end time of the edge ECE burst seen during ELMs as a function of emission frequency. The times are referenced to the start time in the lowest frequency channel, and are averaged over a number of ELMs.

MODELLING and INTERPRETATION. Various mechanisms which might produce the non-thermal hump in the emission profile have been investigated [4]. The only explanation we have found to fit the above observations is the existence of a small population of suprathermal electrons in the region within 30-40 cm of the separatrix. To explain the small relativistic frequency downshift of the hump and the ELMs, their energy must be limited to about 60 keV. The appearance of the hump during the H-mode may be due to an increase in their density, resulting from reduced outward diffusion of suprathermals through the edge transport barrier. At frequencies above the hump the suprathermals are not seen because their emission is re-absorbed by the optically thick thermal plasma.

The measured spectra have been modelled using the formulae for the emission coefficients of moderately non-thermal electrons given in [5]. The parallel energy of the electrons is limited to 60 keV and their perpendicular energy is assumed to be Maxwellian at around the local plasma temperature (2-3 keV). Their density is obtained by fitting the measured intensity of the hump, and is typically $<10^{-4}$ of the thermal electron density. The series of spikes during the ELM may be caused by pitch-angle scattering of some of the suprathermals during the ELM instability, followed by their ejection from the plasma along with some of the thermal density. In the model calculations the pitch-angle scattering is simulated by transferring energy from the parallel to perpendicular direction. Scattering 10-15% of the suprathermal population is sufficient to give the observed intensity. To explain the slightly wider frequency range over which the ELM is observed (relative to the hump) it is necessary in the model to reduce transiently the edge thermal density to about its L-mode value. This causes the radial location at which the thermal plasma changes from optically thin to thick to move inwards, allowing higher frequency non-thermal emission to escape.

The frequency dependent start time of the ECE burst is not necessarily due to radial propagation of the ELM itself, since the suprathermal emission is spectrally broadened. Alternative explanations are a time evolution of the suprathermal distribution function, or radial propagation of the fall in thermal plasma density due to the ELM, which would vary the frequency at which the plasma becomes optically thick. These possibilities are being investigated.

SUMMARY. Observations of ECE from the edge region of JET H-mode discharges have shown non-thermal features which are not present in the L-mode phase. These features are attributed to a small population of moderately suprathermal electrons in the region within 40 cm of the plasma edge. Model calculations including emission from both the thermal plasma and a suprathermal population with energy up to 60 keV and density about 10^{-4} of the thermal plasma provide a consistent explanation of the observed phenomena.

REFERENCES

[1] L Porte et. al., Proc. 18th EPS Conf. on Cont. Fusion and Plasma Phys., (Berlin, 1991)
[2] D Bartlett et. al., Journal of Nuclear Materials, 1064, 176 (1990)
[3] A Zolfaghari et. al., this conference.
[4] L Porte, PhD thesis, to be submitted to the University of Strathclyde.
[5] G Giruzzi et. al., Phys Fluids, 1704, 27 (1984).

EFFECTS OF ENHANCED TOROIDAL FIELD RIPPLE ON JET PLASMAS

G.Sadler, P.Barabaschi, E.Bertolini, S.Conroy, E.Deksnis, J.Dietz, B.de Esch, B.Green, M.Huart, M.Huguet, J.Jacquinot, O.N.Jarvis, A.Khudoleev*, M.J.Loughlin, R.König, J.Last, A.Maas, M.Petrov*, S.Putvinskii, C.Sborchia, D.Stork, B.Tubbing, P.v Belle.

JET Joint Undertaking, Abingdon, Oxon, OX14 3EA, U.K.
*A.F.Ioffe Physico-Technical Institute, St.Petersburg, Russia

The JET machine is equipped with 32 toroidal field coils. In order to study the effect of TF ripple on the confinement of fast particles and, more generally, on the plasma behaviour, a series of experiments was performed using only 16 TF coils. At the position of the outer limiter, this led to an increase of the ripple, $\delta=(B_{max}-B_{min})/(B_{max}+B_{min})$, from 1% to 12.5%. The toroidal field was limited to 1.4 T, with plasma currents in the range between 2 and 3 MA. Additional heating power-levels and energy-input were kept low in order to avoid possible damage to some first wall components made out of inconel.

For all the 16 coil NBI heated discharges, the toroidal rotation was $\leq 0.5\ 10^4$ m/s compared with $4\ 10^4$ m/s for the 32 coil reference plasmas.

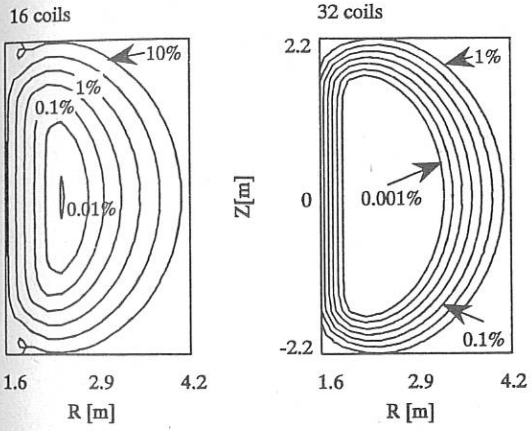

Fig.1:
Comparison of TF ripple maps (contours of log δ) for 16 and 32 TF-coils.

L-mode plasmas: With 16 coils, 2.5 MA inner-wall NBI-heated L-mode discharges showed a reduction of ≈ 30% in the plasma stored energy (diamagnetic) as compared to 32 coil reference discharges. A maximum of ≈10% can be attributed to direct losses of NBI particles ionized in the ripple-well trapping zone. At equal electron temperature ($T_e \approx 3$ keV) and density ($\langle n_e \rangle \approx 1.4\ 10^{19}/m^3$), the ion temperature, T_i, was ≈5 keV and ≈3 keV respectively for the 32 coil and 16 coil discharges. The possibility of a reduction in ion

heating due to pitch-angle scattering of NBI particles while slowing down ($E \leq E_{crit}$) into the ripple-well trapping phase space is under investigation and will be reported elsewhere [1].

H-mode: Although H-modes could be obtained in the double-null X-point configuration with 16 coils only, their quality was severely degraded by elms. The longest elm-free period obtained during 10 MW NBI injection was ≤ 200 ms (with a threshold for elmy H-modes in the region of 1.5-3.5 MW), whereas a power of 1.5 MW was sufficient to form elm-free H-modes in 32 coil reference discharges. The typical density increase for elm-free H-modes was never observed with 16-coils.

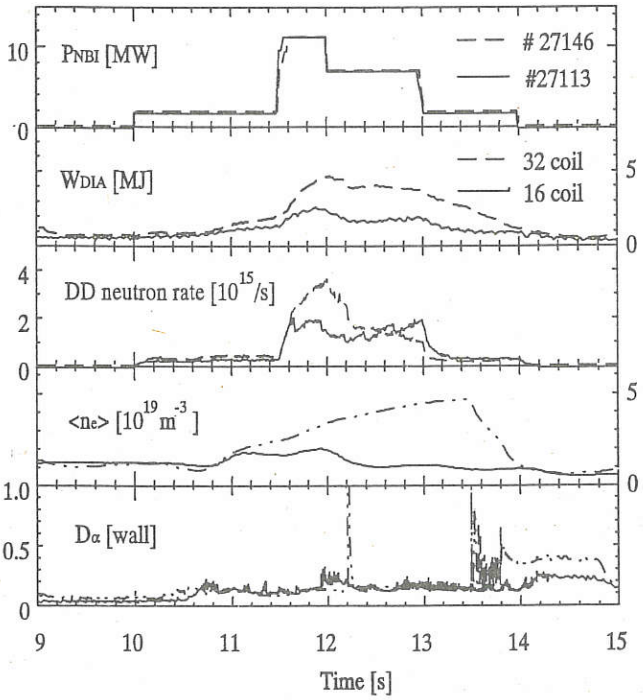

Fig.2: Showing the difference in the quality of H-modes obtained in the 16 coil and 32 coil configuration.

Triton burn-up: The fast particle behaviour was investigated by studying the burn-up of the 1 MeV tritons generated by D-D reactions; the burn-up values obtained in 16 coil plasmas were compared with those from 32 coil reference discharges. The reference discharges were kept as similar as possible to those under investigation by adjusting the NBI power to yield equal 2.5 MeV neutron emission strengths. Theory predicts a reduction of the triton burn-up of ≈ 25% due to ripple-well and stochastic ripple losses; almost all tritons

with trapped orbits are expected to be lost in the 16 coil case. A straight-forward comparison of the 14 to 2.5 MeV neutron yield ratios shows reductions of between 20 and 40%. A more careful analysis using the time dependent 'TRAP-T' code [2], which takes into account slight differences in the background plasma parameters (T_e, Z_{eff}, ..), leads to reductions of between 30% and 60% for 2.5 MA discharges, indicating slightly larger losses than expected. However the uncertainties on the measured plasma parameters used in the calculations are appreciable.

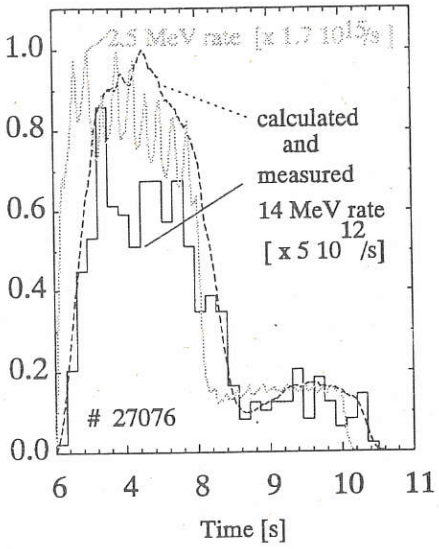

Fig. 3: Showing a 40% deficit in the measured 14 MeV neutron emission yield for a 2.5 MA, 16 coil discharge when compared to the 'TRAP-T' calculated yield. The calculated yields for the 16 coil and 32 coil discharges were identical within 4%.

RF Heating: The loss boundary for fast particles was explored by accelerating H minority ions (2nd harmonic) and NBI injected deuterons (4th harmonic) with the ICRF heating system. A high energy neutral particle analyzer [2] was used to measure fast H^0 energy spectra in the 0.5 MeV to 2.0 MeV range [3]. The intensity of the 3 MeV gamma line from the $^{12}C(D,p)^{13}C+\gamma$ reaction with C impurity ions (threshold energy $\approx$ 0.8 MeV) was used to monitor the fast deuteron content of the plasmas. The 3 MeV γ-ray signature was only present when NBI heating (140 keV D^0) was applied simultaneously, in agreement with calculations with the 'PION' code [5], which show that, under these particular conditions (frequency tuned to 2nd harmonic H minority and $n_H/n_e \approx$ 10 %), the beam ions absorb about 55% of the total RF power.

A scan of the RF resonance position showed that the signals (NPA and I_γ) dropped faster in the 16 coil case than in the 32 coil case when approaching the low field side. Compared to

central heating conditions (R≈ 3 m), a 3.5 fold reduction of fast deuterons and protons (E ≥ 0.8 MeV) was seen with the resonance layer 30 cm off axis on the low field side. Neutron energy spectra, which also reveal the presence or absence of fast deuterons, confirm this behaviour. Furthermore, the RF-heating efficiency decreases when the resonance layer is moved into the region of higher ripple. These results are consistent with expected losses

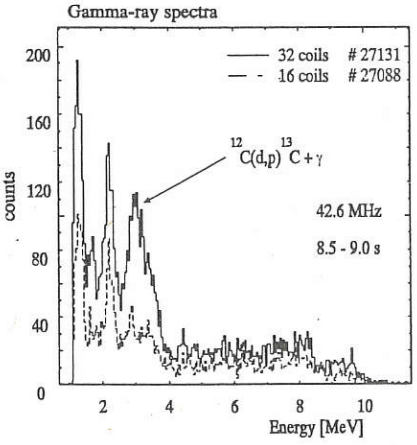

Fig. 4: γ-ray spectra showing the presence of fast deuterons (E ≥ 0.8 MeV) in a 32 coil discharge and their absence in a 16 coil discharge.

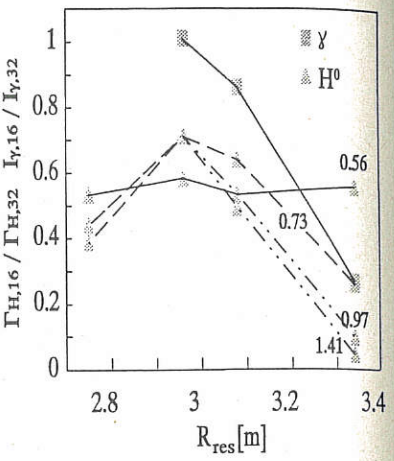

Fig.5: Ratios of fast H neutrals from 16 coil to 32 coil discharges at energies of 0.56, 0.73, 0.97 and 1.4 MeV as a function of the RF resonance position. Also shown are ratios of intensities of 3 MeV γ-rays.

Conclusions: As expected, enhanced ripple has a detrimental effect on the plasma behaviour; H-modes although still obtainable, are of poor quality; the stored energy in L-mode plasmas is low and losses of fast particles are enhanced.

References:

1)B.Tubbing et al., to be presented at the 14th IAEA Conf on Plasma Physics and Controlled Fusion Research, Würzburg, 1992

2)S.Conroy, O.N.Jarvis, G.Sadler and G.B.Huxtable Nucl. Fus. 28 1(1988) 127

3)A.Khudoleev et al. 'Measurements of MeV ICRF driven minoriy Ions', this conference

4)M.P. Petrov et al., 'NPA in the MeV range in JET', this conference

5)L.G. Eriksson, JET Joint Undertaking, private communication

Two-Dimensional Measurement of Heat Load on The First Wall Due to Fast Ion Ripple Loss in JT-60U with Near-Perpendicular NBI

K. Tobita, K. Tani, Y. Neyatani, H. Takeuchi, S. Miura, T. Nishitani and M. Matsuoka

Japan Atomic Energy Research Institute, Naka Fusion Research Establishment
Naka-machi, Naka-gun, Ibaraki, 311-01 Japan

Introduction

Toroidal field ripple produced by a finite number of toroidal field coils can lead to enhancement of fast ion excursions in a tokamak. The ripple-induced fast ion loss has an impact on the realization of a fusion tokamak reactor because of its serious heat deposition on the first wall. In order to predict the local heat load due to fast ion ripple loss, several simulation codes have been developed [1]. Recently heat load to the first wall was one-dimensionally measured in JT-60U using toroidal/poloidal thermocouple arrays. The experimental result has been compared with the orbit-following Monte Carlo (OFMC) code [2], and it showed good agreement [3]. This suggests that our understanding of single particle behavior of fast ions in non-axisymmetric field is reasonably good and that the OFMC code is useful for predicting ripple-induced alpha loss in a burning plasma.

At present, we are performing a further investigation on ripple-induced fast ion loss by introducing infrared thermography. This paper describes the latest results on the two-dimensional measurement of heat deposition on the first wall due to ripple loss and comparison between the experiment and the OFMC computation.

Diagnostics and Experimental Conditions

Heat load on the first wall was measured by a fast infrared TV (IRTV) camera. The IRTV provides a standard television image with time resolution of 16.7 ms. The IRTV views the first wall between two toroidal field (TF) coils. Since fast ions injected by neutral beam injection (NBI) circumnavigate on torus at least several times before their ripple-trapping, heat spots due to ripple loss periodically appear between every TF coil at equal heat flux. The heat flux to the wall is deduced from the temperature rise of the wall surface by calculating the one-dimensional heat diffusion equation. The surface temperature measurement by the IRTV has several advantages such as fast response, sensitivity, wide FOV and spatially good resolution. Only defect is that the measurement gives no information on physical origin of heat deposition on the wall. However some experimental observations indicate that the heat flux comes from ripple-induced fast ion loss as described below.

JT-60U is a tokamak which has the major radius $R_0 = 3.4$ m, the average minor radius $a = 0.9$ m. Its toroidal field is produced by 18 circular coils and the toroidal ripple (δ) goes up to 2.2% at the outer edge of a full-size plasma. The toroidal ripple in JT-60U is illustrated in

Fig.1 (a). The experiment was performed under the conditions of plasma current I_p = 1.5-4.0 MA and toroidal field B_T = 4.0 T. The NBI system is operated with about 15 MW near-perpendicular injection (D^0, 85-95 keV). The power fraction of NBI is E : $E_{1/2}$: $E_{1/3}$ = 78% : 15% : 7%. Throughout the experiments, B_T and I_p are directed clockwise and hence the ion ∇B drift direction orients downwards.

Experimental Results

Heat flux deduced from the IRTV measurement agreed well with that from the thermocouple measurement. Figure 1 (b) shows the two-dimensional profile of heat flux to the first wall. Here TF coils are located at toroidal angles of 0° and 20°, and the toroidal angle is taken in the same direction as I_p and B_T. Poloidal position No. (PP No.) shown in the figure is illustrated in Fig. 1 (a). In this shot, the NBI power P_{NB} is 13.9 MW and the effective safety factor q_{eff} [4] is 2.94. Figure 1 (b) indicates that the heat load on the first wall is localized in both toroidal and poloidal directions: the heat flux is peaked between TF coils on the ion ∇B-drift side.

In addition, parameter scan study showed that the heat load increased with magnitude of ripple δ and/or safety factor q. The reason for the increase in heat load is that the ripple trapping region extends with δ and/or q. These experimental characteristics definitely indicate that the observed heat load is due to ripple-induced fast ion loss.

It is well known that ripple trapping region extends with q, δ and N (being the number of TF coils) in poloidal cross section of a plasma [5]. Besides in the poloidal cross section, the ripple trapping region is expected to extend in the toroidal direction with these parameters. Figure 2 (a) shows the measured toroidal distribution of heat flux as a parameter of the effective safety factor q_{eff}. Here q_{eff} scan was performed by changing I_p. Full width half maximum (FWHM) of the observed heat flux in the toroidal direction increases monotonically with q_{eff}, as shown in Fig. 2 (b). This result bears out the extension of ripple trapping region with q clearly.

By changing the plasma position, we obtained the relation between ripple size δ_{mid} and ripple loss fraction P_{RL}/P_{NB}, where P_{RL} stands for the total ripple loss power deposited to the whole first wall, and δ_{mid} represents toroidal ripple on the outermost magnetic surface on the midplane. As plotted in Fig.3, fast ion ripple loss increases with ripple size. Radiation and charge exchange (CX) losses can be a part of the heat deposition on the first wall. We estimated the loss power due to these processes from the temperature rise of the wall near TF coils and corrected the contribution of radiation and CX. Error bars shown in the figure are mainly determined from ambiguity in the estimation of radiation and CX loss power.

Comparison between Experiment and OFMC Calculation

We compared the measured heat flux with the OFMC [2] computation for a specific shot shown in Fig.1 (b). In the used version of the OFMC code, the radial electric field in the plasma is not taken into account. Computed heat flux distribution is shown in Fig. 4. In the calculation, the number of test particles is 36,000. The calculation indicates that the total heat deposition on the wall comes from ripple-trapped loss of 7.6 % of the injected NB power. The computed ripple loss fraction is in good agreement with the experimental value of 6.8 ± 1.1 %. However we can see little difference between the experiment and the calculation in the position of heat spot. The experimental heat deposition (Fig.1 (b)) is seen in lower PP No. (more outside) at smaller toroidal angles than the calculated one. If we take into account the radial electric field (E_r) which directs inwards in all shots with perpendicular NBI, the calculated heat spot are expected to approach the position of the experimental heat spot; orbits of ripple-trapped ions shift more outwards in the R-direction by $\mathbf{E}_r \times \mathbf{B}_T$ drift and counter-clockwise (the direction decreasing toroidal angle) in the toroidal direction by $\mathbf{E}_r \times \mathbf{B}_p$ drift. Therefore the difference in the position of heat spot is probably caused by the radial electric field in the plasma.

Conclusions

From the surface temperature measurement of the first wall, fast ion loss due to toroidal ripple was investigated in JT-60U. Heat deposition on the wall due to ripple loss localizes in both toroidal and poloidal directions and increases with q and/or δ. Toroidal FWHM of the heat flux due to ripple-induced fast ion loss monotonically increases with q_{eff}. This result indicates that ripple trapping region extends with safety factor in the toroidal direction. The measured heat flux was compared with the OFMC calculation without inclusion of the radial electric field in the plasma and quantitative agreement between them was obtained in overall heat flux. The position of heat spot is, however, slightly different between the experiment and the OFMC calculation. The difference is thought to be due to the drift of ripple-trapped fast ions by the radial electric field.

Acknowledgment

The authors would like to acknowledge Drs. H. Nakamura and M. Nagami for their critical reading of this paper, and members of JT-60 Team for their support to this experiment.

References

[1] S. Putvinskij, et al., ITER-IL-PH-1-9-1 (1989).
[2] K. Tani, M. Azumi, H. Kishimoto, S. Tamura, J. Phys. Soc. Japan **50** (1981) 1726.
[3] K. Tobita, K. Tani, Y. Neyatani, et al., submitted to Phys. Rev. Lett.
[4] H. Ninomiya, JT-60 Team, submitted to Phys. Fluids B.
[5] J.N. Davidson, Nucl. Fusion **16** (1976) 731.

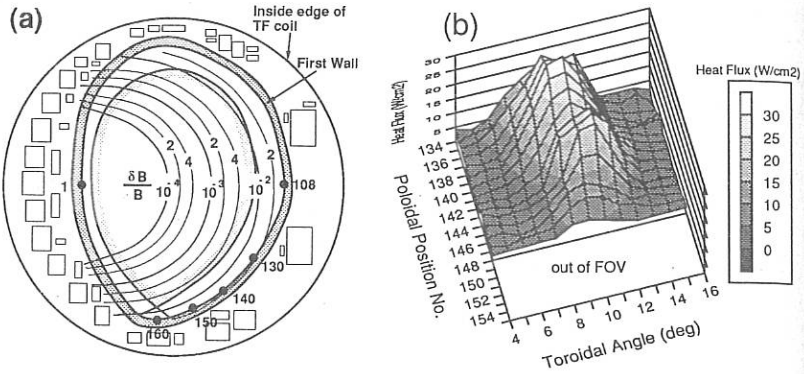

Fig. 1. (a) Poloidal position No. on the first wall and the toroidal ripple distribution in JT-60U. (b) Heat flux on the wall in a NB-heated shot (E14791).

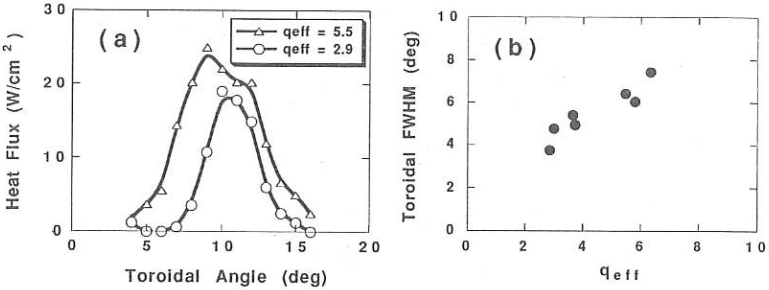

Fig. 2. (a) Toroidal distribution of the heat flux. (b) Dependence of toroidal FWHM on q_{eff}.

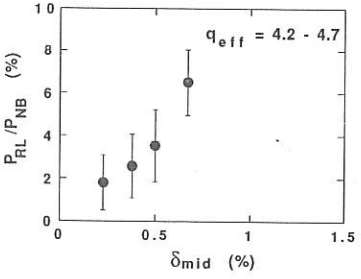

Fig. 3. Dependence of P_{RL} / P_{NB} on δ_{mid}.

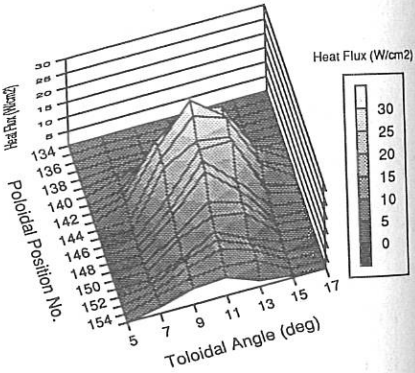

Fig. 4. Heat deposition on the wall computed by OFMC.

Profile measurements of localized fast electrons and ions in TORE SUPRA

V.Basiuk, J.-P.Roubin, A.Bécoulet, J.Carrasco, G.Martin, D.Moreau, B.Saoutic
Association EURATOM-CEA sur la fusion
Centre d'études de Cadarache - F 13108 St Paul-Lez-Durance

The understanding and prediction of ripple related phenomena is an important issue in the design of tokamak reactors. The strong toroidal and poloidal anisotropy of the heat flux to the first wall of TORE SUPRA during additionnal heating has been related to suprathermal particle losses induced by the TF ripple [1]. In this paper we describe a new system of electric collectors designed to diagnose these localized particles and we analyse measurements performed during LHCD, ICRH and NBI heating.

Description of the diagnostic

The diagnostic consists of two arrays of twelve graphite collectors. Each array is located inside a vertical port, one on the ion drift side (top), the other on the electron drift side (bottom). A given collector is related to a known vertical chord across the plasma by the drift trajectory of the localized particles (fig.1) and therefore an array gives the current profile of the particles drifting in its direction and entering the port. The arrays can be set to a potential which can be ramped during the shot (±100 V) in order to plot the characteristic of each collector. This allows to measure the effect of a possible weak density background plasma inside the port and to detect secondary electron emission induced by the fast particles.

Analysis of the collected currents

Measurements have been performed during ohmic and additionnal heating phases. The main parameters of these discharges are summarized on table 1.

During the ohmic phase, the collected currents are weak, and the characteristics are reminiscent of those of Langmuir probes (fig.2). The current values and profiles are the same on each array and can be related to a plasma density of 10^{17} m^{-3} near the port aperture, decreasing to 10^{16} m^{-3} inside the port.

During additionnal heating, the measured profile drastically changes on the side towards which the suprathermal particles are drifting (fig.3), whereas the other side keeps almost the ohmic levels and shapes. During LHCD the characteristics of the bottom array are clearly shifted by a current due to fast localized electrons (fig.2). During ICRH (minority heating), the top array characteristics are shifted but somewhat modified by the presence of secondary electrons created by fast ions. The analysis of the characteristics reveals that these electrons are emitted when the collectors are set to a negative potential but can be recaptured by a positive potential. A secondary electron emission rate of about 2.5 can be deduced from the ionic and electronic saturation values. This value is compatible with the interaction between carbon and fast H^+ ions in the range 100-200 keV generated by the wave.

Consequently, the electronic saturation part of all the characteristics is free of secondary electrons. This current is due to the fast particles and to a small background plasma contribution that can be estimated from the array located on the opposite side. This procedure gives a value of the localized suprathermal particle currents that is free of any spurious component.

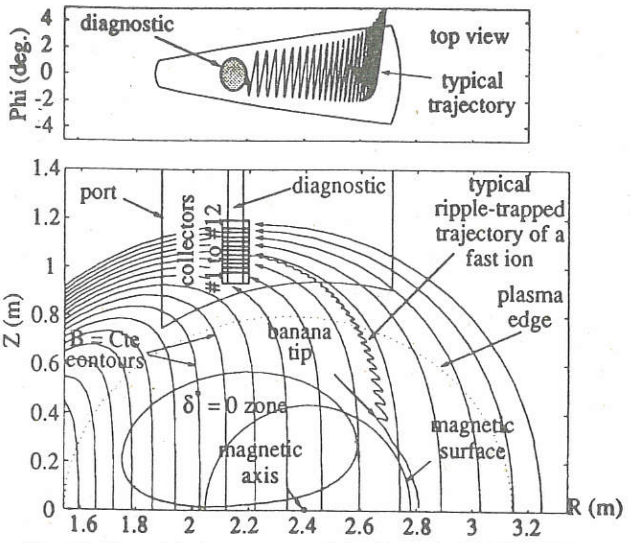

Figure 1: Geometrical arrangement of the diagnostic in TORE SUPRA

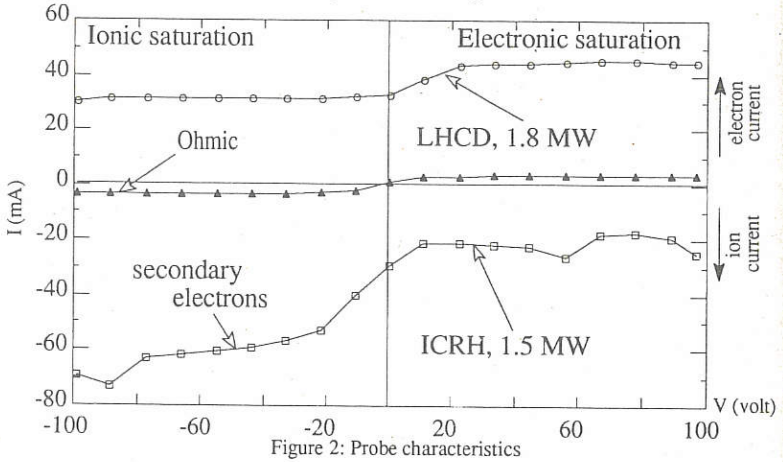

Figure 2: Probe characteristics

Heating	P_{inj} (MW)	mean density (10^{19} cm^{-3})	I_p (MA)	
LHCD	$0 \rightarrow 5$	$2 \rightarrow 3$	$1 \rightarrow 2$	Table 1 : plasma parameters
ICRH (hydrogen minority)	$0 \rightarrow 3$	$2 \rightarrow 3$	$1 \rightarrow 2$	
IDN ($D^\circ \rightarrow D$, 60 keV)	0.3	≈ 3	$1 \rightarrow 2$	
Ohmic		$1.5 \rightarrow 3.5$	$1 \rightarrow 2$	

Ripple losses profiles during additional heating

LHCD experiments:

When LHCD is applied the currents collected by the bottom array suddenly rise and their profile is strongly peaked around a collector connected with the chord R=2.6 m. Hot spots were also observed by IR camera at this point inside the port [1]. The position of this maximum is in good agreement with what is expected from theory. A fraction of the fast electrons generated by the wave in the good confinement zone (fig.1) is brought by collisional scattering on banana orbits. When the banana tip comes outside the good confinement zone, i.e. outside the $\delta^*=0$ contour, a fast electron can be trapped in the ripple well and directly lost to the wall provided its energy is high enough to avoid collisional detrapping (E>40keV for TORE SUPRA conditions). For most of the central magnetic surfaces this mechanism takes place at R≈2.6m where the drift trajectories are tangential to the good confinement zone (fig.1). This geometrical effect is the origin of the observed anisotropy. The position of the maximum can be considered as a direct measurement of the good confinement zone inside the plasma.

The profile of the localized particles is roughly independent of power and density in the experimental range. A regression analysis shows that total collected current varies as $P_{LH}n_e^{-2}$. A Fokker-Planck model describing the ripple losses as a loss cone above a critical energy related to the collisionnal detrapping is on the way and should explained theses scalings.

The total power losses can be estimated considering that the mean energy of the localized electron deduced by hard X-ray measurements is ≈100 keV. For $n_e \approx 3\times10^{19}m^{-3}$ and P_{LH}=3MW, the total collected current on the bottom array is 40 mA. Therefore, taking into account the 18 coils symmetry of the problem we obtain $P_{ripple}/P_{LH} \approx 2$ %. Despite this small value, the strong anisotropy of these losses leads to high local thermal loads on the vessel structure (up to 400 $W.cm^{-2}$ perpendicularly to the drift trajectory of localized particles).

ICRH experiments:

During ICRH (minority regime, resonance on axis) fast ions currents clearly appear on the top array (fig.4). The observed profile is also peaked around the same location (fig.3) but somewhat broader than the fast electron one. The interpretation of this profile is quite the same than for fast electrons. The wave creates fast ions on banana orbit that can be lost in the ripple after diffusion and scattered outside the good confinement zone. The global power losses can be deduced by using the average energy of fast H^+ ions seen by CX measurements (100-200 keV). We also found moderate global losses, typically $P_{ripple}/P_{ICRH} \approx 2$ %, but strong local thermal load at the edge.

A striking feature is the presence of intense fast ions bursts synchronous with the sawteeth crashes. These bursts are seen only on the top collectors and therefore are not related to an edge phenomenon. The rise time of the signal is smaller than the acquisition rate (2 ms). The decay time of these bursts goes from 10 ms for the most central chords to less than 2 ms for the peripheral chords. This is consistent with the theoretical trapping time of the fast ions. This expulsion of fast ions during sawteeth crashes has already been seen by other methods on other tokamaks e.g.[2].

NBI experiments:

Fast localized ions have also been observed during preliminary NBI experiments (P_{NBI}=300kW, E_0=60keV). The profile is peaked again at the same radius. Moreover, as expected by previous Fokker-Planck calculations [3], the power loss is much more important in the case of NBI, because fast ions on banana orbits are directly generated in the high ripple zone. Calculations simulate the total loss current and lead to $P_{ripple}/P_{NBI} > 30$ %.

Conclusions

The interaction of fast particles created by additionnal heating with the TF ripple perturbation in TORE SUPRA has been analyzed by a direct measurement of the localized particles. The good confinement region has been identified thanks to a peak in the measured current profiles and is in agreement with theory. During LHCD and ICRH, the global losses are weak (≈2%) but strongly anisotropic leading to hot spots at the wall. During ICRH, an ejection of fast ions by the sawteeth towards peripheral zones where they get lost in the ripple has been seen. This is a possible scenario of α particle losses in a reactor.

References

[1]: Roubin J.P., Guilhem D., Martin G., Pégourié B., Peysson Y., in Proc. 18th Europ. Conf. on Controlled Fusion and plasma Physics, Berlin, 1991, Part I, p. 54.
[2]: Martin G., Jarvis O.N., Källne J. et al., Phys. Scr. T 16 (1987) 171
[3]: P. Grua and J.-P. Roubin, in Proc. 16th Europ. Conf. on Controlled Fusion and Plasma Physics, Venise, 1989, Part III, p.1225.

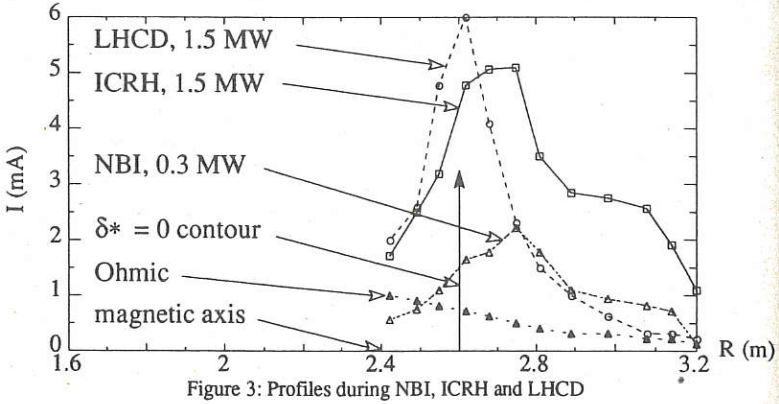

Figure 3: Profiles during NBI, ICRH and LHCD

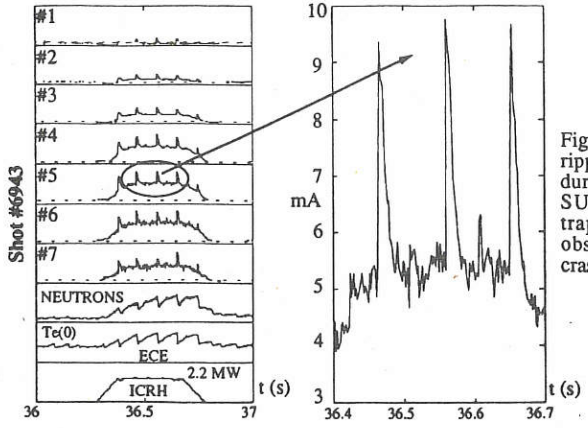

Figure 4: Observation of ripple trapped fast ions during ICRH in TORE SUPRA. Bursts of trapped particles are observed at sawteeth crashes.

Investigation of Microturbulence Drive and Damping Mechanisms in DIII–D

C.L. Rettig, W.A. Peebles, K.H. Burrell†, E.J. Doyle, R.J. Groebner†,
R.J. La Haye†, N.C. Luhmann, Jr., R. Philipona‡, and T.L. Rhodes
Department of Electrical Engineering
University of California, Los Angeles 90024
† *General Atomics, La Jolla, Ca.*
‡ *present address: Swiss Meteorological Institute*

1. Introduction

During DIII–D H–mode discharges, microturbulence is observed to reduce in the plasma edge simultaneous with the $L \rightarrow H$ mode transition and in the plasma core on a longer time scale. Knowledge of the radial electric field profile inferred from CER spectroscopy has allowed the density fluctuations to be sufficiently localized so that edge electrostatic fluctuations can be unambiguously discriminated from those in the plasma core. This has allowed the reduction of edge turbulence simultaneous with the $L \rightarrow H$ transition to be quantified and confirmed with far–infrared (FIR) scattering. Furthermore, strong fluctuations in the plasma interior are observed to decrease after H–mode on a timescale similar to the evolution of the density and electric field profiles in the plasma interior. The improved spatial resolution has allowed a preliminary investigation of the cause for the observed turbulence reduction.

2. Improved Spatial Resolution

Measurements of the poloidally propagating component of tokamak density fluctuations are influenced by the radial electric field, $E_r(r)$, which induces a Doppler shift of the measured turbulence through the $\vec{E} \times \vec{B}$ convective drift [1], proportional to the product of the $\vec{E} \times \vec{B}$ ($\propto E/B$) velocity and the poloidal wavenumber, k_θ [1]. In DIII–D L- and H–mode discharges, the radial electric field is inferred from spatially and temporally resolved measuremnts of the poloidal and toroidal rotation of an impurity species and its pressure gradient [2, 3]. The electric field during co–injected discharges is positive in the plasma core ($r/a \lesssim 0.8$) where the neutral beam induces large toroidal rotation, v_ϕ. In the plasma edge, E_r is negative, arising from poloidal rotation, v_θ, and diamagnetic drift in the steep pressure gradient edge.

The radial variation of E_r and therefore the associated Doppler shift are utilized to enhance the spatial resolution of the FIR fluctuation measurements. It has been observed that the $E \times B$ Doppler shift dominates the measured dispersion characteristics [4], so fluctuations measured in the laboratory frame with a large positive frequency ($\nu \gtrsim 10\nu_{*e}$) must originate from the plasma interior where the radial electric field induces a large positive frequency shift. Conversely, fluctuations measured with a negative frequency must originate from the negative electric field region of the plasma edge. Thus, unambiguous discrimination between the plasma edge and interior is possible, based on the sign of the Doppler shift.

This interpretation has been confirmed by FIR data showing a fast suppression of density fluctuations in the plasma edge region correlated with both a re-

duction in edge D_α and the reflectometer fluctuation signal which is well localized to the edge [5]. This is seen in Fig. 1 which shows the frequency spectrum of the scattered power ($\propto \tilde{n}_e^2$) at $k_\theta = 2\ cm^{-1}$ plotted as a function of time around the $L \rightarrow H$ transition. The scattered power integrated over negative frequencies is reduced sharply at the transition, indicative of a fast reduction of the edge microturbulence ($\rho \geq 0.9$). Approximately 5 ms after the transition, the discharge exhibits an ELM known to be an edge localized disturbance with large fluctuation amplitude. The fluctuation spectrum in the frequency range interpreted as the edge distinctly shows the ELM, while that associated with the interior does not. This is a clear confirmation of the enhanced spatial localization based on the $E \times B$ Doppler shift induced by a radial electric field.

If the scattered signal is separated into frequency bands representing their spatial origin, the time scale and spatial structure of the events becomes clear. As shown in Fig. 2, the scattered power integrated over negative frequencies (corresponding to the edge) is reduced on a timescale of $\simeq 100\ \mu s$ at the $L \rightarrow H$ transition, but the scattered power over positive frequencies is unchanged on this timescale. This agrees with the previous interpretation of reflectometer data which concluded that a rapid suppression of density fluctuations occurred in a narrow (3 cm) edge plasma region [3]. The fluctuation reduction in the edge is of the order $\gtrsim 50\%$. Further, the effects of local electric field shear are observed in the suppressed fluctuations during H–mode. Figure 3 shows the scattered power spectrum during L– and H–mode on a log scale with only the negative frequencies shown for clarity. Although the fluctuations are reduced in H–mode, the frequency spectrum is broader, indicating the presence of local shear in E_r.

3. Reduction of Interior Microturbulence

After the $L \rightarrow H$ transition, the fluctuations in the plasma core are observed to reduce on a longer timescale. Figure 4 shows the frequency spectrum of the scattered power plotted as a function of time beginning 5 ms *after* the $L \rightarrow H$ transition and extending 20 ms into the ELM–free H–mode phase. From the above discussion, the scattered feature centered around 500 kHz indicates that interior fluctuations are steadily reduced over a period of 25–50 ms. Previous studies have shown the normalized core fluctuations ($\tilde{n}_e/\bar{n}$) in DIII–D tend to reduce during the H–mode phase on a timescale of 10–20 ms [6]. However, this was dominated by an increase in $\bar{n}$. The more recent data shown in Fig. 2 were obtained during a boronized discharge which achieveded the enhanced confinement regime known as VH mode (defined such that $\tau_{E,VH}/\tau_{E,H} \gtrsim 1.6$). The global energy confinement time is observed to increase during the period of fluctuation reduction, further continuing to rise to the VH mode confinement value. The fluctuation reduction in boronized discharges (which develop into VH mode) is much greater than that seen in previous non–boronized discharges, as much as 70% in $\tilde{n}$ alone (and much larger in $\tilde{n}/\bar{n}$).

Concurrent with the observed turbulence reduction in the plasma interior, the density and E_r profiles are evolving with a similar time constant. The electron density profile flattens in the confinement region ($0.5 \lesssim \rho \lesssim 0.9$), presumably due to reduced outward particle transport at the far edge ($\rho \gtrsim 0.9$). Thus, if the turbulence is ∇n_e driven, this could explain the observed reduction in $\tilde{n}$. In addition, the radial electric field is increasing in the plasma core ($\rho \lesssim 0.7$) producing stronger E_r shear in the confinement region as a result of the negative contribution

at the edge. Thus, if ∇E_r is capable of turbulence suppression, this might also contribute to the observed reduction.

4. Experiments to Alter the Radial Electric Field

To isolate the effects of the radial electric field on turbulence in the plasma core, several experiments have recently been performed to modify the radial electric field while keeping all other parameters constant to assess the importance of electric field on the local turbulence levels. For example, during discharges with counter neutral beam injection (NBI antiparallel to I_p), the electric field structure is significantly altered in the plasma core (compared to co–injection.) With reversed toroidal beam momentum input, the contribution to E_r made by $v_\phi \times B_\theta$ is reversed, eventually driving E_r negative across the entire plasma cross–section. Preliminary analysis of these discharges has clearly shown the Doppler shifts predicted by the electric field evolution. In addition, a reduction of the short wavelength turbulence has been observed during the initial phase of the L–mode, as E_r is modified in the core. More extensive analysis will be performed in order to elucidate these effects and identify possible causes.

In other experiments, the radial electric field is altered by modifying the toroidal rotation in the plasma core. Toroidal drag is induced on v_ϕ from an external n=1 magnetic field coil which slows the plasma toroidal velocity. Preliminary data have indicated that the fluid velocity is slowed by the additional n=1 error field, reducing E_r in the core, and that the Doppler shift on the FIR scattered signal is reduced relative to the case of no external n=1 error field. Further analysis is needed to determine the effect on turbulence levels.

5. Conclusions

The spatial resolution of the DIII–D FIR scattering system has been improved by knowledge of the spatially varying radial electric field during H–mode discharges. Using this complementary information, the fast ($\simeq 100\ \mu s$) reduction of edge turbulence simultaneous with the $L \rightarrow H$ mode transition has been quantified and confirmed with FIR scattering. Further, the core fluctuations during H–mode have been observed to reduce on a longer timescale similar to that of the density profile evolution (10–50 ms). The core fluctuations are reduced by a much larger amount during boronized discharges which generally lead to VH mode confinement. The improved spatial resolution has allowed preliminary investigation of the mechanism for the observed fluctuation reductions in the interior.

Acknowledgements

Work supported by U.S. D.O.E. Grant No. DE–FG03–86ER53225 and contract no. DE–AC03–89ER51114.

References

[1] R.A. Koch and W.M. Tang, Physics of Fluids 21, 1236 (1978).
[2] R.J. Groebner, K.H. Burrell, and R.P. Seraydarian, Physical Review Letters, 64, 3015 (1990).
[3] K.H. Burrell, *et al*, Physics of Fluids B, 2, 1405 (1990).
[6] R.P. Philipona, et al, Review of Scientific Instruments, 61, 3007 (1990).
[5] submitted to Nuclear Fusion.
[6] Philipona, R., Doyle, E.J., Luhmann, N.C., Jr., in Proceedings of the 18th European Conference on Controlled Fusion and Plasma Physics, Berlin, vol. 1, 287 (1991).

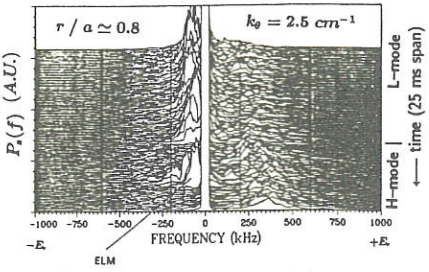

Fig. 1 - Fluctuation spectra across the transition. - Frequency spectra of the scattered power as a function of time across an $L \rightarrow H$ mode transition. The transition occurs at 2180 ms where the negative frequencies reduce. An ELM occurs at 2186 ms when the L-mode spectra transiently returns.

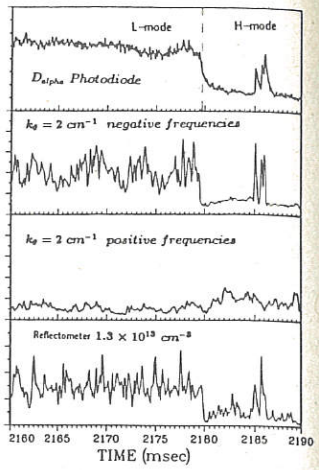

Fig. 2 - Frequency Integrated Scattered Power. - The scattered spectra of Fig. 1 integrated over positive and negative frequency bands. Note the ELM at 2186 ms on the D_α signal and on the edge FIR signal showing the spatial resolution.

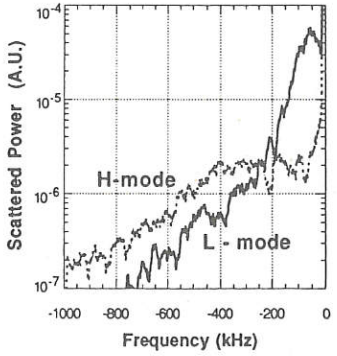

Fig. 3 - Spectra of the Residual Suppressed Fluctuations - Log plot of the scattered power during L- and H-mode of Fig. 1. The broader H-mode indicates the presence of local electric field shear where the fluctuations are suppressed.

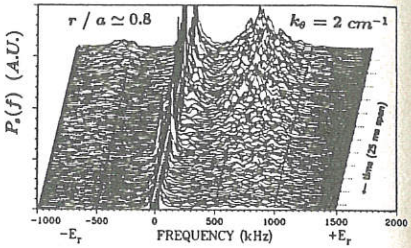

Fig. 4 - Scattered Power Spectra During H-Mode. - Frequency spectra of the scattered power ($\propto \tilde{n}^2$) as a function of time, beginning 5 ms after the transition. The reduction of the positive frequency feature indicates a reduction in the interior turbulence.

EDGE ION DYNAMICS IN H-MODE DISCHARGES IN DIII-D*

R.J. Groebner, K.H. Burrell, P. Gohil, J. Kim, R.P. Seraydarian
General Atomics, San Diego, California 92186-9784, U.S.A.

INTRODUCTION

Recent theoretical and experimental studies have suggested that the dynamics of the ions at the plasma periphery may play an important role in causing the L-H transition. A well-known hypothesis is that the transition is caused by a reduction of microturbulence at the plasma edge due to an increase in shear in the radial electric field E_r.[1-2] This hypothesis is consistent with experimental observations showing that at the L-H transition in a narrow layer just inside the last closed flux surface (LCFS) E_r becomes more negative,[3-12] the shear dE_r/dr increases markedly[5,6,9-12] and profiles of temperature and density steepen.[6,9-12] Furthermore, the H-mode has been generated in limiter discharges with the application of a radial electric field with an electrode inserted into the plasma.[13] If this hypothesis is correct, then it is important to understand the forces which control E_r at the plasma edge. Several mechanisms for generation of a negative E_r have been proposed including ion orbit loss and charge exchange loss,[1,14,15] power flow asymmetry,[16] anomalous Stringer spin-up[17] and self-generation by turbulence.[18] Several of these mechanisms imply that E_r should be related to the ion collisionality parameter ν_i*; experimentally a relationship between T_i and E_r might be expected. Calculations by Hinton and Chu have shown that if ion orbit loss dominates ion transport across the LCFS in H-mode, then the gradient scale length of T_i should be comparable to the poloidal gyroradius $\rho_{i\theta}$. Large values of T_i have been observed near the plasma boundary in H-mode[11,19] and T_i gradients as high as 1 keV/cm have been observed within 1 cm of the LCFS.[11]

The goal of this paper is to present detailed measurements of T_i and E_r at the plasma edge in L- and H-mode with high spatial resolution in order to study the edge ion dynamics. Of primary interest is the relationship between T_i and E_r and the behavior of the edge T_i profile in H-mode. The principle findings are: there appears to be a threshold temperature for T_i required for the transition to occur with T_i at the LCFS in the range of 0.2-0.3 keV at the transition; a correlation between the edge E_r profile and the edge T_i profile has been observed; and values of T_i of 2-3 keV within a few cm of the LCFS and of dT_i/dr of up to 1 keV/cm are observed in the transport barrier in H-mode, with the scale length for T_i being of the order of a poloidal gyroradius.

MEASUREMENTS AND RESULTS

Measurements of the edge values of T_i and E_r in the DIII-D tokamak are made with a high resolution spectroscopy system[12,20] which uses the techniques of active Charge Exchange Recombination (CER) Spectroscopy. Measurements are normally made from the C VI 5290.5 A line or the B V 4944.6 A line. Ion temperature measurements are made from the Doppler widths of these lines, poloidal and toroidal flow velocities v_θ and v_ϕ are made from the Doppler shifts of these lines and the shape of the C VI or B V density profile is determined from the intensity of the signal. These measurements are the required ones for calculating E_r from the lowest order force balance equation for a single species, $E_r = (Z_I e n_I)^{-1}\ dp_I/dr - (\vec{v} \times \vec{B})_r$. Here, Z_I is the charge of the ion, n_I is the ion density and p_I is the ion pressure, e is the electronic charge, v is the mass flow velocity for the ion and B is the total magnetic field. The CER system used for these measurements spans a region of 5 cm in major radius at the outer midplane, has a spatial resolution of 6 mm for measurements of E_r and of 3 mm for T_i and has a minimum averaging time of less than 1 ms.

* This is a report of work sponsored by the U.S. Department of Energy under Contract No. DE-AC03-89ER51114.

A power scan is a useful technique for studying any relationship between E_r and T_i because T_i can be varied with other plasma parameters held nearly constant. Data presented here are for a scan in which the neutral beam heating power was varied by a factor of eight (P_b = 2.5–20 MW). All of the single-null divertor discharges had identical target densities with the plasma current I_p being 1.0 MA and the toroidal magnetic field B_t being 2.1 T. The L-H transition was obtained at all eight power levels used in this experiment. Figure 1 shows the effect of increasing the heating power on the rate of change of T_i for a location which is within 1 cm or less of the separatrix (LCFS). The edge T_i obtained just prior to the transition is in the range of 0.2–0.3 keV for nearly an order of magnitude change in heating power. This observation suggests that a threshold value of T_i may be required to obtain the L-H transition, an idea which is consistent with many studies showing that there appears to be a threshold value of edge T_e required for the transition.[21]

After the transition, the ions at the edge can be heated very rapidly for powers well above the threshold power, as is indicated in Fig. 1. Rapid heating leads to large values of T_i and of dT_i/dr very near the LCFS in the H–mode. Figure 2 shows the temporal history of the T_i profile near the edge for a case with 5.0 MW of heating power. The transition occurred at about 2360 ms and a very rapid increase of T_i occurred subsequently with values of dT_i/dr reaching about 0.74 keV/cm within less than 100 ms and values of T_i reaching 1.5 keV within 2 cm of the LCFS. Increasing the heating power into a fixed target plasma increases the rate at which T_i and dT_i/dr increase and appears to increase the values of T_i which are achieved near the separatrix. T_i values of 3 keV were obtained within about 5 cm of the LCFS for P_b = 15 MW.

The scale length L_{Ti} for the maximum T_i gradient in Fig. 2 is about 1.5 cm. This value is comparable to the poloidal gyroradius of 2.5 cm, a result which was qualitatively predicted by an ion orbit loss model.[14] The exact theoretical prediction for L_{Ti}, $L_{Ti} = \epsilon\, \rho_{i\theta}/2.2$, yields a value of 0.3 cm, which is smaller by a factor of five than the observed value.

A consistent feature of all L-H transitions in DIII–D is that E_r becomes more negative in the transport barrier and that the most negative value of E_r is observed on the chord closest to and inside of the LCFS. Previous studies have shown that E_r can change much faster than 1 ms.[9–11] However, the power scan shows that for heating powers near the threshold value required to obtain the H–mode, E_r can evolve over a period of tens of milliseconds. For a heating power of 2.5 MW, Fig. 3(a) shows that E_r just inside the LCFS continued to become more negative for a period of at least 65 ms. For a power level of 10 MW, Fig. 3(b) shows that E_r also evolved at an observable rate but the rate of change was considerably faster than for the 2.5 MW case. It took ~10–15 ms for E_r to reach its most negative value. Figure 3 also demonstrates that the most negative values of E_r are approximately 35 kV/m, independent of a factor of four change in heating power. Other temporal changes in E_r are observed, including widening of the layer of negative E_r as the H–mode progresses [see

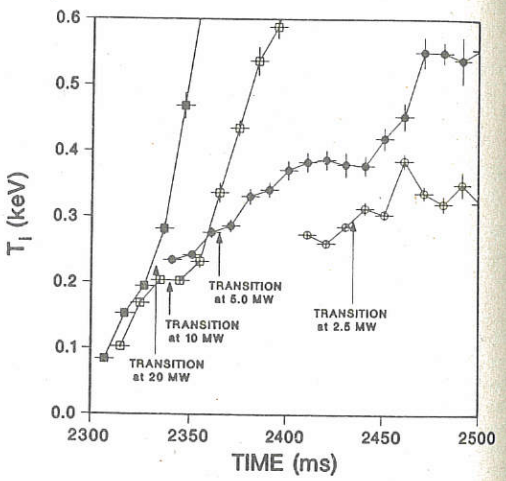

FIG. 1. Time evolution of the T_i value which is within 1 cm and just inside the LCFS (separatrix). Data are shown for heating powers of 2.5 MW, 5.0 MW, 10 MW, and 20 MW. Data were obtained with an averaging time of 10 ms.

data for +65 ms in Fig. 3(a) and for +15, +45 and +65 ms in Fig. 3(b)] and an outward movement of the LCFS due to increasing beta [see data for $R = 2.30$ m at +65 ms in Fig. 3(b)].

These observations and theories which relate E_r to ion physics suggest that there may be a relationship between E_r and T_i. This hypothesis is generally supported by the data from the power scan which show that for nearly identical T_i profiles obtained at different power levels, the observed E_r profiles are very similar. As T_i increases, the corresponding E_r profiles change accordingly. Figure 4(a) shows that for a range of eight in heating power that it is possible to find nearly identical T_i profiles. These profiles are obtained earlier in the discharge as the heating power is increased. The corresponding E_r profiles overlay almost identically with the exception of the highest power case. It can be argued that as the heating power is increased, a given value of T_i is obtained at different values of the density and therefore of ν_i*; thus, for sufficiently high heating power, the correlation between E_r and T_i should depart from that observed at lower power.

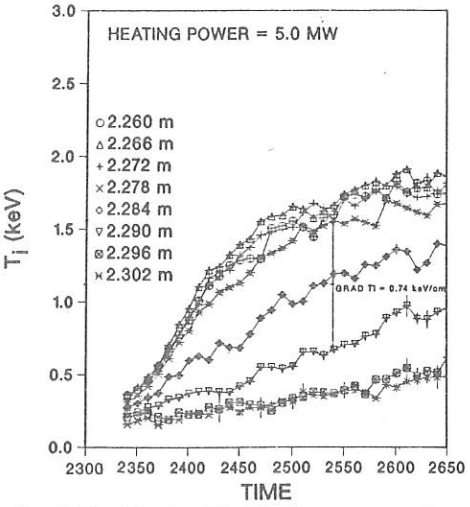

FIG. 2. Time histories of T_i on eight CER chords for $P_b = 5.0$ MW with L-H transition occurring at about 2360 ms. Spacing of adjacent chords is 6 mm. The values of T_i for the outermost chords (at 2.296 m and 2.302 m) are nearly identical, which is a signature that they are at the separatrix or in the scrapeoff layer.

CONCLUSIONS

Data obtained with high spatial resolution near the LCFS show that in

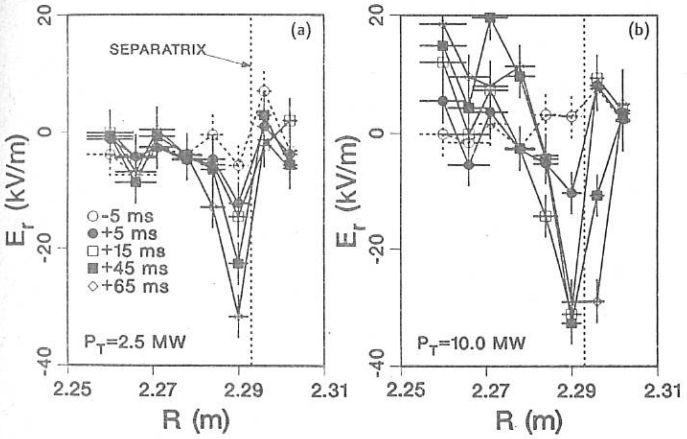

FIG. 3. Time evolution of E_r profiles for (a) 2.5 MW heating power and (b) 10 MW heating power. Open circles show that E_r profiles just prior to the L-H transition are nearly zero inside the separatrix. Location of the separatrix is shown for the time of transition. For the 10 MW case, separatrix moves to larger radii as plasma heats up. Times are shown relative to the L-H transition.

H–mode, there is evidence of a relationship between E_r and T_i, as is expected from several theories for generation of a negative E_r. Large gradients in T_i are observed, as suggested by a theory of ion orbit loss. Further progress on these subjects requires detailed quantitative comparison between the experimental measurements and the predictions of theory.

1 Shaing, K.C., Crume, Jr., E.C., Phys. Rev. Lett. **63** (1989) 2369.
2 Biglari, H., Diamond, P.H., Terry, P.W., Phys. Fluids B **2** (1990) 1.
3 Groebner, R.J., *et al.*, in *Proc. of the 16th Euro. Conf. on Controlled Fusion and Plasma Physics*, Venice (European Physical Society, Petit-Lancy, Switzerland, 1989), Vol. **13B**, p. 245.
4 Burrell, K.H., *et al.*, Plasma Physics and Controlled Fusion **31** (1989) 1649.
5 Groebner, R.J., *et al.*, Phys. Rev. Lett. **64** (1990) 3015.
6 Ida, K., *et al.*, Phys. Rev. Lett. **65** (1990) 1364.
7 Burrell, K.H., *et al.*, Phys. Fluids B **2** (1990) 1405.
8 Hofmann, J.V., Field, A.R., and Fussmann, G., *Proc. of the 17th Euro. Conf. on Controlled Fusion and Plasma Physics*, Amsterdam, 1990 (European Physical Society, Petit-Lancy, Switzerland), Vol. **14B**, p. 1556.
9 Groebner, R.J., *et al.*, *Proc. of the 13th Intnl. Conf. on Plasma Physics and Controlled Nuclear Fusion Research*, Washington, D.C., 1990 (International Atomic Energy Agency, Vienna, 1991), Vol. I, 453.
10 Doyle, E.J., *et al.*, Phys. Fluids B **3** (1991) 2300.
11 Gohil, P. *et al.*, *Proc. of the 18th Euro. Conf. on Controlled Fusion and Plasma Physics*, Berlin, 1991 (European Physical Society, Petit-Lancy, Switzerland) Vol. 13, p. 245.
12 Gohil, P., *et al.*, to be published in *Proc. of 14th Symposium on Fusion Engineering*, San Diego, California 1991.
13 Taylor, R.J., *et al.*, Phys. Rev. Lett. **63** (1989) 2365.
14 Hinton, F.L., and Chu, M.S., Nucl. Fusion **25** (1985) 345.
15 Itoh, S., and Itoh, K., Phys. Rev. Lett. **60** (1988) 2276.
16 Tendler, M., and Rozhansky, V., Comments Plasma Phys. Contr. Fusion **13** (1990) 191.
17 Hassam, A.B., *et al.*, Phys. Rev. Lett. **66** (1991) 309.
18 Diamond, P.H., and Kim, Y.-B., Phys. Fluids B **3** (1991) 1626.
19 Weisen, H., *et al.*, Nucl. Fusion **31** (1991) 2247.
20 Gohil, P., *et al.*, Rev. Sci. Instrum. **61** (1990) 2949.
21 ASDEX Group, Nucl. Fusion **29** (1989) 1959.

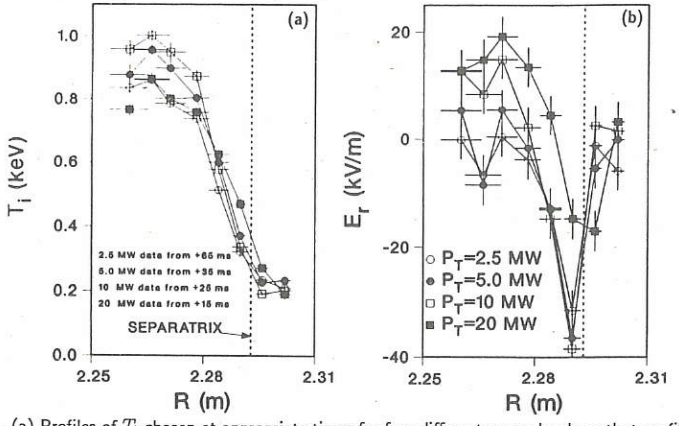

FIG. 4. (a) Profiles of T_i chosen at appropriate times for four different power levels so that profiles are very similar. (b) E_r profiles corresponding to the T_i profiles shown in (a). All target discharges were identical, and location of separatrix is for time of transition. Averaging time was 10 ms and times shown are for midpoint of averaging time. Times are show relative to the L-H transition.

INVESTIGATION OF THE EFFECT OF LARGE CORE CHANGES IN TOROIDAL PLASMA ROTATION AND RADIAL ELECTRIC FIELD ON CONFINEMENT IN H-MODE DISCHARGES IN THE DIII-D TOKAMAK*

R.J. La Haye, R.J. Groebner, A.W. Hyatt, and J.T. Scoville

General Atomics, San Diego, California, USA

ABSTRACT

The plasma toroidal rotation and the radial electric field in the core ($\rho \lesssim 0.9$) of H-mode discharges in DIII-D are greatly altered by the drag produced by application of static, resonant magnetic field perturbations from an external coil ("the $n = 1$ coil"). Transport loss due to turbulent fluctuations can in theory be reduced by E_r shear stabilization or suppression. This is tested experimentally in DIII-D by using "the magnetic braking" of rotation (with concomitant change in E_r) as an independent control. The magnetic braking produces reversal of the core radial electric field, E_r, and E_r shear. However, the plasma maintains a negative edge ($\rho \gtrsim 0.95$) E_r and E_r shear and remains in H-mode with insignificant changes in global confinement, density profile and temperature profiles. The H-mode confinement is remarkably robust to the increasing error fields and the slowed toroidal rotation up to the onset of a locked mode which induces a transition to L-mode, the virtual cessation of plasma rotation and large reconnected islands.

1. INTRODUCTION

Recently there has been considerable theoretical study of the possibility that shear in the radial electric field E_r can stabilize microturbulence[1-5] and thus improve confinement. These theories have been largely motivated to explain the L to H transition when confinement approximately doubles which is now known to be an edge phenomenon. However, the idea of shear suppression of turbulence certainly has much wider possibilities than just the edge of the H-mode plasma. So far, the published experimental data show that edge regions of high E_r shear coexist with regions of improved confinement.[6-10] The further improvement in confinement in the DIII-D VH-mode (1.6~2 times H-mode confinement) may result from the inward extension of the region of high electric field shear.[11] The necessity for a negative E_r and the radial depth of such an E_r shear suppression layer are in theoretical question.

The shear stabilization of microturbulence is thought to result from a radial gradient in E_r which is connected to the plasma fluid rotation velocity $\vec{V}$ through force balance by[12]

$$E_r = \frac{1}{n_i Z_i e} \nabla P_i - (\vec{V}_i \times \vec{B})_r \quad , \tag{1}$$

where E_r is the same for all species i, electrons, majority ions and impurity ions, and n_i is the density, Z_i the ionic charge, e the electron charge, ∇P_i the perpendicular pressure gradient, and $\vec{B}$ the total magnetic field.

2. EXPERIMENT

To vary the plasma rotation and radial electric field E_r, the magnetic braking due to the toroidally localized vertical field of the external "$n = 1$ coil" on DIII-D is used. The $n = 1$ coil is a 56 turn ring of radius 0.9 m placed at the major radius and 3 m above the midplane at toroidal angle $\phi = 289°$.[13] The coil produces a static magnetic field of toroidal modes $n = 0$ and $n = 1$ made up principally of poloidal modes $m = 1$ and 2. The magnetic braking in DIII-D arises from conducting plasma fluid rotating toroidally into the region of the localized $n = 1$

* This is a report of work sponsored by the U.S. Department of Energy under Contract No. DE-AC03-89ER51114.

coil field; the time rate of change of flux produces a plasma "eddy" current which opposes the rotation.

Neutral beams are applied which increase the plasma kinetic energy and lead to H–mode and the usual L to H transition signatures of a drop in recycling D_α light (at 1570 msec) followed by repetitive bursts of D_α, edge localized modes (ELMs) (Fig. 1). (Discharge parameters are $I_p = 0.95\,MA$, $B_T = 1.2\,T$ and single-null divertor with q at the 95% flux surface of 3.5.) The beams spin up the plasma rotation as measured by an analog frequency measure of the Mirnov activity (BDOTLFFREQ) divided by the dominant Mirnov toroidal mode number $n = 2$. At $t = 2000$ msec, the $n = 1$ coil current is ramped linearly in time at a rate slow compared to the energy confinement time. Note that the $n = 1$ coil field magnetically brakes the plasma rotation until at about 2800 msec, a locked mode[13] arises as detected by the "locked mode detector", a set of integrated radial magnetic field B_r loops arranged to measure low frequency $n = 1$ perturbation. All through the slowing down phase caused by the $n = 1$ coil, the plasma remains in H–mode, as noted by frequent ELMs, and as observed in the sharp edge density gradient, enhanced confinement, etc. Between 2000 and 2800 msec, the plasma density and stored kinetic energy drop about 20%. This is attributable to the effect of the ELMs and is typical of discharges without the slowing down of rotation by the $n = 1$ coil.[14]

The ion temperature T_i and toroidal and poloidal rotation profiles are measured by charge-exchange recombination (CER) spectroscopy of HeII and/or CVI.[15] The toroidal rotation profiles of ω_ϕ are shown in Fig. 2 versus effective normalized radius ρ ($\rho = 0$ is the magnetic axis, $\rho = 1$ is the edge/separatrix) at $t = 1990$ msec (before the $n = 1$ coil is turned on), at $t = 2700$ msec and at 2825 msec (just as the locked mode turns on). The approximate locations of $q = 1$, 2, and 3 are from the fitted magnetohydrodynamic (MHD) analysis of the magnetic configuration.[15] For all three times, the plasma is in H–mode. Note the rapid toroidal rotation at 1990, the slower rotation at 2700 (with radial structure from the $n = 1$ coil field dragging the plasma at $q = 1$ and $q = 2$) and the very low toroidal rotation at 2825. The profiles of poloidal rotation are little changed over the three times, indicating that although the magnetic braking occurs initially at a local singular surface, it is quickly transferred throughout the plasma.

The radial profiles of E_r are reconstructed from the profiles of toroidal and poloidal rotation and the MHD analysis. The CVI ion pressure gradient contribution to E_r noted in Eq. (1) is measured from CER T_i profiles and n_e Thomson scattering profiles assuming $n_i \sim n_e$ at any radius. (The absolute n_i is not needed.) Figure 3 shows E_r from $\rho = 0.6$ to 1.0 for $t = 1990$, 2700 and 2825 msec, all in H–mode. The error bar shown is $\pm 1\,\sigma$. The E_r profiles show negative E_r and $dE_r/d\rho$ at the edge. (These CER measurements do not resolve the positive E_r shear at $\rho \approx 1$ observed in previous DIII–D experiments.[9]) As the magnetic braking slows the toroidal rotation, the E_r and $dE_r/d\rho$ in the core ($\rho \lesssim 0.9$) decrease significantly and reverse sign; thus the H–mode is maintained with negative edge E_r and $dE_r/d\rho$ despite the large core changes. The electron density and temperature profiles measured by the 20 Hz Thomson scattering system on DIII–D are shown in Fig. 4 at $t = 1990$ and 2825 msec. The only significant difference is a drop in core density (in agreement with line-averaged density from interferometers) as a result of the ELMs. The ion temperature T_i profiles measured by CER (not shown) are also similar to each other at the two times and similar to the T_e profiles.

Recent theoretical work suggests that microturbulence is suppressed (and confinement thus improved) by decorrelation due to radial shear in the velocity $v_\perp \approx -E_r/B_T$ perpendicular to the equilibrium magnetic field and that the stabilization mechanism does not depend on the sign of $dv_\perp/dr$.[3,16] A simple criterion[16] for shear suppression of microturbulence is $|dv_\perp/dr| > C_s/R_o$ where $C_s = (k_B T_e/m_i)^{1/2}$ is the ion sound speed. This condition is easily satisfied in the edge ($\rho \gtrsim 0.95$) of the DIII–D H–mode discharges reported on here. In the core at $\rho \approx 0.6$, $C_s/R_o \approx 1.5 \times 10^5\ s^{-1}$ with $d(E_r/B_T)/dr \approx -1.0 \times 10^5\ s^{-1}$ at $t = 1990$ msec (before the $n = 1$ coil is turned on) and about $0.2 \times 10^5\ s^{-1}$ at $t = 2825$ msec (when the locked mode begins). Thus at no time does the core radial field shear satisfy the theoretically proposed condition for suppression of microturbulence which is consistent with the lack of an effect on the H–mode confinement despite the extreme change in toroidal rotation produced by the magnetic braking.

3. SUMMARY

Magnetic braking of plasma toroidal rotation by a toroidally localized vertical field is used to vary the plasma rotation and radial electric field profile for investigation of H–mode. This technique is a useful new tool for evaluation of the correlation between rotation, the radial electric field (and its shear) and confinement. The H–mode plasma is remarkably robust to slowing of the toroidal rotation and reversal of the core E_r and shear in E_r. The plasma maintains a reversed edge E_r and edge E_r shear, and remains in H–mode. Comparing otherwise similar discharges with and without the magnetic braking of the $n = 1$ coil field, there are no significant changes in plasma kinetic stored energy or n_e, T_e, and T_i profiles. With the magnetic braking, the plasma stays in H–mode virtually unaffected until the onset of a locked mode induces the H to L transition. As static $n = 1$ fields can slow the rotation of the plasma to produce change in radial electric field, one expects that rotating $n = 1$ fields could be used to speed rotation and increase or vary radial electric shear.[17]

Useful discussion with Keith Burrell is appreciated.

1 Itoh, S., and K. Itoh, Phys. Rev. Lett. **60** (1988) 2276.

2 Shaing, K.C., and E.C. Crume, Jr., Phys. Rev. Lett. **63** (1989) 2369.

3 Biglari, H., *et al.*, Phys. Fluids B2 (1990) 1.

4 Hassam, A.B., *et al.*, Phys. Rev. Lett. **66** (1991) 309.

5 Hinton, F.L., Phys. Fluids B3 (1991) 696.

6 Taylor, R.J., *et al.*, Phys. Rev. Lett. **63** (1989) 2369.

7 Groebner, R.J., *et al.*, Phys. Rev. Lett. **64** (1990) 3015.

8 Ida, K., *et al.*, Phys. Rev. Lett. **65** (1990) 1364.

9 Doyle, E.J., *et al.*, Phys. Fluids B3 (1991) 2300.

10 Ritz, Ch.P., *et al.*, Phys. Rev. Lett. **65** (1990) 2543.

11 Jackson, G.L., *et al.*, General Atomics Report GA-A20787 (1991) to be published in a special issue of Phys. Fluids B.

12 Hinton, F. L., and R. D. Hazeltine, Rev. Mod. Phys. **48** (1976) 239.

13 Scoville, J.T., *et al.*, Nucl. Fusion **31** (1991) 875.

14 Schissel, D.P., *et al.*, Nucl. Fusion **29** (1989) 185.

15 Gohil, P. , *et al.*, Rev. Sci. Instrum. **61** (1990) 2949.

16 Hassam, A.B., Comments on Plasma Physics and Controlled Fusion **14** (1991) 275.

17 Hyatt, A.W., *et al.*, Bull. Am. Phys. Soc. **36** (1991) 2345.

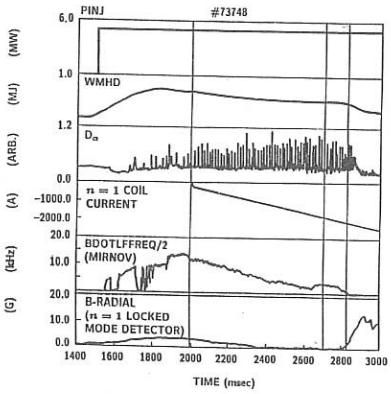

FIG. 1. Neutral beam power (PINJ), plasma kinetic energy (WMHD), D_α light, $n = 1$ coil current, toroidal plasma rotation from analog Mirnov ($\dot{B}_\theta$) frequency (divided by dominant rotating mode $n = 2$) and $n = 1$ $\tilde{B}_r$ locked mode detector (with compensation for $n = 1$ coil field).

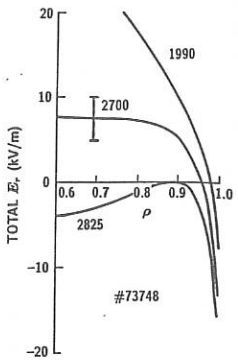

FIG. 3. Reconstructed E_r profiles from CER $[-(\vec{V} \times \vec{B})_r]$ with the ∇P_i contribution included (only $\rho = 0.6$ to 1.0 is shown).

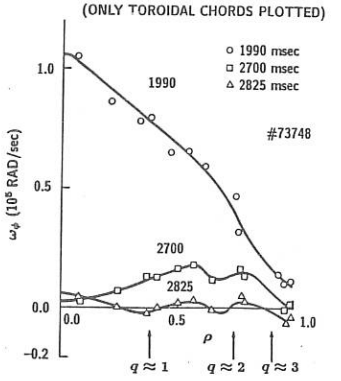

FIG. 2. Toroidal rotation profiles measured by CER at $t = 1990$ msec (before $n = 1$ coil is on) at $t = 2700$ msec and at $t = 2825$ msec (at onset of locked mode). All cases are in H-mode.

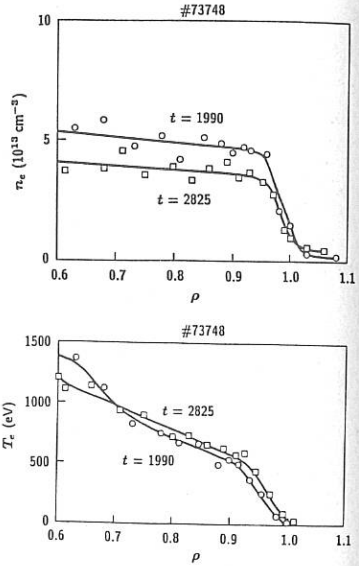

FIG. 4. Thomson scattering profiles of electron density and temperature measured at $t = 1990$ msec (before $n = 1$ coil is on) and at 2825 msec (at onset of locked mode).

CHARACTERISTIC FEATURES OF DENSITY FLUCTUATIONS ASSOCIATED WITH THE L-H-TRANSITION IN THE ASDEX TOKAMAK.

G. Dodel, E. Holzhauer, and the ASDEX-Team*
Institut für Plasmaforschung, Universität Stuttgart, Germany
*MPI für Plasmaphysik, EURATOM Association, Garching, Germany

1. INTRODUCTION

A far-infrared laser system was used to scatter from electron density fluctuations in the ASDEX tokamak [1]. Particular emphasis was placed on the L-H transition which is characterized by the establishment of a transport barrier close to the separatrix [2]. The difference in the behaviour of the fluctuations inside and outside this barrier was investigated. Another topic was the determination of plama rotation from the measured frequency and wavenumber spectra. A number of diagnostics measuring macroscopic plasma parameters was recorded with sampling rates up to 5 MHz to investigate a possible relationship with the density fluctuations.

2. CHANGES IN PLASMA PARAMETERS AT THE L-H-TRANSITION

To investigate the dependence of density flucutations on macroscopic plasma parameters we evaluated Li-beam measurements for the electron density profiles and ECE for the electron temperature. The transition into the H-phase usually occurs on a time scale of 100 μs. The sharp transition of the shoulder of the electron density profile to a steep gradient which marks the transport barrier is situated within a few mm at the separatrix position as determined from magnetic signals. There is experimental evidence that the true separatrix position is up to 1 cm further outwards. Outside the barrier both electron temperature and density drop to values comparable to or below those in the ohmic phase. The decay time of $\leq$ 100 μs for the parameters after the establishment of the transport barrier can be explained by diffusion radially and along open field lines to the walls of the vessel. A further build-up and broadening of the barrier region manifests itself by a rise in temperature and density on a ms timescale inside the separatrix. In many cases an oscillatory transition between the L- and H-mode is observed, the so-called "dithering H-mode".

Fig.1 shows the behaviour of the plasma density at two radial positions as obtained with the Li-beam for an L-H-transition and an ELM demonstrating the fast drop outside the transport barrier and the gradual increase inside [3].

Fig.2 shows the behaviour of the electron temperature as obtained from ECE for a position about 4 cm inside the separatrix for a sequence of two short H-modes demonstrating the continuous increase in T_e inside the barrier after an H-transition.

3. FLUCTUATIONS IN THE BULK PLASMA AT THE TRANSITION

With the onset of NI the plasma in the L-phase starts to rotate in the toroidal direction. The corresponding frequency shift of the scattering signals is in the ion-diamagnetic direction for co-injection. In the dominant wavenumber range $k < 4\ cm^{-1}$ these changes occur on the global momentum confinement timescale of several 10 ms. An attempt was made to measure the plasma velocity. In the bulk of the plasma drift waves are the most probable candidate for an instability. Linear theory predicts a decrease of the phase velocity with increasing wavenumber due to polarization drift and finite Larmour radius effects. Hence, for sufficiently high wavenumbers the propagation velocity of the fluctuations as measured in the laboratory frame should be dominated by the plasma velocity. Measurements were made in the equatorial channel at wavenumbers up to $10\ cm^{-1}$. The frequency shifts observed are as expected from the toroidal plasma rotation measured by spectroscopy [4]. Information on the radial position of the fluctuations could be inferred from temporal correlation with other diagnostics. For instance ELM precursor oscillations which are assumed to exist inside the transport barrier lead to a strong reduction of this frequency shift even if they do not trigger an ELM [5]. This supports the assumption that fluctuations with frequency spectra shifted towards the ion-diamagnetic side occur in the bulk of the plasma.

4. FLUCTUATIONS IN THE PLASMA BOUNDARY AT THE TRANSITION

Fluctuations coming from the separatrix region were localised in two ways:

- Using the outer vertical channel (which sees primarily radially propagating fluctuations).
- Using the equatorial channel (which sees primarily poloidally propagating fluctuations) and correlating the time dependence with macroscopic plasma parameters.

Contributions to the frequency spectra corresponding to the electron-diamagnetic drift direction which come from a region close to or outside the separatrix drop to a level comparable to or below the level in the ohmic phase. This drop occurs simultanously with the drop in density within the minimum time resolution determined by signal-to-noise considerations.

By shifting the plasma position inwards fluctuations outside of the separatrix could be measured using the outer vertical channel. Fig.3 shows the temporal development of the scattering signal power P_S for a dithering H-transition together with the D_α-monitor. One can see, that the level of fluctuations repeatedly drops back to "zero" (i.e. the noise level of the detection system) indicating the return of the barrier to an H-mode like state.

5. FLUCTUATIONS IN THE PLASMA BOUNDARY AFTER THE TRANSITION

A few ms after the transition a narrowband instability is observed to grow, which comes from the region at or outside the barrier and yields scattering signal powers above those in the L-phase. By suitable numerical filtering it can be also detected on a SX-channel (with the same distance from the plasma center as the vertical FIR channel), microwave reflectometry and the D_α signal in the divertor. It propagates in the electron diamagnetic direction. Its poloidal wavelength is estimated to be ≥10cm resulting in a propagation velocity in the laboratory frame of ≥ 6000 m/s for a frequency of 60 kHz. This instability does not lead to a dramatic increase of the D_α signal in the divertor. Taking into account the local electron pressure gradient (which yields the electron diamagnetic drift) and the toroidal plasma velocity the resulting frequency shift into the electron diamagnetic direction can only be explained by a poloidal rotation of the plasma due to a radial **E**-field as measured by spectroscopic methods [6]. Fig.4 shows the scattered power in the frequency band 55-65 kHz (electron diamagnetic direction). One can see a low power contribution in the L-mode, which disappears at the transition. For comparison, the scattered power in the frequency band 600 - 1000 kHz (ion diamagnetic direction) shows the continuous increase of the frequency shift after the L-H transition in the bulk plasma.

6. CONCLUSIONS

With the L-H transition a transport barrier is established inside the separatrix. We have separated the contributions to the scattering spectra coming from inside and outside this transport barrier. Outside the barrier the total fluctuation level as well as T_e and n_e drop to values comparable to or below the ohmic level on a 100 μs timescale whereas inside the barrier they change on a ms timescale. This behaviour is similar to observations reported on Doublet D-III-D. Evidence for poloidal plasma rotation close to the separatrix after the L-H-transition has been found from an instability with narrowband frequency spectra propagating in the electron-diamagnetic direction. In the bulk of the plasma the frequency shift is mainly in the ion diamagnetic direction due to toroidal plasma rotation.

REFERENCES

[1] E. Holzhauer et al., Rev.Sci.Instrum. **61**, 2117 (1990)
[2] ASDEX-Team, "The H-mode of ASDEX", Nucl.Fus. **29**, 1959 (1989)
[3] K. McCormick et al., this conference
[4] A. Kallenbach et al., Nucl.Fus. **30**, 645 (1990)
[5] H. Zohm et al., Nucl.Fus. **32**, 489 (1992)
[6] A. Field et al., to be published in Nucl.Fus.

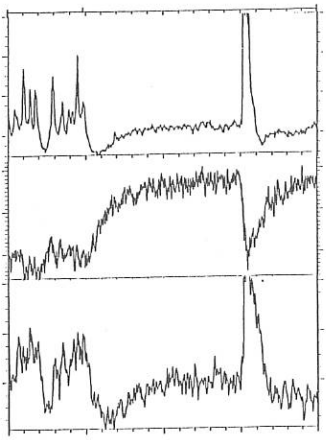

time window 20 ms

Fig.1: Top: D_α - monitor in the divertor chamber Middle: n_e (Li-beam) inside barrier Bottom: n_e (Li-beam) outside barrier

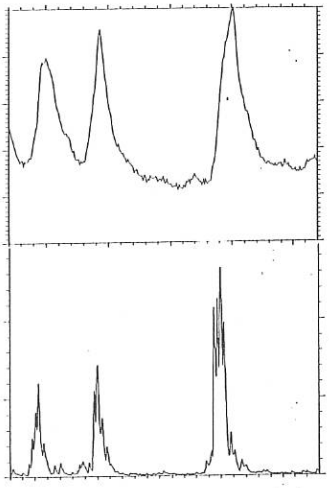

time window 2.5 ms

Fig.3: Top: D_α - monitor in the divertor chamber Bottom: P_S outside separatrix (vertical channel, ΔB=10-60 kHz)

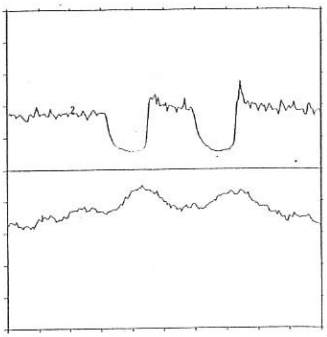

time window 10 ms

Fig.2: Top: D_α - monitor in the divertor chamber Bottom: T_e(ECE) inside barrier(sequence L-H-L-H-L)

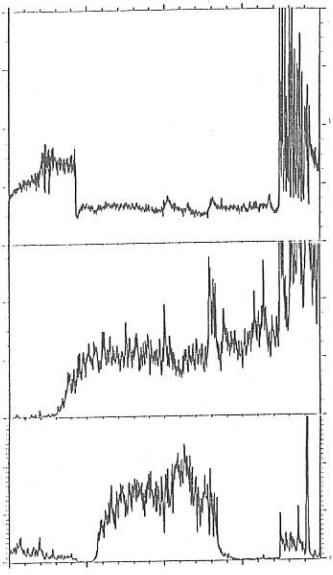

time window 200 ms

Fig.4: Top: D_α - monitor Middle: P_S in the bulk plasma (ΔB=600-1000 kHz, ion diamagnetic direction) Bottom: P_S in the separatrix region (ΔB=55-65 kHz,electron diamagnetic direction)

H-mode power threshold in ASDEX

F. Ryter, U. Stroth, F. Wagner, ASDEX-group, NI-Group

Max-Planck-Institut für Plasmaphysik, EURATOM-IPP Association
D-8046 Garching, FRG

1. Introduction

The H-mode is one of the most promising confinement regimes for a future reactor. It is therefore important to identify the parameters determining the minimum power (power threshold, P_{thres}) necessary to reach it. Moreover, the results could give indication about the underlying physics of the L to H-mode transition. Previous studies performed for ASDEX [1] showed that an open divertor configuration (inducing higher neutral density in the main chamber) required more heating power to obtain the H-mode than the initial closed version. In this paper we present new results from data obtained with the latest closed divertor configuration of ASDEX under boronized conditions. These conditions were favourable for the H-mode which could be reached over an extended operational window.

2. Experimental conditions

The H-mode power threshold for the ASDEX initial closed divertor configuration was described in [2]. Some of the essential results given in [2], for co-NBI, are also found with the new data presented here and are only summarised as follows. In ASDEX the vertical plasma position determines the magnetic configuration as double-null for -5 mm $\leq z \leq$ +5 mm or single-null outside of this z-window. The maximum z-displacement is 40 mm i.e. 10% of the minor radius a = 0.4 m, for the data used here. The power threshold in the single-null configuration for which the ion gradB drift is towards the active divertor is twice lower than the other single-null or the double-null configuration. Moreover, the electron density prior to the H-mode must be above 2 10^{19} m^{-3} in order to access the H-mode in a wide operational window. In this paper, we analyse the dependence of the power threshold versus plasma current (I_p), magnetic field (B_t) and/or edge cylindrical safety factor q_a .

For this purpose, we take all kinds of H-mode discharges (ELMy or ELM-free) into account. The reason for this choice is that we assume the transition physics into the ELMy and ELM-free H-mode regimes to be the same. Discharges showing short H-mode phases after sawtooth crashes are considered to be at the threshold and named marginal (M). These M and the L-mode data are essential to unambiguously determine the power threshold. The power considered here is the total heating power ($P_{tot} = P_{OH} + P_{abs}$) where P_{OH} is the residual Ohmic power and P_{abs} is the NBI power absorbed by the plasma. P_{abs} is quantized by steps of ≈0.2 MW linked with the number of sources in operation.

The operational window of the discharges considered in the following is: 0.2 MA $\leq I_p \leq$ 0.46 MA, 1.1 T $\leq B_t \leq$ 2.8 T, leading to a variation of q_a between 2.3 and 4.5. Hydrogen (H^o) or deuterium (D^o) NBI was injected (co-injection) into deuterium plasmas, with $P_{abs} \leq$ 2.3 MW for H^o and $P_{abs} \leq$ 2.5 MW for D^o. It is observed that the injected species practically play no role in determining the power threshold, provided the background plasma is the same. This can be understood by the fact that the plasma features (transport, profiles) at the time of the L-H transition 30-150 ms after the beginning of the NBI pulse, are essentially determined by the (initial) background species. The background species, shown in [2] to increase P_{thres} by nearly a factor of 2 when changed from deuterium to hydrogen, was not varied in the present set of data.

In the divertor H-mode, the distance between plasma surface and the next protection limiter, which prevents the occurrence of the H-mode when it is smaller than typically 1 cm, was kept large enough so that the data are not biased by this effect.

3. Results

3.a. Main dataset

The essential of the H-mode discharges (main dataset) consists of discharges having the favourable single-null configuration and a density above 2 10^{19} m^{-3} for the reason mentioned in section 2.

A schematic overview of the results is given in Fig. 1. A clear minimum appears approximately along the $q_a = 3$ line. This suggests that two opposite phenomena might be in competition to determine the power threshold. We therefore will separately analyse each side of the minimum to find out whether the power threshold in both regions is governed by different parameters. Due to the linear relation between I_p, B_t and q_a, the identification of the relevant parameter(s) is not straightforward. For this purpose, the power was plotted versus I_p, B_t and q_a. The plot (if any) giving the clearest separation between L and H discharges indicates the relevant parameter. For $q_a \geq 3$, B_t clearly has to be chosen (Fig. 2). Fitting the boundary yields: $P_{thres} = 0.5\ B_t^{1.25}$ [MW, T].

For $q_a \leq 3$, it appears that the B_t dependence of P_{thres} found in Fig. 2 remains, but that an additional strong increase of P_{thres} with decreasing q_a dominates. This behaviour is shown in Fig. 3. The fit of the boundary gives: $P_{thres} = 6.64 - 1.97 q_a$ [MW].

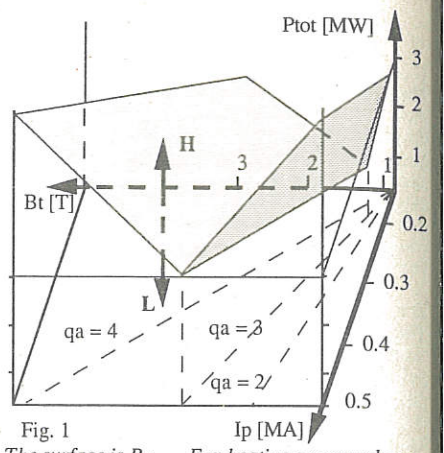

Fig. 1

The surface is P_{thres}. For heating powers above this surface the H-mode is achieved.

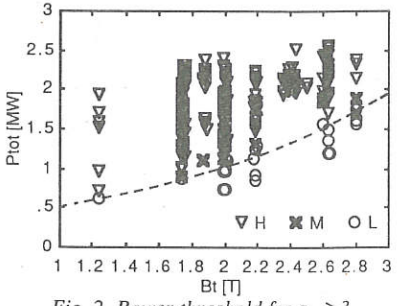

Fig. 2. Power threshold for $q_a \geq 3$

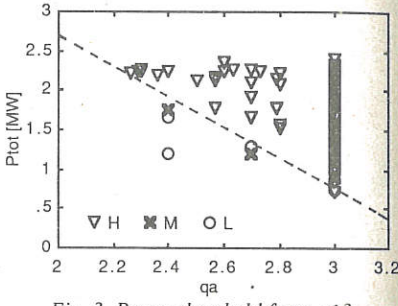

Fig. 3. Power threshold for $q_a \leq 3$

The dashed lines in both figures indicate the fits given in the text.

We can therefore assume, in a first approximation, that the power threshold in the two regions roughly separated by the $q_a = 3$ line have dependences governed by two different parameters: q_a for $q_a < 3$ and B_t for $q_a \geq 3$. The boundary between both regions was analysed in more detail by looking for the experimental minimum of P_{thres} for each available value of the current.

The results are given in Fig. 4. The line drawn in this figure is the intersection of the surfaces of P_{thres} in both regions ($q_a<3$ and $q_a\geq 3$) determined by the fits given above. It is the minimum of P_{thres} for each value of I_p. I_p is introduced by the formula for q_a. The curvature of the line is due to the increase of B_t as I_p is increases along the boundary. The good agreement of the line with the experimental points indicates that the I_p dependence of P_{thres} (if any) is weak. The different dependences found for the two regions suggest different physics in each region, as discussed in section 4.

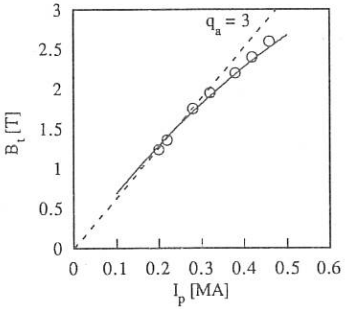

Fig. 4. Minimum of P_{thres} in the I_p/B_t plan: circles are the experimental data, the line is obtained from the fits as indicated in the text.

3.b. Subsets of the data

Discharges with double-null configuration (not included in the main dataset) show a stronger B_t dependence than that given in Fig. 2. No information is available for $q_a < 3$.

ELM-free discharges require a 0.5 - 0.75 MW extra heating compared to the ELMy ones in the whole B_t/I_p window. However, the q_a and B_t dependences of the ELM-free power threshold are comparable to those given in Fig. 2 and 3, as shown by Fig. 4 and 5. This is in agreement with the interpretation that ELM-free discharges are achieved for an edge electron temperature higher than that of ELMy discharges [3].

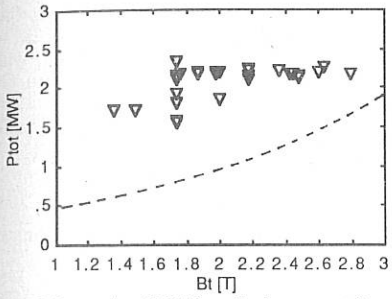

Fig. 5 P_{thres} for ELM-free discharges $q_a\geq 3$ The dashed lines are that of Fig. 2 and 3 respectively

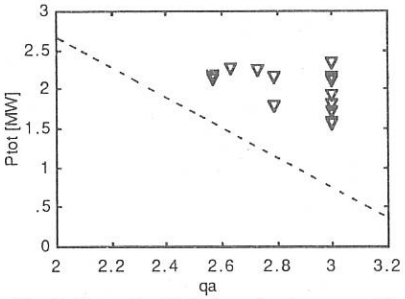

Fig. 6 P_{thres} for ELM-free discharges $q_a\leq 3$

A limited database of ctr-NBI discharges (I_p and B_t reversed) for $q_a \leq 3$ shows the following features. The influence of the divertor configuration on P_{thres} almost disappears. The q_a dependence does not exist any more, but a B_t dependence like $P_{thres} = 0.4\ B_t^{1.25}$ [MW, T] is compatible with the data, in the $q_a \leq 3$ region.

4. Discussion

The q_a dependence of P_{thres} for the main data set in the $q_a < 3$ region can be interpreted as follows. In the low q_a operational window, a strong toroidal asymmetry of the power deposition on the divertor neutralization plates was observed in ASDEX [4]. This effect was linked to the creation of magnetic islands (and ergodic regions) by errors fields due to slight

misalignments of the toroidal field coils. The perturbations of the plasma edge associated with these effects increase strongly as the $q_a = 2$ surface approaches the plasma edge. The asymmetry of the toroidal power deposition for representative discharges of the present work plotted versus q_a (Fig. 7) shows a rapid increase for $q_a < 3$ which can be compared to the increase of P_{thres} of Fig. 3. This is in agreement with numerous indications that the L-H transition happens at the plasma edge and with the observations of JFT-2M showing an increase of the power threshold when error fields are applied on purpose [5]. As small coils misalignment cannot be avoided, induced islands and ergodization may be important for P_{thres} in ITER which will operate at low q_a.

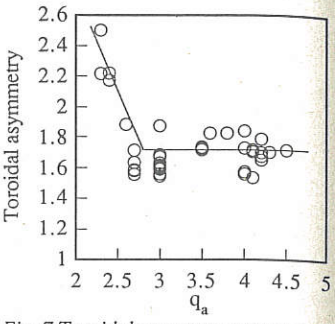

Fig. 7 Toroidal asymmetry versus q_a

The B_t dependence shown in Fig. 3 might reflect the L-H transition physics. Similar dependences were observed in other tokamaks [6 - 8]. The theory [9] presently meeting best the experimental observations does not predict such a B_t dependence whereas the ones described in [10,11] do.

The observations for ctr-NBI could possibly be explained, in the frame of the theory given in [9], by the large amount of beam ions lost to the wall in this case. It must be noticed that the increase of P_{thres} with hydrogen background compared to deuterium background is consistent with the B_t dependence if the gyro-radius plays a role.

5. Conclusion

The H-mode power threshold has a minimum along a line defining two region in the operational window of ASDEX. In the low q_a region, P_{thres} increases with decreasing q_a whereas in the $q_a \geq 3$ region it increases with B_t. The possible implications for ITER can be expressed as follows. The B_t dependence does not seem to restrict the future H-mode operation of ITER. In fact, it can be inferred from the present tokamaks [6-8] that the power threshold increase with machine size is much weaker than that of the typical installed power of the present design. On the other side, ITER being planed to operate at low q_a, the dramatic increase of P_{thres} in this region as described in the present paper, might have consequences for the ITER operation in the H regime. A better identification of this possible problem seems to be necessary as well as a discussion of the compensation of the errors which could be envisaged.

Acknowledgement

The authors are glad to thank K. Lackner for fruitful discussions. The efforts of the technical and experimental teams are greatly acknowledged.

References

[1] F. Wagner, et al., proceedings of the 13th IAEA Int. Conf. on Plasma Physics and Controlled Nuclear Fusion, Washington DC, 1-6 October 1990, Vol.1, 277, (Vienna 1991)
[2] ASDEX Team, Nucl. Fus. **29** 1959 (1989)
[3] H. Zohm, et al. Nucl. Fus. **32** 489 (1992)
[4] J. Neuhauser, et al. proceedings of the 13th IAEA Int. Conf. on Plasma Physics and Controlled Nuclear Fusion, Washington DC, 1-6 October 1990, Vol.1, p. 365, (Vienna 1991)
[5] A. W. Leonard, et al. Nucl. Fus. **31** 1511 (1991)
[6] JFT-2M Group, presented by Y. Miura, proceedings of the 3rd H-Mode workshop,10th-12th June 1990, Vol.1, p 141, ed. by M. Keilhacker, JET.
[7] K. H. Burrell, et al., Plasm. Phys. Contr. Fus. **31**, 1649, (1989)
[8] JET Team, presented by D. J. Campbell, ib.
[9] K. C. Shaing and E. C. Crume Jr., Phys. Rev. Lett. **63**, 2369 (1989).
[10] R. R. Weynants, et al., proc. of the 3rd H-Mode workshop, 1990, Vol.1, p 475, ed. by M. Keilhacker, JET.
[11] A. Rogister, ib. p. 619.

MEASUREMENT OF THE TOROIDAL MOTION OF FINE-SCALE DENSITY STRUCTURES IN JET PLASMAS

A E Costley, P Cripwell and T Fukuda*

JET Joint Undertaking, Abingdon, Oxfordshire, OX14 3EA, UK
*Naka Fusion Research Establishment, JAERI, Japan

Introduction Measurements with a four channel *radial* correlation reflectometer have demonstrated the existence of fine-scale density structures in JET plasmas /1/. Under ohmic and H-mode conditions the radial extent of the structures is small ($\lesssim$ 5 mm). However, under L-mode conditions the radial extent of the structures depends on the beam power and for high levels of beam power (~ 15 MW) is typically $\gtrsim$ 30 mm. The measurements suggest that the structures are moving perpendicularly to the direction of view, ie. toroidally and/or poloidally, but they cannot give the speed or direction of the motion. In this paper we present the first measurement with a *toroidal* correlation reflectometer. From the measurements we determine the toroidal velocity of the structures and we estimate their toroidal extent.

Toroidal Correlation Reflectometer The toroidal correlation reflectometer consists of two independent reflectometers which probe the plasma in the mid-plane through two antennas toroidally separated by 155 mm (figure 1). One of the reflectometers is the standard JET multichannel instrument /2/ while the other has been specially constructed for this measurement. The probing radiation is polarised in the ordinary mode and so reflection is off the plasma frequency layer. Both reflectometers operate at the same radiation frequency (29 or

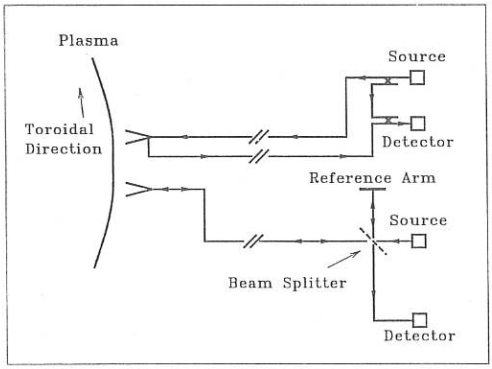

Fig. 1. Schematic of the toroidal correlation reflectometer installed on JET.

34 GHz) so that the two reflecting layers are always at the same radius. For the measurements presented, the reflection layer is located in the boundary of the plasma ($3.75 < R < 4.0$ m). The detection systems in both cases are of the homodyne type and the data is usually recorded with a bandwidth of 100 kHz.

The measurements are analysed using standard spectral analysis techniques /3/. From the analysis, the crosspower spectrum, $G(\omega)$, the crossphase spectrum, $\theta(\omega)$, and the coherence spectrum, $\gamma(\omega)$, are determined. The value of the coherence is between unity (identical signals) and zero. However, for a finite length data set, there is a lower level of statistical significance, γ_r, which represents the coherence between two independent random signals. For our measurements, γ_r is typically 0.18.

Measurements Measurements have been obtained for a range of plasma conditions; ohmic, L-mode and H-mode. In the latter two cases the plasmas are heated by neutral beam injection. The results are qualitatively different for these three cases.

Ohmic In this case, the level of coherence is generally at the random level (γ_r) and the crossphase spectrum shows wide scatter. A typical measurement is shown in figure 2a.

L-Mode In this case, the level of coherence is significant across the entire observed frequency band and the crossphase increases linearly with frequency (figure 2b). As the neutral beam power is increased, the slope of the crossphase decreases.

H-Mode In this case, the level of coherence is significant but the crossphase is independent of frequency (figure 2c).

Interpretation As in the case of the earlier radial measurements, we interpret the results in terms of perturbations in the density profile, ie fine-scale density structures. The measurements do not show any evidence for such structures under ohmic conditions. However, under L-mode conditions the high level of the coherence, combined with the frequency dependence of the cross-phase, suggests that the structures rotate toroidally. The phase difference is due to the rotation and it can be shown that the slope of the cross phase spectrum is simply related to the rotation velocity. It is instructive to compare the rotation velocity of the fine-scale density structures obtained with the toroidal correlation reflectometer with the local plasma rotation obtained independently with the charge exchange (CX) diagnostic /4/. This is done in figure 3 for a wide range of neutral beam powers (2-15 MW). It can be seen that, within measurement uncertainties, the two velocities agree. The uncertainty on the CX includes a contribution due to the uncertainty on the radial location of the reflecting layer.

Further, under these conditions, we can estimate the toroidal extent of the structures from the auto correlation function of the individual reflectometer signals. This will be greater than zero for a time, T_c, which is approximately the time taken by the structures to pass in front of the reflectometer antenna. Hence the toroidal extent of the structures is simply the product of

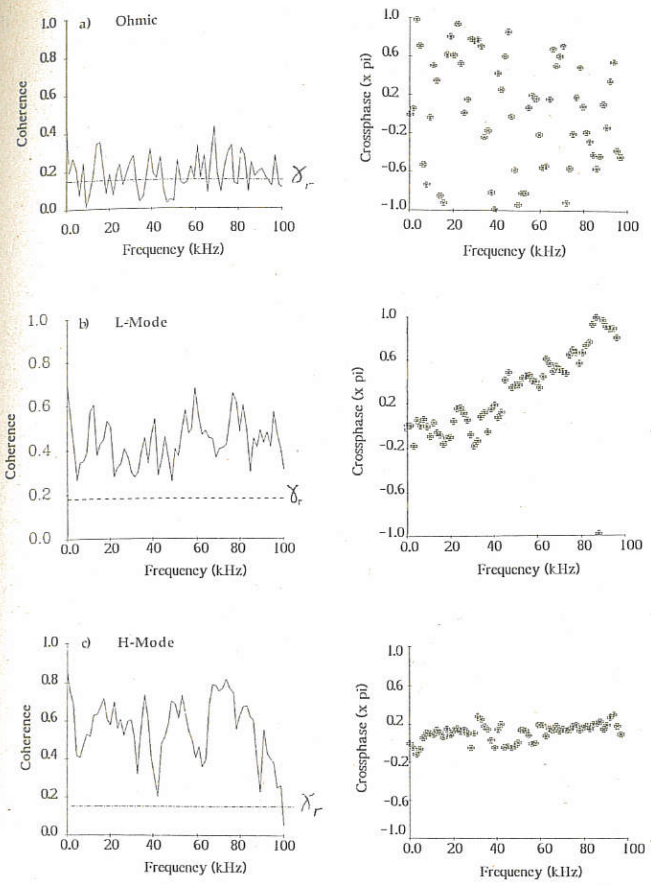

Fig. 2. Coherence and cross phase measurements under (a) ohmic, (b) L-mode and (c) H-mode conditions.

T_c and the toroidal rotation velocity of the plasma. Typically we find the toroidal extent to be in the range 1-5 m. Further work is required to determine any dependence on other plasma parameters. Possibly, the structures have a helical configuration corresponding to the helical magnetic field. In order to investigate this, an additional reflectometer located at a different polodial location is required but such a device has not been installed on JET.

Under H-mode conditions, the frequency independence of the crossphase suggests that the structures are either moving toroidally at very high velocity or, more plausibly, poloidally. The CX diagnostic indicates that under these conditions there is usually a poloidal component to the

plasma motion of similar magnitude to the toroidal component. It is most likely, therefore, that under these conditions the reflectometer measurements are dominated by the poloidal motion.

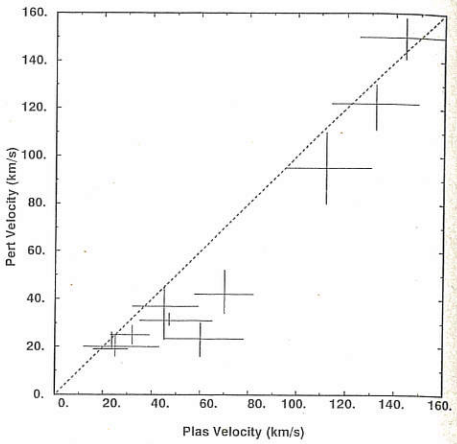

Fig 3. Comparison between the measured toroidal velocity of the perturbations and the toroidal velocity of the plasma measured with the CX diagnostic for a range of neutral beam powers (2-15 MW).

Conclusions A toroidal correlation reflectometer has been constructed and used on JET. The measurements confirm the existence of fine-scale density structures in L-mode and H-mode plasmas. Comparison with CX diagnostic measurements, shows that for L-mode plasmas the structures rotate with the plasma. The toroidal extent of the structures is determined to be in the range 1 - 5m. Under H mode conditions, the structures appear to rotate poloidally. In order to determine the poloidal motion of the structures an additional poloidal correlation reflectomer is required.

Acknowledgement We would like to thank Drs R König and H Morsi for providing the CX rotation velocity data.

References

/1/ Cripwell P and Costley A E, Proc. 18th European Conf. on Controlled Fusion and Plasma Physics, 15C, Part 1, 20, Berlin (1991).

/2/ Prentice R, Sips A C C, Fessey J A and Costley A E, Proc. 17th European Conf. on Contr. Fusion and Plasma Heating, 14B, Part IV, 1500 Amsterdam (1990).

/3/ Bendat J S and Piersol A G 'Random Data : Annalysis and Measurement Techniques' Wiley (1971).

/4/ Boileau A, von Hellermann M, Horton L et al, Pl. Phys and Contr. Fus. 31, 779 (1989).

Plasma Flows and Fluctuations During H-modes in TFTR

C.E. Bush[a], B.C. Stratton, E.J. Synakowksi, N. Bretz, R. Budny, D.S. Darrow, R.Durst[b], R. Fonck[b], E.D. Fredrickson, E. Mazzucato, K.M. McGuire, S.S. Medley, R. Nazikian, S. Paul, A.T. Ramsey, J. Schivell, S.D. Scott, G. Taylor, R.M. Wieland, and S. Zweben
Princeton University, Princeton NJ, USA
[a]Oak Ridge National Laboratory, Oak Ridge TN, USA
[b]University of Wisconsin, Madison WI, USA

Introduction

Popular theories [1-3] of transitions to the H-mode regime are based on the concept of a fundamental interdependence of plasma poloidal and toroidal flows and plasma magnetic and density fluctuations. To understand the physics of the H-mode transition and confinement, the details of the characteristics of the H-mode rotation dynamics and correlation with fluctuations must be studied. In TFTR the transition is usually from a supershot to a circular limiter H-mode [4,5]. However, all of the relevant H-mode phenomena are observed. The density profile is peaked in the center for both the supershot and the resulting H-mode; the main change being a modest increase in confinement in the H-mode edge plasma ($r/a > 0.8$).

The leading model proposed to explain the physics of the H-mode transition is that suppression of edge turbulence due to non-ambipolar sheared ExB flow generation leads to bifurcation to the enhanced confinement regime. The main component of the ExB flow is due to the radial electric field, E_r, which is given by the zeroth order force balance equation

$$E_r = \frac{1}{Z_i e}\left(\frac{T_i}{n_i}\frac{dn_i}{dr} + \frac{dT_i}{dr}\right) + V_\theta B_\phi - V_\phi B_\theta . \qquad (1)$$

where i, V_θ and V_ϕ refer to the same impurity ion (carbon for TFTR).

The parameters in the equation which can be measured (or deduced) on TFTR are V_ϕ, n_i (profile shape), T_i, B_ϕ, B_θ and Z_i. Values of $V_\phi(r)$ and $T_i(r)$ are determined experimentally using charge exchange recombination spectroscopy (CHERS). TFTR has an inner bumper graphite limiter and the main impurity ion is carbon. Line emission for C^{5+} (n = 8 - 7; 5292 Angstroms) is used for the CHERS measurements. An average value of the ExB flow velocity at the plasma edge is inferred from the microwave scattering spectra of density fluctuations. (Spatially resolved measurements for determining $V_\theta(r)$ and $E_r(r)$ are not available on TFTR.)

Results and Discussion

The n_e, n_C, and D_α signals along with $V_\phi(t)$ and $T_i(t)$ for the outer three chords of the CHERS diagnostic are plotted in Fig. 1 for a typical TFTR H-mode plasma. The n_C profile shape is deduced from C^{5+} line brightness data from CHERS. Details of the V_ϕ profile may reflect the dynamics of the transition and the spatial extent of the bifurcation region, although shear in poloidal flow is expected to be much more effective than shear in toroidal flow in suppressing plasma turbulence. Recent theoretical studies [6] indicate that there are some regimes in which V_ϕ should play an effective part in H-mode physics. Usually during the TFTR supershot to H-mode transitions, V_ϕ in the outer 25 cm layer of plasma becomes less positive (+ indicating rotation in I_p direction). This trend is obvious for three outer radial positions of the plasma of Fig. 1. For example at R = 3.14 m, $V_\phi = 0$ just before the transition and spins up in the counter direction ($V_\phi < 0$) during the transition and the

final H-mode. Thus, V_ϕ shifts toward the counter direction at the H-mode transition and $T_i(R)$, $n_e(R)$, and $n_c(R)$ begin to increase within a broad region at the plasma edge (outer 20 to 25 cm). This behavior is also clear in Fig. 2, which is a plot of $V_\phi(r)$ profiles for three times of the H-mode of Fig. 1; before, during, and at the end of the transition. The shift in the profile in the region 2.94 to 3.24 m is obvious. In this plasma, V_ϕ in the core ($R \leq 2.94$ m) remains constant during the transition, while a large change (~ 25 km/sec) takes place at 3.04 m. Also shown are profiles of $T_i(R)$, $n_e(R)$, and $n_c(R)$. The drop in the D_α signal and the change in V_ϕ can be fairly slow for TFTR H-modes. The shift in V_ϕ, i.e. ΔV_ϕ, takes place in 10 ms or less for some H-modes, but often ΔV_ϕ occurs over 10's of milliseconds. Density fluctuation and toroidal velocity data are shown in Fig.3 for a typical TFTR H-mode. Figure 3(a) shows a contour plot of the scattered power due to density fluctuations at the plasma edge. The D_α signal and $V_\phi(r,t)$ for three outer radial positions are shown in Figs 3(b) and 3(c) respectively. Just as in Fig. 1, during the transition ($t > 4.02$ s) V_ϕ at the edge shifts toward the counter direction and at about the same time shift in the microwave scattering spectra begins to take place, indicating a steady increase in poloidal rotation in the direction of electron diamagnetic drift (V_{De}). A decrease in density fluctuations at the transition was not observed; however, high frequency magnetic fluctuations usually decrease. The shift in the spectra beginning at the transition (at ~ 4.02 s) is most likely due to a poloidal spinup at the plasma edge, in the direction of V_{De} and is usually of order $\geq 10^4$ km/s. This poloidal flow is also consistent with the establishment of a radially inward pointing electric field and has magnitude given by $-E_r x B_\phi$. After ELMs begin at 4.15 s, V_ϕ becomes more co- going and the shift in the density fluctuation spectra decreases. This trend away from the H-mode regime is accelerated after 2.5 MW of NBI power is turned off at ~ 4.3 s.

Preferential loss of fast ions, especially counter injected particles at the injected beam voltage (90 - 110 keV) and the 1/2 and 1/3 energies could lead to radial electric fields of magnitudes which are expected to be sufficient to cause effects on turbulence due to shear in the $E_r \times B_\phi$ flow. An indication of possible orbit loss effects is the fact that a mixture of co- and counter-NBI is needed for H-mode transitions on TFTR. Small contributions by energetic fusion product ions such as the 3 MeV proton and 800 keV He-3 ion from the D-D reaction are also possible since they have large banana orbits which intersect the limiters. On TFTR, fast ion probes [7] at the plasma edge, usually at the outer limiter radius, are used to monitor trapped energetic beam and fusion product ions directly.

At the transition, the signal of the fast ion probe near the midplane shows a prompt increase. The probe signal is a measure of the energetic ion flux (EIF) and is plotted in Fig. 4 (a) along with the (b) D_α signal. The prompt increase in the energetic ion flux to the probe just before 4.0 s is clearly correlated with the beginning of the decrease in the D_α signal. In fact, the rate of rise of the EIF signal appears to be greater than the rate of decrease of the D_α signal. There is a second decrease in D_α light 25 ms later at t ~ 4.02 s and a corresponding second prompt increase in EIF. ELMS begin just after 4.04 s and there are corresponding oscillations in EIF. The initial changes in EIF and D_α light appear to be simultaneous. Quantitative determination of whether or not one signal leads the other would have implications as to whether or not the EIF rise is a precursor to or a consequence of the transition.

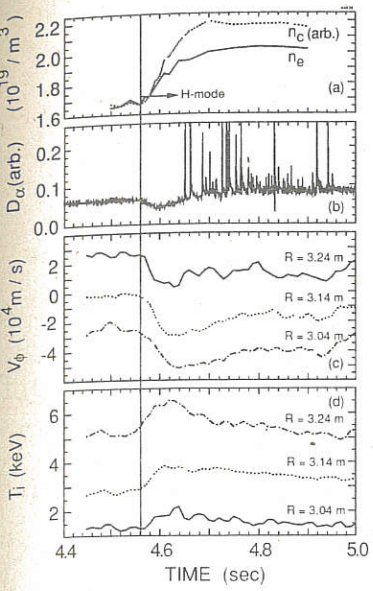

Fig. 1 Variation of plasma parameters for a typical TFTR H-mode. (a) n_c and n_e (b) $D\alpha$ signal (c) Values of V_ϕ for four outer CHERS positions. (Note: Spatial resolution of V_ϕ data ~ ± 2.5 cm).

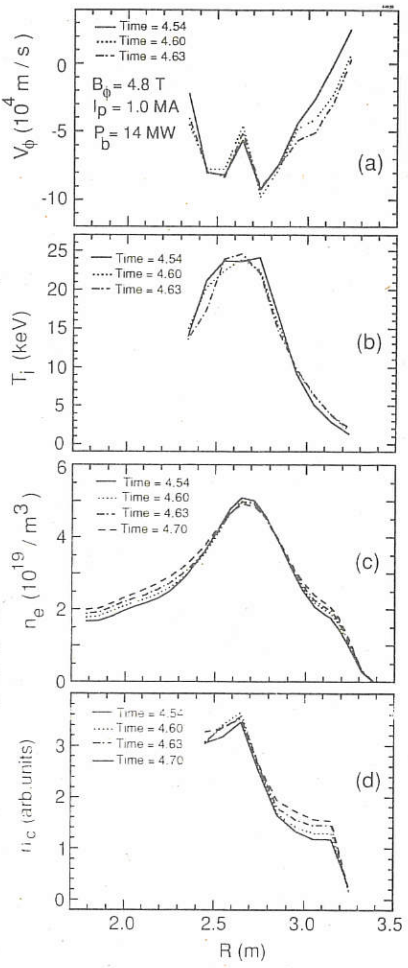

Fig. 2 Toroidal velocity, V_ϕ, and also T_i, n_e, and n_c profiles for an H-mode plasma, before the transition (4.54 sec), during the H-mode ELM free period (4.60 sec), and just at the first ELM (4.63 sec).

Conclusions

Detailed measurements of V_ϕ have been made during supershot to H-mode transitions on TFTR. Also, a measure of the average value of V_θ in the plasma edge is inferred from microwave scattering spectra of density fluctuations. V_ϕ usually shifts toward the counter direction during the transition, with ΔV_ϕ ~ 10 - 35 km/sec at the edge. The shift in the density fluctuation spectra implies an ExB flow velocity of 10 - 20 km/sec in the V_{De} direction. Increases in edge Ti and the gradient in edge carbon concentration are also observed. The prompt fast ion efflux to an edge probe at the beginning of the transition is consistent with a rapid charge up of the plasma which could lead to an inwardly pointing electric field E_r.

References

[1] Biglari, H., Diamond, P.H., and Terry, P.W., Phys. Fluids **B2** (1990) 1.
[2] Shaing, K. C., and Crume, E.C., Jr., Phys. Rev. Letters **63** (1989) 2369.
[3] Hassam, A. B., et al., Phys. Rev. Letters **66** (1991) 309.
[4] Bush, C. E., Goldston, R.J., Scott, S.D., et al., Phys. Rev Letters **65** (1990) 424.
[5] Bush, C. E., et al., submitted for publication in Nuclear Fusion.
[6] Kim, Y. B., Diamond, P.H., and Groebner, R.J., Phys. Fluids B **3** (1991) 2050.
[7] Zweben, S. J., Nucl. Fusion **29** (1989) 825.

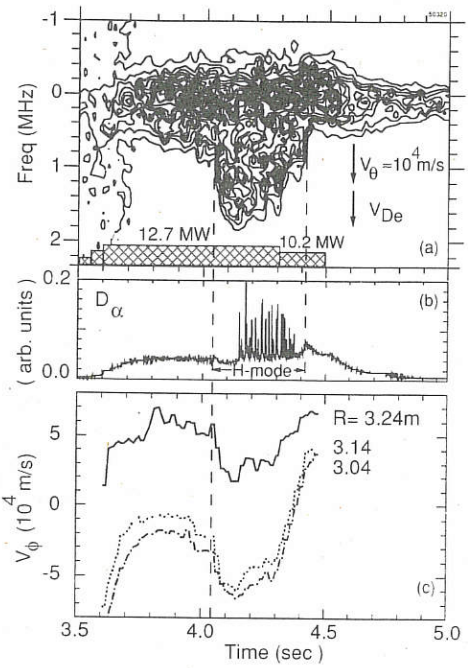

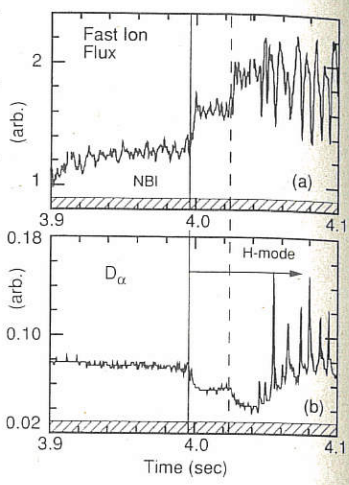

Fig. 4 Time evolution of (a) the fast ion efflux and (b) D_α signal for an H-mode plasma. The fast ion signal increases promptly at the transition.

Fig. 3.

(a) Microwave scattering data showing a shift consistent with a 10 - 20 km/s poloidal rotation in the V_{De} direction. X-mode scattering with $K_\theta = 5.4$ cm.$^{-1}$ (b) Time evolution of D_α light. (c) V_ϕ data for a broad plasma edge.

Autooscillating L–H transitions under ECCD in T–10

Voitsekhovich I.A., Kislov D.A., Parail V.V., Razumova K.A.

I.V.Kurchatov IAE, Moscow, Russia

In the recent experiments on current drive by EC waves (ECCD) in T-10-tokamak it has been found out that the transition from the L-mode into the original autooscillating mode, characterized by the periodic ($\tau \simeq 10^{-5}$ s) release of suprathermal electrons upon the chamber walls with an increase in the launched RF-power occurs. A theoretical analysis of the reasons for the emergence of relaxational oscillations in the near-wall region is realized in a given study.

1. Experimental results.

Periodic releases of fast electrons - registered with SXR-probes (Fig.1) - were observed under ECCD in T-10-tokamak. Autooscillating modes were observed at a rather low plasma density, n_e, only, when the parameter $\alpha = P/n_e$ (P is the power of EC-waves) exceeded $\alpha_{cr} = 2 \cdot 10^{-6} W \cdot cm^3$. With the further increase in α ($\alpha > \alpha_{cr}$) a non-controlled plasma density rise occured with the subsequent reduction in α to the level $\alpha \simeq \alpha_{cr}$. The mentioned autooscillations are developed only when EC-waves give birth to the beam of accelerated electrons; when the radiation was launched strictly-perpendicular to the magnetic field, B, into the plasma, the birth of accelerated electrons and autooscillations did not occur even in the low density modes of operation (at $\alpha > \alpha_{cr}$). According to calculations, EC-waves in T-10 should drive suprathermal electrons in the central part of the plasma column only. The presence of periodic X-ray radiation oscillations at the chamber wall speaks about the emergence of fast electrons in the near-wall zone. It is natural to assume that the emergence of suprathermal electrons at the periphery is caused by their anomalous diffusion along the radius, and the time of that diffusion should be shorter than the time of fast electron cooling due to their collisions with thermal electrons. Then our considerations follow the scheme:

1. Fast electrons run off along the field lines to the chamber wall that results in the emergence of a potential, φ, in the near-wall zone. The magnitude of φ is defined by the equality between the longitudinal electron flux and the ion one.
2. The presence of an inhomogeneous radial electric field results in the emergence of a shear plasma rotation.
3. The shear plasma rotation, in its turn, provides stabilization of the drift-type instabilities [1] which cause an anomalous diffusion of suprathermal electrons.
4. Suppression of the instability reduces the flux of fast particles towards the periphery that results in the reduction in φ.

It is evident that the process described by a given logic scheme can have a cyclic nature under definite conditions.

2. Model of autooscillating L–H transitions.

For a self-consistent representation of L-H transitions the following set of equations is used:

$$n_e V_{Te} \exp(-e\varphi/T_e) + n_b V_b \exp(-e\varphi/T_b) = C_s(n_e + n_b) \quad (1)$$

$$\frac{dn_b}{dt} = \frac{PW/W_0}{VT_b} - \nu n_b - \frac{n_b W}{\tau_i W_0} \quad (2)$$

$$\frac{dW}{dt} = \gamma_0 W - \gamma_1 \varphi \frac{W - W_T}{W + W_0} - \gamma_2 W^2 \quad (3)$$

where $C_S=((2T_e+e\varphi)/m_i)^{1/2}$, $V_{b(e)}=(2T_{b(e)}/m_e)^{1/2}$, n_b is the density, T_b is the temperature of suprathermal electrons, W is the energy density in oscillations, W_T is the level of a thermal noise in the plasma, W_o is the normalization constant, γ_o - γ_2 are constants, other designations are standard ones. According to (1), a potential emerging at the plasma edge provides an equality between the longitudinal electron (thermal and suprathermal) flux and the ion one. A characteristic width of the layer under the potential φ in the radial directions is $\Delta r \simeq (DR/C_s)^{1/2}$, where D is the transversal plasma diffusion coefficient in the limiter shadow. Below we limit ourselves by a zero-dimensional approximation, solving the problem in the narrow near-wall zone, $a-\Delta r \le r \le a$. Equations (2) representing the balance of fast electrons in the zone under consideration takes account of the fact that the diffusive flux from the centre, provided by the presence of oscillations and, as a result, proportional to W, is a source of fast particles at the periphery. The second term in the right-hand side of Eq.(2) takes account of fast particle maxwellization (ν is the frequency of collisions between fast electrons and thermal ones). The third term there represents an anomalous particle diffusion in the process of their interaction with oscillations (life-time of fast electrons due to their anomalous diffusion along the radius is assumed to be equal $\tau_E=\tau_1 W_o/W$, where τ_1 is the parameter independent of W).

The energy density behaviour in oscillations is represented by a purely-model way. Here the first term in the right-hand side represents the linear drive of oscillations with the increment γ (of the order of a drift frequency), the second term phenomenologically represents suppression of oscillations due to a shear plasma rotations in case of the high near-wall potential emergence, $\varphi \simeq T_b$. The presence of a non-linear decrement dependence on the level of energy oscillations reveals the conclusion, which follows from the numerical calculations [1], that with a rise in the amplitude of oscillations their capability of stabilization due to a shear rotation is reduced. The third term in the right-hand side of Eq (3) represents (again in a purely-model way) saturation of an oscillational level due to non-linear processes of the wave redrive within the spectrum.

The sets of equations (1-3) naturally cannot pretend to a quantitative agreement with the experimental results, we speak only about representation of the process dependences on the plasma parameters.

3. Analysis of autooscillations.

The set of equations (1-3) was solved numerically. It has been shown that with an increase in the launched specific power, P/n_e, the discharge makes the transition, in succession, from L-mode into a self-oscillating one first and, finally, into the H-mode (Fig.2). The range of changes in the specific power, within which the selfoscillating mode exist, satisfies the inequality $4.2Vn_eT_b/\tau_1=P_1\le P\le P_2=10^3Vn_eT_b/\tau_1$. For the T-10 parameters it turns out to be rather wide. The time dependence of the quantities W, n_b, φ in one of the autooscillating modes is given in Fig.3. One can see that a high level of oscillations, assisting in the enhanced anomalous transport, results in the fast particle density growth in the near-wall zone (Fig.3c). The enhanced beam particle release upon the limiter provides a steep rise in the plasma surface potential (Fig.3b), $e\varphi \simeq T_b$, and, as a result, the suppression of oscillations practically to the thermal noise level (Fig.3a). The anomalous diffusion of particles in the case is abruptly reduced, the flux of electrons and the potential at the edge drop that, in its turn, provides the growth of oscillations. Thus the described process is periodically repeated in time.

The range of changes in other parameters of the set (1-3), within which the autooscillating solutions exist, is rather wide. This shows that the due regard for a considerable number of plasma effects, within the framework of a given phenomenological set of equations, does not change, in principle, the nature of its solution.

Conclusion.

The realized theoretical and experimental study has shown that the intermediate autooscillating mode characterized by the periodic release of fast electrons upon the chamber walls can emerge under definite conditions in the transition from the L-mode to the H-one. A theoretical selfconsistent model allowing one to qualitatively - represent both the autooscillating L-H mode transition and the stationary self-sustaining one. The role of a fast particle beam in realization of the L-H mode transition has been studied It has been shown that the autoscillating nature of these transitions is provided by diffusion of the very suprathermal electrons from the discharge.

Reference

1. Biglari H. et al, Plasma Phys. and Contr. Nucl. Fus. Res., IAEA, Vienna, 1991, v.2, p.191.

Figure captures

Fig.1. The intensity of SXR-radiation in one of the central channel.

Fig.2. The dependence of the stationary quantities W(a), φ(b) and n_b(c) on RF power for the stable L and H-modes. For autooscillations the maximum and minimum values W, φ and n_b are drawn. $\nu\tau_1=100$, $T_b/T_e=2.5\cdot10^4$, $\gamma_o\tau_1=2000$, $\gamma_1\tau_1T_e/eW_o=130$, $\gamma_2\tau_1W_o=1$, $W_T/W_o=10^{-2}$, $a/\Delta r=250$.

Fig.3. The time dependences of the oscillations energy density, W(a), edge potential, φ(b), and fast electron density, n_b(c), under the parameters of Fig.2 and $P\tau_1/Vn_eT_b=4.8$.

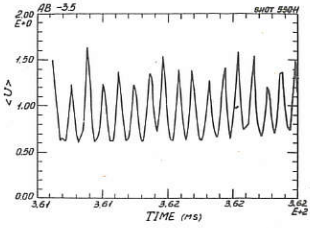

Fig 1

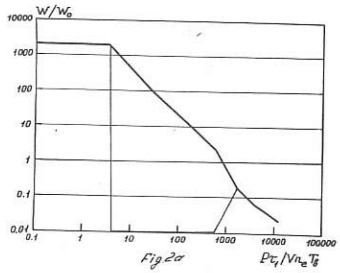

Fig 2a

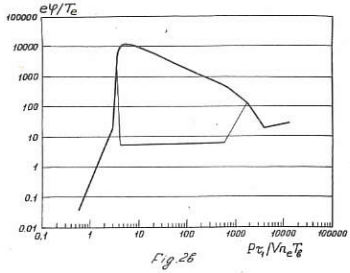

Fig 2b

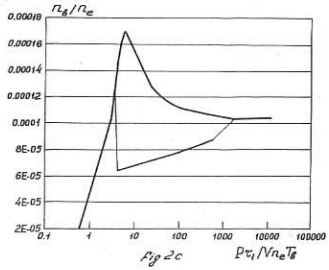

Fig 2c

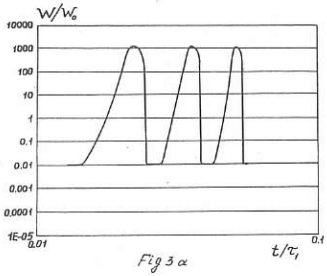

Fig 3a

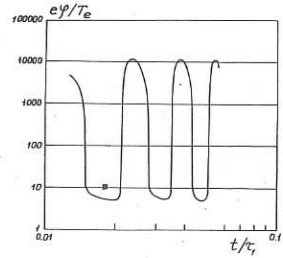

Fig 3b

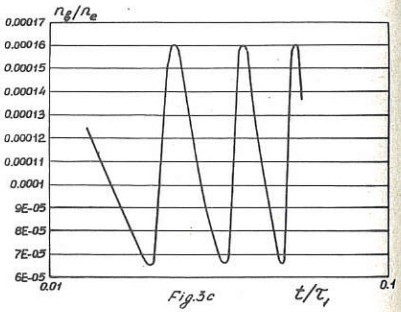

Fig 3c

Rotation in Ohmically Heated Tokamaks: A Detailed Comparison of Experiment with Theory

W. Rowan, M. Calvin, R. Hazeltine, A. Meigs, E. Solano, P. Valanju
Fusion Research Center and Institute for Fusion Studies,
The University of Texas at Austin,
Austin, Texas USA 78712

Comparison of experiments in the Texas Experimental Tokamak (TEXT) with theory leads to a reasonably complete understanding of impurity rotation in Ohmic plasmas. In the experiments, the components of the impurity rotation velocity, $v_{\sigma\phi}$ and $v_{\sigma\theta}$ (σ represents impurity species) were derived from measurements of the Doppler shift of C and O spectral emission. Simultaneously, quantities that might affect rotation were measured: the neutral concentration and the gradients of ϕ, T_i, n_σ, and n_i. The striking results of these comparisons are that plasma toroidal rotation is damped (not quenched) by momentum loss due to ion-neutral charge exchange and that the damping can now be accurately predicted. In the initial stage of this study, it was found that rotation velocity measurements were consistent with then-current theory only for plasma regions with low neutral concentration/1/. This observation led to the conclusion that charge exchange damping should be incorporated into transport theory. Appropriate theory was developed, /2/ and is successfully compared with experiment here. The present work will demonstrate the predictive capability of current theory, identify the principal mechanisms for rotation at the plasma edge, and demonstrate a significant modification of transport by an atomic process.

In the theoretical description that has evolved, ions and impurities have independent perpendicular drifts but a common parallel velocity that is damped by momentum loss due to ion-neutral charge exchange. The species included in the theory are plasma ions, neutrals (same element as the plasma ion), and impurity ions. Impurity ions interact with neutrals only through the plasma ions. Plasma ions are in the plateau regime. The charge exchange

mean free path is large compared to the ion mean free path, but small compared to the gradient scale length. The perpendicular impurity velocity is simply

$$n_\sigma v_{\perp\sigma} = \frac{1}{m_\sigma \Omega_\sigma B} \mathbf{B} \times (\nabla p_\sigma + n_\sigma e_\sigma \nabla \phi)$$

The parallel flow of the ions is impeded (but not necessarily quenched) by charge exchange momentum loss. The collisionality between ions and impurities is sufficiently high that parallel pressure gradients are small, and $v_{\sigma\parallel} = v_{i\parallel} \equiv v_\parallel$

$$v_\parallel = \left\{ \frac{E_r}{B_\theta} - \frac{kT_i}{B_\theta Z_i e} \left[\frac{\partial \ln(p_i)}{\partial r} - k_v \frac{\partial \ln(kT_i)}{\partial r} \right] \right\} F_{cx} \quad \text{with} \quad F_{cx} = \left[1 + \frac{2}{\sqrt{\pi}} \left(\frac{R}{r} \right)^2 \frac{\nu_x}{\omega} \right]^{-1}$$

ν_x is the ion-neutral charge exchange frequency, and ω is the transit frequency. Flow velocities are typically measured in the (θ, ϕ) frame. In that frame,

$$v_\phi \approx v_\parallel \tag{1}$$

$$v_{\theta\sigma} = \frac{T_i}{eB_\phi} \left\{ \frac{1}{Z_\sigma} \frac{\partial \ln(n_\sigma)}{\partial r} - \frac{F_{cx}}{Z_i} \frac{\partial \ln(n_i)}{\partial r} - \left[\frac{F_{cx}}{Z_i} (1 - k_v) - \frac{1}{Z_\sigma} \right] \frac{\partial \ln(kT_i)}{\partial r} \right\} + (F_{cx} - 1) \frac{E_r}{B_\phi} \tag{2}$$

Charge exchange reduces the magnitude of v_ϕ, but for $v_{\theta\sigma}$, it changes the relative contribution of the terms and adds a new dependence on E_r.

Flow velocities are derived from the Doppler shift of impurity spectral emission. The measured spectrum is emitted by a plasma chord. The chord is identified by a tangency radius, a major radius R_T for v_ϕ measurement or a minor radius r_T for $v_{\theta\sigma}$ measurement. The shift of the chordal spectrum is obtained using a non-linear fitting technique. The quantity used to characterize this spectral shift and to facilitate comparison with theory is the apparent velocity $\langle v \rangle$, a velocity that is derived from the shift of the chordal spectrum using the simple Doppler formula. Because the measured spectral shift contains contributions from all points along the observation chord, $\langle v \rangle$ can not be strictly interpreted as a local velocity, although the line emission profile does provide substantial localization. The prediction of theory is obtained by simulating the measured spectrum with an integral along the plasma chord of the predicted local spectrum , and then extracting $\langle v \rangle$ from the simulated spectrum using the same fitting techniques as for the experiment. For the simulation, the

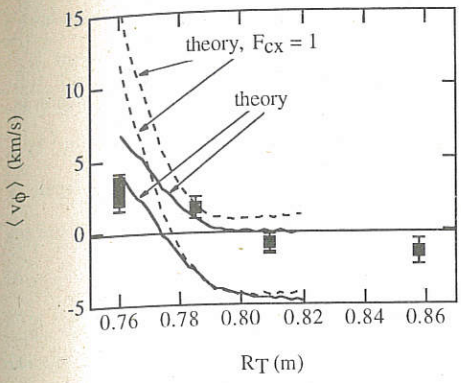

Figure 1. Comparison of measured to predicted $\langle v_\phi \rangle$.

local spectral profile is described as Doppler broadened by thermal motion and Doppler shifted by the component of the theoretical impurity flow velocity, v_σ, along the plasma chord. The quantities required to describe the local profile, T_i and total spectral line emissivity, are measured. All quantities required for evaluation of (1) and (2) are also measured. Comparisons between theory and experiment are in figures 1 and 2. The spectral line used for these measurements was 2270.91, C^{+4}.

The comparison between experiment and prediction is shown in figure 1 for $\langle v_\phi \rangle$. For reference, the high field side of the poloidal limiter is at $R_T = 0.76$ m, and the plasma center is at $R_T = 1$ m. The points represent experiment, the solid lines, upper and lower limits for theory including charge exchange, the dashed lines, upper and lower limits for theory without charge exchange ($F_{cx} = 1$). Upper and lower limits are included to allow for uncertainty in the data used to evaluate (1). At the plasma edge, charge exchange effects reduce the predicted $\langle v_\phi \rangle$ to the observed value. Figure 2 contains the comparison for $\langle v_{\sigma\theta} \rangle$. Charge exchange

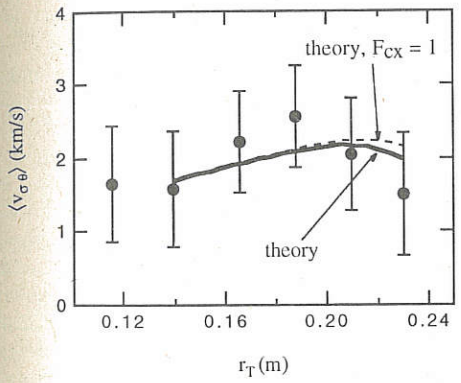

Figure 2. Comparison of measured to predicted $\langle v_{\sigma\theta} \rangle$.

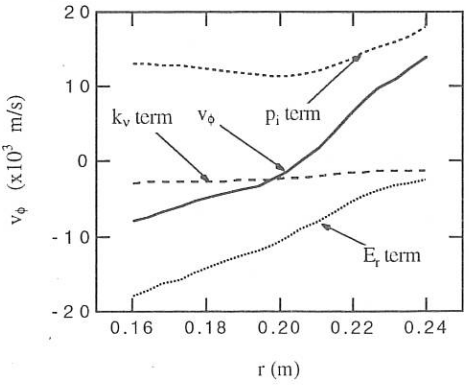

Figure 3. v_ϕ and each of the terms of (1)

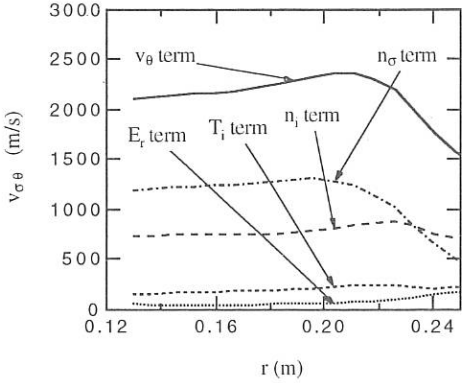

Figure 4. v_θ and each of the terms of (2)

momentum loss does not have a measurable effect on $\langle v_{\sigma\theta} \rangle$.

Each of the terms in the equation for v_ϕ (eqn. 1) is plotted separately in figure 3. Near the plasma edge, the ion pressure gradient dominates. At smaller radii, the E_r term reverses the direction of v_ϕ. The term $k_v \frac{\partial \ln(kT_i)}{\partial r}$ is small in the case of Ohmic discharges in TEXT. For devices with large ion thermal gradients, it could become significant.

Each of the terms in the equation for $v_{\sigma\theta}$ (eqn. 2) is plotted separately in figure 4. The principal contribution to $v_{\sigma\theta}$ is from the diamagnetic term. The interesting new E_r term is unmeasurably small in these experiments where $E_r \approx 20$ to 30 V/cm. For significantly larger values, charge exchange could modify $v_{\theta\sigma}$.

Plasma rotation is a phenomenon of critical importance. This study demonstrates the influence of atomic processes. It also may contribute to understanding of turbulence and L-to-H transition through improvements in understanding of plasma rotation.

/1/ W. L. Rowan, et al. Physics of Fluids B 4, 917 (1992).

/2/ P. M. Valanju, et al., IFS Report No. 540, The University of Texas at Austin, 1992.

DIVERTOR PLATE BIASING AND CURRENT INJECTION ON TdeV

J.-L. Lachambre, P. Couture, A. Boileau, C. Boucher, R Décoste, B. Gregory, C. Janicki, D. Lafrance, G. Le Clair, C. Liu-Hinz, C. MacLatchy, F. Martin, D. Michaud, G.G. Ross, B. Stansfield, M. St-Onge, B. Terreault and Z. Wang

Centre canadien de fusion magnétique, Varennes, Canada, J3X-1S1

INTRODUCTION

TdeV (Tokamak de Varennes) is a medium size tokamak featuring two closed poloidal divertors with electrically insulated neutralization plates. Among the various possible plate biasing combinations, two modes are particularly relevant to the physics of electrical biasing: current injection and plasma biasing in the scape-off layer. While the first mode provides important information on the electrical characteristics of biasing, the latter shows numerous and pronounced effects on the basic plasma parameters of the discharge [1]. This paper summarizes a comparative experimental study of these two biasing modes on TdeV and discusses their similarities and differences.

CURRENT INJECTION

In the current injection mode represented in Fig.1, an electric current is driven in the SOL by an external floating power supply without imposing any potential reference to the plasma. The operating potentials of the neutralization plates adjust themselves with respect to the vacuum vessel so as to leave the SOL potential relatively unaffected. Figure 2 displays plasma potential profiles obtained from Langmuir probe measurements in the equatorial plane for three source voltages, -200, 0 and +300 volts. Over this range, the SOL potential changes by less than +/- 10 V. In either source polarity, the more negative plate experiences most of the potential drop similar to the probes in a Langmuir double probe circuit. The I-V characteristic of the biased plates in the current injection mode is presented in Fig.3 for a double null configuration. One recognizes on this graph all the features of a "double probe" response with two saturation levels for the upper and lower divertor plates. To interpret the data, we use a simple two-temperature model based on planar Langmuir probe theory in absence of magnetic field with the temperatures and saturation currents as free parameters. The fit of Fig.3 clearly shows a zero current offset of ~20 V, indicative of a possible thermoelectric effect due to an asymmetry between upper and lower divertor temperatures, 35 and 40 eV respectively. In order to get a satisfactory fit with reasonable temperature values, we have assumed a serial resistive element of about 0.3 Ω in the lower divertor electric circuit. The nature of this resistance is not understood but we tentatively attribute it to a weak connection to the separatrix

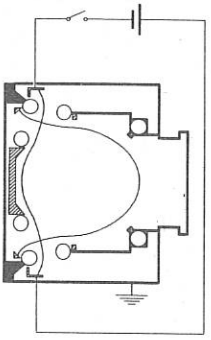

Figure 1 Current injection

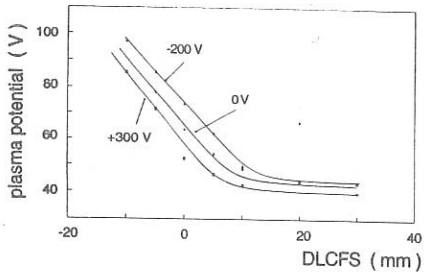

Figure 2 SOL plasma potential profiles for the current injection mode.

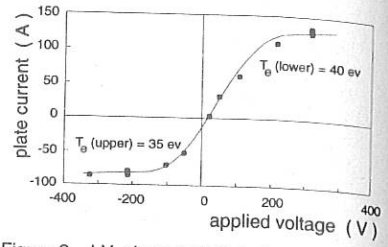

Figure 3 I-V characteristic in the current injection mode .

caused by poor vertical control. In fact, in a single null configuration where the saturation levels are almost doubled, no such resistive element is needed. Assuming the saturation to be caused by the ion flux through the sheath at the plate, we infer an effective width of the wetted area on the plates to be about 22 mm for an electron density of $1x10^{18}m^{-3}$ and a field line inclined at 5°. An improved model should also include, 1) current saturation based on the SOL flux limit imposed by the core particle losses and 2) recycling.

Contrary to the plasma biasing mode, we do not observe significant changes in the basic plasma parameters except for a minor variation of the gas feed; $n_e(r)$ and $T_e(r)$ do not change appreciably in the SOL or the core region. In addition, no detectable modification is seen in the central ion temperature, the intrinsic impurity rotation or the fluctuation level of the electron density inside the separatrix. For a constant fuelling rate, the line density increases slightly with the applied voltage, independent of its polarity, with no saturation as in the case of the current. This result suggests that $J_{SOL}xB$ cannot be the cause of this phenomenon, which, however, might be explained by a small variation in recycling due to power deposition in the divertors. On the other hand, when the density is controlled, the divertor chamber parameters do not show noticeable changes; in particular, the total gas pressures in both chambers are unaffected by either polarity. This is not surprising since JxB or ExB effects are not expected to be important in the divertor chamber because no transverse current is sustained and most of the voltage drop occurs in the plate sheaths. The only observable change is a increase with time of both saturation currents, probably due to the deposition of 50 kW of heating power into the sheaths near the plates. No heating is seen in the SOL because of its very low resistivity.

PLASMA BIASING

In the plasma biasing mode represented in Fig. 4, the power supply voltage is applied between the plates and the grounded vacuum vessel. In this way, a potential difference is established between the separatrix connected to the plates and the first flux surface connected to the first metallic surface at the ground potential. Depicted in Fig. 5, the potential profiles measured by the probes in the equatorial plane support this interpretation. The induced electric field amplitude deduced from these data is proportional to the applied voltage over the full -200 to +200 V range of arc-free biasing. The

equivalent electric network of this biasing mode would be composed of the impedance of the plasma sheaths in front of the neutralization plates, a radial resistive component and finally, to close the loop, a diode-like element representing the plasma sheath at the vessel wall. The I-V curve of this plasma biasing mode is presented in Fig.6. We do not observe the full characteristic of a double resistive Langmuir probe; we only see the resistive behaviour, presumably because saturation on both the plates and the vacuum vessel wall occurs at higher bias voltages. The radial current resulting from the application of a constant bias is observed to be linearly dependent on the edge density, as measured by the outermost interferometer channel and a Li-ablation diagnostic. Since the current does not saturate over the observation range, the 0.66-ohm impedance is attributed to the radial resistance of the SOL. This is further supported by the fact that the biasing current is strongly modulated by the sawtooth heat pulse (>25%) and by perturbative gas puffs. A nonambipolar radial current or an orthogonal conductivity based on viscous damping by neutrals would be consistent with our observations. The former mechanism assumes that electrons and ions are moving across the field according to their mobilities. Retaining the ion channel alone ($j_r = en_i\mu_i E$) and using a separatrix surface of 9.2 m^2, we infer from the observed currents and fields, a mobility of 0.015 m^2/Vs. In addition, it is observed from Li beam measurements, that the SOL e-folding length profile is strongly affected by biasing. To be consistent with this observation, we assume a diffusive flux , Γ_D = -Ddn/dr, of the order of the mobility flux, Γ_μ = $n\mu E$, thus predicting a mobility of 0.03 m^2/Vs, in broad agreement with our evaluation from the I-V curve. On the other hand, the viscosity mechanism based on charge exchange with neutrals leads to a radial current three times lower than the observed value. These two mechanisms could be present simultaneously.

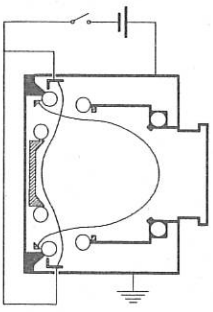

Figure 4 Plasma biasing

The effect of plasma biasing on divertor pressure is illustrated in Fig. 7. The pressure grows according to the direction of the ExB flow; namely, it increases in the upper (lower) divertor chamber with negative (positive) bias. For our standard plasma conditions ($\bar{n}_e$=2.5x10^{19} m^{-3}, I_p=210kA), pressure increases by factors as high as 5, with a strong up/down asymmetry between negative and positive biasing [2]. This asymmetric response is also observed on the current drawn by the plates.

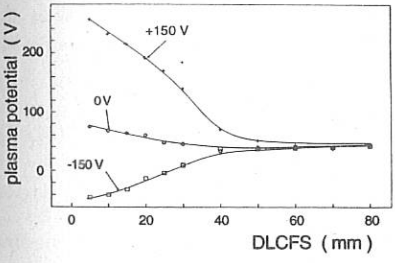

Figure 5 SOL plasma potential profiles for the plasma biasing mode.

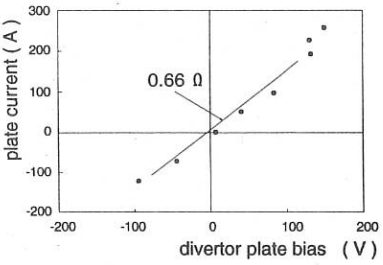

Figure 6 I-V characteristic in the plasma biasing mode.

At higher densities, after boronization, we even observe a corresponding pressure reduction in the opposite divertor chamber. The asymmetry cannot be explained by the ExB flow alone, since, for the same electric field amplitude and proper polarity, the inflow would be the same for each chamber. However, coupled with the electrostatic barrier effect which widens or narrows the SOL, the explanation could make sense since it favours the upper divertor with the present B field direction. In addition, the barrier effect is supported by the fact that pressure increases in the main chamber with a positive bias (Fig. 7). In this case, the main chamber is favouvered over the lower divertor.

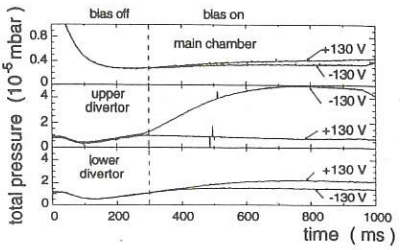

Figure 7 Plasma biasing effects on divertor pressure.

Although the electric field is imposed in the SOL, we observe many effects in the central plasma. As seen from the loop voltage and soft X-ray emission, the impurity content of the core is strongly modified by biasing in an unboronized TdeV, decreasing with negative and increasing with positive polarity [1]. Rotation of intrinsic impurities is also observed, reaching poloidal and toroidal values up to several km/s. Density fluctuations are also seen to be either stabilized or increased with bias [3]. Central electron and ion temperatures do not change appreciably. The global energy and particle confinement times are not substantially modified by biasing over the reduced range of actually applicable voltages, the main influence being on Z_{eff} and recycling. The divertor efficiency is greatly improved by plasma biasing, its impurity retention capability being increased by a factor of 5 with negative bias.

CONCLUSION

Although current injection in TdeV does not produce significant changes in the basic plasma parameters, it is instrumental in supplying essential information not available in the other modes. On the other hand, plasma biasing, defined as the application of a potential difference between the separatrix and the wall, shows marked effects in the SOL plasma as well as in the core. The electric characteristics observed for these modes can be explained to first order by classical plasma sheath considerations and radial nonambipolar transport. In plasma biasing, it appears as if only the separatrix were biased. The mechanism in the divertor chamber that insulates the other highly conducting SOL field lines from the plates to produce the observed fields is under investigation.

[1] P. Couture, A. Boileau, R. Décoste et al. Phys. Lett. A 163 (1992) 204.

[2] B. Terreault et al. Accepted in Nuclear Fusion (1992).

[3] A. Boileau, P. Couture, D. Lafrance, J.-L. Lachambre et al. Accepted in Nuclear Fusion (1992)

Supported by the Centre canadien de fusion magnétique with funds from AECL, Hydro-Québec and INRS.

Edge Fluctuations at Regimes with Improved Confinement on CASTOR Tokamak

J. Stöckel, L. Kryška, F. Žáček, J. Badalec, K.Jakubka, J. Mlynář, P. Magula, P. Kletečka
Institute of Plasma Physics, P.O.B. 17, 182 11 Prague, Czechoslovakia

Abstract
A link between the level of electrostatic fluctuations and particle confinement is investigated experimentally in two regimes with an improved global particle confinement:
- *Lower Hybrid Current Drive regime* (**LHCD**).
- *Edge Plasma Polarization regime* (**EPP**).

It has been found that the edge fluctuations are reduced and their character changes at LHCD. Preliminary results of the spectral analysis of the fluctuations at EPP regime are presented.

Experiments are performed on CASTOR tokamak ($R = 40cm, a = 8.5cm, B_t = 1T, I_p = 12kA$) at densities $\bar{n}_e < 1.5 \cdot 10^{19} m^{-3}$. The particle confinement time is estimated from the global particle balance. Edge fluctuations are monitored by means of multiple tip Langmuir probes located at the midplane near the last closed flux surface (LCFS).

LHCD regime:
A lower hybrid wave ($f_{LH} = 1.25GHz, P_{LH} < 40kW$) is launched into the plasma by a multijunction grill. Typical evolutions of the LHCD shot (shown in Fig. 1) demonstrate that the line average density increases, while hydrogen and impurity line intensities decrease during the LHCD phase of the discharge. The radial density profile broadens in the plasma core, while its steepening is observed at the edge region [1]. Therefore, an improvement of the global confinement time (by a factor of ~ 2) is deduced from the experimental data. At the same time, the level of electrostatic turbulence is significantly reduced in the vicinity of the last closed flux surface. Note also that the HXR intensity from the limiter nearly vanishes during the improved particle confinement phase.

The best confinement and the minimum level of the fluctuations are observed when the LH power is less then the initial OH power input. Simultaneously, the total power $P_{OH} + P_{LH}$ reaches its minimum. The similar results have been obtained at low power LHCD regimes on ASDEX [2].

The spectral analysis shows that the reduction of the edge turbulence is accompanied by changes in the character of the fluctuations. Fig. 2 compares the spectral characteristics of density fluctuations in the vicinity of the last closed flux surface at OH and LHCD discharge phases, averaged over five similar shots. It may be seen that the mean wavenumbers as well as the width of the k-spectrum decrease. The first fact indicates that the poloidal phase velocity of the fluctuations in the laboratory frame increases. The frequency spectra are reduced especially at their low frequency part which is probably caused by the enhanced poloidal rotation. Frequency integrated k- spectra are reduced in the range of $(0.5 - 2.7)cm^{-1}$. Additional measurements indicate a decrease of the correlation length of the density fluctuations at LHCD [3].

Fig. 1.
Evolution of LHCD (thick lines) and Ohmic (thin lines) shots for $P_{LH} = 17kW$.
a) Loop voltage U_l. The drop of U_l between 15th and 20th ms indicates that roughly a half of the plasma current is driven non-inductively in this particular case.
b) Line average density (central chord).
c) Peaking factor p of the density profile defined as $n/n^o = (1 - x^2)^p$. The drop of p from 0.7 to 0.35 indicate significant broadening of the density profile at LHCD.
d) Intensity of the H_α-spectral line. Similar evolutions of this line are observed at different toroidal locations as well.
e) Resulting particle confinement time τ_p/τ_p^{OH} normalized to its initial Ohmic value.
f) Hard X-ray intensity from the limiter.
g) Incident LH power P_{LH}.

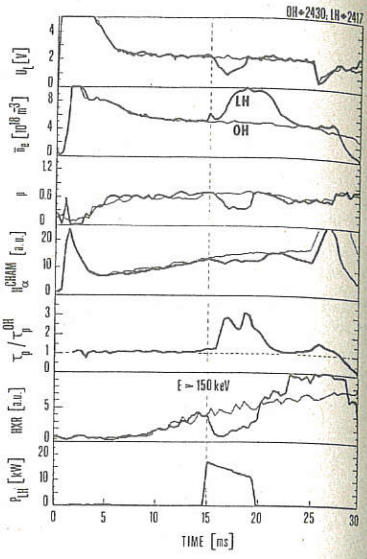

Fig. 2.
Spectral characteristics of the density fluctuations at $P_{LH} = 37kW$ averaged over five similar shots. The fluctuations are monitored at the midplane, 180° toroidally away from the grill.
a) Frequency resolved mean poloidal wavenumbers $\bar{k}_p$.
b) The same for the relative width of the wavenumber spectra $\Delta k_p/k_p$.
c) Frequency spectrum S(f) integrated over wavenumbers.
d) Wavenumber spectrum S(k) integrated over frequencies.

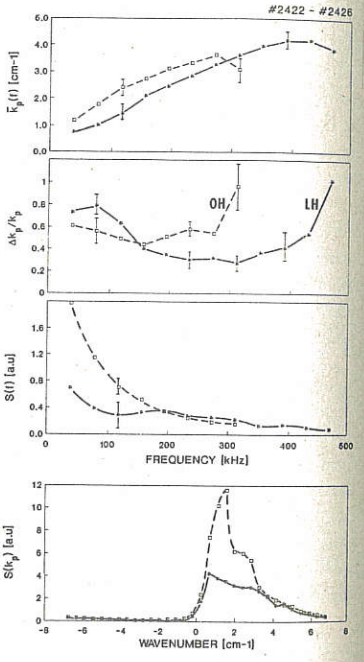

Fig. 3.
Evolution of the shot with limiter biasing, $U_{lim} = +200V$.
a) Loop voltage. b) Line average density.
c), d) and e) Intensities of the H_α-spectral line monitored 180° toroidally away from the limiter, in the limiter section and in front of the waveguide grill.
f) Hard X-ray intensity from the limiter.
g) Resulting particle confinement time τ_p/τ_p^{OH} normalized to its Ohmic value.
g) Limiter current I_{lim}.

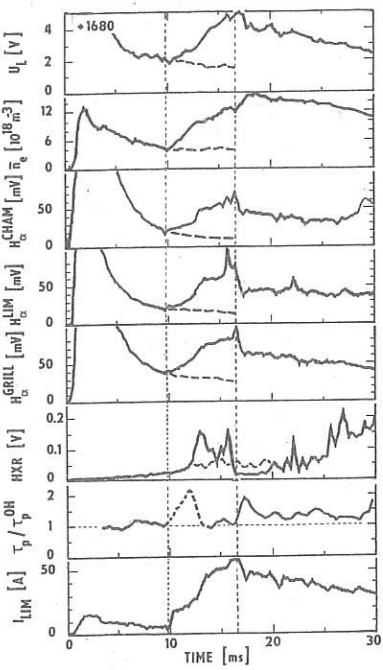

Fig. 4.
Spectral characteristics of the density fluctuations in the shot with limiter biasing. The probe is located in the SOL near the limiter.
a) Frequency resolved mean poloidal wavenumbers $\bar{k}_p$.
b) The same for the width of the wavenumber spectra Δk_p.
c) Frequency spectrum S(f) integrated over wavenumbers.
d) Wavenumber spectrum S(k) integrated over frequencies.

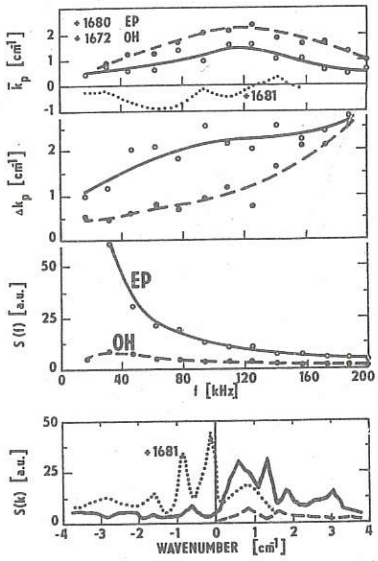

EPP regime:

In this case, the edge plasma is polarized by means of biasing of the circular limiter. Fig. 3 shows an evolution of a shot with limiter biasing ($U_{lim} = +200V$) during a steady state phase of the OH shot. After an initial jump (up to $I_{lim} \sim 20A$), the limiter current increases more slowly. Simultaneously, the line average density and H_α line intensities are increasing as well. This indicates enhanced recycling, which is not, however, localized at the limiter. Radiation of impurities (not shown in the figure), increases as well, but noticeably faster then the hydrogen line intensities. Therefore, we conclude that the initial increase of the plasma density is probably caused by an accumulation of impurities in the plasma.

After reaching the value $I_{lim} \doteq 60A$, the limiter current drops suddenly and a transition to the improved particle confinement occurs. This is manifested by a faster increase of $\bar{n}_e$ and by a sharp drop of H_α and impurity line intensities. The both effects seem to have a transient character. The edge density and the level of the density fluctuations drop at the transition, but not bellow their initial Ohmic values. It is worthwhile to note a sudden drop in the HXR intensity at the transition, starting even before the transition.

The resulting global particle confinement time τ_p, normalized to the corresponding Ohmic value, is shown in the same figure. The initial increase of τ_p (shown by the dashed line) is assumed to be caused by neglecting the multiple ionization of impurities throughout the evaluation. We see that the τ_p/τ_p^{OH} roughly doubles just after the transition, but it remains still slightly enhanced at later time.

It should be noted that a more smooth transition to the improved confinement (but accompanied by a drop of HXR) can be arranged with a lower biasing voltage $U_{lim} = 120 - 140V$. A similar smooth improvement of particle confinement during limiter biasing was reported from HYBTOK-II tokamak [4]. Biasing of the limiter by a negative voltage does not influence the global plasma parameters for $U_{lim} \leq -160V$.

The plasma parameters in scrape-off layer are monitored by a Langmuir probe located near the limiter. Results of preliminary spectral analysis of the probe signals, performed only just after the start of limiter biasing, are depicted in Fig. 4. The poloidal velocity of the density fluctuations roughly doubles in this case. The maximum of the wavenumber spectrum is shifted to lower k-values and, in some shots, it even changes the sign. The last means that, at the given probe radial position, the poloidal rotation of the fluctuations is reversed from ion to electron diamagnetic drift direction. In general, the level of density fluctuations and the width of the wavenumber spectra increase during the initial phase of limiter biasing. The spectral analysis of the edge fluctuations deeper in the plasma and just during the transition is in progress.

Acknowledgement: The work was supported by the grant CSAV No. 41310 and by the IAEA Research Contract No. 6702/RB.

References:

[1] J.Stöckel et al: Proc. 12th IAEA Conf., Vol.I., p.359, Nice 1988.
[2] J.Stöckel et al: Proc. 18th EPS Conference, Vol.III., p.341, Berlin 1991.
[3] F.Žáček et al: IAEA TCM on Research Using Small Tokamaks, Hefei 1991.
[4] Y. Ueshugi et al: IAEA TCM on Research Using Small Tokamaks, Washington 1990.

H MODE INDUCED BY THE BIASED ELECTRODE AND TRANSITION OF LOW DENSITY TO HIGH DENSITY WITH OPTIMIZED GAS PUFFING IN HL-1

L.B.Ran, H.R.Yang, S.K.Yang, S.X.Zhang, Y.Z.Zheng, E.Y.Wang, Z.H.Wang, L.H.Yao, S.Q.Sun, Y.W.Qin, J.F.Dong, Z.C.Deng, H.C.Deng, G.C.Guo, Y.X.Jiang, H.Z.Li, K.H.Li, H.N.Zuo, J.W.Yang, Q.W.Yang, K.Q.Huang, C.J.Yuan and HL-1 Team

Southwestern Institute of Physics, P. O. Box 432
Chengdu, Sichuan 610041 China

H MODE INDUCED BY THE BIASED ELECTRODE

The H mode has been induced on the HL-1 tokamak by the radial electric field created by a electrode with positive bias similar to the works on CCT(1) and TEXTOR(2). This electrode, which is consisted of a carbon head and a ceramics insulator, is inserted 2-4cm inside the limiter. A pulse voltage with amplitude of 0-600V with respective to the wall and duration of 100ms is supplied on the electrode head during the plasma plateau phase of the HL-1 Ohmic discharge in H- and D-plasma over a range of the paramerters: Ip=80-100kA, Bt=2.2-2.6T and $\bar{n}_e$= 0.2-2.0×10^{13}/cm^3.

As the electrode is inserted over 2cm into the last closed flux surface limited by the movable limiter and the bias voltage is higer than ~350V and the bias current is higher than a threshold(see later), the L-H transition takes place. The time evolution of a variety of diagnostic signals in L and H mode is shown in Fig.1, which indicate that at L-H transition the Hα /Dα light drops abruptly; The line averaged density $\bar{n}_e$ increases by a factor of 1-3; The ion saturation current Is at r = 18.5-22.0cm measured by the double Langmuir probe deceases; The edge density n_{eb} reduces evidently as shown in Fig.2 and the e-folding length reduces from ~14mm of L mode to ~4mm of H mode for H -plasma, indicating that the density gradient increases. From above measurements it can be derived that the perpendicular particle diffusion coefficient $D_\perp$ is reduced by a fctor of ~3 and the particle confinement is improved by a factor of 1-3. The central temperature Te(0) measured by the Thomson scattering increases about ~20-30%; The edge temperature T_{eb} decreases significantly as shown in Fig. 3, indicating that the temperature gradient increases. The increase of the density gradient and the temperature gradient would lead to that the transport barrier is formed and that the fluctuation is suppressed. In our experiment it has been indeed observed that the electro-static fluctuation and the magnetic fluctuation are suppressed heavily. The electro-static fluctuation is suppressed to the level of ~20-30% of L mode for D-plasma. The magnetic fluctuation measured by the Mirnov loops is suppressed gradually or suddenly with ~15-20ms time delay. The suppression of the magnetic fluctuation at the outer midplane is heavier than that at the inner midplane, indicating that the effect of bias at the low field side is stronger than the one at the high field side and that the reduction in fluctuation-driven transport across the outer midplane of the plasmsa is more than the one at the inner midplane of the plasma. The form of the transport barrier and the reduction of the fluctuation would lead to the confinement improvement. The diamagnetic measurement shows that the diamagnetic flux DMF increases by a factor of 1-3, indicating that the energy confinement is enhanced. Unfortunately, the intensities of O, Cr, Ni, Mo impurity lines, soft X-ray, hard X-ray and the plasma radiation loss are increased, indicating that the impurity is accumulated and hence leading to confinement degradation which is characterized by the decrease of the diamagnetic flux and the

increase of the electro-static fluctuation after ~40-50ms later as the L-H transition occurs.

The observed time scale of the reduction of the edge density, the edge temperature and the electro-static fluctuation is ~200-300 μs, the time scale of the changes of the global parameters, such as the line averaged density $\bar{n}_e$ and the diamagnetic flux DMF, is ~20-40ms, much slower than the time scale of the edge parameter changes, which is consistent with the observation on DIII-D (3) and the prediction of the theories of Shaing (4) and BDT (5). These observation reveal that the L-H transition starts at the plasma edge and develops gradually into the plasma center.

The electrode current, which is mainly consisted of the radial current and increases the plasma rotation, plays an important role in L-H transition. As the bias voltage is higher than ~350V, only the electrode current is higher than a threshold, which is ~30A for D-plasma and ~40A for H-plasma respectively, the L-H transition can take place.

The isotop effect appears in the L-H transition. The electrode current threshold of the L-H transition in D-plasma is lower than that in H-plasma as related above; The line averaged density $\bar{n}_e$ can be increased from $0.5\text{-}1.0\times10^{13}$ /cm^3 of L mode to $0.9\text{-}1.8\times10^{13}$ /cm^3 of H mode for D-plasma and from $0.2\text{-}0.5\times10^{13}$ /cm^3 of L mode to $0.9\text{-}1.2\times10^{13}$ /cm^3 of H mode for H-plasma, indicating that the L-H transition can take place in higher density of D-plasma than that of H-plasma; The edge density n_{eb} of H mode is reduced ~50-60% and ~30-40% of L mode for D- and H-plasma respectively, and the edge temperature of H mode is reduced ~50-70% and ~30-50% of L mode for D- and H-plasma respectively, indicating that the gradient of the density and the temperature of D-plasma is steeper than that of H-plasma. The electro-static fluctuation of H mode is suppressed to the level of ~20-30% and ~30-40% of L mode for D- and H-plasma respectively. All related above reveal that the L-H transition is easier to take place in D-plasma than in H-plasma.

TRANSITION OF LOW DENSITY TO HIGH DENSITY WITH OPTIMIZED GAS PUFFING

The transition from low-density (LD) to high-density (HD) in ohmic discharge was demonstrated in the HL-1 tolamak with metal wall and limiter configuration. The stainless-steel wall of vacuum vessel was neither carbonized nor gettered for the experiments of the transition from LD to HD. Fig.4 shows the line averaged density $\bar{n}_e$ jumps up , Dα emission drops down, total neutral gas pressure and D_2 pressure fall, but plasma current, loop-voltage, and plasma column displacents remain constant (black lines, #10772). For comparison, dashed lines present parameters wihtout HD transition in normal ohmic discharge (#10802). The density transitions from $3\text{-}4\times10^{13}$ /cm^3 to $7\text{-}10.8\times10^{13}$ /cm^3 within 50-80 ms were observed by switching off intensive He pulse puffing on the HL-1 tokamak. Similar transition from $2.5\text{-}3\times10^{13}$ /cm^3 to $5\text{-}7\times10^{13}$ /cm^3 were obtained by turnning off intensive D_2 pulse puffing. The Murakami paramiter $n_e R_o / B_t$ extended to 4.7×10^{19} m^{-2}/ T for HD transition discharges triggered by He pulse puffing and to 3.3×10^{19} m^{-2} /T triggered by D_2 pulse puffing shown in Fig.5 where black line is from previous data for testing density limit.

the edge density n_{ed}, edge temperature T_{ed} , and their profiles were measured by movable Langmuir probe. Without puffing gas from last closed flux surface (LCFS), T_{ed} profile in SOL always remains E-folding shape, however with continually puffing working gas from LCFS through two valves mounted on the pump limiter, the E-folding profile of T_e in SOL is rerranged (6). A cold layer at plasma edge was established which may protect the limiter and wall against the power loading onto them. The edge density n_{ed} in HD phase are almost constant, although line averaged densities $\bar{n}_e$ are 2-3 times higher than in LD phase. Dependenceof power load in SOL on $\bar{n}_e$ is conincided with the heat flux measurements (6). Puffing working gas from LCFS combined with pump limiter may provide a cold layer at plasma edge and to suppress plasma surface interaction. The lower edge density and lower edge temperture allow us more easily to make the transition from LD to HD on the HL -1 tokamak.

The line averaged density $\bar{n}_e$, plasma current Ip, perpendicular particle flux Γ_o and particle confinement time τ_p in HD are shown in Fig.6. The He gas with pulse width of ~ 60ms was puffed into the D-plasma at 250ms of the dicharge. At the beginning of He gas puffing both $\bar{n}_e$ and $D\alpha$ radiation increased (probablely caused by wall refulling). At He gas puffing stoped and kept D_2 gas puffing, the $\bar{n}_e$ increased continally, but the $D\alpha$ radiation decreased very rapidly after $\bar{n}_e$ reached the plateau (about 9×10^{13} /cm^3), τ_p increased gradually, Γ_o reduced to min., and τ_p increased to max. τ_p in HD is ~2.5-4 times higher than that in the LD.

The relation between τ_p and $\bar{n}_e$ is shown in Fig.7. The τ_p in HD is completely different from HD. In the HD as $\bar{n}_e$ is less than 3×10^{13} /cm^3 , the τ_p is proportional to $\bar{n}_e$ and as $\bar{n}_e$ reach 3×10^{13} /cm^3 , τ_p is saturared. In HD τ_p is proportional to $\bar{n}_e$, no saturation has been found yet.

REFERENCES

(1) R. J. Taylor et al., Phys. Rev. Lett. 63 (1989) 2365
(2) R. R. Weynants et al., Proc. 17th EPS conference, Amsterdam, 1990, VOL14B, partI, P.287.
(3) K. H. Burrell et al., Phys. Fluids B2 (6) 1405.
(4) K. C. Shaing et al., Phys. Rev. Lett. 63 (1989) 2369.
(5) H. Biglari et al., Phys. Fluids B2 (1) 1.
(6) H. R. Yang et al., on 10th PSI Conf., Monterey, USA, March 30-April 3, 1992.

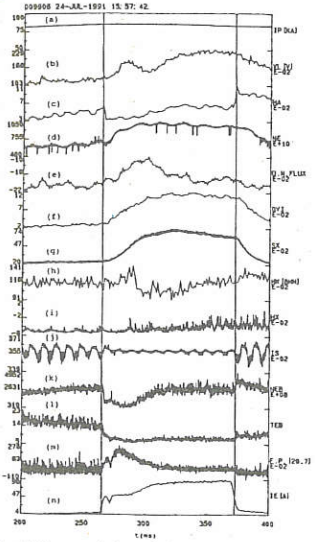

Fig.1 Time evolution of the diagnostic signals of L and H mode

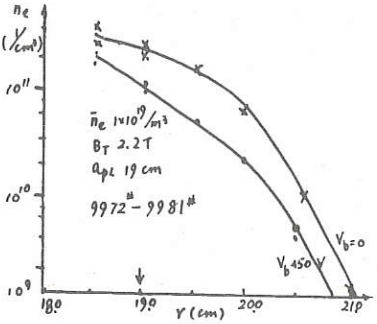

Fig.2 Density profile of L and H mode at the plasma edge

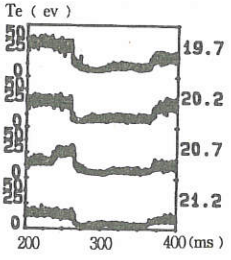

Fig.3 Time evolution of the edge Te of L and H mode at r=19.7-21.2cm

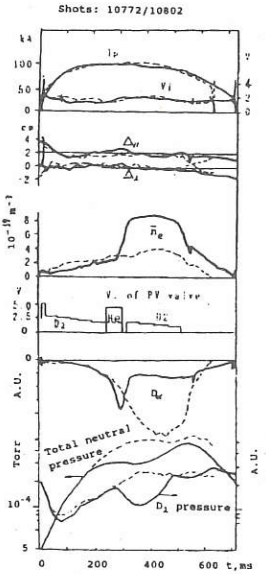

Fig.4 Temporal behavior of Ip, Loop-voltage, plasma column displacements, $\bar{n}_e$, voltage of PV puffing gas valve, D α emission, total neutral gas pressure and D_2 pressure in boundary of vessel with HD transition (black lines, #10772) and W/O HD transition (dashed lines, #10802) on the HL-1 tokamak.

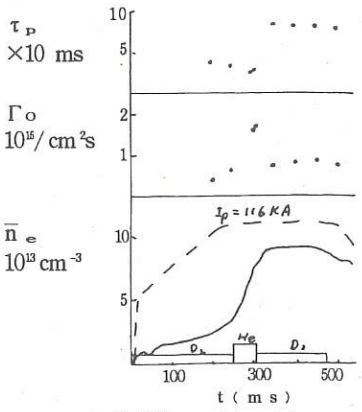

Fig.6 Time evolution of Ip, $\bar{n}_e$, Γ_o and τ_p

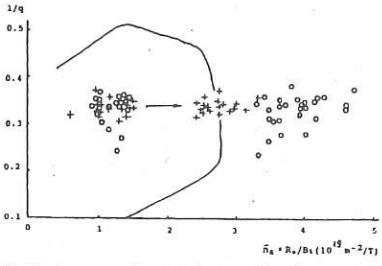

Fig.5 Hugill diagramm for (a) the transition from LD to HD triggered by hard D_2 gas puffing (crosses), (b) the transition from LD to HD triggered by hard He gas puffing (open circles).

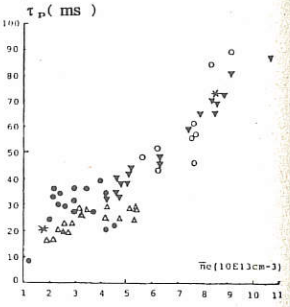

Fig.7 Dependence of τ_p on $\bar{n}_e$
Δ— LD
▼— HD
● o — calculated
※ — measured by Langmuir probe

ELM Precursors in JET

S. Ali-Arshad, D. Campbell, A. Colton[1], P. Cripwell, L. de Kock,
G. J. Kramer[2], M. F. F. Nave[3], G. F. Neill.

JET Joint Undertaking, UK.
[1]Risoe National Laboratory, Denmark.
[2]FOM Institute Rijnhuizen, Nieuwegein; The Netherlands.
[3]Associação IST/EURATOM, Lisbon, and LNETI Sacavém, Portugal.

Edge Localised Modes (ELMs) are observed on JET during H-modes, and at the L-to-H and H-to-L transitions. They are characterised by a D_α spike with a rise-time of <250μs, of duration ~1ms, interpreted as a transient particle loss [1]. The multi-channel reflectometer shows associated disturbances in the outer 20% of the plasma, which are also seen on the magnetics. In this paper these disturbances are discussed. In particular, a high frequency coherent precursor is shown, which appears to play a causal role in ELMs.

Fig. 1 shows a pulse with a sequence of ELMs. The magnetic data show a series of bursts near each ELM. The expanded window shows the magnetic activity at the first ELM in more detail. An oscillation is seen initially. This becomes turbulent, and the turbulence level rises in about 250μs, followed by the sharp rise in the D_α light. The frequency / time contour plot shows that initially (e.g. at 14.94 sec.), the magnetic activity is relatively broad-band, in the range 50kHz to 85kHz. This activity narrows at 14.97 sec. into a coherent mode (75kHz to 85kHz). As this happens, the D_α signal falls. The mode grows in amplitude over the next ~ 25ms and slows down, and then broadens again at the first burst of magnetic activity with a rise in the D_α level. The magnetic activity at this time is similar to that in the initial part of the expanded window. The subsequent turbulence is seen to be much broader, covering the entire frequency range (at 14.99 sec.). After the ELM, the coherent mode starts to grow from low amplitude again, and the process repeats.

These data suggest that particle loss is related to broadening of magnetic fluctuations, ELMs being an extreme case of this behaviour. If the D_α signal is high-pass filtered, additional fluctuations are seen on this signal with an envelope following that of the magnetic fluctuations. The coherent mode, which grows before the appearance of broad-band fluctuations, and around which the broadening starts can be regarded as the precursor causing ELMs.

In ASDEX [2], coherent precursors are observed growing exponentially and leading to turbulence at ELMs. On JET the behaviour is rather different. Before an ELM, the turbulence usually builds up around the precursor frequency. For example, in fig. 1, the activity broadens at the first burst, and subsequently does not narrow down before the next burst at the ELM (nor does the D_α light drop to the level when the activity was coherent). Generally, a sequence of bursts of activity may precede the ELM, with the mode broadening at each until the ELM. Each burst in the sequence (not just the last) thus plays a role in the ELM.

The precursor mode is not always present in a saturated state for many milliseconds before ELMs, as in the case of fig. 1. In some cases it may grow very rapidly before an ELM. Fig. 2 shows the spectrum of such a case on a surface plot. While there is no mode visible before the ELM, the broad-band activity shows peaking near 80kHz (on a contour plot the amplitude at different frequencies is more difficult to see). Since the broad-band activity does not usually have such structure, it is likely that the coherent precursor grows *before* the broad-band

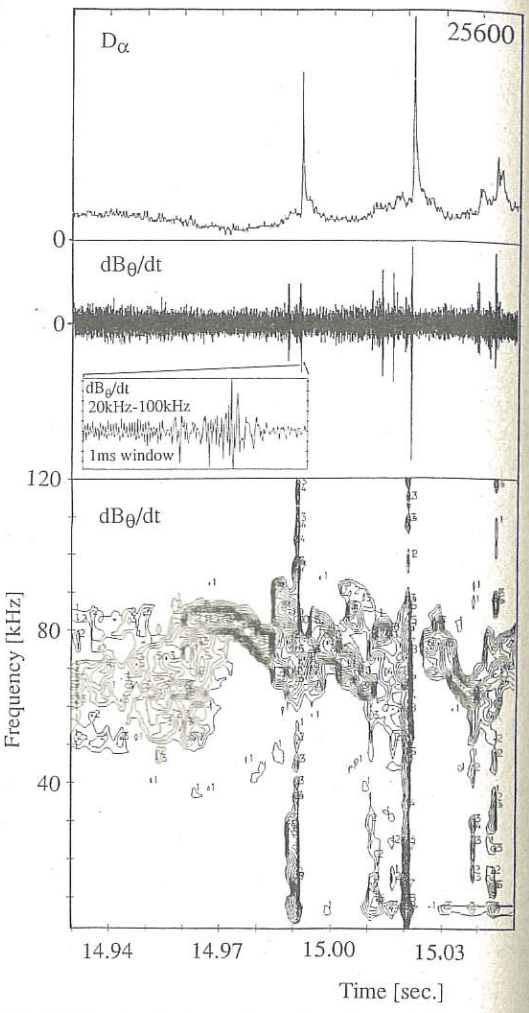

Fig. 1: Coherent oscillations leading to broad-band activity at three successive ELMs. The mode grows and slows down before the ELM, broadening occurs around the mode while the D_α signal rises slowly, then strong turbulence sets in rapidly with the sharp D_α ELM spike.

activity, but the spectral analysis is unable to resolve it separately. The raw data are shown in fig. 3. It is seen that within 2ms, there are in fact two ELMs, a mini one followed by a large one. A burst of activity occurs at each. Closer inspection shows that the first burst contains relatively coherent activity at about 80kHz, while the second is possibly initiated with 1 - 2 growing oscillations at this frequency, followed by strong turbulent fluctuations. As for the case of fig. 1, it is possible that the mini ELM damages the edge plasma, so that the second burst is more strongly unstable and turbulent.

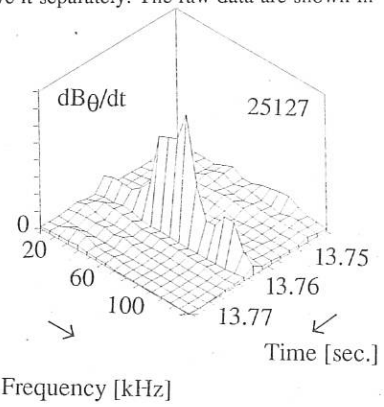

Fig. 2: An ELM without a saturated precursor. Activity is highest at frequencies typical of ELM precursors, suggesting rapid growth of the precursor before the ELM.

Fig. 4 compares magnetic fluctuations with those observed on the reflectometer at the edge. At 8.595 sec., an ELM occurs. The same coherent precursor is seen in both signals. The precursor is clearest on the reflectometer channel reflecting at R=4.18m in this case, and is seen to broaden again, leading to the ELM. From the range of reflectometer channels on which the precursor is observed the radial extent of the precursor is estimated to be ~10cm. It is also seen that the broad-band fluctuations spread outwards at the ELM.

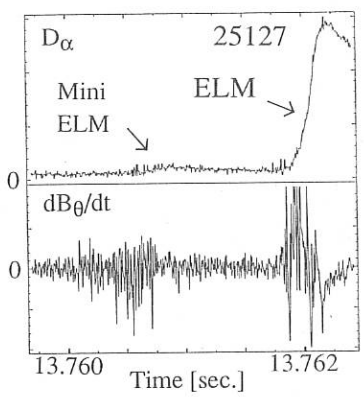

Fig. 3: Raw data for the case of fig. 2 showing two bursts of activity. Each burst grows from noise level.

The coherent ELM precursors in the current JET data set lie in the 50kHz-100kHz band. As in fig. 1 and fig. 4, the frequency may drop as the mode grows, and after the ELM, if the mode reappears, its frequency returns to the higher value (fig. 1). A cross-phase analysis of two coils at the same poloidal position, and toroidally separated by 15cm indicates toroidal mode numbers of $n \geq 8$.

The broad-band fluctuations are always seen at ELMs. The high frequency precursor is often, but not always seen. While acknowledging the possibility of different types of ELMs, (in a couple of cases low frequency modes are seen before ELMs e.g. pulse 27793), it is worth considering diagnostic limitations as a possible explanation for this. On both diagnostics, when the mode is detected, the signal-to-noise ratio is usually low. The magnetic

perturbation would be expected to decay as $(r-r_s)^{-m}$ (where r_s is the resonance surface of the mode). With high mode numbers ($m \geq 24$ at $q_s=3$) it is therefore likely that distance of the resonant surface from the magnetic probe determines whether or not it is observed. Evidence for this is seen in pulse 25996, where the mode is observed on the reflectometer but not on the magnetics. The reflectometer shows that the mode in 25996 is ~10cm further from the magnetic probes than in 25773 of fig. 4. Similarly there are cases where the mode is seen on the magnetics but not on the reflectometer. This may be due to a combination of noise levels and limited spatial coverage. A further limitation is that there is not a large margin between the frequency of the coherent mode and the maximum Nyquist frequencies of the magnetics and reflectometer (125kHz and 100kHz respectively). As in the case of fig. 2 and fig. 3, the mode may also grow very rapidly in some cases, and may escape detection for this reason.

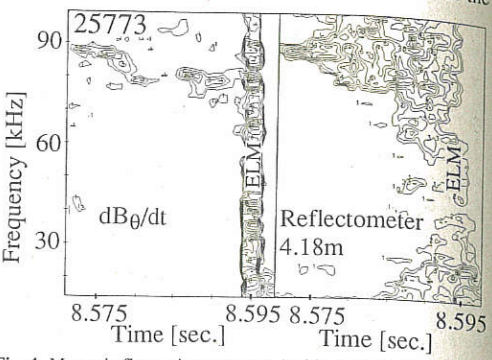

Fig. 4: Magnetic fluctuations compared with density fluctuations at an ELM.

A possible interpretation of the phenomenon is that it is an edge localised disruption. There may be a number of modes appearing at the precursor frequency in the edge, and interaction between these might be the cause of the chaotic edge fluctuations. Alternatively, a single helicity might produce this behaviour by interaction with the walls. A fast loop voltage spike (with a 100μs rise-time) is observed at the time the ELM spike starts on the D_α signal. For a discussion on theoretical aspects see [3].

In conclusion, a high frequency (50kHz-100kHz) precursor to ELMs is usually observed on JET. In many cases this mode grows and broadens, and as this happens, the particle losses from the plasma increase. The broadening then suddenly increases sharply, with a corresponding burst of particle loss, which is distinguished as an ELM.

[1] A. Hubbard *et al., proceedings of the 15th International Conference on Controlled Fusion and Plasma Heating,* Dubrovnik, II 651, (1988).

[2] H. Zohm *et al., proceedings of the 18th International Conference on Controlled Fusion and Plasma Physics,* I 305, Berlin (1991).

[3] G. T. A. Huysmans *et al.*, this conference.

Reflectometry measurements of the m=1 satellite mode in L- and H-mode plasmas in ASDEX

F. Serra, M. E. Manso, A. Silva, J. Matias, F. Wagner[1], H. Zohm[1], A. Kallenbach[1] and P. Varela

Centro de Fusão Nuclear, EURATOM/IST Association, 1096 Lisboa Codex, Portugal
[1]Max-Planck Institut fur Plasmaphysik, EURATOM/IPP Association, Garching

1 - Introduction

In ASDEX, with strong NBI heating, often a large central m=1,n=1 mode is observed on the SXR emission. For $P_{NBI} \geq 1$ MW a mode rotating with the same frequency, the so-called 'm=1 satellite', is seen on the magnetic pick-up coils in the L and H-phases. Magnetic measurements in the divertor chamber suggest that the satellite mode might be located outside the separatrix, on open field lines reaching the divertor /1/. Here we present results from localized microwave reflectometric measurements. The time evolution of the satellite mode frequency is studied for plasmas with different q_a and the mode localization is estimated, confirming that it should be close to but outside the separatrix. The central toroidal rotation velocities of the plasma can be inferred from the measured frequencies of the satellite modes.

2 - Local frequency spectra of the satellite mode

A set of H-mode deuterium discharges was analysed, with q_a at the edge between 2.6 and 3.8, where NBI (Deuterium co-injection, $P_{NI} \geq 2.3MW$) was applied Δ t = 1.2 s after the start of the discharge. Two density layers were probed simultaneously with fixed frequency reflectometry at the plasma edge, in the range $(0.5 - 1.2) \times 10^{13} cm^{-3}$, and local power spectra of density fluctuations were obtained.

As an example, the frequency distribution of the fluctuations detected during # 32225 is shown, as contour plots, in Fig. 1 (a) for $n_e = 0.6 \times 10^{13} cm^{-3}$. The H_α trace (Fig.1(b)) is also presented. A short ELM-free H-mode is observed where the fluctuations are supressed. At the second L-H transition, fluctuations again drop drastically and a coherent (satellite) mode coupled with central m=1, n=1 is clearly detected. Its frequency increases from $f_{L-H} \sim 18$ kHz at the end of the L-phase to a maximum $f_m \sim 24$kHz just before the occurence of the single ELM. The frequencies of the mode agree with Mirnov coil measurements that detect the mode during the L and H-phase, although with lower amplitude in the L-phase. As the layers probed by reflectometry in the L-phase are inside the separatrix but the mode location is outside (as it will be discussed later) the mode is hardly seen by reflectometry before the L-H transition; the high level of turbulence makes it difficult to detect a coherent structure of low amplitude.

As shown in Fig.2(a), the frequencies of the satellite mode grow during the H-phase, from f_{L-H} up to maximum observed values f_m. The highest value of the frequency represents a stationary level of the toroidal rotation velocity of the plasma. In some cases, before the saturation is reached, the (1,1) mode may be supressed due to sawtooth events. In these cases the maximum observed value is below the saturated value. The minimum temporal rate of change of the frequency is observed at plasmas with $q_a \sim 3.3$ and the maximum for $q_a \sim 3.8$; in the example of # 32230 ($q_a = 3.8$) a late transition occurs ($\sim$ 80 ms after NBI) and the maximum observed frequency (30 kHz) is reached soon after ($\sim$ 10 ms), when the mode is supressed.

3 - Relation of satellite frequency and plasma central toroidal rotation

As the magnetic field perturbation $\tilde{B}$ is expected to be frozen into the plasma, the measured frequency (f) of the satellite mode can give an estimate of the central toroidal rotation (f_ϕ) of the plasma. The existence of a pressure gradient in the plasma contributes locally with the diamagnetic electron drift frequency, which can be expressed as a purely toroidal contribution (f_d) to the mode frequency /1/. The central toroidal rotation velocity of the plasma can thus be roughly given (for co-injection) by $v_\phi = 2\pi R(f + f_d)$, where R is the plasma major radius and f_d is evaluated at the q=1 surface. In all the cases analysed there is a decrease in the drift frequency between t_{L-H} and t_s (due to the flattening of the profile close to the resonance surface), but a net increase of the toroidal rotation velocity is observed with maximum values in the range $\sim$ 250 - 350 km/s.

The obtained values of the toroidal rotation frequency at the L-H transition were compared with the frequency derived from the statistical analysis of the charge exchange recombination (CXR) spectroscopy data, for co-injection L-mode discharges /2/:

$$f_\phi[kHz] = 30\left(\frac{M}{\bar{n}_e}\right)^{0.61} \times I_p^{0.3}, \quad [MW, amu, 10^{19}m^{-3}, MA], \tag{1}$$

where M $\sim 1.2(A_b)^{1/2}P_{NI}$ Nm is the torque applied to the plasma, which is higher by deuterium beams (A_b=2) than by hydrogen (A_b=1). As (1) describes the central speed it slightly overestimates the velocity at the q=1 surface.

A good agreement is found between the values measured at the L-H transition and those predicted by the scaling law (1) (see Fig. 2(b)). The above comparison cannot be extended to the H-phase (where the total angular momentum of the plasma changes), as (1) only applies to stationary conditions.

In all the discharges analysed with deuterium an increase in the toroidal velocity during the H-phase is observed . This behaviour corresponds to early L-H transitions ($\sim$ 35 to 80 ms after beam injection), so the speeding up of the plasma may still last during the H phase. In contrast, in discharges with hydrogen injection the values measured for the satellite mode are constant and typically $\sim$ 17 kHz. This is due to the fact that the transition L-H usually occurs later than in deuterium discharges (some 200 ms after the neutral beams start), so the rotation velocity of the plasma is already saturated at the beginning of the H-phase. These results confirm that for the same set of plasma parameters the speed attained with deuterium injection is higher than with hydrogen.

4 - Localization of the m=1 satellite mode

The effect of the coherent fluctuations induced by the satellite mode on the wave propagation can be described using the geometric optics approximation. Fluctuations (with frequency Ω) cause mainly Doppler shifts of the phase φ due to the propagation in the plasma, $\varphi(t) = \varphi_c + \Delta\varphi sin(\Omega t + \delta)$, leading to phase modulations of the detected reflectometric signals (V(t)):

$$\begin{aligned} V(t) \sim & \frac{1}{2} + \frac{A^2 J_0(\Delta\varphi)}{2} + AJ_0(\Delta\varphi)cos\varphi + \cdot \\ & + \sum_{n=1}^{\infty} 2AJ_{2n}(\Delta\varphi)cos2n\Omega t cos\varphi - \sum_{n=0}^{\infty} 2AJ_{2n+1}(\Delta\varphi)sin(2n+1)\Omega t sin\varphi + \ldots \end{aligned} \tag{2}$$

where $J_n(\Delta\varphi)$ is the Bessel function of the first kind, and of order n. The phase modulation $\Delta\varphi$ can be obtained from the relative amplitude of the harmonics (odd or even) of

the frequency (Ω) /3/. The amplitude of the fluctuations ($\delta n_e/n_e$ at the reflecting layer (x_c) can be related with $\Delta\varphi$ by:

$$\frac{\delta n_e}{n_e} = \frac{3c}{8\pi f}(\frac{\nabla n}{n})_{x_c}\Delta\varphi \qquad (3)$$

Fig. 4 shows the frequency spectra of fluctuations, (# 32225) , (a) immediately after the L-H transition and (b) 10 ms after L-H, at two plasma layers: (I) $n_e = 0.6 \times 10^{13} cm^{-3}$ and (II)$n_e = 0.98 \times 10^{13} cm^{-3}$. Three harmonics are observed in the spectra due to the modulating frequency of the pertubation ($\Omega/2\pi \sim 18$ kHz). From the ratio between the first and third harmonic, $J_1(\Delta\varphi)$ /$J_3(\Delta\varphi)$, the values of the amplitude $\Delta\varphi$ were estimated. The temporal evolution of the plasma density profile was modelled from O-mode broadband reflectometry for similar discharges /4/. During the L-phase, with low density gradient ($\sim 0.15 \times 10^{13} cm^{-4}$), the probed layers are located at $r \leq 40cm$ (see Fig.5), inside the magnetic separatrix. Immediately after the transition the gradient at the edge steepens reaching $\sim 0.4 \times 10^{13} cm^{-4}$) at $\sim 10ms$ after L-H; by that time the position of the layers probed at fixed density is estimated to be at (I) r$\sim$ 43 cm and (II)r$\sim$ 42 cm.

From the above study it can be concluded that at the inner layer , (II), the rate of fluctuations decreases during $\Delta t_{L-H} \sim 10$ ms from $\sim 11.3\%$ to $\sim 6.7\%$; for the same time interval, the rate of fluctuations at the outer layer,(I), increases from $\sim 10.8\%$ to a maximum $\sim 31.8\%$. The localization of the mode is therefore shifted outwards from a region around 42 cm, to $r \geq 43$ cm. This is consistent with a mode location close to and outside the magnetic separatrix and a movement outwards during the H-phase by $\geq 1cm$. The spectral analysis shows a subsequent decrease in the rate of fluctuations at both layers. As the probed layers are now roughly at fixed radial positions (the build up of the density gradient at the edge is completed $\sim 20ms$ after L-H), the decrease of the fluctuations suggests therefore that the mode is being displaced further outwards following the displacement of the magnetic separatrix.

5 - Conclusions

The temporal evolution of the so-called "m=1 satellite mode" (coupled to the central m=1,n=1 activity) is studied with microwave reflectometry in H-mode plasmas with q_a between 2.6 and 3.8. The central toroidal velocities of the plasma are inferred from the measured mode frequencies, which increase during the H-phase for the deuterium co-injection discharges; a maximum temporal rate of change of the velocity is obtained for plasmas with $q_a \sim 3.8$, and a minimum for $q_a \sim 3.3$. The localization of the mode is obtained from density profile reflectometry measurements and from the analysis of the local frequency spectra. Results show that the mode should be localized close to and outside the magnetic separatrix, giving further evidence to the previous estimates based on magnetic measurements /1/. During the H-phase the maximum amplitude of the mode is observed to shift outward by ≥ 1 cm, suggesting that the mode is radially moving outward together with the magnetic separatrix.

References

/1/ O. Klüber et al., Nuclear Fusion, Vol. 31, No. 5, 907 (1991).
/2/ A. Kallenbach et al., Nuclear Fusion, Vol. 30, No. 4 (1990).
/3/ E. Mazzucato , Report MATT 1151, Plasma Phys. Lab., Princeton (1975).
/4/ M. E. Manso et al., 18th Eur. Conf. Berlin, Vol. 15C, I-393 (1991).

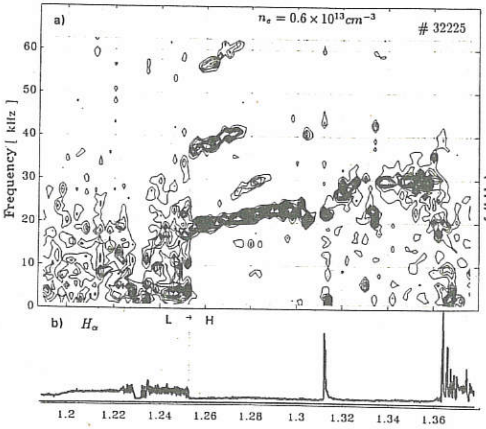

Fig. 1

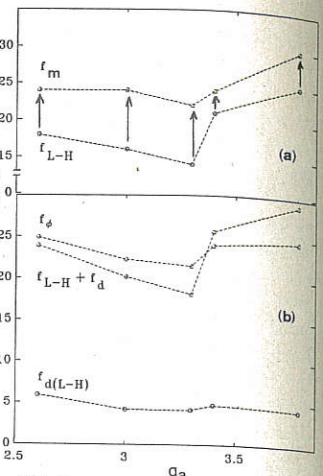

Fig. 2

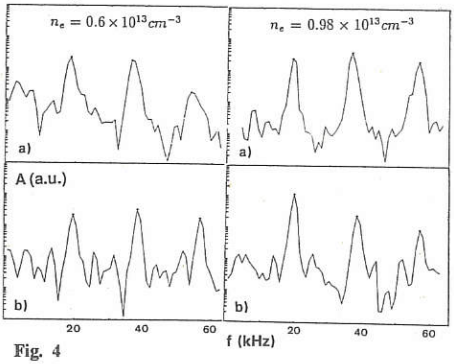

Fig. 4

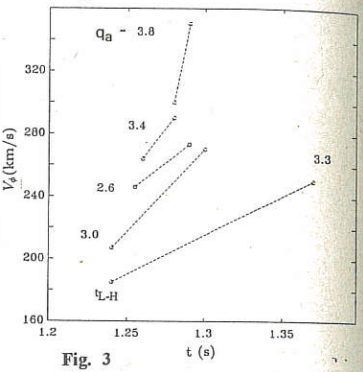

Fig. 3

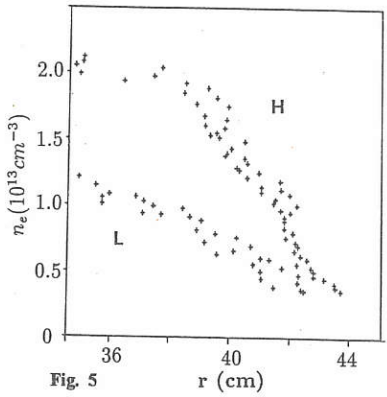

Fig. 5

Fig. 1 a) Contour plot of the power spectrum at n_e=0.6x10^{13}cm^{-3}, b) H_α at the divertor, for #32225.

Fig. 2 a) Frequencies of the satellite mode at the transition, (f_{L-H}), and maximum values (f_m) measured by reflectometry during the H-phase, b) Comparison between f_ϕ and $f_{L-H} + f_d$, for different q_a plasmas.

Fig. 3 Estimate of the central toroidal rotation V_ϕ showing its increase from the transition (t_{L-H}) to a maximum in the H-phase.

Fig. 4 Power spectrum of density fluctuations for a) Δt=1254 - 56 ms, b) Δt=1264 - 66 ms, for #32225.

Fig. 5 Density profiles from reflectometry for the L-phase, and for ~10 ms after the L-H transition.

A QUANTITATIVE ANALYSIS OF THE EFFECT OF ELMS ON H–MODE THERMAL ENERGY CONFINEMENT IN DIII–D*

D.P. Schissel, T.H. Osborne, T.N. Carlstrom, and H. Zohm†

General Atomics, San Diego, CA 92138 U.S.A.

The desire to reach ignition in future tokamaks makes the energy confinement time (τ_E) a critical parameter. The most promising enhanced (over L–mode) confinement regime is the H–mode, discovered on ASDEX with neutral beam heating, and then confirmed with various auxiliary heating sources on numerous machines. The knowledge of how H–mode τ_E depends on different parameters is of crucial importance to the performance predictions for next generation devices. Inter-machine H–mode total and thermal energy confinement (τ_{th}) scalings,[1,2] which are being utilized to predict ITER thermal energy confinement, have been created for discharges where the Edge Localized Mode (ELM) instability has not been present. Confinement scaling research has concentrated on this ELM-free H–mode phase mostly owing to the difficulty of characterizing ELM behavior. To date, long pulse H–mode operation has only been achieved by utilizing ELMs to flush out impurities and prevent radiative collapse of the discharge. Unfortunately, accompanying the ELMs is a decrease of the plasma stored energy due to the expulsion of particles near the edge of the discharge resulting in a reduction of the steep edge electron density gradient. In order to predict ITER's H–mode τ_{th} in the presence of ELMs, an estimated 25% confinement degradation factor has been applied to the ELM-free predictions.[3] Our work, summarized in this paper, indicates that this 25% reduction factor is too large and instead a value of approximately 15% would be more appropriate.

Three types of ELMs have been observed on DIII–D. The first is the giant ELM which is believed to occur with the edge pressure gradient at the ideal ballooning mode limit. Thus, the frequency of these ELMs increases with neutral beam power and decreases with plasma current (I_p). The second, the grassy ELM, is most easily seen when the plasma shaping produces edge conditions stable to ballooning modes. The third, the threshold ELM (or Type III) is observed when the input power is just above the threshold power needed for H–mode. Two methods for determining the effect that ELMs have on τ_{th} are to measure the energy loss per ELM and therefore determine an average power loss due to ELMs. The second method is to accurately follow the temporal evolution of the plasma stored energy (W_T), calculate the time derivative of W_T ($\dot{W}_T$), and then calculate τ_{th}. The latter method can be used for all three types of ELMs where with the threshold ELMs the former method can be difficult in practice since the energy loss per ELM becomes so small. For the discharges analyzed in this paper, the neutral beam power has been kept large enough so that no threshold ELMs were obtained and therefore both methods for determining the effect of ELMs have been utilized.

Previously on DIII–D at 1.1 T, the diamagnetic loop was used to make a quantitative estimate of the average power loss due to ELMs for a current scan ranging between 0.5 MA and 1.4 MA.[4] This analysis was made possible since the diamagnetic loop is sensitive enough to resolve small drops in plasma stored energy caused by individual ELMs. The results presented in Ref. 4 found that the time averaged ELM power loss did not exceed 0.7 MW with 5 MW of neutral beam heating; at most a 15% effect. As the plasma current was increased the ELM frequency decreased while the energy loss per ELM increased resulting in an approximate constant power loss per ELM.

* This work was supported by the U.S. Department of Energy under Contract No. DE-AC03-89ER51114.

† Max-Planck-Institut für Plasmaphysik, Garching bei München, Germany.

Since the publication of Ref. 4, new diagnostic capability on DIII–D makes it possible to determine the thermal stored energy (W_{th}) and therefore τ_{th} from kinetics for both the ELM-free and ELMing phase of the same discharge. This new measurement capability on DIII–D is the multi-pulse Thomson scattering diagnostic. Thomson scattering measures electron density (n_e) and temperature (T_e) profiles with a constant 6.25 msec time resolution. Combining these measurements with ion temperature (T_i) profiles determined by the charge exchange recombination diagnostic and effective charge (Z_{eff}) profiles calculated from visible bremsstrahlung emission makes it possible to calculate W_{th}.

To study the effect of ELMs on τ_{th} by using DIII–D's profile diagnostics, a controlled plasma current ($0.5 \leq I_p(\mathrm{MA}) \leq 2.0$) scan was performed at 2.1 T and with 6.8 MW of deuterium neutral beam heating. These discharges had between 0.1 second and 0.2 seconds of an ELM free H–mode phase before the onset of grassy ELMs at low current and giant ELMs at higher currents. The temporal evolution of one of these discharges at 1.0 MA is shown in Fig. 1. The neutral beam heating was injected beginning at 2.0 sec, the transition to H–mode occurred at 2.04 sec and the first ELM was at 2.18 sec. The energy confinement τ_E rises from the L–mode value to a peak value in H–mode of 0.221 sec and then begins to decrease. This decrease in confinement is expected since it has been demonstrated on numerous tokamaks that in neutral beam heated discharges $\tau_E \sim P_L^{-0.5}$ where $P_L = P_T - \dot{W}_T$ and P_T is the total input power. Given the definition of τ_E and the observation that $\tau_E \sim P_L^{-0.5}$, it follows that $W_T \sim P_L^{0.5}$ and consequently, $\tau_E \sim 1/W_T$ for fixed plasma current, toroidal field and input power. Early in the H–mode phase W_T is small so τ_E is large. As time progresses in the H–mode, W_T increases to a steady state value resulting in smaller values in τ_E until steady state is obtained. In Fig. 1, the calculation of fast ion stored energy (W_f), and therefore τ_{th}, has been derived assuming classical processes and has been normalized to previous results from ONETWO transport analysis.

We first examine the effect of a single ELM on the plasma energy content. This is most easily done with a giant ELM because it expels the largest amount of energy and occurs with the smallest frequency. Since giant ELMs are most prevalent at higher currents we examine a 2.0 MA discharge. Figure 2 illustrates the effect of a single giant ELM on the n_e, T_e, and Z_{eff} profiles for a 2.0 MA single null divertor discharge. The predominate effect of the ELM is to expel particles from the outside of the discharge. The thermal stored energy is reduced by 15% as determined from profile measurements and the total stored energy is reduced by 12% as determined by magnetic measurements; both numbers are within their respective uncertainties of each other.

From the effect of a single ELM we now examine the collective effects of many ELMs on τ_{th} in the 2.1 T current scan. Utilizing the diamagnetic loop to determine the energy loss per ELM we find similar results to what was stated earlier; with increased current the ELM frequency decreased, the energy loss per ELM increased yielding an approximate constant power loss per ELM. The time averaged ELM power loss is at most 1 MW which again is approximately 15% of the input power.

The result of the 2.1 T current scan where τ_{th} is calculated during both the ELM-free and ELMing phases of the same discharge by profile measurements is illustrated in Fig. 3. It is possible that the grassy ELMs at low current effect confinement in a different amount than the giant ELMs at higher current. However, our analysis via the diamagnetic loop indicates that the average power loss due to ELMs is approximately constant. Furthermore, our W_{th} analysis also does not indicate that the ELM effect varies with current. For these reasons we calculate an average ELM effect; the average ratio (R_τ) of ELMing τ_{th} to ELM-free τ_{th} in Fig. 3 is 0.82 ± 0.07. The values of τ_{th} for the ELM-free phases are approximately 20% better than what is predicted by the ELM-free DIII–D/JET H–mode scaling[1] given by $\tau_{th}^{JD} = 0.106\, I_p^{1.03}\, P_L^{-0.46}\, R^{1.48}$ where R is the plasma major radius. Since boronization, H–mode τ_{th} has been superior to the pre-boronization values and the 20% enhancement over the DIII–D/JET prediction is consistent with these observations. It must be stressed that the discharges analyzed in this paper are not VH–mode plasmas. Our present understanding of VH–mode discharges is that ELMs somehow prevent VH–mode confinement behavior and therefore significantly impact τ_E in these cases.

There are at least two pieces of physics that were not included in the above calculation which when included should increase the value of R_τ. The first involves the temporal evolution of l_i. In DIII–D, with the transition from L–mode to H–mode the current profile becomes broader due to the increasing edge temperature; l_i decreases. This decrease of l_i is more pronounced at lower currents where q is larger and the current profile is initially more peaked. The effect of the current profile on global confinement is an active area of research on numerous tokamaks including DIII–D. Initial results from DIII–D current ramp experiments[5] indicate that in highly shaped H–mode discharges τ_E depends weakly on l_i. Therefore, ELM-free τ_{th} will be overestimated relative to the ELMing τ_{th} due to the larger value of l_i. In an attempt to examine the possible effect that a changing l_i has on our results, we assume that the thermal confinement has a $\sqrt{l_i}$ dependence and recompute R_τ. Normalizing τ_{th} by $\sqrt{l_i}$ increases R_τ to 0.87 ± 0.08.

The second effect on R_τ has to do with the temporal evolution of τ_E. Previously it was discussed (Fig. 1) that given the observation that $\tau_E \sim P_L^{-0.5}$, τ_{th} will decrease in time until a steady state value is obtained. Since the confinement analysis in the ELM-free phase was performed when $\dot{W}_T > 0$ but the ELMing τ_E was calculated when $\dot{W}_T = 0$, the ELM-free τ_E has possibly been overestimated relative to the ELMing τ_E. There is no easy way to quantify the reduction in the ELMing τ_E. However, this reduction in ELM-free τ_{th} will only increase R_τ.

On DIII–D, numerous H–mode discharges have been operated for up to 10 sec with the duration limited only by available power supplies. These H–modes were made possible by adjusting the neutral beam power to set the ELM frequency and therefore achieve quasi-steady state conditions. Control of the ELMs was critical for the operation of these steady state plasmas since they determine the impurity accumulation and density rise. Since ITER is planned as a quasi-steady state device, the most ITER relevant ELMs to study are those that allow for long pulse operation. For the DIII–D long pulse H–modes, T_e and n_e profiles during both the ELM-free and ELMing phases were not available. It is possible to calculate W_{th} from $W_T - W_f$. However, the fast ion stored energy is most accurately determined when the fast ion content is small relative to the total energy content. For that reason, it is difficult to calculate a value of τ_{th} with a small uncertainty in the ELM-free phase since the density is low resulting in a large fast ion content. Because of this difficulty, we have chosen to examine the long pulse H–mode discharges at the end of the H–mode phase, the ELMing phase, and compare the calculated value to τ_{th} predicted by the JET/DIII–D ELM-free thermal confinement scaling. Since the long pulse H-modes have been obtained prior to boronization, the predictions of the JET/DIII–D scaling should be valid. The 5.0 sec long H–mode discharges considered have a plasma current range of $1.2 \leq I_p(\mathrm{MA}) \leq 1.7$ at 2.1 T and neutral beam heating range of $3.5 \leq P_b(\mathrm{MW}) \leq 11.1$. For these 13 discharges an average value of R_τ, relative to the JET/DIII–D prediction, of 0.83 ± 0.05 is obtained. This number again is very similar to that obtained for the current scan of Fig. 3.

In summary, the effects of ELMs on τ_{th} has been investigated for a wide variety of plasma currents, neutral beam powers, and length of H–mode duration. Our results indicate that the reduction in confinement due to ELMs, R_τ, of 0.75 presently used for the ITER design is too pessimistic. Research on DIII–D indicates a conservative value of R_τ near 0.85 is more realistic even for H–modes of 5 second duration or approximately 50 confinement times.

[1] Schissel, D.P., *et al.*, Nucl. Fusion **31** (1991) 73.

[2] Christiansen, J.P. , *et al.*, Nucl. Fusion **32** (1992) 291.

[3] ITER Team, ITER Physics, ITER Documentation Series No. 21, IAEA, Vienna (1991).

[4] Schissel, D.P., *et al.*, Nucl. Fusion **32** (1992) 107.

[5] Ferron, J., *et al.*, "The Effect of Current Profile Changes on Confinement in the DIII–D Tokamak," to be presented at the 19th EPS Conf. on Controlled Fusion & Plasma, June 29–July 3, 1992.

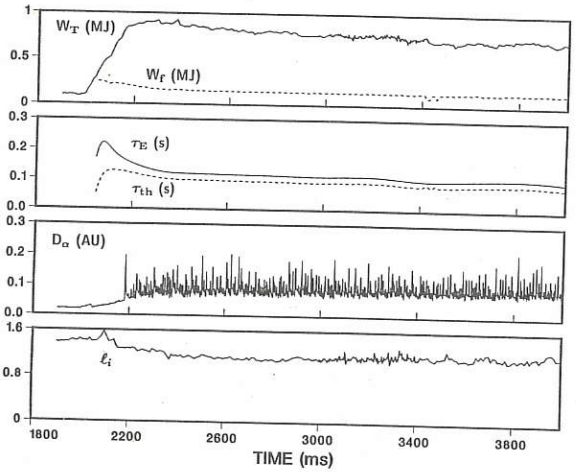

Fig. 1. Temporal evolution of a 1.0 MA H–mode discharge with 6.78 MW of neutral beam heating beginning at 2000 msec.

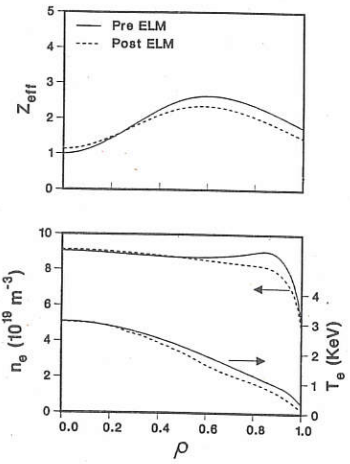

Fig. 2. Effect of a giant ELM on a 2.0 MA H–mode discharge. The plasma profiles are taken 12 msec before and 8 msec after the initiation of the giant ELM.

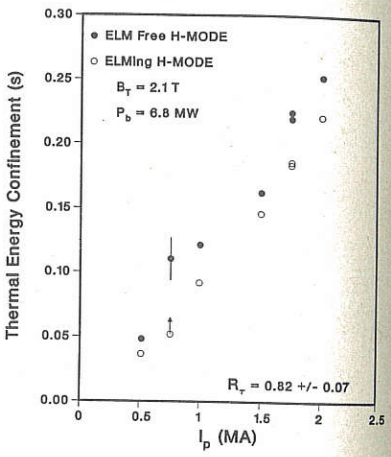

Fig. 3. H–mode τ_{th} increases with plasma current for both the ELM-free and ELMing phases. The average confinement reduction, R_τ, due to ELMs is 0.84. The arrow on the open circle at 0.75 MA indicates that τ_{th} would have been larger if large amplitude MHD activity had not been present at this time.

Steady State H-modes in JET

P.R.Thomas, D.J.Campbell, A.Gondhalekar and C.J.Lowry

JET Joint Undertaking, Abingdon, Oxon OX14 3EA, UK

Introduction: Usually, H-modes in JET are free of ELMs so that the density rises uncontrollably and, with it, the radiated power. When the radiated power approaches the input power, a transition back to the L-mode occurs. During ELM free H-modes, the density profile is extremely steep near the separatrix and, at high densities especially, can even be hollow. Also, impurities are compressed within a narrow zone near to the seperatrix [1]. Such plasma behaviour would be unacceptable in ITER because of the difficulty that it would cause in establishing a steady-state burn.

In contrast to JET, other tokamaks observe H-modes with ELMs to be the normal behaviour. The ELMs affect H-mode plasmas by reversing the inward particle flow at the boundary. This results in a particle efflux with a relatively small additional power loss. Since impurity and hydrogenic ions are all ejected by the ELMs, the radiated power is controlled and stable, steady-state operation obtained. Therefore, the deliberate generation and control of ELMs is an obvious way to produce steady-state H-modes in JET.

This paper will describe the methods of ELM production investigated, the results obtained and a scenario which allowed H-modes of up to 18 seconds duration to be produced at 7.5MW input power. These plasmas reached steady conditions both in the magnetic equilibrium and the target tile temperature. The only limit to their duaration was the shear stress induced in the shaping windings by electrical heating. There are signs however that, in the absence of any active pumping, density control is being lost because of the loading of plasma-facing surfaces with deuterium. The same scenario has been successfully demonstrated at 18MW input power, albeit for shorter pulses.

The Investigation of ELM Production and Control: Compared with other machines, JET H-modes appear to be remarkably immune to ELMs. Whether this is due to low edge collisionality ($\nu^*_e \sim 0.05$), high edge conductivity or, as suggested by a recent experiment in JET [2], its low toroidal field ripple is not entirely clear. Most of the experiments which will be described were directed towards reducing the edge electron temperature in order to increase the edge collisionality or resistivity. This direction of approach is supported by observations of ELMs being triggered by laser ablated impurities in JET. Methods involving positioning of the

plasma close to material surfaces were eschewed, both because of the resultant heating of the surfaces and the lack of reproducibility observed in previous experiments.

However the first experiments was quite different in character, as it involved current density modulation to see if the ELM stability could be affected by the edge current density. Single ramps and one or two cycle oscillations of the plasma current were tried. Although ELMs were observed, there was no convincing evidence that the current modulation was responsible and control of the discharges was certainly not obtained. Such ELMs as were observed seemed to be associated with ICRH power trips which were caused by the plasma/antenna coupling changing with slight equilibrium shifts. As the input power dropped down to approximately the same level as the radiated power, ELMs were triggered.

In the 1990 experimental campaign, steady-state H-mode plasmas had been made by heavy fuelling(140mb-l.s^{-1}) of a deuterium plasma with hydrogen gas[3]. The steady ELMy phase lasted about 2 seconds. Deuterium gas fuelling did not produce the requisite ELMs. When further attempts were made in the 91/92 campaign to use deuterium gas fuelling, with no other measures, the ICRH dominated plasmas were prone to disruption because of locked modes produced at monster sawtooth crashes. Whilst some ELMs were observed, steady-state conditions could not be obtained. However, the other recipes, including the successful one, all use gas fuelling to cool the boundary.

In addition to the use of gas fuelling to modify the edge plasma power balance, modulation of the ICRH was tried. There is some evidence that this had the desired effect in a plasma in which ICRH provided 7.5MW out of 11MW of input and was modulated to a depth of 30% at 20Hz. Whilst a 2 second period of ELMs was produced, their effect on the plasma density was insufficient and the H-mode terminated because the radiated power grew to equal the input power. This technique would appear to be worthy of future investigation, although its application to burning plasmas would appear to be somewhat limited!

Finally a robust ELMy plasma was obtained by moving the ICRH resonance position off-axis in order to suppress the monster sawteeth which had caused the problems described above. By dropping the toroidal field from 2.8T to 2.3T, the 42MHz hydrogen minority resonance was moved about 0.5m inboard of the magnetic axis. The plasma current was limited to 2MA in order to keep shear stresses, induced in the poloidal field coils by electrical heating, low enough to allow an X-point configuration of 20s duration. The H-mode duration was extended gradually to ensure that the X-point target was not overheated. The longest H-mode in the sequence is shown in figure 1. Unfortunately, further optimisation of the ICRH

resonance position and the gas fuelling rate was not possible because the neutron budget for the experiment had been exhausted. The characteristics of this 18.5s H-mode will be described in the next section.

Characteristics of the Long Pulse H-modes: It may be seen from figure 1 that, following an ELM free period of slightly more than 2s, ELMs appear and grow to an amplitude and frequency such that the density and radiated power are stabilised. An steadily increasing baseline on the D_α emission and an increase in density in the final seconds of the H-mode are indicative of increasing saturation of the X-point target with deuterium. Since the gas fuelling rate falls by a factor of two during the H-mode, active pumping of the target plasma would be required to extend the pulse much further. The fall in the fusion rate over the last 5 seconds of the H-mode mirrors the density increase and can be ascribed to the corresponding drop in temperature.

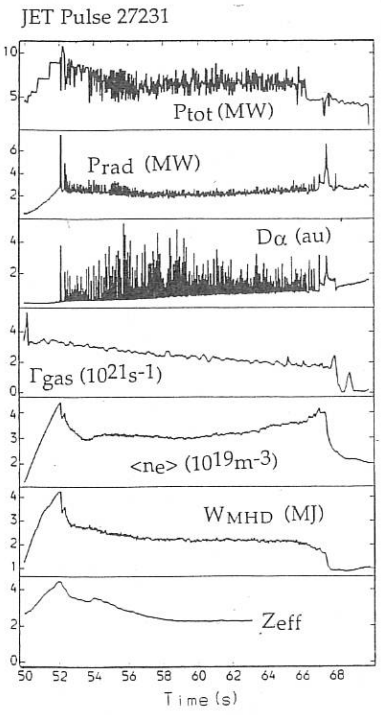

Figure 1: An 18second long H-mode, produced using heavy gas fuelling and off-axis ICRH

The density profile is flat in the interior region with an approximately linear fall off in the outer 15cm.. Fast reflectometer data show that the ELMs are confined to the gradient region and, it seems likely, control the profile shape. The electron temperature displays sawteeth at the largest ELMs, just inside of the density gradient region, with $\delta T_e/T_e$~0.05-0.1. This is reflected in the time averaged thermal conductivity in the outer half of the plasma which increased to $1.4m^2.s^{-1}$ from the ELM free value of $0.5m^2.s^{-1}$. In contrast, the central electron temperature sawteeth are diminished by the off-axis heating to an amplitude of ~150eV in 3keV The global energy confinement shows an enhancement over Goldston L-mode scaling (with A_i=1) of only 1.5. No doubt, this could be improved upon by optimisation of the ICRH resonance position or by taking the heating efficiency into account..

CCD images of the target tiles in D_a and CII light show thermal breakthrough at the strike points in the former but not the latter. From these data the peak temperature of the tiles can be estimated to be between 1200 and 1300°C. The intensity of the hot spots diminishes slightly throughout the H-mode, indicating some cooling of the target in spite of some 75MJ being delivered to it. Either the CCD field of view is atypical or the power is being spread by a radiative target plasma [4]. Z_{eff} falls initially and flattens out at about 2.2, which is indicative that the tile temperature measurements are typical and that no region of the target is being severely overheated. Except for the last few seconds, the internal inductance and the second and third Shafranov moments flatten out so these plasmas can be said to have come into a true steady state.

Discussion: In spite of the disappointingly small energy confinement enhancement, these plasmas do demonstrate that it is possible to make long steady state H-modes. The same condition has been obtained for 3s at 18MW. Interestingly, the high power discharges, which have some 15MW of NBI, show an enhancement over L-mode scaling of 1.6, indicating the optimisation of the long pulses which might be possible if the reliance on ICRH had been reduced or if the resonance position had been changed. It is clear that it was the heavy gas fuelling which was responsible for producing the ELMs. The off-axis ICRH had the function of suppressing monster sawteeth and subsequent locked modes. The systematic diagnosis of the plasmas to elucidate the mechanism triggering the ELMs and the reason for past failures with deuterium puffing is a task for the future.

The difficulties with monster sawteeth during ICRH demonstrate what might happen in a burning plasma. Unfortunately, off-axis α-particle heating is not an option which can be readily realised! It is possible therefore, that reliance will have to be placed on MHD or α-particle instabilities to spread the power deposition and so allow long burn pulses in ITER. The use of heavy gas fuelling to control the target heat load and to facilitate long pulse operation will extend into the JET Pumped Divertor phase. The active target pumping will permit true steady state to be demonstrated and optimised.

References

[1] Giannella et al., EPS Conference Amsterdam, Vol. 14B, Part 1, p247.
[2] B.J.Tubbing et al., this meeting.
[3] D.Stork et al., EPS Conference Berlin, Vol. 15C, Part 1, p357.
[4] G.Janeschitz et al., this meeting.

ELM STUDIES ON DIII-D AND A COMPARISON TO ASDEX RESULTS*

H. Zohm,† T.H. Osborne, K.H. Burrell, M.S. Chu, E.J. Doyle,‡
P. Gohil, D.N. Hill,° L.L. Lao, T.S. Taylor, and A.D. Turnbull

General Atomics, San Diego, California, U.S.A.

1. INTRODUCTION

The H-mode[1] is one of the most promising confinement regimes for a possible tokamak reactor. Up to now, the only way to maintain a steady state H-mode discharge is to allow for periodic Edge Localized Modes (ELMs).[2] ELM studies have been performed on various tokamaks.[3-5] On DIII-D, three ELM categories are known,[6] whereas on ASDEX, only one type of ELM exists.[5] This paper investigates MHD characteristics of different ELM categories on DIII-D and compares them to observations made on ASDEX. We find ELMs observed on ASDEX exhibit the same phenomenon as type III ELMs on DIII-D.

2. EXPERIMENTAL OBSERVATIONS ON DIII-D

In DIII-D, the following ELM behaviour is observed. At heating powers just above the threshold for L-H transition, type III ELMs occur; their frequency decreases with increasing heating power until they are finally stabilized resulting in an ELM-free period. A further rise in heating power leads to occurrence of type I ELMs, and their frequency now increases with heating power.

Ideal ballooning stability analysis of edge plasma has been done using experimental profiles of n_e and T_e and assuming $T_i = T_e$ and $n_i = n_e$ to determine the normalized pressure gradient $\alpha = (2\mu_0 \nabla p)/(B_t^2 R_0)$. To analyze a large number of cases, we assumed an offset linear dependence of the critical pressure gradient α_{crit} on the edge shear S/q^2, where $S = d\ell n\, q/d\ell n\, \psi$ (a more detailed stability analysis is presented in Section 4). This analysis shows type III ELMs are observed at $0.3 \leqslant \alpha/\alpha_{crit} \leqslant 0.5$ and type I ELMs ('giant ELMs') occur at $\alpha/\alpha_{crit} \approx 1$, consistent with a previous analysis.[3] This behaviour is also found in Helium discharges for $0.1 \leqslant S/q^2 \leqslant 0.5$. Therefore, the ideal ballooning mode can be excluded as the mechanism for type III ELMs. When, at $\alpha/\alpha_{crit} \approx 1$, the edge is cooled by strong gas puffing, the edge pressure gradient remains nearly constant (*i.e.*, $n\delta T = -T\delta n$). In this case, type I ELMs become more frequent, although the pressure gradient itself has not changed. This might indicate the ideal ballooning mode limits achievable edge pressure gradient but is not the type I ELM mechanism itself.

The sequence described above can also be observed at constant high input power during the rise of α after onset of the additional heating. In an early phase, where $\alpha/\alpha_{crit} < 0.5$, type III ELMs appear, these are stabilized at higher values of α until, at $\alpha/\alpha_{crit} \approx 1$, type I ELMs appear. Type II ELMs ('grassy ELMs') differ from the scheme described above in that they occur only in strongly shaped plasmas at low S/q^2, where the edge region is found to be in the connection between the first and second stable regime.

The different types of ELMs have different consequences on MHD equilibria. To evaluate effects on equilibria introduced by different types of ELMs, we use the magnetic equilibrium

*This is a report of work sponsored in part by the U.S. Department of Energy under Contract Nos. DE-AC03-89ER51114 and W-7405-ENG-48, and Grant No. DE-FG02-86ER-52126.
†MPI f. Plasmaphysik, D-8046 Garching, F.R.G., EURATOM-Association.
‡University of California, Los Angeles, California, U.S.A.
°Lawrence Livermore National Laboratory, Livermore, California, U.S.A.

fitting code EFIT[8] with input data from Mirnov loops inside the vessel sampled at 200 kHz. A typical example is shown in Fig. 1: a type I ELM changes the energy content of plasma by 15% and also introduces a change in ℓ_i of $\approx 5\%$, indicating a change in current profile. For a typical type III ELM, the energy change is less pronounced (5%) and the change in ℓ_i, if any, is of the order of the resolution of the fitting code (1% to 2%). This is consistent with the signature on integrated Mirnov coils (B_θ, midplane outside): due to the change in internal inductivity, type I ELMs exhibit a spike resembling that observed at a minor disruption; type III ELMs do not show this feature. The effects of ELMs on confinement are discussed elsewhere.[9]

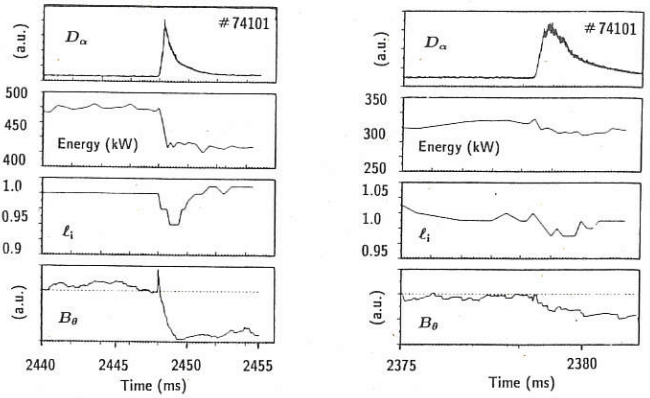

FIG. 1. Change in the equilibrium parameters due to a type I (left) and type III (right) ELM. Note the different time axis.

A further difference between type I and type III ELMs is found in their precursor activity as observed in density and magnetic fluctuations[6]: before type I ELMs, the general broadband fluctuation level slowly increases within 30 to 50 ms before the ELM, whereas type III ELMs always have a coherent precursor with a toroidal mode number of 5 to 10 lasting for up to 10 ms. During both types of ELMs, magnetic and density fluctuations may reach or even exceed L–mode level.

The duration of type I ELMs decreases with increasing heating power[2]: at high heating power (*e.g.*, 10 MW in a discharge with $I_p = 1$ MA and $B_t = 2.1$ T), the typical duration of a type I ELM is 1 to 2 ms. At intermediate heating power, (*e.g.*, 3 MW for conditions mentioned above), type I ELMs may last for up to 15 ms. These 'long' ELMs consist of two phases: first, a 1 to 2 ms phase which resembles the short type I ELM is seen. Then, the D_α emission and fluctuation level returns to L–mode levels. The event ends with an L–H like transition. IRTV camera measurements of the heat flux to the divertor target plates have shown that, during ELMs, a large heat pulse arrives. During a long ELM, this pulse is coincident with the first phase, whereas in the second phase, the heat flux returns to a low level. Figure 2 shows the temporal evolution of magnetic fluctuation spectra measured by a magnetic probe located under the strike point for a long and a short ELM. It can be seen that in both cases, during the initial event lasting 1 to 2 ms, high frequency fluctuations exist. In the case of short ELMs, the fluctuation level drops to H–mode level after this phase, in long ELMs, it transiently returns to

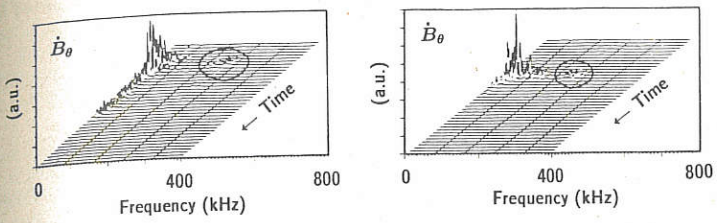

FIG. 2. Temporal evolution of a long (left) and a short (right) type I ELM; circles indicate the high frequency component mentioned in the text. Time interval shown is 10 ms.

L–mode level. The second phase of the ELM does not exhibit high frequency fluctuations. The edge pressure gradient before both events shown in the figure is at the ideal ballooning limit.

Type III ELM · normally last for 1 to 2 ms. At intermediate heating power, there are also 'long' ELMs which exhibit a coherent precursor. The temporal evolution of the D_α emission and the fluctuation spectra during these events suggest they are also compound events consisting of an MHD event followed by an L–phase. Here, the edge pressure gradient is less than 50% of the ideal ballooning limit; therefore, the MHD event is identified as a type III ELM (consistent with occurrence of the coherent precursor).

We conclude that type I and type III ELMs both are MHD events lasting 1 to 2 ms which may be followed by a transient L-phase lasting up to 15 ms. The transient L–phase is only observed at intermediate heating powers: to maintain the H–mode, energy loss caused by an ELM must be balanced by auxiliary heating. As type III ELMs rise in amplitude with increasing heating power, they are more likely to trigger an L–mode at a heating power well above the H–mode threshold. Type I ELMs, which introduce a bigger energy loss, can also trigger L–mode but, at highest heating power, re-heating obviously is sufficient to maintain H–mode.

3. COMPARISON WITH ASDEX RESULTS

As mentioned before, on ASDEX only one type of ELM existed for input powers from the power threshold of the L–H transition up to the β-limit.[5] The ELMs observed on ASDEX were very similar to type III ELMs on DIII–D. ASDEX ELMs occurred at $\alpha/\alpha_{crit} < 1$, became less frequent with rising heating power, and were stabilized at even higher power. They always exhibited a coherent precursor oscillation with mode numbers $m = 10$ to 15 and a frequency $\approx m\omega^*$, where ω^* is the electron diamagnetic drift frequency. Also, energy loss caused by an ELM in ASDEX was of the order of 5% and no change in ℓ_i could be detected. On DIII–D, all these features are typical for type III, but not for type I ELMs. We conclude that ELMs observed on ASDEX exhibit the same phenomenon as type III ELMs on DIII–D.

The duration of ELMs on ASDEX was 0.5 to 1 ms; a compound phenomenon as described above was not observed on ASDEX. For this reason, ELMs on ASDEX were not considered H–L–H transitions, whereas on DIII–D, this sequence triggered by an ELM can occur. Note that the experimental evidence showing that ELMs on DIII–D are a transient return to L–mode as *e.g.*, given in Ref. 2 was obtained during compound ELMs.

4. MHD STABILITY ANALYSIS

In order to study the MHD stability properties of ELMing discharges, we first analyze an equilibrium just prior to a type I ELM. The equilibrium reconstruction uses experimental

profiles of T_e, n_e, T_i, Z_{eff}, and P_{rad}, as well as the radius of the $q = 1$ surface determined from sawtooth inversion radius. Also, the pressure contribution from the fast beam ions is taken into account. This fixes the pressure profile and puts constraints on the current profile. We vary current profile by changing the value of j_{1n}, *i.e.*, current density at the 95% flux surface normalized to average current density. The best fit is obtained for $j_{1n} = 0.51$; we analyzed four different equilibria with $j_{1n} = 0.41$, 0.46, 0.51, and 0.57.

An infinite n ideal ballooning stability analysis using the codes MBC[10] and CAMINO[11] shows most flux surfaces are in the first stability regime and the experimental pressure gradient is well below the critical value. Near the edge, however, where the pressure gradient reaches its highest value, the effect of the edge current becomes important: the last flux surfaces are analyzed to be in the connection region to the second stable regime; the region which has access to the second stable regime widens with increasing edge current. For the values of the edge current given above, the pressure gradient approaches but never reaches the ballooning limit. This result suggests giant ELMs can also occur in plasmas which are stable against ideal high n ballooning modes.

A detailed analysis of the ballooning stability of an equilibrium prior to a type III ELM reveals ideal ballooning stability for the whole profile. In this example, the whole plasma is found to be in the first regime (edge current is significantly lower, *i.e.*, $j_{1n} = 0.23$). This confirms our previous observation that type III ELMs may occur well below the ideal ballooning limit, also consistent with findings on ASDEX. On ASDEX, an ELM model involving finite n resistive ballooning modes which nonlinearly couple to form a peeling mode has been found to give good agreement with experimental findings.[5] It will be an issue of further studies to apply this model to DIII–D discharges.

5. CONCLUSIONS

Our analysis has shown that the type III ELMs observed on DIII–D are similar to the ELMs observed on ASDEX, whereas type I ELMs did not occur on ASDEX. Furthermore, ELMs are found to be MHD events of short duration (1 to 2 ms), which, on DIII–D, may be followed by a transient L–mode phase. This compound event was not observed on ASDEX. A stability analysis of DIII–D discharges indicates type III ELMs occur well below the ideal ballooning limit. Type I ELMs generally occur close to this limit; there are, however, indications they also occur in discharges in which the edge is in the connection region to the second stability regime.

REFERENCES

1. The ASDEX Team, Nucl. Fusion **29** (1989) 1959.
2. Burrell, K.H., *et al.*, Plasma Phys. and Contr. Fusion **31** (1989) 1649.
3. Gohil, P., *et al.*, Phys. Rev. Lett. **61**, (1988), 1603.
4. Kaye, S.M., *et al.*, Nucl. Fusion **30** (1990) 2621.
5. Zohm, H., *et al.*, "ELM Studies on ASDEX," to be published in Nucl. Fusion.
6. Doyle, E.J., *et al.*, Phys. Fluids B **3** (1991) 2300.
7. Ozeki, T., *et al.*, Nucl. Fusion **30** (1990) 1425.
8. Lao, L.L., *et al.*, Nucl. Fusion **25** (1985) 1611.
9. Schissel, D.P., *et al.*, this conference.
10. Moore, R.W., *et al.*, Nucl. Fusion **25** (1985) 1575.
11. Greene, J.M., *et al.*, Nucl. Fusion **21** (1981) 453.

MHD STABILITY MODELS OF EDGE LOCALIZED MODES IN JET DISCHARGES

G.T.A. Huysmans[1], H.J. de Blank, W. Kerner, J.P. Goedbloed[1], and M.F.F. Nave[2]

JET Joint Undertaking, Abingdon, Oxon, OX14 3EA, UK.

[1] *FOM-Instituut voor Plasmafysica 'Rijnhuizen', Nieuwegein, the Netherlands*

[2] *Associação IST/EURATOM, Lisbon, and LNETI Sacavém, Portugal*

Introduction

Edge localized modes (ELMs) are observed in JET H-mode discharges under a wide range of circumstances and their amplitudes and repetition rates vary considerably [1,2]. Small, very frequent ('grassy') ELMs often occur when an H-mode builds up. As the edge electron temperature increases, they become larger and much less frequent. ELMs are observed in the entire range from 'grassy' to 'isolated', and all of them occur with edge pressure gradients well below the ideal ballooning limit. JET high β_p discharges in which large, isolated ELMs are observed with edge pressure gradients close to the ballooning threshold are discussed elsewhere in this conference [3].

In this paper we address the singular ELMs in normal (not high-β_p) H-modes in JET, which are similar to the 'type III' ELMs in DIII-D [4] and ASDEX [5]. We determine how far the edge plasma is below the ideal ballooning limit prior to the ELMs. Subsequently resistive instabilities are considered in two limits. Firstly, we treat resistive (Δ') ballooning modes. For the ELMs we have studied, the edge plasma is found to be unstable for toroidal mode numbers $n \geq 10$. Electrostatic resistive modes are shown to have very low growth rates under the same conditions.

Secondly, free boundary resistive (tearing) modes are treated [6]. These resistive modes with $n = 1$ are destabilized by the current density gradient near the edge, which can be large due to the bootstrap effect of the H-mode pressure gradient. For $n > 1$ the pressure gradient itself is a driving force.

Phenomenology

ELMs are primarily observed as a sharp rise in the D_α signal. During an ELM a short (200μs) broad-band (0–120 kHz) burst of magnetic fluctuations and density fluctuations (microwave reflectometer) are observed as well. Smaller, but otherwise similar, fluctuation bursts which do not give rise to a D_α peak often occur as well. The ELMs and smaller turbulent events occur with irregular intervals and amplitudes, though larger ELMs tend to suppress the activity for some time afterward. This pattern of ELMs preceded by smaller bursts suggests a cascade of particle and energy losses by a locally increased pressure gradient. Alternatively, ELMs are sometimes triggered by enhanced impurity influx, gas puff, or a heat pulse from a sawtooth or fishbone instability arriving at the edge. This indicates that a locally increased pressure gradient and increased resistivity can both trigger an ELM, i.e. the ELM is caused by a resistive MHD mode.

Clues for the underlying instability come from the observations of oscillations in the edge with a well-defined frequency, typically 50–100 kHz, which usually start several milliseconds before the ELM. The ELM precursors are observed with fast pick-up coils (sample rate = 250 kHz) and with the multichannel microwave reflectometer (sample rate = 200 kHz). For details we refer to [2]. The phase differences between two coils indicate toroidal mode numbers n = 8–15, suggesting a ballooning type instability. When several reflectometer channels observe constant-density surfaces near the edge, the precursor activity can be seen to be localized several centimeters inside the separatrix, while the turbulent phase extends further outward.

Because these precursors can exist long before an ELM occurs and are not growing shortly before the onset of turbulence, their effect is probably to change the equilibrium, building up larger gradients near the edge. Subsequently, turbulence sets in quickly at a broad range of frequencies. Exponential growth of a monochromatic precursor, as is clearly seen in ASDEX [6], is visible in JET for at most a few cycles and often not at all.

Resistive ballooning modes

In order to study the ballooning stability, the double-null x-point equilibria were reconstructed from the magnetic and profile data with the IDENTD code [8]. We have selected double-null x-point shots because in those cases the plasma edge is close to the pick-up coils in the outer midplane, so that fast magnetic data are available. The shapes of flux surfaces near the separatrix are accurate, but for a selection of ELMs the edge pressure gradients can be improved locally by (re)considering the following profiles: T_e and n_e from LIDAR Thomson scattering, n_e from the microwave reflectometer (and FIR interferometer), and T_i, Z_{eff} from charge exchange spectroscopy. The uncertainty in dp/dr is almost 100%, taken over 5 cm, sufficiently small for the present discussion.

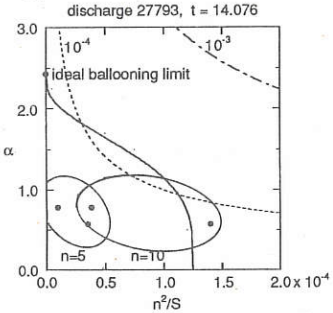

Fig. 1 *Stability diagram of pressure gradient versus resistivity at* $r/a = 0.95$. *Here,* $\alpha = -2\mu_0(dp/dr)r^2/RB_\theta^2$ *and* S *is the Lundquist number. The two ellipses show the observed equilibrium values of* dp/dr *and* S *for toroidal mode numbers* $n = 5$ *and 10.*
Solid line: resistive ballooning stability boundary.
Dashed lines: lines of given growth rate of the electrostatic mode, in units of the Alfvén frequency.

The full equilibrium shape, the current density and locally improved pressure profile are used in the code HBT [7], which recomputes the equilibrium and performs a full ideal MHD ballooning stability analysis using the Suydam method. Figure 1 shows the results for a discharge with high heating power and high Be influx ($Z_{\text{eff}} = 3.5$ near the edge) when the first ELM occurs. The ideal ballooning limit is found to be considerably above the observed pressure gradient and comes closest ($\sim 3dp/dr$) at $r/a = 0.95$.

Subsequently the resistive ballooning curve is constructed by matching the ideal MHD Δ' to the resistive layer solution. We obtain Δ' from the ballooning equation $d^2\xi/d\theta^2 = V(\theta)\xi$ in the limit of high shear by taking a square well potential $V(\theta)$, with depth and width chosen to give the correct values of $\int_{-\infty}^{\infty} V(\theta)\,d\theta$ and the HBT ideal stability limit. Figure 1 shows that only mode numbers $n \geq 10$ can become unstable. Electrostatic modes (dashed lines) grow very slowly in this parameter range.

Free boundary resistive modes

There are a number of experimental observations of MHD activity in tokamak plasmas in which resistive MHD modes localized near the plasma boundary are important. Examples are obviously the ELMs but also the MHD activity during the current rise phase of the plasma startup. For the study of the stability properties of low-n resistive modes localized at the boundary a free boundary description of the MHD modes is essential. The fully toroidal linear resistive MHD code CASTOR [6,9] has been extended to include a vacuum surrounding the plasma up to an ideally conducting wall. At the plasma vacuum interface, the resistive boundary conditions, i.e., continuity of all three components of the perturbed magnetic field, apply.

Before we apply the CASTOR code for the stability analysis of resistive free boundary modes of a JET ELMy H-mode discharge, we first discuss the influence of an x-point on the stability of the ideal and resistive external kink mode. The x-point plasma shape is taken to be quasi-circular with a small perturbation into an x-point at the top and bottom, so that it can be compared to the the case with a circular boundary. The aspect ratio is 4. The growth rates of the $m/n = 3/1$ are plotted in Fig. 2 versus the value of q at the boundary, q_1. The value of q_1 is changed by changing the total current, the shape of the current profiles is fixed. The growth rate is plotted for four different situations, for ideal MHD and for a resistivity of $\eta = 10^{-6}$ and for both a circular and an x-point shape. In ideal MHD, the external kink becomes stable as the $q = 3$ surface moves into the plasma. The resistive external kink mode is still unstable when $q = 3$ lies inside the plasma. At the low q_1 side, a finite resistivity has no influence on the marginal q_1 for the circular case. The x-point and the associated high shear at the edge reduces the growth rate of the $m = 3$ mode. Surprisingly, however, with an x-point the ideal mode is more unstable than the resistive mode for $q_1 < 2.9$. This is due to the more restrictive resistive boundary conditions which do not allow a surface current in the perturbation in combination with the small radial width of the mode due to the high shear. For $q_1 > 3$ the x-point reduces the growth rate, the marginally stable edge current gradient is however not affected by the x-point.

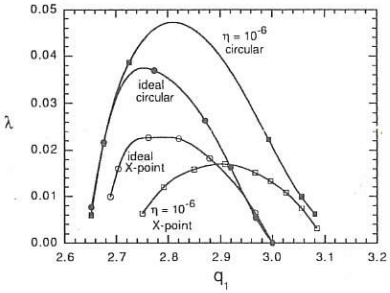

Fig. 2 *The growth rates as a function of q at the boundary for a circular and X-point boundary and for ideal MHD and for a resistivity of $\eta = 10^{-6}$.*

Next, we try to establish the relevance of free boundary tearing modes with respect to the ELMs. The equilibrium of a JET H-mode discharge is reconstructed with the IDENTD code using the magnetic data and the electron pressure profile from the LIDAR diagnostic. The resulting flux surface averaged current density is shown in Fig.3b (marked by (1)).

The growth rate of the $n = 1$ free boundary tearing mode of the actual JET discharge is shown in the lowest curve of Fig. 3a as a function of the resistivity. The ideally conducting wall is placed at 10 times the minor radius. The mode consists of many overlapping poloidal harmonics localized in the high shear region near the boundary, with each harmonic having a maximum at the corresponding rational q-surface. The width of the different harmonics decreases with decreasing resistivity, reducing the overlap of the harmonics. The scaling of the growth rate with resistivity is close to η^{+1}. Extrapolating the growth rate to typical values of the resistivity near the edge, $\eta \sim 10^{-7} - 10^{-8}$ for a temperature of 500 eV, yields a growth rate of the order $10^{-4} - 10^{-5}$ times the Alfvén frequency. This is far to slow to be of relevance.

To determine the dependence of the $n = 1$ tearing mode on its driving force, we have increased the current density gradient at the edge as compared to the actual reconstructed JET equilibrium. This is done by changing the current profile locally near the plasma boundary ($0.8 < \sqrt{\psi} < 1.$). The increase of $<J>'$ must extend to the $q = 3$

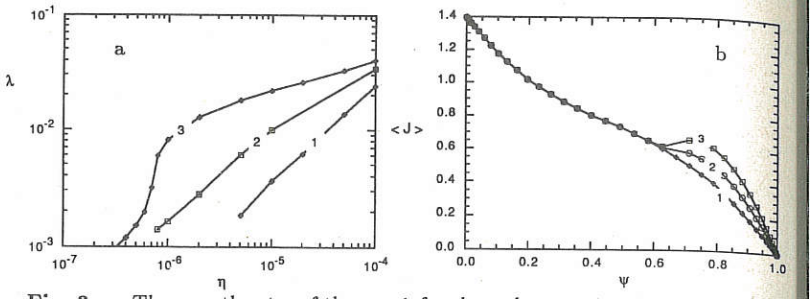

Fig. 3a *The growth rates of the $n = 1$ free boundary tearing mode for the three current profiles shown in* **3b**. *The actual JET equilibrium is marked (1).*

surface to have any effect on the stability of the $n = 1$ tearing mode. The flux surface averaged toroidal current density for the original equilibrium and for two cases with an increased gradient are shown in Fig. 3b. The pressure profile is kept constant. The growth rate of the free boundary $n = 1$ mode of the three cases are shown in Fig. 3a as a function of the resistivity. It is clear that the growth rate increases with an increasing current gradient at the edge. Also, the growth rate decreases more slowly with decreasing resistivity. For the case with the largest current gradients, however, we find a different behavior as a function of resistivity. For this case the growth rate shows a sharp decrease at $\eta = 10^{-6}$. This suggests that the mode can be triggered either by an increase of the edge current gradient or an increase of the resistivity, for example due to the build up of impurities. Increasing the pressure gradient, even beyond the ideal ballooning limit has no effect on the $n = 1$ mode. For higher values of n (= 2,3,..), however, both the current and the pressure gradient can be destabilizing.

Conclusions

Resistive ballooning modes match the observations of long lived ELM precursors in JET. These precursors may cause the pressure gradient to build up closer to the separatrix. The sudden onset of broad band fluctuations in the ELM must be caused by a faster instability, possibly closer to the edge. Our results suggest that the outer flux surfaces are then destroyed by global resistive free boundary modes, driven by the edge current gradient. For values of $n > 1$, the pressure gradient is destabilizing as well. Thus, the combined action of these two types of resistive instabilities causes the observed outflow of particles and energy.

Acknowledgement. We thank G.J. Kramer for providing the reflectometer data.

References

[1] W. Kerner *et al.*, Bull. Am. Phys. Soc. **36** (1991) 2R13, p. 2310.
[2] S. Ali-Arshad *et al.*, 'ELM Precursors in JET', this conference.
[3] T.C. Hender *et al.*, 'High-β_p MHD activity in JET', this conference.
[4] E. Doyle *et al.*, Proceedings of the 18th European Conf. on Controlled Fusion and Plasma Physics, Berlin, Vol. I (1991) p. 285.
[5] H. Zohm *et al.*, Nucl. Fusion **32** (1992) 489.
[6] G.T.A. Huysmans, Ph.D. Thesis, Free University Amsterdam, 1991.
[7] G.T.A. Huysmans *et al.*, (1990), Rijnhuizen Rep. 90-194, Nieuwegein, Netherlands.
[8] J. Blum *et al.*, Nucl. Fusion **30** (1990) 1475.
[9] W. Kerner *et al.*, Proceedings of the 18th European Conf. on Controlled Fusion and Plasma Physics, Berlin, Vol. IV (1991) p. 89.

NEUTRON PROFILE MEASUREMENTS DURING THE TRITIUM EXPERIMENTS IN JET

F B Marcus, J M Adams*, D S Bond*, S Conroy, P J A Howarth, O N Jarvis, M J Loughlin, G Sadler, P Smeulders, P van Belle and N Watkins*

JET Joint Undertaking, Abingdon, Oxon, OX14 3EA, U.K.
*AEA Industrial Technology, Harwell Laboratory, Oxon, OX11 0RA, U.K.

Tritium (t) was injected into a deuterium (d) plasma in the JET tokamak, and fusion powers of up to 1.7 MW [1] were produced. During preparatory experiments, tritium diffusion was also studied. A comprehensive range of neutron and gamma-ray diagnostics [2] was operated during these experiments. The main diagnostic used in this paper, the JET neutron emission profile monitor, is described elsewhere [3]. A tomography code, NEUTOMO [4,5], has been used to determine the 2-D neutron emissivity profile from the line-integral measurements, employing a hybrid pixel/analytic algorithm.

From simultaneous measurements of the neutron emissivity profiles for 14 MeV (R_t) and 2.5 MeV (R_d) neutrons, the ratio of thermal tritium density (n_t) to thermal deuterium density (n_d), can be obtained as a function of radius and time from the ratio of the local emissivities and reactivities. The only other information needed is an approximate measurement of the ion temperature. In plasmas where the neutron emissivities are dominated by the beam-plasma reactivities (S_d and S_t) of a deuterium beam onto a mixed d and t plasma, the ratio is: $n_t/n_d = (R_t/R_d) / (S_t/S_d)$.

A series of diffusion experiments was performed in which two of the 80 keV injectors had a 1% admixture of tritium. In Pulse No. 26114, at 12 s, the deuterium beam power was increased to 8 MW, and at 12.5 s, an additional 1 MW, 80 keV beam with 1% tritium was switched on, giving a tritium power of approximately 13 kW. The 1% tritium beam was turned off at 13.5 s, and replaced with 1 MW of pure deuterium. Tritium diffusion was examined by observing the neutron emissivity profiles evolve in time after the 1 s injection pulse of tritium. During this time, the axial electron and ion temperatures both equalled 7 keV.

The neutron emissivity profiles along a radial chord at the tokamak midplane are plotted versus major radius and time in Fig. 1 (a) and (b), for 2.5 and 14 MeV neutrons, respectively. The shapes of the 2.5 MeV and 14 MeV

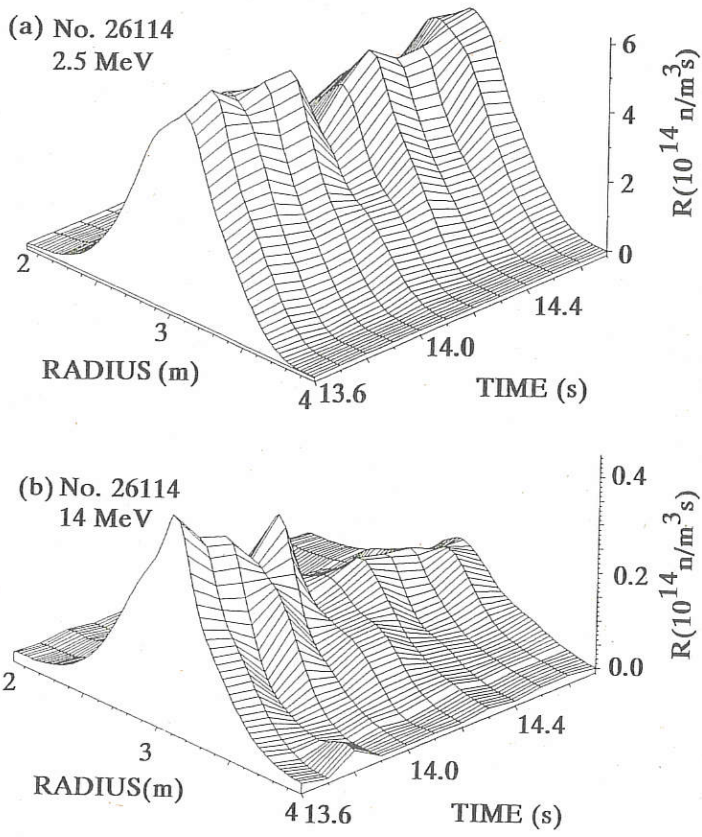

Fig. 1. The (a) 2.5 MeV and (b) 14 MeV neutron emissivity profiles along the radial chord at the tokamak midplane are plotted versus major radius and time for Pulse No. 26114.

neutron profiles were similar, but the time evolutions were different.

After the tritium beam was turned off at 13.5 s, the 2.5 MeV profile stayed relatively constant for the next second, while the 14 MeV profile decayed slowly, but maintained the same shape, except after a sawtooth crash at 14.085 s, which temporarily caused a strong flattening of both profiles. During this decay phase, the neutron emissivity was dominated by beam-plasma reactions. The calculated contribution of thermal d-d fusion reactions to the

2.5 MeV emissivity on axis was approximately 1/6th of the measured value. The ratio of n_t/n_d was obtained as a function of space and time using the emissivity and reactivity ratios. The emissivity values were large enough to obtain the density ratio over ±1/2 of the plasma radius. It was found that, within experimental error bars, the density ratio was constant as a function of major radius; this ratio decreased monotonically with time. The electron density profile was flat over the radial region investigated. Therefore the deuterium and tritium density profiles were also approximately flat.

The remarkable observation that the 2.5 and 14 MeV neutron emissivity profile shapes were the same, even after the sawtooth crash, is now easily understandable. Since the neutron production was mostly from beam-plasma reactions, the two emissivity profiles depended solely on the beam deposition and slowing down profile, or redistribution after a sawtooth crash, and consequently stayed the same shape while the tritium density decayed.

Since n_t/n_d was a constant across the profile, the ratio n_t/n_d could also be obtained from the ratio of the global 14 MeV to the global 2.5 MeV emission. Because the emissivity ratio was a weak function of ion temperature, the reactivity ratio corresponding to the central ion temperature could be used. The global emission values were obtained from integrating the emissivity profiles and from primary or secondary measurements, including activation and fission chambers. Both ratio methods gave similar answers, and both were well described by an exponential decay with a time constant of 1 s. The decay was not affected by the sawtooth crash at 14.085 s; although the emissivity profiles were strongly altered at this time, the ratio remained constant except for the slow time decay.

A cylindrical approximation of the global particle diffusion coefficient gave $D \equiv a^2/5.6\tau = 0.2\ m^2/s$, where τ is the observed tritium decay constant. The radial profile of the diffusion coefficient was analyzed separately [6] using the TRANSP code, which used several measured plasma profiles to predict the 2.5 and 14 MeV emissivity profiles from Fokker-Planck calculations with different particle diffusivity models. To reproduce the observed neutron emissivity profiles, identical conclusions about the spatially constant fraction of tritium density were obtained.

Following the above-mentioned experiments for detailed physics studies, there were two discharges with fusion power up to 1.7 MW, Pulses No. 26147 and 26148, with two PINIs producing 100% t beams. Tomographic inversion of the data was performed to obtain the 2-D neutron emissivity profiles. In Fig. 2,

the global 14 MeV neutron emission and maximum local emissivity are plotted during the high power heating phase from 12 to 14 s. The neutron emissivity initially increased, then decreased on axis and flattened due to the first sawtooth crash. The emissivity again increased on axis, rapidly at first, and then very slowly, even though the global emission was increasing due to the broadening of the profile. The axial emissivity was calculated to be predominantly (> 3/4) due to thermal d-t fusion. This phase was terminated by another crash, after which the emissivity peaked again, but at a lower level due to an impurity influx [1]. The profile remained peaked, but with the intensity continuously decreasing.

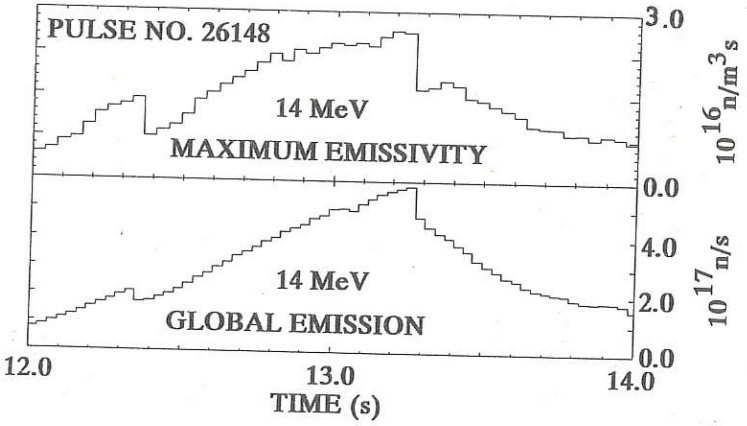

Fig. 2. The 14. MeV neutron maximum emissivity and global emission are plotted versus time during high power heating for Pulse No. 26148.

[1] THE JET TEAM, Nucl. Fusion **32** (1992) 187.
[2] Jarvis, O N, Neutron Measurements from the Preliminary Tritium Experiment at JET, Presented at the Conference on High Temperature Diagnostics, Santa Fe, 1992, to be published in Rev. Sci. Instrum.
[3] Adams, J.M. et al., in Controlled Fusion and Plasma Physics (Proc. 16th Europ. Conf., Venice, 1989), Vol. 1, European Physical Society (1989) 63.
[4] Marcus, F.B. et al., Plasma Phys. and Cont. Fusion **33** (1991) 277.
[5] Granetz, R.S., Smeulders, P., Nucl. Fusion **28** (1988) 457.
[6] Balet, B. et al., to be published in Controlled Fusion and Plasma Physics (Proc. 19th Europ. Conf., Innsbruck, 1992), European Physical Society (1992).

FUELLING OF JET LIMITER AND X-POINT PLASMA BY DEUTERIUM PELLET INJECTION

G.L. Schmidt[(a)], D. Bartlett, L. Baylor[(b)], M. Bures, A. Edwards, M. Gadeberg, N Gottardi, T. Jones, P. Kupschus, P. Lomas, P. Morgan, H. Morsi, P. Nielsen, J. O'Rourke, G. Sadler, D.F.H. Start, P. Stubberfield, A. Tanga, D. Ward
JET Joint Undertaking, Abingdon, Oxon, OX14 3EA, UK
[(a)]Princeton University, Princeton NJ, USA; [(b)]ORNL, Oak Ridge TN, USA

I] Introduction: Pellet fuelling experiments have been undertaken on JET in conjunction with other experimental goals. A multiple barrel pneumatic pellet launcher built at ORNL and operated at JET under a collaboration agreement between JET and the USDoE has been used to produce extended pellet fuelling sequences. In this paper we summarize experiments conducted using a range of pellet perturbations in L-mode (limiter) and H-mode (x-point) plasma configurations heated primarily by ICRH: the observed efficiency and radial distribution of the pellet fuelling source and the effects of and constraints on pellet perturbation size. These issues are important for modeling of pellet fuelling experiments. In future, more specific fuelling experiments will be required to extend plasma parameters by pellet fuelling beyond those obtained in long pulse gas fuelling experiments.

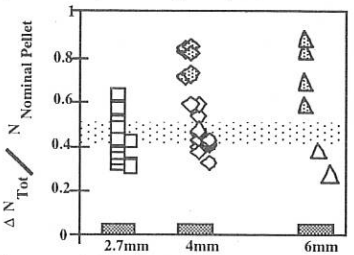

Figure 1:Retained Mass Fuelling Efficiency, 2.7mm (0.9 x 10^{21}), 4mm (3.0 x 10^{21}), and 6mm (10 x 10^{21}) diameter pellets. Fuelling efficiency is generally reduced as pellet penetration is diminished. Shaded points represent penetration to beyond r/a=0.3

II] Pellet Deposition and Fuelling Efficiency: The fuelling of a plasma by an extended sequence of pellets involves the repeated injection of individual pellets over a period of many particle confinement times. Each pellet event in this sequence proceeds through two phases following acceleration of the pellet in the launcher. In JET, the duration of a pellet event is roughly 1 to 2 ms. During the first phase, the pellet penetrates the confined plasma volume. The ablating pellet mass acts to attenuate the energy flux incident on the pellet reducing the ablation rate. The deposited mass is assumed to be ionized locally. During the second phase, this deposited pellet mass redistributes itself symmetrizing the pellet mass perturbation in both the toroidal and poloidal directions. The neutral gas shielding model or its extension to the neutral gas and plasma shield model are commonly used to describe the ablation process. The symmetrizing process is assumed to proceed without radial transport. Although the models can be adjusted to reproduce the penetration depth obtained in JET, and hence to reproduce the ablation rate integrated over the pellet trajectory[1], there are differences between the radial distribution of the deposited mass predicted by the model and that observed in fuelling experiments[2]. These differences could result from an incomplete description of the ablation and shielding process or from a breakdown in the assumption that no mass flow takes place across flux surfaces during the symmetrizing phase of the pellet event. In either case, for pellet fuelling experiments, the measured retained mass and its radial distribution following the pellet event are the

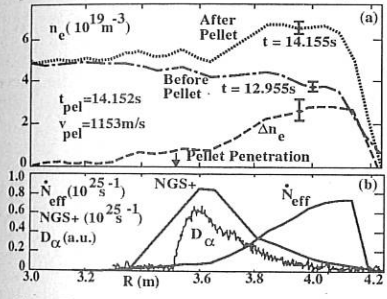

Figure 2: Retained Mass Pellet Source - (a) density profiles before and after pellet event and change in profile -(b) Pellet Dα emission, Δn_e converted to ablation rate Neff, and ablation rate calculated from modified Neutral Gas Shield model.

quantities of interest. The total mass retained in the present experiments has been determined from the increase in plasma electron density, assumed to be symmetric poloidally and toroidally, as measured some 3 to 40 ms following the pellet event. In JET, minimal change in the total particle content beyond that associated with the pellet event itself occurs on this time scale. The retained pellet mass can vary from <40 to 100% of the nominal pellet mass. A retained mass fraction or fuelling efficiency of 0.4 to 0.5 is typical of discharges using auxiliary heating and utilizing shallow pellet penetration during the fuelling sequence. Figure 1 shows the fuelling efficiency for the three pellet diameters used in the JET experiments. A reduction in retained pellet mass from the nominal value occurs for all pellet diameters. Similar results have been observed on other smaller tokamaks using pellets in the ranges of 1 to 2 mm diameter[3]. Little energy loss appears to be associated with this mass loss, however, the effect must be considered in establishing the pellet perturbation and particle source. The radial distribution of the retained pellet mass represents the effective pellet particle source. As illustrated in figure 2, in JET experiments this effective source is shifted radially outward when compared to that predicted by the standard ablation models. The maximum perturbation occurs at larger minor radius than predicted and the effective source near the plasma core at the end of the pellet trajectory is less than predicted.

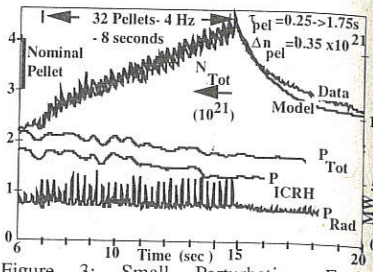

Figure 3: Small Perturbation Fuelling Sequence, 3 MA limiter plasma - measured and modeled total electron content, input and radiated power. Radiation burst at pellet injection is due to direct view by bolometer of pellet trajectory.

III] Pellet Perturbations: The radial distribution of retained pellet mass can be altered by choice of either pellet speed or pellet mass. In JET experiments a range of pellet mass perturbations from 10 to 300% has been investigated at fixed pellet speed of ~1300 m/s.

III-1]Small Perturbation [Injected Mass: n-pel/<n-tot>=0.2-0.4, Retained Mass:0.1- 0.15]: Pellets of 2.7 mm diameter have been employed to simulate a possible ITER steady state fuelling scenario using small density perturbations of from 10 to 15%. An integrated pellet particle flux of 2.9 x 10^{22} was injected using 32 pellets over an 8 second period (figure 3). Average retained mass fuelling efficiency was 40%. As shown, the time evolution of the discharge total particle content can be modeled using the average value of the retained mass for each pellet perturbation, combined with a decay time for the retained mass, which increases linearly from 0.25s to 1.75s during the fuelling sequence. This increase is greater than that of the plasma density. Pellet penetration to r/a ~0.5, outside the sawtooth inversion radius, was generally obtained. The neutron rate was unchanged by the pellet event, confirming that little perturbation of the plasma core occured. In contrast to predictions of the standard ablation model, measured fractional temperature perturbations diminish near the end of the pellet trajectory consistent with a reduced pellet perturbation in this region. Density profiles produced during the fuelling sequence are illustrated in figure 4. The number of radial measurements limits the spatial resolution of the density profile, but the deposition profile of the pellet mass can be estimated. The pellet source function extends further in radius than that associate with the recycling particles, and leads to a modest inversion of the density profile immediately following the pellet event. The profile then relaxes on a 100 ms time scale

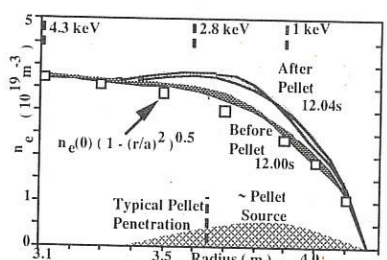

Figure 4: Density profiles 2.7mm fuelling sequence before and after pellet event.

to a shape of the form $n_e(r)= n_e(0)(1-(r/a)^2)^{0.5}$ before the next pellet event.

III-2] Moderate Perturbation [Injected Mass: n-pel/<n-tot> = 1 - 1.5, Retained Mass:0.3 - 0.5]: Pellets of 4 mm diameter increase pellet penetration using a moderate retained mass density perturbation of from 30 to 50%. The fuelling sequence is shown in figure 5. Average particle flux, retained mass efficiency and radiated power fraction are similar to the 2.7 mm case, but pellet penetration is now extended to within the sawtooth inversion radius. Approximately a 20% drop in neutron rate occurs with pellet injection compared with a 50% decrease at a sawtooth crash. Note that in a higher temperature device little change in neutron rate would occur on pellet injection, due to the adiabatic nature of the pellet perturbation and the proportionality of neutron rate to pressure (T > 8 keV). The presence of a pellet source within the inversion radius is important since it allows the sawtooth to provide a mechanism by which pellet mass is delivered to the plasma center [4]. This effect is more clearly seen when the neutron rate is scaled to remove the temperate dependence of the reaction rate (figure 5). The first sawtooth after each pellet event produces the largest increase in core deuteron concentration, as indicated by the scaled neutron rate. The density profile after the pellet in figure 2 represents those seen in the 4 mm case. The profile is more strongly inverted than that following the smaller 2.7 mm perturbation. The inverted profile again relaxes on 100 ms time scale but the 1 second pellet repetition rate, large edge density perturbation, and the recycling of the pellet mass appear to result in a profile broader than that obtained in the 2.7 mm case.

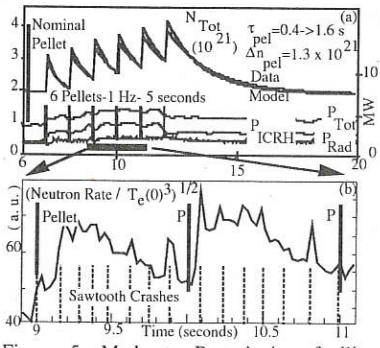

Figure 5: Moderate Perturbation fuelling sequence, 3 MA (limiter) - (a) total electron content, measured and modeled, input and radiated power-(b) ~core deuterium density from the neutron rate scaled by $1/T_e(0)^3$.

High Density: As the density limit is approached, moderate pellet perturbations can still be used in conjunction with the sawtooth to fuel the plasma core (figure 6). Since the pellet size was fixed the nominal pellet perturbation decreased during the fuelling sequence with increasing N_{tot} from 130% to 40%, while a radiated power fraction < 40% was maintained. The density at 3.9 m during and following the fuelling sequence approaches the value n(edge)~ B_T/R 2.37 $P^{0.5}$ proposed as a nominal limit[5]. Further, the density immediately following the pellet perturbation is likely to be higher than the values shown, since only the time point at 7.5s immediately follows the pellet event. Density profiles are broad with $\alpha \sim 0.1$. Retained mass fuelling efficiency diminishes slightly at higher input power (22 MW) but remains >50 % even at high density.

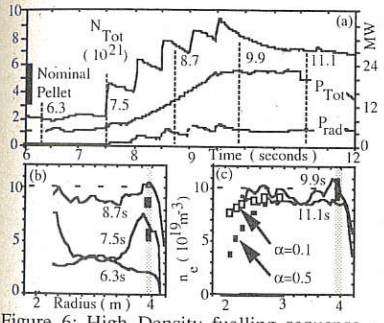

Figure 6: High Density fuelling sequence - (a) total electron content, input (ICRF) and radiated power - (b) and (c) density profiles, nominal edge density limit values at times shown and analytic profiles of the form: $8.5 \times 10^{19} (1 - (r/1.1)^2)^{\alpha}$.

H-mode Operation: In high density H-mode plasmas, moderate pellet perturbations can also be used, but as density approaches the density limit transitions back

to L-mode confinement may follow the pellet perturbation. Figure 7 shows an H-mode pellet fuelling sequence with nominal pellet perturbation of 50%. Retained mass fuelling efficiency was also 50%. Following the first pellet perturbations the volume average density increases but edge density remains $\leq 5 \times 10^{19}$ m^{-3} and little perturbation in the H-mode conditions is observed. With subsequent pellets, however, edge density following the pellets rises above 5×10^{19} m^{-3}. A period of L-mode confinement of increasing duration then follows each pellet event. During this L-mode phase, levels of, and fluctuations in, the Dα emission increase as do radiation losses from the x-point plasma. Although a momentary loss in RF power following the pellet event may contribute to the the loss of H-mode, the plasma response suggests that choice of pellet size and frequency might be used to control H-mode performance in high density plasmas.

III-3] Large Perturbations [Injected Mass:n-pel/<n-tot>=3, Retained Mass:2.3]: The use of large perturbations, retained mass >100%, to fuel the plasma core directly is also possible if an appropriate target plasma can be established. Using 6 mm pellets, nominal mass perturbations of up to 300% have been used in JET. To stop the pellet within the plasma core a target plasma central temperature of ~ 3 keV is required while the central pressure and total stored energy should be sufficient to retain a temperature ≥ 0.5 keV immediately following the pellet perturbation. Given the size of the perturbation, this implies a target plasma central electron density of 5 to 6×10^{19} m^{-3} and a total energy of 3.5 to 4 MJ. A 4 mm pellet event has been used to densify the target, preferentially fuelling the central plasma and ~6 MW of NBI power then used to establish the target plasma temperature. This large perturbation scenario provides significant mass deposition directly within the plasma core, producing a peaked high density profile. Use of 6mm pellets has produced a near triangular density profile filling the entire plasma volume with central density $>2 \times 10^{20} m^{-3}$. In past experiments, following such a perturbation a period of enhanced core confinement has been established. While not suitable for extended fuelling sequences, use of large perturbations in future devices may allow the sustaining of peaked density profiles and enhanced core confinement up to temperatures approaching ignition minimizing auxiliary power requirements.

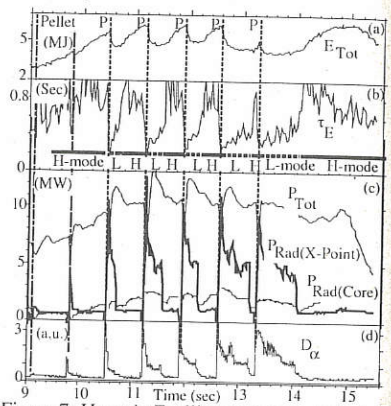

Figure 7: H-mode Fuelling sequence- (a) total stored energy, (b)global confinement, (c)input power (ICRF), power radiated from the confined plasma (core) and from the region of the x-point, (d) Dα emission.

1: Houlberg, W.A. et. al. to be submitted for publication.
2:Baylor L.R. et. al. to be submitted for publication.
3:Buchl et. al., Nuclear Fusion **27** (1987) 1939.
4:Cheetham A.D. et. al. , Workshop on High Temperature Diagnostics, Varenna 1986.
5:Lowry C.G. et. al.,17th EPS Amsterdam (1990), I- 339.

MEASUREMENTS OF THE ELECTRON SOURCE DISTRIBUTION AND IMPLICATIONS FOR PARTICLE TRANSPORT

J O'Rourke, G J Kramer*, R Simonini, A C C Sips

JET Joint Undertaking, Abingdon, Oxon., UK
* On attachment from FOM-'Rijnhuizen, Nieuwegein, The Netherlands

INTRODUCTION

The electron source profile is critical in the study of particle transport in tokamak plasmas. It arises from a number of atomic processes, namely the ionization of neutrals penetrating from the plasma boundary via multiple charge exchange processes, the ionization of neutrals arising from recombination processes (unless a local balance between ionization and recombination is established), and the ionization of partially ionised impurities. The contribution from neutrals is usually inferred using neutral transport codes /1,2/ based on Monte-Carlo algorithms, and requires detailed knowledge of plasma parameters and atomic cross-sections. The contribution from impurity ionization additionally requires knowledge of charged-particle transport. Because of the large number of required parameters calculations of the electron source are subject to considerable errors. The experimental verification of these calculations is usually also unsatisfactory as it relies on (1) spectroscopic data, with the concomitant uncertainties arising from the interpretation of line intensities and the Abel inversion of chordal data, or (2) charge-exchange measurements of the neutral particle distribution, which are not directly related to the electron source.

In this paper we report the first direct determination of the electron source distribution in JET from harmonic perturbations (at 1 - 4 Hz) of the electron density produced by modulation of the gas feed. The density modulations are measured by a 12-channel microwave reflectometer and a 6 channel far-infrared interferometer. We also make use of the information contained in the electron temperature modulations, measured using a 12-channel grating polychromator. Fourier analysis of the data yields the local phase and amplitude of the modulations. The advantages of this technique are the small number of physical assumptions involved, the localised nature of the measurements and the sensitivity afforded by Fourier analysis.

ANALYSIS AND RESULTS

The reflectometer signals measure displacements of the critical density layer corresponding to each reflectometer frequency with a sensitivity of about 0.4 mm. The amplitude of the density modulation is determined from the density gradient:

$\tilde{n}_e = \tilde{R}_{crit} \bullet \frac{\partial n_e(R_{crit})}{\partial R}$. Because of this dependence, the amplitude of the density modulations is subject to larger error than their phase. The linearised particle balance equation is solved for harmonic perturbations of the electron source. Both numerical and analytic /3/ solutions have been used in this study. The linearised electron flux is assumed to have a diffusive form, with D_e constant. The electron source is assumed to be of the form: $S_e=S_a\, e^{(r-a)/\lambda}$. The physics of the problem is governed by the dimensionless parameter $\gamma=\lambda(\omega/D_e)^{1/2}$. For $\gamma< 1$ the localisation of the source can not be resolved. Note that the linearised electron source distribution is not necessarily identical with the 0-th order distribution if impurities ionisation contributes significantly to the source. In this discharge Z_{eff} ~1.2, so that impurity ionisation can be neglected. The heat balance equation is also solved for the temperature perturbations. These provide a consistency check on the amplitude of the density modulations.

Figure 1 shows the evolution of a 3 MA, 3.1 T, X-point discharge with 1 Hz modulation of the gas feed. 7 channels of the reflectometer have critical densities in the plasma. A least-squares fit to the data yields $D_e=0.75m^2sec^{-1}$ with $\lambda<a/40$. Figure 2 shows the sensitivity of the simulations to λ. The results are not sensitive to values of $\lambda \leq a/20$ (because γ becomes too small) and this should be considered as an upper bound on the source decay length. The modulation amplitudes decrease rapidly with modulation frequency and the signals become noisy. Nevertheless, similar results are obtained for modulation at 4 Hz: De = $0.3m^2$ sec^{-1}, λ= a/20.

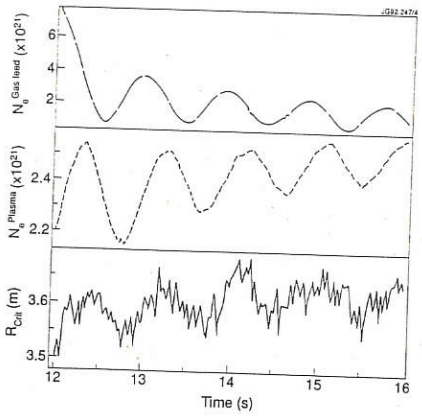

Fig. 1 -- Evolution of the gas feed, particle inventory and major radius of $n_e^{crit} = 2.5 \bullet 10^{19} m^{-3}$ in pulse 24248 (1 Hz modulation).

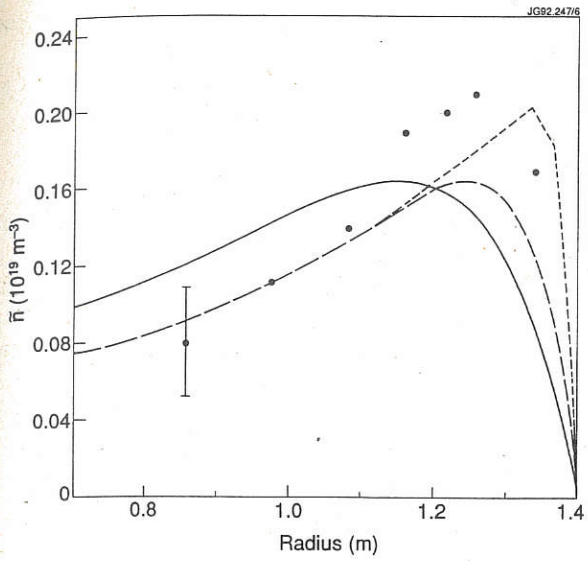

Fig. 2 -- Modulation amplitude versus minor radius. Data (circles), λ = a/5 (solid line), λ = a/20 (dashed line), λ=a/80 (dotted line).

IMPLICATIONS FOR PARTICLE TRANSPORT

Figure 3 compares the electron source distribution determined by gas modulation with that calculated by the 3-D neutral transport code AURORA3. The gas modulation results confirm the shallow penetration of the electron source in JET. Note that the calculated source does not have a simple exponential form. It has a tail which reflects the deep penetration of neutrals through multiple charge exchange but which is not of sufficiently large amplitude to contribute significantly to the particle balance.

With the experimentally determined source (λ=a/20), the particle pinch velocity v_p, can be calculated either (1) from the steady state density profile using the diffusion coefficient obtained above or (2) by a least-squares fit of the form Γ_e=-$D_e\nabla n_e + n_e v_p$ to the time evolution of the particle flux. The 2 calculations are shown in Figure 4. The most important source of error is the uncertainty in the electron density gradient. It should be noted, however, that there is good agreement among the reflectometer, interferometer and LIDAR (Thomson scattering) density profiles. In the outer portion of the plasma the particle pinch velocity exceeds the neo-classical value by nearly an order of magnitude. These results agree with previous deductions of the electron source and conclusions about the magnitude of the inward pinch velocity and its

relation to the neo-classical pinch /1/, but are now made with an experimentally determined source and with density profile measurements having a better spatial resolution.

/1/ A Gondhalekar et al., Bull. Am. Phys. Soc. 30 (1985) 1525 and JET Report JET-P(85)31.

/2/ M H Hughes and D E Post, PPPL Report 1335

/3/ E Barbato and R Giannella, Physics Letters 110A (1985)309

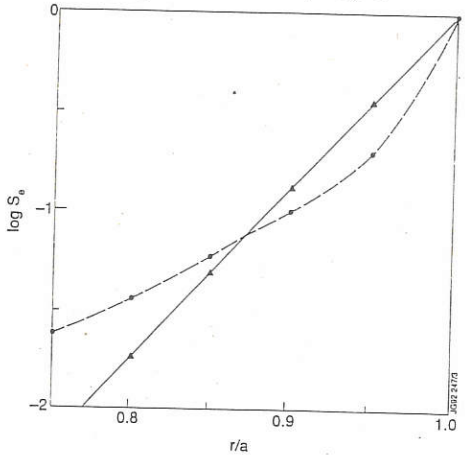

Fig. 3 -- Calculated (circles) and experimentally determined (triangles) electron source distribution versus r/a

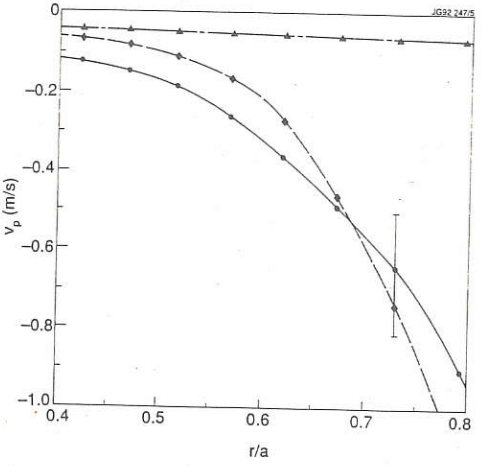

Fig. 4 -- Pinch velocity. Steady-state particle balance with $D_e = 0.75 m^2\ sec^{-1}$ (circles), time-dependent flux analysis (diamonds), neo-classical (Ware) pinch (triangles).

PARTICLE TRANSPORT DURING THE TRITIUM EXPERIMENTS IN JET

B. Balet, J.G. Cordey, T.T.C. Jones, R. König, F. Marcus, G. Sadler, P.M. Stubberfield, M. von Hellermann
JET Joint Undertaking, Abingdon, Oxon, OX14 3EA, U.K.

Introduction Different types of deuterium - tritium discharges have been performed recently in JET [1]; some with a 1% mixture of tritium in one or two neutral beam sources and two discharges with 100% tritium in two neutral beam sources. These discharges have been extensively analysed by the $1^1/_2$D transport code TRANSP [2]. The experimental measurements of the main plasma parameters (T_e, T_i, n_e and Zeff) are used as input data to TRANSP. The consistency of these data is checked by comparing the measurement and simulation of the diamagnetic and MHD energies, the loop voltage and, most importantly, the neutron emission rates. Monte-Carlo techniques are used to simulate the neutral beam injection; TRANSP can therefore estimate the fraction of neutrons produced by thermal-thermal, beam-thermal and beam-beam reactions. The main objective of this preliminary tritium experiment was to produce more than 1 MW of fusion power; this was achieved in hot ion H-mode discharges. However a few tritium decay experiments were performed in conventional H-mode plasmas to determine the particle transport of thermalised tritium and deuterium. We report on the analysis of these pulses below.

Models of particle transport: Three different mixing models have been used to predict the relative amounts of tritium and deuterium in the plasma:

1) The "constant fraction" model where the deuterium density n_D and the tritium density n_T evolve in such a way that their profile shapes are the same.
2) The "constant velocity" model where the radial velocity v defined by Γ/n, where Γ is the particle flux, is the same for both species.
3) The "proportional diffusivities" model which, defining the particle flux $\Gamma = -D\nabla n + n.v$, imposes a tritium diffusivity D_T proportional to the deuterium diffusivity D_D.

The "constant fraction" and "constant velocity" models imply a common driving force for deuterium and tritium or a strong coupling between the two species. The "proportional diffusivities" model implies that the main driving force is the density gradient of each species. The validity of these different models can be assessed by comparing the measurements and simulations of the total neutron yields and the neutron emission profiles from both D-D and D-T fusion reactions (2.5 MeV and 14 MeV neutrons respectively). The detailed description of the neutron measurements is the subject of a companion paper at this conference [3].

Hot ion pulses: In the deuterium-tritium discharges with 100% tritium in two neutral beam sources, the high fluxes of 14 MeV neutrons inhibit the measurement of low fluxes of 2.5 MeV neutrons; the different mixing models give equally good fits to the D-T neutron data and therefore they cannot be distinguished. This is not surprising as this scenario of tritium fuelling by neutral beam injection was chosen precisely because of the insensitivity of the neutron yield to the particle transport model as was shown in preliminary TRANSP studies (3).

In the pulses with a 1% mixture of tritium into one deuterium neutral beam source, both the D-D and D-T neutrons can be measured. Therefore, comparisons can be made with the TRANSP simulations. This is shown in Fig. 1 for pulse No. 26095 where 1% tritium is injected for 3s up to the end of the high neutron yield phase. The deuterium and tritium source rates are similarly peaked on axis and the three different mixing models result in similar deuterium and tritium density profiles. Therefore, all models give equally good fits to both the D-D and D-T neutron data; and they cannot be distinguished in such a discharge.

The tritium decay experiment: Pulse No. 26114 is a deuterium-tritium discharge with a 1% mixture of tritium into one deuterium neutral beam source. The main characteristics of this pulse are shown in Fig. 2. At 12s, the NB power increases to ≈ 9MW, and is kept constant for 3s; this leads to very similar electron and ion temperatures reaching ≈ 7 keV. Some 13 kW of tritium power is injected for 1s between 12.5s and 13.5s. After the tritium source is switched off, the discharge is sawtooth free for ~ 0.6s and the decay of the thermal tritium density is observed.

As in the previous cases and for the same reasons, the different mixing models cannot be distinguished by comparison with the D-D neutron data. However, the three mixing models lead to different tritium density profiles in the decay phase: the "constant velocity" model results in a much more peaked profile than the other models. Therefore, the models can be assessed by comparison with the D-T neutron data. This is shown in Fig. 3 where the measured and simulated D-T neutron rates are plotted. The "constant velocity" model is inadequate to simulate the measurement whereas the "constant fraction" model or a mixing model with $D_T \approx D_D$ equally well reproduce the 14 MeV and the 2.5 MeV neutron yield. This result is further confirmed by the simulations of the line integrated neutron emission rates, as measured by the horizontal and vertical camera of the neutron profile monitor (see Fig. 4).

The TRANSP simulation shows that the ratio n_T/n_D is more or less flat in radius and decays with an exponential time of 1s as also deduced from neutron measurements (4) (see Figs. 5 and 6). The effective tritium diffusivity $D_T = \Gamma_T/\nabla n_T$ is shown in Fig. 7. It is similar to the deuterium diffusivity observed in similar D-D pulses and to the Helium diffusivity observed during H_e injection into D plasma (5). D_T is low in the plasma centre ($D_T \approx 0.25$ m^2/s) and increases sharply towards the edge.

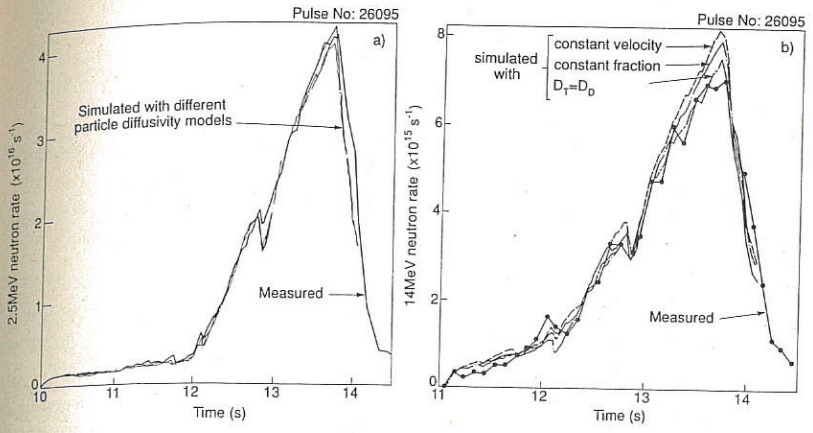

Fig. 1: The measured and simulated rates for (a) 2.5 MeV and (b) 14 Mev neutrons for Pulse No. 26095. The TRANSP simulations use Zeff profile measurements from charge exchange recombination spectroscopy.

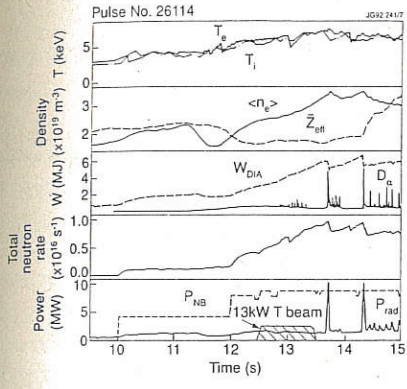

Fig. 2: The time development of the central electron and ion temperatures, the volume - averaged electron density, the line averaged $\bar{Z}_{eff}$, the plasma diamagnetic energy, the D_α emission, the total neutron rate and the NB and radiated powers for Pulse No. 26114.

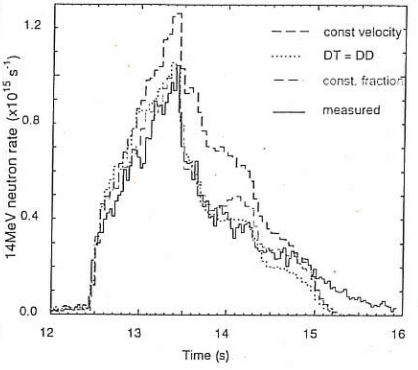

Fig. 3: The measured and simulated rates of 14 MeV neutrons for Pulse No. 26114 using different mixing models.

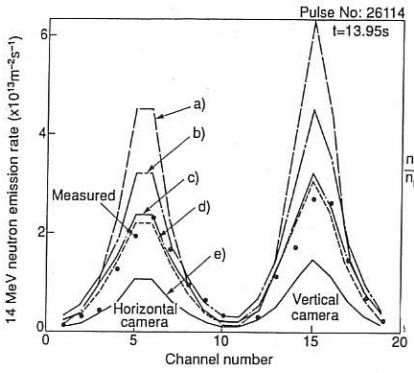

Fig. 4. The measured and simulated line-integrated 14 MeV neutron rates for Pulse No. 26114 using a) the "constant velocity" model, b) $D_T = 1/2\ D_D$, c) the "constant fraction" model, d) $D_T = D_D$, e) $D_T = 2.D_D$.

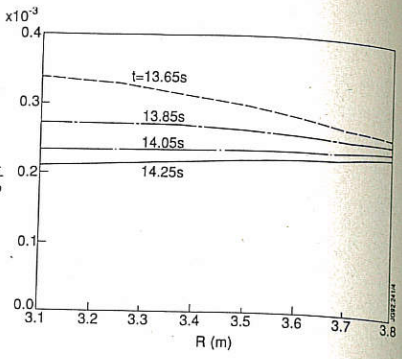

Fig. 5. Ratio of tritium to deuterium density n_T/n_D versus major radius R at different times.

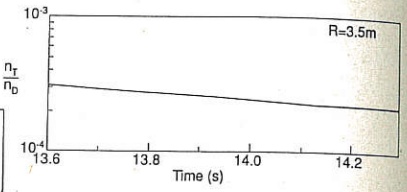

Fig. 6. Ratio of tritium to deuterium density n_T/n_D versus time at R = 3.5 m.

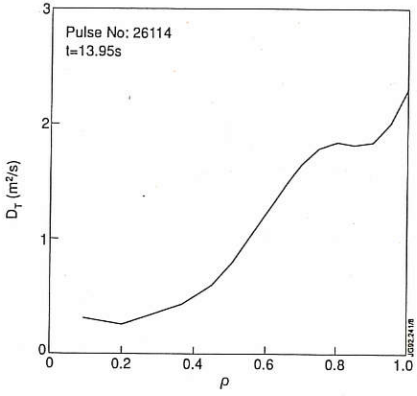

Fig. 7. The effective tritium diffusivity $D_T = \Gamma_T/\nabla n_T$ versus normalised radius ρ at t = 13.95 s.

References

(1) The JET team Nucl. Fusion 32 (1992) 187.

(2) R.J. Goldston, et al., J. Comput. Phys. 43 (1981) 61.

(3) P.M. Stubberfied, et al., Plasma Phys. and Control. Fusion 33 (11) (1991) 1255.

(4) F. Marcus, et al., at this Conference.

(5) T.T.C. Jones, et al., (1991) in Controlled Fusion and Plasma Physics (Proc. 18th European Conf., Berlin, 1991), Vol. 15c, Part 1, p.185.

FIRST RESULTS OF PELLET INJECTION IN ECR AND OHMIC HEATED DISCHARGES IN RTP.

A.A.M. Oomens, D. F. da Cruz Jr., G. van Dijk, J.F.M. van Gelder, J. Lok, J.H. Rommers, A.J.H. Tielemans, and RTP-team

FOM Instituut voor Plasmafysica 'Rijnhuizen', Association Euratom-FOM, P.O. Box 1207, 3430 BE Nieuwegein, The Netherlands

Abstract

A multi-shot pellet injector, built by Risø National Laboratory, is operational at RTP since the fall of 1991. First results of pellet injection both in Ohmic and in ECR-heated discharges are described.

Introduction

The Rijnhuizen Tokamak Project RTP is dedicated to the study of steady state and perturbative transport studies. To manipulate the plasma conditions RTP is equipped with an ECR-heating system, a programmable plasma current and gas feed, and a pellet injector. Next to transport studies, the machinery and its diagnostics will be used to investigate the pellet ablation process in ohmic and ECR-heated discharges. In this paper we report on the initial results on mainly the density behavior when pellets are injected in both kind of discharges.

Experimental conditions

The plasma of the Rijnhuizen tokamak has a major radius of .72 m and a minor radius (a) set to .164 m by two carbon bar limiters. It is contained in a continuous stainless steel vacuum vessel with a minor radius of .23 m. The maximum toroidal magnetic field is 2.4 T (variable in steps of roughly 1 %), and plasma currents up to 150 kA with pulse durations of ≈ 250 ms are obtained. The first wall of the vacuum vessel has been boronized with $B(CH_3)_3$ after extensive baking and glow discharge cleaning. Daily conditioning of the first wall is done by baking overnight ($T \leq 150$ °C) and 15 minutes helium glow discharge cleaning prior to tokamak operation, which results in plasmas with Z_{eff} in the range 1 - 2.

The ECRH-system includes two 60 GHz, 200 kW, 100 ms gyrotrons. One gyrotron is linked up with an antenna at the high field side, the other is connected to a launcher located at the low field side in the equatorial plane of the torus.The latter is used for the experiments described in this paper. The power is injected perpendicular to the magnetic field in the linearly polarized TE_{11} mode. For these measurements the waves have been launched in O-mode polarization at the fundamental frequency, resonant at the plasma center.

Launching of the hydrogen pellets is performed by a multi-shot pellet injector, developed and built by Risø National Laboratory (Denmark) [1]. The pellets are formed and accelerated in a 8-shot unit in which eight pipe guns are placed symmetrically around a liquid helium flow cryostat. The pipe guns are loaded simultaneously and fired successively with

hydrogen driver gas. The injector is able to fire a sequence of pellets every three minutes. The pellets are fired from the low field side in the equatorial plane in radial direction. Pellet masses and velocities are measured with a single integrated diagnostic unit containing a microwave cavity and two optical detectors. Two H_α-monitors have been installed, one with the viewing direction almost along the trajectory of the pellet, the other one views the pellet from the top. Further diagnostic information is obtained from a 19-chord FIR interferometer [2], single point Thomson scattering, a 20-channel ECE-radiometer, a bolometer, and an 80-channel 5 camera SXR tomographic system [3].

Experimental results

Pellets of hydrogen containing 5.10^{18} or 2.10^{19} atoms/pellet have been fired with velocities between 800 and 1000 m/s for the smaller and (400 - 700) m/s for the larger pellets with time intervals between pellets down to 5 ms. Due to shot to shot variations in the sticking of the pellet, the jitter in arrival time at the RTP liner is below 1 ms. The scatter in velocity is less than 5 %, and the number of atoms in a pellet is reproducible within 10 %.

The values of the velocity, as deduced from the time of flight measurement in the injection line, the H_α-measurement, and the various soft X-ray channels are in agreement within the error bars. From the increase in total number of electrons, as deduced from the interferometer, it follows that up to 50 % of the pellet mass is deposited inside the plasma The increase in density due to the driver gas can be neglected. The values for the penetration depth L_p of the pellets, from H_α and interferometer, show that in Ohmic discharges L_p decreases from > 2a (at $n_e(0) = 6 \times 10^{18} m^{-3}$) to ≈ a/2 with increasing density ($n_e(0) = 3 \times 10^{19} m^{-3}$) for the smaller pellets and L_p always >2a for the larger pellets. In ECR-heated discharges in general L_p is slightly reduced for the small pellets, large pellets have $L_p > 2a$ or are followed by a density disruption.

The evolution of the electron density profile following the pellet injection is studied with high time-resolution by means of the interferometer. Typical examples are shown on Figs. 1 & 2. An increase of the line integrated density of 3×10^{23} m^{-2} s^{-1} can still be detected. This high upper limit appears to be not always sufficient for pellets injected in plasmas with high density and temperature. Only for a restricted number of shots the ablation rate could be evaluated trustworthy. Typical values for plasmas with $n_e(0)$: (1 - 2) x 10^{19} m^{-3} and $T_e(0) \approx 700$ eV are in the range (2-3) x 10^{22} atoms/s for Ohmic discharges and (5-7) x 10^{22} atoms/s for ECR-discharges. For pellets arriving in the plasma .5 to 10 ms after switching off the ECR-pulse, the ablation rate still has the high value. This indicates that a suprathermal tail in the electron velocity distribution could be of importance in the ablation process even after an ECR-pulse. The analysis of the ECE- and SXR-data is still in progress, preliminary results are shown in Figs. 3 & 4. The central temperature starts to collapse 50 to 100 μs before the pellet has

arrived, indicating that radial heat diffusivity may be considerably enhanced by the strong temperature gradients during pellet penetration.

In conclusion : A reliable and accurate pellet injector has been installed at the RTP tokamak. Combined with the advanced diagnostics this should allow a detailed comparison of the ablation process in Ohmic and ECR-heated discharges.

Acknowledgement

This work has been performed under the Euratom-FOM association agreement with financial support from NWO and Euratom.

References

[1] H. Sørensen et al., Proc. 17th Symp. on Fusion Techn., Rome, September 14 - 18, 1992.

[2] A.C.A.P. van Lammeren, S.K. Kim, and A.J.H. Donné, Rev. Sci. Instrum. **61**, (1990) 2882 .

[3] D.F. da Cruz, Jr. and A.J.H. Donné, Rev. Sci. Instrum. **61**, (1990).3067.

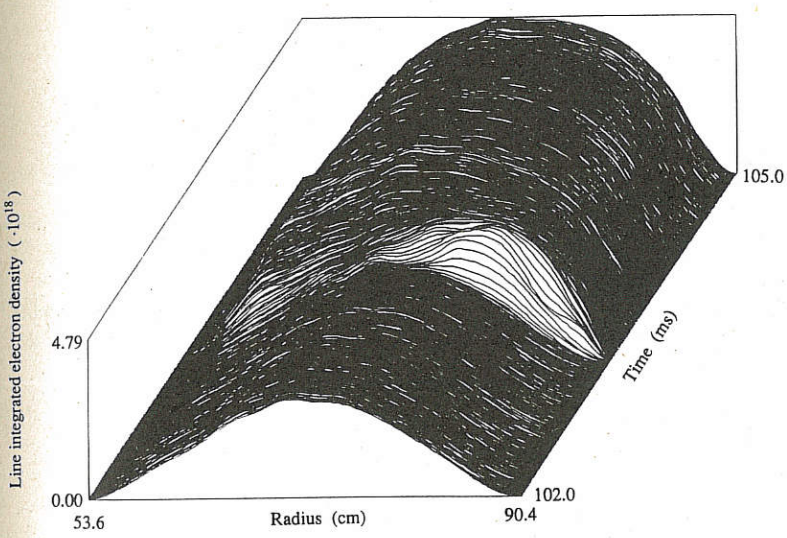

Fig. 1. The time evolution of the (line integrated) n_e- profile (in m^{-2}) during the injection of a small pellet.

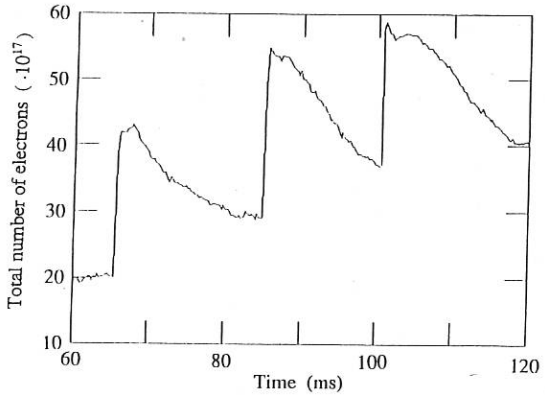

Fig. 2. The time behavior of the total number of electrons, deduced from profile measurements, as a result of the injection of three small pellets.

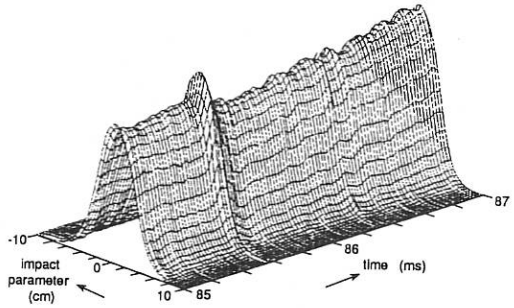

Fig. 3. The time evolution of the SXR - profile measured with the vertical camera. The pellet enters the plasma at t = 85.58 ms.

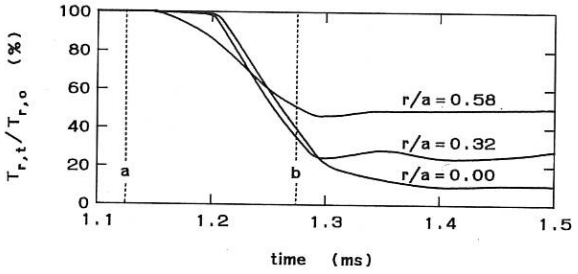

Fig. 4. The decrease of the (relative) electron temperature at various radii from the ECE signals, measured with a time resolution of 50 μs. The pellet enters at t = 1.125 ms (a) and reaches r/a = 0 at t = 1.275 ms (b).

On the Bootstrap Current Calculations Based on Values of the Radial Electron Transport

V. Petržílka

Institute of Plasma Physics, Czechoslovak Academy of Sciences
Za slovankou 3, P. O. B. 17, 182 11 Praha 8, Czechoslovakia

Abstract. A method of computation of anomalous bootstrap current is suggested which uses calculated or experimentally found values of the radial transport velocity. The underlying theory is the drift kinetic equation approach of Shaing to anomalous plasma transport in a toroidal configuration and/or the MHD approach of Klíma and Petržílka to convection and diffusion in a plasma cylinder under the influence of RF fields.

1 Introduction and basic equations

As we plan to use the values of the radial transport for BC estimates, we start from the equation connecting the BC density j^{BC} and the radial transport velocity V_r. We will omit symbols denoting the average value over the magnetic surface. From [1] we obtain

$$j^{BC} = S_1 S_2 V_r \frac{B_p}{\eta_{\|}}, \tag{1}$$

multiplicative terms $S_1(r)$, $S_2(r)$ are computed from [1],

$$S_1 = \left(\sum_{m,n,\omega} \Phi^2_{mn\omega} \frac{m(m-nq)}{\mid m-nq \mid} \right) \left(\sum_{m,n,\omega} \Phi^2_{mn\omega} \frac{m^2}{\mid m-nq \mid} \right)^{-1}, \tag{2}$$

$$S_2 = \left(-A_\Phi \frac{eB_r}{cT_e} - \frac{T_i}{T_e P_i} \frac{dP_i}{dr} - \frac{e}{T_e} \frac{d\phi}{dr} + \frac{T_e + T_i}{T_e P} \frac{dP}{dr} - 0.87 \frac{1}{T_e} \frac{dT_e}{dr} \right) \times$$
$$\left(-A_\Phi \frac{eB_r}{cT_e} - \frac{T_i}{T_e P_i} \frac{dP_i}{dr} - \frac{e}{T_e} \frac{d\phi}{dr} + \frac{T_e + T_i}{T_e P} \frac{dP}{dr} - 1.5 \frac{1}{T_e} \frac{dT_e}{dr} \right)^{-1}, \tag{3}$$

B_p is the poloidal magnetic field, $\eta_{\|}$ is the Spitzer resistivity, $\Phi_{mn\omega}$ denotes the electrostatic fluctuating potential, m, n are poloidal and toroidal wavenumbers, q is

the safety factor, $T_{e(i)}$, $P_{e(i)}$ denote temperature and pressure of electrons and ions, $P = P_e + P_i$, ϕ is the electrostatic potential and

$$A_\Phi = \left(\sum_{m,n,\omega} \Phi^2_{mn\omega} \frac{m\omega}{\mid m - nq \mid} \right) \left(\sum_{m,n,\omega} \Phi^2_{mn\omega} \frac{m^2}{\mid m - nq \mid} \right)^{-1} . \quad (4)$$

As we typically have $m \simeq nq$ for the fluctuating fields, S_1 is much smaller than one while S_2 is of the order of one. In contrast to what has been said about the anomalous transport case in [2] , we see that BC can again be considered as driven by the radial transport. Let us assume that a toroidal current carried by fast electrons driven by an externally applied radiofrequency field is present in addition to the ohmic current. Then, similarly as in [3], we obtain for the total current $J(r)$ inside radius r the following equation

$$\frac{dJ}{dr} = C \frac{\mu_0 V_r J}{\eta_{\|}} + 2\pi r j^{RF} + 2\pi r j^E, \quad (5)$$

where $C = S_1 S_2$, j^{RF} is the current density noninductively driven by RF waves and j^E is the ohmic current density. The equation (5) differs from the basic equations in [3,4] by the multiplicative term $C(r)$ in the first term of the right side. The absolute value of C is - according to the text following eq.(4) - much smaller than one and thus its presence leads to a substantial reduction of the BC-term value in (5) in comparison with [3,4]. We see that when the anomalous transport velocity V_r is known , only the knowledge of the relative values of $\Phi_{mn\omega}$ is necessary for computing the total current $J(r)$ from (5), which is in contrast to [1], where the value of $\Phi_{mn\omega}$ has to be estimated. By taking $\mid C \mid \simeq 1$ and inserting the neoclassical value of V_r in (5), we would obtain an approximate equation for the total current $J(r)$ in case of the neoclassical diffusion.

2 Computational results

Similarly as in [1], we estimate $\mid m - nq \mid \simeq 1$, $\mid nq \mid \simeq 10$; the absolute value of S_1 may then be estimated as $S_1 \leq 0.1$. In what follows, we assume $S_1 = 0.05$ and $S_2 = 1$ for the BC estimates based on the equation (5). We note that a possible dependence of S_1, S_2 on r is neglected. The values of the anomalous diffusion coefficient D_e and of the inward velocity V_p are chosen according to [5],

$$D_e(r) = D_0(1 + 2r^2/a^2), 0.3 \leq D_0 \leq 0.5, \quad (6)$$

$$V_p(r) = -V_0(r/a)^{s_V}, 0.4 \leq V_0 \leq 1, s_V = 2 - 3. \quad (7)$$

The assumption (6) possibly exaggerates the value of D_e for $r \leq 0.3a$ [6].

The temperature, density and j^{RF} profiles are

$$T_{i,e}(r) = T_{0i,e}(1 - r^2/a^2)^{sT_{i,e}} + T_{Bi,e}, \quad (8)$$

$$n(r) = n_0(1 - r^2/a^2)^{s_n} + n_B, \quad (9)$$

$$j^{RF}(r) = j_0^{RF}(cos\pi r/2a)^{s_{RF}}. \quad (10)$$

We choose this centrally peaked profile of j^{RF} for the BC current estimates in this paper. However, it should be remembered that, e.g., recent high density current drive experiments in Tore Supra and JET indicate an off-axis deposition of lower hybrid power and hollow RF current profiles [7].

In Figs.1,2, we present two examples of the anomalous BC computed from eq.(5) (solid line). For comparison, the dashed line represents the neoclassical value of BC computed according to [8], where we assume $T_e = T_i$ for simplicity. For computations of Fig.1, we assume $a = 1m, R = 2.5m, n_0 = 5 \times 10^{19}m^{-3}, s_n = 0.5, n_B = 10^{18}m^{-3}$,very peaked temperature profile with $s_T = 5, T_{0e} = 10keV, T_{Be} = 30eV, Z_{eff} = 2, D_0 = 0.5m^2/s, V_0 = 1m/s, s_V = 2.5, s_{RF} = 2, j_0^{RF} = 1MA/m^2, j_E = 0$. In Fig.2, we assume $a = 0.5m, R = 1.5m$, not so peaked temperature profile with $s_T = 2, T_{0e} = 3keV$ and $V_0 = 0.5m/s$, the other parameters being the same as in Fig.1. The high value of $s_T = 5$ may be a good approximation of central T_e profile in some discharges using lower hybrid and ICRH synergetic effects for reaching high electron temperature in central regions [9].

3 Discussion and conclusion

In frame of the MHD description, the effect of an RF field on diffusion and convection in a plasma column has been studied in [10]. From the equation (4.7) for the electric current density j_z along the z-axis and from the equation (5.10) for the radial velocity V_r in [10] we obtain

$$j_z = \frac{V_r B_p}{\eta_{||}} \frac{\sum_{m,n,\omega} A_e(m - nq)/\omega}{\sum_{m,n,\omega} A_e(m + nqB_p^2/B_z^2)/\omega}, \quad (11)$$

where $A_e(r, \omega, m, n)$ is the RF power density absorbed by electrons from the m, n mode. In deriving (11), terms proportional to d/dr have been neglected in expressions for the time-averaged force density given by the RF field. By using equation (11) instead of (1) and assuming again that V_r is the anomalous transport velocity, we would obtain essentially the same results for the BC values from simple MHD considerations based on diffusion and convection in a plasma cylinder under the action of forces of RF fluctuating fields [10] as from the considerations based on the drift kinetic equation description of the transport in a plasma torus [1]. This should not be surprising as the first order effects of fluctuations may be separated from first order effects resulting from toroidicity [11].

In conclusion we note that there is now clear experimental evidence for the existence of the bootstrap current. The measured value is close to its neoclassical value, but it is not possible to rule out some enhancement due to non-classical (anomalous) effects [12,13]. For gaining more exact values of anomalous BC computed on the basis of the transport velocities, better knowledge of the radial dependence of the fluctuations spectrum would be useful.

4 References

[1] K. C. Shaing, *Phys. Fluids* **31** (1988) 2249.
[2] M. Bornatici, F. Engelmann, A. Nocentini, *Frascati Research Report* LGI.R/-TEO/74/6/E, August 1974; *Rivista del Nuovo Cimento* **5** (1975) 617.
[3] R. Klíma, V. Petržílka, *Czech. J. Phys.* **B35** (1985) 513; *Czech. J. Phys.* **B36** (1986) 1375.
[4] V. Petržílka, *Czech. J. Phys.* **B39** (1989) 1372.
[5] *JET Progress Report* **Vol. 1** (1988), p. 83; *IPP Garching Annual Report* (1988), p. 18; *ibid.* , (1989), p. 38; *ibid.* , (1980), p.28.
[6] M. Keilhacker et al. , *Plasma Phys. Controlled Fusion* **33** (1991) 1453.
[7] D. Moreau, *Plasma Phys. Controlled Fusion* **33** (1991) 1621.
[8] M. N. Rosenbluth, R. D. Hazeltine, F. L. Hinton, *Phys. Fluids* **15** (1972) 116.
[9] J. Jacquinot, *Plasma Phys. Controlled Fusion* **33** (1991) 1657.
[10] R. Klíma, V. Petržílka, *Czech. J. Phys.* **B30** (1980) 1003.
[11] T. E. Stringer, *Research Report JET-P* (1991) 38; to be submitted for publication in *Nuclear Fusion.*
[12] J. C. Cordey, C. D. Challis, P. M. Stubberfield, *Research Report JET-P* (1988) 29.
[13] J. Hawryluk et al. , *Plasma Phys. Controlled Fusion* **33** (1991) 1509.

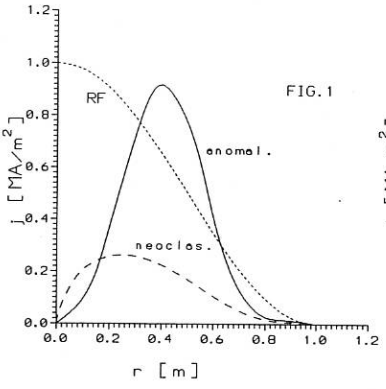

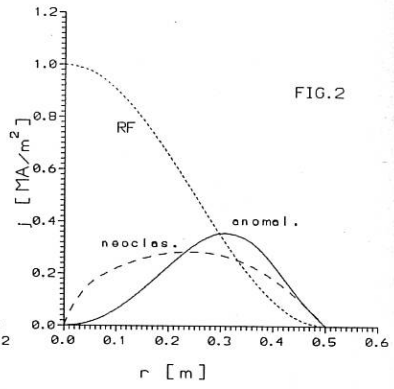

HELIUM TRANSPORT STUDIES ON DIII-D*

D.F. Finkenthal,† D.L. Hillis,‡ M.R. Wade,‡ W.P. West,
J.T. Hogan,‡ K.H. Burrell, R.P. Seraydarian, R.J. Groebner,
P. Gohil, C.C. Klepper,‡ and P.K. Mioduszewski‡

General Atomics, San Diego, California, U.S.A.

INTRODUCTION

The measurement of Helium density profiles in tokamak plasmas is necessary for helium transport studies. These studies are important in predicting the helium ash transport properties for ITER and will have important implications for the design. Poor helium transport in reactors could lead to a buildup of fusion ash, causing fuel dilution and increased radiation that will result in degraded fusion power and possibly quench ignition altogether. Present estimates[1] indicate that He concentrations in the core must be kept below 10% in order to maintain continuous reactor operation. Helium transport studies have begun on the DIII-D tokamak using charge exchange recombination (CER) spectroscopy for helium density measurements. Helium transport behavior has been observed by injecting helium gas puffs into DIII-D plasmas and measuring the He density profile evolution. The profiles are used to calculate the relevant helium transport properties. This paper covers the results obtained from puffing He gas into L-mode plasmas of various electron densities. The results obtained in DIII-D L-mode plasmas are similar to measurements made at TEXTOR and JT-60.

EXPERIMENTAL ARRANGEMENT AND METHOD

The measurement of He^{++} profiles on DIII-D is accomplished using the charge exchange recombination (CER) spectroscopy system previously developed on DIII-D for ion temperature and rotational velocity measurements.[2-4] Neutral deuterium atoms in the beam undergo charge exchange with fully stripped He in the plasma, resulting in excited He^{+} that de-excites via photon emission at characteristic wavelengths. The He $n = 4 - 3$ emission at 4686 Å is chosen because it falls in the visible range. The intensity of this photon emission is proportional to the density of helium present in the plasma (typically a ~1% helium concentration exists in DIII-D plasmas due to He glow discharge cleaning between shots). The present CER system consists of 4 spectrometers with 8 viewing chords each, which are arranged to view across two neutral beamlines. There are 16 chords on the midplane that view the beams tangentially through the plasma and 15 that view vertically from two windows located above and below the midplane. The vertical and tangential view points are interwoven across the plasma half-width, providing excellent spatial resolution. The system is capable of 2 ms time resolution although a signal integration time of 10 ms is typically used for He transport studies. The absolute calibration of the CER system has been accomplished using standard calibration lamps and supplemented with two other techniques involving: (1) injection of the neutral beam into a gas filled torus and (2) neutral beam injection into a pure He plasma.[4] Electron temperature and density profiles are measured continuously throughout the discharge every 16 ms using a multiple pulsed Thomson scattering system. Typical profile measurements of the ion temperature T_i, electron temperature T_e, and electron density ne are shown in Fig. 1 for an L-mode discharge on DIII-D.

DATA ANALYSIS

Data analysis is accomplished by a non-linear least squares fit to the measured He CER spectrum. The He spectra observed on DIII-D are complicated by the presence of a cold line from edge emissions as well as a third, warm component due to CER from thermal neutrals.[3]

* This is a report of work sponsored by the U.S. Department of Energy under Contract No. DE-AC03-89ER51114. Research at the University of California supported by the U.S. Department of Energy under Grant No. DE-FGO3-89ER5116.

† University of California, Berkeley, California, U.S.A.

‡ Oak Ridge National Laboratory, Oak Ridge, Tennessee, U.S.A.

Analysis of the data is greatly facilitated by modulating the beams on and off. The beam-off spectrum is used as a background measurement to subtract out most of the interfering cold and warm components from the beam on spectrum, thereby leaving only the hot charge exchange signal. The DIII–D neutral beams are aptly suited for this task. The beam attenuation in the plasma is calculated by a radiative collisional model using cross sections made available to us from the JET atomic physics database, and has been bench-marked to a code employing Monte-Carlo methods. Modeling of the He transport is performed with the Multiple Impurity Species Transport (MIST) code to deduce the anomalous diffusivity and pinch coefficients, D_A and C_V respectively.

HELIUM GAS PUFF INTO L–MODE PLASMA

Helium transport studies in L–mode were conducted by injecting a 25 ms He gas puff into three double-null divertor discharges with major radius $R = 1.67$ m, plasma current $I_P = 1.6$ MA, toroidal magnetic field $B_T = 2.1$ T and 1.24 MW of modulated (10 ms on, 10 ms off) deuterium neutral beams. The CER system used a 10 ms integration time synchronized with the beam, producing a CER measurement every 20 ms (10 ms with CER signal, 10 ms of background). Figure 2 shows three L–mode helium density profile measurements for low, intermediate and high electron densities with line-averaged electron densities of $\bar{n}_e \sim 3.4$, 4.4, and $5.8 \times 10^{19}\,\mathrm{m}^{-3}$ respectively. The corresponding electron density profile shape is overlayed on the data to show the similarity of shape. Both the helium data and the electron density profiles are normalized to unity at the location of the innermost CER chord at $\rho = 0.32$. Figure 3 plots the time history of the measured charge exchange signal from the plasma core for several CER chords during shot 74762, also normalized to the innermost chord. The resultant rise in He density shortly after the gas puff at 2.30 s can be seen; the He takes about 150 ms to reach the innermost chord at $\rho = 0.23$. Since there is no He pumping on DIII–D most helium transported out of the plasma returns to the core and results in a steady-state profile that becomes fully developed about 200 ms after the gas puff; this indicates that the global He recycling coefficient, R_{He} is about unity. Similar behavior is observed in the low and high density discharges, as shown in Fig. 4. Figure 5 is a plot of the helium density profiles at 2.28, 2.36, and 2.60 s, normalized to the innermost vertical chord at $t = 2.28$ s. The

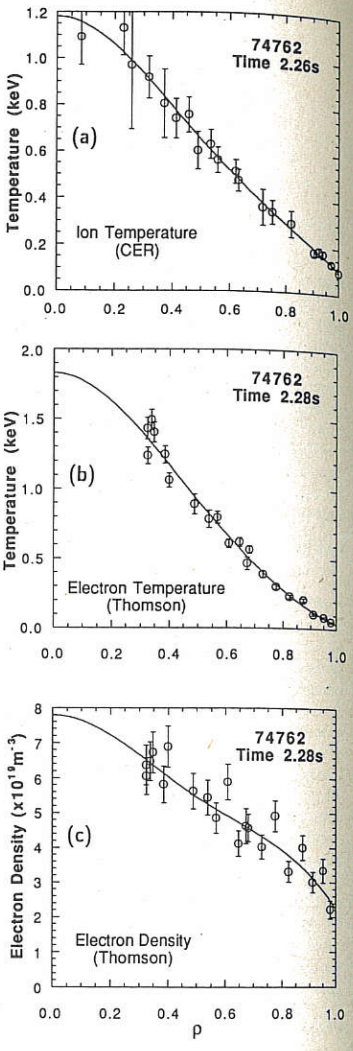

Fig. 1. Typical profile measurements with spline fits for: (a) ion temperature from CER; (b) electron temperature from Thomson scattering; (c) electron density from Thomson scattering.

introduction of the gas puff at 2.3 s can be observed by the initial He density rise at the edge.

Figure 6 features a MIST calculation for shot 74761 at time 2.44 s superimposed on the He density data and shows excellent agreement.[5] The values of the transport coefficients for both the low and the high density L–mode were found to be $D_A = 1.0$ m^2/s and $C_V = 0.95$. These values are similar to results of $D_A = 1.0$ m^2/s and $C_V = 1.50$ found in TEXTOR (no He pumping),[6,7] and values of $D_A = 1.0$ m^2/s and $C_V = 1.0$–1.5 found in JT-60.[8]

SUMMARY AND CONCLUSION

The CER system used on DIII–D has been successfully calibrated for helium density and density profile measurements. The L–mode helium profile measurements have the same shape as the electron density profiles and agree with calculations made by the MIST code. The results of these transport studies on DIII–D are in good agreement with results obtained on TEXTOR and JT-60. These and other recent results[5–7] seem to absolve present concerns about plasma alpha ash removal problems in ITER for L–mode operation. Current and future studies on DIII–D will provide an excellent helium transport data base by measuring and comparing relevant transport properties in L–, H–, and VH–modes, including behavior in ELMing (edge localized mode) H–mode discharges. H–mode studies on DIII–D are currently in progress and the possibility of using ELMs to eject helium is being investigated.[5] Experiments involving helium neutral beam fueling are planned for the fall of 1992. The Advanced Divertor Project (ADP) planned for the spring of 1993 may allow for He pumping and exhaust enhancement studies if proper conditioning of the cryopumps (Argon frost coating) is done.

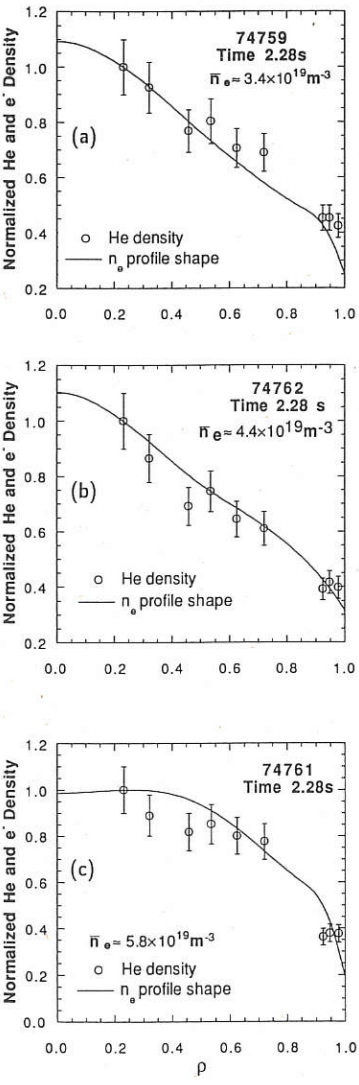

Fig. 2. Relative He density measurements with electron density profile normalized and overlayed to show similarity for (a) low, (b) intermediate, and (c) high density L–mode discharges.

[1] Reiter, D., *et al.*, Nucl. Fusion **30** (1990) 2141.

[2] Seraydarian, R.P., *et al.*, Rev. Sci. Instrum. **57** (1986) 155.

[3] Groebner, R.J., *et al.*, Appl. Phys. Lett. **43** (1983) 920.

[4] Wade, M.R., *et al.*, submitted to Rev. Sci. Instrum. (1992).

[5] Hillis, D.L., *et al.*, Proc. of the 10th Int. Conf. on Plasma Surface Interactions, Monterey, California, 1992.

[6] Hillis, D.L., *et al.*, Phys. Rev. Lett. **65** (1990) 2382.

[7] Hillis, D.L., *et al.*, Proc. of 13th Int. Conf. on Plasma Physics and Controlled Nuclear Fusion Research, Washington, 1990 (IAEA, Vienna 1991), CN-53/G-2-8.

[8] Nakamura, H., *et al.*, Phys. Rev. Lett. **67** (1991) 2658.

[9] Synakowski, *et al.*, Phys. Rev. Lett. **65** (1990) 2255.

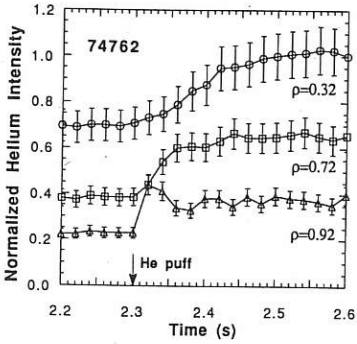

Fig. 3. Measured helium CER signal intensity versus time for 3 chords for the intermediate density discharge.

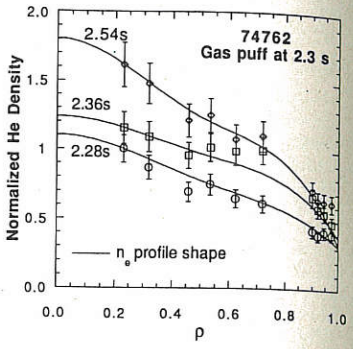

Fig. 5. Comparisons of normalized He and electron density profiles before and after the He gas puff injection at 2.3 s.

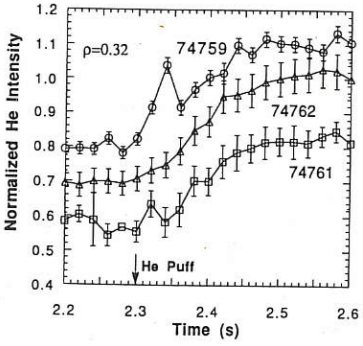

Fig. 4. Comparison of the measured He CER signal intensity versus time at $\rho = 0.32$ in the core for the low, intermediate, and high density discharges.

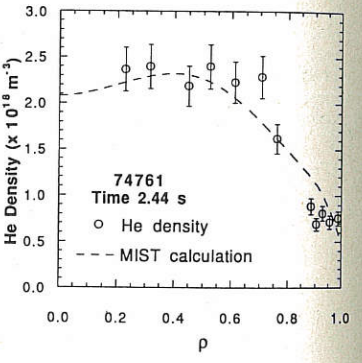

Fig. 6. He density profile versus ρ compared with a He transport simulation (dashed line) with $R_{\mathrm{He}} \sim 1.0$, $D_A = 1.0$ m^2/s, and $C_V = 0.95$.

POLOIDAL ASYMMETRY OF IMPURITY IN CO- AND COUNTER-INJECTION EXPERIMENT AT JET

R Giannella, M Christensen, R De Angelis,* N Gottardi, L Lauro-Taroni, M Mattioli+, D Pasini
JET Joint Undertaking, Abingdon, Oxon., UK
*Associaziome Euratom Enea sulla Fusione, Centro di Frascati, Roma, ITALY
+Association Euratom CEA sur la Fusion, Cadarache, France

Most of the electromagnetic radiation from tokamak plasmas is known to be emitted by line radiation from impurities. Since the early experiments it appeared on JET that the highest levels of the global emissivity E are localized at the very edge of the bulk plasma in the proximity of the last closed flux surface (LCFS). Although these edge levels of radiation may vary in a very wide range depending upon the plasma density and contamination ($E(a) \simeq 2 \bullet 10^4$ to $5 \bullet 10^5$ W/m^3 as measured with a radial space resolution never better than 5 cm), E decays typically by a factor of 4 or larger within 15 cm from the LCFS in the bulk plasma. Polodial asymmetries in the bolometric radiation profiles are observed in the generality of L-modes and ohmic discharges. Besides possible highly localized radiation clouds (as it happens in the case of marves), a clear m=1 up/down modulation is observed with the tomographic bolometer diagnostic in these cases. The relative amplitude of modulation $\tilde{E} / \overline{E}$ is about 0.3 to 0.7. This peripheral asymmetry of the radiation pattern is interpreted as due to poloidal variation of the impurity distribution [ref.1] and is seen to disappear during ELM-free H-modes when a strong increase of the edge plasma temperature occurs. Given the strong contrast in the levels of E between the periphery and the central region of the plasma, it is difficult to assess the radial extent Δr of the poloidal symmetry in emissivity profiles (and therefore in impurity density profiles) with bolometry alone. Using information from soft X-ray tomography we can conclude that typically $\Delta r \leq 30$ cm. In fact this diagnostic generally monitors the emissivity E_{SXR} of photons with energies in excess of 2 keV which is very low at the plasma periphery. Within the experimental uncertainties, and disregarding fast small amplitude modulations connected with the MHD activity or the large amplitude perturbations during the sawtooth crashes, E_{SXR} is uniform over the flux surfaces for $\rho<0.7$ in most cases.

In discharges that are not close to marfe conditions, good in/out symmetry is generally observed for both the global and the soft X-ray emissivity. Radiation and density profiles of injected and intrinsic impurities appear to obey the same symmetry rules.

Experimental observations with counter-injection beam heating

One notable exception has been verified during neutral beams counter-injection experiments where Ni was injected into the plasma using the laser blow off technique. These experiments were run on 3MA, 3 T, upper X-point discharges where the toroidal plasma current was directed counter-clockwise (looking at the tokamak from above) and the ion ΔB drift was

oriented upwards; peak electron densities and temperatures ranged within 2 - 5•$10^{19}$$m^{-3}$ and 3 - 5 keV respectively.

An example of the phenomena observed is given in fig. 1 where, together with other signals, the traces are plotted of the average emissivities along the lines of sight (LOS's) of four different channels of the bolometer arrays. The four LOS's are tangent to flux surfaces very close to each other ($\rho \simeq 0.7$); each plotted signal is obtained dividing the measured brightness by the length of the chord subtended by the LCFS along the corresponding LOS. The relative differences among the various traces are representative of the degree of poloidal asymmetry. The comparison of the two traces from the horizontal cameras

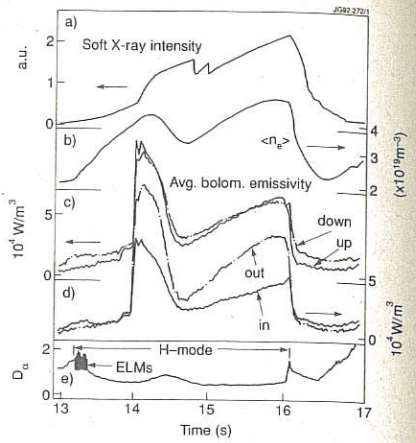

Fig.1 Soft X-ray intensity, avg. el. dens. and Dα together with avg. emissivity along the lines of sight of two channels of the horiz. cameras (c) and two of the vert. camera (d), during ctr-inj. beam heating. Ni is injected at 14.00 sec. Jet pulse # 24375.

shows that the typical up/down asymmetry is strongly reduced after the end of the ELMy phase at the beginning of the H-mode and reappears at the transition back to L-mode. The in/out asymmetry instead, as deduced by the traces from the vertical camera, is practically absent before the Ni injection time (t=14 sec), developing very rapidly thereafter and persisting until the end of the H-mode ($t \simeq 16$sec), while the injected metal impurity is retained within the discharge due to the very high impurity confinement time typical of that phase in high density discharges [ref.2]. After t=16 sec, while the injected Ni and the other impurities accumulated into the discharge during the H-mode are rapidly lost from the bulk plasma, the in/out asymmetry also disappears.

Fig. 2 shows the emissivity E_{SXR} from the tomographic soft X-ray diagnostic for the same pulse at five different times. It can be seen that while no appreciable in/out asymmetry is present before the Ni injection, thereafter the soft X-ray radiation profile is systematically higher on the large major radius side than on the other side of the magnetic axis, as already observed for the bolometric radiation profiles. From the time sequence of the profiles in fig. 2, as well as from the time behaviour of the electron density (fig,. 1) it appears that the asymmetry survives important rearrangements of the electron and impurity distribution profiles: an incipient process of central impurity accumulation (prof. c fig. 2) is interrupted by two

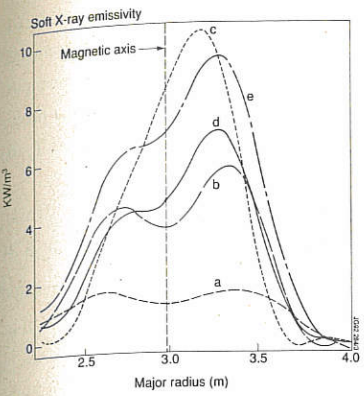

Fig.2 Soft X-ray emissivity on the equatorial plane of the JET tokamak. (a) t=14.00 sec; (b) t=14.25 sec; (c) t=14.70 sec; (d) t=15.00; (e) t=15.70 sec. Jet pulse # 24375.

successive internal collapses of the impurity distribution profiles (fig. 1a). The practical absence of up/down asymmetry is also a characteristic of these strongly in/out-asymmetric profiles of E_{SXR} observed after the injection of nickel into discharges with counter-injected neutral beams heating (fig.3).

When no Ni injection was performed in these discharges the profiles of E_{SXR} were dominated by radiation from light impurities (C and Be) and maintained a good degree of poloidal symmetry (in/out and up/down) through the entire beam heating phase. This latest observation, and the fact that the strong asymmetry after the injection of the metal impurity persists during the whole H-mode phase, suggests that the observed phenomenon is accounted for by a shift towards the large major radii of only those impurities with high atomic mass (or ionic charge). Furthermore the effect appears to increase with the beam power (or the value of β or with the toroidal velocity of the plasma).

Centrifugally driven modulations

One important effect consistent with the experimental observations is driven by centrifugal force F_c acting on the ion populations. Balanced by the pressure force and the parallel amipolar electric field E_{par}, this force produces a selective accumulation of the heaviest ions on the outside of the torus. In the absence of poloidal flows, the $O(\varepsilon)$ in/out poloidal modulation of the impurity density $\tilde{n}_I^c / \overline{n}_I$ is the same for all the collisional regimes [3-4]. A useful approximation to this quantity is given by [3]

$$\frac{\tilde{n}_I^c}{\overline{n}_I} = \left(1 - Z_I \frac{m_{eff}}{m_I} \frac{T_e}{T + Z_{eff}\, T_e}\right) \bullet \varepsilon \bullet \frac{m_I v_\phi^2}{T} \quad (1)$$

where ε is the inverse aspect ratio, v_ϕ is the plasma toroidal velocity, T and T_e the ion and electron temperatures, Z_I and m_I the ion charge and mass of the impurity considered and Z_{eff}, m_{eff} are the mean

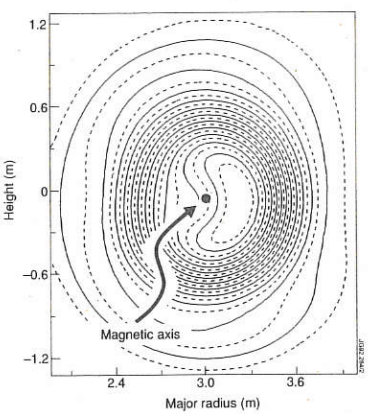

Fig. 3 Contour plot of the soft X-ray emissivity during counter-injection beam heating after injection of Ni into the discharge. JET pulse # 24394.

ion charge and mass of the plasma. From the above expression we see that the higher the ion mass of the background plasma (for constant Z_{eff}) the more the centrifugal effect is attenuated by the electrostatic force. For deuterium plasmas (this is the case for all the data presented here) and impurity ions close to full ionization $m_I/Z_I \simeq m_{eff}/Z_{eff} \simeq 2m_p$, where m_p is the proton mass. Introducing this simplification and disregarding the diference between T and T, the expression in brackets in eq. (1) reduces to $1/(1+Z_{eff})$.

In fig. 4 the relative in/out modulation of the perturbation in the soft X-ray emissivity after injection of Ni in counter injection experiments is plotted versus the parameter $X \equiv \varepsilon\, m_I\, v_\phi^2 / T$. Interpreting this quantity as $\tilde{n}_I^c / \bar{n}_I$ for that impurity we see that the measured asymmetries are consistent with values of Z_{eff} around 3. On the same plot data referring to co-injection experiments are also marked. They correspond to discharges (3 MA, 3 T) run in upper X-point configuration with plasma current and ion ∇B drift directed clockwise and upwards respectively. The amplitudes of the modulations are much smaller than in the counter injection and in some cases even their signs are inconsistent with the prediciton of eq.1.

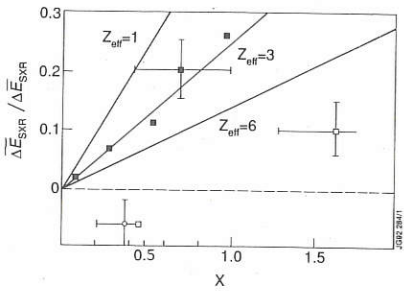

Fig. 4 Relative in/out modulation of the soft X-ray emissivity perturbation after metal injection in beam heated plasmas. ■ Ni, ctr.-inj.; □ Ni, co-inj.; ⊙ Fe, co-inj. The straight lines represent the prediction of eq.(1) for different values of Zeff in D plasma.

The failure of eq. (1) to represent the co-injection data is the evidence that another poloidal force (e.g. friction, viscosity or forces due to fluctuations), different from those considered above and comparable in strength to F_c, is present in that case, contrary to the neoclassical prediction of ref. 3. A recent work [5] analyses the impurity density poloidal modulation in the different collisional regimes in the presence of arbitrary toroidal and poloidal flows. Unfortunately $E_{par}= 0$ is assumed in that paper leading to an overestimate of the centrifugally driven modulations. However the expressions given there predict important modifications and even strong quench of the asymmetries for impurity poloidal velocities several times larger than the ion diamagnetic speed.

References

1. N Gottardi et al. EPS Conf. Amsterdam Vol. 14B Part 1.
2. R Giannella et al. EPS conf. Amsterdam Vol 14B Part 1.
3. S K Wong Phys. Fluids **30** (1987) 818.
4. C T Hsu, D J Sigmar Plasma Phys. Contr. Fus. **32** (1990) 499.
5. W Feneberg Nucl. Fus. **29** (1989) 1117.

SCALING OF IMPURITY TRANSPORT IN JET

D Pasini, R Giannella, L Lauro-Taroni, G Magyar, M Mattioli[(1)]

JET Joint Undertaking, Abingdon, OX14 3EA, UK

(1) Association Euratom-CEA, Cadarache

Introduction

The dependence of impurity transport with I_p, B_T, n_e, T_e and P_{add} has been investigated in JET for limiter L-mode He plasmas. Ni trace impurities were injected by laser blow-off and their progression into the plasma was followed with good spatial and temporal resolution using two soft X-ray cameras[1] (250 μm Be filter). The system uses 38 viewing lines in a vertically oriented fan and 62 in a horizontal fan allowing tomographic reconstruction of the X-ray emission. The spatial resolution (~10 cm) and the temporal resolution of the measurements (1 ms) was sufficient to follow the movement of the impurities between sawtooth crashes. In addition the time evolution of Ni spectroscopic lines was measured using VUV and X-ray spectrometers. The experimental data have been simulated using an impurity transport code where the radial flux was described as the sum of a diffusive and convective term, $\Gamma_z = -D\nabla n_z + Vn_z$. Both the diffusion coefficient D and the inward convection velocity V were taken to be functions of the minor radius and were specified to best reproduce the experimental data, namely, the time evolution of the X-ray emissivity profiles and of the spectroscopic line brightnesses during the quiescent phase of the sawteeth.

Measurements of impurity transport in JET using this technique have already been reported[2,3] for OH, L-mode and H-mode plasmas. These experiments were mostly limited to plasma conditions with $I_p = 3$ MA, $B_T = 3.2$ T and $\langle n_e \rangle \sim 3 \times 10^{-19} m^{-3}$. The results showed clearly the existence of two distinct transport regions in the plasma between sawtooth crashes, with a rather abrupt transition around $r/a \sim 0.4$. The aim of the present experiments was to study the dependence of D(r) and V(r) on I_p, B_T, n_e, T_e and P_{add} and possibly to identify the parameter(s) responsible for the transition. The data obtained confirm the generality of the previous observations. In addition it was found that the location of the transition region depends on the shape of the q profile and that a clear correlation exists between ∇T_e and the value of D in the anomalous transport region. The plasma density itself did not appear to have any significant effect on impurity transport.

Current scan and toroidal field scan

Experiments were performed in plasmas with I_p= 2,3,4 and 5 MA at B_T=3.2 T and at I_p=2 MA with B_T=1.45 and 2.55 T. Ni impurities were injected during the steady phase of the discharges heated with 4 MW of RF power. The time evolution of the tomographically reconstructed X-ray emissivity profiles shows the development of an increasingly hollow X-ray emissivity distribution following Ni injection. This indicates a very rapid transport of impurities in the outer plasma region up to the radius where the profiles peak and a much slower transport on the inside. The position where the profiles peak evolves only very slowly with time. In Figure 1 the Ni X-ray emissivity profiles (background emission subtracted), measured 70 ms after injection, are compared for different values of I_p and B_T. The outward displacement of the peaks when I_p is increased or when B_T is reduced indicates that the central zone of reduced transport become broader the flatter the q profile. The central zone of reduced transport is present only during the quiescent phase of the sawteeth. During a sawtooth crash the transport is greatly enhanced in the central region up to a mixing radius roughly 30 % larger than the inversion radius and this leads to a rapid inflow of impurities when the impurity distribution is hollow (see Ref.3).

In order to reproduce the evolution of the X-ray emissivity profiles it was necessary to assume two regions with distinct transport characteristics: in the central region, whose size had to match the hollowness of the experimental data, the value of D was much smaller than in the outer region. V(r) was taken equal to $2D \cdot r/a^2$. The D profiles used in the simulations are shown in Figure 2. The central value of D is independent of the plasma current within the error bars (50 %) and close to neoclassical predictions but the spatial size of this region increases with I_p and decreases with B_T. In the outer region, the value of D is ~20 times larger than in the central region at 2 and 3 MA, and at 4 and 5 MA it is ~30 times larger.

Density scan and power scan

The density scan and the power scan experiments were done with I_p = 3 MA and B_T=3.2 T covering the following range of parameters: $\langle n_e \rangle$=1 to 4 x 10^{19} m^{-3} with 4 MW of ICRH; P_{add}= 4 to 20 MW at various densities. The impurity confinement time, τ_{imp}, as given by the decay time of the central chord X-ray signal, was found to increase with the plasma density when comparing pulses with similar P_{add} or to decrease with P_{add} when comparing pulses of similar

density. More generally, as shown in Figure 3, the larger the total imput power per particle P_{tot}/n_e where $P_{tot}=P_{OH}+P_{add}$, the shorter τ_{imp}. The diffusion coefficient D for the pulses of Figure 3 are given in Figure 2. The corresponding T_e and n_e profiles are given in Figure 4.

The data shows that the larger P_{tot}/n_e the larger T_e and ∇T_e. Moreover, the larger $\langle \nabla T_e \rangle$ and $\langle T_e \rangle$ in the region (r/a>0.4) the larger the value of the diffusion coefficient in that region. As shown by the comparison of the pulses #27401 and #27397 which have the same values of D and V with similar T_e profiles but different n_e profiles, the plasma density itself doesn't seem to have any strong influence on the transport of impurities in the anomalous transport region. The apparent dependence of τ_{imp} on n_e during the density scan with a constant input power can be explained by the differences in the T_e profiles.

Summary and discussion

These experiments confirmed that two distinct transport regions exist in the plasma with a rather abrupt transition between them. In the central region D is small, close to neoclassical predictions, and in the outer region it is 20 to 30 times larger, clearly anomalous. The size of the central region of reduced transport is larger the flatter the q profile as observed by either increasing the plasma current or reducing the toroidal field. In plasmas with a constant q profile corresponding to 3 MA and 3.2 T, it was found that the value of D scaled with $\langle T_e \rangle$ or $\langle \nabla T_e \rangle$ in the anomalous transport region but did not depend on $\langle n_e \rangle$ or $\langle \nabla n_e \rangle$.

In these experiments there was a strong correlation between the location of the q=1 resonant surface and the region where ∇T_e and D suddenly changed value. However in other experiments the central zone of reduced transport was found to be present even when the temperature profile was strongly peaked on axis, as during a Monster sawtooth (see Ref. 3) or even in the absence of the q=1 surface in the plasma. This may signify that for the anomalous transport to develop both dq/dr and ∇T_e need to be large.

References

1. A W Edwards et al., Rev.Sci.Instrum.59(1986)2142.

2. D Pasini et al., EPS Conference (Berlin 1991) Vol 15 C, I-333.

3. D Pasini et al., Nuclear Fusion 30(1990)2049.

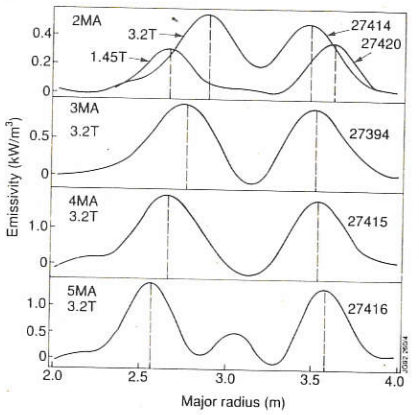

Fig.1 X-ray emissivity profiles 70 ms after Ni injection (background emission subtracted).

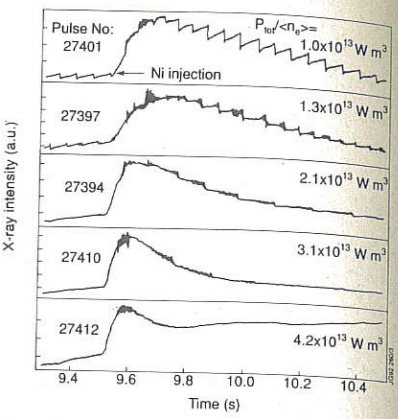

Fig.3 Evolution of the central chord X-ray intensity following Ni injection.

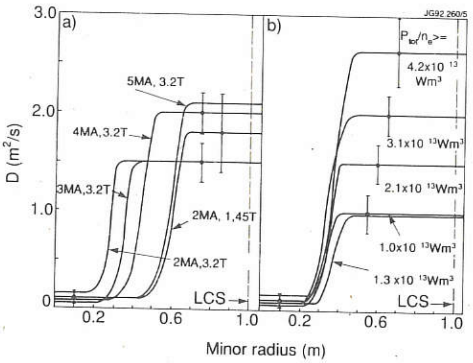

Fig 2 (a) Ni diffusion coefficients used to simulate Ni transport for the the plasma pulses shown in Fig.1. (b) Ni diffusion coefficients used to simulate Ni transport for the plasma pulses shown in Fig.3.

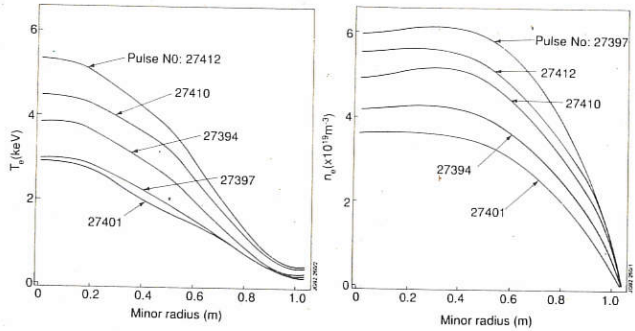

Fig.4 Radial profiles of T_e from ECE and of n_e from interferometric measurements for the plasma pulses shown in Fig.3.

PARTICLE AND IMPURITY TRANSPORT IN JET VERSUS NEOCLASSICAL THEORY

L Lauro-Taroni, R Giannella

JET Joint Undertaking, Abingdon, Oxon, UK

The analysis of impurity transport in recent years has stressed the need for reliable neoclassical predictions against which the experimental data should be benchmarked. During long H-modes, the impurities seem to accumulate in a region close to the separatrix: this behaviour has been identified for metallic (Ni), but also for lighter (O, Be) impurities and has been put in relation with a neoclassical mechanism {1}. A central zone of reduced transport has been identified in various cases and the values of diffusion and convection have been associated with neoclassical ones ({2}, {3}).

The neoclassical coefficients used in the simulation programs {4}, {5} for the comparison with the experimental results are analytical approximating expressions derived under several restrictions: the plasma is assumed to have a circular cross section and a small inverse aspect ratio and the impurity is present in the plasma only as a trace, i.e. the impurity strength $\alpha = n_I Z^2_I / n_i Z^2_i << 1$ with I and i being the impurity and the plasma main ion indeces, respectively. Furthermore, the expressions are valid in the asymptotic collisionality regimes, well away from transitions.

These approximations can be too restrictive for JET plasmas and a computer package {6} has been developed for the calculation of the full set of the general neoclassical transport coefficients for main ions, electrons and up to two impurities according to the neoclassical theory summarized in {7}.In general, the neoclassical transport coefficients L_{ij}^{ab}, linearly relating the fluxes to the thermodynamical forces (gradients), can be factorized in each collisionality regime into the product of two distinct terms: one depending only on the geometry (flux surface averages of quantities equilibrium-dependent) and one depending on the driving physical mechanism.

It is customary to decompose the particle flux across a surface labelled by the generic radial coordinate ψ into a diffusive (diagonal) and convective (non diagonal part): $\Gamma_a^\psi = -D_a^\psi \frac{\partial n_a}{\partial \psi} + n_a v_a^\psi$. This implies that the choice of the arbitrary radial coordinate represented by ψ needs to be consistent: if the gradients are evaluated with respect to the outer minor radius, this same coordinate has to be used for the calculation of the transport coefficients.

GEOMETRY

The well known $2q^2$ dependence of the Pfirsch-Schlüter transport coefficients results from the geometrical factor in the collisional regime in the limit of circular concentric flux surfaces and small inverse aspect ratio:

$$G_{PS} = \left(\frac{4\pi^2 q}{< R^{-2} > V'} \right)^2 \left(< \frac{1}{B^2} > - \frac{1}{< B^2 >} \right) B_0^2 \rightarrow 2q^2$$

$V' = \frac{\partial V}{\partial \psi}$, where V the plasma volume enclosed by the surface ψ, B_0 is the reference magnetic toroidal field and <.> indicates the average over the flux surface. For JET plasmas and in particular for the highly elongated X-point discharges G_{PS} needs to be evaluated properly: the volume increases faster than quadratically with the minor radius, particularly towards the plasma periphery where the Pfirsch-Schulüter contribution to the flux dominates, and the averages $<R^{-2}>$, $<B^{-2}>$ and $<B^2>$ computed numerically differ from their circular limit. From fig. 1 one can see that the departure from the circular cross section is not negligible even in the central zone of the plasma, where the dominant contribution to the flux is from the Banana-Plateau contribution. The BP geometrical factor

$$G_{BP} = \left(\frac{4\pi^2 q}{< R^{-2} > V'} \right)^2 \frac{3 < (\hat{n} \bullet \nabla \vec{B})^2 >}{< B^2 >^2} B_0^2 R_0^2$$

is lower for elongated plasmas than the value of 3/2, its limit for circular concentric flux surfaces.

TRANSPORT IN THE PLASMA CORE

Electrons. Deep fuelled NB discharges have been analyzed: in fact, when a LIDAR electron density profile is available between sawteeth, it presents the characteristic peaked shape already reported in {2}, for pellet fuelled and sawtooth free ohmic cases, with strong gradient for $\rho \leq 0.3$, ρ being the outer normalized minor radius. This feature builds up quickly and persists for a long time indicating a low diffusivity: for pulse #20981 the central peaking shown in fig.2 ($\simeq$700ms after a sawtooth crash) appears to have been determined entirely by the beam electron source and has effectively been simulated by means of a diffusion coefficient D_e = $0.006 m^2/s$ in the internal zone: this value is compatible with the neoclassical diffusion profile.

Helium. The neoclassical diffusion and convection profiles for helium injected into a deuterium plasma has been calculated for the JET shot #23457 {8}. Both D and He are in the bananan regime. Fig. 3 shows the He diffusion profile for $\rho < 0.5$ (curve a) together with the diffusivity from the analytical formula quoted in {4} for this regime (curve b). The typical $\varepsilon^{-3/2}$ divergence for $\rho < 0.05$ is of course removed because D and He transit to the plateau regime. The third curve represents the He diffusivity if carbon with a radially uniform density

profile with a radially uniform density profile, is added, in order to reproduce the experimental Z_{eff}.

So, it is possible to say that neoclassical effects can account up to an averaged value of $D_{He} \simeq 0.1 m^2/s$ in the region $\rho \leq .3$. The resolution of the experimental He profiles is poor so that at this stage it is not possible to exclude the existence of a narrow central neoclassical zone.

Impurities. Simulations of intrinsic (e.g. C, Ni) and injected (e.g. Ni, Fe) impurities require a zone of reduced transport in the central region, for both L- and H-mode discharges (see, for Ni, {3}). The departure from the circular cross section affects all collisionality regime so that its cumulative effect results in lower values in the centre than given by the cylindrical approximation by a factor of $\simeq 2$, leading for the case of H-mode to a $D_{NI} \leq 0.03 m^2/s$.

This is a low value, still, given all the uncertainties, neoclassical mechanism of transport in the centre cannot be dismissed.

TRANSPORT CLOSE TO THE PLASMA EDGE

The accumulation of impurities at the plasma edge, observed during high density H-mode discharges is a convection-dominated phenomenon in a narrow layer $\Delta x \simeq 3cm$ just inside the separatrix {1}. The strong effects of the elongation damping the q^2 factor (see fig. 1) lead to neoclassical predictions for D and v which are very small indeed ($D_{Ni} < 0.01 m^2/s$).

However, Stringer {9} shows that the inclusion of electrostatic fluctuations alter the picture: automatic ambipolarity is broken and a strong radial electric field arises which must be retained explicitly in the general equations that leads to a neoclassical charge dependent convection for the impurities $v_I = \frac{e_I}{T_I} E_r D_I^{NC}$, in order to balance the non-ambipolar part of the fluctuation-driven particle flux.

As in JET periphery highly localised radial electric fields of 40-100 kV/m have been inferred from measurements of poloidal and toroidal rotation velocities {10}, they could account in the case of e.g. NiXIX for an edge temperature $T_i \simeq 500eV$, for a convection velocity of the order of $V_{Ni\ XIX} \simeq 10m/s$.

This value of convection makes a "neoclassical" mechanism of edge impurity accumulation plausible, also keeping in mind that the scale length of this phenomenon is of the order of the ion poloidal Larmor radius and strictly speaking the neoclassical theory breaks down.

References

{1} R Giannella et al., Proc. XVII EPS, Amsterdam (1990)
{2}R Giannella et al., Plasma Physics and Contr. Fus., **34**,687
{3}D Pasini et al, Plasma Phys. and Contr. Fusion, **34**,677
{4}G Fussmann et al., Plasma Phys. and Contr. Fusion, **33**, 1677
{5}G Fussmann et al., J. Nucl. Mater. 162-164 (1989),14 and ref. therein
{6}L Lauro-Taroni et al., JET-R(91)10
{7}S P Hirshman and D J Sigmar, Nucl. Fus. **21**(1981) 1079
{8}T T C Jones et al. Proc. XVIII EPS, Berlin (1991)
{9}T E Stringer, Nucl. Fus., to be published

{10}K Ida, to be submitted to Nucl. Fus.

Fig 1:Pulse No: 22122 t=11.15s

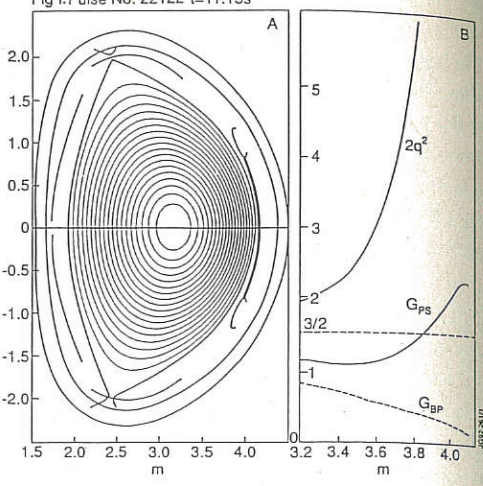

Fig.1 Pulse #21022 t = 11.5 s
A: Flux surfaces configuration from equilibrium code
B: Geometrical factors G_{PS} and G_{BP} and their cylindrical approximations

Fig.2 Pulse #20981 t = 11.5s
A:
(a)- Electron LIDAR profile
(b)- Simulated electron profile
(c)- Integrated electron source
B: Electron Diffusivity for Simulation (solid line)
Neoclassical Electron Diffusivity (dotted line)

Fig 2 Pulse No: 20981 t=11.5s

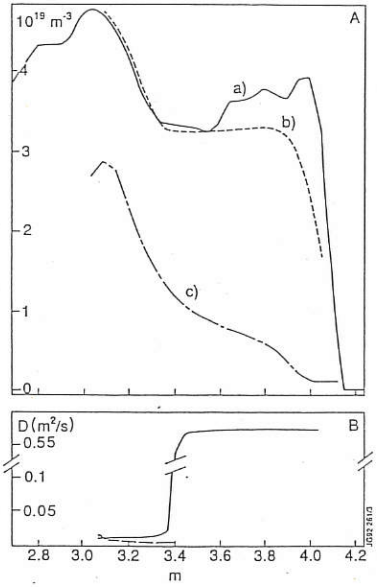

Fig 3 Pulse No: 23457

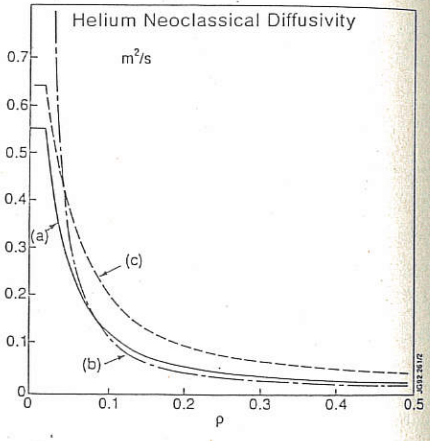

Fig.3 Pulse #23457
(a): Neoclassical Diffusivity for Helium
(b): Neoclassical Diffusivity according to {4}
(c): Neoclassical Diffusivity including collisions with Carbon

COMPONENTS OF Prad AND Zeff DERIVED FROM X-RAY SPECTROSCOPY OF THE MAIN IMPURITIES IN JET

R Barnsley, J Brzozowski[1], I H Coffey[2], K D Lawson[3], I M Melnick[4], A Patel[3], T K Patel, N J Peacock[3].

JET Joint Undertaking, Abingdon, OX14 3EA, UK.

1 Royal Institute of Technology, Stockholm, Sweden.
2 Queens University Belfast, B17 1NN, UK.
3 Culham Laboratory, (UKAEA/Euratom Fusion Assoc.) OX14 3DB, UK.
4 University College London, WC1E 6BT, UK.

INTRODUCTION. We describe techniques to derive P_{rad} components, and impurity concentrations from soft x-ray spectroscopic data. This has particular importance for the JET preliminary tritium experiment (PTE) /1/, when the close-coupledVUV and XUV grating spectrometers were inoperable due to high background radiation.

A new diagnostic at JET, the Bragg rotor spectrometer, gives near-complete coverage of the soft x-ray spectrum between about 0.1 nm and 10 nm. This region contains K-, L-, or M-shell line radiation from highly ionised plasma impurities for which $Z \geq 4$ (Be), and offers the potential to measure all impurity concentrations, and to derive Z_{eff} either from the sum of the components derived from line emission or directly from the continuum level. The extension to longer wavelengths is particularly useful at JET, where radiated power and Z_{eff} are usually dominated by light impurities such as Be and C, whose H- and He-like transitions lie between about 2.5 nm and 10 nm.

Advantages of the soft x-ray region are that the spectrum is relatively uncrowded, and that all likely impurities have strong transitions for which the atomic physics is relatively well known. However, a major problem is the interpretation of central-chord line intensites in terms of local impurity concentrations, particularly for the low-Z ions.

INSTRUMENTATION. The three main design criteria of the Bragg rotor spectrometer /2/ were: **(a)** full coverage of the soft x-ray spectrum, to monitor a range of ionisation stages of any possible impurity, **(b)** high monochromatic sensitivity to monitor trace impurities and give good time resolution for the study of transient events such as impurity injection, and **(c)** the best possible time resolution for representative lines of the few main impurities, with good sensitivity and stable calibration, for routine analysis of radiated power components. This feature, intended to give a standardised set of data for all discharges, was thought to be especially important.

In order to achieve these somewhat conflicting aims the aperture was divided into two independent sections. Aims (a) and (b) are fulfilled by scanning six diffractors sequentially on a hexagonal rotor and aim (c) is met by a side-by-side array of small diffractors or parallel-channel monitor.

The optical configuration (low divergence x-ray collimator and rotating flat diffractor) allows coverage of a broad spectral range with good sensitivity even when using a low f-number beamline. This made it possible to install the instrument outside the JET torus hall, sharing the radiation-shielded tritium-compatible beamline of the Active Phase Double Crystal Monochromator /3/. Both instruments were operated throughout the JET PTE and gave useful data on the intrinsic impurities /4/ (Be, C, O, Al, Cl and Ni) as well as monitoring for unexpected occurrences of any other impurity (Ne, F, P, S, Ar, Cu and Zn have previously been observed).

RESULTS. The JET Active Phase Double Crystal Monochromator was fitted with TlAP crystals and scanned between 1.15 nm and 1.65 nm to monitor H-like lines of Oxygen and Ne-like lines from metals such as Ni and Zn. The Bragg rotor spectrometer, fitted with a selection of crystals and multilayer mirrors, gave full coverage from 0.2 nm to 11 nm and was used mainly to monitor Be, C and Cl. The parallel-channel monitor was not built at this time and so the time resolution was limited to ~1 s by the hexagonal rotor. A full survey spectrum from this instrument is shown in fig. 1. The data from the Bragg rotor spectrometer shows similar time evolution for the same lines (Be Lyα and C lyα) as from the VUV/XUV grating spectrometers, and has been analysed by similar techniques /5/.

In principle it is possible to derive P_{rad} components and impurity concentrations using a transport code together with an instrument absolute calibration, but for low-Z ions the uncertainties are too great at present to yield results which are consistent with independent P_{rad} and Z_{eff} measurements. Errors arise from uncertainties in the parameters of the outer region of the plasma, where low-Z impurities mostly radiate, from the atomic physics and from the instrument absolute calibration. Instead we take the intermediate step of deducing the radiated power components for each impurity, for use as transport code inputs.

Radiated Power. P_{rad} components are derived by fitting a set of coefficients k_z to the individual line intensities I_z, such that the sum $\Sigma_z\, k_z.I_z = P_{rad}$: the total radiated power as measured by bolometry. This technique requires that the time evolutions of the impurity line intensities are sufficiently different from each other to identify their signatures on the bolometry, a condition which can

usually be met by analysing a large enough number of pulses. Figure 2 shows the results of such a fit for the main radiating impurities Be, C, and Cl, in a D-T discharge. The agreement in the Ohmic phase of the discharge is good, but there is up to a factor two discrepancy in the beam-heated phase. There is no data point for C at 12 s, and the resulting interpolation has overestimated the radiated power at that time.

Impurity Concentrations. The main feature of this part of the analysis is use of the P_{rad} components derived by the above technique as inputs to the SANCO time-dependent impurity transport code, which uses measured T_e and n_e profiles, and transport coefficients obtained from experiments at JET /6,7/. This gives derived concentrations which are about a factor two higher than needed for consistency with the visible bremsstrahlung value Z_{eff-vb}, which is considered to be good agreement in view of the uncertainties inherent in modelling central chord data. These interim concentrations are then normalised to Z_{eff-vb} at a time of 6 s, thus only relying on the code to model the relative impurity abundances. The results (fig. 3) are consistent with Z_{eff} up to about 12 s, but do not show the sharp increase at 13 s as recorded by charge exchange spectroscopy. This is partly due to the scanning time resolution of the Bragg spectrometer data, but may also be due to the problems of modelling the light impurity radiation in the H-mode, where the edge profile effects are most severe.

CONCLUSION. The Bragg spectrometers at JET are able to monitor all the major intrinsic impurities, and offer a viable alternative to grating instruments, particularly in D-T experiments where a shielded low f-number beamline is desirable. At the present level of analysis, the derived components of P_{rad} and Z_{eff} are useful only in the Ohmic phase, and are thus complementary to charge-exchange spectroscopy. In future the improved time resolution (~20 ms) of the completed Bragg rotor spectrometer is expected to increase its usefulness as a survey monitor and allow a deeper analysis of the impurity time behaviour.

/1/ The JET Team, Nuclear Fusion, 32 no2, Feb 1992, p187.
/2/ R Barnsley, K D Evans, N J Peacock and N C Hawkes, Rev Sci Instrum, 57(8) (1986) 2159-2161.
/3/ R Barnsley, U Schumacher, E Källne, H W Morsi and G Rupprecht, Rev Sci Instrum, 62(4) April 1991, 889-898.
/4/ R Barnsley, J Brzozowski, I H Coffey, K D Lawson, A Patel, T K Patel, N J Peacock, U Schumacher. APS 9th Top. conf. High temp. plas. diag., Santa Fe, March 1992. Proc. to be publ. in Rev Sci Instrum, 1992.
/5/ K D Lawson et al, Proc. 17th EPS Conf. Controlled Fusion and Plasma Physics, Amsterdam, III p1413-8, 1990.
/6/ D Pasini et al, Proc. 18th EPS Conf. Contr. Fus. and Plas. Physics, Berlin, I
/7/ R Giannella et al, JET-P(91)33

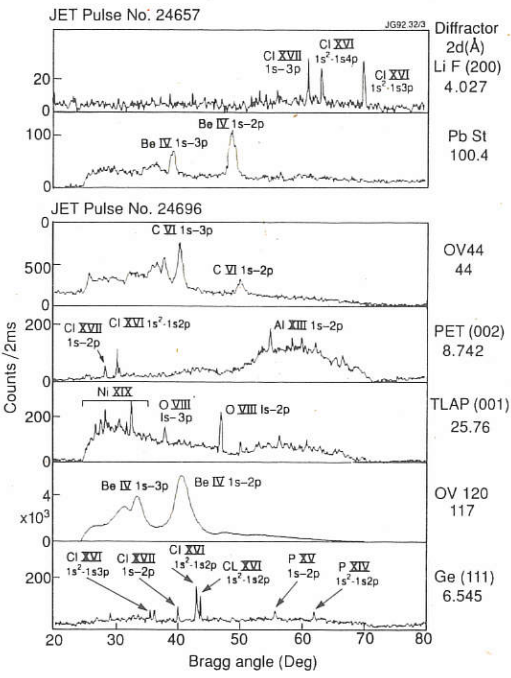

Fig 1: Survey spectra from the Bragg rotor spectrometer. A selection of crystals and multilayer mirrors was mounted to a hexagonal rotor, to survey soft x-ray line radiation from all the main impurities in JET. The spectrum contains H- and He-like lines from the lighter elements (Be, C, O, Al, P, and Cl), and Ne-like Ni lines.

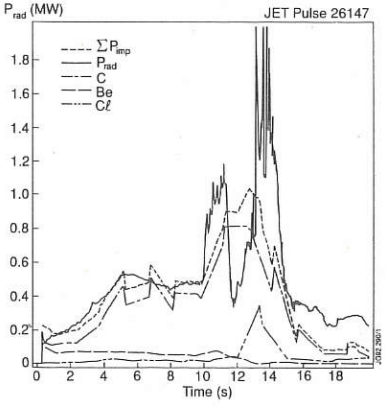

Fig 2: Radiated power components derived by fitting line intensities to the total radiated power (P_{rad}).

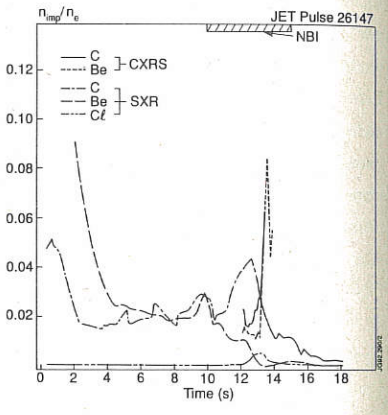

Fig 3: Impurity concentrations derived from soft x-ray spectroscopy (SXR), compared with charge exchange recombination spectroscopy (CXRS).

Effective ion charge and impurity behavior in the Frascati Tokamak Upgrade

D. McNeill,* V. Zanza, G. Mazzitelli, G. Bracco, I. Condrea,**
R. De Angelis, F. Orsitto, L. Panaccione, and S. Segre +
Associazione EURATOM-ENEA sulla Fusione, CRE Frascati
C. P. 65, 00044 Frascati (Roma), Italy

The effective ion charge Z_{eff} is an important measure of the plasma purity in tokamak discharges. In the Frascati Tokamak Upgrade (FTU) diametral average values of Z_{eff} obtained from visible bremsstrahlung and from the Spitzer plasma resistivity for ohmically heated discharges are generally in good agreement. Here we discuss the two types of measurements and relate the behavior of Z_{eff} to the behavior of impurities in the plasma. FTU is a medium-size (plasma major and minor radii 0.93 and 0.30 m, respectively), high toroidal magnetic field (up to 8 T on axis) tokamak with a peak plasma current of 1.6 MA and a plasma duration of up to 1.6 s. The major object of study is high-density plasmas (above 10^{20} m^{-3}) with high heat loads on the limiters.

Bremsstrahlung in FTU is measured with a horizontally viewing fan array of 12 detectors and a vertical array of 4 detectors at 540 nm. The observed intensity profiles are usually much higher than pure bremsstrahlung in the outer 10 cm or so of the plasma. In the steady-state phase of well-centered, MARFE-free discharges, these excess levels are close to the calculated levels of the quasicontinuum emission from hydrogen molecules incident at the discharge edge.[1] Thus, as a first approximation the observed data are corrected by subtracting a fixed fraction of coincident H-alpha signals. This makes it possible to obtain correct diametral average values of Z_{eff} in the conventional manner (assuming a flat Z_{eff} profile and a fixed Gaunt factor) and to establish the level of contamination in the array signals in order to obtain bremsstrahlung emissivity profiles (at least within minor radii of ≈ 0.15 m) from which a radial profile of Z_{eff} can be derived. The variation in the diametral average Z_{eff} with the plasma electron density in a single shot is qualitatively similar to the dependence of Z_{eff} on the line

average electron density in the steady-state phase of sequences of shots (Fig. 1). This kind of variation in Z_{eff} with n_e over sequences of discharges has been reported previously for many machines,[2] but the analogous variation within single shots suggests that similar impurity mechanisms are operating at equivalent electron densities in the time frame of individual discharges in FTU. (At the lowest densities, the assumptions used in the calculation must be checked carefully. For example, the relative contribution of emission from the edge should be greater then and the radial profiles of various parameters may not be well established.) Z_{eff} in the steady-state phase of FTU discharges has been decreasing as contaminating materials have been removed from the vessel and the machine has become conditioned over the last year and a half. Presently $Z_{eff} \leq 1.3$ in dense hydrogen plasmas ($n_e \geq 1 \times 10^{20}$ m^{-3}) and <2.1 in dense helium plasmas ($n_e > 2 \times 10^{20}$ m^{-3}).

Z_{eff} has also been derived from neoclassical theory, including the bootstrap current (<10% of I_p), and from a simple Spitzer resistivity model over a wide range of steady-state discharge conditions.[3] This derivation of Z_{eff} assumes a flat Z_{eff} profile and is based on the measured plasma current and loop voltage together with (as for the bremsstrahlung measurements) the electron temperature profiles from the electron cyclotron emission diagnostic and the electron density profiles from the DCN interferometer. Figure 2 shows the Z_{eff} calculated using the Spitzer and neoclassical resistivities as functions of that calculated from the central bremsstrahlung intensity. The neoclassical values are almost always below the Z_{eff} from bremsstrahlung. Given the errors in the derived values of Z_{eff} (estimated at up to 35% for the bremsstrahlung value) the agreement of the bremsstrahlung value with the Spitzer value is qualitatively satisfactory.

Understanding the variation of Z_{eff} with time and density in FTU plasmas involves questions of plasma initiation and fuelling, as well as transport. Although this topic requires detailed investigation beyond the scope of this paper, here we briefly examine the relationships between Z_{eff} and the impurities observed by visible[4] and UV spectroscopy.

The main light impurity now observed in FTU is oxygen, while

nickel and chromium are the major heavy impurities. Oxygen is desorbed from the walls while the metallic impurities are produced by sputtering from (mostly) the limiter. At the start of operations it was necessary to overcome the radiation barrier owing to oxygen (which occurs within the first 20 ms of the discharge), after which standard 1-1.5 s pulses could be produced. Figure 3 shows the time evolution of the intensities of the O VI 103.2 nm, O V 63.0 nm, O IV 55.4 nm, and Ni XVII 24.7 nm lines together the electron density for a typical discharge. In general, the influx of metallic impurities into a discharge decreases as the electron density rises and, depending on the plasma current, almost disappears at the maximum density attained in ohmic discharges. Measurements of the visible 425.4 nm and metastable 528.0 nm term lines of Cr I, together with the H alpha and beta lines, show that the ratio of the fluxes of chromium and hydrogen at the limiter is $\approx 1\%$ at low n_e and falls by more than a factor of 3 for $n_e > 1 \times 10^{20}$ m^{-3}. Systematic changes in the impurity influxes over the early operating period of FTU have been mirrored in a gradual decline of Z_{eff}.

The behavior of the metallic impurities in these ohmically heated discharges is a peculiarity of high field machines such as FTU or Alcator C and is of interest from the standpoint of plasma-wall interactions. The nominal heat load to the limiter in FTU ($>10^{11}$ W/m^2) should be enough to melt the metal and produce a strong influx of metallic impurities. The presence of a "virtual limiter"[5] may explain the observed low levels of metallic impurities in the plasmas, although this requires further study. In contrast, light impurities are almost absent at low electron densities but predominate at high densities ($n_e > 1 \times 10^{20}$ m^{-3}); however, at present they do not affect Z_{eff}, which is close to 1.

Footnotes and References

* ENEA Guest
** ENEA Fellow
+ Dip. di Fisica, Università degli Studi di Roma II, Tor Vergata (Rome) Italy

/1/ D.H. McNeill, Rev. Sci. Instrum. 57, 2724 (1986)
/2/ P.C. Stangeby and G.M. McCracken, Nucl. Fusion 30, 1225 (1990)
/3/ V. Zanza and S.E. Segre, accepted for publication in Nucl. Fusion
/4/ I. Condrea, R. Bartiromo et al., paper in these proceedings
/5/ A. Sestero, Nucl. Fusion 17, 115 (1977)

Fig. 1. Average Z_{eff} from bremsstrahlung as a function of the line average n_e in the steady-state phase of a large number of FTU discharges (circles) and during two discharges with I_p=700 (solid curve; rising density portion of discharge only) and 350 kA (dashed curve; average of rising and falling density portions of the discharge).

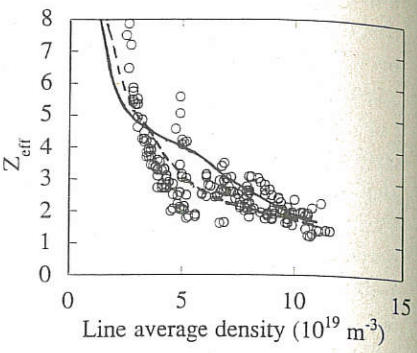

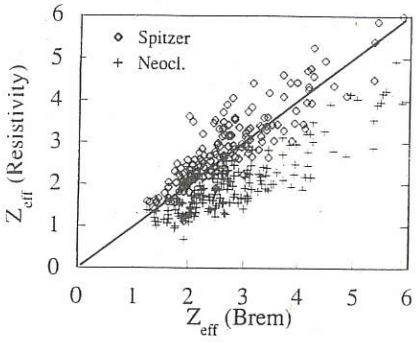

Fig. 2. Z_{eff} from the Spitzer (diamonds) and neoclassical (crosses) resistivities as functions of the value of Z_{eff} from bremsstrahlung data in the steady state phase of FTU discharges. The line corresponds to equality of the resistive and bremsstrahlung values.

Fig. 3. Time evolution of the intensities of the O VI 103.2 nm, O V 63.0 nm, O IV 55.4 nm, and Ni XVII 24.7 nm lines together with the electron density (dashed curve; units of 10^{19} m^{-3}) for a typical discharge.

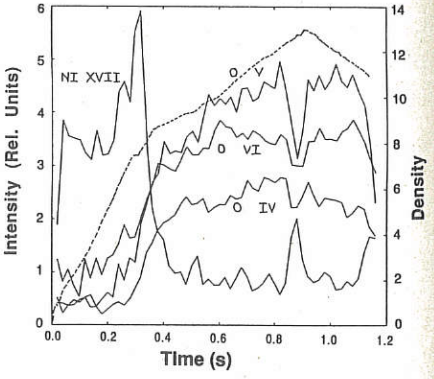

STUDIES OF IMPURITY CONFINEMENT INJECTED BY LASER BLOW-OFF IN THE TJ-I TOKAMAK

B. Zurro, J. Vega, F. Aragón, C. Burgos, L. Pacios and C. Pardo. Asociación EURATOM/CIEMAT. E-28040 Madrid. Spain

1. Introduction. This paper reports studies of particle confinement injected by laser blow-off in the TJ-I tokamak. Injection by laser blow-off of a non-recycling impurity is the most direct and powerful method to measure the particle confinement time in magnetic fusion devices. This technique allowed to obtain an empirical scaling law of particle confinement time in tokamaks (1). We studied, in a former work (2), the impurity confinement behaviour with plasma density and toroidal field, but our data did not fit in the former scaling law, what deserves a more complete study. We address in the present work, to extend these studies to different plasma regimes and using a more complete set of diagnostics to document them. The aims of this work are threefold: to study the dependence of particle confinement with plasma current, explore the influence of a polarized limiter on the penetration and confinement of injected impurities at low plasma currents and to assess the performances of a new detector (3) to support impurity injection experiments.

2. Experimental. Non-recycling impurities are injected into the TJ-I ohmically heated tokamak ($R = 30$ cm, $a = 9.5$ cm, $I_p \leq 60$ kA and $B_T \leq 1.5$ T), by using the laser blow-off technique described in more detailed in Ref. (2). For this purpose iron deposited on a pyrex plate as a thin film, of thickness 1 μm, has been ablated by focusing a Q-switched ruby laser delivering 2 J in 30 nsec, at the plateau of the TJ-I ohmically heated discharge. A vacuum manipulator permits a fine orientation of the plate within an auxiliary chamber evacuated at a pressure of 10^{-7} torr. The target plate can be moved from the outside so many injections can be made without breaking the vacuum.

The arrival of the generated impurity beam at the plasma edge is monitored by optical means, collecting at 90º the light emitted by the particles when interacting with the edge plasma electrons. This light can be guided, for high-resolution spectral studies, to a near-UV and visible monochromator, which has an intensified multichannel detector attached to its focal plane. The evolution of the impurity transient in the plasma core is monitored by a

pyroelectric detector, sensitive to the entire spectrum of plasma radiation, and by this new detector based on the fluorescence of a phosphor. We have realized, in a previous work (2), that the decay time of the perturbation measured in the pyroelectric signature is the same as that deduced from the time evolution of highly ionized ions tracked by a VUV grazing-incidence monochromator.

One of the aims of this work is to assess the performances of this recently developed VUV filter spectrometer (3), to support impurity injection experiments in a tokamak plasma. This system can either follow the radiation intensity signature, lying within a selected spectral range and chord-averaged along a central vertical diameter, or provide radiation spatial scan every 0.5 msec. Depending on the type of interposed filter, between the plasma and the sodium salycilate phosphor used to detect VUV photons, the system is sensitive to radiation coming from high or low-Z ions. The resonant lines of the former ions tend to emit higher energy photons than the latter ones. In addition, an array of ten x-ray detectors with a filter (4), passing radiation with energy higher than 1 keV, is used to follow with space-time resolution the penetration and decay of the injected impurity pulse into the plasma. Therefore, a complete set of radiation diagnostics covering the visible, VUV and x-ray ranges are available for these studies.

3. Results. The impurity confinement time is being studied as a function of plasma current, in order to separate the influence of toroidal field, plasma current and safety factor in the particle confinement time. The final aim is to cover the range between 20 and 45 kA. We show, in Fig. 1, first results obtained at a low plasma current (≈20 kA). In Fig. 1 (a), we show typical signatures of a few relevant monitors in a discharge in which iron was injected around 4 msec after the discharge started-up. The inverted trace, which corresponds to a visible photodiode seing the plasma edge at the injection port, is sensitive to the laser light pulse -narrow feature- and afterwards to the interaction between the injected atomic pulse and the edge plasma electrons which produce some observable emission. The impurity transient in the main plasma is seen by two other traces, the phosphor detector and the pyrolectric, as an enhancement in the radiation. The first detector shows a fluctuating signature, which is not due to noisy detection but rather well reflects actual plasma fluctuations. The radiation impinging onto the sodium salycilate (ss) detector was selected, in this particular case, by a VUV filter passing the radiation lying between 100 - 800 Å. Both detectors are collecting radiation along central chords at two different toroidal positions.

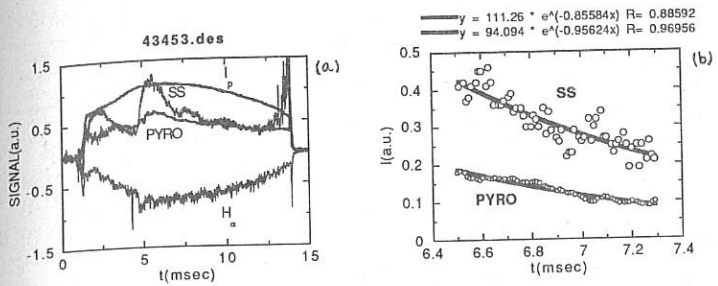

Fig. 1. (a) Signatures of plasma current (I_p), sodium salycilate detector (SS), pyroelectric detector (PYRO) and photodiode edge monitor in a low current discharge (≈ 20 kA), where iron was injected by laser ablation; (b) Analysis of the decay -time of the radiation transient to deduced the confinement time (τ_p = 1.17 (SS), 1.05 (PYRO) msec).

In Fig. 1 (b), the analysis of the perturbation decay time measured in the SS and pyroelectric detectors is shown, given decay times of 1.2 and 1.1 msec, respectively; which agree reasonable well within experimental errors. The signals used in the analysis were obtained by subtracting the background contribution. At a plasma current of 38 kA the decay time was 0.7 - 0.8 msec, for a similar density discharge. The corresponding values of q at the edge for these two discharges (B_T = 1 T) are 7.5 and 3.9. At present we do not know whether the q or the current is the dominant parameter.

In Fig. 2 (a) the perturbation signature seen by several channels of the x-ray detectors in a typical impurity injection experiment is shown for three different plasma chords, their radii are given in this figure. The decay time of the transient measured on the x-ray signals is similar to that provided by the pyroelectric and sodium salycilate detector. Chord-integrated profile evolution of this perturbation detected by the same diagnostic is depicted in Fig. 2 (b), for three times after the injection took place. The background signal was subtracted in the transient profiles presented in this former figure. As can be seen impurity penetration occurs in around 30 μsec. A feature which must be noted, not shown in this figure, is that the perturbed profile, the one resulting after subtracting background, peaks at different position that the unperturbed one. This might indicate that plasma potential and pressure do not have the maximum at the same position. A more quantitative analysis of these preliminary results, using a transport code, will be presented.

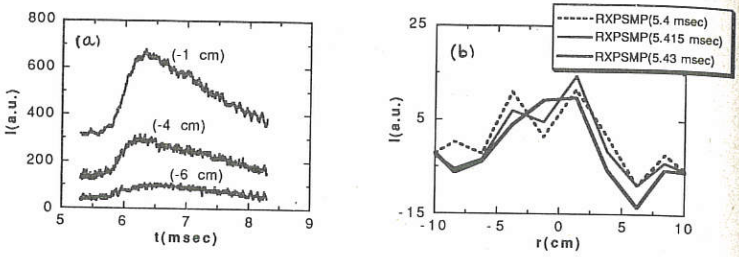

Fig. 2. Results of impurity injection seen by the x-ray array: (a) Time evolution of traces at different plasma chords; (b) Chord-integrated emission profiles showing the impurity penetration into the plasma. The latter were obtained subtracting the background radiation profile. The outer edge, corresponding to positive radii, exhibit a stronger perturbation since the impurities are injected from the low field side.

The possibility of producing an H-like-mode regime (5) by the appropriate polarization of an inserted electrode, is being also studied in the TJ-I tokamak. In this work we address the question of the influence of a polarized electrode on the confinement of impurities injected by laser ablation in this tokamak. Since this transient method is sensitive to the particle central confinement, this method is potentially more powerful to elucidate if there is an improvement of confinement at any radius or only at the plasma periphery. To this aim an electrode inserted 3 cm into the plasma is polarized (± 1 kV) few milliseconds before the laser injection take place and the signature of the impurity transient will be compared for discharges with and without electrode polarization. Preliminary experiments have been performed and the results are being analyzed.

References

(1) E. S. Marmar, J. E. Rice and J. L. Terry, Nucl. Fusion **22**, 1567 (1982).

(2) B. Zurro, F. Mompeán and C. Pardo, Plas. Phys. Controll. Fusion, **30**, 1767 (1988).

(3) B. Zurro, Rev. Sci. Instrum. **62**, 118 (1991).

(4) J. Vega and A. P. Navarro, Proc. 18th Europ. Conf. Controll. Fusion and Plasma Phys. **15C II**, 29 (1991).

(5) R. J. Taylor et al., Phys. Rev. Lett. **63**, 2365 (1989).

Toroidal diffusion of injected impurities in the MT–1M tokamak

S.Zoletnik, G.Veres, J.S.Bakos, G.Bürger, P.N.Ignácz,
B.Kardon, S.Kálvin, G.Kocsis and J.Szigeti

KFKI Research Institut for Particle and Nuclear Physics
H–1525, P.O.Box 49. Budapest, Hungary

Introduction. Injecting small amounts of impurities into tokamak plasmas for diagnostic purposes is a common technique on most present-day tokamaks. In these experiments mainly the radial transport of the injected particles is observed, after the material has been dispersed along the toroidal direction. On the MT–1M tokamak (R=40 cm, a=12.5 cm) aluminium has been injected, using the blow–off technique, in order to investigate the toroidal motion and ionization of the injected impurities. Recently similar experiments have been proposed/1/ to gain information on various plasma parameters by observing the toroidal distribution of subsequent charge states of the injected atoms.

Experiments. All experiments were performed on the MT–1M tokamak with hydrogen gas filling, toroidal magnetic field B_T=1 T, plasma current I_p=17 kA, limiter radius 90 mm, $q_{lim} \approx 6$ and line averaged electron density $2 \times 10^{13} cm^{-3}$. The electron temperature obtained from the Spitzer resistivity formula is 170 eV. The amount of injected material was kept so low, that no perturbation could be observed on the global plasma parameters (e.g. loop voltage, electron density, total radiation, ...etc). The blow–off beam was injected from the bottom side of the torus with 5 cm beam diameter. The beam penetrated into the plasma up to about 2 cm minor radius, the highest amount of ion was deposited at r $\approx$ 5cm.

The light of the Al atoms, Al^+ and Al^{2+} ions around the place of injection was detected by two visible monochromators/2/. Radiation of the Al^{2+}, Al^{3+} and higher ionization state ions was observed by two VUV—soft–X–ray cameras/3/ in three series of experiments: at the place of injection, toroidally 60 and 180 degrees apart.

Using different absorber filters, different energy sensitivity ranges can be selected for the cameras from 5 eV up to 1 keV. As different ions radiate at different photon energies, the cameras can be made sensitive to certain ionization states. In the case of aluminium, using $2mm\ CaF_2$ crystal filter, the cameras detect the line radiation of Al^{2+}/2/. This ion could be seen only in a few cm distance in toroidal direction around the place of injection/2/. Using 0.2 μm Carbon foil filter the cameras are most sensitive to the radiation in the 80–300 eV range. Aluminium ions starting from Al^{3+} up to Al^{7+} all have intensive lines around 100 eV thus there is no way to distinguish between the line radiation originating from the different ionization states/2/. This phenomenon is clearly shown by *Fig. 1.*, where the light of the neutral Al atoms in the blow–off beam is plotted together with the sum of the camera signals. The fast increase in the camera signal at the beginning corresponds to a low ionization state (possibly Al^{3+}), while the slow decay indicates that the radiation of higher ionization states is also measured. This effect complicates the interpretation of the results, but on the other hand can be useful if one is interested in the motion of the injected Al ions regardless of their charge state.

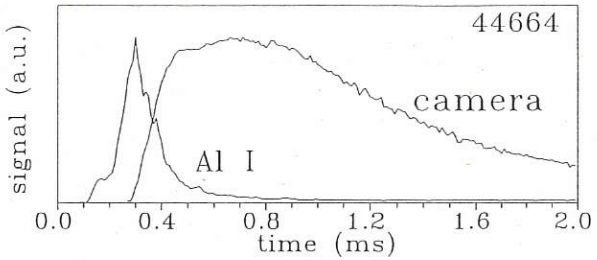

Fig. 1. Time evolution of the 3944 Å neutral aluminium line radiation signal and the sum of all (2 × 16) camera signals (energy range 80–300eV). The camera was located 60° toroidally from the place of injection. Both curves are normalized in amplitude. The timescale refers to the time after the blow-off laser pulse.

Fig. 2. shows the time evolution of selected camera signals measured with carbon filter at different toroidal positions relative to the place of injection. As it can be seen the time evolution depends much on the radial position of the measuring chord in a given toroidal cross-section. Morover, the picture also changes if one moves from one cross-section to another. On *Fig. 2/a,b.* (60° from the injection) the radiation first appears at the central and lower part, while on *Fig. 2/c,d.* (180° from the injection) it appears first in the central and upper part. A characteristic delay, relative to the Al radiation signal can also be observed, which has been discussed elsewhere/2/.

To further analyse the radiation distribution data obtained with the two cameras, a new method of tomography has been developed which can be used both for radiation distributions with localized peaks and for smooth tokamak equilibrium distributions. The tomographic reconstruction of the measurements presented on *Fig. 2.* is shown on *Fig. 3.* Near to the injection (*Fig. 3/a.*) most of the radiation is localized to a spot at the bottom side of the tokamak, while 180° apart the highest radiation levels can be observed on the upper part (possibly two peaks are present). This structure can be observed only for a short time after the injection.

From the above results, the following picture can be outlined of the toroidal diffusion of injected aluminium. From the beam Al^+ ions are deposited in the plasma. During the first $\approx 100\mu s$ they become ionized to Al^{2+}, but as their average toroidal velocity is small/2/, they become ionized to Al^{3+} within a few centimeters. Al IV is the ion which spreads around the tokamak and can be observed at all toroidal cross-sections. About $150\mu s$ after the injection Al ions can be observed in the whole tokamak. The first packet of ions which arrive at a cross-section can be seen at well defined places, they possibly travel along field lines. Later the ions become ionized to higher levels and spread around in all cross-sections.

Computer simulation. To have a clearer theoretical picture about the mechanism of the toroidal dispersal of the injected aluminium, a two dimensional (toroidal and radial) Monte Carlo computer simulation has been developed. The code takes into account the following physical processes:

- ionization of the injected impurities due to the collisions with the electrons of the background plasma (recombination neglected),
- heating of impurities due to the collisions with the ions and electrons of the background plasma.

For the description of the toroidal motion of the impurities, first the model proposed in /5/ was applied, but the agreement with the experimental data was not satisfactory. In the final version the square of the momentum of impurity particles along the field lines has been calculated, taking into account Coulomb collisions with mostly small deflection angles and averaged for the Maxwellian velocity distribution of the background particles:

$$\left\langle \frac{\mathrm{d}p_{tor}^2}{\mathrm{d}t} \right\rangle = \frac{2Z^2}{4\pi\varepsilon_0^2 v} \ln\Lambda \; n^* \mathrm{Erf}(\alpha), \qquad \alpha = v\sqrt{m^*/2T^*} \; .$$

Z is the charge state of an impurity ion and v is its velocity. n^* is the number density of the background particles, T^* is their temperature, m^* is their mass and $\ln\Lambda$ is the Coulomb logarithm.

The result of the simulation is compared with the experimantal data on Fig.4a–4b. The experimental distributions of the line radiation intensity of Al^+ and Al^{2+} were measured with a visible monochromator at 80 mm radial position /2/. The simulated curves correspond to the same radial position. In both cases the data are integrated for the duration of the blow–off pulse.

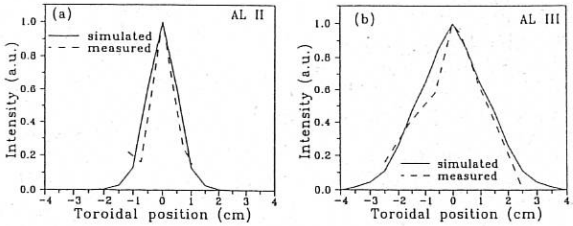

Fig. 4. Toroidal distribution of aluminium ions around the place of injection: a/ for Al^+ and b/ for Al^{2+}. The data are integrated for the duration of the blow–off pulse and taken from the radial position of 80 mm.

Experimental field line tracing. It has been shown above, that the injected Al ions travel in well defined directions. The place where their path intersects a toroidal cross-section could be localized with the VUV–soft-X-ray cameras up to 1m distance from the place of injection. As the parameters of the MT–1M core plasma are in the order of the edge plasma of a big tokamak, it seems possible to inject and follow impurities in the edge plasma of such devices, and thus gain direct information on the magnetic field topology.

References

/1/ P.C. Stangeby, J. Elder, *Plasma Phys. Contr. Fusion* **33**, 1435 (1991)
/2/ G.Kocsis, G.Bürger, P.N.Ignácz, S.Kálvin, B.Kardon, J.Szigeti, G.Veres, accepted for publication in *Plasma Phys. and Contr. Fusion.*
/3/ S.Kálvin, J.S.,Bakos, G.Bürger, B.Kardon, G.Petravich and S.Zoletnik, *Rev. Sci. Instrum* **60** (1989) 2857
/4/ S. Zoletnik, S. Kálvin, submitted to *J. Appl. Phys.*
/5/ P.C.Stangeby, C.Farrel, S.Hoskins, L.Wood *Nucl.Fus.***28** (1988) 1945.

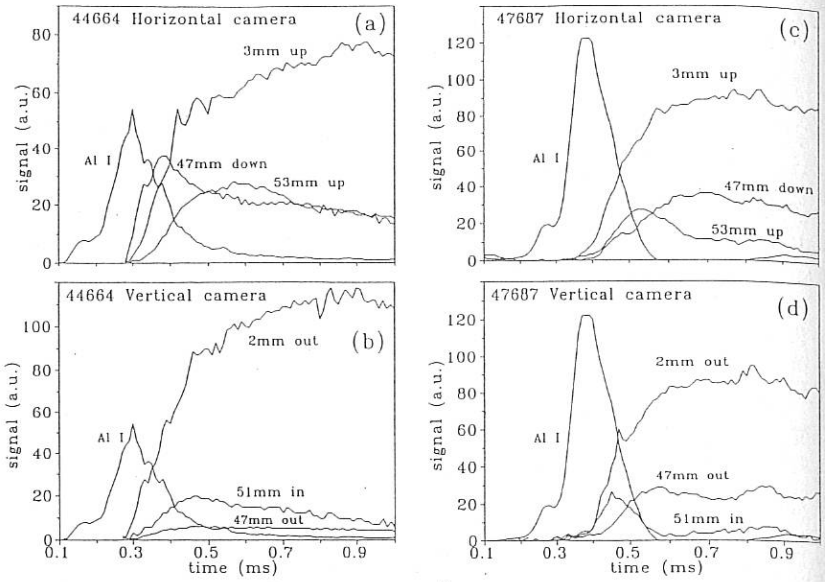

Fig. 2. Time evolution of the 3944 Å neutral aluminium line radiation signal and selected camera signals (energy range 80-300eV). The continuum radiation background has been subtracted from the camera signals. Channel position data refer to the distance of the measuring chord from the center of the cross-section. The camera was located a,b/ 60°, c,d/ 180 ° toroidally from the place of injection. The timescale refers to the time after the blow-off laser pulse.

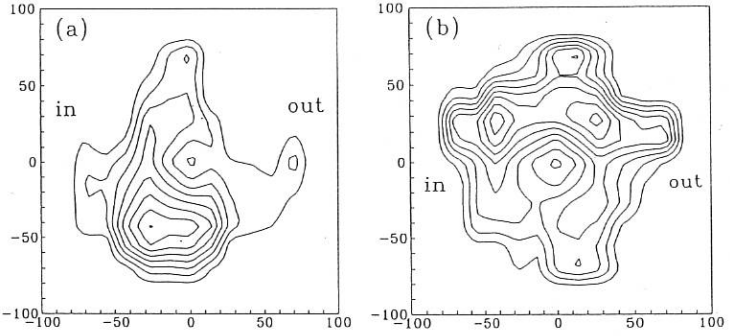

Fig. 3. Tomographic reconstruction of radiation distributions at different toroidal cross-sections.
a/ 60° from injection, shot 44664 at 0.36ms (see Fig. 2/a,b)
b/ 180° from injection, shot 47687 at 0.42ms (see Fig. 2/c,d)

LONG PULSE OPERATION IN JET

M. Brusati, M. Bures, S. Clements, J. Ehrenberg, L. Horton, T.T.C. Jones, K. Lawson[a], P. Lomas, P. Morgan, P. Nielsen, R. Sartori, G. Schmidt[b], M.F. Stamp, D. Summers

JET Joint Undertaking, Abingdon, Oxon, OX14 3EA, UK
[a]Culham Lab., UKAEA/Euratom Association, Abingdon, Oxon, OX14 3DB, UK
[b]PPPL, Princeton University, Princeton (NJ),USA

Introduction

Long pulse operation was performed on JET to investigate the properties of plasmas in full steady state, once complete penetration of the plasma current has been achieved. Emphasis has been put on the plasma wall interaction and the recycling characteristics of the limiter materials when under high energy loading. This information is relevant for the steady or quasi steady state operation foreseen for ITER.

Operation scenario

Limiter Deuterium plasmas with current flat top of duration one minute have been obtained in JET at 2 MA, 1.9 T, with volume average electron densities in the order of $\langle ne \rangle \approx 2\ 10^{19}\ m^{-3}$ and central electron temperatures up to 5 keV. Ion Cyclotron Resonance Heating (ICRH) was used in order to raise the electron temperature and reduce the plasma resistivity, allowing a more efficient exploitation of the primary ohmic flux. ICRH was applied in the H minority heating scheme at 28 MHz during the whole discharge with power up to 5 MW in three successive 20 sec pulses, using 2 antennae in monopole phasing at each step. Further Volt-sec saving was obtained by applying the JET 3.7 GHz Lower Hybrid Current Drive (LHCD) system at 1 MW power level for 50 sec. The combined application of the two RF systems allowed to extend the duration of the basic ohmic discharge by ~ 25 sec, when the plasma termination is caused by the toroidal field system reaching a limiting I^2t value in JET of 10^{11} A^2s. The total energy loading on the toroidal C and Be limiters was in excess of 250 MJ. The impurity content in these discharges corresponded to $Z_{eff} \leq 2$ and was associated with a total radiated power $P_{rad} \leq 1$ MW, of the

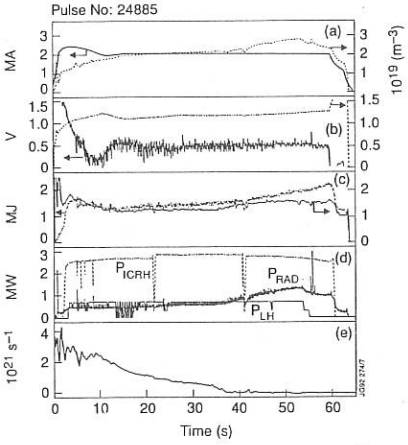

Fig. 1 - Time evolution of the main plasma parameters in a 1 minute long JET pulse. (a) plasm current (—) and volume averaged electron density (—). (b) l_i (—) and loop voltage (—). (c) total stored energy (—) and Z_{eff} (—). (d) RF, LH input and radiated powers. (e) Total gas input.

order of 20 % of the total input power.

Steady state plasma operation

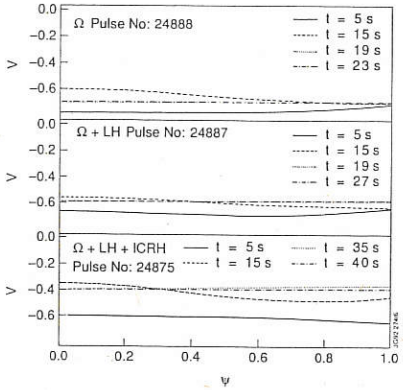

Fig. 2 - Time evolution of the radial profile of the toroidal electric field in the pulse types shown, plotted as a function of the normalized flux coordinate.

In fig. 1 the time evolution of the plasma parameters is shown during a one minute current flat top pulse. The diffusion time of the plasma current was estimated from the time evolution of the plasma internal inductance to the steady state value of $l_i \simeq 1.2$ and through equilibrium analysis which allowed the computation of the radial profile of the toroidal electric field. It was found to agree well with the calculation of the resistive time for the whole plasma cross section, from ~ 18 sec at $T_e \simeq 2$ keV in the ohmic case, to ~ 35 sec at $T_{eo} \simeq 5$ keV when LH and ICRH are applied (fig. 2). A further slower evolution of the plasma current density profile is observed when full recycling conditions are reached later on into the discharge, with a corresponding 10 % increase in l_i.

Recycling and plasma-wall interaction

The plasma density was kept constant throughout the discharge by gas feedback control. The plasma position control was used to maintain continuous contact with top (Be) and bottom (C) toroidal limiters. However the plasma elongation was found to vary between 1.4 and 1.6, thus changing the effective contact area and power loading on limiters and ICRH antennae and LH launcher protection tiles. The gas influx required to maintain the density under feedback control diminished progressively throughout both ohmic and RF sustained discharges, eventually switching off altogether (fig. 1) as the recycling coefficient R_c increased to and above unity. In some cases the plasma density increases by up to 30 % when the $R_c > 1$ condition is attained. This was usually associated with the observation of increased interaction between the plasma and the ICRH antennae

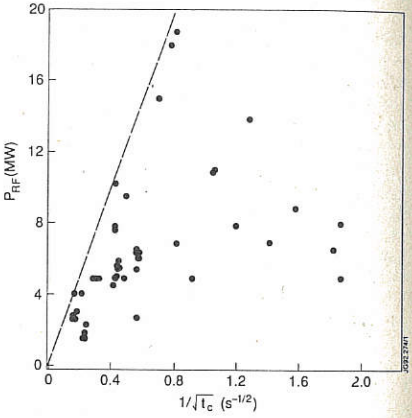

Fig. 3 - Relation between the RF input power and the time t_c when density control is lost. The dashed line indicates the limiting boundary for well conditioned surfaces in JET.

and/or the LH launcher, as seen by the wide angle CCD camera, during changes in the plasma shaping and position. It was accompanied by an increase in low Z impurity concentration, which however accounts for less than 40 % of the build-up in electron density. The time t_c in the discharge when this occurs depends strongly on the state of the walls and, for conditioned surfaces, is a function of the input power P_{in} of the form (P_{in} $t_c^{1/2}$ = const.), indicating that the increased recycling can be associated with structural heating of the limiter material /1/. This is shown in fig. 3 where the left hand edge identifies the limiting boundary $P_{in}\ t_c^{1/2} \simeq 20$ MW $s^{1/2}$ for a well conditioned surface. Calculations have been carried out for JET discharges using a particle balance model /2/ to study the change of the effective particle retention parameter of material surfaces $(D/Kr)^{1/2}$, where D and Kr are respectively the effective diffusion and recombination coefficients for hydrogen in the first wall of JET. Results indicate that a decrease of $(D/Kr)^{1/2}$ by a factor of 3 is required to simulate the measured time evolution of the electron density. This variation can be associated in Beryllium with a temperature rise of less than 200° C /3/. This is consistent with the plasma energy loading at the time $t = t_c$ of ~ 150 MJ on a limiter contact surface A $\simeq$ 6 m^2 and a perpendicular thermal conductivity for Beryllium of $K_c \simeq 120$ W/m-K. In a number of these pulses there was clear evidence of local hot regions on the Be limiter, occasionally leading to the emission of Be droplets during the last few seconds of the current flat top.

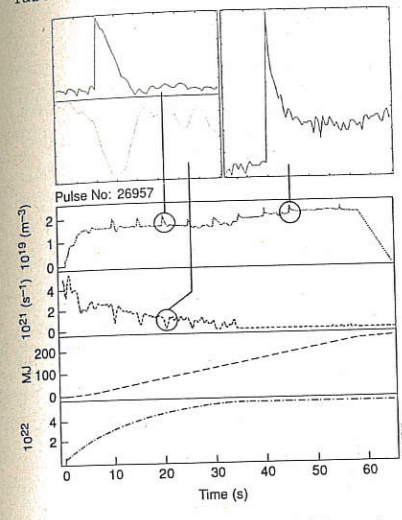

Fig. 4 - Time evolution of (from top) volume average electron density, gas input, total integrated energy and total particle loading for a pellet probing experiment. Density control is lost at ~ 35 s for energy and particle loadings of about 150 MJ and 5 10^{22} respectively. Details are shown of the pellet effect at 20 s (top left) and 45 s (top right). Time scale on the blow-ups is 4 s.

Changes in the pumping capabilities of the limiters have been investigated by probing the plasma periodically with 2.7 mm pellets injected at 0.2 Hz during the current flat-top. At these plasma densities the LH absorption takes place in the outer half of the plasma minor radius. The pellet ablation rate is locally increased by the presence of a fast electron population created by Electron Landau Damping of the LH wave. Before the $R_c = 1$ condition is reached the density decay time τ_d results from the convolution between the pump-out mechanism and the reaction of the density feedback (fig. 4). In the linear density decay regime $\tau_d \simeq \langle n_e \rangle /$ [S exp-(t/τ_f) + k], where S is the change in gas density influx, t the measured delay in S, τ_f the response time of the gas feedback system and k the measured density decay rate. The pump-out time τ_d is of the order of 1 s, corresponding to a particle diffusion coefficient $D_p \simeq 0.3$ m^2/s, and lengthens systematically during the period when $R_c < 1$. The density evolution following a pellet injection, at times $t > t_c$, is characterized by a fast decrease, associated with low τ_d in absence of

gas influx, leading to a stationary state at an increased density level when compared with its value preceeding the pellet fuelling. The density build up corresponds to ~ 30 % of the total particles supplied by the pellet injection. This behaviour can be explained in terms of the plasma reaching a new dynamic equilibrium in conditions of strongly reduced wall pumping.

Conclusions

One minute long pulses have been obtained on JET where the combined application of the ICRH and LHCD systems has allowed to extend the duration of the current flat top by ~ 25 s. These discharges enter into steady state on a resistive time scale, up to ~ 35 s for central electron temperatures $T_{eo} \simeq 5$ keV. Progressive decrease of the gas influx required for maintaining density control occurs throughout the discharge as the limiter recycling coefficient R_c approaches 1. The density rise observed when $R_c \geq 1$ cannot be fully accounted for by the increase in impurity influx alone. The time t_c required to reach the $R_c = 1$ condition is a function of the input power P_{in} of the type $P_{in}\, t_c^{1/2} \simeq 20$ MW $s^{1/2}$ for well conditioned surfaces in JET, indicating that this is due to progressive heating of the limiter surface, which leads to a build-up of fuel and impurity influxes into the plasma.

Pellet probing experiments indicate a plasma pump out time during density control of the order of 1 s and a particle diffusion coefficient $D_p \simeq 0.3$ m^2/s. In full recycling conditions the particle load from the pellet is maintained in the plasma as a new equilibrium is established between plasma and limiting wall materials.

The attainment of a new particle balance equilibrium in full recycling conditions leads to a further peaking of the plasma current density profile with a 10 % variation in the plasma internal inductance.

Acknowledgements

The support of the whole of the JET team is gratefully acknowledged. The pellet experiment has been performed under a collaboration agreement between the JET Joint Undertaking and the US Department of Energy.

References

/1/ M. Pick, K. Sonnenberg, Journal of Nuc. Materials, **131** (1985) 208.
/2/ J. Ehrenberg et al., Proc. 10th Int. Conf. on Plasma - Surface Interactions in Contr. Fus. Devices, Monterrey (USA), 30/3 - 3/4 1992.
/3/ G. Saibene et al., Journal of Nuc. Materials, **176-177** (1990) 618.

EVOLUTION OF THE CURRENT PROFILE IN JET HIGH BOOTSTRAP CURRENT PLASMAS

J O'Rourke, C D Challis, J Jacquinot, D O'Brien, M F Stamp, D Stork, P Stubberfield, F Tibone, B J Tubbing, W Zwingmann

JET Joint Undertaking, Abingdon, Oxon., UK

OVERVIEW: In this paper we report on the production of plasmas in which a large fraction of the plasma current (up to 70% +- 15%) is driven by the Bootstrap effect. These Bootstrap fractions are a factor of 2-3 higher than previous results /1/ and they induce substantial changes in the current distribution. Thus they constitute the clearest evidence to date of the existence of the Bootstrap current on JET and they provide an indication of the steady-state current profiles which can be expected in Bootstrap-dominated plasmas.

Since for constant profiles the Bootstrap fraction scales as β_p, the experiments study low current H-mode plasmas. The JET Ion Cyclotron Resonance Heating (ICRH) system was used because it can operate at low I_p, in contrast to the Neutral Beam Injection (NBI) system which was limited to operation at $I_p \geq 2.0$ MA for injection times greater than 1.5 sec. Another difference with NBI is that the ICRH system does not involve any central fueling of the plasma. This corresponds to the situation expected in a tokamak reactor.

Figure 1 shows the evolution of pulse 25264, a 1 MA, 2.8 T, double-null X-point discharge with 7 MW of D(H) dipole ICRF power. The thermal confinement time exceeds by 70% the prediction of a scaling law derived for elm-free H-modes at lower q_{95} /2/. This allows β_p values close to 2 to be achieved.

The current profile is determined using the EFITJ code /3/, which incorporates magnetic polarimetric (Faraday rotation) and kinetic data self-consistently into the equilibrium identification algorithm. Figure 2 shows the evolution of the loop voltage, the internal inductance and the Faraday rotation angles along 3 (central) lines of sight as determined experimentally and as calculated in TRANSP under the assumption of resistive diffusion with and without the Bootstrap current. The assumption of the Bootstrap current is necessary to obtain a fit to the data. In particular, the presence of the Bootstrap current leads to a 3 sec. period during which the loop voltage is reversed or close to 0 and to a 30% reduction in l_i, in good agreement with the experimental observations. It should be noted that these experiments are among the first in which the current profile changes introduced by the Bootstrap current are sufficiently marked to be corroborated by Faraday rotation measurements. Figure 3 shows the evolution of the calculated Bootstrap current. This reaches 700 KA at the latter part of the H-

mode. The calculation is sensitive to the edge electron density gradient, which is poorly known. The error bars correspond to the range of Bootstrap currents which yield an acceptable fit to the experimental data.

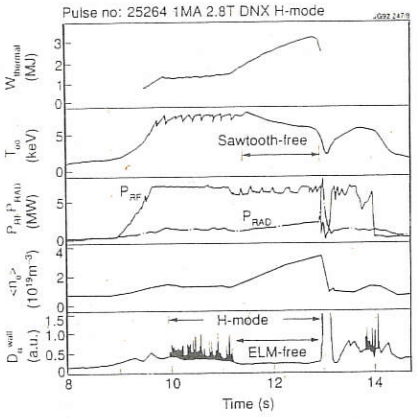

Fig. 1 Evolution of plasma parameters in pulse 25264

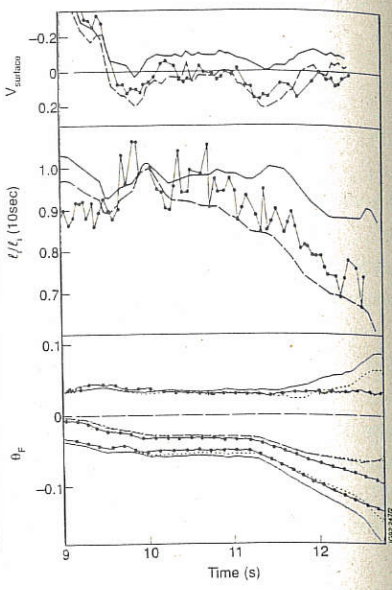

Fig. 2 Evolution of the loop voltage, self inductance and Faraday rotation angles. Data (circles), TRANSP calculation assuming a neo-classical Bootstrap current, (dashed lines), TRANSP calculation without Bootstrap current. (solid lines).

CURRENT PROFILE EVOLUTION: The discharge discussed in the preceding section has distinct ELMy H-mode and ELM-free H-mode phases. In the presence of ELMs, the electron density profile is relatively peaked. The Bootstrap current is about 30% of I_{plasma} and is distributed across the plasma radius. The supression of ELMs leads to a 4-fold increase in the edge density gradient and a larger Bootstrap current which is, however, localised near the plasma periphery. Figure 4 shows the evolution of the total current density at $\overline{\Psi} = 0.8$ during

the H-mode. Although the absolute value of the experimentally determined current differs from that obtained in the field-diffusion calculation, its time variation shows a similar trend.

The duration of the H-modes in these discharges is not sufficient to reach a steady-state. The diffusion calculations indicate that the axial current density decreases by less than 25% during the H-mode phase due to the high electron temperature of the discharge and the large radial distance over which the ohmic current perturbation must diffuse (since the bootstrap current is predominantly driven near the edge). The sawtooth activity, which is only suppressed at 11.2 sec. also suggests a slow evolution of the central current. However, the results imply that in the absence of ELMs the current distribution evolves toward a very hollow profile in response to a flat density profile. The concomitant reduction in magnetic shear and, ultimately, the creation of non-monotonic q-profiles is likely to lead to MHD instabilities. This highlights the importance of achieving control of the density profile in steady-state Bootstrap-dominated plasmas. In the absence of some other forms of density profile control, a sustainable current distribution may only be achievable with ELMs and a Bootstrap current fraction, $I_{Bootstrap}/I_p$, well below unity. (The MHD stability of the present experiments is addressed in another contribution at this conference /4/.)

RELATION TO HEAT AND PARTICLE FLUXES:

The foregoing results suggest that the Ohm's law relating the plasma current and the electric field is well described by the neo-classical expression:

$$J_\phi = j_{bootstrap} + \sigma_{neo} E_\phi \qquad [1]$$

Here we examine the validity of another neo-classical expression of Ohm's law /5/:

$$j_\phi = \sigma_{spitzer}[E_\phi + (\Gamma_r T_e + 0.32 Q_r^{cond})\frac{B_\theta}{n_e T_e}] \qquad [2]$$

In contrast with previous JET work on Bootstrap currents /1/ which used Neutral Beam Injection, these discharges have a power deposition profile which is strongly peaked on axis and are fueled only from the plasma edge. This reduces the uncertainty in the calculation of the electron heat and particle fluxes. Uncertainties arising from Neutral Beam fast ion currents are also avoided. There is a disagreement of some 2 orders of magnitude in the two calculations of the plasma current, demonstrating that the measured fluxes can not be used in equation 2. It may appear paradoxical that the Bootstrap effect is well described by one neo-classical expression (eq. 1) but not by another (eq. 2). A possible explanation for this observation is that the net radial fluxes are a superposition of the neo-classical fluxes (which

obey the above relation) and anomalous fluxes. The mechanism giving rise to the anomalous flux must then be such as not to perturb the parallel dynamics which give rise to the Bootstrap effect.

CONCLUSIONS: A large fraction (approaching unity) of the total plasma current in a Tokamak can be driven by the Bootstrap effect, even in the absence of central fueling. Large Bootstrap current fractions are compatible with H-mode confinement. but control of the density profile will be required in order to ensure that the resulting current distribution can be sustained.

REFERENCES:

/1/ C Challis, C D, et al., Nuclear Fusion 29 (1989) 563
/2/ Schissel, D P, et al., Nuclear Fusion 31(1991)73
/3/ O'Brien, D P, et al., JET-P(91)50
/4/ Hender, T, et al., "High β_p MHD activity in JET", this conference
/5/ Ware, A A , Nuclear fusion 13(1973)793

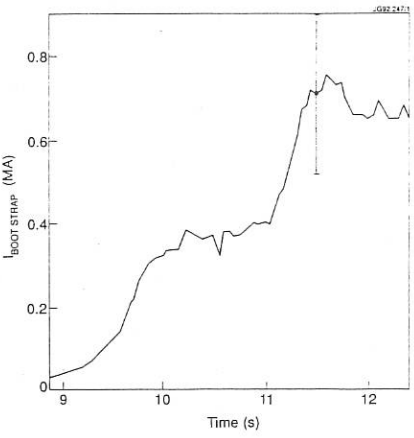

Fig. 3 Evolution of the calculated Bootstrap current.

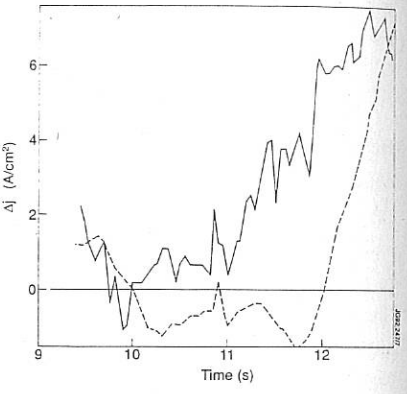

Fig. 4 j(t) - j(10 sec.) at $\overline{\Psi}$ = 0.8. Solid line--EFIT equilibrium reconstruction, dashed line--TRANSP calculation.

BOOTSTRAP CURRENT DRIVEN BY ALPHA PARTICLES IN A FUSION REACTING TOKAMAK*

C. S. Chang
Courant Institute of Mathematical Sciences
New York University
New York, NY 10012, U.S.A.

In a fusion reacting tokamak, bootstrap current driven by plasma density and temperature gradients may supply a major portion of the toroidal equilibrium current. It is important to understand and predict a correct profile shape of the bootstrap current. Local alpha pressure may be small compared to the bulk plasma pressure. However, the alpha pressure is likely to have much steeper radial gradient than the bulk pressure does, and, thus, the alpha-driven bootstrap current is usually enhanced.

Pitch angle scattering yields bootstrap current of order $\epsilon^{1/2}$, where ϵ is the horizontal inverse aspect ratio, while the energy scattering alone can yield bootstrap current of order $\epsilon^{3/2}$ only. Previous calculations of alpha-driven bootstrap current [1] neglected the pitch angle scattering effect and, as a natural consequence, predicted a small amount of bootstrap current of order $\epsilon^{3/2}$. In reality, the pitch angle scattering rate of the slowing-down alpha particles is not negligibly small compared to the slowing-down scattering rate, as demonatrated in Ref. [2] in their evaluation of radial alpha transport rates. For the energetic alpha particles in the burning core of a D-T reacting plasma, the pitch-angle scattering rate is only of order inverse aspect ratio smaller than the slowing-down scattering rate. Considering the fact that the effective pitch angle scattering rate of the trapped particles is enhanced by about the toroidal aspect ratio, it can be easily seen that the pitch angle scattering effect can be as important as the slowing-down scattering effect for the alpha particles in the burning core. Hence, a larger alpha-driven bootstrap current of order $\epsilon^{1/2}$ is expected when a more complete Coulomb collision operator is used. In the present work, we report a variational calculation of the alpha bootstrap current in a general flux surface geometry, which is valid to the lowest order in $\epsilon^{1/2}$.

It can be easily shown from an electron kinetic equation that a parallel flow $U_{\alpha\|}$ of alpha particles in a tokamak results in a parallel current of the amount

$$J_\alpha = Z_\alpha e N_\alpha U_{\alpha\|} \left(1 - \frac{Z_\alpha}{Z_{eff}} F_p\right) + 2eU_{\alpha\|} \int d^3v f_{eo} \frac{v_\|^2}{v_e^2} \frac{N_\alpha Z_\alpha^2}{N_e Z_{eff}} , \qquad (1)$$

where $Z_\alpha = 2$ is the alpha charge number, Z_{eff} is the effective charge number of the plasma ions, N_α is the α-particle density, F_p is the passing fraction of the electrons, v_e is the electron thermal speed, and f_{eo} is the lowest order electron distribution function.

In order to calculate $U_{\alpha\|}$ driven by the free energy in the radial α particle gradients, we use a linearized drift-kinetic equaiton:

$$\vec{v}_\| \cdot \nabla f_\alpha - C_\alpha^\ell(f_{\alpha 1}) = -I\vec{v}_\| \cdot \nabla \left(\frac{v_\|}{\Omega_\alpha}\right) \frac{\partial f_{\alpha o}}{\partial \psi} , \qquad (2)$$

where C_α^ℓ is the linearized alpha collision operator, $I = RB_T$, R is the distance from the toroidal major radius, B_T is the toroidal component of the magnetic field, Ω_α is the alpha gyrofrequency, $f_{\alpha o}$ is the lowest order distribution function of the alpha particles, ψ is the poloidal flux, and $f_{\alpha 1}$ is the first order deviation of the alpha distribution function when expanded in the assumed small parameter "banana width/plasma minor radius." We note here that the small banana width ordering may be questionable near the magnetic axis where the radial drift motion becomes relatively large. This question is being examined and will be reported elsewhere.

Expansion in small collision frequency, then, yields the following usual solution:

$$f_{\alpha 1} = -I\frac{v_\parallel}{\Omega_\alpha}\frac{\partial f_{\alpha o}}{\partial \psi} + G\,, \tag{3}$$

where G is constant along $\vec{B}$ and vanishes in the trapped region; and, in the passing region, it is determined from the solubility condition

$$\{C_\alpha^\ell(-I\frac{v_\parallel}{\Omega_\alpha}\frac{\partial f_{\alpha o}}{\partial \psi} + G)\} = 0\,, \tag{4}$$

where $\{\ \}$ represents bounce average operation.

Solution to Eq. (4) is easily obtained when the alpha collision operator contains pitch angle scattering only, or slowing-down scattering only. Keeping both scatterings in Eq. (4) makes the equation quite complicated. A variational solution of the alpha particle distribution function is obtained and it is used to calculate the alpha driven bootstrap current. By defining a variational functional

$$\mathcal{H} = 2D[y] - S[y,y]\,,$$

where

$$S[y_1,y_2] = -<\int d^3v(y_1/f_o)C(y_2)>\,,$$

$$D[y] = <\int d^3(y/f_o)C(\tilde{g})>\,,$$

and

$$\tilde{g} = -I\frac{v_\parallel}{\Omega_\alpha}\frac{\partial f_o}{\partial \psi}\,,$$

we can easily show that $\mathcal{H}$ is extremal at $y = G$ satisfying Eq. (4).

In order to get a physically valid solution, it is important to choose a trial function which has correct physical behaviors, which are

1) f_1 should be continuous across the trapped-passing boundary $\lambda = \lambda_c$; hence, $y = 0$ at the boundary,

2) the boundary layer, in which the pitch-angle scattering effect is dominant, has a velocity dependent width $\Delta\lambda \sim (v_b^3/v^3)^{1/2}$, where v_b is the alpha speed at which the pitch angle scattering rate is the same as the slowing-down rate,

3) within this pitch angle boundary layer, y should be close to the pitch-angle-only solution G_λ,

4) far away from the pitch angle layer, y should approach the solwing-down-only solution G_v.

Here, λ is the ratio of magnetic moment to the kinetic energy. Based upon the above behaviors, we can construct the following variational trial function

$$y = \frac{(\lambda_c - \lambda)^2 G_v + (\Delta\lambda)^2 (v/v_o - x)^2 G_\lambda}{(\Delta\lambda)^2 (v/v_o - x)^2 + (\lambda_c - \lambda)^2},$$

where the factor $(v/v_o - x)^2$ is included to adjust the pitch angle layer width by a variational parameter x.

Using the above trial function y, Cordey's form for the collision operator [3] C^ℓ_α, and slowing-down α-distribution function, the equation $\delta\mathcal{H}(x = x_*) = 0$ has been solved and the variational parameter x_* has been determined to be

$$x_* = \frac{0.3 s_b^6 + 2.8 s_b^3 + 0.3}{1 + 5.5 s_b^3 + 0.45 s_b^6},$$

where $s_b = v_b/v_o$ and v_o is the alpha particle birth speed. The variational solution for $G = y(x_*)$ is, then, substituted into the alpha particle distribution function f_1 in Eq. (3), and the alpha driven current is, then, calculated from Eq. (1). It is found that the pitch-angle scattering effect indeed raises the alpha-driven bootstrap current to order $\epsilon^{1/2}$. A simple analytic formula for alpha driven bootstrap current $j^\alpha_{bootstrap}$ has been obtained in an arbitrary flux-surface geometry, which is, to the leading order in $\epsilon^{1/2}$

$$j^\alpha_{bootstrap} \simeq -0.58\, \epsilon^{1/2} \left(1 - \frac{2}{Z_{eff}}\right) \sqrt{Z_{eff} \left[\frac{T_e(keV)}{20}\right]^{3/2} + 0.4}\ \frac{I\, cT_\alpha}{eB_o} \frac{\partial S_\alpha \tau_s}{\partial \psi},$$

where $T_\alpha = \int d^3v (m_\alpha v^2/2) f_\alpha$ is an average kinetic energy of the energetic alpha particles, S_α is the alpha birth rate from D-T reaction, τ_s is the alpha-electron slowing-down time, and

$$\frac{1}{f_{\alpha o}} \frac{\partial f_{\alpha o}}{\partial \psi} \simeq \frac{1}{S\tau_s} \frac{\partial S\tau_s}{\partial \psi}$$

has been used. The effect of energy scattering appears in the next order term ($\propto \epsilon$).

The relative magnitude of the local alpha-driven bootstrap current is estimated to be only up to 20 to 30 percent of the local bulk bootstrap current. However, the direction of the alpha-driven bootstrap current follows the sign of $(Z_{eff} - 2)$, yielding a negative current for $Z_{eff} < 2$. This directional change of the alpha-driven bootstrap current may cause a subtle effect on the toroidal equilibrium current profile and stability issues. Volume integrated current driven by alpha bootstrap effect is likely to take less fraction of the total toroidal current because the alpha-driven current may be highly localized in the burning core region.

The banana width near the magnetic axis tends to be larger, and the present theory needs to be modified accordingly. This problem was examined in Ref. [4], but, again, with energy scattering operator alone. Correct inclusion of pitch angle scattering operator may again yield larger alpha bootstrap current near the magnetic axis, which is proportional to $(Z_{eff} - 2)$. This work is in progress and will be reported in the future.

REFERENCES

[1] NOCENTINI,A., TESSAROTTO,M., ENGELMANN,F., Nucl. Fusion **23** (1983) 405.

[2] HSU, C.T., CATTO, P.J., SIGMAR, D.J., Phys. Fluids B **2** (1990) 280.

[3] CORDEY, J.G., Nucl. Fusion **16** (1974) 185.

[4] GOLOBOROD'KO, V.Ya., KOLESNICHENKO, Ya.I., YAVORSKIJ, V.A., Nucl. Fusion **23** (1983) 399.

---

*Work supported by U.S. DOE, Grant Number DE-FG02-86ER53223.

FAST WAVE SPECTRAL PROPERTIES IN ITER TOKAMAK

Elfimov A.G.*, Medvedev S.Yu., Pestryakova G.A.

Keldysh Institute of Applied Mathematics,
Academy of Sciences, Moscow, Russia
*I.N.Vekua Institute of Physics and Technology,
Sukhumi, Georgia

Fast wave excitation in ITER tokamak is proposed to use for ICRF heating and current drive [1]. The spectrum and field structure of fast magnetosonic (FMS) waves in cylindrical current–carrying inhomogeneous plasma have been studied in detail [2], but 2D simulations of fast wave excitation in hot toroidal plasmas (see, for example [3]) show very complicated picture, which is hardly understood. Therefore it is important to examine FMS wave properties in toroidal plasma to interpret them.

The FMS excitation in ITER plasma has been analyzed numerically using 1D [4] and 2D full wave codes, developed on the basis of MHD plasma model with effective collisional damping. In order to find FMS spectrum, which overlaps the Alfven continuum in large tokamaks, it is convenient to investigate the dependence of plasma total active impedance on driving frequency. The special choice of effective damping in numerical calculations enable one to describe correctly local Alfven resonance absorption and to distinguish fast wave eigenfrequencies by maxima on impedance curve.

The spectrum of FMS eigenmodes in 1D approach is shown in Fig.1. Dispersion curves correspond to fast wave excitation by different helical antennae with fixed toroidal (N=–10÷10) and poloidal (M=–4÷4) wave numbers. Two different types of curves are well seen. Ones describe the surface waves with dispersion relation $\omega_S \cong \sqrt{2} v_A k_\parallel$ at sufficiently low frequencies while others – the FMS waves with dispersion relation $\omega_F \cong v_A \sqrt{k_r^2 + k_\parallel^2}$ (v_A – Alfven velocity, $k_r, k_\parallel$ – radial and parallel wave numbers respectively). Dispersion curves of surface and fast waves intersect and fast eigenmodes with different poloidal numbers

are driven at close frequencies. Plasma toroidicity and cross–section elongation and triangularity lead to strong coupling of these modes.

The results of 2D calculations of ITER plasma (aspect ratio A=2.8, elongation κ=2 and triangularity δ=0.4) loading resistance with respect to driving frequency are presented in Fig.2. Each group of maxima on the curve corresponds to the cluster of 1D fast wave eigenfrequencies. Thus the structure of FMS spectrum of toroidal plasma with non–circular cross–section is well interpreted with the help of 1D results. At the same time RF field mode structure significantly depends on plasma geometry and toroidal wave number and contains wide spectrum of different poloidal modes (Fig.3,4). The excitation of fast wave with complicated mode structure in ITER plasma must lead to broadening of absorbed power profile as compared to 1D case.

1. ITER Physics, ITER Documentation series, N 21, IAEA, Vienna, 1991
2. M.J.Ballico, R.S.Cross, Phys.Fluids B, v.2, p.467, 1990
3. A.Becoulet et al., Intern. Workshop "Collective Acceleration in Collisionless Plasma", IES, Cargese, Corsica, France, 1991
4. A.G.Elfimov et al., Proc. Contrib. Papers 16th Europ. Conf. Controlled Fusion and Plasma Phys., Venice, v.1, p.423, 1989

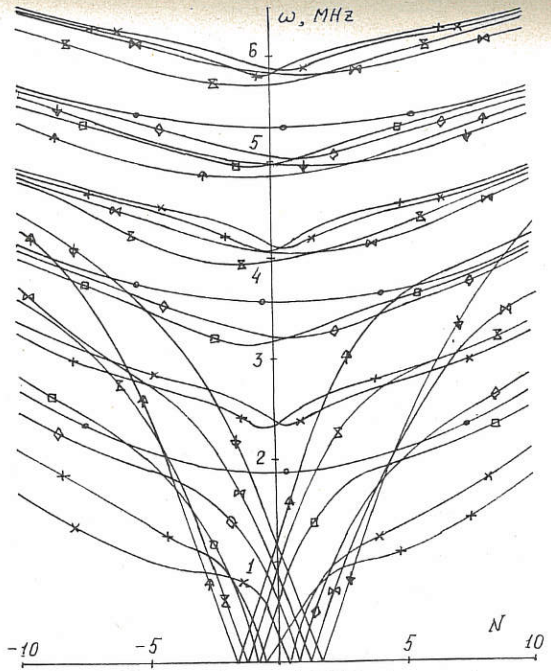

Fig.1 The spectrum of FMS eigenmodes. 1D calculations. ⏚ – M=–4, ⋈ – M=–3, ◇ – M=–2, × – M=–1, ∘ – M= 0, + – M= 1, □ – M= 2, ⧖ – M= 3, ⏃ – M= 4.

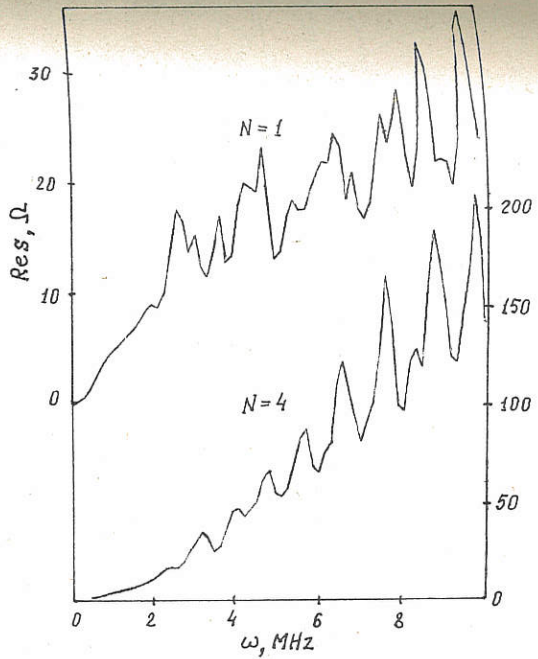

Fig.2 ITER plasma total resistance vs the driving frequency. 2D calculations. Helicoidal antenna with N=+1,+4; M=1.

1-97

I-321

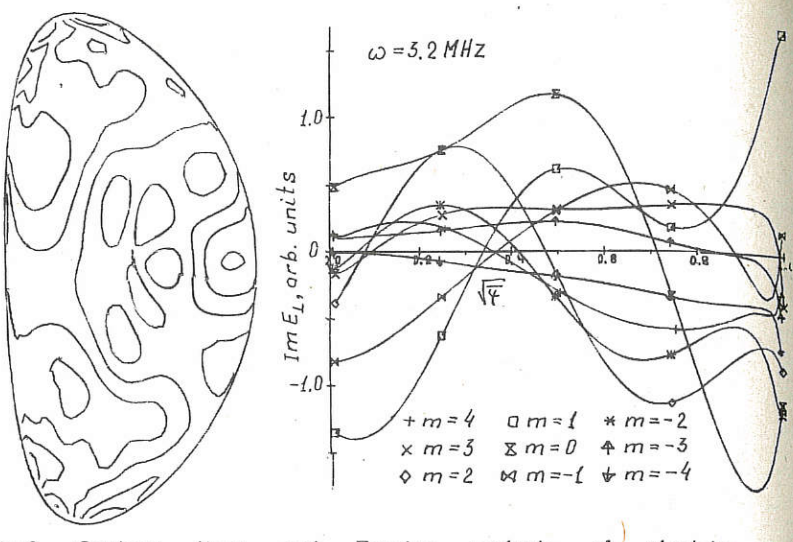

Fig.3 Contour lines and Fourier analysis of electric field component $Im\,E_\perp$ for FMS eigenmode at N=+1, dominant harmonic M=2.

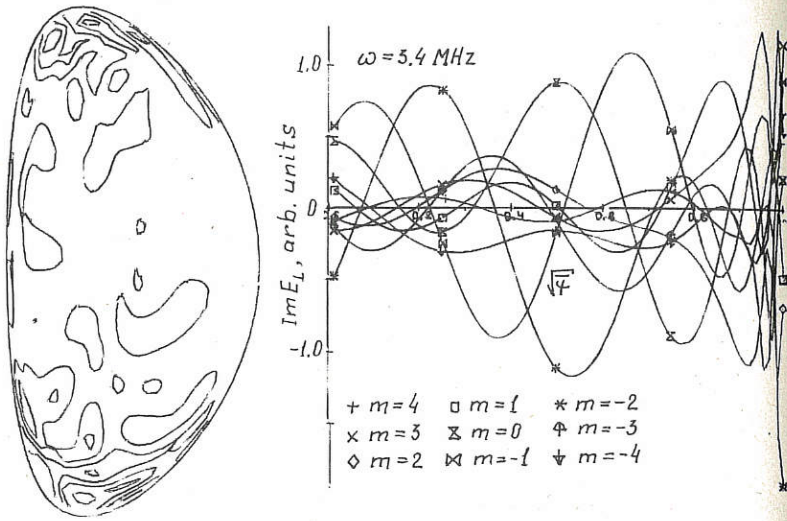

Fig.4 Contour lines and Fourier analysis of electric field component $Im\,E_\perp$ for FMS eigenmode at N=+4, dominant harmonic M=-2.

Expansion of the Ablated Pellet Substance Along the Magnetic Field Lines

P. N. SPATHIS and L. L. LENGYEL
Max-Planck-Institut für Plasmaphysik
Boltzmannstr. 2, D-8046 Garching bei München, F.R.G.

1 Physical and Computational Model

We have constructed a one-dimensional, single-fluid, three-species, single-temperature Lagrangian code to study the quasi-steady, field-aligned expansion of pellet clouds in tokamaks. The gas dynamics of the process, energy deposition, and cloud heating by collisional processes and finite ionization rate dynamics have been incorporated.

The basic model used in these calculations is described in /1/. A source of cold particles of strength $\dot{N}_s$ is specified at $z = 0$. Heating of the pellet cloud by the background plasma is assumed to take place by energy loss to the cloud from an incident beam of fast electrons through collisional processes. As a first approximation, the beam is assumed Maxwellian, with a distribution corresponding to the background plasma temperature, and is subdivided into a small number (typically five) of monoenergetic beamlets, each carrying a heat flux equal to the appropriate fraction of the background plasma heat flux. The energy loss of each beamlet is then computed according to

$$q_e^{(i)}(z) = \Gamma_e^{(i)}(z)\mathcal{E}_e^{(i)}(z),$$

where $\Gamma_e^{(i)}(z)$, $\mathcal{E}_e^{(i)}(z)$ are the number flux and energy of the ith beamlet and satisfy

$$\frac{\partial \Gamma_e^{(i)}}{\partial z} = \frac{1}{\lambda^M}\Gamma_e^{(i)}, \qquad \frac{\partial \mathcal{E}_e^{(i)}}{\partial z} = -eE + \frac{1}{\lambda^E}\mathcal{E}_e^{(i)}.$$

In the above, $\lambda^{M,E}$ are the effective mean free paths for elastic and inelastic collisions respectively /2,3,4/, E is the value of the local electric field and z is the coordinate along the cloud, e being the electron charge. The conductive heat flux within the cloud, on the other hand, is considered local and equal to the sum of the fluxes due to the ionized and neutral components of the cloud. Additionally, it is limited by 20% of the local free streaming flux.

Collisional ionization and three-body recombination are assumed to be the dominant ionization processes.

An attempt has been made to model the electric field set up in the cloud by the incident electron beam and thus a possible electrostatic pellet shielding. In the present approximation the current in the cloud is computed as a sum of two terms, one due to the incident electron beam and one due to the cloud. The latter is in turn expressed using Ohm's law, as given by the corresponding Braginskii equation, and the condition of no

$\dot{N}_s\,(\mathrm{s}^{-1})$	$T_e^\infty\,(\mathrm{keV})$	$z_{\mathrm{ion}}\,(\mathrm{cm})$	$z_{\mathrm{cld}}\,(\mathrm{m})$	$n_h^0\,(\mathrm{m}^{-3})$	$n_h^{\mathrm{ion}}\,(\mathrm{m}^{-3})$	$\int n_h\,dz\ (\mathrm{m}^{-2})$
$6\cdot10^{23}$	1	3.3	1.26	$2.6\cdot10^{24}$	$2.9\cdot10^{23}$	$5.3\cdot10^{22}$
$1\cdot10^{25}$	5	7.0	1.23	$2.6\cdot10^{25}$	$2.6\cdot10^{24}$	$8.8\cdot10^{23}$
$3\cdot10^{25}$	10	9.0	1.35	$7.9\cdot10^{25}$	$6.4\cdot10^{24}$	$2.7\cdot10^{24}$

Table 1: Cloud parameters for three representative scenarios

net current is invoked to give an equation for the field E:

$$j = e\sum_i \Gamma_e^{(i)} + \sigma E + \frac{\sigma k T_e}{e}\left(1.71\frac{\partial}{\partial z}\log T_e + \frac{\partial}{\partial z}\log n_e\right) = 0. \qquad (1)$$

2 Numerical Results

In all of the calculations presented below the background plasma density was taken equal to $n_e^\infty = 10^{20}\,\mathrm{m}^{-3}$. Flow was assumed to take place along a flux tube of 6 mm radius. Initially the code was run for three different values of the background plasma temperature, $T_e^\infty = 1$, 5 and 10 keV, while the mass source strength was chosen such as to give complete depletion of the incident beam at the source location ($z = 0$) at the end of $t = 10\,\mu\mathrm{s}$, typical of the pellet residence time in a flux tube. The results of the calculations are summarized in the accompanying table, where values are given for the ionization length, z_{ion}, total cloud length, z_{cld}, heavy particle number density at $z = 1$ mm from the source, n_h^0, heavy particle number density at the ionization length, n_h^{ion}, and integrated line density, $\int n_h\,dz$. In Fig 1 we give distribution profiles of the various cloud parameters for the case $\dot{N}_s = 6\cdot10^{23}\,\mathrm{s}^{-1}$, $T_e^\infty = 1$ keV. The quantities shown are flow velocity, v, temperature, T, electron and heavy particle number density, n_h, n_e, electric field, E and the number flux and average energy of the incident beams, Γ_e and $\mathcal{E}_e$, respectively. For the electric field, the two curves shown correspond to contributions originating from the first and third summands in Eq (1), E_{b} and E_{cld} respectively. The field points in the direction of decreasing cloud coordinate z. It should be noted that the steep rises observed in the temperature profile, located at the points where the energetic beamlets are successively stopped by the cloud, are an artifact of the discrete number of beamlets used in this approximation. A more accurate calculation would presumably give a smoother temperature profile. The same remark obviously holds for the small peaks in E_{cld}, which is proportional to the temperature gradient. In Figs 2 (a)-(c), on the other hand, we give heavy particle and electron density and temperature profiles for three cases involving the same source strength ($10^{25}\,\mathrm{s}^{-1}$) but different background plasma temperatures: $T_e^\infty = 2$ (a), 5 (b) and 10 (c) keV at times $t = 0.4$, 10 and 70 μs, respectively, these being the times when the incident energy flux is completely depleted at exactly the source plane. The oscillations in n_e seen in the vicinity of the source are caused by the discretization scheme used (splitting of the last cell every time its mass exceeds a threshold value) and the iterative scheme used to take electric field effects into account. Nevertheless, the oscillation amplitudes are small, their magnitude being exaggerated by the logarithmic scale used; they are absent in the region where significant ionization is

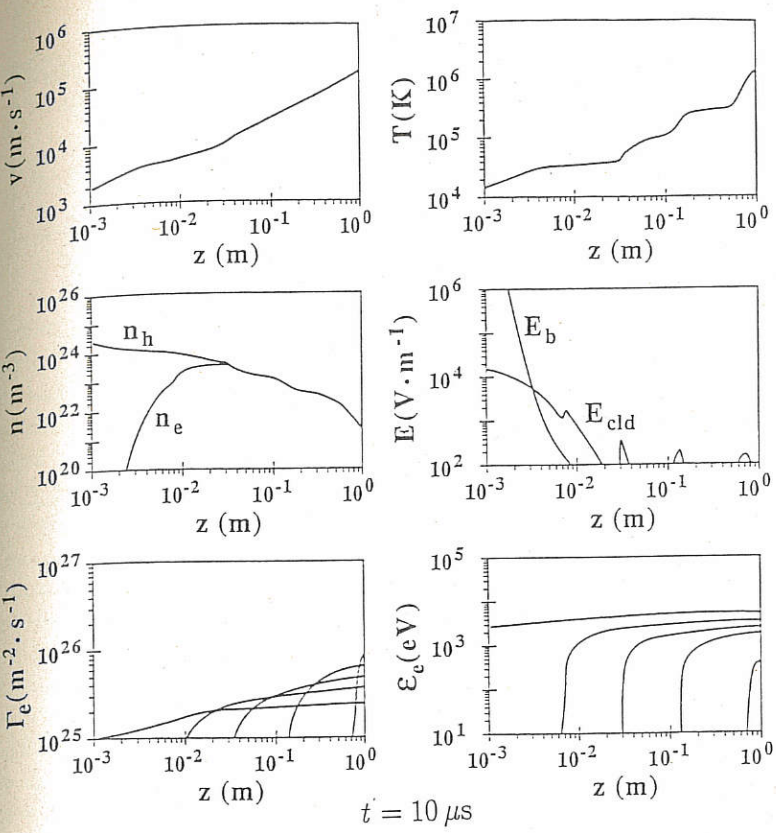

Figure 1: Cloud parameter distributions for the first scenario enlisted in Table 1.

taking place, occuring at a location where the ionization degree is rather small. On the basis of Table 1 and Figs 1 and 2, we note that the ionization length associated with the time instant when total energy depletion occurs at exactly the particle source location seems to be more strongly affected by the ablation rate, or equivalently the line density, than by the background temperature, moving outwards as $\dot{N}_s$ and $\int n_h dz$ are increased. The heavy particle and electron density close to the source and the ionization length are all increasing functions of $\dot{N}_s$. Finally, it should be kept in mind that Figs 2 (a)–(c) correspond to widely different physical times (thus different line integral values), explaining the seemingly odd fact that the ionization length increases with T_e^∞ in moving from the top to the bottom of Fig 2.

In closing, we note that our results agree qualitatively with measured data /5,6/. No detailed comparison is possible, as the local ablation rates are not given in /5,6/.

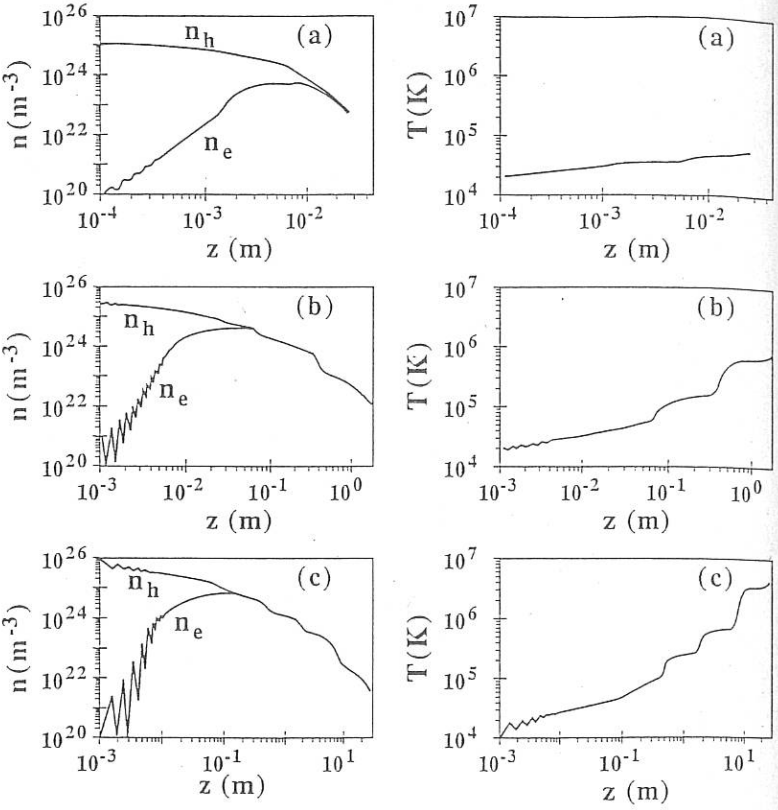

Figure 2: Density and temperature distributions along the cloud length for three background plasma temperatures: (a) $T_e^\infty = 2\,\mathrm{keV}$, (b) $T_e^\infty = 5\,\mathrm{keV}$, (c) $T_e^\infty = 10\,\mathrm{keV}$; $\dot{N}_s = 10^{25}\,\mathrm{s}^{-1}$ in all three cases.

3 References

/1/ P. N. Spathis, IPP Report # 5/38, Jan 1992.

/2/ P.B. Parks, Nucl. Fusion **20**, 311 (1980).

/3/ P.B. Parks and R.J. Turnbull, Phys. Fluids **21**, 1735 (1978).

/4/ L.L. Lengyel, IPP Report # 1/233, Sep 1984.

/5/ R. D. Durst *et al*, Nucl. Fusion **30**, 3 (1990).

/6/ TFR Group, *Europhys. Lett.*, **2** (4), pp. 267–273 (1986).

IDENTIFICATION OF ION CYCLOTRON EMISSION FROM FUSION ALPHA PARTICLES DURING JET DEUTERIUM-TRITIUM EXPERIMENTS

G.A.Cottrell, V.P.Bhatnagar, O. da Costa, R.O.Dendy*, A.Edwards, J.Jacquinot, M.F.F.Nave, M.Schmid, A.Sibley, P.Smeulders & D.F.H.Start
JET Joint Undertaking, Abingdon, Oxon, OX14 3EA, UK.
*UKAEA Culham Laboratory, Abingdon, Oxon, OX14 3DB, UK

Introduction. Ion Cyclotron Emission (ICE), up to 500 MHz, has been observed in deuterium-fuelled tokamaks /1-5/. ICE spectra show narrow ($\Delta\omega/\omega << a/R$) superthermal emission lines with regular spacing proportional to the magnetic field. In JET OH deuterium discharges /2/, ICE line intensities correlate with the DD fusion reaction rate, indicating that charged fusion products provide free energy to drive ICE. The frequencies of the emission lines coincide with harmonics, l, of the deuteron or α-particle gyrofrequency at the outer mid-plane edge ($\omega = l\ \omega_{cD\text{-}edge}$) /4/. ICE signals on JET correlate with inverted sawteeth /5/. With intense neutral beam injection (NBI) on TFTR /3/, broadband emission above ~200 MHz, correlated with the time evolution of the neutron emission. ICE spectra measured above the plasma centre show cyclotron harmonic peaks with $\omega = l\ \omega_{cD\text{-}edge}$.

Results. ICE data were obtained during the JET Preliminary Tritium Experiment (PTE) /6/, using an ICRH antenna as probe, with the aim of evaluating the potential of ICE measurements as a fusion product diagnostic. In the PTE, combined D and T NBI into a single-null 3.1 MA X-point discharge gave a plasma composition ratio (average T to D + T density) of ~ 11% and a maximum neutron emission of 6.0×10^{17} s^{-1}. The spectrum (Fig 1) shows $l < 7$ clear emission lines with spacing 16.7 MHz, matching the IC frequencies of harmonics of deuterons or α-particles at major radius $R = 3.9$ m ($\omega = l\ \omega_{cD\text{-}edge}$). Spectra with D –> D NBI are similar. In both DD and DT plasmas, for $l < 7$, the even-l lines are more intense with each showing *fine structure*, being split into a doublet with $\Delta f / f \sim 0.06$. For l >7, the lines merge into a *continuum*, possibly related to the broadband feature seen on TFTR. In plasmas with intense NBI heating, the issue of whether beam particles or fusion products drive the ICE can be determined by comparing the level of $l = 2$ ICE power at the time of peak neutron emission between similar single-null X-point 3.1MA discharges with *a) only* D -> D NBI (shot 26094 as control, $P_{NBI} = 13.2$ MW), and *b)* (D + T) -> D NBI (shot 26147, $P_{NBI} = 14.2$ MW). In case *a*, the ICE power was $P_{ICE} = 0.12$ μW with total neutron rate 2.7×10^{16} s^{-1}; in case *b*, $P_{ICE} = 3.1$ μW with total neutron rate 5.3×10^{17} s^{-1}. So, by changing from D to (D+T) NBI (at almost constant P_{NBI}), the ICE power increased by a factor of ~26 and the total neutron emission by a factor of ~20. In the DT case, the plasma

was dominated by DT, and not DD fusion reactions, suggesting that the ICE is driven by fusion α-particles. Thus the ICE signal relates to fusion products, not beam particles.

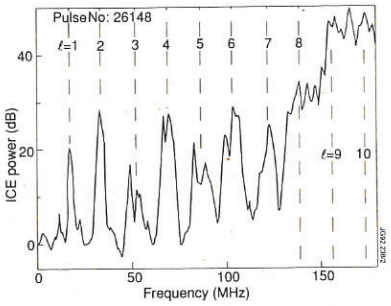

Fig 1: *The ICE spectrum measured in a DT discharge, close to the time of the peak neutron emission.*

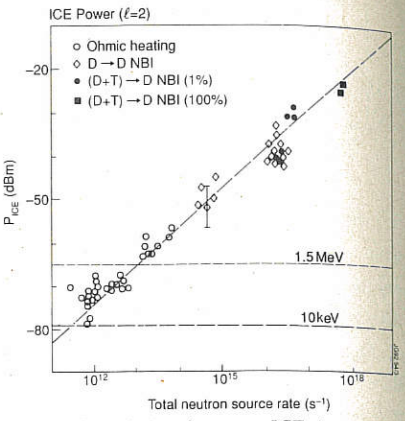

Fig 2: *Correlation between ICE intensity and total neutron emission rate for ohmic and NBI heated JET discharges.*

For a range of JET discharges, the correlation between ICE power and neutron rate is shown in Fig. 2. Reference levels of thermal radiation from a 10 keV bulk D plasma and a population of fusion α-particles (average energy 1.5 MeV) are shown. A single ICE peak fluctuates on the timescale of the data sampling (0.5 ms). Therefore, to compare the evolution of ICE and neutron signals, individual spectra were averaged in the range (10-180) MHz (Fig 3). In the high performance DD and DT PTE cases shown, the onset of the discharge termination phase, or 'X-event', (identified as the the time when the neutron emission starts falling) coincides with a sawtooth collapse coupled to a large ELM /6/. Up to that time, the integrated ICE signal follows the neutron emission, but lags behind by (0.2-0.4) sec; this is similar to D -> D NBI discharges on TFTR /3/. A delay of this magnitude is consistent with the growth-time of the fusion product population.

ICE and ELM activity. In the phase of the discharge before the X-event, time resolved observations show the ICE to increase in bursts of ~ 20 ms, and amplitude $\Delta P_{ICE} / P_{ICE} \sim 1$, correlated with ELMs. The detected ICE signal is proportional to the product of the ICE source power in the plasma and the antenna-plasma coupling resistance, R_c, which is always observed to increase when ELMs occur. Thus, before the X-event, the observed positive ICE-ELM correlation is consistent with changes in R_c and not with fluctuations of the ICE source. Corresponding soft X-ray data reveal only mild perturbations in the outermost few cm of plasma. However, at the time of the X-event, the ICE vanishes in a time < 0.5 ms,

indicating a prompt loss of α-particles from R ~ 3.9 m. After X-events in DD and DT discharges, the ICE vanishes at each large ELM. Simultaneous soft X-ray data show significantly larger ELM perturbations penetrating to a depth ~ 30 cm, encompassing the ICE source. We infer that the large ELMs terminate the ICE by expelling the fast ions, thereby temporarily extinguishing the source. After an ELM, the level of ICE recovers in ~ 60 ms. This is shown in Fig. 4, which also illustrates n=1, m=4-5 MHD activity at 4.5 kHz.

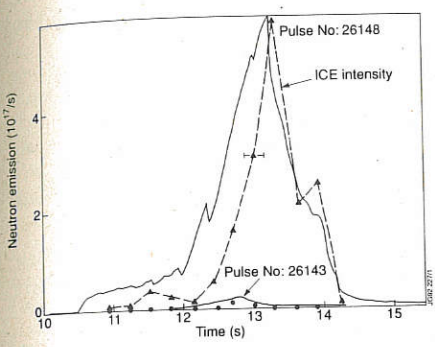

Fig 3: *Evolution of the neutron emission (solid lines) for DT (# 26148) and DD (# 26143) NBI discharges compared with the respective ICE signals (points).*

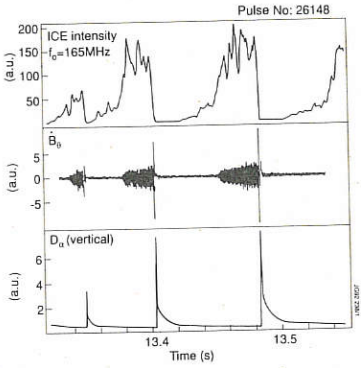

Fig 4: *Correlation, with ELMs, between the ICE, an edge Dα signal and that of an MHD coil mounted at the top of the vessel.*

ICE mechanism. An outstanding question concerns the observed localization of the ICE source at the outer mid-plane edge where the local fusion reaction rate is negligible. In the plasmas observed, the radial birth profiles of DD and DT fusion products are centrally peaked. However, calculations show the existence of a class of fusion products, centrally born within a narrow range of pitch angles (Fig. 5) just beyond the trapped-passing boundary, whose drift excursions reach the outer edge. About 10% of centrally born fusion products belong to this class, which we call class I. The orbits of particles born centrally elsewhere in phase space do not reach the edge. The velocity distribution of the fusion products in the outer midplane edge is therefore exceptionally anisotropic. As the class I ions slow down, their orbits contract, and so, below a certain energy, they no longer pass through the edge. The edge distribution is therefore non-monotonic, resembling a 'bump-on-tail' distribution. Such distributions are potentially unstable to collective relaxation via IC wave-particle /7/ or wave-wave /8/ modes, even when the concentration of fusion products is low; in the PTE, the central α–particle density is ~10^{-4} of the electron density. The essential theoretical feature is the excitation of waves on the fast Alfven and ion Bernstein branches, propagating across the magnetic field with frequencies at IC harmonics. Linear analysis of

shell and ring distributions /8/ indicates that, of the DD fusion products, only 3 MeV protons give instability; the 0.8 MeV ^{3}He and 1 MeV tritons lie below threshold. In the JET PTE plasma, 3.5 MeV α-particles give instability. Subsequent re-partition of energy between fusion proton or α-particle modes and bulk D IC harmonics might generate the observed spectrum.

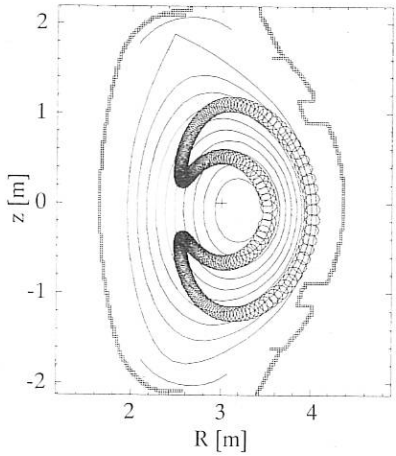

Fig 5: *Calculated orbit of a 3.5 MeV alpha-particle in the flux-surface geometry of JET PTE DT discharge No. 26148 at time 13.2 sec close to the time of maximum neutron emission (see Fig. 3). The particle was born at a point 30 cm from the magnetic axis in the mid-plane with a pitch angle of 65.1°. Similar (class I) orbits, having large radial excursions sufficient to reach the edge, exist in the range 64.4° to 75°. Approximately 10% of the fusion products are centrally born into this class. Below the lower limit, orbits are passing.*

This model may also be consistent with ELM behaviour after the X-event: if a large ELM expels energetic ions from the outer plasma skin of thickness ~ 30 cm, this must include those intersecting the region on large drift orbits, and the ICE signal is extinguished, as observed. However, the central birth of fusion ions continues and, after the ELM, is sufficient to re-build the fast ion population. Thus the ICE signal returns after a delay.

References

/1/ W.H.M.Clark, Proc. 4th Int. Symp. '*Heating in Toroidal Plasmas*' **I**, EUR 9341 EN, 1984

/2/ G.A.Cottrell, et al, Proc. 13th EPS Conf. '*Controlled Fusion and Plasma Heating*', Schliersee, Germany 1986, Vol **10C**, part **II**, 37

/3/ G.J.Greene, et al, Proc. 17th EPS Conf. '*Controlled Fusion and Plasma Heating*', Amsterdam, The Netherlands, 1990, Vol **14B**, part **IV**, 1540

/4/ G.A.Cottrell & R.O.Dendy, *Phys.Rev.Lett.* **60** (1) 33 (1988)

/5/ P.Schild, G.A.Cottrell & R.O.Dendy, *Nuclear Fusion Lett.* **29** (5) 834 (1989)

/6/ The JET team, *Nuclear Fusion* **32** (2) 187 (1992)

/7/ B.Coppi et al, *Phys. Fluids* **29** (12) 4060 (1986)

/8/ R.O.Dendy, C.N.Lashmore-Davies & K.F.Kam, AEA Fusion Report, Culham Laboratory, **AEA FUS 126**, (1991)

MHD LIMITING PHENOMENA IN HIGH PERFORMANCE JET PLASMAS

B Alper, A W Edwards, R D Gill, D Pasini and P Smeulders
JET Joint Undertaking, Abingdon, Oxon, OX14 3EA, UK

Introduction Two types of discharges have been used in the last year on JET to produce plasmas with high neutron yields. The first, the Pellet Enhanced Performance (PEP) H-mode, is characterised by peaked density and pressure profiles with $T_i \sim T_e$. A pellet is injected early in the discharge before the current profile is fully developed and auxilliary heating of typically 8MW of ICRH and 2MW of NBI is applied soon after. Large bootstrap currents produce negative shear near the plasma core[1]. The second type of high performance discharge, the hot-ion H-mode, is characterised by peaked ion temperature profiles, relatively flat density profiles and $T_i > T_e$. Heating is largely from NBI (~14MW), though ICRH is also used in some cases. The high performance phase in both types of discharge is only transitory, lasting typically less than two seconds.

The JET soft X-ray (SXR) camera system, with a real-time trigger facility to provide good time resolution ($5\mu s$), has been used to study the effect of MHD activity on limiting the duration of the high performance phase of these discharges. An analysis of the absolute intensity of SXR emissions has also been used to study impurity accumulation in the plasma core. This is found to lead to significant fuel dilution for both types of discharge.

PEP H-modes Figure 1 shows an example of the nature of MHD activity in a PEP H-mode for shot 24507 during the phase of rising neutron yield. A 4mm pellet was injected into the plasma core at 5 seconds. During the period 5.7s to 6.2s, four small 'crashes' are observed in the SXR emission data. Key features of these events can be seen in the figure. In particular, they have no precursors, the postcursor oscillations are damped – disappearing within 10 - 20 ms and the crashes are very fast. They occur in $\leq 30\mu s$, (the bandwidth limit of the SXR system). Tomographic reconstruction shows a step-wise change with each crash from hollow to flat to peaked emission profiles in the core. Mode analysis of the postcursor oscillations illustrated in the figure, indicates the presence of a dominant (m,n)=(2,1) mode. Another mode with high (m,n) is also present and has been tentatively identified as a (7,4) mode. Though consistent with shear reversal in the plasma core, firm confirmation by mode analysis alone has not proved possible with these data. Faraday rotation measurements, which do show reversed shear, indicate that the centrally peaked q-profile is temporarily flattened with each crash.

Estimates of Z_{eff} in the plasma core have been made using absolute values

of SXR emission combined with electron temperature and density profile data[2]. Profiles of Z_{eff} using this technique are shown in figure 2 at times between each crash. The development of peaked Z_{eff} profiles in the core region is found to be accelerated by these crashes. Accumulation of impurities in the core leads to a significant dilution of deuterium and in many cases leads to a rapid turn-over in neutron yield.

The rapidity and radial extent of these crashes, the absence of any evidence for an m=1 mode and the absence of precursor growth is difficult to explain from an MHD viewpoint[3]. An 'infernal' mode[4] has been proposed as a candidate in PEP-modes but there is little evidence for flattening of the q-profile near q=2, that would be needed in this case.

Fast trigger data have been taken at the termination phase of shot 24532 – a similar PEP H-mode. The line integrated emission profiles, shown in figure 3, are seen to be highly peaked from impurity accumulation prior to termination of the high performance phase. Termination appears more as a gradual erosion of the core emission over a few 100ms with an inward movement of the peak emission from the reduction in Shafranov shift. This contrasts with the rapid crash often observed in hot ion modes (see below).

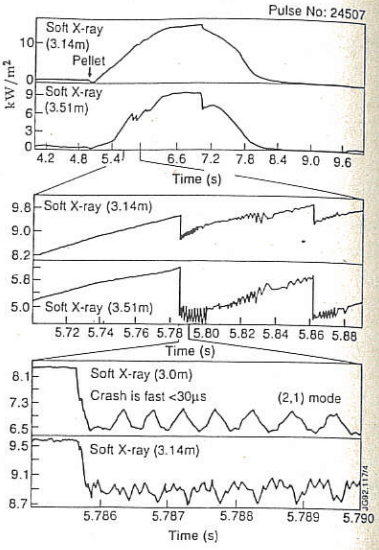

Fig.1 Soft X-ray data showing a series of fast crashes during the development phase of a PEP H-mode.

MHD activity is seen throughout this phase with a (1,1) mode identified near the core and probably a (2,2) mode further out. A movement of the resonant surfaces of these modes to smaller radii is observed through the termination phase. Conventional sawteeth are not observed until after termination of the PEP phase.

Hot Ion H-mode The principal MHD features which characterise hot ion H-mode discharges are sawteeth, edge localised modes (ELMs) and fishbones[5]. Often these phenomena are correlated and their effects on fusion yield depend to a large extent on whether they occur early in the H-mode or at times near peak performance. Relative timings and characteristics can vary greatly from shot to shot but discharge 26591, shown in figure 4, illustrates most of the above features. At 13.2 seconds, (labelled 'a' in the figure), an ELM is seen in both the SXR and C-III

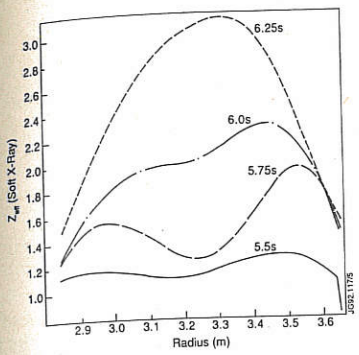

Fig.2 Development of the Z_{eff} profile through the collapses of fig.1 showing the central accumulation of impurities.

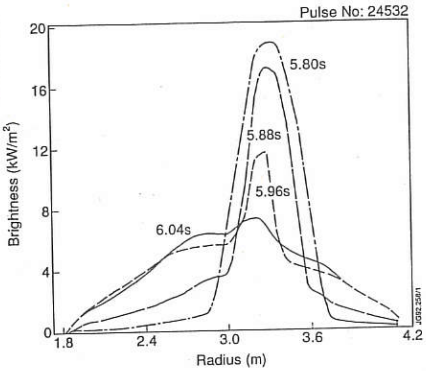

Fig.3 Soft X-ray profiles at 80ms intervals through the final decay phase of a PEP H-mode.

emission. From SXR data it appears to be located in the upper outer quadrant of the vessel. It perhaps flattens the rise in neutron yield but otherwise has no dramatic effect. About 50ms later, a sawtooth collapse, labelled 'b', occurs. SXR emission profiles which were strongly peaked now become flattened and there is a concurrent rapid drop in neutron yield associated with a fall in central temperature. Fishbones, seen in the magnetic signals, cease after the sawtooth crash. A giant ELM, 'c', occurs a further 150ms later at 13.4 seconds. Line integrated SXR emission data show that the giant ELM is localised near the upper X-point dump plates. This ELM is followed, within about 2ms, by a influx of carbon impurities characteristic of a 'carbon bloom'. SXR emission profiles are extremely hollow at this time and the fusion yield continues its rapid decline.

In the highest performance deuterium discharges, 26087 and 26788, the sawtooth and giant ELM occur together at, or soon after, peak performance. The sawtooth collapse occurs about 100μs before the giant ELM, as shown in figure 5 for shot 26087, and has features which extend almost to the edge of the plasma. The giant ELM is localised at the upper X-point dump plates and, similar to shot 26591, is followed within 2ms by a rapid influx of carbon impurities. One or two smaller ELMs may also be associated with these events. As with the PEP-modes, an analysis of Z_{eff} profiles from SXR data shows that there is a strong peaking of impurities with Z_{eff} on-axis reaching values of $\sim$2.8 in the period leading up to the sawtooth crash. An ejection of impurities takes place with the sawtooth collapse and, following the ELM, a rise in edge Z_{eff} is inferred which soon penetrates the core. In this discharge evidence for an increase in carbon inflow occurs about 0.2s before the neutron crash.

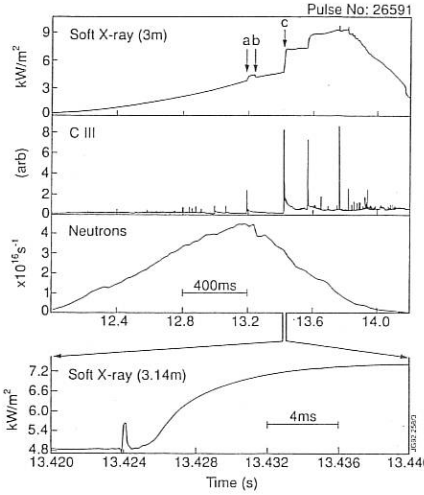

Fig.4 Evolution of a hot ion H-mode. Time 'a' corresponds to an ELM, time 'b' to a sawtooth and 'c' to a giant ELM. Event 'c' is rapidly followed by an increase in SXR edge emissions.

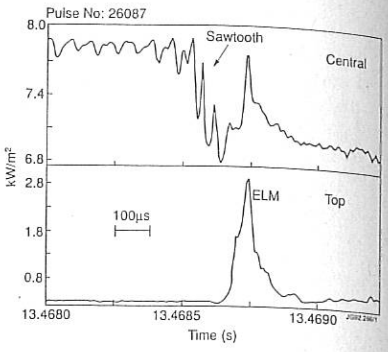

Fig.5 Soft X-ray data showing ~100μs delay between the sawtooth crash and giant ELM, the latter being localised near the upper X-point.

In other examples, when a sawtooth occurs early in the H-mode (eg. in shot 26095, not shown), effects are usually confined to the core region. A temporary flattening in the central peaking of Z_{eff} is seen. There are no associated ELMs, the drop in neutron yield is transitory and no rise in carbon influx is observed.

Conclusions MHD activity has been seen in the soft X-ray emissions of both PEP and hot-ion H-mode high performance JET plasmas. Although no unique instability has been associated with the termination of either of these modes, in most cases MHD activity does affect the nature and speed of the crash. Impurity accumulation in the core is observed in both cases and, particularly in the PEP modes, is accelerated by the MHD activity. This accumulation can result in significant fuel dilution which limits peak neutron yields in JET high performance discharges.

References

[1] M Hugon *et al.*, Nucl. Fusion **32** (1992) 33.

[2] H Weisen *et al.*, Rev. Sci. Instrum. **62** (1991) 1531.

[3] J Wesson, *et al.* Nucl. Fusion **31** (1991) 111.

[4] L A Charlton *et al.*, Nucl. Fusion **31** (1991) 1835.

[5] D Stork *et al.*, this conference.

HIGH-β_p MHD ACTIVITY IN JET

T.C.Hender*, B.Alper, S.Ali-Arshad, H.J.DeBlank, C.D.Challis, C.Gimblett*, J.Han*, J.Jacquinot, G.J.Kramer, W.Kerner, M.F.Nave, D.P.O'Brien, J.O'Rourke, P.Smeulders, M.Stamp, D.Summers, F.Tibone, B.Tubbing, A.Zolfaghari** and W.Zwingmann.
JET Joint Undertaking, Abingdon, OX143EA, UK. ** MIT, Cambridge, USA.
*UKAEA/EURATOM Fusion Association, Culham Laboratory, Abingdon, Oxon, UK.

Introduction High-β_p, and therefore high bootstrap current, is an attractive design regime for a tokamak reactor since it minimises capital expenditure on, and recirculating power used in, external current drive. In JET high-β_p has been achieved by operating open divertor H-mode discharges at relatively low current, $I_p \sim$ 1–1.5MA and moderate toroidal field $B_T(R = 3\text{m}) \sim 2.8$T, with ICRF heating powers in the range $\sim$ 4–10MW.

A typical discharge is shown in Fig. 1. In the Ohmic phase immediately preceding the ICRH, sawteeth oscillations are visible on the central temperature. From Fig. 1 it can be seen that these sawtooth oscillations continue for the initial parts of the additionally heated phase ($t < 52.8$s). The sawteeth acquire an increasingly fishbone character as time proceeds. During this fishbone/sawtooth phase non-correlated ELM type events are also visible on the D_α-trace. Often these ELM's stop at approximately the same time as the sawteeth (though there are discharges in which the sawteeth are absent but the ELM's still occur). Following the cessation of ELM's/fishbones the energy confinement improves and β_p climbs steadily to $\beta_p \sim 2$ (for $I_p = 1$MA) where a rapid reduction in β_p occurs. In some discharges (generally those with $I_p = 1.5$MA) the cycle of β_p increasing and then decreasing rapidly, may repeat itself several times.

Less commonly discharges occur in which large edge relaxations limit the β_p rise. These discharges were avoided experimentally by adjusting the antenna coupling resistance (ie. the plasma–antenna distance) and by altering the gas feed.

In this paper we consider areas directly related to MHD behaviour for these high-β_p discharges. A companion paper [1] considers their bootstrap current properties.

MHD Activity in ELM free period During the ELM free period, preceding the rapid decline in β_p, the density rises monotonically and there is a corresponding improvement in confinement, with τ_E exceeding the JET/DIII-D H-mode scaling by ~ 1.7. As β_p climbs towards $\beta_p \sim 2$ the bootstrap fraction rises to $\sim 70\%$ of the total current [1]. The location of this bootstrap current is dominated by the strong edge density gradients ($dn_e/dr \sim 2 \times 10^{20}\text{m}^{-4}$). The combination of dominantly edge bootstrap current and fairly high central temperature ($\sim$ 6keV) means that in the relatively short time (compared to the central resistive diffusion time) of high-β_p, the central-q varies little. Given that the discharges are sawtoothing initially this implies $q(0) \sim 1$ throughout the high-β_p phase; this view is borne out by TRANSP transport simulations [1].

An alternate determination of $q(0)$ arises from the observed instabilities which precede (and sometimes for a short while) follow the rapid reduction in β_p. These instabilities which occur after the ELM phase are observed on the central (ECE) temperature and SXR chords. From the toroidal SXR cameras it is found that these instabilities are $n = 1$. The temperature fluctuations from the ECE show an odd-m mode about the plasma centre ($R \sim 3.3$m) with phase reversals near $R = 3.07$ and 3.6m (Fig. 2(a)). These temperature

oscillations are very similar to the computed flux surface distortions arising from an $n = 1$ (dominantly $m = 1$) internal kink mode, when the central-q is slightly greater than unity (Fig. 2(b), $q_0 = 1.03$). For the results shown in Fig. 2(b) the linear toroidal stability code FAR [2] has been used to calculate the $n = 1$ eigenfunctions, the amplitude of these eigenfunctions is adjusted to match the observed oscillations, and the mode is assumed to rotate rigidly which gives an equivalence between toroidal angle and time (at a fixed viewing angle).

A comparison between the observed SXR oscillations and theoretical predictions has also been made. In this case the observed SXR line integrals are reconstructed by assuming constant emissivity on the flux surfaces which are distorted by the computed $n = 1$ eigenfunction. The functional form of the emissivity is adjusted to match the averaged emissivity on each SXR chord. For the equilibrium (with $q_0 = 1.03$) used for Fig. 2(b) the reconstructed SXR chords show excellent relative phase agreement with the experimental measurements. Direct tomographic reconstruction also gives the result that the observed oscillations (Fig. 2(a)) are dominantly $m = 1$ in the core. Thus the transport analysis and inference from MHD activity support the view that the central-q changes very little, despite the large bootstrap fraction.

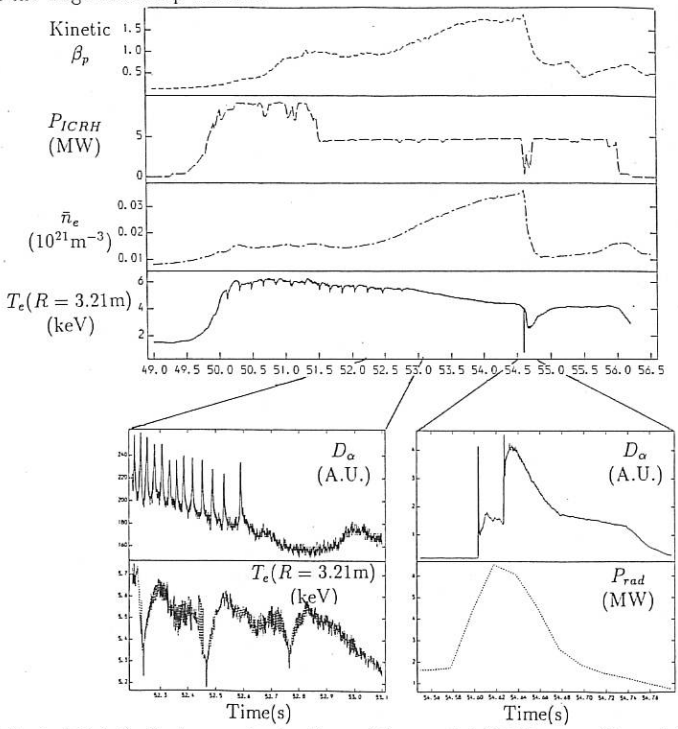

Fig. 1 Typical high-β_p discharge, showing thermal β_p, coupled ICRH power (P_{ICRH}), line average density ($\bar{n}_e$), and electron temperature (T_e). The expanded traces show details of (on the left) transition phase as sawteeth/ELM's cease and (on the right) fast β_p-decline.

β_p–decline There is no correlation between the observed core MHD activity and the rapid β_p-decline. The β_p-decline in fact appears to be related to edge stability, since it is always initiated by a large ELM.

For at least 100msec preceding the β_p-decline the CCD images of one of the ICRF antenna's typically show localised heating of the mid-plane edge carbon protection tiles. This strong heating arises because the short scrape–off layer widths in H–mode cause the plasma to be moved towards the plasma antenna, by the position feedback system which maintains the plasma–antenna coupling impedance constant. As the density rises during the ELM free phase the radiated power steadily increases to $\sim 30-40\%$ of the total input power, immediately before the β_p-decline. The dominant radiating impurity is carbon (perhaps from the ICRF antenna) with significant nickel. At the large ELM initiating the β_p-decline, the radiated power fraction increases to $\gtrsim 100\%$, the ICRF coupling to the plasma is lost (Fig. 1), and the plasma reverts to L–mode confinement. The large radiated power causes a rapid decline in temperature but this recovers in $\sim$ 300msec, and the decline in energy confinement is mainly accounted for by a 2–3 times decrease in density.

As the density rises preceding the β_p-decline, the edge density gradients (and therefore pressure gradients) become very large ($dn_e/dr \sim 2 \times 10^{20}\mathrm{m}^{-4}$). The high–$n$ ballooning analysis given in Fig. 3 shows that the edge pressure gradients are marginally stable over the outer parts of the plasma ($R = 4-4.15$m) immediately preceding the ELM. This is to be contrasted with normal H–mode operation in JET, where the edge pressure gradients are significantly below the ballooning threshold [3]. Thus it may be that the large ELM preceding the β_p-decline is triggered by an ideal ballooning instability.

The multi-channel reflectometer shows evidence for increased high frequency ($\sim$100kHz) density fluctuations near the plasma edge, as the time of the large ELM is approached. Figure 4 shows this result by comparing the power spectra at $n = 1.94 \times 10^{19}\mathrm{m}^{-3}$, for discharges where data is acquired during and 2.1 sec before the ELM. It can be seen that the high frequency activity increases significantly near the ELM timing, perhaps indicating some high–n instability developing.

Discussion It is interesting to contrast the results presented here with those from NBI discharges in JT–60, where a similar bootstrap fraction ($\sim$ 80%) occurs [4]. The JT–60 results show a similar rapid decline in β_p but this is attributed to a near axis bootstrap current causing a strongly non-monotonic q–profile which in turn destabilises an $n = 1$ internal kink mode. In contrast for the JET results, with broad density profiles and bootstrap current driven primarily in the plasma edge there is little variation of the central q–profile. The β_p-decline is not precipitated by any observed central MHD activity but appears to be caused by an ELM instability. These results point to the importance of tailoring the density profile if steady state discharges with a high fraction of bootstrap current are to be achieved.

Acknowledgement We thank G.Sips for his contribution to providing the reflectometer data.

References

[1] J.O'Rourke et al, 'Evolution of the current profile in JET high bootstrap current plasmas', this conference.

[2] L.A.Charlton et al, Jrnl Comp Phys 86 270 1990.
[3] G.T.A.Huysmans et al, 'MHD stability model of ELM's in JET discharges', this conference.
[4] S.Ishida et al, Phys Rev Lett 68 1531 1992.

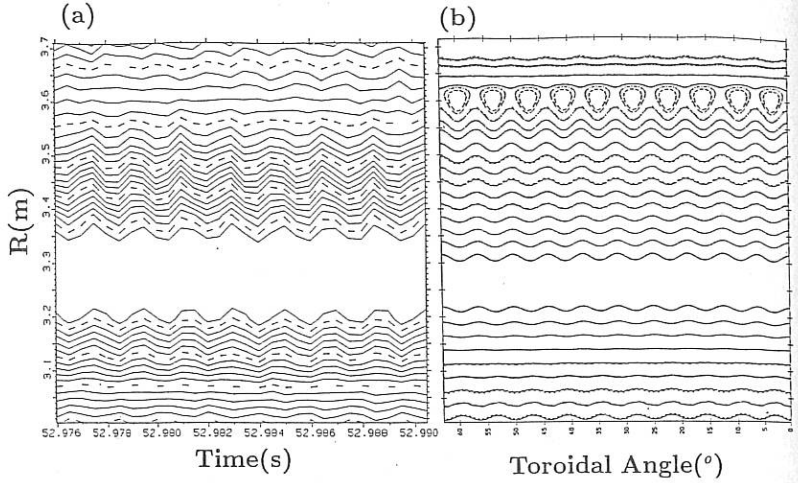

Fig. 2 (a) ECE temperature contours and (b) flux surfaces from $n = 1$ internal kink mode in horizontal mid-plane for Shot 25260. Plasma rotation gives an assumed equivalence between time and angle.

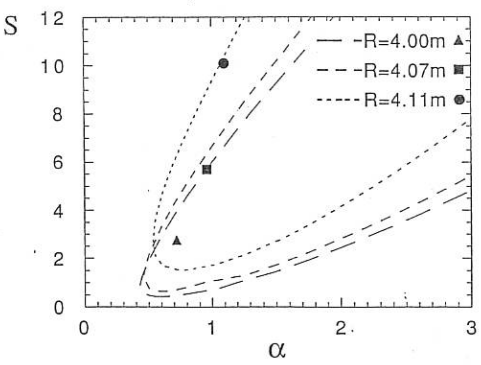

Fig. 3 Marginal stability boundaries in the $S[= r/q(dq/dR)]$ and $\alpha[= -(2\mu_0 r^2/RB_\theta^2)(dP/dR)]$ plane at three major radii; all quantities are evaluated at outboard midplane. The symbols are experimental values 0.1s before β_p decline.

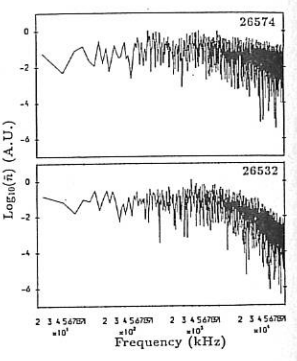

Fig. 4 Power spectra of density fluctuations for $n = 1.94 \times 10^{19} m^{-3}$. For shot 26574 data encompasses a β_p decline and for shot 26532 it is 2.1s before the decline.

HIGH β STUDIES IN THE H-MODE AND HOT ION H-MODE IN JET

D Stork, B Alper, S Ali-Arshad, H J de Blank, H P L de Esch, A Edwards, T C Hender*, R Konig, G J Kramer†, F B Marcus, M F Nave, D P O'Brien, J O'Rourke, P Smeulders, M Stamp, F Tibone, B J D Tubbing, A Zolfaghari ** and W Zwingmann

JET Joint Undertaking, Abingdon, Oxon OX14 3EA, UK
* UKAEA/EURATOM Fusion Association, Culham Laboratory, OX14 3DB, UK
** MIT, Cambridge, USA., † FOM, Rijnhuizen, Neivwegen, Netherlands

Introduction and Database Overview

High β plasmas have recently been studied on JET in two separate regimes. For a given plasma dimension, the power to reach a β limit is minimised either by working at low toroidal field or with a high energy confinement. This dictated the two regimes for the JET study; one set of H-mode plasmas being generated using high Neutral Beam Injection (NBI) power into low toroidal field (< 1.4 T) discharges; the other set of discharges involved studying β-limits in Hot-Ion H-modes where the confinement enhancement H (= τ_E/τ_G with τ_G the Goldston L mode scaling) is significantly above the normal H-mode factor of 2. Thus β-limits were studied in the highest performance regimes. The MHD and confinement behaviour of these regimes will be discussed and the preliminary results of a high n-ballooning analysis presented.

The value of maximum toroidal beta ($\beta_\phi{}^M$) is plotted for the JET database in Fig.1 with the regimes mentioned above being highlighted. The best of the JET discharges in the low B_T regime exceed the Troyon limit for β_ϕ ($\beta_\phi{}^T$ = 2.8 I/aB with I in MA; a in m and B in Tesla) [1], by up to 20% whilst the Hot Ion discharges limit at around 0.85 $\beta_\phi{}^T$. Figure 1 plots $\beta_\phi{}^M$ against the product l_i x I_N (l_i = internal inductance; I_N = I/aB) together with the limit line $\beta_\phi{}^L = 4\ l_i \times I_N$ which has been suggested by experiments on DIIID [2]. The low B_T H-modes on JET are consistent with this limit, given the uncertainties in the knowledge of the inductance (± 10%). The Hot Ion H-modes limit at $\beta_\phi{}^L \simeq 2.7\ l_i\ I_N$.

Characteristics of the low B_T H-modes

The low B_T experiments were all performed at 2MA and 1.5MA to avoid low q, although q_{95} was nevertheless < 3.0. Most discharges were strongly affected by ELMs which began ~ 300 - 400 ms after the application of high NBI power, clipping the rise in β. The ELMs were usually accompanied by sawteeth. There was an energy clip at the first large ELM at which steadily growing n = 1 and 3 modes collapsed and the n = 2 mode increased suddenly to remain strong throughout the high power phase. Most discharges reached β_ϕ values ~ 0.95 - 1.05 x $\beta_\phi{}^T$, the limit of previous JET results [3]. Some discharges achieved higher performance and exceeded the Troyon limit for approximately an energy confinement time (τ_E) before a β_ϕ collapse occurred. Figure 2 shows such a discharge (# 26236) which reached $\beta_\phi{}^M$ ~ 6% (1.2 x $\beta_\phi{}^T$). β_ϕ rolls over about 200 - 300 ms before the first small ELM then collapses with loss of about 0.5 MJ stored energy with the second giant ELM. The n = 3 activity in this discharge does not grow as early as in the other ELM discharges and appears only at the time of the β_ϕ saturation.

Shot 26236 nears a 'Hot Ion' type regime with $T_i(0)$ ~ 12 keV and $T_e(o)$ ~ 5.5 keV at 15.4 secs. The superior performance of this discharge may arise from the initial low target density arising from the burst of ELMs in the low NBI power H-mode prior to the high β_ϕ phase. However, similar β_ϕ values are reached in H-modes where $T_i \sim T_e$, so the effects of the different pressure profiles are not clear. The confinement enhancement factor H of the 'Hot Ion' low-B_T plasma is H ~ 2.1 at the point where β_ϕ begins to roll over. This is somewhat better than the $T_i \sim T_e$ high β_ϕ shots where H ~ 1.7 - 1.9. All the highest β_ϕ shots show similar occurrence of high frequency MHD activity in the range 69 - 121 kHz. This is broadband in nature and grows as β_N (= $\beta_\phi/\beta_\phi{}^T$) exceeds 1 (see Fig.3). This may be the manifestation of

high-n ballooning modes. It is not possible with the diagnostics available to pinpoint the radial location of the activity.

Hot Ion H-modes

These studies at Ip = 3MA and $1.8 \leq B_T \leq 3.1$ T, extended the Hot Ion regime down to $q_{95} \sim 2.8$. Also, Hot Ion H-modes were established before the current profile had fully developed, before the q = 1 surface had entered the plasma and at a low l_i. The behaviour of the Hot Ion H-modes proved to be varied in character but several patterns emerged.

1) The peak normalised β achieved before collapse depended on the purity of the target throughout the H-mode phase.

2) For H-modes with $q \leq 1$ volumes inside the plasma as evidenced by sawtooth activity, the β limit phase was in general associated with a drop in the edge T_e accompanied usually by an ELM within a few 10's of milliseconds. The severity of this collapse varied from a 'deep' collapse of the temperature, including the centre in a sawtooth-like manner accompanied by a large ELM; to a gentle decline of the edge T_i and T_e channels (outside the sawtooth inversion radius) accompanied by levelling of the central temperatures and enhanced edge D_α and CIII light signals indicating an increase in conducted power to the edge. The extremes of this behaviour are shown in Fig.4. Neither of the collapses shown has the same time development as previously-observed 'carbon blooms' in the H-mode on JET [4]. For many shots, gradual saturated behaviour of the β_ϕ and the temperatures was seen for 100-200 ms before a collapse as indicated in Fig.4(a).

3) Many forms of MHD activity, including fishbones, were seen in the H-modes with well-peaked current profiles. There is no regularity in β_ϕ thresholds for low n and fishbone activity however, and it is not clear whether the existence of such activity limits the plasma performance. There are strong bursts of high frequency MHD activity above 69 kHz (as in the $\beta_N > 1$ shots) and these occur generally at high β_ϕ. The threshold for such high frequency activity (β_N^{HF}) is dependent on target Z_{eff} (see Fig.5) and is generally around 0.75 - 0.95 of the peak normalised β_ϕ (β_N^{pk}). This high frequency activity may be linked to high n-modes, the Z_{eff} dependence may indicate resistive ballooning activity.

4) The MHD activity is much lower in the low l_i shots (early H-modes) and is non-existent where no q = 1 surface has entered the plasma. Limiting β_ϕ behaviour is nevertheless seen in these discharges. The collapse is probably due to 'carbon bloom' pollution, but the saturation may be due to insufficient confinement (see below).

5) The confinement enhancement factor for these Hot Ion H-modes (H) is seen to be dependent on toroidal field, varying from ~ 2.2 at 1.8T to ~ 2.9 at fields above 2.8T. There is also evidence of a l_i dependence in some shots similar to the $l_i^{0.68}$ behaviour of global confinement seen in the JET current ramp experiments [5]. In spite of the unfavourable dependences on l_i and B_T, the 3MA/1.8T early H-modes still achieve the highest normalised β_ϕ values (0.88 - 0.91) presumably aided by the lower level of MHD activity.

Ballooning stability analysis

A preliminary stability analysis using a high n-ballooning code based on the method of Greene and Chance [6] has been performed on the data from a low-B_T H-mode (26236; $\beta_N^{pk} \sim 1.2$). Supplemented by the HBT code [7] at low shear. Thermal pressure profiles were established from LIDAR and ECE measurements of $T_e(r)$; Charge Exchange Recombination Spectroscopy (CXRS) measurements of $T_i(r)$ and Z_{eff} (r). Polarimetry measurements of the Faraday rotation profile were used, together with the measured pressures and magnetics as constraints to 2 equilibrium fitting codes (IDENTD and EFIT). The 2 codes being in good agreement can effectively be interchanged. Some results are shown in Fig.6. It can be seen that the plasma profile at 15.6 secs (near the peak β_ϕ value) has a trajectory in the s - α plane ($s = rq'/q$; $\alpha = -2\mu_0 R\, p' q^2/B_T^2$) which limits close to 100% of the Ideal MHD ballooning limit

around the surface $r/a = 0.45$. The data at 15.8 secs, taken in the collapse of β_ϕ, shows that the central pressure is lost due principally to the collapse of the ion temperature.

Conclusions

High β plasmas have been obtained in JET where the peak β value reached exceeds the Troyon limit (of combined stability against free boundary kinks or Ballooning modes) by up to 20%. The best JET discharges are consistent with a β_ϕ-limit of 4 l_i I/aB.

The high β plasmas exceeding the Troyon limit show characteristic broadband high frequency MHD activity, this is also seen at even higher amplitude in many Hot Ion shots at high β_ϕ, although the high performance Hot Ion shots have not exceeded $\beta_\phi \sim 0.85\ \beta_\phi^T$.

The MHD activity in Hot Ion shots at high β_ϕ is varied but the onset of high frequency activity occurs above a threshold β_ϕ which is inversely proportional to Z_{eff}. Collapse phases in the Hot Ion high β_ϕ shots are very fast. The MHD activity is quiescent across the spectrum in shots without a q = 1 surface in the plasma.

An initial ballooning stability analysis shows that the low B_T discharge pressure profile limits at the ideal ballooning limit for $0.35 < r/a < 0.5$. Most of the profile lies below this limit, possibly indicating importance of resistive ballooning modes.

References:

[1] Troyon F., et al., Plasma Phys. Contr. Fusion 26 (1984), 209

[2] Taylor T. S., et al., 13th IAEA Conf. on Plasma Phys. and Contr. Fus. Research, Washington (1990). Proceedings, vol. 1, pp 177-193.

[3] The JET Team (presented by P. Smeulders), ibid [2], vol. 1, pp 219-227.

[4] Stork D., et al., 18th European Conf. on Contr. Fus. and Plasma Phys., Berlin (1991), Europhys. Conf. Abstracts 15(C), I, 357-360.

[5] Cordey J.G., et al., these proceedings.

[6] Green J.M. and Chance M.S., Nucl. Fus. 21 (1981), 453.

[7] Huysmans G.T.A., et al., Fom-Instituut voor Plasmafysica, Rijnhuizen Report, 90-194.

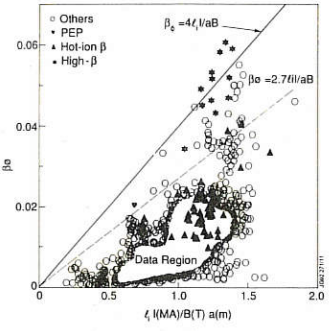

Fig.1: β^M for the JET dataset as a function of ℓ_i I/Ba

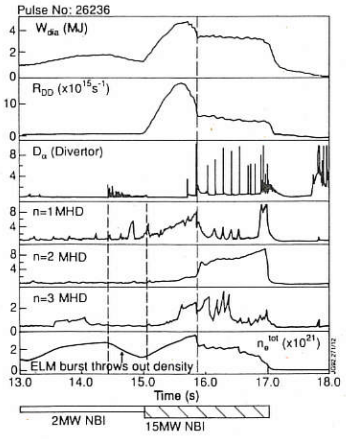

Fig.2:Time development of Shot 26236 (2MA/1.1T) showing low n MHD activity.

Max-Planck-Institut für Plasmaphysik
8046 Garching bei München

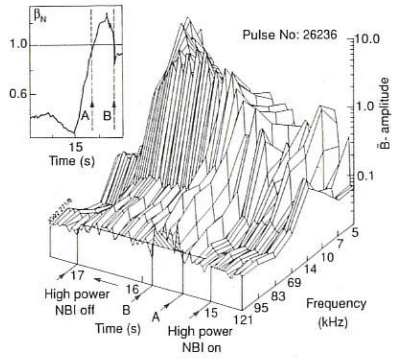

Fig.3: High frequency MHD activity as a function of time during the high power heating phase of $\beta_N > 1$ Shot 26236. The peak at <10kHz represents n = 1 activity at the plasma rotation frequency.

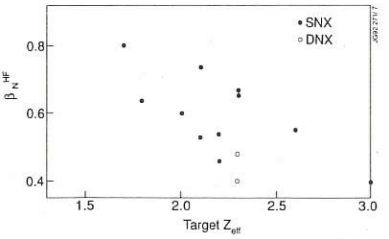

Fig.5: Threshold for onset of high frequency MHD activity (β_N^{HF}) as a function of target Z_{eff} during Hot Ion H-modes (3.1MA/2.8T)

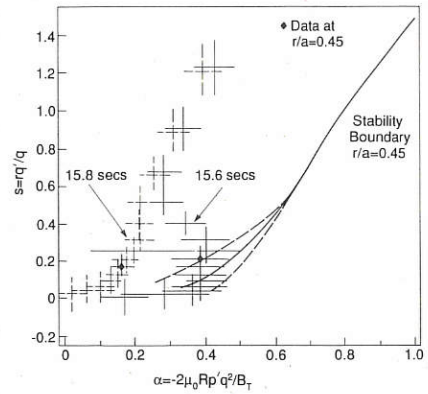

Fig.6: Ballooning stability curve for Shot 26236 at r/a = 0.45 compared to (s, α) profiles at 15.6s and 15.8s (after collapse). The dashed lines around the stability boundary indicates uncertainly due to q profile errors. ◊ indicates the data point to be compared to the curve at each time.

Fig.4: Comparison of collapses of Hot Ion H-modes at high β_N ($=\beta_I/\beta_I^T$)
(a) Limiting behaviour before collapse
(b) Fast collapse setting in without limiting behaviour.

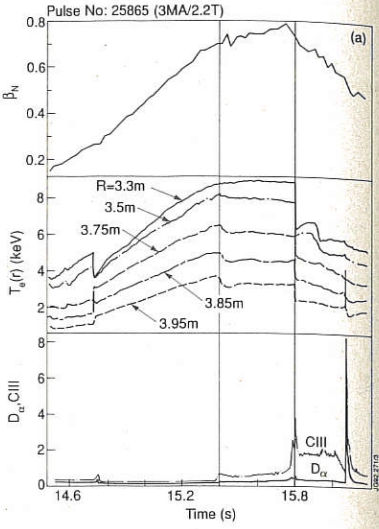

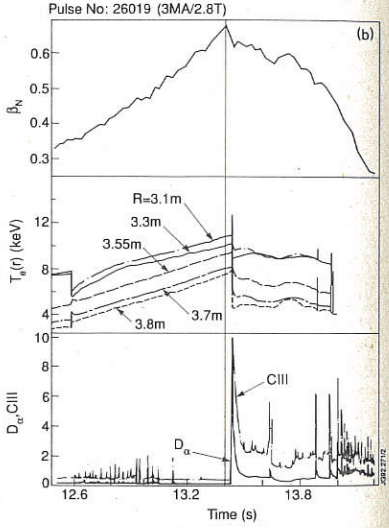

Ideal-MHD Operational Limits for Highly Elongated Tokamaks

G. Eriksson*, A. Bondeson, D.J. Ward, F. Hofmann and L. Villard

Centre de recherches en physique des plasmas, Association Euratom - Confédération Suisse, Ecole polytechnique fédérale de Lausanne, Lausanne, Switzerland

I. INTRODUCTION

The construction of strongly shaped and elongated tokamaks is to a large extent motivated by the theoretical prediction that the beta-limit is proportional to the plasma current [1]. Experimental results confirm the advantageous effects of increased elongation ($\beta = 11\%$ was reached with an elongation $\kappa = 2.34$ in DIII-D [2]). The understanding of beta and other operational limits at very high elongation ($\kappa > 2.5$) is, however, very limited. Notably, it is not clear whether the beta limit can be further increased by an increase in κ or by other types of shaping, whether vertical stability limits the achievable elongation and whether control of current and pressure profiles is necessary.

We report on an ideal MHD stability study in progress with the aim of clarifying the operational limits imposed by $n = 0$ (vertical), 1 (kink) and ∞ (ballooning) stability for tokamaks with elongation from 2 to 3, in particular, for shapes accessible to the TCV tokamak in Lausanne. The shape of the plasma-vacuum boundary is prescribed as:

$$R/a = A + \cos(\theta + \delta \sin\theta + \lambda \sin 2\theta) \quad , \quad Z/a = \kappa \sin\theta \ .$$

The parameter λ modifies the shape of the tips: $\lambda > 0$ makes the tips broader. We refer to configurations with $\delta = 0.5$ and $\lambda = 0.2$ as "TCV dee". For all results presented here, the aspect ratio is $A = 3.7$. Generally, the current profiles are prescribed, and unless otherwise stated, q_0 is held fixed at 1.05. The pressure profiles are either prescribed or optimized at the ballooning limit (in the first stability region). Critical betas are then computed for $n = 0$ and $n = 1$ stability with the pressure profile a scaled version of that which gives the ballooning limit. The $n = 0$ modes are calculated for a resistive wall with the shape of the TCV vacuum vessel. We assume that the $n = 0$ mode can be stabilized by active feedback if the growth time in the absence of feedback is longer than 0.5 ms. The $n = 1$ limits do not take into account wall stabilization. The equilibria, $n = 0$ and $n = 1$ modes are computed with the CHEASE [3], NOVA-W [4] and MARS [5] codes, respectively.

II. CURRENT AND INDUCTANCE LIMITS AT ZERO PRESSURE

It is well known that the circular current limit $q_\psi \geq 2$ does not apply for sufficiently noncircular equilibria (including those with X-points). Figure 1 shows the limit in normalized current $I_N = \mu_0 I_p / aB_0$, set by $n = 1$ stability at zero pressure, as a function of q_0 for different shapes ($\delta = 0.25$, 0.5 and $\lambda = 0$, 0.25) and elongations $\kappa = 2.5$ (1a) and $\kappa = 3.0$ (1b). Here we use a simple current profile: Rj_ϕ is a quadratic polynomial in poloidal flux ψ and vanishes linearly at the plasma edge. At elongation 2.5, the current limit corresponds to $q_\psi = 2$ for $q_0 < 1.2$ and $q_\psi = 3$ for $1.2 < q_0 < 2$. For elongation 3, the limit is no longer related to integer q_ψ but is a smooth function of q_0. The maximum current increases with δ and decreases with λ. It is remarkably constant when expressed in terms of q_{95}, $q_{95} \geq 3.3$ for q_0 between 1 and 2 and $\lambda = 0$. We note that the current limits are similar for elongations 2.5 and 3. In fact, for $q_0 < 1.2$, the limit is even slightly higher for $\kappa = 2.5$.

While $n = 1$ stability is favored by high q_ψ or a large internal inductance, the $n = 0$ (vertical) stability is favored by a low inductance. To illustrate this, we show in Fig. 2 the limits in internal inductance for $n = 1$ and $n = 0$ as functions of elongation for a TCV dee and the same type of current profile as in Fig. 1. While these profiles give a large operating window where both $n = 0$ and 1 are stable for $\kappa = 2$, the window is considerably reduced at

$\kappa = 2.5$ and nonexistent at $\kappa = 3$. We find that at zero beta, the n = 0 stability is almost entirely determined by the internal inductance, while the n = 1 stability is sensitive to the details of the current profile. We have found advantageous results for a class of current profiles with "shoulders" in the outer region of the plasma. An example of such a current profile is shown in Fig. 3a. For $q_0 = 1.05$, this profile remains n = 1 stable for ℓ_i as low as 0.43, while the "standard" profile shown in Fig. 3b gives an ℓ_i-limit of about 0.54. At $\kappa = 3$ and zero pressure, n = 0 stability requires $\ell_i < 0.5$, which can be satisfied for the profile with shoulders but not by the standard profile. (Another way to ensure both n = 0 and n = 1 stability is to raise q_0. This, however, reduces n = 1 the current limit, which is not the case for the profile in Fig. 3a.)

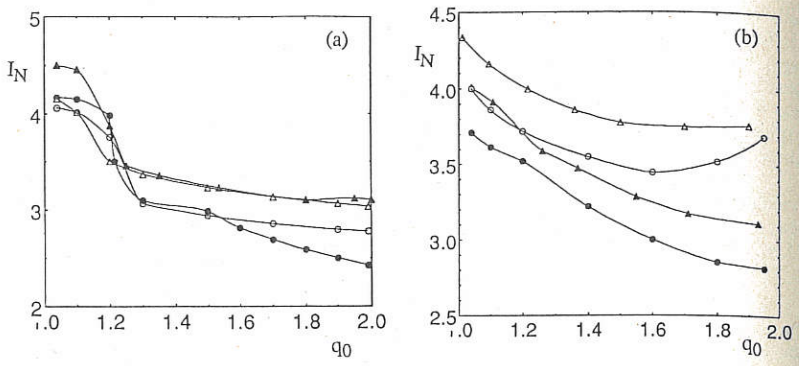

FIGURE 1. Current limit for the n = 1 external kink and different shapes. Circles - $\delta = 0.25$, triangles - $\delta = 0.5$; open symbols - $\lambda = 0$, filled symbols - $\lambda = 0.25$. (a) $\kappa = 2.5$ and (b) $\kappa = 3$.

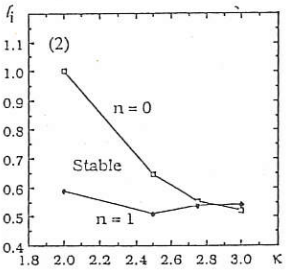

FIGURE 2. Limit in ℓ_i for n = 0 and 1. vs elongation in TCV dee with a simple current profile and $q_0 = 1.05$.

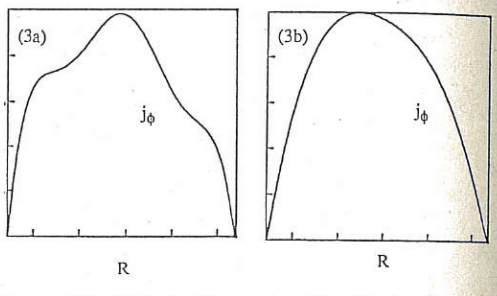

FIGURE 3. (a) Current profile with shoulders and low inductance limit for n = 1. (b) Simple current profile used to generate Fig. 2.

III. BETA LIMITS AT HIGH ELONGATION

III.1 Kink-ballooning limit

Here we present the beta limits imposed by kink and ballooning modes for different shapes (κ = 2, 2.5 and 3; δ = 0.2, 0.5 and 0.8; λ = 0, and 0.2). In this study, the surface averaged toroidal current density I* has been taken as flat in the central region, matched by a cubic polynomial in ψ in the outer region with $I^* = dI^*/d\psi = 0$ at the edge and I^* and $dI^*/d\psi$ everywhere continuous. These profiles give rather high internal inductance, which is favorable for n = 1 stability (but makes the n = 0 unstable at high elongation). The normalized current

was fixed at 2.96 for $\kappa = 2.5$ and 3, and $I_N = 2.22$ for $\kappa = 2$.

Figure 4 shows the beta limits imposed by kink and ballooning stability as functions of elongation for different δ and λ. We see that the effects of δ and λ compensate each other and the highest beta limits are obtained for highly triangular plasmas, δ large and λ small. Furthermore, at high triangularity, $\delta = 0.5$ or 0.8, the limit takes the largest values at elongation $\kappa = 2.5$. The best result obtained here is for $\kappa = 2.5$, $\delta = 0.8$ and $\lambda = 0$, where the limit is 8.3%. It may be noted that this shape is close to that of the DIII-D discharge with record β of 11 % [2]. With correction for the inverse dependence on aspect ratio, $\beta = 8.3$ % at $A = 3.7$ corresponds to $\beta = 10.4$ % at $A = 2.96$, which is close to the experimental result.

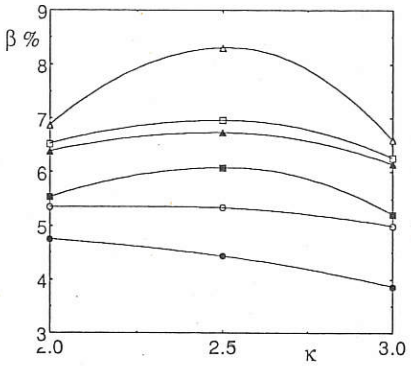

FIGURE 4. Beta limits for kink and ballooning stability and different plasma shapes. Circles - $\delta = 0.2$, squares - $\delta = 0.5$ and triangles - $\delta = 0.8$. Open symbols - $\lambda = 0$, filled - $\lambda = 0.2$.

III.2 Limits imposed by vertical stability

As discussed in Sec. II, an important issue at high elongation is the vertical stability which requires a low internal inductance. Previous studies indicate that the highest beta limits both for kink [2] and ballooning [6] occur for high internal inductance. To examine the effect of the $n = 0$ stability on the beta limits for TCV, we have considered current profiles with different internal inductance in a TCV dee with $\kappa = 3$. Figure 5 shows the beta limits for ballooning (dotted), $n = 1$ (solid) and $n = 0$ (dashed curves) vs. the normalized current for three different sequences of current profiles. In order of decreasing ℓ_i at fixed I_p these are: 1 - standard profile without shoulders and two profiles with 2 - weak and 3 - large shoulders. Figure 6 shows the internal inductance as a function of I_N at the $n = 1$ limit for these equilibria.

The $n = 0$ stability is primarily dependent on the internal inductance. Figure 5 shows that pressure has a strong stabilizing effect on the $n = 0$ mode. The limit in internal inductance increases by about 0.1 when β is increased from 0 to 6 % for these equilibria. (Note that the $n = 0$ mode is stable for $\beta > \beta_{crit}(I_N)$. For the sequence (1) of equilibria with the highest inductance, the $n = 0$ mode requires $\beta > 10$ % for stabilization, which is clearly higher than the $n = 1$ limit, so this sequence is always unstable.) The finite β stabilization appears to be due to an outward shift of the maximum in the current density which redistributes the eddy currents in the wall towards the outboard side. This is strongly stabilizing. Thus, finite pressure widens the class of current profiles stable to both $n = 0$ and 1 at high elongation. We find that the pressure effect on $n = 0$ stability is similar at $\kappa = 2.5$.

The $n = 1$ beta-limit is higher for the cases of higher inductance (curve 1), in agreement with the results of [2]. The two other cases, medium and low ℓ_i (curves 2 and 3) give almost the same values with a maximum of about 4 %. It is clear from Fig. 5 that the equilibrium sequence with the lowest inductance is stable over a fairly large range of plasma current, while

the sequence of intermediate inductance gives a smaller operational window and that of high inductance is always unstable. Figure 5 shows that the ballooning limit is almost independent of the inductance which is different from results for lower elongation reported in [6]. We conclude from Fig. 5 that at $\kappa = 3$, the beta limit is set entirely by the $n = 0$ and $n = 1$ modes, the ballooning limit being always higher.

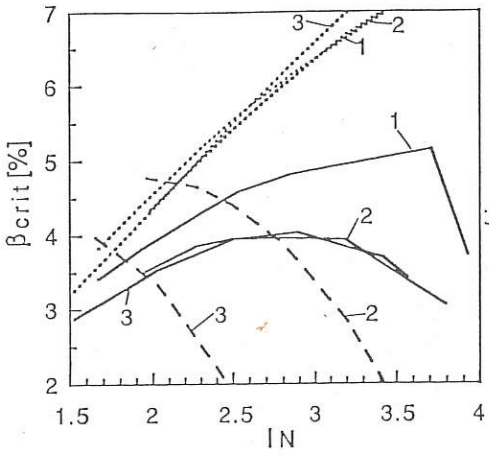

FIGURE 5. Beta limits for ballooning (dotted), n = 0 (dashed) and n = 1 (solid) vs. normalized current for a TCV dee (κ = 3, A = 3.7) and the equilibrium sequences described in Sec. III.2.

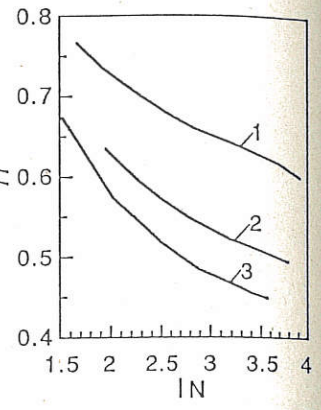

FIGURE 6. Internal inductance vs. normalized plasma current for the same equilibrium sequences as in Figure 5.

IV. CONCLUSION

In conclusion, the beta limit of highly elongated tokamaks increases with triangularity. As a function of elongation, the limit shows a maximum for $\kappa \approx 2.5$. The $n = 1$ and ballooning limits fall weakly at higher elongation. However, vertical stability for high elongation requires operation at low inductance and this causes a more significant decrease of the $n = 1$ beta limit. At high elongation, the beta limit is set entirely by $n = 0$ and $n = 1$ stability. Finite pressure is clearly favorable for vertical stability at high elongation.

Acknowledgement: This research was funded in part by the Swiss National Science Foundation.

References

[1] TROYON, F., et al., Plasma Phys. Controlled Fusion **26** (1984) 209.
[2] LAZARUS, E.A., et al., Phys. Fluids **B3** (1991) 2220.
[3] LÜTJENS, H., BONDESON, A., ROY, A., Comp. Phys. Comm. **69** (1992) 287.
[4] WARD, D.J., JARDIN, S.J., to appear in Nucl. Fusion **32**, 1992.
[5] BONDESON, A., VLAD, G., LÜTJENS, H., to appear in Phys. Fluids **B4**, 1992.
[6] LAO, L.L., et al., Phys. Fluids **B4** (1992) 232.

*On leave from Uppsala University, Sweden

FINE STRUCTURE IN TOKAMAK OPERATING REGION

Li Linzhong, Deng Chuanbao, Li Guoxiang, Guo Dequan, Xie Jikang, Huang Rong
Institute of Plasma Physics, Hefei, 230031, P.R. China

The researches of controlled nuclear fusion have showed that there is a stable operating regime of Tokamak. The boundary of the stable operatiing regime has been studied in detail, but its internal structure has still not been researched. Many experimental phenomena on HT-6B Tokamak showed that different plasma parameters had different discharge characteristics. Therefore, we studied the dependence of discharge characteristics on plasma parameters all-sidely and systematically. We have got the fine structure of stable operating regime of Tokamak/1/.

1. THE REGULATION OF TOKAMAK FINE STRUCTURE

In our experiments of fine structure of operating region, the line average electron density n_e and the safety factor at plasma edge q(a) were used as basic adjustable parameters. All diagnostics on the HT-6B Tokamak were used for measuring various plasma parameters/2/. Through a large number of experimental observations, we have found that:

"In the diagram on the n_e - q(a) parameters plane, the high density limit, the runaway limit, the low q limit, and the high q limit (low current limit) enclosed a stable operation area. There are five subdivied regions with different properties in the area: MIID-oscillation region, transition region, sawtooth region, energetic electron region, and runaway region{Fig.1}. The boundary and size of the five regions are varied slightly with impurity conditions, discharge parameters and device states, but the five regions always exist and always emergy successively in above order with the decrease of n_e."

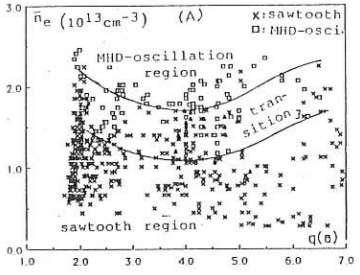

<- Fig.1 (A) distribution of discharge types

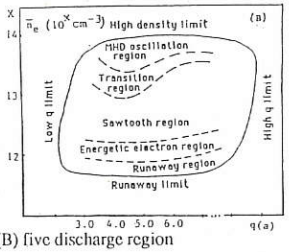

(B) five discharge region

When n_e is too high, because of disruption instability, the discharge is always distroyed. So every Tokamak has a high density limit. In a small region beneath this limit, the fluctuation signals on soft X-ray are the intense MHD-oscillations with high frequency like sine wave. The frequency in HT-6B is about 20 kHz to 25 kHz. We call this region MHD-oscillation region. The signals of m = 2 and m = 3 perturbations are stronger than the other regions. Hard X-ray radiation is much weaker than that in the sawtooth and energetic electron regions. When density is decreased to the range from 0.4×10^{13} to 1.2×10^{13}cm^{-3}, SX signals usually present as strong sawtooth oscillations, so this range is called sawtooth region. When the q(a) is above 5.5, the sawtooth region expands to higher density area. Because of the different n_e , impurities, and plasma current, the m = 1/n = 1 oscillations overlaped on sawtooth are sometimes weak, sometimes obvious. Generally speaking, the m = 1/n = 1 oscillations are weaker at the low n_e part of the sawtooth region, and stronger with the increase of n_e. The period, amplitude, rising speed and dropping slope of sawtooth all somewhat vary with n_e.

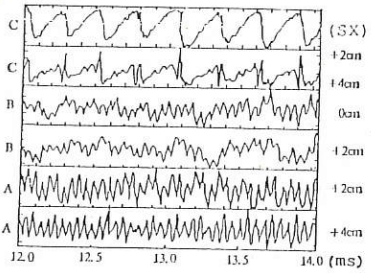

Fig. 2 SX waveform. A: MHD-oscil. region,
B: transition region,
C: sawtooth region

Between sawtooth and MHD-oscillation regions, there is a transition region. In this region, the discharges may be MHD 20kHz oscillation or may be sawtooth. In the duration of a discharge if the n_e changed, the discharge may be changed from MHD-oscillations to sawtooth, or on the contrary, from sawtooth to MHD-oscillations. In this region, the sawtooth are often overlaped by strong m = 1/n = 1 oscillation (Fig. 2).

When electron density ne is below 0.2×10^{13}cm^{-3}, it can be found that the hard X-ray radiation are strengthened enormously by one to two orders than that in transition region and its appearance is earlier than that in sawtooth region. Sometimes on hard X-ray signals tha clear sawtooth oscillations corresponding to soft X-ray sawtooth may be found. In this case, the energetic part of SX energy spectrum rises and its linear part shortens, sometimes even no linear part appears. This area is called energetic electron region. If the electron density be lowered continuously, a great number of

energetic electrons will bombard limiter or wall of vacuum vessel. At this case, a lot of spiles appear on the signals of loop voltage and plasma current, sometimes stronger undulations occure. This is the runaway region.

2. THE RESONANT REGION OF RHF

When the fine structure was studied, the effects of l = 2 and l = 3 RHF (Resonant Helical Field) on each discharge region were also surveyed. The experiments show that the effects of RHF intensely depend on the structure of discharge region. We have found out that a regularity between the effects of RHF and fine structure of discharge region is that:

"In the transition region with lower q(a) and its vicinity, the effect of RHF is most intensely. Its major effect is the suppression of 20 kHz MHD oscillation. Thereby, the discharges change from 20kHz oscillation to sawtooth. Both the l = 2 and l = 3 RHF can suppress the 20 kHz MHD oscillation. They have the effects of prolonging the period and amplifying the amplityde of sawtooth. It is called resonant region. Apart from the resonant region, the effects of RHF decrease gradually and vanish finally." (Fig. 3 and Fig. 4)

On the HT-6B in the range of about q(a) ≤ 4.0, the l = 2 and l = 3 RHF all act. As q(a) increases, the effects of l = 2 reduce, but the effects of l = 3 are still apparent. However, if q(a) is larger than about 4.5, the l = 3 hardly has any effect. When q(a) is lower than 3, because of having no corresponding resonant surface, the effects of l = 3 RHF disappear. The discharge region for best effects of RHF is resonant region with lower q(a) and medium density. This is major operation region of RHF experiments on HT-6B for recent years.

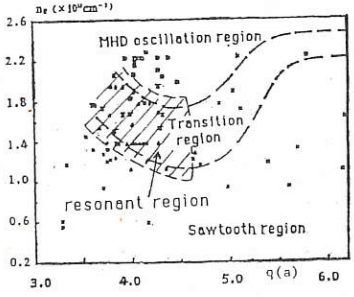

Fig. 3 resoanat region

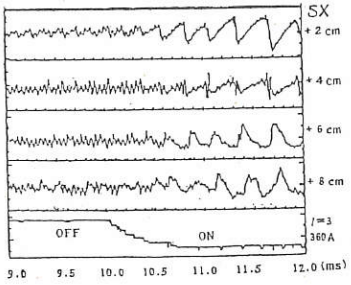

Fig. 4 effect of RHF in resonant region

3. CONCLUSION

According to the experimental studies of the fine structure of discharge region, we can get the conclusions as follows:

(1) The stable operation region of a Tokamak has itself fine structure. In the diagram of n_e against q(a), with decrease of n_e from high value to lower, five discharge regions with different characteristics, appear in succession, that is, MHD-oscillation region, transition region, sawtooth region, energetic electron region and runaway region.

(2) In the MHD-oscillation region, intense MHD oscillations with higher frequency emerges in plasma. In the sawtooth region, sawtooth fluctuation is dominant. In the transition region between above two regions, both sawtooth fluctuation and MHD oscillations with frequency of about 20kHz can appear. In the case of low n_e, energetic electron region and runaway region appear one after one. The boundary of discharge region might shift slightly with the variations of the conditions of impurities and discharge status, but the five discharge regions always exist and their relative position does not change.

(3) In the transition region with low q(a), medium density and its vicinity, there is a resonant region. Its major characteristic are that the RHF has a very strong ability of suppressing MHD turbulence, so it can change the discharge from 20 kHz MHD oscillation to sawtooth, and can prolong period of sawtooth, also amplify amplitude of sawtooth. This region is very sensitive to the external RHF and impurity conditions, so that the experimental phenomena are most plentiful here.

(4) The actions of RHF occure mainly in the resonant region. Apart from this region the effect of RHF reduce and vanish gradually.

4. DISCUSSION

(1) Every Tokamak has its own fine structure of discharge region and maybe it similar to that of HT-6B Tokamak.

(2) Different discharge regions have different discharge characteristics and this cause in different experimental phenomena. so the same experiment carried out in different discharge regions may get different results. Therefore we can suppose that some different results, which come from same experiment on different Tokamak devices, were due to operating in different discharge regions. If the two Tokamak devices operated in same discharge region, the results maybe in agreement.

/1/ Li Linzhong, Huo Yuping, et al., CNIC-00329 (1989)
/2/ Zhao Qingchu, et al., IAEA-CN-44/A-V-5

The high density and high β_{pol} disruption mechanism on TFTR

E. D. Fredrickson, J Manickam, K M McGuire, D Monticello, Y Nagayama, W Park, and G. Taylor
Princeton Plasma Physics Laboratory, Princeton, NJ 08543

J. F. Drake and R. G. Kleva
University of Maryland, College Park, Maryland

Studies of disruptions on TFTR have been extended to include high density disruptions as well as the high β_{pol} disruptions. The data strongly suggests that the (m,n)=(1,1) mode plays an important role in both types of disruptions. Further, for the first time, it is unambiguously shown, using a fast electron cyclotron emission (ECE) instrument for the electron temperature profile measurement, that the (m,n) = (1,1) precursor to the high density disruptions has a 'cold bubble' structure. The precursor to the major disruption at high density resembles the 'vacuum bubble' model of disruptions first proposed by Kadomtsev and Pogutse.

Previous studies of disruptions in hot, high β_{pol} plasmas on TFTR have revealed that the precursor is an (m,n) = (1,1) mode[1]. However, reconstructions of the precursor indicate that it has a kink-like (rather than island-like) structure. This precursor is found to have a very rapid growth rate, often in excess of 10^3/sec. A large, non-thermal burst of electron cyclotron emission lasting 100 - 200 μsec is observed before the thermal transport phase. The thermal transport phase is a rapid (≈200 μsec), structureless collapse of the electron temperature profile.

Studies of disruptions in ohmic plasmas at high density have also found that an (m,n)=(1,1) mode plays an important role. Examples of minor and major disruptions will be discussed below where the precursor has the form of a (1,1) 'cold bubble' or 'vacuum bubble'. Examples of major and minor disruptions in an 0.7MA ohmic plasma are shown in Fig. 1. The minor disruption begins with a growing hollowness of the electron temperature profile measured on the midplane. It is found that this hollowness is due to an (m,n) = (1,1) 'cold bubble' moving into the plasma core. The precursor continues to grow until the disruption takes place, which flattens the electron temperature across the center of the plasma. This event resembles a sawtooth crash, but the inversion and mixing radii are much larger. For the example shown in figure 1, the inversion radius is 0.28m (near q=1.5) and the mixing radius extends nearly to the q=3 surface at r=0.49 m. The measured Λ ($\equiv \beta_{pol}^{equil} + l_i/2$) remains unchanged, suggesting no change in the

internal inductance. Following the disruption, the edge temperature drops and the profile peaks up to a shape similar to that before the disruption, including the flattened region within the q=1 surface (profile 'd'). The sawtooth inversion radius and the region of flatness in the central T_e profile following the minor disruption are only slightly reduced compared to that before the disruption. Thus, although the electron temperature is flattened out to the q≈3 surface, there is no evidence for a similar re-distribution of the plasma current.

The major disruption begins in much the same way as the minor disruption, with the rapid growth of a 'cold bubble' m = 1 mode. Fast data from the horizontally viewing x-ray camera is available at the time of this major disruption, and it shows a vertically asymmetric collapse of the soft x-ray emissivity profile, supporting the model of the cold bubble shape for the precursor. The growth of the precursor for the major disruption ($\gamma \approx 5 \times 10^3\ s^{-1}$) is about 5 times faster than for the minor disruption ($\gamma \approx 1 \times 10^3\ s^{-1}$). While the central electron temperature is even hotter at the time of the major disruption, the temperature beyond the q = 1.5 surface is lower.

At the end of the crash phase the Λ is seen to decrease sharply (Fig. 1), suggesting a redistribution of plasma current. (In this figure, the relative timing between the temperature and magnetics diagnostics was determined from comparison of the synchronized fast soft x-ray camera and Mirnov coil data.) The change in Λ from 1.15 to 0.85 is consistent with a flattening of the current profile to the q ≈ 3 radius (the β_{pol} is ≈ 0.1 at this time). This suggests that in this case either the m=1 mode, or modes excited during the crash, led to a reconnection or a destruction of the magnetic flux surfaces and a broadening of the current profile. The central electron temperature remains about 1 keV for several milli-seconds following the major disruption, then the temperature abruptly drops to less than 100 eV and the current quench phase begins. It is not known at this time what is responsible for this final temperature drop.

The difference between the minor and major disruptions may be understood in the following context: we assume that q(r) is flat and that the bubble is produced by the magnetic reconnection over an annular ring of width δr located at a radius r_s (with $\delta r << r_s$). An estimate of δr can be obtained from the radius r_b of the cold bubble, $\delta r = r_b^2/2r_s$. Taking r_b as the radius of the bubble at the half depth and r_s the radius of the cold plasma shoulder on the T_e profile, we find that for the minor disruption $\delta r \approx 0.037$m while for the major disruption $\delta r \approx 0.021$ m. Thus, the reconnection layers are quite narrow. The effective resistive timescale is approximately $\tau_R = 4\pi(\delta r)^2/\eta c^2$. For the minor disruption

the bubble growth time, $\tau_b \approx 0.8$ms while $\tau_R \approx 3.3$ms (based on the 200 eV edge temperature). Thus, since $\tau_b << \tau_R$, the mode in this case must be categorized as an internal kink. The internal kink has little effect on the current profile, producing a q profile which is flat and close to unity. This conclusion is also consistent with the absence of a large change in the Λ, which would be expected to change significantly as a result of the modification of the current profile by the external kink.

For the major disruption, $\tau_b \approx 0.2$ ms and $\tau_R \approx 0.34$ ms (based on the 100 eV edge temperature) so that $\tau_b \approx \tau_R$. Thus, the formation of the bubble in the case of the major disruption is driven by a quasi-external kink. The external kink can produce a non-monotonic q profile in which q(0) can be significantly greater than unity. Such a profile is unstable to a range of modes with $m \geq 2$ and led to significant broadening and disruption of the current in a recent 3-D resistive MHD simulation of the density limit[2].

The internal (m,n) = (1,1) cold bubble precursor structure has also been seen in disruptions at moderate density and low q(a) ($\approx$ 2.5) (Fig. 2). The density for this case is well below the Greenwald limit, but the phenomenology of the disruption appears similar to those studied above. Again, the edge electron temperature had collapsed and the central electron temperature profile was very flat, implying very rapid thermal transport (and possibly low shear) within the q=1 radius. In the fast ECE data from the grating polychromator and the soft x-ray data it was possible to observe a cold bubble moving downward (at this toroidal location) into the core of the plasma at a speed of 2×10^4 m/s. The growth rate of the precursor mode inferred from this measurement is $\gamma \approx 1 \times 10^4$ s^{-1}.

These studies of high density and high β_{pol} disruptions on TFTR have shown that, while there are important differences, the disruption precursor in both cases has a large growth rate and an (m,n) = (1,1) structure. While it is not known which type of disruption is more relevant to reactor plasmas, in either case the nature of the instability precludes active external feedback control. The high density disruption studies do suggest that active control of the edge temperature might be used to prevent the major disruption.

Acknowledgements -

The authors would like to thank D. Monticello for useful discussions and the TFTR group for its continued support. This work was supported by U.S. DoE Contract No. DE-AC02-76-CHO-3073.

[1]E D Fredrickson, K M McGuire, et al., IAEA, Washington DC, Oct 1990.

[2]R G Kleva and J F Drake, Phys. Fluids B **3** (1991) 372.

Figure 1

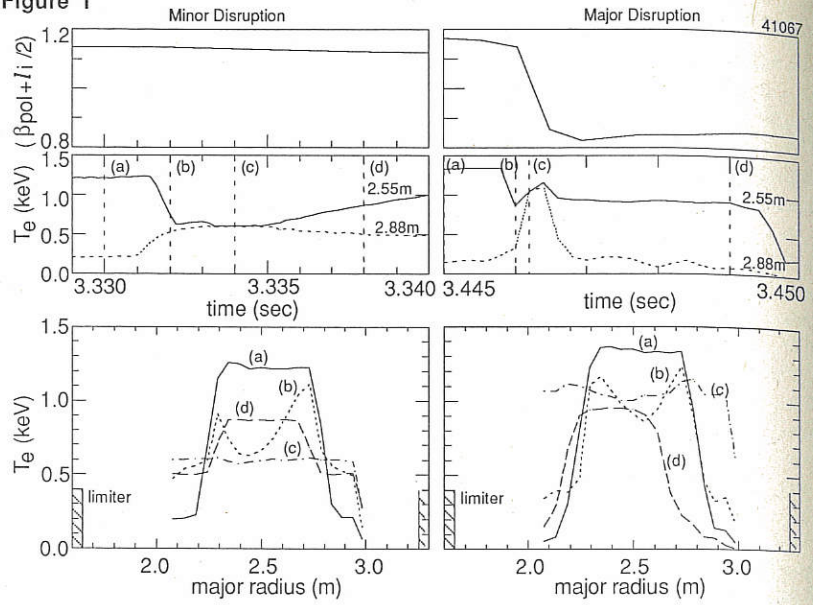

Figure 2

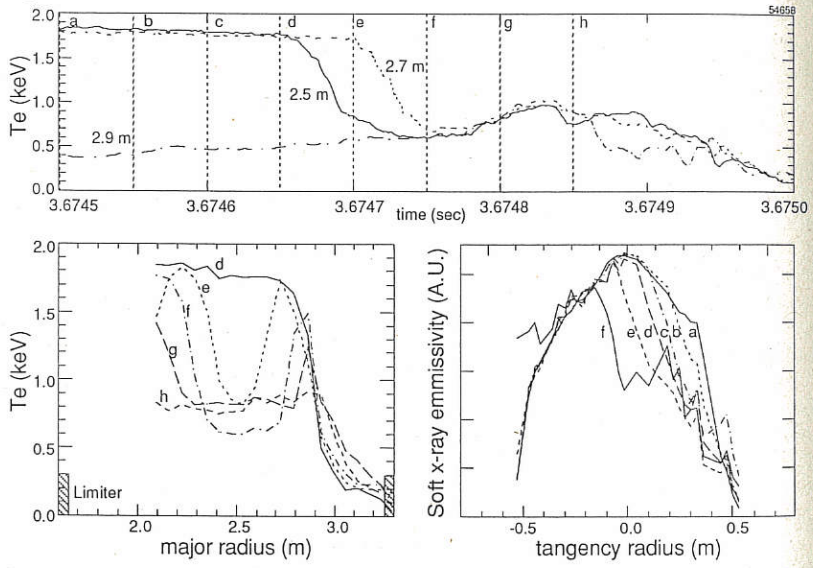

GENERATION AND LOSS MECHANISMS OF RUNAWAY ELECTRONS FOLLOWING DISRUPTIONS IN JET

R D Gill and A W Edwards

JET Joint Undertaking, Abingdon, Oxon., UK

The generation and loss of runaway electrons following plasma disruptions have potentially serious consequences in large tokamaks due to the ensuing damage produced if the electrons are dumped onto the limiter or the vessel walls. In JET, large runaway currents are produced in discharges with carbon limiters, with reduced currents for X-point configurations. Discharges with Be limiters generally produce few runaways. This paper will be concerned with establishing an understanding of the runaway production and loss in carbon limited discharges and using this to both evaluate possible means of runaway control and establish possible reasons for the different behaviour with C and Be.

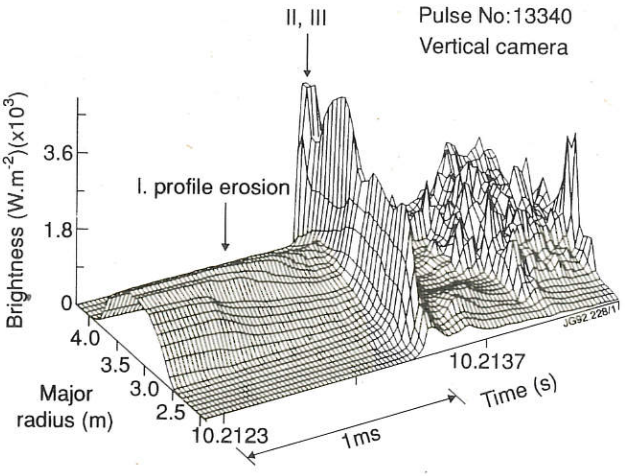

Fig 1 On the soft X-ray signals the disruption appears initially as an erosion of the profile. This is followed by a huge spike on the X-ray emission coincident with the negative voltage spike. After the spike the plasma emission profiles are no longer smooth, with rapid variations in emission for small changes in both time and space.

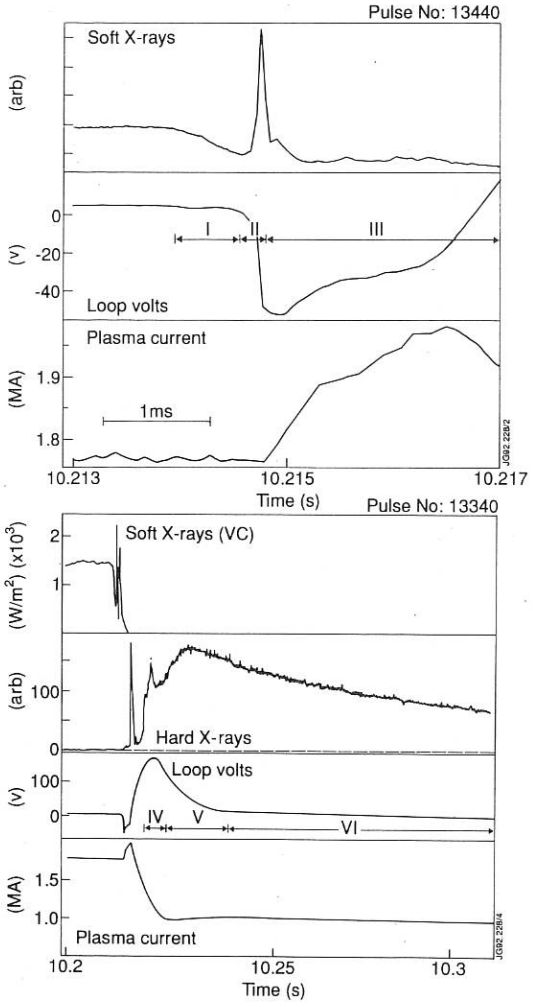

Fig. 2. The different stages of the disruption and runaway generation process are shown. The first three stages are shown in the figure above with the remaining processes shown the figure below which is on a 28 times slower timescale.

Runaway Production

Plasma disruptions are complicated phenomena often preceded by a variety of mhd phenomena. However, the main features of a disruption leading to runaway production may be summarised by the following sequence. The different stages are shown on fig. 2

I Erosion of central profile probably due to the interaction of many modes[2]). The temperature falls, profiles flattens. Generation and trapping of negative voltage within the plasma[3]). This is the start of the disruption.

II Heating of plasma edge, escape of negative voltage spike[3]), greatly increased soft X-ray emission due to impurity influx.

III Rapid drop of T_e and soft X-ray emission, large increase in loop volts, start of generation of runaways.

IV Bulk plasma cold, gradual build up of runaway current resulting in drop of loop volts.

V Loop volts drop to about zero, runaways now have MeV energies and are located at small R.

Either VIA Runaways dumped on wall due to inadequate control of their position. Plasma current drops to zero.

or VIB Runaways stabilised at small major radius (R) and lose energy mainly by synchrotron radiation. Substantial plasma current (I) remains.

These stages are illustrated in figure 2. The sharp spike on the soft X-rays marks the point at which runaway production starts. This increased X-ray emission is initially produced by the influx of the impurities into the plasma[4]), but the impurities also cool the plasma with a subsequent decrease in X-ray emission coincident with the drop in the loop voltage. Analysis of soft X-ray signals from detectors with different filters confirms this picture with the density increasing rapidly by a factor of ~2 in 60μsec followed by an extremely rapid fall in plasma temperature. This is the point at which the runaway generation is taken to start as the drop in electron temperature will increase the ratio of the electric field (E) in the plasma to the Dreicer electric field substantially where

$$E/E_D \propto Z_{eff}\, I/n_e\, T_e^{1/2}$$

Once the runaway regime has been reached the energy of the runaways may be calculated approximately from $W^2 = p^2c^2+m^2c^4$ with $p = \int eEdt$. The value of T_e during the runaway phase is not well known, but it must be quite small (ten's of eV) as the loop volts, V, is large when dI/dt=0. An estimate for W may be found by using the measured value of V. This does not allow for differences which may exist between the E at the centre of the plasma compared with the value outside the vacuum vessel where V is measured. This calculation shows that the runaway energy increases up to 35 MeV over a timescale of 12 ms in approximate agreement with the characteristic rise time seen in the hard X-ray signal (fig. 2). The build-up of the runaways has also been clearly observed by a Ge PHA system which records a spectrum in the 0-400 keV region. After a substantial runaway current is produced the loop volts drop to ~0 and the hard X-ray signal then shows a smooth decay. At this time the current channel is stabilised at a small minor radius. In other discharges the position of the runaways is not stabilized and then the runaways are frequently dumped on the vessel walls causing damage.
The hard X-ray signal originates in bremstrahlung from runaway - background plasma interactions. This radiation is highly peaked in the direction of the runaways and is observed in the hard X-ray detectors only after scattering from material in the region of the main horizontal ports. The efficiency of detection above threshold depends only weakly on energy and the observed decay represents a gradual loss of energy from the runaway beam principally by

synchrotron radiation. Typical timescales are about 75 ms which correspond to synchrotron loss times of relativistic electrons in orbits with radii 12 cms. This is very much less than the major radius of the orbit and probably corresponds to the effective radius of the electrons as they move in the combined toroidal and poloidal field. An alternative explanation would be that the electrons were scattered from their original trajectories parallel to **B.** A scattering angle of ~5° would be sufficient to account for the observed decay time.

Avoidance of runaway damage

1) The runaways build up over a period of 15 ms after the negative voltage spike which itself appears ~ 1 ms after the initial disruptive event. The runaway generation could be prevented by decreasing E/E_D during this period compared with the values which occur "naturally". One possibility would be to admit gaseous substance immediately after the start of the disruption to produce higher n_e, T_e and lower Z_{eff}. Clearly H or He would be suitable. The fact that Be limited discharges produce many fewer runaways than C is possibly due to this effect.

2) If runaways are produced then if their position was properly controlled at the plasma centre their energy would be dissipated by synchrotron radiation which would be distributed over relatively large areas of the torus walls. This would not cause damage to the vessel walls. That this is sometimes possible is proved by the stable runaway discharge illustrated by the figures.

3) A crude, but probably effective means of limiting runaway damage to the machine would be to use a sacrificial limiter which would be moved to intercept the relativistic beams. However this method would seem to have disadvantages compared with methods (1) and (2).

References

1) J A Wesson et al., Nuclear Fusion 29 (89) 641
2) A Bondeson et al., Nuclear Fusion 31 (91) 1695
3) J A Wesson et al., Nuclear Fusion 30 (90) 1011
4) D J Ward et al., Controlled Fusion and Plasma Heating (Dubrovnik EPS) 1 (88) 330.

DENSITY TURBULENCE AND DISRUPTIVE PHENOMENA IN TEXTOR

G. Waidmann, M. Jadoul*, G. Kuang

Institut für Plasmaphysik, Forschungszentrum Jülich GmbH,
Association EURATOM-KFA, D-5170 Jülich, F.R.G.

*Laboratoire de Physique des Plasmas - Laboratorium voor Plasmafysica,
Association EURATOM-Etat belge - Associatie "EURATOM Belgische Staat",
Ecole Royale Militaire - Koninklijke Militaire School, Brussels, Belgium

Introduction

Disruptive processes are observed in tokamak plasmas not only at the operating limits (density limit or q-limit) but can be found under a variety of experimental conditions. Large forces are exerted then on vessel components and support structures. The sudden release of stored plasma energy presents a serious erosion problem for the first wall already in the next generation of large tokamak machines. Strong energy losses from the plasma and an influx of impurities are already present in minor plasma disruptions which do not immediately lead to a plasma current termination. The rapid loss of energy confinement was investigated within the framework of a systematic study on plasma disruption phenomena in TEXTOR.

Density fluctuations and disruptive evolution

A frequent precursor situation found prior to a disruption in TEXTOR /1,2/ and other tokamaks is the simultaneous appearance of several MHD modes. The most prominent ones are the $m = 2$ and $m = 1$, $n = 1$ modes. A 10-channel ECE system was used to detect and localize T_e-oscillations associated with MHD activities. A collective 2mm-wave scattering diagnostic was installed to study the density fluctuation behaviour in different radial regimes of the TEXTOR plasma /3/. The appearance of MHD activity is also recognized by a periodic enhancement of the scattered mm-wave power above the normal fluctuation level of an Ohmic plasma. Fig. 1 shows the last 100 ms before disruption for a discharge with I_p = 350 kA, q(a) = 3.8 and $\bar{n}_e = 2.0 \times 10^{13}$ cm^{-3}. A drastic change appears, however, when a mode locking process occurs. Fig. 2 demonstrates for the

same shot the change in the fluctuation level when an energy quench happens after the overlapping of two MHD modes, here m = 2 and m = 1. The scattering volume was close to the surface where the rational q = 2 is expected. For a given radial wave vector $\vec{k}_r$ = 22.5 cm^{-1} the evolution of three frequencies is shown. The scattered power for high frequencies (f ≥ 0.7 MHz) grows exponentially from a small fluctuation level to a rather high value. Fig. 2 shows for the same time interval two ECE-signals from the neighbourhood of the scattering volume. Deeper inside the plasma (R[EC3] = 197 cm) a T_e-drop is recorded whereas further out (R[EC9] = 206 cm) a steep heat pulse is detected. Between these two radial positions the rise of the density fluctuation amplitude (R[SCAT] = 200 cm) was measured. At the very time of the growing density fluctuation the $T_e(r)$-profile erosion is shown in Fig. 3. In time steps of 100 μsec the beginning $T_e(r)$-profile collaps is visualized. This is the start of the final energy quench phase. The arrow in the figure marks the radial position of the scattering volume in the equatorial plane of the plasma.

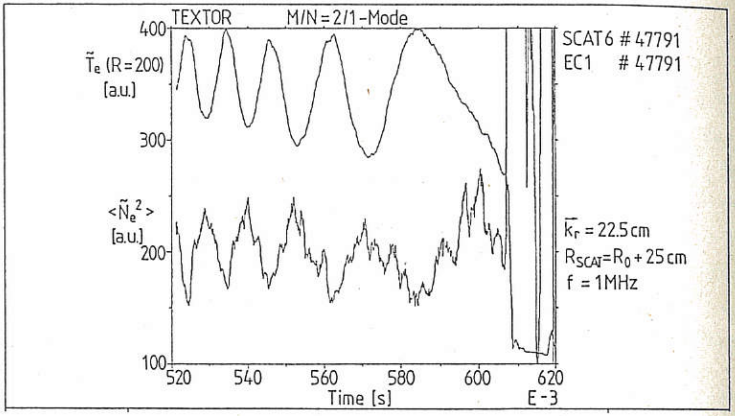

Fig. 1 M = 2 mode precursor detected by ECE (top) and periodic enhancement of collective wave scattering (bottom) show a strong phase correlation prior to the plasma disruption.

MHD-triggered strong turbulence

The evolution of the density fluctuation spectrum from the time of MHD precursors to the final energy quench is shown in Fig. 4. The spectral density function $S_K(f)$ is plotted versus frequency f in a logarithmic presentation. A typical decay index $\gamma \approx 3$ is found

here in the MHD active phase. A remarkable change of the spectrum is observed with the onset of the T_e-profile erosion. The decay index changes finally to $\gamma \approx 1.5$. The higher fluctuation frequencies, measured up to f = 2 MHz, show up clearly now. The spectrum has changed its shape and amplitude. The frequency broadening of the spectrum emphasizes the turbulent development of the fluctuations. The prompt emission of a single, steep heat pulse HP, detected by the outermost ECE channel at R = Ro + 31 cm in Fig. 2, tells that a new heat loss channel has been opened.

In the radial regime between the q = 1 and q = 2 surface a field line stochastisation is expected to occur and was numerically already modelled /4/. This leads to a perturbation in the local pressure equilibrium. T_e-perturbations, i.e. T_e-drop, are detected by ECE measurements. Density perturbations show up in this phase of dynamic changes even in the line integrated interferometric measurements. Very pronounced impurity increase is seen from CV-carbon line emission. Strong turbulent density fluctuations, initiated by MHD-mode interaction, seem to be the responsible process for the enhancement in the scattered power and the abrupt loss of energy confinement.

The turbulent density fluctuations are still observable in the current decay phase when, after impurity influx and strong loop voltage increase, a transient megawatt Ohmic heating takes place in the decaying plasma. A turbulent phase was recognized already for a short time interval early in the current ramp-up when skin effects play a role. During this critical start-up phase current disruptions are encountered occasionally.

The frequency spectra observed before the disruptive phase can be interpreted as drift wave turbulence phenomena. The amplitude of the fluctuations increases during the MHD development but the decay index remains essentially constant. In the energy quench, however, and during current decay after the disruption another type of turbulence must be present. The sudden frequency broadening into the MHz range requires another physical explanation. Rapid radial density changes observed by a multichannel FIR-interferometer can qualitatively explain via their Doppler shift the frequency increase in the spectrum.

References

/1/ G. Waidmann, G. Kuang, Nuclear Fusion, 32, No. 5 (1992)
/2/ G. Kuang, M. Jadoul, G. Waidmann, Verhandlungen der DP, DPG-Frühjahrstagung Hannover, March 1992
/3/ M. Jadoul, G. Waidmann, Controlled Fusion and Plasma Physics (1989), Proc. 16th EPS Conf., Venice, Vol 13B, Part II, p 529
/4/ A. Bondeson et al., Nuclear Fusion, 31, No. 9 (1991) 1695

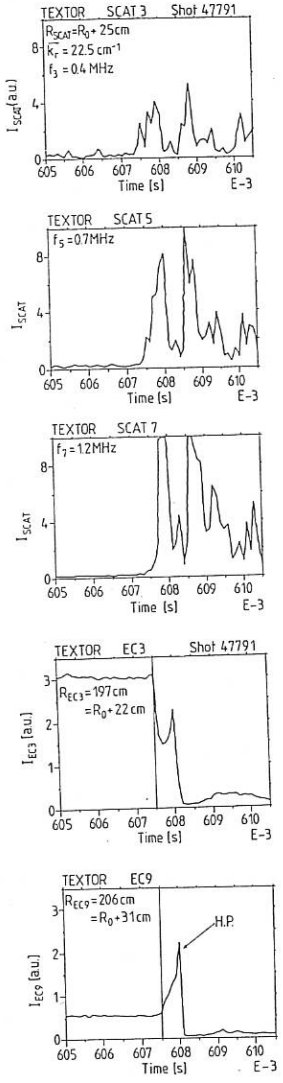

Fig. 2

Scattered wave power at frequencies f = 0.4, 0.7 and 1.2 MHz from a radial position R_{SCAT} = Ro + 25 cm and two ECE-signals from the neighbourhood of the scattering volume

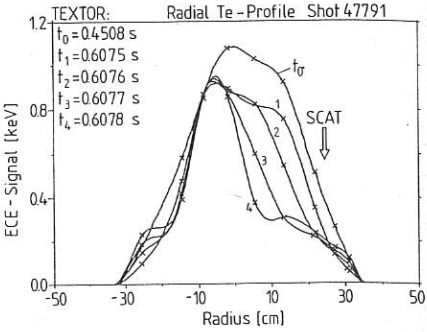

Fig. 3 T_e-profile evolution at the beginning of the energy quench, the time of enhanced scattering of wave power

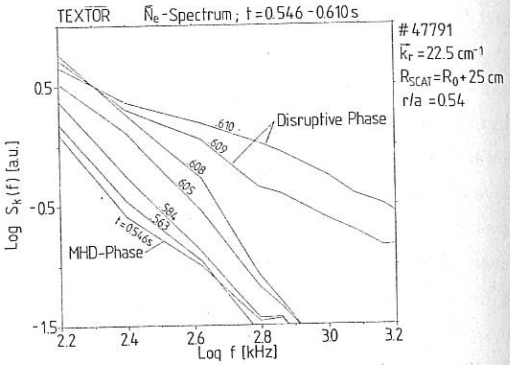

Fig. 4 Electron density fluctuation spectrum at different times in the evolution from MHD-precursors to the energy quench phase

Electron Density Profile and Microturbulence Modification by MHD Instabilities

D.L. Brower, C.X. Yu[1], Y. Jiang,
J.Y. Chen[2], H. Lin[2], N.C. Luhmann, Jr., W.A. Peebles, X.Z. Yang[3], S.J. Zhao[1]

Department of Electrical Engineering, and Institute of Plasma and Fusion Research,
University of California, Los Angeles, California 90024, USA

[1] University of Science and Technology of China, Hefei, PRC
[2] Fusion Research Center, The University of Texas, Austin, Texas 78712, USA
[3] Institute of Physics, Academia Sinica, Beijing, PRC

Detailed information on the evolution of the electron density profile has been obtained during large-amplitude tearing instabilities, locked modes and disruptions on TEXT-Upgrade. For tearing instabilities, density islands which can be directly correlated with magnetic islands are observed as a localized flattening about the mode rational surface. As a precursor to a major disruption, the density island rotation is slowed as the amplitude increases eventually leading to a locked mode, in a fashion analogous to that for magnetic islands. The resulting distorted density profile can persist for several milliseconds prior to the actual disruption, immediately after which the edge density increases dramatically creating a hollow density profile. Previously, the effect of tearing instabilities on the plasma magnetic surfaces and temperature profiles has been well documented. Here, similar information is available for the electron particle distribution providing further insight into the nature of the instabilities. For the case of quasi-steady-state MHD activity on TEXT, perturbation of the plasma profiles, in particular the density and potential, can be correlated with changes in the microturbulent density fluctuation amplitude and frequency spectra. This information can be used to investigate the nature and drive of the electrostatic fluctuations.

It is experimentally observed that Mirnov activity can significantly affect the spectral distribution and magnitude of the turbulent density fluctuations through changes in local parameters and their scale lengths. Typical density profiles viewing the island X-point and O-point are shown in Fig. 1(a), for during large-amplitude MHD activity with f_{MHD}=1 kHz. At the O-point, the density profile is strongly modified by the dominant m=2,n=1 tearing mode as flattening occurs in the region of the q=2 surface. Time-averaged density profiles tend to broaden as well with increasing magnetic island size.[1] The radial extent of the flattened region in the density profile can be defined as the density island width. Island widths can also be deduced from the Abel-inverted profile of the density perturbation, as shown in Fig. 1(b). The island width on the high-field side of the torus is measured to be $\simeq$10 cm while that on the low-field side is ($\simeq$6 cm) for $f_{MHD} = 1\ kHz$. Both the density island width and the maximum perturbation to the line averaged density at approximately $r_{q=2}$ [see Fig. 1(c)] are larger on the high-field side and vary inversely with of f_{MHD}.

In order to investigate the relation between MHD activity (i.e. tearing modes) and plasma microturbulence, the density fluctuation frequency spectra for poloidal wavenumbers k_θ at varying levels of Mirnov activity have been examined. The time-averaged (i.e. over approximately 10 cycles) turbulent spectra, as measured via heterodyne far-infrared laser scattering during discharges with low ($\tilde{B}_\theta/B_\theta \leq 10^{-3}$, $f_{MHD} = 7.1\ kHz$), moderate ($\tilde{B}_\theta/B_\theta \simeq 5 \times 10^{-3}$, $f_{MHD} = 5.0\ kHz$) and large ($\tilde{B}_\theta/B_\theta \geq 10^{-2}$, $f_{MHD} = 2.4\ kHz$) amplitude Mirnov oscillations, are shown in Fig. 2, for $k_\theta = 12\ cm^{-1}$ [$k_\theta \rho_s \simeq 0.9$]. As previously reported,[1] for gas-fueled plasmas in TEXT with densities $2 \times 10^{19}\ m^{-3} \leq \overline{n}_e \leq 4 \times 10^{19}\ m^{-3}$ and quiescent MHD activity (i.e. low amplitude), the frequency spectra [see Fig. 2(a)] are typified by a distinct

large-amplitude broadband peak at negative frequencies, which corresponds to propagation in the electron diamagnetic drift direction. The measured dispersion relation for the turbulent density fluctuations agrees well with that predicted for electron drift waves when an $E_r \times B_\phi$ spectral shift is included. Since the $E_r \times B_\phi$ correction accounts for the bulk of the spectral shift, unambiguous identification of the electron drift wave dispersion is difficult. However, a roll-over in the dispersion relation for $k_\theta > 7\ cm^{-1}$ is consistent with finite ion temperature and mass effects which are theoretically expected.[2] In addition, the spectral width $\Delta\omega/\omega_e^* \geq 4$ appears to be a real feature of the turbulence and not due to a radially varying electric field across the sample volume.

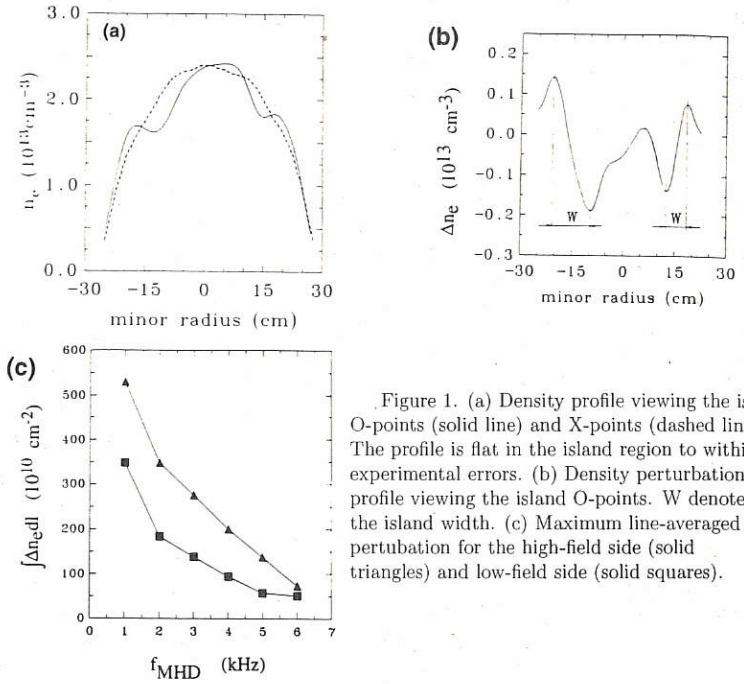

Figure 1. (a) Density profile viewing the island O-points (solid line) and X-points (dashed line). The profile is flat in the island region to within experimental errors. (b) Density perturbation profile viewing the island O-points. W denotes the island width. (c) Maximum line-averaged density pertubation for the high-field side (solid triangles) and low-field side (solid squares).

At moderate to high levels of MHD activity, the frequency spectra at each wavenumber measured are significantly modified, as shown in Figs. 2(b) and (c). A notable feature readily distinguished from these broadband spectra is that the large-amplitude negative frequency peak shifts towards zero frequency as the MHD amplitude increases. The fluctuation mean frequency decreases linearly with increasing MHD frequency. Time-resolved frequency spectra show virtually no change in either $\overline{\omega}$ or $\Delta\omega$ when looking at island X and O points. This implies that their is no m=2 component to the plasma potential or radial electric field, consistent with measurements.[3]

Changes in the fluctuation amplitude which correlate with f_{MHD} and consequently the plasma parameter L_n indicate that an increase in the turbulence magnitude, $S_k \propto \tilde{n}_k^2$, directly correlates to a decrease in the density scale length. From the time-resolved density fluctuation amplitude data (integrated over all frequencies), as shown in Fig. 3(a) for $k_\theta = 9\ cm^{-1}$,

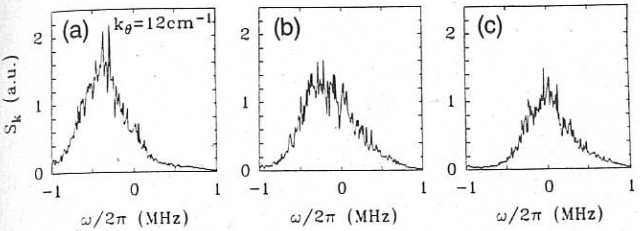

Figure 2. Time-averaged frequency spectra for $k_\theta = 12\ cm^{-1}$ with (a) low, (b) moderate, and (c) large amplitude Mirnov oscillations. Negative (positive) frequency corresponds to the electron (ion) diamagnetic drift direction in the laboratory frame of reference.

clear maxima and minima are observed which correlate with the island X-point and O-point, respectively. The density fluctuation amplitude, which is typically percent level, is modulated by $\Delta\tilde{n}_k/\tilde{n}_k \simeq \pm 20\%$ during the MHD cycle for large magnitude islands. Similar observations are made at the other values of k_θ investigated. Recalling the density profile information provided in Fig. 1, one can readily see that $\tilde{n}_k$ and L_n at the island radius are inversely proportional. Mixing length estimates of the density fluctuation amplitude give the saturated limit as

$$\frac{\tilde{n}}{n_e} \simeq \frac{1}{\overline{k}_\theta L_n} \quad , \tag{1}$$

for the case of isotropic turbulence. Since n_e changes are small and $\overline{k}_\theta$ does not appear to change, one would expect $\tilde{n}$ to scale inversely with L_n. The relationships between the time-averaged fluctuation amplitude, L_n at the island (q=2) radius, and f_{MHD} are provided in Fig. 3(b). Here S_G refers to the portion of the total fluctuation level S_k which can be attributed to electron drift wave type turbulence originating in the island region. While both S_k and S_G decrease with increasing L_n, better agreement with the mixing length estimate is achieved by using the parameter S_G.

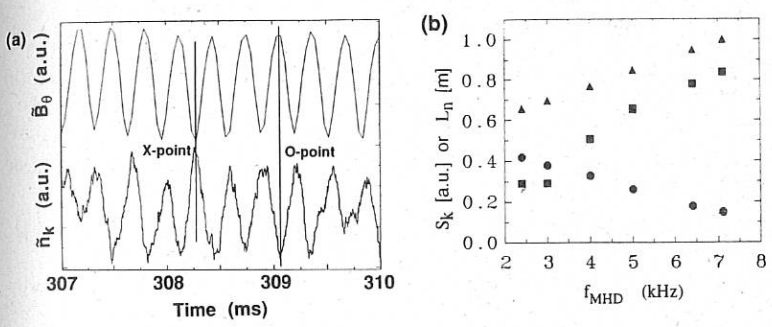

Figure 3. (a) Temporal evolution of the magnetic and density fluctuations. (b) Time-averaged fluctuation amplitude S_k (triangles) and S_G (squares), and island region density scale length L_n (circles) for $k_\theta = 7\ cm^{-1}$.

Changes to the density profile are measured with a 15 channel [channel spacing $\Delta x = 3$ cm] interferometer. Data for vertical chords ranging from x = -0.7 to -15.7 cm, where the negative sign denotes the high-field side, are shown in Fig. 4(a) for a time period about a major disruption [t=355 ms] on TEXT-Upgrade. Large-amplitude Mirnov oscillations [$\Delta n_e/n_{eo} = 15\%$ at x=-9.7 cm] are clearly seen on the interferometer traces with phase changes occuring at x = 17.3 [not shown], -3.7 and -15.7 cm at time -7.5 msec before disruption. Distortions in the profile are observed due to the island structure. The Mirnov oscillations persist until -5 msec at which time the island rotation ceases leading to a locked mode which continues up to the actual disruption. The density profile during the locked mode phase at -4 msec is shown in Fig. 4(b) and looks quite similar to that observed at an island O-point. This shape is maintained up to the disruption, immediately after which the density increases dramatically [see Fig. 4(a)] and the profile becomes hollow as shown in Fig. 4(b) for +0.2 msec. After a few milliseconds, the Mirnov oscillations resume and the profile evolves to a shape that is roughly centrally peaked as the plasma continues to decay. From this data, a tomographic reconstruction can be generated by producing multiple views during a Mirnov cycle as the plasma rotates by the interferometer view.[4] This provides a real-time 3-D view of the plasma electron distribution as the island rotation frequency slows approaching the locked-mode phase and subsequent disruption.

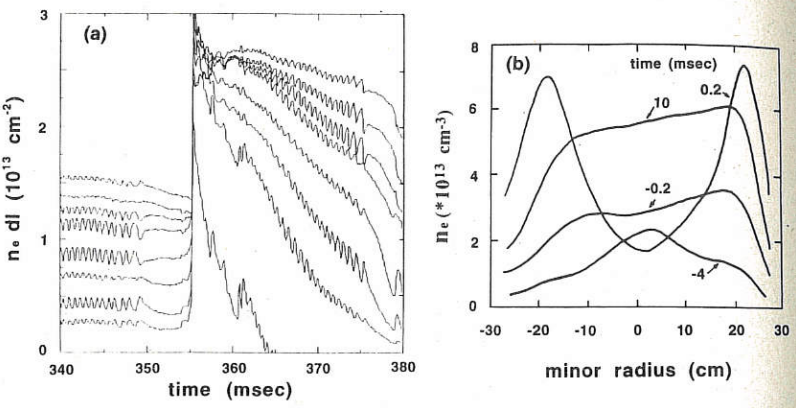

Figure 4. (a) Line-averaged density for chords from x = -0.7 to -15.7 cm with $\Delta x = 3$ cm. (b) Inverted profiles with negative (positive) corresponding to times before (after) the disruption.

This research is supported by the U.S. DoE under grants DE-FG03-86ER-53225 [TASK VIIA] and DE-FG05-88ER-53267.

[1]C.X. Yu, D.L. Brower, S.J. Zhao, R.V. Bravenec, J.Y. Chen, H. Lin, N.C. Luhmann, Jr., W.A. Peebles, Ch.P. Ritz, P.M. Schoch, X.Z. Yang, Phys. Fluids B **4**,381(1992).

[2] Horton, W., in Basic Plasma Physics II, edited by A.A. Galeev and R.N. Sudan (North-Holland, New York, 1984),p.383.

[3]X.Z. Yang, Zhang, B.Z. , Wootton, A.J. , Schoch, P.M., Richards, B., Baldwin, D., Brower, D.L., Castle, G.G., Hazeltine, R.D., Heard, J.W., Hickok, R.L., Li, W.L., Lin, H., McCool, S.C., Simcic, V.J., Ritz, Ch.P., Yu, C.X., .Phys. Fluids B **3**,3448(1991).

[4]J. Howard, W.A. Peebles, D.L. Brower, S.K. Kim, N.C. Luhmann, Jr., Rev. Sci. Instrum. **61**,2829(1990).

INVESTIGATION OF TEARING MODES WITH TOROIDAL COUPLING IN A TOKAMAK WITH ARBITRARY PLASMA CROSS-SECTION AND ASPECT RATIO

C.V.Atanasiu,* L.E.Zakharov,** A.A.Subbotin,** and N.V.Chudin**
*Institute of Physics and Technology of Radiation Devices,
R-76900 Măgurele- Bucharest, Romania
**I.V.Kurchatov Institute of Atomic Energy,
123182 Moscow, Russia

For an axisymmetric toroidal geometry, the individual poloidal harmonics are coupled together, while the toroidal harmonics remain independent; thus, there can be many resonance surfaces for each toroidal mode number and, correspondingly, many $\Delta'_{m/n}$ parameters. The effect of the toroidicity on the tearing modes has been examined in /1,2/. In the present paper, a system of Euler equations of the potential energy functional for toroidal tearing modes in a tokamak with arbitrary cross-section and aspect ratio, has been drawn. Starting from this equations, a numerical algorithm has been developed in order to calculate the perturbations of the flux function and the $\Delta'_{m/n}$ parameter. Writing the general expression of the potential energy W in terms of the perturbation of the flux function instead of the plasma displacement, one obtains the energy functional for the tearing modes /3/. Using a coordinate system α,θ,ζ with straight field lines and considering a pressureless axisymmmetric toroidal configuration, the potential energy can be reduced to the following simple functional /4/ :

$$W = -\frac{1}{8\pi}\int d\alpha\, d\theta\, d\zeta \left\{ \frac{g_{11}}{\sqrt{g}} \left(\frac{\partial\psi}{\partial\theta}\right)^2 - 2\,\frac{g_{12}}{\sqrt{g}}\,\frac{\partial\psi}{\partial\theta}\,\frac{\partial\psi}{\partial\alpha} + \right.$$

$$\left. + \frac{g_{22}}{\sqrt{g}} \left(\frac{\partial\psi}{\partial\alpha}\right)^2 + \psi\,\frac{\partial u}{\partial\theta} \left(\frac{4\pi}{c}\,\frac{F'}{\Psi'} \right)' \right\}, \qquad (1)$$

where the perturbation of the flux function ψ has the expression :

$$\psi = - \frac{\Psi'}{\Phi'} \frac{\partial u}{\partial \theta} + \frac{\partial u}{\partial \zeta} , \quad \mu = - \frac{\Psi'}{\Phi'} , \qquad (2)$$

and $\Psi(\alpha)$, $F(\alpha)$ and $\Phi(\alpha)$ represent the poloidal flux, the poloidal current and the toroidal flux, respectively; g_{ik} is the metric tensor. A Gaussian system of units is used. Note that the m=0 harmonic of the perturbation is absent.

Considering the usual harmonic representation for the perturbation of the flux function ψ :

$$\psi = \sum Y_m(\alpha) \cos(m\theta - n\zeta) , \qquad (3)$$

one obtains the 1-D functional for a set of harmonics $Y_m(\alpha)$

$$W = \frac{n}{4} \int d\alpha \sum_{m=-\infty}^{\infty} \sum_{j=-\infty}^{\infty} \left\{ f_{1j} Y'_m Y'_{m+j} + 2(m+j) f_{2j} Y'_m Y_{m+j} + \right.$$

$$\left. + m(m+j) f_{3j} Y_m Y_{m+j} + \left(\frac{4\pi}{c} \frac{F'}{\Psi'} \right)' \frac{Y_m^2}{\mu - n/m} \right\} \qquad (4)$$

In an arbitrary coordinate system α, ω, ζ, the coefficients f_{ij} are given by the following relations :

$$f_{1j} = \left\langle \frac{g_{22}}{rD} \cos j\theta \right\rangle_\omega , \quad f_{2j} = \left\langle \left[\frac{g_{12}}{r^2 \left\langle \frac{D}{r} \right\rangle_\omega} - \frac{g_{22} \theta_\alpha}{rD} \right] \sin j\theta \right\rangle_\omega ,$$

$$f_{3j} = \left\langle \frac{g_{11} \theta_\omega - 2 g_{12}^2 \theta_\omega \theta_\alpha + g_{22} \theta_\alpha^2}{rD} \cos j\theta \right\rangle_\omega , \quad \sqrt{g} = rD \qquad (5)$$

θ_ω and θ_α are the derivatives of θ in function of the general poloidal angle ω and of the flux-surface label α, respectively. By minimizing, one obtains a system of Euler equations of the potential energy functional :

$$\frac{d}{d\alpha} \left(f_{10} \frac{dY_m}{d\alpha} \right) - m^2 f_{30} Y_m - \left(\frac{4\pi}{c} \frac{F'}{\Psi'} \right)' \frac{Y_m}{\mu - n/m} + \sum_{\substack{j=-\infty \\ j \neq 0, j \neq -m}}^{\infty} \left\{ \frac{d}{d\alpha} \left(f_{1j} \frac{dY_{m+j}}{d\alpha} \right) \right.$$

$$\left. - m(m+j) f_{3j} Y_{m+j} + (m+j) \frac{d}{d\alpha} \left(f_{2j} Y_{m+j} \right) + m f_{2j} \frac{dY_{m+j}}{d\alpha} \right\} = 0 . \qquad (6)$$

Considering only the terms with j=0, one obtains the equations for uncoupled modes.

In a condensed form, the system of equations (6) reads as follows :

$$\mathbf{Y}'' = \mathbf{f}^{-1}(\mathbf{G}\,\mathbf{Y} + \mathbf{V}\,\mathbf{Y}') + S\,\delta_{m}(\alpha-\alpha_{m/n}) \qquad (7)$$

where f,V and G are matrices, while Y is the vector of the flux function perturbations. To obtain a well posed system, a source term has been added in the r.h.s of the equations (7); S is a constant, while the Dirac operator δ_m must be considered as a vector with a single non-zero element corresponding to the resonant surface of the harmonic m/n.

To solve the system (7) with boundary conditions Y=0 for α=0 and α=∞, a nonstandard integration algorithm has been developed. Over the full region a sweep method has been applied; excepting a thin layer around the resonant surfaces, coefficients corresponding to the Runge-Kutta integration method have been written, while in the vicinity of the resonant surfaces, analytic expressions with an error of $O(x^3)$ have been drawn ($x = a-a_{m/n}$). This algorithm has been checked on a cylindrical case, where an analytical solution exists /5/.

As an example of computation, the mode m/n = 2/1, with a parabolic dependence of $\mu(\alpha)$ has been considered. The metric coefficients, as well the dependence of the ellipticity, the magnetic shift, the triangularity etc on α , have been determined from the MHD equilibrium equations. To determine the $\Delta'_{m/n}$ parameter, the same definition as in /4/ has been considered :

$$\Delta'_{m/n} = \left.\frac{Y'_m}{Y_m}\right|_{\alpha_{m/n}+\varepsilon} - \left.\frac{Y'_m}{Y_m}\right|_{\alpha_{m/n}-\varepsilon} \qquad (8)$$

(In paper /4/, for the determination of the $\Delta'_{m/n}$ parameter the coupling effects have not been taken into account.)

The following investigated dependencies are presented : $\Delta'(\varepsilon(\alpha_o))$ for $\alpha_o/R=0$ and fixed $\alpha_{m/n}$ (Fig.1) and $\Delta'(\alpha_o/R)$ for $\varepsilon(\alpha_o)=0$ and fixed $\alpha_{m/n}$(Fig.2). To outline the coupling effects,

in Fig.1 and Fig.2 the dependencies of $\Delta'_{m/n}$ on the ellipticity $\varepsilon(\alpha_o)$ and the aspect ratio α_o/R have been calculated with coupling (curves (a)) and without coupling - by forcing the non-diagonal terms to be zero (curves (b)).One can see that the coupling of the modes leads to an increased value of the $\Delta'_{m/n}$ parameter - i.e. a more unstable tearing mode is obtained.

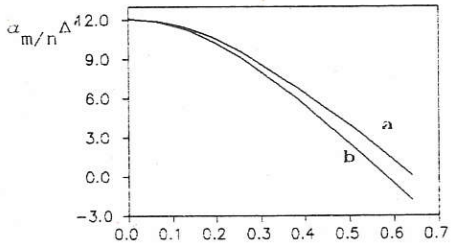

Fig.1 $\Delta'(\varepsilon(\alpha_o))$ dependence for $\alpha_o/R=0$, $m=2$, $\alpha_{m/n}=0.9$
a) with coupling
b) without coupling

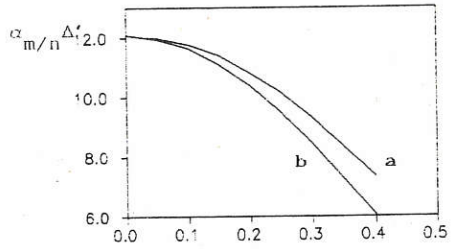

Fig.2 $\Delta'(\alpha_o/R)$ dependence for $\varepsilon(\alpha_o)=0$, $m=2$, $\alpha_{m/n}=0.9$
a) with coupling
b) without coupling

/1/ Glasser A.H., Greene J.M., Johnson J.L., Phys. Fluids, 19,4, 567(1976)

/2/ Connor J.W., Hastie R.J., Taylor J.B., Phys. Fluids B3, (7), 1532(1991)

/3/ Zakharov L.E.,Plasma Physics and Contr. Nucl. Fusion Res., vol.I,689, Innsbruck(1978)

/4/ Zakharov L.E., Subbotin A.A., Chudin N.V., Atanasiu C.V., Plasma Physics and Contr. Nucl. Fusion Res. vol.2, 113, Washington(1990)

/5/ Zakharov L.E., Int. Rep. IAE-3540/16 I.V.Kurchatov Inst., Moscow (1982) (in Russian)

INTERNAL MHD PERTURBATIONS IN T-10 TOKAMAK.

P.V.Savrukhin, D.A.Kislov, E.S.Lyadina, G.E.Notkin, Yu.D.Pavlov
I.V.Kurchatov Institute of Atomic Energy, 123182 Moscow, Russia

ABSTRACT. Internal structure of the plasma perturbations at the density limit disruptions in T-10 were studied with the use of three arrays soft x-ray imaging system. It was found that coupling of the m=1 and m=2 modes leads to energy quench at density limit, while separate evolution of the modes does not effect on gross plasma stability.

1. INTRODUCTION. One of the common features of almost all density limit disruptions is an appearance of plasma perturbations with m=2, n=1 poloidal and toroidal symmetry. Growth of the 2,1 perturbations depends on the m=2,n=1 mode stability, on intensity of interaction of different internal perturbations (m=1,2,3,et.) and on strength of the external error fields due, for example, to coil misalignment and coil feeds. This can lead to wide spectrum of mechanisms of disruption depending on peculiar conditions of experiments.

Growth of the m=2,n=1 mode is often accompanied by appearance of m=1,n=1 mode prior the disruption. Complicated behavior of the m=1 mode and its interaction with the m=2 mode at the major disruptions was observed as early as T-4 experiments [1]. Experiments indicated that disruption is preceded either by the m=2 and m=1 modes coupling [1-3] or by growth of only m=1 precursor [4-6]. Sometimes m=1 mode does not rotate and only m=1 erosion in r<r(q=2) zone is observed [7]. "Giant" rotating m=1 mode was observed at the energy quench in T-10 plasma during ECRH [8,9]. Maximum of the "giant" m=1 perturbations is at the radii two time larger than that of the normal m=1 mode often accompanied sawteeth. However, experiments on TFR indicated that the m=1 perturbations induced by the growth of the m=2 mode are localized at the same surface as normal m=1 sawtoothing mode, but have higher frequency [10]. Moreover, sometimes there is no direct connection with the m=1 mode [11]. Physical nature of appearance of the m=1 mode was analyzed in number of theoretical studies [12,13], however simultaneous growth of the 2/1 and 1/1 modes observed in experiments does not allow to reveal directly reasons of the mode appearance.

To reveal role of interaction of the internal modes at density limit disruption we analyzed structure of the plasma perturbations in high-qL discharges (qL=3.3-4) with different behavior of the modes: m=1 mode growth without m=2 mode destabilization (2.1), simultaneous growth and coupling of the m=1 and m=2 modes (2.2), growth of the m=1 and m=2 modes without coupling (2.3), coupling of decaying m=1 mode with growing m=2 mode (2.4) and growth of the m=2 mode without m=1 mode destabilization (2.5).

2. EXPERIMENTAL RESULTS. Studies of internal perturbations were made with the use of the soft x-ray imaging system consisted of three arrays and allowed to reconstruct local perturbations characterized by the m=0,1,2 poloidal symmetries [14]. This permits one to study m=1,m=2 modes without severe restrictions on symmetry. To maintain the accurasy of the reconstruction of small oscillations perturbed part of the sygnals can be processed separately. Time resolution of the system is up to 0.01msec.

2.1. Destabilization of the m=1 perturbations is observed during on-axis ECRH (Pab=0.7MW) with intensive gas puffing by additional valves. Time evolution of the soft x-ray intensity at the central part of the plasma column is represented in Fig.1a,b. Fig.1c. represents radial profiles of the relative amplitude and phase of the soft x-ray oscillations at time moments indicated in Fig.1b [t=426msec(1), 430msec(2), 432msec(3)]. Amplitude of the perturbation grows at first stage (1)-(2). Second stage (2)-(3) is characterized by the mode decay and displacement of the hot core. In spite of large amplitude of the m=1 oscillations (in comparison with normal sawtoothing m=1 mode) they produce no effect on gross plasma stability and decay after a few milliseconds.

2.2. Continuation of the density rising resulted in increase of power radiated from the plasma edge and Te(r) contraction. This leads to growth of the m=2 and m=1 perturbations at disruption at t=460.1msec (Fig.1a,1d). Radial profiles of the relative amplitude and phase of the soft x-ray oscillations just prior the disruption are shown in Fig.1e (t=459.8msec). Modes m=1 and m=2 are coupled and have large amplitude at low field side. Dependence of phase of the oscillations at r=13-14cm on the poloidal angle is shown in Fig.1f (t=459.8msec). The m=2 mode is poloidally asymmetric. This experiments indicate that in T-10, as in many other tokamaks, coupling of

the m=1 and m=2 modes play a significant role in density limit disruption.

2.3. Growing m=1 and m=2 modes without coupling were observed just after H-pellet injection into ECRH-heated plasma with intensive gas puffing. Temporal evolution of the soft x-ray intensity at the central part of the plasma column is shown in Fig.2a,2b. Vertical arrow marks moment of pellet injection. Oscillations m=1 and m=2 have different frequencies just after pellet injection and in spite of relatively large amplitude they do not lead to the energy quench. Amplitude of the m=2 mode decreases with time (till t=420.0-420.5msec) while m=1 oscillations continue to grow.

Fig.2.c. represent radial profiles of the relative amplitude and phase of the soft x-ray oscillations at time marked in Fig.2.b [t=420.2msec(1),422.0msec(2),423.98msec(3)]. Hillocks at the profiles represent m=1 and m=2 modes localization. Maximum of amplitude of the m=1 mode decays and moves outside (1),(2),(3). The m=2 mode appears ones again,

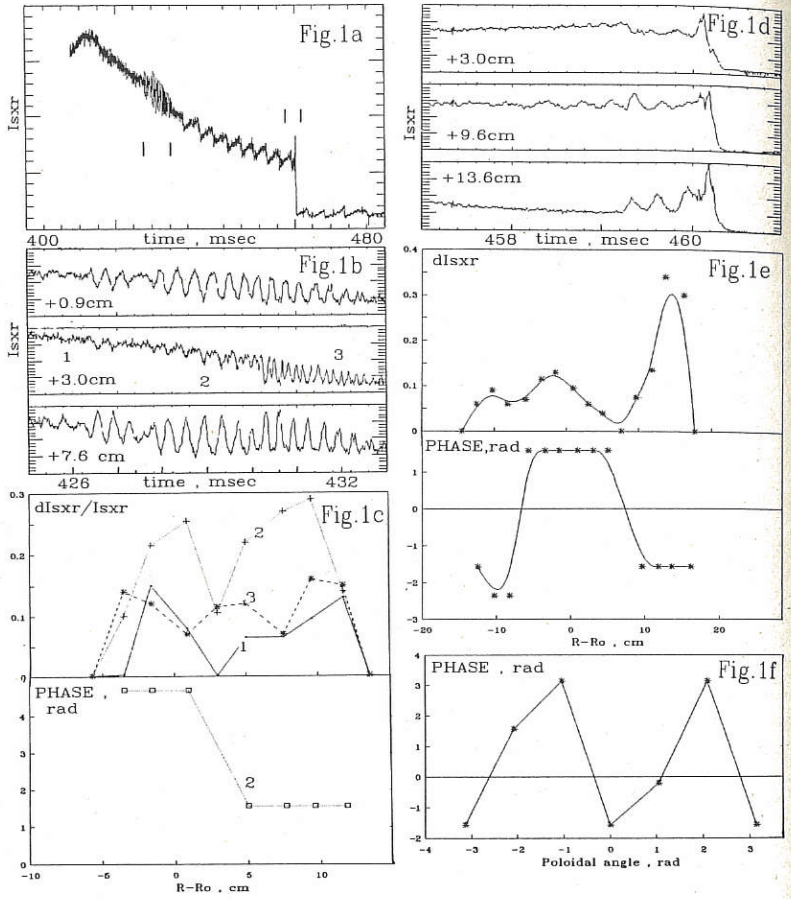

Fig.1a,1b,1d. Time evolution of the soft x-ray intensity. Fig.1c,1e. Radial profiles of the relative amplitude and phase of the soft x-ray oscillations. Fig.1.f. Dependence of the phase of the soft x-ray oscillations on the poloidal angle.

but with frequency equal to the frequency of m=1 mode.
2.4. Coupling of expanding m=1 mode with m=2 mode is observed when the distance between the surfaces of mode localization became sufficiently small. The modes interaction is stronger at low-field side. Dependence of the phase of the oscillations at r=14-15cm on the poloidal angle is represented in Fig.2d (t=422.0msec). The modes remains poloidally asymmetric. Growth of the m=2 mode continues until the first minor disruption occurs at t=424.5msec (Fig.2b). Tomographic images of the local soft x-ray emissivity are shown in Fig.2e. Frames A(t=419.19msec) and B(419.27) represent images of the emissivity observed just after pellet injection, while images C-H represent

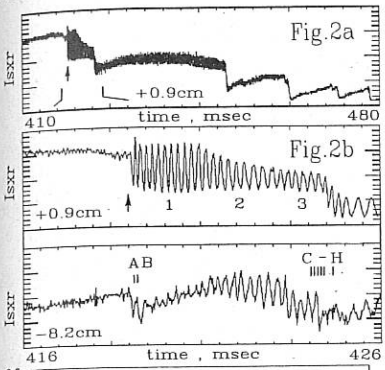

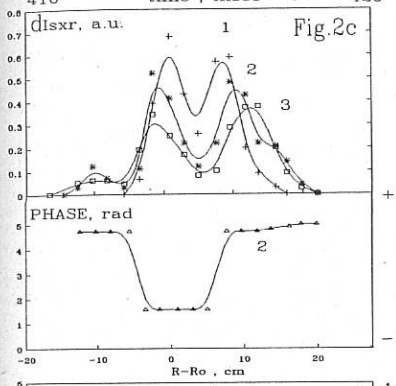

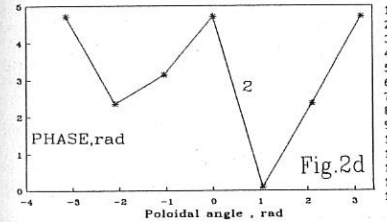

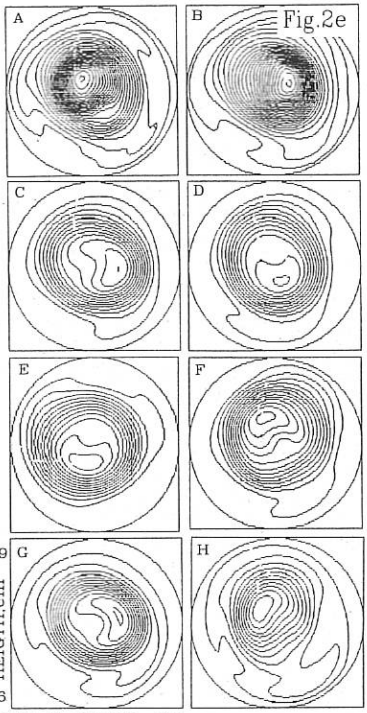

1 A.B.Berlizov,S.V.Mirnov,G.E.Notkin,et al.,IAE-2742(1976)
2 EQUIPE TFR, In Proc.6ICPP(1976),IAEA-CN-35/A8,v.1.,p.279
3 G.Waidmann,G.Kuang,In Proc.18EPS(1991),Vol.15C,p.II-45
4 N.R.Sauthoff,et al.,Nucl.Fusion,18(1978)1445
5 E.D.Fredrickson,et al.,In Proc.13ICPP(1990),IAEA-CN-53/
6 J.Howard,M.Persson, Nucl.Fusion,32(1992)361 /A-VII-9
7 J.A.Wesson,et al.,Nucl.Fusion,29(1989)641
8 D.Kislov,E.Lyadina, In Proc.17EPS(1990),Vol.14B,p.315
9 V.V.Alikaev,et al. Proc.13ICPP(1990),IAEA-CN-53/A-II-6
10 EQUIPE TFR, Nucl.Fusion,17(1977)1283
11 D.C.Robinson,K.McGuire, Nucl.Fusion,19,1(1979)115
12 R.G.Kleva,J.F.Drake Phys.Fluids B3(1991)372
13 A.Bondeson,et al.,Nucl.Fusion,31(1991)1695
14 G.A.Bobrovskii,et al. Rev.Sci.Instr.,30,62(1991)886

Fig.2a,2b. Time evolution of the soft x-ray intensity. Fig.2c. Radial profiles of the relative amplitude and phase of the soft x-ray oscillations. Fig.2d. Dependence of the phase of the soft x-ray oscillations on the poloidal angle. Fig.2e. Tomographic images of the local soft x-ray emissivity.

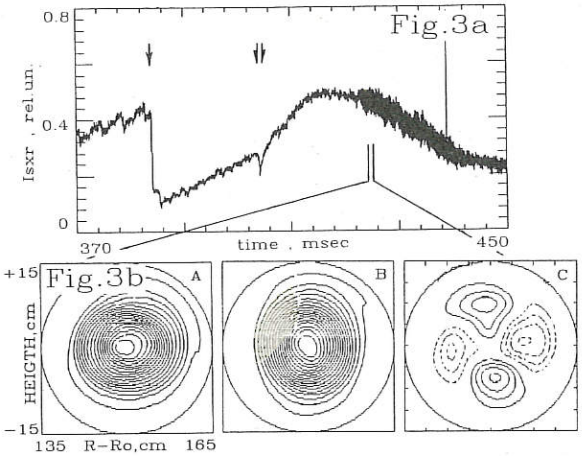

Fig.3a. Time evolution of the soft x-ray intensity.
Fig.3b. Tomographic images of the local soft x-ray emissivity Isxr (A,B) and local perturbations of Isxr(C).

temporal evolution of the internal perturbations at the first minor disruption [C(424.20), D(424.24), E(424.28), F(424.32), G(424.40), H(424.66)].

2.5. Slowly growing and saturated m=2 modes without m=1 mode destabilization was observed in OH-plasma after subsequent injection of two pellets (H-pellet at t=385msec and C-pellet at t=405msec). Temporal evolution of the soft x-ray intensity is represented in Fig.3.a. Single and double arrows mark times of H- and C- pellets injection respectively. Injection of H-pellet induces cooling of the plasma and stabilization of sawteeth, while injection of C-pellet initiates appearance of continues m=2 mode. Mode m=2 is poloidally symmetric in the case. It does not induce disruption and only leads to density decay. Tomographic images of the local soft x-ray emissivity are shown in Fig.3b. Frames A(t=425.04msec) and B(425.11) represent images of the emissivity observed with horizontal and vertical positions of X-point of m=2 islands. Frame C represent image of perturbation of the soft x-ray emissivity at the same time as shown in the Frame B. Dashed contours represent negative perturbation of the emissivity.

3. CONCLUSIONS. Tomographic studies of the internal MHD perturbations in T-10 tokamak revealed that either growth of the m=1 mode without m=2 modes destabilization, or m=2 mode growth in the absence of the m=1 mode, or growth of the m=1 and m=2 modes simultaneously but without coupling do not lead to energy quench and disruption in T-10 plasma.

Simultaneous growth and coupling of the m=1 and m=2 modes is important to the triggering of the energy quench at the density limit disruption. Coupled m=2 mode is poloidally asymmetric with more strong interaction with the m=1 mode at the low-field side of the plasma.

ACKNOWLEDGMENTS: The authors would like to thank the ECRH Group, Pellet Group, and T-10 staff for their technical assistance and Drs. V.Alikaev, Yu.Esipchuk, N.Ivanov, A.Kislov, and K.Razumova for their support of the experiment.

THE SAWTOOTH COLLAPSE IN ROTATING JET PLASMAS

R. Büchse*, D.J. Campbell, A.W. Edwards, R.D. Gill
JET Joint Undertaking, Abingdon, Oxon, OX14 3EA, U.K.
*Max-Planck-Institut für Plasmaphysik, 8046 Garching, F.R.G.

INTRODUCTION The variety of sawteeth in JET can be divided into two main groups: precursorless sawteeth /1/ and sawteeth with $m = n = 1$ precursors. The latter are predominantly found in NBI heated discharges with a corresponding fast toroidal plasma rotation. Their collapse phase is analysed with high spatial resolution by means of a rotational soft X-ray tomography code. It is found that a complete collapse is a sequence of two energy loss processes. Either of these may be stabilized during the collapse, giving rise to different types of sawtooth behaviour.

TOMOGRAPHIC RECONSTRUCTION METHOD The method is an extension of an algorithm developed for the circular plasmas in ASDEX /2/. Its static version performs the tomography in flux coordinates rather than the polar coordinates of the original Cormack method. The rotational version used in the investigations of this paper also makes use of the rotation of MHD modes to increase the poloidal resolution. It has been tested /3/ in numerical simulations and by reconstructing pellet induced snakes. Snakes are far too localized to be resolved by static tomography. The snake size deduced from rotational tomography (fig. 1) is in very good agreement with that deduced from the raw data traces /4/, clearly demonstrating the reliability of the method. Since the data from about a quarter rotation cycle is needed for one reconstruction, the rotational method is restricted to sawtooth collapses in which the emissivity changes little during that time. This is fulfilled in strongly beam-heated plasmas where rotation frequencies of up to 20 kHz are achieved.

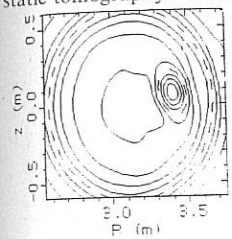

Fig. 1: *A pellet snake* (#9550).

EXPERIMENTAL RESULTS **Partial sawteeth** flatten the temperature profile only near the radius r_1 of the $q = 1$ surface. Incomplete reconnection has long been believed to account for this effect. The temporal evolution of the soft X-ray contours shown in fig. 2 supports this mechanism. The plasma core is displaced radially and an $m = 1$ island grows opposite the core (figs. 2A,B). After the displacement has increased from 2cm to 12cm within 200μs the process comes to an end (fig. 2C). Then, on a much slower timescale the core moves back towards the plasma centre (fig. 2D). The peak emissivity stays constant. Since the direct consequence of reconnection is a flattening of the q-profile it seems likely that the collapse trigger is related to the shear around r_1. In the development of the instability

$q(r)$ changes, the instability drive is removed and the collapse is stabilized. Obviously, this is the case before the centre has been reconnected. The X-ray contours after the collapse are in agreement with the T_e contours /5/.

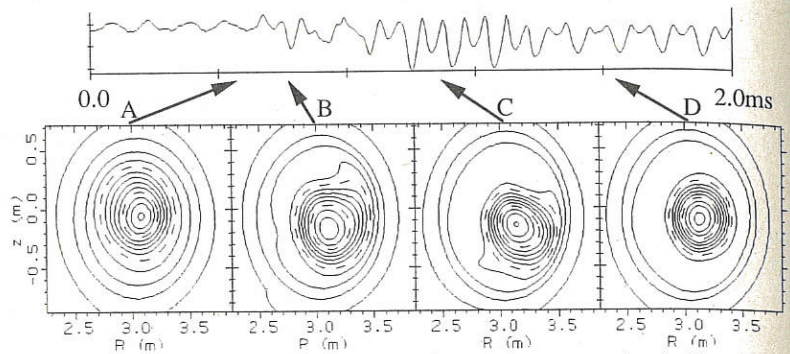

Fig. 2: *Partial sawtooth collapse.* ***Top:*** *Signal from central soft X-ray diode.* ***Bottom:*** *Contours of constant soft X-ray emissivity.* (#26023, $I_P = 3MA$, $B_\phi = 3T$, $\bar{n}_e = 1.7 \times 10^{19} m^{-3}$, $a = 1.03m$, $P_{NBI} = 4MW$)

Complete sawteeth are the extreme opposite of partial sawteeth. The collapse is followed by very small or no postcursor oscillations. During the early crash phase the same dynamics as for the partial collapse are found (fig. 3A,B). However, the

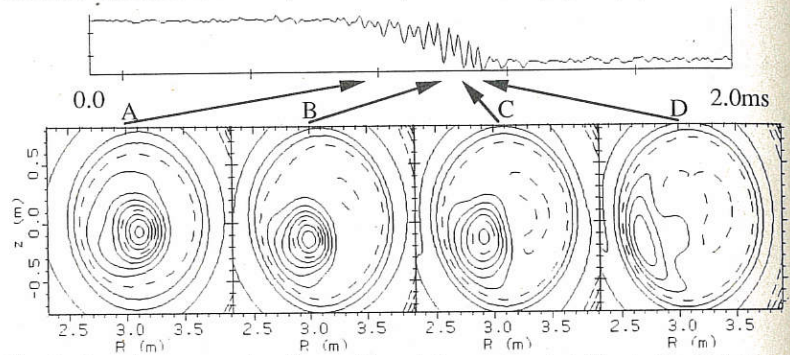

Fig. 3: *Complete sawtooth collapse. The relative peak emissivities in the contour plots are 1.0, 0.94, 0.85 and 0.64, respectively.* (#26040, $I_P = 3MA$, $B_\phi = 3T$, $\bar{n}_e = 1.3 \times 10^{19} m^{-3}$, $a = 1.02m$, $P_{NBI} = 15MW$)

island size and the displacement of the hot core increase further and eventually the peak emissivity starts to decrease (fig. 3B→C). Finally the profiles across the whole plasma core have been flattened ($\simeq 50\mu s$ after fig. 3D). Since the emissivity in the *non-reconnected* core drops it must be concluded that reconnection is not the only process of plasma redistribution. Rather, an additional mechanism for fast transport

of energy across closed flux surfaces is necessary to explain the observations. This is supported by the analysis of the following type of sawteeth.

Intermediate sawteeth exhibit postcursor oscillations of considerable amplitude. Tomography reveals that they represent indeed an intermediate stage between the partial and the complete collapse. At first, as in the previous two cases, an island grows (fig. 4A). Then, just as in the complete collapse, energy is transported across closed flux surfaces. However, this process is stabilized before the whole pressure is released from the core as can be seen from the presence of the remnant of the core in the lower part of fig. 4B.

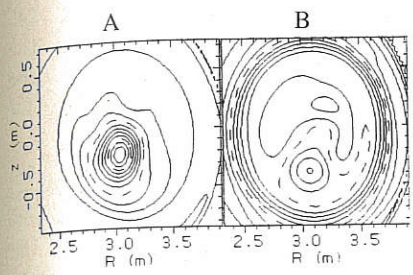

Fig. 4: *Intermediate sawtooth collapse. Emissivity contours before (A, max.=1.0) and after (B, max.=0.3) the collapse. (#26095, $I_P = 3MA$, $B_\varphi = 3T$, $\bar{n}_e = 1.3 \times 10^{19} m^{-3}$, $a = 1.08m$, $P_{NBI} = 7MW$)*

INTERPRETATION The experimental observations can be combined to obtain a qualitative picture of the sawtooth collapse (see fig. 5). The collapse starts by reconnective plasma mixing in the vicinity of the resonant surface. In some cases the resulting changes make the plasma stable against further reconnection (*partial sawteeth*), in other cases a second instability boundary is crossed, leading to fast energy flow across closed flux surfaces. In some of these cases the resulting loss of central pressure makes the plasma stable against further loss before all the central pressure is released (*intermediate sawteeth*), in other cases the pressure release is complete (*complete sawteeth*).

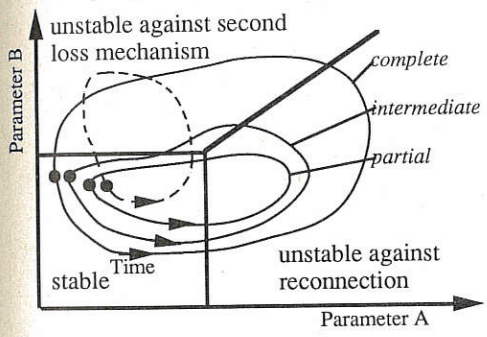

Fig. 5: *Schematic stability diagram. Each particular type of collapse discussed in this paper is represented by a certain path in stability space. The real picture might be more complicated. In particular stability might depend on more than two parameters. However, in this schematic diagram parameter A is likely to increase with the shear at r_1, parameter B with β_P inside r_1.*

The presence of two loss processes is confirmed by a more quantitative analysis of the complete collapse in fig. 3. Two growth rates are found for the core displacement. The change from the slow ($\gamma_1 \simeq (300\mu s)^{-1}$) to the fast growth rate

($\gamma_2 \simeq (100\mu s)^{-1}$) coincides with the onset of the central pressure release. Much smaller values of γ_1 are also to be found, underlining the sensitive dependence on the local shear. γ_2 however shows very little variation, pointing towards a more global stability criterion like a critical value of the core β_p.

Additional support comes from the compound sawtooth behaviour in JET. Complete or intermediate collapses are often preceeded by one or more partials. The time interval between complete collapses is, however, basically independent of the number of partial collapses. This striking behaviour can in principle be explained if there are two different trigger conditions involved in the two types of event.

A two-stage process for the sawtooth instability provides a probable explanation for some of the seemingly inconsistent observations made in different tokamaks: Depending on machine parameters and plasma profiles, stabilisation of the collapse will happen at different stages during both loss processes and thus give rise to the complex spectrum of observations.

Other JET results support the important role of the local shear: reduced shear at r_1 has been found by analysing pellet ablation clouds /6/. Current profile modifications by local current drive /7/ and by a change of the heating scenario from CO-NBI to CTR-NBI /8/ change the sawtooth behaviour dramatically. The findings in this paper are also consistent with the low values of $q(0)$ typically found in JET, since *incomplete* reconnection is involved in the two-stage process.

CONCLUDING REMARKS Although the proposed outline of the collapse is in qualitative agreement with many observations, a number of important questions obviously remain to be answered. In particular, the question as to the nature of the second loss process arises. The growth of stochastic regions has been considered to play a role during the collapse in experimental /9/ as well as in theoretical /10/ work.

Another important question is how the fast precursorless sawteeth /1/ fit into this picture? One might speculate that they are represented by the dotted loop in fig. 5, which does not enter the reconnection region.

We gratefully acknowledge valuable discussions with J. O'Rourke and J. A. Wesson.

REFERENCES

/1/ A. W. Edwards et. al., Phys. Rev. Lett. 57(2), 210 (1986)
/2/ R. Büchse et. al., Proc. 17th EPS Conf. Amsterdam (1990), Vol. 14B I, p. 391
/3/ R. Büchse, to be published
/4/ A. Weller et. al., Phys. Rev. Lett. 59(20), 2303 (1987)
/5/ E. Westerhof et. al., Nucl. Fus. 29(6), 1056 (1989)
/6/ R. D. Gill et. al., Nucl. Fus. 29(5), 821 (1989)
/7/ D. F. H. Start et. al., this conference
/8/ A. W. Edwards et. al., this conference
/9/ M. A. Dubois et. al., Nucl. Fus. 23(2), 147 (1983)
/10/ A. Y. Aydemir et. al., Phys. Fluids B1(4), 774 (1989)

A COMPARISON OF JET SAWTOOTH BEHAVIOUR IN PLASMAS WITH CO- AND COUNTER NEUTRAL BEAM INJECTION.

A.W. Edwards, A. Bickley, R. Büchse*, C.D. Challis, R König,
F. B. Marcus, J. O'Rourke and D. Stork.
JET Joint Undertaking, Abingdon, Oxon, OX14 3EA, U.K.
*Max-Planck-Institut für Plasmaphysik, 8046 Garching, F.R.G.

Introduction. Experiments have been performed on JET with neutral beam injection counter to the plasma current direction, (counter-NBI), to assess the behaviour of global parameters in this heating regime and to compare them with other experiments. With counter-NBI on ASDEX, for example, peaking of the electron density profile and accumulation of impurities was often observed /1/. Sawtooth activity was also stabilised for a few sawtooth periods /2/. This paper reports on a detailed study of sawtooth activity during the JET counter-NBI experiment. A brief comparison is also made with sawtooth behaviour for NBI in the plasma current direction, (co-NBI), a description of which is given in /3/.

General Counter-NBI Pulse Characteristics. Fig. 1 shows on overview for a 3.1MA/2T discharge. In contrast to pulses at higher toroidal field where Zeff rises and then saturates, Zeff decreases during the later phase of the heating pulse.

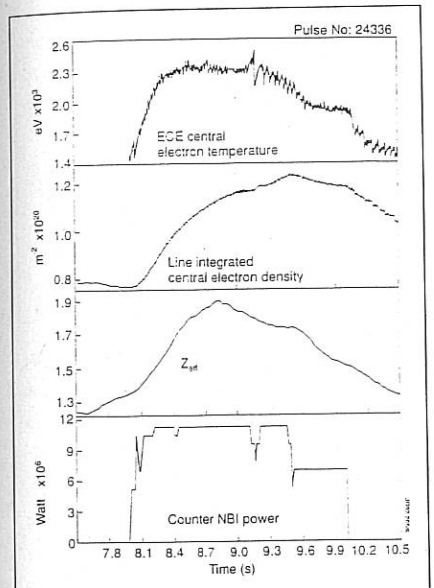

Fig. 1 Overview of Plasma Parameters

For all counter-NBI pulses the sawtooth behaviour changes following the first crash during the heating pulse, small amplitude sawteeth being observed. The period is very short, of the order of 30 milliseconds (ms). This compares with a value close to 100ms for the ohmic sawteeth preceding the heating pulse and contrasts strongly with the behaviour in co-NBI, where the sawtooth period is longer than the corresponding ohmic sawtooth period. The sawtooth period gradually increases during the heating pulse, whilst remaining well below the ohmic sawtooth period. For discharges with a toroidal field above 2T, the nature of the sawtooth crash remains the same.

For the 3.1MA/2T shots, the sawtooth behaviour changes in the later part of the high power heating pulse giving larger amplitude, longer period sawteeth, which are then stabilised during the low power phase at the end of the heating pulse.

Fig 2a shows electron temperature profiles before and during the counter-NBI heating pulse, for the 3.1MA/2T shot of Fig 1. These profiles, which are flat in the centre, are typical of those measured for all counter-NBI discharges. The electron density profiles are also flat over the centre of the profile. The corresponding profiles of the safety factor, (q), determined from an equilibrium code that uses Faraday rotation data to constrain the fit, are shown in Fig 2b. These show a broad central region over which q is close to 1. Sawtoothing has begun at about 5secs and within 0.5secs the current profile has come into equilibrium. The sawtooth inversion radius at 7.55secs, as determined from tomographic inversion of the soft X-ray data, is 0.5m. This is in good agreement with the radius of the q=1 surface.

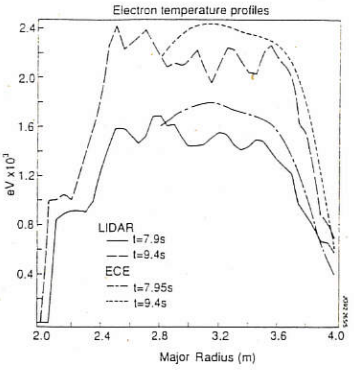

Fig. 2a

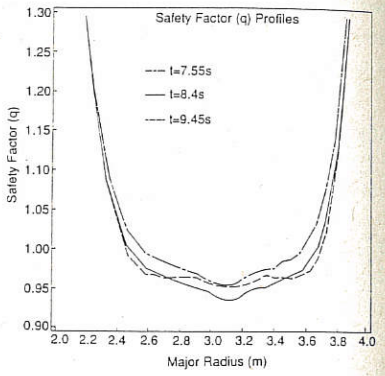

Fig. 2b

Electron temperature and safety factor profiles. The error on q-on-axis is ± 15%. The relative error point-to-point and from one profile to another is much smaller.

The Counter-NBI Sawtooth Crash. Fig. 3 shows the soft X-ray data for a counter-NBI sawtooth crash during the early phase of the NBI heating pulse. Prior to the crash, the channel at 3.59m shows the presence of a large saturated m=n=1 island, which is also seen in Fig3A. This island lies close to the sawtooth inversion radius measured during the ohmic phase of the discharge, that is at 2.6m and 3.6m. An m=n=1 island then grows in the centre, displacing the core off-axis and fully reconnecting the central region. Fig 3B shows the core displaced off-axis at the end of this phase, close to the sawtooth inversion radius that is now measured to lie between 2.8m and 3.35m. Upon completion of the crash the central region is left flattened with the original m=n=1 island remaining, as shown in Fig3C.

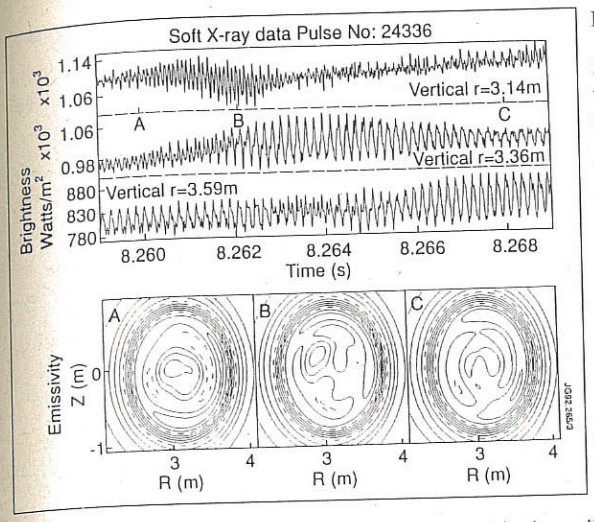

Fig. 3

Soft X-ray data for a typical counter-NBI sawtooth crash.

The top traces show the line integrated signals for 3 vertical chords.

The bottom plots show the tomographically inverted local soft X-ray emission.

For the 3.1MA/2T discharges, the sawtooth activity is modified later in the heating pulse. An example is shown in Fig 4. A growing m=n=1 mode is seen which displaces the core off-axis. Before reconnection is complete, a second process leads to the rapid loss of central plasma energy. This behaviour is typical of that seen for co-injection sawteeth and is covered in more detail in /3/. The sawtooth inversion radius measured for this sawtooth crash is 0.5m, equal to that found for the ohmic phase of the discharge.

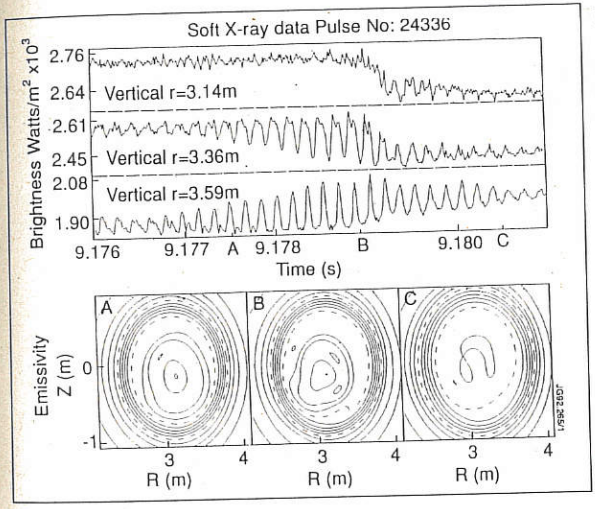

Fig. 4

Soft X-ray data for a sawtooth crash during counter-NBI. This crash, which occurs late in the heating pulse of a 2T discharge, is more typical of a co-NBI sawtooth crash.

The top traces show the line integrated signals for 3 vertical chords.
The bottom plots show the tomographically inverted local soft X-ray emission.

Interpretation of the Counter-NBI Sawteeth. Ohmic q-profiles measured in other JET operating regimes are normally parabolic with a q-on-axis (q_0) falling to about 0.75 /4/. In comparison, the ohmic q-profile measurements for counter-NBI show a broad profile in the centre with q_0 below and close to 1. Steady state simulations show a substantial beam driven current (j_{bdc}) in the central region (r/a<0.1). For 3.1MA/2T discharges this can reach 300KA/m^2, which is 25% of the total current density of 1.2MA/m^2. j_{bdc} has a high radial gradient and acts counter to the plasma current direction. If j_{bdc} is sufficiently large, this will 'overcome' the effect of neo-classical resistivity, which lowers q_0, and raise the central q. As q_0 reaches 1, two q=1 surfaces will be present in the plasma. Under these conditions, as q_0 rises above 1, an ideal instability is predicted. If the off-axis minimum in q is below 1, then the flux within the central q=1 surface will be reconnected, lowering q_0 from a value above 1 to a value below 1. The outermost q=1 surface will be unaffected by the reconnection which occurs within the central q=1 volume.

As the electron density increases during the heating pulse, the fraction of j_{bdc} to total current density decreases, slowing the rate of rise of q_0. This leads to an increase in the sawtooth period during the heating pulse. For discharges with a toroidal field above 2T, this is the only consequence of the increase in the electron density, the type of sawtooth behaviour described above being seen throughout the heating pulse. For the 3.1MA/2T pulses, the sawtooth behaviour changes in the later part of the heating pulse to that which is more typical for JET in co-NBI /3/. Only one q=1 surface is observed in the plasma at this time and the sawtooth crash occurs within a large inversion radius, equivalent to that measured during the ohmic phase. In this case, the fraction of j_{bdc} to total current is clearly not sufficient to drive q_0 above 1 in the centre.

Concluding Remarks. Small amplitude, high frequency sawteeth have been observed on JET during counter-NBI. These can be explained by a beam driven current in the centre, counter to the plasma current direction, driving q-on-axis above 1. This leads to an ideal instability that causes the central flux to be reconnected, driving q_0 below 1. This is the opposite of normal JET sawtooth regimes, where the sawtooth crash leads to an increase in the central q.

References

/1/ O. Gehre et al., Phys. Rev. Lett 60 (1988) 1502.

/2/ R. Büchse et al., Proc. 17th EPS Conf. Amsterdam (1990), Vol 14B I, 391.

/3/ R. Büchse et al., this conference.

/4/ J. Blum et al., Nucl. Fusion 30 (1990) 1475.

INVESTIGATION OF THE SAWTOOTH PRECURSOR OSCILLATIONS OF ELECTRON DENSITY AND ELECTRON TEMPERATURE IN OHMIC TOKAMAK DISCHARGES ON TEXTOR

H.R.Koslowski and A.Krämer-Flecken
Institut für Plasmaphysik, Forschungszentrum Jülich GmbH, Ass. EURATOM-KFA,
Postfach 1913, D-5170 Jülich, Germany

The m=1 precursor oscillations and the sawtooth crash in Ohmic discharges have a fixed phase relation. The outflow of heat and density during the crash has no radial symmetry. The enhanced transport is via the X-point of the rotating island.

Precursor oscillations can be observed in tokamak discharges over a wide range of plasma parameters. These oscillations are commonly attributed to the evolution of a rotating m=1 mode. They start during the ramp up phase several ms before the sawtooth crash and grow exponentially in amplitude. The typical frequencies of these oscillations on TEXTOR are in the range from 2kHz up to approx. 4kHz. The duration of the precursor phase is about 3ms. The modulation of the line integrated electron density and the ECE signals are a few %, depending strongly on the radial position of the measurement.

The sawtooth precursor oscillations and the sawtooth crash have been measured in a series of Ohmic discharges in the TEXTOR tokamak (R=1.75m, a=0.46m). The main plasma parameters are: $\overline{n_e}=4.4 * 10^{13}\mathrm{cm}^{-3}$, I_p=400kA, B_t=2.25T. The applied diagnostics were the HCN interferometer, measuring the line integrated electron density at nine vertical probing beams and the ECE radiometer with nine channels at various radial positions, measuring the local electron temperature. Both diagnostics have sufficient time resolution (50μs for the HCN interferometer, 40 μs for the ECE measurement) to resolve the fast oscillations.

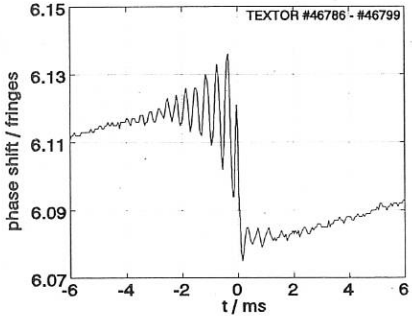

Fig. 1 Line integrated electron density at R=R_0=1.75m after averaging of 428 sawtooth events.

The good reproducibility of the individual sawtooth events allows the application of a coherent averaging procedure to the density and temperature signals in order to increase the signal to noise ratio. The ECE signal from the plasma centre serves as a reference for the times of the sawtooth crashes during the flat top phase of the discharge. This signal shows only a small modulation due to the precursor oscillations, thus allowing a precise determination of the sawtooth

crash. About 50 sawteeth are detected during the flat top of a discharge. The signals are averaged by superposing a constant interval of the time traces around the sawtooth crash. Figure 1 shows the line integrated electron density measured with a probing beam at the geometrical centre of the torus at R_0=1.75m. By averaging of more than 400 sawtooth periods the signal to noise ratio is increased by a factor of ~20 compared to the original raw data, whereas the amplitude of the precursor oscillation shows nearly no decrease. Therefore the precursor oscillations and the sawtooth crash must have a fixed phase relation, otherwise the amplitude of the precursors should have the same damping in amplitude as the average noise level. The measurement of the line integrated electron density is made along vertical chords, so it projects the plasma onto a horizontal plane. The finding can be explained only, if the projection of the rotating m=1 island, which is associated with the precursor, onto the probing beams has a well defined phase. We can conclude, that the m=1 island has a fixed position within the laboratory frame when the sawtooth crash occurs.

The precursor period in this series of discharges is 320μs when the precursor starts and the rotation slows down to a period of 380μs just before the crash. There are some oscillations visible after the crash. These postcursor oscillations are present in many investigated discharges. Their frequency is nearly equal to the precursor frequency. The postcursor oscillations have a duration of about two periods and have the same phase as the precursor.

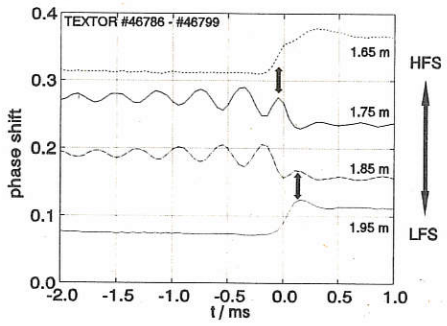

Fig. 2 Line integrated electron densities of four probing beams. The signals at 1.75m and 1.85m show precursor oscillations with opposite phase, thus underlining the m=1 character of the precursor.

The coherently averaged signals for the central four interferometric probing beams are shown in figure 2. The opposed oscillations of the signals at R=1.75m and R=1.85m, which are located on the high field side (HFS) and on the low field side (LFS) with respect to the magnetic axis, demonstrates clearly the m=1 behaviour of the precursor oscillation. The beams at R=1.65m and R=1.95m are located outside of the q=1 surface, showing no modulation but only the inverse sawtooth caused by the outflow of electrons due to the sawtooth crash. The sawtooth crash time can be determined to approx. 200μs. An inversion of the line integrated electron density (the time for the inversion was chosen 3ms before the sawtooth crash to avoid the perturbation due to the m=1 mode) using a matrix method yields the equidensity surfaces which are approximately equivalent to the flux surfaces. This calculation yields the position of the magnetic axis at R_{mag} ~ 1.80m. The probing beams at

1.75m and 1.85m are tangential to the same flux surface (with r=5cm) and because the Shafranov shift profile is rather flat in the centre (as comes out from the inversion and is in good agreement with equilibrium calculations for TEXTOR /1/) the beams at 1.65m and 1.95m are located on opposite sides of the flux surface with r=15cm. The nearly equal modulation amplitudes for the inner two probing beams confirm the calculation. Looking closer at the signals measured at 1.65m and 1.95m major radius reveals, that the onset of the inverse sawtooth is delayed in the channel at the LFS, i.e. the outflow of the density starts at the HFS. The analysis of SXR data from the TEXT tokamak showed for some sawtooth events that the crash on different sides of the plasma centre was not simultaneous /2/.

The common picture for the magnetic m=1 island is that it has a crescent shape, the profiles have a localized flattening around q=1 on one side (the so-called O-point), whereas the profile gradients at the opposite side of the q=1 surface (X-point) become larger due to the displacement of the hot core. A simulation of the HCN data for a probing beam intersecting the q=1 surface under the assumption of a rotating m=1 island shows the same modulation as the measured signals. The maximum amplitude of the phase shift signal is found when the beam crosses the island in the vicinity of the X-point, whereas the minimum is measured when the beam intersects the flattened island. From these model calculations one can conclude that the outflow of density and temperature during the internal disruption has no radial symmetry around the q=1 surface, but is localized at the X-point (this is also predicted by a theoretical model, see ref. /3/). The delay between the inverse sawteeth at the HFS and the LFS is correlated with the rotation of the island (see fig. 2, where the inverse sawtooth on the HFS appears, when the X-point of the island is located there, the arrows indicate the times when the X-point of the island is at the HFS and LFS, respectively). A similar behaviour was found from the tomographic analysis of SXR and ECE data in TFTR /4/.

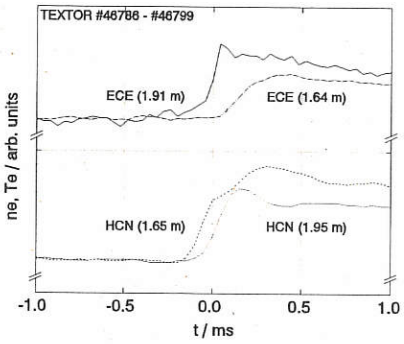

Fig. 3 Asymmetric behaviour of the sawtooth crash.

The same analysis for the ECE data yields that the sawtooth crash in the electron temperature starts at the low field side. Figure 3 shows in the upper part two ECE signals measured at R=1.64m and R=1.91m on the HFS and LFS, respectively. The temperature outflow on the high field side is significantly delayed. The lower part of the picture displays the corresponding HCN signals showing the opposite behaviour. This finding seems to be contradictory, but can be explained in a straightforward way: on TEXTOR the

diagnostics for the electron temperature and the electron density are 180° apart in the toroidal direction. The respective diagnostics observe at a given time opposite points of the rotating m=1 island at the inner and outer sides of the torus. Therefore these results are another indication, that the sawtooth crash is coupled to the m=n=1 mode.

A further asymmetry is found in the amplitudes of the inverse sawteeth. Figure 3 shows that the amplitudes on the side where the crash starts (HFS for the HCN data and LFS for the ECE) are larger than the corresponding signal amplitudes on the opposite sides, indicating that the outflow of density during the crash phase is not constant in time.

The coherent averaging procedure has been applied to many Ohmic discharges with different plasma conditions (variation of $\overline{n_e}$, I_p, B_t), thus allowing to study the dependence of the precursor period on various plasma parameters. As an example, figure 4 shows a plot of the precursor period versus the plasma current. The precursor period increases with the plasma current. The scatter within the data at the same current is due to the variation of density. We have included shots with $\overline{n_e}$ in the range from 1.5 to 4.4*10^{13}cm^{-3}. The magnetic field was 2.25T for all shots. The precursor period was averaged over the last 4-5 oscillations before the sawtooth crash. An additional result is that the precursor period increases when the toroidal magnetic field is decreased. In most of the discharges with precursor activity the m=1 island is found to take a fixed position within the torus when the sawtooth crash occurs. In some cases the averaging procedure results in the decrease of the precursor amplitude, i.e. the m=1 mode has a random orientation within the vacuum vessel at the crash time. Then the coherent averaged data shows no time delay between the inverse sawteeth on the HFS and LFS (which may be still present in an individual sawtooth). The reversal of the toroidal magnetic field had no effect on the localization of the asymmetry.

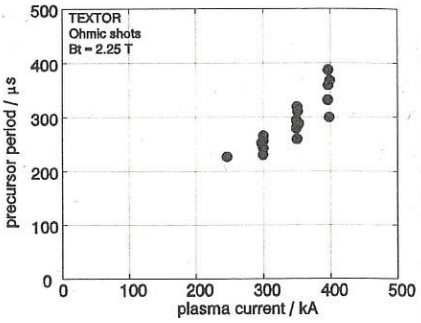

Fig. 4 Precursor period vs. plasma current. The data are measured at different averaged electron densities.

/1/ P. Börner, A. Kaleck, Proc. 12th Eur. Conf. on Controlled Fusion and Plasma Physics, Budapest, part I, p. 187, Eur. Phys. Soc. Geneva 1985
/2/ J. A. Snipes, K. W. Gentle, Nuclear Fusion, **26**, 1507 (1986)
/3/ A. Rogister *et al.*, Proc. 13th Intern. Conf. on Plasma Physics and Contr. Nuclear Fusion Research, Washington 1990, vol. 2, p. 231, IAEA, Vienna, 1991
/4/ Y. Nagayama *et al.*, Phys. Rev. Lett. **67**, 3527 (1991)

THE INFLUENCE OF MODE LOCKING BY RESONANT HELICAL FIELDS ON FLUCTUATION INDUCED PARTICLE TRANSPORT IN TOKOLOSHE TOKAMAK

GW van Vuuren, DE Roberts, JD Fletcher, MA Hellberg*, MJ Alport*, JAM de Villiers
Atomic Energy Corporation of South Africa, PO Box 582, Pretoria 0001, R.S.A.
*Dept of Physics, University of Natal, King George V Avenue, Durban 4001, R.S.A.

INTRODUCTION

We report studies of electrostatic, fluctuation-induced, edge particle transport in *Tokoloshe* tokamak plasmas during controlled mode locking with external, helical (ℓ =2, 3) coils. The measurements were made on reference plasmas characterised by periods of both high and low Mirnov activity and on plasmas locked to fields imposed by the coils. The fluctuation induced transport, $\tilde{\Gamma}$ was estimated from $\tilde{i}_{\rm sat}$ and $\tilde{\phi}_f$ measured with a four-tip Langmuir probe array which could be moved radially up to 2.5 cm into the plasma from the limiter. Electron temperatures and temperature fluctuations were measured with two of the tips configured as a double probe using the technique of [1]. Data were recorded at a 1 MHz sampling rate and all transport analyses were calculated from ensemble averaging over 16 blocks of 128 μs (= 2.048 ms).

RESULTS

Reference plasmas (I_p =120 kA, B_ϕ =0.6 T, R_0 =0.52 m, a =0.24 m) have large m/n =2/1 and 3/1 islands present, rotating at $\simeq$ 8 kHz. The onset of high Mirnov activity varies from shot to shot, but the $\tilde{B}_\theta(m=2)$ trace shown in Figure 1(b) is representative of the activity on the type of shot studied. Figure 1(a) shows the radial profile of the fluctuation induced particle transport, peaking at $\rho(=r/a) \simeq$0.93. These data were obtained between 14 and 20 ms during the 'flat-top' period of the plasma current in the presence of strong gas puffing. The temporal evolution of $\tilde{\Gamma}$ at ρ =0.93, or 1.5 cm, into the plasma from the limiter is shown in Figure 1(b), measured during discharges which exhibited periods of high and low Mirnov activity. The particle transport increases linearly throughout the duration of the discharge up to the major disruption. The temperature and associated fluctuations are shown in Figure 1(c) at three different radial positions, in the region of peak $\tilde{\Gamma}_r$. The temperature is roughly constant at $\approx$ 18$\pm$4 eV and the temperature fluctuations are small ($0.02 \leq \tilde{T}_e/T_e \leq 0.11$ or $\tilde{T}_e/T_e \lesssim 0.5\tilde{i}_{\rm sat}/i_{\rm sat}$) at each radius. Saturated ion current and floating potential fluctuation levels as a function of time are shown in Figure 1(d), taken at ρ =0.93, on the same timescale as 1(b). The fluctuation levels for both $\tilde{i}_{\rm sat}/i_{\rm sat}$ and $\tilde{\phi}_f/T_e$ increase during the low Mirnov activity phase and then decrease while the m =2 tearing mode amplitude starts to grow. Both levels remain constant at about 1.5 $\times$ their levels prior to the growth of the m =2 mode, even after the mode amplitude decays again.

Figure 2 shows data from discharges in which the islands were locked by a resonant ℓ =2 coil pulse for both directions of helical coil current. The coil was switched on at t =10.5 ms and locking of the islands usually occurred 0.5 ms later. Results from the two coil current directions were very similar. Figure 2(a) shows the radial profile of the particle transport

during locking, with the reference results shown as filled circles for comparison. Data for this figure were taken during the locked phase, usually from $t \simeq 12 \rightarrow 17$ ms. Figure 2(b) shows the temporal evolution of $\tilde{\Gamma}$ before and after locking for several shots at ρ =0.93. In some cases the plasma unlocked after ≈7 ms as shown by the $\tilde{B}_\theta(m=2)$ signal in Figure 2(b). The transport first increases linearly, as expected, during the period of high Mirnov activity. Immediately after locking, $\tilde{\Gamma}$ drops to a value $\approx 1/2$ of that prior to locking and remains at this value throughout the locked phase. With the coil current in the opposite direction this effect is again observed, but with $\tilde{\Gamma}$ dropping to only 1/3 of its reference value. In the few cases where the plasma unlocked, the transport once again increases, but at a rate faster than that prior to locking. In most cases, however, the plasma undergoes a major disruption after a period (≈ 5 ms) of locking. Figure 2(c) shows the temperature and associated fluctuations during the locked phase at the three radial positions shown in Figure 1(c). The temperature is, again, roughly constant and slightly lower than the reference case at ≈ 12±2 eV, but the relative level of temperature fluctuations are very large ($0.62 \leq \tilde{T}_e/T_e \leq 0.92$ or $\tilde{T}_e/T_e \lesssim 2.5\tilde{i}_{\rm sat}/i_{\rm sat}$) at each radius. Saturated ion current and floating potential fluctuation levels are shown in Figure 2(d) as a function of time at ρ =0.93, on the same timescale as Figure 2(b). The $\tilde{\phi}_f/T_e$ fluctuation level increases during the low Mirnov activity period and during the growth of the m =2 island, but, at locking, drops to $\approx 1/2$ the value immediately before locking. During locking, the level increases monotonically again at a similar rate to that before locking up to the major disruption. The ratio $\tilde{i}_{\rm sat}/i_{\rm sat}$ is about the same as during the high Mirnov phase in Figure 1(d) and does not seem to depend on whether the mode is rotating or locked.

DISCUSSION

The broad peak in the radial particle transport (Figure 1(a)) occurs about 1.5 cm into the plasma at $\rho \simeq 0.93$. Both ϕ_f and $\tilde{\phi}_f$ peak in this region giving rise to a velocity shear layer of width ≈ 0.8 cm. The radial electric field changes sign across this layer which in turn changes the direction of the phase velocity. The phase angle between $\tilde{i}_{\rm sat}$ and $\tilde{\phi}_f$ also changes sign in this region so the particle transport remains positive at each radial position as observed on many tokamaks.

The profile during locking (Figure 2(a)) retains essentially the same shape as that before locking, but is smaller at each radius. No change is observed in the phase spectrum or phase velocity in both magnitude and sense before and after locking. The coherency between the fluctuating quantities is only slightly higher during locking. Power spectra of both $\tilde{i}_{\rm sat}$ and $\tilde{\phi}_f$ are broadband and essentially featureless with maximum power between 50 and 100 kHz during both reference and locked cases, but the amplitudes during locking are lower. The monotonic increase of $\tilde{\Gamma}$ with time (Figure 1(b)) takes place in the presence of strong gas puffing throughout the discharge. The reduction in $\tilde{\Gamma}$ during the locked phase (Figure 2(b)) is a direct result of the reduction in $\tilde{i}_{\rm sat}$ and $\tilde{\phi}_f$ as can be seen from spectral analysis. A global analysis (Fletcher et. al., this conf.) suggests the main effect of locking is to change the particle source function. Since the locked island orientation at the probe is different with different coils and coil current directions, the similarity of the $\ell = \pm 2$ and $\ell = \pm 3$ results

suggests that they are reasonably representative of the global picture.
The edge electron temperature (Figure 1(c) and 2(c)) is essentially unchanged by locking, but the dramatic increase in $\tilde{T}_e/T_e$ during the locked phase could have serious consequences for the contribution to particle transport deduced from the measured quantities. Standard fluctuation induced transport theory requires a measure of $\tilde{n}_e$ and $\tilde{\phi}_p$, but both of these quantities are difficult to measure in a tokamak. Instead, the edge density is derived from $n_e \simeq i_{\rm sat}\sqrt{m_i}/(Ae\sqrt{T_e})$ (where A is the probe area) and the plasma potential fluctuations from $\phi_p \simeq \phi_f + 3.6T_e$ giving

$$\frac{\tilde{n}_e}{n_e} = \left\{ \left(\frac{\tilde{i}_{\rm sat}}{i_{\rm sat}}\right)^2 - \frac{1}{4}\left(\frac{\tilde{T}_e}{T_e}\right)^2 - \frac{1}{2}\frac{\langle \tilde{n}_e \tilde{T}_e \rangle}{n_e T_e} \right\}^{\frac{1}{2}} ; \frac{\tilde{\phi}_p}{T_e} = \left\{ 13.0\left(\frac{\tilde{T}_e}{T_e}\right)^2 + \left(\frac{\tilde{\phi}_f}{T_e}\right)^2 + 7.2\frac{\langle \tilde{T}_e \tilde{\phi}_f \rangle}{T_e^2} \right\}^{\frac{1}{2}}$$

Relative fluctuation levels of n_e and ϕ_f, then, also involve temperature fluctuations, but these are normally negligible during reference cases. The levels of $\langle \tilde{n}_e \tilde{T}_e \rangle / 2n_e T_e$ and $\langle \tilde{T}_e \tilde{\phi}_f \rangle / T_e^2$ are small ($\lesssim 0.05$) at all radial positions used and are therefore neglected. With values obtained from *Tokoloshe* during the reference cases the error in using $\tilde{i}_{\rm sat}/i_{\rm sat}$ instead of $\tilde{n}_e/n_e$ is $\approx$ 3% and using $\tilde{\phi}_f/T_e$ instead of $\tilde{\phi}_p/T_e$, about 15%. The large temperature fluctuation levels at the edge cannot be ignored during the locked phase since now these errors for $\tilde{n}_e/n_e$ are $\simeq$ 40% and could be up to 100% for $\tilde{\phi}_p/T_e$. Our results contain no *direct* spectral information of $\tilde{T}_e$ so it is impossible to estimate the overall effect on $\tilde{\Gamma}$, however, an estimate can be obtained from the auto-power spectrum of $\tilde{i}_{\rm sat}$. These show that the $\tilde{T}_e$ are low frequency with $\gtrsim$ 80% of the spectral power between $0 \leq f \leq 50$ kHz. It is possible that the phase angle between $\tilde{\phi}_f$ and $\tilde{T}_e$ has a noticeable effect on $\tilde{\Gamma}$ only when the T_e fluctuation levels are high and this could lead to the observed drop in ϕ_f fluctuation levels. Preliminary results taken from discharges in which the islands were locked by the $\ell = 3$ coil show that the phase angle between $\tilde{i}_{\rm sat}$ and $\tilde{\phi}_f$ changes by $\Delta\alpha \simeq 90°$ after locking, which could suggest a phase shift in one or both of the fluctuation quantities — more likely $\tilde{\phi}_f$ because of its strong T_e dependence. The drop in $\tilde{\phi}_f/T_e$ is due to a decrease in $\tilde{\phi}_f$ rather than an increase in T_e since the latter remains more or less the same before and after locking. The strong dependence of $\tilde{\phi}_f/T_e$ on $\tilde{T}_e/T_e$ suggests that this drop could be due to the high level of $\tilde{T}_e$ during locking which may be coherent, but also out of phase with $\tilde{\phi}_f$.

[1] ROBINSON, D. C., RUSBRIDGE, M. G., Pl Phys., **11**, 73 (1969).

Figure 1: (a) Edge $\tilde{\Gamma}(r)$ (b) $\tilde{\Gamma}(t)$ at ρ =0.93 for the reference case with typical $\dot{\tilde{B}}_\theta(m=2)$ trace shown above the graph. (c) T_e and associated relative fluctuation levels. Nominal limiter position is at ρ =1.00, (d) $\tilde{i}_{\rm sat}/i_{\rm sat}$ and $\tilde{\phi}_f/T_e$ as functions of time.
Figure 2: (a) as Fig 1, but during locking of high Mirnov activity. (b) as Fig 1. but with locking and subsequent rerotation of m =2 islands. (c) as Fig 1 but during a period of $\approx$ 4 ms of locking. (d) as Fig 1. but during both high Mirnov activity and the locked phase.

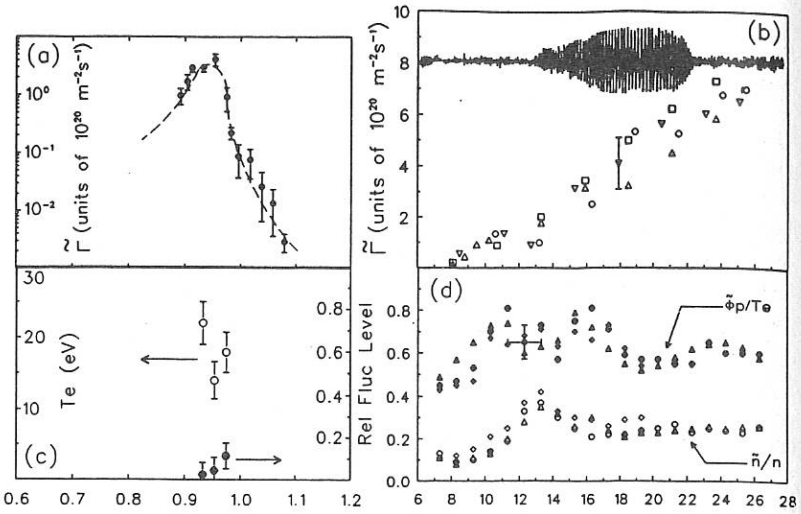

FIGURE 1

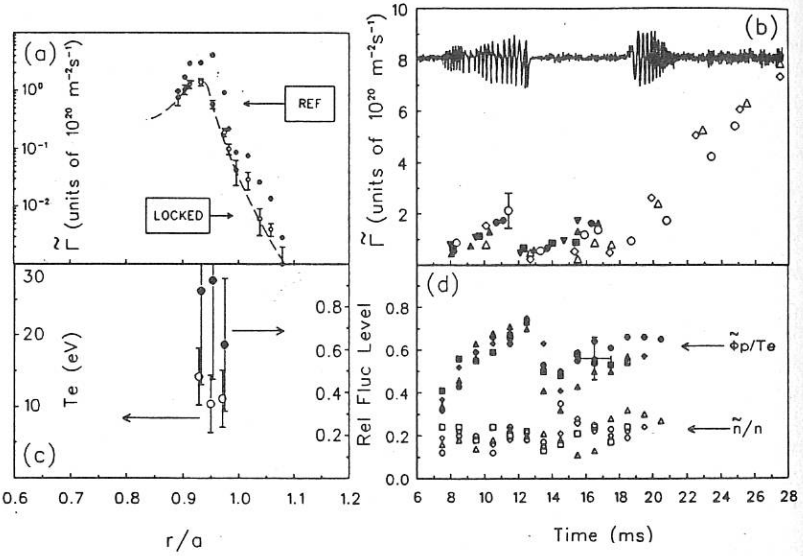

FIGURE 2

SAWTOOTH OSCILLATIONS WITH q_0, THE SAFETY FACTOR ON AXIS, BELOW UNITY

D. Anderson[1], Ya.I. Kolesnichenko[2], M. Lisak[1], F. Wising[1], Yu.V. Yakovenko[2]

[1]Institute for Electromagnetic Field Theory and Plasma Physics, Chalmers University of Technology, Gothenburg, Sweden

[2]Institute for Nuclear Research, Ukrainian Academy of Sciences, Kiev, Ukraine

Introduction

Present theories of sawtooth oscillations in tokamaks are in agreement with a number of experimental facts, e.g. observed plasma flow patterns, precursors, postcursors, time scales etc. Although these parameters may vary between different discharges, there are two standard models, based on ideal MHD, which seem to explain two basic classes of sawteeth. One is the model of Kadomtsev [1], based on a rigid shift of the plasma core. It is characterized by a cold plasma crescent enclosing a hot central plasma region. The other model was proposed by Wesson [2], and is based on a quasi-interchange flow of the plasma. It is characterized by the formation of a hot crescent surrounding a cold plasma center.

However, none of these models are consistent with recent experimental results on q-profiles. In particular, Faraday rotation measurements in JET show values of $q_0 \approx 0.6$-0.8 before a sawtooth, and the corresponding change at the crash is only $\Delta q_0 \approx (1\text{-}2)\%$ [3]. Furthermore, the q=1 surface ($r=r_s$) survives the collapse, a fact which is evidenced by the snake phenomenon. Pellet as well as impurity snakes, localized at the q=1 surface, are only partly contracted at sawteeth, and recover fully during the intermediate phases. The pellet measurements also indicate small values of the shear near q=1. These observations are thus in disagreement with the basic assumption of the Wesson model [2], that $1-q_0 \approx 10^{-2} - 10^{-3}$, as well as with the result of the Kadomtsev model [1], that $q(r) \geq 1$ after a sawtooth.

A model with $q_0 < 1$

In order to remove these discrepancies, we propose a new model [4]. The main feature of this is that the crashes are considered to involve two kinds of plasma motions occuring simultaneously: (i) a rigid shift of the plasma core, and (ii) a quasi-interchange flow in the vicinity of the q=1 surface. This is reasonable if the $q^{-1}(r)$ - profile has a "head-and-shoulder" shape, i.e q_0 is well below unity and the shear near q=1 is small. Note that the two models mentioned above represent limit cases of the new model. Sawteeth dominated by motion of kind (i)/(ii) will be referred to as "shift-dominated"/"interchange-dominated" respectively. Figs. 1 and 2 show possible changes in topology of the magnetic field for such crashes, and we note that full reconnection of the magnetic field lines leads to $q_0 < 1$, provided that two (rather than one) current layers arise.

We introduce the helical flux ψ as (see [5] for notations)

$$\psi(r,\omega) = R\int_0^r dr\ r\ \mathbf{e}_2\cdot\mathbf{B}_* = B_T\int_0^r dr\ r\left[\frac{B_p(r,\omega)}{\varepsilon B_T} - 1\right] \tag{1}$$

Assuming $q_0 < 1$ after the crash, we may write the conservation laws for magnetic flux and volume as follows (we assume that $dq/dr \geq 0$ before the crash):

$$\psi^-(r_1^-) = \psi^-(r_2^-) = \psi^+(r_1^+) = \psi^+(r_2^+) \tag{2}$$

$$\frac{\partial\psi^-(r_1^-)}{\partial r_1^-}\,dr_1^- = \frac{\partial\psi^-(r_2^-)}{\partial r_2^-}\,dr_2^- = \frac{\partial\psi^+(r_1^+)}{\partial r_1^+}\,dr_1^+ = \frac{\partial\psi^+(r_2^+)}{\partial r_2^+}\,dr_2^+ \tag{3}$$

$$dV_1^- + dV_2^- = dV_1^+ + dV_2^+ \tag{4}$$

where $dV = 2\pi R\,rdr$, the subscript 1/2 label values at $r<r_s/r>r_s$ and minus/plus denote values before/after the crash. We assume that the volume V_2^- contributes to the formation of the whole plasma mixing region, whereas the volume V_1^- takes part only in producing the volume V_2^+. We also introduce the flux surface function $W(\psi)$, determining the fraction of the volume dV_2^- producing the cold plasma core with $q < 1$. These restrictions of the conservation laws correspond to the physical picture described in Figs. 1 and 2, and we may now split Eq. 4 as follows:

$$\begin{aligned} dV_1^+ &= W\,dV_2^- \\ dV_2^+ &= (1-W)\,dV_2^- + dV_1^- \end{aligned} \tag{5}$$

In order to demonstrate our model we consider the limit case $q_{10}^+ = q_{10}^-$, and for simplicity we assume

$$W = \begin{cases} \text{const}, & r_2^- < r_{20}^- \\ 0, & r_2^- \geq r_{20}^- \end{cases} \quad \text{where} \quad \left(\frac{r_{20}^-}{r_s^-}\right)^2 = 1 + \frac{1}{W}\left(\frac{r_s^+}{r_s^-}\right)^2 \tag{6}$$

The system of equations (1), (2), (3), (5) and (6) has a unique solution which determines the only possible profile of q(r) resulting from the crash, provided q(r) before the crash as well as the radius of the q=1 surface after the crash are known. Taking a physically and experimentally reasonable "head-and-shoulder" $q^{-1}(r)$-profile before the crash and assuming $(r_s^-/r_s^+)^2=2$, we obtain the q-profiles and flux profiles before the crash (dotted lines) and after the crash (solid lines) shown in Fig. 3. The q-profile has changed negligibly, apart from the contraction of the q=1 surface.

Application of model to JET experiments with NBI

We have also analyzed the behaviour of fast particles at sawteeth using our new model. The Fokker-Planck equation is solved numerically to obtain the distribution function of the injected fast ions before the crash. Since the fast ions are expected to follow the magnetic field lines [5] we can write the formula for conservation of the number of fast particles as

$$f_1^+ \, dV_1^+ = W \, f_2^- \, dV_2^-$$
$$f_2^+ \, dV_2^+ = (1-W) \, f_2^- \, dV_2^- + f_1^- \, dV_1^- \qquad (7)$$

where f is the distribution function. Using Eqs. (1), (2), (3), (5) and (7) we obtain an expression for the fast ion distribution function after the crash:

$$f_1^+ = f_2^-$$
$$f_2^+ = \frac{\nu_1 \, f_1^- + (1-W) \, \nu_2 \, f_2^-}{\nu_1 + (1-W) \, \nu_2} \qquad (8)$$

where $\nu = |q^{-1}(r) - 1|^{-1}$. The density and temperature profiles of the thermal ion population are obtained similarly. The radial distributions of the neutron emissivity before and after the crash are then calculated and integrated along the lines-of-sight of the JET neutron profile monitor, c. f. Fig. 4. The flux surface geometry obtained from MHD equilibrium calculations is used during the integration. In addition, the change of the global neutron emission is also calculated and compared with the experimental results. The model is found to be consistent with the experimentally observed change in neutron flux (within error bars of the experimental data), provided the q(r)-profile is chosen properly (Fig. 5). Note that this q-profile is consistent with experimentally inferred constraints, e. g. the observed small changes of q_0 during crashes and the persistence of the q=1 surface as evidenced by the snake observations.

Conclusions

We have presented a new model for sawtooth oscillations which is consistent with experimental observations of q-profiles, in particular with observations of q_0 well below unity after a crash. The model contains the models of Kadomtsev [1] and Wesson [2] as limit cases, and its predictions for fast ion behaviour are in agreement with JET NBI experiments.

Acknowledgements

This work was carried out under JET contract no. JT1/13435.
We gratefully acknowledge valuable discussions with the helpful JET staff.

References

[1] B.B. Kadomtsev, Sov. Journ. of Plasma Phys. **1** (1976) 389.
[2] J. A. Wesson, Plasma Phys. Contr. Fusion **28** (1986) 243.
[3] J. O'Rourke et al., Proc. 17th EPS Conf., Amsterdam, **14B** (I) (1990) 343.
[4] Ya. I. Kolesnichenko et al., Preprint CTH-IEFT/PP-1991-25
[5] Ya. I. Kolesnichenko et al., Nucl. Fus. **32** (1992), to be published

Figure captions

Fig. 1 Evolution of $\mathbf{B}_*$ during a shift-dominated crash: (a) the initial state; (b) shift of the large hot plasma core and formation of a small cold bubble; (c) the hot core is enclosed by a cold crescent which is perturbed by a colder island with $q<1$; (d) the final axisymmetric state with a cold plasma core and $q_0<1$. Notations: dotted line represents the q=1 surface ($\mathbf{B}_* = 0$); clockwise directed field lines - $q>1$; counter-clockwise directed lines - $q<1$; A and B - reconnection layers; bold arrows indicate direction of plasma motion.

Fig. 2 Evolution of $\mathbf{B}_*$ during an interchange-dominated crash with successors: (a) the initial axisymmetric state; (b) shift of the hot plasma core and formation of a large cold bubble, (c) formation of a cold core with $q<1$ enclosed by a hot crescent; (d) formation of the q=1 surface with reduced radius; (e) the final axisymmetric state with a cold core and $q_0<1$.

Fig. 3 Safety factor q(r) and flux $\psi(r)$ before the crash (dotted) and in the final axisymmetric state (solid lines) assuming $q_0^+=q_0^-=0.8$.

Fig. 4 Pulse #20981. Measured (solid) and calculated (broken) neutron-flux at channels 1-10 corresponding to the q-profiles of Fig. 5.

Fig. 5 Pulse #20981. Calculated q-profiles before (solid) and after (broken) sawtooth assuming $q_0^+=q_0^-$.

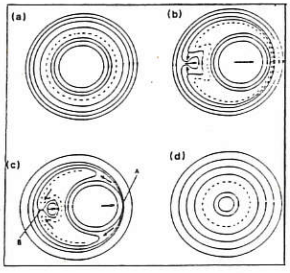

Fig. 1

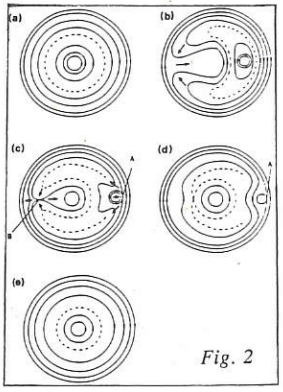

Fig. 2

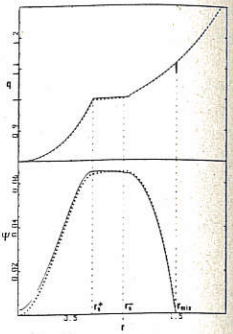

Fig. 3

Fig. 4 Neutron flux #20981

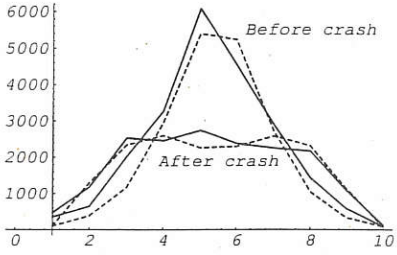

Fig. 5 q-profile #20981

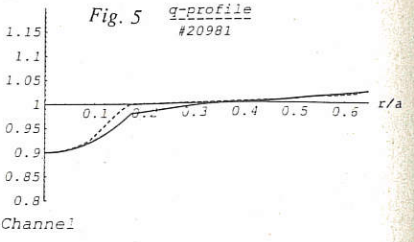

SAWTOOTH ACTIVITY AND PHOTONEUTRON PRODUCTION

G.C.Guo[1], Y.Z.Zhong[1], J.F.Dong[1] and B.Z.Fu[1]
J.W.Yang[2], G.Y.Zhang[2], W.X.Liang[2], D.F.Gong[2] and M.L.Shi[2]

(Southwestern Institute of Physics, Chengdu, Sichuan 610041, China)

1. SAWTEETH

The sawtooth activity in HL-1 exhibits some complexity. The analysis is mainly relying on soft X-ray measurements. The characteristics of sawteeth are significantly difference under different discharge conditions. Main five types of sawtooth were observed during sawtoothing discharges, and most of them were detected in high density and current 'flat-top' phase. The changes of the mode behaviour superimposed on sawteeth imply the presence of different crash mechanisms.

In most of sawtoothing discharges, the sawteeth with classic growing m=1 oscillations predicted by Kadomtsev model before sawtooth crash are often observed (Fig.1). The growth-rates of the m=1 oscillations ($\gamma = 2\text{-}5 \cdot 10^3\ s^{-1}$) in a wide spectrum of discharge parameters are obtained, and almost no consistent growth-rates could be found for a given set of discharge parameters. But the value of growth-rate γ for deuterium plasma is larger than that in hydrogen discharges. The sawteeth without precursor oscillations for all of soft X-ray channels were frequently observed during the current rise and/or 'flat-top' phase. They occur generally in low q_a ($q_a \approx 2 - 2.3$) discharges (Fig.2). According to the analysis of discharge conditions , the occurrence of sawteeth of no m=1 precursor oscillations appears to be to have relation with the flat current density (j) profile, because there are relatively flat Te and j profiles in the plasma central region in low q_a discharges in HL-1. Fig.3 shows a type of sawteeth with large m=1 oscillations, m=1 oscillations occur throughout the sawteeth, with almost no change in amplitude and frequency through the sawtooth crash. The type of sawtooth is very simular to that in TEXT obtained[1]. Occasionally, 'compound' sawteeth were observed for some operating regimes. They are interspersed among normal sawteeth (shown in Fig.4), it implies that a small and/or localized changes of plasma parameters may significantly affect the sawtooth characteristics. In general, the successor oscillations are often observed follow the partial crash, and no precursor oscillations preceding the full crash. But in our results, the m=1 oscillations observed are large growing precursor preceding the partial crash rather than successor follow the partial. And there are the small m=1 oscillations with unchange in amplitude and/or frequency superimposed on complete relaxation. This feature of compound sawtooth in HL-1 is different from other Tokamak devices[2,3]. In relatively high plasma current (Ip>120kA), high density ($\bar{n}_e \geqslant 4 \cdot 10^{13}\ cm^{-3}$) discharges, the sawteeth with successor oscillations were observed during current and density rise phase, when the line integrated electron density increases sharply (as shown in Fig.5). It seems to imply the presence of different mechanisms for the m=1 mode due to the different j profiles during the phase in the centre region.

---

[1] Soft X-ray group
[2] Neutron group

2. ENERGY OF RUNAWAY ELECTRON AND PHOTONEUTRON

(1) The Energy of Runaway Electron

Runaway electrons (R.E) exist in tokamak plasma and sometimes these elctrons can reach the energy level beyond 10Mev. In normal ohmic discharge, if the duration time of plasma are sufficiently long, the runaway electron can enter a steady state, in this case, the confinement time τ_r of R.E exceeds 400ms in HL-1 tokamak. The energy of R.E is determined by accelerated electric field produced by loop voltage (46.8Mev/v.s in HL-1) and the cyclotron radiation losses due to curvature of trajectories. When a disruption occures, the plasma current falls sharply and the loop voltage gives rise to a high level, it may exceed 100v for period of 10ms or longer, in this case, the original R.E or superthermal electron which exist in plasma may be accelerated to several tens Mev.

The energy of R.E are shown on Fig.6, as function of time for different conditions (4, 5).

(a) Pure acceleration by electric field, the loop voltage signal from shot 10153 has been used.

(b) Including cyclotron radiation, pitch angle $\theta = 0$.

(c) Considering in the presence of small vertical velocity component of R.E, the radius of cyclotron decrease and the cyclotron radiation power are enhanced, we take the mean pitch angle obtained with coulomb scattering, $\theta = 60^0/\lambda$, λ is the Larmor radius of R.E.

The results of calculation show that the energy of R.E induced by parallel electric field may reach 70Mev and 80Mev in normal and disruptive ohmic discharge respectively. After deducting the cyclotron radiation losses and their enhancement the energy of R.E are about 55Mev and 65Mev respectively. The estimated actual values which are lower than calculation cover range from 15Mev to 30Mev.

(2) Photoneutron Production

The strong photoneutron emission measured by BF_3 long counter has been observed during major disruption or at the end of normal ohmic discharge in HL-1 takamak. The experiment in laboratory shows that this detector is insensitive for γ - rays and hard X-rays. We assume that all the runaway electrons are brought to rest in the limiter material (Molybdenum in HL-1), the energetic bremsstrahlung which completely escapes from limiter, only are wholly absorbed in the vacuum vessel wall material (stainless steel, main compositions are Nickel and Chromium), therefore, the photonuclear reactions are 58Ni (γ,n) 57Ni (T=12.2Mev) and 52Cr(γ,n) 51Cr(T=12.0Mev), the estimated photoneutron yield is $6.3 \cdot 10^{-4}$ neutrons per 30Mev electron (for Nickel) (6). The intrinsic efficiency of detector which has been calibrated is roughly 10%, the measured photoneutron yields cover the range from 10^8 to 10^{10} neutrons per discharge, the average intensity during photoneutron emission is about $2.5 \cdot 10^{10}$ neutrons/s. Fig.7 show photoneutron and hard X-ray signals in disrption discharge for hydrogen plasma.

REFERENCES

(1) J.A.SNIPES, et.al. Nuclear Fusion, V01. 26, No.11 (1986)
(2) S.B.KIM. Nuclear Fusion, V01.26, No.9 (1986)
(3) C.JANICKI, et.al. Nuclear Fusion, V01.30, No.5 (1990)

(4) O.N.JARVIS et al., Nucl. Fusion 28 (1988) 1981
(5) M.CFATELIER et al., "Runaway Electrons Dynamic and Confinement in TORE-SUPRA ", 16th EPS, Venice, 1989, Part I, 19.
(6) H.BOLT and A.MIAHAVA, "Runaway Electron -Materials Interaction studies", ISSN 0915-6356, NIFS-FECH-1, Nagoya, Japan, March 1990.

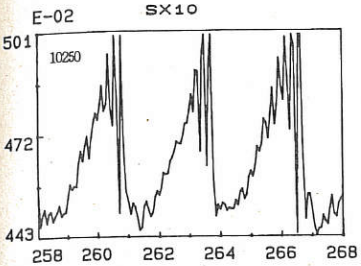

Fig.1 Sawtooth signals with classic growing m=1 oscillations in hydrogen plasma, $\bar{n}_e = 4.6 \cdot 10^{13}$ cm^{-3}

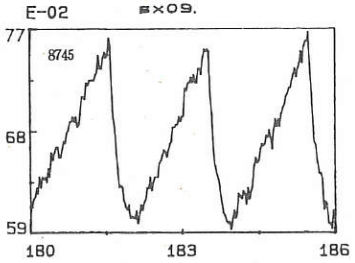

Fig.2 Sawteeth without m=1 oscillations in low q_a hydrogen discharge, $\bar{n}_e = 3.2 \cdot 10^{13}$ cm^{-3}

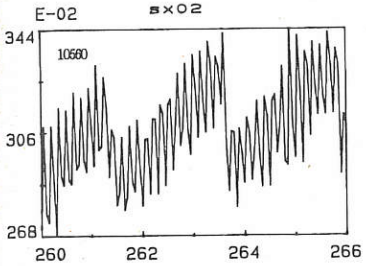

Fig.3 Sawteeth with large m=1 oscillations in deuterium plasma.

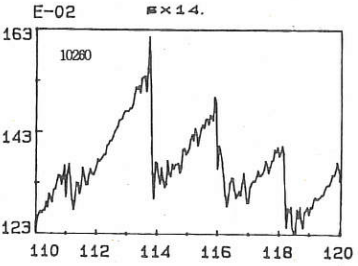

Fig.5 Sawteeth with successor oscillations in deuterium plasma.

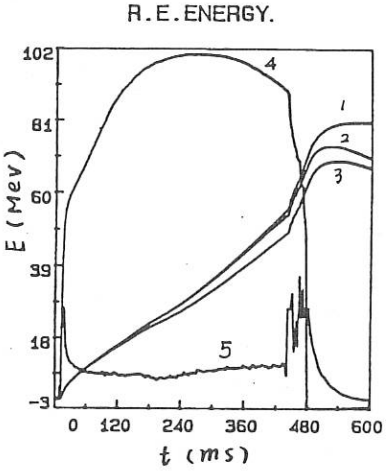

FIg.6 The energy of R.E
Curve 1, pure acceleration by electric field.
Curve 2, after deducting the cyclotron radiation loss at zero pitch angle.
Curve 3, cyclotron radiation power enhance due to the radius of cyclotron radiation decrease. pitch angle = $60°/\lambda$.
Curve 4, plasma current.
Curve 5, loop voltage.

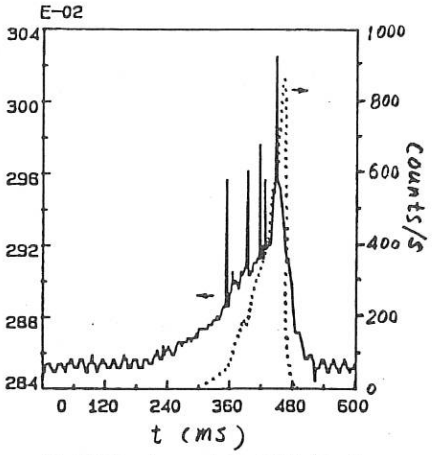

Fig.7 Photoneutron emission (dotted line) and hard X-ray (solid line) signal.

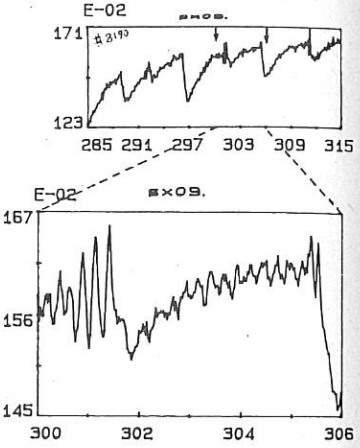

Fig.4 Compound sawteeth in hydrogen plasma, $\bar{n}_e = 6.5 \cdot 10^{13}\,cm^{-3}$

MHD PROPERTIES OF LOW-ASPECT RATIO TOKAMAK PLASMAS

M Gryaznevich, A Bondeson*, R Duck** T C Hender, D C Robinson, A Sykes
AEA Fusion, Culham Laboratory, Abingdon, Oxon, OX14 3DB, UK
(Euratom/UKAEA Fusion Association)
*Centre de Recherches en Physique des Plasmas, Lausanne, Suisse
**Dept of Pure and Applied Physics, UMIST, Manchester, UK

Introduction The improvement of both ideal and resistive stability in low-aspect ratio tokamaks has been theoretically predicted in /1/. The first experimental investigation of the stability properties of low-aspect ratio tokamak plasmas has been carried out in the START (Small Tight Aspect Ratio Tokamak) experiment. No major disruptions have been observed for aspect ratios 1.3 - 1.6.

Experimental Apparatus The main parameters of START are presented in /2,3/. Discharges used for this analysis have $R/a = 1.3-1.6$, $R \sim 0.2$m, $\kappa \sim 1.4-2.0$, $\delta \sim 0.4$, $I_{pl} \sim$ 90-140kA, $B_{tor} \sim 0.5$T, q_ψ (a) $\sim$ 6-12, $\bar{n}_e \sim 4-8\times10^{19}m^{-3}$. The soft-X-ray imaging system used for investigation of the internal mode structure consists of two arrays with seven horizontal channels (separation $\Delta \sim 6.5$cm at $R = 0.2$m) and 11 vertical channels ($\Delta \sim$ 3cm at the equatorial plane), as shown in Fig 1. Two symmetrical sets each of 44 Mirnov probes arranged as shown in Fig 1 were used for cross-correlation analysis. The typical equilibrium flux contours from magnetic reconstruction, an associated CCD-image in visible light and the positions of the poloidal field coils are also shown.

Axi-Symmetric Stability Low aspect ratio plasmas are naturally elongated /4/, the elongation κ being strongly dependent upon the current density profile as well as the aspect ratio. START plasmas are observed to be vertically stable despite the absence of any active feedback stabilisation. The elongation can be as high as 2.0 for broad current profiles, consistent with the increased natural elongation predicted at tight aspect ratio. Attempts to increase the elongation beyond this natural value lead as expected to vertical instability, the plasma position then drifting vertically subject to passive stabilisation from the vessel structure and poloidal field coil cases /5/.

Disruptions in START In all START discharges so far (>8300) no major disruptions have occurred whilst the aspect ratio is less than two, over a considerable range of plasma current (60-220kA) and density ($\bar{n}_e \sim 1-8.10^{19}m^{-3}$). Several explanations for this stability improvement at low aspect ratio have been proposed: high edge q-values; increase in the geometrical shear near the edge; decrease in saturated island size due to strong toroidal and shaping effects causing coupling with stable modes /1/; smaller island sizes making overlap much less likely. Several attempts have been made to induce a major disruption. The range of q-values in these shots is quite high, $6 < q_\psi < 12$, although the shear near the plasma edge is also very high. The toroidal field value is already rather low and any further reduction in the initial value inhibits breakdown /3/.

The plasma current value is limited by the stresses in the poloidal field coils. A fast current increase induced at different times in the discharge can produce a disruption only when the aspect ratio is above two. The density limit disruption seems not to have been achieved so far, despite the fact that the Murakami parameter $M = \bar{n}R/B = 3-4$ at $q_\psi \sim 10$ ($q^* \sim 5$).

An increase in the initial filling pressure (which it is thought leads to a greater peaking of the current density profile) usually causes the appearance of an internal reconnection, Fig 2. This is accompanied by a negative spike on the loop voltage and a positive spike on the plasma current. During the reconnection no significant change of plasma position is observed. The increase in the plasma current can be explained by a flattening of the current density profile assuming flux-conservation. An accompanying increase in the plasma elongation supports this explanation as the vertical field decay index remains constant. Although the increase in the plasma current can reach 40% this event never terminates the discharge. Several such events can occur during a discharge producing non-regular sawtooth-like behaviour of the SXR-emission.

Kink Mode Observation Accompanying these reconnections a strong asymmetry of the plasma shape is observed. Figure 3 shows some examples of such perturbations observed in the CCD-images. The helical structure of the perturbation possibly indicates a large amplitude internal kink mode. This non-linear saturation of the kink instability has been predicted theoretically /6/ but has not to our knowledge previously been observed in tokamaks. In START it may be that the conducting central column assembly acts as a partial shell. The observed saturation of the kink mode may be related to the absence of the major disruption in START.

Precursor Analysis MHD-fluctuations with frequencies of 6-30kHz and edge amplitudes up to $\delta B_\Theta/B_\Theta \sim 1.1\%$ do not terminate the discharge at low-aspect ratio, although they can be accompanied by a sawtooth-like internal reconnection, as described above. Typical magnetic and SXR precursors to the reconnection event are shown in Fig 4. Analysis shows them to be dominantly n = odd, but the poloidal mode number can vary. The precursor fluctuations in B_Θ show strong peaking near the inboard mid-plane (Fig 5). The theoretical explanation for these precursor oscillation is still under investigation. The SXR oscillation seems to be well fitted by a dominantly $m/n = 2/1$ instability as calculated with the FAR code /7/; the flux surfaces for this instability have a rich satellite structure as shown in Fig 6. For this simulation the equilibrium has gross parameters $(R/a, \kappa, I_p, B_{tor})$ matched to the experiment and $q_o = 1.2$. By assuming constant SXR emission on a given flux surface the SXR chord integrals can be calculated for the case shown in Fig 6; these reconstructed SXR chords show a reasonable match in relative phase with the experiment. It should be noted however, that free-boundary simulations with $q_o = 0.6$ giving a dominantly $m = n = 1$ mode can also be made to fit the Mirnov probe data, but are difficult to reconcile with the SXR waveforms.

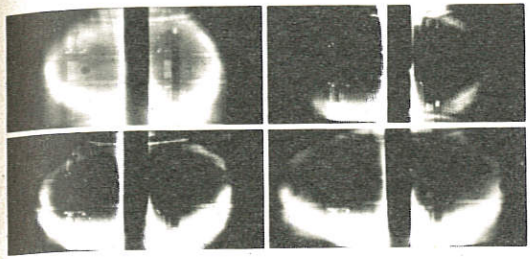

FIG.3
Asymmetry of the plasma shape accompanying the internal reconnection

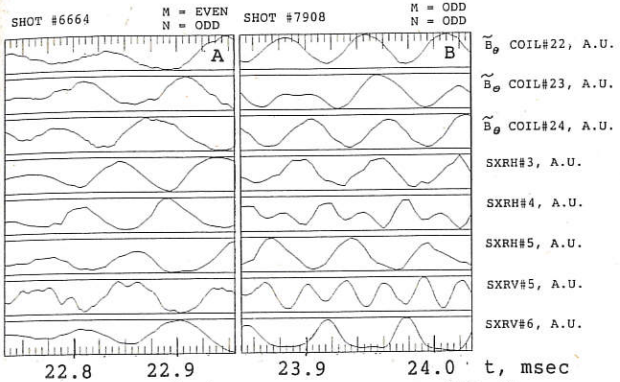

FIG.4. SXR and Mirnov precursor oscillations

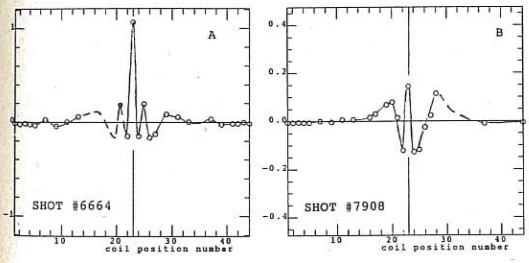

FIG.5. Results of correlation analysis of precursors shown in Fig.4: relative amplitudes of Mirnov probe signals for case a and b (SXR m = even/odd)

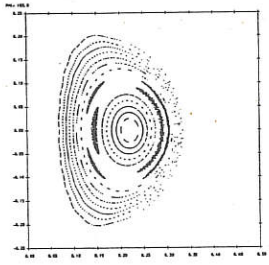

Fig. 6. Perturbed flux structure for $m/n = 2/1$ (result of FAR simulations)

Conclusions The absence of the major disruption in low-aspect ratio configurations is an important result supporting the Spherical Torus Reactor concept /8/. The measured structure of the precursor to the internal reconnection event which is observed in some shots is in agreement with a theoretical model and shows a rich satellite tearing mode structure. The natural elongation effect in a low aspect ratio tokamak allows START plasmas to be vertically stable for $\kappa \leq 2.0$ without any active feedback stabilisation.

/1/ B A Carreras et al, Proc of Plasma Phys & CNFR, Kyoto, IAEA, 1986, V2, p53
/2/ A Sykes et al, this conference, invited papers
/3/ A Sykes et al, AEA FUS 132, 1991; Nucl Fus, 1992
/4/ Y-K M Peng, D J Strickler, Nuclear Fusion 26, (1986), p769
/5/ M Gryaznevich et al, Proc 18th IOP Plasma Phys Conf, 1991, Colchester, p177
/6/ L Zakharov, Sov Journ of Plasma Phys, V7, n1, (1981), p8
/7/ L A Charlton et al, Jnl Comp Phys, 86, (1990), p270
/8/ Y-K M Peng & J B Hicks, Proc 16th SOFT, Fusion Technology 2 p1287, 1990.

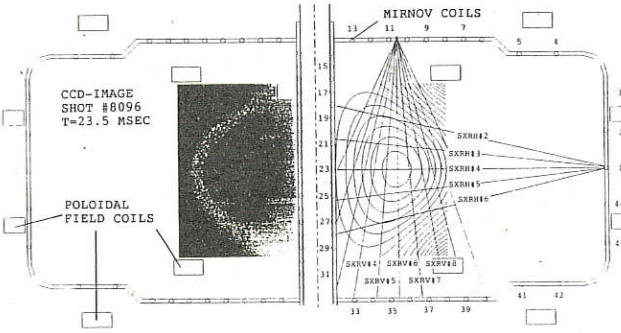

FIG.1
Diagnostic frames and SXR views. On the left side CCD-image shot #8096.

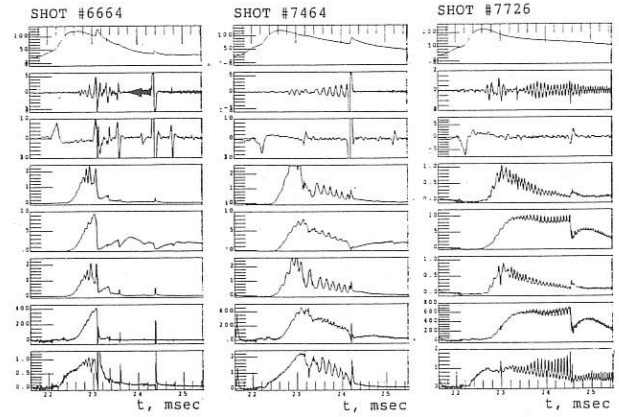

FIG.2. Typical traces for shots with internal reconnections.

EXCITATION OF FAST DENSITY OSCILLATIONS BY PELLET INJECTION AND ITS RELATION WITH SAWTOOTH ACTIVITY IN TEXTOR PLASMAS

K.N.Sato[1], H.Akiyama[2], S.Kogoshi[3], N.Noda[1], M.Sakamoto[1], K.H.Dippel[4], K.H.Finken[4], G.Fuchs[4], H.R.Koslowski[4], H.Soltwisch[4], KFA TEXTOR Team[4]

1) National Institute for Fusion Science, Nagoya 464-01, Japan
2) Kumamoto University, Kumamoto 860, Japan
3) Science University of Tokyo, Noda 278, Japan
4) IPP, KFA Julich, Association Euratom-KFA, D-5170 Julich, Germany

[1] Introduction

Ice pellet injection experiments have been widely carried out with various toroidal plasmas, and some interesting phenomena have been found until now. One of them is the unique oscillation of soft X-ray emission region after pellet injection observed in Alcator C[1], JET[2], JT-60[3] and W7-AS[4], which has sometimes been called the "Snake" oscillation.

A deuterium (hydrogen) ice pellet with a size of 1.4 mm (ϕ and l) and with velocities in the range of 400~900 m/s has been injected into ohmically heated plasmas in the TEXTOR tokamak (B_t=2.25 T, Ip=220~430 kA, n_e=1~4x10^{19} m^{-3}), and a couple of interesting phenomena have been studied. Fast oscillations of large perturbation in density and slight one in temperature have been observed just after the pellet injection. The structure of the activity has been analyzed in detail, and the relation with sawtooth activities has been discussed.

[2] Excitation of Fast Density Oscillations by Pellet Injection

Excitation of fast and large density oscillations has been observed in the core region of pellet-injected TEXTOR plasmas. The phenomena are prominent in density since the oscillations have been detected clearly by the FIR interferometer and the soft X-ray systems, they have, however, only marginally by the ECE measuring system. The phenomena seem to be similar to those observed by soft X-ray measurements in the Alcator C and JET, and to recent results in JT-60, although there exist several differences.

Typical results of electron line densities obtained by the 9-channel FIR interferometry are shown in Fig.1(a). The fast oscillation of large perturbation is clearly seen in the core region (on channels No.5 and No.6) just after the pellet injection. The oscillation seems more likely to occur when a pellet is injected more deeply into the plasma.

The frequency is typically around 0.7-2 kHz and the oscillation usually terminates after about ten msec. In some cases, however, it appears not only immediately after the injection (which we call the first oscillation), but also some tens of milliseconds after the termination of the first oscillation, as shown in Fig.1(b). Here, we call it the second oscillation. Sometimes, the first and the second ones seem to interact with each other (Fig.1(c) and (d)), possibly depending upon the timing (or phase) of pellet injection with respect to the sawtooth activity before the injection. These second oscillations are the unique features in the TEXTOR plasma, which have not been observed on other experiments.

The frequency of these phenomena in the TEXTOR is between those in Alcator C (~5kHz) and JET/JT-60 (0.03~1kHz). The oscillations start immediately after the injection in Alcator C and TEXTOR, while in JET and JT-60 a certain build up time (~10ms and/or 0.2~0.3 sec) is needed. Also, the duration times differ from each other, and again the TEXTOR case is

between Alcator C (~1ms) and JET/JT-60 (0.2~2 sec).

The structure of these activities has been analyzed in detail. Poloidally it rotates in the electron diamagnetic drift direction with a mode number m=1, as shown in Fig.2. Here, a correlation on amplitudes of ch.17 and ch.23 has a large value in the frequency range 0.8-1.7 kHz, and a correlation on phase in this frequency range brings about the result of the mode number m=1. On the other hand, toroidally it seems to rotate in the plasma current direction with the mode number almost n=1 or at least odd. More detailed study will be needed to have a precise conclusion, however, the location of the oscillation suggests that it should be n=1.

Observations by the soft X-ray system indicate the location of the first oscillation to be almost near or very slightly inside the sawtooth inversion radius, as seen in Fig.3. This is similar to the case in JET, however, it is not the case in Alcator-C and JT-60.

[3] Relation of Oscillations with Sawtooth Activity

Excitation of the fast density oscillations might have some relation with sawtooth (ST) activity before the pellet injection.

As mentioned in the previous section, in some cases the oscillation revives once again after its first termination with a certain interval (Fig.1(b) and (c)), or without an interval by interacting the first and the second oscillations with each other (Fig.1(d)). The characteristics of these oscillations and precursors of ST activity have been compared.

Frequencies of the first, the second and a precursor oscillations differ from each other. The precursor frequency is always larger than the other two. The first oscillation is slower than the second one, and sometimes its frequency changes gradually in time. This may be due to the rapid change of plasma parameters just after pellet injection, and also might have some relation with ST activity. On the other hand, the mode structure of these three is similar to each other, that is m=1. From analysis of the soft X-ray signals, one can conclude locations of the oscillations, as in Fig.3. The precursor and the first oscillations seem to localize near the ST inversion region, however, the actual location of the first oscillation is more inside than that of the precursor.

Many cases have been examined with respect to the injection timing (or phase) as to the ST oscillation. In the case in Fig.4(a), the injection timing is at 95% of the ST period normalized by previous several ST activities. One could deduce a reason of the oscillation to be because of an accumulation of the ST activity (95%); that is the memory effect. However, the case in Fig.4(b) shows that the first oscillation still may occur even with the phase of 20%. On the other hand, this example might lead an argument that the ST activity may be a cause of the second oscillation, because it exists at about 100%. But, examples in Fig.4(c) and (d) are of 52 and 56%, respectively, and have different features of the first and the second oscillations.

Thus, these three (precursor, 1st and 2nd) oscillations differ from each other in frequency and location, they have, however, similar mode structures and from the comparison there may result a useful information on sawtooth activity of tokamak plasmas. The characteristics of the phenomena seem to be qualitatively similar in the several machines (Alcator-C, JET, JT-60 and TEXTOR), however there exist several differences in quantitative features. One explanation of these phenomena might be the persistent trapping of particles ablated from a pellet inside magnetic islands by some reasons[5,6], however more detailed studies will be necessary to identify the mechanism clearly.

References

1) J.Parker et al. : Nuclear Fusion 27 (1987) 853.
2) A.Weller et al. : Phys. Rev. Letters 59 (1987) 2303.
3) Y.Kamada et al. : JAERI-M 90-123.
4) A.Weller : private communication.
5) G.Kurita et al. : IAEA-CN-53/D-4-1, part B (1990).
6) S.I.Itoh et al. : Comm'ts Plasma Phys. Cont'ld Fusion 13 (1990) 141.

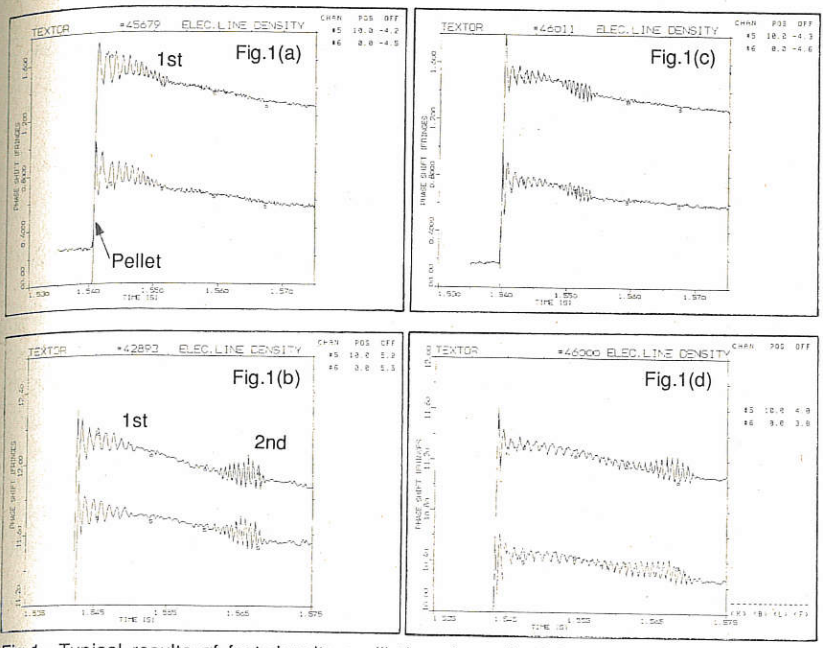

Fig.1 Typical results of fast density oscillations by pellet injection, (a) without the 2nd oscillation, (b) with the 2nd one after a certain interval, and (c)&(d) interacting (1st and 2nd ones) with each other.

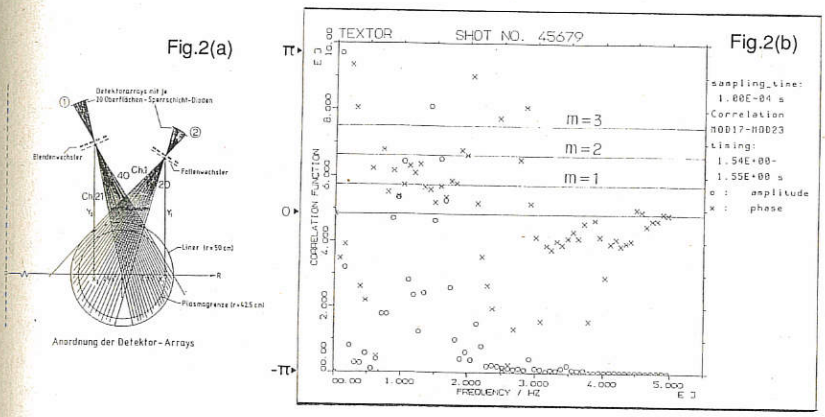

Fig.2 (a) Mode analysis of the oscillation by the multichannel soft X-ray system, and (b) a typical result of the analysis, where correlation functions of amplitude (O) and phase (X) are presented.

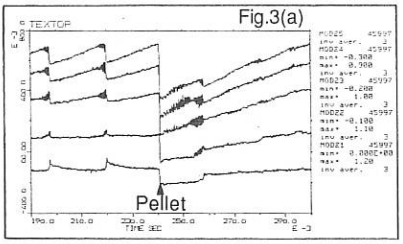

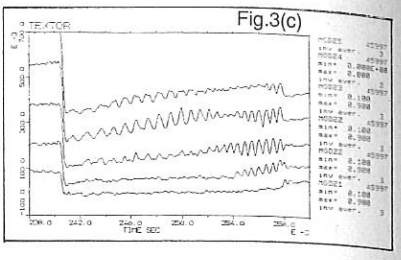

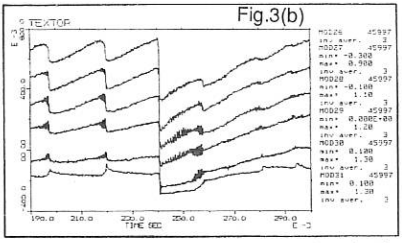

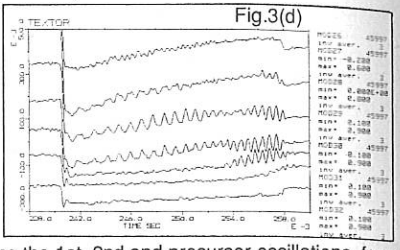

Fig.3 A typical result of soft X-ray signals showing the 1st, 2nd and precursor oscillations, from which locations of the oscillations and of inversion radii can be deduced.
(a) Ch. 21~25. (b) Ch. 26~31. (c) and (d) Time expansion of (a) and (b), respectively.

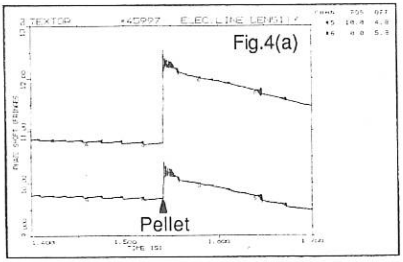

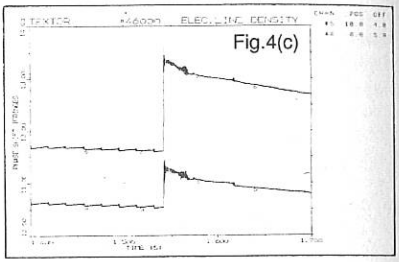

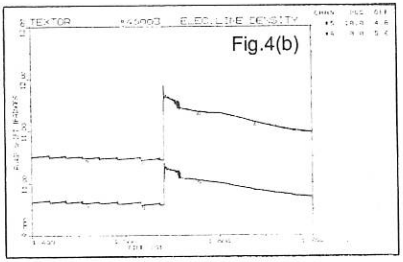

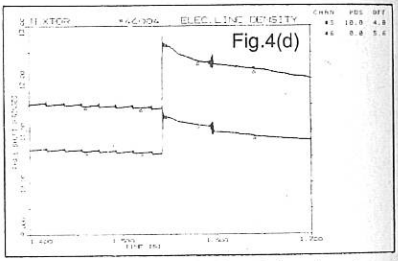

Fig.4 Several results of the density oscillations with various pellet injection timing (or phase) with respect to sawtooth activities.

First Measurements of Fast MHD Fluctuations in JET by ECE Correlation Radiometry

A M Zolfaghari*, D V Bartlett, A E Costley, P Cripwell, S E Jones*, J Kesner*
S C Luckhardt*, L Porte, J J Ramos*, R J Smith, P P Woskov*

JET Joint Undertaking, Abingdon, Oxon, OX14 3EA, UK
**MIT Plasma Fusion Center, Cambridge, Massachusetts, 02139 US*

INTRODUCTION. The experimental study of MHD activity in JET has become increasingly important in the study of plasma stability and confinement of high performance discharges. In plasmas with high beta and large pressure gradients a variety of MHD modes can be destabilized. Pressure perturbations due to MHD modes can produce fluctuations in the electron temperature and density and therefore in the electron cyclotron emission (ECE), which can be related to the frequency spectrum and spatial structure of such modes[1]. Heterodyne radiometry, which measures ECE with good spatial resolution and radial coverage of the plasma, is suitable for detection of these modes. In this paper we will present the first measurement of fast MHD mode fluctuations in JET high beta discharges using this technique.

EXPERIMENTAL TECHNIQUE AND SETUP. It has been shown[2] that the fluctuations in the ECE signal caused by MHD modes can be related to the component of the MHD mode displacement vector normal to the isobaric surface at the radius corresponding to the emission frequency. Therefore the radial structure (location, wavelength and extent) of the MHD mode perturbations can in principle, be determined by analyzing the ECE fluctuation measurements at various spatial locations which are recorded on different channels of an ECE radiometer. The data is analyzed using temporal and spatial correlation techniques. The instrument used to perform these measurements on JET is a multichannel heterodyne radiometer[3]. It has 44 frequency channels equally spaced in 4 bands covering the frequency range 73 to 127GHz which span a significant fraction of the plasma cross-section (at first, second and third harmonics of the electron cyclotron frequency), the precise range depending on the toroidal field. A fast data acquisition system was used to make simultaneous measurements at up to 1MHz sampling rate on any 8 channels of the radiometer.

MEASUREMENT CONDITIONS. ECE measurements have been taken on high beta low toroidal field H-mode discharges. Most of these discharges have reached beta values near the Troyon limit (β^T). Those with the highest performance exceeded the Troyon limit before a beta collapse occurred[4]. In particular, discharge #26236 reached a maximum beta of 6% which exceeded the Troyon limit by 20% before the beta collapse. Fast ECE measurements were made during shot #26236 on 8 channels of the radiometer

in the time interval t=15.4 sec. to t=16.1 sec. Due to low toroidal field and possible cutoff in the second harmonic, the radiometer recorded X-mode ECE from the third harmonic of the electron cyclotron frequency. The optical thickness of the plasma for the 3rd harmonic X-mode radiation at R=3.8m was estimated to be τ_3~0.7 (optically grey). Taking into account that the inner wall of the vacuum vessel is smooth, so that the first inner wall reflection will not significantly spread the instrumental antenna pattern, we can expect to have a well collimated beam for two passes through the plasma. Therefore, we estimate that 75% of the observed emission intensity comes from a spot of diameter less than 50cm (perpendicular to the line of sight) and about 5cm thick, centered on the nominal resonance location. The remaining 25% will be made up of contributions from the whole resonance layer (a vertical cylinder at fixed major radius). The radial resolution of each channel is ~8cm. The 8 channels acquiring data covered the range of 73 to 82GHz which corresponded to radii from R=4.16m to R=3.70m (R_0=3.0m , a=1.2m). The radius corresponding to each frequency channel was obtained from the total magnetic field (B_T+B_p) profile calculated by the JET magnetic equilibrium code.

OBSERVATIONS AND ANALYSIS. Figure 1a shows some of the parameters for shot #26236 along with the ECE signal from R=4.11m. The Magnetic signals show an increase in n=1,2 and 3 mode MHD activity before the beta collapse. Figure 1b shows both the DC-coupled signal and the AC fluctuations (>500Hz) on one ECE channel recorded by the fast data system. The noise which is visible on the lower trace is dominantly due to statistical fluctuations in the black-body radiation. Its level is proportional to the signal intensity, and therefore falls at the beta collapse. However, note that from approximately 100 msec before the beta collapse the level of fluctuations on the ECE signal rises despite the decrease in signal level. This rise in fluctuation level is due to the perturbations caused by the increase in the MHD mode activities. Figure 2 shows the power spectra (up to 100kHz) of the ECE fluctuation signal from R=4.11m for two 20msec periods, one immediately before the beta collapse and the other at 200msec before the beta collapse. The power spectrum immediately before the beta collapse shows peaks at 10kHz, 20kHz and 30kHz corresponding to n=1,2 and 3 mode MHD activity (the plasma toroidal rotation frequency measured by charge exchange spectroscopy is ~10kHz). This agrees with the results from the magnetic signals in figure 1a. Additionally the power spectrum shows a mode at 23kHz, which has not yet been identified. This mode was also observed on the soft X-ray signals. The spectrum from 200msec before the beta collapse does not show any strong MHD mode activity.

In order to study the spatial extent of these modes, we have performed spectral analysis on the data from all 8 active channels in the time period before the beta collapse. The

n=2 and 3 modes were strong only in the region close to the edge of the plasma and were not detected further inside (Figure 3) . However the n=1 and the 23kHz mode remained strong and showed significant coherence between all channels throughout the region probed. Spectral analysis of the data in the period leading up to the beta collapse shows that the n=1 mode is present both before and after the collapse, whereas the 23kHz mode which is present on all channels, begins at about 150msec before the beta collapse, grows in amplitude and then disappears completely at the collapse. This interesting behavior seems to suggest that this mode may be related to the cause of the beta collapse.

SUMMARY. ECE correlation radiometry has been used to measure fast MHD fluctuations on JET high beta discharges. n=1,2 and 3 MHD modes and a mode at 23kHz have been detected on the ECE signals preceding the beta collapse in a high beta discharge which exceeded the Troyon limit. The n=2 and 3 modes were detected only on the edge region of the plasma, whereas the n=1 and the 23kHz mode were extended over a large radial range. The 23kHz mode which is detected in all the channels grows rapidly before the beta collapse and disappears at the beta collapse.

REFERENCES

[1] S Luckhardt, J Kesner, J J Ramos, P. Woskov, A. Zolfaghari, MIT Plasma Fusion Center Report PFC-JA/91-16 (1991).
[2] A Zolfaghari et. al. , Diagnostics for Contemporary Fusion Experiments (Varenna, 1991), p1085
[3] L Porte et. al., Proc. 18th EPS Conf. on Cont. Fusion and Plasma Phys. (Berlin, 1991), Vol. 15C,p IV-357.
[4] D Stork et. al., this conference

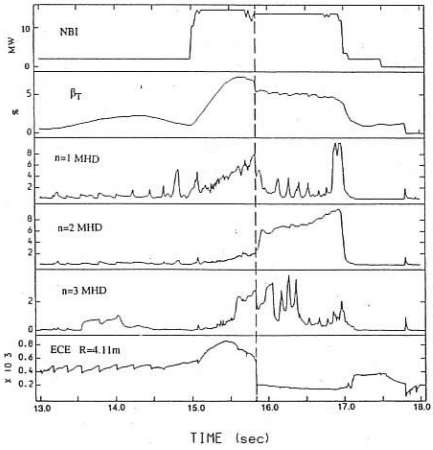

Figure 1a: Overview of JET discharge #26236. The dashed vertical line marks the β-collaps.

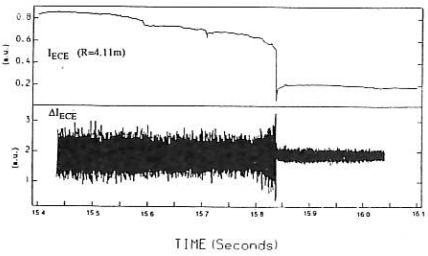

Figure 1b: DC-coupled signal and the AC Fluctuations on the ECE channel viewingthe plasma at R=4.11m.

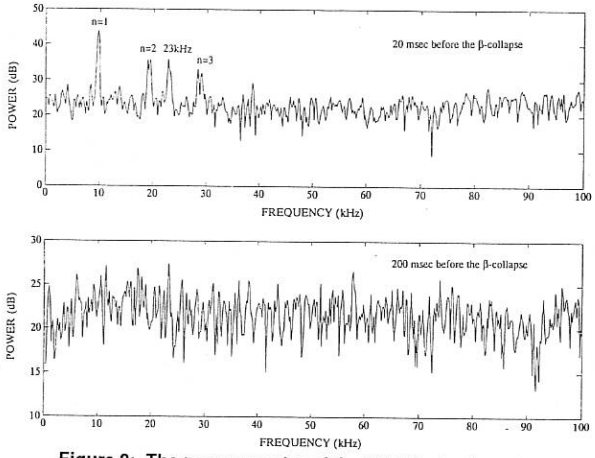

Figure 2: The power spectra of the ECE fluctuation signals (R=4.11m) for two 20 msec periods before β-collapse.

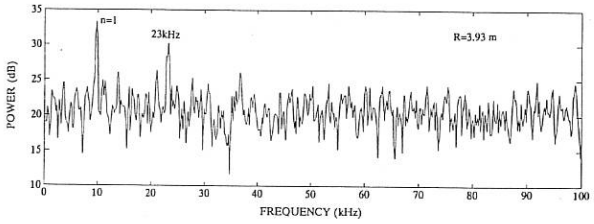

Figure 3: The power spectrum of the ECE fluctuation signal from R=3.93m, 20 msec before the β-collapse.

Fluid Rotation and Resonant Magnetic Perturbations in COMPASS-C.

P. G. Carolan, R. Fitzpatrick, T. C. Hender and A. W. Morris.
Culham Laboratory, Abingdon, Oxon, OX14 3DB, UK.
(UKAEA/Euratom Fusion Association)

1 Introduction

The application of resonant magnetic field perturbations (RMPs), most importantly those with helicity $m = 2, n = 1$, can lead to large magnetic islands and locked mode effects [1]. Plasma rotation effects, including poloidal flow damping, play an important role in a phenomenological resistive MHD model [2] which is used to interpret the experimental results on mode locking in COMPASS-C. In this paper we examine the changes of toroidal velocity occurring at the time of RMP mode locking and unlocking and show how they can be reconciled with the theoretical model. These effects are important because the threshold above which error fields lead to driven islands and reduced confinement and/or disruptions is predicted to be very low in large tokamaks, such as ITER ($b_r(2,1)/B_\phi \sim 10^{-5}$) [3]. One scheme to raise the threshold, and hence reduce the required engineering accuracy, is to use NBI to increase the plasma rotation velocity. It is, therefore, important to establish experimentally the role of plasma rotation velocity in the penetration of magnetic fields to form islands.

2 Experimental Arrangements

The results presented here were obtained from the COMPASS-C tokamak (major radius $R = 0.557$m; minor radius of limiter $a = 0.2$m; plasma current $I_p < 200$kA; toroidal field $B_\phi < 1.75$T, thin vacuum vessel of circular cross section) COMPASS-C was equipped with a large number of saddle coils which were installed outside the vacuum vessel at a radius of 0.278m (centred on $R = 0.576$m) and could be connected together to give a wide variety of RMP fields [1]. In this paper we concentrate on COMPASS-C RMP configurations for which the (2,1) harmonic was dominant.

A high resolution spectrometer, incorporating an echelle-grating [4] and a multichannel detector, was used to measure simultaneously the toroidal rotational velocity and temperature of impurity ions in COMPASS-C. Absolute velocity calibration was derived from measurements in opposing toroidal directions obtained on sequential discharges. Fast time resolution was facilitated by image-dissecting the dispersed spectrum into three photomultiplier channels [4]. The high light throughput, together with a high resolution in velocity measurements and a fine time resolution (sub-km s^{-1} and $\sim 50\mu$s), are important for mode locking experiments in ohmic discharges where the velocities are smaller, and the impurity line intensities weaker, than are typically available from neutral beam heated discharges. In the post-boronisation operation [5] of COMPASS-C, emission in the near UV (282.1nm) from Boron IV ($1s2s\,^3\mathrm{S}$–$1s2p\,^3\mathrm{P}_2$) afforded sufficient intensity to allow passive spectroscopic methods to be used.

3 Results and Interpretation

3.1 Mode penetration

In Fig. 1 are shown the waveforms of the current, I_c, in the RMP saddle coil and the three spectrometer channels for a representative discharge ($I_p = 100$kA, $B_\phi = 1.1$T and $q_\psi \sim 4.3$)

which experienced an induced $m = 2, n = 1$ mode locking event. The spectrometer line–of–sight is tangential to the minor axis of the torus and, in this case, is in the direction of the plasma current. Thus, during the mode locking (t = 130ms→ 170ms) the decrease in the signal of the 'blue' channel is accompanied by an increased signal in the 'red' channel, showing a shift of the B IV ion drift velocity in the direction of the plasma current.

The temporal behaviour of the toroidal velocity, $v_{\phi \mathrm{B\,IV}}$, derived from the three spectral signals, is shown in Fig. 2 and is compared with the multichannel estimates of $v_{\phi \mathrm{B\,IV}}$. In this case the signals from the three channel system were integrated over the same light collection periods as the slower ($\sim$ 17 ms) multichannel device which had $\sim$ 100 channels encompassing the Doppler broadened spectrum. This validates the use of the three channel system to measure the ion temperatures and velocities where the interpretative algorithm assumes a simple Gaussian shape to the spectrum (*e.g.* no interfering spectral lines).

We interpret the mode locking event shown in Fig. 1 as the sudden onset of magnetic tearing, induced by the RMP fields, and resulting in the formation of a stationary (2,1) island. This interpretation is consistent with a phenomenological model [2] of the interaction of RMP fields with rotating plasmas. It is proposed that, as a result of both viscous and inertial effects, a *rotating* plasma is able to resist tearing until a critical threshold field-strength is exceeded.

It can be seen in Fig. 1 that the toroidal velocity is not *directly* affected by the RMP field since the velocity only changes significantly at the time of mode penetration. The shift in toroidal velocity, as shown in Fig. 2 is from an initial value of about 10 km s^{-1} in the *electron* drift direction to a final value, after mode penetration, of about 22 km s^{-1} in the *ion* direction. Using the standard neoclassical result [6], we calculate, for COMPASS-C conditions, that the B IV ions will drift, relative to the fuelling ions, by less than about 3 km s^{-1} in the *electron* drift direction. It follows that in the unperturbed plasma, the fuelling ions in the vicinity of the radiating B IV ions are probably rotating comparatively slowly ($\sim$7 km s^{-1}) in the *electron* direction. The E×B drift must, therefore, be in the *electron* direction, implying the presence of an inward pointing radial electric field. This is consistent with previous more direct measurements (*e.g.* [7]).

The spectroscopic data shows a $\sim$ 32km s^{-1} velocity shift of the fuelling ions at mode penetration in contrast to the $\sim$ 49km s^{-1} velocity shift (corresponding to a mode frequency of $\sim$ 14kHz) obtained from the magnetic data of the $m = 2$, $n = 1$ mode. It is assumed that the mode and plasma fluid are 'tied' together at the rational surface, and that the plasma is subjected to strong poloidal flow damping. The apparent discrepancy in velocity shifts may be explained by the presence of shear in the toroidal velocity profile which means that the *shifts* in velocity will differ at the $q = 2$ radius and the radius of the B IV emission. A single-fluid model which includes perpendicular viscosity is used in a simple description of the radial transport of toroidal momentum. It is assumed that the velocity is clamped at the plasma edge and viscosity-profile effects are neglected. In equilibrium, (*i.e.* $\partial/\partial t = 0$), we obtain for the perturbation to the toroidal (angular) velocity profile following penetration: $\Delta f_\phi(r) = \Delta f_\phi(r_s)$ for $r \le r_s$, and $\Delta f_\phi(r) = \Delta f_\phi(r_s)\dfrac{\ln(r/a)}{\ln(r_s/a)}$ for $r_s \le r \le a$, where $\Delta f_\phi(r_s) = \Delta f_s/n$, $\Delta f_\phi(r_{\mathrm{B\,IV}}) = \Delta v_{\phi \mathrm{B\,IV}}/(2\pi R_{\mathrm{B\,IV}})$, and Δf_s is the change in mode frequency at $r = r_s$ ($r_s/a \sim 0.67$). The velocity shear explanation for the discrepancy is applicable if $r_{\mathrm{B\,IV}} > r_s$. Here, $R_{\mathrm{B\,IV}}$ and $r_{\mathrm{B\,IV}}$ are the major and minor radii of the B IV emission. For the discharge under consideration, the difference between $\Delta f_\phi(r_s)$ and $\Delta f_\phi(r_{\mathrm{B\,IV}})$ ($\sim$7kHz, assuming $R_{\mathrm{B\,IV}} \sim 0.72$m) can be reconciled by the velocity shear explanation if the shell of radiating B IV ions lies at $r_{\mathrm{B\,IV}}/a \sim 0.82$ (*i.e.* about 4 cm from the edge). Similar results are found for a wide collection of discharges with $q_\psi \sim 3.2 \rightarrow 5.8$. These results are in accord with estimates from impurity transport modelling which give the peak of B IV emission (282.1nm)at 5cm $\pm$ 2cm from the plasma edge. It is also plausible from the Doppler B IV ion temperature measurement of $T_i \sim 60eV$ compared with the central $T_i \sim 200eV$.

Another effect considered is that the difference in frequency shifts between the B IV ions and the $m = 2$ mode could be attributed, at least partly, to changes in electron diamagnetic drift

speed following mode locking. Although we have no direct profile information, it is assumed that the mode velocity arises from a combination of the diamagnetic and $\mathbf{E} \times \mathbf{B}$ drifts, as observed in other devices. The observed reductions ($\lesssim 30\%$) in the diamagnetic energy correspond to a $\sim$ 2kHz reduction in the electron diamagnetic frequency which is much less than the required $\sim$ 7kHz to account for the differences in frequency shifts.

3.2 Mode Unlocking

There is a 'spin-up' event soon after the RMP is switched off in which both the MHD frequency and the B IV velocity are observed to revert to their pre–penetration values on a timescale of a few milliseconds. Figure 3 shows a comparison between the frequencies obtained from the B IV velocity and the $m = 2$ Mirnov coil signals during the 'spin–up' phase.

The strong correlation between the two frequencies is explicable because the decay of the perturbed velocity profile is rapidly dominated by a single eigenfunction (*i.e.* that with the slowest decay rate). A simple model [2] which neglects the variation of viscosity and density across the plasma cross–section yields: $\dfrac{\Delta f_\phi(r_{\rm B\,IV},t)}{\Delta f_\phi(r_s,t)} = \dfrac{J_0(2.405\, r_{\rm B\,IV}/a)}{J_0(2.405\, r_s/a)} = 0.53 \pm 0.04$, using $r_s/a = 0.67 \pm 0.03$ and $r_{\rm B\,IV}/a = 0.82 \pm 0.05$ (as found previously). The observed ratio of $\Delta f_\phi(r_s,t)$ to $\Delta f_\phi(r_{\rm B\,IV},t)$ is 1.92 ± 0.04 in the discharge under consideration, which agrees well with the calculated value.

This good agreement points strongly to the validity of the velocity shear model. It is unlikely that the more indirect physical effects arising from changes in the diamagnetic velocity would allow the two frequency shifts to remain in close proportion during the greater portion of the spin-up phase. We therefore conclude that the discrepancy between the shifts in the B IV and the mode frequency is dominantly due to shear in the perturbed velocity profile.

4 Conclusions

A phenomenological resistive MHD model can account for the significant disparity of toroidal frequency shifts, observed during mode locking experiments, between an impurity ion species (B IV at the plasma periphery) and the MHD modes. It is necessary in accounting for the experimental results to incorporate in the model poloidal flow damping and velocity shear. In summary, our results indicate the validity of a phenomenological resistive MHD model in explaining error field effects and point to the potential for ameliorating these effects in large tokamaks by increasing the fluid velocity (*e.g.* by NBI).

References

[1] A. W. Morris, *et al.* Phys Fluids B **4**, 413 (1992).

[2] R. Fitzpatrick and T. C. Hender, Phys Fluids B **3**, 413 (1991).

[3] R. J. LaHaye Bull. Amer. Phys. Soc. **36**, 2402 (1991)

[4] R. A. Bamford, P. G. Carolan and C. A. Bunting to be publ. Rev. Sci. Instrum. (1992).

[5] H. G. Esser, S. J. Fielding, *et al.* J. Nucl. Mat. **186**, 217 (1992).

[6] Y. B. Kim, P. H. Diamond, and R. J. Groebner, Phys. Fluids B **3**, 2050 (1991).

[7] V. I. Bugarya, *et al.* Nucl. Fusion **25**, 1707 (1985).

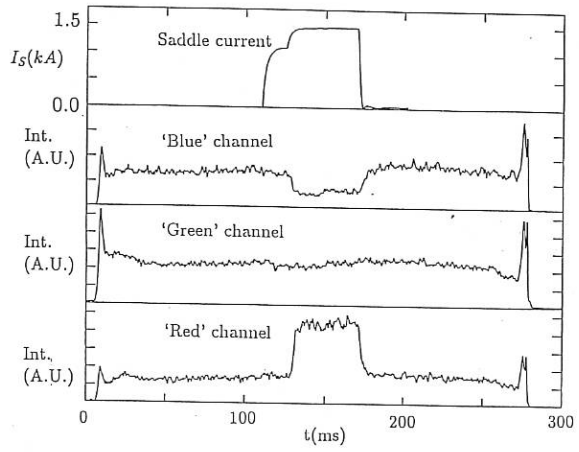

Figure 1: Waveforms of the three channel system and the current applied to the saddle coil ($m = 2, n = 1$). (Shot 6167)

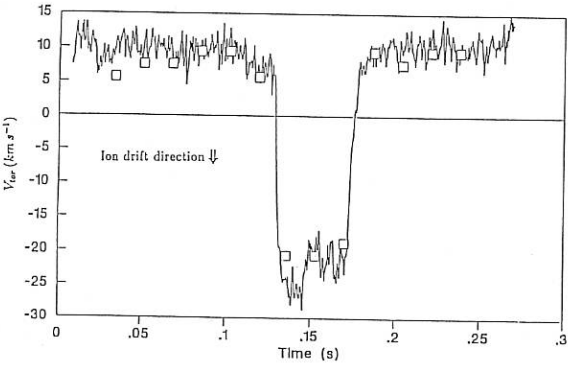

Figure 2: Comparison between the drift velocity estimated from the three channel system and from the multichannel detector (discrete points). (Shot 6167)

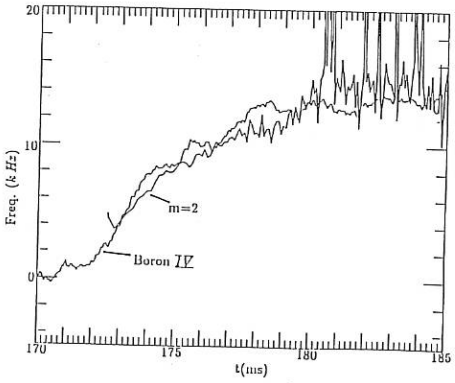

Figure 3: Comparison between the toroidal frequency acceleration, during the mode unlocking phase, obtained from the Boron IV, multiplied by 1.9, and that obtained from $m = 2$ Mirnov coils. (Shot 6167)

A STUDY OF THE DIFFERENCE IN CONFINEMENT PROPERTIES BETWEEN LARGE ROTATING AND LARGE LOCKED MODES ON TOKOLOSHE TOKAMAK.

J. D. Fletcher, D. E. Roberts, G. Nothnagel, G. W. van Vuuren, J. A. M. de Villiers.
Atomic Energy Corporation of South Africa, P.O.Box 582, Pretoria 0001, R.S.A.

INTRODUCTION

Tokoloshe tokamak has a low aspect ratio (R = 0.52 m, a = 0.24 m) and is equipped with three sets of fully toroidal stellarator-like windings [1]. One of these windings viz., the $\ell = 2$, was used to lock rotating (m/n=2/1 and m/n=3/1) magnetic islands during high ($\tilde{B}_\theta/B_\theta \geq 0.5\%$) Mirnov activity when the tearing mode amplitude is slowly increasing and the frequency slowly decreasing over several energy confinement times ($\tau_{Ee} \lesssim 1.8$ ms). These locked modes are stable for several energy confinement times and do not change significantly the time to disruption. The difference in confinement properties between large rotating and large locked modes is studied and, using the results of measurements of fluctuation induced particle transport (see Van Vuuren et.al. this conf.), the fraction of particle flux due to fluctuation induced transport is compared to the total particle flux. The principal diagnostics used in this study are: a vertically viewing, single channel, 2 mm μ-wave interferometer for line averaged electron density and a horizontally viewing surface barrier diode array from which an intensity profile is obtained. Measurements have been made for reference shots, and for shots where the islands were locked by the resonant external helical field for both directions of current in the external winding.

OBSERVATIONS

Interferometer results for reference shots show that during the period of high Mirnov activity (12 $\rightarrow$ 18 ms) (Fig.1(a)), the line integrated electron density rises monotonically to $\approx 2.6 \times 10^{19}$ m^{-3} before disruption (Fig.2(a)) due to strong gas puffing throughout the discharge. Soft X-ray intensity profiles for reference shots are broad and nearly parabolic in shape and become more peaked towards the end of the discharge (Fig.3(a)). The central intensity increases monotonically (from $\approx$ 12 ms) up to the disruption. The discharge duration for all the reference shots is $\lesssim$ 18 ms. The $\ell = 2$ coil is energised during high Mirnov activity by a pulse with peak current of 1400 A and duration $\gtrsim$ 10 ms, (Fig.1(b)), which is sufficient to lock the tearing mode for 4 $\rightarrow$ 6 ms (Fig.1(c)). These locked mode discharges disrupt $\lesssim$ 2 ms earlier than the reference shots. When the mode is locked by the $B_\phi, I_p, I_\ell = (--+)$ configuration [2] the line integrated density rises at a slower rate (33% down c.f. reference case) after locking, reaching a maximum value of $\approx 2.2 \times 10^{19}$ m^{-3} (Fig. 2(b)). For the $(---)$ configuration the line integrated density rises at a still slower rate (58% down on reference case) after locking, reaching a maximum value of $\approx 1.7 \times 10^{19}$ m^{-3} (Fig. 2(c)). Soft X-ray intensity profiles for both locked mode configurations show the same spatial evolution as the reference discharges. For the $(--+)$ configuration (Fig.3(b)) the central X-ray intensity increases monotonically up to the disruption. For

the $(- - -)$ configuration (Fig.3(c)), however, the intensity flattens off and the central intensity is $\lesssim$ 50 % less than relative to the reference shots at disruption. When a short duration ($\lesssim 2$ ms) helical current pulse was used (which resulted in $\lesssim 2$ ms locked phase after which rerotation occurred) no effect on the central soft X-ray intensity was observed.

DISCUSSION AND CONCLUSIONS

The results for the $(- - +)$ configuration show that large stationary locked modes can be benign over several energy times and do not significantly affect the build up of the line averaged electron density or the central soft X-ray intensity. The $(- - -)$ results indicate that locking leads to a modest decrease in central confinement. These different results suggest that the locking position, which is determined by the phase of the islands, the externally imposed field and any stray fields, determines to what degree edge conditions are modified to impact significantly on central confinement. The change in the total electron density, N_e, is given by the particle balance equation

$$\frac{dN_e}{dt} = S - \nabla.(\tilde{\Gamma} + \Gamma_{\rm other})$$

where $N_e = \int n_e(r) dV$, V is the plasma volume and $n(r) \approx n_{e0}(1 - (r/a)^2)$. S includes all the source terms, $\tilde{\Gamma}$ is the fluctuation induced particle flux and $\Gamma_{\rm other}$ includes all other particle loss channels. $\tilde{\Gamma}$ (see Van Vuuren et.al. this conf.) and dN_e/dt have been measured for both large rotating and large locked modes. For plasmas locked by the $(- - +)$ configuration, both dN_e/dt and $\tilde{\Gamma}$ are reduced by $\sim$ 33%, whilst for the $(- - -)$ configuration a larger reduction of $\sim$ 55% in both quantities is observed. With $\tilde{\Gamma} = 7.9 \times 10^{20}\,s^{-1}$ and assuming $\Gamma_{\rm other} \ll \tilde{\Gamma}$, S is calculated to be $1.8 \times 10^{21}\,s^{-1}$. An independent estimate of S $\approx 1.2 \times 10^{21}\,s^{-1}$ can be made from the gas puff and is 50% less than the calculated S. This implies that fluctuation induced particle transport is at least as important as particle losses through other channels, as is seen on many tokamaks. The reduction of dN_e/dt and $\tilde{\Gamma}$ during locking is due to a reduction in S, a change in $\Gamma_{\rm other}$, or both. A decrease in S could be due to the locking changing interaction with the limiter. In conclusion, the presence of large stationary locked modes does not necessarily lead to decreased confinement, however, the locking position can be important in determining the ultimate effect. This probably depends on the degree of concentricity of the outer flux surface with the fully poloidal limiter.

REFERENCES

[1] D.P. Coster, J.A.M. de Villiers, J.D. Fletcher, G. Nothnagel, J.R. O'Mahony, D.E. Roberts, D. Sherwell, in Contr. Fusion and Plasma Physics, (Proc. 14th EPS Conf. Madrid, 1987), European Physical Society, (1987) 240

[2] D.E.Roberts, D.Sherwell, J.D.Fletcher, G.Nothnagel, J.A.M. de Villiers, Nucl Fusion 31, 319 (1991)

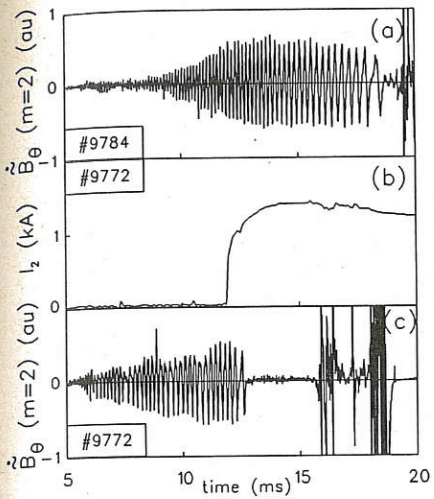

Fig. 1 (a) $\dot{\bar{B}}_\theta$ for a reference shot ($I_2 = 0$) terminating in a major disruption.
(b) Current pulse in the $\ell = 2$ coil.
(c) $\dot{\bar{B}}_\theta$ for a shot locked by the $(---2)$ configuration.

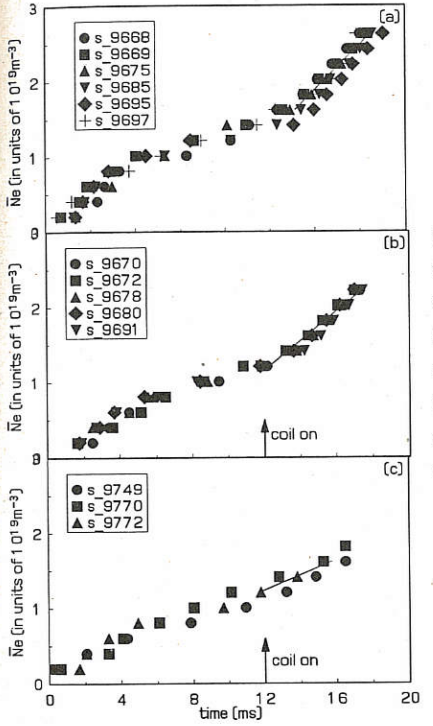

Fig. 2 Line integrated electron density traces $\overline{N}e$ (along a diameter) for (a) reference discharges (b) discharges locked by the $(--+2)$ configuration and (c) discharges locked by the $(---2)$ configuration. The different symbols represent different discharges and the solid lines are regression fits to the data points.

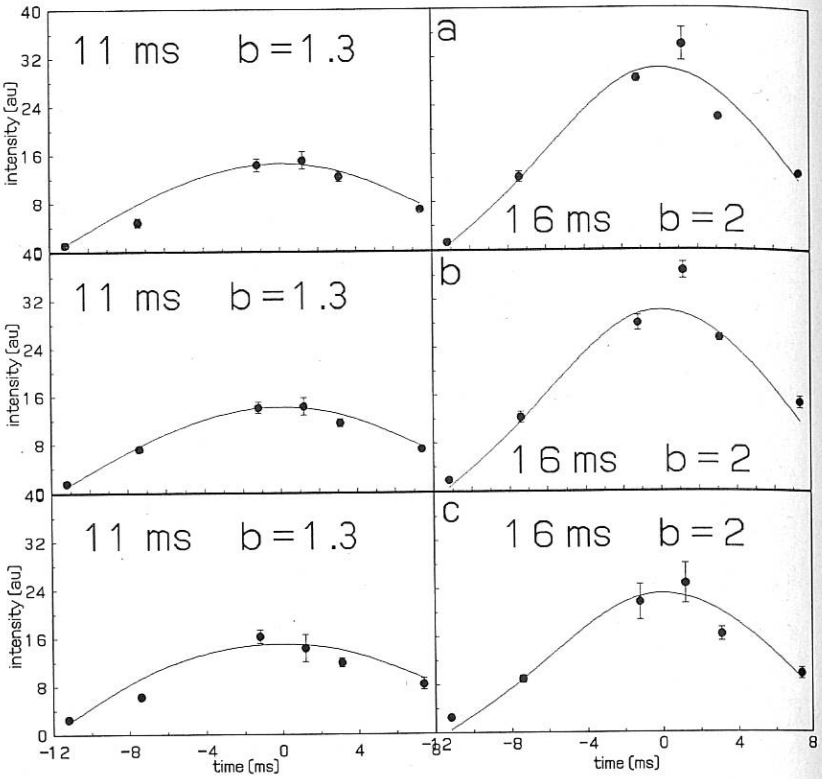

Fig. 3 Soft X-ray intensity profiles averaged over the shots listed in Fig.2 at 11 and 16 ms into the discharges respectively for (a) the reference configuration (b) the $(--+2)$ configuration and (c) the $(---2)$ configuration. The fitted curves are of the form $k(1-(r/a)^2)^b$.

ACTIVATION/INHIBITION OF PLASMA INSTABILITIES CAUSED BY RESONANT MAGNETIC FIELDS

Araujo M.S.T.; Vannucci A.; Caldas I.L.

INSTITUTO DE FÍSICA DA UNIVERSIDADE DE SAO PAULO
C.P. 20516 - CEP 01498 - SAO PAULO - BRAZIL

I - Introduction

Investigations concerning the influence of Resonant Helical Fields (RHF) on confined plasmas have been already carried out in several tokamaks /1,2/, including the TBR-1 - a small tokamak with minor radius a=0.08m and major radius r=0.30m /3/. This work, in particular, reports some detailed analysis done with the objective of determining the physical mechanisms that may give rise to disruptive instabilities, when RHF are applied. The external perturbations, corresponding to the components m/n=2/1, 3/1 and 4/1 were created by a set of helical windings located externally around the torus. The poloidal magnetic fluctuations were detected by a set of 10 pick-up coils placed inside the vacuum vessel. The output signals were Fourier-analysed and the time evolution of each MHD component, ranging from m=0 to m=4, could be separately obtained. Spectral analysis performed over some time intervals, along the discharges, allowed the determination of the characteristic frequencies of the different modes before, during and after a disruption takes place.

II - Instability Activation

When rather intense helical currents (I_{hel}~400-500A) were applied, it could be frequently observed the occurrence of both minor and major disruptions. In fig.1, for example,a minor disruption was detected approximately 0.3ms after the ramp-up of the helical pulse, at t=1.92ms (fig.1c), which caused a small drop of the plasma current (fig.1a); at the same time the plasma column is observed to shift towards the inner direction (fig.1d). At t=2.68ms, the appearence of a major disruption is identified, destroying the confinement. In fig.2 the time evolution, of the m=0 to m=4 components, can be observed. The spectral analysis done over the last moments before the loop voltage negative spike indicated a dominant presence of the m/n=2/1 mode, along with the m/n=1/1 (fig.3).

III - Inibition effect

When lower intensity helical currents ($I_{hel} \lesssim 300A$) were used, a strong reduction of the MHD activity was often observed. This feature can be easily identified in fig.4, which shows a pulse of $I_p \sim 8kA$ lasting for 7ms, approximately. At t=2.0ms, an helical pulse of 200A was applied (fig.4d), causing the MHD amplitude attenuation observed in fig. 4c and also, in more details, in fig.5. Performing the spectral analysis before, during and after the application of the helical pulse (fig.6), it could be observed that the m=2 mode was indeed the most intensely inhibited by the RHF (fig.6b). After the helical pulse has ended, the m=2 amplitude exhibits, again, the same magnitude of the other modes (fig.6c).

IV - Interaction between magnetic islands

Estimating the rational magnetic surfaces localizations and also the half-widths of the corresponding magnetic islands, just before the occurance of minor and major disruptions, the Chirikov criterion (table I) indicated that the minor disruptions could be triggered by an external ergodization of the plasma columnum while, in a major disruption, this ergodization would also comprise the internal region, leading to the total destruction of the confinement.

V - Conclusions

The activation or inhibition of plasma instabilities in TBR-1 Tokamak could be performed using resonant magnetic fields of different intensities. When $I_{hel} \lesssim 300A$ a strong reduction of the MHD activity was often observed while, for $I_{hel} \sim 400\text{-}550A$, it could be frequently observed the development of minor and major disruptions. The Chirikov criterion showed that minor disruptions were preceded by an ergodization of the external part of the plasma column while, before a major disruption, the ergodization also comprised the internal region.

References

/1/ F.Karger et al., Nuclear Fusion **25**, 1059 (1985).

/2/ D.C.Robinson, Nuclear Fusion **25**, 1101 (1985).

/3/ A.Vannucci et al, Nuovo Cimento **10D**, 1193 (1988).

TABLE I

Rat.Surf. Position (cm)	Half-width (cm)	Chirikov criterion	Rat.Surf. Position (cm)	Half-width (cm)	Chirikov criterion
$r_{0,1}$=1,8	$\Delta_{1,1}$=2,1	—	$r_{1,1}$=1,8	$\Delta_{1,1}$=2,3	—
$r_{2,1}$=5,2	$\Delta_{2,1}$=1,0	$S_{1,2}$=0,9	$r_{2,1}$=4,8	$\Delta_{2,1}$=1,2	$S_{1,2}$=1,1
$r_{3,1}$=6,6	$\Delta_{3,1}$=0,7	$S_{2,3}$=1,2	$r_{3,1}$=6,0	$\Delta_{3,1}$=0,6	$S_{2,3}$=1,4
$r_{4,1}$=7,7	$\Delta_{4,1}$=0,6	$S_{3,4}$=1,2	$r_{4,1}$=7,0	$\Delta_{4,1}$=0,6	$S_{3,4}$=1,2
Minor Disruption			Major Disruption		

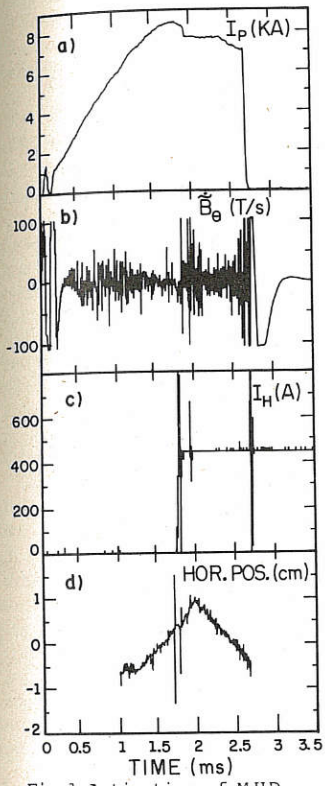

Fig.1-Activation of MHD instabilities due to a $I_{hel} \sim 450$ A.

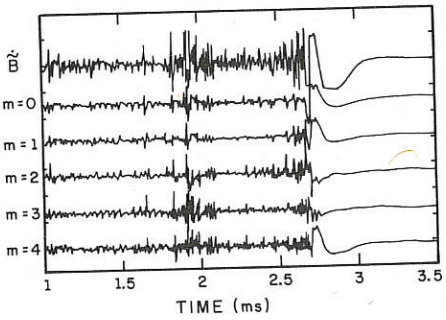

Fig.2- m = 0 to m = 4 MHD components corresponding to the pulse in fig. 1.

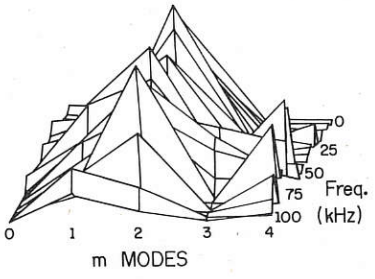

Fig.3- Spectral analysis showing the dominant presence of the m/m = 2/1 mode, along with the m/m = 1/1.

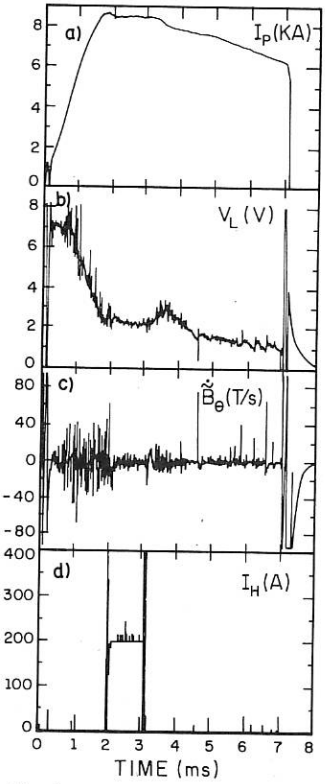

Fig.4- Inhibition of MHD activity due to a I_{hel}~200 A.

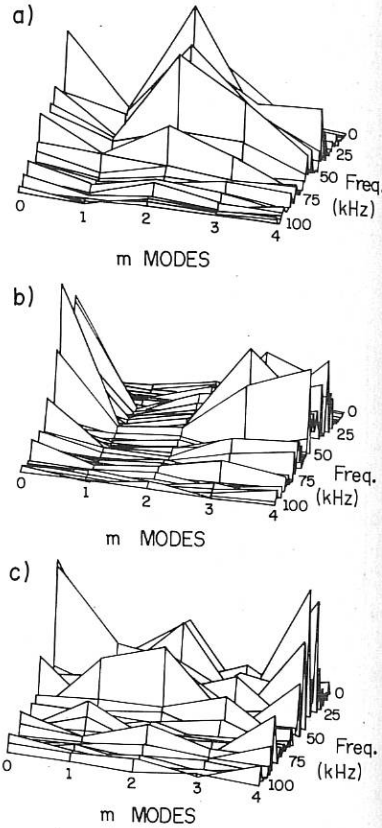

Fig.6- Spectral analysis done before, during and after the helical pulse application.

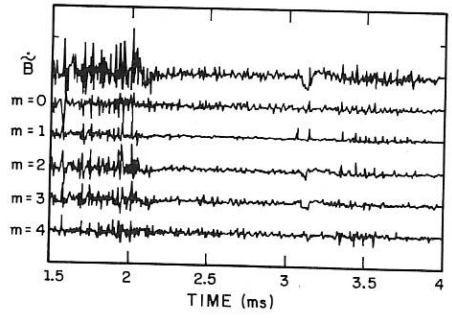

Fig.5- m = 0 to m = 4 MHD components corresponding to the pulse in fig. 4.

FEEDBACK STABILISATION OF RESISTIVE TEARING MODES IN TOKAMAKS

A W Morris, R Fitzpatrick, T C Hender and M R O'Brien
AEA Fusion, Culham Laboratory (Euratom/UKAEA Fusion Association), Abingdon, UK

Introduction

The likely consequences of disruptions in a device the size of ITER are sufficiently severe that it is worth investigating a variety of schemes for disruption control. The majority (but not all) of tokamak disruptions are preceded by an $m = 2, n = 1$ tearing mode, and it has been demonstrated that control of these can delay or prevent a disruption [1]. It has long been known that radially localised axisymmetric current perturbations can stabilise resistive tearing modes by changing the stability of the current profile $J_0(r)$ [2], but it has also been proposed [3, 4] that localised heating or current drive inside magnetic islands (e.g. at the O-point) could be used to control the non-linear evolution of the island. This is addressed in greater detail here, for $m = 2, n = 1$ modes, considering realistic deposition profiles; the poloidal and toroidal extent of the deposition zone, as given by an ECRH antenna pattern for example; the use of the scheme in a feedback loop and, finally, the application to error-field-driven tearing modes [5]. The profile control effect [6, 7] is referred to as "DC" current drive, the island heating scheme as "phased" current drive. This paper will consider Electron Cyclotron Current Drive, although ECCD is not the only possible scheme.

Basic Principles and Model

Local phased heating and current drive have both been investigated, and it is concluded that current drive is considerably more efficient, does not have to compete with bulk heating and is less dependent upon anomalous transport and so in principle more predictable. In addition, local heating is ineffective when J_0 is small or non-inductively driven at $q = 2$. The model is for cylindrical geometry using the normal formalism of non-linear tearing modes [8]. The stabilisation arises from a reduction of the electric field that drives the tearing mode current and thus takes effect very rapidly, on the collision timescale for the resonant electrons [9]. For COMPASS-D [10] this is 10–100μs ($2\omega_{ce}$ ECCD), compared to mode growth times of 0.1 $\sim$ 5ms and rotation frequency $f_{m=2} \sim$ 10kHz. This is considerably faster than for axisymmetric profile control where there is a delay $\sim \mu_0 \sigma d^2$ for a drive profile of width d, $\lesssim$ 5ms for COMPASS-D.

Current drive profiles $\delta J_{\parallel d} = J_1 \exp[-(r - r_0)^2/d^2]$ are assumed (Lorentzian-like profiles behave similarly [11]). The angular variation may be matched to the antenna pattern, and duty-cycle effects may be included for feedback on rotating modes. $\delta J_{\parallel d}$ is normalised to $J_1 \equiv \frac{1}{4\pi^2} \int_{-\pi}^{\pi} d\phi \int_{-\pi}^{\pi} \alpha P_0(\theta, \phi) d\theta$ for direct comparison with ray-tracing output (α is a current drive efficiency, and $P(0)$ the power density). The results presented here lead to requirements for J_1 and hence the total installed ECRH power required, even if it is only used for 50% of the time as with feedback on a rotating mode. For example if 100kW ECRH were predicted, then the mean power used would be 50kW for phased control with a 50% duty cycle.

The tearing mode equation is averaged over flux surfaces in the usual way using the formalism of ref [12], and it is the concentration of the driven current on the helical-flux surfaces in the island that makes the stabilisation efficiency high. The result is an equation for the evolution of the island width W [11]:

$$0.82\tau_R \frac{d(W/a)}{dt} = a\Delta'(W) + \frac{a}{W}\frac{1}{s}\frac{J_1}{J_{0,av}} C_J \qquad (1)$$

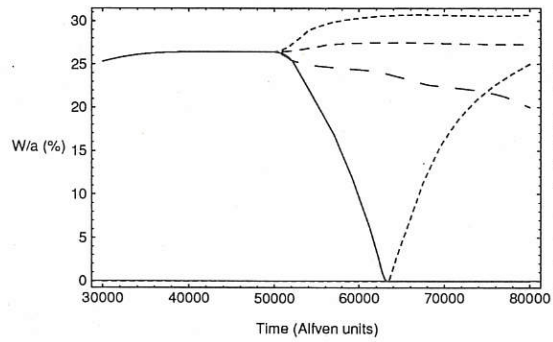

Figure 1: *Evolution of (2,1) island width with O/X-point current drive, started at* $t = 5 \times 10^4 \tau_A$, *co and counter to the equilibrium current.* ————: *O-point co;* - - - - -: *O-point, counter;* – – –: *X-point co;* —— ——: *X-point counter. Here* $q = 1.1\sqrt{[1+(r/0.66a)^4]}$

s is the shear, rq'/q, and $J_{0,av.} \equiv I_p(r_s)/\pi r_s^2$. C_J is negative for current drive at the O-point parallel to the equilibrium current and is defined for finite deposition width as follows:

$$C_J \equiv \frac{\int_{-\pi}^{\pi}\int_{-\pi}^{\pi} P_0(\theta,\phi) I_2(\xi) d\xi d\phi}{m\int_{-\pi}^{\pi}\int_{-\pi}^{\pi} P_0(\theta,\phi) d\theta d\phi}; \qquad I_2(\xi_0) = 16\sqrt{2}\int_{\cos\xi_0}^{\infty} \frac{\langle \delta J_{\|d} \rangle}{\sqrt{\Omega - \cos\xi_0}} \frac{\langle \cos\xi \rangle}{\langle 1 \rangle} d\Omega. \qquad (2)$$

The integral I_2 is defined for a pencil beam at $\xi = \xi_0$. $\Omega \equiv 8(r - r_{q=2})^2/W^2 + \cos\xi$ is a flux surface label with $\xi \equiv m\theta - n\phi$, and $\langle \cdots \rangle$ denotes a flux surface average. Any other localised DC current drive (e.g the effects of odd-parity components of $\delta J_{\|d}$) is included in $\Delta'(W)$ [11].

The stabilising effect of phased current drive has also been established by numerical simulations using the reduced MHD equations including an RF-induced electric field. This field is specified to be constant on surfaces of constant helical flux and peaked at the O or X-point with a prescribed radial width ($0.2a$). Fig 1 shows the effect on W when the electric field is applied to a saturated island at $t = 5 \times 10^4 \tau_A$. All combinations of O/X-point and co/counter drive are shown, and in all cases $J_1/J_{0,av} = 5 \times 10^{-2}$. It is seen that co-drive at the O-point is best, as predicted. J_1 is held constant in this simulation so the O-point co-drive case flips into positive feedback as W reaches zero: this would not occur in a real system where J_1 would be feedback controlled.

Current Drive Profiles and Antenna Patterns

Since the stabilising effect arises from currents flowing on helical flux surfaces, with any non-helical components only having an influence via the DC effect, the phased scheme is naturally localised to the island. Thus it is expected that it is insensitive to the width and location of the current drive profile as long as it overlaps the island, depending mainly on the magnitude of the driven current density in the environs of the magnetic island.

Figs 2,3 show the effect on C_J of variations in the width and location of $\delta J(r)$. C_J is found for the case of a narrow antenna pattern and the current being injected over half a rotation period (i.e. 50% duty cycle) – this is the optimum for rotating $m = 2$ modes. For a stationary mode with the power injected exactly at the O-point, a factor ~ 3 improvement is found. Gaussian profiles are used, although a very similar result is obtained for $\delta J \propto [1 + (r - r_s)^2/d^2]^{-2}$. It is seen that the deposition width is unimportanmt if it exceeds the size of the magnetic island (but of course, the total driven current required rises linearly with the width: J_1 is constant in Fig 3). Further, Fig 3 shows that it is not essential that the resonance (for ECCD) be located exactly at the $q = 2$ surface – unlike DC stabilisation where it is rather critical [13] to avoid destabilising the $m = 2$ mode. The localisation requirements

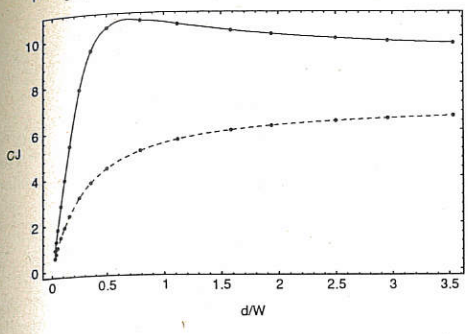

Figure 2: *C_J as a function of deposition width. Note the difference between X-point (- - -) and O-point (___) current drive (the O-point case is multiplied by -1 for comparison). This shows that stabilisation efficiency is not sensitive to the width of the current-drive profile.*

can be quantified: $|r_0 - r_s| \lesssim 0.5d$ for the DC scheme to be effective, and $|r_0 - r_s| \lesssim d$ for the phased scheme, and any destabilisation is weaker and decreases with increasing d/W (Fig 3).

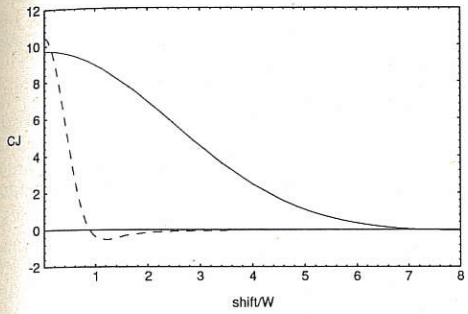

Figure 3: *C_J as a function of deposition position for O-point drive, for $d/W = 0.5$ (dashed line) and $d/W = 3.53$ (solid line).*

Use of Phased Current Drive in a Feedback Loop

The formalism is almost identical to that for magnetic feedback [14, 15], and is again based on the simple non-linear island evolution equation. This reveals that for a given $\Delta'_0(0)$, a certain level of current drive is required to allow a saturated island to be reduced to zero. Of course, if the feedback were always present, the island might never grow to significant and the power requirement would be reduced. For $\Delta'(W) = \Delta'_0(0)(1 - W/W_{sat})$ the current required to reduce W to zero from W_{sat} can be directly compared with that required for linear stability in the DC scheme (for a Gaussian profile centred exactly on $q = 2$):

$$\frac{\delta I_{CD}(DC)}{I_p(r_s)} = \frac{d^2 s}{2ar_s} a\Delta'_0(0); \qquad \frac{\delta I_{CD}(Phased)}{I_p(r_s)} = \frac{W_{sat} d}{ar_s} \frac{s\sqrt{\pi}}{2C_J} a\Delta'_0(0) \tag{3}$$

Thus is is seen that for typical values of C_J (~ 10) the phased scheme is rather better than optimised DC profile control, a factor ~ 5 for $d \sim W_{sat}$. For a Lorentzian-type profile, more appropriate for transport-broadened current drive [16], the improvement is more marked. Ray tracing calculations with transport indicate that $\lesssim$ 200kW for COMPASS-D at $2\omega_{ce}$ should provide adequate power for phased control with $a\Delta' \sim 10, W_{sat} \sim 0.1a$ and $I_p \sim$ 150kA. This is well within the range of the COMPASS-D 2MW ECRH facility. For an ITER-sized tokamak, where it is estimated that $\sim$ 20MW would allow DC control [17], the phased scheme might

require only $\sim 5MW$:- with higher power the deposition zone could be broadened and so the accuracy with which the $q = 2$ surface has to be located would be reduced.

Control of Error-field-driven Tearing Modes

It has been shown experimentally and theoretically [5, 12, 18] that helical error fields can lead to large magnetic islands in some circumstances. In this case Eq. 1 may be written (including the phased stabilisation term, and assuming constant phase shift between island and driving field):

$$I_1 \tau_R \frac{d(W/a)}{dt} = a\Delta'(W) + \frac{C_{error}}{W^2} \frac{a}{W} \frac{1}{s} \frac{J_1}{J_{0,av}} C_J. \quad (4)$$

It can be seen that it is possible in principle to reduce the amplitude of the stationary island with phased current drive, but not to reduce it to zero. However, it is observed experimentally [5] that if the source of error field is reduced, the stationary island "unlocks", starts to rotate and decays away. This is understood in terms of the viscous drag from the rest of the (rotating) plasma overcoming the electromagnetic mode-locking force as the island size reduces. Thus it is likely that with C_{phased} sufficiently large, W will be reduced to the point where the mode unlocks and W obeys Eq 1, and can now be reduced to zero if it does not decay naturally. For the scheme to be reliable, the antennae must be located to allow control of a stationary mode locked with its O-point at any toroidal phase.

Conclusions

It has been shown that for realistic current drive profiles, phased ECCD is an attractive option for control of the $m = 2, n = 1$ tearing mode. The power requirements can be substantially less than for conventional profile control techniques, and the requirements on the radial localisation and positioning of the driven current are less exacting. Application to an ITER-sized device should be practicable and the requirements on poloidal localisation (i.e. width of the antenna pattern) present no problem if ECCD is used (but may eliminate LHCD). It is also shown that it should be possible to control stationary tearing modes driven by error fields with phased ECCD with appropriate location of antennae, and a single system would allow both DC and phased mode control.

References

1 A W Morris et al. *Physical Review Letters*, **64**, 1254, (1990).
2 A H Glasser, H P Furth, and P H Rutherford. *Physical Review Letters*, **38**, 234, (1977).
3 P H Rutherford. *in Basic Phys Processes of Tor. Fus. Plasmas, Varenna 1985*, **2**, 531, (1985).
4 Y Yoshioka, S Kinoshita, and T Kobayashi. *Nuclear Fusion*, **24**, 565, (1984).
5 A W Morris, P G Carolan, R Fitzpatrick, T C Hender, T N Todd. *Phys. Fl. B*, **4**, 413, (1992).
6 M R O'Brien, M Cox, T C Hender, D C Robinson, and D F H Start. *Proc. 13th EPS. Conf on Controlled Fusion and Plasma Heating, Schliersee*, **2**, 270, (1986).
7 E Westerhof. *Nuclear Fusion*, **30**, 1143, (1990).
8 P H Rutherford. *Physics of Fluids*, **16**, 1903, (1973).
9 R O Dendy and M R O'Brien. *Nuclear Fusion*, **29**, 480, (1989).
10 R J Hayward et al. *in Proc.15th SOFT*, **1**, 361 (1988).
11 A W Morris and R Fitzpatrick. *AEA Fusion Report*, **AEA FUS 141**, (1991).
12 R Fitzpatrick and T C Hender. *Phys. Fl. B*, **3**, 644, (1991).
13 G Giruzzi, T J Schep, and E Westerhof. *NET Report No. 96, EUR-FU/80/89-96*, (1990).
14 S Ali-Arshad et al. *Proc. IAEA TCM on Avoidance and Control of Tokamak Disruptions, (Culham 1991)*.
15 T C Hender, R Fitzpatrick, and A W Morris. *AEA Fusion Report*, **AEA FUS 141**, (1991).
16 M R O'Brien, M Cox, and J S McKenzie. *Nuclear Fusion*, **31**, 583, (1991).
17 D E Post et al. *ITER Documentation series, No. 21 (IAEA, Vienna, 1991)*.
18 T C Hender, A W Morris, R Fitzpatrick, et al. *AEA Fusion Report*, **AEA FUS 150**, (1991).

NONLINEAR MECHANISM FOR THE SUPPRESSION OF ERROR FIELD MAGNETIC ISLANDS BY PLASMA FLOW

R.D. Parker

Centre de Recherches en Physique des Plasmas, Association Euratom-Conféderation Suisse, Ecole Polytechnique Fédérale de Lausanne
21 Av. des Bains, CH-1007 Lausanne, Switzerland

Introduction

Non-axisymmetric magnetic field perturbations generated, for example, by errors in the alignment of the field coils are known to lead to reduced confinement in a tokamak,e.g.[1,2]. By inducing the formation of small, stationary, magnetic islands on all rational surfaces they can enhance radial transport and under certain circumstances interact with MHD instabilities to trigger the onset of locked modes[1,2] leading, in some cases, to a disruption of the plasma discharge.

Given the stationary nature of the error field islands it is natural to consider whether they can be reduced significantly by the viscous drag of a sheared flow resulting from a bulk rotation of the plasma. In this paper, we examine this interaction by modelling the nonlinear growth and saturation of force-reconnected magnetic islands driven by a corrugated boundary in a slab plasma with an initially uniform flow. A systematic parameter study is made of the time asymptotic steady state revealing a transition to a *"suppressed state"* as a function of the flow velocity, which becomes discontinuous for sufficiently small viscosity. As such, a critical velocity, V_c, is defined and its dependence on: corrugation amplitude, δW (which is proportional to the error field amplitude, δB), viscosity, ν, and resistivity, $\eta = 1/S$,(S is the Lundquist no.), are delineated. Other parameters to be explored include the wall separation, X_w, and the wavenumber of the perturbation, k_p.

This study follows on from a preliminary numerical investigation[3,4] in which the flow suppression mechanism was first demonstrated. From the nonlinear simulations in the present study a simple intuitive model of the process based on the induced velocity shear,V' and the resistive layer width, Δ_η has been developed. This predicts a scaling for the critical velocity as: $V_c \propto \delta B\, S^{-2/5}\, \nu^{-2/3}$ in good agreement with numerically determined values of V_c ,although the scaling with viscosity diverges toward small ν. The reasons for this divergence are discussed in the light of changes occuring in the flow structure in the limits $\nu >> \eta$ and $\nu << \eta$.The scaling does not appear to be predicted by an alternative, analytical treatment of the phenomenon[5].

Besides the flow suppression mechanism, a variety of fascinating nonlinear phenomena were observed in different regions of the parameter space such as: flow amplified islands, flow induced secondary reconnection and hysteresis. These are discussed in the last section.

To investigate the mechanism of mode-locking it is also necessary to include the interaction of internally as well as externally driven reconnection processes in the presence of flow. This is the subject of the next stage in this study although preliminary simulations with a tearing unstable plasma have already demonstrated cases of full and partial mode-locking[4].

Numerical Model

The basic numerical model adopted is that of a 2-D, plane-slab plasma sandwiched between two, perfectly-conducting walls (at $x = \pm X_w$) with periodic boundary conditions in the y-direction (of periodicity length L_p). An approximately sinusoidal perturbation of the walls is introduced along the y-direction to provide a selfconsistant source of field error. Details of this can be found in ref.[3]. The initial equilibrium is $B = Bo \tanh(x)$, It has a line of field reversal at x=0 along which reconnection can occur and is maintained by a y-directed electric field and a non-uniform resistivity profile. To produce the plasma flow an initially uniform ExB drift is driven in the y-direction by maintaining a potential diffence between the walls.

To follow the evolution of the plasma in response to the error field, the visco-resistive MHD equations are integrated in time using a semi-implicit, spectral (in y)/ finite diffence (in x)scheme. Since, for the moment, we are only interested in externally driven reconnection the tearing instability is stabilized by reducing the wall separation to $X_w=1$, with Kp=0.35.

transition to the unsuppressed state should therefore be $V_c = 1/2\Delta_\eta V'(1-1/2\Delta_\eta/X_w)$ where the second term should be negligibly small at small resistivity. From linear theory we know that $\Delta_\eta \propto S^{-2/5}$ so taking this as well as the dependence found for the velocity shear into account we arrive at the scaling: $V_c \propto \delta B\, \nu^{-2/3}\, S^{-2/5}$ where the correction due to momentum conservation has been neglected.

Although the model is an over-simplification of what actually happens it appears to capture the essential features of the mechanism and consequently predicts a scaling for V_c in surprisingly good agreement with the computed dependence on S and δB and to a lesser extent on ν. See figs.1(a) and (b). Runs made with $S=10^4$, $\nu=10^{-4}$, $X_w=1.$, $K_p=0.35$ and $\delta W=0.04$, 0.02, 0.01, 0.005 and 0.0025 for a range of flow velocities showed $V_c \propto \delta W$ to a high precision. Since V' is also $\propto \delta W$ it thus confirms that V_c is affected by the size of the error field directly through the modification of the induced velocity shear.

The intuitive model is too simplistic to correctly predict more than just the general trend in the dependence on viscosity and this is evidenced by the changes in flow cross section observed in the limits of small and large viscosity.

When $\nu\sim\eta$, that is, when the viscous layer width, $\Delta_\nu \sim V/V'$, is roughly equal to the reconnection layer width, Δ_η, the situation is close to that of the intuitive model. See fig.2(b). However when $\Delta_\nu > \Delta_\eta$ the trough in the flow flairs out beyond the reconnection layer, although with the maximum velocity shear still occuring at the edge of the layer as in fig.2(a).

At the other extreme with $\Delta_\nu < \Delta_\eta$, the suppression of the flow is concentrated around the edges of the reconnection layer where the conflict with the flow, due to ideal coupling, is strongest. Thus, instead of one trough, two narrower troughs are formed as shown in fig.2(c). In the centre of the layer, where the resisitivity completely decouples the field from the fluid, the flow is left to pass through the island almost unretarded. The two narrow troughs cannot penetrate as low as a single broader trough with the same velocity shear so a smaller than expected flow velocity is needed to allow the island to become unsuppressed. This change in the flow structure when $\nu \ll \eta$, therefore appears to be why V_c is smaller than that predicted by the scaling of the intuitive-model towards small ν.

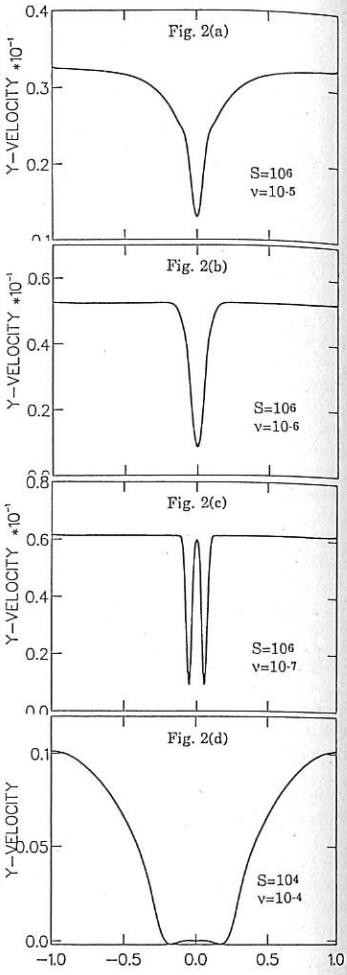

Fig.2 Flow cross-sections for: suppressed islands with Prandtl no. (a) $P_r=S\nu=10.$, (b) $P_r=1.0$,(c) $P_r=0.1$ and (d) for an unsuppressed island.

Time Asymptotic Behaviour

Several interesting features of the saturated behaviour can be seen in fig.3 which shows the transition between the suppressed and unsuppressed states as a function of flow velocity for several different values of the viscosity, and $S=10^3$. The first thing to note is that for sufficiently large viscosity the transition ceases to be discontinuous. This also occurs for large resistivity. To understand this we note that with finite resistivity some relative motion of the

field to the fluid is allowed outside the reconnection layer. The flow therefore does not have to entirely vanish in the island for it to become unsuppressed, It is however only significant for relatively large resistivity. If the viscosity is also large the consequent flair-out of the trough beyond the reconnection layer can allow the island to expand some distance beyond the layer before the flow is made low enough to completely unsuppress the island. The higher the viscosity the more the flow is reduced outside the reconnection layer and so the larger the suppressed island can reach while still in a suppressed state. Eventually for sufficiently large viscosity the flow can be reduced to where the island can reach its unsuppressed size without passing through a discontinuity, as shown in fig.3.

Perhaps the most surprising observation is the flow induced amplification of the unsupressed island well above its zero flow width. This can occur if it is still stable above about 10% of the Alfvén velocity with $\nu \ll \eta$. In fig.3, where $S=10^3$, the marginal case occurs for $\nu=10^{-4}$ although this varies depending on the other parameters. As the viscosity is made smaller the amplification begins at a smaller velocity but quickly approaches a limiting case below $\nu=10^{-5}$. This confirms that the amplification only occurs when the flow is a significant fraction of the Alfvén velocity.

Fig. 3

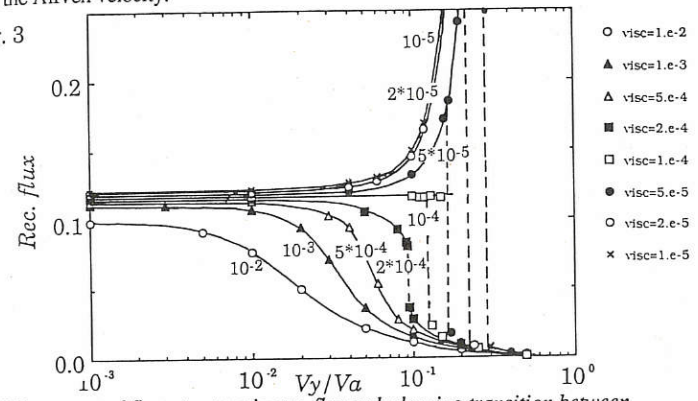

Fig.3 Reconnected flux at saturation vs. flow vel. showing transition between suppressed and unsuppressed islands for different viscosities and $S=10^3$.

Another feature of these flow enhanced states is a form of hysteresis. By restarting a simulation from a solution with $V<V_c$ and slowly increasing the flow at the boundary it is possible to obtain a stable unsuppressed state for $V>V_c$. In effect, there is a finite basin of attraction for the unsuppressed state distinct from that of the the suppressed state. V_c therefore only represents the flow velocity below which the suppressed attractor becomes unstable. A different critical velocity can be defined above which the unsuppressed state becomes unstable.

Changes in the long time behaviour of the suppressed states were also observed. At large S ($S \geq 10^5$) and small ν ($\nu \leq 10^{-5}$) the supressed island is very narrow and during its evolution it can undergo a spontaneous transition during which secondary islands are formed at the x-points. The increase in the number of islands produces a large rise in reconnected flux without greatly increasing the island width. It tends not to occur, however, in cases where the island eventually becomes unsuppressed.

Acknowledgement: This work was partly supported by the Swiss National Science Foundation.

References

[1] P.R. Thomas et. al., Plasma Phys.& Controlled Fusion,IAEA,Vienna,Vol.1,353,(1985).
[2] J.T. Scoville et. al., Nucl. Fusion, 31, 875, (1991)
[3] R.D. Parker, R.L. Dewar, Comput. Phys. Com., **59**, 1, (1990).
[4] R.D. Parker, PhD Thesis, ANU, Canberra, (1987).
[5] R. Fitzpatrick, T.C. Hender, Phys.Fluids B, **3**, 644, (1991).

Flow Suppression Mechanism

In the absense of flow, the error field induces reconnection of the field lines to form the usual magnetic island structure which generally extends well beyond the reconnection layer. With flow, however, the strong ideal coupling of the field outside the reconnection layer constrains the magnetic field lines to keep the same topology as the fluid flow and so tends to obstruct the further development of the island. A narrow filamentary island is therfore formed within the reconnection layer and dragged partially out of phase with the boundary corrugation by the flow. Since further reconnection is blocked the driving energy of the error field is diverted into shifting the flow out of the magnetic island. Once the flow is removed, however, the island is nolonger topologically constrained and so recontinues its growth, pushing the flow aside as it does. See fig.2(d). Viscous drag causes a finite velocity shear to build up to a maximum around the separatrix of the island. Measurements of the maximum velocity shear, V', over a range of parameters show a clear scaling with viscosity and perturbation amplitude as $V' \propto \delta B\, \nu^{-2/3}$. If we assume, for simplicity, that the flow is only removed from the region of the suppressed island and that its width is equal to the reconnection layer width, Δ_η, then it is clear that the lowest the flow velocity can fall is $\Delta V = 1/2 \Delta_\eta V'$. If the initial flow velocity, V, is greater than ΔV then the island is theoretically unable to proceed and so must remain suppressed. Taking into account conservation of momentum, the critical initial velocity for

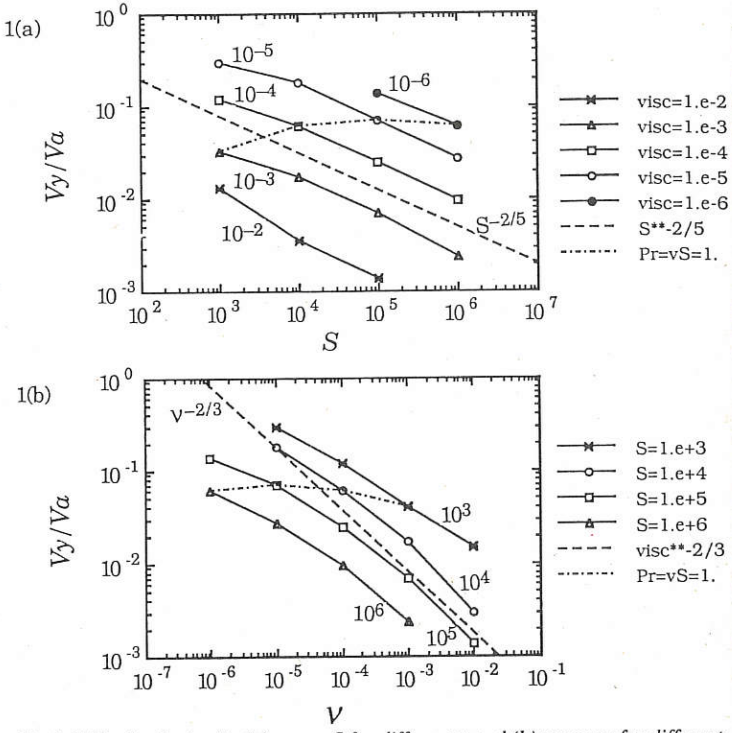

Fig.1 Critical velocity, V_c (a) versus S for different ν and (b) versus ν for different S with $\delta W=0.02$, $X_w=1.$ and $K_p=0.35$. These are compared respectively with the $S^{-2/5}$ and $\nu^{-2/3}$ scalings of the simple model. Also shows theweak dependence of V_c on S and ν at constant Prandtl number, $P_r=S\nu=1$.

Observations of Beam Ion Losses in TFTR During TAE Modes and Other MHD Activity

D. S. Darrow, E. D. Fredrickson, H. E. Mynick, R. Nazikian,
R. B. White, K.-L. Wong, S. J. Zweben
Princeton University, Plasma Physics Laboratory, Princeton, NJ 08543, USA
M. Tuszewski
Los Alamos National Laboratory, Los Alamos, NM 87545, USA

Abstract

Direct measurements of fast NBI ion losses have been made near the outer midplane during MHD activity in TFTR. Bursts of beam ion loss are seen coincident with the TAE mode activity. Particles lost during TAE activity are lost at the full injection energy of 100 keV, and only the total efflux of fast ions changes during the mode, not the pitch angle or energy of the lost ions. Reductions in neutron source strength indicate that ~ 10 percent of the beam ions can be lost in a single burst, with a cumulative loss of as much as 50 percent. Other MHD activity can cause large losses of beam ions, including passing ions.

I. Introduction

Toroidal Alfvén Eigenmodes (TAEs) have become a topic of recent concern due to their potential impact upon tokamak reactors.[1-4] These are toroidal eigenmodes of the Alfvén wave which are driven unstable by resonances with toroidally-circulating particles whose velocity exceeds[5] $v_A/3$, where $v_A = \frac{B_T}{\sqrt{\mu_0 \rho}}$ is the Alfvén velocity. In a reactor, alpha particles are anticipated to provide the free energy to drive the mode. The mode is of importance due to its potential ability to expel fast ions of all sorts, including the alpha particles and beam ions.

Experiments on TFTR[2] and DIII-D[3] have utilized neutral beam ions, under suitable conditions, as superalfvénic particles. In both experiments, repeated short bursts of high-frequency (~ 100 kHz) Mirnov activity were observed, which coincided with reductions in the neutron production rate. More recent experiments on DIII-D[6] have found significant sputtering of carbon tiles near the outside midplane during TAE-unstable discharges. This has been the most direct evidence of TAE-induced beam ion losses. The present work describes recent measurements of the beam ion losses due to TAE modes in TFTR, as well as losses from other MHD activity.

II. Beam Ion Loss During the TAE

To obtain conditions in which the 100 keV deuterium beam ions are super-alfvénic in TFTR ($v_b > v_A$), plasmas must be run at low toroidal field (1 to 1.5 T) and moderately high densities ($\geq 3 \times 10^{19}$ m^{-3}) so that the Alfvén speed is low.

Beam ion losses are detected with the TFTR midplane fast ion probe.[7-9] It is moveable radially, along a line 0.35 m below the midplane and, for plasmas in experiments reported here ($R = 2.40$ m, $a = 0.75$ m), can be positioned at minor radii varying from 1.04 m to 1.18 m. The probe detects fast ions which have trajectories such that they can pass through two collimating apertures and then strike a flat scintillator. The position of the light created identifies the gyroradius and pitch angle of the particle which produced it, and that light is recorded by an intensified videocamera (to obtain an image) and by a photomultiplier tube (to obtain the total intensity from the scintillator with fast time response). The probe detects only ions travelling in the direction of the plasma current, and only those with pitch angles (relative to the toroidal field) between 40° and 85°, and gyroradii between 2 cm and 12 cm.

Figure 1 shows data from a plasma with $R = 2.40$ m, $a = 0.75$ m, $B_T = 1.5$ T, $I_p = 500$ kA, $\bar{n}_e = 2.3 \times 10^{19}$ m^{-3}, and $P_{inj} = 10$ MW. The typical signatures[2] of a TAE are evident: periodic bursts of high-frequency magnetic activity, coincident with reductions in the neutron production rate, and increases in the beam ion loss. The frequency of the Mirnov signal within the bursts varies as expected from the mode frequency,[1] $\omega = \frac{v_A}{2qR}$. The beam ion loss is integrated over all pitch angles and energies that the probe can view; the only substantial contribution to the signal comes from 100 keV neutral beam ions. In addition, it is apparent that the magnitude of the ion loss is correlated with the amplitude of the magnetic activity, and that only the bursts with largest amplitude cause substantial dips in the neutron rate. In this figure it can be seen that the beam ion loss is sychronous with the mode activity, rising after the magnetic burst starts, and falling after the end of each burst. However, in some of the bursts, the ion loss does not peak until after the Mirnov activity has subsided, suggesting that the process of expulsion of the ions may take ~ 0.5 msec, although low-frequency Mirnov activity may also expel particles during the intervals between high-frequency bursts.

During the bursts, the rate of beam ion loss is approximately 1.5 times what it is without the mode activity. A SNAP calculation on a discharge similar to the one which produced the data in Fig. 1 indicates that 16% of the neutral beam ions escape the plasma due to first-orbit losses. First-orbit loss (and possibly stochastic TF ripple loss) most likely comprise the steady background loss rate. The 50% increase in the loss rate due to the bursts would then imply a loss of about 8% of the beam ions, which is of similar magnitude to the reduction in the neutron rate observed. Although the beam loss rate is seen to increase with every Mirnov burst, the neutron rate drops significantly only during some. This intermittency will be the subject of future investigations.

III. Energy and Pitch Angle of Ions Lost During TAEs

Figure 2 shows the sintillator image under two circumstances, for a discharge similar to that in Fig. 1. In 2(a), the image has been integrated over several bursts of the mode, and in 2(b), the image is that seen immediately after the neutral beams have been turned off, at which time the TAEs are no longer excited but the plasma parameters have not changed significantly from their values when the modes were present. The images show contours of constant intensity (the actual intensities of the contours differ between the two images). The maximum intensity corresponds to ions with a gyroradius of $\rho = 7 \pm 1$ cm, the gyroradius of the 100 keV deuterons at the probe position. The pitch angle at maximum intensity is $\chi = 57°$, while the boundary between trapped and passing particles is the line $\chi = 47°$. The images in Fig. 2 indicate that, although the total beam ion loss from the plasma seen by the probe is being increased by the TAE, the loss continues to occur at the same place in the energy/pitch angle space.

IV. Losses During Other High-Frequency MHD Activity

Beam injection into plasma with densities $\sim 25\%$ lower than those used in the TAE experiments ($\bar{n}_e = 1.8 \times 10^{19}$ m^{-3}, $B_T = 2$ T, $I_p = 420$ kA, $P_{inj} = 10$ MW, $R = 2.40$ m, $a = 0.75$ m) can result in Mirnov bursts which have characteristics qualitatively similar to those of the TAEs: Mirnov activity at 25–50 kHz, neutron drops, and increased beam ion losses. These modes, however, do not fit the frequency scaling expected of TAE modes: $\omega = \frac{v_A}{2qR}$. These modes do, however, show similar radial distributions of frequency and amplitude in the beam emission spectroscopy (BES[10]) signals. Figure 3(a) shows the time-history of the midplane probe signal, with spikes of beam ion loss many times the MHD-quiescent background level. Figure 3(b) shows the image at the detector for a particularly intense burst of this sort. In this image, the loss of trapped particles is seen, approximately as in the TAE case (the intensity has saturated the camera at the center of the loss, preventing detection of the exact location of peak loss). It also, however, possesses an additional feature not seen in any of the TAE cases to date, the loss of passing particles (the feature with pitch angles below $\chi = 47°$).

V. Summary

Energy and pitch-angle resolved measurements of beam ions lost during TAEs indicate that particles are lost at the same energy and pitch angle both when the mode is present and absent. This observation

is most likely explicable by enhanced velocity-space diffusion of fast ions induced by the mode, or by stochastic ripple diffusion[7] of ions in the fields of the mode. Under similar conditions, but with lower density, intermediate frequency (25- 50 kHz) MHD modes act to expel passing beam ions at their full injection energy.

VI. Acknowledgements

The authors wish to acknowledge useful discussions with Prof. W. Heidbrink of the University of California at Irvine and the assistance of the TFTR group. This work was supported by U.S. Department of Energy Contract DE-ACO2-76-CHO-3073.

References

[1]G. Y. Fu and J. W. Van Dam, *Phys. Fluids B* **1**, 1949 (1989).

[2]K.-L. Wong, R. J. Fonck, S. F. Paul, et al., *Phys. Rev. Lett.* **66**, 1874 (1991).

[3]W. H. Heidbrink, E. J. Strait, E. Doyle, G. Sager, R. T. Snider, *Nucl. Fusion* **31**, 1635 (1991).

[4]C. Z. Cheng, *Phys. Fluids B* **3**, 2463 (1991).

[5]H. Biglari,F. Zonca, and L. Chen, Princeton Plasma Physics Laboratory Report Number PPPL-2789, October, 1991.

[6]W. H. Heidbrink, to appear in *Phys. Fluids B* **4** (1992).

[7]R. L. Boivin, Ph.D. Thesis, Princeton University (1991).

[8]R. L. Boivin, S. Kilpatrick, D. Manos, and S. J. Zweben, *Rev. Sci. Instrum.* **61**, 3208 (1990).

[9]D. S. Darrow, R. L. Boivin, and S. J. Zweben, to appear in *Rev. Sci. Instrum.*

[10]R. J. Fonck, P. A. Dupperex, and S. F. Paul, *Rev. Sci. Instrum.* **61**, 3487 (1990). S. F. Paul, and R. J. Fonck, *Rev. Sci. Instrum.* **61**, 3496 (1990).

Figure Captions

Figure 1 Time histories of signals from Mirnov coil, neutron detector, and midplane fast ion probe during several TAE modes. Modes are designated by the enhanced high-frequency Mirnov signal. Note that the beam ion loss signal increases during each Mirnov burst, and that the amount of the increase varies in proportion to the Mirnov amplitude.

Figure 2 (a) Intensity pattern seen on midplane detector, integrated over an interval containing several TAE bursts. A gyroradius/pitch angle grid is overlaid on the pattern. The gyroradius is that the ion would have if all its velocity were perpendicular to B, i.e. this coordinate is the energy of the particle, not the actual radius of orbital motion. The pitch angle is $\chi = arccos(v_{tor}/v)$. (b) The pattern for similar plasma conditions immediately after beam injection has ended, so that TAE modes are no longer being excited. Note that the feature due to beam ion loss is at exactly the same position and has the same shape as the feature when TAEs are present.

Figure 3 (a) Beam ion loss signal versus time showing pronounced bursts of beam ion loss. (b) Intensity pattern seen on the detector during a Mirnov burst whose frequency scaling did not fit the TAE frequency, but under similar conditions. Note that, in this instance, passing particles are lost ($\chi < 47°$).

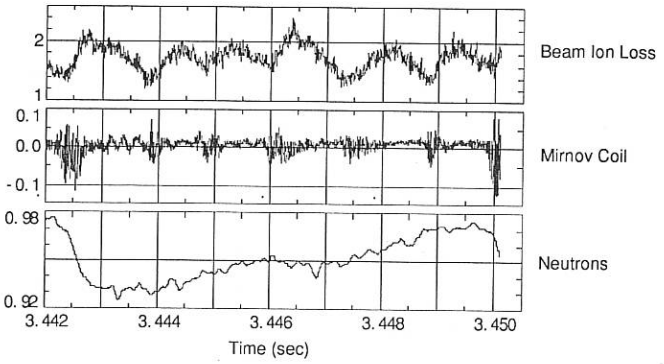

Figure 1

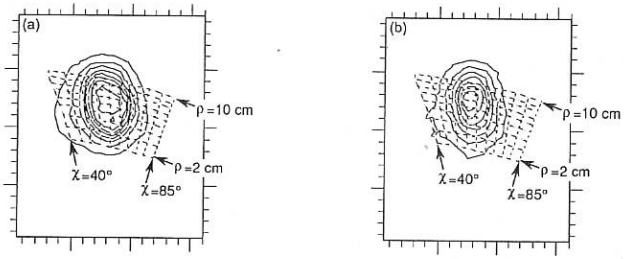

Figure 2

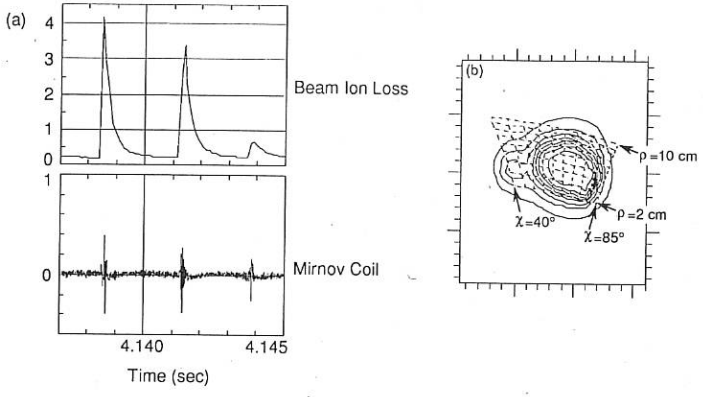

Figure 3

GLOBAL ALFVÉN EIGENMODES IN DIII–D*

A.D. Turnbull, M.S. Chu, E.J. Strait, W.W. Heidbrink,† H. Duong,†
L.L. Lao, J.M. Greene, M.S. Chance,‡ and T.S. Taylor

General Atomics, San Diego, California, U.S.A.

1. INTRODUCTION

Global Alfvén modes, such as the Toroidicity-Induced Alfvén Eigenmode (TAE), pose a serious threat for strongly-heated tokamaks since they can result in saturation of the achievable beam β at moderate levels and they may also cause serious α-particle losses in future ignited devices. The DIII–D tokamak has a unique capability for study of the resonant excitation of these instabilities by energetic beam ions. TAE modes have now been observed in DIII–D over a wide range of operating conditions, including both circular cross-section and elongated ($\kappa \sim 1.8$) discharges. Equilibrium reconstructions of several representative discharges, using all available external magnetic and internal profile data, have been done and analyzed in detail. The computed real mode frequencies of the TAE modes are in good agreement with the experimentally observed mode frequencies and differ significantly from the estimated kinetic ballooning mode frequencies. The TAE calculations include coupling to the Alfvén and acoustic continuum branches of the MHD spectrum and generally indicate that the simplified circular cross-section, large aspect-ratio assumptions made in analytic calculations are poor approximations to the actual TAE mode structures. In particular, the global TAE modes are almost always coupled to one or more continuum branches by toroidicity, poloidal shaping, and finite β effects. Estimates of the various resonant excitation and damping mechanisms, including continuum damping, have been made and the total is found to be in reasonable agreement with the experimental threshold.

2. COMPARISON: THEORETICAL AND EXPERIMENTAL FREQUENCIES

In low field, beam-heated DIII–D discharges, MHD modes are observed which rotate with respect to the plasma at a real finite frequency. Typically, modes with toroidal mode numbers n in the range $3 \lesssim n \lesssim 10$ are observed. The real frequency, when corrected for Doppler shift due to the plasma rotation, is in approximate agreement with the frequency of TAE modes as predicted by the simple formula [1] $\omega \sim V_A/2qR$, where V_A is the Alfvén speed, R is the major radius, and q is the value of the safety factor at which the modes peak; typically $q \sim 1.5$ is taken. The results from a typical sequence of similar shots are shown, for example, in Fig. 1 (solid points). Here, the Alfvén speed was varied by systematically changing the toroidal field, keeping the total current set at 0.6 MA, density 3×10^{19} m^{-3} and beam power constant at 5 MW. The straight line corresponds to $\omega = V_A/2qR$ with $q = 1.5$. The diamonds are the predictions for kinetically destabilized ballooning modes [2], which are also predicted to have a real nonzero frequency in the plasma frame. We note in passing that these are not in agreement with the observed frequency dependence, thus eliminating those modes as being responsible for the observations.

The equilibria were reconstructed using all available profile and magnetic data, as described in Ref. 3, for shots 71515 and 71524. They were then analyzed using the two ideal MHD stability codes CONT [4] and GATO [5]. The CONT code computes the singular eigenvalues of the ideal MHD equations, providing both the real frequencies and spatial locations of the stable Alfvén

*This is a report of work sponsored by the U.S. Department of Energy under Contract Nos. DE-AC03-89ER53277, DE-AC03-89ER51114, and DE-AC02-76-CHO-3073.
†University of California, Irvine, California, U.S.A.
‡Princeton Plasma Physics Laboratory, Princeton, New Jersey, U.S.A.

and acoustic continuum modes. The result is a global picture of the MHD continua, including the continuum gaps induced by both toroidicity [4] and shaping [4,6]. The GATO code has been modified to compute the real part of the eigenvalues and eigenvectors of the ideally stable modes. The continuum is discretized and the logarithmic singularities of the continuum modes are truncated by the finite mesh. Global modes, however, are well represented and appear in gaps within the appropriate continua. The gap extrema predicted by the CONT and GATO codes are in extremely good agreement.

The spectrum predicted from the CONT code for shot 71515 is shown in Fig. 2 for toroidal mode number $n = 3$. The solid curves are the continuum branches (labeled with the dominant poloidal mode number for $m \leqslant 9$), plotted as the normalized square of the frequency against the radial position at which the mode is resonant. The dotted curves are the envelopes of the gaps for all n. The experimentally-measured density profile was used in both the CONT and GATO calculations. For clarity, acoustic continua are not shown in Fig. 2. The lowest gap near $\omega^2 \gtrsim 0$ is due to finite β [4]. The next gap is the toroidicity-induced gap and the third gap is created by the coupling of poloidal harmonics m and $m+2$ ($m = 3, 4, \ldots$) induced mostly by the elongation of the discharge [6] ($\kappa \sim 1.7$). The GATO calculations, which in this case, included full coupling between the Alfvén and acoustic branches (*i.e.*, compressibility included) as well as the presence of a finite vacuum and the correct DIII–D wall location, revealed two groups of closely-spaced TAE-like modes with frequencies lying within the TAE gap near $\omega^2 = 0.101$ and 0.133. Within each group, the TAE-like eigenmodes comprise a global component, coupled to singular Alfvén and acoustic continuum harmonics. The Fourier analysis of the perpendicular displacement is shown in Fig. 3 (a) and (b) for two eigenmodes typical of the respective groups. For the lower frequency mode at $\omega^2 = 0.101$ in Fig. 3(a), the $m = 4, 5$ TAE-like structure is coupled to several higher $m, m+1$ TAE-like components and a singular $m = 16, 17$ continuum component near the edge. There is also a small $m = 3$ continuum component near the center, as expected from Fig. 2. On the other hand, the higher frequency mode ($\omega^2 = 0.133$) in Fig. 3(b) is dominated by the $m = 3, 4$ TAE component with smaller higher m TAE structures and several high m ($m \sim 12$) continua inside the edge. The small $m = 3$ singular branch is also present near the center. The multiple modes in each group are a result of coupling to the higher harmonics — both global harmonics from the multiple local gaps ($m, m+1$ for $m > 4$) and continuum harmonics where the TAE gap is intersected by the continua [7] as in Fig. 2.

The frequencies computed for these two modes are also shown as circled crosses in Fig. 1. The agreement with the observed frequency is extremely good. We have also looked for experimental evidence of multiple modes in shot 71515, as predicted by the GATO code. However, TAE activity in this particular shot was relatively weak and, although there is some suggestion from the data that two or more modes are present at slightly different frequencies, the evidence is inconclusive. Nevertheless, more detailed analysis of the similar, but lower field shot 71524, where the TAE activity was much stronger, does reveal the existence of at least two distinct TAE modes separated in frequency by about 20%. These are also indicated in Fig. 1 by the circled pluses. The stability analysis for this shot, however, was limited to the incompressible case, in which acoustic coupling is eliminated. A conducting wall was also imposed on the plasma surface. Incompressibility introduces a downward frequency shift of about 25% and, together with the change in boundary conditions, modifies the coupling between the various poloidal harmonics. Nevertheless, the results do indicate that there are probably at least two modes in this shot, analogous to those shown in Fig. 3. For reference, the eigenvalue of the highest frequency eigenmode from that analysis is shown in Fig. 1 (open circle); the correct frequency is probably about 25% higher than that shown.

3. STABILITY THRESHOLDS

Resonance between energetic particle drift motion and the rotating TAE wave introduces an imaginary part to the otherwise real ideal MHD eigenvalue which, in the absence of dissipation,

can result in an exponential growth rate [1] $\gamma_\alpha > 0$; in DIII–D, the energetic particles are the injected neutral beams. The mechanism is essentially an inverse Landau interaction with energy transferred from the fast particles to the wave. The condition for resonance is that the parallel beam velocity $V_\parallel$ be near V_A, with $\gamma_\alpha > 0$ for $V_\parallel > V_A$. The growth rate γ_α is proportional to the fast-ion beta β_b.

Additionally, however, it has been shown that a secondary resonance exists [8] at $V_\parallel \gtrsim V_A/3$ as a result of the coupling of poloidal modes m and $m+1$. Several damping mechanisms also compete with the fast-ion drive. For a TAE mode localized near a particular surface, the overall growth rate normalized to the real frequency can be written $\gamma \sim \gamma_\alpha - (\gamma_{CD} + \gamma_{IL} + \gamma_{EL})$, where γ_α is the destabilization from the fast particles. The other three terms represent the various damping contributions. Specifically, γ_{CD} is from continuum damping, which results from phase mixing of the wave with nearby continuum modes. γ_{IL} is the Landau damping from resonance between the wave and background ions ($V_{\parallel bg} \lesssim V_A$), including a secondary resonance when $V_{\parallel bg} \lesssim V_A/3$ analogous to the fast-ion inverse-Landau driving mechanism. Finally, γ_{EL} is the dissipation due to energy lost from the wave to the electrons. For passing electrons, this is from collisionless Landau damping and is essentially negligible. Inclusion of finite conductivity and parallel electron dynamics for trapped electrons, on the other hand, has been shown to result in much larger damping rates [9] and this latter contribution is the dominant damping mechanism in our case; the overall growth rate is largely a balance between this and the fast particle drive, though the other two terms do contribute. The condition $\gamma > 0$ for instability then becomes an expression for a threshold β_b, above which the TAE modes are destabilized.

Expressions for the various growth rate terms have only been derived in the specific case of large aspect ratio, circular cross-section, and are meant to be applied at the location of the TAE mode [8–10]; a general theory for realistic cross-sections is still unavailable. Nevertheless, we can apply the local formulae at the $q = 1.5$ location, which is roughly where the GATO calculations predict the modes peak. This naive application of the simplified theories, while not entirely applicable in DIII–D, is still probably valid to within a factor of order one. We find for shot 71524 that the TAE mode should be unstable over a range of toroidal mode numbers $3 \leqslant n \leqslant 9$, which is in complete agreement with the observations. Analysis of the other shots is still in progress.

In conclusion, TAE modes have been observed in DIII–D and the observed frequencies are in extremely good agreement with the results of full MHD calculations. Moreover, multiple TAE modes with the same toroidal mode number have been identified in both the experimental observations and the calculations; these are separated in frequency by about 20% in either case. The threshold beam β_b, as calculated from simplified formulae, is also in good agreement with the observations.

REFERENCES

[1] G.Y. Fu and J.W. Van Dam, Phys. Fluids B **1** (1989) 1949.

[2] H. Biglari and L. Chen, Phys. Rev. Lett. **67** (1991) 3681.

[3] L.L. Lao, J.R. Ferron, R.J. Groebner, W. Howl, H. St. John, E.J. Strait, and T.S. Taylor, Nucl. Fusion **30** (1990) 1035; D. Wroblewski and L. L. Lao, Phys. Fluids B **3** (1991) 2877.

[4] C.Z. Cheng and M.S. Chance, Phys. Fluids **29** (1986) 3695; M.S. Chu, J.M. Greene, L.L. Lao, A.D. Turnbull, and M.S. Chance, General Atomics Report GA-A20714 (1992), submitted to Phys. Fluids B.

[5] L.C. Bernard, F.J. Helton, and R.W. Moore, Comput. Phys. Commun. **24** (1981) 377.

[6] R. Betti and J.P. Freidberg, Phys. Fluids B **3** (1991) 1865.

[7] A.D. Turnbull, M.S. Chu, M.S. Chance, J.M. Greene, L.L. Lao, and E.J. Strait, General Atomics Report GA-A20746 (1992), submitted to Phys. Fluids B.

[8] R. Betti and J.P. Freidberg, Massachusetts Institute of Technology Report PFC/JA-91-25, submitted to Phys. Fluids B (1991); H. Biglari, F. Zonca, and L. Chen, submitted to Phys. Fluids B (1992).
[9] R.R. Mett and S.J. Mahajan, University of Texas Report IFSR #543 (1992).
[10] F. Zonca and L. Chen, Phys. Rev. Lett. **68** (1992) 592; M.N. Rosenbluth, H.L. Berk, D.N. Lindberg, and J.W. Van Dam, Phys. Rev. Lett. **68** (1992) 596.

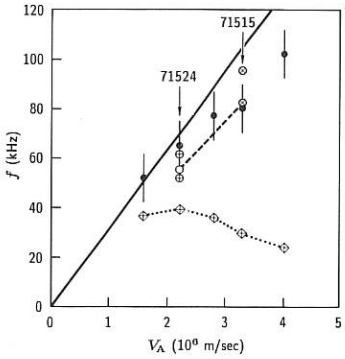

FIG. 1. Frequencies of TAE modes in a sequence of DIII–D shots with varying toroidal field.

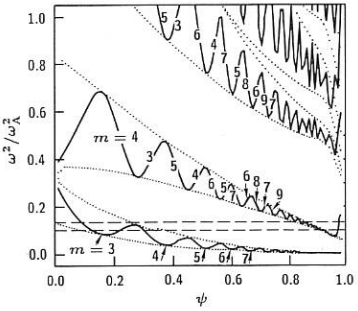

FIG. 2. Continuum shear Alfvén spectrum for shot 71515 with $n = 3$. The TAE mode frequencies computed with GATO are indicated by the broken lines at $\omega^2 = 0.101$ and 0.133.

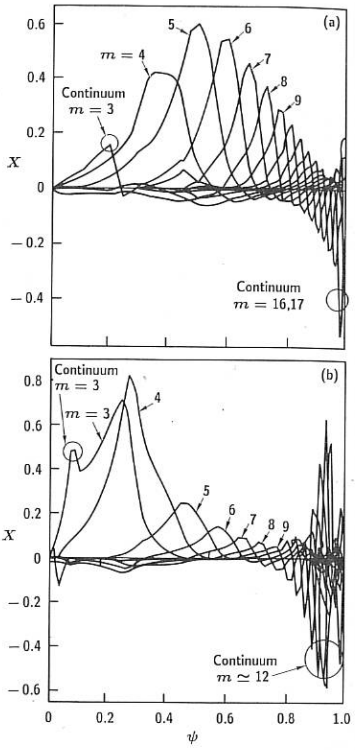

FIG. 3. Fourier decomposition of $X = \xi \cdot \nabla\Psi/|\nabla\Psi|$ for two TAE modes at (a) $\omega^2 = 0.101$ and (b) $\omega^2 = 0.133$.

Energetic Particle Driven instabilities at JET

M.F.F.Nave[1*],D.Borba,[1] P.Cripwell, M.von Hellermann,
W.Kerner, F.Porcelli, G.Sadler, P.Smeulders

JET Joint Undertaking, Abingdon, Oxon, OX14 3EA, UK

[1] Associação IST/Euratom, Centro de Fusão Nuclear,
Instituto Superior Técnico, 1096 Lisboa Codex, Portugal

* Laboratorio Nacional de Engenharia e Tecnologia Industrial,Lisboa, Portugal

Experimental results

i) central modes

Fishbones are a common feature of auxiliary heated JET discharges, and are observed in the signals of several diagnostics, in both low and high beta regimes. As the typical fishbone bursts, first observed in PDX /1/, these are central modes, with a main m=1, n=1 mode structure. At JET they appear either in the form of short repetitive bursts (lasting a few milliseconds, with a repetition time of 10-20 milliseconds) or as continuous oscillations *(fig.1)*, with frequencies ranging from 1 to 25 kHz.

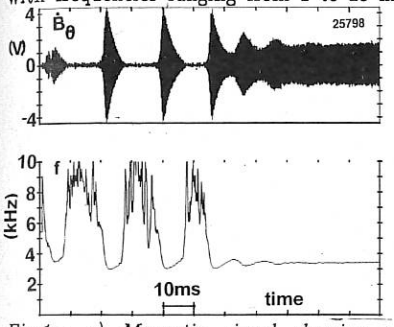

Fig.1– a) Magnetic signal showing a sequency of bursts that develops into a continuous oscillation,
b) corresponding frequency evolution.

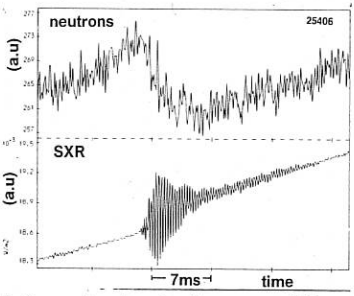

Fig.2– a) signal from a Silicon detector shield with Inconel, measuring mostly neutrons.
b) corresponding SXR signal near the sawtooth inversion radius.

In the low β regimes, the presence of a high frequency, 3-10 times that of the bulk plasma rotation at the q=1 radius, clearly distinguishes fishbones from other m=1, n=1 oscillations. Sawtooth precursor/postcursor oscillations, for instance, always have frequencies comparable to that of the plasma rotation.

In high β regimes, the fishbone frequency decreases and becomes comparable to that of oscillations around the sawtooth collapse. In low β regimes, the soft-X rays and electron cyclotron emission signals show the bursts localized around the q=1 radius. However, for high β, fishbone oscillations extend to outer regions, making it possible to observe fishbones with the reflectometer near the edge. A ballooning behaviour is also observed. Close to the Troyon limit fishbones are observed contributing to the saturation of the β parameter.

Interaction with fast particles is found for the largest amplitude events ($b_\theta/B_\theta \sim 10^{-3}$) observed in high beta regimes. For β_ϕ above 70% the Troyon limit,

the total neutron rate may fall by 9-19% during a burst *(fig.2)*. However, for the majority of JET discharges the rate of losses caused by fishbones is low (below the detection threshold ~ 5%). This may be due to the low amplitudes (one to two orders of magnitude smaller than the fishbone bursts observed in PDX), and to the large size of the JET plasma which leads to a better confinement of the fast particles.

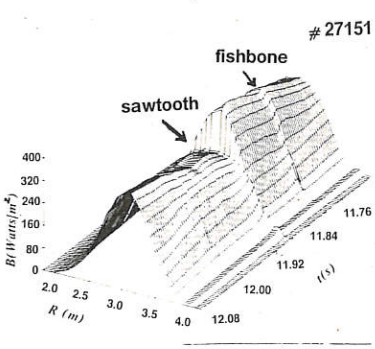

Fig.3– SXR profiles showing a fishbone and a sawtooth collapse. For the fishbone the maximum decrease in SXR emision is around q=1, where the profiles are flattened.

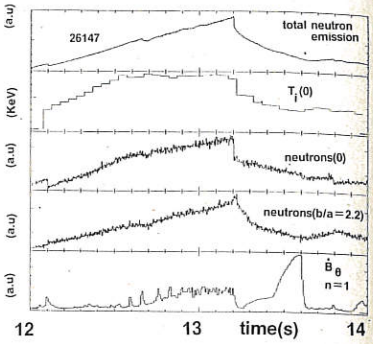

Fig.4– Time traces of a)the Total neutron emission rate, b) The ion Temperature;c) neutron emission in the centre, and d) near the edge; and e) the n=1 activity, mostly fishbones, measured at 45° above the midplane.

An important aspect of JET operation in the 1991/92 campaign was the study of high performance discharges (/2,3/), where fishbones are a prominent feature. Fishbones with increasing amplitude were the main low mode number activity observed before the termination of the good confinement phase.*(figs.4 and 5)*. These large amplitude fishbones cause drops in the central electron temperature and the central SXR intensity *(see fig3)*, and their onset maybe associated with a roll-over of the neutron emission in the centre *(fig.4)*.

ii) outer modes

A new observation from JET high performance discharges is that outer modes may also interact with energetic particles. After the termination of the good confinement phase, large amplitude ELMs are observed associated to losses of fast ions near the edge, measured by the ion cyclotron emission diagnostic /4/ *(fig.5)* in both DD and DT discharges. In some DT discharges, these ELMs are preceded by non central n=1 modes, possibly fishbone-type modes with m>1.

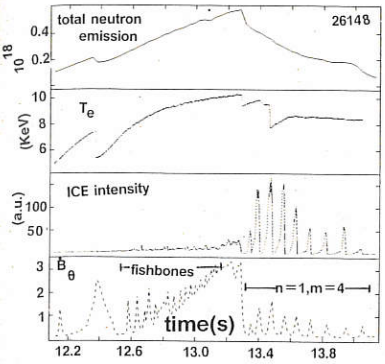

Fig.5– Time traces of the total neutron emission, central electron temperature, ion cyclotron emission (ICE) intensity measured at the edge, and n=1 magnetic activity.

Comparison with the theory

i) linear predictions

Ideal models which include the effects of finite Larmor radius and fast particles, predicts two types of m=1, n=1 modes, normally referred to as the kink and the fishbone modes/5/. The kink is a slow mode with frequencies close to zero in the rest frame, while the fishbone is a faster mode with frequencies ranging from the ion diamagnetic frequency, ω_{*i}, for a low value of the density of the energetic ions, n_h, to the drift frequency of the energetic ions, ω_{Dh}, for high values of n_h.

Some of the JET observations could be explained by the models, both qualitatively and quantitatively. Observations at low-β confirm the existence of two types of m=1,n=1 oscillations, with two distinct frequencies. As predicted fishbone oscillations are the faster ones and are always observed to rotate in the direction of the ion diamagnetic drift. The observed fishbone frequency in the rest frame of the plasma, ω, is also in good agreement with the predicted frequencies. For neutral beam injection heated discharges, we find $\omega \cong \omega_{*i} \cong \omega_{Dh}$; while in discharges with ion cyclotron radio frequency heating, where $\omega_{*i}/\omega_{Dh} \cong 10^{-1}$-$10^{-2}$, we find $\omega_{*i} \leq \omega \leq \omega_{Dh}$.

Other observational aspects are not well understood. The large experimental error bars make it difficult to explain the observation of fishbones during sawteeth-free periods. Another difficulty, is the observation in high-β regimes that all m=1 n=1 oscillations observed are slow, possibly indicating that only the kink branch may be present.

ii) non-linear model

A simple heuristic non-linear model has been developed to study the fishbone repetition cycle . Including ion-diamagnetic effects in resistive MHD two fluid theory an expression for the growth rate for the fishbone mode can be obtained /5/. The growth rate is proportional to the density of resonant super-thermal ions, and the mode decay is due to plasma resistivity. An equation for the density of the resonant ions is obtained assuming that a constant source of ions is provided by auxiliary heating, and the loss of fast particles is due to the ergodization of fast particle orbits. In this model the loss rate is proportional to the square of the mode amplitude.

The following non-linear system of equations describes the evolution of the mode amplitude, A, and the density of fast ions, n_h:

$$\partial A/\partial t = - \gamma_\eta A + \gamma_{MHD}(n_h/n_0)A$$

$$\partial n_h/\partial t = S_h - \gamma_L n_{crit} A^\nu$$

γ_{MHD} is the ideal MHD stability parameter; γ_η is the resistive damping; S_h is the source of fast ions; $\gamma_L n_{crit}$ is a measure of the fast particle loss rate. One expects $1 \leq \nu \leq 2$; $\nu=1$ assumes a secular loss of the resonant ions, while $\nu=2$ corresponds to losses following orbit stochasticity.

The comparison with the experimental data shows a good agreement with the model. Qualitatively the model predicts both bursts and continuous oscillations, and the observed relation between amplitude and the period of repetition of the bursts. A fit of the cycle solution with the experimental bursts is obtained for $\nu=2$ (see *fig.6)*, suggesting that orbit stochasticity is the main loss mechanism.

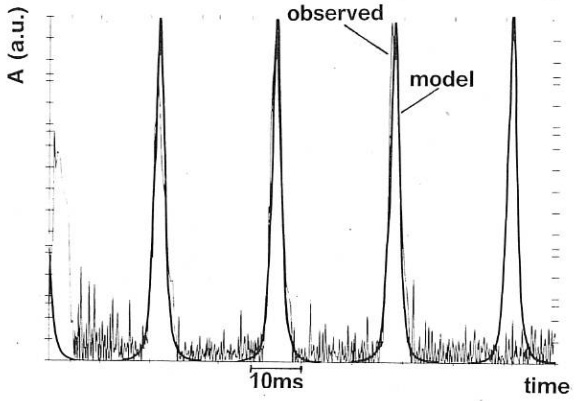

Fig.6– Fishbone amplitude measured by a magnetic pick-up coil and the amplitude obtained with the model, for $\nu=2$.

References

/1/McGuire,K. et al., Phys.Rev.Lett.**50,**891 (1983)
/2/Stork,D, et al.,"High β studies in the H-mode and Hot ion H-mode in JET", This conference.
/3/The JET Team, NucLear Fusion **32,** 187 (1992)
/4/Cottrell,G.A. et al."Identification of ion cyclotron emission from fusion alpha particles during JET DT experiments", This conference.
/5/Coppi,B.,Migliuolo,S.,Porcelli,F.,Phys.Fluids **31**,1630 (1988)

Acknowledgements

We would like to thank W. Core, G.Cottrell, O. da Costa, J.Hastie, and R.Stankiewicz for useful discussions.

PLASMA CHARACTERISTICS DURING SOFT DISRUPTIONS

E.Lazzaro, A.Simonetto,A.Tanga*
Istituto di Fisica del Plasma, Associazione EURATOM- ENEA-CNR, via Bassini 15, 20133 Milano, Italy

Introduction

A significant class of disruptive discharges in tokamaks is characterized by an irreversible but rather slow current decay occurring while the electron temperature is still high.For definitiveness we refer to typical JET cases , such as that shown in Figs.1-2 where the observed rate of current decay is of the order of 2-3MA/s and the electron temperature T_e measured by the ECE polychromator may decay as fast as 6keV/s in the center and 1.5 keV/s at the position of the q=2 surface.The influx of impurities is moderate and Z_{eff} ~6. The Ohmic resistance R_{Ohm} calculated with the proper plasma geometry and the ECE profiles is of the order of 1 μΩ plasma during the disruptive decay and these observations cannot be reconciled with a the model of a choking effect of the plasma caused solely by a sudden inflow of impurities which may drive a radiative collapse of the plasma temperature to a few eV on a ms time scale.The discharge evolution is conveniently described by the trajectories on the plane of the parameters l_i (internal inductance) and q(a) (safety factor).Inspection of the path followed (Fig.3) shows that the soft disruption phase often traces backwards the current ramp up phase , where an accelerated peaking up of the current profile may be associated to the effects of observed enhancement of MHD activity [1], as measured by the poloidal and toroidal magnetic pick-up coils (Fig.4).

The observed irreversible process suggests that the effective resistance R_{eff} of the plasma may be due indeed to temperature independent MHD effects .The problem is discussed comparing the difference between the effective and the Ohmic resistances with the expected value of a model based on the coupling of unstable tearing modes with resonant surfaces close together, around the q=2 surface where a saturated background mode is assumed . The time scales of the process observed require that the power input to the plasma be evaluated considering the full coupling with the external active and passive circuit elements since it is incorrect to assume the trapping of the poloidal flux between the plasma and the vacuum vessel , which in JET has a toroidal time constant of 0.03 s.

Evaluation of effective plasma resistance from power input

To analyse the dynamics of a class of soft disruptions evolving on time scales longer than the time constant of the vessel surrounding the plasma , it is necessary to establish the power balance in the form:

$$R_{eff} I_p^2 = -\frac{1}{2}\frac{d}{dt}\left\{[L_{ext} + L_i] I_p^2\right\} - \frac{I_p^2}{2}\frac{d}{dt}[L_{ext} + L_i] + V_l I_p = P_{input}$$

where the loop voltage V_l is due to the mutual coupling with all the external active and passive circuit elements:

$$V_l = -\frac{d\psi}{dt} = -\sum_{k \neq p} \frac{d}{dt}[L_{pk} I_k]$$

In particular in the case of JET the main elements of the poloidal field system coupled with the plasma include the iron cored transformer coil (labeled k=1), the shaping coils (k=s) and the vacuum vessel (k=v). This leads to the simplified model :

$$R_{eff}I_p + \frac{d}{dt}[L_pI_p] = -\frac{d}{dt}\{L_{p1}I_1 + L_{ps}I_s + L_{pv}I_v\}$$

$$R_vI_v + L_v\frac{dI_v}{dt} = -\frac{d}{dt}\{L_{vp}I_p + L_{vs}I_s + L_{v1}I_1\}$$

The plasma radial displacements and changes in the current profile causing variations of both the internal inductance and the external and coupling inductances are taken into account.A finite fraction of the power sloshing between the transformer inductor and the plasma during the disruption is dissipated by the vessel, and it has been calculated using JET technical data.A numerical program of data interpretation embodying this model has been written and used to calculate $R_{eff} = P_{input}/I_p^2$ and R_{Ohm}.with neoclassical corrections,using the instantaneously measured T_e and Z_{eff} , for scores of JET discharges.For shot #20757 the maximum ohmic dissipation of ~8 MW and the maximum power input of ~18 MW occur at t=52 s ewhen there is a the peak of the MHD activity over all the spectrum of poloidal harmonics m.At this time R_{eff} ~5μΩ and R_{Ohm} ~2μΩ, as read from the time evolution in Fig. 5. It is illuminating to note that between t=51.75 anf t =52.05 the ECE T_e profile which initially was smooth, appears strongly flattened (Fig.6)in the radial interval where the self consistently calculated q(ψ) takes on the rational values m/n=3/2,2/1,5/3,7/4, 9/5...

These observations support the conjecture that the relevant mechanism of accelerated, irreversible decay of the plasma current is the onset of an effective resistivity related to the coupling of resistive modes when they overlap even on a limited radial interval and saturate to relatively small island sizes..

Effective resistivity due to tearing mode coupling

We adopt the usual , single fluid,reduced MHD description in cylindrical geometry with constant mass density ρ and a magnetic field and a velocity field given by:

$$B = \nabla \times (\psi \underline{e}_z) + B_0 e_z = \nabla\psi \times e_z + B_0 e_z$$

$$\underline{v} = \nabla \times (u\underline{e}_z) = \nabla u \times e_z;\ w_z = e_z \cdot \nabla \times \underline{v} = -\nabla^2 u$$

The scalar stream functions w_z (i.e. u) and ψ evolve according to the nonlinear ,coupled equations:

$$\frac{\partial\psi}{\partial t} + \underline{v}_\perp \cdot \nabla\psi = -\eta J_z + E^w$$

$$\frac{\partial w_z}{\partial t} + \underline{v}_\perp \cdot \nabla w_z = \frac{1}{\rho}[B \cdot \nabla \underline{J} - \underline{J} \cdot \nabla \underline{B}]$$

We consider a multiple time scale approach with $t_0=t, t_1=\varepsilon t, t_2=\varepsilon^2 t, \varepsilon \sim a/R << 1$ and decompose ψ in a background with a saturated helical deformation with $\underline{k}_0=\{0.m,/r,n/R\}$, (centered around m=2,n=1) evolving on the slowest time scale t_2, a driven mode (e.g. m=3,n=2) and a test mode (e.g. m=5,n=3) evolving on the fast time scale t_0

$$\psi = \psi_{eq}(r,t_2) + \sum_{k_0}\psi_{k_0}(r,t_2)\exp[ik_0 \cdot \chi] + \varepsilon\sum_{k_1}\psi_{k_1}(r,t_1)\exp[ik_1 \cdot \chi + \gamma t_0]$$
$$+ \varepsilon\psi_k(r,t_1)\exp[ik \cdot \chi + \gamma t_0] + c.c.$$

where $\underline{k}_1=\underline{k}-\underline{k}_0$.The function w_z is assumed to evolve on the fast timescale and is decomposed in a similar way but with $w_{eq}=0$ and $w_{k0}=O(\varepsilon)$ .By separation order by order in ε and grouping terms with the same phase a set of coupled tearing modes equations is obtained.The coupling terms depend on the radial gradients of the current, and the vorticity in the resonant layers for each mode,which are assumed to scale as:

$$\frac{\partial J_k}{\partial r}:\frac{\partial J_{k_1}}{\partial r}:\frac{\partial J_{k_0}}{\partial r}:\frac{\partial J_{eq}}{\partial r}=1:1:\varepsilon:\varepsilon^2\ ;\ \frac{\partial^2 u_k}{\partial r^2}:\frac{\partial^2 u_{k_1}}{\partial r^2}:k^2u_k:k_1^2u_{k_1}=1:1:\varepsilon:\varepsilon$$

On the fast time scale the driven and test mode are linearly unstable and their growth rate is increased by the coupling with the static background,[2,3] according to the tearing mode equations of the type:

$$\gamma\psi_k+ik(r-r_s)\frac{nq'}{mr_s}B_{\theta 0}(r_s)u_k=[\frac{\sum_{k_0}|k_0\psi_{k_0}|^2}{\gamma\rho\mu_0}+\frac{\eta}{\mu_0}]\Delta\psi_k$$

$$\gamma\frac{\partial}{r\partial r}\left(\frac{r\partial u_k}{\partial r}\right)\approx\frac{1}{\rho}[i\sum_{k_0}k_0\psi_{k_0}\frac{\partial J_{k_1}}{\partial r}]$$

and the growth rate turns out to be:

$$\gamma=(0.55)^{5/8}[\Delta']^{1/2}a(\frac{nq'}{r_s})^{1/4}\left(\frac{\sum_{k_0}|k_0\psi_{k_0}|^2}{B_\phi^2}\right)^{3/8}\tau_A^{-1}$$

The test mode grows exponentially on the fast time scale but it saturates to an island size smaller than the background mode , allowing the equilibrium and helical background fluxes to decay on the slowest time scale t_2 driven by the convective terms involving the coupling of the k ,k_0 and k_1 modes:

$$\frac{\partial\psi_{eq}}{\partial t}\approx\varepsilon^2\frac{\sum_{k_0}|k_0\psi_{k_0}|^2}{\gamma\rho\mu_0}\nabla^2\psi_{eq}-\varepsilon^2\frac{2\gamma\sum_{k_0}k_0^2Re(\psi_{k_0}\psi_{k_1}\psi_k^*)/B_o^2}{[\gamma\tau_A^2/\tau_R+\sum_{k_0}|k_0\psi_{k_0}|^2/B_o^2]}$$

The second term vanishes by phase averaging and therefore the magnetic energy diffuses at an effective rate essentially independent of the ohmic resistivity, and dictated by the amplitude of the background modes (around m=2,n=1) and the growth rate of the test and driven modes, leading to an "effective resistivity" due to MHD activity

$$\eta_{eff}=\eta_{Sp}\frac{\varepsilon^2(\tau_R/\tau_A)}{(0.55)^{5/8}[\Delta']^{1/2}a(\frac{nq'}{r_s})^{1/4}}\left(\frac{\sum_{k_0}|k_0\psi_{k_0}|^2}{B_\phi^2}\right)^{5/8}$$

For the JET cases considered, the expected enhancement factor, related to the measured MHD activity amplitude, is in the range 2 to 10,in agreement with the observed increase of the resistance.

E.L.- Work done under Euratom Mobility Contract No 131-83-7 FUSC
*A.T. -JET Joint Undertaking,present address:JAERI Naka Research Instit.Nakamachi,Nakagun,Ibaraki Ken 31101, Japan

References

[1]D.Campbell, E. Lazzaro, M. Nave et al.,Nucl.Fus. **28** (1988) 981.
[2[G.Murtaza,P.H.Shukla,M.Y.Yu .Phys.Fluids **28** ,427(1985)
[3]P.H.Diamond,R.D.Hazeltine,Z.G.An,B.Carreras,H.R.Hicks, Phys.Fluids **27** 1449 (1984)

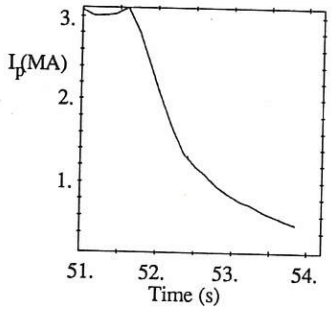

Fig.1- Plasma current I_p vs.time during the slow disruption phase of JET shot N_0 20757

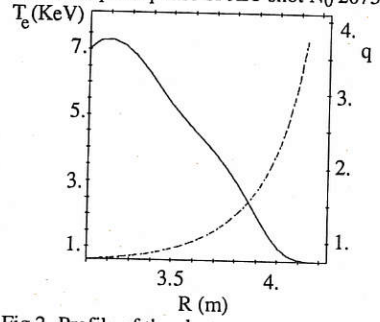

Fig.2 -Profile of the electron temperature $T_e(R)$ at t = 51.75 (full line):$T_e(R_0)$ ~7 keV. Safety factor q(R) (dashed line) at the same time.

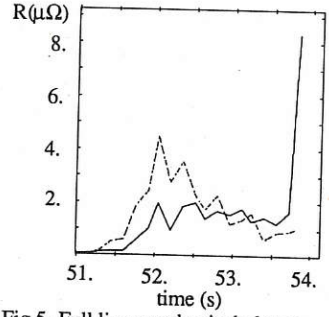

Fig.5- Full line:neoclassical plasma resistance R_{Ohm} calculated from $T_e(R)$,vs time.Dashed line : R_{eff} calculated from the detailed power balance.

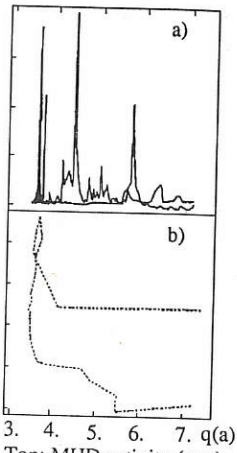

Fig.3 -Top: MHD activity (a.u.) vs q(a) during the evolution of the discharge (20757). Bottom:Internal inductance l_i vs q(a).

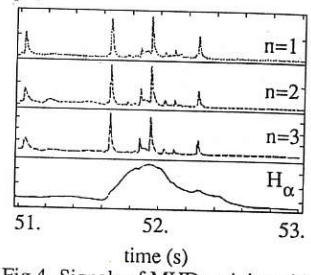

Fig.4 -Signals of MHD activity with mode number n=1,2,3 and time trace of Z_{eff}

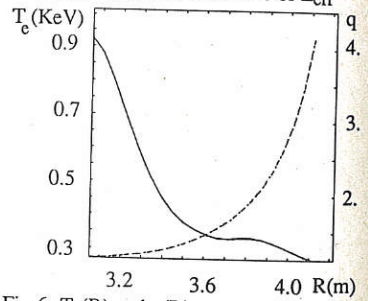

Fig.6 -$T_e(R)$ and q(R) at t = 52.05 at the peak of MHD ,when R_{eff} ~2.5R_{Ohm}

Disruption Behavior of Plasma and Vacuum Vessel in JT-60U

Y. Neyatani, K. Ushigusa, M. Matsukawa and H. Ninomiya
Japan Atomic Energy Research Institute, Naka Fusion Research Establishment
Naka-machi, Naka-gun, Ibaraki-ken, 311-01, Japan

INTRODUCTION

Understanding of the plasma and vacuum vessel behavior during disruptions is very important to estimate the validity of the design and design of a next generation tokamak. The JT-60 Upgrade (JT-60U) has a toroidally continued vacuum vessel with the toroidal resistivity of 160 μΩ. As the high-beta with high current plasma is not discharged so far, a toroidal current has a major part of the eddy current during disruptions. The toroidal current was measured directly and the behaviors of the plasma and the eddy current were studied in the current quench phase. The vessel vibration caused by the toroidal current was also investigated. The measurement of a poloidal current due to vertical displacement events is now under preparation.

DESCRIPTION OF ANALYSIS TOOLS

(1) **Diagnostics** In JT-60U, a direct measurement of the toroidal eddy current on the vacuum vessel was performed by Rogowski coils for the first time /1/. Two Rogowski coils were installed inside and outside the vacuum vessel and the eddy currents were obtained by subtracting these signals. The effects of the error fields by the feeders of poloidal field coils were numerically cancelled using the data of the coil excitation tests. The drift of the integration circuits was reduced by an auto adjustment for each shots. After that, the accuracy of the eddy current reached up to 1%. The plasma motion during disruptions was monitored by a high speed visible TV with a frame rate of 1000 frames/sec. A gate shutter with typical gate time of 50 μs was utilized to procure static pictures of the plasma during disruptions.

The laser displacement sensors were utilized for the vibration measurement of the vacuum vessel. The head of a port was chosen for this measurement (see Fig.4) because the vessel displacement cannot be measured directly owing to the thermal insulator. These sensors have a sensitivity of 0.15mm/4Tesla to the poloidal magnetic field. However, even in the 6 MA discharges, the poloidal magnetic field is within 1 Tesla at the locations of the sensors, so, the effect of the magnetic field is within the error of 50 μm. The frequency response of these sensors are 3 kHz.

(2) **Magnetic Fitting Code** The magnetic fitting code was developed to evaluate the axisymmetric eddy current, electromagnetic load in the vacuum vessel and the plasma motion during disruptions. The original static FBI (Fast Boundary Identification) code /2/, which determined the plasma boundary by the method similar to the filament current method in ISX-B /3/, was modified to include the transient eddy current on the vacuum vessel. Figure 1

shows the location of the magnetic probes and flux loops in JT-60U. Seventeen probes for the tangential magnetic field B_ω, sixteen probes for the normal magnetic field B_ρ and fifteen flux loops are installed inside the vacuum vessel. The plasma current is treated as a sum of four filament currents I_{pFk} (k=1 ~ 4) in this code. Using some unknown coefficients (I_{ED0}, A_m, B_m ; m=1 ~ 5), the eddy current in the vacuum vessel can be expressed with

$$I_{ED}(\theta_i)=I_{ED0}+\sum_{m=1}^{M}\{A_m\cos(m\theta_i)+B_m\sin(m\theta_i)\}$$

where i is the number of i-th filament current at the poloidal angle θi in the vacuum vessel (i=1~100). In order to determine unknown currents and coefficients (I_{pFk}, I_{ED0}, A_m, B_m), the conventional least squares method is used so as to keep the total filament currents inside the plasma outermost surface equal to the plasma current measured by the Rogowski coil.

The error of this code could be estimated for comparing the total fitted eddy current with the measured one by Rogowski coils (Fig.2). In a typical locked mode disruption, (closed circles), the total eddy current obtained from the code agrees well with measured one within the error of 100 KA. In the case of disruption by a vertical instability (open circles), the difference increases with the eddy current over 0.2 MA. One of the candidates of this displacement may be halo currents in the scrape-off layer, because the asymmetric toroidal component from the halo currents cannot be expressed by the Fourier components used in the fitting code. The plasma boundary obtained by the fitting code is consistent with the observation of the high speed visible TV within an accuracy of 10 cm.

PLASMA AND EDDY CURRENT BEHAVIORS

The current decay starts after 5 ~20 ms of the thermal quench. In this current quench of JT-60U, the fastest current decay is $Ip/(dIp/dt)_{MAX}$ ~ 5 ms which is almost same with that in JT-60 /4/ and JET /5/. The toroidal eddy currents are generated up to 30-50% of the plasma current just prior to plasma terminations. The scatter of these percentage is due to the difference of the current decay rate and the mutual inductance between the plasma and the vacuum vessel caused by the plasma position and current distributions. With a typical plasma location and a shape ($-0.2 < Z_j < 0.2$ m, $0.72 < a_p < 1.04$ m , Z_j : vertical plasma position, a_p : plasma minor radius), the maximum toroidal eddy current increases with the plasma current (see Fig.3). It supposes the electromagnetic force from the toroidal eddy current is proportional to $I_{Tor} \times B_{Pol} \sim I_p^2$.

Although the plasma cross section is elongated-shaped single divertor, the observation of the visible TV and the result of the magnetic fitting code show that most of the plasmas move to the inward direction during disruptions. Figure 4 shows the time evolution of the typical disruption caused by a locked mode MHD activities. The plasma starts to move inward with the decay of the plasma current. When the current decays rapidly, the magnetic field by the vertical field coils becomes larger than that by the other PF coils. Then the plasma

is pushed inward. The total radial electromagnetic force of the vacuum vessel was 750 tons with the inward motion. The downward motion was observed only when a plasma disrupted by a vertical instability. In this case, the plasma moved downward with the constant plasma current. The inward force by the vertical field coil was not dominant until the plasma current started to decay.

VIBRATION OF THE VACUUM VESSEL

The maximum displacement was measured in the poloidally tangential direction and the vibration with the same frequency was observed at the normal and toroidal directions. In a 4 MA disruption with an inward plasma motion, the vacuum vessel vibrated with the maximum amplitude of 0.55 mm and the frequency of 82 Hz as shown in Fig.5. Where, Δ shows the distance between the head of the port and the laser displacement sensor. The offset in this figure means a displacement of the spacer of TF coils, which is utilized as a base of the sensors. It was found in the PF and TF coils excitation tests without a plasma. The measured amplitude was 40% lower than the design value of 4 MA disruption with a downward plasma motion. It is because that the rigidity near the port is 20 % higher than the design value owing to the closed welding pitch of square tubes which are utilized to space the inner and outer skin of the vessel wall, and the maximum stress is evaluated to be 30 % lower for an inward motion than for a downward motion in accordance with the design calculations. This consistency is within a error of the displacement measurement of ± 50 μm which is equivalent to 10 % of the measured value.

The maximum amplitude of the vessel vibration increases with I_p^2 as shown in Fig.6. The parameters of plasma just prior to the current quench are $-0.2 < Zj < 0.2$ m and $0.72 < a_p < 1.04$ m. This dependence is consistent with electromagnetic force from the toroidal eddy current. From this scaling, an amplitude at 6 MA disruption is expected to be 1.3 mm that is within the design limit of 2 mm. The vessel force from the poloidal eddy current is supposed not so large in JT-60U, because the discharge with vertical displacement events have not been tried so far, excepting with a low plasma current within 1.2 MA.

ACKNOWLEDMENT

The authors are very grateful to Dr. H. Horiike for your advice. They would like to thank the members of the JT-60 Facility Division II for their help in the vibration measurement of the vacuum vessel.

/1/ Y. Neyatani et al. : 14th Symposium on Fusion Engineering 1991, to be published.
/2/ S. Tsuji et al. : JAERI Report, JAERI-M 86-006 (1986).
/3/ D. W. Swain et al.: Nucl. Fusion **22** (1982) p.1015.
/4/ JT-60 Team : JAERI Report, JAERI-M 89-033 (1989) p.33-37.
/5/ J.A. Wesson et al.: Nucl. Fusion **29** No.4 (1989) p.641-666.

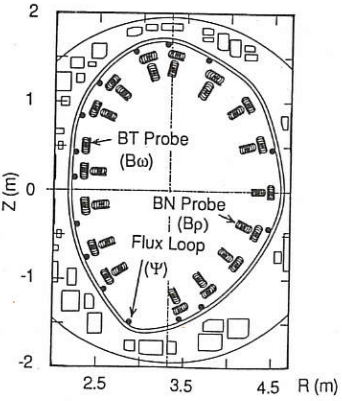

Fig.1 Locations of the magnetic probes and flux loops.

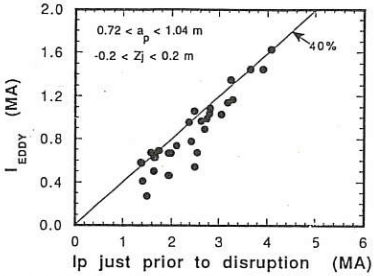

Fig.3 Toroidal eddy current as a function of the plasma current just prior to a disruption.

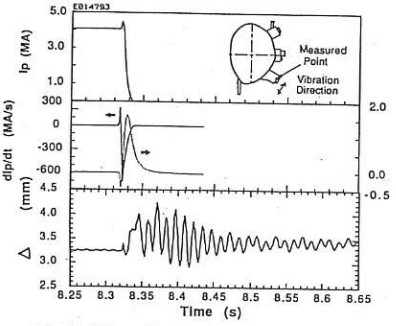

Fig.5 The vibration of the vacuum vessel (Δ) at a disruption.

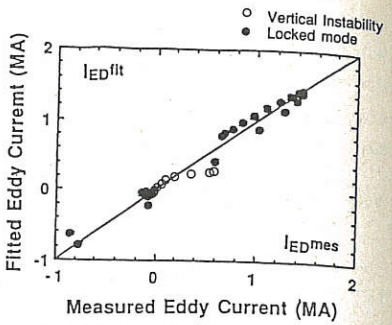

Fig.2 Fitted total eddy current against measured eddy current.

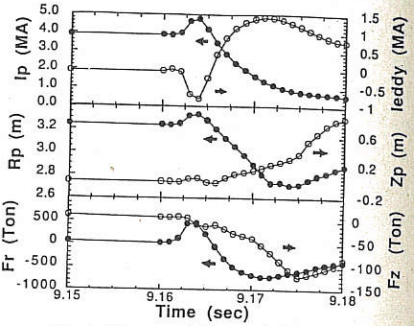

Fig.4 Time evolution of the current quench during a disruption by locked mode.

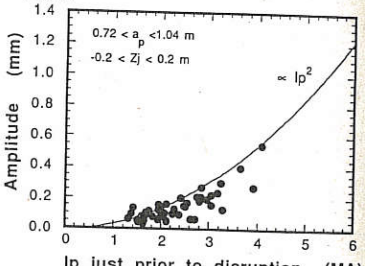

Fig.6 Maximum amplitude of the vibration of the vacuum vessel as a function of the plasma current just prior to disruptions. Plasma parameters just prior to current quench are $-0.2 < Zj < 0.2$ m and $0.72 < a_p < 1.04$ m.

Discharge scenarios for the first operational phase of ASDEX Upgrade

U. Seidel, O. Gruber, P. McCarthy, S.C. Cha (†), W. Köppendörfer, A. Krause, V. Mertens, W. Woyke, ASDEX Upgrade Team
Max-Planck-Institut für Plasmaphysik, Euratom Association
D-8046 Garching, Germany

I. Introduction

The first phase of plasma operation in ASDEX Upgrade, started in April 91 and concluded in August 91 with the production of a 400 kA plasma in the standard single-null configuration, was devoted to successful tests of predesigned discharge scenarios /1/ for the different phases of the experiment.

The main objective of designing a "discharge scenario" for a tokomak is to determine the control input - both, analog and discrete - to the power supply facilities, which cause them to apply a voltage program to the PF coils, establishing the presumably required poloidal field conditions for the desired discharge. In the case of ASDEX Upgrade this design procedure is greatly complicated by power limitations, because the reactor-relevant positioning of the main poloidal field coils outside the toroidal field coils rather far away from the plasma requires relatively high power and energy. This appears especially in the highly dynamic phase of plasma build-up. Further particular properties of the ASDEX Upgrade device, such as the unstable vertical position of the final divertor plasma with an elongation of about 1.6 and the induced currents in the all-metal vacuum vessel, impose further conditions, which the control program design has to deal with.

The quantitative elaboration of the control program was based on and verified by applying different numerical tools, including IPP's electromagnetic diffusion code FEDIFF /2/, the Princeton Tokomak Simulation Code (TSC) /3/ and a special plasma preprogramming code (PCC) which allows utilization of a data-base with approximately 7,000 precalculated MHD equilibria for the purpose of discharge planning.

II. Discharge Scenario

Figure 1 shows for an actual ASDEX Upgrade discharge the behaviour of those electromagnetic variables by which the plasma equilibrium can be instantaneously controlled and, for some selected and characteristic times, the contour plots of the resulting plasma cross-section. Also indicated are different discharge phases, each distinguished by particular technical and physical conditions, the desired final equilibrium state and the strategy applied to achieve it.

I.1. Plasma Initiating Phase

This first phase of the discharge starts with the application of the breakdown voltage (U_{loop}) to the $0.5...1.0 \cdot 10^{-4}$ mTorr He atmosphere in the vessel, induced by the interruption of the OH-coil current, and ends when the plasma current - raising rapidly under the still applied breakdown voltage - reaches about 100kA. Due to the high power involved, the voltage supply program in this phase, once

(†) deceased

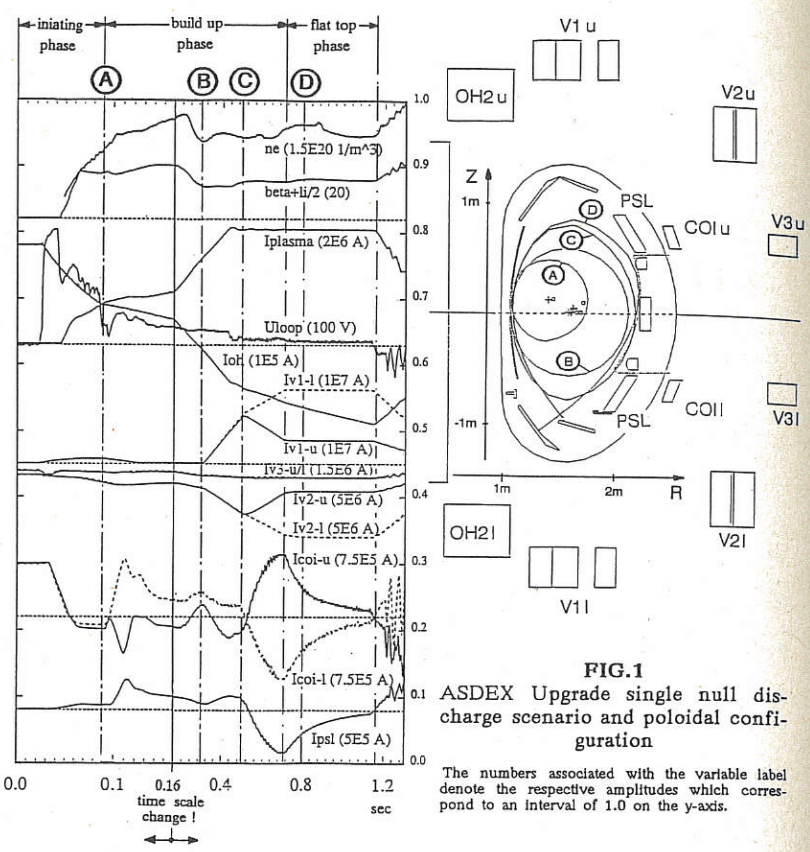

FIG.1
ASDEX Upgrade single null discharge scenario and poloidal configuration

The numbers associated with the variable label denote the respective amplitudes which correspond to an interval of 1.0 on the y-axis.

started, cannot be corrected by online feedback and must work reliably also under not completely reproducible conditions. The power available in the main PF-coil circuits is even not sufficient to exert the actually desired complete control over all currents. Especially the fast build-up of the required equilibrium field during the first rise of the plasma current can be accomplished only by the use of the inner control coil circuits (COI), in the first place installed for the fast position feedback control of the plasma. The decay of the initial currents in these coils is chosen such as to reach approximately zero and leave the circuit ready for feedback actions in the next discharge phase, when the plasma produced is balanced by the correspondingly preset currents in the V2 and V3 coils alone. Due to the rapid current changes, especially in the OH and COI coils, currents up to 100 kA are induced in the all-metal vessel, which, on the one hand, delay the build-up of the ignition voltage and, on the other hand, produce, together with the preloaded or induced currents in the PF coils, a mainly vertical

poloidal field at the position in the vessel where the discharge is expected to initiate. However, the amplitude of the initial current in the COI coil and the starting time of its decay can be chosen, such that the total vertical field goes through zero when the breakdown voltage becomes maximal which satisfies the necessary condition for reliable initialization of the discharge. Apprehensions with respect to the destabilizing shape of the equilibrium field in this early plasma phase, mainly caused by the induced currents in the V1 coils, turned out to be unfounded. Though in this phase too far away from the passive stabilization structure, the plasma position will be sufficiently stabilized by the action of the vessel in conjunction with the stabilizing effect of the large positive dI_p/dt in the plasma.

The scheme outlined works well up to an ignition voltage of about 25 V. Beyond this value the induced voltages in the PF-coils exceed the capability of the supplies to compensate them and the first plasma current rise may be too fast, to can be followed by the build-up of the equilibrium field. As a compromise between this requirement of a moderate ignition voltage, on the one hand and reliable ionization during the plasma initiation, on the other, a initial gas pressure of about $1.0 \cdot 10^{-4}$ mT, prefilled by a gas pulse of 60 msec duration immediatly before breakdown, turned out to be favourable. Under this condition a reliable ignition at a voltage of about 15 V could be reached an approx. 70 % of the gas shows up in the final plasma. To ensure also shot-to-shot reproducibility with respect to the gas balance and its consequence for the discharge, helium was used as filling gas in this first operational phase instead of hydrogen.

II.2. Plasma Build-up and Flat-top Phase

After the OH-coil voltage is switched down to the operation voltage of the static OH-coil power supply, the rate of plasma current rise reduces substanttially. The power required to set up the necessary equilibrium field reduces in correspondence, now allowing the application of feedback control of the plasma current, and the radial and - indispensable for the elongated plasma - vertical plasma position. As the COI-coil currents in the Fig.1 show, the feedback system, once actuated, starts immediately to correct the vertical displacement remaining after the uncontrolled initial phase.

Subsequently, to ensure sufficiently close magnetic coupling of the plasma column to the stabilizing passive conductor loops during the phase of increasing plasma elongation, the major radius of the discharge is expanded, while maintaining still its circular cross-section and the contact the inner-wall limiter. The elongation is then accomplished by exitation of positive currents in the so-called "divertor coils" (V1) simultaneously with the further rise of the plasma current to its flat-top amplitude of 350 kA. For safety reasons, this value must not be exceeded in this first operation phase. Possible loss of control over the unstable vertical plasma position might have led to uncontrollable self- induction of stabilizing "halo" currents and consequently to untolerable forces in some internal vessel components.

The plasma build-up finally concludes with the transition of the limiter plasma to the desired lower single-null divertor configuration, which is basically performed by the unsymmetrically driven V1 currents and, to maintain the global equilibrium, by a corresponding change of the V2 currents.

The termination of the discharge is presently done by linearly decreasing of I_p and all PF currents on a slow rate leading again to the inner limiter equilibrium

sequence C,B,A of Fig.1. This method will finally be replaced by a shut- down program which reverses the build-up procedure.

III. Plasma Control Code (PCC)

As the COI currents in Fig.1 indicate considerable feedback actions take place during the build-up phase which illustrates how desirable it is to have obtained beforehand a well-adapted control program for the poloidal field. Additionally, since the feedback controlled objects are restricted for the time being to just a few global equilibrium parameters, any detailed adjustment of the plasma shape must be accomplished anyway by preprogram control alone.

To satisfy this need for a precalculated command input to the power supplies, a computer program (PCC) was developed which allows the determination of such a control input in a systematic way, taking into account the imposed technical constraints.

The code is based on a collection of about 7,000 precalculated MHD equilibria for ASDEX Upgrade, each characterized by a "driving vector" with all currents influencing the equilibrium and β_p and l_i as elements, on the one hand, and by a set of parameters, describing mainly the geometry of the plasma, on the other. By a regression analysis of this database quadratic equations for these geometrical equilibrium parameters in terms of the elements of the "driving vector" are derived and utilized by the PCC algorithm. Based on this, and an arbitrary set of given desired trajectories for arbitrarily chosen equilibrium parameters and a prediction for $\beta_p(t)$ and $l_i(t)$, PCC calculates the command inputs which should force the real discharge to follow as closely as possiblethe desired trajectory. Closeness is measured by a performance index, defined as the time integral over the square of the differences between actual and the desired equilibrium parameters, multiplied by specific weighting factors for each of the parameters considered. Their choice allows the user to adjust the precision with which the desired equilibrium parameter will be met by the actual one and to balance possibly contradictory aims. An additional penalty term in the performance index measures the requirements of voltages and currents and ensures economical use of the available power and energy. The electromagnetic properties of the PF system enter the PCC procedure of minimizing the performance index as subsidiary condition to take into account the ability of the resulting command input program to anticipate the effects of mutual induction between the different circuits and to take appropriate actions. The imposed constraints with respect to the maximal available voltages of the power supplies and the maximal admissible currents in the coils can also be added to the conditions PCC will take into account. Since vessel currents are not included in the equilibrium database, PCC can be applied only to discharge phases with negligible vessel currents. For phases, satisfying this condition, results in accordance with TSC calculations were obtained by PCC.

/1/ O.Gruber and ASDEX Upgrade Project Group, "ASDEX Upgrade, Start-up and Operation" from "Tokamak Start-up", Ettore Majorana Internat. Science Series, Physical Sciences: Volume 26; 131-141; Plenum Press 1986

/2/ H.Preis "Die Finite-Element-Netzwerkmethode für dreidimensionale Wirbelstromberechnungen in Experimenten zur kontrollierten Kernfusion"; Archiv für Elektrotechnik 65 (1983); 233-239

/3/ S.C.Jardin, N.Pomphrey, J.DeLucia; J.Comput. Phys. 66 (1986) 481 pp

Performance of the Equilibrium Control System for ASDEX Upgrade

Woyke, W.; Gernhardt, J.; Gruber, O.; Jülich, A.; Lackner, K.; Mc. Carthy, P.J.; Seidel, U.; ASDEX-Upgrade Team.
Max-Planck-Institut für Plasmaphysik, Euratom Association
D 8046 Garching, Germany

1. Introduction

ASDEX Upgrade utilizes a feedback control system for the plasma current (I_p), position and shape, which is novel in its algorithm for the determination of the plasma equilibrium, its fully digital implementation, and its combined use of internal (inside the TF-coils for position control) and external (outside the TF-coils for shape control) poloidal field coils. The large distance V-coils - plasma surface and the complex, asymmetric plasma shape preclude a control algorithm as used so far and require a detailed shape and position identification as input for the feedback system. A passive stabilizing conductor PSL with a relatively long time constant (L/R-time 0.57s) is used to slow down the unstable Z-motion of vertical elongated plasmas. It allows an elaborate digital control system, whose intervention time has been fixed to 1.5ms.

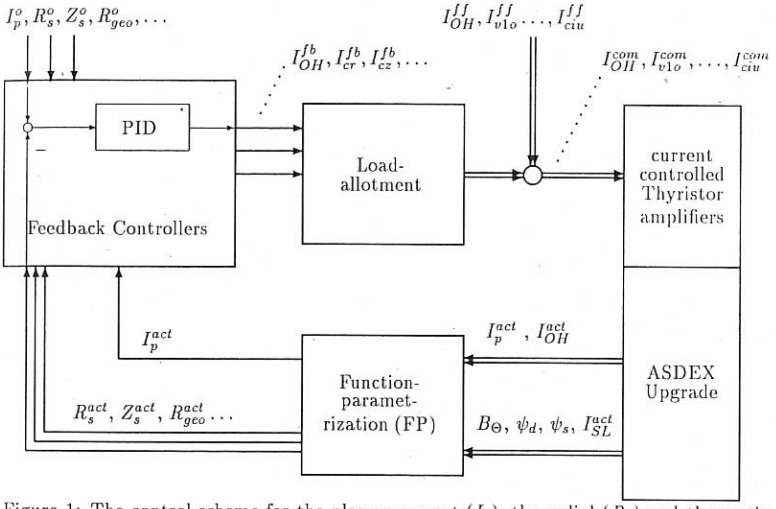

Figure 1: The control scheme for the plasma current (I_p), the radial (R_s) and the vertical (Z_s) plasma position current centre position

2. The feedback control system

The feedback control scheme is shown in Fig.1. The plasma equilibrium determination proceeds via a function parametrization technique [2] using 34 magnetic measurements as input (poloidal field B_θ, poloidal flux differences ψ_d, flux of saddle loops ψ_s and the current of the PSL I_{SL}^{act}). It calculates the actual values (^{act}) of 6 equilibrium parameters ($R_{geo} \ldots$)

and of the current centre position (R_s, Z_s). In the first stage three of nine single-input, single-output PID feedback controllers (with an anti-windup algorithm) compute, from the difference between the intended values (°) of I_p, R_s and Z_s and the corresponding actual values, the corrections (^{fb}) for the OH transformer current (I_{OH}) and the radial (I_{cr}) respectively vertical (I_{cz}) control currents. By means of the load allotment matrix

$$\begin{pmatrix} I^{com}_{cio} \\ I^{com}_{ciu} \end{pmatrix} = \begin{pmatrix} 0,5 & 0,5 \\ 0,5 & -0,5 \end{pmatrix} \begin{pmatrix} I^{fb}_{cr} \\ I^{fb}_{cz} \end{pmatrix} + \begin{pmatrix} I^{ff}_{cio} \\ I^{ff}_{ciu} \end{pmatrix}$$

these control currents are mapped to the corrections for the inner control coils I_{cio} and I_{ciu}. In adhanced operation with load compensation of the internal by the external coils and with shape control this mapping will be more complex. The sum of feedback (^{fb}) and feedforward (^{ff}) signals result in the commands (^{com}) for the thyristor amplifiers of the poloidal field coils. We tuned the current controllers of the thyristor amplifiers to high proportional feedback gains to have good agreement of the commands with the actual values of the PF coil currents ($I_{OH}, I_{v1o}, \ldots, I_{ciu}$). The result were sufficient to suspend the integral control gains. The algorithm of function parametrization, of feedback control and of load allotment are implemented in a network of transputers, which work in parallel [1].

3. Design and test of the feedback control algorithms

For the analysis and design of the feedback control system a nonlinear lumped-parameter model was derived. Though this multi-input/multi-output model is of high order, single-input/ single-output channels can be approximated with high accuracy by low-order models using methods of optimal reduction in the frequency domain. The design of the feedback controllers is based on these reduced order models neglecting the coupling between various channels. It leads to rules for the tuning of the feedback gains in dependence of the most important time constants. Though only conventional PID-control is applied, the vertical position feedback control is approximately as good as time-optimal control would be [5]. The comparison to the design procedure of optimal output feedback control, which utilizes the full lumped parameter model, results in nearly the same gains for the PID-controllers.

In a next step the envisaged control algorithm was implemented in the Tokamak Simulation Code TSC [4] and fed with the FP parameters to simulate the "closed loop" operation. Intensive tests in all phases of a plasma shot showed that the gains of the feedback controllers had to be adapted slightly owing to some differences of time constants and to the voltage limitations of the thyristor amplifiers for the PF-coils. The resulting set of gains then could be used for all discharge simulations and worked properly; especially parameter jumps occuring at limiter/divertor transitions did not influence the feedback control. It turned out that the feedback controller could cope well with the necessary control requirements owing to the various points of operation (start-up, heating, flat-top and shut-down).

4. The set into operation

The first plasma discharges of ASDEX Upgrade up to a plasma current of 200 kA were started in a preprogrammed mode, where the feedback control circuits were disabled, thus setting the feedback gains to zero. So the troubleshooting concerning the software and hardware problems could be done without the additional complication due to the feedback control. In a second stage the feedback control of the plasma current was used first, followed by the plasma position control of circular inner limiter-bounded plasmas. Nearly all position

control was done using the R_s and Z_s coordinates of the current centre, defined as

$$R_s^2 = \frac{1}{I_p A_p} \int R^2 j_t dA \qquad Z_s = \frac{1}{I_p A_p} \int Z j_t dA$$

where the integration of the toroidal current density j_t is over the plasma cross-section A_p. This particular definition has the advantage that R_s^2 and Z_s are exact integrals of the poloidal magnetic field B_θ on a closed poloidal contour enclosing the plasma. In a few discharges the geometrical centre $R_{geo} = \frac{1}{A_p} \int R dA, Z_{geo} = \frac{1}{A_p} \int Z dA$, was controlled instead of R_s, Z_s. A few feedback gains had to be adapted slightly during this test phase.

In a third stage of operation vertically unstable elongated plasmas either inner limiter-bounded or in single-null divertor configuration were studied. As an example, the results for a lower SN discharge (#1288) are described in Fig. 2. At $t = 94$ms the feedback control is switched on at a plasma current of about 100 kA. Up to the current flat-top phase there is a serious difference between the intended value I_p° and the actual I_p^{act} values of the plasma current (Fig. 2a). Therefore, the plasma current controller adds an equivalent feedback value I_{OH}^{fb} to the preprogrammed value I_{OH}^{ff} to get the command value I_{OH}^{com} to be compared with I_{OH}^{act}. As a consequence, the current-controlled thyristor amplifiers apply the maximum negative voltage of $\approx -3V$ per turn to the OH coil, resulting in the highest possible ramp rate of $I_p \approx 0.7MA/s$. Due to the anti-windup fo the PID-controller the overshoot at the beginning of the flat-top phase is very small.

The radial position control (Fig. 2c) catches the plasma in about 50 ms and leads it to a major radius of 1.65 m. The control current I_{cr}^{act} necessary for this action is rather small (Fig. 2e), since the preprogrammed PF currents (^{ff}) are calculated by the PCC code quite well [3]. The vertical position control starts at a shift of 0.12 m and brings the plasma centre to the intended midplane position in a few tens of ms. During the change to an elongated divertor configuration ($b/a \approx 1.6$) the plasma is shifted to $Z_s^\circ = 0.14$m by means of the control coils (I_{cz}) and the vertical feedback controller. Control currents I_{cz}^{act} up to 20 kA (Fig. 2e) have to be used for this, as the current induced in the PSL works against this shift. An overshoot of 2 cm decreases to zero within 200 ms.

5. Conclusion

At the current stage of operation the feedback control of the plasma current and of the plasma position works reliable and seems to be well optimized. Further steps of operation will require the feedback control of the current-load from the inner to the outer PF-coils and additional shape control will be applied utilizing the outer PF-coils. Thus the remaining six feedback controllers have to be put into operation.

References

[1] Richter, H.; Raupp, G.: IEEE 7th conf. Real Time '91, pp. 308
[2] Mc. Carthy, P.J. et al.: This volume
[3] Seidel, U. et al.: This volume
[4] Jardin,S.C.: Multiple Time Scales, Computational Techniques, Vol. 3, pp.185
[5] Woyke, W. et al.: 15th SOFT, Utrecht(1988), pp. 1648

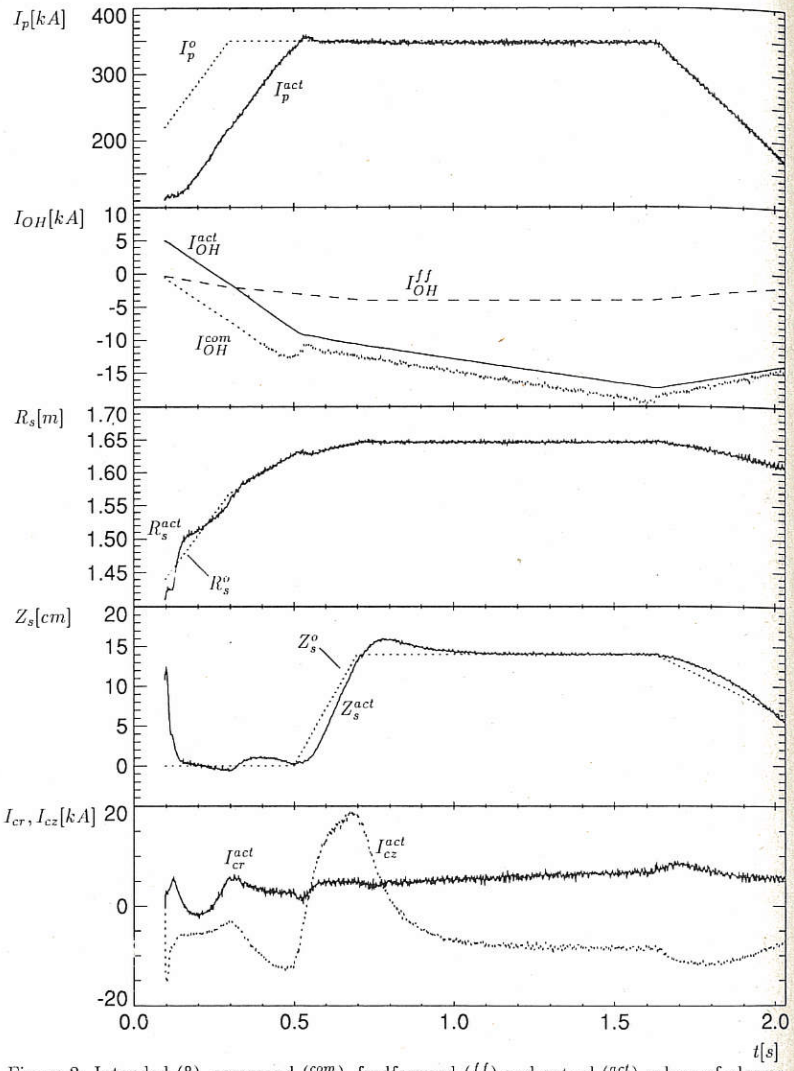

Figure 2: Intended ($^{\circ}$), command (^{com}), feedforward (^{ff}) and actual (^{act}) values of plasma current (a), OH current (b), current centre R_s (c) and Z_s (d), and radial and vertical position control currents I_{cr}, I_{cz}(e) of bottom SN discharge #1288.

MHD Equilibrium Identification on ASDEX-Upgrade

P.J. Mc Carthy[1], W. Schneider, K. Lackner, H.P. Zehrfeld,
K. Büchl, J. Gernhardt, O. Gruber, A. Kallenbach, G. Lieder, R. Wunderlich,
and ASDEX-Upgrade team.

Max-Planck-Institut für Plasmaphysik , EURATOM Association,
D-8046 Garching bei München, Germany

[1]On attachment from University College, Cork, Ireland

A central activity accompanying the ASDEX-Upgrade experiment is the analysis of MHD equilibria. There are two different numerical methods available, both using magnetic measurements which reflect equilibrium states of the plasma. The first method proceeds via a function parameterization (FP) technique, which uses in-vessel magnetic measurements to calculate up to 66 equilibrium parameters. The second method applies an interpretative equilibrium code (DIVA) for a best fit to a different set of magnetic measurements. Cross-checks with the measured particle influxes from the inner heat shield and the divertor region and with visible camera images of the scrape-off layer are made.

1. FP: Function Parameterization

Function parameterization is the numerical determination, by statistical regression on a database of simulated states, of simple functional representations of parameters characterizing the state of a particular physical system, where the arguments of the functions are statistically independent combinations of diagnostic raw measurements made on the system [1,2].

The chief advantage of the method is, that once the functional representations, in the form of linear or quadratic polynomials, have been determined offline, online parameter recovery essentially reduces to the evaluation of a low order polynomial with fixed coefficients, whose arguments are linear combinations of the raw measurements.

1.1 Database generation

An equilibrium database was generated using an extended version of the Garching Equilibrium Code [3]. By randomly selecting values for 12 input parameters (the magnetic axis position, seven poloidal field (PF) coil currents and three toroidal current density profile parameters) some 7000 limiter and divertor equilibria were generated using the ASDEX-Upgrade configuration of PF coils and vessel geometry.

After each successful convergence, (execution time $\approx$ 0.5 sec on a Cray YMP) an extensive list of relevant equilibrium parameters is calculated ($\approx$ 1000 items requiring $\approx$ 1.0 sec). These include a representation of the entire plasma boundary and, in particular, the poloidal flux or field values evaluated at the sites of the measurements which are later to be used for equilibrium reconstruction. These parameters, together with all PF coil currents and a 41 x 65 grid of poloidal flux values, are stored on disk in a combined dataset of $\approx$ 3500 words.

1.2 Determination of FP coefficients

Currently, 34 magnetic signals (14 flux differences, 19 B_θ values and the current flowing in the in-vessel passive stabilizing conductor) are used for the real-time determination of equilibrium parameters for input to the AUG plasma feed-back control loop

and between-shot analysis. A regression model involving all 34 measurements would be numerically unreliable, however, since there are a number of near-exact linear dependences between the 34 simulated measurement variables in the database. To overcome this problem, a dimension reduction is made using the well-known technique of principal components analysis (PCA). This procedure, which entails the eigendecomposition of the correlation (or covariance) matrix of the simulated measurements, yields 34 uncorrelated linear combinations (eigenvectors) with corresponding database variances (eigenvalues). Many of the eigenvalues are close to zero, and the corrsponding linear combinations are then effectively constants of the database and carry no information for an individual equilibrium. The remaining eigenvectors, termed principal component (PC) variables, are retained as predictors for the FP regression.

The poloidal flux outside the plasma boundary and an incomplete family of moments of the toroidal current density, including a representation of the current centre given by

$$R_s^2 = \int R^2 \, j_t \, dA / I_P \qquad z_s = \int z \, j_t \, dA / I_P,$$

are known to be linear functions of the external measurements, and the FP coefficients for such parameters are accordingly determined by linear regression against the PC's. Most equilibrium parameters, however, require higher order models. Numerical experimentation with a variety of functional forms showed that a full quadratic model (i.e. mixed 2nd degree terms included) in 12 – 14 PC's yields an acceptable recovery accuracy in practice. Typical rms errors for geometric quantities are 3 – 6 mm for the 14 PC model (with a total of 120 terms) which is used for between-shot analysis.

The plasma boundary in AUG can be variously determined by the inboard heat shield, the outboard ICRH antenna limiter, an upper x-point or finally a lower x-point magnetic separatrix. Because of zeroth and first order discontinuities in parameter behaviour at transitions between these four *categories*, a separate quadratic regression is required for each. A critical function of the FP algorithm is, accordingly, the identification of the plasma category to determine which set of coefficients are to be used for parameter recovery. This is accomplished by linear recovery of the flux at 12 candidate positions on the belt limiter and antenna, and a quadratic regression of the upper and lower x-point fluxes which is restricted to equilbria in the neighbourhood of a limiter-divertor transition. The highest flux among the 14 candidates then determines the category.

Basically the same algorithm is implemented in the R2 transputer configuration for real-time control of the plasma equilibrium; however, processing constraints limit to 6 the number of quadratically modelled parameters which are reconstructed every 1.7 msec with a smaller 12 PC model of 91 terms.

2. DIVA: interpretative equilibrium calculation

In contrast to FP, DIVA uses flux differences from loops situated outside the vacuum vessel. These measurements can be exactly satisfied by allowing currents at the flux loop positions which can be interpreted as vessel currents. Basic to the computational approach for an interpretation of equilibrium states by magnetic measurements is the approximate representation of the plasma current density in terms of internal parameters. These internal parameters are subjected to an optimization procedure which determines a best fit to the experimentally measured in-vessel poloidal field measurements. The resulting current density is imbedded in Piccard-type iteration cycles resulting in equilibrium states with optimum poloidal current and plasma pressure profiles.

It should be noted that DIVA can also be used in a predictive manner; this applies to standard MHD equilibria as well as to the inclusion of such extensions as halo currents, pressure anisotropy and flow.

3. Results

FP results are primarily scalar quantities such as (R,z)mag, (R,z)curr, (R,z)geo, (R,z)xp, $\beta_{pol} + li/2$, ... but also include a 24-point reconstruction of the plasma boundary. This is illustrated in Fig. 1 by a sequence of poloidal cross-sections for shot # 1288 at different time points: the first is an inner limiter configuration (t= .350 s), the second an outer limiter case (t= .5 s); after t= .65 s the configuration switches into a lower divertor and stays there till about 2.15 s; finally it returns to an outer limiter before termination. The result of DIVA for the same shot at t= 0.8 s is shown in Fig. 2, demonstrating good agreement between the different methods.

4. Comparison with other diagnostic measurements

Firstly, the images of the plasma edge contours from several CCD-cameras have been used as an indicator for the plasma shape evolution. Since the interpretation of these images is very difficult due to perspective and optical distortions, equivalent images of the plasma edge region emission due to excitation processes were calculated by a computer program. The transition from a limiter to a divertor plasma in He discharges is diagnosed qualitatively due to the poloidal shape of the radiating edge layer and with a camera which observes the x-point directly.

Secondly, category transitions have been compared with spectroscopically determined particle influxes, an example of which is shown in Fig. 3. Below the plasma current and the line-averaged density, the category (from FP) indicates the different configurations. The particle flux inferred from visible emission shows a clear decay as the plasma moves away from the inner limiter. The same is found for the spectroscopically determined particle influx resulting from the plasma - inner heat shield interaction measured by a 12 chord visible spectroscopy system. As the plasma separates from the inner limiter, the observed particle fluxes are reduced by about a factor of 3. This is shown in the next-to-lowest trace by the helium influx in the midplane of the heat shield measured using the He II (468.6 nm) transition. The switching time is, within the limited temporal resolution, in good agreement. The bottom signal is the measured He flux in the divertor region; here there is a prominent increase when the configuration changes from outer limiter to divertor.

5. Conclusion

The above-described data interpretation systems are used routinely to reconstruct the plasma parameters on AUG both for real-time control of the discharge and for more extensive between-shot analysis. They depend on reliable magnetic measurements and are continuously cross-checked and improved by calibrating the results against the above-mentioned (and other) experimental observations.

REFERENCES

1. Wind, H., 'Function Parametrization' in "Proceedings of the 1972 CERN Computing and Data Processing School", CERN 72-21, 1972, pp. 53–106.

2. Braams, B.J., Jilge, W., Lackner,K., *Nucl. Fusion* **24** (1986) 699–708.

3. Lackner, K., *Comput. Phys. Commun.* **12** (1976) 33–44.

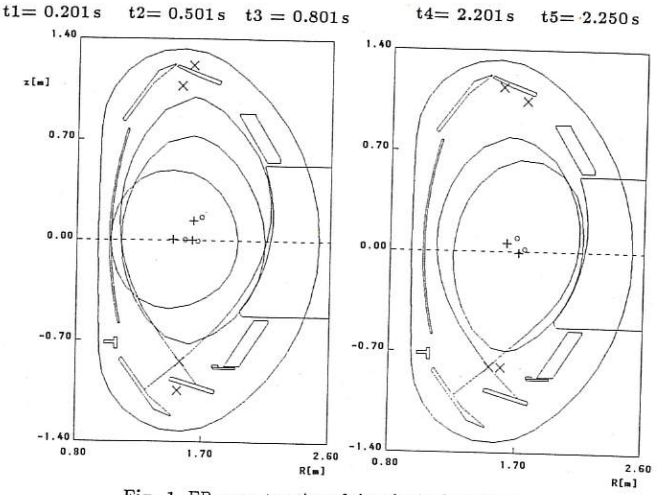

Fig. 1 FP reconstruction of the plasma boundary.

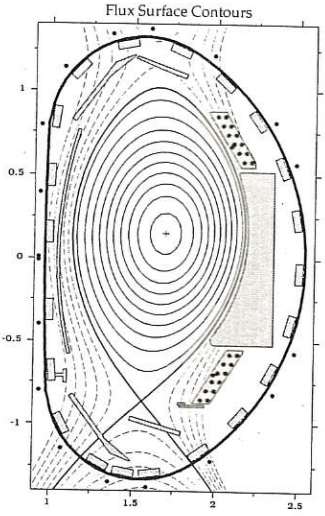

Fig. 2 DIVA Equilibrium at t= 0.8 s.

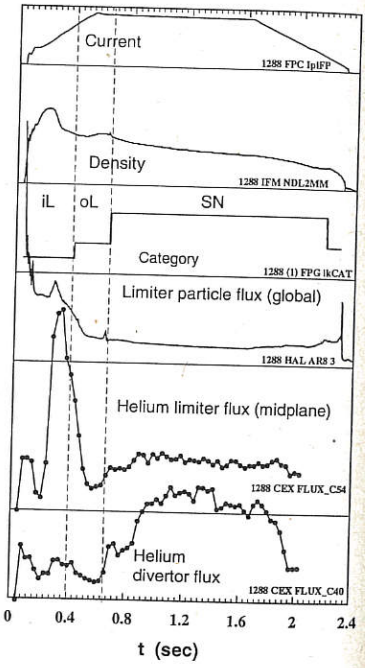

Fig. 3 Comparison of FP category with other diagnostic data.

VOLT-SECOND CONSUMPTION AND CURRENT RAMP EXPERIMENTS ON FTU

G. Apruzzese, F. Crisanti, D. Frigione, H. Kroegler, L. Lovisetto,
G. Mazzitelli, S. Podda
and
P. Buratti, M. Zerbini, F. Romanelli, O. Tudisco
Associazione EURATOM-ENEA sulla Fusione Centro Ricerche Energia Frascati,
C.P.65 - 00044 Frascati (Rome), Italy

1 - Volt-second Consumption

The Volt-second consumption in FTU /1/ has been evaluated both during the plasma start-up and during the current ramp-up from a flat top level to an higher flat top level. The Poynting definition was used to work out the resistive volt-second consumption; the equilibrium reconstruction ODIN code /2/ was used to get the physical quantities necessary ($\beta_p+l_i/2$, β_p, l_i, V_p, L_e). The Ejima parameter $E=\Delta\Phi_{surface}/\mu_0 RI_p$, where $\Delta\Phi_{surface}$ is the flux consumption inside the last magnetic surface, R is the major radius, I_p is the plasma current, has been evaluated for a large set of shots in H_2, D_2 and He. The database covers a large variation of plasma parameters: I_p=.35÷1.1 MA; dI_p/dt~2÷9MA/s; n_e~1.5÷10×10^{-19} m^{-3}; for the whole database it was B_T=6T, R=.93m, a=.28m, b/a~1.04. The flux necessary to get the plasma break-down can be estimated in 0.1 volt-second for the first 50 kA of the plasma current and it is included in all the computations. The total flux consumption (internal plus external) obtained from the equilibrium code outputs was cross-checked with the total flux measured by the poloidal circuit currents variation: the two results were quite well in agreement (about 5%). The mean Ejima parameter obtained for the examined shots was E~1.15. In Fig.1 is shown the Ejima resistive parameter, $E_R=\Delta\Phi_{Resistive}/\mu_0 RI_p$, that is obtained considering only the resistive Volt-second necessary to the plasma ramp-up: the medium value is E_R~0.7-0.8. The points describing the ramp-up starting from a current flat top show a lower value for E_R (up to E_R~0.35); moreover the flux consumed in these shots is compatible with the plasma flat top resistive voltage. Both the E and the E_R values are larger than the ones obtained from other machines (for instance in DIII-D E~0.7-0.8; E_R~0.4-0.5 /3/). A possible cause for this discrepancy could be related to a lack of position control during the early stage of current ramp-up; this fact could lead to a strong interaction with the limiter with a consequent influx of impurities and an increase of the resistive loop voltage. A more physical explanation could be that the normalisation factor ($\mu_0 RI_p$) used in the definition of Ejima parameter is not the best one. We could define, for example, the normalisation factor as the external flux $\Delta\Phi_{external}=I_p L_{pe}$, where $L_{pe}=\mu_0 R[\ln(8R/a)-2]$ is the external plasma inductance: in

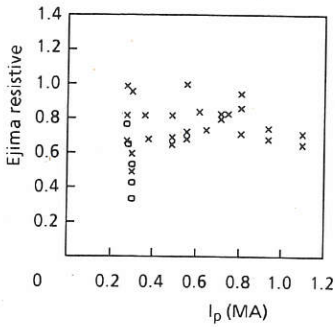

Fig 1: Ejima resistive parameter for a selected set of shot of the used data base. The circle refers to current ramp-up

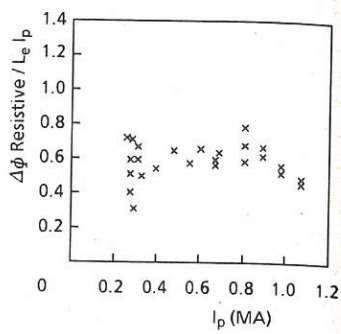

Fig 2: The Ejima resistive parameter renormalized with the external flux L_eI_p for the same shots of Fig. 1

Fig.2 there are the same points of Fig.1 renormalized in such a way. The use of this new normalization allows to our results to agree with the JET or DIII-D results: $E=\Delta\phi_{surface}/I_pL_{pe}\sim0.9$, $E_R=\Delta\phi_{Resistive}/I_pL_{pe}\sim0.5$-$0.6$. It is obvious that our definition is as arbitrary as the traditional one; however it has the merit to give the same result for machines quite different in size and shape and it uses as normalisation factor a quantity ($\Delta\phi_{external}$) with a more physical meaning.

2 - Current Ramp Experiments

2.1 Numerical interpretation of data

Current ramp-down experiments have been performed on FTU at rates up to 9 MA/s, (faster than used in previous experiments /4,5/) in order to study current diffusion with transiently decoupled current and electron temperature profiles. As the current profile j(r) is not directly measured in FTU, its evolution has been calculated by the JETTO code /6/, and the resulting plasma internal inductance has been compared to the measured one.

The following measured quantities are used as inputs to the code: the electron temperature profile $T_e(r)$ from ECE Michelson interferometer, major and minor plasma radius R_0 and a from magnetics, the density $n_e(r)$ from the DCN interferometer, and Z_{eff} as deduced from bremsstrahlung emission assuming a flat profile. Cylindrical simmetry has been assumed; sawtooth effects were taken into account by applying the Kadomtsev reconnection model when $q(0)<q_{ocrit}$. The input parameter q_{ocrit} was chosen such as to reproduce the measured sawtooth period.

The code is initialized by an assumed q profile and evolved to simulate the stationary phase that precedes the current ramp; the reliability of initialization has

been checked by verifying that it does not influence the electric field profile in the stationary phase.

The code provides the time evolution of the j(r) profile, from which the time evolution of internal inductance l_i, of the sawtooth inversion radius and of the loop voltage are obtained. Results with two different assumptions for electrical conductivity (Spitzer with and without trapped particles corrections) were compared with experimental data.

2.2 Experimental results

In this paper we present the results of FTU shot 3322 (magnetic field 4 t; line average density 5.2×10^{19} m^{-3}), in which the current varies from 500 to 280 kA in 40 ms at a rate of 5.5 MA/s, about six times faster than the L/R decay rate. The quantities R_0 and a were kept constant during the current ramp; Z_{eff} and the density profile hardly changed.

The internal inductance has been obtained using the $\beta_p+l_i/2$ values from magnetics and the kinetic β_p obtained assuming $T_e=T_i$. During the ramp down phase, l_i increases almost linearly and strongly overshoots the final value. The β_p shows an even stronger overshoot: the values at 500 kA is 0.27; the transient value at the end of the ramp is 0.65 and the final value is 0.37. The measured l_i is compared in Fig. 3a with the one calculated using the two conductivity models. Taking into account the uncertainties introduced by measurement errors, and by the assumption of uniform Z_{eff}, we find that both models are in reasonable agreement with the data. Also the on axis loop voltage calculated from both models agreed within errors with the one from equilibrium reconstruction.

Data shown in Fig. 3a concern a global quantity; in order to check the calculation of the current profile in the plasma core, we compared the evolution of the sawtooth inversion radius obtained from the ECE grating polychromator, with the evolution of current density at r=9 cm from JETTO; the latter gives an indication of the time required to modify the current profile in the sawtooth region, and decreases after the current ramp with the same delay as the sawtooth inversion radius (Fig. 3b).

3 - Conclusions and further work

Current diffusion in a 5.5 MA/s current ramp-down experiment on FTU tokamak was studied by the JETTO code; no evidence of anomalous current diffusion was found.

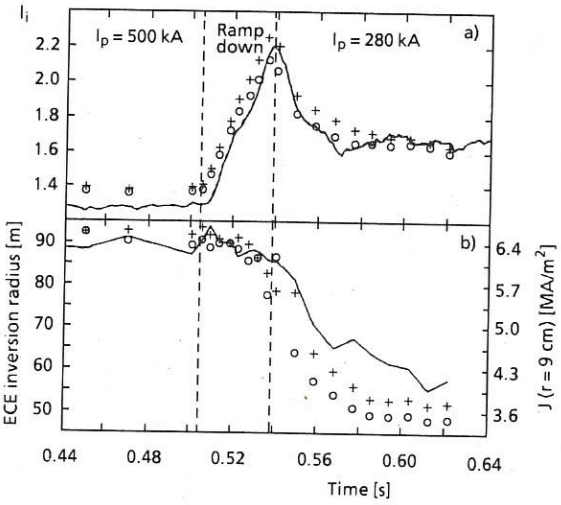

Fig 3: a) Time evolution of internal inductance: from experiment (solid line), from calculation without trapped particle corrections (+) and from calculation with trapped particles corrections (○). b) Time evolution of ECE measured inversion radius (solid line) and current density at r=9 cm from JETTO. (Symbols as before)

Given the experimental uncertainties, simulations assuming Spitzer resistivity agree with measured data both taking into account and neglecting trapped particles corrections.

Further work will concern current ramps at higher magnetic field in order to increase the temperature and consequently the importance of trapped particles corrections. The dynamic behavior of the energy confinement time will also be studied.

References

/1/ R. Andreani et al., Proc. of the 13th Symposium on Fusion Enginering, Knoxville, Tennessee, October 2-6, 1989

/2/ F. Alladio, F.Crisanti, Nucl. Fusion **26**, 1143 (1986)

/3/ Iter Phisics R&D reports task PH11, September 1990

/4/ M.M. Shoucri et al., Nucl. Fusion **30**, 2536 (1990)

/5/ E.D. Fredrickson, Nucl. Fusion **27**, 1897 (1987)

/6/ G. Cenacchi, A Taroni, ENEA RT/TIB/88/5

Stabilization of Axisymmetric Modes and the Effects of Plasma Deformability in Elongated Tokamak Plasmas Using Active Feedback Coils Inside and Outside the Vacuum Vessel

D. J. Ward, F. Hofmann Centre de Recherches en Physique des Plasmas, Association Euratom–Confédération Suisse, EPFL, Lausanne

In this paper we study the feedback stabilization of the vertical instability in a highly elongated ($\kappa = 3$) TCV plasma using a combination of active coils inside and outside the vacuum vessel. The TCV is a tokamak under construction at the CRPP in Lausanne. It is designed to create plasmas with a variety of cross-sectional shapes with elongations up to $\kappa = 3$. We calculate axisymmetric stability using the NOVA-W code.

In previous studies using NOVA-W [1], it has been shown that the eigenfunction of the axisymmetric mode will be modified under the influence of active feedback in such a way that the effectiveness of the system that detects the vertical displacement by means of magnetic flux measurements is greatly reduced, and thereby the active feedback system becomes less effective or ineffective. In this study we find that fast internal coils very close to the plasma surface can induce an enhanced deformation of the eigenfunction. We shall also demonstrate in this study that a feedback system using a combination of many flux loops and poloidal B-field pickup coils is susceptible to these same problems, and that a large number of distributed flux and B_p measurements used to determine vertical position does not always improve matters.

Figure 1 shows a cross-section of the TCV vacuum vessel, active feedback coils, flux-loops and B_p coils, and the TCV equilibrium used in this study. Also shown are the contours of perturbed plasma flux for the case without active feedback. We are using an equilibrium with a growth rate ($\gamma \approx 6000s^{-1}$) which is several times faster than the expected operational limit of the growth rate imposed by the power supplies ($\gamma = 2000s^{-1}$). We choose this more unstable equilibrium because we cannot model all the destabilizing aspects of a real feedback system such as finite bandwidth and voltage limits of power supplies, and because this equilibrium, being very unstable, exhibits very interesting behavior.

There are two active feedback coils inside the vacuum vessel in the corners on the outboard side. There are also 8 active feedback coils outside the vacuum vessel on the outboard side, as well as 8 external coils on the inboard side. The magnetics measurements are composed of a combination of poloidal flux measurements from 38 flux loops just outside the resistive wall (shown in Fig. 1 by an 'X') and poloidal field measurements from 38 B_p-coils just inside the vacuum vessel wall (each is noted by 'c'). These measurements can be used in any combination as a way to determine the vertical position of the plasma as input for the feedback system. In this study we number the flux-loop, B_p-coil pairs (which are up-down symmetric about the midplane) from #1 at the inboard midplane to #20 at the outboard midplane. The numbering is shown in Fig. 1. We use a two time-scale feedback system [2] using both the internal and external active coils. The voltage applied to the internal coils is equal to some gain (proportional plus derivative) multiplied by a measure of the vertical displacement which is composed of a combination of perturbed flux and B_p measurements. The voltage applied to the external coils is proportional to the current in the internal coils. In the case we consider first, the voltages applied to all external coils are of the same magnitude. The internal coils provide the fast response necessary to stabilize these highly elongated plasmas, but they have power limitations, so this two stage system allows the current in the fast internal coils to return to zero by replacing their stabilizing force by that of the more powerful, but slower, external coils.

Figure 2 shows the plot of perturbed flux for the TCV plasma under active feedback using all feedback coils (internal and external). When the complete set of flux loops are used (but no B_p measurements) the plasma cannot be made stable with this coil configuration. This is due to the fact that the sum of the flux-loop signals goes to zero as the feedback gain is increased to large values. In Ref. [1] it was shown that the deformation of the eigenfunction under active feedback can cause the measured signal at a pair of flux loops to go to zero, rendering the feedback system ineffective. We see here that using a combination of a large number of flux-loop measurements does not necessarily improve matters. The contour of zero-flux is shown as a dotted line in Fig. 2. The flux loops inside this contour measure positive flux, while those outside measure negative flux. It is not necessary that the flux be zero at *each* of the detector pairs for the feedback system to be made ineffective, but only that the measured fluxes add positive and negative values to give an *overall sum* that decreases at the same rate that the gain increases. In this configuration, a relatively small modification of the eigenfunction is sufficient to make the sum of the flux measurements go to zero as the gain is increased to large values.

It is apparent from the fact that the zero-flux contour in Fig. 2 lies so close to most of the flux loops that most pairs of flux loops if used by themselves would be ineffective. However, a single pair of well placed flux loops can be better than the complete set that surrounds the plasma. An example of an *effective* single pair of flux loops is pair #17. Comparing Fig. 1 and Fig. 2 we see that the influence of the internal coils induces a deformation in the eigenfunction that produces a bulge in the perturbed flux to the outboard side. This in turn increases the detected flux signal at these flux loops. In

Figure 1

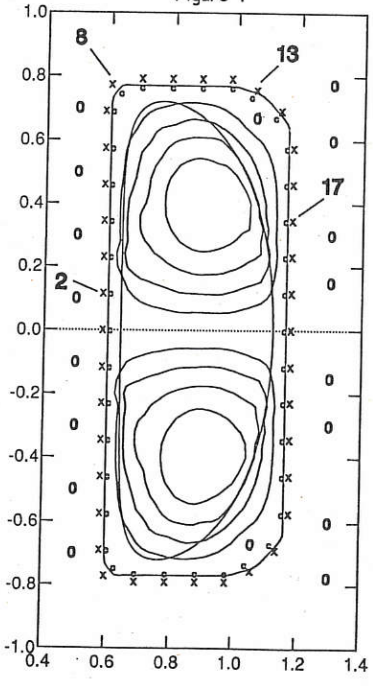

Figure 2

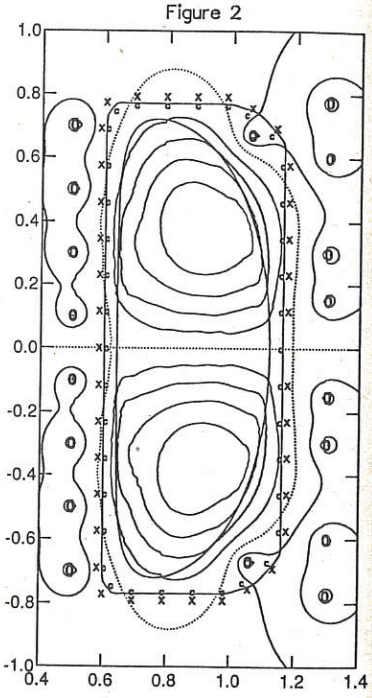

this case one can take advantage of the deformation in the eigenfunction due to the influence of the internal coils to use flux loops that would be quite ineffective without this deformation. The flux-loop pairs that are effective when used by themselves are at positions #10, #11, #17, #18, and #19.

When the complete set of B_p-coils are added to the set of flux loop measurements in a weighted sum [3], the plasma can be stabilized with the active feedback system described above. The deformation of the eigenfunction under the influence of the feedback system is unable to make the sum of the magnetic measurements go to zero. In fact, if the measurement from the corresponding pair of B_p-coils is added to the measurement from a single pair of the flux loops, the combination is effective for *most* of the pairs. However this is not true in all cases, and one must still be careful in choosing the location of the flux-loop, B_p-coil pairs. In some cases the sum of a negative flux measurement plus a positive B_p measurement yields a null signal. The *ineffective* locations for the single flux-loop, B_p-coil pairs are at positions #7, #8, #9, #12, #13, #14, and #15.

We find that the deformation of the eigenfunction due to active feedback is virtually the same when flux-loop pair #17 is alone used as when the complete set of flux-loop and B_p-coil measurements is used for this case. This is quite different from previous results for the PBX-M configuration [1]. This appears to be due to the fact that the active feedback system using internal coils and many nearby external coils on both the inboard and outboard sides imposes a particular deformation of the eigenfunction that is not significantly affected by this change in the detection system. This is not necessarily the case if the distribution of the coil currents in the active coils were changed.

The effectiveness of a particular feedback system is very sensitive to the distribution of currents in the active coils. Changing the relative weights of the feedback gains on the various coils changes the eigenfunction, and it changes the way that the eigenfunction can be deformed in order to defeat the detection system. In the feedback system used in Fig. 2 there is a voltage of equal magnitude applied to all external coils. Now we consider calculations where the voltages on the external coils are weighted such that the voltage applied to the coils farther away from the midplane is proportionately higher than the voltage applied to those close to the midplane, and the voltage applied to the inboard coils is smaller than that applied at the outboard coils. With this weighting of the voltages the resulting currents in the external coils provide a more uniform radial field inside the vacuum vessel.

This completely changes the deformation of the eigenfunction under active feedback, and it is such that the detection system using the full configuration of flux-loops and B_p-coils is no longer effective. Figure 3 shows the ways that the eigenfunction changes under the effect of the different coil current distributions. In Fig. 3 we show the ratios of the mth poloidal harmonic of the radial component of the eigenfunction to the first harmonic, $\xi_{\psi m}/\xi_{\psi 1}$, at the plasma edge for $m = 2, 3, 4$. These are displayed versus the corresponding growth rate, γ, for that case. The feedback gain is increasing as the growth rate decreases, i.e., it is increasing as one moves to the left along the curves. The ratios $\xi_{\psi m}/\xi_{\psi 1}$ are shown for three cases. The first case (case A) uses the combination of internal and external coils with equal voltage applied to the external coils as in the case shown in Fig. 2. The second case (case B) has only the external coils activated (with equal weighting) and the internal coils remain passive, and the third case (case C) uses a combination of internal and external coils with the voltages on the external coils weighted in order to give a more uniform radial field as discussed above. All three cases use a detection system using the full combination of all flux-loops and B_p coils shown in Fig. 2. In each case the ratios for $\xi_{\psi 2}/\xi_{\psi 1}$ are shown by squares,

the ratios for $\xi_{\psi 3}/\xi_{\psi 1}$ are shown by circles, and the ratios for $\xi_{\psi 4}/\xi_{\psi 1}$ are shown by triangles (case A by small open symbols, case B by solid symbols, and case C by large open symbols).

The difference in the deformation of the eigenfunction is quite clear between these three cases. For example, the values for $\xi_{\psi 2}/\xi_{\psi 1}$ for case A evolve with increasing gain (decreasing growth rate) in the opposite direction to the other two cases. Likewise, the values for $\xi_{\psi 3}/\xi_{\psi 1}$ for case B evolve in the opposite direction from the other cases. For case B and case C the deformation is such that the plasma cannot be made stable. The total magnetic measurement of the vertical displacement goes to zero at the same rate that the gain is increased. Increasing the gain only serves to further modify the eigenfunction. The plasma in case A can be made stable (points to the left of the vertical line in Fig. 3), but the eigenfunction changes to a large extent after the plasma becomes stable, and the magnitude of the stable eigenvalue seems to be limited.

CONCLUSION

We see that the deformation of the eigenfunction plays a crucial role in the ability of the feedback system to successfully stabilize the plasma. It is important to understand the deformation of the eigenfunction resulting from a particular choice of active coils in order to choose an appropriate set of magnetic measurements to determine the vertical displacement. The use of internal and external active coils imposes a particular deformation that allows one to choose a small number of well placed measurements. A large number of magnetic measurements distributed around the plasma does not necessarily improve matters, and in fact can be much less effective than a small number of well placed measurements. The deformation of the eigenfunction is also strongly affected by the distribution of currents in the external coils.

[1] D. J. Ward and S. C. Jardin, LRP 434/91, CRPP-EPFL, Lausanne (September 1991). To appear in Nucl. Fusion **32** (1992) #6 or #7.

[2] F. B. Marcus, F. Hofmann, S. C. Jardin, et al., Nucl. Fusion **30** (1990) 1511.

[3] F. Hofmann and G. Tonetti, Nucl. Fusion **28** (1988) 519.

Figure 3.

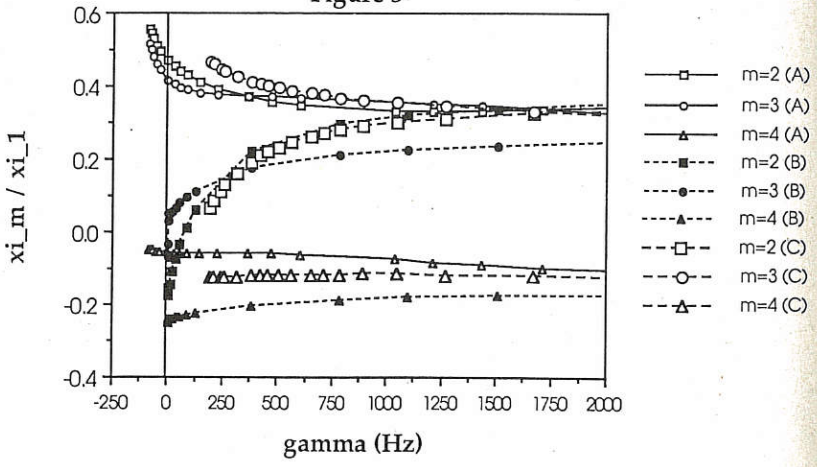

PLASMA PERFORMANCE, EQUILIBRIUM AND STABILITY IN SPHERICAL TOKAMAK GLOBUS.

V.A. Belyakov, S.E. Bender, A.A. Kavin, Ju.A. Kostsov, O.A. Minyaev, V.I. Vasiliev
D.V.Efremov Scientific Research Institute of Electrophysical Apparatus, St. Petersburg ,Russia
V.E. Golant, A.N. Levitsky, N.V. Sakharov, O.V.Fedorov, K.G. Shakhovets
A.F. Ioffe Physical - Technical Institute of the Russia Academy of Sciences, St.Petersburg ,Russia
A.R. Polevoy, P.N. Yushmanov
I.V. Kurchatov Institute of Atomic Energy, Moscow, Russia

Introduction

In comparison with a conventional tokamak (aspect ratio $A=R_o/a>2.5$) a tight aspect ratio tokamak ($A<2$) allows to obtain plasma characterized by high toroidal beta (b_T=15-20%),low poloidal beta (b_p=0.2-0.3), naturally large elongation ($k=b/a=2-2.5$), large plasma current, strong paramagnetism and strong magnetic helical pitch /1/. These features combined result in a unique physics regime.

The Globus device is an inductively driven low aspect ratio tokamak (A = 1.6). The main parameters of Globus tokamak are: plasma major radius R_o=0.5 m, plasma minor radius a = 0.31 m, plasma elongation $k=b/a=1.6-2.4$, plasma triangularity d = 0.2 - 0.5, plasma current I_p=0.5-1 MA, vacuum toroidal magnetic field $B_{TO}<0.67$ T, inductively driven discharge duration up to t_p = 0.5 sec. In order to achive high beta an auxilary heating (up to 4 MW of NBI) is planned to be used. The designed poloidal field system permits to produce both limiter and divertor configurations in the wide range of plasma parameters.

The main goals of Globus experiments are:

-Investigation of plasma stability, energy and particle confinement in low aspect ratio plasmas;

-High beta experiments and non-inductive current drive;

-Study of shape control and diagnostic of highly elongated plasmas;

-Exploration of engineering problems concerning of spherical tokamak.

Plasma performance.

The analysis of plasma scenario was performed using 0-D power balance code and 1.5-D time dependent transport code "ASTRA". Calculations are performed for plasma parameters: R_o=0.5 m, a_p=0.31 m, $k_{0.95}$=2.0, $d_{0.95}$=0.4, B_T=0.6 T, Z_{eff}=2.5, $<n_e>=0.4\ 10^{20}$ m^{-3}.

The features of reference(I_p=0.5 MA) and high current (I_p=1MA, P_{aux}=1.5 MW) mode of operation are listed in Table 1.

Table 1. Reference and high current mode of operation.

	Reference mode (I_p=0,5 MA, P_{aux}=0 MW)	High current mode (I_p=1 MA, P_{aux}=1.5MW)
t_E , ms	14.0	12.0
b_p	0.26	0.21
b_T , %	3.9	<17.0
b_{Troyon} , %	8.0	16.0
V_p , V	1.6	0.58
L_p , мH	0.5	0.49
l_i (3)*	0.61	-
l_i (3)	0.72	0.80
t_p , sec	0.43	0.49
F_{tot} , Vs	0.72	0.82

where t_E - energy confinement time, $t_E=t_{ITER-P}$; b_p ,b_T - poloidal and toroidal beta; $b_{Troyon}=3I_p/aB_T$; U_p - resistive voltage; L_p- plasma inductance, calculated for l_i=0.65; l_i(3) - internal inductance , defined in terms of the internal poloidal magnetic energy; l_i(3)* - with current MHD-mixing; F_{tot} - volt-second consumption.

Proposed evolution of plasma current, density, position and shape with start-up from inner wall correspondes to practically constant values of internal inductance l_i(3)=const and safety factor $q_{(a,t)}$=const with peaked current profiles. The analysis shows, that auxiliary power of 1.5 MW of NBI is sufficient to reach high b_T, close to Troyon limit.

Plasma equilibrium and poloidal field system

The designed poloidal field system of Globus tokamak is shown in Fig.1, where OH1 - central solenoid, OH2-OH5 - coils for compensation of stray magnetic field from OH1 inside plasma volume, PF1-PF4 - poloidal field coils, AC1-AC2 - coils for feed-back control of plasma vertical position.

At the moment of plasma break-down the coils (OH2...OH5) provides the precize compensation of the stray field produced by central solenoid. The field errors do not exceed 2 G for 0.2 m < R_o < 0.6 m.

The volt-second capability of poloidal field system is 0.72 Vs for I_p=0.5 MA and 0.82 Vs for I_p=1.0 MA. The volt-second capability of central solenoid with initial premagnetization is about 0.6 Vs. This value is limited by the allowable stresses in bronze (=170 MPa) and an overheating.

Free boudary MHD equilibrium calculations show that plasma elongation of 1.6 occurs naturally when only a dipole vertical field is applied. When a quadrupole shaping field is applied a high elongation (k=2.4) and triangularity (d=0.5) can be obtained.

In limiter mode of operation plasma elongation does not exceed the value k=2.0 if X-point is outside of vacuum vessel. A sequence of equilibria obtained are shown in Fig.2 and possible plasma configurations are listed in Table 2.

Table 2. Possible plasma configurations in Globus tokamak (divertor regime)

Used PF coil	Plasma elongation	Plasma triangularity
PF3 and PF4	2.1	0.2
PF2, PF3 and PF4	2.2	0.3
PF1, PF2, PF3 and PF4	2.4	0.5

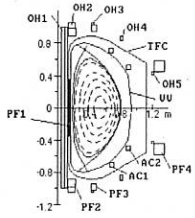

Fig.1 Poloidal field coil system

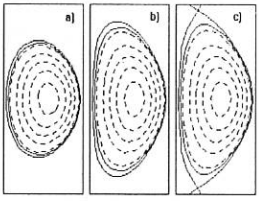

Fig.2 Sequence of plasma equilibries
a - natural elongation: k=1.6,d=0.2
b - limiter configuration: k=2,d=0.4
c - divertor configuration with maximum elongation and trianqularity: k=2.4, d=0.5

Control of plasma vertical instability

High plasma elongation and a small distance between plasma boundary and vacuum vessel wall (Fig.1) require a careful control of plasma vertical instability.

The necessary condition of vertical stability can be expressed by the stability margin as:

$$f_s = \frac{dF_z^{stab}/dz}{dF_z^{ext}/dz} > 1 \qquad (1)$$

where: F_z^{stab} is the stabilizing vertical force acting on the plasma due to the flux-conserving eddy currents flowing in the passive structure;

F_z^{ext} is the destabilizing vertical force acting on the plasma due to curvature of the external field.

In Globus tokamak the stability margin f_s varies in the range of 1.5 to 1.8 depending on plasma current density profile $l_i(3)=0.85-0.55$. The condition (1) is not sufficient for plasma vertical stability. If we take into account the finite conductivity of the passive structure (vacuum vessel and coils) the system plasma - passive structures shows an intrinsic instability with respect to plasma vertical movements, measured by the growth time t_G. Taking into account the vacuum vessel (Vessel material - steel with specific resistance $7\ 10^{-7}$ Ohm m, wall thickness h=1-1.5 mm) the growth time t_G varies in the range of 0.16 to 0.33 depending on plasma current profile. The passive stabilizing effect is improved taking into account the control coils (AC1 and AC2). In this case the growth time t_G increases by factor of two.

The numerical simulation of active plasma control shows that plasma vertical position control accuracy within 1 cm with disturbance rate up to 3 G/ms is possible if high speed current reversive convertor (f_{max}=3 kH, P=0.5 MVA) is used.

/1/ Y.-K.M.Peng, D.J.Strickler, Nuclear Fusion, vol.26, No.6, 769 (1986).

RAPID CONTROLLED SHUTDOWN OF A BURNING PLASMA

G.W. Pacher and H.D. Pacher
The NET Team, c/o Max Planck Institut für Plasmaphysik, Garching b. München, Germany

Abstract:
The shutdown phase of an ignited plasma in a next step device such as ITER is simulated, with a view to maximizing the speed of decrease of fusion power without initiating a disruption. In order to prevent melting of the cooling tubes of the divertor in case of failure of the cooling system, the desired time scale is typically 10 s or less. For the various scenarios simulated here (current rampdown, helium poisoning, and fuelling decrease), the decrease of fusion power is always appreciably slower than this, typically 15 s or more to reach one third of the initial value. It is likely, therefore, that rapid shutdown in the space of 10 seconds or faster will have to be disruptive, and that measures will have to be taken to alleviate as much as possible the effect of these programmed disruptions on the plasma-facing components.

Introduction:

The 1.5 D ASTRA transport code [1] has been employed to simulate various scenarios for rapid shutdown of a burning plasma in a next step device. Rapid shutdown will be necessary for instance in the case of failure in the cooling of the plasma-facing components. Because of the high heat loads on the divertor plates for typical scenarios in the high-recycling regime [2], the time-scale before melting of the cooling tubes occurs (which could cause major damage) will be of the order of 10 seconds, and this defines the target for controlled, non-disruptive discharge termination. For all the scenarios investigated, the initial condition is a nearly steady-state sub-ignited burn corresponding to ITER parameters ($\langle n\rangle=1.2\times10^{20}$ m^{-3}, $\langle T\rangle=10$ keV, $Z_{eff}=1.66$, ref.[2]). The dimensions chosen for the simulation are I=22 MA, R=6 m, a=2.15 m, $\kappa=2$, B=4.85 T, so that $q_{edge}=3$. The corresponding fusion and external heating powers are 1.1 GW and 20 MW respectively, i.e. C=0.9 ($C\equiv P_\alpha/(P_\alpha+P_{ext})$). The effect of sawteeth is modeled by increasing locally the resistivity with respect to the neoclassical value so as to clamp q at unity inside the q=1 surface. H-mode confinement is postulated: the anomalous heat diffusion coefficient is taken as constant in the cross-section, and is adjusted to give an energy containment time equal to 90% of the value predicted by ITER H-mode scaling, derated by 25% [2] for the effect of ELM's (to approximate the effect of sawteeth, the heat diffusivity is also increased for radii smaller than twice the q=1 radius). The alpha particle fraction in steady state is taken to be 10% of the electron density, and this concentration is taken constant over the cross-section. Oxygen concentration is also constant at 0.1%. The carbon concentration varies with local electron density according to the ITER guidelines ($(0.9+0.6\times(7/n_{20})^{2.6})$%) [ref.2]. The ratio of deuterium to tritium ions is taken to be unity.

As an initial condition, temperature, density, and current profiles close to those for steady-state are prescribed. The profiles are then allowed to relax for 10 seconds, in order to adjust the approximate profiles to the actual transport coefficients, with an external heating power of about 20 MW, which is feedback-controlled to give a fusion power of about 1100 MW. At 10 seconds, the control power is set to zero, and the controlled shutdown is initiated. Three major types of intervention are simulated: A) rapid decrease of the plasma current in order to reduce the plasma confinement, B) poisoning of the discharge by helium ash at constant electron density to reduce the density of reacting particles, and C) termination of edge fuelling to reduce the overall density of the plasma. Finally, scenarios D) which combine fuelling and current decrease are presented.

A). Rampdown of Plasma Current

At 10 seconds in the simulation, a negative loop voltage of 3 volts is applied, and the plasma current profile is allowed to evolve as the plasma current is reduced. The density profile is held fixed for this simulation, $n_e(r)\propto(1-(r/a)^2)^{0.5}$. The temperature profiles evolve according to the local energy balance. Two cases are investigated: for both cases, the global energy confinement time in steady-state

is that corresponding to ITER H-mode scaling with ELM's, but for the first. case (A1), the heat diffusivity is taken to vary according to ITER-H-mode scaling also during the rampdown, whereas for the second case (A2), a transient dependence is postulated such that $\tau_E \propto I_p^{1.3} I_i^{0.68}$, a scaling law that has been shown [3] to fit JET and TFTR current ramp experiments. For both simulations (Fig.1), a pronounced negative current density layer occurs at the plasma edge, somewhat more pronounced in the second case (A2) because of the slower cooling due to improved confinement during the rampdown.

B) Poisoning by Helium Ash

For this simulation (case B), the helium density is allowed to increase from the initial concentration of 10% of electron density according to the local fusion power density. As deuterium and tritium are consumed, the electron density is held fixed (parabolic to the power one-half). For the ions, helium and deuterium/tritium, outward diffusion is taken to be balanced by the inward pinch, so that the helium ash remains where it is produced. Electron and ion temperature profiles evolve, and the current density profile adjusts accordingly at a fixed total plasma current of 22 MA.

C) Termination of Edge Fuelling

Fuelling of the plasma is simulated by imposing a neutral pressure at the edge such that the volume average particle density in steady-state is 1.25×10^{20} m^{-3}. The particle diffusion constant is taken to be D_a=0.5 m^2/s. Two different pinch coefficients S (pinch velocity equals $-2D_a Sr_{eff}/a^2$) are considered: S=0.7 (case C1), giving a density profile with a broad central peak similar to the guidelines of ref.2, and a case with one-fiftieth of this value, S=0.014 (C3), giving a very flat density profile. At 10 seconds, the neutral (D-T) density at the edge is decreased. Its speed of decrease, and hence also of the fuelling rate of the plasma, is determined by the balance between pumping speed (taken to be 10^{22} particles/second [4]) and the number of particles coming from the plasma and the wall. In the simulations, the rate of decrease of neutral pressure at the plasma edge is adjusted to correspond to a certain rate of decrease of the total number of particles in the plasma. For the first case (C1 no outgassing) 10^{22} part./s are removed from the plasma. For case C2 (with outgassing), the particle source from the wall and from the plasma are assumed to be equal, so that 0.5×10^{22} part./s are removed from the plasma. As the edge plasma density decreases, the number of particles per second evacuated are assumed to decrease proportionally.

For these scenarios, it is therefore the available pumping speed at the time of detecting the cooling system failure, and the wall outgassing characteristics, that determine the maximum speed of decrease of the density of reacting particles.

Results of Basic Scenarios

For the conditions indicated, it is seen that the speed of decrease of fusion power to one-third of the original value is appreciably longer than the desired 10 s time frame (Table I). The shortest time constant found for the decrease of fusion power is 13 seconds in a case which is probably not realistic (i.e. current decrease with 3V negative loop voltage, no credit in confinement due to the current distribution). For all the cases considered, except those for which the density decreases because of termination of fuelling, the problem of violating the density limit early during the shutdown exists as the fusion power (and external heating power) is decreased at constant density.

To illustrate this point, we have used the Borrass scaling for the limiting density [5], varying as $\{(\text{power/area at separatrix})^{0.57}/q_{edge}^{0.1}\}$. Normal nearly ignited operation at 1100 MW fusion power is taken to be at 90% of this limit, since high density operation is required to alleviate divertor operating conditions. In Table I, we have indicated the time after shutdown initiation when the density limit is reached. When this occurs, the shutdown of fusion power is likely to be disruptive, with deleterious consequences for plasma-facing components, and the damage will be the greater the larger the total stored plasma energy at that time, thermal and magnetic. In the Table, the stored energies are indicated as percentages of initial energy, and the magnetic energy content is estimated as proportional to $(l_i \times I_p^2)$. For all scenarios, the time to reach the density limit is shorter than the time

constant for the decrease of fusion power. For most scenarios, virtually all the initial energy is still available at the projected time of disruption.

D) Combined Scenario - Stop of Edge Fuelling with Current Decrease

In order to improve the situation with respect to the density limit, and still attain rapid fusion power decrease, combined scenarios of forced rampdown of plasma current, along with stop of edge fuelling, have been investigated. (Clearly, termination of edge fuelling and helium poisoning are incompatible, because the former implies pumping, whereas the latter implies stop of pumping; fuelling with e.g. helium instead of hydrogen does not eliminate the problem with the density limit.). For these simulations, outgassing from the wall is taken to be negligible, i.e. 10^{22} particles/s are removed from the plasma initially. The confinement is taken to improve with internal inductance, as above. The results are shown in the last three rows of Table I. The typical time for fusion power decrease remains 15 s or longer, with three different negative loop voltages, -1 (case D1), -2 (D2), and -3 V (D3). However, the stored magnetic energy at the density limit decreases appreciably as the negative loop voltage increases, and the total stored energy (initially approx. 600 MJ thermal and 600 MJ magnetic) decreases appreciably for all these cases compared to the simpler scenarios.

Discussion and Conclusion

For the conditions and scenarios investigated, controlled, non-disruptive shutdown in less than 10 seconds is not obtained. The reason for this is that, in order to alleviate divertor power load, normal operation is likely to be close to the limiting density, and that this density depends on the power input to the scrape-off layer. In the present analysis, we have taken a variation as $P^{0.57}$ (scaling for JET [6] gives a variation as $P^{0.5}$; the result would be only marginally different). As a result, when the fusion power decreases, the density limit is rapidly violated. In a normal shutdown, the external heating power would be increased to avoid violating the density limit. In the event of cooling system failure, however, this action would not reduce the power load on the divertor plates. If a disruption due to violation of the density limit results, the present simulations indicate that at least 75% of the initially stored plasma energy (thermal and magnetic) is still present at the time of disruption. An appreciable fraction of this energy would probably be deposited on the divertor plates.

In order to minimize the consequences of loss of cooling to the divertor plates, it would appear therefore that the correct action is to induce a disruption by pushing the plasma against a sacrifical component. Given that the poloidal field system must be able to follow the current ramp-up and heating to ignition scenarios [2], radial movement of the plasma inward, (to reduce the plasma radius such that q=1.5 results), is easily possible in 10 seconds. A low-q disruption would then occur, leading to energy deposition mainly on the inboard sacrificial limiter element against which the plasma is pushed. This is more likely to minimize damage than a vertical disruption, which would of course be faster and even easier to initiate.

References:

1) G.V. Pereverzev et al., "ASTRA, An Automatic System for Transport Analysis in a Tokamak", IPP Report 5/42, August 1991
2) D.E. Post et al., ITER Physics, IAEA/ITER/DS/21, ITER Documentation Series, IAEA, Vienna (1991)
3) C.D. Challis et al., "The Plasma Current Scaling of Energy Confinement", JET report P(92)15
4) D. Leger, P. Dinner, et al., ITER Fuel Cycle, IAEA/ITER/DS/31, ITER Documentation Series, IAEA, Vienna (1991)
5) K. Borrass, "Scrape-off Layer Based Model for the Disruptive Tokamak Density Limit...", in Proc. 17th EPS Conference on Contr. Fusion and Plasma Heating, Amsterdam 1990, vol. 3, 1393
6) The JET Team, "Recent JET results and Future Prospects", Proc. of XIIIth International Conference on Plasma Physics and Controlled Nuclear Fusion Research, Washington, D.C., Oct. 1990, IAEA-CN-53/A-1-2

Action	time const. for P_{fus} (s)	time to density limit (s)	energy at density limit (thermal/magn %)	case
current decrease (V_f=-3V)	13	1.5	97/96	A1
current decrease (-3V) ($\chi \propto I^{1.3} l_i^{0.68}$)	19	1.6	98/96	A2
poisoning (He accumulation)	17.5	1.5	98/100	B
fuelling stop (no outgassing)	19	12.5	57/100	C1
fuelling stop (with outgassing)	31	16	70/100	C2
fuelling stop w. flat profile	15	8	71/100	C3
fuelling stop & current rampdown (-1V)	16.5	10	63/89	D1
fuelling stop & current rampdown (-2V)	15.5	8	69/85	D2
fuelling stop & current rampdown (-3V)	15	7	72/80	D3

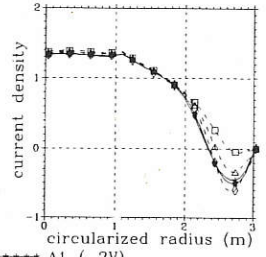

Fig.1 – Current density 10s after start of current decrease; open symbols for combined scenarios

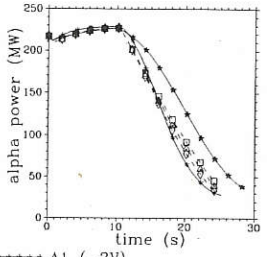

Fig.2 – Decrease of alpha power with current decrease; open symbols for combined scenarios

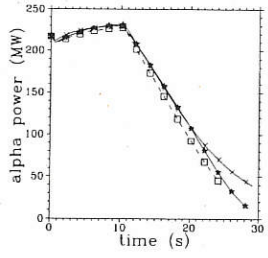

Fig.3 – Decrease of alpha power with helium poisoning and density decrease; open symbol denotes combined scenario

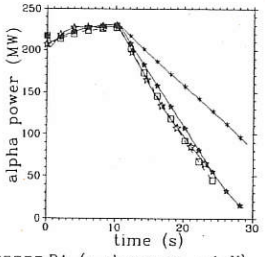

Fig.4 – Decrease of alpha power with density decrease, w./wo. outgassing, w. flat profile, and combined scenario

NEUTRAL BEAM HEATING IN ALVAND IIC TOKAMAK

M. GHORANNEVISSE, M. MORADSHAHI, AND M. AVAKIAN

Physics department; Islamic Azad University; Iran

Nuclear Research Center AEOI Tehran.

P. o. Box: 11365-8486 Tehran Iran

1. INTRODUCTION:

Neutral beam have a wide applications in tokamak experiments. It used to heat; fuel; adjust electric potentials in plasmas and diagnose particles densities and momentum distributions. It may be used to sustain currents in tokamaks to extend the pulse length.

A 5KV; 500 mA Ion source have been constracted by plasma physics group; AEOI [1] and it used to produce plasma and study the plasma parameters [2].

Recently this Ion source have been neutralized and it adapted to a neutral beam source; and it used to heat a cylendrical DC plasma and the plasma of ALVAND IIC Tokamak which is a small research tokamak with a minor radius of 12.6 cm, and a major radius of 45.5 cm [3].

In this paper we report the neutralization of the Ion beam and the results obtained by injection of this neutral beam into plasmas.

2. NEUTRALIZATION OF ION BEAM

Fig 1 shows the experiment set up equipments.

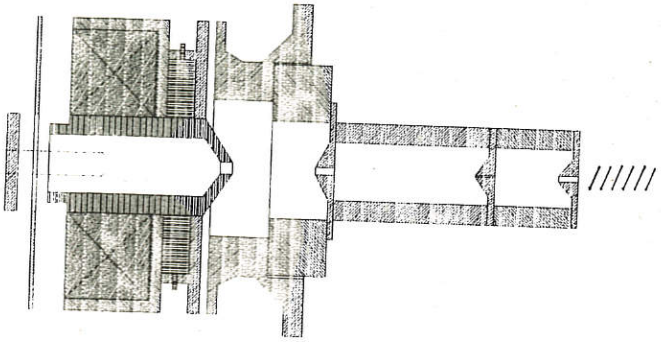

Fig 1) Shematic view of neutral beam source.

Accelerated Ion beam leave the final accelerator grid and passthrough a heated cylindrical tangstan coil with 5 cm lenght and 0.01 cm diameter.

The neutralization percent is determind by Faraday cap measurement of Ion beam current betore heating the neutralization coil (2.2 mA) and after it (0.8 mA) which shows a 60% neutralization of Ion beam.

3. INJECTION OF NEUTRAL BEAM INTO A CYLINDRICAL DC PLASMA.

The generated neutral beam have been injected into a cylindrical DC plasma. Using a double probe the plasma electron density and temperature are measured (n_e=9.8 x 10^{11} , T_e = 4.69 ev). We compared it with Ion beam injection case (n_e= 8.2 X 10^{11} cm^{-3} , T_e = 5.23 ev) and we

found an improvement in electron density. The generated plasma Ion wave was as figure (2) ($f=5x10^{6}$ HZ).

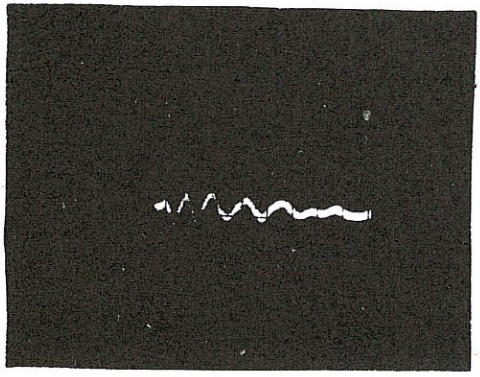

(Figure 2)

4. INJECTION OF NEUTRAL BEAM INTO THE TOKAMAK PLASMA.

This neutral beam have been injected into ALVAND IIC tokamak plasma. We were concerned to investigate the alternation of the average electron density in the length of vertical small diameter of torus in presence or absence of neutral beam. This done by use of a zebra stript type microwave interferometer. Figures 3 and 4 show the results;

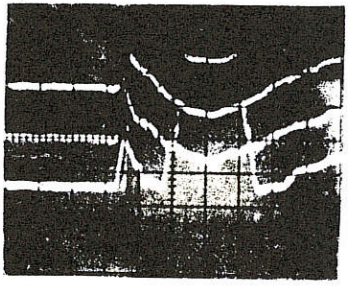

(figure 3)

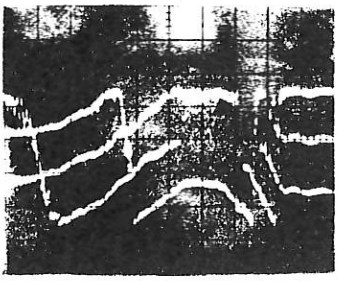

(figure 4)

it show that the average electron density rise from 1.6 x 10^{13} / cm^3 to 2.3 x 10^{13} /cm^3 as we determined theoretically

REFERENCES:

[1] M. GHORANNEVISS: Recent Development in an Ion source for plasma Heating proc.
Third summer school on plasma physics.
TSINGDAO/ P.R. China August 15 - 22; 1990

[2] M. GHORANNEVISS; Collisionless argon plasma produced by a DUO plasmatron source.
PROC. ICPIG X X Belgrade ; March 1989

OPERATIONAL START-UP AND VESSEL CONDITIONING OF THE NOVILLO TOKAMAK

L. Meléndez-Luqo, R. López-Callejas, R. Valencia-Alvarado, E. Chávez-Alarcón, S. Colunga-Sánchez, H. Jiménez-Domínguez and E. Gaytán-Gallardo.

INSTITUTO NACIONAL DE INVESTIGACIONES NUCLEARES
Apartado Postal No. 18-1027, Col. Escandón
México 11801, D.F., MEXICO.

The first results of design, construction and start stage of the Novillo Tokamak are presented. The main parameters of the device are: $R_o = 0.23m$.. $a = 0.08m$. $a_p = 0.06m$. $q \approx 3$. $B_t \approx 0.5T$. $B_p = 0.04T$. $I_p = 12kA$. $n_e = 2x10^{19}m^{-3}$. $T_e = 150eV$. $T_i = 50eV$ [1]. The vacuum vessel has a wide accessibility to all major forms of diagnostics covering approximately 25% of the total area. We have obtained tokamak discharges with base pressure as low as $1.0x10^{-6}$ Torr. after a vessel conditioning. Using approximately 70% of OHT energy, the plasma current has been more than 11 kA. At the current stage of the Novillo project, plasma measurements have been restricted to magnetic probes and a more sophisticated diagnostic like a 2mm microwave interferometer and a 9mm reflectometer (figure 1), and now a 32 channel acquisition data system are setting on the tokamak and will be available soon.

VACUUM VESSEL

Two different methods of wall conditioning were employed, namely vacuum baking and the Taylor discharge cleaning process. Wall and seal preparation was followed by the use of these two methods after a initial pressure of 10^{-7} Torr with a turbomolecular system was attained. A mass spectrometer was used to perform the residual gas analyses. One of the important objectives of conditioning is to eliminate oxygen

from walls. The vacuum baking was actually very effective to reduce the initial pressure in more than one magnitud order in a short time. The discharge cleaning process brought oxygen level to an insignificant amount with respect to the initial value [2]. A sample of spectra and data obtained during wall conditioning of the vacuum chamber of the "Novillo" Tokamak are presented in the figure 2.

INSTRUMENTATION

The design, construction and tests of the electric and electronic instrumentation to generate discharges cleaning conditioning and the main discharge in the Novillo Tokamak are presented. The instrumentation for the discharge cleaning consists of the following parts: 1) an AF pulsed power oscillator that in the tank circuit energyzes the primary coil in a pulsed mode, thus inducing the discharge in the tokamak toroidal volume. 2) a time base that controls and synchronizes the process. This system provides an effective method for inducing Taylor's pulsed discharges in hydrogen with a peak to peak current up to 500 A and a duration up to 40 ms, at a rate of 2 pps within a pressure interval from $6x10^{-5}$ to $4x10^{-4}$ Torr. The instrumentation for the main discharge consists of the following parts: 1) five capacitor banks having the characteristics summarized in table I. 2) five energy sources for charging the capacitor banks. 3) a time base that synchronizes the secuence of discharge of the banks [3]. We have obtained tokamak discharges within a presure interval from $1x10^{-5}$ to $4.6x10^{-4}$ Torr (figure 3).

STUDY OF BREAKDOWN

As a result of the experimental study of breakdown in the Novillo Tokamak, it was shown that the presence of a stray vertical magnetic field from the toroidal coil makes the breakdown hard. The compensation of this stray field lead to better breakdown conditions and initial stability of tokamak discharges.

This work is being carried out wiht partial support from the IAEA under project MEX/1/015.

BANK	TOROIDAL	OHT		VERTICAL	
		FAST	SLOW	FAST	SLOW
Capacitance (mf)	0.0625	0.175	18	0.736	45
Voltage (kV)	18	12	1.7	1.7	0.25
Energy (J)	10125	12600	26010	1063	1406
Maximal Current (A)	1500	4197	6031	1006	1157
Inductance (mHy)	9	1.43	1.43	2.1	2.1
Current rise time (ms)	1.17	0.785	7.96	1.95	15
Decay time constant (ms)	31	17	17	20	20

TABLE I. MAIN PARAMETERS OF THE ENERGY SOURCES OF THE NOVILLO TOKAMAK.

REFERENCES

/1/ J. Ramos S. et al. Rev. Mex. de Fis 29 No. 4 (1983) 551-592.

/2/ R. valencia A. et al. ACONDICIONAMIENTO DE LA CAMARA DE VACIO DEL TOKAMAK NOVILLO. Sent to Rev. Mex. de Fis.

/3/ R. López C. et al. Rev. Mex. de Fis. 38, No. 2 (1992) 279-289.

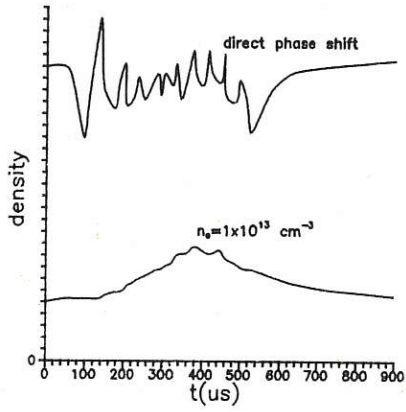

FIGURE 1. CURVES FROM THE REFLECTOMETER (ABOVE) AND THE INTERFEROMETER (BELOW)

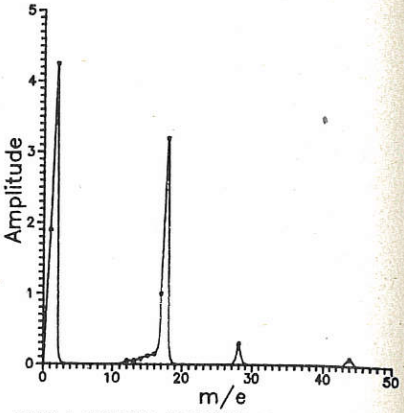

FIGURE 2. SPECTRUM OF RESIDUAL GAS IN NOVILLO TOKAMAK AFTER 48 HS TAYLOR DISCHARGES CONDITIONING. PRESSURE = 7.4x10^{-4}Torr.

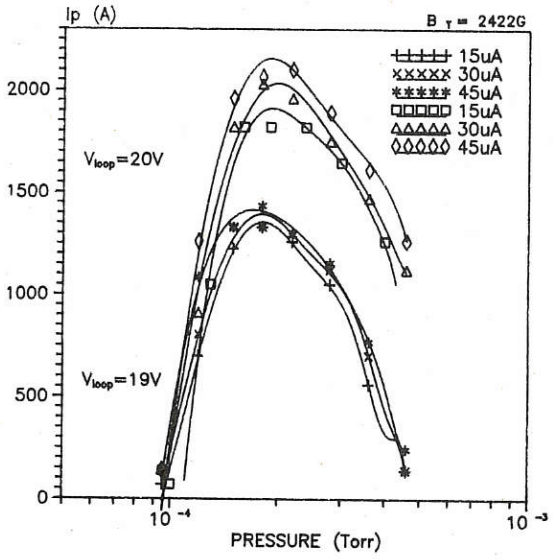

FIGURE 3. BREAKDOWN CURVES WITH TWO DIFFERENT OHT VOLTAGES FOR DIFFERENT PREIONIZATION CURRENTS

Topic 2:

Stellarators

Confinement Studies in Recent NBI Experiments of Heliotron E

F.Sano, K.Kondo, H.Zushi, S.Sudo[1], M.Sato[1], T.Mizuuchi, H.Matsuura[2], K.Hanatani, M.Nakasuga, H.Okada, S.Besshou, Y.Nakamura, K.Nagasaki, Y.Ijiri, M.Iima, T.Senju, K.Yaguchi, T.Baba, S.Kobayashi, K.Toshi, K.Sakamoto, M.Wakatani, T.Obiki

Plasma Physics Laboratory, Kyoto University, Uji, Japan
1) National Institute for Fusion Science, Nagoya, Japan
2) College of Engineering, University of Osaka Prefecture, Osaka, Japan

1. Introduction

The Heliotron-E vacuum magnetic field has the rotational transform ($0.52< \iota/2\pi <2.5$) sensitive to the low-mode perturbation field, and therefore one of the targets for the Heliotron-E plasma-confinement improvement was to explore the ways of the control of these potentially dangerous resonances in addition to the built-in strong magnetic shear as the countermeasure. A small toroidal field can add a shallow magnetic well which leads to a possible stabilization of inherent microinstabilities. The inward magnetic-axis shift can contribute to the restoration of the helical symmetry for its orbit control as well as to the increase in its magnetic shear. In connection with configuration control, this paper discusses the correlation between the vacuum magnetic-mapping results and the plasma-transport experiments[1] from the viewpoint of the quality of the magnetic-flux-surface structure. Furthermore, in order to investigate the transport behavior especially at the peripheral region, the material-limiter-inserted plasma characteristics were compared with those without limiter with special regard to the edge configuration control.

2. Vacuum magnetic surface mapping

In order to clarify the plasma confinement characteristics in Heliotron E, the full two-dimensional scan of the flux-surface mapping is particularly beneficial for the direct observation of the vacuum separatrix as well as the incidental islands topology. Concerning the desirability of the magnetic surface control, the key elements in this study were the effects of (i) the magnetic-axis shift, (ii) the applied toroidal field (the α^* effects), (iii) the superimposed perturbation field(e.g., by means of the m=1/n=1 island-formation coils), and (iv) the rail-type carbon-limiter insertion inside the separatrix. The performed surface mapping is based on the well-known "stellarator diode" method, but here we adopted the "directed electron beam" method rather than the conventional "emissive filament" method. One of the features of this method is the comparatively high reliability of determining the vacuum-magnetic-surface impedance independently of the electron-gun emission properties. The tiny electron gun could be scanned in steps of less than 1 (mm), horizontally and/or vertically, at the fixed toroidal angle(#5.5 port). The observed range of the vacuum impedance was on the order of 1-30 (MΩ) inside the determined separatrix under the DC 500 (G) main magnetic field, and therefore we could observe the $\iota/2\pi=1$ island that is vulnerable to the earth magnetic field. It is desired that these 2D-mapping results can furnish definite and reliable information about the high-field vacuum magnetic structure with predictable extrapolation as well as about the origins of the probable external error fields. Previous 1-D scan measurements[2-4] suggested the presence of a low- level magnetic braiding($\iota/2\pi>2$), an $\iota/2\pi=1$ island, etc. The present study deals with a more detailed 2D-topological analysis of the magnetic field structure. The location of the separatrix is one of the sensitive measures of the diagnostic accuracy when

compared with the numerical field-line tracing. The observed impedance-contour characteristics revealed the evident structure of the closed, nested magnetic-flux surfaces(more correctly, drift surfaces of the directed 15 eV electrons) inside the separatrix. Although the determined separatrix radius is slightly less than the original design value for the standard configuration, no apparent anomalies except for the $\iota/2\pi=1$ island due mainly to the earth magnetic field were seen in the core region within the present detection level. On the other hand, the detailed analysis of the ergodicity of the separatrix layer and of the presence of "natural" and/or "induced" magnetic islands at the edge as well as of their removal by the error-correcting fields will be of special importance. In this connection, the poisonous effect of the m=1/n=1 superimposed perturbation field (e.g., $B_{1,1}/B_0 = 6 \times 10^{-4}$) was studied in order to check the dynamic response of the magnetic lines of force as shown in Fig.1 together with the numerical prediction. The measured result was in general accordance with the prediction in terms of both the island phase topology and the island width. It was also confirmed that the α^* application can expand or shrink the separatrix radius dependently on its sign and that the determined magnetic axis can be shifted in accordance with the calculation. Moreover, the limiter insertion was found to modify the nested surface structure in terms of the corresponding connection length. Figure 2 shows the shrunk, closed impedance contours which were separated by the limiter head (inserted at $r_L/a_s=0.7$, where a_s is the plasma radius of the standard configuration) from the outer open contours (SOL) that were otherwise represented by the closed topology.

3. NBI transport experiments

The magnetic configuration studies of NBI plasmas should be based upon the above surface-mapping results with special reference to the observed topology of the corresponding confinement volume. The impedance contours in the limiter SOL can serve as a working model of the connection-length behavior there. For the normal standard configuration (natural divertor), on the other hand, the $\iota/2\pi=1$ island observed at $B_h=500$ (G) is expected to be diminished down to a few percent of the plasma radius at $B_h=1.9$ (T) [4], practically leading to no degradation of the global configuration quality in the high-field plasma experiments. For the NBI plasmas, it was already reported[5] that the global energy confinement scaling with respect to the plasma radius, a_p, is not contradictory with the a_p^2 scaling under the natural-divertor configurations where the plasma radius is varied ($0.7<(a_p/a_s)^2<1.2$) with the toroidal-field parameter, $\alpha^*=B_t/B_h$. For the carbon-limiter configurations, this size-scaling result could be checked out again in the much wider range of $0.4<(a_p/a_s)^2<1$ under the different boundary conditions. Here the dominant plasma-wall-interaction area is almost localized near the limiter head, which can be predicted from the mapping results of Fig.2. Experimentally, the limiter insertion drastically decreased the thermal load onto the vacuum chamber as well as the bolometric loss, CX-loss, $H\alpha/D\alpha$ emissions,etc. The thermal load onto the limiter, on the other hand, was found to reach almost 50% of the absorbed ECH/NBI power for the limiter plasmas. It was also confirmed that the plasma pressure was shrunk according to the insertion of the limiter inside the separatrix, but the definite degradation of energy confinement was not observed. To the first-order approximation, the natural-divertor and carbon-limiter experiments were mutually complementary as shown in Fig.3, and the results showed a greater confidence in expecting the a_p^2 dependence of the NBI plasma energy confinement under the assumption of unchanged loss-cone behavior. When assumed the a_p^2

scaling, the carbon-limiter NBI plasma confinement under the fixed radius a_p=15(cm) and the inward axis-shift Δ_v= -2 (cm) at B_h=1.9 (T) is enhanced by 40% as compared with the predicted standard scaling of τ_E^{fit}[1], as shown in Fig.4. This marked improvement is reflected also in the local power balance analysis. At the normalized radius of r/a_p=2/3, the local χ_e(cm^2/s) is found to decrease as compared with that of the without-limiter plasma when we take the Gyro-reduced Bohm type scaling as the reference. Another feature of the limiter plasmas is the reduction of the emission intensities due to heavy-impurity ions (Fe), suggesting the lowered impurity source rate originated from the reduced CX neutral particles. From the viewpoint of MHD activities, the limiter insertion could modify the pressure profile on the magnetic surfaces near the limiter head, generally leading to an increase in pressure gradient. Here the response to the MHD at the rational surface was marked, exciting the sawtooth and/or the burst-like fluctuations($\tilde{n}_e$, $\tilde{B}_\theta$, $\tilde{H\alpha}/\tilde{D\alpha}$, etc.) in the typical frequency range of 10(kHz). It was also shown that these activities could be effectively controlled with a shallow-well formation or with a magnetic-island application. Especially, the m=1/n=1 island application was confirmed to suppress the limiter-driven sawtooth through the decrease in pressure gradient at the $\iota/2\pi$=1 surface only with a small degradation of the confinement when the field-perturbation level was optimized.

4. Conclusion

The 2D-vacuum-magnetic-surface mapping was advantageous for the experimental understanding of the confinement behavior related to the configuration control of the NBI plasmas in Heliotron E. The low-field mapping results revealed the predictable nested surface structure and the separatrix topology which were in general accordance with the calculation. The detailed analysis of the probable error fields other than the earth magnetic field still remains, but the present method was found to have the potential for solving that problem. NBI transport experiments showed the a_p^2 dependence of τ_E in both the natural-divertor and carbon-limiter configurations. In the limiter plasmas, the inward-axis-shift confinement improvement was also obvious, accompanied with lowered local transport. In addition, it was conceivable that, contrary to the conditions of high magnetic shear, the effective radius of the plasma under the outward-axis-shift and very-low-shear conditions was significantly reduced even when a low-level perturbation field was superimposed. As a result, to obtain the robust edge structure, it was suggested that the reduction of the island structure as well as stochastic region at the periphery (produced not only by unavoidable fabrication errors but also toroidal effects) can be the next target for improving the confinement from the viewpoint of configuration studies, which will also contribute to the investigation of plasma-β effects.

/1/ F.Sano et al., Nucl.Fusion 30(1990)81.
/2/ T.Obiki et al., Plasma Physics and Controlled Nuclear Fusion Research 1990, Vol.2(IAEA,Vienna,1991), p.425.
/3/ R.Takahashi et al., Jpn.J.Appl.Phys. 28(1989)2604.
/4/ T.Mizuuchi et al., J.Nucl.Mater. 176-177(1990)1070.
/5/ F.Sano et al., 1st Intern. TOKI Conference on Plasma Physics and Controlled Nuclear Fusion Research 1989, NIFS-PROC-3,p.192.

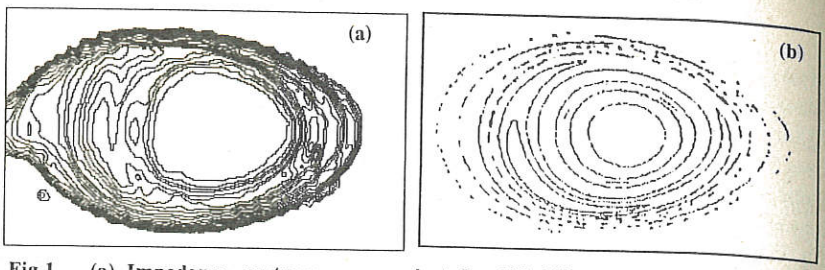

Fig.1 (a) Impedance contours measured at Bh=500 [G] when the m=1/n=1 perturbation field ($B_{1,1}/B_0=6\times10^{-4}$) was superimposed in order to study its dynamic response to the surface structure.
(b) Numerical field-line tracing in the same situation as that of (a). The agreement between these two results is globally good.

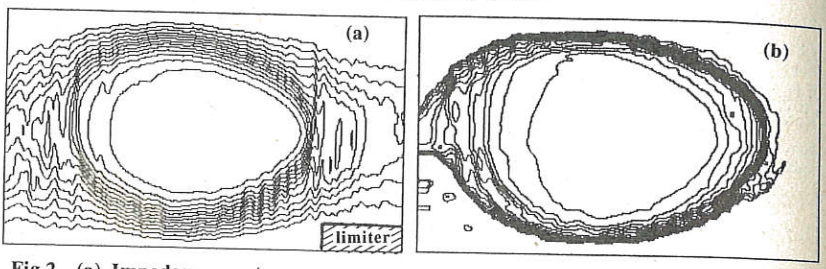

Fig.2 (a) Impedance contours measured at Bh=500 [G] when the carbon limiter was inserted at $r_L/a_s=0.7$ in order to study the resulting modification of the edge structure.
(b) Impedance contours measured at Bh=500 [G] for the standard natural-divertor configuration. The observed $\iota/2\pi=1$ island can be reduced materially in the high-field plasmas.

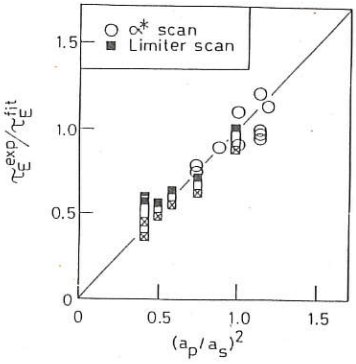

Fig.3 Global energy confinement scaling as a function of a_p^2 in NBI experiment under the α*- and limiter- scan experiments.

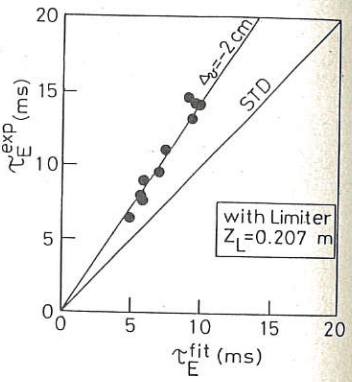

Fig.4 Improvement of the global energy confinement at Δv=-2 (cm) with limiter plasmas.

ELECTRON HEAT TRANSPORT IN THE LMFP-REGIME FOR THE STELLARATORS W7-A, W7-AS AND L2

K.S. Dyabilin*, U. Gasparino, H. Maaßberg, H. Renner, H. Ringler
W7-AS Team† and ECRH Group†
Max-Planck Institut für Plasmaphysik
Association EURATOM-IPP, D-8046 Garching, Germany
* General Physics Institute, Moscow, Russia

Introduction

The reduction of the neoclassical transport losses in the long mean free path (LMFP) collisionality regime ($1/\nu$-regime) is an essential part of the configurational optimization of future stellarator experiments /1/. Whereas the neoclassical transport reduction within the plateau collisionality regime is mainly important for ions (the anomalous electron transport is expected to dominate here), the diffusion of electrons trapped in local magnetic field ripples in the LMFP regime can degrade the global confinement properties. Within the optimization concept of general stellarator configurations some degrees of freedom exist in the mixture of the main Fourier harmonics of $|B|$ on flux surfaces which determine the neoclassical transport properties.

So far, however, no comparative analysis of the experimental transport properties in the LMFP-regime for different stellarator configurations is available. In this paper we compare the electron heat conduction in low density ECRH discharges with highly peaked T_e profiles found in the stellarators W7-A, L2 and W7-AS. This type of discharges is best candidate for the analysis of the electron heat transport. For these conditions, the global energy balance is mainly determined by the electron heat transport, radiative losses and collisional power transfer to the ions are small. The ECRH power deposition for launching from the low field side is found to be highly localized consistent with ray-tracing calculations. The analysis is based on measured profiles of electron density and temperature.

Magnetic Configurations

L2 in Moscow ($R \simeq 1$ m, $a < 13$ cm, $B = 1.34$ T) is a classical stellarator with a very large helical ripple (up to 20%). W7-A in Garching ($R = 2$ m, $a < 9$ cm), the predecessor of W7-AS, was a classical stellarator with very small field ripples (less than 2.5%) and W7-AS is partly optimized (Advanced Stellarator) with modular coils. In W7-AS ($R = 2$ m, $a < 18$ cm), being a rather flexible system, quite different magnetic configurations can be realized, they have all a very complex magnetic field topology (high number of Fourier harmonics in $|B|$ on flux surfaces). While the W7 stellarators are characterized by rather low shear, L2 has a moderate one. The fraction of ripple trapped particles as well as the averaged radial drift are quite different.

In Fig. 1, the $|B|$-contours for L2 and two W7-AS configurations at about $0.4 \cdot a$ are shown. For L2, the (2,1) component (poloidal and toroidal mode number) is dominant additional to the curvature term (1,0). The W7-A configuration is quite similar, only the amplitude is much smaller: in W7-A, the (1,1) component is the dominant one.

---

† for the teams see H.J. Hartfuß; this conference

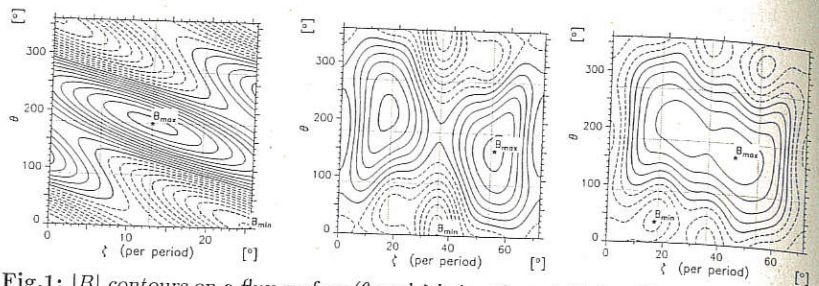

Fig.1: *$|B|$ contours on a flux surface (θ and ζ being the poloidal and toroidal magnetic coordinates) of L2 (left plot, $r = 6$ cm effective radius) and W7-AS at $\iota \simeq 0.31$, $r = 7.5$ cm for standard configuration (central plot) and increased current in the larger special coils (by 18%, right plot).*

The two W7-AS configurations of Fig. 1 at the same $\iota \simeq 0.3$ differ in the ratio of the currents in the larger special coils and the modular coil compound. The W7-AS3 configuration which is the standard case (central plot) has series connection of the main toroidal field system while in the W7-AS31 configuration (right plot), the current in the larger special coils is increased by 18%. The dominant components, (1,0), (0,1) and (1,1) are nearly identical for both configurations, however, the higher harmonics are reduced in the W7-AS31 configuration (comp. also Fig. 4). Comparable flexibility in the W7-AS configurations is also obtained by applying an additional B_z-field. A rather large number of $|B|$ Fourier harmonics is necessary to describe the neoclassical transport properties in W7-AS correctly. This is done by using the DKES code (/2/) which calculates the full neoclassical transport matrix. The experimental results of the electron heat transport analysis in the three devices are compared with the neoclassical predictions.

Transport Analysis

We solve the electron energy balance with the usual ansatz $-n_e \cdot \chi_e^{\exp} \cdot T_e'$ for the electron heat flux. A parametrized $\chi_e^{\exp}$ profile is estimated by a least-squares fit of T_e obtained from the energy balance to the experimental data measured by Thomson scattering. Some uncertainty for the innermost part of the $\chi_e^{\exp}$ profile is introduced by rather large errors in the central T_e' and the very narrow profile of the ECRH power deposition which is modelled corresponding to ray-tracing calculations. The error bars in the $\chi_e^{\exp}$ profiles (solid lines in Figures 2 and 3) are obtained by error analysis (functional variance) of the least-squares fits. The $\chi_e^{\exp}$ profiles are compared to the neoclassical predictions for the electron heat diffusivity (the transport matrix element related to T_e'), convective terms (related to n_e' and to E_r) are disregarded. DKES code results (dot-dashed lines) and the axisymmetric contribution (dotted lines) are calculated with constant Z_{eff} (no profiles available). In the LMFP collisionality regime, the neoclassical transport coefficients depend on the radial electric field, E_r. For the highly peaked T_e profiles with $T_e \gg T_i$, the "electron root" (solution of the ambipolarity condition of the particle fluxes with $E_r > 0$ and scaling with T_e) can exist which reduces significantly the electron transport coefficients in the $1/\nu$-regime. In this comparison of the different

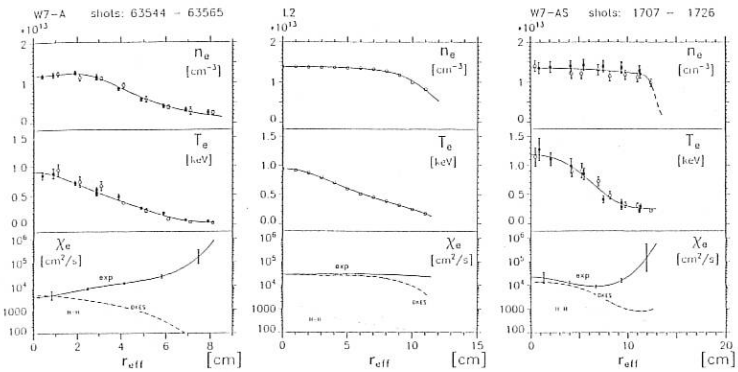

Fig. 2: *Transport analysis for comparable ECRH discharges in W7-A (left plot, $\iota_a = 0.52$, $B = 1.27$ T, $P_{abs} \simeq 120$ kW), in L2 (central plot, $B = 1.34$ T, $P_{abs} \simeq 140$ kW; the dots do not represent original n_e and T_e measurements) and in W7-AS (right plot, standard configuration, $\iota_a \simeq 0.53$, $B = 1.26$ T, $P_{abs} \simeq 200$ kW)*

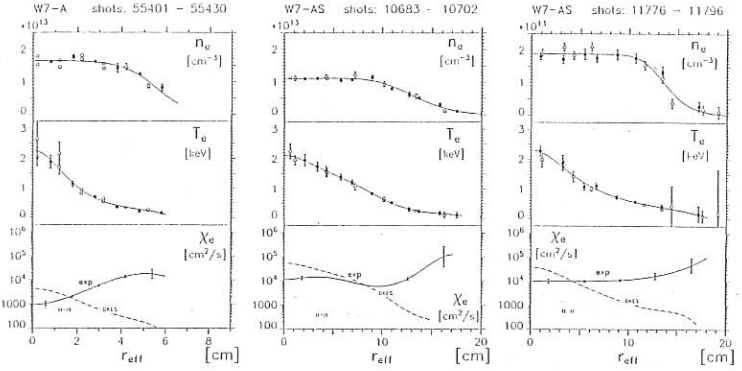

Fig. 3: *Transport analysis for comparable ECRH discharges in W7-A (left plot, $\iota_a = 0.48$, $B = 2.55$ T, $P_{abs} \simeq 175$ kW) and in W7-AS standard configuration at $B = 2.57$ T, $\iota_a \simeq 0.34$, (in the middle: $P_{abs} \simeq 150$ kW and on the right: $P_{abs} \simeq 290$ kW)*

configurations, however, we calculate χ_e^{neo} with $E_r = 0$ which leads to an upper estimate of the neoclassical heat losses. The configurational dependence of the transport properties in the LMFP regime is characterized by an equivalent "effective ripple", $\langle \epsilon_h \rangle$ (see Fig. 4), by fitting the DKES results to an analytical model /4/. In general, $\langle \epsilon_h \rangle$ is not directly related to the main helical Fourier component of $|B|$.

In Fig. 2, we compare ECRH discharges at low power level for W7-A, L2 and W7-AS. Both the magnetic field strength (≈ 1.3 T) and the densities are very similar. In the W7-A example, χ_e^{exp} is much larger than χ_e^{neo} in the main part of the plasma. For the L2

discharge, the DKES result fits quite well to χ_e^{exp}. At outer radii the expected decrease in χ_e^{neo} being related to lower T_e and higher collisionality ν_e^* is completely compensated by the strongly increasing $\langle \epsilon_h \rangle$ (see Fig. 4). Contrary to W7-A, for the L2 stellarator χ_e^{neo} is much larger than the axisymmetric part. In the W7-AS case, the central χ_e^{exp} is close to the neoclassical one, but much larger at outer radii, similar to W7-A. The discharges shown im Fig. 3 have quite similar central electron temperatures, but differ in density and heating power. For the high T_e at full field (2.5 T), the neoclassical prediction exceeds χ_e^{exp} in the central part. The extremely peaked T_e profile in the W7-A case leads to very small χ_e^{exp} (rather close to the low neoclassical plateau value) For the W7-AS discharges, the χ_e^{exp} are comparable while the DKES results show significant differences. Both discharges have equivalent energy confinement times (τ_E depends on the ratio n_e/P_{abs} /4/ being very similar). All these low density ECRH discharges show electron heat diffusivities rather close the neoclassical predictions in the central region. These losses in the LMFP-regime are dominated by the radial drift of ripple trapped particles (contrary to the tokamak "banana" regime) leading to a very strong unfavourable T_e-dependence in the neoclassical transport coefficients. The resulting limitation of the achievable central electron temperature is roughly consistent with the experimental findings.

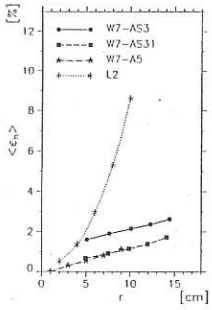

Fig.4: *Effective ripple, $\langle \epsilon_h \rangle$, obtained by fitting DKES results in LMFP regime by an analytical model /3/ for W7-AS at $\iota \simeq 0.31$ (W7-AS3 and W7-AS31), W7-A at $\iota \simeq 0.51$ (W7-A5) and L2 configurations (comp. Fig. 1).*

Conclusions

The comparative analysis of low density ECRH discharges in W7-A, L2 and W7-AS shows that the neoclassical transport in the unfavourable $1/\nu$ regime is consistent with the experimental results in the central region. The quite different neoclassical properties characterized by $\langle \epsilon_h \rangle$ are shown in Fig. 4. Neoclassical transport in the LMFP regime is minimum in W7-A and maximum in L2, the W7-AS standard configurations are in between. These results are in reasonable agreement with the analysis of the experimental electron energy balance showing an analogous relation for χ_e^{exp} in the central region. In W7-AS, field configurations can be realized with neoclassical confinement properties as good as in W7-A according to reduced amplitudes of the higher field harmonics.

References

/1/ C. Beidler et al.; Fusion Technology, **17** (1990), 148

/2/ W.I. van Rij and S.P. Hirshman; Phys. Fluids B, **1** (1989), 563

/3/ K.C. Shaing et al.; Plasma Phys. and Contr. Nucl. Fus. Res. (1985), **2**, 189

/4/ H. Renner et al.; Plasma Phys. and Contr. Nucl. Fus. Res. (1991), **2**, 439

DIFFUSIVE AND CONVECTIVE TRANSPORT MODELLING FROM ANALYSIS OF ECRH-STIMULATED ELECTRON HEAT WAVE PROPAGATION

V. Erckmann, U. Gasparino, L. Giannone,
H.J. Hartfuß, H. Maaßberg, M. Tutter,
W7-AS Team†, IPF-ECRH Group† and KFK-Gyrotron Group‡
Max-Planck Institut für Plasmaphysik
Association EURATOM-IPP, D-8046 Garching, Germany

Introduction

ECRH power modulation experiments in toroidal devices offer the chance to analyze the electron heat transport more conclusively: the electron heat wave propagation can be observed by ECE (or SX) leading to radial profiles of electron temperature modulation amplitude and time delay (phase shift). Taking also the stationary power balance into account, the local electron heat transport can be modelled by a combination of diffusive and convective transport terms. This method is applied to ECRH discharges in the W7-AS stellarator ($B = 2.5$ T, $R = 2$ m, $a \leq 18$ cm) where the ECRH power deposition is highly localized.

In W7-AS, the T_e modulation profiles measured by a high resolution ECE system are the basis for the local transport analysis (see /1/). As experimental errors limit the separation of diffusive and convective terms in the electron heat transport for central power deposition, also ECRH power modulation experiments with off-axis deposition and inward heat wave propagation were performed (with 70 GHz o-mode as well as with 140 GHz x-mode for increased absorption). Because collisional electron-ion coupling and radiative losses are only small, low density ECRH discharges are best canditates for estimating the electron heat flux from power balance.

Transport Modelling

For ECRH power modulation (ΔP_{ECRH} typically less than 10%), the time dependent electron energy balance is linearized with respect to the electron temperature modulation, $\tilde{T}_e$, and Fourier transformed for the m different harmonics of the modulation frequency, f_{mod} (square wave ECRH power modulation). The linearisation was confirmed by amplitude scans of the modulated power, $\tilde{P}_{\mathrm{ECRH}}$, and by the fact that only odd harmonics of the modulation frequency were found. A modulation of density and ion temperature is neglected.

$$\frac{3}{2} i m \omega n_e \tilde{T}_e + \frac{1}{r} \frac{d}{dr} r \tilde{q}_e = \tilde{P}_{\mathrm{ECRH}} + \tilde{P}_{\mathrm{ei}} + \tilde{P}_{\mathrm{rad}}$$

with $\omega = 2\pi f_{\mathrm{mod}}$, $\tilde{P}_{\mathrm{ei}}$ and $\tilde{P}_{\mathrm{rad}}$ being the Taylor expansions with respect to $\tilde{T}_e$ of the collisional power transfer and the radiative loss, respectively. The linearized diffusive ansatz for the electron heat flux is used: $\tilde{q}_e = -n_e\{\bar{\chi}_e \tilde{T}_e' + \tilde{\chi}_e \bar{T}_e' - \bar{v}_e \tilde{T}_e\}$, where $\bar{\chi}_e$ and $\bar{v}_e$ being the stationary heat diffusivity and convection velocity, respectively. For the

† for the teams see H.J. Hartfuß; this conference

‡ G. Dammertz, G. Gantenbein, T. Geist, M. Kuntze, H.U. Nickel, B. Pioszyk and M. Thumm

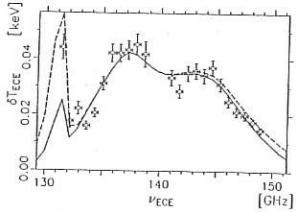

Fig.1: *Asymmetry in the ECE simulation arising from a symmetric (with respect to the effective radius) T_e-modulation in presence of strong $\bar{T}_e'$ versus the ECE frequency. The dashed line reflects the effect of multiple wall reflections, measured ECE (x-mode 2nd harmonic) data are also shown.*

modulation of the heat diffusivity, $\tilde{\chi}_e$, the ansatz $\chi_e \propto T_e^\alpha$ is used (e.g., $\alpha = \frac{3}{2}$ for the neoclassical plateau dependence). The *1st* order electron heat flux can be written in the form

$$\tilde{q}_e = -n_e\{\bar{\chi}_e \cdot \tilde{T}_e' - (\bar{v}_e - \alpha\bar{\chi}_e\frac{\bar{T}_e'}{\bar{T}_e}) \cdot \tilde{T}_e\}.$$

On the other hand, an assumed dependence of χ_e on T_e' leads in the linearization only to a modification of $\bar{\chi}_e$. E.g., the ansatz $\chi_e \propto (T_e')^\beta$ increases $\bar{\chi}_e$ by a factor of $1+\beta$. Consequently, the comparison of $\bar{\chi}_e$ from the heat wave propagation analysis with χ_e^{pb} from the stationary power balance may allow a conclusion on the T_e' dependence of χ_e. A modulation of the convection velocity, $\tilde{v}_e$, is disregarded in this paper. The linearized power balance equations for the m harmonics of f_{mod} are solved numerically by a standard complex difference scheme. The least-squares fit of the resultant amplitudes, $|\tilde{T}_e|$, and time delays, Δt, to the experimental data obtained from the cross-correlation of the ECE channels with the ECRH power modulation results in the profiles of $\bar{\chi}_e$ and $\bar{v}_e$. Within the fit, polynomials are used to represent these profiles (the polynomial coefficients being the fit parameters).

Experimental Results

The analysis of the electron heat wave propagation is a very sensitive tool for local transport investigations depending on the reliability of the basic assumptions as well as on the quality of the measured $|\tilde{T}_e|$ and Δt. The $\tilde{P}_{\mathrm{ECRH}}$ profile can be deduced directly from the measured $\tilde{T}_e$ profile for high modulation frequencies ($f_{\mathrm{mod}} \geq 5$ kHz, depending on the requested spatial resolution). At these frequencies, the transport term in the electron energy balance is of minor importance. As no direct measurements of $\tilde{P}_{\mathrm{ECRH}}$ are available so far, the results of ray-tracing calculations are used which are based on absorption coefficients for Maxwellian distribution functions. The absorption turned out to be well above 90%. A suprathermal electron component is indicated in discharges with high local ECRH power densities for central deposition at low electron densities. The relativistically down-shifted emission from these suprathermal populations is located within the ECRH power deposition profile and can be detected in the low frequency channels (for low field observation: the outer part of the spectrum with respect to the major radius) of the stationary ECE temperature profile where the plasma becomes optically thin. Low frequency ECE channels which are affected by suprathermal emission are excluded in the analysis of the heat wave propagation.

The $|\tilde{T}_e|$-profiles obtained from the ECE measurements on the inner and outer part of profile (at high and low frequencies) are generally not symmetric. For the experimental conditions, however, the parallel heat conduction is much too high to allow significant temperature gradients on flux surfaces. The modulation experiments with off-axis power

deposition show significantly higher $|\tilde{T}_e|$ on the outer part of the profile. Fig. 1 shows a simulation of the ECE temperature modulation for off-axis modulated ECRH power deposition (at $r \simeq 6$ cm with 140 GHz) within a discharge heated by 3 gyrotrons (70 GHz with central deposition) and with highly peaked electron temperature ($T_e(0) \simeq 3.2$ keV). A $\tilde{T}_e$ profile symmetric in the effective radius, r, was assumed resulting in an asymmetry of about ± 4 eV. In modulated on-axis power deposition experiments, the outer $\tilde{T}_e$ are also higher. The power measured within a frequency channel of the ECE radiometer is determined by the highly non-linear balance of local emission and re-absorption. The presence of strong stationary electron temperature gradients can lead to a small asymmetry in the $\tilde{T}_e$ profiles (see /2/). Furthermore, the modulation of the Shafranov shift must be taken into account in case of strong $\bar{T}_e'$. In phase with the heat wave propagation, an additional Shafranov shift of about 0.03 cm (for a stationary $\beta_e(0) \simeq 0.3\%$) and a $\bar{T}_e'$ of up to -350 eV/cm leads to an increase of the outer $|\tilde{T}_e|$ of up to 10 eV (correspondingly, the inner $|\tilde{T}_e|$ are decreased). This β-modulation effect is maximum in the innermost region for central deposition.

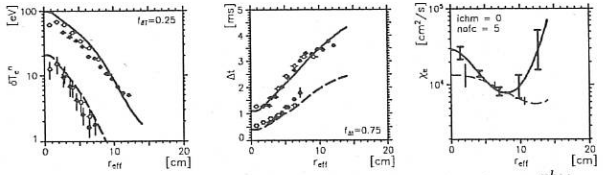

Fig. 2: *Electron heat diffusivity, $\bar{\chi}_e$ (solid line in the right plot; χ_e^{pb} from stationary power balance is given by the dashed line) obtained from fit of $|\tilde{T}_e|$ and Δt to experimental data for the fundamental (solid lines) and the 3rd harmonic (dashed lines) of the ECRH modulation frequency ($f_{\mathrm{mod}} = 92$ Hz at 70 GHz). $\alpha = 0$ and $\bar{v}_e = 0$ is assumed, 5 fit-parameters are used for the $\bar{\chi}_e(r)$ representation.*

In Fig. 2, the transport analysis for a discharge with $T_e(0) = 1.8$ keV and $n_e(0) \simeq 2.4 \cdot 10^{13}$ cm^{-3} heated with 2 gyrotrons ($P_{\mathrm{ECRH}} = 270$ kW with central deposition) is shown. For these discharges, the experimental evaluation of the electron heat wave propagation is rather good. For this example, only diffusive transport ($\bar{v}_e = 0$) and no dependence of χ_e on T_e ($\tilde{\chi}_e = 0$) are assumed. The fit of the simulated $|\tilde{T}_e|$ (left plot) and Δt (central plot) to the experimental data simultaneously for the fundamental and the 3rd harmonic of f_{mod} yields the $\bar{\chi}_e$-profile (solid line in the right plot) which exceeds the one from stationary power balance, χ_e^{pb} (dashed line), in the innermost and the outer region. The fit can be improved in the simulation if the absorbed ECRH power is slightly reduced ($\approx 70\%$). Taking the $\tilde{\chi}_e$-term in $\tilde{q}_e$ into account, the slope of the $|\tilde{T}_e|$ profile steepens and $\bar{\chi}_e(r)$ increases with α. Including a convective transport term ($\bar{v}_e \neq 0$) leads to an increased heat diffusivity and an additional inward heat pinch in this case, however, the fit quality remains similar. In general, the correlation between the convective term and the diffusive term is rather large.

A more complex example is shown in Fig. 3. These discharges at rather low density ($n_e(0) \simeq 2.4 \cdot 10^{13}$ cm^{-3}) heated with 3 gyrotrons at 70 GHz ($P_{\mathrm{ECRH}} = 510$ kW with central deposition) have highly peaked electron temperatures $T_e(0) \simeq 3.2$ keV (see also Fig. 1). In this example, the heat wave was generated by an additional 140 GHz gyroton ($P_{\mathrm{ECRH}} \simeq 30$ kW) with central deposition. Both diffusive and convective

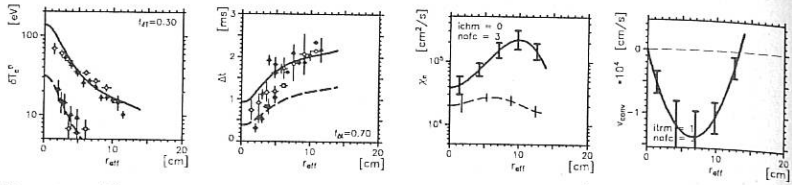

Fig. 3: *Electron heat diffusivity, $\bar{\chi}_e$, and convection velocity, $\bar{v}_e$ (f_{mod} = 69 Hz at 140 GHz with central deposition, comp. Fig. 2). $\alpha = 0$ is assumed, altogether 5 fit parameters are used for both the $\bar{\chi}_e(r)$ and $\bar{v}_e(r)$ profiles.*

transport terms are included in the least-squares fit, only the $\tilde{\chi}_e$ term was omitted ($\alpha = 0$) resulting in a rather high heat diffusion ($\bar{\chi}_e \gg \chi_e^{pb}$) compensated by an inward heat pinch ($\bar{v}_e < 0$). The quality of the fit is only moderate, no improvement is obtained including $\tilde{\chi}_e$ terms in the analysis. Omitting the convective inward term, however, leads to $\bar{\chi}_e(r)$ values being a factor of 3 to 5 larger than those from stationary power balance, χ_e^{pb} (dashed line) with much lower fit quality (the slope of $|\tilde{T}_e|$ is not reproduced). The stationary heat flux related to these $\bar{\chi}_e$ and $\bar{v}_e$ profiles are in full contradiction to the stationary power balance. Off-axis deposition experiments with 140 GHz power modulation in equivalent discharges were performed showing rather strong asymmetries in $|\tilde{T}_e|$ (with large scatter of the experimental data). Here, no significant convection term was obtained by the fitting. These findings indicate that these evaluations are very critical for this type of discharges.

Summary and Conclusions

The electron heat flux modelled by both diffusive and convective transport terms is estimated by least-squares fits of simulated heat wave propagation to the electron temperature modulation amplitude and time delay. Profiles of the heat diffusivity and the convection velocity are obtained. The dependence of these local transport coefficients on local plasma parameters (e.g. T_e or T_e' in the diffusivity χ_e) can be analyzed. This procedure is applied to ECRH power modulation experiments in the W7-AS stellarator where the heat wave propagation is analyzed by ECE measurements. The interpretation of the ECE measurements, however, is rather complex even if effects related to suprathermal emission and wall reflection in the region where the plasma is optically thick seem to be negligible. The reliability of the heat wave propagation analysis and the transport modelling depends sensitively on the accuracy of the experimental data as well as on the validity of the basic assumptions. An independent estimation of the ECRH power deposition profile by high frequency ECRH power modulation experiments is advisable. Together with the stationary power balance, the analysis of ECRH-stimulated electron heat wave propagation seems to be a powerful tool to get more informations on the anomalous electron transport.

/1/ L. Giannone et al.; submitted to Nucl. Fus. (1992)

/2/ W.H.M. Clark; Chap. 2.4, Plasma Phys. (1983), **25**, 1501

Towards higher ß in the Stellarator Wendelstein W 7AS.

Renner H., Ringler H., Kisslinger J., Kühner G. and the W7AS-team*, NBI-group**
Max-Planck Institut für Plasmaphysik, Association EURATOM-IPP, D-8046 Garching, Germany F.R.
ECRH Group***, Institut für Plasmaforschung der Universität Stuttgart, D-7000 Stuttgart, Germany F.R.

Introduction

The W 7AS stellarator (R = 2m, a ≤ 0.18m; modular coils: 5 periods) as the first representative of the line of "Advanced Stellarator" is being operated since summer 1988 / 1, 2, 3 /. W 7AS has been constructed as a partly optimized device to follow the conventional stellarator W 7A. The optimization applied to W 7AS leads to an improvement of the equilibrium by the reduction of the PS-currents compared to the conventional stellarator by a factor of 2. The equipment for plasma generation and heating includes ECRF (electron cyclotron heating: 4 gyrotrons at 70 GHz with 200 kW each), NBI (neutral beam injection heating: balanced tangential injection with 1.5 MW), ICRF (ion cyclotron heating: "experimental antenna" with 1 MW). Usually a currentless plasma is produced by ECRF using the second harmonic scenario at 1.25 T with a cut-off density of $3\ 10^{19}m^{-3}$, or the fundamental heating scenario up to densities of $6\ 10^{19}m^{-3}$ at the main field 2.5 T. The plasma generated by ECRF is used as a target plasma for NBI heating. A startup scenario down to a magnetic field of 0.6 T using ICRF was also successful and allows operation away from particular resonant values of the magnetic field. During NBI heating under good confinement conditions, fed by the particle flux, the density is steadily growing and exceeds the cut-off densities of ECRF application. Restricted by radiative collapse maximum densities up to $3\ 10^{20}m^{-3}$ were obtained. The high ß values are almost entirely a consequence of the increased electron density. Wall conditioning by carbonization and boronization reduced the impurity concentration and opened the way to high densities / 4, 5 /.

Configurational effects

Due to perturbations of the equilibrium, similar to the W 7A stellarator, the global confinement in W 7AS depends strongly on the edge value of the rotational transform, ι(a), and the total ι(r) profile. For the low-shear stellarator W 7AS a degradation of both energy and particle confinement is found for low-order rational values of the rotational transform and values of 5/n corresponding to "natural islands" related to the particular magnetic configuration. This behaviour may be explained by the formation of extended islands and ergodic regions at the position of resonant magnetic surfaces within the plasma volume. Field perturbations at the plasma edge are seen to reduce the particle confinement and deteriorate the energy confinement by shrinking the electron temperature profiles. For good confinement, away from rationals, the control of the boundary value of the rotational transform counteracting the effect of plasma currents stemming from finite ß conditions or associated to transport (bootstrap current) is essential to establish quasistationary conditions. By means of current control either by small loop voltages, ECRF current drive or unbalanced beam injection optimum confinement can be achieved. Generally, the influence on the confinement can be minimized by introducing moderate shear. The profile of the transform becomes modified by the secondary currents (Fig.1).

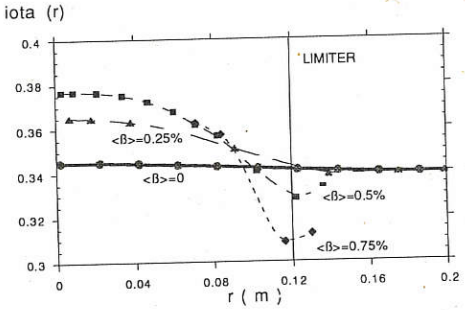

Fig.1: Plasma pressure effects on iota profiles at ι(a)=0.34. KW-code calculations / 7 / with parameter <β>, β0/<β>=2. Plasma radius a=0.12m restricted by limiter.

In addition net-currents up to 5 kA, as confirmed by theoretical calculations as bootstrap currents for parameters of W 7AS, have to be included in case of high temperature plasmas. Under these conditions, due to the different current density profiles the compensation of the bootstrap current leads to positive shear , where "resonances" always exist inside the plasma. Such perturbations are indicated by localized fluctuations as detected by means of magnetic probes, ECE-, soft X -measurements and reflectometry. In the low-shear stellarator optimum confinement in low collisionality ($10^{-3} \leq \nu^* \leq 10^{-2}$) discharges is obtained for values of the rotational transform ι(a) in the vicinity of 1/3, 1/2, 2/3.
Proceeding to higher ß and densities, respectively for NBI discharges, the strong dependence of confinement on the boundary value of the transform becomes partly smoothed out / 6 /. Fig.2 demonstrates this behaviour for a set of discharges at rotational transform around 1/2. The plasma current needs not to be controlled and remains below a value of 1 kA.

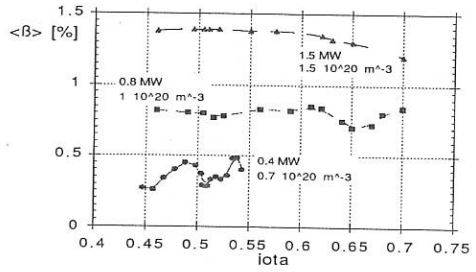

Fig.2: Averaged <ß> values depending on the rotational transform at the boundary ι(a): experimental data for varying input power and density. The plasma radius is fixed by limiter to a=0.11m. Magnetic Field B_0 = 1.25 T.
NBI: H^0 / D_2-plasma.

With increasing <ß> significant shear is introduced at the boundary (Fig.1), where steep pressure gradients are localized. The effect of the bootstrap current and Ohkawa currents is only small due to the low temperatures. Under these conditions the introduced negative shear narrows the perturbed regions and the effect on the confinement becomes less pronounced. Additionally, with increasing collisionalities ($\nu^* > 10^{-1}$) island formation and ergodization should play a minor role for the heat transport. Depending on the connection length for particular values of the rotational transform electron parallel transport losses scale down and become comparable to the perpendicular anomalous losses. At the lower electron temperatures and the significantly broader ion temperature profiles the ion heat conduction and charge exchange losses become important for the energy balance. Cooling at the boundary by gas puffing or formation of radiative boundary layers seem also beneficial to reduce configurational effects on the confinement and may indicate a rather complicated influence of atomic processes for the 3D structure of the plasma boundary at W 7AS / 5 /. In this context the generation of radial electric fields may also play a role for the different behaviour.

Plasma parameters

The plasma density appears to be the most significant parameter to enhance the energy replacement time and to proceed to high ß values. Remarkably, the global confinement of ECRF and NBI heated discharges in W 7AS is rather good described by the Lackner-Gottardi-scaling as derived for tokamaks / 7 /. To apply this scaling to net-currentfree operation in a stellarator, the plasma current has to be replaced by the rotational transform: $\tau_{E,LG}$ [s] $= 0.17 * R * a^2 * B^{0.8} * \iota^{0.4} * (n/P)^{0.6}$ with major radius R [m], plasma radius a [m], ι rotational transform, av. density n [10^{20} m^{-3}] and input power P [MW]. The parameter range covered includes ECRF-plasmas at low collisionality $\nu^* \geq 10^{-3}$ with central electron temperatures up to 3 keV where electron heat transport is dominating and towards higher densities in NBI-plasmas, $\nu^* \geq 10^{-1}$ with T_i and $T_e \sim 0.2$- 0.4 keV. Here the electrons and ions are stronger coupled and the ion heat conduction becomes important. Due to the scaling with density n and power P the highest value for the energy replacement time is obtained for high values of n/P. For ECRF-discharges a maximum energy confinement of 40 ms is achieved operating close to $n_{cut\text{-}off} = 6\ 10^{19}$ m^{-3} for 70 GHz and lowering the input power. Maximum plasma pressure <ß> can be realized under conditions of a high product n*P (Fig.3). Increasing the density the plasma becomes terminated by a radiative collapse starting with temperature reduction in the core. The achievable density grows almost proportional to the input power. The reduction of impurities and radiative losses by different measures as applied in W 7AS have improved the plasma parameters significantly by increasing density. Under clean

conditions maximum densities of 3 10^{20} m^{-3} were obtained at temperatures $T_e=T_i \geq 0.2$ keV (τ_E still being ≈ 30ms) with NBI-heating of 1.5 MW.

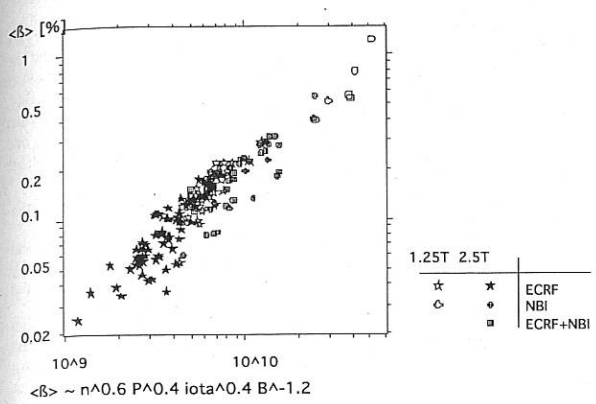

Fig.3: Averaged <ß> versus $n^{0.6}p^{0.4}{}_{iota}{}^{0.4}B^{-1.2}$ based on the LG-scaling (density n [cm^{-3}], input power P [W], magnetic field B [T]). Experimental data documented by profile measurements.

Based on theoretical studies of equilibrium and stability limits of <ß> at about 2% are expected. So far within the operational range up to <ß> values of 1.4 % (at 1.25T) no limitations by MHD instabilities have been observed for the heating power available at present. At low rotational transform a significant Shafranov shift of ca. 5 cm is observed and needs to be compensated by vertical fields depending on the pressure to prevent plasma wall interaction and impurity recycling. Note, for a constant ratio n/P the energy replacement time can be saved at a high level even for increasing input power. The possibility of high density operation, especially with high densities at the boundary, is important for save power and particle exhaust in large devices. The density range in W 7AS exceeds that of an equivalent tokamak and a formal Murakami parameter of M=n*R/B ≈ 20 [$10^{19}m^{-2}T^{-1}$), with averaged density n , major radius R and main field B , is calculated.

Magnetic flux measurements

On the way to the "advanced stellarator", W 7AS is the first representative one with a reduction of the PS-currents by a factor of 2. The evalution of the displacement of the plasma column on the basis of soft-X data has already indicated the expected reduction of the Shafranov shift / 4 /.

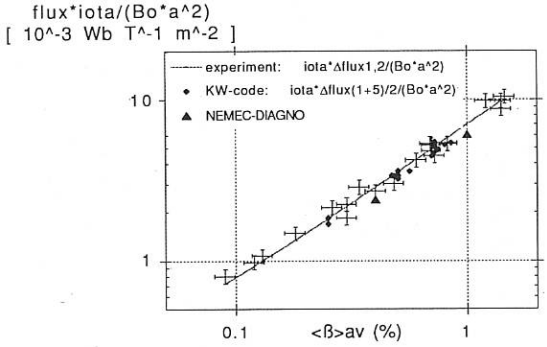

Fig.4: Comparison of experimental data and theoretical results based on equilibrium codes: KW-code, NEMEC-DIAGNO. Normalized values of the flux are related to averaged <ß> values.

Using external loops the vertical field components related to the secondary currents for finite ß plasmas can be directly measured and compared to theoretical predictions. Theoretical data for changes of magnetic flux depending on the plasma pressure have been calculated using the KW-code / 8 / and the NEMEC/DIAGNO-code / 9 / both for the diamagnetic loops and the flux loops.

To determinine the energy content of the W 7AS plasmas two approaches are possible: (1) For the flux loops, which are installed at the surface of the vacuum vessel, an almost linear relation of the flux and the plasma pressure was found rather weakly dependend on pressure profiles and the current density distribution of the bootstrap current: $\Delta flux_{loop}$ [Wb] ~ <ß> * (B_o * a^2) / ι , where $\Delta flux_{loop}$ is the induced magnetic flux, ι the rotational transform, a the effective plasma radius and B_o the toroidal magnetic field on axis. After the compensation of the perturbing stray fields associated with the net-current of the plasma, vertical field B_Z and nonstationary currents in the different magnets of the W 7AS arrangement a simple measurement of the voltage induced in the flux loops allows to evaluate the energy content of the plasma: W [kJ] ~ $\Delta flux_{loop}$ [Wb] * ι * Bo . (2) On the other side the energy content W can be derived from diamagnetic measurements $\Delta flux_{dia}$: W [kJ] ~ $\Delta flux_{dia}$[Wb] * B_o with high accuracy.

For the accessible parameter range up to <ß>-values of 1.4% and independent of the heating scheme a good agreement within 10% of magnetic measurements and kinetic data integrating measured temperature and density profiles is found. Systematic deviations still being within the error range, caused by anisotropic pressure effects, can be recognized for ECRF and NBI discharges at high power level and low densities.

Experimental data from the flux loop measurements are presented in Fig.4. The averaged diamagnetic <ß> values for different discharges varying the heating power from 0.1 MW to 1.6 MW, the magnetic field B_o between 1.25 T and 2.6 T, the plasma radius a between 0.11 m and 0.18 m and the rotational transform ι between 0.3 and 0.63, are plotted and compared to data as obtained from the different equilibrium codes. ($\Delta flux_{loop}$ = 1 10^{-3} Wb corresponds to vertical field component of 3.3 10^{-3} T produced by PS-currents for the choosen loops #1and #2 out of a set of 6 coils per period). The remarkable agreement has to be considered as a significant proof of the concept for the advanced stellarator to minimize the PS-currents and consequently to improve the equilibrium proceeding to higher <ß> operation.

Summary and conclusions

Proceeding to higher densities and ß in NBI discharges, the sensitive dependence of the confinement properties on the boundary value of the rotational transform becomes smoothed out at still favourable confinement conditions. For typical NBI discharges (ν*>1) the ß profiles are rather broad with strong gradients close to the plasma radius a. In this regime the pressure driven currents introduce significant shear. Such changes of the rotational transform profile are indicated by changes of the MHD-mode activity. Even with the presence of localized MHD-modes no disagreement with the empirical scaling of the confinement time τ_E was observed. For the main field of 2.5 T and a rotational transform of ~1/3 a volume averaged <ß> of 0.7% at a line av. density of 3 $10^{20}m^{-3}$ was achieved in W 7AS. By reducing the main field to 1.25 T, ß was further increased to <ß> >1% with a NBI power of 1.5 MW. Magnetic fluxes associated with the equilibrium of finite ß plasmas are analyzed. The experimental data agree with results of the equilibrium calculations based on KW-code and VMEC-code and verify quantitatively the reduction of the secondary currents in the optimized magnetic configuration of W 7AS.

References

/ 1 / Renner,H. et alt., Plasma Physics and Controlled Fusion **31**, (1989), p. 1579
/ 2 / Ringler,H. et alt., Plasma Physics and Controlled Fusion **32**, (1990), p. 933
/ 3 / Weller,A. et alt., Plasma Physics and Controlled Fusion **33**, (1991), p. 1559
/ 4 / Renner,H. et alt., 13th Conf. Pl. Ph., (1990), Washington, IAEA-CN 53/C-1-2
/ 5 / Grigull,P. et alt., Journ. of Nucl. Mat /PSI (1992), Monterey to be published
/ 6 / Renner,H. et alt., 8th Int. workshop on stellarators, Kharkov, USSR (1991), IAEA Techn.Com., p. 35
/ 7 / Lackner,K., Gottardi, N.A.O., Nuclear Fusion **25**, p. 1593
/ 8 / Kisslinger,J.,Wobig,H. 12th EPS Budapest (1985), Vol. 1, p. 453
/ 9 / Gardner,H.J., Nuclear Fusion **30** (1990), p. 1417

* ** *** see Hartfuß, H.J. this conference.

THE OPTIMUM ION CONFINEMENT MODE IN W7-A STELLARATOR INDUCED BY FAST ORBIT LOSSES OF THE NEARLY PERPENDICULAR NBI

U. Gasparino, M. Kick, H. Maaßberg, H. Renner,
H. Ringler, F. Sardei, W7-AS Team† and NBI Team†

Max-Planck Institut für Plasmaphysik
Association EURATOM-IPP, D-8046 Garching, Germany

Introduction

The general discussion of improved confinement properties in both tokamaks and stellarators has concentrated on mainly two effects: the reduction of the plasma fluctuation level and the role of sufficiently large radial electric fields. Especially for the tokamak L-H transition, the generation of radial electric fields by ion orbit losses at the plasma edge affects the fluctuation level. A consistent analysis of radial electric field and its impact on fluctuations, however, is not available so far and the basic effect for confinement improvement is still an open question. In this context, a new analysis of the optimum ion confinement regime found in the W7-A stellarator /1/, the predecessor of W7-AS, can contribute to the issue of improved confinement (see e.g. /2/).

In the W7-A stellarator ($R = 2$ m, $a \lesssim 9$ cm) with nearly perpendicular neutral beam injection ($P \leq 1$ MW), optimum ion confinement with ion temperatures of up to 1 keV could be obtained in high density ($\sim 10^{14}$ cm^{-3}) NBI discharges. For this density regime, the highest T_i values found in stellarators or torsatrons so far were measured. In these NBI discharges in W7-A, where T_i significantly exceeded T_e very high E_r values (up to -500 V/cm) were inferred from the analysis of Doppler shifted impurity lines. The analysis of the ion energy balance was in strong conflict to the neoclassical predictions disregarding radial electric fields. In this paper, we first analyse pure ECRH discharges (W7-A and W7-AS) at moderate densities. Then, we discuss for a NBI discharge in W7-A with optimum ion confinement the effects of the fast beam ions on the radial electric field and the confinement of thermal ions. For the neoclassical transport analysis, a DKES code /3/ database is used where strong radial electric fields are included also in the plateau collisionality regime. From the ambipolarity condition of all particle fluxes the radial electric fields are estimated and compared with the measured ones.

Ion Confinement in ECRH Discharges

ECRH discharges with n_e close to the cut-off density ($6.3 \cdot 10^{13}$ cm^{-3} for fundamental o-mode at $B = 2.5$ T) and moderate T_e are the best candidates for the analysis of the ion energy confinement. For the W7-A discharge shown in Fig. 1 with an ECRH input power of 150 kW, the collisional ion heating, P_{ei}, of 35 kW (radiation loss only 15 kW) leads to central T_i of 280 eV measured by active CX; the flat and broad T_i profile is confirmed by the CX energy spectra for the full aperture of the diagnostic beam (indicated by the radial error bar). The outer T_i and E_r data were obtained from Doppler spectroscopy. With the profiles of Fig. 1, the ambipolar electric field was calculated. As the ion transport coefficients in the plateau collisionality regime are

† for the teams see H.J. Hartfuß; this conference

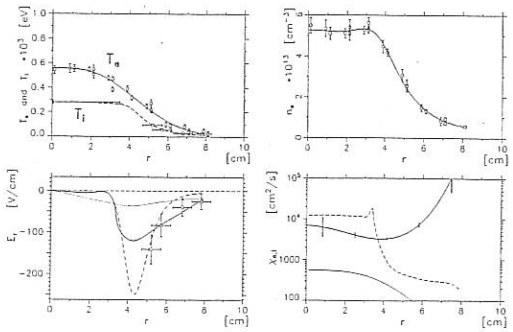

Fig. 1: *ECRH discharges in W7-A (shots 61003-61057): T_e and T_i (left upper plot), n_e (right upper plot), radial electric field (lower left plot) measured and predicted (DKES transport coefficients with E_r dependence - solid line, and for $E_r = 0$ - dot-dashed line) and E_{res} (dotted line); in the right lower plot, neoclassical heat diffusivities, χ_e^{neo} (lower thin solid line), χ_i^{neo} (dashed) and the experimental χ_e^{exp} (thick solid line).*

significantly decreased for $|E_r| > E_{res} = \pm v_{th} Br/R$ (then, the tokamak-like "banana" orbits disappear, dotted line in Fig. 1), the ambipolar E_r (solid line) is smaller than the one where the ion transport coefficients for $E_r = 0$ were used (dot-dashed line, this simple approach is mostly used in plateau regime). Especially for large aspect ratio (extended plateau regime and E_{res} being small), the reduction in the ion transport coefficients is important. This reduction in the neoclassical χ_i at $r > 4$ cm shown in Fig. 1 (broken line, lower right plot) is essential for the improved ion energy confinement also in ECRH discharges in W7-A. The neoclassical ion heat flux with E_r included is up to 5 cm in very good agreement with the collisional ion heating. At outer radii, however, an anomalous convective flux which is related to a particle diffusion coefficient with D^{an}/χ_e^{exp} within the range of 0.1 ... 0.3 (χ_e^{exp} is the solid line in Fig. 1, lower right plot) and CX losses of the same order of magnitude are indicated. For both the particle sources and the CX losses a consistent neutral density profile with a reasonable decay length in the n_e gradient region but with rather high edge density (close to 10^{11} cm^{-3}) is required. This is confirmed by the fact that the CX fluxes were unaffected by the diagnostic beam (with density of about 10^9 cm^{-3}) at outer radii.

For an equivalent ECRH discharge in W7-AS ($R = 2$ m, $a < 18$ cm), similar electron and ion temperatures ($T_e(0) \simeq 600$ eV and $T_i \simeq 350$ eV) were obtained. In this discharge, the ECRH input power was 140 kW, the radiation loss nearly 40 kW and P_{ei} about 80 kW (within 13 cm). The neoclassical prediction of the ion heat transport with ambipolar E_r (no measurements available) is up to 13 cm in good agreement with the collisional power transfer. The ambipolar E_r values are smaller than for the W7-A discharge and rather close to the larger resonant values E_{res}. In this case, no significant reduction in the ion transport coefficients due to the ambipolar E_r is obtained. These results are important with respect to the rather low ion confinement properties in W7-AS for NBI discharges with the mainly tangential injection.

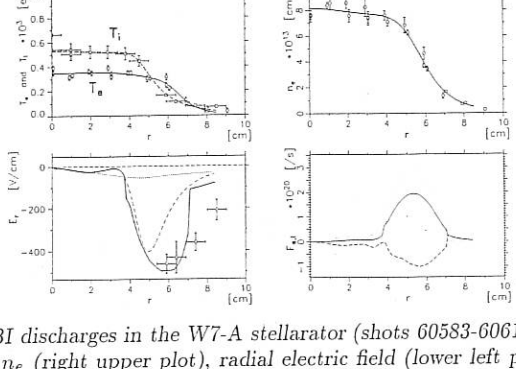

Fig. 2: *NBI discharges in the W7-A stellarator (shots 60583-60615): T_e and T_i (left upper plot), n_e (right upper plot), radial electric field (lower left plot) measured and predicted (comp. Fig. 1) and, in the right lower plot, the ambipolar neoclassical particle fluxes, Γ: electrons (solid), fast beam ions (dotted) and thermal ions (dashed line).*

Optimum Ion Confinement in NBI Discharges

High power NBI nearly perpendicular to the magnetic field ($90° \pm 1.5°$) in W7-A was not expected to give good performances. For densities up to 10^{14} cm^{-3}, more than 30% of the input power was transmitted (shine through). For these injection conditions which were dictated by the strongly limited access to the plasma, losses of ripple trapped fast beam ions were significant despite of the very small helical ripple (2.5%) in W7-A. The experimental findings, however, were contrary to the pessimistic predictions. In the currentless pure NBI phase of the discharges, optimum confinement properties could be obtained: $\tau_p > 200$ ms (n_e linearly increasing in time) and τ_E up to 6 ms. In the discharge shown in Fig. 2 at the time of maximum energy content (later, the discharge terminated by radiative collapse) 750 kW were injected (shine through: ~ 320 kW) leading to ~ 300 kW electron and only ~ 130 kW ion heating if orbit losses are omitted, and radiative losses about 150 kW. Despite the small fraction of ion heating power, T_i (broken line) exceeded T_e (solid line) in the central part of the plasma: the collisional power transfer being rather close to the ion heating power. For these typical findings, the ion energy balance is strongly violated if simple expressions for the ion heat flux are used (as in /2/) in which the ion transport coefficients in the plateau regime do not depend on the radial electric field. With a more accurate treatment (DKES code or /4/) the ion transport coeffients are reduced within the T_i gradient region by more than one order of magnitude for E_r values close to the measured ones. For these strong $E_r \gg E_{res}$ the E × B rotation forces the ion orbits very close to the magnetic flux surfaces, and the tokamak-like large banana type orbits disappear. The measured strong E_r values (Fig. 2), however, exceed by a factor of 2.5 the values obtained from the ambipolarity condition using only the thermal particle fluxes. The fast beam ion component must be taken into account (see the particle fluxes in Fig. 2).

The local fast ion fluxes are approximated by means of the energy convolution within the DKES code database. Only isotropic distribution functions can be treated so far. In this approach (contrary to Monte-Carlo simulations), the ambipolar E_r can be easily estimated. The stationary beam ion distribution is calculated under the assumption

of slowing-down on flux surfaces, transport effects are omitted. The beam particle density gradient turns out to be the main driving force for the neoclassical transport. Furthermore, for the direct loss of ripple trapped beam ions, depending on the ambipolar potential, a rough approach is used based on the analytic representation of the bounce invariant. Without radial electric fields, more than 50 kW can be lost by ripple trapped beam ions for the discharge of Fig. 2. Consequently, the plasma must be charged up to reduce these losses, or significant non-ambipolar thermal losses close to the plasma edge must be assumed. The direct orbit losses are important only for $r > 6$ cm, however, they are omitted in the estimation of the ambipolar E_r. Only the diffusive transport of the fast beam ions is included. In this approach, the ambipolar E_r (solid line) fits rather well to the experimental data within the gradient region, the deviation at outer radii is attributed to the omitted fast ion orbit losses (at very low plasma density and temperature). These losses had been estimated from LIF measurements of sputtered iron from the vacuum vessel and were found to be in good agreement with Monte-Carlo simulations if a strong E_r was assumed. Within the range of 4 to 7 cm, the fast beam ion flux dominates in the ambipolarity condition and determines the E_r values. The corresponding particle flux balance shows a curious result within the gradient region (lower right plot): The outflux of fast beam ions and electrons is related to an influx of thermal plasma ions. For this ion inward pinch related with the strong E_r (the equivalent ion heat pinch is only very small), the thermal ion transport coefficients are reduced by more than one order of magnitude (comp. also χ_i^{neo} in Fig. 1). As a consequence, the thermal ion contribution to the energy balance is negligible which is in full agreement with the experimental results. Equivalent NBI discharges in W7-AS with almost tangential injection behave quite different: $T_i < T_e$ with T_i typically less than 500 eV are found and the neoclassical ion heat conduction is a main loss channel (see /5/).

Summary and Conclusions

The optimum ion confinement in the W7-A stellarator is attributed to ambipolar radial electric fields ("strong ion root" with $E_r > E_{res}$) which reduce significantly the local ion transport coefficients also in the plateau collisionality regime. This "strong ion root" is also responsible for the good ion confinement in ECRH discharges with higher densities. High power NBI nearly perpendicular to the magnetic field and the resulting fast ion distribution drive the neoclassical E_r to very large values. This is shown in neoclassical simulations where the fast ion distribution is included in the ambipolarity condition where several roots can exist. Equivalent to tokamak L-H mode transition models /6/, the optimum ion confinement mode is attributed to the fast beam ion losses (the mathematical background is nearly identical). Within the NBI phase in W7-A, however, no bifurcation (like the L-H mode transition) was observed. For the optimum confinement conditions the density fluctuation level within the plasma measured by microwave scattering was significantly reduced (perhaps as a consequence of the strong poloidal plasma rotation). The improved confinement in W7-A, however, is attributed to the direct role of the strong radial electric fields on the ion loss channel and not to the reduction of the fluctuation level.

References

/1/ H. Wobig et al.; Plasma Phys. and Contr. Nucl. Fus. Res. (1987), **2**, 369

/2/ K. Itoh et al., Report **NIFS-117** (1991)

/3/ W.I. van Rij and S.P. Hirshman; Phys. Fluids B, **1** (1989), 563

/4/ H. Maaßberg et al.; EPS (1985), ECA 9f, **1**, 623

/5/ V.I. Afanasiev et al.; EPS (1991), ECA 15C, **2**, 209

/6/ S.I. Itoh and K. Itoh; Phys. Rev. Lett. (1988), **60**, 2276

19th EPS Conference on Controlled Fusion and Plasma Physics
Innsbruck, Austria, 29 June - 3 July 1992

Local Neutral Particle Density in the W7-AS Stellarator

J. Junker, M. Kick, H. Maaßberg, F. Sardei, U. Stroth, S. Zöpfel,
WVII AS-Team* and NBI-Team**

Max-Planck Institut für Plasmaphysik
Association EURATOM-IPP, D-8046 Garching, Germany

ECRH Group***

Institut für Plasmaforschung der Universität Stuttgart
D-7000 Stuttgart, Germany

Introduction:
Ion temperatures as obtained from line integrated CX-flux measurements generally must be corrected for systematic errors by a reconstruction technique /1/ which employs measured n_e, T_e and Z_{eff} profiles and a neutral density n_0 profile which is calculated from a Monte - Carlo transport code /2/. The reconstruction technique is an iteration which starts from the non corrected ion temperature profile as obtained from the line-averaged passive fluxes. This non corrected ion temperature will be called passive ion temperature in the following. For the reconstruction technique the knowledge of the neutral particle density profile is very important. Reliable estimates of the neutral densities in the toroidal section of the stellarator W7-AS where the CX measurements are made, are not available from the DEGAS code /3/. This is due to the poor knowledge of the neutral density sources, which in this region are essentially determined by strongly asymmetric wall recycling.
By using a diagnostic beam of fast neutrals a space resolved measurement of the ion temperature profile is obtained. This active ion temperature profile together with the line integrated fluxes and the passive ion temperature allows an estimate of the neutral particle density and its profile. For this analysis the following steps are required and will be described in detail:

1. Active measurement of the ion temperature profile.
2. Measurement of the line integrated fluxes and the passive ion temperature profile.
3. Correction of the active ion temperature profile due to the calculated absorption of the neutral particle flux by electron impact ionization and charge exchange collisions with plasma ions (impurity ions are neglected).
4. Determination of the neutral particle density profile from a least-squares fit which minimizes simultaneously for all lines of sight the deviations of the calculated fluxes at different energies from the passively measured ones.

*,**,***see Hartfuß this conference

Experimental Setup:
The CX-diagnostic on W7-AS consists of 4 analyzers from Joffe Institute /4/, which are mounted on a lift in such a way that their lines of sight are in one vertical plane. The lift can be moved in the vertical direction. The plasma is observed at 40 degrees to the plasma axis. The diagnostic injector injects its neutral beam vertically, thus allowing space resolved measurements at the crossing points with the lines of sight of the analyzers.

Evaluation:
Series of shots are required for complete temperature profiles, because only 4 temperature points of a profile are measured per shot. The temperatures are separately evaluated for each analyzer in the usual way /5/. The evaluation treats the following equation:

$$\Phi(E,L) = \int_0^L g n_i \frac{e^{-\frac{E}{T_i}}}{T_i^{\frac{3}{2}}} n_0 < \sigma_{CX} v > (T_i, E)\sqrt{E} \cdot e^{-\int_0^l \frac{n_i < \sigma_{CX} v > + n_e < \sigma_{ei} v >}{v} \cdot dl} \, dl \qquad (A)$$

where g is a geometrical factor, $< \sigma_{CX} v > (T_i, E)$ the rate coefficient of charge exchange and $< \sigma_{ei} v >$ the rate coefficient of electron impact ionization. The ion impact ionization can be neglected.

After the ion temperature profile is actively measured, the electron density n_e and temperature profile T_e from the Thomson diagnostic and the Z_{eff} value from the soft-X diagnostic are used to calculate the neutral particle absorption by electrons and ions, which is represented by the second exponential in (A). The cross-sections used are taken from Riviere /6/. A constant Z_{eff} over the plasma radius is assumed.
After the neutral particle fluxes are corrected, the ion temperature can be evaluated along the injected diagnostic beam. With this corrected ion temperature profile T_i, which represents the true ion temperature, and the ion density profile n_i, the line-integrated neutral particle fluxes Φ are simulated assuming a neutral particle density profile which has constant densities on the flux surfaces. Then the assumed neutral particle density profile is varied to fit the calculated neutral particle fluxes to the measured fluxes for all lines of sight and automatically the passive ion temperature is fitted to the measured one.
The passive ion temperature is taken as the slope of the energy dependend neutral particle fluxes $\Phi(E)$. The fluxes are the integral over a real temperature function weighted by the neutral density n_0 and the ion density n_i along the line of sight L (see equation (A)). Therefore this passive ion temperature is a kind of „line-averaged ion temperature", which will generally be different from the real ion temperature. This passive ion temperature is used as an indicator for the accuracy of the assumed n_0 profile, which will be the result of the evaluation.

Results:
For all investigated NBI-heated (400-800 kW) and ECR-heated (120-320 kW) plasma discharges neutral particle density profiles with edge densities and central densities of the order of $10^{10}\,cm^{-3}$ and $10^{7}\,cm^{-3}$ respectively are observed. The absorption of neutral particles by electron- and ion-collisions are relevant only between plasma densities of 10^{13} and $10^{14}\,cm^{-3}$. For the active ion temperature correction at lower densities no influence is observed, and at densities higher than 10^{14} cm^{-3} active evaluation is not possible, because the signal of the diagnostic injector cannot be discriminated from the passive background signal. In this density region the temperature corrections are up to -10% of the temperature value. The correction depends on the plasma density as well as the diameter, which increases with decreasing ι values (0.3-0.5) and can be reduced by the limiters ($r_{eff} \approx 12...18\,cm$). In a typical example

(Fig. 1) /7/, an NBI heated (700 kW) discharge ($B = 2.5\,T$, $\iota = 0.529$, $n_e = 7 \cdot 10^{13}\,cm^{-3}$), the temperature correction in the core is $\Delta T_i = -30\,eV$. The ion temperature decreases from the actively measured to the corrected temperature because the absorption is lower for higher energies of the neutral particles. With the profiles of ion density (Fig. 2), electron temperature (Fig. 3) and density, and the calculated neutral particle density profile (Fig. 4) the line integrated fluxes and the passive ion temperature profile has been evaluated and compared with the measurements. The neutral density profile has been varied iteratively until the calculated and the measured passive particle fluxes agree. Fluxes of high energy channels in which non thermal contributions are expected are ommitted in the fit procedure. The deduced passive ion temperature profile agrees within 40 eV, i.e. 10%, with the measured one. A sensitivity study indicates the following impact of a variation of the neutral density profile: Increasing the minimum level of the neutral particle density profile by 10% the calculated passive temperature increases about 5 eV or 1.5% in the core. Changing the maximum level by 10% leads quantitatively to the same result as changing the minimum level, but in the opposite direction. If the gradient is varied by 10% the passive ion temperature varies about 6%. If the steep gradient regions are radially shifted 10% outwards, the passive ion temperature is drastically inreased (55%). The neutral particle fluxes are similarly sensitive.

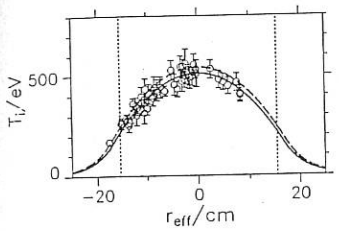

Fig. 1: Ion temperature actively measured (dashed) and the corrected ion temperature (solid line). Limiters dotted in all diagrams.

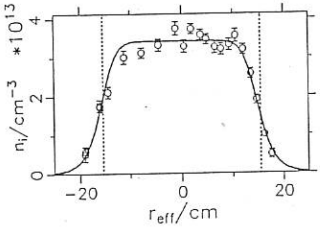

Fig. 2: Ion density approximated by $\frac{n_e}{Z_{av}}$, the averaged $Z_{av} = 2$.

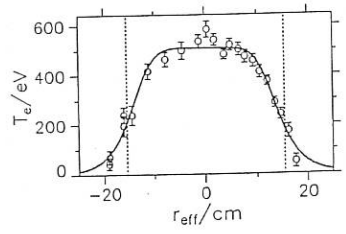

Fig. 3: Electron temperature measured by Thomson diagnostic (points) and profile fit (solid line).

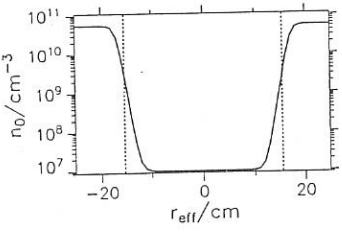

Fig. 4: Neutral particle density profile (solid line), which results in the best approximation for the passive ion temperature profile and neutral particle fluxes.

The steep gradient regions of the neutral particle density profile coincide within 1 cm with those of the ion density profile. The spatial resolution of the measurements is also 1cm. The decay length of n_0 is 0.5 cm. This compares to a decay length of 1.3 cm as derived from the DEGAS code simulations of limiter recycling for an equivalent discharge. The short decay length observed seems to require the presence of a neutral source strongly localized at the plasma edge near the port of the diagnostic injector (cold gas cloud from the injector). There are two analyzers showing fluxes in full agreement with the simulated ones (Fig. 5). The other two can deviate up to a factor of 2. The main reason is the insufficient assumption of neutral particle densities beeing constant on flux surfaces. A further reason in separatrix bounded discharges is the lack of information in the plasma edge on the ion temperature, the ion density and electron density.

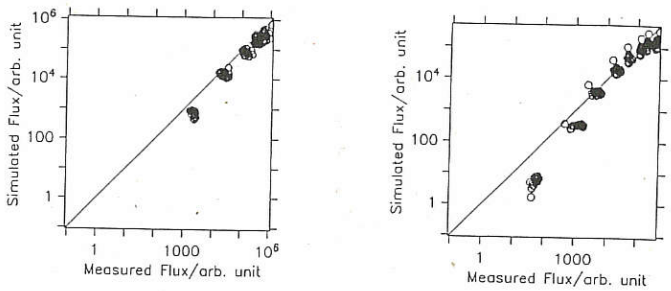

Fig. 5: Comparison of neutral particle fluxes between measurement and simulation for two analyzers. The curvature is caused by flux channels of higher energy because there are non-thermal neutral particles from the NBI heating. These are mainly slowing-down particles. The channels used for the temperature measurement are located on the straight line.

Conclusions:

The procedure described is a simple way, with simple assumptions, of determining the neutral particle density profile with an accuracy of 10% to 20% in the gradients and a factor of 2 in the absolute values. The plasma discharges investigated have typical neutral particle densities of the order of $10^7\,cm^{-3}$ in the centre and $10^{10}\,cm^{-3}$ at the edge. The evaluation of neutral particle density profiles is more accurate for steeper gradients of the ion temperature profiles and can be improved by CXRS measured ion temperatures which complete the temperature profiles at the plasma edge. Finally it can be concluded, that the CX diagnostic affords an additional possibility of n_0 profile measurements, which can be compared with DEGAS code computations, if sufficient information about the neutral particle sources is available.

/1/ U. Stroth et al., Nuclear Fusion, Vol. 29, No. 5, 761 (1989)
/2/ M. H. Hughes, H. E. Post, J. Comput. Phys. 28, 43 (1978)
/3/ F. Sardei et al., EPS, ECA 15-CII, 193 (1991)
/4/ V. V. Afrosimov et al., Sov. Phys. Tech. Phys., Vol. 20, No. 1, 33 (1975)
/5/ V. V. Afrosimov, M. P. Petrov, and V. A. Sadovnikov, JETP Lett., 18, 300 (1973)
/6/ A. C. Riviere, Nuclear Fusion, Vol. 11, 363 (1971)
/7/ V. I. Afanasjev et al, EPS, ECA 15-CII, 209 (1991)

2-7

ECH POWER DEPOSITION CONTROL IN CHS

S. Kubo, H. Idei, M. Hosokawa, Y. Takita, H. Iguchi, I. Yamada,
H. Arimoto, M. Ueda*, K. Ida, K. Matsuoka, S. Morita,
K. Nishimura, S. Okamura, C. Takahashi, H. Yamada,
M. Fujiwara, N. Noda, A. Sagara, H. Sanuki, J. Todoroki, K. Toi

National Institute for Fusion Science
Nagoya 464-01, Japan
**INPE, Brazil*

INTRODUCTON

Electron cyclotron heating experiments at the second harmonic resonance in the Compact Helical System (CHS) have been carried out using the 53.2 GHz, 200 kW gyrotron. CHS is the l=2, m=8 heliotron/torsatron type device with the specific feature of low aspect ratio (A_p 5)/1/. The main objective of this machine is to establish the plasma confinement database of helical systems at the low far end of aspect ratio. Especially, transport study is the critical issue. For this campaign, it is of much importance to have well defined power deposition and its controllability. This capability also enables the control of the distribution function in the velocity space as well as the real one, which will provide a way to clarify the effect of loss cone on the confinement. The density clamping or pumping out phenomena has been reported during high power ECH experiments commonly in tokamaks /2/ and helical systems /3,4/ without substantial verification of the mechanism. One of the possible candidates for the mechanism is the presence of loss cone into which electrons are accelerated by ECH /5/.

Here, the microwave complex to focus the power and control the polarization and the focal point is described with the result from cold test and plasma experiment. Estimates of the power deposition profile during on and off axis heating and finally, the particle confinement degradation observed during ECH in CHS and the effort to clarify its mechanism are reported.

FOCUSING SYSTEM

In order to realize the local heating, the microwave complex for 53.2 GHz is installed on the CHS. This system is composed of a stair cut Vlasov antenna, a reflecting mirror, a reflecting corrugated polarizer, and a steerable focusing mirror as shown schematically in Fig. 1 a). The focusing reflector just in front of the stair cut Vlasov antenna is designed so

as to focus the total radiated power on the reflecting polarizer. The reflecting polarizer of in principle $\lambda/4$ corrugated plate is set to obtain a correct polarization for the second harmonic heating. The steerable focusing mirror transforms the incoming elliptical Gaussian beam into the circular one. Low power test of this system indicates more than 60% of input power of TE_{02} circular mode can be focused on the mid-plane of the CHS vacuum vessel with the 2.5 cm $1/e$ spot size and desired polarization. Fig. 1 b) shows the contour plot of the focused power measured on the mid-plane of CHS.

Fig. 1. a) ECH focusing system on CHS.
b) Beam profile measured on the position of CHS mid-plane. Contour lines are plotted by every 2 dB step.

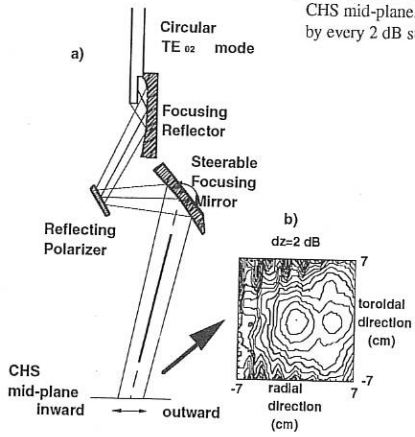

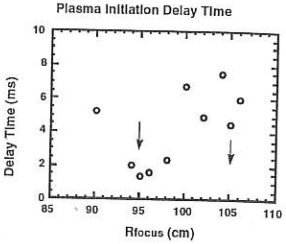

Fig. 2. The delay time of the plasma initiation as a function of the focal position. The magnetic axis is at R=95 cm. Arrows indicate the resonance positions.

One of the good demonstrations for well defined beam would be the time delay of the plasma initiation after the application of the microwave pulse. Fig. 2 shows this delay time as a function of the focal position. The resonance points exist at the magnetic axis (95 cm) and near the periphery of the confinement region (105cm) in this case.

POWER DEPOSITION PROFILE

Power deposition profiles are reduced from the change of electron temperature and density profiles at the ECH power turn off. This method relies on the following formula

$$\Delta P(r) = \left[\frac{\partial}{\partial t}\left\{\frac{3}{2} n_e(r,t)\, T_e(r,t)\right\}\right]_{t=t_0+\varepsilon}^{t=t_0-\varepsilon},$$

here, $\Delta P(r)$ is the local input power difference at time $t = t_0$. Time interval ε should be sufficiently shorter than the local heat diffusion time scale. Since only single point Thomson scattering system is available for the electron pressure profile measurement at

the moment, it is difficult to estimate the difference of time derivative for a short time interval. Fig. 3 a) and b) show the change of kinetic plasma pressure profiles during ECH and about 1 ms after the ECH power turn off for on and off axis heating. These profile changes indicate that the power deposition profile is well controlled and is drastically varied when the focal point is changed, although the time interval of 1 ms is not sufficiently short. The increase of the pressure at $\rho = 0.2 - 0.5$ for the off axis case may indicate the diffusion effect for this long time interval. The power deposition profiles inferred from these data agree qualitatively with the ray tracing calculation which includes the multi-reflection effects on the wall. For more precise estimates of the power deposition profile, fast response electron temperature diagnostic with high spatial resolution, for example second harmonic ECE , is desired.

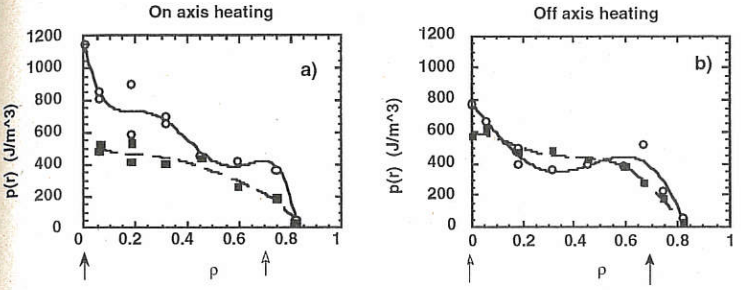

Fig. 3. Plasma pressure profiles during ECH (open circles) and those at 1 ms after ECH power turn off for a) on axis and b) off axis heating case. Arrows indicate the equivalent normarized radius of the resonance point on the midplane. Closed arrows correspond to the focal point.

Transport analyses using these deposition profiles are underway. The estimate of the electron heat conductivity gives roughly the same results as those reported previously /6/.

PARTICLE CONFINEMENT DEGRADATION DURING ECH

The degradation of the particle confinement during second harmonic ECH is investigated by focusing the power on the resonance at about 1/3 of plasma radius. In order to study the effect of loss cone, two configurations are chosen in which the heating position is at the inside (high field side) or at the outside (low field side) with respect to the magnetic axis. In Fig.4 are shown the density profiles for the cases of inside and outside heating with open and closed signs, respectively. Data points with circles and boxes correspond to those from Thomson scattering for the core density and fast Li beam probing for the edge density, respectively. The differences of the electron temperature profile for these

tow cases were within error bar of the Thomson scattering measurement. It should be noted that the density profile is more flat or even hollow and the edge density gradient is steeper in case of outside resonance heating than those of inside heating. The intensity of the H_α line normalized by the averaged density as a measure of the particle confinement is stronger in case of outside heating than that of inside one. These results indicate that the degradation of the particle confinement or pumping out of the electron density is enhanced in the case of outside heating. These experimental results indicate that the degradation of the particle confinement has close correlation with the confinement of helically trapped electrons produced at the second harmonic resonance region. The particle orbit calculation and analysis of the loss region of helically trapped particles for CHS also support the above statement /7/. More precise and quantitative study is under planing to confirm these preliminary results and the model.

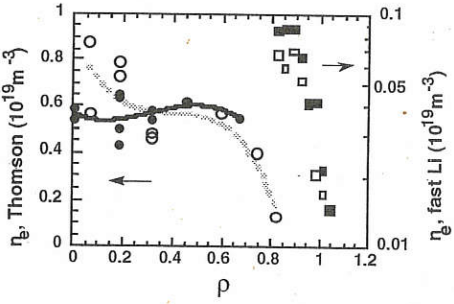

Fig. 4. Electron density profile measured by Thomson scattering (circles), and fast Li beam probing (boxes). Open and closed marks correspond to the case of outside and inside resonance heating, respectively.

SUMMARY

The microwave power from gyrotron at 53.2 GHz is injected for second harmonic ECH in CHS with linear polarized and Gaussian like focused beam. Well localized power deposition profile is inferred from the pressure profile change at the ECH power turn off. The particle confinement degradation phenomenon during ECH is investigated with this local heating capability. Improved understanding of second harmonic ECH plasma and its confinement is expected by making full use of this heating system.

/1/ K. Matsuoka, et al. ,Proc. IAEA conf. Plasma Phys. and Controlled Fusion,Nice(1988).

/2/ D. C. Sing et al., 17th Eur. Conf. Cont. Fusion . ECA Vol. 14B part III p.1133 (1990).

/3/ H. Zushi et al. , PPLK report PPLK-R-27 (1988).

/4/ F. Sardei et al., 17th Eur. Conf. Cont. Fusion . ECA Vol. 14B part II p.471 (1990).

/5/ K. Itoh et al., PPLK report PPLK-R-25 (1988).

/6/ H. Yamada et al.,18th Euro Conf. Cont. Fusion, ECA Vol. 15C part II p.137 (1991).

/7/ H. Sanuki, J. Todoroki and T. Kamimura, Phys. Fluids B **2** , 2155 (1990).

DENSITY PROFILE AND PARTICLE TRANSPORT OF NBI-HEATED PLASMAS IN THE LOW-ASPECT-RATIO HELIOTRON/TORSATRON CHS

H.Iguchi, K.Ida, S.Morita, H.Yamada, S.Okamura, K.Matsuoka, R.Akiyama, H.Arimoto, M.Hosokawa, H.Idei, K.Itoh, O.Kaneko, T.Kohmoto, S.Kubo, K.Nishimura, N.Noda, T.Ozaki, A.Sagara, S.Sakakibara, H.Sanuki, Y.Takeiri, Y.Takita, C.Takahashi, M.Ueda #, I.Yamada

National Institute for Fusion Science, Nagoya 464-01, Japan

Instituto Nacional de Pesquisas Espaciais, Brazil

and

K. Uchino, H. Takenaga, K. Muraoka, M. Maeda*

Department of Energy Conversion, Kyushu University, Fukuoka 816, Japan

*Department of Electrical Engineering, Kyushu University, Fukuoka 812, Japan

1. Introduction Transport phenomenon is the critical issue in a low-aspect-ratio helical device like CHS against its favorable MHD characteristics. Much effort has been made to evaluate local transport coefficients experimentally in CHS for neutral beam heated plasmas. The electron thermal diffusivity was found to be higher than the neoclassical prediction in the plateau regime by a factor of 20 to 50. The ion thermal diffusivity had less anomaly but had the same order of magnitude ($\chi_e \approx \chi_i \approx$ 5-10 m^2/s at 1 Tesla).[1] The parallel viscosity was studied experimentally by observing toroidal rotation profile,[2] in which necessity of introducing the anomalous perpendicular viscosity (momentum diffusivity) of the order of the thermal diffusivity was pointed out. The particle diffusivity so far has not been evaluated mainly due to a difficulty in the determination of local particle sources. Especially in the magnetic configuration with an inward-shifted magnetic axis, where global confinement time was optimum in CHS,[3] the plasma was wall-limited and strong recycling occurred on the inboard wall. On the other hand, a peaked density profile was observed in the inward-shifted magnetic axis, while the density profile flattened in outward-shifted one.[4] Two explanations for the density peaking are possible; 1) The particle diffusivity is reduced with an inward-shifted magnetic axis. 2) The inward flow velocity is increased with an inward-shifted magnetic axis. In order to clalify this point, it is necessary to study particle transport by determining the particle diffusivity and the convective velocity separately. The first effort along the line is described in this paper, where the relationship between the density profiles and the local particle transport is examined for the steady state neutral beam heated plasma in a plateau regime based on new experimental observations of neutral hydrogen density.[5]

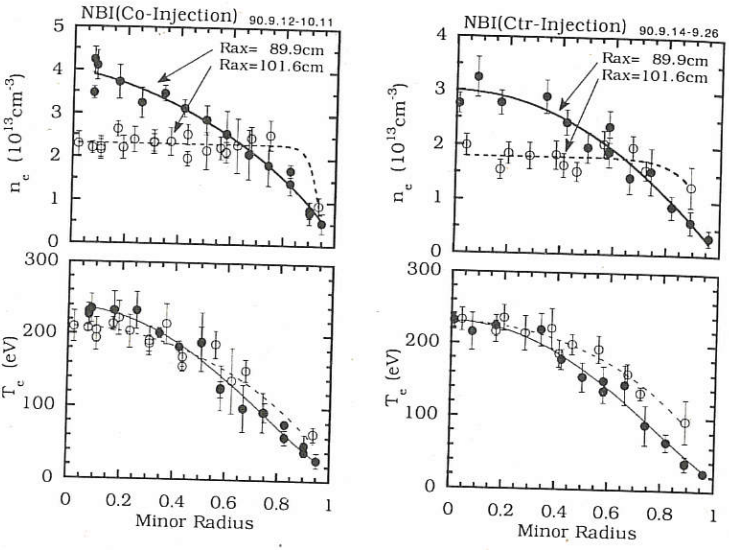

Fig.1 The electron density and temperature profiles for different magnetic configuration.

2. Density profile Figure 1 shows a comparison of electron density and temperature profiles for two different magnetic configurations. The data on the left hand side are for co-injection of the neutral beam and those on the right hand side are for counter-injection. Density profiles were peaked for plasmas with an inward-shift of the magnetic axis for both co- and counter- injection. The peakedness parameter, which is defined as central density divided by average density, was around 2 in this density regime. In contrast to the density profile, the temperature profile changed little with the magnetic axis shift. In the case of tangential beam injection, toroidal momentum input drove toroidal rotation. It was observed that the toroidal rotation was damped due to the neoclassical parallel viscosity in the configuration with an outward-shifted magnetic axis.[2] Good coincidence between density peaking and the toroidal rotation velocity was suggested, but there has been no model to connect these two parameters directly. Little difference was observed in both density profile and toroidal rotation velocity between co- and counter- injection, which is different from tokamak experiments. The density profile became less peaked even in inward-shift of the magnetic axis when strong gas puffing was applied to obtain higher densities ($\langle n_e \rangle > 5 \times 10^{13}$ cm^{-3}).

3. Neutral density In order to understand the particle transport, it is important to measure the local neutral hydrogen density three-dimensionally and two diagnostic methods were used. A method of laser induced fluorescence tuned to Hα emission was used to directly measure the local hydrogen atom density inside the plasma. Hβ emission profiles were also measured using

fibre optics arrays (an 8 channel toroidal array and two sets of 34 channel poloidal arrays observing poloidal cross sections vertically and horizontally). Strong local emission was observed around the inboard wall where the vertically elongated elliptic plasma was in contact with it, indicating that strong recycling occurred there. On the other hand, the emission profiles were rather uniform at the cross section where the plasma is horizontally elongated. This is because plasma was detached from the wall in this section. In order to measure the toroidal extent of the strong emission near the inner wall, a calibrated TV camera with an Hα optical filter was used. Details of these diagnostics and the experimental results have been reported elsewhere.[5)]

4. Particle transport The experimental data were extensively analyzed for the plasma with a peaked density profile in co-injection case (Fig. 2 (a)) using the particle simulation code DEGAS. Since it is difficult to simulate the actual CHS vacuum chamber and plasma with helically rotating structure in a toroidal direction, we carried out simulation in two simplified plasma and wall configurations. One was a simple torus with a vertically elongated elliptic cross section and the other was one a with horizontally elongated cross section. Each configuration simulated the neutral behavior at the corresponding plasma cross section. At the vertically elongated cross section it was well simulated when we assumed that the local neutral source from the position where plasma touched the wall was three times as large as that from the uniform source at the entire wall. It was also found that the total neutral source at the vertically elongated cross section was 2.5 times as large as that at horizontally elongated cross section. The overall particle source from recycling was determined by the combination of these two simulations, in which the weight of each was determined using the data from the TV camera observing near the inboard wall. In addition to this, the particle source from the neutral beam was evaluated from the birth profile calculation by the use of the transport code PROCTR

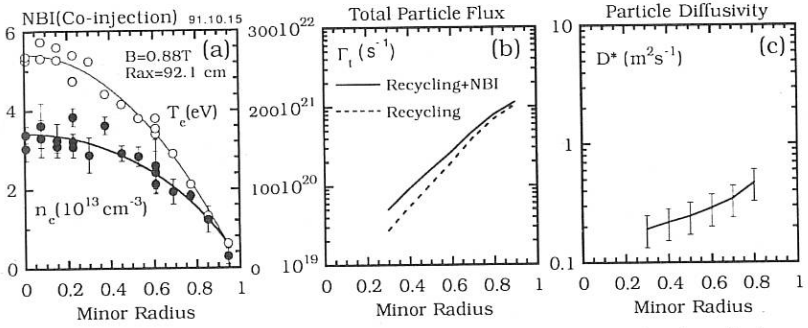

Fig.2 (a) Profile data for the transport analysis. (2) Total Particle flux as a function of minor radius. (c) Apparent diffusivity D* calculated from (a) and (b).

-MOD. The neutral source in the central region was dominated by the source from the beam. At the outer half plasma radius, the particle source was dominated by recycling. The neutral source from the gas puffing was estimated from the gas flow rate at the gas puffing port. The recycling rate was higher than 0.9 in this experiment and the contribution from gas puffing was neglected. The total particle source in the plasma was thus evaluated as a function of the magnetic flux surfaces. The results are shown in Fig. 2(b). Particle transport processes are often described using effective diffusivity and convective inward flow velocity. However, because we only have experimental data for steady state operation, it was impossible to separate diffusivity and convective velocity. We define an apparent particle diffusivity D* as $\Gamma = -D^* \text{ grad } n_e$. The radial profile of D* thus evaluated is shown in Fig. 2(c). The error bars in the figure correspond to uncertainty in the profile fitting of the density. In these calculations we assumed $Z_{eff} = 1$. Even if we assumed only naked carbon in the core contributes to $Z_{eff} = 3$ of a typical value for NBI plasma in this density regime, which gave unreasonably high carbon concentration, the error for D* was estimated to be not more than 50%. Similar measurements have been carried out for an outward-shifted magnetic axis configuration, although the average density was one half and the data set was still in a preliminary stage. Particle confinement time was about half of that in inward-shifted case. When we consider the result and the flattened density profile, the particle confinement seems to be degraded in the core region for an outward-shifted magnetic axis compared with the inward-shifted one. We do not have any data of neutral density for the counter-injection of the beam, which is the subject of future work.

5. Conclusion We have evaluated an apparent particle diffusivity D* for the steady state neutral beam heated plasma with peaked density profile. Although it does not correspond to a real physical process, it is a good indication of the global particle confinement characteristics. It is necessary to carry out time resolved measurements to separate diffusivity and convective velocity for the better understanding of the particle transport, which is under planning. The effect of the radial electric field must also be considered but is not included in this discussion.

Acknowledgement We also thank Profs. T. Ohbiki and S. Sudo of Plasma Physics Laboratory, Kyoto University for giving us a chance to use the tunable dye laser. This work has been carried out under the collaboration program of National Institute for Fusion Science.

References

[1] H.Yamada, et. al., Proc. 18th EPS Conf., Berlin, Part II (1991) p137 .

[2] K. Ida, et. al., Phys. Rev. Letters 67 (1991) p58.

[3] H.Iguchi, et. al., Proc. 8th Stellarators Workshop,Kharkov (IAEA Viena, 1991) p75.

[4] O.Kaneko, et. al., Proc. 13th IAEA Conf.,Washington (1991) Vol. 2, C-1-4 .

[5] K.Uchino, H.Takenaga, et. al., Research Report of Plasma Engineering Laboratory, Kyushu Univ. No.274 (1992), to be published in J. Nuclear Materials.

TRANSPORT STUDIES USING MODULATION OF DIMENSIONLESS PARAMETERS IN THE ADVANCED TOROIDAL FACILITY*

M. Murakami, T. S. Bigelow, B. A. Carreras, R. A. Dory, J. B. Wilgen, L. R. Baylor, G. R. Dyer, A. C. England, D. P. Hutchinson, R. C. Isler, T. C. Jernigan, H. Ji[a], C. H. Ma, S. Morimoto[a], O. Motojima[a], D. A. Rasmussen, M. Sato[a], W. R. Wing, H. Yamada[a], and the ATF Group

Oak Ridge National Laboratory, Oak Ridge, Tennessee, U.S.A.

Modulation of dimensionless plasma variables in ECH plasmas in the Advanced Toroidal Facility (ATF) torsatron was used to explore anomalous transport mechanisms underlying the behavior of the global energy confinement scaling. The energy confinement scaling can be expressed by a leading term that characterizes the turbulence length scale and a residual term describing the source of the turbulence [1]. The leading term can distinguish the short wavelength turbulence (corresponding to gyro-reduced Bohm scaling) from the long wavelength turbulence (Bohm scaling) for dominant energy loss mechanisms. The earlier regression analyses [2] of the global energy confinement time τ^*_E, from data in a multi-shot database representing diverse conditions with both NBI and ECH plasmas in ATF, suggested that the gyro-reduced Bohm scaling was more closely followed than the Bohm-like scaling, although the discrimination was not strong. The determination of the remaining terms, in particular, the dependences of collisionality ν_* and beta β, tended to be less certain because of the problem of collinearity of the control variables and also the variation of other parameters (e.g., heating power profile shape). To alleviate these problems, new experiments were performed in which individual dimensionless plasma parameters were modulated during single discharges. These experiments have utilized the unique ATF capabilities of long pulses (up to 20 s) and external magnetic configuration control.

In order to establish the leading term of the energy confinement, the magnetic field dependence in the global scaling was studied using second-harmonic ECH (to produce similar power deposition profiles) at B = 0.96 T and 0.64 T with two different gyrotrons (53 and 35 GHz, respectively). Figure 1 shows a comparison of the experimentally observed stored energy with the predictions of gyro-Bohm and Bohm scaling. The gyro-Bohm is a closer fit than Bohm scaling, as indicated by the smaller variance (by a factor of

* Research sponsored by the Office of Fusion Energy, U.S. Department of Energy, under contract DE-AC05-84OR21400 with Martin Marietta Energy Systems, Inc.

a Permanent address: National Institute for Fusion Science, Nagoya 464-01, Japan

two) for the gyro-Bohm scaling. The data also show that the isotope effect on confinement in ATF is small, possibly with a slightly negative dependence of atomic mass A_i, in contrast to tokamaks [3]. These ECH experiments confirmed earlier results [2] that the leading term of the confinement time is the gyro-Bohm scaling, which may result from short-wavelength turbulence.

The second experiment was aimed at establishing the additional dependences to the gyro-Bohm scaling, $\tau_E = \tau_{gB} \nu_*^{\alpha} \beta^{\gamma}$, in a fixed magnetic geometry where other dimensionless parameters such as rotational transform and key configuration parameters (e.g., magnetic well and shear) remain constant. The experiment involved modulation of one dimensionless variable (ν_* or β) while keeping the other constant. This was accomplished by simultaneously modulating the ECH power and the electron density (with gas feedback) such that $\tilde{n}/n = (-2/3)\tilde{P}/P$ for ν_* modulation and $\tilde{n}/n = (4/9)\tilde{P}/P$ for β modulation, both based on the gyro-Bohm scaling. Figure 2 shows the time evolution of the resulting global and local plasma parameters in the ν_* scan. The modulation period (80 ms) was chosen to be longer than both the energy and particle confinement time, and the modulation was applied (at 0.16 s) after the quasi-stationary discharge was established. For the given ECH power modulation ($\tilde{P}/P \approx 25\%$), the amplitude and phase of the density feedback demand were adjusted to give the specified line-average density modulation ($\tilde{n}/n \approx 15\%$). A polar diagram (Fig. 3) based on Fourier analysis at the modulation frequency (12.5 Hz) shows that a modulation amplitude of 50% in ν_* (at $\rho \approx 2/3$) with a negligible β modulation (3%) resulted in a modulation of 8% in the normalized confinement time, implying that $\alpha \approx -1/6$. An experiment was also carried out for β modulation. Regression analysis on both the ν_* and β scans yields $\alpha = -0.18$ and $\gamma = +0.36$ for the modification to the gyro-Bohm scaling. Using the dimensionless correction from these experiments provides as good a fit to the multi-shot NBI and ECH data as did the regression, by mitigating the usual problem of collinearity of control parameters with "orthogonal" variation of the dimensionless parameters.

Of the theoretical models compared in Ref. [3] with tokamak data, dissipative trapped electron mode (DTEM) models (developed for tokamaks) give an opposite dependence on ν_* ($\alpha = +0.4$), implying that DTEM may not govern the global confinement. However, the DTEM could play other roles (e.g., core confinement or constraining electron density profiles). A simple resistive MHD turbulence model shows that the ν_* dependence is close to the data ($\alpha = -0.4$), but the β dependence is opposite to that from the experiment. However, a more favorable trend of confinement with increasing β may result from the modification of the curvature term by β self-stabilization. The magnetic configuration

modulation experiments [4] show that the energy confinement improves as the magnetic well radius expands, as might be expected from stabilization of resistive interchange turbulence.

The favorable ν_* and β dependences ($\alpha = -0.18 \pm 0.05$, and $\gamma = 0.36 \pm 0.10$) observed in these experiments imply excellent prospects for improving confinement by increasing the heating power (implying higher β and higher temperature) in ATF. Long pulses and modulation techniques could be used to establish the dependence of confinement on critical stability factors: magnetic shear, hill/well, and trapped particle fraction. Furthermore, comparisons with tokamaks and stellarators could lead to a better understanding of the anomalous transport mechanisms in toroidal devices.

REFERENCES

[1] J. P. Christiansen, J. G. Cordey, K. Thomsen, Nucl. Fusion **30** (1990) 1183. [Note: the sign of the exponent of the resistive fluid turbulence in Table II should be +1, not −1].

[2] R. A. Dory, M. Murakami, W. R. Wing, ATF Group, Comments Plasma Phys. Controlled Fusion **14** (1991) 237.

[3] F. Wagner et al., 17th EPS Conf.on Controlled Fusion and Plasma Heating (Amsteldam, 1990, ECA), 14B, Pt. 1, p. 58.

[4] M. Murakami et al., in Radio Frequency Power in Plasmas, AIP, New York, 1992 (AIP Conference Proc., **244**).

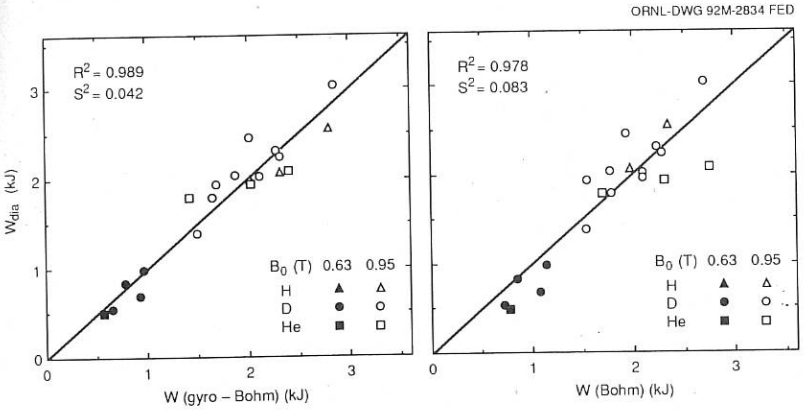

FIG. 1. Comparison of measured plasma stored energy with predictions of the gyro-Bohm scaling ($\propto B^{0.8}p^{0.4}n^{0.6}A_i^{-0.2}$) and Bohm-like scaling ($\propto B^{0.5}p^{0.5}n^{0.5}$).

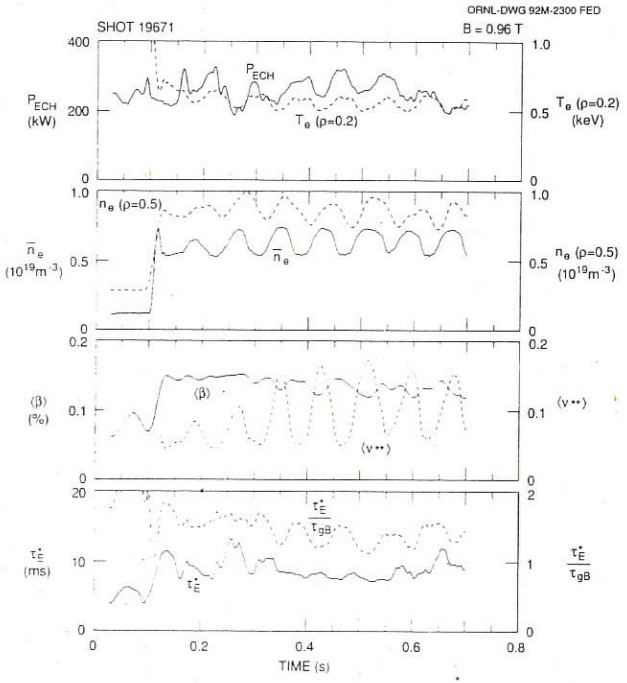

FIG. 2. ν* scan with constant β.

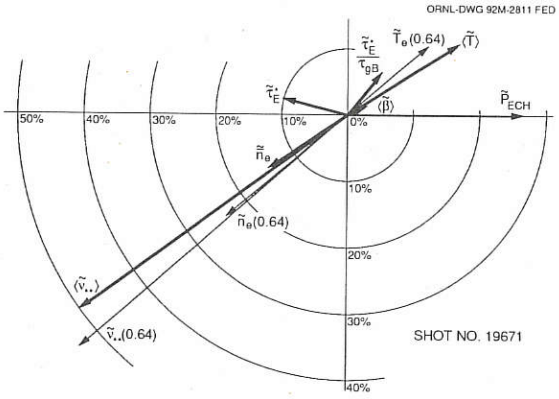

FIG. 3. Polar diagram of the relative modulation of global (shown by bold arrows) and local (by fine arrows) plasma parameters for the ν* scan.

2-10

FLUCTUATION STUDIES OF ECH PLASMAS IN THE ATF TORSATRON*

J.H. HARRIS, G.R. HANSON, J.B. WILGEN, J.D. BELL[1], M. MURAKAMI, B.A. CARRERAS, L.R. BAYLOR, S. ACETO[2], T. S. BIGELOW, R.J. COLCHIN, J.L. DUNLAP, N. DOMINGUEZ, G.R. DYER, A.C. ENGLAND, R.C. ISLER, T.C. JERNIGAN, J.N. LEBOEUF, D.K. LEE[1], J.F. LYON, C.H. MA, A.L. QUALLS, D.A. RASMUSSEN, C.E. THOMAS, T. UCKAN, J. ZIELINSKI[2]
Oak Ridge National Laboratory, Oak Ridge, Tennessee, USA

M.G. SHATS, K.M. LIKIN, K.A. SARKSYAN, L.M. KOVRIZHNYKH
General Physics Institute, Moscow, Russian Federation

A principal goal of experiments on the ATF torsatron ($R = 2.1$ m, $\bar{a} = 0.27$ m, $\iota_0 = 1/q_0 \approx 0.3$, $\iota_a = 1$) in 1991 has been the study of turbulent fluctuations in long pulse (1–20 s), low-collisionality ECH discharges ($B = 0.94$ T, $\bar{n}_e \approx 4\text{–}7 \times 10^{12}$ cm^{-3}, $T_{e0} \approx 1$ keV). These plasmas are macroscopically quiet, but exhibit anomalous outward transport (gyro-Bohm scaling) very much like that seen in tokamaks, suggesting that the underlying transport mechanisms in the two types of toroidal plasmas are similar [1]. The flexible magnetic configuration of ATF makes it possible to change (even during a single discharge) properties—rotational transform, magnetic well, shear, trapped particle confinement—that are expected to influence turbulence and transport.

The fluctuation diagnostics installed on ATF include a heavy-ion beam probe (HIBP), a microwave reflectometer, a fast reciprocating Langmuir probe (FRLP) and a 2-mm microwave scattering diagnostic. Together, these diagnostics make it possible to measure fluctuation amplitudes and other characteristics from the plasma core to the edge. During the 1991 operating period, fluctuation data from the various diagnostics have been combined to yield a picture of the turbulence as a function of normalized radius (ρ) which can be

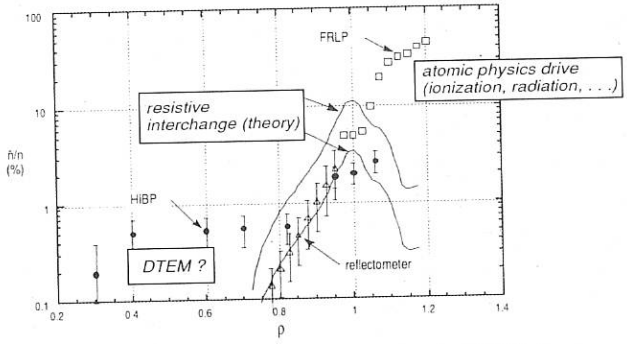

FIG. 1. Radial profile of normalized density fluctuations in ATF ECH plasma.

*Research sponsored by the Office of Fusion Energy, U.S. Department of Energy under Contract DE-AC05-84OR21400 with Martin Marietta Energy Systems, Inc.

[1]Computing and Telecommunications Division, Martin Marietta Energy Systems, Inc., Oak Ridge, TN 37831, USA.
[2]Rensselaer Polytechnic Institute, Troy, NY 12181, USA.

compared with theoretical concepts (Fig. 1).

The edge plasma fluctuations show characteristics similar to those seen in tokamaks, provided the radial position is normalized to the radius of the velocity shear layer [2]. This supports the hypothesis that drive mechanisms that do not depend on plasma current, such as radiation, ionization, charge exchange, etc., are responsible for the observed edge turbulence.

In the gradient region, $0.7 \leq \rho \leq 0.9$, the fluctuations exhibit significant radial correlation lengths $L_c = 2$–5 cm and no radial propagation ($k_r \approx 0$). The measured fluctuation amplitudes $\tilde{n}/n$ are smaller than those predicted by simple mixing length estimates by a factor of 2–10, but are comparable to amplitudes predicted theoretically [3] for resistive interchange turbulence driven by the unfavorable average magnetic curvature in this region. Single-shot configuration variations which vary the magnetic curvature during a discharge indicate that this region governs the overall energy confinement in ATF: global confinement improves as the volume of the magnetic well region expands. This supports the conclusions of early high-β experiments on ATF [4] that demonstrated transient access to the second-stability regime for interchange instabilities.

In the plasma core, measurements using 2-mm microwave scattering [5] show features like those expected for dissipative trapped-electron modes (DTEM). Signals from scattering volumes on the small-major-radius side of the torus, where helically trapped particles are well confined, show features in the density fluctuation spectrum for $k_\theta \rho_s \sim 1$ that are absent in the fluctuation spectra measured on the large-major-radius side of the torus, where helically trapped particles are poorly confined (Fig. 2). Operation near the marginal stability condition for such instabilities could conceivably account for the persistence of flat and hollow density profiles in stellarator experiments (including ATF) with ECH alone.

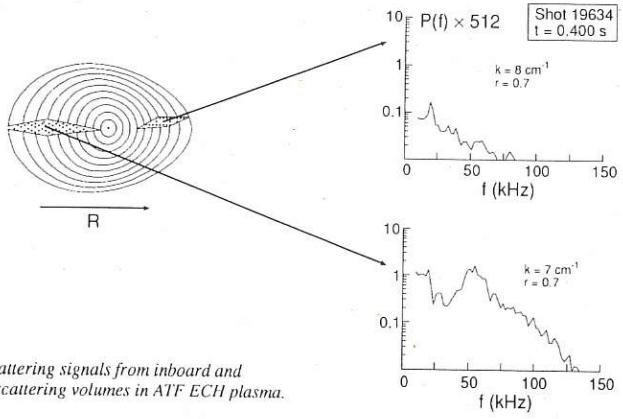

FIG. 2. Scattering signals from inboard and outboard scattering volumes in ATF ECH plasma.

REFERENCES

[1] MURAKAMI, M., ACETO, S.C., ANABITARTE, E.,et al., Phys. Fluids B **3** (1991) 2261.

[2] RITZ, C.P., RHODES, T.L., LIN, H., et al., in Plasma Physics and Controlled Nuclear Fusion Research (Proc. 13th Int. Conf. on Plasma Physics and Controlled Nuclear Fusion Research, Washington, D. C., 1990), Vol. 2, IAEA, Vienna (1991) 589.

[3] DIAMOND, P.H., CARRERAS, B.A., Phys. Fluids B **1** (1989) 1011.

[4] HARRIS, J.H., MURAKAMI, M., CARRERAS, B.A., et al., Phys. Rev. Lett. **63** (1989) 124.

[5] BATANOV, G.M., KOLIK, L.V., SAPOZHNIKOV, A.V., et al., Fiz. Plazmy **15** (1989) 527 (in Russian).

Results of the Heavy Ion Beam Probe Measurements on the Advanced Toroidal Facility*

S. C. Aceto, J. G. Schwelberger, K. A. Connor, and J. J. Zielinski, *Rensselaer Polytechnic Institute, Troy, NY 12180-3590, U.S.A.*

J. C. Glowienka, R. C. Isler, M. Murakami, J. D. Bell, and T. Uckan, *Oak Ridge National Laboratory, Oak Ridge, TN 37831-8072, U.S.A.*

*Research sponsored by the Office of Fusion Energy, U.S. Department of Energy, under contract DE-AC05 84OR21400 with Martin Marietta Energy Systems, Inc. and contract No. 19X-SB078C with Rensselaer Polytechnic Institute.

1 Introduction

A heavy ion beam probe (HIBP) has been used to measure radial potential and density profiles in the Advanced Toroidal Facility (ATF). It has also been used to measure density and potential fluctuations at multiple radial locations. These measurements have been primarily made during ECH discharges, although some data have been obtained during neutral-beam-heated discharges.

2 Potential Profiles

Potential profiles have been obtained under a variety of conditions during ECH discharges. Fig. 1 shows typical radial potential profiles obtained in ECH discharges with two different values of the line-averaged density. Predicted profiles from a model are also shown. The potential is measured relative to the ATF vacuum vessel. The high density case corresponds to a line-averaged density of 1.0×10^{13} cm^{-3}; while the low-density case corresponds to a line-averaged density of 5.0×10^{12} cm^{-3}. The trend of the measured profiles can be described as follows. At low-line averaged densities, the potential is peaked in the center and is approximately 250 to 300 V above the potential at the last closed flux surface. As the density is increased, the central potential begins to drop, both in absolute magnitude and in relation to the edge potential. Finally, during the high density ECH discharges, a small potential well begins to form. Using the experimentally measured electron density and temperature profiles, a comparison has been made with the predictions of neoclassical theory. The model used is based on that of Hastings, et al. [1], where a self consistent field is determined using an ambipolarity constraint on the non-ambipolar particle fluxes. The results shown are those obtained using a three-species model in which one species is an oxygen-like impurity ion. The ion temperature and density profiles needed to perform the analysis are obtained from the PROCTR-MOD code [2], with the central ion temperature used being that determined from neutral particle analysis. Two features deserve emphasis. The first is that the overall trends of the measured and predicted potential profiles are in agreement: at low density both have a central potential higher than the edge potential, while at high density, both have a central potential less than the edge potential. The second is that the magnitudes of the measured and predicted values can differ by a factor of two or more. This difference is well above that of the estimated uncertainty in the potential measurement of $\pm$ 60 V. An investigation of the sensitivity of the model predictions to uncertainties in the temperature and density of each species and in gradients is under-way. The trend of the measured potential profiles as the magnetic configuration is varied is also consistent with the expectations of neoclassical theory.

3 Density Profiles

The density profile is related to the secondary beam current by the equation

$$I_{ds} = 2\kappa I_{prim}\sigma_s^{1>2}\lambda_s n_s \exp[-\int_{P1}^{SV} n(\rho)\sigma^1(\rho)dl - \int_{SV}^{P2} n(\rho)\sigma^2(\rho)dl]$$

where I_{ds} is the detected signal, κ is the secondary emission coeffiecient of the detector, I_{prim} is the primary beam current, $\sigma_s^{1>2}$ is the effective cross section for Cs^+ to Cs^{2+} electron impact ionization, n_s is the electron density at the sample volume, λ_s is the length of the sample volume, $P1$ is the injection point, SV is the sample volume location, $P2$ is the detector point, σ^1 is the total effective cross section for Cs^+ to other charge states, σ^2 is the total effective cross section for Cs^{2+} to other charge states, and dl is the arc length along the trajectory. The subscript s indicates values at the sample volumes and the effective cross sections are the ionization rates divided by the velocity of the beam ions. In a radial sweep of the sample volumes, I_{ds} is recorded as a function of time, which can be transformed into a function of normalized radius ρ. This equation can be used N times for N different locations of the sample volume, giving a system of N equations. Since the absolute value of $I_{prim}\kappa$ is unknown, the relation

$$\int_0^1 n_e(\rho)d\rho = \bar{n}_e$$

is used to uniquely determine the electron density profile, where ρ is the normalized plasma radius, $n_e(\rho)$ is the electron density, and $\bar{n}_e$ is the line average density measured by the 2-mm microwave interferometer. Thus, the first equation, applied N times, and the second relation, together with a knowledge of the electron temperature profile and the trajectories of the heavy ions allow a unique determination of the density profile from the HIBP signal, using a simple iterative method. An example of the density profile obtained fron the HIBP is shown in Fig. 2 and compared with the profiles obtained from FIR interferometry and Thomson scattering. The largest errors in the HIBP density measurement are caused by errors in the edge temperature and in the trajectory calculations. The effective cross sections vary strongly as a function of the electron temperature in the range below 50 eV, near the edge of the plasma. Also, uncertainties in the coordinates of the injection point and the detector point can introduce errors in the measurement that appear as a shift of the profile on the ρ axis.

4 Fluctuations

The (HIBP) has also been used to measure density and potential fluctuations in the plasma from the plasma edge to near the center. The typical density fluctuation level for a low-density ECH discharge is shown in Fig. 3. Near the edge of the plasma, the rms density fluctuation level in the frequency range of 6-500 kHz is approximately 2.5-3.0%. It gradually falls at locations farther inside the plasma to a value of about 0.5% near the plasma center. A large potential fluctuation has been observed during the density ramp-up phase when the neutral beams are turned on. The fluctuation is on the order of 400 to 800 V with a frequency of 30 kHz. It is present only in sample volumes inside of ρ=0.5 and is highly coherent with the Mirnov loop signals. The time-dependent behaviour of this fluctuation is shown in Fig. 4, where one of the raw HIBP detector signals is plotted with the 2-mm interferometer signal. The fluctuation appears in three distinct bursts over a period of 30 ms as the density is ramped up.

References

[1] D. E. Hastings, W. A. Houlberg, and K.C. Shaing, Nucl. Fusion, **25** 445, (1985).

[2] H. C. Howe, ORNL/TM-11521, (1990).

Figure 1. Measured and modeled potential profiles for low-density and high-density ECH discharges.

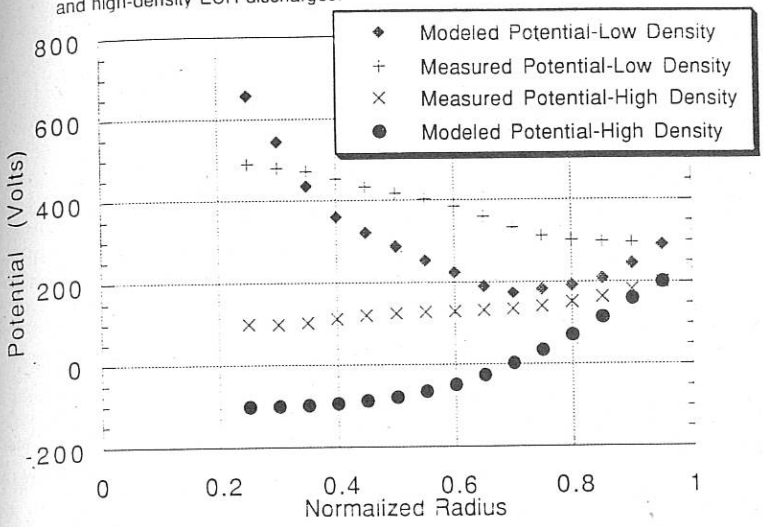

Figure 2. Comparison of electron density profiles obtained from FIR interferometer, Thomson scattering, and the heavy ion beam probe (HIBP).

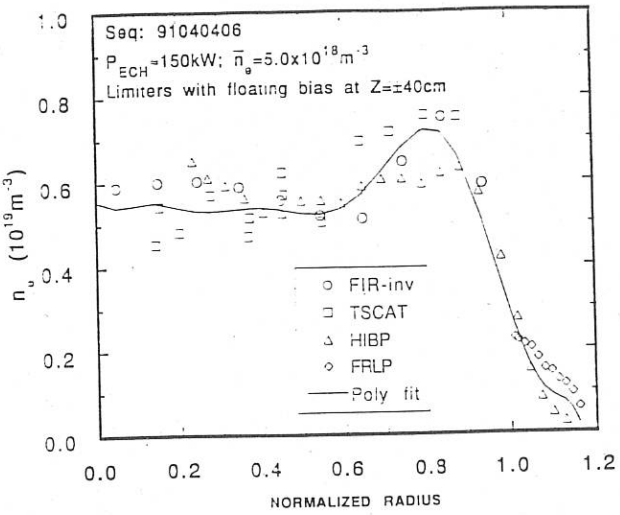

Figure 3. Density fluctuation level in a low-density ECH disharge.

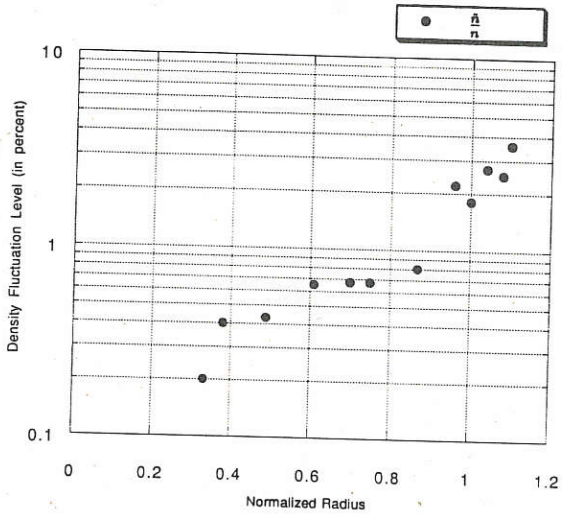

Figure 4. Potential fluctuation during density ramp-up after the neutral beam is turned on.

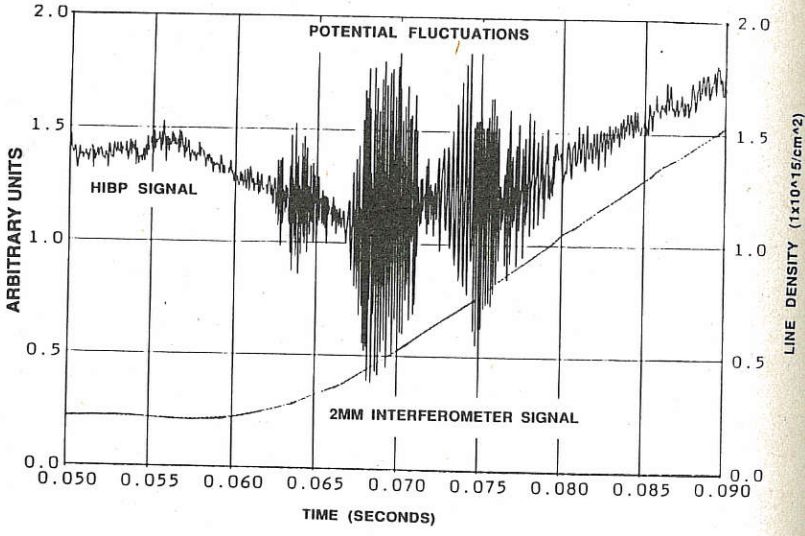

A GENERAL SOLUTION OF THE RIPPLE-AVERAGED KINETIC EQUATION (GSRAKE)

C.D.Beidler*, W.D. D'haeseleer†
*IPP-EURATOM Association, †The NET Team
Max-Planck-Institut für Plasmaphysik
W-8046 Garching bei München, Germany

Abstract — A General Solution of the Ripple-Averaged Kinetic Equation, GSRAKE, is presented and results are obtained for the simple model magnetic field of a stellarator. No assumptions are made as to the relative sizes of the collision frequency, ν, and poloidal precessional frequency, Ω, so that the solution is valid throughout the entire *long-mean-free-path* regime. The solution treats both localized and non-localized particles and the boundary conditions fully account for the interaction between these two classes of particles. All drift terms present within the framework of the ripple-averaged theory are included; in particular, for localized particles $\Omega = \Omega_E + \Omega_{\nabla B}$ is comprised of both the $\mathbf{E} \times \mathbf{B}$ and ∇B precessional frequencies. The solution is thus equally valid in the $\Omega_E \gg \Omega_{\nabla B}$ and the $\Omega_E = 0$ limits. A comparion of the results is also undertaken with those of the FLOCS code (D'haeseleer, Hitchon and Shohet, J. Comp. Phys. 95, (1991) 117). GSRAKE results are in good agreement with those obtained from FLOCS and require only a tiny fraction of the computer time necessary for the latter code.

The Ripple-Averaged Kinetic Equation for Localized Particles — Consider the simple model for the magnetic field strength of a stellarator

$$B/B_0 = 1 - \epsilon_t \cos\theta - \epsilon_h(r)\cos\eta\,,$$

where $\epsilon_t = r/R_0$ is the inverse aspect ratio, ϵ_h is the magnitude of the stellarator's helical ripple and η is the phase angle of this local ripple. In the *long-mean-free-path* regime, where $\mathcal{J} = \oint v_\parallel dl$ is an adiabatic invariant of a ripple-trapped particle's motion, the guiding-center drift-kinetic equation may be time averaged over the bounce motion of localized particles to yield the "bounce-averaged" kinetic equation

$$\langle\dot{r}\rangle \frac{\partial F_m}{\partial r} + \langle\dot{\theta}\rangle \frac{\partial f}{\partial \theta} + \dot{k}^2 \frac{\partial f}{\partial k^2} = \frac{\nu_{eff}}{A'(k^2)} \frac{\partial}{\partial k^2}\left(A(k^2)\frac{\partial f}{\partial k^2}\right),$$

where $\langle\dot{r}\rangle$ and $\langle\dot{\theta}\rangle$ are the bounce-averaged radial drift velocity and poloidal precessional frequency, respectively, and $\nu_{eff} = \nu/2\epsilon_h$ where ν is the 90 degree deflection frequency. This "effective" collision frequency is the frequency with which localized particles are collisionally removed from the helical-ripple wells. $A'(k^2) = 4K(k)$ and $A(k^2) = 8(E(k) - (1-k^2)K(k))$ are functions of the complete elliptic integrals of the first, $K(k)$, and second, $E(k)$, kinds with the argument being the pitch-angle variable

$$k^2 = (\kappa/\mu B_0 - 1 + \epsilon_t \cos\theta + \epsilon_h)/2\epsilon_h\,,$$

with $\kappa = mv^2/2$ and $\mu = mv_\perp^2/2B$. Localized particles satisfy $0 \le k^2 < 1$, with the limits corresponding to particles trapped at the bottom of a helical-ripple well and to those marginally trapped, respectively.

The constraint that the particle flux be ambipolar generally requires the formation of a radial potential, $\Phi(r)$. Given this assumption and the model magnetic field, the ripple-averaged drift terms for localized particles are given by

$$\langle\dot{r}\rangle = v_d \sin\theta, \qquad \langle\dot{\theta}\rangle = \Omega_E + \Omega_t \cos\theta + \Omega_h\langle\cos\eta\rangle, \qquad \dot{k}^2 = -\omega_k \frac{A(k^2)}{A'(k^2)} \sin\theta,$$

where $v_d = eT/(qRB)$ is the ∇B drift velocity (T being the particle's kinetic energy in eV), $\langle \cos\eta \rangle = 2E(k)/K(k) - 1$ and

$$\Omega_E = -\frac{(d\Phi/dr)}{rB_0}, \qquad \Omega_t = \frac{v_d}{r}, \qquad \Omega_h = \frac{v_d}{\epsilon_t}\frac{\partial \epsilon_h}{\partial r}, \qquad \omega_k = \frac{\epsilon_t}{2\epsilon_h}\Omega_h.$$

The Ripple-Averaged Kinetic Equation for Non-Localized Particles — Blocked particles (executing tokamak-like banana orbits) and passing particles have $k^2 > 1$ and are referred to as *non-localized* particles. For such particles it is possible to average the kinetic equation over the time it takes to traverse a **single** ripple well; i.e. quantities averaged in this way do not vary over a single ripple but do change over longer scale lengths. The variable k^2 is inconvenient to use for non-localized particles because of its range $1 < k^2 < \infty$. Instead, the variable $\zeta^2 = 1/k^2$ will be employed. The ripple-averaged kinetic equation may then be expressed

$$\langle \dot{r} \rangle \frac{\partial F_m}{\partial r} + \langle \dot{\theta} \rangle \frac{\partial f}{\partial \theta} + \dot{\zeta}^2 \frac{\partial f}{\partial \zeta^2} = \frac{2\nu_{eff}}{K(\zeta)} \mathcal{E}^{3/2} \frac{\partial}{\partial \zeta^2}\left(\mathcal{E}^{1/2} \zeta^2 E(\zeta) \frac{\partial f}{\partial \zeta^2} \right),$$

with

$$\mathcal{E} = \frac{\zeta^2 \kappa}{\mu B_0} \approx \zeta^2 + \epsilon_h(2 - \zeta^2), \qquad \langle \dot{r} \rangle = v_d \sin\theta \left(1 + \frac{2\epsilon_h}{\mathcal{E}} \frac{E(\zeta)}{K(\zeta)} \right),$$

$$\langle \dot{\theta} \rangle = \begin{pmatrix} + \\ - \end{pmatrix} \frac{\iota v}{R} \left(\frac{\epsilon_h}{2\mathcal{E}} \right)^{1/2} \frac{\pi}{K(\zeta)}, \qquad \dot{\zeta}^2 = (\zeta^2)^2 \frac{\epsilon_t}{2\epsilon_h} \sin\theta \langle \dot{\theta} \rangle,$$

where ι is the rotational transform. This is really two equations — one for each sign of $\langle \dot{\theta} \rangle$ — which will be referred to as the equations for the *forward* and *backward* distribution functions (the reason for this choice of names will shortly become clear).

Method of Solution — The poloidal dependence of f is expanded in Fourier series,

$$\begin{pmatrix} f_\ell \\ f_{f,b} \end{pmatrix} = \frac{\partial F_m}{\partial r} \left[\begin{pmatrix} Z_\ell(k^2) \\ Z_{f,b}(\zeta^2) \end{pmatrix} + \begin{pmatrix} Y_\ell(k^2) \\ Y_{f,b}(\zeta^2) \end{pmatrix} \sin\theta + \begin{pmatrix} X_\ell(k^2) \\ X_{f,b}(\zeta^2) \end{pmatrix} \cos\theta + \cdots \right]$$

being assumed for the localized, forward and backward distribution functions, respectively. One then obtains the following sets of coupled equations (assuming that the Fourier *ansatz* is terminated at the θ terms)

$$\frac{\Omega_t}{2} Y_\ell - \frac{\omega_k}{2} \frac{A(k^2)}{A'(k^2)} Y'_\ell = \nu_{eff} \left(Z'_\ell + \frac{A(k^2)}{A'(k^2)} Z''_\ell \right)$$

$$v_d - (\Omega_E + \Omega_h \langle \cos\eta \rangle) X_\ell - \omega_k \frac{A(k^2)}{A'(k^2)} Z'_\ell = \nu_{eff} \left(Y'_\ell + \frac{A(k^2)}{A'(k^2)} Y''_\ell \right)$$

$$(\Omega_E + \Omega_h \langle \cos\eta \rangle) Y_\ell = \nu_{eff} \left(X'_\ell + \frac{A(k^2)}{A'(k^2)} X''_\ell \right)$$

for the localized distribution function (where the primes denote d/dk^2) and

$$\begin{pmatrix} + \\ - \end{pmatrix} (\zeta^2)^2 \frac{\epsilon_t}{2\epsilon_h} \Omega_\theta \frac{Y'_f}{2} = \mathcal{C}(Z_f)$$

$$v_d \left(1 + \frac{2\epsilon_h}{\mathcal{E}} \frac{E(\zeta)}{K(\zeta)} \right) - \begin{pmatrix} + \\ - \end{pmatrix} \Omega_\theta X_f + \begin{pmatrix} + \\ - \end{pmatrix} (\zeta^2)^2 \frac{\epsilon_t}{2\epsilon_h} \Omega_\theta Z'_f = \mathcal{C}(Y_f)$$

$$\begin{pmatrix} + \\ - \end{pmatrix} \Omega_\theta Y_f = \mathcal{C}(X_f)$$

$$C(Z_f) = \nu_{eff}\mathcal{E}\left(\frac{2E(\zeta)}{K(\zeta)}(2\mathcal{E}-\epsilon_h)-\mathcal{E}\right)Z_f' + 2\nu_{eff}\mathcal{E}^2\zeta^2\,\frac{E(\zeta)}{K(\zeta)}\,Z_f''$$

for the forward distribution function with $\Omega_\theta = (\mp v/R)(\pi/K(\zeta))\sqrt{\epsilon_h/2\mathcal{E}}$ (the primes in the forward equations denote $d/d\zeta^2$). The equations for the backward distribution function are obtained by replacing the f subscripts with b and flipping the sign of all terms in which $(\pm)$ appears. These equations are solved by finite differencing (second-order accuracy) on a mesh with non-uniform spacing. Non-uniform spacing is desirable as the distribution function can become very localized about $k^2 = 1$ at very-low ν.

Boundary Conditions — The phase-space flux of particles must be conserved at the $k^2 = 1$ boundary, i.e.

$$-J_\ell \dot{k}^2 f_\ell = J_f \dot{\zeta}^2 f_f + J_b \dot{\zeta}^2 f_b$$

where J_x is the appropriate Jacobian. Defining *forward* as the direction in which collisionless trapping can take place, the *trapping probability*, P_t, is calculated to be consistent with the flow velocities on either side of $k^2 = 1$, i.e. $P_t = -(J_\ell \dot{k}^2)/(J_f \dot{\zeta}^2)$. It then follows that $J_b = -J_f(1-P_t)$. To make use of these conditions the sets of equations must be written in "flux" form; e.g. for the localized equations

$$\frac{(\Omega_t+\omega_k)}{2}Y_\ell + \frac{1}{2A'(k^2)}\left[(\widetilde{J_\ell \dot{k}^2})Y_\ell\right]' = C(Z_\ell)$$

$$v_d - (\Omega_E + \Omega_h\langle\cos\eta\rangle)X_\ell + \omega_k Z_\ell + \frac{1}{A'(k^2)}\left[(\widetilde{J_\ell \dot{k}^2})Z_\ell\right]' = C(Y_\ell)$$

$$(\Omega_E + \Omega_h\langle\cos\eta\rangle)Y_\ell = C(X_\ell)$$

where $C(\mathcal{Z}_\ell)$ is shorthand for the collision operator and the tilde indicates that the poloidal dependence of $J_\ell \dot{k}^2$ has been factored out. Numerical differentiation at mesh point n (where n is the mesh point just below $k^2 = 1$ for localized particles and just below $\zeta^2 = 1$ for forward and backward particles) is then possible using, for example,

$$-\left[(\widetilde{J_\ell \dot{k}^2})Z_\ell\right]_{n+1} = \left[(\widetilde{J_f \dot{\zeta}^2})Z_f\right]_n + \left[(\widetilde{J_b \dot{\zeta}^2})Z_b\right]_n$$

Results — The FLOCS code solves the *time-dependent* ripple-averaged kinetic equation by central differencing on a 2D mesh (θ, k^2) using a time-relaxation scheme. The variable k^2 is used for all particles; a multi-mesh approach (with successively coarser mesh spacings) makes it possible to handle $0 \le k^2 \le 100$ when so desired. To investigate low-ν transport, however, it is usually sufficient to consider the region $0 \le k^2 \le 3$ with a single mesh. Results from FLOCS and GSRAKE are compared in the accompanying figures for a stellarator with $\epsilon_t = 0.05$ and $\epsilon_h = 0.063$ in the limit $\Omega_E \gg \Omega_h, \Omega_t$. In Figure 1, plots of the $\sin\theta$ dependence of the distribution function are shown for $\nu_{eff}/\Omega_E = 0.1$ (only the results for Y contribute directly to the particle and heat fluxes); agreement for the other constituent parts of f is equally good. Note that this excellent agreement is obtained even though the GSRAKE *ansatz* for f is limited to a very small number of harmonics. Figure 2 gives FLOCS and GSRAKE estimates of the monoenergetic diffusion coefficient

$$D = -\frac{v_d}{2\pi}\left(\frac{\epsilon_h}{2}\right)^{1/2}\left\{2\int_0^1 dk^2\, Y_\ell(k^2)K(k) + \int_0^1 d\zeta^2\left(K(\zeta)+\frac{2\epsilon_h}{\mathcal{E}}E(\zeta)\right)\left(\frac{Y_f(\zeta^2)+(1-P_t)Y_b(\zeta^2)}{\mathcal{E}^{3/2}}\right)\right\}$$

as a function of collision frequency. Also shown are results from a guiding-center Monte-Carlo code and from the DKES code (Hirshman, et al., Phys. Fluids 29, (1986) 2951).

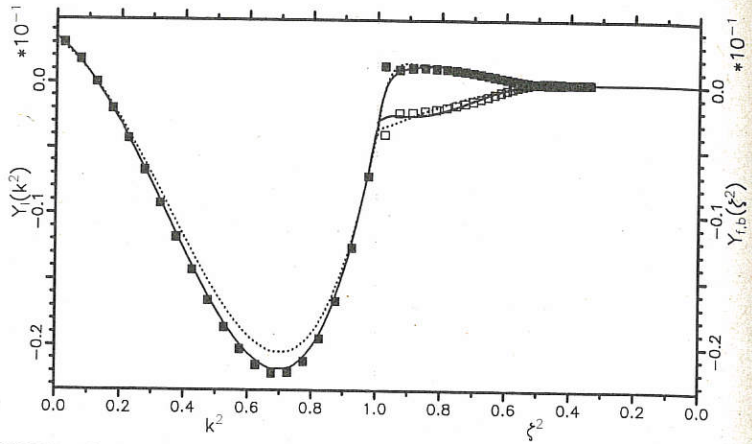

FIGURE 1. The $\sin\theta$ dependence of the perturbed distribution function is shown for localized particles as a function of k^2 (Y_ℓ, left half of the figure), and for forward-moving and backward-moving particles as a function of $1/k^2 \equiv \zeta^2$ (Y_f and Y_b, respectively, right half of the figure). Results from the FLOCS code are given by the blackened squares for Y_ℓ and Y_f and by the open squares for Y_b. Two sets of GSRAKE results are illustrated; the solid line gives the solution when the Fourier ansatz for the distribution function is truncated at the 2θ terms, while the dotted line shows the results when the ansatz is truncated at the θ terms. In this figure the limiting case $\Omega_E \gg \Omega_{\nabla B}$ is illustrated. CPU times (CRAY XMP) — FLOCS: 590 seconds; GSRAKE: < 1 second.

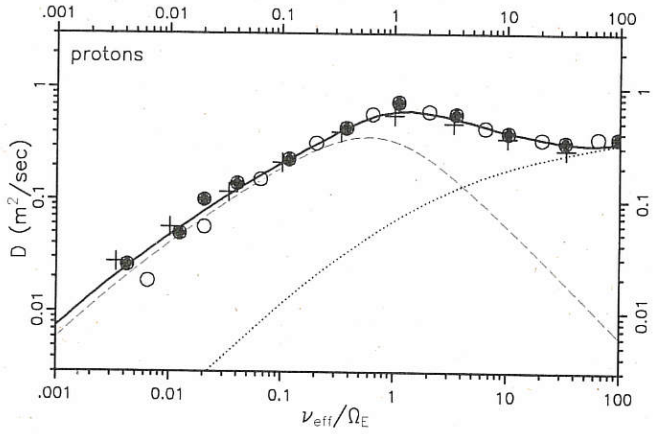

FIGURE 2. The monoenergetic diffusion coefficient as a function of normalized collision frequency for a stellarator with $R_0 = 20$ m, $B_0 = 4$ T, $\epsilon_t = 0.05$, $\epsilon_h = 0.063$ and $T = 12$ keV. GSRAKE results are given by the solid line (composed of 20 data points per decade), FLOCS results are shown as crosses (+). Numerical estimates of D from a guiding-center Monte-Carlo simulation are shown by solid circles (•), DKES results by open circles (o). The expected "axisymmetric" contribution to D is given by the dotted line while the broken line is an analytic approximation for the expected helical-ripple transport.

Influence of electric fields on the heating efficiency in the W7AS Stellarator

A. Teubel and F.-P. Penningsfeld

Max-Planck-Institut für Plasmaphysik,
D-8046 Garching, FRG

Abstract: A version of the neutral beam injection code FAFNER which now takes into account a radial electric field is applied to the W7AS Stellarator. With increasing electric potential (from -5kV to +5kV) the heating efficiency decreases for co and increases for counter injection. This is different to the W7A Stellarator, where the confinement of the fast ions was strongly enhanced by negative as well as positive electric potentials.

Introduction: The presence of radial electric fields E_{rad} can strongly influence the confinement of fast ions as known from W7A /1,2/ where the ions were injected nearly perpendicularly ($|v_{||}/v| < 0.1$). In W7AS however, the effect of E_{rad} on the heating efficiency η_h is expected to be less important because of tangential injection ($|v_{||}/v| > 0.75$). However quantitative numerical results concerning $\eta_h(E_{rad})$ and the heating profile are not available . For a proposed concept of injection in the W7X Stellarator /3/ with $|v_{||}/v| = 0.35\text{-}0.65$ the investigation of this problem is also of interest.
The 3-dimensional computer code FAFNER simulates the injection of fast neutral particles into a toroidal plasma and the paths of the resulting ions. The global efficiency, the losses (i.e. shine through, charge exchange, and orbit losses to the wall and the limiters), the birth profile and the heating profile can be calculated for actual discharges. The field configuration, calculated with a MHD code, the measured density and temperature profiles, as well as the beam parameters are taken as input parameters. Now a new version of this Monte Carlo code treats the guiding centre part in magnetic coordinates (toroidal magnetic flux Ψ, toroidal and poloidal angle Φ and Θ, respectively /4/). The use of these coordinates has several advantages, mainly the separation of the slow motion across the field lines from the fast motion along the field lines and the natural representation of quantities which are constant on magnetic surfaces (e.g., the electric potential, densities, and temperatures). Additionally the energy conservation is inherently fulfiled.

Electric field and guiding centre orbits: For simplicity and comparison with /1/ the electric potential is assumed to be $V(\Psi) = V_0 \cdot (1 - \Psi / \Psi_b)$. Ψ_b specifies the outermost flux surface (effective radius $r \approx \text{const} \cdot \sqrt{\Psi}$, r_b=22.3cm). In the case of W7AS injection (full particle energy E_0=45keV, ion species mix E_0: $E_0/2$: $E_0/3$ = 0.5: 0.3: 0.2) it is found that even a relatively strong assumed electric potential

$|V_0|$=5kV ($|E_{max}|$=500V/cm) does not change the orbit topology of passing particles. This is different to the case of nearly perpendicular injection in W7A, where the toroidal plasma resonance plays an important role /2/.
The orbits of fast ions shown in Fig.1 are the outermost closed orbits in the sense that particles starting outside this region cross the plasma edge and therefore are lossed particles. With increasing V_0 (from -5kV to +5kV) the loss region increases for co injection and decreases for counter injection. Because of the larger gyroradius this effect is stronger for smaller B-field strength. The presence of limiters (r_{lim}=18cm<r_b) additionally enhances the orbit losses.

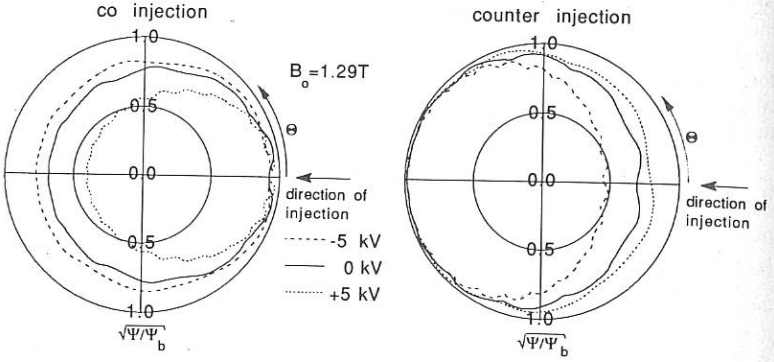

Fig 1: Projection of fast ion drift orbits onto a poloidal plane for different electric potentials, typical initial kinetic ion energy $E_0/2$=22.5keV, $v_{||}/v$ = +0.85 and -0.85 for counter and co injection, respectively

Loss mechanisms V_0=0: The dependence of shine through, charge exchange and orbit losses (including limiter losses) on the line averaged electron density $\int$ndr are shortly discussed. Taking the input quantities from shot series 13556 ($\int$ndr=$9\cdot10^{15}$cm^{-2}) and scaling only the central density the following results are obtained (Fig.2). Orbit losses are nearly independend (4%-8%) on $\int$ndr for co injection but increase from 5% to 30% with density for counter injection (outward shift, see Fig.1). At high densities $\int$ndr>$3\cdot10^{15}$cm^{-2} the orbit losses are dominant for counter injection whereas the heating for co injection is very efficient (η_h>90%). In the low density region $\int$ndr<$1\cdot10^{15}$cm^{-2} the heating is mainly limited by shine through losses. Also the charge exchange losses are enhanced (>10%). Thus the efficiencies for co and counter injection are approximately equal at low densities.

Influence of an electric field on the heating efficiency: The effect of an assumed radial electric field is discussed for a shot series at full (B_0=2.56T: shot series 13556) as well as at half magnetic field strength (B_0=1.26T: shot series 17916). As known from measurements a positive V_0 can be excluded nevertheless these results are presented for completeness also.

1. dependence on ∫ndr for V_0=-5kV (Fig.2): For co injection with its inward shifting the simulations for V_0=-5kV yield approximately the same results as for V_0=0kV. A small deterioration of the efficiency from 75% to 65% is obtained in the counter case for $\int ndr > 4 \cdot 10^{15} cm^{-2}$. In the low density region the co and counter heating efficiencies are not affected by an electric field (more central birth of ions).

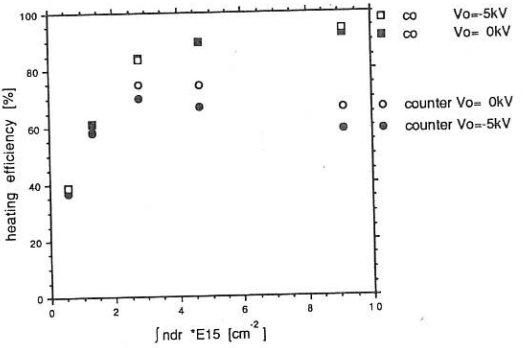

Fig 2: Heating efficiencies as a function of the line averaged density ∫ndr with -5kV and 0kV. Parameters are taken from shot series 13556 and only the central density is scaled

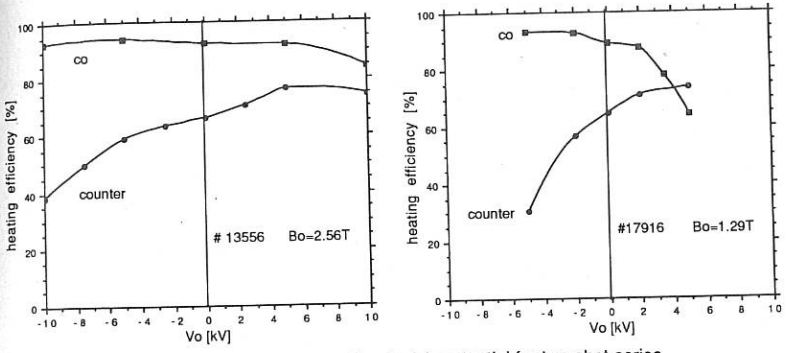

Fig 3: Heating efficiencies in dependence on the electric potential for two shot series

2. dependence on V_0 (Fig.3): For co injection at full field (B_0=2.56T) the heating efficiency is nearly independent of V_0 even at very high electric fields ($|V_0|$=10kV). For counter injection the efficiency increases nearly linearly with V_0. At half field operation, i.e. shot series 17916 ($\int ndr = 4.5 \cdot 10^{15} cm^{-2}$), the electric field has a much stronger influence on η_h. The efficiency increases from 30% to 70% for counter and decreases from 95% to 60% for co injection. The dependence of the outermost closed orbits on the electric potential gives an qualitative understanding of these results (Fig.1). E.g., for co injection the area of the loss region increases with V_0 causing a decreasing of η_h.

3. Balance of kinetic energy: With the power P_{neu} of injected neutral , the heating power P_{heat} , and the power losses P_{loss} the quantity $g_{kin} = (P_{heat} + P_{loss}) / P_{neu} - 1$ is a measure for the transfer of potential field energy to the kinetic energy of the fast ions during their guiding centre motion ($E_{kin}+E_{pot}=E_{tot}$=const). For W7AS this energy transfer is of less importance (e.g., shot series 17916: $|g_{kin}|<12\%$ for $|V_0|$=5kV and $|g_{kin}|<3\%$ for $|V_0|\leq$2kV).

4. Heating profiles for shot series 17916 (Fig 4): For V_0=0 a comparison of the birth profiles with the heating profiles clearly shows the inward shifting for co and outward shifting for counter injection. The strongest influence of the electric field on the heating profile is found for counter injection and negative potential. In this case the loss region as well as the outward shift are enhanced. For co injection and V_0=+5kV the increasing inward shift is dominated by the increasing loss region.

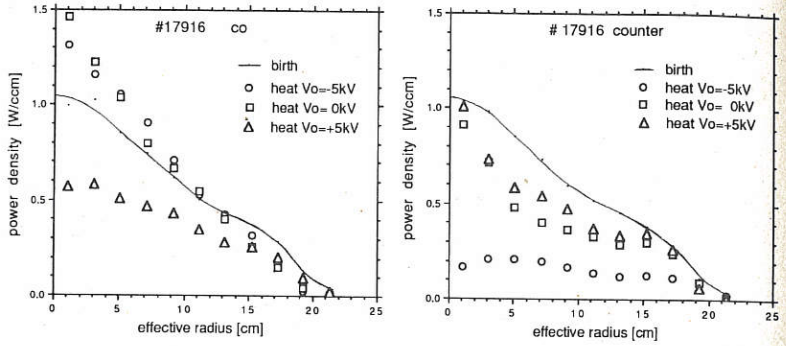

Fig 4: Birth and heating profiles for different electric potentials for co and counter injection

References

/1/ F.-P. Penningsfeld, W. Ott, and E. Speth: Proceedings of the 12th European Conference, Vol. 9F Part 1, 397, Budapest (1985)

/2/ K. Hanatani, F.-P. Penningsfeld, and H. Wobig: International Stellarator / Heliotron Workshop, Kyoto (1986)

/3/ F.-P. Penningsfeld and E. Speth: Proceedings of the 3rd Workshop on Wendelstein W7X, 186, Ringberg (1989)

/4/ T. S. Chen: Report IPP 0/50, Garching (1988)

CHANGE OF ADIABATIC INVARIANT IN TRAP-DETRAPING PROCESSES IN STELLARATOR

S.V.BULANOV, S.G.SHASHARINA

General Physics Institute, Russian Academy of Sciences,
Vavilov Street, 38, Moscow, Russia

Low-collisional transport in stellarator is governed by the locally trapped particles and the so-called transition particles which collisionlessly change their orbits from the locally trapped to the toroidally trapped and vice versa /1/. To study the transport of these particles we need to solve the drift kinetic equations which, in the stellarator case, are

$$dr/dt = v_d(\varepsilon_t sin(\theta)+l\varepsilon_t sin(\lambda)), \tag{1}$$

$$d\theta/dt = (v_H/r)((d\varepsilon_H/dr)cos(\theta)+(d\varepsilon_t/dr)cos(\lambda))+\Omega_E + u/qR, \tag{2}$$

$$d\phi/dt = u/R, \tag{3}$$

where $v = \mu B_o/R\omega$ is a gradient drift velocity, ω is a gyro frequency, $\Omega = (dV/dr)/r\,\omega$ is an electric drift frequency, $V = e\Phi(r)/m$, with $u = (2(E-\mu B))^{1/2}$ being the parallel velocity, $B = B_o\,(1-\varepsilon_t cos(\theta)-\varepsilon_h cos(l\theta-M\phi))$ the stellarator magnetic field, ϕ and θ toroidal and poloidal angles, ε_t and ε_h the toroidal and helical modulations, $R = R_0(1-\varepsilon_t cos(\theta))$. This set of the equations is three dimensional. That is why introducing the adiabatic invariant, J, which eliminates one degree of freedom is of great help here,

$$J = R \oint u\, d\phi\ . \tag{4}$$

The main difficulty arising at calculation of J is connected with the finite rotational transform, $1/q$, through which the angles are related to each other, $\theta = \phi/q + const$.

This relationship makes the evaluation of J quite difficult. That is why the regular procedure to evaluate J was proposed only for the case of negligibly small $1/Mq$ /2/. The other approaches /1,3/ used approximations for B.

We propose here a regular procedure to evaluate the corrections to the invariant J (in comparison with that found earlier /2/) taking into account the relationship between the toroidal and poloidal angles. The main idea is to introduce new (fast and slow) variables, λ and s, no longer related to each other,

$$\lambda = l\theta - M\phi, \quad s = ((\phi/q) - \theta)/(1 - 1/Mq). \tag{5}$$

Leaving in B only the first order terms in $1/qM$, we reduce equation of motion, $R\, d\phi/dt = u$, to

$$(dy/d\tau)^2/2 = 1 - \cos(y) + \Delta A - \alpha y, \tag{6}$$

whis is similar to the energy integral of the nonlinear oscillator equation of motion. The change of adiabatic invariant due to the separatrix crossing has been evaluated in the cases of "fast" and "slow" crossing in /4.5,6/, and here we present the application of the approach developed in /6/ to the case described by (6).

In Eq.(6)

$$\Delta A = A - 1 - \alpha\pi \ , \ \alpha = \alpha_0 |\sin(y)| \ .$$

$$A = (E - \mu B_0(1 - \varepsilon_t \cos(s))/\mu B_0 \varepsilon_h \ , \quad \alpha_0 = \varepsilon_t/qM\varepsilon_h \ . \tag{7}$$

$$y = \lambda - \pi \ , \ \tau = t\,(R/M)\,(\mu B_0 \varepsilon_h)^{1/2}.$$

The locally trapped particles satisfy $\Delta A > -2\pi\alpha$. We imply that $\alpha \simeq |\Delta A| \ll 1$ which means that we are interested at near separatrix behavior of the locally trapped particles in stellarator. Expanding the solution in α, $y = y_0 + y_1 + \ldots$, yields

$$y_0 = 4\ arctg(e^{\tau}) - 2\pi, \tag{8}$$

$$y_1 = C(dy_0/d\tau) + (dy_0/d\tau) \int ((\Delta A - \alpha_0\ y_0)/(dy_0/d\tau)^2)d\tau \tag{9}$$

The asymptotes of the solution at $\tau \to \infty$ are

$$y_1(\tau \to +\infty) = (\Delta A/8)\ e^{\tau}.\quad y_1(\tau \to -\infty) = -((\Delta A+2\pi\alpha)/8)\ e^{-\tau} \tag{10}$$

The turning points of the locally trapped particle are defined by $d(y_0+y_1)/d\tau = 0$ as τ goes to ∞. This gives

$$\tau_2 = (1/2)\ ln(32/|\Delta A|).\quad \tau_1 = -(1/2)\ ln(32/|\Delta A+2\pi\alpha|). \tag{11}$$

The invariant then yeilds

$$J = (2R(\mu B_0 \varepsilon_h)^{1/2}/M)\ S.\qquad S = S_0 + S_1. \tag{12}$$

$$S_0 = \oint (dy_0/d\tau)^2\ d\tau = 16.$$

$$S_1 = 4 \int_{\tau_1}^{\tau_2} (dy_0/d\tau)\ (dy_1/d\tau)\ d\tau = 2\ \Delta A\ (\tau_2 - \tau_1) - 4\alpha\pi\tau_1. \tag{13}$$

In particular, the separatrix ($\Delta A = -2\pi\alpha$) value of the invariant, $J = J_s$, is

$$J_s = (16\ R\ (\mu B_0 \varepsilon_h)^{1/2}/M)\ (1-(\pi\alpha/8)\ L).\quad L = ln(\pi\alpha/16). \tag{14}$$

Thus, we rigorously derived the longitudinal invariant for the locally trapped particles in stellarator near the separatrix. We also investigated the case of deeply trapped particles and found that the effect of the finite α are not important there. With the help of Eq.(15) we evaluated the trapping probability: /1,4/

$$P = -Q\left(\sigma\left(\frac{2\varepsilon_h(dV/dr)}{\mu B_0(d\varepsilon_H/dr)}+1\right)+\frac{\varepsilon_h(dV/dr)\ \pi\alpha_0}{\mu B_0(d\varepsilon_H/dr)\ 8\varepsilon_h}ctg(s)(L+1)\right), \qquad (15)$$

$$Q = 4\ (\mu B_0\varepsilon_h)^{1/2}(d\varepsilon_H/dr)/(\varepsilon_t\pi\omega\varepsilon_h). \qquad (16)$$

REFERENCES

/1/ L.M.Kovrizhnykh, S.G.Shasharina, Nucl.Fusion 30, 453 (1990)
/2/ J.R.Cary, C.L.Hedrick, J.S.Tolliver, Phys.Fluids 31, 158 (1988)
/3/ T.E.Stringer, Nucl.Fusion 12, 689 (1972)
/4/ J.R.Cary, D.F.Escande, J.L.Tennyson, Phys.Rev A34, 4156 (1986)
/5/ A.V.Timofeev, Sov.Phys.JETP 48, 656 (1978)
/6/ S.V.Bulanov, S.G.Shasharina, submitted to Nuclear Fusion

α-PARTICLE BEHAVIOUR OUTSIDE THE LAST CLOSED MAGNETIC SURFACE IN DIVERTOR STELLARATORS.

F.Alladio, P.Batistoni, A.Mancuso

Associazione EURATOM-ENEA sulla Fusione, C.R.E. Frascati
C.P. 65 - 00044 Frascati, Rome (Italy)

Introduction

The stellarator approach to controlled magnetic fusion offers the well known advantages of net toroidal current free, steady state operations as the rotational transform necessary for the magnetic toroidal confinement is provided by steady currents flowing in external windings. Usually stellarators are characterized by high aspect ratios (A>10), however the exploration of more compact aspect ratios is interesting due to the reduced winding size and the higher use of the magnetic field volume. However, the combination of toroidal effects with the helical ripples of the magnetic field raises concern about the alpha particles confinement, necessary for steady ignition. Recently /1/, investigations have been made on the amount and the spatial distribution of direct collisionless losses of alpha particles in stellarators with varying aspect ratios $3<A<12$. The studied configurations have been idealized stellarators with l=2 poloidal winding number and with helicoidal surface currents distributed on circular tori, flowing with constant pitch in toroidal coordinates, that means a higher pitch in the outside and a lower pitch in the inside of the torus. The choice of this winding law has turned out to be a rewarding one since it has allowed a fully analytical treatment of the 3-D vacuum field and has permitted an easy access to low aspect ratios. The parameters of one of the most interesting configurations so far considered are: $R^*/a^*=2.15$ as the aspect ratio of the surface current distribution, A=4.35 as the plasma aspect ratio, M=9 as the toroidal winding number, taxis = 0.108 and tedge = 1.15 as the values of the rotational transform at the axis and at the edge respectively. The toroidal field has the usual ideal form B_0R_0/R. All the configurations are characterized by very low ergodicity of the vacuum field, strong shear at the edge and pronounced separatrix features. The modulation of the magnetic field strength due to the helical ripple is constant along the field lines.

Divertor Characteristics

Figure 1 shows the Poincare' plot of the magnetic structure of the A=4.35 stellarator configuration at $\phi=0, 2\pi/4M$ and $2\pi/2M$. The quite ordered structure of the magnetic field lines around the X-points of the closed magnetic surfaces points out that the so obtained configuration can be viewed as a stellarator endowed with a divertor. Regions of chaotic magnetic field lines seem to be present, conversely, outside the last closed magnetic surface far from the divertor region, in particular on the outboard of the torus.

Orbit Calculation

A collisionless orbit calculation, based on the Boozer /2/ coordinates (ψ,θ_0,χ), (where $2\pi\psi$ is the toroidal magnetic flux, θ_0 is an angle which labels the field line, χ is the generalized magnetic potential) has been performed /1/. The use of Boozer coordinates is particularly suitable for studying the drift orbits in the complex field of a stellarator since the slow motion across the field lines is well separated from the rapid motion along these lines, moreover it requires only the knowledge of the magnetic field strength and of its derivatives. However the disadvantage is the restriction to integrating particle orbits within the last closed flux surface since the

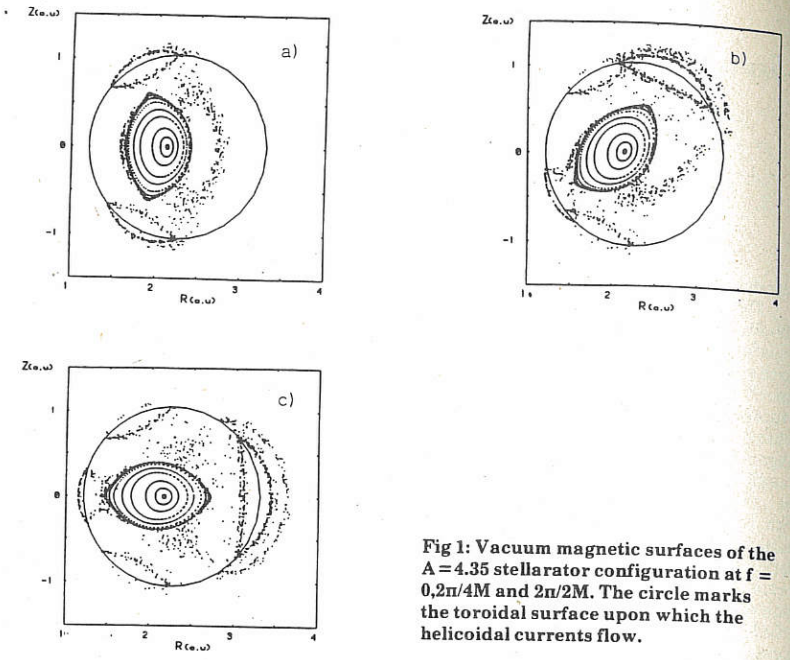

Fig 1: Vacuum magnetic surfaces of the A = 4.35 stellarator configuration at f = 0,2π/4M and 2π/2M. The circle marks the toroidal surface upon which the helicoidal currents flow.

Boozer coordinates are not defined outside this surface, while a correct evaluation of particle losses requires a realistic modelling of the boundary. The magnetic field strength B is represented in Boozer coordinates by Fourier decomposition $B=B_0 \Sigma_{p,q} \delta_{p,q}(\psi) \cos[p\theta-q\phi]$; 15 harmonics have been kept for this configuration. It has to be remarked that in the low aspect ratio cases the helicity coefficient is comparable with the toroidicity coefficients. So far only the vacuum field (zero β case) has been considered for the computation of alpha particle containment. In the ORBIT code, the particles are started with a random uniform distribution in pitch, toroidal and poloidal angles and with a radial birth distribution given by $(1-\psi/\psi_{edge})^2$. To obtain a reactor relevant estimate of the confinement capabilities of the studied configurations, the normalized Larmor radius of 3.5 MeV alpha particles has been fixed to $\rho_L/\langle a\rangle = 0.02$ which means $B_0\langle a\rangle = 14$ T·m, where $\langle a\rangle$ is the average minor radius. Particle orbits are followed up to a preset time limit, typically 100 τ, where $\tau=2\pi R_0/v$ is the toroidal transit time of a passing particle, or until they cross the plasma boundary (i. e. the last closed flux surface). As a first step the aim of this work has been to determine the loss cone and to study the orbit behaviour outside the last closed magnetic surface. To do this, when particles cross this surface, their orbits have been further followed by means of a Lorentz code.

Alpha Particle Orbits and Confinement

In a helical/toroidal field particle orbits can be roughly divided into three groups: transit particles with $v_\parallel/v_\perp > \max[(2\varepsilon_h)^{1/2}, (2\varepsilon_t)^{1/2}]$, toroidally trapped particles with $(2\varepsilon_h)^{1/2} < v_\parallel/v_\perp < (2\varepsilon_t)^{1/2}$ if $\varepsilon_t(\psi) > \varepsilon_h(\psi)$, and finally localized particles with $v_\parallel/v_\perp < (2\varepsilon_h)^{1/2}$, where $\varepsilon_h=(\delta_{2,M}(\psi)/\delta_{0,0})$, $\varepsilon_t=(\delta_{-1,0}(\psi)/\delta_{0,0})$. This classification is

somewhat artificial because of the possibility of transitions from one orbit type to another. This is particularly true for high energy particles since their drift orbits largely deviate from the birth flux surface and hence experience varing ripple amplitudes along the orbits. In the A=4.35 configuration it has been found that almost all the toroidally trapped particles become become helically trapped when moving in the external plasma region. Moreover in this configuration all the helically trapped particles are lost, as well as the transition particles. With increasing aspect ratio the toroidally trapped particles tend to disappear, and the localized particles are better and better confined. Toroidally trapped particles may be subject to helical ripple induced stochastic diffusion leading to significant delayed losses. However this effect is not important for the configurations that we have studied, with low to moderate aspect ratios, since the trapped particles are primarily lost by orbit conversion into helically trapped particles. The prompt collisionless losses are as high as 17% for A=4.35, yet the aspect ratio $A \geq 7$ is able to provide an almost perfect containment with $f_{cont} \geq 94\%$. For the A=4.35 case the loss region is almost symmetric around $v_{\parallel}/v=0$, while the same region becomes more and more asymmetric towards the $v_{\parallel}/v<0$ (counter-streaming) side, as a result of the fact that the deeply trapped particles are better confined than the marginally trapped particles as discussed above.

Orbit Behaviour Outside the Last Closed Magnetic Surface

At the exit on the last closed magnetic surface, the escaping alpha particles are found in narrow helical strips which closely follow the X - point path /1/, when it is in the inner or upper side of the torus ($\pi > \theta > \pi/2$), as the toroidal magnetic field $B_0 > 0$ has been selected. This loss distribution depends on the constant minimum B contours and is also a consequence of the fact that the trapping occurs in the inside of the torus (since in the high field side the particles have smaller $v_{\parallel}$). The tori where the helical currents flow have been assumed as boundaries for the escaping alpha particles and two different situations have been studied. In the first one the surface currents are very close to the plasma. In this case the escaping alpha particles are strongly focused in the X-point region /1/ for all the aspect ratios considered, i.e. far from the coils that would generate the corresponding torsatron configuration. In the second case, the currents generating the configurations have been moved far from the plasma (see Fig. 1) leaving the closed magnetic surfaces unchanged, and the space between the last closed magnetic surface and the currents has become much larger than previously. Here the escaping particles emerge from the plasma region as they are on the inner side with respect to the X-point and move along the inner separatrix tails as in the previous case, but now have sufficient space to be reflected, cross the X-point private region and reach the other separatrix tail (Fig.2a). Here they remain trapped and start to drift following closely the X-point, typically along one field period (Fig.2b), eventually jumping from one separatrix tail to the other at a turning point. This mechanism is observed in the majority of the escaping particles. Thus, although it remains to compute whether these orbits are stable on longer time scales, they are observed to remain confined in the X-point region without reaching the walls at least for a few bounce periods. The particles which emerge from the last closed surface in the inner side of the torus (i. e. close to $\theta=\pi$) also remain trapped in the X-point region, but their drift motion is not toroidally limited to one field period (see Fig.3).

Implications for a Stellarator Reactor Design

The loss of a fraction of alpha particles in a fusion reactor has implications both for the plasma power balance and for the wall loading. The total losses and the spatial distribution of lost particles has been found to strongly depend on the boundary location and in any case is affected by the presence of X-points. If the boundary is close to the plasma, the particles which are not contained within the last closed magnetic surface reach the wall with a strong focusing on one separatrix

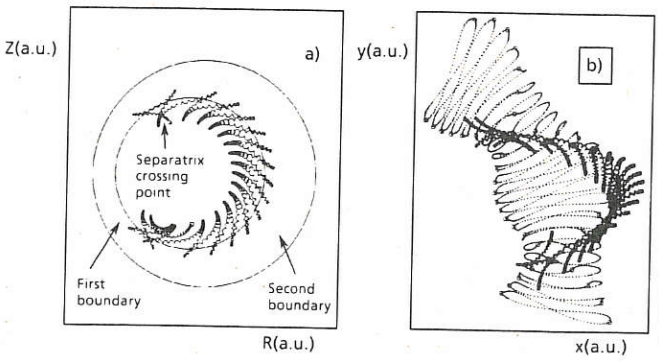

Fig 2: Poloidal projection a) and top view b) of the orbit of an alpha particle trapped on one side of the X-point, outside of the last closed magnetic surface

tail. This fact opens the possibility of reducing the damage to the superconducting magnets and even the chance of exploiting the charged fusion product escape for direct electrical conversion. The strong focusing of the escaping particles implies that a limited space will be required to collect the related flux. However the computed direct losses are rather large when compared to the tokamak case, and increase dramatically with decreasing aspect ratio. However the fraction of lost trapped particles is not direclty related to the aspect ratio, but rather to the closing of the contours of costant minimum B in the plasma region. The approach of optimization of the magnetic configuration has been successfully pursued by the Wendelstein VII-X design team /3/. In the Wendelstein VII-X case the remarkable properties of the quasi-helical symmetry permit a strong reduction of the toroidicity coefficients $\delta_{1,0}(\psi)/\delta_{0,0}(\psi)$ with a corresponding improvement in the fast particle confinement. However this method seems successful only for A>10 because of the difficulty of obtaining such optimized stellarators with coils that are sufficiently far from the plasma at lower aspect ratios. On the other hand, the results found in the present work show that in standard stellarator configurations with low aspect ratios and with pronounced separatrix features, the alpha losses can be strongly reduced by confining the escaping particles in the X-point region. Although many important aspects still remain to be studied, such as the effect of finite β, the importance of collisions and of diffusion, these results could perhaps relieve the most critical issue on the road to low aspect ratio stellarator/torsatron devices, i. e. the losses of charged fusion products.

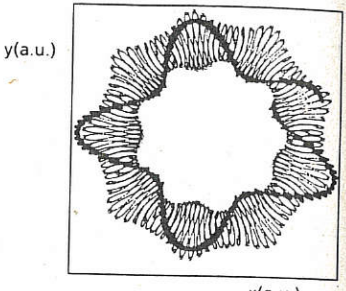

Fig 3: Top view of the orbit of an alpha particle trapped on one side of the X-point, outside of the last closed magnetic surface

References

/1/ F. Alladio et al.: Proc.18th Eur.Conf. on Controlled Fusion and Plasma Physics, Berlin ,1991, Part II, 117

/2/ A.H. Boozer: Phys.Fluids **23**, 904 (1980)

/3/ J. Nuhrenberg and R. Zille: Phys. Letters **129A**, 113 (1988)

MODE ACTIVITY AT HIGH PLASMA PRESSURE IN THE STELLARATOR WENDELSTEIN W7-AS

A. Weller, R. Jaenicke, J. Kisslinger, A. Lazaros, H. Maaßberg, F. Sardei, C. Schwab
W7-AS Team* , ECRH Group**, NI Group***

Max-Planck-Institut für Plasmaphysik, Association EURATOM-IPP
D-8046 Garching, Germany

Introduction - W7-AS is a low shear modular stellarator ($R = 200\,cm,\ a \leq 18\,cm$), in which low order rational values of the rotational transform ι are aimed to be excluded from the confinement region. The stabilisation of ideal MHD modes counts mainly on the existence of a magnetic well in the vacuum configuration. Experimentally, coherent mode activity is found in a wide parameter range by several diagnostics. The highest amplitudes are observed during NBI: i): beam driven modes [1,2] with frequencies $\sim 20 - 40\,kHz$ in the lower density and β regime ($n_e \lesssim 1 \cdot 10^{14}\,cm^{-3}$, $\langle\beta\rangle \lesssim 0.5\%$), and ii): modes with frequencies $\lesssim 10\,kHz$ in the high density, high β regime ($n_e \gtrsim 2 \cdot 10^{14}\,cm^{-3}$, $\langle\beta\rangle \gtrsim 0.8\%$). The highest-β plasmas are achieved with boronized walls at $B = 1.25\,T$ by creating a target plasma with 2nd harmonic ECRH, which is then heated by $1.5\ MW$ NBI with balanced injection. The second type of mode activity is presented in this paper and is discussed on the basis of stability analysis predictions.

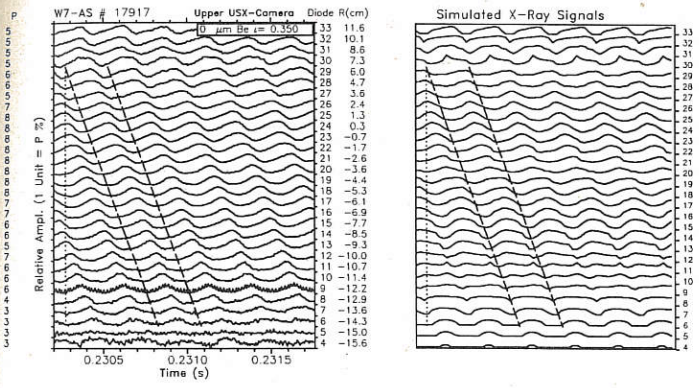

Fig. 1. Measured and simulated X-ray modulation due to a low frequency $m = 3$ mode during NBI and high β ($\langle\beta\rangle \simeq 0.9\%$, $P_{NBI} \simeq 1.5\,MW$).

Mode Characteristics - The experimental observations are based on X-ray fluctuation measurements with the W7-AS X-ray camera system. The relative amplitudes of the signal modulation reaches typically $\tilde{A}/A \simeq 20\%$ from which modulations of the plasma density and temperature of $\lesssim 10\%$ can be inferred. The observed rotation frequency of $f = 4 \ldots 8\,kHz$ can be explained by the diamagnetic drift in the direction of the electrons (which is opposite to the beam driven modes). The excitation of these modes occurs

*,**,*** see Hartfuß, this conference

above a threshold of the plasma pressure corresponding to $\langle\beta\rangle \gtrsim 0.8\%$ in a narrow band of the vacuum boundary rotational transform $\iota(a)$ which is just above the value of a low order rational value. One of the experimental aims of the X-ray imaging system is to identify particular rational surfaces by radially localized measurements. The measurements, however, are not always consistent with predictions of the ι profiles, if a close localization of the MHD activity at the resonant surface is assumed. In contrast to the beam driven modes at low density the modes discussed here are pressure driven, since they decay much slower compared with the decay of the fast ion component after NBI switch-off.

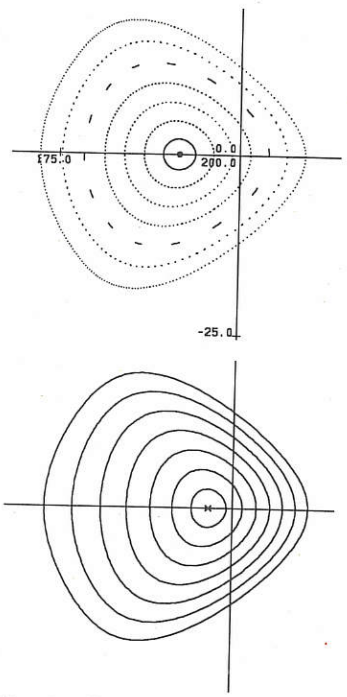

Fig. 2. Poincaré plot of vacuum flux surfaces (top) and equilibrium flux surfaces for a case with $\langle\beta\rangle = 0.87\%$ (bottom) with $\iota \gtrsim 1/3$ calculated with the fixed boundary code VMEC. The configuration is shifted inward by a vertical field ($B_z/B = 0.05$).

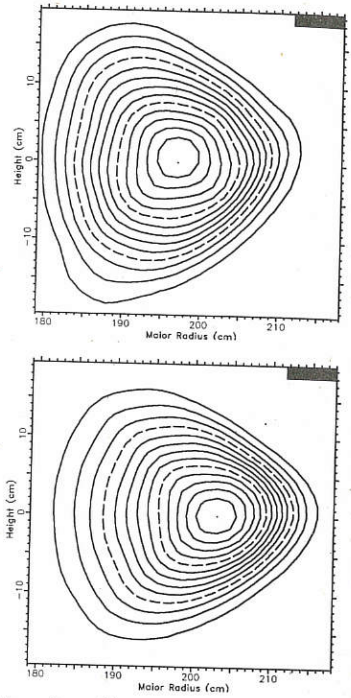

Fig. 3. Contours of constant X-ray emissivity from tomographic reconstructions of signals from the X-ray imaging system on W7-AS. The plasma pressure for the case on the top is about half the value of the case on the bottom ($\langle\beta\rangle = 0.9\%$, $\iota \gtrsim 1/3$).

The highest β values are obtained in the vicinity of $\iota = 1/3$, where $m = 3$ modes could be identified, and in addition $m = 5, 2$ and 3 are seen around $\iota = 2/5, 1/2$ and $2/3$, respectively. In low β-plasmas characteristic phase reversals occur in the X-ray fluctuations at particular locations in the plasma cross section. These nodes are the consequence of the line integrated measurement, by which the perturbed emission cancels out along the line of

sight. The number and location of the nodes is used for the determination of the poloidal mode number m. At high β the situation is more complicated, since typically the signals phases are shifted continuously from one side of the plasma to the opposite (see left side of fig. 1) and no clear maxima or nodes are seen in the radial profiles.

Mode Simulation with Inclusion of Equilibrium Effects - The observation of "sliding phases" in the soft X-ray modulation has been explained as a consequence of the horizontal outward shift of the inner magnetic surfaces against the outer surfaces (Shafranov shift)[3]. Although, resulting from a stellarator field optimization in W7-AS, this shift has been reduced by a factor of ~ 2 compared with a conventional stellarator, the plasma center can be shifted by $\sim 5\ cm$ at low rotational transform ($\iota \sim 1/3$). This can be seen from figures 2 and 3, in which the change of the equilibrium topology induced by the plasma pressure (Pfirsch-Schlüter currents) as predicted for the vacuum configuration and the fixed boundary equilibrium code VMEC [4] are compared with tomographic reconstructions of the soft X-ray emissivity, which is expected to be constant on the magnetic surfaces.

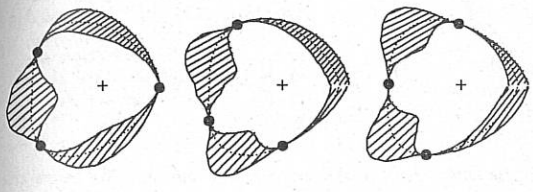

Fig. 4. Topology of an $m = 3$ mode assumed for simulation of X-ray signals (3 rotation angles). The straight lines indicate the viewing chords across the mode structure, which is squeezed at the outside due to the Shafranov shift.

From flux conservation considerations the eigenfunction of the mode varies slowly in poloidal direction, where the magnetic surfaces are compressed and vice versa. A simple model, which uses model surfaces similar to the calculations, has been used for a simulation of the measured X-ray oscillations. The mode structure is assumed to be localized between two unperturbed surfaces and the lengths of the different line of sights through the mode structure was taken as an estimate for the perturbed signal at different poloidal rotation angles of the mode. Fig. 4 shows the mode structure used in the model for generating the simulated signals shown in fig. 1 (right), which are in good agreement with the observed signals (left). In particular, the structure in fig. 4 illustrates, that two signal periods (in the case of an $m = 3$ mode) occur, as the mode propagates from top to bottom of the plasma cross section. In addition, the direction of mode rotation can be deduced from the simulations. At high rotational transform, where the Shafranov shift is considerably smaller, the observed X-ray modulation shows again the characteristic phase reversals in accordance with the expectations from the equilibrium surfaces.

Experiments with Relation to Stability Analysis Predictions - The global ideal MHD stability has been investigated with the code CAS3D [5] for a few W7-AS 3D equilibria, as calculated with the VMEC code. In the presence of a strong vertical field ($B_z/B \sim 0.02$) the magnetic well in the vacuum configuration becomes marginal. In this case the modes are predicted to be more unstable compared with configurations with lower vertical field ($B_z/B \sim 0.015$) corresponding to a magnetic well of 0.5%. In both cases the vertical field leads to a significant inward shift of the plasma column (~ 6 and $\sim 4.5\,cm$, respectively). For pressure profiles, which are similar to typical measured profiles, the $m = 3$, $n = 1$ mode was found to be unstable for equilibria with the resonance of the rotational transform $\iota = 1/3$ inside the plasma volume. The unstable modes are fairly well localized around the resonant rational surfaces. In most of the cases they are

also inside the region of violated Mercier criterion. The calculated perturbed pressure contours of the $m = 3$ mode in the marginal well case are shown in fig. 5. This mode structure exhibits similar features underlying the simulation calculations of the modulated X-ray signals (fig. 4). In the unshifted configuration, the magnetic well is of the order of 2%, but although this case has not yet been analyzed in detail, modes with low order mode numbers are expected to be ideally stable in the experimentally accessible β-range.

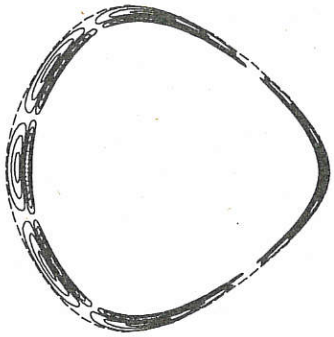

Fig. 5. Perturbed pressure $p_1 = -p_0' \xi^s$ due to an $m = 3$ mode, calculated for $\langle\beta\rangle = 1.1\%$, $\iota \gtrsim 1/3$ and marginal vacuum well with the code CAS3D. (ξ^s : scalar displacement out of the magnetic surface s). In poloidal direction contours represent 3 maxima and 3 minima, respectively. In radial direction the mode is usually localized close to the rational surface ($\iota = 1/3$).

The threshold of the MHD activity found in the experiments seems to be below the predictions of the initial ideal stability analysis calculations. In order to study the effect of a varying magnetic well and varying shear on the mode amplitudes, the vertical magnetic field was varied in the experiment in the range $B_z/B = 0.0015 \ldots 0.0145$ keeping all other controllable parameters constant (in particular $\iota(a)$ and the plasma pressure). No significant change of mode characteristics was observed. The shear was varied by applying toroidal currents ($\lesssim 4\,kA$) in both directions induced by the OH transformer. By adjusting the vacuum rotational transform, $\iota(a)$ was kept constant. Again, however, no significant dependence of the mode amplitudes was detected. Possibly, the effect of these toroidal currents on the ι profile was too small. A reliable knowledge about this profile is an important issue in any case, since additional internal currents (usually bootstrap- and beam driven currents have to be compensated by small OH-currents in order to get a configurationally stable situation) can lead to modifications with respect to the equilibrium and stability predictions. Therefore, further studies are required on the basis of well documented experiments and more realistic input parameters in the stability analysis calculations. Although sometimes very pronounced mode activity is observed, this does not lead to any confinement degradation, and it is believed, that the present operational range is significantly below a hard stability β limit.

References

[1] Lazaros, A. et al., (Proc. 18th Euro. Conf. Berlin, 1991), Part II (1991) 197.
[2] Hartfuß, H. et al., (Proc. 19th Euro. Conf. Innsbruck, 1992), this conference.
[3] Renner, H. et al., (Proc. 19th Euro. Conf. Innsbruck, 1992), this conference.
[4] Hirshman, S.P. and Betancourt, O., J. Comput. Phys. 96 (1991) 99.
[5] Schwab, C. , In: Theory of Fusion Plasmas, Editrice Compositori Bologna (1990) 667.

FINITE ION GYRO RADIUS STABILIZATION OF IDEAL MHD BALLOONING MODES IN OPTIMIZED STELLARATORS

J. Nührenberg, L.-J. Zheng

Max-Planck-Institut für Plasmaphysik
IPP-EURATOM Association, D-8046 Garching bei München

The stabilizing effects of a finite ion gyro radius (FGR) have been known for a long time. Since gyrokinetic theory and the ballooning representation were developed, an expression for this effect in tokamak configurations became available from the kinetic approach /1/. Later, similar results have also been obtained from the two-fluid approach /2, 3/ which will be used here.

Optimized stellarators /4/ have low shear, the increase of ι from the centre to the boundary being $\approx 1/6$. The ideal MHD ballooning modes tend to be localized in one period of the configuration (rather than being toroidally extended) and the β limit is determined by the competition between the local bad-curvature drive and the average curvature although this is smaller than the local one. In the low-frequency regime the FGR effect is non-oscillatory and non-negligible compared with the average-curvature term so that one may expect a stabilizing effect.

This problem is treated within the framework of Braginskii's two-fluid equations /5/. In the low-frequency regime, the continuity and momentum equations of the two fluids –together with Maxwell's equations– are used to construct an FGR-modified energy principle in general 3D configurations (a subsidiary large-aspect ratio approximation is only employed for the treatment of the gyro-viscous stress tensor) for localized modes. As a first application, the ballooning-mode equation with FGR modification is obtained from this principle for 3D equilibria.

The basic set of equations is obtained from Braginskii's two-fluid equations without resistivity, in the zero-electron-mass limit, and with the quasi-neutrality condition instead of Coulomb's law

$$\frac{\partial N}{\partial t} + \nabla \cdot (N\boldsymbol{V}) = 0$$

$$-\nabla P + \boldsymbol{J} \times \boldsymbol{B} - \nabla \cdot \boldsymbol{\Pi}_i = N M_i \frac{\mathrm{d}\boldsymbol{V}}{\mathrm{d}t}$$

$$-\nabla P_i + qN(\boldsymbol{E} + \boldsymbol{V} \times \boldsymbol{B}) - \nabla \cdot \boldsymbol{\Pi}_i = N M_i \frac{\mathrm{d}\boldsymbol{V}}{\mathrm{d}t}$$

$$\nabla \times \boldsymbol{B} = \boldsymbol{J}$$

$$\nabla \times \boldsymbol{E} = -\frac{\partial \boldsymbol{B}}{\partial t}$$

$$\nabla \cdot \boldsymbol{B} = 0$$

where $\mathbf{\Pi}_i$ is the ion-gyroviscous pressure tensor, defined in [13], q the elementary charge and other symbols have their usual meanings. Those without subscript denote the quantities of the single fluid. Here the energy equations are not included; instead the various fluid responses will be obtained from

$$\boldsymbol{B}\cdot\nabla P_e = 0, \quad \boldsymbol{B}\cdot\nabla N = 0$$

the first one of which entails $\boldsymbol{B}\cdot\boldsymbol{E}=0$. The equilibrium flow is given by $\boldsymbol{V}_{o\perp} = \boldsymbol{V}_D + \boldsymbol{V}_E$ – the equilibrium diamagnetic and $\boldsymbol{E}\times\boldsymbol{B}$ flows – with $\boldsymbol{V}_D = B_o^{-2}(P'_{io}/qN_o)\boldsymbol{B}_o\times\nabla s$ and $\boldsymbol{V}_E = B_o^{-2}\Phi'_o\boldsymbol{B}_o\times\nabla s$ ($' = \mathrm{d}/\mathrm{d}s$, s the flux label) and $\nabla\cdot\boldsymbol{V}_o = 0$. Equilibrium-velocity related viscosity and inertia are neglected. Perturbed quantities are denoted by lower-case letters. The perturbation of the magnetic field is expressed as $\boldsymbol{b} = \nabla\times(\boldsymbol{\xi}_\perp\times\boldsymbol{B}_o)$ which corresponds to the gauge $\boldsymbol{B}_o\cdot\boldsymbol{a}=0$ with $\boldsymbol{a}$ the perturbed vector potential /6/. The responses $\boldsymbol{e}$, p_e, ϕ, n are given by

$$\boldsymbol{e} = -\frac{\partial\boldsymbol{\xi}_\perp}{\partial t}\times\boldsymbol{B} - \nabla\phi, \quad p_e = -\xi^s P'_e \text{ (with } \xi^s = \boldsymbol{\xi}\cdot\nabla s), \quad \phi = -\xi^s\Phi', \quad n = -\xi^s N'.$$

Here – and later on – the subscript o for the equilibrium quantities is omitted. The relation between $\boldsymbol{v}_\parallel$ and $\boldsymbol{v}_\perp$ is obtained from the continuity equation

$$N\boldsymbol{B}\cdot\nabla\frac{\boldsymbol{v}_\parallel}{B} = -N\nabla\cdot\boldsymbol{v}_\perp + N'\left(\frac{\partial\xi^s}{\partial t} + \boldsymbol{V}\cdot\nabla\xi^s - \boldsymbol{v}\cdot\nabla s\right).$$

Parallel momentum balance yields

$$\boldsymbol{B}\cdot\nabla p_i = -P'_i\boldsymbol{B}\cdot\nabla\xi^s - \boldsymbol{B}\cdot\nabla\boldsymbol{\pi}_i - NM_i\boldsymbol{B}\cdot\frac{\partial\boldsymbol{v}}{\partial t}.$$

With $\mathcal{O}(\nabla\cdot\boldsymbol{v}_\perp) \sim \mathcal{O}(\nabla\cdot\frac{\partial\boldsymbol{\xi}_\perp}{\partial t})$ (see below) $\sim \mathcal{O}(\frac{\partial\xi^s}{\partial t})$ (limitation on field compression for unstable modes) $v_\parallel/L_p \sim \mathcal{O}(\omega\xi^s)$ is obtained so that – with $\mathcal{O}(\boldsymbol{B}\cdot\nabla\boldsymbol{\pi}_i) \lesssim \mathcal{O}(NM_i\boldsymbol{B}\cdot\frac{\mathrm{d}\boldsymbol{v}}{\mathrm{d}t})$

$$p_i = -\xi^s P'_i$$

is obtained for the ion pressure response in the low-frequency regime $\omega \ll 2\pi V_i/L_p$ with β the plasma β, V_i the ion thermal velocity, and L_p the period length. The perpendicular momentum balance is tedious and here greatly simplified with the approximation of localized modes $[|\nabla s|^{-1}(\boldsymbol{B}\times\nabla s)\cdot\nabla\boldsymbol{\xi}_\perp \sim B|\nabla s|^{-1}\nabla s\cdot\nabla\boldsymbol{\xi}_\perp \gg \boldsymbol{B}\cdot\nabla\boldsymbol{\xi}_\perp]$ which leads to $(\boldsymbol{B}\times\nabla s)\cdot\nabla\boldsymbol{\xi}_\perp = -\boldsymbol{B}\times\nabla\xi^s$. In the low-frequency limit this yields

$$\boldsymbol{v}_\perp = \frac{\partial\boldsymbol{\xi}_\perp}{\partial t} + \frac{\boldsymbol{B}\times\nabla p_i}{qNB^2} + \frac{\boldsymbol{B}\times\nabla\phi}{B^2} = \frac{\partial\boldsymbol{\xi}_\perp}{\partial t} + \boldsymbol{V}\cdot\nabla\boldsymbol{\xi}_\perp.$$

With this result the inertia term in the momentum balance becomes $NM_i(\frac{\partial}{\partial t}+\boldsymbol{V}\cdot\nabla)^2\boldsymbol{\xi}_\perp$, which only leads to a frequency shift for marginally stable modes. This shows that without taking into account the gyro-viscous stress tensor, the equilibrium electric field and the Hall effect make no contribution to the stability. When the gyro-viscous effect is taken into account, the situation changes because of

$$NM_i\left(\frac{\partial}{\partial t} + \boldsymbol{V}_D\cdot\nabla\right)\frac{\boldsymbol{B}\times\nabla p_i}{qNB^2} + NM_i\boldsymbol{V}_D\cdot\nabla\frac{\boldsymbol{B}\times\nabla\phi}{B^2} = \frac{M_i}{qB^2}\boldsymbol{B}\times\nabla(-\boldsymbol{v}\cdot\nabla P_i)$$

for localized modes and $\frac{M_i}{qB^2}\boldsymbol{B}\times\nabla(-\boldsymbol{v}\cdot\nabla P_i) + (\nabla\cdot\boldsymbol{\pi}_i)_\perp = \mathcal{O}(\epsilon)NM_i\frac{\mathrm{d}\boldsymbol{v}_\perp}{\mathrm{d}t}$ with ϵ the inverse aspect ratio.

Therefore, when inverse-aspect-ratio order contributions of the stress tensor are neglected the perpendicular momentum balance yields

$$NM_{\mathrm{i}}\left[\left(\tfrac{\partial}{\partial t}+\tfrac{1}{2}\boldsymbol{V}_{\mathrm{D}}\cdot\boldsymbol{\nabla}+\boldsymbol{V}_{\mathrm{E}}\cdot\boldsymbol{\nabla}\right)^{2}-\tfrac{1}{4}(\boldsymbol{V}_{\mathrm{D}}\cdot\boldsymbol{\nabla})^{2}\right]\boldsymbol{\xi}_{\perp}=\boldsymbol{\nabla}(\boldsymbol{\xi}_{\perp}\cdot\boldsymbol{\nabla}P)+\boldsymbol{J}\times\boldsymbol{b}+\mathrm{j}\times\boldsymbol{B}$$

so that the following energy relation results

$$NM_{\mathrm{i}}\int_{V}\left[\left(\frac{\partial}{\partial t}+\frac{1}{2}\boldsymbol{V}_{\mathrm{D}}\cdot\boldsymbol{\nabla}+\boldsymbol{V}_{\mathrm{E}}\cdot\boldsymbol{\nabla}\right)\boldsymbol{\xi}_{\perp}\right]^{2}\mathrm{d}\tau=-\delta W_{\mathrm{MHD}}-\delta W_{\mathrm{FGR}}$$

with δW_{MHD} the familiar MHD part and $\delta W_{\mathrm{FGR}}=\tfrac{1}{4}NM_{\mathrm{i}}\int_{V}(\boldsymbol{V}_{\mathrm{D}}\cdot\boldsymbol{\nabla}\boldsymbol{\xi}_{\perp})^{2}\mathrm{d}\tau$ the stabilizing FGR contribution.

Deriving the ballooning-mode equation from the energy principle is a trivial extension of previous work /7/. The ballooning-mode equation for marginal modes can then be written in the form /8/

$$\frac{\mathrm{d}}{\mathrm{d}\overline{\phi}}\left\{a^{-1}[1+(\overline{\sigma}\overline{\phi}+\tilde{\sigma})^{2}]\frac{\mathrm{d}F}{\mathrm{d}\overline{\phi}}\right\}+(\overline{D}\;\overline{\phi}+\tilde{D})F+C_{\rho_{\mathrm{i}}}\left(\frac{\sqrt{g}}{V'}\right)^{2}a^{-1}[1+(\overline{\sigma}\overline{\phi}+\tilde{\sigma})^{2}]F=0$$

with $C_{\rho_{\mathrm{i}}}=\tfrac{1}{4}M_{\mathrm{i}}N\frac{V'^{2}}{F_{\mathrm{T}}'^{2}}(\boldsymbol{V}_{\mathrm{D}}\cdot\boldsymbol{\nabla})^{2}\approx\tfrac{1}{2}\pi^{2}A^{2}\frac{\beta_{\mathrm{loc}}'^{2}}{\beta_{\mathrm{loc}}}(M_{\mathrm{p}}\frac{\rho_{\mathrm{i}}}{a})^{2}$; here β_{loc} is the local β value , A the aspect ratio, a the plasma radius, and ρ_{i} the local ion gyro radius.

Results for optimized stellarators (see Fig. 1) as well as tokamaks (see Fig. 2) show that a significant stabilization of the ballooning mode occurs for poloidal node numbers M_{p} with $M_{\mathrm{p}}\frac{\rho_{\mathrm{i}}}{a}\approx 0.3$.

REFERENCES

/1/ W. M. Tang, J. W. Connor, and R. J. Hastie. *Nucl. Fusion* **20**, 1439 (1980).

/2/ J. W. Connor and R. J. Hastie. *Plasma Phys.* **27**, 621 (1985).

/3/ P. Andersson and J. Weiland. *Phys. Fluids* **31**, 359 (1988).

/4/ W. Lotz, J. Nührenberg, and C. Schwab. In *Plasma Physics and Controlled Fusion Research* (Washington, 1990). Nucl. Fusion Suppl. Vol.**2**, (IAEA, Vienna, 1991) 603.

/5/ S. I. Braginskii. In *Rev. of Plasma Physics.* M.A. Leontovich ed. (Consultants Bureau, New York, 1965), Vol.1, 205.

/6/ T. M. Antonsen, Jr. and Y. C. Lee. *Phys. Fluids* **25**, 132 (1982).

/7/ D. Correa-Restrepo. *Z. Naturforsch.* **33a**, 789 (1978); **37a**, 848 (1982).

/8/ J. Nührenberg and R. Zille, in *Theory of Fusion Plasmas.* A. Bondeson, et al. ed. (Societá Italiana di Fisica, Bologna, 1987), p.3.

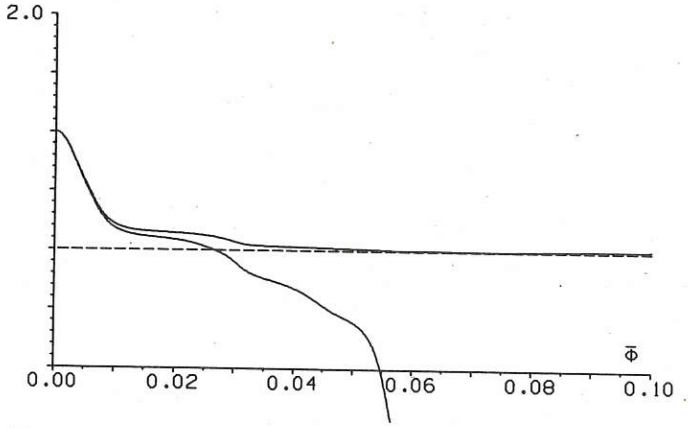

Fig. 1: Ballooning solutions without and with FGR stabilization in an $n \to \infty$ ideally unstable Helias equilibrium with bell-shaped pressure profile at $\iota_r = \frac{9}{11}$. $\bar{\phi}$ is the normalized magnetic coordinate $0 \leq \bar{\phi} \leq 1$ on the closed field line. The local values of β and β' are approximately 0.06 and 0.16, respectively. $M_p \frac{\rho_i}{a} \approx 0.3$ is obtained from the definition of C_{ρ_i}.

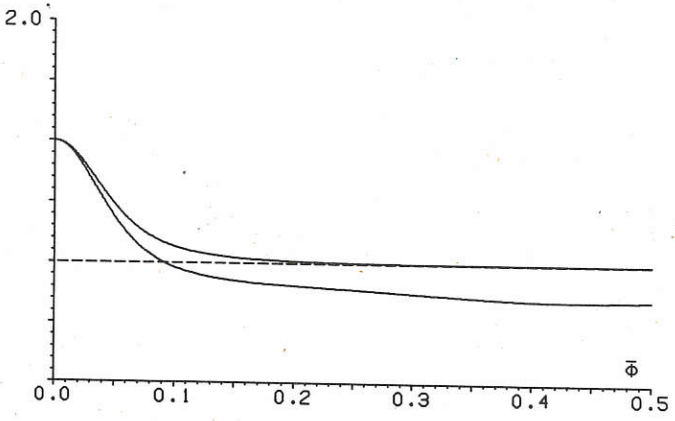

Fig. 2: Ballooning solutions without and with FGR stabilization in an $n \to \infty$ ideally unstable Tokamak equilibrium at $\iota_r = \frac{3}{4}$; $\beta_{loc} \approx 0.017$, $\beta'_{loc} \approx 0.071$, $M_p \frac{\rho_i}{a} \approx 0.4$.

LINEAR MHD STABILITY COMPUTATIONS IN 3D PLASMAS

W. A. Cooper, Y. Nakamura*, M. Wakatani*, R. Gruber†, S. Merazzi‡, D. V. Anderson° and U. Schwenn*
Centre de Recherches en Physique des Plasmas,
Association Euratom-Confédération Suisse,
Ecole Polytechnique Fédérale de Lausanne,
Lausanne, Switzerland

The equations that govern the global and local magnetohydrodynamic (MHD) stability properties of three dimensional (3D) plasma confinement configurations constrained to have nested magnetic flux surfaces with a noninteracting hot electron species are presented. In the absence of hot particles, the model reduces to the ideal MHD limit. Specific applications presented here will concentrate on the 10 field period LHD torsatron device and toroidal ripple effects in the JET Tokamak within the ideal MHD model. Applications to problems in which an energetic species plays an important role will be deferred to future work.

The energy principle within a plasma with a noninteracting hot electron current layer can be written as [1,2]

$$\delta W_p = \frac{1}{2}\int\int\int d^3x \left[C^2 + \Gamma p|\nabla\cdot\xi|^2 - D|\xi\cdot\nabla s|^2\right], \tag{1}$$

where the vector $\mathbf{C}$ corresponds to a modified perturbed magnetic field, the second term describes the compressibility of the plasma, D constitutes the MHD instability driving term, ξ is the perturbed displacement vector and s is the radial variable the labels the magnetic flux surfaces. We introduce a modified Boozer magnetic coordinate system [3] (s,θ,ϕ) applicable to plasmas with anisotropic pressure and expand the perturbation as

$$\xi = \sqrt{g}\xi^s\nabla\theta\times\nabla\phi + \eta\frac{\mathbf{B}\times\nabla s}{B^2} + \left[\frac{J(s)}{\Phi'(s)\sigma B^2}\eta - \mu\right]\mathbf{B}, \tag{2}$$

where $\sqrt{g}$ is the Jacobian, σ is the firehose stability parameter of anisotropic plasmas [4], $\Phi(s)$ is the equilibrium toroidal magnetic flux function and $J(s)$ is the effective toroidal plasma current function determined from $\mathbf{K} = \nabla\times(\sigma\mathbf{B})$. The components of the perturbation are $\xi^s = \xi\cdot\nabla s$, η and μ. The perturbed magnetic energy contribution is decomposed as $\sqrt{g}C^2 = \sqrt{g}C^sC_s + \sqrt{g}C^\theta C_\theta + \sqrt{g}C^\phi C_\phi$, where the the components in the contravariant representation are

$$\sqrt{g}C^s = \sqrt{g}\mathbf{B}\cdot\nabla\xi^s = \left[\Psi'(s)\frac{\partial\xi^s}{\partial\theta} + \Phi'(s)\frac{\partial\xi^s}{\partial\phi}\right], \tag{3}$$

$$\sqrt{g}C^\theta = \frac{\partial\eta}{\partial\phi} - \Psi'(s)\frac{\partial\xi^s}{\partial s} - \frac{1}{\sigma B^2}\left[\sigma B^2\Psi''(s) + \frac{I(s)\mathbf{j_p}\cdot\mathbf{B}}{|\nabla s|^2} + \sigma p'(s)\Psi'(s)\right], \tag{4}$$

$$\sqrt{g}C^\phi = -\frac{\partial\eta}{\partial\theta} - \Phi'(s)\frac{\partial\xi^s}{\partial s} - \frac{1}{\sigma B^2}\left[\sigma B^2\Phi''(s) + \frac{J(s)\mathbf{j_p}\cdot\mathbf{B}}{|\nabla s|^2} + \sigma p'(s)\Phi'(s)\right]. \tag{5}$$

The poloidal magnetic flux and effective current flux functions are denoted by $\Psi(s)$ and $I(s)$, respectively. The prime denotes a derivative with respect to s. The components of

C in the covariant representation are related to the contravariant components through the metric elements g_{ij}. The instability driving term is

$$\sqrt{g}D = \frac{\sqrt{g}B^2}{|\nabla s|^2}\left(\frac{\mathbf{j_p}\cdot\mathbf{B}}{B^2}\right)^2 + \frac{\sqrt{g}[p'(s)]^2}{B^2} - p'(s)\frac{\partial\sqrt{g}}{\partial s} + \left[\Psi'(s)\Phi''(s) - \Phi'(s)\Psi''(s)\right]\left(\frac{\mathbf{j_p}\cdot\mathbf{B}}{B^2}\right) \tag{6}$$
$$+\frac{\sqrt{g}p'(s)}{(\sigma\sqrt{g}B^2)}\left[J(s)\Psi''(s) - I(s)\Phi''(s)\right] + (\sqrt{g}\mathbf{B}\cdot\nabla)\left\{\left[I(s)\frac{g_{s\theta}}{\sqrt{g}} + J(s)\frac{g_{s\phi}}{\sqrt{g}}\right]\frac{\mathbf{j_p}\cdot\mathbf{B}}{\sigma|\nabla s|^2B^2} + \frac{p'(s)B_s}{B^2}\right\}.$$

Imposing the incompressibility constraint eliminates μ algebraically from the problem. The application of a Fourier decomposition to ξ^s and η in the Boozer angles and a finite hybrid element discretisation in the radial variable reduces the problem to a special block pentadiagonal matrix eigenvalue equation that is amenable to solution with an inverse vector iteration technique, as implemented in the TERPSICHORE code [5].

Applying the covering space concept [6], we derive the 3D ballooning equation

$$\frac{\partial}{\partial\theta}\left\{\left[C_p + C_s(\theta-\theta_k) + C_q(\theta-\theta_k)^2\right]\frac{\partial\chi}{\partial\theta}\right\} + (1-\lambda)\left[d_p + d_s(\theta-\theta_k)\right]\chi = 0, \tag{7}$$

with eigenvalue λ in the Boozer magnetic coordinates. The coefficients are

$$C_p = \left[\frac{g_{ss}}{\sqrt{g}} - \frac{\sigma B_s^2}{(\sigma\sqrt{g}B^2)}\right], \tag{8}$$

$$C_s = 2\frac{q'(s)\Psi'(s)}{\Phi'(s)}\left[\frac{J(s)B_s}{(\sigma\sqrt{g}B^2)} - \frac{g_{s\theta}}{\sqrt{g}}\right], \tag{9}$$

$$C_q = \frac{[q'(s)\Psi'(s)]^2}{(\sigma\sqrt{g}B^2)}\sigma|\nabla s|^2, \tag{10}$$

$$d_p = \frac{p'(s)}{[\Psi'(s)]^2}\left[\frac{\sqrt{g}p'(s)}{B^2} + \frac{[J(s)\Psi''(s) - I(s)\Phi''(s)]}{\sigma B^2} - \frac{\partial\sqrt{g}}{\partial s} + \sqrt{g}\mathbf{B}\cdot\nabla\left(\frac{B_s}{B^2}\right)\right], \tag{11}$$

$$d_s = -\frac{q'(s)}{\Psi'(s)}\sqrt{g}\mathbf{B}\cdot\nabla\left(\frac{\mathbf{j_p}\cdot\mathbf{B}}{B^2}\right) \tag{12}$$

where $q(s) = d\Phi/d\Psi$. The Mercier criterion obtained from the asymptotic analysis is

$$< h_q >< d_p > - < h_q >< d_q > + < h_q d_q > + < h_q >< h_q d_q^2 > - < h_q d_q >^2 \leq \frac{1}{4}, \tag{13}$$

where $h_q = 1/C_q$, $d_q = -q'(s)\mathbf{j_p}\cdot\mathbf{B}/B^2$ and $< f >$ denotes the flux surface average of f. A detailed derivation of this formulation will be published elsewhere [7].

The ideal MHD stability of an LHD torsatron configuration (once considered as the standard operating configuration for the device, with its magnetic axis shifted inwards with the poloidal field system by 10 cm) is summarised in Fig. 1. The pressure profile is chosen as $p(s) = p(0)(1-s)^2$ and the toroidal current vanishes within each flux surface. The MHD stability stability imposed by the low $n = 1, 2, 3$ families of modes all yield β limits close to $\beta \simeq 4.95\%$. In the LHD device, the rotational transform $\iota = 1$ surface lies inside the plasma. In terms of ideal MHD behaviour, this constitutes one of the essential features that distinguishes it from the ATF torsatron. As a result the low n structures

in LHD are fully internal in nature, vanishing close to the plasma-vacuum interface even when the conducting wall is placed at a great distance. The Mercier stability indicates a first unstable domain bounded by $0.5\% \leq \beta \leq 2.2\%$. A second Mercier unstable domain that encompasses the region where the magnetic shear vanishes in this torsatron device is triggered at $\beta > 3.6\%$. The *stable* domain between the two unstable regions is not actually fully stable. Mercier instability persists but only very locally about resonant surfaces with rational rotational transform values within one period ($\iota_p = 1/18$, $1/17$, $1/16$, $1/15$, etc). It could be argued, however, that local flattening of the pressure profile about these surfaces would render stability without altering significantly the β value that could be achieved. Localised ballooning modes become unstable at $\beta = 1.5\%$ and remain unstable to $\beta > 5\%$ without any indication of second stability. The dominant ballooning structures are localised about magnetic field lines that cross the outer edge of the prolate up-down symmetric cross section. The ballooning modes on the more conventional field lines that cross the outer edge of the oblate up-down symmetric cross section become unstable when $\beta > 3.7\%$ and impose the inner stability boundary at $\beta > 4\%$ in Fig. 1. The large variation of ballooning stability from field line to field line calls into question the applicability of ballooning stability predictions based on the stellarator expansion method. The poloidal field design in the LHD device permits a significant enhancement of the magnetic well through an outward shift of the magnetic axis. The magnetic well can play a big impact in the stabilisation of localised pressure driven modes to improve the predictions of the 3D ideal MHD model that we present here. On the other hand, the outward axis shift deteriorates particle confinement and erodes the quality of the outer magnetic flux surfaces. The flexibility of the LHD device should allow a quantitative experimental evaluation ot the tradeoff between MHD stability versus particle confinement and flux surface fragility to determine the optimal operational conditions in torsatrons.

The effects of toroidal field ripple on ideal MHD ballooning stability in JET are investigated with a simplified model in which the toroidal coils are infinitely elliptical [8]. Selfconsistent 3D MHD equilibria are calculated with the VMEC code [9]. The pressure profile is bell-shaped to model the H-mode and the toroidal current profile is prescribed as rounded box-like in shape. The magnitude of the ripple depends on the coil discreteness and on the gap between the coils and the plasma. The critical β value as a function of the inverse number of coils is shown in Fig. 2 for cases in which the plasma-coil gap is 20, 30, 40 and 50 *cm*. With 32 coils, the β value is virtually unaltered when the coil plasma distance exceeds 30 *cm*. With 16 coils, the critical β degrades when the gap is smaller than 40 *cm*.

*Kyoto Univ., Japan; †GASS/CSCS, Manno, Switzerland. ‡IMHEF/EPFL, Lausanne, Switzerland; °NERSC/LLNL, Livermore, USA; *MPIPP, Garching, FRG.

REFERENCES

[1] J. L. Johnson, R. M. Kulsrud and K. E. Weimer, *Plasma Phys.* **11** (1969) 463.
[2] D. B. Nelson and C. L. Hedrick, *Nucl. Fusion* **19** (1979) 285.
[3] A. H. Boozer, *Physics Fluids* **23** (1980) 904.
[4] H. Grad, in *Magneto – Fluid and Plasma Dynamics, Symposia in Applied Mathematics* (American Mathematical Society) **18** (1967) 162.
[5] D. V. Anderson, W. A. Cooper, R. Gruber, S. Merazzi and U. Schwenn, *Int. J. Supercomp. Appl.* **4** (1990) 34.
[6] R. L. Dewar and A. H. Glasser, *Physics Fluids* **26** (1983) 3038.
[7] W. A. Cooper, *Plasma Phys. Contr. Fusion* (1992) in press.
[8] J. L. Johnson and A. H. Reiman, *Nucl. Fusion* **28** (1988) 1116.
[9] S. P. Hirshman and O. Betancourt, *J. Comput. Phys.* **96** (1991) 99.

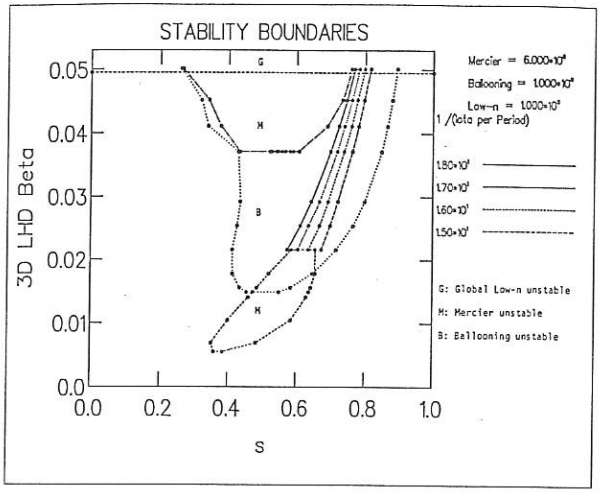

Figure 1: The MHD stability boundaries in the LHD torsatron imposed by global low n modes, Mercier modes and ballooning modes.

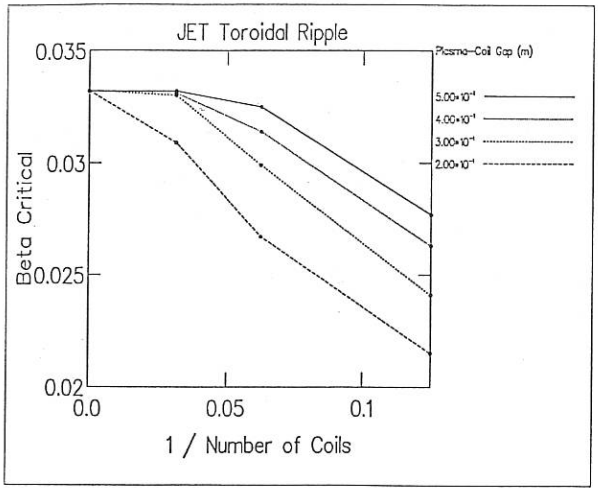

Figure 2: The β limit imposed by ballooning instabilities versus the inverse number of toroidal coils in JET for plasma-coil gaps of 50, 40, 30 and 20 cm.

INTERCHANGE MODES IN TORSATRONS AND HELIACS

Juan Antonio Jiménez and Antonio Varias

Asociación Euratom-CIEMAT
Av. Complutense 22
E-28040 Madrid, Spain

Nicolás Domínguez

Oak Ridge National Laboratory
Oak Ridge, Tennessee 37830, U.S.A.

Introduction

A stability condition for localized perturbations applicable in principle to torsatrons and heliacs (but not excluding to extent it to other kind of stellarators as, for example, Helias) will be developed [1].

The criterion is be obtained by expanding the equilibrium quantities around the radial position where the second derivative of the volume is equal to zero (V"= 0). Then we evaluate the Mercier criterion and solve the ballooning equation.

The reason to choose this particular point is the following. It is the transition point from a region with magnetic well to a region with magnetic hill, and unstable stellarator configurations have unstable regions around that surface. In this way it will be found in this region the minimum of the Mercier criterion. That minimum must not be exactly where V"= 0. This is the reason we do the expansion and we do not evaluate just the criteria on the point where V" = 0. With this approach we expect to gain insight on the unstablilizing mechanism for stellarators.

In contrast to other methods, like the stellarator expansion, no average is done in any generalized toroidal angle.

After fixing the notation, we will determinate the quantities necessary to evaluate the criterion and the algorithm to obtain them. We have tested the algorithm by applying it to axisymmetric configurations in the large aspect ratio limit and to helically symmetric configurations, where analytical calculations are possible. Next, we consider a general l=2 stellarator [2] with an undefined number of periods and an l=2 stellarator modelling the ATF torsatron. In the last case, the analytical and numerical results were in good agreement up to a <ß> of 1.5% approximately. Current effort is devoted to heliacs.

Coordinates

We work in magnetic coordinates (s,θ,ξ), where s is the flux label and (θ,ξ) are generalized angles. The contravariants components of the magnetic field are:

$$B^s = 0 \qquad B^\theta = \frac{1}{\sqrt{g}}\left[F_P'(s) - \partial_\xi \lambda_B\right] \qquad B^\xi = \frac{1}{\sqrt{g}}\left[F_T'(s) + \partial_\theta \lambda_B\right]$$

We will assume Fourier expansions in the (θ,ξ) angles relating geometrical coordinates (R,Φ,Z) to magnetic coordinates (s,θ,ξ).

Equilibrium

We assume the following equilibrium quantities are known:

- Flux functions $F_T'(s)$, $F_P'(s)$, $I'(s)$, $J'(s)$, $p'(s)$
- Fourier coefficients $R_{mn}(s)$, $Z_{mn}(s)$, $\Phi_{mn}(s)$

From the condition $J^s=0$ we obtain the following differential equation for $\lambda_B(s,\theta,\xi)$:

$$g_{\xi\xi}\left(\partial^2_{\theta\theta}\lambda_B\right)+g_{\theta\theta}\left(\partial^2_{\xi\xi}\lambda_B\right)-2g_{\theta\xi}\left(\partial^2_{\theta\xi}\lambda_B\right)+A(s,\theta,\xi)\left[\partial_\theta\lambda_B+F_T'(s)\right]+B(s,\theta,\xi)\left[\partial_\xi\lambda_B-F_P'(s)\right]=0$$

$$A(s,\theta,\xi)\equiv\frac{g_{\theta\xi}}{\sqrt{g}}\left(\partial_\xi\sqrt{g}\right)-\frac{g_{\xi\xi}}{\sqrt{g}}\left(\partial_\theta\sqrt{g}\right)+\left(\partial_\theta g_{\xi\xi}-\partial_\xi g_{\theta\xi}\right)$$

$$B(s,\theta,\xi)\equiv\frac{g_{\theta\xi}}{\sqrt{g}}\left(\partial_\theta\sqrt{g}\right)-\frac{g_{\theta\theta}}{\sqrt{g}}\left(\partial_\xi\sqrt{g}\right)+\left(\partial_\xi g_{\theta\theta}-\partial_\theta g_{\theta\xi}\right)$$

After resolving this equation it is possible to calculate all the quantities involved in the Mercier and ballooning criteria.

Large aspect ratio Tokamak and straight heliac

As first example we consider the case of a tokamak with circular magnetic surfaces and large aspect ratio, with the Fourier coefficients ordered in terms of the inverse aspect ratio parameter:

$$R(s,\theta)=R_0(s)+R_1(s)\cos\theta \qquad R_0(s)\approx 1/\varepsilon \qquad R_0'(s)\approx\sqrt{\varepsilon}$$
$$Z(s,\theta)=\qquad R_1(s)\sin\theta \qquad R_1(s)\approx 1 \qquad R_1'(s)\approx 1$$
$$\Phi=\xi$$

To order $\sqrt{\varepsilon}$ we obtain: $$\lambda_B(s,\theta)\equiv F_T'(s)\left[\frac{R_0'(s)}{R_1'(s)}-\frac{R_1(s)}{R_0(s)}\right]\sin\theta$$

As second example we use an analytical helically symmetric equilibrium [3] with circular flux surfaces in the $z=$ const. planes. Assuming a Fourier representation for $\lambda_B(s,\theta)$:

$$\lambda_B(s,\theta)=\sum_{n=1}^{\infty}\lambda_B^{[n]}(s)\sin n\theta$$

we can obtain analytically all the Fourier coefficients,and we see that $\lambda_B^{[n]}(s)\approx O(1/n)$.

Large aspect ratio *l*=2 stellarator and heliac

One of the simplest 3-D magnetic surfaces are those of an stellarator with *l*=2 in the winding law. In this case the parametrization is as follows:

$$R(s,\theta,\xi)=R_0(s)+r(s)+r_h(s)\cos(\theta-N\xi)$$
$$Z(s,\theta,\xi)= \quad r(s)-r_h(s)\sin(\theta-N\xi)$$

and the correspondent ordering is an extension of the former mentioned for the Tokamak.

$R_0 \approx 1/\varepsilon$ $\quad N \approx 1/\varepsilon$ $\quad r/R_0 \approx \varepsilon$ $\quad r_h/r \approx \sqrt{\varepsilon}$ $\quad N$: *number of periods*

$r \approx 1$ $\quad R_0' \approx \sqrt{\varepsilon}$ $\quad r' \approx 1$ $\quad r_h' \approx \sqrt{\varepsilon}$ $\quad \varepsilon \equiv r/R_0 << 1$

A large aspect ratio is required for a fast convergence of the series but moderate plasma aspect ratio devices, like ATF, are well described with few terms (taking into account just the *l*=2 contributions to the total magnetic configuration). For this case, the equation for $\lambda_B(s,\theta,\xi)$ gives:

$$\lambda_B(s,\theta,\xi)=\lambda_B^{(1/2)}(s,\theta,\xi)+\lambda_B^{(1)}(s,\theta,\xi)+\ldots$$

$$\lambda_B^{(1/2)}(s,\theta,\xi)=\frac{F_T'(s)}{V'(s)}\left\{R_0R_0'r\sin\theta+\left[\frac{2R_0^3r_hr'-2R_0^3rr_h'+V'(s)NR_0(rr_h'-r_hr')}{r^2N^2+4R_0^3}\right]\sin(2\theta-N\xi)\right\}$$

$$\lambda_B^{(1)}(s,\theta,\xi)=\lambda_{B\,1,0}^{(1)}(s)\sin\theta+\lambda_{B\,1,1}^{(1)}(s)\sin(\theta-N\xi)+\lambda_{B\,3,1}^{(1)}(s)\sin(3\theta-N\xi)+\lambda_{B\,4,2}^{(1)}(s)\sin(4\theta-2N\xi)$$

We obtained all the equilibrium quantities from VMEC code [4] and they were used to evaluate the integrals involved in the Mercier criterion by two methods, using the analytical expressions and by numerical calculation. The quantities here compared are:

$$Int\ 1=\left\langle\frac{\sqrt{g}}{g^{ss}}B^2\right\rangle \qquad Int\ 4=\left\langle\frac{\sqrt{g}}{B^2}\right\rangle \qquad \langle\cdot\rangle=\int_0^{2\pi}d\theta\int_0^{2\pi}d\xi$$

The values given to the parameters for the last surface comes from a simplified border of ATF in order to adjust to our parametrization requirements, that is, 12 field periods, a major radius of 2.1 m. and average plasma radius of 0.27 m. At low ß (0.2%) we obtain a good agreement as seen in the figures.

$\left\langle \frac{\sqrt{g}}{g^{ss}} B^2 \right\rangle$ $\left\langle \frac{\sqrt{g}}{B^2} \right\rangle$

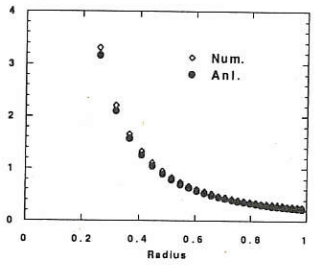

Fig. 1: Results for analytical and numerical calculations for the integral #1.A total of 50 Fourier modes were employed in the equilibrium calcutation with VMEC.

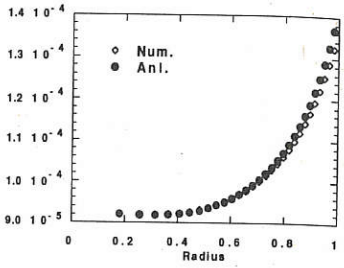

Fig. 2: Results for integral #4.The number of radial points is 31.Here they appear more concentrated near the boundary because VMEC's surface label is the toroidal flux.

But for <ß> >1.5% both methods are increasingly different as we increase the plasma pressure. This happens because our parametrization of the surfaces is too restrictive (too simple). For instance, we could release the condition that forces $\boldsymbol{R}$ and $\boldsymbol{Z}$ to share the same Fourier coefficients. This is the way to describe a heliac, increase the number of modes used in the magnetic surfaces which leads inevitably to more complicated equations.

[1] A. Varias, J.A. Jiménez and N. Dominguez, APS Conference 1991, Bull. Am. Phys. Soc., **36**, 2R17 (1991) 2310.
[2] S.P.Hirshman, Private communication.
[3] P. Merkel and J. Nührenberg, Comput. Phys. Commun. **31** (1984) 115.
[4] S.P. Hirshman, W.I. van Rij and P. Merkel, Comput. Phys. Commun. **43** (1986) 143.

IDEAL MHD STUDIES OF THE TJ-IU TORSATRON

C. Alejaldre, E. Ascasibar, L. García, A. López-Fraguas, A. Varias
Asociación EURATOM-CIEMAT para Fusión
B. Carreras and N. Dominguez
Oak Ridge National Laboratory

Introduction

The TJ-I Upgrade device is a 6 periods, $l=1$ torsatron with a total number of 5 coils. The 6 turns, helical coil has a major radius R_0= 0.6 m and a minor one of 0.24 m. The helix pitch is not uniform, it follows the law:

$$\zeta = 1/6\ (\theta + 0.4\ \sin\theta)$$

where ζ and θ are the usual toroidal and poloidal angles.

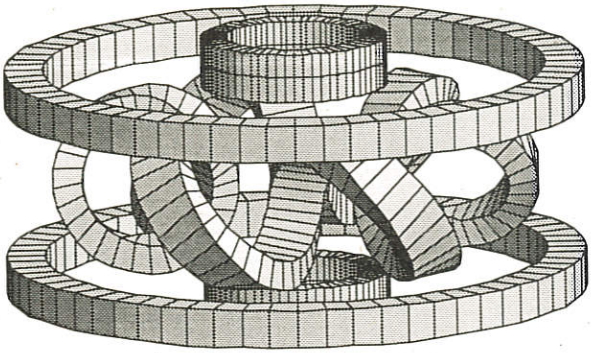

Figure 1
TJ-IU coil configuration

TJ-IU intents to fill up the gap until the main device of CIEMAT, TJ-II, becomes operational. For this reason, very stringent conditions were imposed upon the device, namely: simplicity of construction, it had to be built at CIEMAT workshops, it should use all the available TJ-I tokamak systems (power supplies, hall, control and data acquisition system.. and therefore its name), it should be small and with a low magnetic

field (0.5 T) to lower the cost. Figure 1 shows the final coil configuration. Initial operation of the device is expected in June 1992.

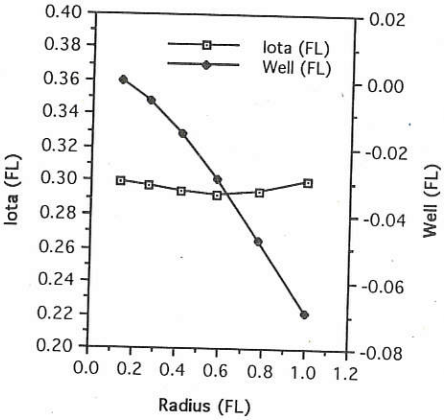

Figure 2
Vacuum magnitudes for the reference case

The strong modulation of the helical coil produces a deep vacuum magnetic well that is the main stability mechanism in the machine since its shear is almost negligible. See fig. 2 where the vacuum iota and magnetic well profiles obtained from a field line following code are shown for the configuration with the magnetic axis at its "standard" position, 0.58 m. For this reference configuration the current settings are: I_{hc} = 280 kA, $I_{vf,ex}$ = - 122 kA, $I_{vf,in}$ = - 49 kA. The average radius of the last closed magnetic surface inside the vacuum chamber is <a> = 10 cm. The average toroidal field at axis is 0.52 T with a magnetic ripple of 7.6%.

Equilibrium and Stability Studies

Using the fixed boundary version of the 3D code VMEC [1], equilibria for two different configurations of the machine have been obtained and a sequence of zero-net current equilibria has been generated. Figure 3 shows the equilibrium magnetic axis shift for the standard configuration, and figure 4 shows the flux surfaces at four toroidal positions for the standard case and <ß> ≈ 2%. It can clearly be appreciated the Shafranov shift of the surfaces and the helicity of the magnetic axis. The position at

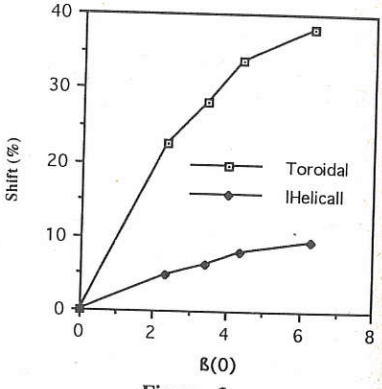

Figure 3
Toroidal and helical shifts when the pressure increases

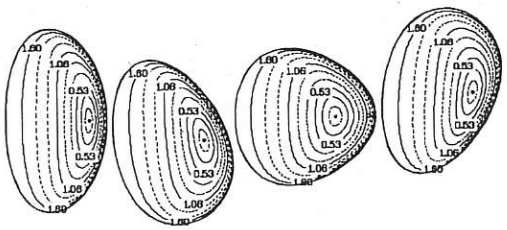

Figure 4

Flux surfaces of the standard configuration at $<\beta> \approx 2\%$ for four toroidal positions. ($\zeta = 0^o$, 15°, 30° and 45°)

$\zeta = 30^o$ corresponding to the most triangular cross section is the chosen for microwave injection. The pressure profile used is the usual $p \propto (1-\Phi)^2$, where Φ is the toroidal flux normalized to 1 at the edge. The two configurations considered are the "standard" one for which the parameters such as plasma volume, magnetic well depth, etc., have been optimized and the "inward" configuration, characterized for a position of the magnetic axis in vacuum shifted 6 cm. towards the axis of the machine.

The equilibrium quantities obtained have then been used to evaluate the 3-D Mercier stability criterion for local instabilities [2]:

$$D_M = D_S + D_W + D_I + D_G \geq 0$$

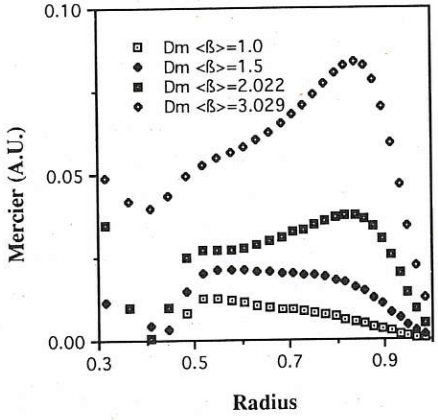

Figure 5

The Mercier criterion (D_M) in arbitrary units for several values of the pressure versus radius.

where D_S gives the contribution of the shear, D_W is the contribution of the magnetic well, D_I gives the contribution of net currents and D_G is the contribution of the geodesic curvature. A positive D_M satisfies the stability criterion for Mercier modes. Figure 5 summarizes the results obtained for the standard configuration. It shows that it is stable to Mercier modes for the whole

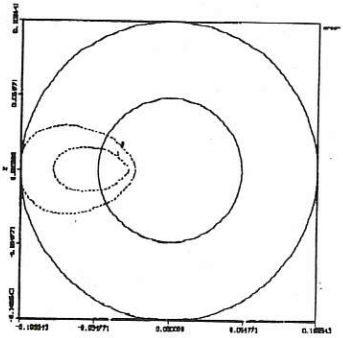

(a) Standard configuration

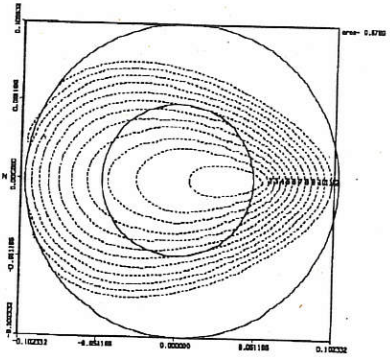

(b) Inward configuration

Figure 6
B-min contours for two TJ-IU configurations

radius and pressures considered even at <ß> = 3%. The valley in the criterion at average radius 0.4 is due to the passing through a lower order resonance of the iota profile that should flatten the pressure profile. We have chosen Mercier modes for our ß studies since they have been shown to give a limit to the pressure in other torsatrons [3].Nevertheless an study is under way to check the TJ-IU stability to ballooning modes. From the Mercier studies we can conclude that the ß-limit in TJ-IU is well above the achievable ß value for the 200 kW available initially of ECH heating power, although the possibility to inject 600 kW of ICH in a second phase will force the plasma stability to its theoretical limit.

This stability picture changes dramatically when we push the magnetic axis inwards, toward the center of the machine. The stabilizing vacuum magnetic well is destroyed and the configuration becomes unstable to Mercier modes even at very low values of the pressure. This strong stability antagonism between both configurations, will permit us to experimentally check the influence, if any, on the stability of the machine, of the amount of trapped particle population that as can be seen from figure 6 changes considerably in both configurations.

REFERENCES

[1] Hirshman, S.P., Van Rij, W.I., Merkel, P., Compt. Phys. Commun. **43** (1986) 143.

[2] Bauer, F., Betancourt, O., Garabedian, P., Wakatani, M., The BETA Equilibrium, Stability and Transport Code, Springer-Verlag, New York (1987)

[3] Carreras, B.A., Dominguez, N., Garcia, L., Lynch, V.E., Lyon, J.F., Cary, J.D., Navarro, A.P., Nucl. Fusion **28** (1988) 1195.

PROGRESS IN THE STUDIES OF URAGAN-2M STABILITY AND TRANSPORT PROPERTIES

N.T. Besedin, D.L. Grekov, I.M. Pankratov, O.S. Pavlichenko,
A.A. Shishkin, A.V. Zolotukhin
Institute of Physics and Technology, Kharkov, Ukraine

C.D.Beidler, J. Kißlinger, H. Maaßberg, F. Rau, H. Wobig
Max-Planck-Institut für Plasmaphysik, Garching, Germany

B.A. Carreras, N. Dominguez, V.E. Lynch
Oak Ridge National Laboratory, Oak Ridge TN, USA

Construction of the new experiment URAGAN-2M has been completed recently at the Kharkov Institute of Physics and Technology. (URAGAN-2M is an $\ell = 2$ torsatron with $m = 4$ field periods, 16 TF coils and 6 pairs of VF coils; the major radius of the device is $R_0 = 170$ cm, the minor radius of the helical windings is $a_h = 44.5$ cm and the maximum value of the magnetic field strength on axis is $B_0 = 24$ kG.) Theoretical efforts to support the upcoming experimental program have been continued and lead to the new results described below (previous results may be found in References /1-3/).

(1) **Mercier Stability** — Using a more accurate model of the URAGAN-2M helical windings (20 filaments for each of the two half poles which comprise a single helical winding as opposed to the 3 filaments used previously) it is found that for parabolic profiles Mercier stability is improved up to peak beta values of $\beta_0 = 3\%$ (instead of the 1.5% obtained previously /2/) for the so-called "Thin" configuration which has a rotational transform $\iota > 0.5$ and an average plasma radius of $\bar{a} = 23.3$ cm. Reducing the plasma radius to $\bar{a} = 15$ cm, $\beta_0 = 5\%$ is limited by equilibrium constraints. By increasing the toroidal field it is possible to realize the so-called "Fat" configuration with $\iota < 0.5$ and with $\bar{a} = 24$–29 cm. This configuration has access to the 2nd stability regime for Mercier modes at low β_0 values when narrow pressure profiles are realized, as is illustrated in the two frames of Figure 1. In the left-hand frame, the Mercier criterion is shown for several values of β_0 as a function of normalized radius assuming the pressure profile $P = P_0(1 - s)^4$, where s is the normalized toroidal flux. For $\beta_0 > 1.6\%$ the configuration is Mercier stable at all radii and becomes increasingly more stable as β increases. The right-hand figure shows the radially localized regions of Mercier instability (i.e. $D_m < 0$) for the pressure profile $P = P_0(1 - s)^2$; the second stability regime for Mercier modes is obtained for $\beta_0 > 5\%$.

(2) **Variation of the Neoclassical Transport** — Significant variation of the neoclassical transport level in URAGAN-2M configurations is possible using unbalanced currents in adjacent pairs of toroidal field coils to produce a "Low Mirror" or "High Mirror" in $|B|$ on the magnetic axis. This was shown for the "Thin" configuration in

Reference /1/ and is illustrated for the "Fat" configuration in Figure 2 of this paper. This figure compares the actual magnitude of the configuration's helical ripple, ϵ_h, with its *effective* helical ripple for $1/\nu$ transport, $<\epsilon_h>$ (the effective helical ripple is defined so that $\epsilon_h = <\epsilon_h>$ for an ideal single-helical-harmonic stellarator). As this figure shows, it is possible to achieve large variations in $<\epsilon_h>$ among these configurations, especially on axis. This variation has a significant effect on the expected plasma parameters as is indicated by results for the "Thin" configuration from the 1-D transport code TEMPL, given in Figure 3. The temperature profiles shown in this figure were calculated for a typical ECR-heating scenario under the assumption that electron transport may be described as the sum of neoclassical and anomalous losses (the anomalous contribution being given by an empirical formula which has been found to describe W VII-AS discharges); ion transport is taken to be neoclassical. These results predict that the peak electron temperature may be varied in the range 1.0 keV $< T_e(0) <$ 1.7 keV.

(3) **The Bootstrap Current** — As Figure 3 also illustrates, the bootstrap current is strongly affected by the choice of magnetic field configuration. For this particular simulation with an ECRH power input of $P_{in} = 400$ kW, peak values of the current density are found to be 25 A/cm^2 (total current $\approx$ 4.8 kA) for the Low Mirror case and 4 A/cm^2 (total current $\approx$ 1.6 kA) for the High Mirror case. This analysis is based on use of the DKES code /4/, a numerical solution of the drift kinetic equation.

This control of neoclassical effects (transport and bootstrap current) through variation of the current ratio in adjacent pairs of TF coils has quite different properties than the well-known approach of using vertical field coils to shift the plasma column (a method used successfully on the ATF and CHS experiments). The latter method results in a significant change in the harmonic content of $|B|$ which is accompanied by changes in the global magnetic properties (e.g. rotational transform, shear, vacuum magnetic well) and thus the MHD properties of the device. In contrast, the redistribution of TF coil currents in URAGAN-2M changes the magnitude of the magnetic field ripple without altering the global magnetic properties of the device. As a consequence, the Mercier and resistive interchange stability conditions in Low Mirror and High Mirror configurations are found to be quite similar.

/1/. C.D. Beidler, N.T. Besedin, V.E. Bykov, et al., in **Plasma Physics and Controlled Fusion Research 1990** (Proc. 13th Int. Conf. Washington D.C., USA, 1990), Vol. 2, IAEA, Vienna (1991) 663-675.
/2/. C.D. Beidler, N.T. Besedin, B.A. Carreras, et al., Proc. 8th Int. Stellarator Workshop, Kharkov, USSR (1991) 327-338.
/3/. B.A. Carreras, N. Dominguez, V.E. Lynch, et al., in **18th European Conf. Controlled Fusion and Plasma Physics** (Proc. 18th Int. Conf. Berlin, Germany, 1991), Vol. 15C, Part II, (1991) 149-152.
/4/. S.P. Hirshman, K.C. Shaing, W.I. van Rij, et al., **Phys. Fluids, 29**, (1986) 2951-2959.

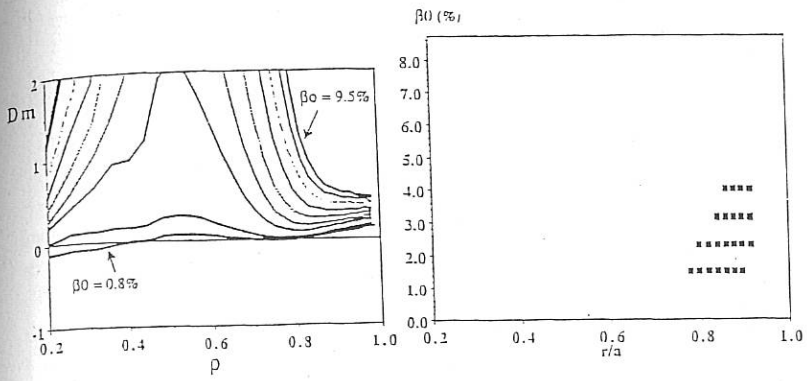

FIGURE 1. Left — Mercier criterion as a function of normalized radius for the "Fat" configuration with the pressure profile $P = P_0(1-s)^4$ for central beta values of (from bottom to top) 0.8%, 1.6%, 3.3%, 4.2%, 5.25%, 6.4%, 7.3%, 8.5%, and 9.5%. Mercier stability is guaranteed when $D_m > 0$. Right — radially localized regions of Mercier instability for given β_0 values for the "Fat" configuration with $P = P_0(1-s)^2$.

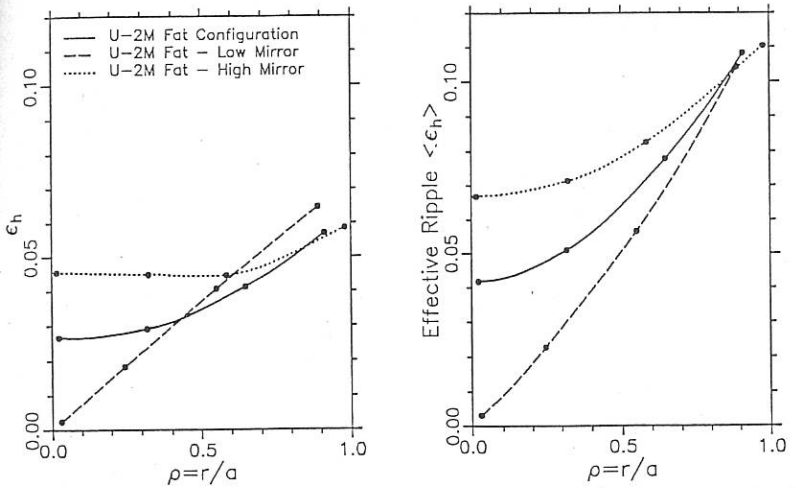

FIGURE 2. The radial dependence of the magnitude of the helical ripple, ϵ_h is shown in the left-hand frame for three different cases of the URAGAN-2M "Fat" configuration. In the right-hand frame, plots of the effective helical ripple for $1/\nu$ transport, $<\epsilon_h>$, are shown for the same cases.

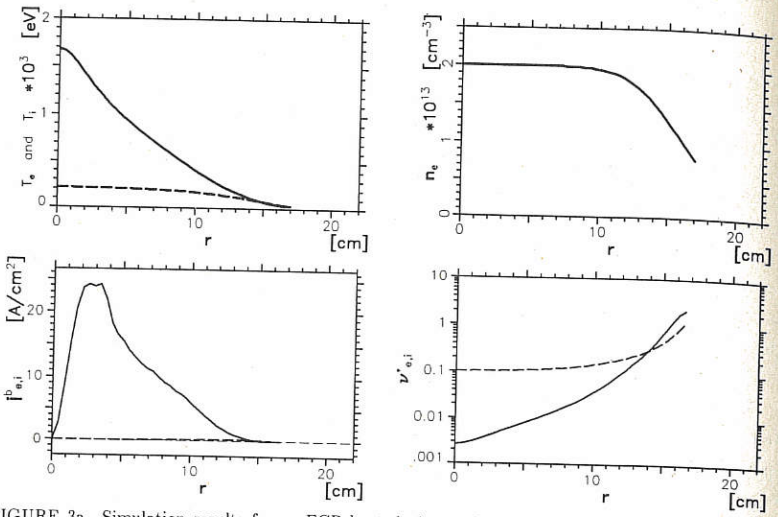

FIGURE 3a. Simulation results for an ECR-heated plasma (P_{in} = 400 kW) for the URAGAN-2M Low-Mirror configuration with $\epsilon > 0.5$ (the so-called "Thin" case) are presented, beginning in the upper-left-hand corner and proceeding clockwise: (1) temperature profiles for electrons (solid line) and ions (broken line) determined by the TEMPL code; (2) the assumed density profile for both ions and electrons; (3) the normalized collision frequency, ν^*, for each particle species; and (4) the radial profile of the bootstrap current (carried almost exclusively by the electrons) as calculated by the DKES code. Other parameters of interest are $B_0 = 1.9$ T and $Z_{eff} = 4.0$.

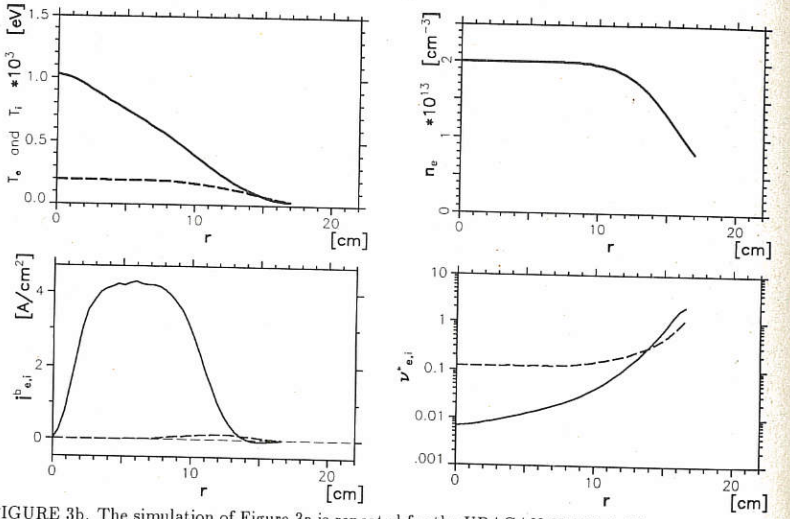

FIGURE 3b. The simulation of Figure 3a is repeated for the URAGAN-2M High-Mirror configuration with $\epsilon > 0.5$.

DESTRUCTION OF ALFVÉN MODES ON A TORUS DUE TO LARGE NONAXISYMMETRY

Albert Salat

Max-Planck-Institut für Plasmaphysik, D-8046 Garching bei München

The spectrum of ideal MHD plasmas in axisymmetric toroidal geometry contains the coupled Alfvén-slow-mode continuum. Modes in a continuum are not square integrable which manifests itself in a radial divergence of the displacement $|\boldsymbol{\xi}| \sim |\psi - \psi_0|^{-1}$ around a magnetic surface $\psi = \psi_0(\omega)$ /1/, /2/. This feature makes the continuum attractive for local plasma heating. Within the resonant surface $\boldsymbol{\xi}$ is determined by a system of ODEs with the operator $\mathbf{B} \cdot \nabla = B^\theta \mathrm{d}/\mathrm{d}\theta + inB^\phi$, i.e. in the variable θ, where θ and ϕ are poloidal and toroidal angles, respectively. $B^\theta = \mathbf{B} \cdot \nabla\theta$, etc., and $\boldsymbol{\xi} \sim e^{in\phi}$. The aim of the paper is to point out qualitative changes in the spectrum and the mode structure of $\boldsymbol{\xi}$ if the axisymmetry of the torus is sufficiently perturbed. Some model assumptions are introduced for simplification.

The equations of ideal MHD may be written in the form /3/

$$\frac{\partial \mathbf{S}}{\partial \psi} = \mathrm{A} \cdot \mathbf{S} + \mathrm{C} \cdot \mathbf{R} ,$$

$$\mathrm{H} \cdot \mathbf{R} = \mathrm{K} \cdot \mathbf{S} ,$$

where $\mathbf{R}$ and $\mathbf{S}$ are vectors defined by $\mathbf{R} = (v^\theta, v^\phi, b^\theta, b^\phi)^T$, $\mathbf{S} = (v^\psi, p^*)^T$ and the matrix operators A, C, H, K contain only derivatives within the magnetic surfaces. $\mathbf{v} = i\omega\boldsymbol{\xi}$ and $p^* = p + \mathbf{B} \cdot \mathbf{b}$, with p and $\mathbf{b}$ being the perturbations of the pressure P and magnetic field $\mathbf{B}$, respectively. The continuous spectrum is given by those values of ω^2 for which

$$\mathrm{H} \cdot \mathbf{R}(\theta, \phi) = 0 ,$$

has a bounded solution with periodicity in θ and ϕ. One possible representation of $\mathrm{H} \cdot \mathbf{R} = 0$ is /4/

$$[\, \mathbf{B} \cdot \nabla \, \mathrm{M} \, \mathbf{B} \cdot \nabla + \omega^2 \rho \, \mathrm{N} \,] \cdot \mathbf{X} = 0 , \qquad (1)$$

where $\mathbf{X} = (u, v)^T$ contains the coefficients u, v of the tangential components $\xi^i = u B^i + v j^i$, $i = \theta, \phi$, and

$$\mathrm{M} = \begin{pmatrix} \gamma P \, \mathbf{B} \cdot \mathbf{B} \, / \, B_* & \gamma P \, \mathbf{B} \cdot \mathbf{j} \, / \, B_* \\ \gamma P \, \mathbf{B} \cdot \mathbf{j} \, / \, B_* & \mathbf{j} \cdot \mathbf{j} - (\mathbf{B} \cdot \mathbf{j})^2 \, / \, B_* \end{pmatrix}, \quad \mathrm{N} = \begin{pmatrix} \mathbf{B} \cdot \mathbf{B} & \mathbf{B} \cdot \mathbf{j} \\ \mathbf{B} \cdot \mathbf{j} & \mathbf{j} \cdot \mathbf{j} \end{pmatrix} .$$

$\mathbf{j} = \mathrm{curl}\, \mathbf{B}$ and $B_* = \gamma P + B^2$. ρ is the mass density, and $\boldsymbol{\xi} \sim e^{i\omega t}$ is assumed. In a coordinate system with straight field lines $q = B^\theta / B^\phi$, the safety factor, is constant on $\psi = const$. Defining new coordinates x, y by

$$\theta = x , \qquad \phi = q\, x + y ,$$

one obtains $\mathbf{B} \cdot \nabla = B^\theta \, \mathrm{d}/\mathrm{d}x|_{y=const}$, so that equs. (1) become ODEs in x, with coefficients $\mathrm{M}(x, qx + y)$ etc. Assuming ergodic field lines q is irrational and the coefficients M, N are quasiperiodic in x.

For small plasma β the Alfvén continuum decouples from the slow modes. Neglecting a first order term one obtains from equs. (1)

$$\left[\frac{\mathrm{d}^2}{\mathrm{d}x^2} + (E - V) \right] U(x) = 0 , \tag{2}$$

where $E = \rho\omega^2/(B^\theta)^2$, $V = -(B^\theta)^{-1}\mathrm{d}[aB^\theta \mathrm{d}a^{-1}/\mathrm{d}x]/\mathrm{d}x$, $a = (\nabla\psi)^2/B^2$ and $U = v/a$. This is the Schrödinger equation with quasiperiodic potential $V = V(x, qx)$ if E is considered independent of x. For ease of numerical evaluation a Kramers-Kronig model for V is taken,

$$V = - F \sum_{r=-\infty}^{+\infty} \delta(x - 2\pi r) - G \sum_{r=-\infty}^{+\infty} \delta(x - 2\pi r / q) ,$$

so that equ. (2) goes over into a recursion from one δ function to the next.

The spectrum of equ. (2) is given by those values of E for which the winding number $w(E)$ (devil's stair case type) is not constant /5/. $w = \lim_{x\to\infty} \Phi(x)/x$, $\tan\Phi = \sqrt{E}U(x)/U'(x)$.

Figures 1 – 3, beginning with $F = 0$ (axisymmetric case) show a sequence of Alfvén modes $U(\theta, \phi)$, $0 \leq \theta, \phi \leq 2\pi$ at increasing nonaxisymmetry $|F|$. G is a measure of toroidicity and is kept constant at $G = 0.8$ throughout. $q = (\sqrt{5} - 1)/2$ is used. Fig. 2: $F = 0.5$. Fig 3: $F = 0.57$. Figures 1 – 3 refer to the "same" mode with fixed $w = w_{(m,n)} = (m + nq)/2$, $(m, n) = (6, -8)$. (m and n are also the number of nodes of $U(x)$ on toroidal and poloidal cuts of the torus, respectively.) At $F = F_0$, slightly above $F = 0.57$, a coherent (6,-8) Alfvén mode ceases to exist. The continuous spectrum, in the region around $w = w_{(6,-8)}$, goes over into a point spectrum. This is in agreement with the general theory of the quasiperiodic Schrödinger equation which, for sufficiently irrational q and sufficiently large $V(x, qx)$, permits both a continuous and a (dense) point spectrum /5/. Numerically, the continuous spectrum can be distinguished from the point spectrum by monitoring the Liapunov exponent Λ_Φ of the winding number equation /6/, /7/. Figure 4 shows a section of the continuous spectrum at $F = 0.4$ (upper trace) and the functions $w(E)$ (middle trace) and $\Lambda_\Phi(E)$ (lower trace). Λ_Φ vanishes in the continuous spectrum outside the gaps $w = w_{(m,n)} = const$. In Fig. 5, at $F = 0.7$, the continuous spectrum is empty, and $\Lambda_\Phi \neq 0$ outside $w(E) = const$ also. Modes in the point spectrum can be found by considering the *boundary value* problem $U_0 = U_{N+1} = 0$ of the recursion, where U_i is the value of $U(x)$ at the i-th δ function pulse, and N is a sufficiently large number /6/, /7/. For F approaching F_0 the continuum modes collapse onto a single field line, i.e. they become infinitely thin transverse to $\mathbf{B}$. Along $\mathbf{B}$ they fall off to zero in both directions with a finite

decay length. Fig. 6 shows the result of this collapse of the $w_{(6,-8)}$ mode, at $F = 0.7$. (Needles instead of infinitely thin ridges are an artefact of the plotting routine.)

An overview of the spectrum for $0 < E < 1$ at 21 values of nonaxisymmetry F is given in Fig. 7. Continuous spectra are rendered as thin lines while point spectra are indicated by vertically elongated bars. The transition at large nonaxisymmetry from a continuous spectrum to a dense point spectrum with ensuing collapse of modes from a resonant surface onto a single field line is not limited to the δ-function model considered here but occurs for smooth profiles as well.

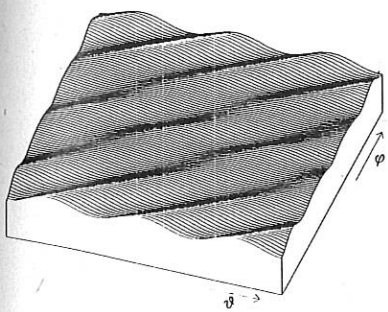

Fig. 1

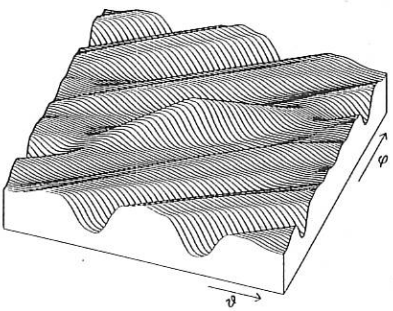

Fig. 2

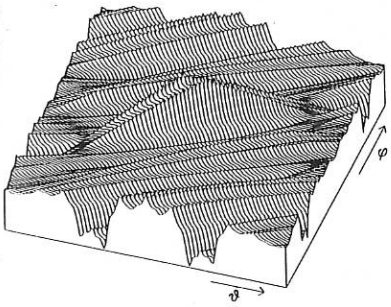

Fig. 3

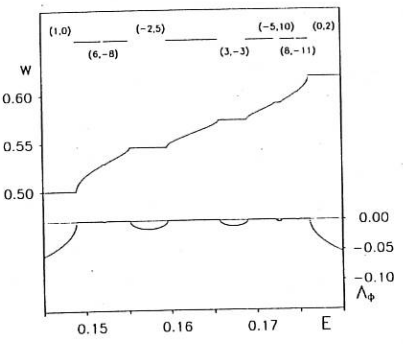

Fig. 4

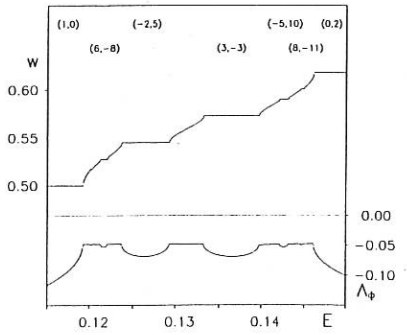

Fig. 5

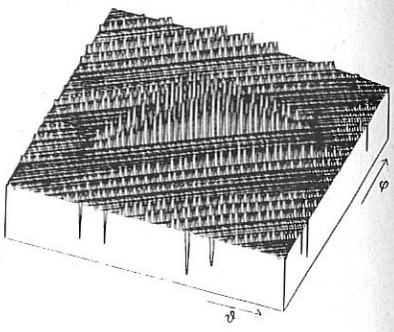

Fig. 6

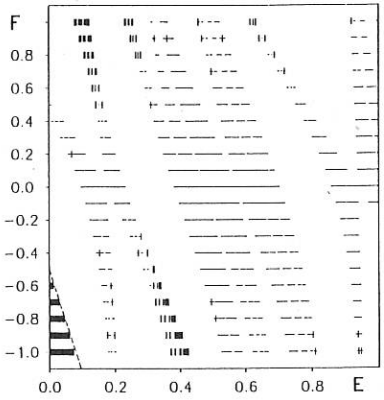

Fig. 7

/1/ J. P. Goedbloed, Phys. Fluids **18**, 1258 (1975)

/2/ Y.P. Pao, Nucl. Fusion **15**, 631 (1975)

/3/ J.A. Tataronis, J.N. Talmadge and J.L. Shohet, Comments Plasma Phys. Controlled Fusion **7**, 29 (1982)

/4/ J.A. Tataronis and A. Salat, E. Canobbio, H.P. Eubank, G.G. Leotta et al. (Eds.) *Heating in Toroidal Plasmas* Proc. 2nd Joint Grenoble - Varenna Int. Symp., Como, Italy (1980), Vol. II, p.655, EUR-7424 EN (1981)

/5/ B. Simon, Advances Appl. Math. **3**, 463 (1982)

/6/ A. Salat, Phys. Rev. A **45**, 1116 (1992)

/7/ A. Salat, Plasma Phys. Contr. Fusion, to be published.

STUDY OF MAGNETIC SURFACES WITH ISLANDS USING THE PIES CODE

A. López Fraguas and A. Salas
Asociación Euratom/Ciemat para Fusión
E-28034 Madrid, Spain

A. H. Reiman, D. A. Monticello, and J. L. Johnson
Plasma Physics Laboratory, Princeton University*

Introduction

The PIES code[1] determines MHD equilibrium configurations by direct integration along the field lines and does not assume the existence of good magnetic surfaces. Therefore it can be used for systems with magnetic islands and/or stochastic regions. In the case of good magnetic surfaces its predictions have been compared with known analytical solutions in some simple test cases, and with the predictions of another well known equilibrium code for more complex configurations[2]. In both cases the agreement was very good.

The work presented here is an application of PIES to configurations with large magnetic islands. For this purpose we use the TJ-II flexible heliac[3], which is very appropiate due to its versatibility and small shear. This provides a very stringent test of the code, because of the complicated shape of the magnetic surfaces (the cross sections are strongly bean shaped and have a helical magnetic axis). In the configurations studied the rotational transform per period is equal to 1/3 somewhere inside the plasma, and is close to 1/3 over the entire volume of the plasma (this is a consequence of the small magnetic shear). To be more specific, the rotational transform changes from 4/3.02 at the magnetic axis to 4/2.92 at the plasma boundary (the number of periods is 4). As should be expected, there is a large third order island.

The shape of the plasma boundary (it must be a good magnetic surface) is given to the code as part of the input. The assumptions used for the islands are that both p and j/B are constant inside them and continuous across the separatrices. The net toroidal current is set to zero. The pressure is taken to be proportional to the square of $(1-\psi/\psi_b)$, where ψ/ψ_b is the relative toroidal flux (equal to 1 at the boundary). We have investigated the change in the magnetic structure when the central pressure is increased.

Zero pressure

First we study the zero pressure case, with no plasma currents. In this case the structure of the magnetic field can be independently obtained by following the field lines of the magnetic field created by the currents in the external coils. When this structure is compared with the predictions of the PIES code, the agreement is good if the number of surfaces and of modes is

* Supported by the U.S. Department of Energy under Contract DE-AC02-76-CHO-3073 with Princeton University

adequate[4]. For all the runs considered in this paper the number of surfaces is 30, and the modes retained by the PIES code are the following:

$$0 \le m \le 5, \qquad -10 + m \le n \le 10 + m,$$

where n is the toroidal number per period. This non-rectangular mode selection takes into account the approximate helical symmetry of the configuration. For inner calculations of the code we take $0 \le m \le 10$, $-30 \le n \le 30$. Without this factor of two padding for both m and n the results were completely wrong (Poincaré plot mostly stochastic).

In Fig.1(a) and Fig.2(a) we show the Poincaré plots for the vacuum run. The first figure shows the true shape of the surface sections (for ϕ=0), and in the second figure a mapping has been performed so that the boundary section appears circular. (There is a change of phase $\theta \rightarrow \pi + \theta$, so that left and right are inverted. The reason for this is that we wanted the θ=0, ϕ=0 line to cross the magnetic island, so that we would get sufaces inside the island in the Poincaré plots.) In the first part of Fig.3 we show the rotational transform profile. The ι=4/3 resonance appears very clearly.

Finite pressure

Once we were satisfied that the code was working satisfactorily with zero pressure, we started increasing the value of the pressure. For each β_0 we made a restart of the code from the previous run (which had a smaller β_0), so that the initial background coordinates for each run were the quasi-magnetic coordinates for the last iteration of the previous run. In this way we went up gradually from the initial value β_0=0 up to β_0=6.e-4. The results can be seen in the figures, specially in Fig.2 and Fig.4. As the pressure increases, the central width of the island

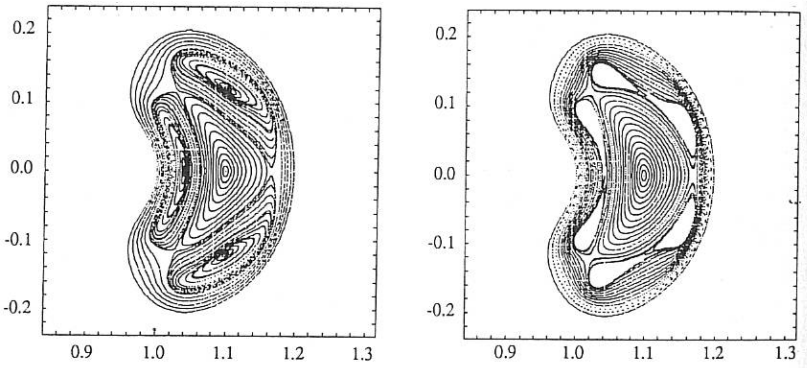

Fig.1. Poincaré plots at ϕ=0 (true shape).

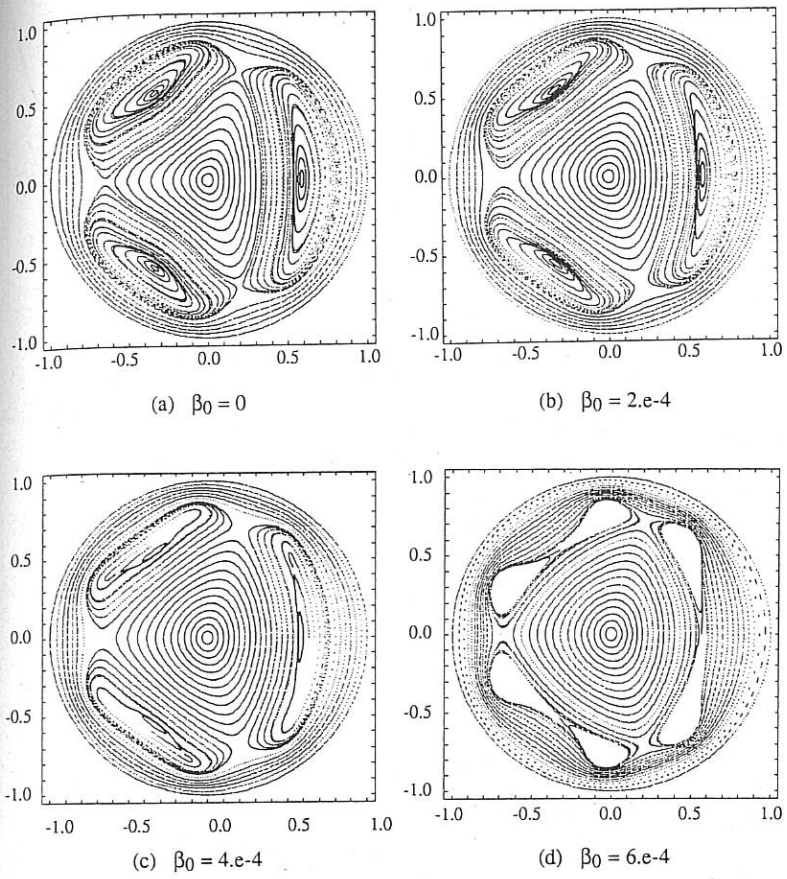

Fig.2. Poincaré plots at ϕ=0 (representation such that the boundary looks circular).

decreases, until the island seems to split around β_0 = 6.e-4. However, since the maximum value of the poloidal number retained by the code in these runs is m=5, the m=6 modes, which presumably become very important when the island is splitting, are not taken into account. Therefore this result can only be considered provisional until more poloidal modes are retained. At least m=6 modes are needed, and perhaps one must go up to m=12. We are currently working on it.

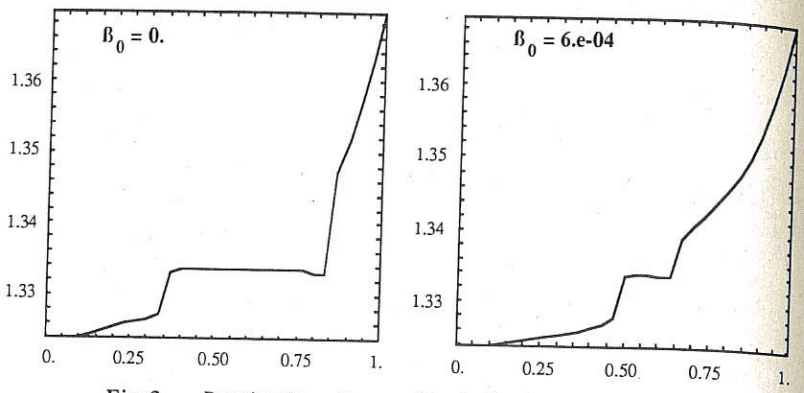

Fig.3. Rotational transform profiles for β_0=0. and for β_0=6.e-4 .

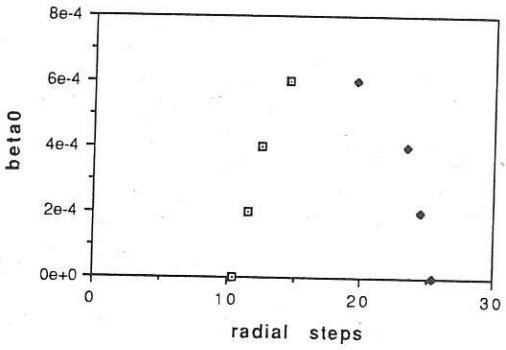

Fig.4. Positions of the island edges at θ=0, ϕ=0.

Conclusions

1. The PIES code is applicable to complex configurations with large islands.
2. In the case considered (ι/N=1/3 resonance for TJ-II), the third order island seems to split when β_0 increases. But the number of poloidal modes retained ($0 \leq m \leq 5$) is too low to make a categoric assertion.
3. Work is in progress using more poloidal modes to confirm the splitting.

References

1 A. H. Reiman and H. S. Greenside, J. Comput. Phys. **75**, 423 (1988)

2 J. L. Johnson *et al*, Proc. of 14th Int'l Conf. on the Numerical Simulation of Plasmas, Annapolis, MD (1991)

3 C. Alejaldre *et al*, Fusion Technology **17**, 131 (1990)

4 A. Salas *et al*, 33rd Annual Meeting of the DPP of the APS, Tampa, Florida (1991)

MODIFIED VACUUM FIELDS AND COMPENSATION OF ISLANDS FOR THE STELLARATOR W 7-AS

C. Beidler, E. Harmeyer, U. Gasparino, J. Kißlinger, G. Kühner, H. Maaßberg, F. Rau, H. Ringler, H. Wobig, W7-AS Team, ECRH-Group, W7-X Team
Max-Planck-Institut für Plasmaphysik
IPP-EURATOM Association, W-8046 Garching bei München, Germany

Three types of modifications are investigated for Wendelstein 7-AS by vacuum field calculations, in order to broaden the range of accessible topologies for the experiment: a variation of the magnetic field modulation (mirror ratio) near the magnetic axis, a superposition of quadrupole fields, and the compensation of magnetic islands. The first type is possible with different currents in the non-planar 'modular' and the large 'special' coils, the second one requires certain current polarities in the axisymmetric coils (OH-transformer and B_z-system), for the third type a system of in-vessel current loops is proposed. Magnetic field properties are analyzed from line tracing and with the use of Fourier harmonics of the magnetic field at a value of $B = 2.5$ T for ECR power input in the toroidal plane $\varphi = 36°$.

Vacuum flux surfaces of W 7-AS with $\iota = 0.34$ and increased mirror ratio on axis, $MR = (B(36°) - B(0°))/(B(36°) + B(0°)) = 10$ %, are shown in Fig. 1, obtained by a coil current ratio $CR = I_{sp}/I_{mod} = 1.6$. One of the typical values of 'good' confinement in W 7-AS, $CR = 1$ and ι near 1/3 at the edge, has $MR \approx -2.5\%$, see Fig. 2, left data points. For this configuration the axis field in the 'triangular' plane exceeds that in the 'elliptical' plane of ECR input. A configuration with $MR = -10\%$ is obtained for $CR \approx 0.6$. Trapped particle fractions $f_t = 0.25$ to 0.30 are estimated at a minor radius $r = 3$ cm for $CR = 1$ with $\iota = 1/3$ and 1/2, the values increase to 0.37 and 0.48 for $CR = 1.6$ and 0.6, resp. Trapped particles influence neoclassical properties in the long-mean-free-path regime; neoclassical heat and particle losses scale with the effective ripple $\epsilon_{eff}^{3/2}$. This quantity is estimated from the Fourier harmonics of $|B|$. Fig. 3 compares four cases with increased mirror ratio and $\iota \approx 1/3$ at the plasma edge. The case with $MR = 15\%$ has an inward shift of the magnetic axis. The largest effective ripple applies for the 'inverse' mirror, $MR = -10$ %. The moderate drift optimization of W 7-AS ensures $\epsilon_{eff} < MR$ for all cases. Except for $MR = 10\%$ the values increase towards the edge via toroidicity and the 'modular' ripple caused by the gaps between the coils. The DKES code allows one to evaluate the Onsager matrix of transport coefficients. Results without radial electric field have been obtained for a limited number of mirror ratios so far. In comparison to W 7-AS with $CR = 1$ and $\iota \approx 1/3$, they indicate a reduction of the particle transport Γ_{11} by a factor up to two when increasing the mean free path for a moderate mirror ratio $MR = 3.2$ %, whereas some degradation is seen at $MR = \pm 10\%$. The geometrical factor G_b and the quantity $G_b \cdot f_t/(1-f_t)$ of the bootstrap current in the lmfp regime are derived from Fourier coefficients of the field. Fig. 4 indicates that the increase of this current at larger MR stems mainly from the increase in f_t. Experiments in W 7AS at $MR = 10\%$ were recently initiated and continue earlier studies at lower MR-values. A maximum of $T_e(0)$ is seen near $B = 1.26$ T on axis, similar as under standard operation, see Fig. 5.

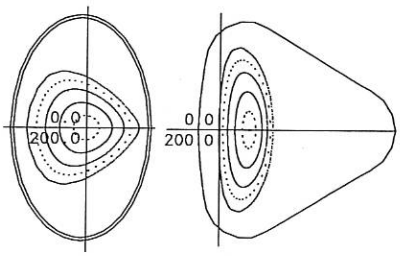

Fig. 1: *Poincaré plots for increased $MR = 10\%$, $\varphi = 0$ and $36°$. Compared to standard conditions of W 7-AS, the 'triangular' surfaces are larger than the 'elliptical' ones. This impacts the limiter efficiency and is important for edge studies.*

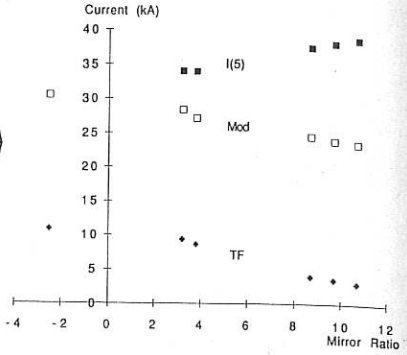

Fig. 2: *Coil currents for various mirror ratios in centered configurations with $\iota \approx 0.34$ at the edge and $B = 2.5$ T on axis at the ECR input plane. The left points are for the standard low-ι-case, $MR = -2.5\%$. Moderately different data apply for an additional vertical field, e.g. yielding an inward axis shift of 3 and 2 cm at $\varphi = 0$ and $36°$, resp., for $I_z = 0.5$ kA in the B_z-system.*

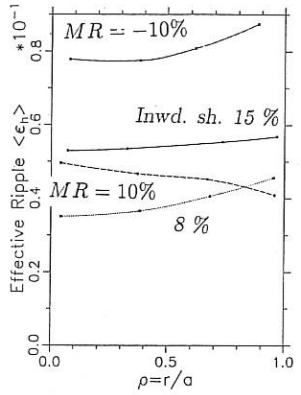

Fig. 3: *Radial profiles of the 'effective' ripple for increased mirror ratio. Values are below the geometrical and modular ripple. The configuration with 'inverted' mirror ratio on axis, $MR = -10\%$, yields the highest value, whereas an inward shift appears to be useful.*

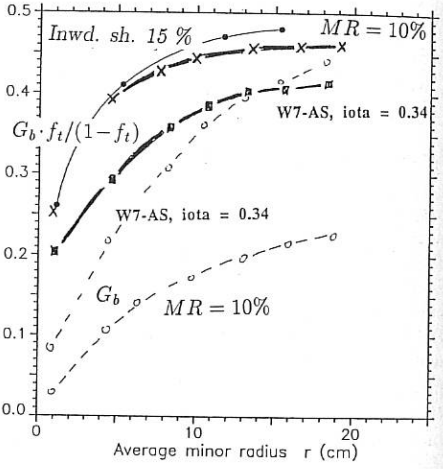

Fig. 4: *G_b and $G_b \cdot f_t/(1-f_t)$, geometrical factors of the bootstrap current in the lmfp regime, which determine this current together with the T_e-profile.*

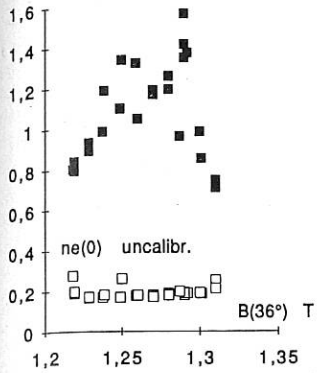

Fig. 5: $T_e(0)$ from Thomson scattering and $n_e(0)$ in the vertical midplane, obtained in an initial experiment at $MR = 10\%$ and a gyrotron output power of 0.4 MW, varying the magnetic field on axis. The bootstrap current < 5 kA is compensated by an OH-current, $V_l \approx 0.1$ V.

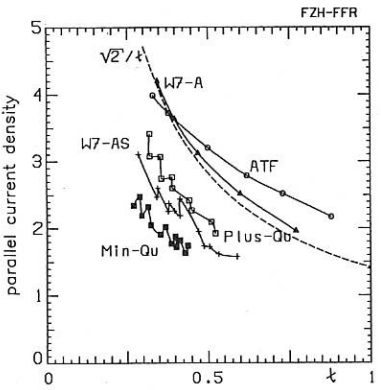

Fig. 6: Pfirsch-Schlüter currents, $\langle |j_\parallel / j_\perp| \rangle$ vs ι for various vacuum fields. The classical stellarator W 7-A follows the theoretical expectation $\sqrt{2}/\iota$. In W 7-AS these currents are improved by a factor 2, with some change by superposed quadrupole fields; an increased mirror ratio has little effect.

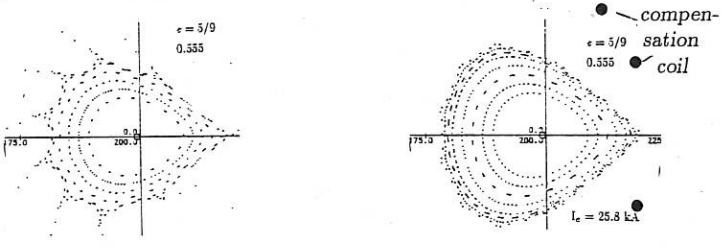

Fig. 7: Poincaré plots of magnetic surfaces at $\varphi = 0°$ with $\iota \approx 5/9$ at the edge: without current (left) and with 25.8 kA in the compensation coils (right). The compensation coils have a toroidal extension of about 60 cm and follow helically the tip of the surfaces.

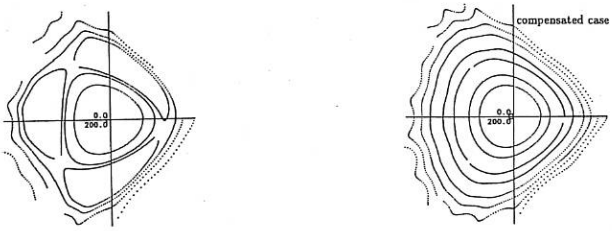

Fig. 8: Perturbed magnetic surfaces with $\iota = 1/3$ in the plasma volume (left) and compensated case (right) with currents in compensation coils in two of the 5 field periods ($\varphi = 216°$ 1.5 kA, $\varphi = 288°$ 0.38 kA).

A quadrupole field with stagnation point at $R = 2$ m can be introduced in W 7-AS by balancing the vertical fields of the two largest pairs of B_z-coils with currents of 6 and -3.76 kA, resp., yielding a normalized field gradient $1/R \cdot dB_z/dR = -2 \cdot 10^{-2}$ T m^{-2}. The field gradient can be doubled by utilizing all poloidal field coils. Positive quadrupole fields introduce horizontally elongated (oblate) magnetic surfaces, negative ones vertically elongated (prolate) surfaces, accompanied by a change of the rotational transform and the shear. Negative quadrupole fields introduce negative shear in a range of $0.27 < \iota < 0.44$, for example -7 % at $\iota = 0.34$ on axis, whereas under standard operation of W 7-AS the shear is small. Simultaneously, the value of the Pfirsch-Schlüter currents changes by about 10 %, see Fig. 6; positive quadrupole fields lead to increased PS currents. This degradation can be reduced by an inward shift. Effects of quadrupole fields on the bootstrap current remain to be studied.

Vacuum fields in W 7-AS are associated at rational $\iota = 5M/N$ with chains of N 'natural' magnetic islands and a radial corrugation of the magnetic surfaces in their vicinity. The amplitude of the deformation and the size of the islands increase with ι and the minor radius of the surfaces. For large ι-values the configuration is bounded by a separatrix which reduces the plasma radius. The deformation of the surfaces and the island size can be considerably reduced by superposition of appropriate harmonic field components produced by an additional coil system, e.g. by using two current loops (compensation coils) inside the vacuum vessel in each field period. For $0.35 < \iota < 0.55$ rather small currents between 10 and 26 kA-turns at $B = 2.5$ T, compared to typical currents of about 0.5 MA-turns in the module coils, are sufficient to smooth the corrugation and to reduce the island size, see Fig. 7 as an example. Larger currents in the coils cause some surface deformation again with a poloidal phase shift and interchanged O and X points of islands. This feature allows one to sweep the position of the contact region between plasma and target plates at the edge, when energizing the coils with AC-currents.

Symmetry-breaking error fields, e.g. due to small construction inaccuracies of the device, can be largely compensated by a proper choice of currents in each coil. For $\iota = 1/3$, three rather large islands have been observed experimentally as the effect of $m = 1$ error fields. In Fig. 8 this perturbation is simulated by the field of a tilted circular coil and can be compensated with currents of 1.5 and 0.38 kA in the loops at $\varphi = 216$ and 288°, respectively.

Summary and Conclusion: 1) An increase of the mirror ratio of the magnetic field near the axis increases the fraction of trapped particles, and thus influences neoclassical properties in the long-mean-free-path regime. Such configurations could be useful to investigate the relative amount of anomalous and neoclassical losses, to analyze details of the bootstrap current and of ECR-induced currents. Experiments at 1.25 T were initiated for $MR = 10\%$, comparison to the case with $MR = -10\%$ appears to be interesting. 2) Superposed 'negative' quadrupole fields introduce some reduction in the parallel current density and introduce negative shear. 3) The installation of additional in-vessel coils would allow one to influence the harmonics of the magnetic field, and thus to improve the aspect ratio at large ι-values by smoothing the existing corrugation near the edge. AC currents in such coils allow for sweeping of the contact region of the existing limiters or of possible divertors, adjusted currents offer the possibility to compensate external error fields. 4) Combination of the various modifications are also possible, and would broaden the range of experimental parameters further.

OPTIMIZATION OF COILS AND A SWEEP COIL SYSTEM FOR W7-X

P. Merkel, J. Kißlinger

Max-Planck-Institut für Plasmaphysik
IPP-EURATOM Association, W-8046 Garching bei München, Germany

1. Optimization of coils for W7-X

An extended version of the NESCOIL code /1/ has been applied to optimization studies of the W7–X coil system. Modifications of the proposed W7–X coil system /2/ are necessary in order to provide sufficient space between plasma and coils for the recently proposed divertor concept /3/ and satisfy additional coil constraints: Not only the local coil curvature, but also an appropriately weighted average coil curvature should not exceed prescribed values /4/ and sufficiently large coil–coil distance has to be guaranteed. On an outer boundary a surface current is determined such that the vacuum field $\vec{B}$ of the W7–X configuration is closely approximated. This is achieved by approximate solution of that Neumann problem which makes the normal component of $\vec{B}$ on the prescribed plasma boundary vanish. Modular coils are then obtained by discretizing the surface current into a finite number of filaments which represent the centres of the finite-size coils. This Neumann problem step is embedded in the nonlinear procedure of optimizing the outer surface, which is formulated as a minimization problem. The parameters determining the shape of the outer surface are the independent variables, and the function to be minimized consists of a sum of terms describing the accuracy of solution of the Neumann problem and several penalty terms introduced in order to satisfy the constraints. Penalty terms control the filament-filament distance and the local and weighted average filament curvatures while the minimum and maximum plasma-filament distances are prescribed by constraining tori (dashed lines, Fig.1). The optimized current– carrying surface (solid line) is obtained by varying the surface in the domain bounded by the constraining tori. In Figs.1a-b the Poincaré plots of the fields produced by 10 (Fig.1a) and 8 (Fig.1b) coils per period are shown. The divertor concept /3/ depends on the transition between the closed magnetic surfaces and the ergodic region, in which the field lines are not closed any more. The optimization computations have shown that this change of the field topology at the plasma boundary is more pronounced if the boundary value problem (vanishing normal field component at the prescribed plasma boundary) is solved with high accuracy, but with the consequence that the shape of the current filaments is then more complicated. In the 10-coil case a field is realized with a chain of thin islands at $\iota = 5/5$ (not shown in the plot) and with an ergodic region beginning slightly above $\iota = 1$. In the field produced by 8 coils per period the islands at $\iota = 5/5$ are larger and there are no closed surfaces outside these islands. In order to achieve a small field ripple it was necessary to choose a larger plasma-coil distance for the $N = 8$ coil case than for the $N = 10$ coil case. The ripple induced by the modular coils has to be sufficiently small ($\leq 10^{-3}$ on the magnetic axis) in order to make sure that the transport properties are not affected by the field variation. The principal ripple component B_{0N} on the magnetic axis is $B_{0N}/B_{00} = 4.4 \cdot 10^{-4}$ for the $N = 10$ case and $B_{0N}/B_{00} = 1.3 \cdot 10^{-3}$ for the $N = 8$ case. As a consequence, also the average length of the modular coils is larger for the 8-coil case: $L_{(N=8)} = 9.7$ m, $L_{(N=10)} = 8.6$ m. The weighted average coil edge curvatures obtained are $F_{(N=8)} = 0.3$, $F_{(N=10)} = .33$. For comparison, the corresponding value for the W7AS coils is $F_{W7AS} = 0.4$.

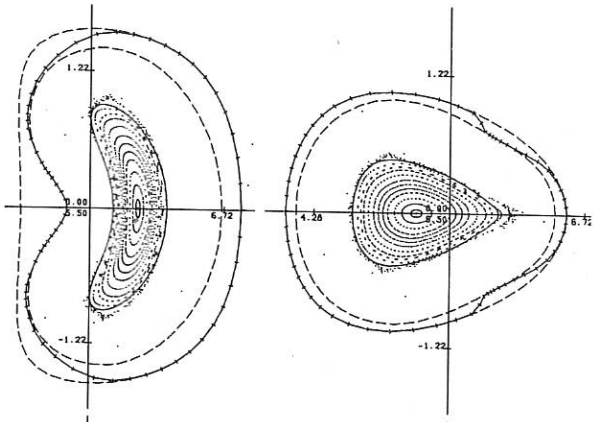

Fig.1a

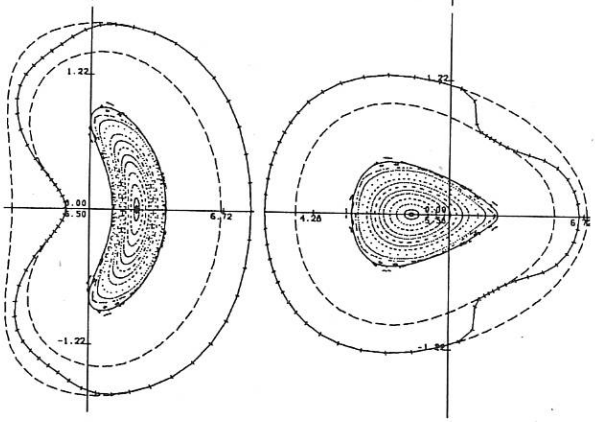

Fig.1b

Fig. 1a-b: Poincaré plots of W7-X field configurations produced by 10 (Fig.1a) and 8 filaments (Fig.1b) per period are shown. The optimized surface (solid line), on which the filaments are determined, is obtained by varying the surface in the region bounded by the constraining tori (dashed lines). Data of the cases: major plasma radius $R = 5.5$ m, aspect ratio $A = 10$, number of periods $n_p = 5$, magnetic field $B = 3$ Tesla. Data of 10 coil case: rotational transform $0.86 < \iota < 1.$, magnetic well $\delta V'/V' = .0085$, minimum filament – filament distance $d = 0.24$ m, coil cross-sections $q = 0.18 \times 0.22$ m^2 and weighted average coil edge curvature $F = .33$ and data of 8 coil case: $0.86 < \iota < 1.$, $\delta V'/V' = .006$, $d = 0.285$ m, $q = 0.20 \times 0.235$ m^2, $F = .3$.

/1/ P. Merkel, Nucl. Fusion **27** (1987) 867 and P. Merkel, In: Theory of Fusion Plasmas, Varenna, Italy, EUR 11336 EN, 25.

/2/ Wendelstein 7-X Proposal.

/3/ E. Strumberger, Proc. 18th European Conf. on Contr. Fusion and Plasma Physics, Berlin 1991, Vol. 15C, Part II, 173.

/4/ J. Sapper, priv. comm. (1991).

2. Sweep coil system

Sweeping the strike points of the outflowing plasma on the divertor target plates is a method to prevent excessive heat load on these plates. In Wendelstein 7-X, these target plates may be located in those regions where the diversion of field lines is a maximum. When large islands exist in the boundary region they are especially suited for divertor action. In this case control of island size and the position of O-points and X-points is desirable. This can be achieved by superimposing a magnetic field with Fourier components $B_{m,n}$ corresponding to the rational value of the rotational transform $\iota = m/n$.

In Wendelstein 7-X, a sweep coil system is considered which consists of two current loops in each field period inside the vacuum tube. These loops (dimensions of about 0.3 by 2 m) follow the helical edge of the magnetic surfaces and can be located behind the target plates (Fig.2, Fig. 4). Fig. 3b shows a Poincaré plot of a configuration very similar to that of Fig. 1, produced by a slightly different, smoother coil set. Closed surfaces exist in a radial domain of a few centimeters outside the islands. The separatrix and islands can be used for divertor application by locating the target plates in the domain of the islands. DC currents in the sweep coils allow one to control the size and phase of the islands and also to introduce an ergodic region at the plasma boundary. In Fig. 3a, currents of 17 kA enlarge the existing islands and there are no closed surfaces outside of them. Feeding the sweep coils with the same currents in opposite direction, causes the islands to shrink and to split into 10 smaller ones, corresponding to the next-order rational of $\iota = 10/10$; see Fig. 3c. Larger currents in this direction again cause an increased island size with interchanged locations of the O- and X-points (Fig. 3d). An important quantity for divertor action is the length of a field line (inside an island, near the separatrix), which connects two target plates. In the configuration without currents in the sweep coils (Fig. 3b, standard case) this connection length is 10-12 toroidal transits. It varies with the size of the islands: in the case of Fig. 3a it is only about 6 and in Fig. 3c it is about 20 toroidal transits.

Energizing the coils by AC currents introduces a sweeping effect; the strike points oscillate on the target plates because of the time-dependent size of the islands. Another type of sweeping is possible by holding the island size constant and shifting the position of the islands in the poloidal direction. This is achieved by using opposite currents in the upper and lower sweeping coils; see Fig. 4 as an example. Oscillating currents of 20 kA shifts the X-point about 5cm on the target plates. Since the X-points are included in the equilibrium field and need not be generated by the sweep coils, only rather small currents are necessary to obtain the desired shift of the strike points.

The magnetic field of the sweep coils preserves the 5-fold symmetry of the basic field in the above cases. A further application of the sweep coil system is the compensation of symmetry-breaking error fields, e.g. due to small construction inaccuracies of the device. This is achieved by an individual choice of current in each sweep coil. An example is studied in /5/. Combinations of the various functions of the sweep coils are also possible.

/5/ J. Kißlinger, F. Rau, Modified Vacuum Field Topologies and Compensation of Magnetic Islands in W 7–AS, this conference.

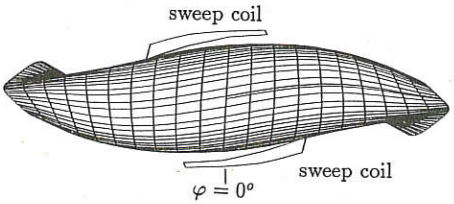

Fig. 2: Perspective view of sweep coils drawn as filament loops and one field period of a magnetic surface near the separatrix.

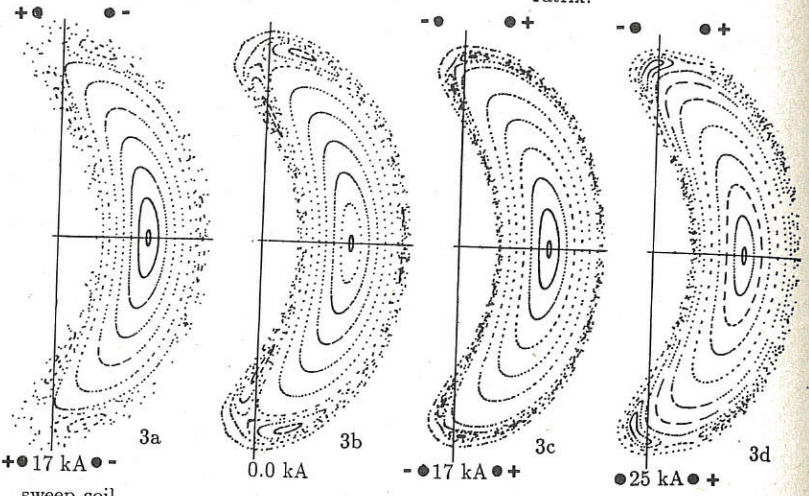

Fig. 3: Poincarè plots at the toroidal angle $\varphi = 0$ of a W7-X configuration modified by different currents in the sweep coils. The average magnetic field is 3 T.

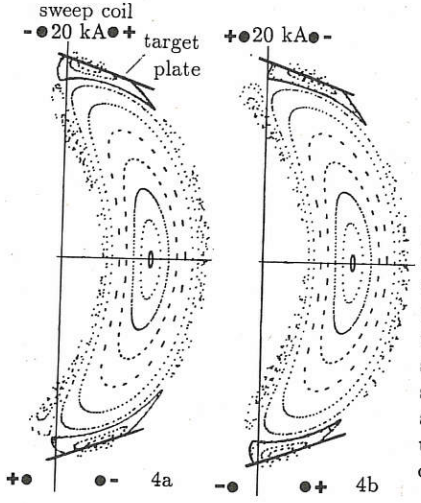

Fig. 4: Poincarè plots of the same configuration as in Fig. 3 but using opposite currents in the upper and lower sweep coils; thus the generated field does not modify the island size but introduces a poloidal shift of the islands. The locations of the sweep coils and of tentative target plates are also indicated. The boundaries of the upper and lower islands show the variation of the strike points.

ANISOTROPIC PRESSURE NUMERICAL 3D MHD EQUILIBRIA

S. P. Hirshman*, **W. A. Cooper**, S. Merazzi†, R. Gruber†
Centre de Recherches en Physique des Plasmas,
Association Euratom-Confédération Suisse,
Ecole Polytechnique Fédérale de Lausanne,
Lausanne, Switzerland

We introduce the energy functional

$$W \equiv \int\int\int d^3x \left[\frac{B^2}{2\mu_0} + \frac{p_{\|}}{\Gamma - 1}\right], \tag{1}$$

and demonstrate that its minimisation can be used to determine three dimensional (3D) magnetohydrodynamic (MHD) equilibria with anisotropic pressure. We express the parallel pressure as

$$p_{\|}(s,B) = M(s)[\Phi'(s)]^{\Gamma} \frac{1 + p(s,B)}{\left\langle 1 + p(s,B)\right\rangle^{\Gamma}}, \tag{2}$$

where $M(s)$ is the plasma mass function, $\Phi(s)$ is the toroidal magnetic flux function, Γ is the adiabatic index and $p(s,B)$ is the function that controls the anisotropy in the pressure. We constrain the poloidal magnetic flux function Ψ to be a flux surface quantity, thus the magnetic flux surfaces remain nested. We introduce a coordinate system (s,u,v) where s labels the magnetic flux surfaces, u is the periodic poloidal angle variable and v is the geometric toroidal angle. We then vary W with respect to an artificial time parameter t in such a manner that the plasma mass function, the magnetic flux functions and the coordinates s, u and v remain invariant. The energy functional acquires the form

$$\begin{aligned}\frac{dW}{dt} = &-\int\int\int dsdudv F_R \frac{\partial R}{\partial t} - \int\int\int dsdudv F_Z \frac{\partial Z}{\partial t} \\ &- \int\int\int dsdudv F_\lambda \frac{\partial \lambda}{\partial t} \\ &- \int\int_{s=1} R\Big(p_\perp + \frac{B^2}{2\mu_0}\Big)\Big(\frac{\partial R}{\partial u}\frac{\partial Z}{\partial t} - \frac{\partial Z}{\partial u}\frac{\partial R}{\partial t}\Big).\end{aligned} \tag{3}$$

The distance from the major axis is R and the distance from the horizontal midplane is Z. The function λ is a periodic stream function that iteratively renormalises the poloidal angle to minimise the spectral width that is required to describe the MHD equilibrium state [1]. The perpendicular pressure is $p_\perp$. The last term constitutes the deformation of the plasma-vacuum interface boundary that vanishes by definition for fixed boundary calculations. The coefficients F_R and F_Z correspond to the cylindrical MHD force components $F_R = \sqrt{g}R\nabla v \times \nabla Z \cdot \mathbf{F}$ and $F_Z = \sqrt{g}R\nabla R \times \nabla v \cdot \mathbf{F}$, respectively, where

$$\mathbf{F} = -\nabla\Big(p_\perp + \frac{B^2}{2\mu_0}\Big) + (\mathbf{B}\cdot\nabla)(\sigma\mathbf{B}). \tag{4}$$

These can be written as

$$\begin{aligned} F_R = {} & \frac{\partial}{\partial u}\big[\sigma\sqrt{g}B^u(\mathbf{B}\cdot\nabla R)\big] + \frac{\partial}{\partial v}\big[\sigma\sqrt{g}B^v(\mathbf{B}\cdot\nabla R)\big] \\ & -\frac{\partial}{\partial u}\Big[R\frac{\partial Z}{\partial s}\Big(p_\perp + \frac{B^2}{2\mu_0}\Big)\Big] + \frac{\partial}{\partial s}\Big[R\frac{\partial Z}{\partial u}\Big(p_\perp + \frac{B^2}{2\mu_0}\Big)\Big] \\ & +\frac{\sqrt{g}}{R}\Big[\Big(p_\perp + \frac{B^2}{2\mu_0}\Big) - \sigma R^2(B^v)^2\Big], \end{aligned} \tag{5}$$

$$\begin{aligned} F_Z = {} & \frac{\partial}{\partial u}\big[\sigma\sqrt{g}B^u(\mathbf{B}\cdot\nabla Z)\big] + \frac{\partial}{\partial v}\big[\sigma\sqrt{g}B^v(\mathbf{B}\cdot\nabla Z)\big] \\ & +\frac{\partial}{\partial u}\Big[R\frac{\partial R}{\partial s}\Big(p_\perp + \frac{B^2}{2\mu_0}\Big)\Big] - \frac{\partial}{\partial s}\Big[R\frac{\partial R}{\partial u}\Big(p_\perp + \frac{B^2}{2\mu_0}\Big)\Big], \end{aligned} \tag{6}$$

where B^u and B^v are the poloidal and toroidal components of the magnetic field in the contravariant representation. The effective plasma current density field is defined as $\mathbf{K} = \nabla\times(\sigma\mathbf{B})$, where $\sigma > 0$ is the firehose stability parameter that characterises plasmas with anisotropic pressure [2]. The vanishing of F_λ corresponds to the condition that $\mathbf{K}\cdot\nabla s = 0$, which implies that the effective current density lines lie on flux surfaces. To diagnose the quality and accuracy of a 3D equilibrium state computed through the simultaneous minimisations of F_R, F_Z and F_λ, it is useful to evaluate the flux surface average of the radial MHD force balance relation given by

$$\mathbf{F} = -\frac{\partial p_\parallel}{\partial s}\bigg|_B \nabla s + \mathbf{K}\times\mathbf{B}. \tag{7}$$

The vanishing of this equation constitutes a form of the 3D Grad-Schlüter-Shafranov equation.

This formulation of the 3D anisotropic pressure MHD equilibrium problem lends itself to an easy adaptation of the techniques that resulted in the development of the preconditioned VMEC code for scalar pressure equilibria [3]. The internal MHD forces and the preconditioning algorithm that is designed to improve the convergence properties of the steepest descent energy minimisation method utilised in VMEC have been appropriately modified to treat the condition $p_\parallel \neq p_\perp$. A more detailed description of the derivation will appear elsewhere [4].

As an application, we consider a fixed boundary calculation in an ATF torsatron configuration [5]. To model an energetic trapped particle layer induced by radio frequency heating or neutral beam injection, we choose the factor $p(s,B)$ as

$$p(s,B) = p_h(s)\Big[\frac{B_{min}(s)}{B}\Big]^8, \tag{8}$$

with $p_h(s) = p_c s^3(1-s)^2$. The hot particle pressure thus vanishes both at the origin

and at the edge. The radial variable s is proportional to the volume enclosed. The plasma mass function required to compute the thermal component is chosen as $M(s) = M(0)(1-s)^2$ and the effective toroidal plasma current is prescribed to vanish within each flux surface. We consider two cases in which the peak β value due to the energetic species remains fixed at 4.83%. The perpendicular (parallel) pressure component contributes 2/3 (1/3) to the β values we quote here. Choosing $M(0) = 0.4$ and $p_c = 120$, we obtain an equilibrium in which the total $\beta = 0.55\%$, the thermal $\beta = 0.16\%$ and the perpendicular hot particle $\beta = 0.55\%$. Choosing $M(0) = 3.67$ and $p_c = 12$, we obtain an equilibrium in which the total $\beta = 1.79\%$, the thermal $\beta = 1.52\%$ and the perpendicular hot particle $\beta = 0.38\%$. The rotational transform profiles for these cases are shown in Fig. 1 and the differential volume $dV/d\Phi$ profiles are shown in Fig. 2. In the low β case, the hot particle pressure induces a weak magnetic well region in the middle third of the plasma volume. At moderate β, the thermal pressure gradient digs a magnetic well in the centre of the plasma.

Acknowledgements

This work was sponsored in part by the Ecole Polytechnique Fédérale de Lausanne, by the Fonds National Suisse pour la Recherche Scientifique, by Euratom and by the Office of Fusion Energy, United States Department of Energy, under Contract No. DE-AC05-84OR21400 with Martin Marietta Energy Systems, Inc.

•ORNL, Oak Ridge, Tennessee, USA; †IMHEF/EPFL, Lausanne, Switzerland; ‡GASS/CSCS, Manno, Switzerland.

References

[1] S. P. Hirshman and J. C. Whitson, *Phys. Fluids* **26** (1983) 3553.

[2] H. Grad, in *Magneto – Fluid and Plasma Dynamics*, *Symposia in Applied Mathematics* (American Mathematical Society) **18** (1967) 162.

[3] S. P. Hirshman and O. Betancourt, *J. Comput. Phys.* **96** (1991) 99.

[4] W. A. Cooper, S. P. Hirshman, S. Merazzi and R. Gruber, *Comput. Phys. Commun.* (to be published).

[5] M. Murakami, B. A. Carreras, L. R. Baylor, G. L. Bell, T. S. Bigelow, A. C. England, J. C. Glowienka, H. C. Howe, T. C. Jernigan, D. K. Lee, V. E. Lynch, C. H. Ma, D. A. Rasmussen, J. S. Tolliver, M. R. Wade, J. B. Wilgen and W. R. Wing, *Phys. Rev. Lett.* **66** (1991) 707.

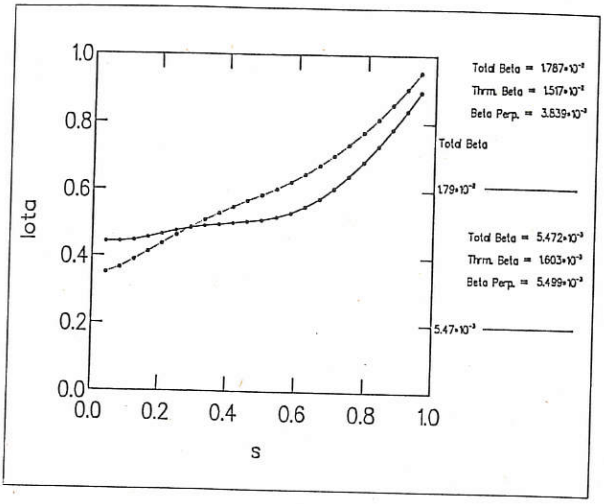

Figure 1: The rotational transform profile in an ATF configuration for cases with total $\beta = 1.79\%$ and total $\beta = 0.55\%$ with fixed peak hot $\beta = 4.83\%$.

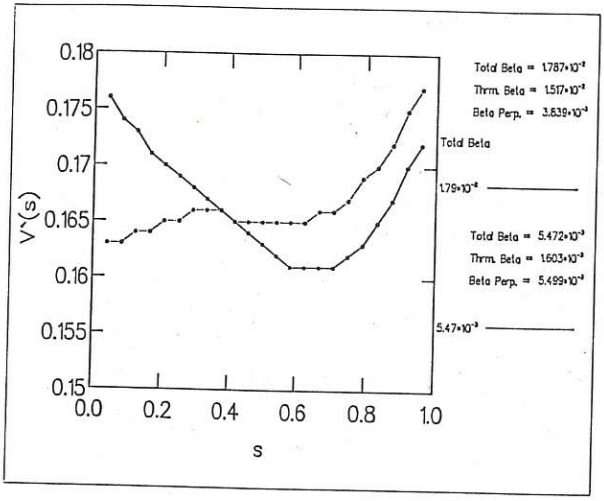

Figure 2: The differential volume profile in an ATF configuration for cases with total $\beta = 1.79\%$ and total $\beta = 0.55\%$ with fixed peak hot $\beta = 4.83\%$.

Topic 3:

Alternative Magnetic Confinement Schemes

CONFINEMENT STUDIES OF A HIGH CURRENT DENSITY RFP IN THE EXTRAP T1 UPGRADE DEVICE

J. R. Drake, J. H. Brzozowski, P. Brunsell, G. Hellblom, P. Karlsson,
S. Mazur, P. Nordlund,A. Welander and K.-D. Zastrow
Alfvén Laboratory, Royal Institute of Technology
S 100 44 Stockholm Sweden

Confinement studies have been carried out on the Extrap T1 device operated in the reversed field pinch (RFP) mode. Extrap T1 is a small device with a major radius of R = 0.5 m and a high aspect ratio, R/a = 8.9. For these experiments, the device has been operated with a resistive shell with measured, toroidally-averaged flux penetration times of $\tau_{sv} = 500$ μs (vertical) and $\tau_{sR} = 300$ μs (radial). The pulse lengths are about 600 μs, which is slightly longer than the shell penetration time.

The purpose of these experiments is to study energy confinement in a high aspect-ratio, high current-density RFP device with a resistive shell. The device can be operated with high current densities which exceed 20 MAm^{-2} on axis. For these discharges, the average electron density is relatively high, $\langle n \rangle \approx 1 \times 10^{20}$ m^{-3}. Therefore, although the average current density $\langle j \rangle$ exceeds 5 MAm^{-2}, the important parameter $\langle j \rangle / \langle n \rangle \approx I/N$ is maintained less than 1×10^{-13} Am, where N is the line density.

The plasma diagnostics for the device include a single chord CO_2 laser interferometer ($\langle n \rangle$), single point Thomson scattering (T_e, n_0), VUV and visible spectroscopy (T_e, Z_{eff}) surface barrier diodes for soft X-ray measurements (T_e), bolometry (P_{rad}), surface probes (Γ_p, T_i) and comprehensive magnetic diagnostics for both equilibrium and magnetic fluctuation studies.

The equilibrium vertical magnetic field for these discharges, with pulse lengths longer than the shell time, is controlled by adjusting the current distribution in the inboard and outboard primary windings, using passive elements in the primary circuit. The equilibrium position can be controlled to within a few millimetres.

Plasma discharge pulse data are presented in Fig. 1. The toroidal plasma current is initiated at time zero. The current rises and reversal occurs at about 75 μs. Burn-through of impurities occurs at around 100 to 150 μs and the current reaches 50 kA at 150μs. There is a corresponding decrease in the calculated resistivity and the ohmic power input after burn-through. During the initial stage of the discharge, fluctuations are evident on $\langle B_\phi \rangle$ and $B_\phi(a)$. This type of activity is generally seen during the start of the discharge.

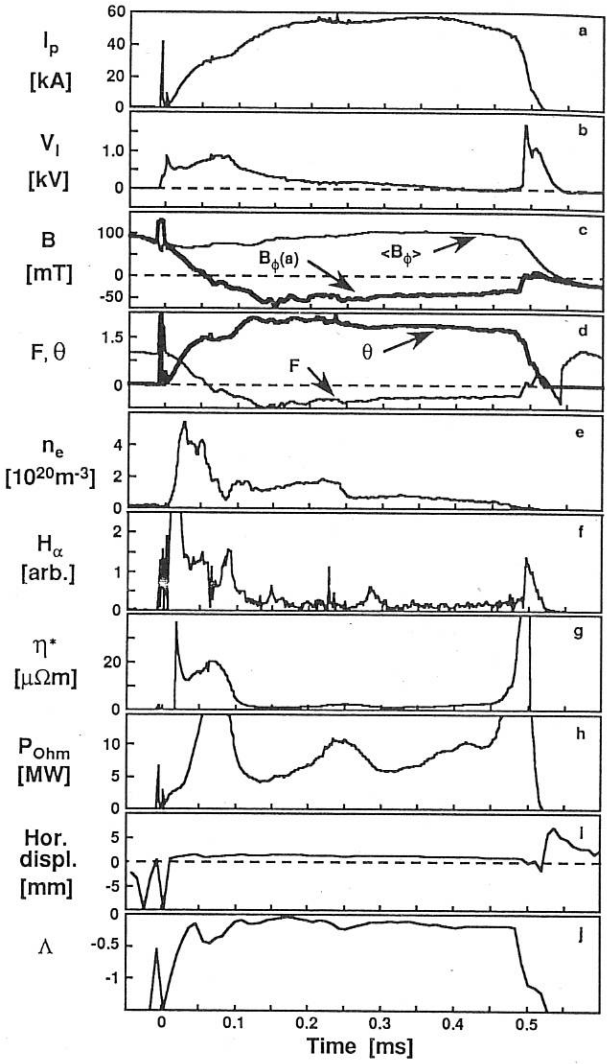

Fig. 1. Plasma discharge pulse data. a) Plasma current. b) Loop voltage. c) Average toroidal field and toroidal field at the liner. d) F and θ. e) Line averaged density from interferometer. f) Hydrogen Balmer alpha intensity. g) Calculated resistivity. h) Calculated ohmic power input. i) Horizontal Shafranov (flux surface) displacement at liner. j) Shafranov lambda.

In this discharge, about midway during the pulse, the character of the discharge changes. There is an is an increase in the loop voltage and a corresponding increase in the calculated resistivity and ohmic power input. There is also a decrease in the density at this time. Furthermore, there is an increase in the Hα intensity indicating that the the particle confinement is temporarily degraded. However this event does not lead to a termination of the discharge. The discharge recovers and the plasma resistivity decreases again. Also, the fluctuation activity seen on the pinch and reversal parameters decreases. The values of these parameters decrease slowly during the second half of the pulse. Typical values of the parameters are $F \approx -0.4$ and $\theta \approx 1.9$.

The resistivity is calculated from the measured loop voltage. This calculation requires a knowledge of the toroidal and poloidal current profiles to estimate the inductive component of the loop voltage and to account for the helicity factor in the resistive component of the loop voltage. Internal magnetic probe studies have been carried out and are described in a separate paper presented at this conference [1]. The current profile information derived from the internal magnetic probe data provide the basis for the models used to calculate the resistivity.

The electron temperature has been measured using Thomson scattering, soft X-ray intensity ratios with different filters and vacuum ultraviolet (VUV) spectroscopy and the spectroscopic Z_{eff} has been measured using calibrated VUV spectroscopy. The spectroscopy measurements are described in a separate paper presented at this conference [2]. A typical value of $Z_{eff} \approx 3$ can be used for the later half of the discharge. Assuming Spitzer resistivity and $Z_{eff} \approx 3$, the calculated conductivity temperature is 85 eV which is a lower limit on the actual temperature. The electron temperature measurements give a value $T_e \approx 120$ eV during the second half of this type of discharge. The discrepancy between the observed conductivity and the Spitzer conductivity, assuming the same current profiles and $T_e = 120$ eV, corresponds to an anomalous loop voltage given by,

$$V_a / V_l = (1 - \eta\,(\text{Spitzer})/\eta(\text{observed})).$$

For the parameters for these discharges, this ratio is about $V_a / V_l = 0.40$. The implication is that of the total power input, about 60% enters the Spitzer electron heating channel and 40% is anomalous power input. At least a part of the anomalous power leads to ion heating. Ion energies of 100 eV have been measured at the plasma boundary using surface probes [3].

The energy confinement for this discharge has been estimated using the temperature data and the line-of-sight integrated interferometer data, assuming a flat temperature profile and a parabolic density profile. The relevant parameters describing the confinement are presented in Table 1.

The T1 device has a small minor radius and a large aspect ratio and therefore it is of interest to compare the energy confinement in this device with other, larger RFP experiments. An expression for the energy confinement time, assuming ohmic heating with $\eta^* \propto f(\theta) Z_{eff} T_e^{-3/2}$, where f includes profile factors and possible anomalous heating factors, is given by [4,5],

Table 1. Energy confinement data.

$\langle n \rangle$	7×10^{19} m^{-3}
T_e	120 eV
β_θ	0.16
I/N	7×10^{-14} Am
I_p	56 kA
V_ϕ	120 V
Z_{eff}	3
τ_E	17 μs
τ_E/a^2	0.005 sm^{-2}

$$\tau_E = 7 \times 10^3 \, [T_e/(T_e+T_i)]^{3/2} \beta_\theta^{5/2} \, a^2 \, I^3 / [f(\theta) Z_{eff} N^{3/2}]$$

An aspect of RFP devices is that there is little variation in β_θ for different devices and for different currents [5]. The observed confinement parameters presented in Table 1 are in fair agreement with other RFP devices for a scaling law $\tau_E \propto a^2 \, I^3 / N^{3/2}$ where β_θ is about 0.15. These devices include a substantial range of aspect ratios and discharge currents.

This work is supported by Euratom through a contract of association between Sweden and Euratom.

References

[1] P. Nordlund et al, paper presented at this conference.
[2] K-D. Zastrow et al, paper presented at this conference.
[3] H. Bergsåker et al, paper presented at this conference
[4] S. Ortolani and G Rostagni, Nuc. Instr. and Meth. 207 (1983) 35.
[5] H.A.B. Bodin, R.A. Krakowski and S. Ortolani, Fus. Technology 10 (1986) 307.

Reversed Field Pinch Equilibria and Profile Dynamics in a High Aspect Ratio Geometry

P. Nordlund, S. Mazur and J.R. Drake

Fusion Plasma Physics, Alfvén Laboratory, Royal Institute of Technology, 100 44 Stockholm, Sweden

Introduction

The Reversed Field Pinch (RFP) magnetic field configuration is believed to result from a dynamic balance between heating and diffusion, on the one hand, and magnetic relaxation on the other [1-2]. The former tends to peak the current density distribution and shrink the current channel, while the latter acts to restore a broader more stable current density profile. Through the relaxation process poloidal flux, injected by the ohmic heating circuit, is dynamically converted into toroidal flux and the RFP configuration is maintained.

Experimentally RFPs achieve their best performance in the low pinch parameter regime ($\Theta = B_\theta(a)/\langle B_\phi \rangle \leq 1.6$). At high Θ most RFP experiments report enhanced fluctuation levels and increased plasma resistance. Often large coherent oscillations are seen on external signals [3-5]. These oscillations have been found to result from macroscopic redistributions of the current in the plasma [6-7]. In the low aspect ratio MST reversed field this behavior is present also at low Θ [8].

In this paper high current density RFP equilibria for $\Theta \approx 1.8$ and $\Theta \approx 2.2$ in a very high aspect ratio ($R/a = 8.8$) device with a distant resistive shell are presented. The time evolution of the profiles, in these regimes, is compared and the behaviour prior to termination is discussed. An estimate of the pressure profile is also presented.

Experimental

The magnetic field profiles were measured using an 8×3 coil insertable magnetic probe, allowing simultaneous measurements of B_ϕ, B_θ and B_r at eight equally spaced positions over the radius. The probe was inserted into sustained, high current density RFP plasmas, typically 13-17 MA/m^2 on axis, in the Extrap T1-Upgrade machine. The device has a distant resistive shell and the vacuum region is 15% of the minor radius. The global performance of RFP plasmas in T1-U are presented at this conference [9]. With the probe inserted there was a somewhat shorter pulse duration and a significant increase in the plasma resistance. However, the behaviour of edge field diagnostics (F&Θ) were similar to those of unperturbed discharges and the pulse lengths were slightly longer than the shell penetration time.

Polynomials of typically tenth order are fitted to the probe data, using least square fits. In estimating the mean field distributions, additional edge field diagnostics in the interspace between the liner and the shell are used to improve the edge fit. The resulting field profiles are shift corrected, including a first order toroidal correction, and expressed in terms of a cylindrical coordinate ρ originating at the magnetic axis. The current densities are then analytically differentiated from the shift corrected polynomials. By means of careful calibration and alignment the estimated error associated with measurement of the magnetic field could be reduced to $\leq 4\%$. The error bars drawn in figs. 2, 5 correspond to the standard deviation from the best estimates, calculated from the propagation of $\pm 4\%$ systematic perturbations of the calibration matrix.

Time Averaged Field Profiles

In fig.1 mean magnetic field profiles for $\Theta = 1.77$ (fairly standard operation in Extrap T1-U) and for $\Theta = 2.22$ (high Θ operation) are shown. The raw data are taken for several shots and averaged over 60 μs, which is longer than the typical relaxation/diffusion time period in these perturbed discharges. This means that they represent the mean field configurations about which the plasma is maintained through the driven diffusion/relaxation process. At higher Θ, a more narrow B_ϕ-profile with a deeper reversal is found.

The difference is more evident when examining the $\mu = \mu_0(\mathbf{J}\cdot\mathbf{B})/B^2$ and $q = rB_\phi/RB_\theta$ profiles shown in fig. 2. Note that a flat and broad mean μ–distribution is obtained for relatively high Θ ($\Theta = 1.77$). Forcing the configuration to very high Θ results in a peaking of the μ–profile. However, indications are found that μ starts to saturate in the regime of $\mu(0)a \approx 3.5$. The result is that at $\Theta = 2.22$ the mean μ–distribution becomes more narrow and peaked but very flat or slightly hollow near the axis. As previously discussed [6-7], this may be interpreted as indications for the presence of a lower limit for the on axis safety factor $q(0) = 2/R\mu(0)$. In our experiment, we find that the plasma tends to keep q(0) above 0.065, corresponding to $q(0)\,R/a \approx 0.57$. Note that the reversal surface moves inward at higher Θ.

Profile Dynamics

We now focus on the time evolution of the profiles in the $\Theta \approx 1.8$ and $\Theta \approx 2.2$ regimes. In both cases it is possible to resolve a trend of peaking and narrowing followed by a flattening and broadening of the μ–distribution. In other words the current channel narrows as the parallel current density ($J_\parallel$) in the central region increases followed by a suppression of $J_\parallel$ on axis and an increase in $J_\parallel$ in the edge region. On the average the plasma remains at the mean distribution described above. In the $\Theta \approx 1.8$ case, no dominant frequency in this current redistribution is observed and the behavior is quite irregular. Here, no clear correlation between the fluctuations in q(0) and q(a) is found. In the $\Theta \approx 2.2$ regime (fig.3) a higher fluctuation level is observed. The fluctuations are more coherent and cyclic oscillations with a time period typically ranging from 10 to 30 μs are seen. In this case the amplitude of the fluctuations in q and μ is relatively larger in the edge region. Also, a clear negative correlation between oscillations in q(0) and q(a) is seen.

A common behaviour towards the end of these perturbed discharges is that the toroidal plasma current decays faster than the toroidal flux (Θ decreases). During this time in the discharge there is a rapid increase in the plasma resistance and an enhanced fluctuation level. Here we find that the toroidal current density is strongly suppressed in the central region while there is a relative increase in the poloidal current density in the edge region resulting in a hollow μ–profile (fig.4). This behaviour is often followed by loss of field reversal and a disruptive termination of the discharge.

Estimation of the Pressure Profile

By assuming zero pressure at the wall and integrating the equilibrium pressure balance equation $(\boldsymbol{J}\times\boldsymbol{B} = \nabla p)_{cyl.}$ an estimate of the pressure profile may be obtained. As evident from this equation the pressure is directly related to the difference between the $J_\phi B_\theta$ and the $J_\theta B_\phi$ terms, which is very small in low beta plasmas. Thus, pressure estimates based on insertable magnetic probe measurements are inherently sensitive to experimental errors in the field profiles. However with the experimental technique adopted, we were able to estimate the pressure profile with useful accuracy in the beginning of the sustainment phase where the best reproducibility is achieved. The result, calculated from the $\Theta = 1.77$ mean distribution above, normalized to the on axis magnetic pressure, is shown in fig.5. We find

that the pressure profile, which appears close to parabolic, may be characterized by values of $\beta_0 = 0.09 \pm 0.03$ $\beta_\theta = 0.19 \pm 0.07$ and $<\beta> = 0.09 \pm 0.03$. Accordingly, the energy confinement time is estimated to be $\tau_E = 5\mu s \pm 2\mu s$ with the probe inserted.

As a confirmation of these results we note that at this time in the discharge, interferometer measurements show that the chord averaged electron density is about $10^{20}m^{-3}$. The electron temperature obtained from line ratios of O^{+5} in the VUV region [10] is about 55 eV. Assuming a parabolic density profile for which $n_e(0) = 3/2<n_e>$ and taking $T_i = T_e$, an independent rough estimate of the on axis beta-value can be calculated. The resulting estimate of the central beta becomes $\beta_0 = 0.082$ for $Z_{eff} = 2.0$, which is in good agreement with the probe results.

Discussion and Conclusions

High current density RFP plasmas have been studied using an insertable magnetic probe in the high aspect ratio (R/a=8.8) Extrap T1-U machine. Mean field distributions for $\Theta \approx 1.8$ and $\Theta \approx 2.2$ are presented. It is found that flat and broad μ-profiles can be achieved at relatively high Θ ($\Theta \approx 1.8$). At very high theta ($\Theta \approx 2.2$) the mean μ–distribution becomes more narrow and peaked, but slightly hollow near the axis. Indications are found that $\mu(0)$ starts to saturate at $\mu(0)a \approx 3.5$, corresponding to $q(0)R/a = 2/\mu(0)a \approx 0.57$.

Turning to the time evolution of the profiles, a general trend of peaking followed by flattening and broadening of the parallel current density distribution is found. The fluctuations about the mean profiles were larger at higher Θ, particularly in the edge region. At $\Theta \approx 2.2$, a clear negative correlation between oscillations in q(0) and q(a) were seen which was not evident for the $\Theta \approx 1.8$ case.

Towards the end of these perturbed discharges, which generally last slightly longer than the shell penetration time, the plasma tends to develop a hollow μ-profile. During this time enhanced fluctuations and increased V_{loop}/I_p are observed. This behaviour is often followed by loss of field reversal and a disruptive termination of the discharge.

Estimates of the pressure profile consistent with independent measurements of the central pressure have been obtained. Values of $\beta_\theta = 0.19 \pm 0.07$ and $<\beta> = 0.09 \pm 0.03$ are found leading to an estimation of the energy confinement time of $\tau_E = 5\mu s \pm 2\mu s$. With the probe retracted τ_E is about 10 μs. The difference is due to an increase in the power input needed to sustain the toroidal plasma current when the probe is inserted.

This work has been supported by the European Communities under an association contract between Euratom and Sweden.

References:

[1] Ortolani S., Physics of Alternative Confinement Schemes,Varenna(1990) 87.
[2] Schnack D. D., Physics of Alternative Confinement Schemes,Varenna(1990) 631.
[3] Antoni V., Ortolani S., Phys. Fluids **30** (1987) 1489.
[4] Watt R. G., Nebel R.A., Phys. Fluids **26** (1983) 1168.
[5] Tsui H. I. W., Cunnane J., Plasma Physics and Controlled Fusion **30** (1988) 865.
[6] Antoni V., Martin P., Ortolani S., Nuclear Fusion **29** (1989) 1759.
[7] Ueda Y. et al., Nuclear Fusion **27** (1987) 1453.
[8] Prager S. C. et al., Phys. Fluids B**2** (1990) 1367.
[9] Drake J. R. et al, This conference.
[10] Zastrow K-D. et al., This conference.

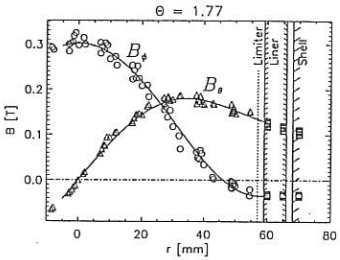

Fig. 1a. Mean magnetic field profiles at Θ = 1.77

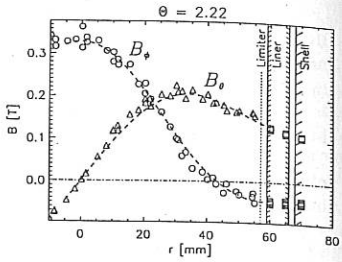

Fig. 1b. Mean magnetic field profiles at Θ = 2.22

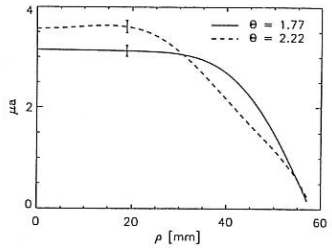

Fig. 2a. Mean μ-profiles

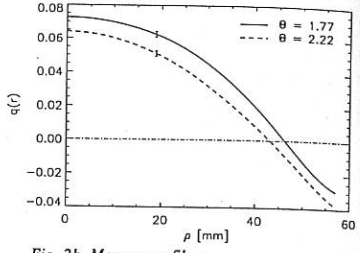

Fig. 2b. Mean q-profiles

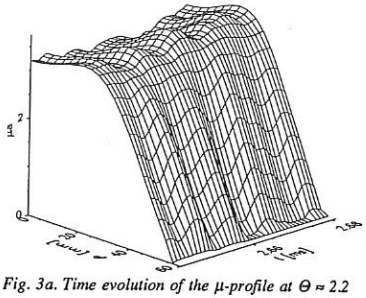

Fig. 3a. Time evolution of the μ-profile at Θ ≈ 2.2

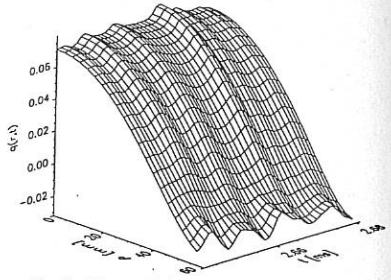

Fig. 3b. Time evolution of the q-profile at Θ ≈ 2.2

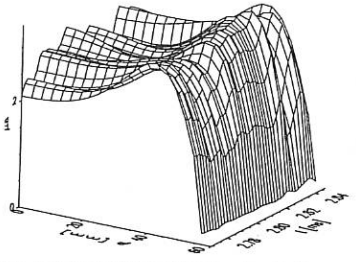

Fig. 4. Time evolution of μ before termination

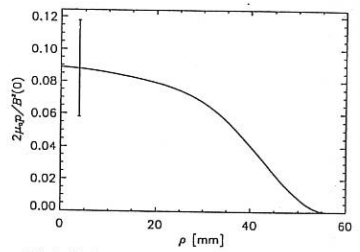

Fig.5. Estimate of the pressure profile (Θ = 1.77)

STABILITY OF KINK MODES IN A NONCIRCULAR Z PINCH SURROUNDED BY A RESISTIVE AND A CONDUCTING WALL

Z. X. Jiang and C. Wahlberg
Department of Technology, Uppsala University, Box 534, S-751 21 Uppsala, Sweden

1. INTRODUCTION. A perfectly conducting wall is frequently used to improve the MHD stability of plasma pinches. In particular, the presence of a conducting wall is crucial for the RFP configuration. Without a wall an RFP is very unstable to current-driven and pressure-driven external modes. However, experiments on OHTE[1] have demonstrated the possiblity of operating an RFP with a resistive shell, and in recent times thin-shell experiments have aslo been performed on other devices. In the present work, the dispersion relation of the free-boundary m = 1 kink mode is evaluated for a noncircular surface current pinch surrounded by both a resistive shell and a conducting wall. The noncircularity is due to the presence of a an external octupole field, simulating the proposed poloidal divertor RFP in the Extrap device[2]. The effects on the growth rate of the kink mode due to variation of the proximity of the walls, the noncircularity of the plasma cross section, and the resistivity of the shell are investigated.

2. MODEL. We use an equilibrium surface current model in which the plasma surface at $r = r_s(\varphi)$ is separated from a thin resistive shell at $r = r_1$ by a vacuum regin I. Moreover, the shell is separated by a vacuum region II that extends to a radius $r = r_2$, where a perfectly conducting wall is situated. Denoting the mean radius of the pinch by $R_P = < r_s(\varphi) >$, the total axial current by I_P and the (uniform) mass density by ρ_m, the expressions appearing in the following are written in dimensionless form, with all lengths given in units of R_P, magnetic fields given in units of $B_P = \mu_0 I_P/2\pi R_P$, and the time scale given in units of the Alfvén time $\tau_A = 2\pi R_P^2/I_P(\mu_0/\rho_m)^{1/2}$. In the case of incompressible perturbations and a uniform axial magnetic field inside the pinch, it can be shown[3] that i) the induced current density in the plasma vanishes ($\mathbf{J}_1 \equiv 0$), and ii) the plasma motion is curl-free. In such a case the dynamics of the pinch can be described in terms of the following five quantities: A function $\eta(\varphi,z,t)$ denoting the perturbed position of the plasma surface $[r_s = 1 + \eta(\varphi,z,t)]$, a potential function $\phi(r,\varphi,z,t)$ describing the plasma flow ($\mathbf{v} = \nabla\phi$), and the three potential functions $\Omega_i(r,\varphi,z,t)$, $\Omega_{eI}(r,\varphi,z,t)$ and $\Omega_{eII}(r,\varphi,z,t)$ describing the unknown parts of the magnetic fields inside the plasma, and in the vacuum regions I and II, respectively. The full magnetic fields inside the pinch, and in the vacuum regions, are then given by, respectively

$$\mathbf{B}_{int} = B_i\,\mathbf{e}_z - \nabla\Omega_i, \tag{1}$$

$$\mathbf{B}_{ext\ I,II} = B_e\,\mathbf{e}_z - \mathbf{e}_z \times \nabla\Psi + r^{-1}\,\mathbf{e}_z - \nabla\Omega_{eI,II}. \tag{2a,b}$$

The axial fields B_i and B_e are allowed to be different in order to be able to simulate the paramagnetism of the RFP. The octupole field is described by $\Psi = \lambda r^4\cos(4\varphi)$, where λ denotes the strength of the octupole field (compared with B_P) and is used as an expansion parameter of the problem. The solution of the problem then amounts to solving $\nabla^2\phi = 0$, $\nabla^2\Omega_i = 0$ and $\nabla^2\Omega_{eI,II} = 0$ in the plasma region and in the two vacuum regions, respectively, and then applying the appropriate boundary conditions at the surfaces $r = r_s$, $r = r_1$ and $r = r_2$. These boundary conditions are formulated in Ref.3. Furthermore, across the resistive shell we use the thin-shell approximate boundary conditions formulated in Ref.4.

3. RESULTS. Considering the m = 1 kink mode perturbation $\eta(\varphi,z,t) = (8/3)\lambda\cos(4\varphi) + \eta_1 \times \exp[pt + i(\varphi - kz)] + \eta_{SB}$, where the first term represents the equilibrium noncircularity of the plasma, and the term η_{SB} denotes the m = 3 and m = 5 "sidebands" generated by the first order m = 1, m = 4 interaction[3], the dispersion relation, to leading order in λ, is obtained in the form

$$p^2 + D_1(k) + \lambda^2\left[C_0 - \frac{C_1C_3}{p^2 + D_5(k)} - \frac{C_2C_4}{p^2 + D_3(-k)}\right] = 0, \tag{3}$$

where $D_m(k) = (kB_i)^2 - \alpha_m^{-1}[1 + \beta_m(m - kB_e)^2]$ {$\alpha_m = I_m(k)/[kI'_m(k)]$ and I_m (and K_m below) are modified Bessel functions} are the dispersion functions of the circular system [$\omega^2 = D_m(k)$], and the coefficients C_0 - C_4 are complicated functions of k, B_i, B_e, r_1,r_2, p and $s = \tau_w/\tau_A$, where τ_w is the time constant of the shell. The quantities $D_m(k)$ and C_0 - C_4 coincide with the corresponding quantities in Ref.3 (which deals with the same mode without wall effects) except that the quantities β_m {$= K_m(k)/[kK'_m(k)]$ in Ref.3} are now given by $\beta_m = [v_mW_m(k,kr_2) + psU_m(kr_1,kr_2)W_m(k,kr_1)/r_1] / [kv_mU_m(k,kr_2) + kps\ U_m(k, kr_1)U_m(kr_1,kr_2)/r_1]$, where $v_m = (r_1^2k^2 + m^2)/(r_1^3k^2)$, $U_m(x,y) = I'_m(x)K'_m(y) - I'_m(y)K'_m(x)$ and $W_m(x,y) = I'_m(y)K_m(x) - K'_m(y)I_m(x)$. In the case $r_{1,2} \to \infty$, Eq.(3) agrees with the corresponding result in Ref.3, while for the circular case ($\lambda = 0$) the dispersion relation obtained by Gimblett[4] is recovered.

Fig.1 shows the destabilizing effect of the plasma noncircularity (solid curve; a circular pinch is marginal at k = 0) as well as the stabilizing effect of the conducting wall (dashed curve). $\lambda = 3/80$ in the figure, corresponding to 10% noncircularity of the plasma cross section. Furthermore, s = 0 so that no effect of the resistive shell at $r = r_1$ is present.

In Fig.2 the parameters are chosen such that the pinch is stable with a perfectly conducting wall instead of a resistive shell at $r = r_1$, and unstable if the wall is moved to the position $r = r_2$. For a finite value of the shell resistivity, energy is dissipated in the system and the problem is no longer self-adjoint, so that p is complex. The figure illustrates how the relevant (m = 1) roots to Eq.(3) move in the complex p-plane as the shell resistivity is varied. It is seen that the transition from the two stable modes with purely imaginary p in the case $s = \infty$ to the two modes with real p in the case s = 0 takes place by interplay with a third mode (curve c). This is the interesting mode which causes instability. The curves start ($s = \infty$) from the points where the plasma is stable, and by decreasing the time constant of the shell the stable modes become slightly damped, and, in addition, the purely growing mode appears. Furthermore, the two damped, oscillating modes coalesce and transform into two purely decaying modes at a critical $s = s_c$, in the figure given by $s_c \approx 2.5$. When $s \rightarrow 0$, one of the purely decaying modes moves to minus infinity and the remaining modes transform to the two modes $p = \pm p_0$ of the unstable pinch in the absence of the shell.

Fig.3 illustrates how the growth rate of the purely growing mode in Fig.2 varies with the wave number k, and with the shell penetration time s. It is seen that the marginal wave numbers are not affected by s, whereas the growth rate is reduced by approximately 50 % as s is increased from s = 1 to s = 100.

Finally, Fig.4 shows how the growth rate of purely growing mode is reduced by increasing the internal field (B_i) and by moving both the shell and the conducting wall closer to the plasma. The difference between the curves **a** in Figs. 3 and 4 is that i) B_i is increased from 0.7 to 0.8, and ii) r_2 is reduced from 2.0 to 1.5. The reduction in the growth rate is about a factor four. Furthermore, with the other parameters remaining unchanged, the shell and the wall are moved from $r_1 = 1.3$, $r_2 = 1.5$ to $r_1 = 1.25$, $r_2 = 1.4$ from curve **a** to curve **c** in the figure, resulting in a reduction of the growth rate with an additional factor eight.

REFERENCES

1. R. R. Goforth et. al., Nucl. Fusion **26**, 515 (1986)

2. B. Lehnert, Fusion Technol. **16**, 7 (1989), and Comments Plasma Phys. Controlled Fusion **14**, 185 (1991)

3. C. Wahlberg, Phys. Fluids B **2**, 1601 (1990)

4. C. G. Gimblett, Nucl. Fusion **26**, 617 (1986)

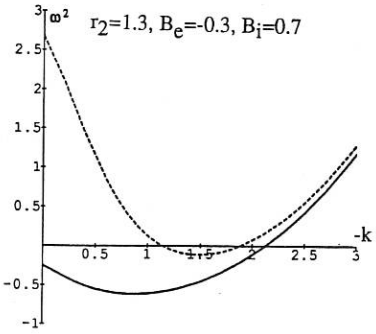

Fig.1. The dispersion relation for s=0, λ=3/80. The dashed line corresponds to r_2=1.3; the solid to r_2=∞.

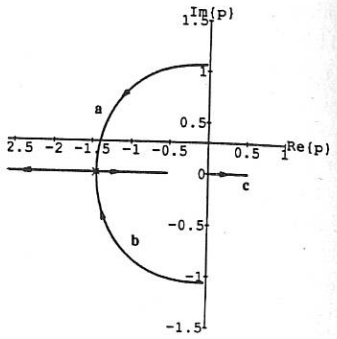

Fig.2. Complex p-plane corresponding to λ=3/80, B_e=-0.3, B_i=0.7, r_1=1.3, r_2=2 and k=0.5. The arrows indicate how the roots of p move as the resistivity is increased.

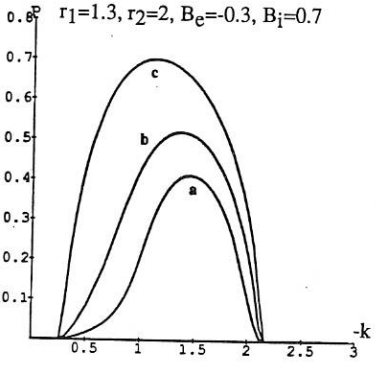

Fig.3. Growth rate versus k for different long time constant of a shell with λ=3/80. Curve (a) corresponds to s=100; curve (b) to s=20; curve (c) to s=1.

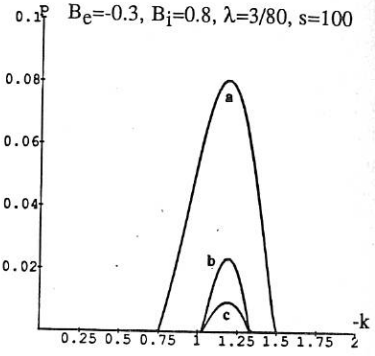

Fig.4. Growth rate versus k for different proximities of a shell and wall. Curve (a) corresponds to r_1=1.3, r_2=1.5; curve (b) to r_1=1.3, r_2=1.4; curve (c) to r_1=1.25, r_2=1.4.

STUDIES OF EDGE PLASMA AND IMPURITIES IN EXTRAP T1 USING SURFACE PROBES.

H. Bergsåker[1], *I. Gudowska*[1], *B.Emmoth*[1] *and E. Tennfors*[2]

1) Manne Siegbahn Institute of Physics, 104 05 Stockholm, Sweden.

2) Alfvén Laboratory, Royal Institute of Technology, S-100 44 Stockholm, Sweden.

Introduction. Dedicated plasma surface interactions studies is a necessary step towards finding means of reducing impurities and improving the recycling properties of the wall in fusion plasma devices. This is a report on surface probe measurements in the T1 device in a series of reversed field pinch disharges with deuterium plasma. The objectives have been to study the flux and energy of particles hitting the wall, in order to identify which processes are responsible for impurity production and for the recycling behaviour. For the T1 device, see also [1-3].

Experimental. The dimensions of T1 are R/a = 0.5 m/0.055 m. The wall consists of 316L stainless steel bellows. The device is operated at room temperature. The RFP discharges had $\sim$ 0.5 ms duration, 40 kA plasma current, density n_e = 1-2 $\cdot$ 10^{14} cm^{-3} and central electron temperature kT_e = 50-100 eV during current flat top. The magnetic field at the wall was mainly poloidal, $B_\theta \approx 0.17$ T.

Cylindrical graphite probes with 9 mm diameter have been exposed as shown in figure 1. The exposure time has been from one to 220 discharges. The front surface of the probes has been parallel to the wall, and probes have been exposed with the front surface at minor radii rangeing from 55 mm to 89 mm. Probes exposed at 55 mm are subjected to the same flux of particles as the wall, whereas retracted probes receive a more collimated flux, eventually only neutrals, since it is expected that the gyro motion of ions prevents penetration into the portholes. After exposure the probes were taken to a surface analysis facility, where retained deuterium and impurities were measured with ion beam analysis techniques.

Results. Figure 2 shows the areal density of deuterium and stainless steel components (Fe,Cr,Ni and Mo), collected on the front surface of the probes versus exposure time. The data are from probes at r = 55 and r = 79 mm. It can be seen that the trapping rate of deuterium on the probes at wall radius is constant up to about 20 shots exposure time. At higher fluence there is saturation. The composition of the steel deposits was in good agreement with the composition of SS316.

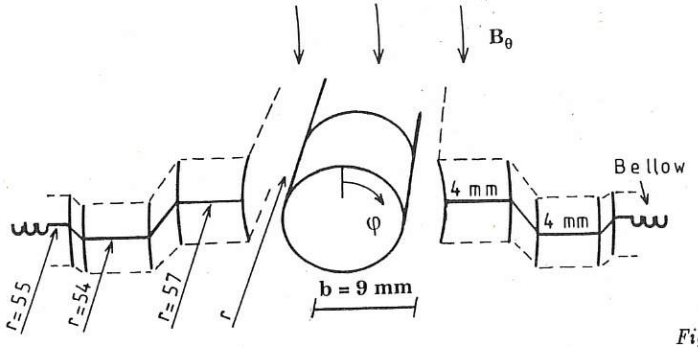

Figure 1.

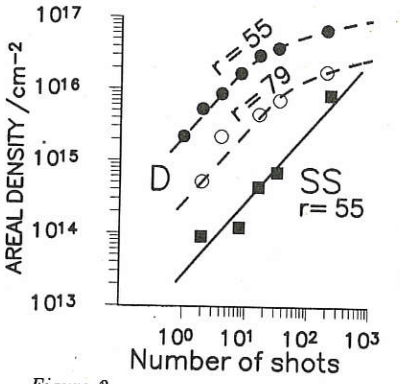

Figure 2.

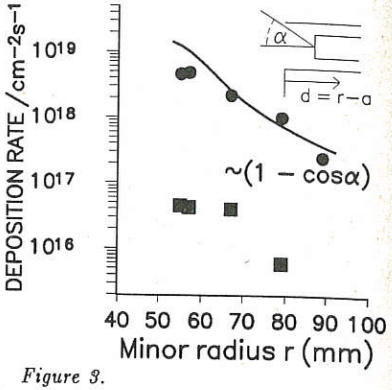

Figure 3.

The collection rate of metals was roughly constant and 1-2% of the deuterium trapping rate. In addition to the steel components, oxygen, silicon, chlorine and tungsten were detected on the probes. Figure 3 shows deuterium and metal deposition on the front surface of probes which were retracted into the port holes. Deuterium and impurities were also measured on the cylindrical side of the graphite probes which were exposed with the front surface at $r = 55$ mm. A maximum in the deposition was consistently observed on the right hand side, as seen from the plasma, where the deposition rate was similar to the front surface. An example of this is shown in figure 4.

Discussion. At wall radius, $7 \cdot 10^{16}$ D/cm^2 was retained in graphite after exposure to 220 discharges. For monoenergetic implantation this corresponds to an implantation energy in excess of 300 eV [4] . To relate the retention of deuterium in graphite probes to the incident flux and energy, we apply the phenomenological local saturation model [4,5]; the retained areal density of deuterium

$$\Phi_{ret} = \int_0^\infty c(x)dx \tag{1}$$

is then obtained from the depth profile $c(x)$:

$$c(x) = \max\left[n_s,\ (1-R)N\Phi_0 S(x)\right], \tag{2}$$

where N is the exposure time in number of discharges, Φ_0 is the incident fluence per discharge, and where the reflection probability R and the implantation range distribution $S(x)$ both depend on the angular and energy distribution of the incident particles. For graphite $n_s = 0.42 n_C$ at room temperature. The incident flux can be derived from Φ_{ret} at low fluence if the probability of reflection is known, and at high fluence $\Phi_{ret}(N)$ gives information on the energy distribution through the energy dependence of $S(x)$. We apply the procedure recommended by Wampler [5], approximating $S(x)$ as exponential for Maxwellian energy distribution and cosine distribution of angles of incidence. The best fits, indicated with dashed lines in figure 2, are obtained for $kT_i = 105 \pm 10$ eV and $\Phi_0 = 3.3 \cdot 10^{15}$ D/cm^2 incident per discharge at wall radius, and $kT_i \approx 30$ eV and $0.5 \cdot 10^{15}$ D/cm^2 per discharge at $r = 79$ mm.

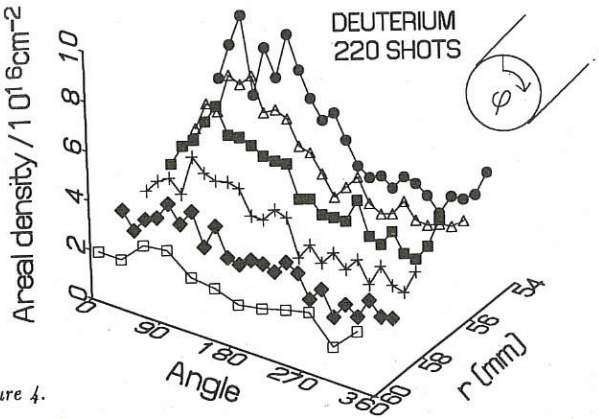

Figure 4.

If the electron temperature at the edge is high, the energy of ions hitting the wall may be dominated by acceleration in the electrostatic sheath. In the present case, in order to have a reasonable fit to saturation with near monoenergetic ions it is necessary to assume an implantation energy above 300 eV, consistent with $kT_e \sim 100$ eV at the plasma edge, which seems excessive.

Since the gyro radius of 100 eV D^+ at the plasma edge is 12 mm, ions with energy less than 100 eV can not penetrate further than $\sim$ 20 mm into the ports, and the deuterium which was collected beyond $r \approx 75$ mm should have been exclusively neutrals. The solid line in figure 3 shows the reduction of the transmission of isotropic neutrals through the port which is expected from the geometry.

The maximum in deuterium implantation and impurity deposition at the sides of the graphite probes (figure 4) can be explained either as a result of rapid ion drift in toroidal direction, or with a gyro radius effect. The deposition pattern can also be due to neutrals which originate in a plasma region with rapid toroidal drift.

If we first consider the case of ions or neutrals with Maxwellian velocity distribution drifting with velocity $v = w\sqrt{2kT/m}$ in toroidal direction, then the flux density to a cylinder surface oriented as in figure 1 can be written:

$$\Phi(\varphi) = n\sqrt{\frac{2kT}{m}} \frac{\int_0^\infty u e^{-(u-w\sin\varphi)^2} du}{\int_{-\infty}^\infty e^{-(u-w\sin\varphi)^2} du}$$

$$= n\sqrt{\frac{kT}{2\pi m}}\left[e^{-w^2\sin^2\phi} + \sqrt{\pi}\,\mathrm{erfc}(-w\sin\varphi)w\sin\varphi\right] \qquad (7)$$

How this relation compares with the distribution of deuterium from figure 4 at r=56 mm is shown in figure 5. There is a reasonable fit for w=0.2. If kT is in the range 10 to 100 eV, this means a drift velocity of $0.6 \cdot 10^4$ to $1.8 \cdot 10^4$ m/s. A toroidal drift can occur due to the density gradient in combination with ion gyro motion (diamagnetic drift) or to grad B and curvature. In either of these cases $w = 0.2$ for D^+ corresponds to $kT \approx 100$ eV. A rapid curvature drift could also explain why a lower ion temperature

is derived from the retracted probes, since the fastest particles would have the highest drift velocity, and consequently reduced transmission through the port.

The effect of ion gyro motion on the angular deposition on cylindrical probes has been assessed in more detail through Monte Carlo simulation of ion orbits. The dots in figure 5 represent the deposition pattern of ions with isotropic Maxwellian velocity distribution, $kT_i = 100$ eV and an axial density gradient with 10 mm e-folding length. There is qualitative agreement.

However, the asymmetric deposition could in principle also be due to an $E \times B$ drift of cold ions. For $kT = 10$ eV this would require a radial electric field of 12 V/cm in order to attain $w = 0.2$. It is expected that langmuir probe measurements in the plasma edge will resolve this ambiguity. The probes collect particles without time resolution, and the resulting energy distribution may be due to the time evolution rather than to an instantaneous distribution of energies.

Conclusions. Particle fluxes to the wall have been inferred from trapping on surface probes during RFP operation in the T1 device. A total flux density at the wall of $\sim 10^{19}$ D cm^{-2} s^{-1} can be inferred. From the retention versus fluence characteristic on graphite probes at wall position an ion energy distribution corresponding to $kT_i \approx 100$ eV is derived. The spatial distribution of deuterium and impurities collected on probe cylinders can be interpreted either as a toroidal $E \times B$ drift with velocity of the order 10^4 m/s, or as a Larmor radius effect for ions with $kT \approx 100$ eV. The deposition rate of stainless steel components on probes at the wall position is $\sim 1\%$ of the deuterium flux, which is compatible with uniform physical sputtering [6].

References.

[1] J.R. Drake et al. this conference.
[2] P. Nordlund, S. Mazur et al. this conference.
[3] K.-D. Zastrow et al. this conference.
[4] S.A. Cohen and G.M. McCracken, J.Nucl.Mater. 84(1979)157.
[5] W.R. Wampler, D.K. Brice and C.W. Magee, J.Nucl.Mater. 102(1981)304.
[6] J. Bohdansky, Nucl.Fus. Spec. Iss. 1984 p. 61.

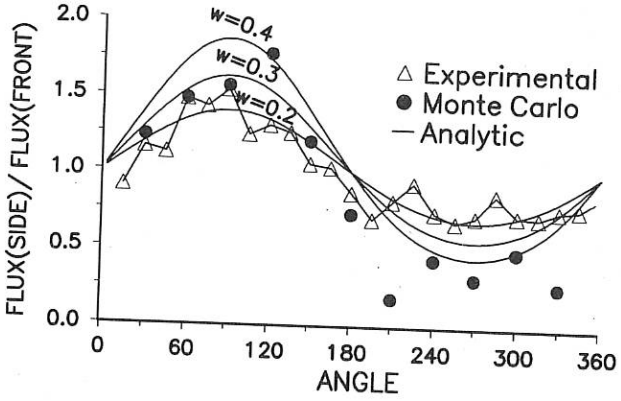

Figure 5.

Plasma spectroscopy at the Extrap-T1 RFP experiment

K.-D. Zastrow, P. Hörling, J.H. Brzozowski[♣] and E. Källne

Department of Physics I, [♣]The Alfvén Laboratory,

Royal Institute of Technology, S-10044 Stockholm

The reversed field pinch (RFP) experiments performed on the Extrap-T1 device[1] are the subject of several papers presented at this conference[2,3,4]. In this paper, we concentrate on the spectroscopic measurements in the vacuum ultraviolet (VUV) and visible wavelength region from a series of reproducible discharges in deuterium. From the spectra we derive electron temperature, carbon and oxygen concentration, Z_{eff} and particle confinement time.

1 VUV spectroscopy

Instrumental

Spectra in the wavelength range 100 - 1100 Å are recorded with a McPherson 251 grazing incidence spectrometer [5], equipped with a toroidal grating of 450 ℓ/mm and an open microchannel plate as detector. The spectral resolution is $\approx$ 3.3 Å over the whole wavelength range. The integration time of the spectra is 30 μsecs. The instrument has been absolutely calibrated using the branching-ratio technique. To this end we have performed discharges with up to 50 % helium added to the normal hydrogen filling gas. In addition, line ratios from naturally abundant impurity ions have been used to obtain the calibration.

Fig. 1 shows a typical spectrum from the RFP sustainment phase. The strongest lines stem from oxygen in ionisation stages O^{3+}- O^{5+}. Spectra are analysed by means of a least squares fit[6], with wavelengths for the observed ions as input. The time history of line intensities is studied from spectra taken at different times during discharges from a series with reproducible plasma parameters. (Deuterium filling gas, plasma current 50 kA, discharge duration 0.5 msec)

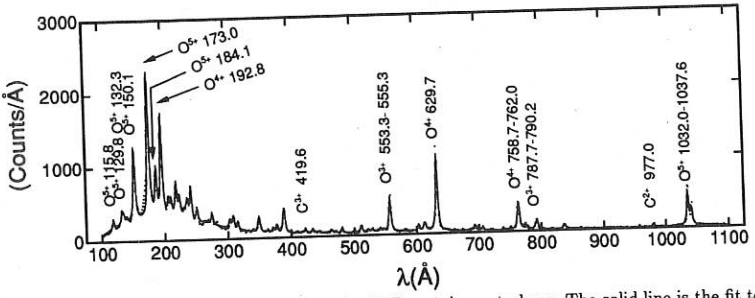

Figure 1: Typical VUV spectrum from the RFP sustainment phase. The solid line is the fit to the experimental values. Spectral lines of $O^{5+}$and those used in this paper are labelled.

Electron temperature, impurity concentrations and Z_{eff}

During the RFP sustainment phase we observe mainly line radiation from O^{5+}. From this ionisation stage we may infer the electron temperature by means of line ratio measurements[7]. During the build-up phase we use O^{4+}. This result is presented in figure 2. In the analysis we have considered, that line ratios in $O^{5+}$are both a function of the electron temperature and the electron density at the typical level for T_e (50 - 100 eV) and n_e (0.5 - 3 10^{14} cm^{-3}) in these discharges. The line ratios of O^{5+}line are density dependent, since the first excited state ($2p\ ^2P$) has an excitation energy of only 12 eV. Thus, the populations of higher excited states will be determined by excitation not only from the ground state but also from the first excited state.

The particle confinement time for these discharges is $\approx 20\mu$sec (see figure 3), which means that the particle diffusion coefficient should be of the order $D \approx a^2/\tau_P \approx 10^6$ cm^2/sec. The radial profiles of He-, Li- and Be-like carbon and oxygen ion densities should thus be rather broad, and the shell like structure of the emission is not expected to be pronounced. For this reason, we can measure electron temperatures far above the temperature of maximum fractional abundance from the lines emitted from O^{5+}. This also permits the measurement of line average impurity ion densities using a 0-dimensional model. The numerical line-of-sight integration in the model is simply replaced by the multiplication with the observed plasma column length. When the emission stems from a narrow region, the derived electron temperature from O^{5+}will be close to 30 eV [8].

The line average concentrations of the most abundant ionisation stages C^{2+}, C^{3+}, $O^{4+}$and $O^{5+}$are derived from absolute line intensity measurements based upon the electron temperature presented above and the electron density from interferometry. For C^{2+}we use the intensity of the line at 977.0 Å , for C^{3+}we use 419.6 Å , for O^{4+}both 629.7 Å and 758.7-762.0 Å are used, and the concentration of $O^{5+}$is based upon the observation of 1032.0-1037.6 Å . Typical oxygen concentrations are 3-6 %, whilst carbon concentrations are below 0.5 %. Thus, Z_{eff} is dominated by oxygen, and is typically in the range 2-3. In figure 2 we present the result for Z_{eff} together with the concentrations of $C^{3+}$and O^{5+}. The atomic data for the analysis have been collected by H.P. Summers, J. Lang and R.W.P. McWhirter[9].

It should be pointed out, that Z_{eff} calculated in this way represents a lower limit, since $C^{4+}$and $O^{6+}$are not observed, though certainly present given the electron temperature, and other impurities like nitrogen, chlorine and silicon are not included in the calculation.

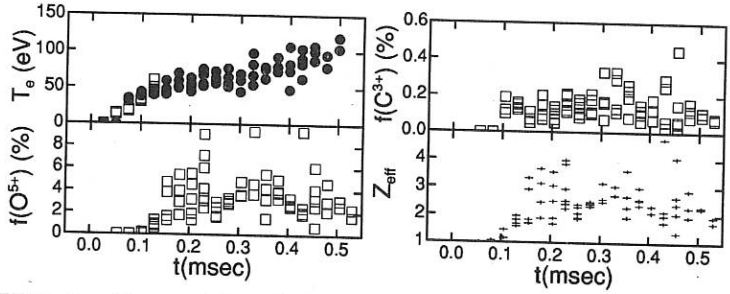

Figure 2: Time evolution of the electron temperature obtained from line ratio O^{5+}150.1/(1032.0-1037.6) (•) and from O^{4+}192.8/(758.7-762.0) (□), line average concentration of $O^{5+}$and $C^{3+}$and Z_{eff} calculated from the measured concentrations of C^{2+}, C^{3+}, $O^{4+}$and O^{5+}. The apparent decrease in Z_{eff} after 0.3 msec is probably due to the production of O^{6+}, which does not emit line radiation in the wavelength interval observed by the VUV spectrometer. Each point in the figures corresponds to a spectrum taken during 30 μsec in a series of reproducible discharges in deuterium (# 24081 - #24197)

2 Visible spectroscopy

Instrumental

Several instruments are used in the visible wavelength region. Time evolution studies on the μsec scale are performed with narrow band filters and small monochromators, equipped with photomultiplier tubes. For spectroscopy, a 1/2 m and a 1 m spectrometer, equipped with an optical multi channel analyser (OMA), are used to cover 400 Å and 100 Å respectively, with 1024 channels. Light is transported to these instruments by optical fibres. All instruments have been absolutely calibrated using a standard tungsten lamp. The 1/2 m spectrometer has been used for the branching ratio calibration of the VUV spectrometer.

Particle confinement time

Hydrogen influx and particle confinement time are derived from the intensity of Hα+Dα and Hβ+Dβ (see Fig. 3). The number of photons emitted per ionisation event depends on the electron density, and this dependence is considered. The atomic data for this analysis stem from the classical paper of Johnson and Hinnov[10]. In the model that relates the particle influx to the hydrogen line radiance, we assume electron density and temperature to be constant up to $r = 0.6a$, and then drop towards $r = a$. For the calculation of τ_P from the particle influx, we have assumed a fraction of 4 % O^{5+}, constant in time (see figure 2).

From the observation of Hβ and Dβ with the 1/2 m spectrometer, we find the fraction of hydrogen in these discharges to be $n(D)/(n(H)+n(D)) = 90\% \pm 5\%$. We note, that the results obtained from Hβ+Dβ during the RFP sustainment phase are in agreement with those obtained from Hα+Dα. During the build-up phase, however, the calculated flux is generally higher. A comparison of the particle influx with the particle flux to the wall measured by surface probes is presented in another paper at this conference[4].

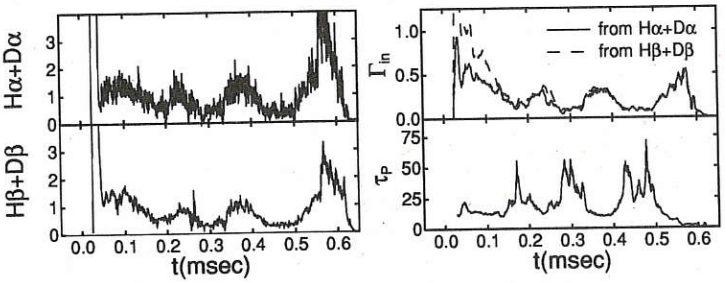

Figure 3: Observed intensity of Hα+Dα in 10^{17} cm^{-2} sr^{-1} s^{-1}, intensity of Hβ+Dβ in 10^{16} cm^{-2} sr^{-1} s^{-1}, calculated hydrogen influx Γ_{in} in 10^{20} cm^{-2} s^{-1}, and particle confinement time τ_P in μsec for a typical discharge (#24088). The frequency of oscillations in τ_P resembles that seen in the local external magnetic diagnostics and in the radial magnetic field profiles[3].

Visible spectra

We have performed a scan of the emission in the wavelength range from 2400 Å to 7000 Å with the 1/2 m spectrometer both during RFP start-up and sustainment phase. The spectrum is dominated by $O^{1+}$to O^{3+}, but also carbon, nitrogen, chlorine, silicon, sodium and calcium have been identified.

In the analysis, we make use of the assumption, that all j-sublevels of excited states are populated according to their statistical weight. This procedure is very fruitful, and helps in the resolution of even the most crowded spectra. However we have observed a few multiplets, where this assumption fails. One such multiplet is presented in figure 4, together with the shape it should have according to statistical weights.

As can be seen, the lines from the lowest j-sublevel are not observed. Of the three sublevels, it is only j=2 which may decay to ^1D states, and thus there is the possible explanation, that the rate of these transitions is enhanced by collisions or electromagnetic fields.

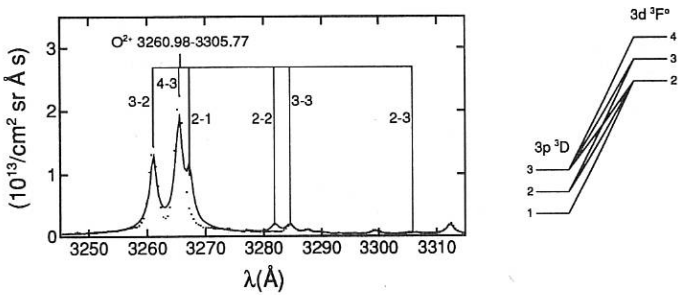

Figure 4: Multiplet $O^{2+}(3d^3F^o \rightarrow 3p^3D)$ as observed with the 1/2 m spectrometer ($\cdots$) together with the shape of the multiplet expected from statistical population of the j-sublevels (—). The transitions from j=2 are not seen. This indicates, that the depopulation to other, possibly singlet, states is faster than the equilibration between j-sublevels.

References

[1] P. Brunsell, J.R. Drake, S. Mazur, and P. Nordlund. *Physica Scripta*, **44**,358, 1991.

[2] J.R. Drake et al. This conference.

[3] P. Nordlund, S. Mazur et al. This conference.

[4] H. Bergsåker, I. Gudowska et al. This conference.

[5] R.J. Fonck, A.T. Ramsey, and R.V. Yelle. *Appl. Optics*, **21**(12)2115, 1982.

[6] J.H. Brzozowski, E. Källne, and K.-D. Zastrow. *Physica Scripta*, **43**,283, 1991.

[7] K.-D. Zastrow, J.H. Brzozowski, E. Källne, and H.P. Summers. In *Course and Workshop on Diagnostics for Contemporay Fusion Experiments*, International School of Plasma Physics, Varenna, Italy, September 1991.

[8] S. Ortolani, M.E. Puiatti, P. Scarin, and G. Tondello. *Plasma Physics and Controlled Fusion*, **27**,69, 1985.

[9] H.P. Summers, J. Lang, and R.W.P. McWhirter. Private communication.

[10] L.C. Johnson and E. Hinnov. *J. Quant. Spectrosc. Radiat. Transf.*, **13**,333, 1973.

RFP SET UP AND CONFINEMENT IN SWIP—RFP DEVICE

ZHANG Peng, FANG Shuiquan, Li Jieping, LUO Cuiwen

LI Qiang, ZHANG Shiyou, YI Ping, XU Ying

Southwestern Institute of Physics

P. O. Box 15, Leshan, Sichuan, China

1. INTRODUCTION

Great progresses have been made on reversed field pinch study at present time[1,2]. SWIP—RFP is a reversed field pinch device of Southwestern Institute of physics[3]. It has a thin stainless steel liner of vacuum chamber ($R/a=0.48m/0.1m$). The set—up RFP has been studied in different conditions of gas filling pressure, initial toroidal field, aided reversal field and plasma current. RFP have been realized in three cases of time matched operation of self—reversal effect and toroidal field control. In this paper, the experiment results of RFP configuration are given. RFP configuration can be established with a passive crowbar and the aids of self—reversing of plasma and a slow control of toroidal field, the plasma current duration over 300μs is obtained and plasma current value ranges from 15 to 30KA.

2. ELECTROMAGNETIC AND PHOTOELECTRICITY MEASUREMENTS

In SWIP—RFP device, magnetic evolution is measured by magnetic probes inserted inside the liner and external pick—up coils. A poloidal single loop is used to measure poloidal voltage of plasma V_θ and toroidal magnetic flux. Another toroidal single loop is used to measure toroidal voltage V_ϕ. Plasma current I_p is measured by a Rogowski coil. Currents of poloidal magnetic field circuit I_{ep} and toroidal magnetic field circuit I_{et} are both measured by current divider. Electrostatic probes give ion saturation current signal I_{ps}. H_α signal $I_{H\alpha}$ and visible light signal I_{VL} are also measured.

3. SET UP RFP

The conditions of the set—up RFP have been studied in different cases for H_2 filling pressures $P_0=0.3-2Pa$, charging voltage of poloidal bank $\langle V_p\rangle=12.6-14.4$ KV, charging voltage of initial toroidal field bank $\langle V_i\rangle=0.68-1.02$ KV, charging voltage of reversed field bank $\langle V_r\rangle=0.56-0.83$ KV, with a passive crowbar.

Table 1, Reverse time of $B_{\phi w}$ and $\langle B_\phi \rangle$ for Pa, $\langle V_i \rangle$, $\langle V_r \rangle$, $\langle V_p \rangle$

H_2 filling pressures, P_0(Pa)	0.8	0.8	1	1
initial toroidal, $\langle V_i \rangle$(KV)	0.68	0.68	0.77	0.77
reversal toroidal, $\langle V_r \rangle$(KV)	0.74	0.56	0.56	0.56
poloidal bank, $\langle V_p \rangle$(KV)	12.6	12.6	12.6	14.4
reverse time of $B_{\phi w}$, $\triangle t$(μs)	60	210	127.5	112.5
reverse time of $\langle B_\phi \rangle$, $\triangle t$(μs)	210	360	285	270

The set—up RFP configuration has been established[4] under $P_0(H_2)=0.3$—2Pa in different conditions for plasma current, initial toroidal field and reversed toroidal field. The set—up RFP discharge have been realized by three methods: (a) Reversed field is supplemented by the control of toroidal field circuits after the plasma self—renersal effect. (b) The toroidal field at outside wall $B_{\phi e}$ is reversed before the reversion of toroidal field at inside wall $B_{\phi w}$. (c) The toroidal field at inside wall $B_{\phi w}$ and the toroidal field at outside wall $B_{\phi e}$ reverse nearly at the same time.

4. RFP CONFIGURATION EXPERIMENTS

Fig. 1 shows RFP configuration for the condition: $P_0(H_2)=1$Pa, $\langle V_p \rangle=12.6$KV, $\langle V_i \rangle=0.68$KV, $\langle V_r \rangle=0.56$KV. From this figure, following conclusion can be reached: $B_{\theta w}$ (Poloidal field at inside wall), I_{pa}, I_{Ha} and I_{VL} are consistent mutually. Fig. 2 is obtained in the same conditions as above but $P_0(H_2)=0.3$Pa, it shows that the sustained time of RFP configuration becomes shorter and I_p is smaller.

Table 2. V_ϕ, I_p, τ_p for $\langle V_p \rangle=14.4$KV, $\langle V_i \rangle=0.68$KV, $\langle V_r \rangle=0.56$KV

$P_0(H_2)$ (Pa)	1.5	0.8	0.5
V_ϕ (V)	202	242.2	222.2
I_p (KA)	16.5	21	15
τ_p (μs)	280	320	280

The distribution of RFP configuration is shown in Fig. 3, the profiles of B_θ and B_ϕ are given at $t_1=100$μs and $t_2=160$μs. The F—Θ curve is shown in

Fig. 4 in which maximum $\Theta=1.85$ corresponds to $F=-0.25$. The time between the breakdown of gas and the set up of RFP configuration is 160μs. The horizontal displacement of plasma column has been measured, it varies from a few mm to 12mm, it is below 10mm usually. The conductivity temperature Teσ of plasma is roughly estimated to be 20eV. Theoretical study points out that the necessary condition of stability requires $\Theta<2.1$ [5] or $\Theta<2$ [6] and the sufficient condition requires $\Theta<1.73$ [5] when $\beta=0.1$. The research of Robinson[7] about MHD stability indicates that a stable region exists.

5. CONCLUSION

Time of set—up RFP ranges from 60μs to 210μs under different conditions. The set—up RFP discharges have been realized in three cases of matched time between self—reversal effect and toroidal control.

I_p, τ_p, V_ϕ and the time of the set—up RFP configuration are all different, when the coordination among $P_0(H_2)$, $\langle V_p\rangle$, $\langle V_t\rangle$, $\langle V_l\rangle$ changes. Bigger value of I_p and longer τ_p can be obtained when better coordination is chosen. I_p, B_θ, I_{VL}, $I_{H\alpha}$ and $I_{p\alpha}$ can all be consistent mutually. Furthermore, RFP configuration can be sustained more than 300μs with a passive crowbar.

ACKNOWLEDGEMENTS

The authors are grateful to Professor Ding Honchang for the proofreading on the words of this manuscript, also thank all members of the SWIP—RFP group for their continuous cooperation in running the device and preparation of the experiments.

This work is supported by the National Natural Science Foundation of China.

REFERENCES:

[1]. Ortolani. s, plasma physics and controlled Fusion V31. (10) P1665(1989).

[2]. Bodin. H. A. B, Nucl. Fusion, V30 (9) P1717 (1990).

[3]. Zhang Peng, et al., Reversed Field Pinch experiment in SWIP—RFP device. SWIP Research Report 1991. 12.

[4]. Zhang Peng, et al., " set up RFP experimental studies on SWIP—RFP" SWIP Research Report 1991. 12.

[5]. Zhang Peng, Chinese Physics, V9. (1)156 (1989); Nucl. Fusion Plasma phys, 7(3) 147 (1987).

[6]. Kondoh. y, Nucl. Fusion. V21. (12). 1607 (1982).

[7]. Robinson. D. C, plasma phys v13. 439(197), Nucl. Fusion V18. 939(1978).

Fig.1 1Pa

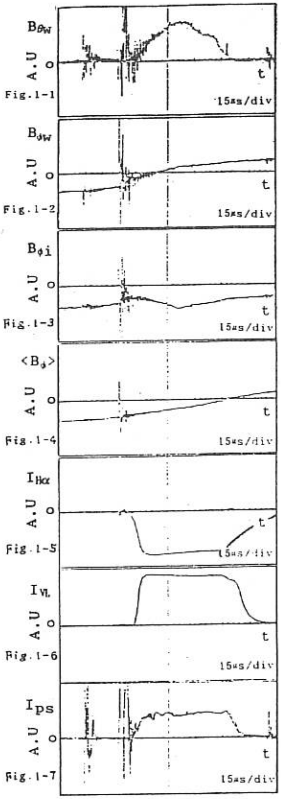

Fig. 2 0. 3Pa

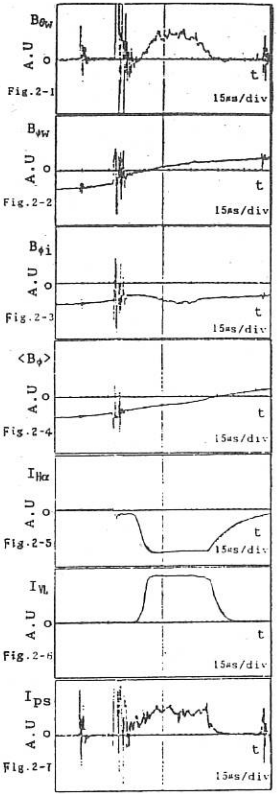

Fig. 1 and Fig. 2 Pulse forms for two discharges with different filling pressures

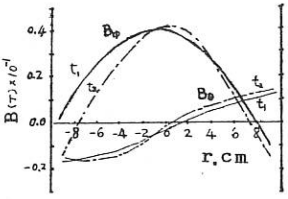

Fig. 3 Profiles of B_θ and B_ϕ

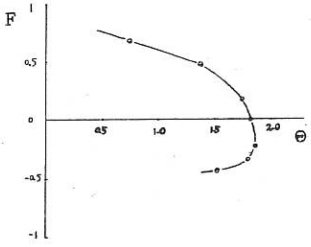

Fig. 4 F—Θ curve.

ION TEMPERATURE MEASUREMENTS IN THE REVERSED FIELD PINCH PLASMAS

A. Schiavi, A. Buffa, S. Costa
Istituto Gas Ionizzati del CNR, EURATOM-ENEA-CNR Association
Corso Stati Uniti 4, 35020 PADOVA, ITALY

INTRODUCTION In this paper are presented ion temperature measurements in the Reverse Field Pinch ETA BETA II obtained by a neutral particle energy analyser. Previously ion temperatures of the plasmas were obtained by Doppler broadening of the CV 2271Å radiation line /1/. Recently the ion temperature measurements are achieved from the energy spectrum of the neutral atoms which are born inside the plasma by charge exchange reactions with a time of flight neutral particle analyser.

THEORY Supposing cylindrical symmetry and maxwellian velocities distributions, characterized by local temperature, for each ion species, the charge exchange neutral atom and energy outflux are /2/:

$$\frac{d\Gamma}{\Delta\Omega dE} = \int_{-a}^{a} n_i(r) n_0(r) \sigma(E) \sqrt{\frac{e}{2m[\pi T_i(r)]^3}}\, E\, \alpha(r)\, \exp\left(-\frac{E}{T_i(r)}\right) dr \quad \left[\frac{\text{part}}{m^2 eV \text{ster sec}}\right] \quad (1)$$

$$P_{cx} = 4\pi \int_0^{\infty} E\, \frac{d\Gamma}{\Delta\Omega dE}\, dE \quad (2)$$

where E is the atom energy; $\alpha(r) = \exp\left(-\int_r^a n_i(r')\sigma(E)dr'\right)$ represents the attenuation for the outgoing neutrals due to ionization or re-charge-exchange; $\sigma(E)$ is the charge exchange cross section; the other symbols have their conventional interpretation.

EXPERIMENTAL SETUP AND TESTING A time of flight neutral particle analyser is used to measure neutral atom fluxes from ETA BETA II plasmas. This instrument observes the plasma through two 0.15mm wide slits: the one is fixed, the other is moveable. A wheel with 48 radial slits rotates in front of the fixed slit at 8000 rpm. The flight distance is 4.45 m; the detector is an electron multiplier Hamamatsu R595, without the window and with Cu-BeO dynodes. The vacuum inside the instrument is about 10^{-7} torr. During the two slit overlap a stream of radiation and particles goes into the instrument. The overlapping interval is about 5μsec and the light spikes specify

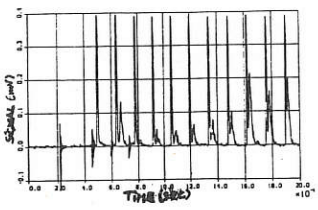

Fig 1: Output signal

the opening instants. The atom fluxes become voltage signals, due to the current produced by the multiplier (Fig.1) and particle energy is obtained from the arrival time $\left(E=\frac{m\ell^2}{e2t^2} \text{ in eV}\right)$. With our time of flight we observe particles with energy from 1500 eV to 30 eV (the lower limit is fixed by the efficiency of the Cu-BeO).

In our description we can distinguish two methods in the signal analysis: in the first we determine ion temperature of the innerest plasma regions and make a rough power losses evaluation employing the relation (2) with suitable simplification; in the second one, more complex, we find radial ion temperature profile and global particle emission power losses fitting the experimental energy spectrum of the neutral atoms with numerical codes.

The simplified equation used for the ion temperature evaluation in the rough data analysis is /3/:

$$\frac{1}{\sigma(E)\,E}\,\frac{d\Gamma(E)}{dE} = \Delta\Omega\; 2a\; n_i(0) n_0(0) \sqrt{\frac{e}{2m[\pi T_i(0)]^3}}\; \exp\left[-\frac{E}{T_i(0)}\right] \qquad (3)$$

and represents the experimental neutral particle fluxes for energies greater than about three times the axial temperature.

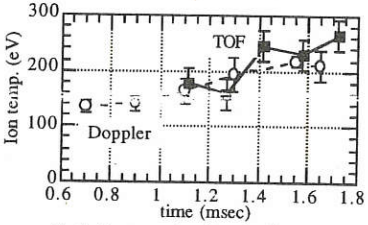

Fig 2: Ion temp. in a "standard" shot

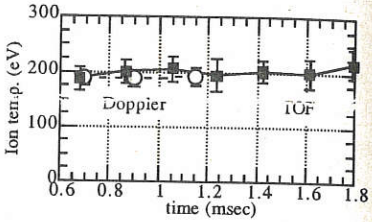

Fig 3: Ion temp. in a "high theta" shot

We have at first compared the TOF with the spectroscopic ion temperature measurements for plasmas obtained in different conditions. Fig. 2,3,4 are ion temperatures of shots where we have measured neutral fluxes simultaneously with measurements of Doppler broadening of the 2271 Å CV radiation line. The results obtained with the two diagnostics are within the error bars. These ion temperature values are not comparable with those of next graphs because of modifications made on the ETA BETA II experiment.

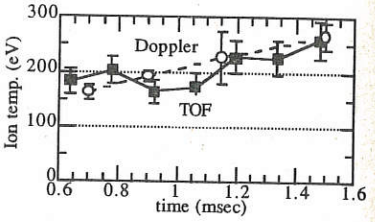

Fig 4: Ion temp. in a "low density" shot

EXPERIMENTAL RESULTS We present here TOF measurements obtained utilizing the rough technique of signal analysis in three different RFP plasma conditions of ETA BETA II. We report either the results obtained by a single shot analysis and the results obtained from the signal average of many shots. Fig. 5,6,7 show, with the plasma current,

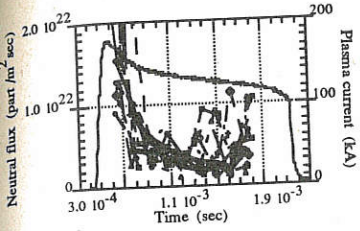

Fig 5: Neutral fluxes

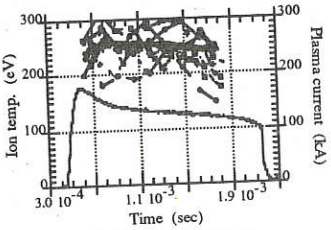

Fig 6: Ion temperatures

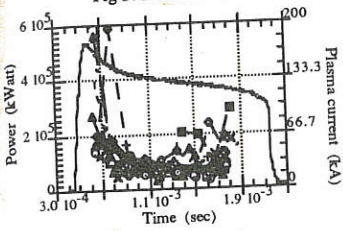

Fig 7: Power emission

experimental total fluxes, ion temperatures and power losses for 12 shots produced in "standard" condition (plasma current ≃ 130 kA, theta value ≃ 2 and filling pressure ≃ 0.45 mtorr) and their average value (marked line). The dispersion of the single signal around the average value is mainly due to the discharge not-reproducibility.

Fig. 8,9,10 show the measured total fluxes, ion temperatures and power losses for the average signal values of 12 shots produced in "standard" condition, of 10 shots produced in "high theta" condition (plasma current ≃ 120 kA, theta value ≥ 2.6, filling pressure ≃ 0.45 mtorr) and of other 10 shots produced in "low density" condition (plasma current ≃ 150 kA, theta value ≃ 2.2, filling pressure ≃ 0.37 mtorr). On comparing the three results, we can observe that in low density plasmas there is the lowest attenuation for escaping particles, so there are the largest power losses and the lowest temperatures; we can observe furthermore for all kind of plasmas that in the reversed field pinch formation phase there is a large loss of neutral particles with low energy; during current flat-top neutral flux has a minimum whereas the average single particle energy increases. Ion temperature reaches initially its maximum

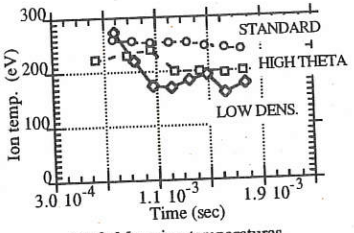

Fig 9: Mean ion temperatures

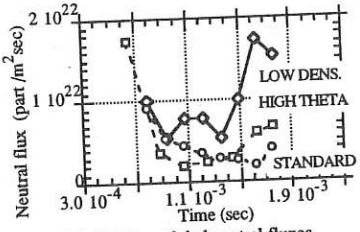

Fig 8: Mean global neutral fluxes

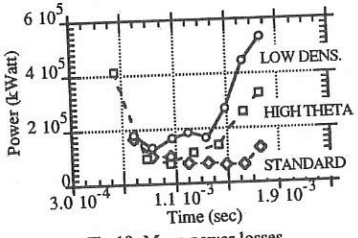

Fig 10: Mean power losses

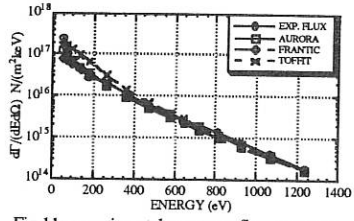

Fig 11: experimental spectrum fits vs energy

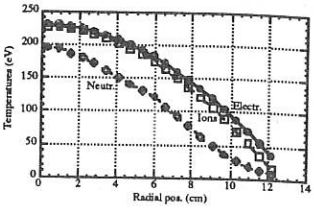

Fig 12: Ion, electr. and neutr. temp. radial profiles

value and remains approximatively constant during current flat-top, excluding the low density plasma case in which the ion temperature diminishes, probably because of the great losses.

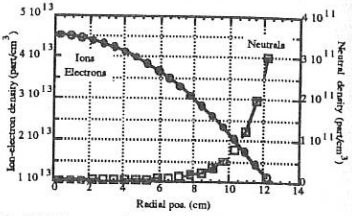

Fig 13: Electr. and neutra. density radial profiles

CODES UTILIZATION A more detailed and complete neutral flux analysis can be obtained by numerical codes. These codes, on the basis of the knowledge of neutral influx, radial profiles of electron and ion densities and temperatures, give radial profile of neutral density and temperature and evaluate neutral atom outflux spectra through eq (1) /4/. We have used a code with the Monte Carlo method (AURORA /5.6/) and two codes solving the neutral particle steady-state equation (FRANTIC /7/ and TOFFIT /8/), to fit experimental neutral atom flux spectra. Fig. 11,12,13 are an example of the results obtained. These three codes are in good agreement and have given a good fit of neutral flux spectrum.Global flux and power losses obtained with codes are greater than those obtained by the rough analysis (about 20%), because our time of flight analyser detects particles within a limited energy range.

CONCLUSIONS We have reported the results of the analysis of neutral atom fluxes observed with a time of flight analyser which allows a careful measure of ion temperature and power losses. On such test basis we are going to employ a similar instrument on RFX, together with a E || B neutral particle analyser which is adequate to measure the neutral particle flux in a higher energy range.

ACKNOWLEDGMENTS One of the authors thanks the Leybold S.p.A., Milano (ITALY), whose financial support allowed him to complete his research. The authors thank Mr E. Baseggio, Mr G. Mella, Mr I. Molon for their irreplaceable collaboration in the experiment conduction.

REFERENCES

/1/ Carraro L., Costa S. et al., Proc. 18th EPS Europ. Conf., Berlin, part II, 557 (1991)
/2/ Voss D.E., Ph. D. Thesis, Princeton University (1980)
/3/ De Chambrier A. LRP 345/88 Echole Polytechnique federale Lausanne (1988)
/4/ Schiavi A.,Tesi di Laurea, Universita' di Padova (1991)
/5/ Huges M.H.,Post D.E. Jou. of comp. Phys.,28, 43 (1978)
/6/ Bignami A., Chiorrini R. ENEA-RT/FIMA(82) 10 (1982)
/7/ Tamor S, Jou. of comp. Phys., 40, 104 (1981)
/8/ Costa S. et al. GIP 86/03 Ist. Gas Ionizz., Padova (1986)

GENERATION OF FAST ELECTRONS BY MAGNETIC RECONNECTION PROCESSES IN RFP PLASMAS

M. ERBA[1], P. MARTIN[2], S. ORTOLANI, A. ROSSI[3]

Istituto Gas Ionizzati del C.N.R.,
Associazione EURATOM-ENEA-CNR,
I-35020 Padova, Italy

1. INTRODUCTION

The dynamics of partially relaxed magnetic field profiles such as the Reversed Field Pinch (RFP) is well described within the framework of MHD theory. In particular a stable, relaxed field distribution immersed in a dissipative plasma departs from this state by resistive diffusion thus becoming subject to resistive instabilities whereby it then relaxes back again and the process is cyclically repeated.

It is generally recognized that the magnetic relaxation phenomena also affect plasma transport. In fact, transport is likely to be dominated by parallel diffusion in magnetic field structures stochasticized by the vigorous broad spectrum of perturbations. Two intriguing pieces of experimental evidence have been clearly brought out by recent measurements:

a) the ion temperature sometime exceeds the electron temperature and it is generally higher than the value expected from equilibration with the joule heated electrons (see Ref. [1] and those quoted therein);

b) a population of energetic electrons with energies corresponding to the core hot region is observed in the outer region of the plasma [2,3,4].

The most widely accepted interpretations of these two evidences are that:

a) a direct and anomalous ion heating channel is present through which magnetic energy, released during relaxation, is transferred to ion kinetic and thermal energy, this process involving viscous dissipation of velocity fluctuations.

b) electrons from the core travel unconfined in the stochastic magnetic field and substantially contribute in the edge to the parallel current density profile (the so called Kinetic Dynamo Theory - KDT [5]).

Thus, if the anomalously strong ion heating still may find an explanation within the MHD theory, the energetic electrons due to their non-collisional nature have been generally described by a kinetic model, although their presence has been still indirectly related to MHD processes in that they are originated by stochastic magnetic fields which are a result of resistive instabilities.

In this paper we propose that also the observed energetic electrons are due to magnetic reconnection processes which take place during relaxation. As pointed out by Taylor [6], reconnection proceeds via thin resistive layers characterized by high current densities. We think that the drift velocities associated with these current densities can explain the presence of the observed fast electrons. Thus magnetic reconnection, related to resistive MHD instabilities, would be the basic mechanism determining both the magnetic field dynamics and the whole thermodynamic properties of confined plasmas in driven partially relaxed magnetic configurations.

2. MAGNETIC RECONNECTION MODEL

As a starting point we assume that the evolution of MHD instabilities characteristic of the RFP profile dynamics can be described in its nonlinear saturated regime by a stationary Sweet Parker-

---

1 Scuola Normale Superiore Pisa, Italy.
2 Dipartimento di Fisica, Universita` di Padova, Italy
3 Dipartimento di Fisica, Universita' di Ferrara, Italy.

like reconnection model [7,8]. The basic features of an elementary reconnection process involving a magnetic field $B^{\dagger}$ are shown in Fig. 1.

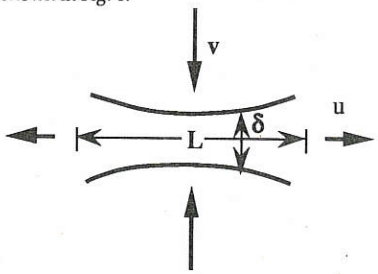

Fig. 1

The incompressible flow continuity equation and pressure balance give:

$$V L \approx u \delta \qquad \text{and} \qquad \frac{1}{2}\rho u^2 \approx \frac{B^{\dagger 2}}{2\mu_o} \tag{1, 2}$$

where L and δ are the length and the width of the reconnection layer, V and u are the inflow and outflow fluid velocities respectively.
From these we obtain:

$$u \approx \frac{B^{\dagger}}{(\rho\mu_o)^{1/2}} \approx V_A \tag{3}$$

where ρ is the mass density and V_A the Alfvén velocity; therefore:

$$V \approx \frac{\delta V_A}{L} \tag{4}$$

The reconnection time, defined as $\tau \equiv \frac{L}{V}$ can then be estimated as:

$$\tau = \frac{L^2}{\delta V_A} \tag{5}$$

Writing Ohm's law in the simple form:

$$VB^{\dagger} = \eta J^R \tag{6}$$

where η is the plasma electrical resistivity, and expressing the current density in the layer with its order-of-magnitude form:

$$J^R \approx \frac{B^{\dagger}}{\mu_o \delta} \tag{7}$$

gives:

$$\delta \approx \frac{\eta}{\mu_o V} \approx \frac{\eta L}{\mu_o \delta V_A} \tag{8}$$

or:

$$\delta \approx L S^{-1/2} \tag{9}$$

where the Lundquist number S is defined as $S \equiv \frac{L\mu_o V_A}{\eta}$.

The reconnection time, after defining the global resistive diffusion time as $\tau_R \equiv \frac{\mu_o L^2}{\eta}$ and the Alfvén transit time as $\tau_A = \frac{L}{V_A}$ can finally be estimated as:

$$\tau \approx (\tau_R \tau_A)^{1/2} \tag{10}$$

an expression already found for RFP [1] by means of dimensional arguments. This scaling for τ, which is that typical for the Sweet-Parker reconnection, has an experimental confirmation when one plots the experimental values of relaxation times for various RFPs experiments vs. the experimental value of $(\tau_R \tau_A)^{1/2}$ [1]. A slightly different scaling, still compatible with that reported in Eq. (10), has also been found in MST [9].

In order to estimate L for the actual RFP experiments it is useful to remind that in the Sweet-Parker model L is the maximum length that the resistive layer can occupy compatibly with the geometry of the system. In the present case the reconnection layer extends along the direction of the wave vector k of the perturbation, whose module for the poloidal wave number m=1 is $k \sim \frac{n}{R}$, where R is the major radius of the torus and n the toroidal wave number. Recalling that the most unstable linear modes in the RFP have $n \approx \frac{2R}{a}$, where a is the plasma column minor radius, we get:

$$L \approx \frac{2\pi R}{n} \approx \pi a \qquad (11)$$

3. CURRENT DENSITY ESTIMATE AND COMPARISON WITH EXPERIMENTS

Using the reconnection model described in the previous section it is possible to calculate the electric current density in the reconnection layer J^R, but a quantitative comparison with the experimental observations would require an estimate of the magnetic field $B^\dagger$ annihilated in the reconnection process. In fact, while in Tokamaks for the m=1, n=1 mode which nearly totally reconnects, $B^\dagger = B^*$, where B^* is the magnetic field perpendicular to the m=1, n=1 helix, the picture in the RFP reconnection is not so clear, since multiple modes with different helicities are simultaneously present. For our order of magnitude estimates we shall use a fraction ε of the poloidal magnetic field at the wall B, i.e. $B^\dagger = \varepsilon B$. This choice allows us to express all the results in terms of quantities characteristic of the macroscopic global behaviour of the plasma and of the parameter ε.

Expressing the average equilibrium current density J^M as $J^M = \frac{B}{\mu_0 a}$ and considering that $L \approx \pi a$, we find:

$$J^R \approx \frac{B}{\mu_0 a} S^{1/2} \approx \varepsilon J^M S^{1/2} \qquad (12)$$

Recalling that we have assumed the density to be uniform and considering the definitions of the drift velocities $v_D{}^R \equiv J^R/ne$ and $v_D{}^M \equiv J^M/ne$, we can write, introducing the electron streaming parameter ξ,:

$$v_D{}^R \approx \varepsilon S^{1/2} v_D{}^M \approx \varepsilon \xi S^{1/2} v_{th} \qquad (13)$$

where v_{th} is the electron thermal velocity. Eq. (13) shows that the electrons associated to the current in the reconnection region are typically faster than those which carry the average equilibrium current density. The acceleration of electrons to velocities of the order of $v_D{}^R$, which takes place in the resistive layer, can then be an explanation for the presence of fast electrons in RFPs. The observation of fast electrons in the edge region should then be related in general to the presence of resonant surfaces (and resistive layers) throughout the plasma. For RFP profiles this is particularly the case in the neighbourhood of the toroidal field reversal surface where there is a high spatial density of resonant surfaces.

In an attempt of obtaining a quantitative estimate of an average electric current density due to reconnection we can conceive that reconnection processes and the associated current sheets are present in the plasma only during the cyclical relaxation phase of duration proportional to τ while the period of the oscillation scales with the diffusion time τ_R. This means that, on the

average, during the discharge the density of electrons carrying the current density J^R is not that istantaneous during the process, n, but rather a lower time averaged density which can be expressed as :

$$<n^R> = n\frac{\tau}{\tau_R} = n\,S^{-1/2} \qquad (14)$$

where the factor τ/τ_R represents a sort of duty-cicle of the relaxation process and accounts for the time interval during which fast electrons can be produced. The above estimate is therefore in agreement with the experimental observation of a small population of fast electrons.

Using $<n^R>$ we can also define a time averaged current density in the reconnection layer, $<J^R>$, which can be directly compared with experimental observations, as

$$<J^R> = <n^R>\, e\, v_D{}^R = n\,S^{-1/2} e\, v_D{}^R \approx \varepsilon J^M \qquad (15)$$

The parameter ε can vary between a lower limit of $\approx 10^{-2}$, which is the measured background fluctuation amplitude and an upper limit of 1. Taking $\varepsilon \approx 10^{-1}$ for an order of magnitude estimate, we obtain, using experimental data typical of three machines, ZT40-M [2], TPE1R-M [3] and ETA-BETA II [4] where fast electrons have been detected, $\frac{v_D^R}{v_{th}} \approx 1$ $\frac{<n^R>}{n} \approx 1\%$ and $\frac{<J^R>}{J^M} \approx 0.1$, values which are in reasonable agreement with the measured quantities.

4. CONCLUSIONS

On the basis of the interpretation proposed in this paper the generation of fast electrons would be a phenomenon present in almost every configuration for plasma magnetic confinement although perhaps more evident in RFP plasmas, where there are many resonant surfaces and a correspondingly active magnetic field dynamics. In the KDT model [5] the fast electrons produced in the central hot region of the plasma would reach the edge where they can be measured; this would be possible because the magnetic field lines become stochastic under the action of magnetic reconnection, degrading the confinement properties of the configuration. On the other hand in our model fast electrons and stochasticity of field lines are different problems, although they have the same origin: the reconnective modes which destroy the magnetic field surfaces are also the cause of the generation of fast electrons in the resistive layers. Moreover since the drift velocity and the fluctuation amplitude scale in opposite ways with S, the presence of fast electrons is not necessarily a symptom of bad confinement.

While the model presented here allows to describe qualitatively a mechanism for the generation of fast electrons, for a more quantitative comparison with experiments further developments are necessary. In particular a better definition of the reconnecting magnetic field and of the effective time duration of the generation process as well as of the number of simultaneously occurring reconnection processes is required.

REFERENCES

[1]Giubbilei M., Martin P. and Ortolani S., Plasma Phys. Controll. Fusion 32 (1.990) 405.
[2]Ingraham J.C., Ellis R.F., Downing J.N. et al., Phys. Fluids B 2(1) (1990) 143
[3]Yagi Y., Shimada T., Hirano Y. et al., in Controlled Fusion and Plasma Physics (Proc. 17th Eur. Conf. Amsterdam 1990) Vol.III, EPS Amsterdam (1990) 545.
[4]Antoni V., Bagatin M., Desideri D., Martines E. and Yagi Y., in Controlled Fusion and Plasma Physics (Proc. 18th Eur. Conf. Berlin 1991) Vol.15 c Part.III, EPS Berlin (1991) 69.
[5]Jacobson A.R. and Moses R.W., Phys. Rev. A 29 (1984) 3335 .
[6] Taylor J.B., Rev. Modern Physics 58 (1986) 741.
[7]Sweet, P. A., 'The neutral poin theory of solar flares,', in *Electromagnetic Phenomena in Cosmical Physics*, edited by B. Lehnert, p.123, (1958), Cambridge University Press.
[8] Parker, E.N., Astrophys. J. Suppl. Ser. 8 (1963) 177.
[9]Chartas G., Ph.D. Dissertation, University of Wisconsin 1991.

Relaxed states for a driven Reverse Field Pinch

R. Paccagnella

Istituto Gas Ionizzati, EURATOM-ENEA-CNR Association
I-35020 Padova, Italy

Some years ago a "minimum energy" principle [1] has been proposed by J.B. Taylor to explain the main properties of a magnetic fusion device: the Reverse Field Pinch (RFP). Later it has been pointed out [2] that relaxation theory can also be applied to other devices such as multipinches, spheromaks etc. In the case of RFP, Taylor's relaxed state can be considered a sort of zero-order description of the magnetic field profiles. In fact, experimental observations show a deviation from the predicted state. In particular the condition of flat $\mu = J \cdot B/B^2$ profile, is not satisfied, especially in the external plasma region near the conducting wall.
Many relaxation theories have been proposed [3,4,5,6,7] to overcome the limits of the Taylor's theory.
In this paper a modification of the Taylor's theory is discussed, which takes into account the fact that the RFP is a driven system.

I. Relaxation theory for a driven system

As it is well known, the Taylor's relaxed state [1] is obtained after minimisation of the magnetic energy under the constraint of constant total magnetic helicity. The relaxed state is shown to be force-free. Taylor's theory is very simple but has some difficulties when compared with experimental observations of magnetic fields.
In the attempt to improve the agreement between theory and experiments it is useful to reconsider Taylor's basic assumptions.
One of the crucial points is the conservation of total magnetic helicity. In fact magnetic helicity is exactly conserved only in the case of an ideal plasma, i.e. for $\eta = 0$. However in that case, total magnetic helicity is not the only invariant, there are in fact infinitely many conserved quantities [1,2]. Taylor's hypothesis of the existence of a single invariant can be considered reasonable only in the limit of very high (but finite) plasma conductivity. He overcame this difficulty using the argument that total magnetic helicity could possibly vary on a longer time scale than magnetic energy. No rigourous proof has been given in order to justify this statement. For a driven system the time variation of magnetic helicity is given by:

$$\frac{\partial K}{\partial t} = 2V\phi - 2\int_v \eta \vec{J}\cdot\vec{B}\, dv \qquad (2)$$

where V is the toroidal loop voltage, Φ is the total toroidal flux. In deriving (2) explicit use of Ohm's law has been done. Therefore in a driven system magnetic helicity can be conserved also in presence of dissipative effects when the rate of helicity input balances the rate of helicity consumption. From the observation that experimentally steady state conditions can be obtained and maintained in a driven RFP, the assumption of helicity conservation appear to be reasonable. Now in a system in which the total toroidal flux is preserved, if the toroidal loop voltage is held fixed (this is the case during the current flat-top) it follows from eq. (2) a constant rate of helicity consumption.

It is quite obvious at this point to suggest the minimisation of energy subject to this new constraint. Note that a similar constraint has also been used and justified in Reference [7].

It is easily shown, considering a constrained variation with $\delta B=0$ at the plasma edge, that the relaxed state is given by:

$$\nabla\times\vec{B} = \frac{\mu}{\eta}\vec{B} - \frac{1}{2}\frac{\nabla\eta}{\eta}\times\vec{B} + \nabla t \qquad (3)$$

where μ = const., η should be considered as a normalized resistivity and t is an arbitrary scalar function. It is interesting to note that for constant η and t, equation (3) gives the Taylor relaxed state. Whereas in the more interesting limit, $\eta = \eta(x)$, the relaxed state is non "force-free", which is consistent for a driven system with a non-zero Poynting vector at the plasma boundary. The final state should be also an equilibrium state, therefore, assuming that the gradient of t has no component parallel to the magnetic field, the perpendicular component of equation (3) can be rewritten in terms of pressure gradient, which determines together with the function μ/η the final state. A more complete relaxation theory would be necessary in order to find the relaxed state without arbitrariness. However we observe that the perpendicular terms in equation (3) are of order $\beta = 2\mu_o p/B^2$, with respect to the parallel terms, therefore resistivity largely determines the magnetic field profiles.

In order to complete the study of the relaxed state given by (3) it should be also necessary to find the solutions of (3) corresponding to the minimum energy content. Due to the lack of analytic solutions of (3) for arbitrary η and pressure profiles, a numerical linear stability

study can be done. In Ref.[8] an extensive study has been performed of states described by a particular choice of J/B ratio, and it has been shown that MHD stable cylindrically symmetric solutions of the force-free part of (3) exist.

II. Comparison with experimental results

In defining RFP operation regimes two parameters are very useful and widely used:

$$F = \frac{B_{tw}}{\langle B_t \rangle} \ , \quad \theta = \frac{B_{\theta w}}{\langle B_t \rangle}$$

where B_{tw} and $B_{\theta w}$ are the toroidal and poloidal magnetic field at the wall, and $< B_t >$ is the average toroidal field over the plasma cross-section.
In Fig.1 the F-Θ plot shows the experimental points from ETA-BETA II compared with Taylor's states (BFM) and with the model obtained from (3) (cylindrical symmetric force-free solutions are considered).

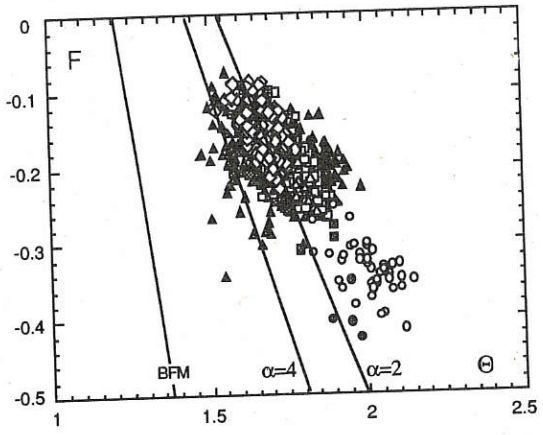

Fig.1

In solving (3) the "classical" dependence of η on temperature has been assumed $\eta \approx T^{-3/2}$ and a suitable temperature profile has been chosen

$$T(r) = T(0)\,(1 - \Delta_T\, r^{\alpha})$$

where r is the normalized radial position, $2 \leq \alpha \leq 6$ and Δ_T is related to the normalized difference between central and edge temperature (usually $\Delta_T \approx 0.8 - 0.9$) .

It is clear from Fig.1 that the experimental points are quite well approximated by the curve obtained with the model presented here. It is clear that an even better approximation of the experimental points can be obtained assuming a non zero pressure.

To conclude this section I want to make some comments concerning Ohm's law. It is well known that in cylindrical symmetric RFP models a "classical" Ohm's law is not compatible [9] with the sustainment of a steady state field reversal. Therefore the presence of a dynamo electric field is invoked. Now in deriving (3) explicit use of Ohm's law has been done. It is therefore clear that (3) holds only if the dynamo electric field can be assumed to conserve helicity. This has been rigourously proved [10]. Hence making a direct reference to a modified Ohm's law (containing a dynamo electric field), projecting it parallel to $\mathbf{B}$ and taking into account (3), for a steady state cylindrical plasma, it is obtained:

$$\frac{\vec{E}_d \cdot \vec{B}}{B^2} = \mu - \frac{E_z B_z}{B^2} \qquad (4)$$

Note that in (4) the constant E_z is determined from the condition that E_d preserves helicity. From (4) it is quite easy to estimate the power dissipated by fluctuations in a RFP plasma [11]. The interesting point is that, in our model, this power does not depend on the resistivity profile (at least in the force-free limit) and for typical RFP profiles is in the range 20 -30% of the total input power.

REFERENCES

[1] Taylor J.B., Phys. Rev. Lett. **33**,1139(1974).
[2] Taylor J.B., Rev. Mod. Phys. **58**,741(1986).
[3] Bhattacharjee A., Dewar R.L., Monticello D.A., Phys. Rev. Lett., **45**,347(1980).
[4] Turner L., Christiansen J.P., Phys. Fluids **24**,893(1981).
[5] Hameiri E., Hammer J.H., Phys. Fluids **25**,1855(1982).
[6] Bhattacharjee A., Kwok Y-C., Phys. Fluids **29**,1156(1986).
[7] Montgomery D., Phillips L., Phys. Rev. A **38**,2953(1988).
[8] Antoni V., Merlin D., Ortolani S, Paccagnella R., Nucl. Fusion **26**,1711(1986).
[9] Caramana E.J., Baker D.A.,Nucl.Fus. **24**,423(1984).
[10] Bhattacharjee A., Hameiri E., Phys. Rev. Lett. **57**,206(1986).
[11] Phillips J.A., Backer D.A., Gribble R.F., Munson C., Nucl. Fus. **28**,(1988)1241.

ELECTRON DIFFUSION AND ENERGY LOSS IN A REVERSED FIELD PINCH PLASMA.

V. Antoni, * M. Bagatin and * E. Martines

Istituto Gas Ionizzati del CNR, Euratom-ENEA-CNR Association, Padua (Italy)
* Dipartimento di Ingegneria Elettrica, University of Padua, Padua (Italy)

Introduction Plasmas confined in a Reversed Field Pinch (RFP) configuration exhibit a turbulent behaviour characterized by a relatively high amplitude of the magnetic fluctuations (b/B~1% in experiments with plasma current I~100 kA, where b is the fluctuating field and B the mean field) /1/. As a consequence a wide stochastic region takes place into the plasma, resulting in an enhanced electron energy loss. A theoretical model, the Kinetic Dynamo Theory (KDT) /2/, has been proposed to couple the diffusion of energetic electrons with the sustainment of the configuration. In this paper the main experimental results of the ETA BETA II device (a=0.125m, R=0.65m) /3/ supporting this model are summarized. A numerical code, solving the KDT model equations in cylindrical coordinates, is presented and the results are compared with the experimental data obtained on ETA BETA II at different reversal parameters.

Experimental results An important feature, common to most RFP experiments /3,4,5/, is a flow of energetic electrons in the edge region along the magnetic field lines, in direction opposite to that expected from the externally imposed electric field. On ETA BETA II, by taking the difference between the energy flux densities on the electron and on the ion drift side of a limiter inserted into the plasma (q_e and q_i respectively), the energetic electrons contribution has been derived (including non-linear effects and thermal response of the equipment /6/). The difference q_e-q_i is reported in fig.1 as a function of the parameter $\Theta = \frac{B_\theta(a)}{\langle B_z \rangle}$ (where <....> is the volume averaged value), which has been shown to be strongly related to MHD stability and magnetic fluctuations properties /7/. The fraction of power carried by energetic electrons over the total power lost by transport, $f^{ee} = \frac{q_e - q_i}{q_e + q_i}$ /3/, is reported in fig.2. It is worth nothing that f^{ee} decreases from 90% at standard Θ down to 60% at high Θ. By equating the energy loss to the wall to the energy flux density intercepted by a limiter inserted into the plasma /8/: $\int_0^x (q_e - q_i)dx' = f^{ee} \frac{VI}{S} L_{eq}$ (where VI is the ohmic input and S is the plasma surface), an equivalent collection length L_{eq} can be obtained for a limiter

insertion x. Thus the magnetic diffusion coefficient $D_m = \langle \Delta r^2 \rangle / L$, where $\langle \Delta r^2 \rangle$ is the mean square radial excursion of a field line in a longitudinal distance L, has been derived by the approximation $D_m \simeq x^2/L_{eq}$ /8/. The Θ dependence of the magnetic diffusion coefficient D_m at x=2 mm is reported in fig.2: the increase with Θ is due to the larger amplitude of magnetic fluctuations, as, in quasi-linear approximation /9/, $D_m \simeq (b/B)^2 \Lambda$, where Λ is the longitudinal autocorrelation length of the magnetic fluctuations ($\Lambda \simeq a$ for a RFP).

KDT modelling of RFP configurations The KDT model /2/ is based on a drift kinetic equation for the electron distribution function, with a Spitzer-like electron-ion collision term /10/ and an additional term describing the diffusion due to the magnetic field stochasticity /11/:

$$\frac{\partial f_1}{\partial t} - \frac{eE_{//}}{m}\frac{\partial f_0}{\partial v_{//}} = \left(\frac{\partial f_1}{\partial t}\right)_{coll} + \left(\frac{\partial f_1}{\partial t}\right)_{diff}$$

(where $E_{//}$ and $v_{//}$ are the electric field and the velocity parallel to B). This equation is solved in stationary conditions for a small perturbation f_1 of the maxwellian f_0, self-consistently with Ampere's law in force-free approximation /2/. The model assumes a isothermal and isodense plasma, and is solved in cylindrical geometry instead of slab geometry with the same boundary condition $\partial f_1/\partial r = 0$ as in ref. /2/. It is worth noting that the solutions are odd in the cosine of the angle between velocity and magnetic field, leading to the absence of particle density perturbation and of particle and energy radial fluxes, whereas there is a radial flux of parallel current density /2/. The numerical code requires as input parameters the applied electric field E_0, the on-axis magnetic field B_0, the average temperature $\langle T_0 \rangle$ and the average density $\langle n_0 \rangle$ of the background f_0, the minor radius a of the vessel and the magnetic diffusion coefficient $D_m(r)$. The main outputs of the model are the perturbed electron distribution function f_1, the magnetic field $B_z(r)$ and $B_\theta(r)$, and from them the parallel current density $j_{//}(r)$, the plasma current I and the pinch and reversal parameters Θ and F ($F = B_z(a)/\langle B_z \rangle$). The fast electrons energy flux at the edge parallel to the magnetic field $q_{//}^{ee}$, as well as their temperature T^{ee} and density n^{ee}, have been calculated according to the expressions

$$q_{//}^{ee} = \int \frac{1}{2} m v^2 f_1 v_{//} d^3v \qquad n^{ee} = \int f_1 d^3v \qquad T^{ee} = \frac{1}{n^{ee}} \int \frac{1}{2} m v^2 f_1 d^3v$$

where the high energy portion of f_1 is integrated over the velocities forming an angle with the magnetic field less than $\pi/2$. In this way the contribution of energetic electrons flowing on one side has been taken into account. The experimental conditions of the Θ scanning described in the previous section have been reproduced by imposing the experimental values of the electric field and of the plasma current I. Moreover $\langle T_0 \rangle = 70$ eV, constant, and $\langle n_0 \rangle \sim 3 \div 5 \cdot 10^{19}$, varying linearly with I, have been assumed. Finally a radially uniform D_m,

3.5 times the edge value and varying with Θ as shown in fig.2, has been used. In this way, magnetic field profiles as shown in fig.3 (for two cases of standard and high Θ) have been obtained. The parallel current density profiles relative to these two cases are shown in fig.4 and compared with the profiles which would be expected from a purely local Ohm's law with Spitzer resistivity.

Discussion Substituting the experimental values of the parameters into the code, different configurations are obtained. In fig.5 the F and Θ parameters of these configurations are compared with the experimental values, and the Bessel Function Model (BFM) curve is also reported as a reference. F and Θ are systematically lower than the experimental values and the discrepancy can be accounted by pressure profile and toroidal equilibrium effects. The energy flux density is reported in fig.6: it decreases with Θ and the absolute values are of the same order of the experimental ones (a better agreement at higher Θ could be obtained taking into account a lower $\langle T_0 \rangle$). In the same figure are also shown the temperature T^{ee} and the density n^{ee} of the energetic electrons: T^{ee} exhibits a tendency to increase with Θ whereas n^{ee} shows a tendency to decrease. In terms of relative values, $\frac{T^{ee}}{\langle T_0 \rangle} \simeq 5$ and $\frac{n^{ee}}{\langle n_0 \rangle} \simeq 2\%$, confirming previous estimates based on the assumption of a half-maxwellian perturbation f_1 /12/.

In conclusion the KDT is widely supported by experimental results of ETA BETA II. Solving the equations of the model in cylindrical coordinates and taking the experimental values of E_0, D_m, I, $\langle T_0 \rangle$ and $\langle n_0 \rangle$, the profiles of the magnetic field in RFP configuration at different Θ have been obtained. It is confirmed that energetic electrons carry most of the current density at the edge in opposition to $E_{//}$.The resulting energy flux density is in fairly good agreement with the experimental values, and it is found that T^{ee} and n^{ee} are weakly dependent on the parameter Θ.

Acknowledgements The authors wish to acknowledge helpful discussions with Prof. F. Pegoraro.

References

/1/ H.A.B. Bodin, Plasma Phys. and Contr. Fusion **29**, 1297 (1984)
/2/ A.R. Jacobson, R.W. Moses, Phys. Rev. A **29**, 3335 (1984).
/3/ V. Antoni, M. Bagatin, D. Desideri, N. Pomaro, Plasma Phys. and Contr. Fusion **34**, 699 (1992).
/4/ J.C. Ingraham, R.F. Ellis, J.N. Downing, C.P. Munson, P.G. Weber, G.A. Wurden, Phys. Fluids B **2**, 143 (1990).
/5/ Y. Yagi, T. Shimada, I. Hirota, Y. Maejima, Y. Hirano, K. Ogawa, K. Namichi, K. Iochi, J. Nucl. Mater. **162-164**, 702 (1989).
/6/ V. Antoni, M. Bagatin, D. Desideri, G. Serianni, Proceedings of 10th Int. Conf. on Plasma-Surface Interaction, Monterey, USA (1992) to be published.

/7/ V. Antoni, D. Merlin, R. Paccagnella, S. Ortolani, Nucl. Fusion **26**, 1711 (1986)
/8/ V. Antoni, M. Bagatin, E. Martines, submitted to Plasma Phys. and Contr. Fusion.
/9/ A.B. Rechester, M.N. Rosenbluth, Phys. Rev. Lett. **40**, 38 (1978).
/10/ R. Härm, L. Spitzer, Phys. Rev. **89**, 977 (1953).
/11/ R.W. Harvey, M.G. McCoy, J.Y. Hau, A.A. Mirin, Phys. Rev. Lett. **47**, 102 (1981).
/12/ V. Antoni, M. Bagatin, D. Desideri, E. Martines, Y. Yagi, 18th Eur. Conf. on Contr. Fusion and Plasma. Phys., Berlin, III, 69 (1991).

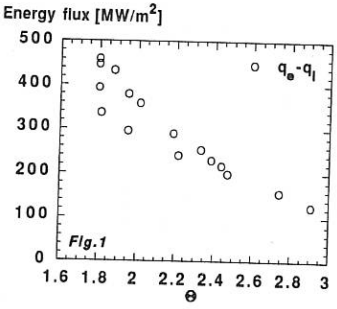

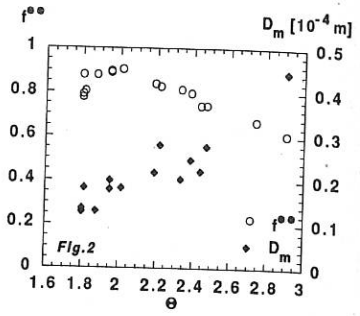

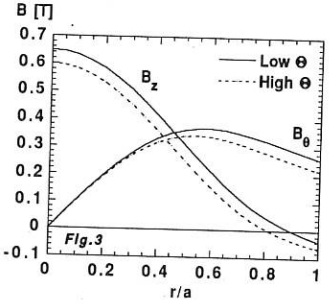

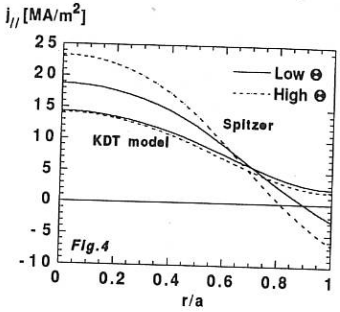

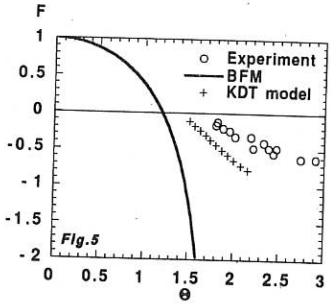

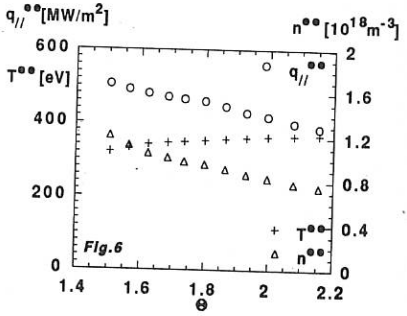

Self-similar Solutions for Trapping and Diffusion of Magnetic Flux During Formation of Field-Reversed Configuration

A. B.Bud'ko, E.T.Karlson, M.A.Liberman
Department of Technology, Uppsala University,
Box 534, S-751 21, Uppsala Sweden

A field-reversed configuration is formed in a Θ-pinch through the application of an initial axial magnetic field which is frozen in a preionized plasma. The external Θ-pinch field is subsequently raised in the opposite direction to the initial field, and the outer forward field lines connect to the inner reversed field lines forming a closed magnetic field configuration. The stability in the final phase of the FRC strongly depends on the amount of the magnetic flux that has been trapped during the previous phases of the FRC formation. Particularly, increasing the fraction of the trapped magnetic flux should result in structures that are amenable to wall stabilization. It is the reason why the study of the dynamics of Θ-pinch plasma during the FRC formation is one of the most important /1/. Experimental results /1-4/ indicate that the diffusion of the magnetic flux depends on the plasma motion and radial structure of the column during the phases of expansion and implosion. We present analytical self-similar solutions describing the phases of compression and expansion for nonmagnetized, and for fully magnetized classical and turbulent plasma. These solutions allow to estimate trapping and losses of magnetic flux in course of plasma motion before the magnetic field lines reconnection.

The plasma magnetohydrodynamic (MHD) transport equations to be solved are

$$\frac{\partial n}{\partial t} + \nabla \cdot (n\,\mathbf{u}) = 0\ , \tag{1}$$

$$\frac{\partial \boldsymbol{B}}{\partial t} = \nabla \times \left[\boldsymbol{u} \times \boldsymbol{B} - \frac{c\,\boldsymbol{R}}{e\,n}\right], \tag{2}$$

$$\rho\left(\frac{\partial \mathbf{u}}{\partial t} + (\mathbf{u}\cdot\nabla)\,\mathbf{u}\right) = \frac{1}{c}\mathbf{j} \times \mathbf{B} - \nabla P, \tag{3}$$

$$\frac{3}{2} n \left(\frac{\partial T}{\partial t} + (\boldsymbol{u}\cdot\nabla T)\right) + P\,(\nabla\cdot\boldsymbol{u}) = -\nabla\cdot(q_e + q_i) + \frac{j^2}{\sigma} + \frac{\boldsymbol{j}\cdot\boldsymbol{R}_T}{en}. \tag{4}$$

Cylindrical geometry is used in this model with variation in radial direction only. The radial velocity $u_r \equiv u$ and axial magnetic field $B_z \equiv B$ are the only nonzero components of $\mathbf{u}$ and $\mathbf{B}$ respectively. Eqs.(1) - (4) together with the corresponding boundary conditions determine the plasma dynamics.

The figure of merit for the diffusion of the magnetic field due to finite plasma conductivity is the magnetic Reynolds number $Rm_o = uL/\nu_m$. More accurate estimate is the ratio of the characteristic time for the magnetic flux losses to the characteristic implosion or expansion time

$$Rm_{eff} = \left(\Phi \Big/ \left|\dot{\Phi}(t)\right|\right) \Big/ \left(R \Big/ \left|\dot{R}(t)\right|\right), \quad \text{where } \Phi = 2\pi \int_0^{R(t)} B(r,t)\, r\,dr \text{ is the trapped magnetic flux.}$$

For a classical nonmagnetized plasma ($\Omega_e\tau_e << 1$), the thermal force is negligible compared with the Ohmic heating, and the ratio of thermal conduction heating to Ohmic heating is small of order $\Omega_e\tau_e$. Thus, only the Ohmic heating term is responsible for diffusion of the magnetic field. Since we consider essentially subsonic flow according to the experimental conditions, the equation of motion (3) is reduced to the condition of uniformity of total pressure.

We seek self-similar solutions of the system of Eqs.(1)-(4), using the method /7/, introducing self-similar coordinate $\xi = r/R(t)$, where R(t) corresponds to the outer boundary of the plasma column, and assuming that the hydrodynamic variables are separable functions of ξ and t

$$u(r,t)=\dot{R}(t)\xi, \quad n(r,t)=n_0\alpha^{-2}(t)\,N(\xi), \quad B(r,t)=B_0\alpha^{\mu}(t)\,B(\xi), \quad B(r,t)=B_0\alpha^{\mu}(t)\,B(\xi). \qquad (5)$$

Separation of variables in Eqs.(1) - (4) implies the following time dependence for the dimensionless radius

$$\alpha(t) = \left(1 + 2\chi\, t / t_0 \right)^{-1-3/2\zeta}, \qquad (6)$$

where, $\mu = -(4\zeta + 5)/(2\zeta + 3)$ and $\lambda = 2(\zeta + 1)/(2\zeta + 3)$ are the self-similar exponents, χ and ζ/χ are separation constants.

For the magnetic Reynolds numbers and magnetic flux we find

$$Rm_0=\chi(2\zeta + 3)/\zeta, \quad Rm_{eff}=(2\zeta + 3),$$

$$\Phi=\Phi_0(1 + 2\chi\, t/t_o)^{-1/2\zeta}, \quad \Phi_0=2\pi\, B_0\, R_0^2 \int_0^1 H(\xi)\,\xi d\xi \qquad (7)$$

Typical experimental conditions during the main time of the FRC formation correspond to the fully magnetized plasma. Using for the Eqs.(1) - (4) the asymptotic expressions for the kinetic coefficients in the limiting case $\Omega_e\tau_e >> 1$, $\Omega_i\tau_i >> 1$, one can see that the Ohmic heating is not the only important dissipative mechanism. Terms accounting for the transverse ion heat conductivity and for thermogalvanomagnetic effects are of the same order. The self-similar profiles $N(\xi)$, $H(\xi)$, $\Theta(\xi)$ can be obtained from the system of equations for both cases unmagnetized and fully magnetized plasma /6/

The time dependence of the self-similar solutions is determined by the dimensionless parameters χ and ζ. The case of negative χ corresponds to solution which describes the process similar to the "explosion" or collapse, when the radius, magnetic field, magnetic flux and other variables tend to zero or to infinity within a finite time interval. Here we shall consider solutions for a positive $\chi > 0$, which for particular values of parameter ζ are listed in

Table I. Regimes of self-similar dynamics of Θ-pinch plasma with classical transport coefficients.

$\zeta < -3/2$	Heating and compression with flux trapping with increase of the external magnetic field.
$-3/2 < \zeta < -5/4$	Heating and expansion with flux trapping with increase of the external magnetic field.
$-5/4 < \zeta < -1$	Heating and expansion with flux trapping with decrease of the external magnetic field.
$-1 < \zeta < 0$	Cooling and expansion with flux trapping with decrease of the external magnetic field.
$\zeta > 0$	Heating and compression with flux losses with increase of the external magnetic field.

From the self-similar ansatz it follows that all of MHD variables are proportional to the radial compression. It means that these solutions do not describe the very first phase of plasma motion, particularly because this phase is not self-similar. However, the time interval during the formation of the self-similar motion is much less then the characteristic time (half - period) of the external magnetic field. Magnitude of the magnetic field B_o, when the plasma motion attracts to self-similar solution, can be expressed in terms of the experimentally observed magnitude of the maximum radial compression. Using Eqs.(5)-(7) we find

$$B_0 = B_{max}\left(\frac{R_0}{R_{max}}\right)^{-(4\zeta_1+5)/(2\zeta_1+3)}, \qquad (8)$$

where $\zeta_1 < -3/2$ corresponds to the first phase, and B_{max} can be chosen as amplitude of the external magnetic field ignoring the small variation of the external field during the second phase. The magnitude of the magnetic field $B = B_1$, when the plasma is converted towards the discharge tube walls in course of the expansion phase from $R = R_{max}$ and the total trapped flux are

$$B_1 = B_{max}\left(\frac{R_0}{R_{max}}\right)^{-(4\zeta_2+5)/(2\zeta_2+3)}, \quad \Phi = \Phi_0\left(\frac{R_0}{R_{max}}\right)^{\left[(2\zeta_2+3)(4\zeta_1+5)^2-(2\zeta_1+3)\right]/(2\zeta_1+3)^2} \qquad (10)$$

where $-5/4 < \zeta_2 < 0$ corresponds to the expansion phase.

It follows from Eq.(10) that the main part of the magnetic flux is trapped during the expansion phase.

The possibile reason for magnetic flux losses during the Θ-pinch evolution before the phase of the FRC formation is the anomalous diffusion of the magnetic field due to anomalous resistivity of a turbulent plasma /2-4/. If plasma becomes turbulent during the first stage of compression it may be significant for the trapping and diffusion of magnetic flux. Using the self-similar solutions for turbulent plasma one can estimate the possible magnetic flux losses in course of FRC formation in this case.

We assume that the hydrodynamic equations retain their form, but the transport coefficients are changed. The classical collision frequency is to be replaced by some effective frequency ν_{eff} depending on the type of instability, which is responsible for turbulence. If the Buneman instability dominates the effective collision frequency is $\nu_{eff} = \text{const}\cdot\omega_{pe}$. Thus, we return to Eqs.(1)-(4) with the new expression for ν_m .Using self-similar variables we obtain the following expression for the time dependence of the radial implosion

$$\alpha(t) = 1 - \chi\,\frac{2\zeta+3}{\zeta}\,\frac{t}{t_0}, \qquad (11)$$

while Eqs.(5)-(7) retain their form. Eq.(11) demonstrates that the time dependence of the radial implosion is linear and it is independent of the time evolution of the external magnetic field.

Analysis of the possible regimes depending on values of the parameters χ and ζ is represented in Table II. It demonstrates that if plasma becomes turbulent with Buneman transport, loss of magnetic flux may occur during the expansion phase before the plasma has reached the discharge tube walls (these solutions correspond to $\zeta < -1$, $\chi > 0$). The peculiarities of the plasma dynamics for the case when plasma becomes turbulent with the Buneman transport are vanishing of the plasma density, and creation of hot plasma near the

axis at $\xi \to 0$, while the energy density N, Θ remains regular near the axis $\xi = 0$.

The model of the Bohm transport corresponds to the following expressions for the effective collision frequency, conductivity and electron heat conduction

$$\nu_{eff} = \text{const}\cdot\Omega_e, \quad \sigma = e^2 n/m_e\nu_{eff}, \quad \kappa = nT/m_e\nu_{eff}\,. \tag{12}$$

Taking into account Eq.(12) and introducing the self-similar variables, we find the time dependence for the dimensionless radial implosion and for the magnetic field in the following form

$$\alpha(t) = \left[1 - \chi\,\frac{4\zeta+5}{\zeta}\,\frac{t}{t_0}\right]^{(2\zeta+3)/(4\zeta+5)}, \quad B(t) = B_0\left[1 - \chi\,\frac{4\zeta+5}{\zeta}\,\frac{t}{t_0}\right]^{-1} \tag{13}$$

Eqs.(5) for the time dependence of n(t), T(t) and Φ(t) remain valid. The conclusion about the possible regimes depending on the value of the parameters χ and ζ remain here about the same as for the case of Buneman transport. Thus, for the Bohm transport loss of magnetic flux may also occur during the expansion stage.

Table II. Regimes of self-similar dynamics of Θ-pinch plasma with turbulent transport coefficients.

	$\chi > 0$	$\chi < 0$
$\zeta < -3/2$	Collapse, infinite increase of the external magnetic field and the trapped flux.	Expansion and flux losses with decrease of the external field
$-3/2 < \zeta < -5/4$	Buneman transport: expansion with flux trapping with increase of the external field Bohm transport: infinite expansion and flux losses with increase of the external field	Buneman transport: Collapse and flux losses with decrease of the external field. Bohm transport: Compression and flux trapping with decrease of the external field.
$-5/4 < \zeta < 0$	Expansion and flux trapping with decrease of the external field.	Collapse and flux losses with increase of the external field.
$\zeta > 0$	Collapse and flux losses with increase of the external field.	Expansion and flux trapping with decrease of the external field.

The obtained solutions show that the magnetic flux is trapped during the implosion phase when the external Θ-pinch field is subsequently raised and than it is about constant. The efficiency of the flux trapping is determined by the magnitude of the effective magnetic Reynolds number Rm_{eff} (ζ). During the expansion phase flux trapping is possible if the plasma is classical, and flux is lost during this phase if the plasma becomes turbulent. The amount of the trapped magnetic flux can be expressed in terms of the time of external magnetic field variation and the plasma column radial compression.

/1/ M. Tuszewski, D.P. Taggart, R.E. Chrien et al. , Phys. Fluids **B 3**, 2856 (1991).
/2/ M.I. Kutuzov, V.N. Semenov, V.F. Strizhov, Sov. J. Plasma Phys. **7**, 520 (1981).
/3/ S.O. Knox, H. Meuth, F.L. Ribe, E. Sevillano, Phys. Fluids **25**, 262 (1982).
/4/ J.C. Dooling, T.M. York, M. Niimura , J. Plasma Physics **43**, 419 (1990).
/5/ F.S. Felber, M.A. Liberman, A.L. Velikovich, Phys. Fluids **31**, 3675(1988).
/6/ A. B.Bud'ko, E.T.Karlson, M.A.Liberman, to be published.

STUDIES OF CURRENT DRIVE AND PARTICLE FLUX IN THE SPHEX SPHEROMAK

P.K.Browning, G.Cunningham, S.J.Gee, A.al-Karkhy, R.Martin, G.Roe
and M.G.Rusbridge
Physics Department, UMIST, Manchester M60 1QD, U.K.

The gun-injected spheromak SPHEX has been described in [1], in which it was shown that the plasma could be divided into the central column extending along the geometric axis between the central gun electrode and the pole of the flux-conserver, and the toroidal annulus surrounding it. The gun drives the central column directly; power is transmitted to the annulus by a coherent global oscillation at ≈ 20 kHz with n=1 symmetry. The electric field in the column is much larger than could be supported by the plasma resistivity alone; we shall show that the additional field is involved in driving the n=1 mode. In [1] we presented measurements of the associated Poynting vector, showing that the power flow reaches 10 MW/m^2 at the interface between column and annulus.

In the present paper we present probe measurements of the "dynamo" current drive $\langle \tilde{v} \times \tilde{b} \rangle$ and the particle flux $\Gamma = \langle nv \rangle$ associated with the n=1 mode; we also present results suggesting that there are significant temperature fluctuations correlated with those of density. The probe used for the dynamo and particle flux measurements is a development of that used for measurements of the Poynting vector described in [1]; the present probe contains three orthogonal magnetic pick-up coils and five standard Langmuir tips, arranged so that all three components of the electric field can be measured; alternatively, one pair can be used as a double Langmuir probe to measure the particle density. The arrangement of coils and tips is shown in fig.(1).

We seek to determine only the parallel component of the dynamo, $D_{||} = \langle \tilde{v} \times \tilde{b} \rangle . b_0$, where b_0 is a unit vector parallel to the mean field B_0. Only the normal component of velocity v then enters, so we may substitute $v = \tilde{E} \times B/B^2$ to obtain to second order

$$D_{||} = (\langle \tilde{E}.\tilde{b} \rangle - \langle \tilde{E}_{||} \tilde{b}_{||} \rangle)/B_0 = (\langle \tilde{E}_\perp \tilde{b}_\perp \rangle + \langle \tilde{E}_r \tilde{b}_r \rangle)/B_0 \qquad (1)$$

where $\perp$ denotes a component normal to B_0 and in the plane locally tangent to the flux surface. To determine the particle flux due to fluctuations, the four tips in the end face of the probe are used, one pair as a Langmuir probe biassed at about 2.2 T_e (which minimises the effect of temperature fluctuations [2]), and the orthogonal pair as an electric field probe oriented to determine the $E_\perp$ component.

Fig.(3) shows the measured particle flux along the equatorial radius of the flux-conserver (see fig.2). The fluctuations are large, but there is clear evidence for an outward flux of about 6 x 10^{22} ions/m^2sec from the central column into the annulus, and some evidence for an outward flux near the flux-conserver wall.

Fig.(4) shows the profile of $D_{||}$ along the equatorial radius. Each point is determined from averaging over a period of 400 μsec in the sustainment phase of the spheromak plasma and over 6 successive shots. The main feature is a strong peak in the central column, which is of opposite sense to the applied electric field. It derives principally from the second term in eq.(1); the first term is small everywhere except very near the axis, where by symmetry the two terms must be equal.

It has been shown [2] that temperature fluctuations correlated with those of density may be determined from the variation with bias of the current fluctuation level in a double Langmuir probe. A typical result is shown in fig.(5), where the experimental points fit well the theoretical curve for $\eta = -0.25$, where $\eta = (\tilde{T}_e/T_{e0})/(\tilde{n}/n_0)$ and subscript 0 denotes average quantities. (For comparison, a curve for the isothermal case $\eta = 0$ is also shown.) Thus, the temperature fluctuations are anti-correlated with the density.

In discussing these results we first consider the particle flux measurements. If we assume that the plasma content of the annulus is maintained entirely by the flow from the central column, we have $dN/dt = \Gamma A$, or in the steady state $N/\tau = \Gamma A$ where N is the total ion content of the annulus, τ is the particle confinement time, and A is the area of the interface between column and annulus. Taking the column to be a cylinder 0.15 m in radius by 0.4 m long, and a mean density in the annulus of 4 x 10^{19} m^{-3}, we obtain a particle confinement time of 200 μsec, similar to the observed decay time of the density after shorting the gun electrode.

The potential difference between the column and the annulus implies that the column is rotating [1]; as a result, the outward plasma flow will also carry angular momentum across the interface, contributing to the observed slow rotation of the annulus also described in [1]. The torque exerted on the annulus is given by $\mathbb{T} = \Gamma A m_i a^2 \omega$ where a is the column radius and $\omega/2\pi \approx 40$ kHz is its rotation frequency. From the observations we estimate $\mathbb{T} = 0.23$ Nm. This may be compared with the estimate of $\mathbb{T} = 0.03$ Nm obtained in [1] from the observed spin-down time of the annulus after shorting the gun and removing the current drive.

In the central column, the dynamo $D_{||}$ is about 350 V/m and directed pposite to the applied electric field E = -475 V/m; the net current drive -125 V/m is comparable to the -40 V/m estimated from the Spitzer esistivity [1]. Evidently the central column is acting as an electric otor, with $D_{||}$ representing its back e.m.f.; as described in [1], the pinning central column radiates power through the n=1 mode to drive urrent in the annulus.

It is of interest to examine whether the mode also provides a "dynamo" the annulus to drive the current there, where the D.C. electric field ust vanish. However, present results are not sufficiently accurate to give clear answer; with $T_e \approx 16$ eV and current density $j \approx 6 \times 10^5$ A/m^2 in the nnulus, the required current drive is about 10 V/m. The results in fig.(4) re of this order, but the level of correlation between $\tilde{E}$ and $\tilde{b}$ is only bout 0.1, and so both random and systematic errors must be considered efore we can be certain of the mechanism of current drive.

In any case, it seems unlikely that the n=1 mode can provide the urrent drive throughout the annulus, since [1] the power flow is totally bsorbed within a few cm of the interface. We have therefore considered an lternative possibility: as we have seen, there are temperature luctuations and therefore also fluctuations of conductivity $\tilde{\sigma}$. We also bserve a large parallel component of the fluctuating electric field $\tilde{E}_{||}$ due o the n=1 mode in the interface, with an amplitude reaching 2000 V/m. Thus, if these fluctuations are correlated, they will drive a D.C. current given by $j = \langle \tilde{\sigma}\tilde{E}_{||} \rangle$. While this is at present speculative, we hope in future experiments to measure the effect definitively.

In conclusion, we have definitely observed the dynamo process which provides the back e.m.f. necessary to oppose the large electric field along the geometric axis, confirming the speculation in [1] that this large field drives the n=1 mode and thus radiates power into the annulus; we have also observed a substantial flux of plasma from the column into the annulus, and have shown that this flux is more than sufficient to maintain the observed toroidal rotation of the annulus; and we have shown that there exist temperature fluctuations in the plasma and have proposed a mechanism of rectification of the n=1 mode power based on their existence.

References:

[1] P.K.Browning et al, Phys.Rev.Lett. 68, 1718 (1992)

[2] D.C.Robinson and M.G.Rusbridge, Plas.Phys. 11, 73 (1969)

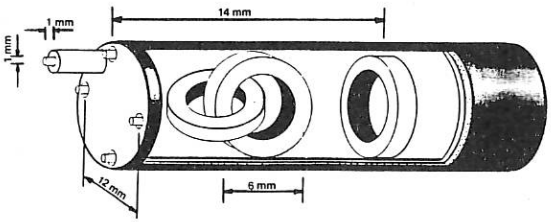

Fig. 1 Schematic of the particle flux and dynamo probe

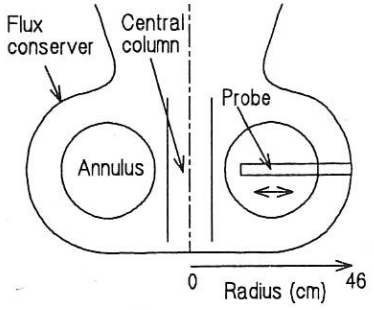

Fig. 2 Flux conserver schematic, showing the radial traverse of the probe

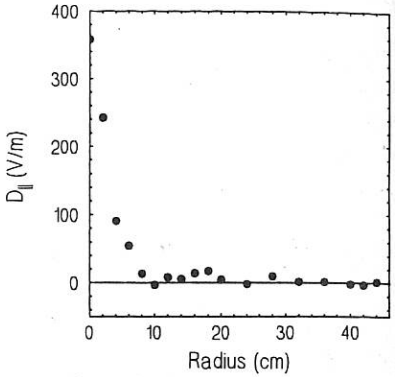

Fig. 4 Distribution of the "dynamo" $D_{||}$ along equatorial radius

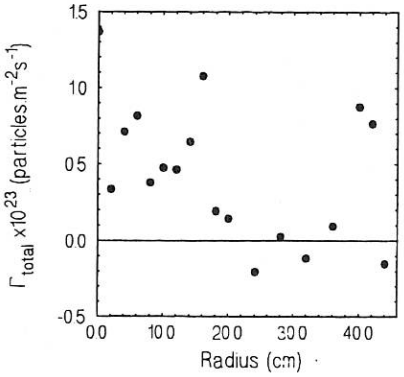

Fig. 3 Measured particle flux along traverse shown in fig. 2

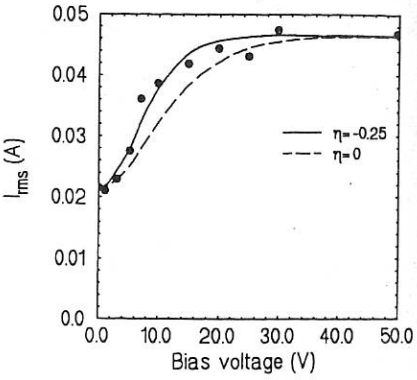

Fig. 5 RMS probe current fluctuation level as a function of probe bias voltage

TOROIDAL CURRENT ENHANCEMENT WITH STRONG POLOIDAL PLASMA CURRENT DRIVE IN FBX-II SPHERICAL TORUS

Masaru IRIE

WASEDA UNIVERSITY

3-4-1 Ohkubo , Shinjuku, Tokyo 169, JAPAN

1. INTRODUCTION The FBX is designed to study an ultra-low aspect ratio plasma, Spherical Torus. The current device FBX - II /1/ has a spherical vacuum chamber / shell with 1.6 m in diameter and can accommodate a plasma with a cross section of 60 mm x 60 mm and aspect ratio of 1.6. The plasma current can be driven both toroidally and poloidally with mechanicaly simple " Split Coil " system which also supply toroidal multipole field with local average minimum field , Min-B.

This plasma dimension is virtually the same as the largest spheromaks. However mainly because of the existence of toroidal field coils - even though they are slim enough to be accommodated within a flux hole of a spheromak plasma - she is free from major spheromak instabilities against tilting and shifting.

A small magnetized plasma gun injects a seed plasma into this toroidal multipole field and settles down in Min-B region. In this way initial plasma density has strong spatial dependence. After this phase, a main plasma is activated solely inductively . This start up method does not allows a plasma to contact to any materials inside the plasma chamber.

2. EXPERIMENTAL ANALYSIS Experimentally obtained plasma profiles are analysed and classified with an aid of Grad - Shafranov equation in cylindrical co-ordinates in a form reported by Kondoh et. al /2/.

$$\left(\frac{\partial^2}{\partial R^2} - \frac{1}{R}\frac{\partial}{\partial R} + \frac{\partial^2}{\partial z^2} \right) \phi = -2\pi\mu_0 R \left(j_{\perp t} + j_{\parallel t} \right)$$

, where:

$$j_{\perp t} = 2\pi R \frac{dP}{d\phi} \quad ; \quad j_{\parallel t} = \frac{dI}{d\phi} Bt$$

$$jp = \frac{dI}{d\phi} Bp$$

When a plasma is operated in far slower time scale than Alfven transit time, " a force free partially relaxed state model " are often used for simplicity , which neglects the effect of pressure.

$$P = 0$$

Because of this strong localization of the seed plasma, ordinary selection of current flux function has some difficulty. In order to solve this problem we adopted a current profile configuration including a region of plasma outside the separatrix /3/, unlike some idealized equilibria which require a cutoff of a plasma at the separatrix . Throughout our experiment looking for toroidal current drive efficiency, we reached simple and efficient model for a current flux for our plasma configuration. This model is

$$I = I_0 \left(1 - \left| \left(\phi - \phi \right) / \phi_{max} \right|^{\alpha} \right)$$

where I_0 is a value of I (current flux function) on ϕ_{max}.
Here a current profile itself is defined and the shape factor α is effective to dominate flux profiles and not too sensitive to minor exper imental errors. The operation window is established with a guideline obtained from these analysis, which will be published elsewhere /4/.

3. EXPERIMENT In the process of experiments , new operation window is found for toroidal plasma current drivre, where toroidal current is more efficiently driven under strong poloidal plasma current condition, rather than under steady toroidal field condition like TOKAMAK type operation. An experimentaly found optimum " Poloidal " plasma current is over 400 kA in its peak and toroidal plasma current is nearly doubled to reach 100 kA.

In Fig. 1. time history of current (in A T) in toroidal and ohmic heating / multipole coil current (I_{OH}) as well as a poloidal plasma current(I_{PT}) is shown. In this mode of operation, toroidal field coils and ohmic heating coils are interconnected in series and toroidal coil has 4.5 times larger AT to drive poloidal plasma current.

A plasma current starts 0.3 ms after the poloidal field flux swing, and ramps up for 0.6 ms. After this stage, the toroidal plasma current decreased with a time constant of 0.2 ms when e. m. f. activated by ohmic heating coils in the reverse direction to drive the toroidal plasma current.

The poloidal profiles of the plasma is shown in Fig. 2 with two different shape factors (α = 2 on the upper side and α = 3 on the lower side). In these figures equilibrium field coils which makes the spherical shell surfaces as the main separatrix even after the shell skin time , are abbreviated to avoid complexity. FBX-II is symmetrical to its horizontal axis. Four internal coils which is used as both multipole field coils and ohmic heating coils , are installed vertically. In the figure, two sections of six toroidal field coils / rods are displayed parallel to the symmetric axis as well.

In Fig. 2. a. vacuum field is shown at 0.25 ms after the flux swing. Typical quadrupole field is seen here. After this stage a toroidal plasma current (I_{PT}) ramps up to the nominal value. In Fig. 2. b. at 1.0 ms, the plasma suffers strong field reversal caused by both toroidal and poloidal coil currents . The effect of the shape factor is fairly clear especially in the posotion of the magnetic axis of the plasma.

4. CONCLUSION Global characteristics of the FBX - II plasma is classified with the help of newly developed current flux model in this field. Typical operation regime is introduced and the validity of the shape factor is demonstrated. In this way new operational window for FBX experiment is found which has helical plasma current with high shear.

ACKNOWLEDGMENTS The author is grateful to experimental support of current and former members and students in our laboratory, especially Dr. N. Saitou, Mrs. H. YOSHIKAWA, H. Sonehara, H. KUSAMA and H. SOMEI.

This work is partially supported by the following organizations.
Ministry of Education (Grant in aid for science and engineering),
Institute of Electromagnetic Application Research,
Science and Engineering Research Institute, Waseda University

REFERENCES

/1/ M. Irie et al., 17th EPS Conference on Controlled Fusion and Plasma Heating : ECA 14B, 626 (1990)

/2/ Y Kondoh et al., J. Phys. Soc. Japan 53, 3427, 1984

/3/ DC Barnes et al., Proc. III Symp. Phys. Tech. Compact Toroids Mag. Fus. Energy. Prog.: 134 (1980)

/4/ M. Irie, to be published

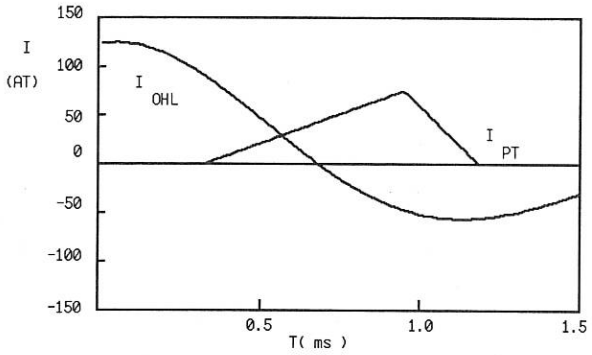

Fig. 1 : Schematic diagram of ohmic heating coil current (I_{OHL}) waveforms and toroidal plasma current (I_{PT})

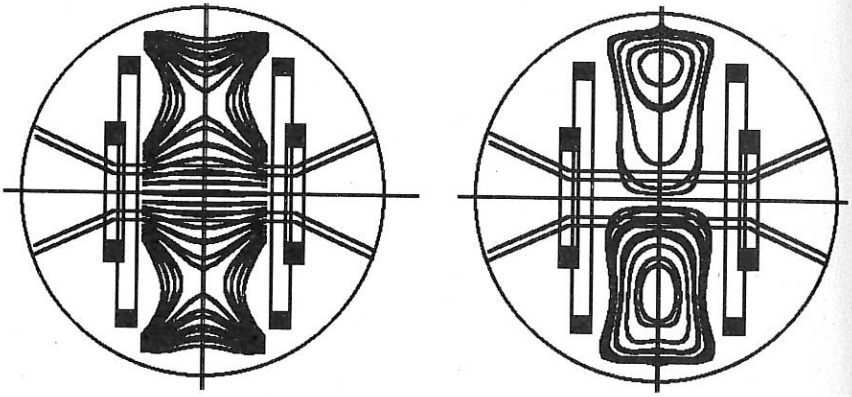

Before plasma current initiation (0.25 ms) Fig. 2. a.

Compressional phase (1.0 ms) Fig. 2. b.

Fig. 2. Schematic diagrams of the plasma flux contours with FBX ohmic heating/ multipole field coils. Part of toroidal field coils are displayed. α=2 on the upper side and α = 3 on the lower side of each diagram.

PARAMETRIC INVESTIGATION OF THE ROTAMAK DISCHARGE IN A 10-LITRE SPHERICAL VESSEL

N. Donaldson, R. Hahnheuser, I.R. Jones, G. Staines and S. Xu

School of Physical Sciences, Flinders University
G.P.O. Box 2100, Adelaide 5001, AUSTRALIA

The Rotamak Apparatus and Experimental Procedure

The rotamak is a compact torus device in which a rotating magnetic field (RMF) is used to generate and maintain the toroidal plasma current. Descriptions of prior work undertaken in the area of rotamak research, both experimental and theoretical, can be found in /1/ and the references contained therein.

The rotamak device used in the experiments consisted of the following components:

- a spherical Pyrex vessel of 28 cm inner diameter fitted with side arms, a vacuum system and access ports for probes,
- a 2-channel RF system capable of producing 40 msec duration pulses of 0.5 MHz oscillations. The waveforms of the pulses were programmable and the oscillations in the two pulses were dephased by 90°. The RMF was produced by feeding these two pulses to a pair of orthogonally oriented coils,
- a pair of circular coils and a suitable DC power supply to produce the required equilibrium magnetic field. In this paper, this field is characterised by its amplitude, B_v, at $r = z = 0$ *in the absence of plasma* (cylindrical coordinates (r, ϕ, z) with the origin at the centre of the discharge vessel).

The characteristics of the plasma/field configuration produced in a rotamak device are determined by the filling pressure of the working gas, p ; the amplitude of the equilibrium magnetic field, B_v ; the total available RF power, P_{max}. For these experiments, $p = 4 - 16$ mTorr H_2 and $B_v = 0 - 110$ gauss. RF pulses having a large power for the initial 5 msec of the pulse followed by a lower, constant power output for the remaining 35 msec were used. The expectation was that the initial high power level would assist in the ionization of the fill gas. Three levels of P_{max} were used for the 35 msec, constant power portion of the RMF pulse: 111 kW, 165 kW and 232 kW. Note that each RF channel provided just half of this total available power. The two RF channels were connected to the RMF coils by the circuit shown in Fig 1. Here, L ($\sim 220\mu$H) is the vacuum inductance of one of the RMF coils, $R_c (= 2.5\Omega)$ is its resistance, C is a series capacitor used to tune out the inductive impedance and R_p represents the antenna loading due to the presence of plasma. The coils marked M are decoupling coils which are used to cancel out the small

amount of mutual inductance which inevitably exists between the nominally orthogonal RMF coils.

The presence of the plasma introduces the loading R_p and decreases the value of L from its vacuum value by an amount ΔL, say. Both R_p and ΔL varied from the time at which the RMF was triggered ($t = 0$) until the steady-state discharge was attained at about 15 msec. In all rotamak experiments undertaken to date, the tuning capacitor C has been used to cancel the inductive impedance presented by $(L - \Delta L)$ at $t = 20$ msec. *i.e.* the tuning of the circuit has always been made for the steady-state situation.

The circuit and plasma parameters presented here were all obtained at the fixed time of $t = 20$ msec *i.e.* for the steady-state discharge.

Current Drive in the Rotamak Discharge

The values of driven toroidal current I_ϕ (at $t = 20$ msec), obtained for a large selection of (p, B_v, P_{max}), are plotted versus B_v in Fig 2. This diagram shows that I_ϕ is primarily determined by B_v and that, to a good approximation, I_ϕ varies linearly with B_v.

We observe that for a given P_{max}, it is not possible to establish a rotamak discharge if B_v exceeds a certain critical value, B_{vc}. The reasons for this is not yet understood.

Fig 3 shows a plot of P_p, the RF power dissipated in the plasma (*i.e.* in the two resistors, R_p, of the equivalent circuit) versus I_ϕ. Two features are worthy of note. Firstly, by increasing the value of P_{max}, it is possible to increase B_{vc} and the corresponding maximum driven current, I_ϕ^{max}. It is also possible to increase B_{vc} by increasing the filling pressure at a fixed value of P_{max}; this trend is especially noticeable in the change from 4 to 8 mTorr. From the current drive viewpoint, the scaling of I_ϕ^{max} with P_p is pessimistic ; the fitted curve is parabolic. Secondly, it is clear that, provided P_p is larger than a certain minimum value, a range of discharges can be generated which have the same driven current but widely different RF power dissipation.

The Rotamak Discharge as a Circuit Element

Fig 4. shows the equivalent circuit for one RF channel at $t = 20$ msec. The maximum available power (for one channel), $P_{max}^{(1)}$, is:

$$P_{max}^{(1)} = \frac{P_{max}}{2} = \frac{\hat{V_0}^2}{8R_G}$$

The corresponding values of ($P_{max}^{(1)}$ (watts); R_G (Ω)) for the three levels of P_{max} used are : (55,000 ; 20.0) ; (82,500 ; 20.4) and (116,000 ; 22.8).

The measured peak values of the coil current, $\hat{i}$, are plotted versus the measured values of R_p in Fig 5 for discharges having different (p,B_v,P_{max}) combinations. Circuit theory

yields the following relationship between $\hat{i}$ and R_p:

$$\hat{i} = \frac{\sqrt{8R_G P_{max}^{(1)}}}{(R_G + R_c + R_p)}$$

The calculated curves obtained using the above three combinations of $P_{max}^{(1)}$ and R_G are shown in Fig 5 ; there is good agreement between theory and data.

The measured RF power deposited in the plasma from one channel, $P_p^{(1)}$, is plotted versus $\hat{i}$ in Fig 6 for a variety of discharges having different (p, B_v, P_{max}). Circuit theory yields the following relationship between $P_p^{(1)}$ and $\hat{i}$:

$$P_p^{(1)} = \hat{i}\sqrt{2R_G P_{max}^{(1)}} - \hat{i}^2 \frac{(R_G + R_c)}{2}.$$

Curves calculated using the above three combinations of $P_{max}^{(1)}$ and R_G are shown in Fig 6 and, again, there is a good agreement between theory and data. This agreement between circuit analysis and data leads us to believe that we have measured the important RF quantities, $\hat{i}$, R_p and P_p, in an accurate and self-consistent manner.

Fig 7 sheds some light on our inability to obtain rotamak discharges for B_v-values larger than a critical value, B_{vc} (for a given value of P_{max}). In this graph, the ratio $\frac{B_\omega}{B_v}$ is plotted versus I_ϕ for a large variety of discharges. Here, B_ω is the amplitude of the applied RMF, calculated from a knowledge of $\hat{i}$ and the geometry of the RMF coils. We see that rotamak discharges cannot be maintained if the ratio $\frac{B_\omega}{B_v}$ drops below ~0.45.

Rotamak Plasma Parameters

Fig 8 shows the line-averaged electron number density, $< n_e >$, measured across a diameter in the $z = 0$ plane by means of a 4.3 mm microwave interferometer, plotted against the total RF power dissipated in the plasma, P_p. $< n_e >$ is seen to be approximately proportional to P_p, regardless of the initial values of p and B_v.

The electron temperature, measured using a double Langmuir probe, was found to be spatially uniform and it increased only slightly with increasing values of P_p. T_e lay in the range 11 ± 2 eV for all the discharges investigated.

/1/ I.R. Jones, *Small Plasma Physics Experiments II* (World Scientific, Singapore, 1990) pages 3-51.

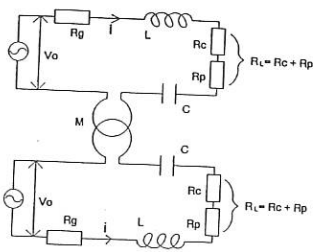

Fig. 1

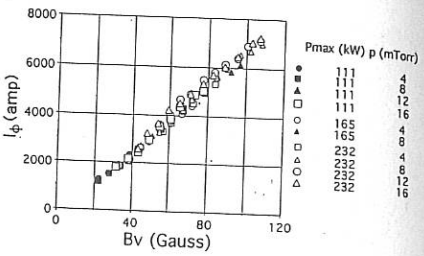

Fig. 2

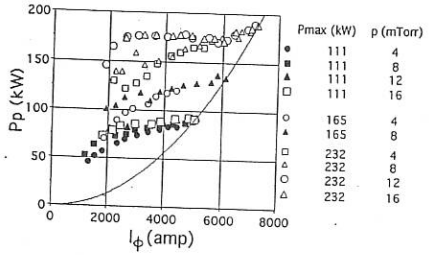

Fig. 3

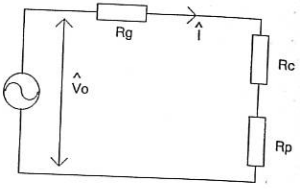

Fig. 4

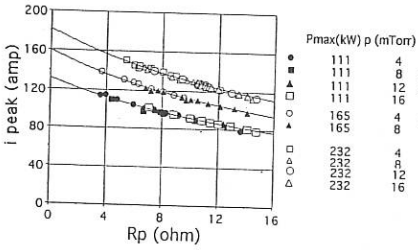

Fig. 5

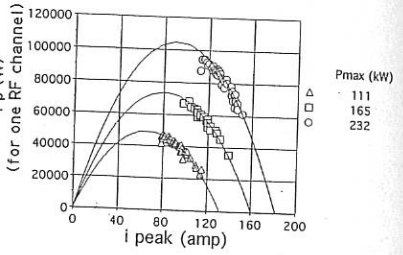

Fig. 6

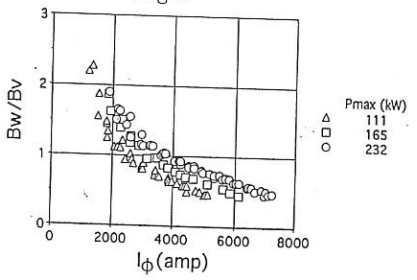

Fig. 7

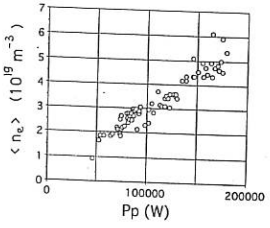

Fig. 8

AN ALTERNATIVE CONFIGURATION OF AXIALLY PINCHED SPHERICAL TORUS

S.Sinman and A.Sinman*
Electrical and Electronics Engineering Department,
Middle East Technical University, 06531
*Nuclear Fusion Laboratory, Nuclear Research Center,
Turkish Atomic Energy Authority, 06100
Ankara - TURKEY

INTRODUCTION

The spherical torus is a very small aspect ratio (A<2) confinement concept obtained by retaining only the indispensable components such as the toroidal field coils imboard to the plasma torus. The general class of spherical tori which includes the spherical tokamak (q>1), spherical pinch (1>q>0) and spherical RFP (q<0) have magnetic configurations unique in comparison with conventional tokamak and RFPs.

In this study, a conceptual design developed for a new spherical pinch system is presented. The numerical model at that of the design is the composition based on the methodes and principles of such as z-pinch, shock heating and the Peng's and Taylor's papers on the features of spherical torus plasma [1] and the current drive by helicity injection [2].

DESIGN CONSIDERATION

In order to generate compact toroids (CT), together with the conventional system components such as spark gap switches and capacitor bank etc., the different types of magnetically driven plasma guns are used. For this conceptual design of spherical torus the C-gun is very convenient.

The C-gun is a novel and alternative version of conventional magnetically driven plasma gun with a very high helicity injection efficiency. The vertical two electrodes placed on the toroidal plane of flux conserver facing each other and the back strap at the outside of it are the main structure of the C-gun and it has successfully been used on our previous experimental studies on CTs [3]. In principle, this system proposed is composed by 20 C-guns placed around the flux conserver symmetrical with respect to the z axis.

The pre-determined system parameters are as follows: for strongly paramagnetic configuration, the pinch parameter of $F=\langle B_t\rangle_s/\langle B_t\rangle_v$ is about 0.3-0.42; the toroidal magnetic helical pitch $T=\langle B_p\rangle_s/\langle B_t\rangle_v$ is in the range of 1.2-1.4; the aspect ratio A=1.2; the safety factor at the edge q(a), is between 0.6-0.8; the energy level of capacitor bank per gun is 226 kJ; the charging voltage is 95 kV; the loop current per gun is 500 kA; the form factor of elliptically shaped plasma at the center is 6.25; the aspect ratio of pushed plasma belt is 4.67; the overall efficiency is 0.28 and the radius and height of flux conserver are 35 cm and 50 cm respectively. This values have been selected for the operating gas of He at the pressure range of 0.1-0.3 Torr.

Therefore, all of pre-determined system parameters are very realistic.

FORMULATION

The magnetic field configuration at the model of conceptual design combined with our previous experimental results [3] are very complex.

The toroidal and poloidal current components of the belts pushed toward the center (see next paragragh) are translated into poloidal and toroidal magnetic fields. After the reconnection, the closed magnetic surfaces are formed in axial and radial directions.

In this study; a generalized analytical model is not concluded, but as it is seen at the results of numerical model, phases and the phenomenon of the belts pushed toward the center which are simultaneously produced by all of the C-guns are very different. In this procedure, the analytical model must be time varying. On the other hand, the mentioned phases depend on the self organization process.

For this reason, the numerical model of conceptual design is a composition of some well known principles. The given expressions are in drived forms.

The electron temperature of plasma belts produced by the C-guns and pushed toward the center of flux conserver, as is evaluated in Ref. [4], is given by the alternative form of

$$T_e=[eM/3K(3Mm)^{1/2})]\{(E/p)/P_c[1+(2.405/R_{wb})/P_cp]\}$$

where T_e is shock heated electron temperature, e is the electronic charge, m and M are the electron and ion masses, k is Boltzmann constant, E is the electric field of C-gun at poloidal frame, p is operating gas pressure, P_c is the collision probability and R_{wb} is the distance between the belt and wall of the flux conserver.

The helicity injection [2,5], can be applied to the C-gun. In this case, the helicity existence rate is

$$dK/dT_p=2[V_{cg}(Bs)_{ex}-\mathbf{E}.\mathbf{B}]$$

where T_p is operating half period of the C-gun, V_{cq} is the voltage applied to the C-gun, $(Bs)_{ex}$ is net flux on the area framed by the plasma belt and flux conserver. The first term represents the injection of helicity and the second term is its resistive dissipation.

From the pressure balance, for the plasma column compressed at the center, the plasma temperature may be written as

$$T_i(0)+T_e(0)=(\text{reduced beta})B_t^2(0)/4C_0N_e(0)k$$

where the reduced beta=$\langle\text{beta}\rangle_v^t\langle\text{beta}\rangle_v^p/(\langle\text{beta}\rangle_v^t+\langle\text{beta}\rangle_v^p)$, $B_t(0)$ is magnetic field density of 20 C-guns at the center, C_0 is permeability of free space, $N_e(0)$ is the central total electron density and k is Boltzmann constant.

At the system proposed; in the flux conserver, one of the operating gases of He, D and H in the pressure range of 0.1-0.3 Torr are used and the C-guns are triggered all together in this neutral gas medium. Thus the Axially Pinched Spherical Torus (APST) which has produced at the center of flux conserver will be surrounded by a gas mantle. On the other hand, the E-layer produced by the energetic helical electrons, will transform into a concentric geometry with the APST. Because of the reconnection, due to the pinch current and the poloidal field of E-layer are parallel each other, APST will be translated into the Taylor's force free mode. For this reason, this system is very different from the conventional z-pinch.

In the stability and equilibrium parameters of FRC, using the transformation of current and flux vectors, one can write $<beta>_v=1-1/2(r_s/r_w)$. As it can be seen in this expression, the volume averaged beta is independent from the pressure profile. Here, r_s and r_w are the radia of seperatrix and flux conserver respectively.

The energy confinement time can be written in the form of

$$t_E=W_3/[P_{12}+P_4-(dW_{12}/dt_{12}+dW_4/dt_4)]$$

where W_1 and W_2 are the plasma storage energies in the belts by shock and ohmic heating respectively, $W_3(W_1,W_2,W_4)$ is the plasma storage energy in central plasma column at equilibrium mode by axially pinching, P_{12} is the input power, P_4 is the additional heating power by current drive, t_{12} is the replacement time and t_4 is the sustainment time.

RESULTS

By means of spark gap switches which are triggered at the same time, the plasma belts containing the shock and ohmic heated electrons (1.24 keV and $5x10^{16}$ cm^{-3}) are pushed toward the center all together by the Lorentz forces. The shock and ohmic heated thermal electrons, interacting with the self generated toroidal magnetic field, under different angles with respect to the magnetic field vector, move on the alternative helical orbits having various pitches. Thus in the first 5 us which is the half period of the C-gun , the system arrives into equilibrium state and the current channel confines itself by reconnecting the toroidal field of helices and the poloidal field of the long pitches. The rise time of the guns' loop current are about 2-3 us and the operating half period of the guns are between 10 us and 12 us. After 6-7 us from the triggering of spark gaps, hot belts come together at the center of flux conserver and hence the central cylinderical current channel of 4 cm in diameter and 25 cm in length which is composed by 20 guns' loop currents (10 keV, 10-12 MA and $2.86x10^{18}$ cm^{-3}) are collapsed by the self generating toroidal magnetic field and then it converts into an elongated hot and dense spherical torus.

CONCLUDING REMARKS

The main points achived on this study have been: i) The energies and densities of thermal and mono energetic electrons in the belt produced by the C-gun are very important parameters for the reconnection phase. Expected values must be in the ranges of U_e=25-100 eV and $\langle n_e \rangle = 10^{16}$-$10^{17}$ cm^{-3}. In this case due to the self organization process the reconnection probability is about 80 %; ii) It has been supposed that the self generated toroidal and poloidal magnetic field productions and the reconnection come into existance together with the magnetic helicity injection. The experimental data of the C-gun has verified this mechanism; iii) The analytical model of equilibrium and the stability conditions of FRC may be applied to this proposed APST. For this purpose in that model, the transformation between the azimuthal and axial current densities are necessary; iv) Selecting the geometry of flux conserver (radius and height) and the distance between the electrodes and the electrical characteristics of C-gun, to control of the elongated plasma is possible; v) The volume averaged beta is about 0.78-0.98 and the global energy confinement time is 4-5 us; vi) As the belts are pushing towards the center, the D shapes will change. In the equilibrium phase, the toroidal flux at the inside of toroid will become $CN_gI_z \, Ln(R_o+a/R_o-a)$ where C is a shaping constant, N_g is the number of C-guns, I_z is the closed axial loop current of toroid, R_o is the major radius to magnetic axis of the elongated plasma and a is value of r at plasma surface. As it is clearly seen here, the strong paramagnetism at the pinch phase will be demonstrated with a non linear property.

REFERENCES

[1] PENG,Y.K.M., STRICKLER,D.J., Nuclear Fusion 26 (1986)769.
[2] TAYLOR,J.B., TURNER,M.F., Nuclear Fusion 29 (1989) 219.
[3] SINMAN,S.,A,SINMAN.,Plasma Physics and Controlled Nuclear Fusion Research 1986 (Proc. 11th Int. Conf. Kyoto, 1986) Vol.2, IAEA, Vienna (1987) 731 and TCMs on Research Using Small Tokamaks, Nice-France 1988 and Arlington-Virginia-USA 1990,IAEA, TECDOC-519 (1989) 185 and IAEA, TECDOC-604 (1991) 181.
[4] BROWS,S.C., in Introduction to Electrical Discharges in Gases, John Wiley and Sons, Inc., New York (1966) Chap.6.
[5] JENSEN,T.H., CHU,M.S., Phys. Fluids 27 (1984) 2881.

CENTRALLY PEAKED TEMPERATURE PROFILES DUE TO THE ETTINGHAUSEN EFFECT

M. G. Haines and J. P. Chittenden

Blackett Laboratory, Imperial College of Science, Technology and Medicine, London SW7 2BZ, United Kingdom.

Abstract

A two temperature one−dimensional Z−pinch plasma is modelled close to equilibrium. A full set of transport coefficients is employed which includes both the Ettinghausen heat flow (the inward radial electron heat flow in the direction of $\underline{J} \times \underline{B}$) and the Nernst term in Ohm's law (where a radial temperature gradient can affect the axial current distribution). One of these effects is almost always important, and together they cause any positive radial temperature gradient (e.g. caused by a skin effect) to nbe reduced or reversed. Centrally peaked temperature profiles can the occur. These effects are also instrumental in the preferential inward drift of the collisionless high energy tail, and the subsequent formation of a runaway electron beam with singular orbits on the axis of the Z−pinch.

1.Introduction

It is very usual for the cross phenomena that are contained in the full Ohm's law and electron heat−flux equations of Braginskii (1957), especially those orthogonal to the driving force and the magnetic field, to be ignored in theoretical models. Two of these terms are present even in a one−dimensional description of a magnetically confined plasma, and exist purely because of the velocity dependence of the collision frequency. One term describes the inward electron heat−flux in the direction of $\underline{J} \times \underline{B}$ (the Ettinghausen effect) while the other is a term in the direction of $\nabla T \times \underline{B}$ in Ohm's law (the Nernst effect).

2. One−dimensional transport

Employing the notation of Braginskii, the radial component of electron heat−flux for a symmetric Z−pinch with only radial dependence of variables is

$$q_{er} = - \kappa_{\perp e} \frac{\partial T_e}{\partial r} - \frac{T_e}{e} \beta_\wedge J_z \qquad (1)$$

where the transport coefficients are given by the more accurate results of Epperlein and Haines (1986). The term with coefficient $\beta_\wedge$ is the Ettinghausen effect. The ratio R_1 of this term to the cross−field thermal conduction in the limit of $\omega_e\tau \to \infty$ is

$$R_1 = \frac{J_z B_\theta L_T \beta_1''}{n_e T_e c \, \gamma_1'} \qquad (2)$$

where L_T is the scale−length of the temperature gradient. For an ionic charge of $Z=1$ Epperlein and Haines give $\beta_1''= 1.5$ and $\gamma_1'= 4.66$. If furthermore there is pressure balance, and if the scalelength L_T is equal to the pinch radius a, the ratio of terms, R_1, is approximately 2/3. Under such conditions the Ettinghausen effect cannot be neglected.

Of course, the cross-field ion thermal conductivity is larger by the ratio $(m_i/m_e)^{\frac{1}{2}}$, but if the electron and ion temperature temperatures are sufficiently decoupled the electron temperature distribution will be determined significantly by the Joule heating, by the electron heat-flux, and hence also by the Ettinghausen effect. In a Joule-heated Z-pinch under pressure balance at constant radius Haines (1982) showed that this decoupling depends only on the line density N; the decoupling is stronger at low N.

Ohm's law can be written as

$$E_z + \frac{v_r B_\theta}{c} = \frac{\alpha_\perp}{n^2 e^2} J_z + \frac{\beta_\wedge}{e} \frac{\partial T_e}{\partial r} \qquad (3)$$

where we note that the coefficient for the Nernst effect is identical to the Ettinghausen coefficient in Eq(1), i.e. it obeys Onsager's relation.

The ratio R_2 of the Nernst term to the perpendicular resistivity term is

$$R_2 = \frac{n_e T_e c \ \beta_1''}{L_T \ J_z B_\theta} \qquad (4)$$

for $\omega_e \tau \to \infty$. We can see that R_2 depends inversely on the parameters in Eq (2) for R_1. Indeed R_2 is approximately $0.5/R_1$. It follows therefore that if the Ettinghausen effect is small ($R_1 \ll 1$) the Nernst term is large ($R_2 \gg 1$). In a situation where $L_T \simeq a$ and there is pressure balance we have R_1 and R_2 of order 1, and neither term can be neglected.

We now consider a one dimensional simulation of a Z-pinch with and without these two effects

3. Numerical simulation

A one-dimensional, time-dependent, two-temperature MHD code was employed, and run in time until an almost self-similar set of profiles was obtained. The examples presented here are for a relatively high line density N of $10^{20} m^{-1}$ where it might have seemed a good approximation to put $T_e = T_i$ and to neglect the cross-phenomena being considered here. Figure 1 shows radial profiles of electron and ion temperature for the two temperature model *without* the $\beta_\wedge$ terms. We note that T_e is very strongly decoupled near the surface of the pinch where the density is low. (The density profile is approximately parabolic, and goes to zero at r/a = 1.) Elsewhere in Fig.1 we find T_e is almost exactly equal to T_i, and that both temperatures increase with radius.

Figure 2 illustrates the same case but *with* the $\beta_\wedge$ terms included. There is a remarkable difference. The almost singularly high electron temperature at the surface of Fig.1 has almost completely been eliminated, and both T_e and T_i have maxima at the axis, albeit rather weak for this high line density. These results will have a profound effect, reducing the onset of micro-turbulence markedly.

The current density distribution under the same two conditions is shown in figure 3. *Without* the cross-phenomena there is an almost singular skin effect, though not arising from the usual electromagnetic skin effect because there is only a weak skin effect for the electric field for an evolving Joule-heated equilibrium (Haines, 1960). This high surface current density arises essentially because of the high electron temperature: Indeed each drives the other in a thermal instability. *With* the cross-phenomena included we find that not only is the current density reduced near the surface because of the reduction of electron temperature, but $\partial J/\partial r$ actually becomes negative because of the effect of the residual positive electron temperature gradient (Fig.2) in the Nernst term. In both cases there is a local rise in J_z near the axis where $\omega_e \tau$ becomes less than 1, with a consequent reduction of perpendicular resistivity.

4.Runaway electrons

The essential physics behind the Ettinghausen effect is that the relatively hot and collisionless electrons experience the axial electric field E_z (set up to drive the axial current). In the presence of the azimuthal magnetic field B_θ, these electrons have a guiding-centre drift, cE_z/B_θ, radially inwards towards the axis. On arriving within one Larmor radius of the axis they will change their motion to singular orbits (Haines, 1978), and move along the axial direction with their full velocity. In the presence of the axial electric field they will be able to run away if the Dreicer condition for them is satisfied. The off-axis electrons that are magnetised are unable to run away, but instead the high energy tail is preferentially filtered to the axis by the drift motion described above.

5.Conclusions

We have shown that the combined effect of the Ettinghausen and Nernst cross-phenomena is to drastically reduce the high electron temperature and current density in the low-density coronal plasma near the surface of the Z-pinch, and instead a maximum temperature occurs on the axis. This is because of the inward heat-flow in the direction of $\underline{J} \times \underline{B}$. The Nernst effect causes a reduction in current density near the surface where there is a weak positive temperature gradient.

REFERENCES

Braginskii,S.I.,Zh. Eksp. Teor. Fiz.**33**, 459 (1957)
Epperlein,E.M.,Phys.Fluids **29**, 1029 (1986)
Haines,M.G.,Phys.Scripta T2/2, 380 (1982)
Haines,M.G.,Proc.Phys.Soc. **76**, 249 (1960)
Haines,M.G.,J.Phys.D: Appl. Phys **11**, 1709 (1978)

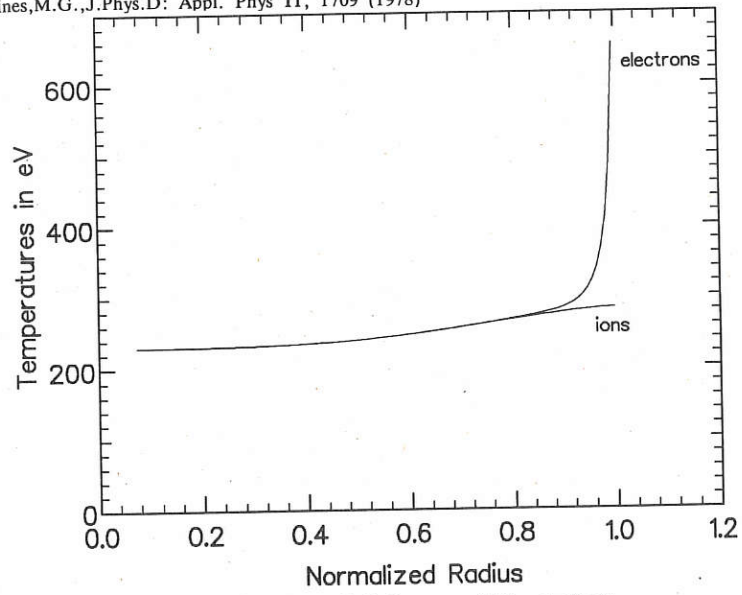

Figure 1. Temperature profiles without Ettinghausen and Nernst effects.

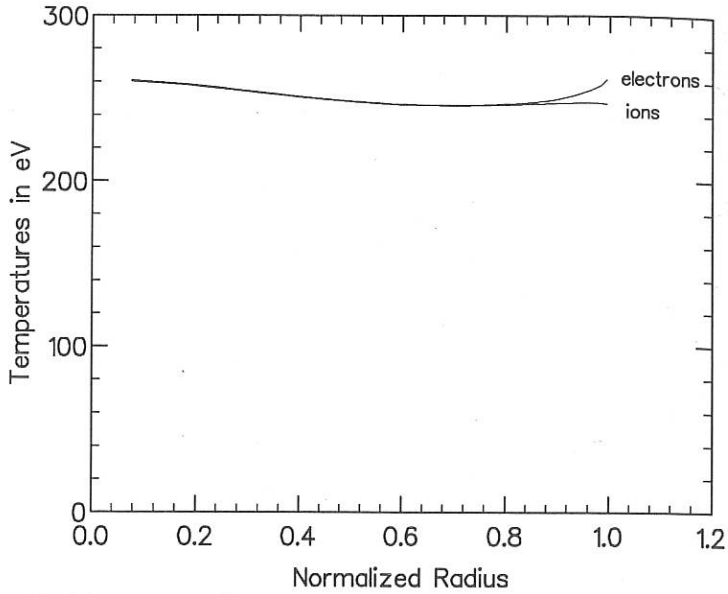

Figure 2. Temperature profiles with Ettinghausen and Nernst effects.

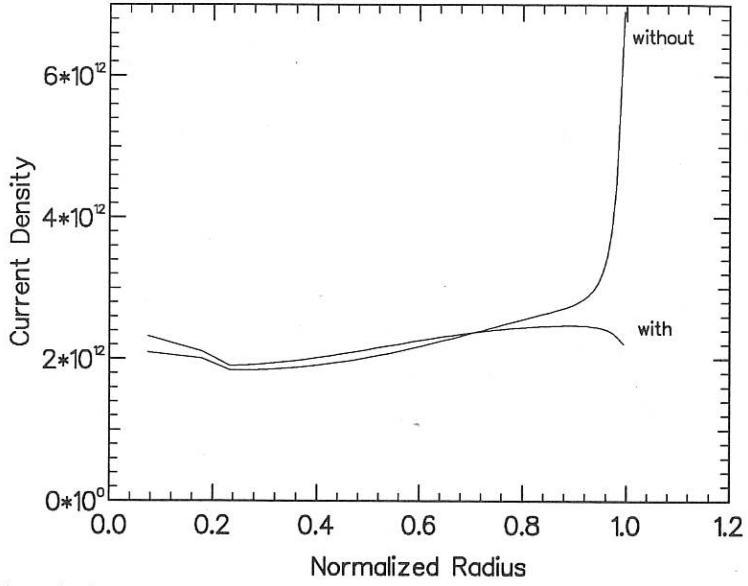

Figure 3. Current density profiles with and without $\beta_\wedge$ terms.

VISCOUS EFFECTS ON EQUILIBRIUM STATES OF ISOLATED Z-PINCHES

T. MIYAMOTO
Atomic Energy Research Institute, Nihon University
Kanda-surugadai, Chiyoda-ku, Tokyo, Japan

1. INTRODUCTION

Various steady states of Z-pinches have been investigated by many authors/1-6/. The Bennett pinch/1/ corresponds to a Z-pinch with infinite viscosity and thermal conduction/2/. The solution appropriate to conventional, isotropic Z-pinches is obtained for zero viscosity and infinite thermal conduction/2/. The temperature and current density are almost constant/4,5/ at Pease-Braginskii current/2,3/. It corresponds to the assumption of the latter solution. In the parabolic density profile obtained under this assumption, the electron drift velocity is infinite at the plasma periphery. In the gas embedded Z-pinch, this difficulty is removed because of the thermal conduction at the plasma periphery/5/. Recently, Robson studied the steady state of an isolated Z-pinch under the assumption that the electron drift velocity is limited to the ion acoustic velocity by anomalous resistivity/6/, which has observed in a transient phase of Z-pinches. It is not clear whether the anomalous resistivity must always exist in the steady state of the isolated Z-pinch. It is noticed that the viscous effect is not negligible at the periphery where the density falls zero. The viscous effects are examined in this paper.

2. CANCELLATION OF APPLIED FIELD BY VISCOUS EFFECTS

We examine the steady state of an isolated Z-pinch, which is cylindrically symmetric and infinite in length. All quantities depend only on the plasma radius r. The radial and azimuthal motions are neglected. The applied field E_z and temperature T are assumed to be constant. Then, the momentum conservation equations for hydrogen plasma are given by

$$0 = -\nabla p_j - \nabla \cdot \pi_j \pm e n_j (E + v_j \times B) \mp R \quad \text{for } j = i, e \ , \tag{2.1}$$

where π's and R are stress tensors and the momentum transfer from ions to electrons by collisions (see Ref.7 for the detailed form), and the upper sign is chosen for ions. The radial pressure equilibrium and the azimuthal field B are given by

$$\frac{d}{dr}(n_i + n_e)T = \sigma E_r - iB \ , \quad \frac{1}{r}\frac{d}{dt}(rB) = \mu_0 i = e(n_i v_i - n_e v_e) \ , \tag{2.2}$$

where σ is charge density, which is not negligible at the plasma periphery. Equations (2.2) give a parabolic density profile, if the electric force term is neglected. The axial momentum equation are written as

$$\sigma E_z = \frac{1}{r}\frac{d}{dr} r(\pi_{izr} + \pi_{ezr}) \quad , \tag{2.3}$$

where $\pi_{jzr} = -n_j T \tau_j f_j (\omega_j \tau_j) dv_j/dr$ and $\omega_j = eB/m_j$ for j = i, e, and $\tau_e = (m_e/m_i)^{1/2}(n_i/n_e)\tau_i$. The electron Larmor frequency increases steeply with the radius, so $\omega_e \tau_e >> 1$ except the vicinity of the axis. On the other hand, $\omega_i \tau_i$ is not much greater than unity in most region. Even if $\omega_i \tau_i >> 1$, $f_e/f_i \sim m_e/m_i$. If $\omega_i \tau_i \sim 1$, the inequality holds $f_e/f_i << m_e/m_i$. The ratio of electron stress to ion's satisfies $\pi_{ezr}/\pi_{izr} << (m_e/m_i)^{3/2}(dv_e/dr)/(dv_i/dr)$. The electron drift velocity magnetic field is of order of ion's one, so the ratio π_{ezr}/π_{izr} is extremely small quantities. Thus, we can neglect the electron stress term.

On the contrary, if the charge density σ is neglected in Eq.(2.3), the ion viscous force must be compensated by the electron's one. This means that the electron Larmor radius must be finite as well as ion's, and also that the radial gradient of the electron drift speed must be so high that the electron viscous force is comparable with the ion's one. The parabolic density profile is obtained under this assumption.

The axial component of the generalized Ohm's law is obtained from Eqs.(2.1), and rewritten using (2.3) as

$$\eta i = E_z + \frac{1}{en_e r}\frac{d}{dr} r\left(\pi_{ezr} - \frac{m_e}{m_i}\pi_{izr}\right) \sim \left(1 - \frac{\sigma}{en_e}\frac{m_e}{m_i}\right)E_z \quad , \tag{2.4}$$

where $\eta = m_e/n_e e^2 \tau_e$ is resistivity, and electron viscous term is also neglected. The ion density n_i exceeds substantially n_e at the plasma periphery, because of large ion Larmor radius. At the radius given by

$$(n_i - n_e)/n_e \sim n_i/n_e = m_i/m_e \quad , \tag{2.5}$$

the externally applied field is completely canceled by the effective field that results from the ion viscous effect. Even if the resistivity is constant, the current decreases near the periphery of the column, and vanishes with the density. The ion and electron densities must vanish at the plasma surface, satisfying Eq.(2.5).

3. VISCOUS-NONVISCOUS HYBRID MODEL

We will approximately solve the problem, instead of solving it exactly. When the effective electric field resulted from the ion viscous term increases steeply, especially in Z-pinches in which the ion Larmor radius is much smaller than the plasma radius. Therefore, we divide the plasma column into two regions (i) zero viscosity region ($0 < r < r_1$) and (ii) infinite viscosity region ($r_1 < r < r_p$).

In the region (i), Eqs.(2.2) give the parabolic profile $n = n_o(1 - r^2/a^2)$, where a is the plasma radius for the uniform current at which n = 0. The line density and the total current in this region ($r < r_1$) are given as N_1

$= N_o(r_1/a)^2(1 - (r_1/a)^2/2)$ and $I_1 = I_o(r_1/a)^2$, where $N_o = n_o\pi a^2/2$ and $I_o = i_o\pi a^2$ are the line density and the total current for the Z-pinch in which the whole column is consisted of the region (i), and in which the Bennett relation is given by $\mu_o I_o^2 = 16\pi N_o T$.

In the region (ii), the electron and ion drift velocities are constant. The density is obtained as

$$n = 2n_o\,(2(r_1/a)^2 - 2 + (a/r_1)^2)\,\frac{C(r/r_1)^{A-2}}{(1 + C(r/r_1)^A)^2}\quad , \tag{3.1}$$

solving Eqs.(2.2) under the boundary conditions that n, dn/dt and $i = e(n_i v_i - n_e v_e)$ are continuous at the radius r_1. The constant C is given by $C = 1 + D \pm [(1+D)^2 - 1]^{1/2}$, where $D = [2(r_1/a)^2-1]^2/[(r_1/a)^2(1-(r_1/a)^2)]$, and where the plus must be chosen for $r_1/a > 1/2^{1/2}$, and the minus for $r_1/a < 1/2^{1/2}$ due to physical reasons. The density and current profiles are shown for several values of r_1/a in Fig.1. The line density N_2 and current I_2 in the region (ii) are obtained, integrating from r_1 to the plasma radius r_p ($\rightarrow \infty$), which does not equal a in general. The line density $N = N_1 + N_2$ and the current $I = I_1 + I_2$ are expressed as

$$(N/N_o)^{1/2} = I/I_o = [1-(r_1/a)^2+(2(r_1/a)^4-2(r_1/a)^2+1)^{1/2}] \quad . \tag{3.2}$$

The line density N and the total current I versus r_1/a are drawn in Fig.2. Equation (3.2) shows that the Bennett condition also holds in this model.

Next, we must determine the characteristic radius r_1, where the viscosity is significant. The viscous force vanishes for the parabolic density profile, if $\omega_e\tau_e \gg 1$ and $\omega_i\tau_i \gg 1$. However, $\omega_i\tau_i$ increases only gradually with the radius. The ion viscous effect increases with radius, but decreases rapidly as well as the electron's after $\omega_i\tau_i$ exceeds unity. If the ion viscosity is important at the plasma boundary, $\omega_i\tau_i$ must be less than unity or not exceed greatly unity. The electric field resulting from the ion viscous force becomes dominant with decreasing electron density under this condition. In other words, the plasma boundary will appear within a radius at which $\omega_i\tau_i$ is not much higher than unity. Hence, we assume that $\omega_i\tau_i \sim 1$ at the radius r_1. Using the the parabolic density profile, we obtain

$$\frac{r_1}{a} = [\,1 + (\frac{e\mu_o I_o \tau_{io}}{4\pi\, am_i})^2]^{1/2} - \frac{e\mu_o I_o \tau_{io}}{4\pi\, am_i}\quad , \tag{3.3}$$

where τ_{io} is the ion-ion collision time at r = 0. Equation (3.3) is approximated as $r_1/a - 1 = e\mu_o I_o \tau_{io}/(8\pi\, am_i)$ at the periphery. This is reasonable results. The present model also holds, when the resistivity is assumed to be anomalous at the plasma periphery/6/. The radius r_1 is determined from the condition, however, that the electron drift speed can not exceed the ion acoustic speed. It gives the questionable result that the

resistivity is anomalous at the whole column in the Bennett pinch.

4. CONCLUSIONS

The difficulty of the parabolic density profile obtained in the simplified model of the isolated Z-pinch is removed by the viscous effect without introducing any anomalous effects. The viscous effect generates the effective electric field that cancels the externally applied field. The effect is consequence of the finite ion Larmor radius effect. The related ion orbits were discussed in detail by Haines/8/. The present results seem to support the recent experimental result/9/, which denied the existence of the anomalous resistivity in a steady state. The characteristic plasma radius is determined by $\omega_i \tau_i \sim 1$ at both gas-embedded Z-pinch and isolated Z-pinch. It is determined by the radius of maximum thermal conduction in the former, and of maximum viscosity in the latter.

REFERENCES :

1) W.H.Bennett, Phys.Rev., **45**, 890(1934).
2) R.S.Pease, Proc.Phys.Soc., **B70**, 11(1957).
3) S.I.Braginskii, JETP **6**, 494(1958).
4) M.G.Haines, Proc.Phys.Soc., **76**, 250(1959).
5) D.W.Scudder, Phys.Fluids, **26**, 1330(1983).
6) A.E.Robson, Phys.Rev.Let., **62**, 2816(1989) ; Phys.Fluids, **B3**(6),1461(1991).
7) S.I.Braginskii, Review of Plasma Physics, Vol.1, p.205(1965).
8) M.G.Haines, J.Phys.D **11**,1709(1978).
9) E.S.Figura, G.H.McCall, and A.E.Dangor, Phys.Fluids, **B3**(19), 2835(1991).

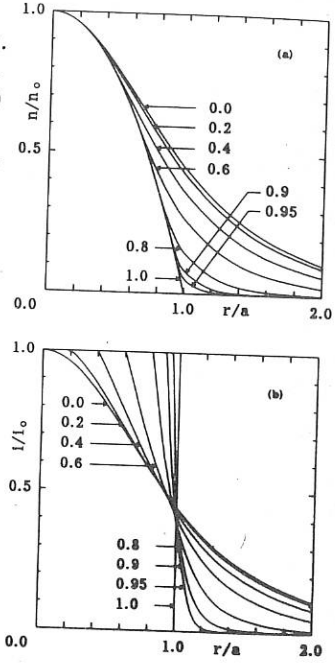

Fig.1 The density (a) and current (b) profiles for several value of r_i/a.

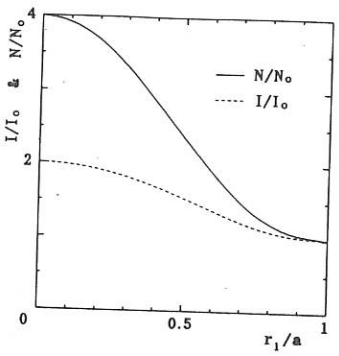

Fig.2 The line density N and the total current I normalized by those of the Z-pinch with uniform.

FIGARO: A Large Larmor Radius Stability Code

M. Coppins
Blackett Laboratory, Imperial College, London SW7 2BZ, U.K.
and
J. Scheffel
Alfven Laboratory, Royal Inst. of Technology, S-100 44 Stockholm, Sweden

Abstract

GARO is a linearized initial value code for studying large Larmor radius stabilization cylindrical geometry. It is based on the Vlasov fluid model and uses integration ng equilibrium ion trajectories to determine the time evolution of the perturbed ion tribution function. The method and its implementation are described and preliminary ults for the $m = 0$ mode in the z-pinch are presented.

Introduction

e availability of high current (~ 1 MA) generators for the z-pinch [1–3] has rendered e collisionless regime accessible experimentally. In this regime ideal MHD is inapplica- e and cannot be used to evaluate the stability properties of the device. The theoretical proach to be adopted depends on the size of the ion Larmor orbits, which, in turn, pends on N, the pinch line density

$$\epsilon \equiv \frac{\overline{a}_i}{a} = \alpha N^{-1/2} \tag{1}$$

ere $\overline{a}_i$ is the average ion Larmor radius, a is the pinch radius, and the constant α is 71×10^8 m$^{1/2}$ for hydrogen, and 8.08×10^8 m$^{1/2}$ for deuterium.

If the line density is greater than about 7×10^{19} m^{-1}, the value of ϵ is sufficiently nall that a fluid like approach is possible. Studies [4–6] using the Chew-Goldberger- ow (CGL) [7] equations have shown that a very large enhancement of linear stability is ilikely for small Larmor radius. In terms of pinches formed from cryogenic fibres (for hich $N \propto r_f^2$, where r_f is the fibre radius) this means that a dramatic improvement in near stability is probably not possible if the fibre radius is above about 20 μm.

The collisionless, finite or large Larmor radius stability of the z-pinch is therefore n important theoretical issue of experimental relevance. It is also an extremely difficult ne to solve. Previous work has concentrated on various simplified subsets of the total roblem. For instance, betatron (or singular) orbits have been neglected [8] or they have een treated, but all other particle types have been neglected [9]; approximate solutions or the finite Larmor radius (FLR, $\epsilon \sim 0.1$) but not the large Larmor radius (LLR, $\epsilon \sim 1$) ase have been found [10], and the simple case of a skin current equilibrium has been olved exactly [11]. In this paper we describe a linearized initial value code, FIGARO,

which is designed encompass all aspects of the problem. It includes all classes of particle, it is applicable in both the FLR and LLR regimes, and it can treat arbitrary equilibria. At present the code is restricted to $m = 0$, fixed boundary modes.

2. Method

FIGARO is based on the Vlasov fluid model [12], which treats the ions fully kinetically, using the exact Vlasov equation, and the electrons as a cold background fluid maintaining quasineutrality. Instead of solving the Vlasov fluid eigenvalue equation, which involves a non-Hermitian operator and formidable trajectory integrals, we use an initial value formulation. A perturbation is applied and its time evolution is followed. After a few growth times the fastest growing mode (i.e., the one with the highest value of $\mathrm{Im}(\omega)$) will dominate the behaviour.

The method used in the code is based on integrating the first order Vlasov equation along the unperturbed ion trajectories of an ensemble of particles to obtain the time dependent values of the first order ion distribution function, at the time dependent positions of the particles in phase space. Moments are taken from these values of f_1 to advance the perturbed fluid variables and fields.

For the equilibrium we make the standard Vlasov fluid assumption that $f_0 = f_0(H)$ where $H = \frac{1}{2}m_i v^2 + e\Phi_0$ is the particle energy. Thus the equilibrium is isotropic in velocity space, implying an isotropic equilibrium pressure. Vlasov fluid equilibria satisfy $\nabla P_0 = \vec{j}_0 \times \vec{B}_0$, like ideal MHD [12]. For equilibrium distribution functions of this form we can write the linearized Vlasov equation as follows

$$\frac{df_1}{dt'} = -\frac{e}{m_i}\vec{E}_1 . \frac{\partial f_0}{\partial \vec{v}'} \tag{2}$$

where $d/dt'$is the time derivative, and $\partial/\partial\vec{v}'$ is the velocity space gradient, following the unperturbed trajectories. Moments are taken of f_1 to obtain to obtain n_1 and $\vec{u}_{i1}$ (the perturbed ion number density and fluid velocity), and the other perturbed fluid and field variables can be calculated from the following equations

$$\vec{u}_{e1} = \vec{u}_{i1} - \frac{n_1}{n_0}\vec{u}_{e0} - \frac{\vec{j}_1}{n_0 e} \tag{3}$$

$$\vec{j}_1 = \frac{1}{\mu_0}\nabla \times \vec{B}_1 \tag{4}$$

$$\vec{E}_1 = -\vec{u}_{e0} \times \vec{B}_1 - \vec{u}_{e1} \times \vec{B}_0 \tag{5}$$

$$\frac{\partial \vec{B}_1}{\partial t} = -\nabla \times \vec{E}_1 . \tag{6}$$

Notice that Eq. (5) is the linearized electron fluid equation.

Plan of Code

ral to the numerical scheme is a one dimensional (radial) configuration space grid. D formulation is possible because we consider only a single Fourier mode (for $m = 0$, urbed variables are proportional to e^{ikz} and are independent of θ).

An ensemble of N particles is moved across this grid following equilibrium ion tra- ories. Each particle carries with it values of f_0 and f_1. The particles f_0 is a constant ie motion (from the zeroth order Vlasov equation). The value of f_1 is time dependent is calculated by advancing the first order Vlasov equation (2).

One cycle of the calculation therefore basically proceeds as follows:

Advance both the particle equations of motion (using $\vec{B}_0$ and $\vec{E}_0$) and the first order sov equation (using $\vec{E}_1$) for all N particles. A fourth order Runge-Kutta scheme is l for these particle integrations.

Values of f_1 are now known at the N new particle positions in phase space. Moments taken to obtain ion fluid variables n_1 and $\vec{u}_{i1}$ at the grid positions by averaging over particles in each cell. For cell j the calculation is as follows [13]

$$n^j = \frac{n_0^j}{K^j} \sum_{k=1}^{K^j} \frac{f_{1k}}{f_{0k}}, \qquad \vec{u}_{i1}^{\,j} = \frac{1}{K^j} \sum_{k=1}^{K^j} \frac{f_{1k}}{f_{0k}} \vec{v}_k \tag{7}$$

ere k is the label for the individual particles in cell j, and K^j is the total number of ticles in the cell.

The ion fluid variables are used to update $\vec{u}_{e1}$, $\vec{B}_1$ and $\vec{E}_1$. Since a two step method x-Wendroff) is used to advance $\vec{B}_1$, each cycle of the calculation is composed of a f timestep followed by a full timestep.

The following boundary conditions are imposed on the fluid variables and fields

$$r = 0: \quad u_{i1r} = u_{e1r} = \vec{B}_1 = E_{1r} = E_{1z} = 0 \tag{8}$$

$$r = a: \quad u_{i1r} = u_{e1r} = \vec{B}_1 = E_{1z} = 0 \tag{9}$$

ice that Eq. (9) applies only to a fixed boundary. The particles are reflected from outer boundary.

Preliminary Results

test the code we need to reproduce a known result. In the collisionless regime the y point of contact with previous theory is the zero Larmor radius limit, where we uld recover the CGL result. Because the code needs to resolve Larmor orbits, this it is actually not accessible. The minimum value of ϵ which we can use is 10^{-3}.

Another difficulty arises when we try to choose a suitable equilibrium. In principle require one with a very high CGL growth rate, so that the code will converge quickly.

Strangely enough, this is impossible to find. Because of the form of f_0 used in the Vlasov fluid model, we must assume a uniform equilibrium temperature. It can be shown [14] that fixed boundary $m = 0$ modes do not exist if the equilibrium density falls to zero at the edge. Thus we must impose a non-zero equilibrium edge pressure. However, making $P_0(a)$ finite significantly reduces the CGL growth rate (if it is sufficiently large, the pinch can be absolutely stable to $m = 0$) [5]. Preliminary tests of the code have been carried out using an equilibrium with uniform j_0 and $P_0(a) = 0.1P_0(0)$.

We use $ka = 10$, again because of the relatively large CGL growth rate. For the limiting case $\epsilon = 10^{-3}$ the code gives a growth rate which is about 20% lower than CGL. The eigenfunction structure is qualitatively similar to the CGL one (i.e., the inner 70% is essentially unperturbed) but the peak in the eigenfunction is shifted by about 10% in radius. Increasing ϵ to 10^{-2} causes a reduction in the growth rate by about 90%. Thus it would seem that the instability properties depend sensitively on ϵ in the small Larmor radius limit. This would explain the discrepancies with CGL. The growth rate appears to increase with ϵ beyond $\epsilon = 0.1$ for $ka = 10$.

Acknowledgements

We would like to thank T. Arber, A. Friedman and Z. Mikic for useful discussions.

References

1. J.D. Sethian *et al*, in *Physics of Alternative Magnetic Confinement Systems*, ed. S. Ortolani and E. Sindoni (Societa Italiana di Fisica, 1991) p. 511.
2. D.W. Scudder *et al*, *ibid* p. 519.
3. P. Choi *et al*, in *Proc 8th IEEE Pulse Power Conf.* (IEEE, New York, 1991) p. 173.
4. M. Coppins, Phys. Fluids B **1**, 591 (1989).
5. J. Scheffel and M. Coppins, *m=0 Z-pinch Stability Reconsidered*, Alfvén Laboratory Report *TRITA-ALF 1991:02* (Royal Inst. Tech., Stockholm, 1991).
6. M. Coppins and J. Scheffel, "Anisotropic Z-Pinch Equilibria and their Stability", Phys. Fluids B (in press).
7. G.F. Chew, M.L. Goldberger and F.E. Low, Proc. Roy. Soc. **A236**, 112 (1956).
8. H.O. Åkerstadt, J. Plasma Phys. **41**, 137 (1990).
9. A.S. Sharma, Nucl. Fusion, **23**, 1493 (1983).
10. H.O. Åkerstadt, Phys. Scr. **37**, 117 (1988).
11. T.D. Arber and M. Coppins, Phys. Fluids B **1**, 2289 (1989).
12. J.P. Freidberg, Phys. Fluids **15**, 1102 (1972).
13. A. Friedman and Z. Mikic (private communication).
14. T.D Arber (private communication).

THE INTERRUPTED Z - PINCH DYNAMICS MODELING

P. Kubeš, J. Kravárik, J. Hakr, P. Kulhánek, J. Píchal

Czech Technical University, Faculty of Electrical Engineering
Technická 2, 166 27 Praha 6, Czechoslovakia

The z-pinch had been formed in the discharge between two cone-shaped copper electrodes (top angle 90° and diameter 10 mm each, interelectrode distance 10 mm) placed in a glass vacuum chamber filled with the air under the pressure 5 kPa - see Fig. 1. The used energy source - 3 μF condenser battery - was charged to a voltage of 18 kV and the discharge current reached its maximum 50 kA at a time 1μs after the breakdown.

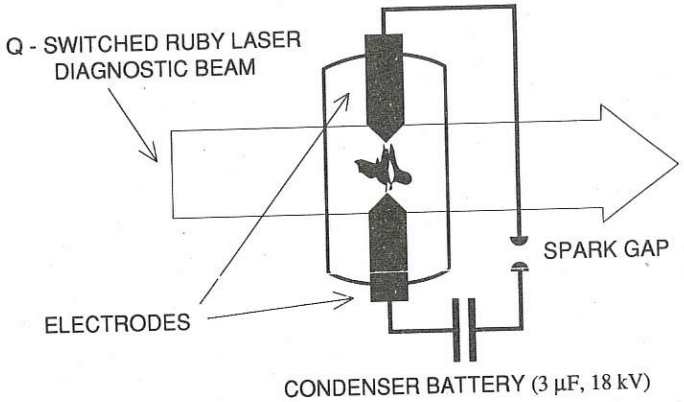

Fig. 1.: Experimental apparatus

The discharge was studied by the Michelson interferometry and Schlieren methods. The Michelson interferometry enabled average the electron density calculations under the assumption of z-pinch cylindrical geometry. The Schlieren method [1] with variable diameter of the focal point disk screen was used to study the small scale concentration gradients in the filaments of the discharge.

Both methods, the Michelson interferometry and the Schlieren method, comprise a ruby laser switched in the Q-regime as the light source. The laser light pulse duration was 0.04 μs. Due to the synchronization and the delay of the light pulse from the discharge ignition, there was a possibility to get a series of experiments. The experiments were carried out every 0.1 μs during the 1 μs time interval after the discharge ignition, the results were registered with a camera. During every discharge there was taken one snap only, but the sequence of measurements was very well acceptable for the discharge evolution study due to the discharge good repeatability (25% variance about a mean). For the discharge evolution obtained from the Schlieren diagnostics see [2].

The densest part of the discharge - the z-pinch - has cylindrical shape during the first 0.2÷0.3 μs after the discharge ignition. Later, by the discharge current some 30 kA, the

z-pinch disrupts in its central part, where the current channel is largest and the electric and magnetic fields relatively weak, into two parts. These parts are connected with the electrodes and turn to the plasma jets throwing plasma in opposite directions towards the discharge center - see Fig. 2. The plasma jets are stable from the moment of their formation (0.4 μs after discharge ignition) to their disintegration at the end of the first current halfperiod (2 μs).

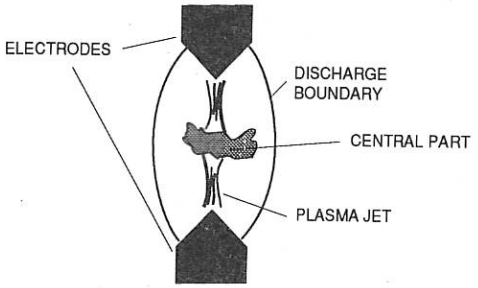

Fig. 2.: Schema of the discharge

Both plasma jets have filamentary structure. The filaments are oriented along the axis of the device, that is parallel with the electric field. Every filament has length 1÷3 mm, diameter about 10 μm and electron density $(6\div9)\times10^{24}$ m^{-3} and creates the plasma jet densest part. The filaments are visible during the whole plasma jets existence and stable during the Schlieren photography exposition.

The electron density n as a function of distance r from the z - pinch axis is in steady state given by

$$n(r) \approx 1 - \left(\frac{r}{R}\right)^2 \quad , \qquad (1)$$

where R is the distance between the discharge outer boundary and the axis. The measured unsteady profiles $n(r)$ for various moments after the plasma ignition are presented on the Fig. 3 - see [2]. The convex shape (maybe $1/r$) could be caused by the plasma transport from the discharge boundary towards the discharge center.

There are no interferometric contours at the interferograms of the plasma flows and the discharge center, hence there is no possibility of direct electron density calculations. In this case, the density lower limit can be defined by the electron density in the neighborhood of the current layer. The results of measurements indicate excellent stability of the plasma jets as well as the filaments. Using the MHD equations for their life time estimation, one obtains for the plasma jets values of the life time 10^{-9} s and for the filaments about 10^{-11} s. We suppose, that the radial plasma flow from the discharge boundary to the plasma jet region through the filamentary interspace is the discharge stabilizing factor.

The force density accelerating the plasma ions with the mass m and the fluid velocity v towards the discharge axis is

$$f = mn\frac{dv}{dt} = j \cdot B + \nabla p \quad , \qquad (2)$$

$p = p_e + p_i$ being the plasma pressure, j the discharge current and B the plasma internal magnetic field induction.

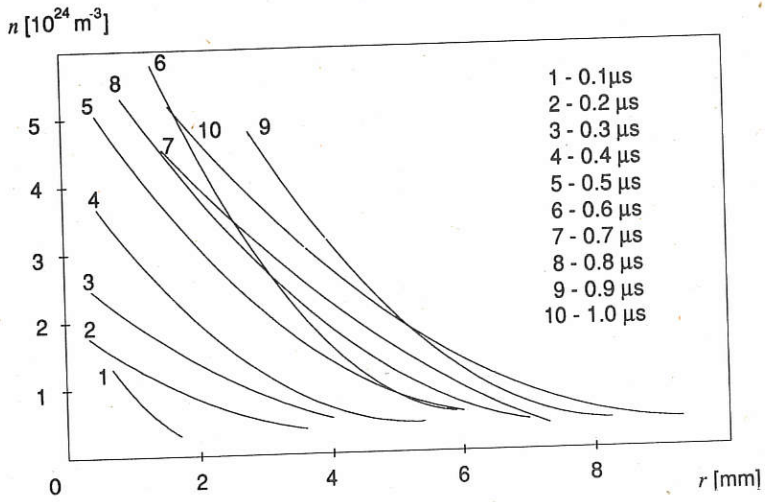

Fig. 3.: The electron density n as a function of distance r from the z-pinch axis in various moments after the plasma ignition

Assuming cylindrical geometry, isothermal process, $T_e = T_i$, $n_e = n_i = n$ and plasma transport described by density

$$n(r) = n(R)\frac{R}{r} \tag{3}$$

one obtains

$$\frac{dp}{dr} = -2\,n(r)\frac{kT_e}{r} \tag{4}$$

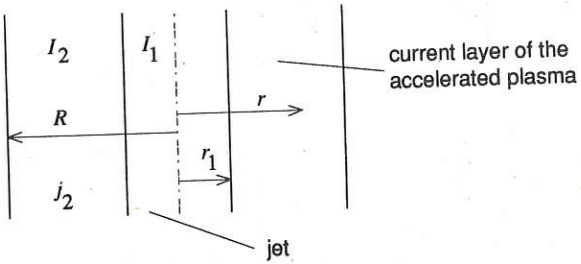

Fig. 4: Model geometry and variables destination

Simplifying the z-pinch geometry see Fig. 4 and assuming $j_2 = const$, $I_1 = 0.2\ I$, the Eq. (2) can be rewritten in the following form

$$f = \frac{\mu_0 j_2 I_1}{2r} + \frac{\mu_0 j_2^2 (r^2 - r_1^2)}{2r} - \frac{2mkT}{r} \quad . \tag{5}$$

After the integration and simple algebraic manipulations of the Eq.(5), the fluid velocity v is given by

$$v = \sqrt{\frac{\mu_0}{n(R)mR}\left[\int_R^{r_1} j_2 I_1 dr + \int_R^{r_1} j_2^2 (r^2 - r_1^2) dr\right] - \frac{4kT_e}{m}\ln\frac{R}{r_1}} \quad . \tag{6}$$

Magnitudes $I = I_1 + I_2$, $n(R)$, R and r_1 are known from the experiment - see [2]. The velocity dependence $v(r,t)$ is presented in Fig 5 .

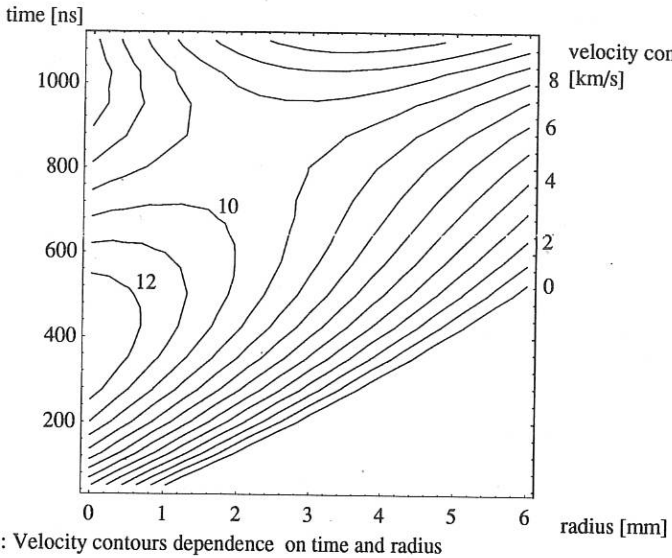

Fig 5.: Velocity contours dependence on time and radius

References:

[1] Kubeš P. et al.: Czech. J. Phys. B 35 (1985) 155
[2] Kubeš P. et al.: Czech. J. Phys. B 42 (1992) at print.

Stabilization of Long Wavelength Sausage and Kink Modes of a Z-pinch by Nonlinear Radial Oscillations.

A.B.Bud'ko, E.T.Karlson and M.A.Liberman
Department of Technology, Uppsala University,
Box 534, S-75121, Uppsala, Sweden

A number of experiments with fiber-initiated dense Z-pinches /1/, with compressional /2/, and gas-embedded Z-pinches /3/, with imploding gas-puff Z-pinches /4/ and the straight Extrap configuration /5/ performed in the last decade demonstrated sufficiently improved stability of Z-pinch configurations. The striking stability with respect to the sausage modes can be explained, in principle, by ideal MHD theory /6/ as well as by finite plasma conductivity effects /7/. The global kink mode can not be stabilized by the appropriate choice of the unperturbed profiles neither within the scope of the ideal MHD /8/ nor taking into account finite ion Larmor radius and viscous damping effects /9,10/.

In this report we shall demonstrate that stabilization of the global kink modes can be explained by the assumption that pinch in not in a stationary but in a dynamic equilibrium.

The dynamic equilibrium of a screw pinch subject to nonlinear radial oscillations is described by the self-similar solutions obtained by Kulikovskii /11/

$$u_r(r,t) = \dot{R}(t)\,\eta \ , \ \rho(r,t) = \rho_0\,\alpha(t)^{-2}\,N(\eta) \ , \ P(r,t) = P_0\,\alpha(t)^{-2\gamma}\,P(\eta) \ ,$$

$$B_\varphi(r,t) = B_{\varphi 0}\,\alpha(t)^{-1}\,B_\varphi(\eta) \ , \ B_z(r,t) = B_{z0}\,\alpha(t)^{-2}\,B_z(\eta) \ , \qquad (1)$$

$$\tau_A^2\ddot{\alpha} + \alpha^{-1} - \beta\alpha^{1-2\gamma} - b\alpha^{-3} = 0 \ .$$

Here $N(\eta)$, $P(\eta)$, $B_\varphi(\eta)$, $B_z(\eta)$ are dimensionless functions of the self-similar variable $\eta = r/R(t)$ representing the self-similar profiles; $u_r(r,t)$ is the radial velocity; $\alpha = R(t)/R_0$ is the instantaneous normalized pinch radius with minimal and maximal values α_1 and α_2 ; R_0 is the pinch radius in stationary equilibrium; γ is the adiabatic index; $\tau_A = R_0\sqrt{4\pi\rho_0}/B_{\varphi 0}$ is the Alfven transit time; $\beta = 4\pi P_0/B_{\varphi 0}^2$ and $b = B_{z0}^2/B_{\varphi 0}^2$ are dimensionless parameters.

Small perturbations of the dynamic pinch equilibrium are described by the linearized equations of the ideal MHD

$$\partial\rho'/\partial t + \nabla\cdot(\rho'\,\vec{u} + \rho\,\vec{u}') = 0 \ , \qquad (2)$$

$$\partial P'/\partial t + \vec{u}\cdot\nabla P' + \vec{u}'\cdot\nabla P + \gamma P'\,\nabla\cdot\vec{u} + \gamma P\,\nabla\cdot\vec{u}' = 0 \ , \qquad (3)$$

$$\partial\vec{B}'/\partial t - \nabla\times(\vec{u}\times\vec{B}') - \nabla\times(\vec{u}'\times\vec{B}) = 0 \ , \qquad (4)$$

$$\rho'\left(\partial\vec{u}/\partial t + (\vec{u}\cdot\nabla)\,\vec{u}\right) + \rho\left(\partial\vec{u}'/\partial t + (\vec{u}\cdot\nabla)\,\vec{u}' + (\vec{u}'\cdot\nabla)\,\vec{u}\right)$$

$$+ \nabla P' - \frac{1}{4\pi}(\nabla \times \vec{B}') \times \vec{B} - \frac{1}{4\pi}(\nabla \times \vec{B}) \times \vec{B}' = 0 , \qquad (5)$$

where primes denote the perturbed variables.

Since the unperturbed variables in Eqs.(2)-(5) are time-dependent the perturbation evolution is not exponential and can hardly be traced analytically in the general case. We assume that the oscillation period is small compared with the perturbation growth time, what is correct for the long-wavelength sausage and kink modes. Under this assumption we can average the linearized equations over the oscillation period neglecting the slow time variation of the perturbed variables. Introducing the particle displacement $\vec{\xi} = \partial\vec{v}/\partial t$ the result can be written in the form

$$\langle\rho\rangle\, \partial^2\vec{\xi}/\partial t^2 = \vec{F}(\vec{\xi}) , \text{ where } \vec{F}(\vec{\xi}) = \vec{F}_0(\vec{\xi}) + \left\langle\rho\right\rangle \nabla\cdot\vec{\xi} + \vec{\xi}\cdot\left\langle\nabla\rho\right\rangle\Big\rangle \left\langle\partial\vec{u}/\partial t + (\vec{u}\cdot\nabla)\,\vec{u}\right\rangle$$

Here $\vec{F}_0(\vec{\xi})$ is the force operator corresponding to the stationary pinch stability problem /8/ but with the averaged zeroth-order functions. In spite of the modification the force operator $\vec{F}(\vec{\xi})$ conserves the self-adjointness property that simplifies numerical and analytical analysis of the problem.

The crucial point in the subsequent analysis is that the averaged values of particle acceleration $d\vec{u}/dt$ and force acting on a particle $\rho d\vec{v}/dt$ are not equal to zero and enter into the force operator $\vec{F}(\vec{\xi})$. In a certain sence this is equivalent to the presence of an effective gravitation field $\vec{g} = -d\vec{u}/dt$ in the local frame of reference associated with a moving particle. This effective (nonuniform) gravitation field produced by radial oscillations is described by the following parameters:

$$\Omega_1^2(r) = \frac{\langle\rho g\rangle}{r\langle\rho\rangle} = \frac{\rho_0}{r\langle\rho\rangle T}\int_{\alpha_1}^{\alpha_2} \frac{\alpha^{-2}\,\ddot{\alpha}(\alpha)\,N(r/R_0\alpha)}{\dot{\alpha}(\alpha)}\,d\alpha, \quad \Omega_2^2 = \frac{\langle g\rangle}{r} = \frac{1}{T}\int_{\alpha_1}^{\alpha_2}\frac{\ddot{\alpha}(\alpha)}{\dot{\alpha}(\alpha)}\,d\alpha$$

Assuming $\vec{\xi} \propto \vec{\xi}(r)\exp(\sigma t + im\varphi + ikz)$ after some straigthforward algebra one can obtain the following second-order equation for ξ_r

$$\frac{d}{dr}\left(G_0\frac{d(r\xi_r)}{rdr}\right) + G_1\frac{d(r\xi_r)}{rdr} - G_2\xi_r = 0 , \qquad (6)$$

$$G_0 = \frac{\rho\sigma^2 + \frac{f_1^2}{4\pi}}{\Delta}\left(\rho\sigma^2\left(\gamma P + \frac{B^2}{4\pi}\right) + \gamma P\,\frac{f_1^2}{4\pi}\right), \quad G_1 = \frac{1}{\Delta}\left(\rho\sigma^2\left(\rho\sigma^2 + \frac{f_1^2}{4\pi}\right)\left(\Omega_1^2 + \Lambda_{\varphi,z} - \Omega_2^2\right)\rho r\right)$$

$$G_2 = \rho\sigma^2 + \frac{f_1^2}{4\pi} + \frac{B_\varphi}{2\pi}\frac{d}{dr}\left(\frac{B_\varphi}{r}\right) + \Omega_{2r}^2\frac{d\ln(\rho)}{dr} + r\frac{d}{dr}\left\langle\frac{kB_\varphi f_2}{2\pi r^2\Delta}\left(\rho\sigma^2\left(\gamma P + \frac{B^2}{4\pi}\right) + \gamma P\frac{f_1^2}{4\pi}\right)\right\rangle$$

$$-\frac{\rho^2}{\Delta}\left(\left(m^2 + k^2r^2\right)\left(\rho\sigma^2 + \frac{f_1^2}{4\pi}\right)\left(\Omega_1^2 + \Lambda_{\varphi,z}\right)\Omega_2^2 + \frac{k\sigma^2}{2\pi}f_2B_\varphi\left(\Omega_1^2 + \Lambda_{\varphi,z} + \Omega_2^2\right)\right)$$

$$-\frac{k^2}{4\pi^2r^2\Delta}\left(B_\varphi^2\left(\gamma P f_1^2 + \rho\sigma^2B^2\right)\right) - r\frac{d}{dr}\left\langle\frac{1}{\Delta}\left(\Omega_1^2 + \Lambda_{\varphi,z}\right)\rho^2\sigma^2\left(\rho\sigma^2 + \frac{f_1^2}{4\pi}\right)\right\rangle ,$$

where the following designations have been used: $B^2 = B_\varphi^2 + B_z^2$, $f_1 = \frac{m}{r}B_\varphi + kB_z$,

$$f_2 = \frac{m}{r}B_z - kB_\varphi,\quad \Delta = \rho^2\sigma^4 + \left(\frac{m^2}{r^2} + k^2\right)\left(\rho\sigma^2\left(\gamma P + \frac{B^2}{4\pi}\right) + \frac{1}{4\pi}\gamma P f_1^2\right),$$

$$4\pi\Lambda_{\varphi,z} = \frac{\left\langle B_\varphi\right\rangle d\left(r\left\langle B_\varphi\right\rangle\right)}{rdr} - \frac{\left\langle B_\varphi\, d\left\langle rB_\varphi\right\rangle\right\rangle}{rdr} + \frac{\left\langle B_z\right\rangle d\left\langle B_z\right\rangle}{dr} - \frac{\left\langle B_z\, dB_z\right\rangle}{dr} .$$

Here and below (excepting the expression for $\Lambda_{\varphi,z}$) by all the zeroth-order variables we mean their average values and omit the averaging brackets for the sake of simplicity.

The boundary conditions are usual and follow from the requirement that the velocity perturbation is regular on the axis and that the total pressure and the normal component of the magnetic field are continuous on the outer boundary.

The boundary value problem was solved numerically by the shooting method. We chose the following shape of the self-similar profiles

$$N(\eta) = 1 - \eta^2\,,\ P(\eta) = \frac{1}{4}\left(1 - \eta^2\right)^2\,,\ B_\varphi(\eta) = \eta\sqrt{\frac{1}{2} - \frac{1}{3}\eta^2}\,,\ B_z(\eta) = 0\ .$$

In Figs.1,2 the dispersion curves for the sausage (m=0) and kink (m=1) modes are plotted for the oscillation amplitude $0.24R_0$ (curves 2) and $0.42R_0$ (curves 3) in comparison with stationary equilibrium case (curves 1). The numerical solution demonstrates that the suppression of the kink mode by the effective gravity produced by the oscillations leads to the total stabilization of this mode in the long-wavelength limit. Reduction of the growth rates corresponding to the m = 0 mode is much less and does not exceed one-half of its value corresponding to a stationary equilibrium even in strongly nonlinear regime.

The growth rates of the kink modes in the long-wavelength limit for a weak gravitational field can be obtained analytically with the aid of the perturbation theory (weakness of effective gravity does not imply small oscillation amplitude). Expanding Eq.(6) together with the boundary conditions in the small parameters $\Omega_1^2\tau_A^2$, $\Omega_2^2\tau_A^2$, k^2 we obtain

$$\sigma^2 = \frac{1}{4M} k^2 \alpha_2^3 \ln(1/k)\, B_\varphi^2(\alpha_2) + \Omega_2^2, \qquad (7)$$

where M is the mass per unit length and the terms of order of unity are ignored compared with the logarithmic term. The first term in the right-hand side of Eq.(7) represents the growth rate of a stationary pinch /12/ and the second one corresponding to the gravity effect predicts a stabilizing correction for $\Omega_2^2 < 0$ (opposite to the Rayleigh-Taylor instability condition). The correction obtained is independent of k, thus providing m=1 mode stability for small k in agreement with the numerical results. The wavenumber k_0 corresponding to the growth rate vanishing is obtained as the solution of the equation

$$k_0^2 \ln(1/k_0) = -4M\Omega_2^2/(\alpha_2^3 B_\varphi^2(\alpha_2)) \ .$$

The values of k_0 given by this expression are very close to the ones obtained by the numerical solution of the boundary value problem even for oscillation amplitudes comparable to the pinch equilibrium radius.

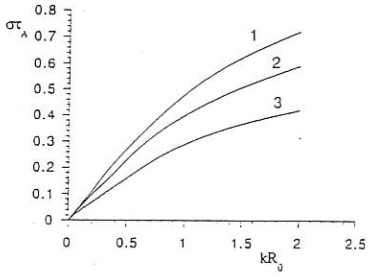

Fig.1

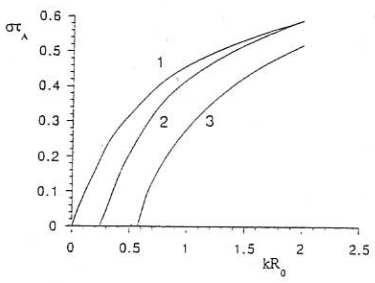

Fig.2

/1/ J.D.Sethian,A.E.Robson,K.A.Gerber,A.W.DeSilva, Phys.Rev.Lett. **59**, 892 (1987).
/2/ M.G.Haines, J.Phys.D Appl.Phys. **11**, 1709 (1978).
/3/ A.E.Dangor,M.B.Favre-Domingues,S.Lee,E.Kahan, Phys.Rev. A**27**, 2751 (1983).
/4/ F.S.Felber,F.J.Wessel,N.C.Wild et.al., J.Appl.Phys. 69, 3831 (1988).
/5/ J.R.Drake, Plasma Phys. Contr. Fusion **26**, 387 (1984).
/6/ M.Coppins,I.D.Culverwell,M.G.Haines, Phys. Fluids **31**, 2688 (1988).
/7/ I.D.Culverwell,M.Coppins, Phys. Fluids B**2**, 129 (1990).
/8/ J.P.Freidberg, Rev. Mod. Phys. **54**, 801 (1982).
/9/ H.O.Åkerstedt, J. Plasma Phys. **41**, 45 (1989).
/10/ G.Eriksson, Physica Scripta **35**, 851 (1987).
/11/ A.G.Kulikovskii, Dokl. Akad. Nauk SSSR **114**, 984 (1957).
/12/ J.Nycander,C.Wahlberg, Nucl. Fusion **24**, 1357 (1984).

IDEAL AND RESISTIVE MHD ANALYSIS OF ROTATIONAL INSTABILITIES IN FRC

P. H. Sakanaka, M. Machida, R. Y. Honda, E. A. Aramaki, L. A. Berni

M. A. A. Santiago[1], K.-H. Tsui[1], and M. Tavares Azevedo[1]

Physics Department, UNICAMP, C.P. 6165, 13081 Campinas, SP, Brazil

Abstract

A global ideal and resistive one dimensional MHD model is used to study the rotational mode in the field reversed configurations. We have developed codes to calculate complex eigenvalues (oscillation frequencies and growth rates) for m-modes in one dimensional field reversed configurations for the ideal and resistive MHD theory. We have found that the growth rate as function of rotation rate presents a maximum, for any value of m; also it is larger for larger m, up to m = 4, and then it decreases quickly as m increases beyond this value. We have also found that the resistivity dependence is not large on the growth rate. These results agrees qualitatively with experimental data obtained from TC-I machine at Universidade Estadual de Campinas.

1 Introduction

The prospect of field reversed configurations (FRC) to be competitive with other fusion devices relies on the understanding of the stability properties. Current machine performance indicates a confinement time far better than the ideal MHD value [1,2] due to finite Larmor radius (FLR) stabilization [3,4]. However FLR effects are not expected to be significant in high field and large dimension FRCs where MHD descriptions will prevail when resistivity is taken into account. It is well known that FRCs usually have inherited some rotational velocity for peculiar reasons. The resistivity is only considered in the singular layer r_0 where the magnetic field vanishes. Ideal MHD solution on both sides are matched across r_0 with the local resistive solution. Here, we use a global scalar resistivity to study the FRC rotational stability and compare it with the results of the UNICAMP experiment [5,6], TC-1, where under some discharge parameters the $m = 4$ mode are observed.

[1]Instituto de Física, Universidade Federal Fluminense, 24024, Niterói, RJ, Brazil.

2 Basic Equations

We consider a reversed field Θ-Pinch configuration with angular rotation Ω in the θ direction and field lines in the z direction. The general equations to describe the equilibrium and stability are

$$\rho \frac{d\vec{v}}{dt} = \frac{1}{4\pi}(\nabla \times \vec{B}) \times \vec{B} - \nabla p, \tag{1}$$

$$\frac{\partial \vec{B}}{\partial t} = \nabla \times (\vec{v} \times \vec{B}) - \frac{\eta c^2}{4\pi} \nabla \times (\nabla \times \vec{B}), \tag{2}$$

$$\nabla \cdot \vec{B} = \nabla \cdot \vec{v} = 0. \tag{3}$$

Here the resistivity η is assumed to be constant and small in the sense that the diffusion time $\tau_R = 4\pi r_0^2/\eta c^2$ is larger than the inverse growth rate of instabilities. Linearizing the basic equations to the first order in η and using the condition $\nabla \cdot \vec{\xi} = 0$ we obtain the perturbed equations in the variables $\xi_{r,\theta,z}$ and its second and third order derivatives [7].

In the limit of zero resistivity, these equations reduce to the perturbed ideal MHD equations, such as the one given by Freidberg (1970) [1].

These equations are solved numerically and the results are used to interpret the UNICAMP's TC-1 experiment.

3 Comparison with Experimental Data and Conclusions

We observe in the experiment that the $m = 4$ mode grows always at a rotation around $\Omega \sim 0.41$. The time associated with the numerical $m = 4$ growth rate is about $0.53\mu s$ which is close to the experimentally observed time of $0.4\mu s$. It is also observed that the mode stabilizes, and stays with non-linearly large amplitude, when the rotation vanishes. In numerical calculations for $\Omega = 0$ the growth rate is zero in both $m = 4$ modes, resistive and ideal. The growth rate increases with Ω as we can see in figure 1. This figure shows the imaginary part of the growth rate against the rotation Ω, for the resistive $m = 4$ mode ($\eta \neq 0$). The stabilization of $m = 4$ mode is interpreted as due to the non-linearity (large amplitude mode). This stabilization is observed for a time of the order of $1.5\mu s$ which is close with our results for $\Omega = 0$ ($1.1\mu s$). Around $\Omega = 0.40$ we obtained the growth rate $\gamma = 2 \times 10^6 s^{-1}$ which corresponds to $\tau_R \sim 0.5\mu s$.

We can conclude that the numerical code calculates the growth rate of x the $m = 4$ mode, consistent with the experimental data. We will be calculating the eigenvalues for other modes to compare them with different experimental conditions for the machine. The rotation may be responsible in determining the behaviour of the plasma in the UNICAMP's machine.

Finally we must study the case of $\Omega > 0.45$ because this behavior is still not understood properly by us.

Acknowledgement

This work was supported by Fundação de Amparo à Pesquisa do Estado de São Paulo and Conselho Nacional de Desenvolvimento Científico e Tecnológico.

References

[1] J. P. Freidberg and J. A. Wesson. Phys. Fluids **13**:1117 (1970).

[2] D. W. Hewett and R. L. Spencer. Phys. Fluids **26**:1299 (1983).

[3] C. E. Seyler. Phys. Fluids **22**:2324 (1979).

[4] D. C. Barnes, J.L. Schwarzmeier, H.R. Lewis, and C. E. Seyler. Phys. Fluids **27**:2616 (1986).

[5] R. Y. Honda, M. Machida, E. A. Aramaki, and P. Porto. Proc. of IV Latin American Workshop on Plasma Physics. p. 355, Buenos Aires, Argentina (1990).

[6] E.A. Aramaki, M. Machida, R.Y. Honda, P. Porto, and L. A. Berni. Proc. of IV Latin American Workshop on Plasma Physics. p. 359, Buenos Aires, Argentina (1990).

[7] M. A. A. Santiago, M. Tavares-Azevedo, K.H. Tsui, and P.H. Sakanaka. Proc. I Brazilian Meeting on Plasma Physics. p. 185, Santos, Brazil (1991).

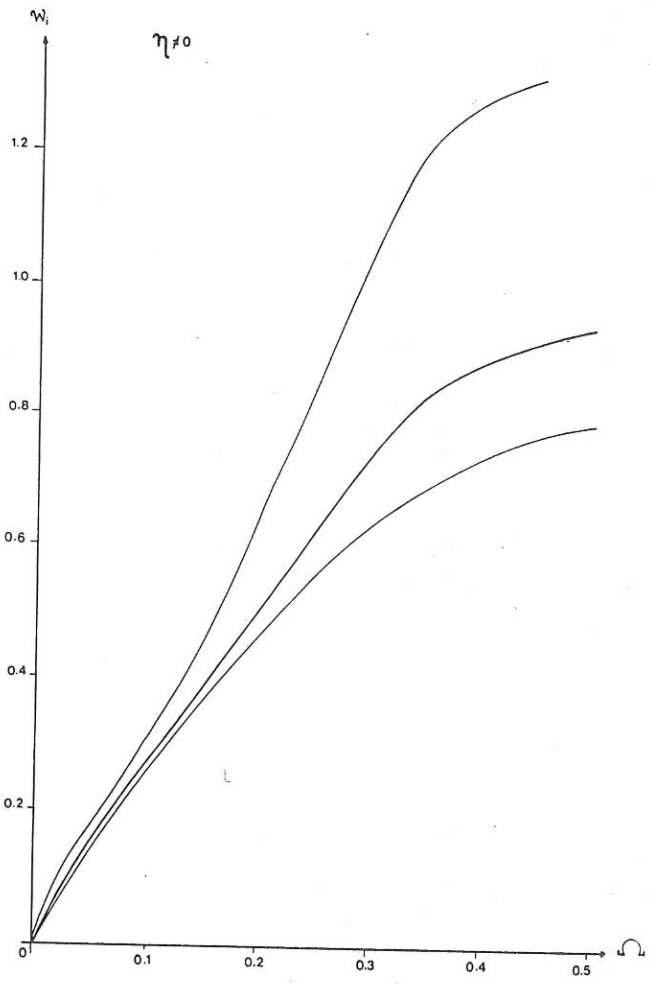

Fig.(1) Growth rate against rotation for m=4 resistive mode.

DISCRETE ALFVÉN WAVES IN REVERSED FIELD PINCHES

P. H. Sakanaka, H. Shigueoka[1], C. A. Azevedo[2], and A. S. Assis[1]

Physics Department, UNICAMP. C.P. 6165, 13081 Campinas, SP, Brazil

Abstract

This paper presents an analysis of the spectrum in the stable branch of the magnetized circular plasma column under the ideal magnetohydrodynamics point of view. There are two continua, slow and Alfvén, with improper eigenvalues, and discrete points of proper eigenvalues outside these continua. These continua are due to two singularities of the linearized stability equation for the ideal MHD plasma – Hain-Lüst equation.

We present an analytical solution for discrete modes; we show that an accumulation point of these discrete modes occurs at the lower edge of the Alfvén continuum. There is no accumulation point found at the upper edge of the slow continuum nor on the upper edge of the Alfvén continuum, according to our calculations.

1 Introduction

The spectrum of a cylindrical magnetohydrodynamic equilibrium has been studied by many authors, Appert et al. (1974) [1], Goedbloed (1975) [2], and others. The conclusion is that there should be two continuous spectra, slow and Alfvén, separated by discrete spectra.

In this paper we show an analytical solution for discrete Alfvén modes. We demonstrate that the discrete modes accumulate at the lower edge of the Alfvén continuum. However, we have found that there is no accumulation of the discrete modes at the upper edges of the slow and Alfvén continua.

2 Discrete Spectrum of Cylindrical Plasma

Our starting point is the Hain-Lüst equation, derived by Hain and Lüst (1958) [4]:

$$\frac{d}{dr}\left[f(r)\frac{d}{dr}\left(r\xi_r\right)\right] + g(r)\left(r\xi_r\right) = 0, \tag{1}$$

where the coefficients f and g are defined as in Azevedo (1991) [3].

[1]Universidade Federal Fluminense, 24024, Niterói, RJ, Brazil.
[2]Universidade do Estado do Rio de Janeiro, RJ, Brazil.

The equilibrium is obtained by solving the equation written in the form

$$\frac{1}{r}\frac{d}{dr}(rB_\theta) = \mu(r)B_z - \frac{B_\theta}{B_\theta^2 + B_z^2}\frac{dp}{dr}, \quad (2)$$

$$\frac{dB_z}{dr} = -\mu(r)B_\theta - \frac{B_z}{B_\theta^2 + B_z^2}\frac{dp}{dr}, \quad (3)$$

where $\mu(r)$ represents the coefficient of equation $\nabla \times \vec{B} = \mu(r)\vec{B}$ such that $\mu(r) = \vec{J} \cdot \vec{B}/B^2$. In the case in which $p'(r) = 0$, it is the force-free equilibrium where $\nabla \times \vec{B}$ is parallel to $\vec{B}$. Equations (2) and (3) are solved upon specifying two profiles, such as, $\mu(r)$ and $p(r)$.

Equation (1) is the eigenfunction equation for the r-component of the Fourier analysed plasma displacement $\vec{\xi}(r,\theta,z,t) = \sum_{m,k_z} \vec{\xi}(r)exp(im\theta + ik_z z - i\omega t)$, where m is the azimutal mode, k_z is the wave number in the axial direction, and ω is the frequency of oscillation.

We have obtained an analytical solution for the discrete eigenmodes (Shigueoka (1991) [5]). We have assumed the independent profiles of the equilibrium equations (2) and (3) to be $p(r) = p_0(1 - p_2r^2 - p_4r^4 - p_6r^6)^{\alpha_p} = p_0 + p_1r^2 + \cdots$, and $\mu(r) = \mu_0(1 - a_2r^2 - a_4r^4 - a_6r^6)^{\alpha} = \mu_0 + \mu_1r^2 + \cdots$, where $p_1 = -\alpha_p p_0 p_2$ and $\mu_1 = -\alpha\mu_0 a_2$. The coefficients b_0, b_1 and B_{z1} which provide the magnetic field profiles, $b(r) = \frac{B_\theta}{r} = b_0 + b_1r^2 + \cdots, and B_z(r) = 1 + B_{z1}r^2 + \cdots$, are obtained by introducing p(r) and $\mu(r)$ into equations (2) and (3).

We now assume a limiting case in which ω^2 is small, $k_z \ll 1/a$, $p' \ll \mu_0 B_0/2$ and profile of $\rho(r)$ such that $\omega_A^2 = \frac{F^2}{\rho} \cong const.$

The Hain-Lüst equation can then be rewritten

$$r^2\frac{d^2}{dr^2}(r\xi_r) + r\frac{d}{dr}(r\xi_r) + \left[\lambda^2r^2 - m^2\right]r\xi_r = 0, \quad (4)$$

where $\lambda^2 = -h^2m^2/(\omega^2 - \omega_A^2)$. One can recognize the Bessel's equation of order m whose solution is the Bessel's function of the first kind, $r\xi_r = J_m(\lambda r)$ for $\omega^2 < \omega_A^2$. If the plasma is limited by a conducting wall at $r = a$, then $a\xi_r(a) = 0$ and the eigenvalues are zeroes, $p_{m\nu}$, of Bessel's function, that is, $\lambda a = p_{m\nu}$; $m, \nu = 1, 2, 3, \cdots$. The solution with $\nu = 1$ is named first radial mode and its corresponding eigenfunction has no zero in the interval $0 < r < a$. Other solutions with higher ν correspond to solutions which have $\nu - 1$ zeros in the same interval.

ν	$m=1$		$m=2$		$m=3$	
	Anal.	Num.	Anal.	Num.	Anal.	Num.
1	0.003269	0.003942	0.007280	0.008710	0.010613	0.012964
2	0.000975	0.001158	0.002710	0.003233	0.004534	0.005550
3	0.000464	0.000550	0.001422	0.001695	0.002550	0.003125

Table 1: $\Delta\omega^2$ analytically $(h^2m^2/p^2_{m\nu})$ and numerically calculated $(\omega^2_A - \omega^2_{DAW})$

Thus, one obtains an expression for the eigenvalues $\omega^2 = \omega^2_A - \frac{h^2m^2}{p^2_{m\nu}}$.. The difference between the eigenfrequency and the Alfvén frequency is given by $\Delta\omega^2 = -\frac{h^2m^2}{p^2_{m\nu}}$ which goes to zero as ν increases, that is an accumulation.

As an example we take the following values to calculate ω^2: $m = 1$, $k = 0.1$, $p_0 = 0.02$, $\alpha = 1$, $\rho_0 = 1, \alpha_p = 1$, $a_2 = 1$, $p_2 = 1$, $q_0 = 1$, $\mu_0 = 0.4$. We obtain $h = 0.02006$ and the eigenvalue results in $\omega^2 = 0.03837$.

This simple solution, however mathematically precise, is the first analytical solution for the discrete Alfvén waves. The solution found in (2) shows the nature of the global discrete Alfvén modes from which we can draw some conclusions: these solutions are Sturmian and that they lie below the lower edge of the Alfvén continuum.

From these results one can also observe that the perturbations are essentially transversal, however a small longitudinal component exists in discrete modes. This component is proportional to the plasma pressure (p_0) and the current density (μ_0).

In table 1 one sees a list of $\Delta\omega^2$, the difference between the square of discrete eigenfrequencies and the square of the Alfvén frequency, as calculated analytically and numerically.

3 Conclusion

We have studied the discrete spectra of cylindrical magnetohydrodynamic plasmas. The discrete eigenvalues lie outside the two continua, slow and Alfvén, in the stable branch of the MHD spectrum. We have shown that there is an accumulation point at the lower edge of the Alfvén continuum, but we have not found accumulation points at the upper edge of the Alfvén continuum, nor at the upper edge of the slow wave continuum.

Analytical solutions for discrete Alfvén waves were determined. From the analytical expression for the eigenmode, one can draw many relevant conclusions, such as, the discrete modes are quasi-transversal waves with a small longitudinal component proportional to the plasma pressure and the current density; for low radial modes, (k_r) small, and low azimuthal modes, (m) small, the modes are global, however as m grows, it becomes more and more like surface waves; and, for a low m-mode, as the radial modes increases, it becomes more and more acentral mode, restricted to perturbations around the magnetic axis.

The longitudinal component of the discrete modes is small, but it plays an important role in the solar arc prominence plasma heating as shown in Azevedo (1991), the tokamak plasma heating, and for the magnetosphere plasma oscillation (Shigueoka (1991)).

Acknowledgement

This work was supported by Fundação de Amparo à Pesquisa do Estado de São Paulo.

References

[1] K. Appert, B. Balet, R. Gruber, F. Troyon, and J. Vaclavik. *Phys. Fluids*, **17**:1471, (1974).

[2] J. P. Goedbloed. *Phys. Fluids*, **18**:1258, (1975).

[3] C.A. de Azevedo, A. S. de Assis, H. Shigueoka, and P.H. Sakanaka. *Solar Physics*, **131**:119, (1991).

[4] K. Hain and R. Lüst. *Z. Naturfor.*, 13a:936, (1958).

[5] H. Shigueoka. *Estudo Espectral das Ondas de Alfvén em Plasma Cilíndrico.* Tese de Doutoramento, Universidade de São Paulo, São Paulo, (1991).

HOT SPOT X-RAY AND MICROWAVE EMISSION OF THE DPF-78 PLASMA FOCUS

P. Antsiferov[1] , D. Franz, R. Pfau, A. Rupasov[2], H. Schmidt, D. Schulz
Institut für Plasmaforschung, Universität Stuttgart, Germany
[1] Institute for Spectroscopy, Troitzk, Russia
[2] P.N. Lebedev Physics Institute, Moscow, Russia

Introduction

Hot spot (micropinch) formation in plasma focus devices depends strongly on proper admixing of appropriate amounts of heavy gases to the standard hydrogen/deuterium filling. Rapid radiative collapse is essential for such hot spots (i.e. strongly localized high density/temperature plasmas) to be formed. Plasma focus devices are intensive sources of high energy particles (accelerated electrons and ions,neutrons) as well as radiation from the microwave to the hard X-ray region. Intense X-ray argon line emission from hot spots occuring in the DPF-78 plasma focus (28 kJ, 60 kV, $\tau/4 \approx 1.5$ μs) was studied using 1) a transmission grating spectrometer, 2) a quartz crystal spectrometer, 3) an X-ray streak camera and 4) a pinhole camera equipped with an X-ray PIN-diode array.

Angular resolved measurements of the μ-wave emission in the X-, R-, and E-band (8 - 90 GHz) - mostly from discharges in pure D_2 - revealed the expected strong temporal correlation between the REB and μ-wave pulses.

X-ray spectroscopic measurements

X-ray spectra of n->1 transitions in multiply charged ions of Ar represent an important channel for obtaining information on compressed plasma in pinch devices. Spectral lines of interest ($3 \text{ Å} \le \lambda \le 4 \text{ Å}$) were detected with a high-quality quartz (2d= 6.68 Å and 8.5 Å, resp.) bent crystal spectrograph of the Johann type. The measured line widths - mostly due to plasma broadening - were greater than the spectral resolution of the spectrometer ($\Delta\lambda/\lambda < 10^{-3}$). Spectra of resonance transitions in He-like and H-like argon from single discharges with a spatial resolution in the mm range could be recorded on Kodak DEF film.

Spectra (from single and multiple discharges) with low spectral but about the same spatial resolution of 1 mm were recorded with a transmission grating spectrograph using a grating with 10^3 lines/mm and an additional slit of 60 μm near (70 mm) to the source. The grating was positioned 600 mm from the source and 920 mm from the film (-> $d\lambda/dx$ = 10.8 Å/mm). Numerous spectra with various amounts of noble gas admixtures (argon, krypton, xenon) confirmed that high intensity lines of highly ionized argon are predominantly emitted from the micropinches and not from the surrounding long (25 - 30 mm) pinched plasma column (see Fig. 1).

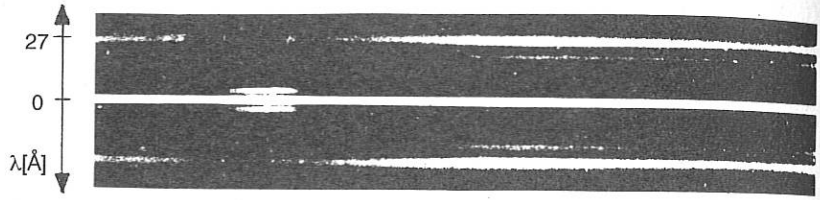

Fig.1: Spatially resolved spectrum (310 Pa D_2 , 20 Pa Ar,5 shots; transmission grating spectrograhp). The 4 Å radiation is emitted by plasma points inside the plasma column.

The percentage of heavy gas admixture strongly influences the final pinch, especially the probability of micropinches to occur, which was found earlier in various plasma focus devices [1,2].In the DPF-78 argon admixture above 10 Pa (to 300 to 500 Pa D_2) results in the appearance of micropinches in the plasma column with dimensions of 200 to 500 μm. Increasing the argon filling above about 20 Pa and especially by adding small amounts of heavier gases (2 to 4 Pa Kr or 0.1 to 0.5 Pa Xe) one can observe micropinches with dimensions of 20 to 50 μm. There exists an upper limit for the heavy gas admixtures. This limit is found because heavy gas admixture may also strongly influence the intial (breakdown) phase of the discharge, which again influences the final (pinch) phase. The appearance of the observed highly compressed micropinches seems to be caused by strong radiation energy losses through multiply-charged ion line emission [3]. In Fig.2 examples of two enlarged pictures taken with a quadratic pinhole (450 μm) are shown. From densitograms one can determine the dimensions of the micropinches using the shadow technique.

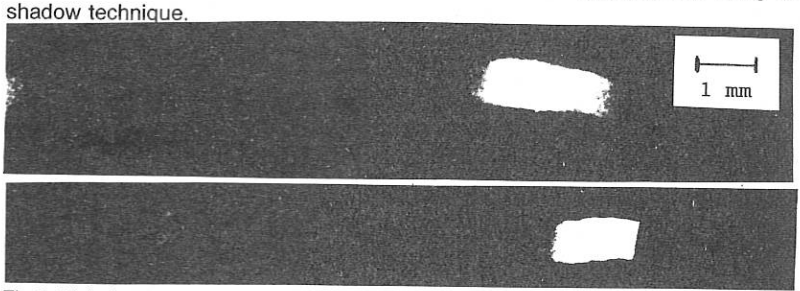

Fig.2: Pinhole pictures from two discharges, upper: (D_2 ,Ar, Kr) = (250,15,5)Pa, lower: (D_2 ,Ar,Kr) = (250,20,3)Pa; electrode left.In the upper picture only one micropinch region at the right can be seen, whereas in the lower picture multiple micropinch activity is recorded.

The most prominent diagnostic features in the range n=2 -> n=1 transitions are the dielectronic sattelites, i.e. the transitions of type a (1s2l - 2l'2l) and b (1s2l2l' - $1s^2$2l' (see Fig.3 for case b). The ratio of the intensity of these lines to the intensity of the parent line I_{par} (1s-2p and $1s^2$-1s2p) is a function of the plasma temperature T_e in stationary conditions [4]. Investigating a highly transient plasma we can only interpret measured ratios I_{sat}/I_{par} in terms of some mean temperature. Intensity ratios

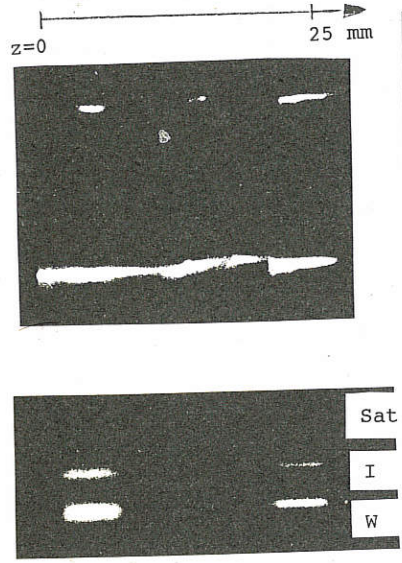

Fig.3: Space resolved spectra of three single micropinches taken during one discharge, together with two pinhole pictures (filter 10 μm Al and 25 μm Al resp.).The axial scales of the pinhole pictures and the spectra are equal. The brightes micropinch occurs nearer to the electrode. [H]lines are seen as well in the spectra (but not shown in the presented range).

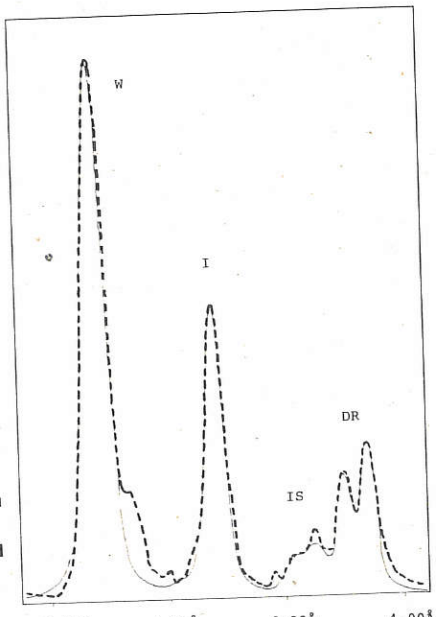

Fig.4: Ar[He]-transitions with [Li]-sattelites. Dashed line: experimental spectrum; Solid line: Model simulation. The discrepancy between the two spectra on the right wing of the resonance line (W) is due to $1s2l3l'$-$1s^2 3l'$ transitions which are not included in the modelling program. Parameters from the simulation: T_e=900 eV, n_e=9·10^{21} cm^{-3}

of He-like sattelites to Lyman α can be measured rather accurate. The case of Li-like sattelites needs a special deconvolution procedure in order to separate the dielectronic part and the collisionally excited part [5]. An example of the comparison between a simulated and an experimentally recorded spectra from a single micropinch is presented in Fig. 4. Finally the ratio of the intensities of Lyman α to the resonance line gives the ionization temperature T_z, i.e. a temperature which would exist in the case of equilibrium conditions. The value of T_e for 200 to 500 μm micropinches measured both by He-like and Li-like sattelites is in the range of 0.9 to 1.4 keV, T_z is not higher than 0.7 keV. So we can conclude about the ionizing transient character of the plasma.

In some spectra Doppler shifts between lines emitted from separated micropinches occuring during the same discharge could be measured, corresponding to relative velocities perpendicular to the column axis of the order of 10^7 cm/s.

Some micropinches reveal an interesting spectral feature in the region of the He-like/Li-like n=2 -> n=1 transitions: The dielectronic part of the sattelite transitions 1s2l2l' - $1s^2$2l' is less broadened than the intercombination line. A comparison with the intercombination line is substantial, because the resonance line can be broadened due to optical thickness of the emitting plasma. Having in mind the transient character of the micropinch plasma we can conclude that the process of increasing of the temperature T_e is accompanied by increasing of the plasma velocities (radial or turbulent) which cause the line broadening.

Micropinch Dynamics

An X-ray streak camera [6] was used to determine the lifetime of single micropinches. For this purpose the whole (horizontal) pinch column is imaged by means of an oblique positioned slit (200 μm) to the vertical 'slit' of the streak camera which consists of a 300 μm wide strip of CsI on the photocathode. Measured lifetimes range from 200 to 400 ps.

With a ten channel PIN-Diode array [7] the times of appearance of various micropinches along the pinch column could be identified in comparison with pinhole pictures. There is a tendency that micropinches which are formed more distant from the anode occur at later times relative to the ones formed nearer to the anode.

Microwave emission

From extensive angular resolved measurements of the μ-wave emission in the X-, R-, and E-band (8 - 90 GHz) - mostly from discharges in pure D_2 - it was found that 1) a strong temporal correlation exists between the REB and μ-wave pulses (FWHM: 3 - 10 ns) measured (minus)end-on, 2) μ-waves are also emitted +end-on, but about a factor 100 less in intensity and only 10 - 20 ns after the onset of the electron pulse, 3) heavy gas admixtures reduce the μ-wave intensity but do not influence the time correlation, 4) no correlation between neutron yield and μ-wave intensity exists.

References

[1] K.N. Koshelev et al., J. Phys. D:Appl. Phys. 21,1827 (1988)

[2] P. Antsiferov et al., Proc.18th ECCFPP, Berlin 1991, Part II,p.221

[3] Koshelev, K.N., Pereira,N.R., J.Appl. Phys. 69, R21 (1991)

[4] Sobelman,I.I., Vainshtein, L.A., Yukov, E.A.: Excitation of Atoms and Broadening of Spectral Lines, Springer-Verlag,1981

[5] F. Rosmej, Ph.D. Thesis, Universität Bochum, 1991

[6] We want to acknowledge the help of Dr. Sigel and Dr. Tsakiris from the Max Planck Institut für Quantenoptik, Garching, who borrowed their X-ray streak camera to us.

[7] The PIN-Diode array was kindly given to us by Prof. L. Pina, Technical University of Praha, CSFR.

THE RELATIVE ROLE OF THE MACROSCOPIC AND MICROSCOPIC PHENOMENA IN THE PLASMA FOCUS PERFORMANCE

V. Zambreanu and V. Zoita
Institute of Atomic Physics
IFTAR, L22, P.O.Box MG-7, Magurele, Bucharest, R-76900, Romania

The last stages of the plasma focus device (PFD) operation was investigated using a broad set of diagnostics with the aim of finding a correlation between the characteristics of the neutron emission and the macroscopic plasma dynamics and of evaluating the importance of the macroscopic phenomena in the neutronic performance of such a device.

The experiments were carried out on the IPF-2/20 plasma focus device (stored energy is 20kJ at 20kV; 450 kA peak discharge current) /1/. The electromagnetic quantities were measured by the following devices: the time derivative of the discharge current (dI/dt) by a magnetic probe located between the collector plates; the collector voltage (U) by a fast resistive voltage divider; the time derivative of the magnetic field (dB/dt) due to the plasma current by a magnetic probe placed in front of the coaxial electrodes. The evolution of the plasma configuration in the collapse, pinch and post-pinch phases was investigated using an image converter streak camera and a four-channel refractometric system (interferometry, schlieren, shadow) based on pulsed (2ns duration) UV TEA nitrogen lasers /2/. The plasma focus neutron yield and fluence anisotropy were measured by means of

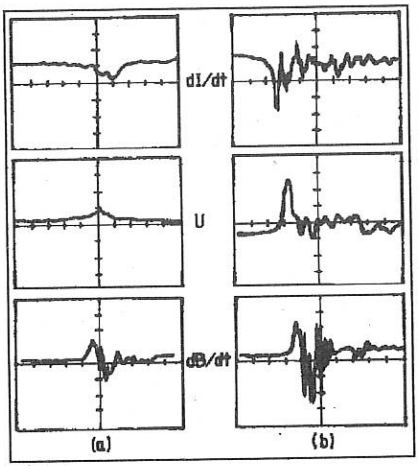

Fig.1
Two sets of electromagnetic signals for (a) low ($5x10^6$) and (b) high (10^8) neutron yields (in neutrons/discharge).

a five-channel Ag activation system. Four activation detectors were placed in the horizontal plane containing the PFD electrode axis at various angles with respect to this axis: the experiments reported here were performed with the four detectors at angles 0°, 30°, 60° and 90° with respect to the electrode axis. The absolute calibration of the activation system was done using a PoBe neutron source, while a relative calibration of the four anisotropy detectors was also done by placing them at locations that were equivalent to each other from the neutron field point of view and irradiating all detectors simultaneously by the same plasma focus discharge. A fifth activation detector placed at 270° was used as a monitor. The neutron emission rate was recorded by a scintillator-photomultiplier detector placed axially at 3.5m from the electrode end.

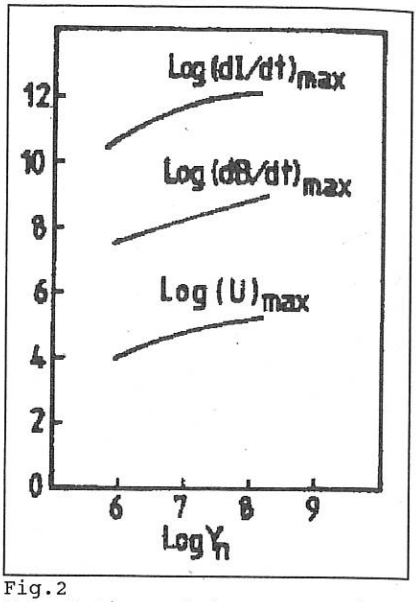

Fig.2
Correlation between maximum amplitudes of the electromagnetic signals and neutron yield

The electromagnetic measurements have shown that in discharges with high neutron yields the electromagnetic signals are systematically characterized by large peak amplitudes and high frequency oscillations (See Fig.1 where the time scale is 100ns/div. and the amplitude scales -one div.-are: 1.39×10^{11}A/s for dI/dt, 11.3kV for U and 4.33×10^{7}T/s for dB/dt). The existence of a correlation is clearly seen in Fig.2 where the maximum amplitudes of the three electromagnetic signals are plotted against the corresponding neutron yield as measured over a large number of discharges on the IPF-2/20 PFD.

The streak camera measurements showed no correlation between

the radial velocity of the plasma sheath at the end of the collapse phase and the neutron yield for this PFD. On the other hand the refractometric studies pointed out very clearly that high neutron yields are correlated with high rates of change of the plasma structures during the pinch and post-pinch phases. These studies evidenced another importance fact: the presence of well developed macroscopic instabilities does not necessarily lead to high neutron yields.

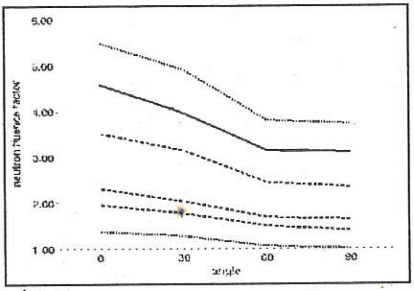

Fig.3
Neutron fluence factor measured at 0°, 30°, 60° and 90° for six discharges of increasing yield: 2.4×10^8 (bottom) and 8.9×10^8 (top) (neutrons/discharge)

The measurements of the neutron fluence at various angles with respect to the electrode axis pointed out not only the fact that the fluence anisotropy increases with increasing neutron yields, but also that higher values of these quantities correspond to higher rates of change of the pinch and post-pinch plasma structures (as seen in the interferometric and shadowgraphic measurements). Fig.3 shows the neutron fluence measured at four angles for six discharges of increasing yield. On the y-axis it was represented a neutron fluence factor proportional to the product of the neutron yield by the fluence anisotropy. The neutron emission rate was also recorded during the yield and fluence anisotropy measurements and in Fig.4 the peak emission rate is plotted against the end-on/side-on anisotropy for a series of discharges with increasing neutron yields (lowest point: 1.9×10^8; highest point: 9.4×10^8).

The correlated use of the information provided by the electromagnetic and optical diagnostics methods shows that the electromagnetic behaviour of the plasma focus configuration during the last phases is dominated by resistive rather than inductive effects. Moreover, it turns out that higher rates of change of the electromagnetic quantities systematically lead to

better neutronic performance.

During the collapse phase any significant transfer of electromagnetic energy to the plasma particles should be prevented by the high value of the magnetic Reynolds number, $R_m \approx 2\mu_0\sigma v_r$, where σ is the plasma electrical conductivity and v_r is the radial collapse velocity. However at the end of the collapse, when $v_r \rightarrow 0$ and R_m becomes less than one, a fast magnetic field diffusion starts accompanied by energy transfer to the plasma particles. This process is obviously dominated by the plasma electrical conductivity rather than by the plasma sheath velocity. v_r could however play an important role in the energy transfer process during the pinch expansion phase through the $v_r \times B$ field /3/. Actually, in /4/ it was found that a pulse of accelerated ions is produced during the explosive expansion of the pinch column confirming the role of field-particle interactions in the energy transfer process.

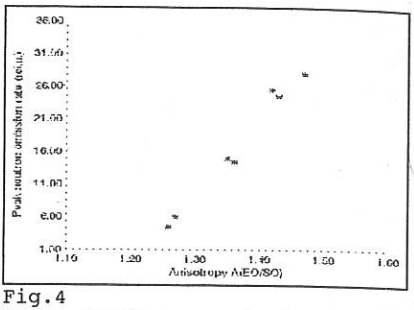

Fig.4
Peak neutron emission rate versus end-on/side-on A(EO/SO) fluence anisotropy

The neutron diagnostics results clearly show that high neutron yields are associated with stronger neutron anisotropies and higher peaks in the emission rate. Combining the results of Fig.2 with those in Fig.4 it follows that the dominant processes in the neutronic performance are those which govern the power (not energy) flow in the system. Since the electromagnetic power flow turns out to be dominated by resistive (known to be highly anomalous) effects we may conclude that the microscopic processes are the important ones in the neutronic performance of the PFD.

/1/ Nuclear Fusion Special Suppl. 1991, p. 232
/2/ I. Baltog et al., Beitr. Plasmaphys. 25, 263 (1985)
/3/ P. Choi et al., Phys. Letters A 128, 80 (1988)
/4/ V. Zambreanu and C. Doloc, "An electrodynamic model for the ion behaviour in the last phases of the plasma focus discharge", accepted for publication in Plasma Phys. and Contr. Fusion,(1992)

INVESTIGATION OF CHARGED PARTICLE AND X-RAY PULSES EMITTED FROM PF-TYPE DISCHARGES

M.Sadowski, A.Szydłowski, J.Żebrowski, E.M.Al-Mashhadani
Soltan Institute for Nuclear Studies,
05-400 Otwock-Świerk n. Warsaw, Poland

High-current plasma discharges of the PF-type are pulsed sources of different energetic particles, e.g. fast deuterons /1-3/, accelerated impurity ions /4-5/, fusion reaction products /6/, as well as high-energy electrons /7-8/. Such discharges are also sources of intense X-rays /9-10/. In order to understand physical processes occurring within the plasma region there are necessary detailed studies of those corpuscular and X-ray pulses.

The main aim of this paper is to report on recent studies of intense corpuscular beams and X-rays emitted from a large PF-360 facility /8,11/. These studies have been performed with the device equipped with coaxial electrodes made of 300-mm-long copper tubes of 120 and 170 in diameter, respectively. The facility has been operated under initial pressure charged from 3.0 to 10.0 torr (D_2 +admixtures) at the energy levels ranging from 120 kJ/30 kV up to 164 kJ/35 kV.

In order to performed ion measurements use was made of nuclear track detectors of the CN- and CR- type. To measure the angular distributions the detector were placed at different angles at a chosen distance from the PF region. To investigate the ion emission along the z-axis there was applied an ion pinhole camera. Using different absorption filters in front of the track detectors it was possible to perform a rough energy analysis of the registered ions. The ion measurements have shown that angular distributions, as obtained at higher operational energy, are similar to those observed in experiments performed at lower energy /5/. Ion pinhole pictures taken along the z-axis have also demonstrated similar features to those observed in the previous experiments /12/. In general, the ion angular distributions have revealed a distinct anisotropy, but they can be approximated by relatively smooth curves, as shown in Fig.1.

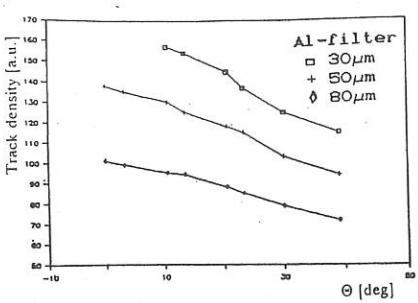

Fig. 1. Angular distributions of high-energy ions emitted from PF-360 facility, as measured for 30 shots performed at p_0=5 torr D_2, U_0=34 kV, W_0=144 kJ, Y_n=1.7x10^{11}.

The space-resolved ion pinhole pictures taken end-on have confirmed that among numerous low- and medium-energy ions there are emitted narrow bunches of high-energy ions, as shown in Fig.2.

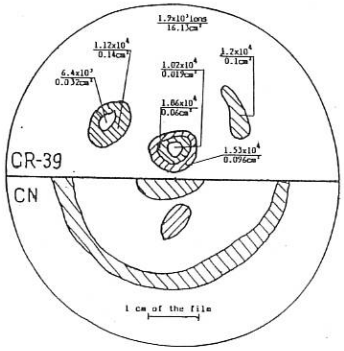

Fig. 2. Ion density map from a pinhole picture taken end-on for a PF-shot performed at p_0=4 torr D_2, U_0=34 kV, W_0=166 kJ, Y_n=7.3x10^9.

track detectors has just been started.

The measured angular distributions of deuterons have been extrapolated to small and large angles. Taking into account deuterons of energy ranging from 10 keV to 1 MeV, and using the beam-target model, corresponding energy spectra of fusion neutrons and protons have been computed, as shown in Fig.3. It can be seen that, if the theoretical model is adequate, the neutron energy spectrum (observed at $\Theta=\Pi/2$) should be around 2.5 MeV, while the maximum of the proton energy spectrum (observed at $\Theta=0$) can be shifted to about 4.0 MeV.

Simultaneously with the ion studies there were performed detailed investigations of REBs emitted through the hollow inner electrode in the up-stream direction. Time-integrated measurements have been

During the described ion studies particular attention has been paid to fusion reaction protons. Using 80-μm-thick Al-foils and CR-39 detectors it was possible to eliminate all the ions except for very fast deuterons of energy > 3.9 MeV and fusion protons of energy > 2.9 MeV. Analyzing dimensions of etched craters one could determine the number of registered protons. It has been found that at the distance of 340 mm there are registered about 4.3x10^3 fusion protons per cm^2 per shot. A comparison of this number with the fusion neutron yield, as measured with separate neutron counters, shows that efficiency of the proton registration has been very low. To verify the data a calibration experiment with various

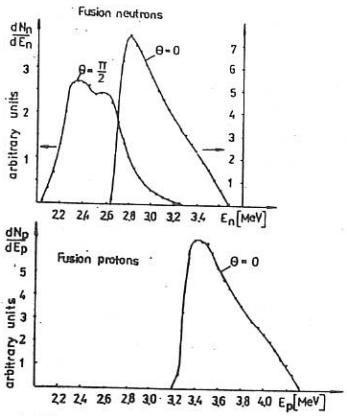

Fig. 3. Energy spectra of fusion neutrons and protons, as computed on the basis of the beam-target model.

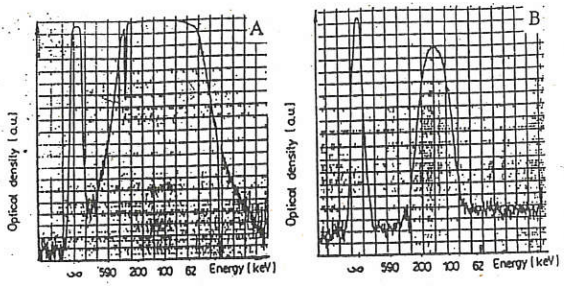

Fig. 4. Energy spectra of REBs, as measured for W_0=154 kJ shots: A - p_0=4 torr D_2, 6 μm Al-filter; B - p_0=3.8 torr D_2 + 0.25 torr Ar, 26 μm Al-filter.

carried out with a magnetic spectrometer /8/. The REB energy spectra have ranged from about 50 keV to above 800 keV, as shown in Fig.4. With 6-μm-thick Al-filters, eliminating electrons of energy <36 keV, even one shot gives a strongly saturated REB picture. With thicker (>30 μm) Al-filters and using Ar admixture, one can obtain unsaturated pictures which correspond to lower REBs yields. It has been found that with an increase in the neutron yield there is also observed an increase in the REB emission.

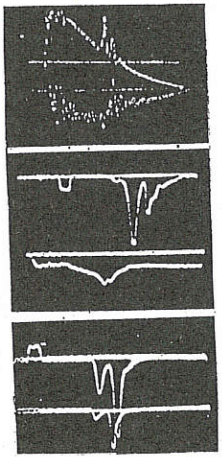

Fig. 5. Voltage and current waveforms, and comparison of neutron and r_{min} signals with REB pulses for 132 kJ shot at 4 torr D_2.

Time resolved REB measurements have been performed with the Čerenkov-type detectors /8/. It has been observed that there appear usually 2 groups of REBs pulses shifted by 80-200 ns, as shown in Fig.5C. The FWHM value for individual REB pulses varies from 20 to 100 ns. Using different Čerenkov radiators and filters it was possible to perform a rough energy analysis. It has been found that the population of REBs > 360 keV is usually 3-5 times smaller than that > 215 keV (detected with plastic and diamond radiators placed behind a 30-μm-thick Cu filters).

Simultaneous X-ray measurements have been performed with different pinhole cameras and scintillation detectors. Hard X-ray signals appearing before the neutron-induced signals, as shown in Fig.5B, could be identified. Side-on observations of soft- and hard-X-rays have confirmed close correlations of those pulses with the current peculiarity and the REBs emission.

Particular attention has been paid to studies of a fine structure of the X-ray emitting plasma region. On the basis of numerous observations, as carried out with different X-ray pinhole cameras equipped with very thin (<10 μm) Be-filters, it has been proved that the PF pinch column has a complex microstructure. The continuous quasi-axial filaments, as observed for very high current PF discharges /10/, have not been found in the PF-360 device, but it has been shown that even with the pure D_2 filling numerous hot spots can appear, as presented in Fig.6A. Using an additional heavy gas, e.g. Ar admixture (up to 30 percent), one can easily increase amount and intensity of the X-ray hot spots, as shown in Fig.6B.

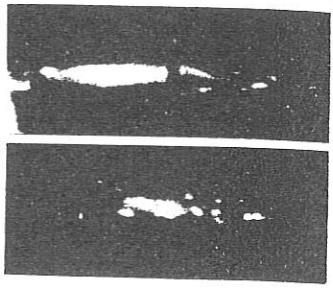

Fig. 6. X-ray pinhole pictures showing hot spots, as observed for PF-360 shots: A - p_0=4 torr D_2, W_0=138 kJ, $Y_n=1.4\times10^{10}$; B - p_0=3.9 torr D_2 + 0.2 torr Ar, W_0=154 kJ, $Y_n=1.8\times10^{9}$.

The experimental results presented above can be summarized as follows:

1 - The charged particle emission characteristics are similar to those obtained for other medium-scale experiments, although some quantitative differences are observed.
2 - The REBs emission demonstrates the multi-spike character, while for PF shots with higher neutron yields there is observed also an increase in the REBs yield , in the maximum electron energy, and in the FWHM of the spectrum.
3 - The microstructure of the PF pinch column is confirmed and the operational conditions are found when numerous X-ray hot spots are generated in the PF-360 facility.

/1/ R.I.Gullickson, H.L.Sahlin, J.Appl.Phys. 49, 1099 (1978)
/2/ M.Sadowski, H.Schmidt, H.Herold, Phys.Lett. 83A, 435 (1981)
/3/ W.Stygar, G.Gerdin et al., Nucl.Fusion 22, 1161 (1982)
/4/ A.Moser, M.Sadowski et al., J.Appl.Phys. 93, 2959 (1982)
/5/ M.Sadowski, J.Żebrowski et al., Plasma Phys.Contr.Fusion 30, 763 (1988)
/6/ U.Jäger, L.Bertalot, H.Herold, Rev.Sci.Instrum. 56, 77 (1985)
/7/ V.Nardi, W.H.Bostick et al., Proc.I LAW, Vol.I, p.114, Cambuguira 1982
/8/ M.Sadowski, L.Jakubowski et al., Proc. 18th Europ.Conf, Pt II, p.233, Berlin 1991
/9/ K.H.Schönbach, L.Michel, H.Fischer, Appl.Phys.Lett. 25, 547 (1974)
/10/ M.Sadowski, H.Herold et al., Phys.Lett. 105A, 117 (1984)
/11/ H.Herold, A.Jerzykiewicz, M.Sadowski, H.Schmidt, Nucl.Fusion 29, 1255 (1989)
/12/ M.Sadowski, J.Żebrowski et al., Proc. 4th Int.Workshop PF, p109, Warsaw 1985

FUSION REACTION YIELD IN FOCUSED DISCHARGES WITH VARIABLE ENERGY AND PLASMA FINE STRUCTURE

A. Bortolotti, J. S. Brzosko, P. De Chiara, H. Kilic, F. Mezzetti, V. Nardi, C. Powell and J. Wang
Stevens Institute of Technology Hoboken, N. J. 07030, USA
University of Ferrara, 44100 Ferrara, Italy
Cooperative Research Program

Summary. The same linear correlation between the distribution parameters (ΔT and Max ΔV) of the radial current density J_r between electrodes and the fusion reaction yield per pulse, Y, in the plasma focus (PF) pinch was quantitatively determined from different PF machines. Contact prints of current-sheath fragments (CSF) ejected from the pinch are obtained from 2.5-MeV-D^+ ions. CSF's show the same submillimetric fine structure of the pinch.

Introduction. The D-D fusion reaction yield, Y, per pulse of focused discharges is monitored by changing the capacitor bank voltage V by a factor 2 without any change in construction parameters of two plasma focus machines PF1 ($C_1 \cong 50\ \mu F$, $L_1 \cong 20$ nH) and PF2 ($C_2 = 1.2 \cdot C_1$, $L_2 = 2 \cdot L_1$) with Mather's geometry. The interval $\Delta = 1_2 + (\Delta W)/W$ of the capacitor bank energy W on which the scaling $Y \sim W^2$ applies, is greater for PF2, where the corresponding variation ΔI_2 of the peak electrode current I_2 is smaller (in agreement with $L_1/C_1 > L_2/C_2$) than for PF1. Suitable figures of merit (in terms of ΔI, ΔW, L, C, etc.) are used for determining the relative importance of (i), the induced variations of the fine structure of the current sheath (and its fragments), and of (ii) the variations of the insulator surface at the breech, with bearing on the initial stage of the current sheath formation. Magnetic probe data monitor the current sheath structure and propagation speed /1/. The D-ion emission from the pinch is monitored in a wide energy interval from 50 keV to 25 MeV for clarifying the links between the pinch fine structure and the set of leading macroscopic parameters of the PF discharges.

The MeV-deuteron induced radioactivity ($\beta+$) in the plasma was measured when the PF chamber was filled with deuterium and doped with HZ-nuclei (carbon or nitrogen): This method can differentiate fusion reactivity and spectral characteristics for low energy ions, $E \lesssim 0.1$ MeV (D+D fusion), medium energy ions, 0.5 MeV < E < 3 MeV (HZ+D reactions)/2/. The results are assessed in terms of high-reactivity plasma domains (hot-spots).

Current Distribution. The radial current J_r is determined from the magnetic probe signal of the time variation $\dot{B}_\theta$ ($\propto J_r$)) of the azimuthal magnetic field between the electrodes /1/. For the discharges (> 90% of the total) in which a multiplicity of current sheaths form we determine the bearing on Y (D+D reactions) of the time spacing ΔT between the first two current sheaths. Two current sheaths are considered as time resolved if the $\dot{B}_\theta$ signal changes sign between the two leading continuous peaks, both with the same amplitude sign. Fig. 1(A) reports the PF geometry and the location of the $\dot{B}_\theta$ probes and of the CR-39 targets on which D^+ tracks are etched. The values of the linear correlation coefficient r for (Y,ΔT) from different groups of N discharges under different pressure and voltage conditions, are

* Work supported by AFOSR, Bolling AFB, DC (USA) and MURST, Roma (Italy).

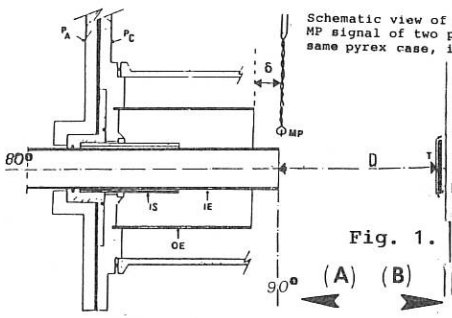

Schematic view of PF, magnetic probe MP and target T in (A). MP signal of two probes with opposite orientation, inside the same pyrex case, in (B).

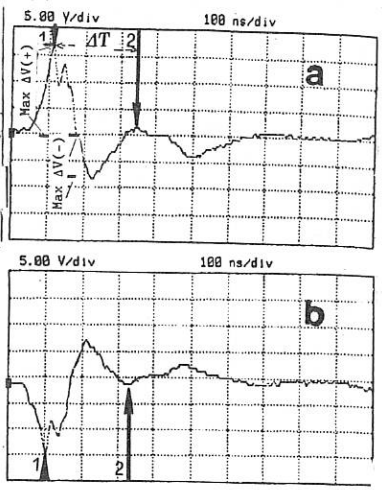

Fig. 1.

TABLE I-A STATISTICAL ANALYSIS OF PROBE DATA FOR PF(I)-U.F.E. AND PF(II)-S.I.T. (ΔT VS. Y)

PROBE		LIN.COR.COEF.	CONFIDENCE LEVEL(1-P)
1 (6 TORR)	PF(I),17KV	-.11	80%
2 (3 TORR)	PF(II),16KV	-.36	85%
2 (5 TORR)	PF(II),16KV	-.12	65%
2 (8 TORR)	PF(II),16KV	-.33	95
2 (ALL PRESSURES)	PF(II),16KV	-.21	>95%
3 (ALL PRESSURES)	PF(II),16KV	-.30	80%

TABLE I-B STATISTICAL ANALYSIS OF PROBE DATA FOR PF(II): (MAX ΔV/Δ V) VS.Y

2 (ALL PRESSURES)	16KV	-.12	70%
3 (ALL PRESSURES)	16KV	-.38	70%

reported in Table I-A. These data were obtained from two identical machines PF(I) and PF(II) with the above PF-1 characteristics and clearly indicate that the smaller is the time spacing ΔT between leading current sheaths, the higher is the fusion yield Y. The value of r and its confidence level, 1-P(r,N), are affected by the capacitance coupling of the probes with the plasma via boiled-off material from the pyrex case of the probes, a pyrex capillary tube of 3 mm to 4 mm in diameter. The determination of this capacitance coupling and of its bearing on the $\dot{B}_\theta$ signal from the inductive coupling was carried out with two probes in the same pyrex case. The two identical probes (each with a 1.2 mm diameter loop, and an anti-inductive shielding connection to the H.P. signal monitor) have opposite orientations. The two Fig. 1(B) signals from these two probes of opposite-orientation had a different amplitude reduction [x1/10-for (a); x1/12.5 for (b)] before entering the H.P. digitizer/display system. Consistently, the maximum amplitude Max ΔV(+) of the leading composite peak 1 in (a), is higher by a factor 1.25 than the absolute amlplitude of peak 1 in (b). This means that no plasma/probe capacitance coupling is affecting the $\dot{B}_\theta$ signal for at least the first 100 nsfromthe time t_o the leading current sheath starts to sweep the probe. The trailing current signal has a peak 2 with absolute value in (b) equal to that of 2 in (a). This means that the plasma/probe capacitance coupling is a function of time, with an appreciable contribution to the probe signal of about 25% of its amplitude at the time t_o + 230 ns of the peak 2. A conclusion is that for single-probe data, the value of r and of its confidence level 1-P can be modified by rotating the plane of the probe loop by 180°. The probe 3 of Table I is the same as probe 2, but for a 180° rotation of the probe loop. The corresponding data are consistent with the above conclusion and provide an assessment of the capacitance coupling effect on r. The overvoltage surges and restrikes at the PF breech (from the resistive surge [of amplitude IL(plasma)] of the radially imploding current sheath) are the direct cause of the dip of absolute value Max ΔV(-) in B_θ signal

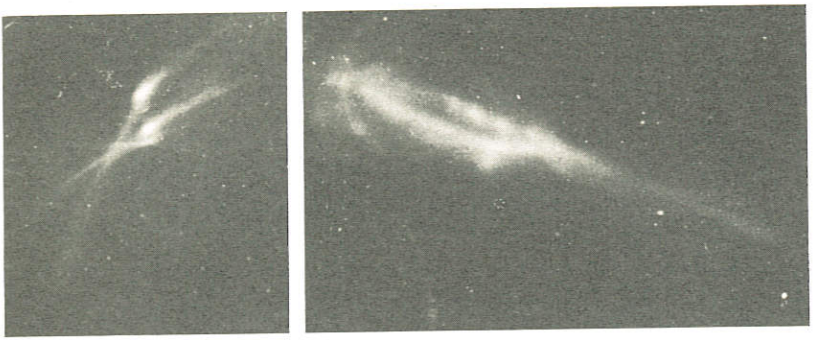

Fig. 2. Contact-print image of axially-ejected plasmoid impacting on a screened CR-39 target T. The image is formed by the non-uniform distribution of D-ion tracks with energy E > 2.5 MeV in (A) E > 1.5 MeV in (B)(D=10 cm). Note hot spots. The electrode axis intercepts the center of (A), and (B)at low right.

TABLE II

CONTACT PRINT OF CURRENT SHEATH FRAGMENTS VIA ETCHED ION TRACKS, ON CR-39 TARGETS (TARGET EXPOSED TO A SINGLE DISCHARGE)

TARGET DISTANCE D (CM)	FILLING PRESSURE (TORR)	MYLAR SCREEN THICKNESS (μM) AND E	OCCURRENCE RATIO: N(C.P.)/N(TOT.) 16 KV DISCHARGES	
10	3(P (8	25 (E)1.5 MEV)]	9/13 (69%)	Y(6)=(0.4 TO 1.6$\bar{Y}$(6)
		50 (E)2.5 MEV)]	5/53 (9%)	Y(5)=(0.2 TO 1.0$\bar{Y}$(5)
25	3(P (5	50 (E)2.5 MEV)]	4/25 (16%)	Y(4)=(0.9 TO 1.1$\bar{Y}$(4)
	5(P (7	50 (E)2.5 MEV)]	3/25 (12%)	Y(7)=(0.6 TO 1.5$\bar{Y}$(7)

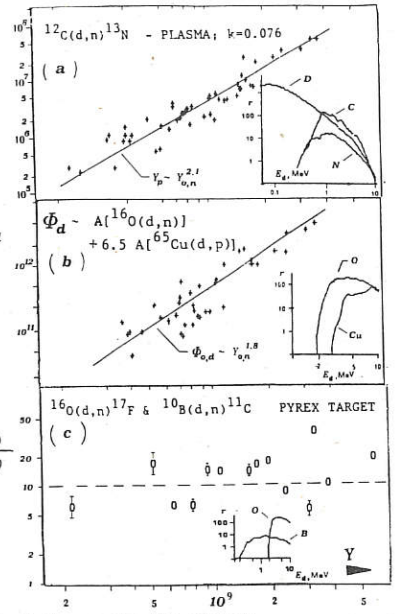

Fig. 3. High-Z fusion reactionyield per discharge Y_p (from D+HZ nuclei) in (a), total fluence Φ_d of fast D ions (E > 0.5 MeV) ejected from the pinch in (b), ratio of the radioactivity A of two nuclear reactions (D + O, D + B) induced from the D-ion bombardment of an azimuthaly-symmetric target - in (c) - covering the solid angle $0 \lesssim \vartheta \lesssim 2\pi$, $25° \lesssim \varphi \lesssim 120°$, as functions of the D+D fusion yield, Y, in the same discharge. The numerical factor 6.5 in (b) accounts for the different values of the geometry-dependent efficiency of the detectors and of the cross-sections of the two fusion reactions. $k = \varrho_{HZ}\varrho_d / (\varrho_{HZ} + \varrho_d)$ in (a); $r = (d\Phi_d/dE)\cdot\sigma(E)$ in (c). ϱ_{HZ}, ϱ_d are the density (cm^{-3}) of HZ and D nuclei, respectively, in the PF filling gas.

between peaks 1 and 2 of Fig. 1. Table I-B reports the linear correlation coefficient (and its confidence level) for Y, Max $\Delta V/\bar{\Delta V}$, where Max ΔV = Max $\Delta V(+)$ + Max $\Delta V(-)$ and $\bar{\Delta V}$ is the mean value of Max ΔV for all discharges at the same voltage. This is consistent with the view that a too high velocity of radial implosion of the leading current sheath (note position of probe) will induce a detrimental restrike at the breech which crowbars the pinch. We also find that the correlation coefficient for the number of peaks $\nu(\dot{I})$ in the $|dI/dt|$ signal and that $\nu(\dot{B})$ of the B signal from the same shot, in a series of N discharges is r = 0.32 with 1-P(r,N) = 90%. The time spacing between

peaks of the $\dot{B}_\theta$ signal is systematically smaller than the time spacing between corresponding peaks of the dI/dt signal of the same discharge. This indicates that the trailing current sheaths after rolling-off the interelectrode gap, may linger from 45 ns to about 150 ns in the region after the probe before pinching on the axis.

Contact Prints. Fragments of the PF current sheaths are forwardly ejected in the axial direction from the pinch region after the pinch disintegration. A CR-39 target (T) is axially located at a distance D (10 cm or 25 cm) from the end of the positive center electrode, with orientation orthogonal to the elextrode axis. A mylar foil of thickness 50 μm (or 25 μm thick, in other tests) covers the T-surface and screens out all D^+ ions of energy E < 2.5 MeV (or E < 1.5 MeV). The distance between screen and target is < 1 mm. The contact print of the impinging current sheath fragment (or plasmoid) with sharply-defined boundaries is formed from the non-uniform distribution of etched D-tracks on the CR-39 surface. Optical photographs of the plasmoid image formed on the CR-39 by ions with E > 2·MeV are reported in Fig. 1 (D = 10 cm). Equally sharp images are obtained for D = 25 cm with both 50 μm or 25 μm thick screens. A clear plasmoid contact print is not formed in all discharges. Table 2 summarizes the results from 120 discharges. Each target (5 cm x 10 cm) is exposed to only a single shot. A new screen is used for each target even though no detectable damage was observed on the screen after the exposure. If N(C.P) is the number of discharges in which a contact print is formed, out of N (Total) discharges under the same conditions, we find that the occurrence ratio R = N (C.P.)/N(Total) with the 25/50 μm screen does not appreciably depend on the PF filling pressure P in the interval 3 Torr ≤ P ≤ 8 Torr. With the 50 μm screen we also find that R does not depend on D in the interval D = 10 cm/25 cm. The majority of the contact prints from > 2.5 MeV ions shows clearly the same filamentary structure and the same hot spot abundance of the pinch previously described in the literature/3/. Contact prints are formed independently on the Y(D+D) value of a discharge. In the last column at right (of Table II) we indicate the range of the Y values (in terms of the mean value $\bar{Y}$) for the set of discharges (at one pressure value) which exhibit the broadest range.

Nuclear Reactivity. The nuclear reactivity data of Fig. 3 have been obtained by following the same method we have reported in /2/. The data provide further confirmation of the hot-spot structure of the pinch, and of the concentration of the nuclear fusion reactions in these regions of high density. A lower bound for the density in the hot spots was and is set at 10^{22} cm^{-3}.

Conclusions. The same fine structure on a submillimetric scale is observed in the self-field dominated plasma of a variety of PF experiments. Both ion-filter and nuclear reactivity data indicated that the energy spectrum of D^+ ions in the plama extends from 0.5 MeV to>2.5 MeV and that the localized regions of acceleration and confinement have linear extension substantially smaller than 1 mm.

*25 MeV D-ions from collective field acceleration of the PF electron beam are detected at 180°.

References.

1. V. Nardi, et al, IEEE Transactions of Plasma Science, Vol. 16, 3, p. 368, 1988.
2. J. Brzosko & V. Nardi, Physics Letters A, Vol. 155, p. 162, 1991.
3. W. H. Bostick, et al, J. Plasma Physics, Vol. 8, p. 7, 1972. Nuclear Fusion, Supp., Vol. 3, 109 (1974).

PARAMETRIC STUDY OF MIRROR PLASMA BASED NEUTRON SOURCE FEF-II

N. Mizuno
Department of Physics, College of Humanities & Sciences
Nihon University
Sakurajousui, Setagaya-ku, Tokyo, 156 Japan

H. Yamaguchi and T. Kawabe
Institute of Physics, University of Tsukuba
Tsukuba, Ibaraki, 305 Japan

S. Hirayama
Department of Mechanical Engineering
Kanagawa Institute of Technology
Atsugi, Kanagawa, 243-02 Japan

The feasibility of the plasma based neutron source for the testings of the fusion reactor materials and fusion nuclear engineering has been requested for the decision of the construction of the neutron source in very near future. We have been working on the design study of the mirror plasma based neutron source, FEF[1]. Recently, design study of the new version of the neutron source FEF-II has been started, aiming early construction[2]. One of the characteristics of FEF-II is introduction of sloshing ions of deuterium, which is injected by NBI into the mirror confined plasma, so that larger neutron flux is expected in the surrounding area of the turning point of the sloshing ions. In this paper, we describe the results of the investigation of the dependence of the 14MeV neutron flux on the parameters of the plasma, magnetic field and heating power of the FEF-II to find the optimum plasma parameters.

FEF-II is the two component systems for the plasma, and use of multi-pole field (Version 1) or RF plugged cusp

(Version 2) for MHD stability. Version 1 of FEF-II is shown in Fig.1. In FEF-II , we consider $n_e = n_i = 4\times 10^{14}$ cm^{-3}, T_e = 3 kev, T_i = 20 kev and central cell length is 330 cm, respectively. Details of major plasma and reactor parameters are shown in Ref.2 except those of the sloshing ions.

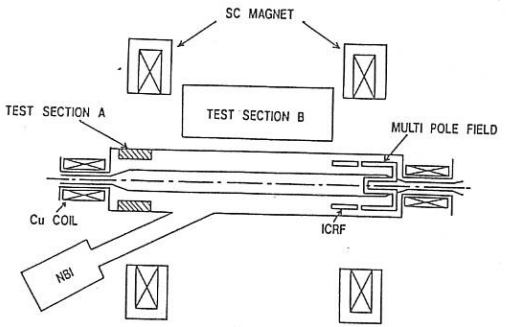

Fig.1. Schematics of FEF-II (Version 1).

Configuration of the magnetic field of FEF-II is basically long solenoid with mirror field at both end. The target plasma is produced by pellet injection of fuel and RF power in the mirror. The sloshing ions are generated by the oblique injection of NBI. The neutrons are producted by the fusion reaction between the sloshing ions of deuterium and the target plasma ions and among ions of the target plasma. The distribution function of the sloshing ions in the velocity space $f_s(v,\zeta,t)$ is obtained by the Fokker-Planck equation[3] to find the axial dependence of the neutron flux on FEF-II , where ζ is the cosine of the pitch angle. In Fokker-Planck equation, we include the term of the charge exchange loss of the sloshing ions and the production of the sloshing ions beside the Coulomb collision term. We assume the charge exchange loss as f_s/τ_{cx} and the production term as

$$S = \frac{I}{\pi e \,\Delta v\, v_o^2 \Delta\zeta\, V} \exp\left[-\left(\frac{v-v_o}{\Delta v}\right)^2 - \left(\frac{\zeta-\zeta_o}{\Delta\zeta}\right)^2\right],$$

where I is the NBI current, V is the volume of plasmas, v_o is the velocity of producted sloshing ions, ζ_o is the cosine of injection angle and τ_{cx} is the charge exchange time. In the first calculation of the temporal variation of the sloshing ions, we set I = 100 A, V = 9.4×10^4 cm^3, $m_D v_o^2/2$ = 100 keV, $m_D(\Delta v)^2/2$ = 1 keV, $\Delta\zeta$ = 0.01 and mirror ratio R = 3.4 as constant.

The sloshing ion density around the turning point is higher than that of the midplain since peaked angular distibution is formulated near the loss-cone angle. We obtain the axial distribution of the neutron production rate and study the dependence on the injection angle and the injection energy of NBI. The dependence on ζ_o of the neutron production is found to be small as shown in Fig.2, so we can choose the optimum injection angle as 45° for R = 3.4. The dependence on NBI energy of the neutron production rate is shown in Fig.3. We can see that the neutron production is higher at higher NBI energy. This is due to that the charge exchange loss of the sloshing ions is smaller in the case of the higher energy injection so that more sloshing ions is trapped in the mirror. It is found that the selection of the NBI energy is the trade off with the engineering feasibility of NBI.

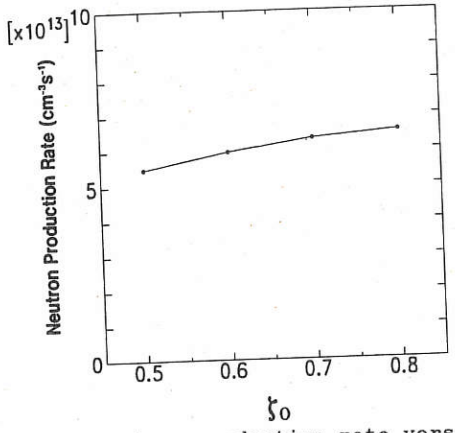

Fig.2. Neutron production rate versus ζ_o.

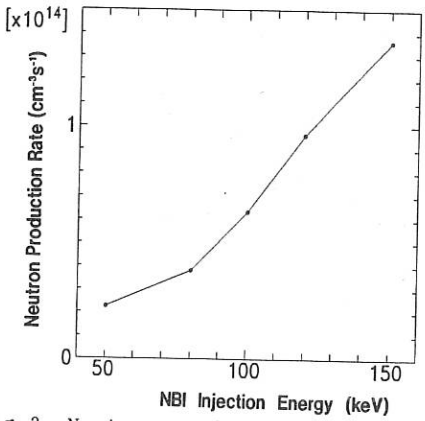

Fig.3. Neutron production rate versus NBI injection energy.

REFERENCES

1) T.Kawabe, S.Hirayama, et al., "The Physical and Engineing Aspects of Fusion Engineering Test Facility based on Mirror Confinement (FEF)", Fusion Technology, Nov./Dec. Vol.10, part 2B, 1102 (1986)

2) T.Kawabe and S.Hirayama, Proc. International School of Plasma Physics, Piero Caldirora, Physics of Alternative Magnetic Confinement Schemes, SIF, Bologna, pp 459-476 (1991)

3) N.Mizuno, H.Irie and M.Sato, J. Phys. Soc. Japan, Vol.54, 1830 (1985)

Direct conversion of a fusion energy into an electric one in the DRACON-trap

V.M.Glagolev, B.N.Kuvshinov, M.A.Proshin, A.V.Timofeev

I.V.Kurchatov Institute of Atomic Energy, Moscow, Russia

The fusion reactor with direct conversion of thermal charged particles energy into an electric one has essential advantages over the reactor with a thermal cycle. The direct conversion is desirable, in particular for the reactors with $D-^3He$ plasma. The development of the $D-^3He$ reactor based on DRACON has been started in [1] (Fig.1). The possibility of direct conversion (recuperation) of a plasma energy outflowing from such a trap, according to the block-diagramm proposed in [2], is analyzed in a given paper. The usage of such a block-diagramm is possible without a bundle-divertor and the plasma energy recuperation can be started at the plasma column perephiry in the DRACON magnetic field.

In the block-diagram [2] the recuperation occurs under drift in the cross fields (electric and magnetic), and, in this case, the magnetic field should decrease in its magnitude in the direction of the electric drift. Due to conservation of transversal, μ, and longitudinal $J_{\|}$, invariants the drift in the crossed fields should result in a reduction in transversal and longitudinal energy components ($\epsilon_{\perp} \propto B, \epsilon_{\|} \propto B^2$). The kinetic energy of particles transits into the electric field energy, since ions are displaced counter-electric field and electrons, co-field. The fraction of kinetic energy which makes transition into the electric one (recuperation efficiency) is given by the expression

$$\eta(\vec{r}) = 1 - b(\vec{r})sin^2\theta_0 - b^2(\vec{r})cos^2\theta_0, \qquad (1)$$

where θ_0 is the pitch-angle of a particle at the entry to the recuperator, $b(\vec{r}) = B(\vec{r})/B(\vec{r}_0)$, $\vec{r}$ and $\vec{r}_0$ are the current and initial coordinates of a particle. From (1) it follows that, for example, at $\theta_0 = 45^0$ the efficiency 80% is attained with an about three times reduction in the magnetic field within the recuperator.

Due to a transversal inhomogenety the DRACON magnetic field is acceptable for recuperation according to the block-diagram given in [2], and for the required electric field production in the mirrors of curvilinear pieses (CRELs) in DRACON at the plasma column periphery the sectioned electrodes with sustained contributed electric potential should be installed. The electrodes should have an electric (non thermal!) contact with the plasma. For sustaining an electric contact the electrodes should freely receive electrons from the plasma and emit them into it. An electric current passing through the electrodes, when the recuperator is in operation, transfers the energy released in it to the powerload [2]. As noted above, in the process of recuperation the drift trajectories of electrons and ions diverge. In that part of the recuperator, where ions enter, the electrodes should emit electrons (these electrodes should be heated to increase the emission). Hot electrons enter another part of the recuperator. In order to provide the obstacle-free sink of a negative charge through the mirrors a cool plasma should be introduced into this part of the recuperator. The opportunity to sustain the electric contact of the plasma confined in the adiabatic trap with end electrodes was demonstrated in [3].

In the process of recuperation hot particles should not be in the direct contact with electrodes. Installing electrodes in the CREL-mirrors, this condition is satisfied for the particles trapped in the DRACON mirrors, as well as for the particles which are reflected from the CREL-mirrors. At the same time, passing particles, diffusing outwards could enter the electrodes. However, the modes of operation, in which the main contribution into a diffusive flux is done by the particles trapped between the CREL-mirrors, are characteristic for DRACONs. The diffusion coefficients of such particles are rather high due to the fact that their toroidal drift is not copmensated by the rotational transform. A small fraction of the energy flux

transferred by passing particles can be received by narrow ring-like limiters separating the plasma column from the recuperation region, or removed through divertors.

In the process of recuperation the charged particles are removed from the plasma. At rather long distances from it the magnetic field of a DRACON transits, in a natural way, into a magnetic field of the recuperator discussed in [2]. The general view of the proposed device is shown in Fig.2.

We have also considered another modification of recuperation according to the block-diagram [2] with the usage of a divertors, see Fig.3. A given modification is more compact. However, due to the presence of a zero magnetic field point in the divertor the particles trapped between the CREL-mirrors can realize transitions into the passing ones, the energy of which will probably be removed by a thermal cycle, see above. The probability of transition can be found only on the basis of numerical calculations for an ensemble of particles trajectories entering the divertor. The analysis of separate trajectories, made by us, allows to hope that this probability is not great. The recuperation efficiency equal 0.9 was achieved in the motion along these trajectories.

The proposed direct conversion techniques of plasma thermal energy into the electric one is possible, in principle, in other closed traps too. The necessary condition for this is the presence of trapped particles the drift of which (super-banana drift-type in stellarators) determines the losses from a trap.

References

[1] V.M.Glagolev et al., Report at the USSR-U.S.A. Workshop on low-radioactive $D-^3He$ thermonuclear systems. I.V.Kurchatov Institute of Atomic Energy, Moscow, 81 (1991).

[2] A.V.Timofeev Fizika Plazmy, 4, 826 (1978).

[3] G.F.Abdrashitov, V.I.Volosov, V.A.Kubarev, Yu.N.Yudin, Report at the Workshop on the mirror traps, Moscow, 109 (1989).

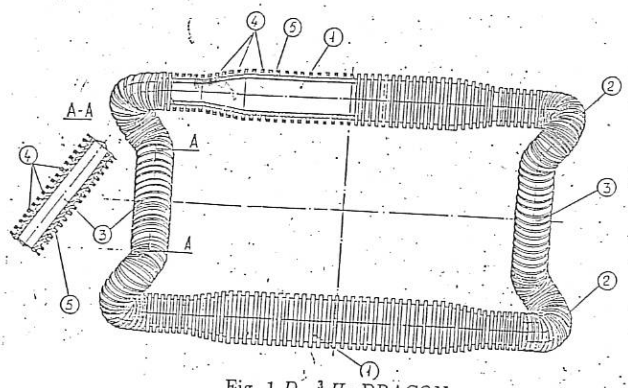

Fig. 1 $D-^3He$ DRACON reactor
1. Straight piece (mirror) 2. Heliac solenoids 3. Stabilizer
4. Coils 5. Shield against a neutron flow.

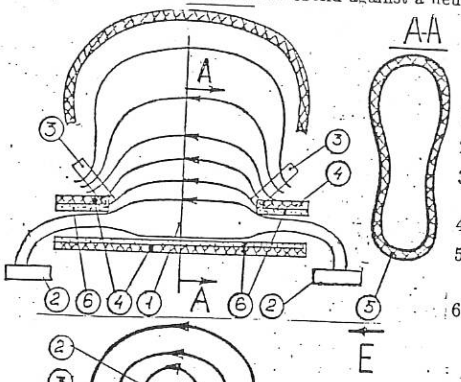

Fig.2
DRACON with the built-in convertor

1. Mirror
2. End electrodes in CREL
3. End electrodes in the con vertors
4. Mirror coils
5. Converter coil (cut in th A-A cross section)
6. Shield againts a neutro flux

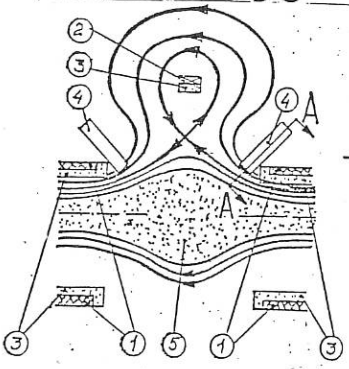

Fig.3
Converter with a separatrix

1. Mirror coils
2. Converter coil
3. Shield againts a neutron flux
4. End electrodes in the convert
5. Plasma of passing particles

ELECTRODYNAMICS OF PLASMA-MOLECULAR SYSTEMS WITH DRIFT MOTION OF CHARGED AND NEUTRAL PARTICLES

S.S.Moiseev
Space Research Institute, Moscow, Russia

N.V.Suyazov
Institute of General Physics, Moscow, Russia

I.P.Yakimenko
Institute for Theoretical Physics, Kiev, Ukraine

Lately, the great attention has been drawn to the development of the statistical theory of the combined plasma-molecular systems, i.e. the theory in which the free (plasma) and bond (atoms and molecules) particles are treated at the common methodological basis as equivalent dynamical subsystems taking an active part in different electrodynamical and gasdynamical processes in total (plasma-molecular) system. The reason for this is found both in the general theoretic considerations and in an extremely wide spreading of plasma-molecular systems in nature and laboratory. In order to estimate the spectrum of possible applications of this theory it is enough to mention far and near cosmos, controlled fusion devices, working medium of gas lasers, dusty plasmas, etc.

However, for such estimation it is necessary to have the clear and conclusive evidences of an active and (or) definite role of molecular subsystem in the physical processes proceeding in plasma-molecular systems. In a number of recent papers (see, for example, the book /I/ and references placed therein) such evidences have been given in a variety of cases of equilibrium and nonequilibrium plasma-molecular systems. At the same time a very interesting class of plasma-molecular systems with directed motion of charged and neutral particles have not been considered in these papers. Here, we study the electromagnetic properties of the systems of such kind.

Let us start from the general expression for the dielectric permittivity tensor describing a plasma-molecular system

at the linear level of approximation

$$\overleftrightarrow{\varepsilon}(\vec{k},\omega) = \overleftrightarrow{I} + \sum_{\sigma} \overleftrightarrow{\chi}_{\sigma}(\vec{k},\omega) + \sum_{\mu} \overleftrightarrow{\chi}_{\mu}(\vec{k},\omega) \qquad (I)$$

where $\overleftrightarrow{\chi}_{\sigma}(\vec{k},\omega)$ and $\overleftrightarrow{\chi}_{\mu}(\vec{k},\omega)$ are the susceptibilities of the subsystems of free (σ) and bond (μ) charged particles. The former one is determined in the standard way /2/ whereas the molecular susceptibility is calculated in the case of atom-oscillator model as /3/

$$\overleftrightarrow{\chi}_{\mu}(\vec{k},\omega) = -\frac{4\pi i n_{\mu}}{\omega^2} \int dx\, d\vec{P} \int_0^{\infty} d\tau\, e^{i(\omega + i\nu_{\mu} - \vec{k}\cdot\vec{V})\tau} \sum_{\ell,\ell_1} e_{\mu}^{\ell} e_{\mu}^{\ell_1} \qquad (2)$$

$$(\vec{V} + \alpha_{\mu}^{\ell}\vec{v})\, e^{-i\alpha_{\mu}^{\ell}\vec{k}\cdot\vec{r}}\, \overleftrightarrow{\beta}_{\mu} \cdot \left(\frac{\partial}{\partial \vec{P}} + \alpha_{\mu}^{\ell_1} \frac{\partial}{\partial \vec{P}_1}\right) f_{0\mu}(x,\vec{P})$$

Here,

$$\overleftrightarrow{\beta}_{\mu} = \left\{\left[\omega - \vec{k}\cdot\left(\vec{V} + \alpha_{\mu}^{\ell_1}\vec{v}_1\right)\right]\overleftrightarrow{I} + \left(\vec{V} + \alpha_{\mu}^{\ell_1}\vec{v}_1\right)\vec{k}\right\} e^{i\alpha_{\mu}^{\ell_1}\vec{k}\cdot\vec{r}_1},$$

$$\vec{r}_1 = \vec{r}\cos\omega_{\mu}\tau - (1/m_{\mu}\omega_{\mu})\,\vec{p}\sin\omega_{\mu}\tau,$$

$$\vec{p}_1 = \vec{p}\cos\omega_{\mu}\tau + m_{\mu}\omega_{\mu}\vec{r}\sin\omega_{\mu}\tau,$$

$$\frac{\partial}{\partial \vec{p}_1} = \cos\omega_{\mu}\tau \frac{\partial}{\partial \vec{p}} + (1/m_{\mu}\omega_{\mu})\sin\omega_{\mu}\tau \frac{\partial}{\partial \vec{r}},$$

ω_{μ}, ν_{μ} and n_{μ} are the eigen-frequency, dissipative constant and averaged number density for the molecular subsystems of μ-species; $\ell, \ell_1 = a, b$; $e_{\mu}^{a} = -e_{\mu}^{b} \equiv -e_{\mu}$; $\alpha_{\mu}^{a,b} = \mp m_{\mu}/m_{\mu}^{a,b}$, $m_{\mu} = m_{\mu}^{a} m_{\mu}^{b}/M_{\mu}$, $M_{\mu} = m_{\mu}^{a} + m_{\mu}^{b}$, $x \equiv (\vec{r},\vec{p})$ and $X \equiv (\vec{R},\vec{P})$ are the variables describing the internal degrees of freedom and the motion of atoms as a whole; $f_{0\mu}(x,\vec{P})$ are the unperturbed distribution functions for the neutral particles of μ-species.

Choosing the function $f_{0\mu}(x,\vec{P})$ in one or another way one can investigate the electromagnetic processes in corresponding equilibrium or nonequilibrium plasma-molecular

system. In particular, in case of "cold" molecular system with drift

$$f_{0\mu}(x,\vec{P}) = \delta(\vec{r})\,\delta(\vec{p})\,\delta(\vec{P}-\vec{P}^{\circ}_{\mu}),\quad \vec{P}^{\circ}_{\mu} = M_{\mu}\vec{U}^{\circ}_{\mu} \qquad (3)$$

and then

$$\overleftrightarrow{\chi}_{\mu}(\vec{k},\omega) = -\frac{\omega^2_{p\mu}}{\omega^2}\,\frac{1}{(\omega-\vec{k}\cdot\vec{U}^{\circ}_{\mu})^2 + i\nu_{\mu}(\omega-\vec{k}\cdot\vec{U}^{\circ}_{\mu}) - \omega^2_{\mu}} \qquad (4)$$

$$\left\{(\omega-\vec{k}\cdot\vec{U}^{\circ}_{\mu})^2\overleftrightarrow{I} + (\omega-\vec{k}\cdot\vec{U}^{\circ}_{\mu})(\vec{k}\vec{U}^{\circ}_{\mu}+\vec{U}^{\circ}_{\mu}\vec{k}) + k^2\vec{U}^{\circ}_{\mu}\vec{U}^{\circ}_{\mu}\right\}$$

where the molecular "plasma" frequency $\omega^2_{p\mu} = 4\pi e^2_{\mu} n_{\mu}/m_{\mu}$ has been introduced.

Using the general electromagnetic field equations /2/

$$\left[\overleftrightarrow{\varepsilon}(\vec{k},\omega) - \frac{k^2c^2}{\omega^2}\left(\overleftrightarrow{I} - \frac{\vec{k}\vec{k}}{k^2}\right)\right]\cdot\vec{E}(\vec{k},\omega) = 0 \qquad (5)$$

together with the expressions for the susceptibilities of such type as it is given by Eq.(4) we can study all eigenmodes in the system under consideration and their stability. For example, as far as pure transverse excitations they can exist only in such geometry that $\vec{U}^{\circ}_{\sigma,\mu}\cdot\vec{E} = 0$. Otherwise, the small but finite (of order $U^{\circ}_{\sigma,\mu}/c$) longitudinal component takes place of necessity. However, in all cases these excitations (pure or quasi-transverse ones) tend to be stable.

Contrary to this, the longitudinal excitations exibit the instability of very interesting and nontrivial type. To show this let us substitute the dielectric permittivity tensor (I) in the standard dispersion equation for longitudinal excitations $\vec{k}\cdot\overleftrightarrow{\varepsilon}(\vec{k},\omega)\cdot\vec{k}/k^2 = 0$ and use the molecular susceptibility (4) and analogous expression for an electron susceptibility $\overleftrightarrow{\chi}_e(\vec{k},\omega)$ (by the way, it has the form of Eq.(4) at $\omega_{\mu} = 0$ and $\mu \to e$). As a result, we obtain the equation

$$(\tilde{\omega}^2 - \omega_{pe}^2 + i\nu_e\tilde{\omega})(\tilde{\omega} + \omega_\mu - \vec{k}\cdot\vec{V}^\circ + i\gamma_\mu) = -\alpha_\mu\omega_{pe}^2 \quad (6)$$

where $\tilde{\omega} = \omega - \vec{k}\cdot\vec{U}_e^\circ$, $\vec{V}^\circ = \vec{U}_\mu^\circ - \vec{U}_e^\circ$, $\gamma_\mu = \nu_\mu/2$, $\alpha_\mu = \omega_{p\mu}^2/2\omega_\mu$. This equation gives one the possibility to analyze the stability of the system under consideration with respect to the longitudinal excitations.

Omitting the details of this analysis we list here only its final results: (i) plasma-molecular system with directed motion of charged and neutral particles is unstable in the domain of anomalous Dopler effect /4/ (i.e. at the condition $\omega - \vec{k}\cdot\vec{U}_\mu^\circ \simeq -\omega_\mu$); (ii) this anomalous Dopler instability is realized if the threshold condition

$$(\alpha_\mu/\gamma_\mu) > (\nu_e/\omega_{pe}) \quad (7)$$

is fulfilled.

These results clearly demonstrate the definite role of molecular subsystem in certain class of electromagnetic phenomena in plasma-molecular media. For example, the threshold condition defined by Eq.(7) essentially depends on the molecular parameters α_μ and γ_μ while in a number of previous papers /5,6/ the latter one has not been taking into consideration at all.

/I/ Yu.L.Klimontovich, H.Wilhelmsson, I.P.Yakimenko, A.G.Zagorodny. Statistical Theory of Plasma-Molecular Systems, Moscow Univ., Moscow, I990

/2/ A.G.Sitenko. Electromagnetic Fluctuations in Plasmas. Academic Press, New York, I967

/3/ G.F.Goryunova, I.P.Yakimenko. In: Proceeding of the Invited Papers I987 Intern.Conf. on Plasma Physics, ed. by A.G.Sitenko, vol.2, p.735, World Scientific, Singapore, I987

/4/ V.L.Ginzburg. Theoretical Physics and Astrophysics, Nauka, Moscow, I98I

/5/ J.Neufeld. Phys.Rev. II6, 785 (I959)

/6/ V.N.Tsytovich, V.D.Shapiro. Z.Tech.Fiz. 34, 875 (I964)

D-^{3}He FUSION REACTOR BASED ON A DIPOLE MAGNETIC FIELD

A.Hasegawa
Department of Communication Engineering,
Osaka University, Osaka 565, Japan

T.K.Fowler
Department of Nuclear Engineering,
University of California, Berkeley CA USA
and
M.E.Mauel
Department of Applied Plysics, Columbia
University, New York, USA

In view of considerable difficulty that a D-T based fusion reacter is expected to face in obtaining public acceptance by simultaneously satisfying environmental, safety and economical issue, interests in fusion based on advanced fuel are increasing rapidly. Recent discovery of relatively abundant ^{3}He deposition on the moon surface has stimulated such interests even further.

Although for ignition it takes approximately four times higher density and temperature than a D-T based fusion, the D-^{3}He fusion is attractive from the point of view of safetyand environmental impact because of much reduced (to a few percent) level of neutron emission and negligible level of tritium inventory (both of which are consequence of a D-D reaction). Reduced level of neutron flux in a D-^{3}He fusion reator provides inherent safety from possible melt-down of the reactor structure in case of accidental stoppage of coolant circulation. It also provides much longer life time for the wall material, reduces radioactive waste substantially and reduces operational and consructioncost which may over balance the fuel cost.

In addition the significantly reduced level of neutron flux allows reconsideration of alternative concepts which wereabandoned for D-T reactors such as a confinement using a floating superconducting ring.

A D-^{3}He fusion reactor requires:

1. a high beta plasma ($\beta \simeq O(1)$) to suppress synchrotron radiation loss,
2. a semi-open geometry to take advantage of direct conversion of high energy charged fusion products,
3. stationary operation due to a large start up energy and
4. inherent plasma stability.

The dipole plasma confinement using a floating superconducting ring current as shown in the figure satisfies these requirement.

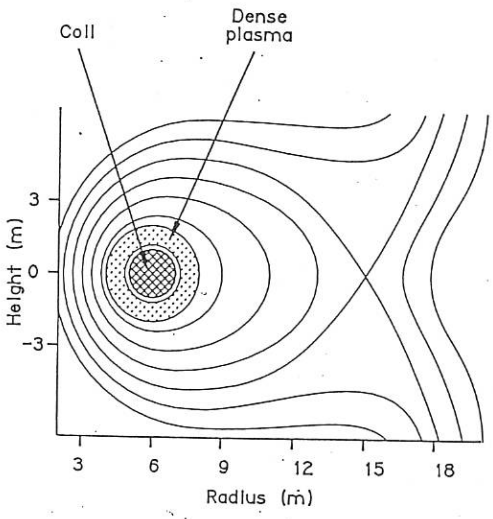

(E.Teller *et al.*, LLNL Report UCRL-JC-106807)

The plasma which is confined in bad curvature is made stable by providing pressure gradient slower than $d\ln p/d\ln V = -\gamma$ where V is the flux tube volume given approximately by $V \simeq r^4$. The magnetically floating ring is made of a superconducting core surrounded by layers of thermal and neutron shields with builtin refrigerator driven by radiation power from the fusion. The fuel plasma is produced by neutral beam injection and inward diffusion induced by RF which breaks the third adiabatic invariant. The charged particle fusion products diffuse out to the X point by the break down of the first adiabatic invairant and guided out by the axial field for direct conversion. The plasma beta is limited by the ballooning instability and preliminary calculation shows stable confinenment to beta exceeding unity. Anomalous plasma diffusion toward the floatingring is unlikely to occur because the plasma should climb up the steep magnetic hill. The detail of the design will be published elsewhere[1,2]

Reference

1 E.Teller, A.J.Glass, T.K.Fowler, A.Hasegawa and J.F.stantarius, "Space Propulsionby Fusion in a Magnetic Dipole ", Fusion Technologies, to be published.

2 A.Hasegawa, L.Chen, M.E.Mauel, H.Warren and S.Murakami, "A Description of D-He^3 Fusion Reactor Based on a Dipole Magnetic Field ", Fusion Technologies, to be published.

PROPOSED EXPERIMENT WITH INJECTION OF A SMALL ANGULAR SPREAD BEAM IN THE OSCILLATED REB REGIME

V.Piffl, P.Šunka, M.Člupek, J.Rauš
Institute of Plasma Physics ČSAV, Prague, Czechoslovakia

The problem of the effective energy deposition of the injected relativistic electron beam (REB) in a plasma remains traditionally in the focus of the experimental investigations, especially at GOL (Novosibirsk) and REBEX (Prague) devices. Recently the experimental way to the dense ($10^{15}cm^{-3}$) bulk plasma heating by the microsecond intensive (50-70 kJ) REB was paved [1]. The generation of the overthermal electrons is the other interesting phenomenon experimentally demonstrated in REB-plasma systems. Ten per cent of the injected REB energy can be transformed into the high current density, low impedance (100kA, 10kV) electron stream applicable in further for classical collisional heating of a dense plasma.

Search for the optimal conditions of the overthermal plasma electrons generation in REB-plasma system is one of the aims of the proposed experiment at REBEX machine. Consequently the relatively small experimental devices with the injection of a nanosecond REB (1-10 kJ) into a magnetized plasma could be used for heating of dense gaseous targets or very thin foils to study the matter in extremal conditions (high ionized states of ions) in the future.

Though, the physical mechanism of the overthermal plasma electrons generation remains in many features open, the basic picture of the beam-plasma interaction in propagating regime is relatively well described. If a REB with small angular spread is injected into a homogeneous magnetized plasma, the two-stream instability results in excitation of the small-scale Langmuir turbulence.It is generally accepted

that the turbulence is responsible for observed transfer of the beam energy to the plasma in most experiments. The distribution function of the plasma electrons being non-maxwellian with a high-energetic tail which carries a considerable part of the plasma energy. The energy deposition is non-uniform along the plasma column with a maximum located near the beam entrance, as the angular spread of the beam electrons is continually growing along the interaction path [2]. The heating efficiency did not exceed 30 per cent.

Surprisingly a comparable heating efficiency was demonstrated at the REBEX experimental facility for the case of an inhomogeneous plasma column and a reflected relativistic beam with a larger angular spread (20°).

In our experiments [3] the oscillating high-current relativistic electron beam (350 kV, 2-4 $kA.cm^{-2}$, 110 ns, 20μm Al anode foil) was used. Longitudinal plasma density profile can be controlled. The plasma column ($n_e=10^{14}$- $5x10^{15}cm^{-3}$, $T_e \approx 1$ eV) is terminated at both ends by thin conducting foils. Behind the exit foil there is a section of a vacuum chamber without plasma. Using a movable collector, two regimes of REB-plasma interaction can be realized. If the collector is far enough from the exit foil, most of the REB electrons are reflected back into the plasma from a virtual cathode created near the foil-vacuum boundary. Putting the collector close to the foil, regime with purely propagating REB is established. In our experimental conditions the results of extensive multichannel measurements of plasma diamagnetism can be summarized as follows:

a) The heating efficiency is always 2-3 times higher in the reflected regime than in the propagating one. About 30% of the beam energy was deposited in plasma in the reflected beam regime.

b) In an inhomogeneous plasma the highest energy deposition

rate is observed in regions of reduced plasma density, independently on their location along the system. Thus the desired distribution of the beam energy deposition can be controlled by initial plasma density profile.

To put the REBEX experiment to a new way we attempt to increase the energy deposition above 30 % by application of a beam with smaller angular spread ($\theta<10^{o}$) in the OREB regime.

The aim of the proposed experiment is the following:

1) To prove the possibility to achieve a heating efficiency higher than 30 per cent.

2) To distinguish the role of the angular spread caused by pitch angle and by scattering in the anode foil.

3) To get new information on the role of the reflected beam in enhancement of the heating efficiency.

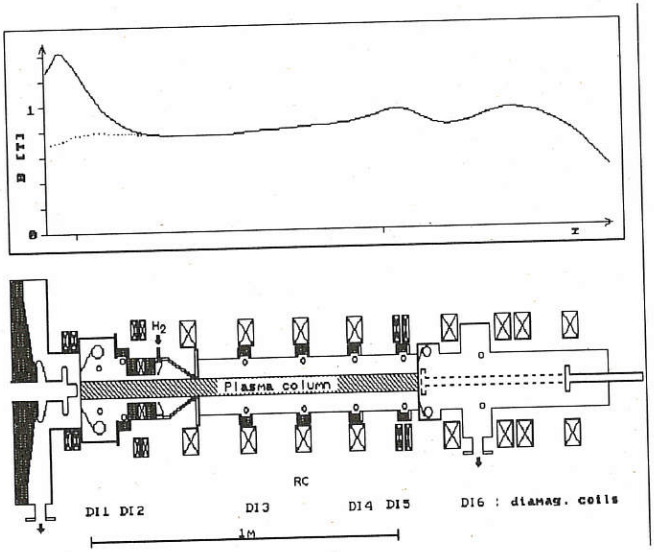

Fig.1

The schematic of the renewed experimental REBEX facility is shown in Fig.1. The main features of the new arrangement are the following :

a) The pitch angle of peripheral beam electrons is substantially reduced ($0<10^{o}$) also for the beam with a high current density (5 $kA.cm^{-2}$), by increasing the external magnetic field (1,5 T) in the diode region.

b) The ultrathin anode Al/mylar foils (down to 60 nm/1,5 μm) will be used to reduce the angular velocity beam spread.

c) The role of the reflected beam in enhancement of the heating efficiency will be studied by varying the thickness of the terminating foil and by the magnetic field strength.

The modified REBEX facility will start to operate in summer 92.

References:

[1] A.V.Burdakov, V.S.Koidan, V.Piffl at al.: Bulk plasma heating by a microsecond E-beam in the GOL-3 facility INP Novosibirsk, preprint 92-8, February 92

[2] A.K.Arzhanikov, A.V.Burdakov, V.S.Koidan at al.: Physics of the REB-plasma interaction
Physica Scripta, Vol.T2/2, 303-309,(1982)

[3] V.Babický at al.: New results on REB plasma heating in the REBEX machine
Proc. of the 8th Int. Conf. on High-Power Particle Beams, Novosibirsk, 1990, 225-232

CONFINEMENT OF LASER-PRODUCED PLASMA BY A STRONG EXTERNAL MAGNETIC FIELD

R.Miklaszewski, A.Farynski, H.Fiedorowicz, M.Mroczkowski, P.Parys, T.Pisarczyk and M.Szczurek

Institute of Plasma Physics and Laser Microfusion
00-908 Warsaw 49, P.O.box 49, Poland

Abstract

First results of a novel experiment with magnetically confined laser-plasma are presented. The laser plasma is created by irradiating solid target with a focused Nd-glass laser. The target was placed on the axis of the two, single-turn magnetis coils which provided a magnetic field up to 500 kGs in the target region. The expanding laser plasma is confined by the magnetic field and an elongated plasma column is formed along the axis. The plasma column emitts strong soft X-radiation. The pinhole photographs show that the plasma column is at least 5 mm long. To study the interaction of the expanding laser plasma with a magnetic field the laser interferometry was used.

1. Introduction

The interaction of the expanding laser plasma with an external magnetic field is a problem interesting from several points of view. Firstly the plasma column formed by a magnetic field of the laser plasma seems to be a promising method of creating a lasing medium for soft X-rays generation. Secondly an external strong magnetic field should reduce the energy losses in the indirect heated targets (cavity targets). And last but not least several interesting physical phenomena can be observed and investigated.

2. Experimental arrangement and results

The experimental setup consists of three main parts: magnetic field generator, plasma chamber and Nd-glass laser system. The magnetic field (up to 500 kGs) is generated by two, single-turn magnetic coils which are located inside of the plasma chamber. The coils with internal diameter of 6 mm are supplied by the high current pulse produced by a condenser bank. The scheme of the experiment is shown in Fig.1.

The laser targets (plastic or glass foils) are placed between the coils on their axis. The laser system produces the laser heating pulses with energy up to 30J in 1 ns pulse.

To study the interaction of the laser plasma with external magnetic field we have used two kinds of plasma diagnostic methods: laser interferometry and X-ray imaging. The X-ray images of the plasma have been obtained using the pinhole camera equipped with two pinholes of about 220-μm and covered with beryllium filters (thickness of the filters 10-μm and 20-μm). To probe the laser plasma we have used a fraction of laser heating pulse converted into second harmo-nic (in the KDP

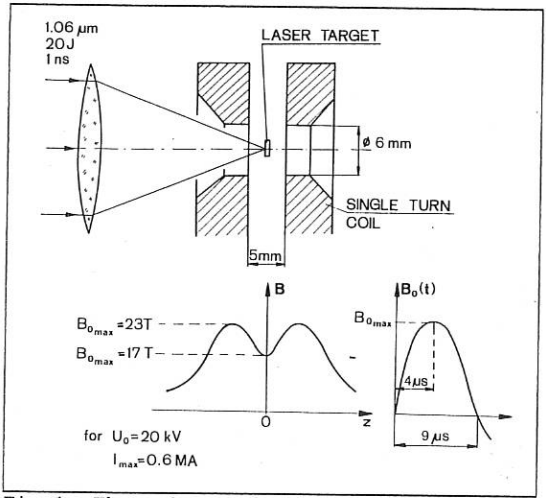

Fig 1: The scheme of the experiment

crystal). The laser probe pulse could be delayed according to the laser heating pulse from 1 ns to 40 ns and it was possible to make oneframe interfe-rograms of the plasma for determined time moment of the plasma expansion. Time duration of the probe pulse was about 0.8 ns.

The interferograms of the plasma have been processed using the computer digitise system.

Typical X-ray images of the expanding plasma for magnetic induction B=0 and B=18T are presented in Fig.2(a) and 2(b) respectively. From the images [Fig.2(b)] one can see that the laser plasma is confined by the magnetic field and an elongated and uniform plasma column is formed at the distance of about 2mm from the laser target surface. A diameter of the column is less than 1 mm. Close to the target surface the plasma is of ellipsoidal shape.

The density distributions of the expanding laser plasma without (B=0) and with external magnetic field (B=18T), obtained from the interferograms for time delay Δt = 20ns are presented in Fig.3(a) and 3(b), respectively.

It is seen that characteristic plasma blob of semi-ellipsoidal shape is created at the distance of about 0.5 mm from the target surface. The electron density of the blob reaches the maximum value of $3.5 \cdot 10^{19}$ cm^{-3}. In the same place and for the same time moment the electron density of the plasma expanding without magnetic field is $6 \cdot 10^{18}$ cm^{-3} [Fig. 3(a)]. For larger time delays Δt=30ns and Δt=40ns the electron density of the plasma decreases but the characteristic shape of the plasma blob remains.

3. Numerical simulation

2-D numerical code based on the single fluid, two temperature, MHD equations was prepared for modelling of a laser plasma expansion into external magnetic field. The complete set of MHD equations with the Braginski transport coefficients and supplemented with equation for a laser light absorption (via inverse Bremsstrahlung) was solved for initial and boundary conditions corresponding to the experiment described above.

The isodense contours obtained by numerical simulation of a

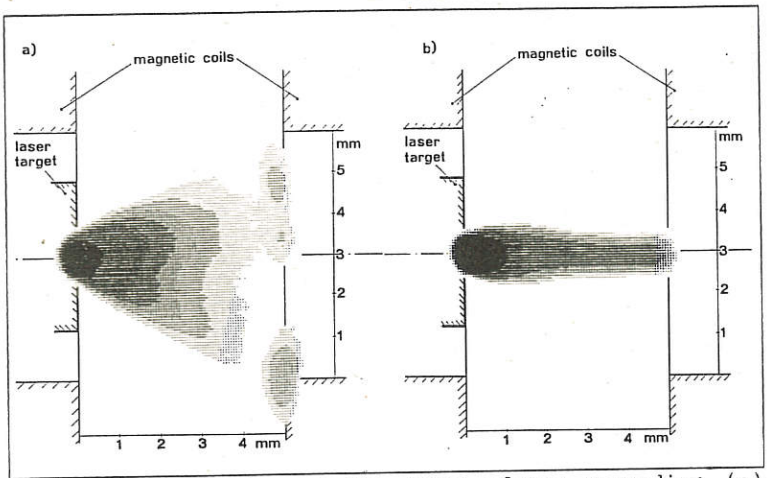

Fig 2: X-ray images of the laser plasma expanding (a) without (B=0) and (b) with an external magnetic field

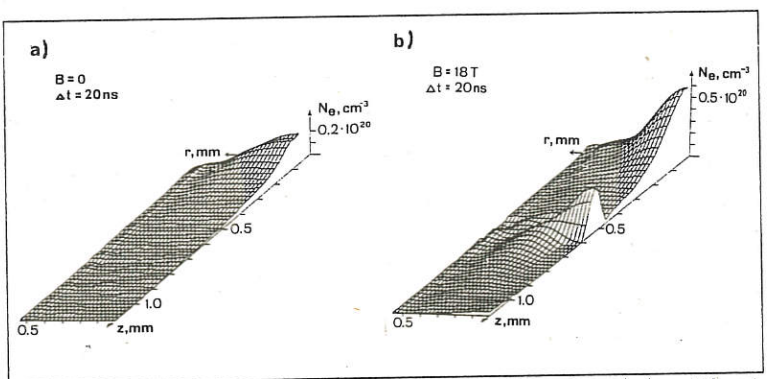

Fig 3: Spatial distribution of plasma density (a) without (B=0) and (b) with an external magnetic field

laser plasma expansion are presented in Fig.4. From these preliminary computations several conclusions can be drawn out:

1. The radially expanding laser plasma is confined by external magnetic field from the very beginning of the phenomena.
2. Due to higher plasma density in the corona area, the absorption of laser light occurs on the distance much longer then in the case without external magnetic field.
3. Distortion of a magnetic field lines, caused by radial motion of a hot plasma results in appearance of radial component of magnetic induction. This is the reason why an

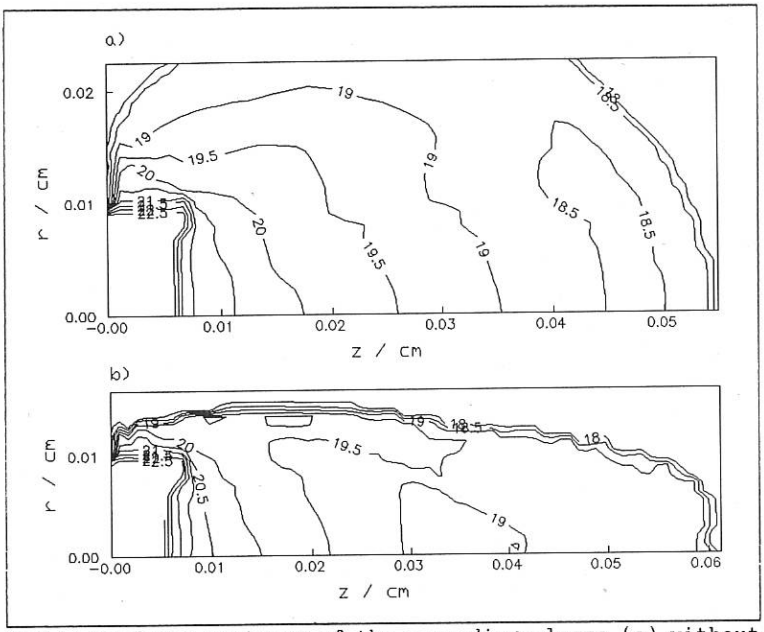

Fig 4: Isodense contours of the expanding plasma (a) without (B=0) and (b) with an external magnetic field (B=18T) obtained from numerical simulation for Δt=1ns (labels correspond to logarithm of the plasma density)

initially axial magnetic field can hamper axial flow of a laser plasma.

6. Conclusions

We have presented preliminary results of the experimental investigations of the interaction of a laser plasma with an external strong magnetic field. The most important finding of these investigations is that the elongated and uniform plasma column is formed on the axis of the magnetic coils.

Acknowledgement

This work was supported by the State Committee for Scientific Research of Polish Government under grant 2 0141 91 01/p01.

AUTHOR INDEX

ceto S. I-525,I-529
dams J.M. I-67,I-251
anasyev V.I. I-151,II-1031
garici G. II-885
gren O. II-1369
roldi A. II-973
kiyama H. I-403
kiyama R. I-517
-Karkhy A. I-639
l-Mashhadany E.M. I-691
lava M.J. III-1923
lejaldre C. I-565
leksandrov V.O. I-111
lexandroaei D. III-1957
lexandrov V.O. II-997
li-Arshad S. I-227,I-335,I-339
lladio F. I-23,I-545,II-1525
llen J.E. III-1973,III-1977,III-2033
lper B. I-331,I-335,I-339,II-1051
lport M.J. III-1895
matucci W.E. III-1895
nabitarte E. II-1183
nderson D. I-391
nderson D.V. I-557
nnaratone B.M. III-1977
ntani S.N. II-1009
ntoni V. I-631
ntsiferov P. I-683
oyama K. III-1765
postol I. III-2049
ppala N.P. III-1943
ppel L.C. I-31
pruzzese G. I-463
ragon F. I-299
rakawa M. II-1337
ramaki E.A. I-675
raujo M.S.T. I-419
rhipenko V.I. II-1203
rimoto H. I-513,I-517
sakura N. II-949
scasibar E. I-565,II-933
shida H. II-1405
shkenazy J. III-2117
ssis A.S. II-1549
ssis A.S. I-679,III-1619,III-1667,III-1785
tanasiu C.V. I-367
umayr F. II-1163
ustin M.E. I-115
vakian M. I-479
xnäs I. II-1175,III-1875
zevedo C.A. I-679,III-1619
zizov E.A. I-47
aang S. II-1071
aba T. I-489
aboolal S. III-1819
achin I.V. II-1345
achmann P. II-747
adalec J. I-219
aelmans T. II-747
agatin M. I-631
agdasarov A. I-371
agryansky P.A. II-1123
ahrim B. III-2049
ahrim C. III-2049
aity F.W. II-893
aker K.B. III-1591
akos J.S. I-303
albin R. II-783,II-791
aldzuhn J. II-1119
Balet B. I-3,I-19,I-59,I-63,I-263,II-881
Barabaschi P. I-167
Baranowski J. II-1211
Barnsley R. I-291
Barrett P.J. III-1803
Bartiromo R. II-957,II-961,II-1127
Bartlett D.V. I-119,I-147,I-163, I-255,I-407,II-973
Basiuk V. I-175
Basu B. II-1373,II-1509
Batani D. II-1207,III-2017
Batchelor D.B. II-913
Batistoni P. I-545
Baumgärtel K. III-1571
Baylor L.R. I-255,I-521,I-525
Bazdenkov S.V. II-1453
Beaumont B. II-885
Becker G. II-1457
Becoulet A. I-175,II-885,II-905
Behrisch R. II-843
Beidler C.D. I-533,I-569,I-581
Belik V.P. II-1039
Bell J.D. I-525,I-529
Bell M.G. I-39
Bell R. I-39,II-949
Belli M. II-1207
Belmont G. II-1297
Belyakov V.A. I-471
Bender S.E. I-471
Bengtson R.D. I-91
Benova E. II-1517,III-2041
Berbece D. II-1561
Berge G. II-1401
Berger By G. II-885
Bergsåker H. I-607
Berk H. II-1469
Bernabei S. II-949,II-957
Berni L.A. I-675
Bertolini E. I-167
Berton F. I-23
Bertrand P. II-807,II-1005,III-1737,III-1741
Besedin N.T. I-569
Besshou S. I-489,II-1131
Bharuthram R. II-1445
Bhatnagar V.P. I-327,II-897,II-901
Bibet P. I-159,II-885
Biborosch L. III-2029
Bickley A. I-379
Bigelow T.S. I-521,I-525
Bilbao L. II-1253
Bingham R. II-1271,III-1627
Birdsall C.K. III-1993
Bizarro J.P. I-27,II-885
Blazquez J.F.M. II-1237
Blumenfeld L. III-2055
Boedo J. I-155
Boerner E.D. II-1275
Bohm M. III-1875
Boileau A. I-215
Bollanti S. II-1207
Bond D.S. I-251
Bondarenko E.A. II-1261
Bondeson A. I-343,I-399
Bonhomme G. III-1737,III-1879
Bonitz M. III-2091
Bonoli P.T. II-965
Boozer A.H. II-863,III-1713
Bora D. III-1575,III-1583,III-2021
Borba D. I-439

Borisov N.D. III-1587
Bornath Th. III-2091
Bornatici M. II-1493
Borrass K. II-735
Bortolotti A. I-695,II-1253
Bosch H.-S. II-747
Bosia G. II-897
Bosia P. II-901
Boucher C. I-215
Boucher D. I-59
Boucher I. III-1883
Bowles J. III-1935
Braams B. II-747
Bracco G. I-23,I-127,I-295
Braithwaite N.St.J. III-1973
Brambilla M. II-925
Branas B. I-99,II-1075
Brasilio Z.A. II-803
Bravanec R.V. I-115
Bravo E. III-1607
Bretz N. I-203
Breun R. II-839
Brouchous D. II-839
Brower D.L. I-115,I-363
Browning P.K. I-639
Brusati M. I-3,I-119,I-307,II-897,II-973,II-977
Bruschi A. I-23
Bryant D.A. III-1627
Brzosko J.S. I-695
Brzozowski B.P. I-595
Brzozowski J. I-291,I-611
Büchl K. I-459,II-743
Büchse R. I-375,I-379
Bud'ko A. I-635,I-671,II-1261
Budnikov V.N. II-997,II-1203
Budny R.V. I-39,I-43,I-203
Buffa A. I-619
Bulanin V.V. I-111
Bulanov S.V. I-541,II-1305,II-1317,II-1429
Buneman O. III-1579
Buratti P. I-23,I-127,I-463
Bures M. I-3,I-19,I-255,I-307,II-881,II-897
Bürger G. I-303
Burgos C. I-299,II-1135
Burrell K.H. I-11,I-179,I-183,I-243,I-275
Bush C.E. I-203
Bustamante E.G. II-1183
Buzhinskij O.I. I-47
Cabral J.A.C. II-1111
Cabral-Prieto A. III-1947
Cabrit B. II-1083,III-1591
Caldas I.L. I-419,II-803
Calderon M.A.G. II-1183
Callen J.D. II-1413
Calvin M. I-211
Campbell D.J. I-227,I-239,I-375,
II-735,II-881,II-897
Caner M. III-2117
Capes H. I-107
Capitain J.J. II-885
Carlson A. II-783,II-787
Carlstrom T.N. I-235
Carolan P.G. I-411
Carrasco J. I-175,II-885
Carreras B.A. I-521,I-525,I-565,I-569,II-1417
Carroll III J.J. III-1895
Carter M.D. II-913
Castejon F. II-933,II-1135
Castiglioni S. II-1087
Castro R.M. II-803
Catto P.J. I-91
Cercek M. II-1171,III-1761
Cereceda C. II-1513
Cermak I. III-1989
Cha S.S. I-451
Chakraborty B. II-1257
Challis C.D. I-15,I-311,I-335,I-379
Chance M.S. I-435,II-949
Chang C.S. I-315
Chang T. II-1509
Chankin A.V. II-779
Chao J.K. III-1615
Chatelier M. I-159
Chavez-Alarcon E. I-483,III-1947
Chekroud D. III-1729
Chen F.F. III-1701,III-1789
Chen H.H. III-2059
Chen J.Y. I-363
Chen X.P. I-107
Cherkhani R. III-1737
Chernobaj A.P. I-47
Cherubini A. II-901
Chevlaier G. III-1701
Chittenden J.P. I-655
Chiu C.Y. III-1615
Chiu S.C. II-893
Chiueh T.H. III-1615
Cho S. III-2133
Chodura R. II-871
Choi E.H. III-2133
Chou A.E. II-1071
Chou C.K. III-2059
Christensen M. I-279
Christiansen J.P. I-15
Chu M.S. I-243,I-435
Chu R. III-1811
Chu T.K. II-949
Chudin N.V. I-367
Cicconi G. II-1187,III-2037
Ciubotariu-Jassy C.I. III-1681
Claaßen H.A. II-771
Clement S. I-307,II-723,II-727,II-735,II-823
Clupek M. I-713
Coffey I.H. I-291
Cohen D. II-1017
Cohen R.H. II-1275
Colborn J.A. II-965
Colchin R.J. I-525
Colton A. I-227
Colunga-Sanchez S. I-483,III-1947
Compant La Fontaine A. III-2113,III-2125
Conceicao P. II-977
Condé H. II-1047
Condrea I. I-295,II-1127
Connor J.W. II-1393
Connor K.A. I-529
Conrads H. II-775
Conroy S. I-67,I-167,I-251
Cook D. II-937
Cooper W.A. I-557,I-589
Coppi B. I-139
Coppins M. I-663
Cordey J.G. I-15,I-191-59,I-63,I-263
Core W.G.F. II-1035
Correa-Restrepo D. II-1329,III-1753
Correia C. II-1063
Corti S. I-151,II-1031
Costa S. I-619
Costley A.E. I-163,I-199,I-407
Cottrell G.A. I-327,II-881,II-897
Coulon J.P. I-107
Couture P. I-215
Cowley S.C. II-1393
Cox M. II-897,II-1341
Cripwell P. I-199,I-227,I-407,I-439
Crisanti F. I-463
Cross R.C. II-815
Cruz-Jimenez S. III-1947
Cunningham G. I-639
Cuperman S. III-2117

Cupido L. II-1063
D'haeseleer W.D. I-533,II-755
da Costa O. I-327
da Cruz Jr. D.F. I-267
da Silva R.P. II-803,II-973
Darrow D.S. I-203,I-431
Das A.C. II-1257,III-1611
Dawson J.M. II-1271,III-1627
De Angelis R. I-279,I-295
de Blank H.J. I-247,I-339
de Esch B. I-167
de Esch H.P.L. I-339
de Gentile B. I-27
De Haas J.C.M. I-83,I-87
De Kock L. I-227,II-723
De la Luna E. II-1075
De Luca F. I-23,I-75
De Nicola S. II-1313
De Villiers J.A.M. I-387,I-415,II-795
DeBlank H.J. I-335
DeBoo J.C. I-11
DeChiara P. I-695
Decker D.T. II-1509
Decoste R. I-215
Decyk V.K. III-1839
DeEsch H. II-897
DeGrassie J.S. II-893
Deksnis E. I-167
DeMichelis C. II-847
Dempers C.A. III-1773
Dendy R.O. I-327
Deng C.B. I-347
Deng H.C. I-223
Deng Z.C. I-223
Deutsch C. II-1245
Deutsch H. III-2095
Devynck P. I-107,II-1079
Di Lazzaro P. II-1207
Diamond P.H. II-1417
Dias J.M. II-1111
Diaz-Pinto A. III-1607
Diebold D. II-839
Dietz J. I-167
Dimits A.M. II-1275
Ding W.X. III-1765
DiPeso G. III-1993
Dippel K.H. I-403
Dmitriev V.I. I-47
Dodel G. I-191
Domier C.W. II-1071
Domier D.W. III-1939
Dominguez N. I-525,I-561,I-565,I-569
Donaldson N. I-647
Dong J.F. I-223,I-395
Donné A.J.H. II-1091,II-1143
Donoso G. III-1795
Dory R.A. I-521
Doyle E.J. I-179,I-243
Drachev V.P. II-1123
Drake J.F. I-351
Drake J.R. I-595,I-599
Drawin H.W. I-159
Dubois M.A. I-103,II-1409
Duck R. I-31,I-399
Dudnikova G.I. III-1639
Dumitrascu N. II-1561
Duncan P.J. III-1729
Dunlap J.L. I-525,II-949
Duong H. I-435
Durst R. I-203
Dwivedi C.B. III-1611
Dyabilin K.S. I-493
Dyachenko V.V. II-997
Dyakov V.E. II-933,II-941
Dyer G.R. I-521,I-525
Eberhagen A. II-1107
Edery D. II-855,II-1421
Edlinger J. III-2149
Edwards A.W. I-255,I-327,I-331,I-339,I-355, I-375,I-379,II-897,II-1051
Ehrenberg J. I-307
Ekiel-Jezewska M. III-1951
Elevant T. II-881
Elfimov A.G. I-319
Elliott J.A. III-1725
Emmoth B. I-607
Endler M. II-783,II-787
Engelhardt W. II-743
England A.C. I-521,I-525,II-949
Erba M. I-623
Erckmann V. I-497
Erdweg M. II-827
Erents S.K. II-723
Eriksson L.-G. I-343,II-881,II-897, II-1469,II-1485
Esipov L.A. II-997
Estrada T. I-99,II-1075
Euringer H. II-775
Fahrbach H.U. II-961
Fajans J. III-1811,III-1899
Fang S. I-615
Farynski A. I-717
Fasoli A. III-1863
Fedele R. II-1293
Fedorov O.V. I-471
Feix G. III-1643
Feix M. III-1741
Feneberg W. II-1477,II-1481
Fernandes C. II-1063
Ferron J.R. I-55
Fiedler S. II-1163
Fiedorowicz H. I-717
Fielding S.J. I-31
Fijalkow E. III-1741
Finken K.H. I-155,I-403
Finkenthal D. I-275
Fischer B. II-1095
Fishman H. II-949
Fitzpatrick R. I-411,I-423
Flå T. II-937,II-1309,III-1951
Fletcher J.D. I-387,I-415,II-795
Flora F. II-1207
Foltin M. III-2067,III-2075
Fonck R. I-203,II-839
Fontanesi M. III-2017
Foote J.H. II-1191
Foster C.A. I-159
Fowler T.K. I-711
Franz D. I-683
Fredrickson E.D. I-39,I-203,I-351,I-431
Freidberg J.P. II-1401
Freysinger W. III-2079,III-2083,III-2087
Friaca A.C.S. III-1647
Friedland L. II-1017
Frieling J. II-1035
Frigione D. I-463
Froissard P. I-119,II-973,II-977
Fröjdh M. II-1441
Fu B.Z. I-395
Fuchs C. I-403,II-835
Fujiwara M. I-513
Fukuda T. I-87,I-199
Fussmann G. II-831,II-835
Gabris R. III-2129
Gadeberg M. I-255
Galassi A. III-2017
Galkowski A. II-1537
Gandy R. I-115
Gangadhara R.T. III-1671
Ganguli A. III-1943

Garbet X. I-107,II-1079,II-1433
Garcia D. III-1607
Garcia L. I-565,II-1417
Garcia-Cortes I. II-791
Gasparino U. I-493,I-497,I-505,I-581,II-1001
Gavrilescu C. III-1969
Gaytan-Gallardo E. I-483,III-1947
Gee S.J. I-639
Gentle K.W. I-115
Georgieva M. II-1353
Géraud A. I-159
Gernhardt J. I-455,I-459
Gervais F. I-107,II-1079
Gettelfinger G. II-949
Ghanashev I. II-1517
Ghanem E.-S. I-131
Ghendrih Ph. II-851
Ghizzo A. II-807,II-1005,III-1737,III-1741
Ghorannevisse M. I-479
Giammanco F. II-1241
Giannella R. I-279,I-283,I-287
Giannone L. I-497,II-783,II-787
Gibson K.J. I-31
Gil C. I-107
Gill R.D. I-331,I-355,I-375,II-1051
Gimblett C. I-335
Giruzzi G. II-905,II-1103
Gladuschak V.I. II-1219
Glagolev V.M. I-703
Glosik J. III-1989,III-2083
Glowienka J.C. I-529
Goedbloed J.P. I-247
Gohil P. I-183,I-243,I-275
Golant V.E. I-471
Goldfinger R.C. II-913
Golubyatnikov G.Yu. III-1831
Gondhalekar A. I-151,I-239,II-1031
Gonella C. III-2055
Gong D.F. I-395
Gonhhalekar A. I-147
Goniche M. II-885
Goree J. II-1365
Gorini G. I-75,II-1047
Gormezano C. I-15,I-119,II-897,II-973
Goruppa A.A. III-1977
Gottardi N. I-255,I-279,II-723,II-727
Goulding R.H. II-893
Gowers C. I-15
Graffmann E. II-771
Green B. I-167
Greene J.M. I-435
Greenfield C.M. I-11
Greenough N. II-949
Greenwald R.A. III-1591
Gregory B. I-215
Grek B. I-39
Grekov D.L. I-569
Grésillon D. II-1079,II-1083,III-1591
Gribok V.A. II-929
Grigull P. II-1167
Grill V. III-2075,III-2095
Grisham L. I-43
Groebner R.J. I-179,I-183,I-187,I-275
Grosman A. II-847,II-851
Grozev D. III-2041
Gruber O. I-451,I-455,I-459,II-743
Gruber R. I-557,I-589
Gryaznevich M. I-399
Gudowska I. I-607
Günther K. II-875
Guo D.Q. I-347
Guo G.C. I-223,I-395
Guo S.C. II-1437
Gusakov E.Z. II-1203
Gusev V.K. II-1219
Gyergyek T. II-1171,III-1761
Hadjoudj Y. III-1915
Hahnheuser R. I-647
Haines M.G. I-655
Hakr J. I-667
Hall D.S. III-1627
Hamilton R.L. II-1349
Han J. I-335
Hanada K. I-79
Hanatani K. I-489,II-1131
Hansel A. III-2079
Hansen B.M.S. II-1397
Hanson G.R. I-525
Hanssen A. II-1279
Hanuise C. III-1591
Harbour P.J. II-723
Harmeyer E. I-581
Harris G. I-107
Harris J.H. I-525,II-949
Hartfuß H.J. I-497,II-1001,II-1099
Harvey R.W. II-893
Hasegawa A. I-711
Hastie R.J. II-1393
Hatakeyama R. III-1705,III-1709, III-1765,III-1919
Hatcher R. II-949
Hazeltine R. I-211
Hegna C.C. II-1413
Heidbrink W.W. I-435
Heijnen S.H. II-1059
Heikkinen J.A. II-1021,III-1923
Hellberg M.A. I-387,II-1397,II-1477,III-1819
Hellblom G. I-595
Heller M.V.A.P. II-803
Hender T.C. I-335,I-339,I-399,I-411,I-423
Hennequin P. I-107,II-1079,II-1409
Hensler E. II-1389
Herrmann H. II-949
Hershkowitz N. II-839,II-909
Hess W. II-847
Hesthaven J.S. III-1903
Heuraux S. III-1915
Hidalgo C. II-783,II-791
Higashijma S. II-1131
Hill D.N. I-243,II-751
Hill K.W. I-39
Hillis D.L. I-275
Hirano Y. II-917
Hirayama S. I-699
Hirshman S.P. I-589
Hoang G.T. I-27,I-103,II-885,II-945
Hoenen F. I-155
Hoffman D.J. II-893
Hofmann F. I-343,I-467
Hofmann J.V. II-1155
Hogan J.T. I-275
Hogeweij G.M.D. I-71,I-75
Holzhauer E. I-191
Honda C. II-1159
Honda R.Y. I-675
Hong J.S. III-2033
Honzawa T. II-1337,III-1603,III-1911
Hörhager M. III-1685
Hori M. III-1965
Hörling P. I-611
Horton L.D. I-307,II-1035
Hoshino K. II-1191
Hosokawa M. I-513,I-517
Howarth P.J.A. I-251
Huang K.Q. I-223
Huang R. I-347
Huart M. I-167
Hübner G. II-1541
Hübner K. II-1485
Hugenholtz C.A.J. II-1059

Hugill J. I-31
Hugon M. I-3,I-119
Huguet M. I-167
Humbert P. II-1249
Hutchinson D.P. I-521
Hutter T. I-27,I-107
Huysmans G.T.A. I-247
Hyatt A.W. I-187
Ianopol B. III-1957
Ida K. I-513,I-517
Ide S. II-953,II-969,II-985
Idei H. I-513,I-517
Ignacz P.N. I-303
Ignat D. II-949
Iguchi H. I-513,I-517
Iima M. I-489
Ijiri Y. I-489
Ikeda Y. II-953,II-969,II-985
Ikegawa M. III-2109
Ikehata T. III-1891,III-1985
Imai T. II-953,II-969,II-985
Ingesson L.C. II-1143
Inoue M. III-1651
Inovenkov I.N. II-1305,II-1317
Intrator T. II-839
Irie M. I-643
Irzak M.A. II-1025
Ishii H. II-917
Ishii S. III-1961
Isler R.C. I-521,I-525,I-529,II-949
Its E.R. II-997
Iwama N. III-1961
Jacchia A. I-23,I-75
Jäckel H.J. II-723,II-823
Jackson G.L. I-11
Jacquinot J. I-167,I-311,I-327,I-335, II-881,II-897,II-901
Jadoul M. I-359
Jaeger E.F. II-913
Jaenicke R. I-549
Jafelice L.C. III-1647
Jäger H. II-1151
Jakovenko V.P. I-47
Jakubka K. I-219
Jakubowski L. II-1215
James R.A. II-893
Janeschitz G. II-723,II-727
Janicki C. I-215
Jardin S. II-949
Jarmen A. II-1441
Jarvis N. II-881
Jarvis O.N. I-67,I-167,I-251
Jaspers R. I-155
Jasperse J.R. II-1373,II-1509
Jassby D.L. I-39,I-43
Jelic N. II-1171,III-1761
Jenichen F. II-835
Jensen V.O. II-1545
Jernigan T.C. I-521,I-525
Ji H. I-521
Jiang Y. I-363
Jiang Y.X. I-223
Jiang Z.X. I-603
Jimenez J.A. I-561
Jimenez-Dominguez H. I-483,III-1947
Jobes F. I-39
Joffrin E. II-855,II-945,II-1421
Johnson D.W. I-39
Johnson J.L. I-577
Johnson L.C. I-39
Jones I.R. I-647
Jones S.E. I-163,I-407,II-949
Jones T. I-255,II-881
Jones T.C.C. I-19
Jones T.T.C. I-3,I-263,I-307
Jong R.A. II-751
Jülich A. I-455
Junker J. I-509
Junker W. II-743
Kahlbaum T. III-2009
Kaita R. II-949
Kajiwara T. II-1159
Kakehi Y. III-2109
Kakoulidis E. II-767
Kallenbach A. I-231,I-459,II-835
Källne E. I-611
Källne J. II-1047
Kalvin S. I-303
Kamp L.P.J. III-1745
Kanaev A.I. I-47
Kaneko O. I-517
Kantor M.Yu. II-1219
Kaplan Z. III-2117
Kardaun O.J.W.F. I-7,I-35
Kardon B. I-303
Karlson E.T. I-635,I-671
Karlsson P. I-595
Karpman V.I. II-1283
Karttunen S.J. II-1005
Katsonis K. II-1245,III-2063
Katsouleas T. II-1301
Kaufmann A.N. II-937,III-1951
Kaufmann M. II-743,II-747
Kauschke U. III-1981
KavinA.A. I-471
Kaw P.K. II-1301
Kawabe T. I-699,III-2155
Kawachi T. II-981
Kawaguchi N. III-1651
Kawai Y. III-1733,III-1807,III-1855,III-1887
Kawashima H. II-893
Kaye S. II-949
Kennel C.F. II-1349
Kerner W. I-247,I-335,I-439
Kesner J. I-407,II-949
Khan M. II-1257
Kholin N.N. III-2137
Khristova D. II-1353
Khudoleev A.V. I-151,I-167,II-1031
Kick M. I-505,I-509
Kilic H. I-695,II-1253
Kim J. I-183
Kim S.K. III-2133
Kinsey J. I-131
Kirsanov V.I. II-1305,II-1317
Kishino T. I-79
Kisigami Y. I-79
Kislov D.A. I-207,I-371
Kiss`ovski Zh. III-2013
Kißlinger J. I-501,I-549,I-585,I-569,I-581
Kitajima M. III-2155
Kiyama H. II-799
Kiyama S. II-799,III-1781
Klepper C.C. I-275
Kletecka P. I-219
Kleva R.G. I-351
Klinger T. III-1677,III-1843
Knorr G. II-807,III-1721
Kobayashi J. III-2109
Kobayashi S. I-489
Kocsis G. I-303
Koepke M.E. III-1895
Kogoshi S. I-403
Kohmoto T. I-517
Kolesnichenko Y.I. I-391
Komori A. III-1733,III-1807,III-1851, III-1855,III-1887
Kondo K. I-489,II-1131
Kondoh T. II-953,II-969,II-985
Kondoh Y. II-917

König R. I-167,I-263,I-339,I-379, II-881,II-1035
Konings J.A. I-71
Kono M. III-1851,III-1855,III-1887
Köppendörfer W. I-451
Korchinsky G.M. II-1377
Korn J. III-1717
Korneev D.O. I-111
Korolev A. III-1599
Korotkov A.A. II-1031,II-1039,II-1043
Kortshagen U. III-2145
Koslovski H.R. I-383,I-403
Kostsov Y.A. I-471
Kovan I.A. I-47
Kovrizhnykh L.M. I-525
Koyama K. II-1225
Kozochkin S.M. II-1229
Krafft C. II-1297
Kramer G.J. I-15,I-227,I-259,I-335,I-339
Krämer M. II-1095
Krämer-Flecken A. I-95,I-383
Krasilnikov A.V. I-47
Krasnikov Yu.I. II-1123
Krause A. I-451
Kravarik J. I-667
Kremp D. III-2091
Krieger K. II-831
Krishan V. III-1671
Krlin L. II-1013
Kroegler H. I-463
Krumm P. III-1773
Kryska L. I-219
Kuang G. I-359
Kubarev Y.V. III-2137
Kubes P. I-667
Kubo H. III-1631
Kubo S. I-513,I-517
Kugel H. II-949
Kuhn S. II-1549,III-1685,III-1777, III-1785,III-2001
Kühner G. I-501,I-581
Kukharkin N.N. II-1453
Kulhanek P. I-667
Kupfer K. II-885,II-905
Kupschus P. I-255
Kurasawa T. II-1405
Kurdel M. III-2095
Kuroki H. III-2155
Kus A. I-7,I-35
Kusaka S. III-1931
Kusano K. III-1631
Kuus H. II-885
Kuvshinov B.N. I-703
Kuyanov A.Yu. II-1521
Kwak J.K. III-2133
Kyriakakis G. II-767
La Haye R.J. I-179,I-187
Lachambre J.-L. I-215
Lackner K. I-455,I-459
Lafrance D. I-215
Laing E.W. II-1505
Lakhina G.S. III-1623
Lalousis P. II-1525
Lao L.L. I-11,I-55,I-243,I-435
Larenz R.W. II-1381
Larsson J. III-1749
Lashkul S.I. II-997
Last J. I-167
Laurent L. I-27,II-1433
Lauro-Taroni L. I-279,I-283,I-287
Laviron C. I-107,II-1079
Lawande S.V. II-1257
Lawson K.D. I-3,I-19,I-291,I-307
Lazaros A. I-549
Lazzaro E. I-443
Le Clair G. I-215
Le Gourrierec P. III-2125
LeBlanc B. II-949
Leboeuf J.N. I-525
Leclert G. III-1883,III-1915
Lecoustey P. II-855,II-945,II-1421
Lee D.K. I-525
Lehnert B. II-1529
Lengyel L.L. I-323
Lesourd M. II-727,II-823
Letardi T. II-1207
Leubner C. III-1667
Leuterer F. II-957,II-961
Levinton F. II-949
Levitsky A.N. I-471
Leys C. II-1147
Lezius M. III-2071,III-2075
Li G.X. I-347
Li H.Z. I-223
Li J. I-31,I-615
Li K.H. I-223
Li L.H. I-347
Li Q. I-615
Li W.L. I-115
Liang W.X. I-395
Liberman M.A. I-635,I-671,II-1261,III-1599
Lieder G. I-459
Likin K.M. I-525
Lim C.S. II-1501
Lin H. I-363
Lindinger W. III-2079,III-2083,III-2087
Lingertat J. II-727,II-823
Linhart J.G. II-1253,II-1265
Liniers M. II-791
Lisak M. I-391
Litaudon X. I-27,II-885
Liu W.D. II-1103
Liu-Hinz C. I-215
Loarte A. II-723
Lohr J.L.T.C. II-893
Lok J. I-267
Lomas P.J. I-3,I-19,I-147,I-255,I-307, II-881,II-897
Longinov A.V. II-921,II-929,II-933,II-941
Lontano M. II-1087
Lopes Cardozo N.J. I-71,I-75,I-123,I-155
Lopez-Callejas R. I-483,III-1947
Lopez-Fraguas A. I-565,I-577
Loughlin M.J. I-167,I-251
Loureiro C. II-1063
Louvet P. III-2113,III-2125
Lovisetto L. I-463
Lowry C.J. I-239,II-723,II-727
Lozneanu E. III-1769
Luckhardt S.C. I-407,II-949
Luhmann Jr. N.C. I-363,I-179,II-1071,III-1939
Lukac P. III-2067,III-2129
Lukinov V.A. II-921,II-929
Luo C. I-615
Lyadina E. I-371
Lynch V.E. I-569,II-1417
Lynov J.-P. II-811,II-1283,III-1903,III-1907
Lyon J.F. I-525
Ma C.H. I-521,I-525
Maafa N. II-1083
Maas A.C. I-151,I-167,II-1031
Maaßberg H. I-493,I-497,I-505,I-509, I-549,I-569,I-581
Mace R.L. III-1819
Machida M. I-675
Maciel H.S. III-1835
MacLatchy C. I-215
Maeda H. II-1191
Maeda M. I-517,II-1159
Maehara T. I-79

Maekawa T. I-79,II-981
Maggi C.F. II-823
Magula P. I-219
Magyar G. I-283
Maier H. III-2001
Majeski R. II-839
Makino K. I-79
Malaquias A. II-1111
Maluyta D.D. II-1229
Mancuso A. I-545
Mandl W. II-1035
Manhood S.J. I-31
Manickam J. I-43,I-351,II-949
Mank G. I-155
Mansfield D.K. I-39
Manso M.E. I-231,II-1063
Mantica P. I-23,I-75
Marcus F.B. I-67,I-251,I-263,I-339,I-379, II-881,II-897
Margreiter D. III-2095
Märk T.D. III-2067,III-2071,III-2075,III-2095
Martin F. I-215
Martin G. I-175
Martin P. I-623,II-1361,III-1795
Martin R. I-639
Martin T.J. II-1393
Martin-Solis R. I-147
Martinell J.J. II-1461
Martines E. I-631
Mase H. III-1891,III-1985
Mast K.F. II-835
Matias J. I-231
Matsui T. III-2121
Matsukawa M. I-447
Matsumoto K. II-989,III-1961
Matsumoto Y. II-1225
Matsuoka K. I-513,I-517
Matsuoka M. I-171
Matsushima I. II-1225
Matsuura H. I-489
Matsuura O.T. III-1619
Matthews G.F. II-823
Matthieussent G. II-1297
Mattioli M. I-279,I-283,II-847
Mauel M.E. I-711
Mayberry M.J. II-893
Mayer H.-M. II-835
Maynard G. II-1245,III-2063
Mazur S. I-595,I-599
Mazzitelli G. I-295,I-463,II-1127
Mazzucato E. I-203,II-1055
McCarthy P.J. I-451,I-455,I-459
McCormick K. II-763,II-767,II-1163
McCracken G.M. II-779
McCune D.C. I-39,I-43
McGuire K.M. I-43,I-203,I-351
McKee G. II-839
McLoud W.S. II-1397
McNeill D.H. I-295,II-1127
McWilliams R. III-1935
Medley S.S. I-203
Medvedev S.Yu. I-319
Meigs A. I-211
Meis C. III-2113
Meister C.-V. III-2159
Melendez-Lugo L. I-483,III-1947
Melnick I.M. I-291
Merazzi S. I-557,I-589
Merkel P. I-585
Mertens V. I-451,II-743
Meyer R.L. III-2113
Mezzetti F. I-695
Michaud D. I-215
Michelsen P. II-1067,II-1283
Micozzi P. II-1525
Mieno T. III-1859,III-1919
Miklaszewski R. I-717
Mikoshiba H. III-1651
Miljak D.G. II-815
Minami T. I-79
Minardi E. II-1465
Minyaev O.A. I-471
Mioduszewski P.K. I-275
Mirnov S.V. I-47
Mirrashidi P. III-1993
Miura S. I-171
Miyakuni S. III-1709
Miyamoto T. I-659
Mizuno K. II-1191
Mizuno N. I-699
Mizuuchi T. I-489,II-1131
Mjølhus E. II-1279,II-1349
Mlynar J. I-219
Mohamed-Benkadda M.S. II-855
Mohanty S.R. II-1195
Moiseev S.S. I-707
Molinari V. III-2037
Monakhov I.A. I-47
Monier-Garbet P. II-847
Monterde P. II-1183
Monticello D.A. I-351,I-577
Moradshahi M. I-479
Morales G.J. I-135,III-1839
Moreau D. I-27,I-159,I-175,II-885, II-905,II-945
Moreira A. II-1063
Morera J.P. II-1421
Morgan P.D. I-3,I-119,I-255,I-307,II-1485
Morimoto S. I-521
Morin M. III-2055
Morita S. I-513,I-517
Moroz P.E. II-909
Morris A.W. I-31,I-411,I-423
Morsi H. I-3,I-255
Morsi H.W. I-19
Moser F. II-1497
Motojima O. I-521
Mroczkowski M. I-717
Muir D. I-59
Murakami M. I-521,I-525,I-529
Muraoka K. I-517,II-1159
Murawski K. III-1635
Murmann H.D. II-961
Mynick H.E. I-431
Myra J.R. I-91
Nagao K. III-1733
Nagasaki K. I-489,II-1131
Nagasawa T. III-1815
Nagashima K. I-83,I-87
Nagayama Y. I-351
Naito O. II-953
Naitou O. II-985
Nakach R. II-1409
Nakamura M. I-79,II-981
Nakamura Y. I-489,I-557
Nakasuga M. I-489,II-1131
Nambu M. III-1693
Nappi C. II-1313
Nardi V. I-695,II-1253
Naujoks D. II-843
Naumova N.M. II-1305,II-1317
Navarro A.P. II-933
Nave M.F.F. I-227,I-247,I-327,I-335, I-339,I-439
Nazikian R. I-203,I-431,II-1055
Neger T. II-1151
Neill G.F. I-227
Nejoh Y. III-1655,III-1799
Nemoto M. II-953,II-985
Nenovski P. III-1635

Neubert T. . . . III-1579
Neudatchin S.V. . . . I-59
Neuhauser J. . . . II-743,II-747,II-767
Neves J. . . . II-1063
Neyatani Y. . . . I-171,I-447
Nguyen F. . . . II-851
Niedermeyer H. . . . II-783,II-787
Nielsen A.H. . . . II-811
Nielsen P. . . . I-3,I-19,I-255,I-307
Nilson D.G. . . . II-1191
Ninomiya H. . . . I-447
Nishida Y. . . . III-1815,III-1927,III-1931
Nishikawa K.-I. . . . III-1579
Nishimura K. . . . I-513,I-517
Nishio R. . . . III-2121
Nishitani T. . . . I-171
Noda N. . . . I-403,I-513,I-517
Nonaka S. . . . III-2045
Nordlund P. . . . I-595,I-599
Norimine T. . . . III-1855
Nothnagel G. . . . I-415,II-795
Notte J. . . . III-1811
Novik K.M. . . . II-997
Nührenberg J. . . . I-553
Nunes F. . . . II-1063
Nycander J. . . . III-1903,III-1907
O'Brien D.P. . . . I-63,I-311,I-335,I-339
O'Brien M.R. . . . I-147,I-423,II-897,II-1341
O'Rourke J. . . . I-15,I-255,I-259,I-311, I-335,I-339,I-379
Obiki T. . . . I-489,II-1131
Ochando M.A. . . . I-99,II-791
Ochirov B.D. . . . II-1229
Oda T. . . . II-1191
Oda Y. . . . II-859
Odajima K. . . . II-1191
Ogawa T. . . . II-1191
Ohasa K. . . . II-1191
Ohkubo K. . . . II-989
Ohno N. . . . II-1115,III-1807
Øien A.H. . . . III-1997
Okabayashi M. . . . II-949
Okada H. . . . I-489,II-1131
Okada T. . . . II-1159,III-2099
Okamura S. . . . I-513,I-517
Ongena J. . . . II-1147
Ono M. . . . II-949
Oomens A.A.M. . . . I-71,I-267
Orishich A.M. . . . III-1689
Orsitto F. . . . I-295
Ortolani S. . . . I-623
Osborne T.H. . . . I-11,I-235
Osborne T.O. . . . I-243
Owadano Y. . . . II-1225
Oyevaar Th. . . . II-1091
Ozaki T. . . . I-517
Paccagnella R. . . . I-627
Pacher G.W. . . . I-475,II-755
Pacher H.D. . . . I-475,II-755
Pacios L. . . . I-299
Pakter R. . . . III-1697
Palladino L. . . . II-1207
Panaccione L. . . . I-295
Pantis G. . . . I-143
Parail V.V. . . . I-207
Pardo C. . . . I-99,I-299
Paris P.J. . . . II-1187,III-1863
Park C.W. . . . III-2133
Park H.K. . . . I-39
Park J.K. . . . III-2133
Park W. . . . I-351
Parker R.D. . . . I-427
Parlange F. . . . II-885,II-945
Parys P. . . . I-717
Pasini D. . . . I-279,I-283,I-331
Patel A. . . . I-291
Patel T.K. . . . I-291
Pättikangas T.J.H. . . . II-1005,II-1021
Paul S. . . . I-203,II-949
Pavlenko V. . . . II-1441
Pavlichenko O.S. . . . I-569,II-933
Pavlov I.P. . . . II-1025
Pavlov S.S. . . . II-921,II-933
Payan J. . . . I-107,II-1079
Peacock N.J. . . . I-291
Pech P. . . . II-1167
Pecquet A.L. . . . I-107,II-855,II-1421
Pécseli H.L. . . . II-811,II-1067
Pedit H. . . . III-1777
Pedrosa M.A. . . . II-791
Peebles W.A. . . . I-363,I-179,II-1071,III-1939
Pegoraro F. . . . I-139,II-1425,II-1429
Pégourié B. . . . I-103,I-159
Penningsfeld F.-P. . . . I-537
Pereira J. . . . II-1063
Pereverzev G.V. . . . II-961,II-1489
Persson H. . . . II-1369
Pestryakova G.A. . . . I-319
Peters M. . . . I-75
Petrov A.A. . . . I-47
Petrov M.P. . . . I-151,I-167,II-1031
Petrov V.G. . . . I-47
Petrov Y.V. . . . II-1219
Petrzilka V. . . . I-271
Petty C.C. . . . II-893
Peurrung A.J. . . . III-1899
Peysson Y. . . . I-27,I-159,II-885
Pfau R. . . . I-683
Pfirsch D. . . . II-1329,III-1753
Philipona R. . . . I-179
Philipps V. . . . II-827
Phillips P.E. . . . I-115
Pichal J. . . . I-667
Pickalov V.V. . . . II-1143
Piel A. . . . II-1199,III-1677,III-1843
Pierre T. . . . III-1879,III-1883,III-1915
Pietrzyk Z.A. . . . II-763
Piffl V. . . . I-713
Piliya A.D. . . . II-1203
Pinsker R.I. . . . II-893
Pironkova A. . . . III-2013
Pisarczyk T. . . . I-717
Plapp B.B. . . . III-1659
Platonov Yu.Ya. . . . II-1039
Pöckl M. . . . II-1163
Podda S. . . . I-463
Poll H.U. . . . III-2095
Ponomarenko A.G. . . . III-1689
Popa G. . . . II-1179,II-1561,III-1757,III-1969
Popel S.I. . . . II-993
Popov G.H. . . . III-1803
Porcelli F. . . . I-439,II-897,II-901,II-1469
Porkolab M. . . . II-893,II-965
Porte L. . . . I-119,I-163,I-407
Porter G.D. . . . II-751
Portnov D.V. . . . I-47
Poschenrieder W. . . . II-1167
Potempski S. . . . II-1537
Poutchy L. . . . II-847
Powell C. . . . I-695
Prasad G. . . . III-1575,III-1583,III-2021
Prater R. . . . II-893
Praxedes A. . . . II-1111
Praxmarer C. . . . III-2079,III-2083
Preische S. . . . II-949
Probert P. . . . II-839
Proshin M.A. . . . I-703
Prudsky V.V. . . . II-1345
Pryadko J.M. . . . II-1321
Puerta J. . . . II-1513

Pulker H.K. III-2149
Punithavelu A.M. III-2025
Punjabi A. II-863
Putvinskii S. I-167
Qin Y.W. I-223
Quallis A.L. I-525
Quéméneur A. I-107,II-1079
Radford G. II-727
Ramachandran H. I-135,III-1839
Ramos G. II-1461
Ramos J.J. I-407
Ramponi G. II-973
Ramsay D. II-1505
Ramsey A.T. I-39,I-203
Ran L.B. I-223
Rao N.N. III-1643
Rasmussen D.A. I-521,I-525
Rasmussen J.J. II-811,II-1283,III-1907
Rau F. I-569,I-581
Raus J. I-713
Rauth T. III-2075
Rawat R.S. II-1195,III-2141
Razdobarin G.T. II-1219
Razumova K.A. I-207,I-371
Reale A. II-1207
Rebut P.-H. II-731
Reiman A.H. I-577
Reiter D. II-739,II-747
Rem J. II-1425
Renberg P.U. II-1047
Renner H. I-493,I-501,I-505
Rensink M.E. II-751
Retterer J.M. II-1509
Rettig C.L. I-11,I-179
Rewoldt G. II-1437
Rey G. II-885
Reyna L.G. III-2103
Rhee C. III-2133
Rhodes T.L. I-179,II-1071
Riccardi C. III-2017
Rice W.K.M. III-1819
Richards B. I-115
Righi E. II-881
Rille E. III-2149
Rimini F. I-119,II-897,II-973
Ringler H. I-493,I-501,I-505,I-581
Rizzato F.B. III-1697
Roach C.M. II-1139
Roberts D.E. I-387,I-415,II-795,II-1397
Robinson D.C. I-31,I-399
Rodriguez L. II-933
Rodriguez-Yunta A. I-99
Roe G. I-639
Rognlien T.D. II-751
Rohde V. II-1199
Röhr H. II-743
Romanelli F. I-463,II-1437
Romannikov A.N. I-47
Rommers J.H. I-267
Roney P. II-949
Rosatelli C. II-1187
Ross D.W. I-115
Ross G.G. I-215
Rossi A. I-623
Roth J. II-831,II-1167
Roubin J.-P. I-175,II-1433
Rousculp C. III-1827,III-1831
Rowan W.L. I-115,I-211
Rubenchik A.M. II-1229
Rudyj A. II-783,II-787
Ruiz J. II-1513
Rupasov A. I-683
Rusbridge M.G. I-639,III-1725,III-1729
Rusbüldt D. I-155,II-775
Ruscanu D. II-1179
Rynn N. III-1935
Ryter F. I-7,I-195,II-889
Sabbagh S.A. I-43
Sabot R. I-103,II-1409
Sadler G. I-3,I-67,I-167,I-251,I-255,
I-263,I-439,II-881,II-1485
Sadowski M. I-691,II-1211,II-1215
Safronov V.P. III-2137
Sagar R. III-2141
Sagara A. I-513,I-517
Saha S.K. I-107,II-1079
Saibene G. II-723,II-727
Saito K. II-917
Sakakibara S. I-517
Sakamoto K. I-489
Sakamoto M. I-403
Sakanaka P.H. I-675,I-679,II-1233,III-1619
Sakasai A. I-87
Sakawa Y. III-1965
Sakharov A.S. II-1305,II-1317,II-1429
Sakharov I.E. II-997
Sakharov N.V. I-471
Sakurai S. II-859,II-1115
Salas A. I-577
Salashchenko N.N. II-1039
Salat A. I-573
Salmon N.A. II-1107
Salomaa R.R.E. II-1005
Salvetti A. II-1241
Samain A. II-851,II-855,II-1421,II-1433
Samm U. II-759
San Jose M.A.G. II-1183
Sanchez J. II-1075
Sandeman J. III-1725
Sanduloviciu M. III-1769,III-1957,III-2029
Sano F. I-489,II-1131
Santiago M.A.M. I-675,III-1785
Santos J. II-1063
Sanuki H. I-513,I-517
Saoutic B. I-175,II-885,II-905
Sardei F. I-505,I-509,I-549
Sarksyan K.A. I-525
Sartori R. I-3,I-307
Sasao M. I-67
Sato K.N. I-403,II-1191
Sato M. I-489,I-521,II-953
Sato N. III-1705,III-1709,III-1765,III-1919
Sato N.Y. III-1705,III-1709,III-1985
Sato T. III-1631,III-1965
Sattler S. II-1099
Sauer K. III-1571
Sauthoff N. II-949
Savrukhin P. I-371
Sawada K. II-981
Sawahata M. II-985
Saxena Y.C. III-1575,III-1583,III-1847,
III-1867,III-2021
Sayal V.K. III-1823
Sborchia C. I-167
Scafati A. II-1207
Schamel H. II-1385,III-1717
Scheffel J. I-663
Scheier P. III-2071,III-2095
Schep T.J. II-1425
Schiavi A. I-619
Schina G. II-1207
Schissel D.P. I-11,I-235
Schivell J. I-203
Schlanges M. III-2091
Schlüter H. III-1981,III-2145
Schlüter M. II-1449
Schmid M. I-327
Schmidt G.L. I-59,I-255,I-307
Schmidt H. I-683
Schneidenbach H. III-2009

Schneider R.S. II-747,III-1697
Schneider W. I-459
Schoch P.M. I-115
Schoon N. II-1147
Schram D.C. II-1143
Schrittwieser R. III-1757,III-1773
Schüller F.C. I-71,I-123,I-155,II-1091
Schulz D. I-683
Schumacher U. II-835
Schupfer N. III-1785
Schwab C. I-549
Schweinzer J. II-763,II-1163
Schwelberger J.G. I-529
Schwenn U. I-557
Scott B.D. II-1449
Scott S.D. I-39,I-43,I-203
Scoville J.T. I-187
Segre S.E. I-127,I-295
Seidel U. I-451,I-455
Seki M. II-953,II-969,II-985
Seki S. II-949
Selenin V.L. II-1203
Semenov I.B. I-47
Semenov V.V. II-1219
Sen A. II-1301
Senju T. I-489
Senties J.M. II-1183
Seraydarian R.P. I-183,I-275
Sergeyev A.A. I-111
Serichol N. III-1607
Serra F. I-231,II-1063
Sesnic S. II-949
Sethia G.C. III-2021
Shah H.A. II-1317
Shakhovets K.G. I-471
Shapiro V.D. II-1271
Sharapov V.M. I-47
Sharma R.P. II-1325
Sharma S.K. III-1567,III-1595
Sharma S.R. III-1823
Shasharina S.G. I-541
Shatalin S.V. II-997
Shats M.G. I-525
Shcherbinin O.N. II-997,II-1025
Sheridan T.E. III-1895
Sherwell D. II-795,II-1397
Shevchenko V. II-1271
Shi M.L. I-395
Shigueoka H. I-679,III-1619
Shiina S. II-917
Shimada T. II-917
Shinno H. III-2155
Shirai H. I-83
Shirokikh A.V. II-1229
Shishkin A.A. II-1353,III-2013
Shivarova A. II-1039
Shmaenok L.A. II-1557
Shmykov V. III-1965,III-2121
Shoji T. II-807,II-1005,III-1721,III-1741
Shoucri M. III-1733
Shoyama H. II-1293,II-1445,III-1587,
Shukla P.K. III-1611,III-1643
Sibley A. I-327
Sicha M. III-1989
Silva A. I-231,II-1063
Simonchik L.V. II-1203
Simonetto A. I-443
Simonini R. I-259
Sindoni E. III-2017
Sing D.C. I-115
Singer C. I-131
Singh A.K. III-1847,III-1867
Singh D.P. II-1241
Singh S. II-1337,III-1603,III-1911
Sinman A. I-651
Sinman S. I-651
Sipilö S.K. II-1021
Sips A.C.C. I-259
Sitenko A.G. II-1287
Skalny J.D. III-2129
Skiff F. III-1863
Skladnik-Sadowska E. II-1211
Skorik M.A. III-1973,III-1977
Skovoroda A.A. II-1521
Sluijter F.W. III-1745
Smeulders P. I-251,I-327,I-331,
Smith D. I-335,I-339,I-439
Smith G.R. III-2083
Smith R. II-1275
Smith R.J. I-163
Snipes J.A. I-407
Snytnikov V.N. I-39
Sobehart J. III-1689
Solano E. III-2103
Söldner F.X. I-211
Soltwisch H. II-957,II-961,II-1063
Sørensen J. I-403
Sosenko P.P. II-839
Sotnikov S.M. II-1287
Spangler S.R. I-47
Spathis P.N. III-1659
Squire J.P. I-323
Srivastava M.K. II-965
Srivastava M.P. II-1257
St.-Onge M. II-1195,III-2141
Stäbler A. I-215
Staikov P. II-743
Staines G.W. III-2041
Stallings D.C. I-647
Stamate E. II-913
Stamp M.F. II-1179
Stankiewicz R. I-119,I-307,I-311,I-335,
Stanojevic M. I-339,II-727,II-819
Stansfield B. II-1469,II-1537
Start D.F.H. II-1171,III-1761
Stenflo L. I-215
Stenzel R.L. I-3,I-19,I-255,I-327,
Stepanov A.Yu. II-881,II-897,II-901
Stepanov K.N. II-1533,III-1587
Stephan K. III-1827,III-1831,III-1871
Steuer K.-H. II-997
Stevens J. II-933
Stöckel J. III-2095
Stork D. II-743,II-961
Stotler D. II-949
Strait E.J. I-219
Stratton B.C. I-167,I-311,I-339,I-379,II-897
Stratton B.E. I-43
Strel'tsov A.P. I-435
Stroth U. I-203
Stubberfield P.M. I-39
Su J.J. II-1229
Subbotin A.A. I-7,I-35,I-195I-509,
Suchy K. I-15,I-63,I-255,I-263,I-311
Sudarshan A. II-1271,III-1627
Sudo S. I-367
Suemitu H. II-1501
Suganuma K. III-1567,III-1595
Sugawara M. I-489,II-1131
Sugimoto H. II-981
Sugimoto M. II-985
Sumini M. III-2099
Summers D.D.R. I-1405
Summers H.P. III-1887
Sun S.Q. III-2037
. . . . . I-3,I-307,I-335,II-723,
. . . . . II-727,II-779,II-823
. . . . . II-823,II-1035
. . . . . I-223

Sunka P. I-713
Surendra M. III-1993
Sutcliffe M. III-1725
Suyazov N.V. I-707
Suzuki K. III-2121
Sykes A. I-31,I-399
Synakowski E.J. I-39,I-203
Szczurek M. I-717
Szigeti J. I-303
Szydlowski A. I-691
Tabares F.L. I-99
Tagle J.A. II-723
Taglieri G. II-1207
Takahashi C. I-513,I-517
Takahashi H. II-949
Takahashi S. II-985
Takamura S. II-859,II-1115,III-1807
Takasa A. II-985
Takeiri Y. I-517
Takenaga H. I-517,II-1159
Takeuchi H. I-171,II-953,II-969,II-985
Takita Y. I-513,I-517
Takiyama K. II-1191
Takizuka T. I-51
Talasman S.J. III-1957
Talvard M. II-855,II-1103,II-1421
Tamano T. III-1631
Tamaoki M. III-1733
Tammen H.F. II-1091
Tanabe T. III-1985
Tanaka M. II-1357,III-1733,III-1855, III-1859,III-1887
Tanaka S. I-79,II-981
Tanaka T. II-839
Tang W.M. II-1437
Tanga A. I-3,I-19,I-255,I-443,II-881,II-897
Tani K. I-171
Tanizuka N. III-1651
Tanzi C. II-973
Tarditi A. II-1187
Taroni A. I-3,I-15,I-19,II-727,II-901
Tartari U. II-1087
Tashaev Y.N. III-2137
Tataronis J.A. II-909,II-1009
Tavares-Azevedo M. I-675
Taylor G. I-39,I-203,I-351
Taylor T.S. I-11,I-55,I-243,I-435
Telesca G. II-771,II-1147
Tennfors E. I-607
Terreault B. I-215
Terumichi Y. I-79,II-981
Teubel A. I-537
Theimer G. II-783,II-787
Thomas C.E. I-525
Thomas P.R. I-239,II-727,II-819
Thomsen K. I-19
Thomsen K. I-3,I-63
Throumoulopoulos G.N. I-143
Tibone F. I-15,I-19,I-311,I-335,I-339
Tichy M. III-1989
Tielemans A.J.H. I-267
Timm R. III-1677
Timofeev A.V. I-703,II-1521
Tobita K. I-171
Todoroki J. I-513
Toi K. I-513
Tokar M.Z. I-95,II-739,II-759
Tolstyakov S.Yu. II-1219
Toma M. III-2029
Tomie T. II-1225
Tonon G. I-27,II-885,II-945
Torres-Silva H. II-1233
Torvén S. II-1175,III-1875
Toshi K. I-489
Towner H.H. I-39
Tracy E. II-937
Tran M.Q. III-1863
Tribaldos V. II-1001
Truc A. I-107,II-1079
Tsintsadze L.N. II-1485
Tsois N. II-767
Tsui K.-H. I-675
Tsytovich V.N. II-993,II-1271,II-1321,II-1333
Tubbing B.J.D. I-15,I-167,I-311,I-335, I-339,II-897
Tuchida K. III-2121
Tudisco O. I-23,I-463
Tugarinov S.N. I-47
Turnbull A.D. I-243,I-435
Turner M.F. I-31
Tuszewski M. I-431
Tutter M. I-497,II-1001
Uberoi C. III-1663
Uchino K. I-517,II-1159
Uckan T. I-525,I-529
Ueda M. I-513,I-517
Uehara K. II-1473
Uehara M. III-1835
Umesh G. III-1943
Urrutia J.M. III-1827,III-1831
Ushigusa K. I-447,II-953,II-969,II-985
Vahedi V. III-1993
Valanju P.M. I-115,I-211
Valencia-Alvarado R. I-483,III-1947
Valeo E. II-949
Vallet J.C. II-847,II-855,II-945,II-1421
Valovic M. I-31
Van Belle P. I-67,I-167,I-251,II-881
Van Blokland A.A.E. II-1091
Van Bruggen-Kerkhof M.J. III-1745
Van de Pol M.J. II-1059
Van Dijk G. I-267
Van Gelder J.F.M. I-267
Van Houtte D. I-27,II-885,II-945
Van Lammeren A.C.A.P. I-123
Van Milligen B.Ph. I-123
Van Oost G. II-771,II-1147
Van Toledo W. II-1111
Van Vurren G.W. I-387,I-415
Vannucci A. I-419
Varandas C.A.F. II-977,II-1111
Varela P. I-231,II-1063
Varias A. I-561,I-565
Varma R.K. III-2025
Vaselli M. II-1241
Vasilescu C. III-2049
Vasiliev V.I. I-471
Vega J. I-99,I-299
Veres G. I-303
Verga A.D. II-1325
Verheest F. III-1623
Verma A. II-863
Verreck M. I-123
Vietzke E. II-827
Vila J. II-1183
Villain J.P. III-1591
Villard L. I-343
Villasenor J. II-965
Vladimirov S.V. II-993,II-1333
Vlases G. II-723,II-727,II-735
Vogl G. III-2149
Voitsekhovich I.A. I-207
Volkov V. I-371
Vollmer O. I-7
Von Goeler S. II-949
Von Hellermann M.G. I-63,I-263,I-439, II-881,II-1035,II-1485
Voss K. II-949
Vshivkov V.A. III-1639
Wade M.R. I-275

Wagner F. I-7,I-195,I-231
Wahlberg C. I-603
Waidmann G. I-95,I-359
Wakatani M. I-489,I-557,II-1131
Walder G. III-2095
Walsh M.J. I-31
Walters P.E. II-795
Wang E.Y. I-223
Wang J. I-695
Wang Z.H. I-215,I-223
Ward D.J. I-3,I-19,I-255,I-343,I-467
Warrick C.D. II-897
Watkins M.L. II-731
Watkins N. I-251
Weiland J. II-1441
Weinlich M. II-787
Welander A. I-595
Weller A. I-549
Werthmann H. II-925
Wesson J. II-897
West W.P. I-275
White R.B. I-431
Wieland R.M. I-43,I-203
Wilgen J.B. I-521,I-525
Wing W.R. I-521
Winkler C. III-2095
Winter H. II-1163
Winter J. I-11
Wising F. I-391
Wittenberg R.W. II-1477
Wobig H. I-569,I-581,II-867
Wolf G.H. I-95
Wolf U. II-1385
Wolfe S. II-953
Wolff H. II-1167
Wolle B. II-1035,II-1485
Wong K.-L. I-431
Wootton A.J. I-91,I-115
Woskov P.P. I-407
Woyke W. I-451,I-455
Wunderlich R. I-459
Wurtele J.S. III-1811
Wyller J. II-1309
Xie J.K. I-347
Xu S. I-647
Xu Y. I-615
Yadav L.L. III-1823
Yaguchi K. I-489
Yakimenko I.P. I-707,II-1377
Yakovenko Yu.V. I-391
Yamada H. I-513,I-517,I-521
Yamada I. I-513,I-517
Yamagiwa K. III-1859
Yamaguchi H. I-699
Yamamoto T. II-985
Yang H.R. I-223
Yang J.W. I-223,I-395
Yang Q.W. I-223
Yang S.K. I-223
Yang X.Z. I-363
Yao L.H. I-223
Yao Q. III-1713
Yi P. I-615
Yu C.X. I-363
Yu M.Y. II-1533
Yuan C.J. I-223
Yugami N. III-1927,III-1931
Zacek F. I-219
Zagorodny A.G. II-1377
Zaitsev F.S. II-1341
Zakharov A.P. I-47
Zakharov L.E. I-367
Zakharov Yu.P. III-1689
Zakouril P. III-1989
Zambreanu V. I-687
Zanza V. I-127,I-295
Zaporowski B. III-2005
Zarnstorff M.C. I-39,I-43
Zastrow K.-D. I-595,I-611
Zebrowski J. I-691,II-1215
Zehrfeld H.P. I-459
Zelazny R. II-1537
Zenevich V.A. III-2087
Zerbini M. I-127,I-463
Zhang G.Y. I-395
Zhang P. I-615
Zhang S. I-615
Zhang S.X. I-223
Zhao S.J. I-363
Zhelyazkov I. II-1517,III-1635,III-2041
Zheng L.-J. I-553
Zheng Y.Z. I-223
Zhong Y.Z. I-395
Zhuravlev V. II-1075
Zhykharsky A. II-1553,II-1557
Zielinski J.J. I-525,I-529
Zilker F. II-1063
Zohm H. I-231,I-235,I-243,II-743
Zoita V. I-687
Zoler D. III-2117
Zoletnik S. I-303
Zolfaghari A. I-163,I-335,I-339,I-407
Zolotukhin A.V. I-569
Zöpfel S. I-509
Zuo H.N. I-223
Zurro B. I-99,I-299,II-1135
Zushi H. I-489,II-1131
Zvonkov A.V. II-1521
Zweben S.J. I-43,I-203,I-431
Zwingmann P.W. I-311,I-335,I-339